# AURORAL PHENOMENA AND SOLAR-TERRESTRIAL RELATIONS

Proceedings of the Conference in Memory of Yuri Galperin
Moscow, Russia
3-7 February 2003

Editors: L. M. Zelenyi, M. A. Geller, and J. H. Allen

Yuri Galperin, a prominent Russian scientist and pioneer of magnetospheric research, suddenly passed away on December 28, 2001. His death was a severe blow to Russian science, to the institute where he worked and to the many scientific programs in which he participated. At the beginning of February 2003, Yuri Galperin's colleagues held a conference in his memory. This book contains the memorial conference Proceedings.

This volume is published by the Scientific Committee on Solar-Terrestrial Physics (SCOSTEP) as the first handbook of the current, comprehensive international scientific program "Climate and Weather of the Sun-Earth System" (CAWSES), with financial support from the National Aeronautics and Space Administration. The editors thank all the authors who submitted their papers.

Papers from the conference were assembled in Moscow by T.M. Mularchik, D.V. Chugunin and L.I. Masyuk with early help from L.V. Zinin. Joe Allen edited some papers (about one-third of the text) to improve the translation into English. After review of his editing by the authors and others it is hoped that no errors were introduced. This volume of Proceedings was printed by Colt Reproduction Center and special help was given by J. Colt, M. Lynn, and M. Fryxl in preparation of the text and pictures.

The opening papers are tributes to Yuri as a scientist, educator, teacher, facilitator of international space science cooperation and personal friend. He participated directly in much of the work presented in these scientific papers or inspired and encouraged his colleagues to continue their work. His colleagues dedicate this book to Yuri's memory.

--- JHA 2004/10/21

# C O N T E N T S

## Foreword



**I. IN MEMORIA**



**II. THERMAL PLASMA**



**III. AURORAL AND IONOSPHERIC CURRENT SYSTEMS**

# Yuri Galperin

M. A. Geller

SCOSTEP President

On December 28, 2001, the international Space Science community lost a beloved colleague, Professor Yuri Ilich Galperin. The Russian Space Science community felt an especially acute sense of loss since Prof. Galperin was a colleague and mentor to many in that community.

With Prof. Galperin's passing, SCOSTEP, ICSU's Scientific Committee for Solar-Terrestrial Physics, also lost an eminent solar-terrestrial scientist who was active in SCOSTEP science as well as in SCOSTEP leadership. Prof. Galperin's scientific achievements are well known internationally. He authored over 200 publications, which include three books. He also was a great champion of international cooperation in science and believed that it could set an example of people from diverse backgrounds peacefully working together for a better world.

Prof. Galperin was the COSPAR representative on the SCOSTEP Bureau from 1997 until his death. I had the very great pleasure of working with him in that capacity, particularly after my election as SCOSTEP President in 1999. SCOSTEP always benefited from his wise counsel, especially during the time when it was engaged in planning for its future program CAWSES (Climate and Weather of the Sun-Earth System).

Speaking personally, it was always a pleasure to have conversations with Yuri. He was a cultured man and knowledgeable on a wide variety of topics. He was also very concerned about the world's future. He was one of the first of my international colleagues to express his sympathy and outrage for the tragic events of September 11, 2001. He saw those events as attacks on the world's civilization and humanity. They were not just the concern of one country but also, a matter of concern for all civilized people.

Over the period February 4-7, 2003, a memorial symposium was held at the Russian Institute of Space Sciences in Moscow, Yuri's long-time home institution. This memorial volume presents many of the papers from that meeting.

I wish to thank Dr. Richard Fisher, Director of NASA's Sun-Earth Connection Division and Dr. Madhulika (Lika) Guhathakurta, NASA's Living with a Star Program Scientist, for supplying SCOSTEP with the funds to produce this volume. I hope that all reading it will honor Professor Yuri Galperin's memory by dedicating themselves to pursuing the peaceful, international cooperation in science to which he was so dedicated.

# Yuri Ilich Galperin

L. M. Zelenyi[1], T. M. Mularchik[1], and L. V. Zinin[1,2],

[1] Space Research Institute, Moscow Academy of Sciences, Moscow, Russia
[2] Kaliningrad State University, Kaliningrad, Russia

Yuri Ilich Galperin was born on 14 September 1932 in Moscow. His father, a well-known linguist Ilia Romanovitch Galperin was a professor of English language and literature in the Moscow Institute of Foreign Languages. His mother, Nadezhda Mikhailovna, taught French in the same Institute. Thanks to his parents, Yuri spoke both English and French freely and was reading Shakespeare in the original when he was still a schoolboy.

Nevertheless he chose astronomy, probably the most poetical of precise sciences. In 1950 he began studying astronomy in the Department of Mechanics and Mathematics of Moscow State University. His favorite teacher in the University was the prominent Russian astronomer Prof. Iosif Shklovsky, who at that time was involved in research into night airglow of the upper atmosphere. After graduating from the University Yu. I. Galperin was appointed to the Upper Atmosphere department of the Institute of Physics of the Atmosphere headed by V. I. Krasovsky, where I. S. Shklovsky also worked. Such an alliance of two outstanding scientists had a decisive role in determining the direction of research in the Institute, and created a most favorable atmosphere for scientific growth of their young specialists. Both of Yuri's supervisors highly appreciated his independence of mind, erudition, intuition in physics and talent.

At that time many countries were preparing for the International Geophysical Year (IGY), a program of globally coordinated observations of geophysical phenomena during 1957-1958. The Institute of Physics of the Atmosphere organized three stations for these observations: Loparskaya (beyond the Polar circle), Roschino (near Leningrad- now St. Petersburg) and Zvenigorod (near Moscow). They were equipped with high-resolution spectrographs, designed in the Optical Institute in Leningrad. These spectrographs had characteristics superior to those in use all over the world at that time. Each of the observational stations was equipped with three spectrographs, for registration of visual, near UV and near IR spectral regions.

The most interesting results were obtained at the Loparskaya station, where Yuri Ilich Galperin spent three observational seasons. He managed to register and classify a great number of auroral spectra. The most interesting was the wide hydrogen line Hα exited by protons entering the upper atmosphere. Up to that time there were only 5 such spectra in the world, and he added 17 more. The line profile corresponded to the dispersion of precipitated protons after charge exchange with hydrogen atoms, this provided information on their distribution function. Yu. I. Galperin proved from these measurements that auroral protons were injected from the magnetosphere, but not directly from solar corpuscular fluxes, as was generally believed at that time. Thus, his studies of near-Earth space started with ground-based observations. His PhD thesis was devoted to this problem.

In Loparskaya he observed a variety of auroras and admired their beauty and mystery. He used to say that any theoretician should spend at least one season at the observatory to see with his own eyes the phenomena he is going to explain. Indeed, many of these phenomena now have been explained and Yuri made a significant contribution to that achievement.

As soon as the satellite era started, the department headed by V. I. Krasovsky began to develop space equipment. One of the first instruments created in the department was a device for detection of particles with energies of about 10 KeV. This energy was estimated from the heights of auroras. The instrument was mounted on the third Soviet satellite (SPUTNIK III) that was launched on May 15, 1958. The measurements showed that such particles were intense enough and had a pitch angle distribution that was typical for particles captured into the geomagnetic trap. According to modern terminology, these are ring current particles. At that time it was a sensational scientific result that contradicted existing opinion on the determining role of a relatively low-power source – high-energy particles of cosmic rays.

In 1961–1962 the department headed by V. I. Krasovsky carried out two big experiments on KOSMOS-3 and KOSMOS-5 satellites. Many measurements were conducted above the auroral oval of low-energy particles and of photoelectrons with energies more than 30 eV. However, after information on the planned American high altitude thermonuclear explosion appeared in the press, their scientific program was urgently modified and was now oriented on investigation

of the influence of this explosion on the magnetosphere. KOSMOS-5 was the only satellite that managed to register the effects at the moment of the explosion. Measurements of the completely changed inner magnetosphere were carried out until spring 1963, and then continued by many other satellites, by ELECTRON-1 and ELECTRON-2 in particular. Yu. I. Galperin interpreted these results in his doctoral thesis (the Highest Russian degree, next after the PhD). This thesis was based on his original measurements during and after the explosion. He modeled the physical pattern of formation of the artificial radiation belt that appeared as the result of the explosion and its characteristics and decay time. He discovered a number of new effects (such as $\gamma$-dawn – scattering of $\gamma$-radiation beyond the horizon; long-term conservation of heavy ions due to vertical drift in the equatorial ionosphere anomaly; and hot plasma upwards breakthrough in the equatorial zone, etc.).

In 1967, the Space Research Institute (IKI) of the Academy of Sciences of the USSR was founded. Scientific groups involved in space research in different institutes were transferred to IKI. Among them was the group from the department of V. I. Krasovsky, led by Yu. I. Galperin. This was the start of Yuri Galperin's Laboratory of Physics of Auroral Phenomena, which he headed all these years.

In 1967, while still in the Institute of Physics of the Atmosphere, his laboratory designed and prepared a major experiment to investigate auroral particles using equipment that filled a whole satellite. Yuri's main idea was that the satellite and all its instruments should work as a unified space laboratory. Previous satellites, KOSMOS-3, KOSMOS-5 and others that were launched from the Kapustin Jar launch site near Volgograd (Stalingrad at that time) had orbit inclinations of 49 degrees. Therefore these satellites reached the auroral oval only above North America and south of Australia. To enable their new satellite to traverse the auroral oval and polar cap a higher inclination angle was necessary. Such an orbit was possible only if the satellite was launched from the Plesetsk launch site. The laboratory staff waited with their completed equipment for the launch site to be opened for use, although there was a considerable risk to lose their satellite – it could be given to another group. But this risk was justified – such an orbit significantly increased the possibilities to make the desired observations.

The satellite KOSMOS-261 was launched on 20 December 1968, and a second satellite with identical equipment, KOSMOS-348, was launched on 13 June 1970.

KOSMOS-261 was actually the starting point of an international collaboration called the INTERKOSMOS program (a program of collaboration of several European countries and the USSR in the field of space research). This satellite was equipped with Soviet instruments. Scientific groups from the other countries participating in the program conducted ground-based measurements of ionospheric and thermospheric characteristics, synchronised with the measurements on the satellite. Then, both satellite- and ground-based measurements were analyzed together. During these experiments the diffuse auroral zone was found – a large-scale region of the polar ionosphere where low-energy electrons precipitate equatorward from the auroral oval.

Four satellites from the KOSMOS series contained only Soviet instruments, and the next three: AUREOL-1 (1971–1972), AUREOL-2 (1973–1974), and AUREOL-3 (1981–1986) – had Soviet and French instruments on board. These three satellites comprised the Soviet-French project ARCAD. The first two satellites produced interesting results: the spot-like cusp shape was established, a global pattern was determined for the evolution of the energetic spectra of protons, their injection from the tail into the inner magnetosphere, their drift in the magnetosphere and their precipitation in the diffuse zone.

The most successful was the third satellite – AUREOL-3. It was a favorite child of Yuri Galperin because so many of his ideas were realized in it. Most of them are obvious now, but 25 years ago they were absolutely new. In all of his space projects Yuri tried to provide for obtaining a complete set of plasma measurements on one satellite.

Yuri's old friend, Jean-Jacques Berthelier wrote about it: "Those involved in Soviet-French collaborative projects think that Yuri represents better, than anyone else, in the long history of such projects, the successes and discoveries of the Soviet and French teams. His deep and broad knowledge in the field of ionospheric and magnetospheric physics, and his friendly leadership made a deep impression on every new participant of the project".

Scientific instruments developed during the ARCAD project were a significant progression in space technology. New techniques for measurement of space plasma were used and a record (for that time) sensitivity was reached in measurement of low-frequency waves and low-energy particles. Several improvements were made in the structure and serving systems of the satellite. Many organizations in the USSR and France took part in the design, development, and production of scientific instruments for the ARCAD project. This alliance of scientists and engineers on this project became a real alliance of like-minded persons.

Yuri was extremely critical during the interpretation of the results, especially in the case of thermal plasma measurements. He clearly realized that the non-uniform distribution of the potential field around the satellite significantly distorted recorded fluxes of soft particles. Therefore he insisted on the equipotentialization of

AUREOL-3 and preparation of special new and electromagnetically clean solar panels. Soviet and French groups carried out joint tests of the scientific instruments and satellite systems to establish their electromagnetic compatibility.

Improvements in solar panels decreased their electromagnetic disturbances 1000-fold and significantly increased their durability – they retained their effectiveness during the 6 years of the satellite's work. (Similar panels were afterwards mounted on the INTERKOSMOS Bulgaria-1300 satellite). In the 1980's it was a real breakthrough in the field of thermal and super-thermal plasma measurements.

Control systems of earlier satellites only permitted up-linking several commands per hour, whereas the new instruments needed more flexible control opportunities and therefore needed more frequent commands. The required increase was achieved due to the French-made computer that controlled the entire instrumental complex. Apart from the satellite's telemetry a French broadband telemetry system was used, that down-linked data continuously to several receiving stations situated in Toulouse (France), Tromso (Norway), Apatity and Zvenigorod (Russia), Kerguelen and Adélie Land (Antarctic), Kourou (French Guiana), Sugadaire (Japan) and Shriharikote (India).

Operation of the satellite was planned in such a way that measurements taken on board could be coordinated with those carried out by other satellites, ground-based geophysical observatories and the work of powerful radio transmitters. Apart from that, timing of the launches was optimized to ensure the possibility of their coordinated work.

Here is an example of one series of such experiments. In autumn 1981 several industrial explosions were carried out during construction work near Alma-Ata. Several laboratories used this opportunity for the MASSA experiment (investigation of magnetosphere-atmosphere connections during seismically active events). The effect of the explosion's large-scale acoustic wave on the upper atmosphere and ionosphere were studied. Timing for the powerful explosion (10 trucks of explosives) was coordinated with passage of the AUREOL-3 satellite. As a result, electrostatic VLF- and ELF-noises as well as an intense MHD-wave were recorded in the corresponding flux tube. These results were confirmed later during further industrial explosions, which were carried out at times coordinated with passages of the satellite.

During the ARCAD project novel results were obtained: new phenomena in the cusp, auroral oval and the sub-auroral zone were investigated, new types of velocity dispersion of injected ions were discovered; research on magnetospheric events caused by artificial influences was carried out (MHD waves excited in the MASSA experiment, particle precipitation caused by VLF radiation of a ground-based transmitter, MHD waves from the plasma jet from a rotating rocket launched from a ship in the North Atlantic, etc.).

In 1984 an international conference dedicated to the results of the ARCAD-3 project took place in Toulouse. Presentations made at that conference showed the significance of the research carried out during the project. It was a real success from both scientific and human points of view. The joint Soviet-French team was an example of productive and fruitful cooperation in space.

Yuri conducted experiments on other satellites, for example: KOSMOS-184, INTERKOSMOS-19, and KOSMOS-1809. By analysis of the first measurements of ionospheric plasma drift carried out on the KOSMOS-184 satellite, Yuri and his colleagues discovered a new phenomenon occurring in the disturbed magnetosphere – a narrow stream of ions drifting at supersonic velocity in a western direction close to the plasmapause (the "polarization jet"). This phenomenon, which they discovered in 1973, was rediscovered by American scientists in 1977, and called the Sub-Auroral Ion Drift (SAID). Appearance of polarization jet in the ionosphere causes a whole range of serious changes, creating strong plasma inhomogeneities that are easily registered from the Earth's surface using ionosondes. For many years Yuri collaborated with a group of the Yakutian Institute of Space Physics and Aeronomy. They made observations on a latitude chain of oblique sounding ionosondes for more than 20 years. Analysis of these observations and synchronous satellite measurements has shown that the polarization jet is a direct result of a deep particle injection at sub-auroral latitudes during the expansion phase of strong substorms. At present modeling of this phenomenon is underway in the laboratory.

Yu. I. Galperin and Ya. I. Feldshtein had long discussions in the 1980's with the geophysical community concerning the mapping of auroral features to the magnetosphere. They proposed morphological mapping based on the similarity of characteristics of the plasma populations at different altitudes along a magnetic flux tube using "natural tracers" – specific plasma features, that retain their typical signatures regardless of the altitude of observation, such as the auroral oval and polar cap boundaries, soft electron boundary (SEB), polar diffuse auroral zone, etc. Most investigators thought that the auroral oval was projected on the boundary plasma sheet at distances of 50–100 Earth radii. Yu. I. Galperin and Ya. I. Feldshtein stated that it was projected on the central plasma sheet. At first this opinion caused serious objections, but gradually the number of its supporters increased and now it is a totally accepted point of view, and no one remembers how many arguments it caused at the beginning.

In the 1990's Yu. I. Galperin and J. -M. Bosqued developed a "Minimum-B" concept of a steady arc's source. They supposed that the magnetic field in the "arc's root" in the near-Earth neutral sheet forms a minimum in its radial profile. This property arises in the model from a supposed tailward gradient of the integral cross-tail linear current density and makes it possible to generate a double-sheet Birkeland current loop associated with the arc. This model is in quantitative accord with experimental data from the AUREOL-3 satellite. Assuming that the steady homogeneous arcs observed at and near the equatorial edge of the auroral oval are due to the Min-B structure in the tail, a typical arc width of 10–20 km is just the magnetic flux projection of the FAC generator region in the near tail.

Yu. I. Galperin actively collaborated with many scientific groups in different parts of our country and many research directions commenced thanks to him. He encouraged a group from Kaliningrad University to start modeling the electric field around a satellite immersed in plasma and calculation of low energy ion trajectories in its vicinity. Yuri constantly supported this group as they developed a time-dependant model of the polar wind.

A long-term collaboration between Yu. I. Galperin and Professor A. V. Volosevich, Mogilev University, concerned modeling of non-linear waves and localized moving structures in magnetosphere. The authors published a series of papers while working on that problem. Recently they modeled three-dimensional quasi-stationary structures of density and electrostatic potential variations that are in good agreement with three-dimensional small-scale moving structures of the soliton type that were observed by the FAST, POLAR and GEOTAIL satellites.

Thermal plasma measurements were one of Yuri's major fields of interest. He clearly understood the problems of such experiments. He made many efforts both to obtain good experimental results and for their interpretation.

Yuri took an active part in the INTERBALL project, using the experience he had gained during the ARCAD-3 project. He participated in several experiments carried out on the INTERBALL-2 satellite, mostly those dealing with measurement of thermal and super-thermal plasma.

He looked ahead to the importance of multipoint measurements. Yuri was a principal inspirer of the closely-spaced multi-satellite project ROY which is intended to study small-scale plasma structures during magnetic field annihilation in thin current sheets and strong turbulence in critical magnetospheric regions.

Yuri had a unique personality and was an expert in nearly every field of magnetospheric research. Until his last days he admired the wonders and puzzles of nature. As a real scientist, he was fond of new developments, changes, scientific "sensations" and scientific "revolutions". He had an intuitive feeling for magnetospheric physics. Many of his predictions, which were based upon both his thorough knowledge of the experimental data and his profound physical intuition, were confirmed in later experiments.

However amazing it may seem, although getting older, he was becoming even less conservative. Being an enthusiastic, dynamic person, he was ready to rush to the Earth's end to a scientific conference, for discussions on technical details of a project, or a PhD examination. His last trip, a scientific visit to Japan in Autumn 2001 to the Solar-Terrestrial Environment Laboratory, STEL, was particularly fruitful. There he continued work on his old projects, finished a paper on multiple scales in auroral plasmas, and planned and discussed future collaboration of his laboratory with colleagues from STEL.

His life was bright and interesting. He managed to do so many things in only one day, while others could not do them in a week. His working day began early, and these first hours spent at home with a book or at the computer were the most productive for him. The family atmosphere was exceptionally favorable to his work. He loved his "warm house" where he was happy to work and happy to rest. From his family he took his power for work and human relations. His wife Natasha created an atmosphere of love and comfort at home. His son Michael is a promising microbiologist and a father of two charming daughters.

Yuri left a deep track in space plasma research in Russia and in the whole world. Many problems that he was thinking over till his last days remain unsolved and need future investigation. Answering these questions will help us to make new steps towards understanding the miracles of the near-Earth space.

# Yuri Galperin, Russian space research pioneer

D. Stern

Greenbelt, Maryland

Yuri Ilich Galperin was born in Moscow, where his father was a professor of languages, and was evacuated during the war to the Urals together with his mother.

In school he earned a gold medal for an essay on classical Russian literature and reported on OTHELLO and HAMLET, which he read at age 14 in the original. However, when he entered Moscow University, after 10th grade, he chose astronomy as his subject.

His teacher and mentor was Iosif Shklovsky, a highly original astronomer who made major contributions to solar research and radio astronomy. Shklovsky's irreverent style (e.g. in his collected stories "Echelon" – in English, "Five Billion Vodka Bottles to the Moon") earned him trouble with the authorities and the admiration of his students, and Yuri all his life tried to emulate Shklovsky's style.

Another mentor was Valerian Krassovsky, who helped develop infrared sensors for the Red Army in Second World War and later (on his own) provided the technology to astronomers, to survey the sky in new wavelengths. Galperin was denied a regular appointment to a government research institute after graduation, and Krassovsky therefore arranged for him to be posted to an arctic station, where he studied the polar aurora (northern lights) 1955–1958. At that time only 5–6 observations of the rare aurora caused by fast protons existed: Galperin added 17 more.

Astronomer friends were amused: "Why would you study such an uninteresting thing as aurora?" But attitudes changed after October 1957, when Sputnik was launched. By that time Krassovsky was designing the payload of what became SPUTNIK III, the first large scientific satellite, and Galperin was invited to join him – provided he let another researcher take over the sophisticated auroral equipment he had built up. Yuri never hesitated: SPUTNIK III was launched in May, 1958, and Galperin became deeply involved in explaining its observations of the radiation belt.

Krassovsky's team was also responsible for KOSMOS-3 and KOSMOS-5, orbited in 1962–1963, and after a while he transferred responsibility for them to Galperin. "I am the richest man on Earth" he would say, "I had seven satellites" – those two, KOSMOS-261 (1968) and KOSMOS-348 (1970), and the three AUREOL satellites, a Soviet-French collaboration. In those days Yuri's interest was focused on low-energy electrons, emitted by sunlight from the top of the Earth's atmosphere, hard to observe because they had to be speeded up by an electric voltage of 3,000 – 11,000 volts before reliably registering in the detector.

KOSMOS-5 was in orbit in the summer of 1962 when the US announced it would detonate a hydrogen bomb above the atmosphere near Johnson Island, west of Hawaii. The time was known (the US had warned ships to avoid the area), the Russian military was anxious to observe the explosion, and KOSMOS-5, though not designed for such work, was the only spacecraft, which could do the job. Galperin, 30 years old, was therefore called before a panel of senior officers and asked to make the necessary arrangements.

He told the generals that even though the satellite would be in a good position at the time of the explosion, "that is impossible, because it is unattainable". KOSMOS-5 stored its data in an electronic memory, and once 200 minutes were accumulated, it stopped accepting data. It therefore needed to download data less than 200 minutes before the explosion, and unfortunately it was not expected to be within range of any Soviet tracking station during that time.

After Galperin repeated his message for the second or third time, the presiding general turned to him and told him: "Young boy, please tell us what is needed – and what is possible, we will decide ourselves". As things turned out, the data were downloaded (probably from a ship) in the vicinity of Great Britain, and the satellite was above Korea when the explosion took place 9000 kilometers (5600 miles) away. Although the explosion itself was below the spacecraft's horizon, delayed effects were observed and information was obtained, including radiation levels expected by Cosmonauts due to be launched in the following months.

KOSMOS-261, in December 1968, was supposed to observe particles of the polar aurora. However, the "Kosmodrom" for orbits reaching the polar region was not ready, and orbits from the existing one at Kapustin Yar could at most graze the auroral zone. Yet the launch could not be delayed. Galperin therefore turned the mission into a collaboration with scientists in other Eastern Bloc countries, helping train them with space instrumentation. By then such a collaboration program –

officially named INTERKOSMOS – was being prepared, and Galperin's spacecraft, which was quite successful, became de-facto the first of the series.

In 1967 the Soviet “Center for Cosmic Research” in Moscow was started (IKI, Institut Kosmicheskih Issledovanii) and Galperin's lab became part of it. At first the change was merely organizational: the building of IKI still had to be constructed, and meanwhile labs were given temporary lodgings in various parts of Moscow. Yuri's lab, in which he constructed instruments for KOSMOS-348, was housed in the basement of an apartment building in Moscow. That led to a disaster, which nearly scuttled the effort.

The anniversary of the October Revolution was a holiday, the lab was locked, instruments were carefully covered and the staff went home. Galperin was preparing to return when a woman from his lab phoned, very upset: “Yuri, there is no laboratory any more”. During the holiday a major water main had burst and flooded the lab and its neighborhood, “even cars were ... just swimming in water.” By the time firemen pumped out the water, all instruments were dirty.

The lab was also building instruments for a manned spacecraft, but Galperin decided he would try to rebuild everything. He went to Dnepropetrovsk (now in the Ukraine), to the plant where the spacecraft was being built, and asked the chief engineer, a woman, to give the project 3 months grace. She readily consented, and even gave him later a second extension, that time insisting on a firm deadline. It was barely met, the satellite was launched in mid-June 1970 and worked well.

The AUREOL series (AUREOL–1 in 1971, AUREOL–2 in 1973, AUREOL–3 in 1981) was a collaboration with France. It grew out of a Paris conference on space science, in which Shklovsky and Galperin represented Soviet science. In the pecking order of the Soviet delegation, these two were near the bottom, while the engineers and managers were at the top. However, as Galperin said, “from the French point of view scientists are much more important than engineers,” and the scientists enjoyed their brief moment in the spotlight.

At IKI Galperin headed the Auroral Laboratory and for a while also chaired one of its departments. In recent years he was active in INTERBALL, a 4-satellite mission simultaneously observing distant regions of the Earth's magnetosphere and the polar cap where auroras initiated in those regions could be seen. He was also active in planning a Russian spacecraft mission ROY (“swarm”) of multiple spacecraft, and had just come back from a scientific visit to Japan when he died.

# Yuri Galperin, a teacher and a friend

J. -A. Sauvaud

Centre d'Etude Spatiale des Rayonnements, Toulouse, France

In the first trimester of 1972, after the launch of the Soviet-French AUREOL satellite, I went to Moscow with Francis Cambou to meet scientists in IKI. During this trip I received my first real course of true space research: and what a course!

My teacher was a 39 year old, French-speaking doctor of science from Moscow state university, named Yuri Galperin. At that time I did not know that Yuri had been involved in 1958 in the first soft-particle space experiment on Sputnik III, nor that he would become my friend for over 30 years. Typically French, we were quite proud of ourselves and happy to be in Moscow; the experiments were working and we were getting data from space. The next question was: how best to analyse the data? In front of us was a high level team led by Professor Yuri Galperin.

On December 28, 2001 I received the very sad news that my close friend Yuri Galperin had passed away. I feel a deep sadness and great loss.

From 1972 to the end of 2001 is 30 years, the time to live, to build, to be happy, discouraged, to have new friends, new enemies, to win and lose visible or invisible battles. Thirty years during which friendship and mutual understanding counted no less than the scientific discoveries made together.

A characteristic of Yuri Galperin was his deep wish to understand Nature; and Nature knows how to make us humble. The work never stopped. The intellectual capacity of Yuri to treat, understand and exploit information was stunning. Several examples are quite famous. With his team, he used data from tens of AUREOL orbits to deduce that the cusp was a spot of limited dimensions centred on the noon meridian; and he hence derived the cross polar cap potential drop. This work was published in 1974 in the French journal Annales de Géophysique. In 2002 and 2003, a team led by H. U. Frey published papers in the Journal of Geophysical Research and in Nature showing the first images of the cusp taken by a far UV camera: it is a small spot centered at noon.

In 1978 Yuri showed that inside the inner magnetosphere, the particles causing the diffuse aurora are accelerated by the betatron and Fermi processes. This result, obtained from the passes of AUREOL when telemetry was available, was published in Journal of Geophysical Research. Ten years later, a team from the USAF Geophysics Laboratory corroborated this result using millions of particle spectra from the DMSP satellites. Later, during the eighties and beginning of the nineties, Yuri was worried about the ideas prevailing in the scientific community about the structure of the Earth's plasma environment, particularly about the determination of the location where substorms are initiated. In two magistral papers published with Y. Feldstein in Review of Geophysics, he gained acceptance for his views, which in turn reoriented this field of research.

He was even at the centre of a re-discovery. In 1973, Yuri discovered a new phenomenon in the disturbed magnetosphere, a fast plasma flow which he called the "polarization jet". In 1977, the polarization jet was discovered again in good faith by Americans, and named "Sub Auroral Ion Drift". This gives an idea of the level of international communications at that time! But that was not the only difficulty Yuri encountered.

The scientific carrier of Yuri is clearly brilliant, he was constantly at the forefront of magnetospheric research. He was able to see what others still did not see. He also had the gift of listening to others and gently, almost inadvertently, helping them to understand themselves better. As shown by the emotion manifested by hundred of Russians and foreigners during the memorial dedicated to him in 2003, Yuri is in our hearts, as we too are all in his heart.

# A few recollections of Yuri

B. G. Fejer

Center for Atmospheric and Space Science, Utah State University,
Logan, UT 94322-4405, USA

It was both a great honor and pleasure to know and work with Yuri Galperin. We first met in the late 1980's at a workshop near Washington, DC. Although this workshop was not focused on Yuri's main areas of research, his very broad and deep scientific knowledge and warm and unassuming personality made a deep impression on all participants. In the following years, we had the opportunity to meet in various places, and to extend our scientific and cultural discussions.

We started working together after Yuri's visit to Logan, Utah in the summer of 1995. The main subject of our work was the Polarization jet, a phenomenon discovered by Yuri and in which he was the world's foremost expert. In 1998, we were awarded a grant from the Joint US/Russia Research in Space Science (JURRISS) of NASA, which allowed us to further expand our scientific work and personal interactions. Yuri visited Logan again in the summer of 2001.

I have very happy memories of Yuri, particularly from his visits to Logan. On these occasions, we often had long discussions during which I greatly benefited from Yuri's deep insight and knowledge. In the evenings, we used to walk from the university to downtown Logan for dinner, usually in the company of my wife Fran. Our dinners were especially enjoyable occasions with long conversations about history, travel, people, and politics. Yuri's visits always produced significant accomplishments and wonderful memories. These memories of Yuri will always be with us.

# Yuri Galperin, a scientist and a friend

J. -J. Berthelier,

Centre d'Etude des Environnements Terrrestre et Planetaires, Saint-Maur, France

Born in a family with a deep and wide culture in Russian and foreign literature and arts, Yuri Galperin inherited many facets of its personality from his family circle and his education in a rather intense period in the history of his country. All of those who approached him have indeed been impressed by his open mind, his personal interest in the surrounding world and people and his impressive knowledge and attraction towards arts and history: he really behaved as if nothing should remain unknown to him. This attitude certainly explains for a large part how he became familiar with many subjects in space physics and his ability to initiate so many scientific collaborations and tie close links with colleagues and friends all over the world.

His attraction for wide horizons probably counts among the reasons that pushed him to specialize in Astronomy after completing his studies in mathematics at Moscow State University. Astronomy stays indeed at the crossroad of a number of complementary routes in human thought such as mathematics, physics, philosophy and even poetry. This choice offered him the opportunity, as a young student, to meet several strong personalities among university professors and scientists. Quite often he liked to recall the qualities that he discovered and recognized in these individuals who left a great impression upon him: their intuition, their ability to keep a wide field of view and an independent spirit. In the political context of those years, this latter quality has to rely on a solid sense and practice of humour that Yuri was also fond of.

Good luck is often a prerequisite to success but one has to be able to seize it when it is within reach. For Yuri, and he liked to recognize it, this was the advent of space exploration with its impressively fast rise in the late fifties, especially in the USSR. This definitely opened to him the way for a long and fruitful career. Nevertheless, even in this period where new and attractive horizons were almost continuously unveiled, it was necessary to distinguish the most valuable fields to explore and be able to remain steadfast in front of the unavoidable difficulties and failures. More importantly these latter had often to be turned into new initiatives and incentives to provide the necessary inflexion to explore previously unforeseen new domains.

In several occasions during his career Yuri did show that he really possessed these necessary qualities. This was the case after he completed his astronomy courses. He was looking for a position in a laboratory at Moscow University but did not get it. He turned this disappointment to the best account and decided to leave for the North and, for a while, to run optical experiments in an auroral observing station in the Murmansk district. This rather original and unplanned step led him to enjoy one of the most attractive and fruitful periods of his young life. While making several discoveries in the physics of proton aurora, he devoted himself to long hours of observation of the mysterious and magnificent displays of northern lights acquiring a unique personal closeness with auroral phenomena and, simultaneously, filling his personal inclination towards poetry. Long after he asserted that such an experience was a kind of unique education for those who engage in the field of magnetospheric physics and Sun-Earth connections. Another outcome of this period had much importance for him personally: he lived and worked in this remote auroral station in close association with Tania Mularchik and Volodia Gladyshev who were to become among his closest friends or, I should better say, life members of the "Galperin family" in the sense that Yuri liked to give to this expression.

Another occasion was given to him to seize the instant when he had an instrument in orbit when the US performed a powerful nuclear test in the upper atmosphere. For sure, neither this instrument nor the soviet space and military organizations were prepared to perform such measurements. Nevertheless his rapid and convincing plea towards the scientific and military administration won against a seemingly hopeless situation and he obtained nearly optimal conditions to achieve the measurements he was looking for.

This period marked also the real beginning of his career as a space scientist and experimenter. Other papers in this introduction provide more detailed and documented reports on his main achievements. Most of them were accomplished after he joined IKI at the end of the sixties where he founded and guided for many years the Auroral Physics Laboratory. Among the oldest souvenirs, historical and, sometime, "heroic" stories that he was so pleased to tell with a mixed touch of emotion and humour, he kept in particular favour his participation in preparations for the historical orbital flight of Yuri Gagarin. He was proud to have, in some way, "entered

into History" by being one of the 900 or so people who contributed to give the green light for the launch when they signed the official document, committing themselves, each in their own domain, to the success of the flight.

One cannot think of Yuri without remembering his personal involvement in international cooperation, a domain which was in line with his interest in the outside world and his ability to tie close links with other people and other cultures. He was indeed one of the driving elements of the cooperative program that was organized between the USSR and foreign countries under the aegis of the Intercosmos organization. This allowed him to initiate a number of research projects with teams from Czechoslovakia, Poland, Hungary, and Bulgaria and to develop collaborative studies that were essential for scientists in these countries. Even if it is delicate for me to say this, I believe that when he embarked on the French-Soviet cooperation in space, this was an event of particular importance for his scientific projects and also for his personal life. One of the obvious reasons was his familiarity with French culture and history acquired from his early age from his mother and in which he was immersed his life long. Again, one can also find a glimpse of Yuri's destiny in the time when this new era of cooperation started. It was at the end of 1968, and, when in Paris, Yuri said that he felt in his discussions and personal contacts with people remnants of the recent events that he considered as a definite mark in French history. The "children", as he liked to call them, which were born from the French-Soviet collaboration, the ARCAD and later the INTERBALL satellites, that provided him and the participating teams a large amount of new data and that were of great importance for Yuri's work. I remember in particular how he was happy to organize the first symposium where the initial results from the ARCAD-3 project were presented. Yuri was indeed a driving force behind the official organization. His wide scientific knowledge, his numerous friends scattered among the administration, laboratories and technical institutes were essential in the success of these missions. Above all, his personal ability to understand and interface with colleagues with often quite different ways of thinking and working, were the basic components which allowed the system to work and helped it to move forwards over more than 30 years in spite of the technical and funding difficulties and political fluctuations that one can easily imagine. At this point I cannot avoid remembering one of the greatest adventure in Yuri's life when he led the Soviet party at Kerguelen Island to take part in the ARAKS project. For many reasons, scientific and not, this trip to Kerguelen and the life in this remote spot turned out to be a summit and later provided Yuri an inexhaustible stock of good stories that he was so fond to tell about during the "night sessions" that we shared with him at his home or on the launching sites during the preparation of satellites. Last but not least, many of us on the French side owe a particular debt to Yuri who "opened the door" of his country for us. Russia, its people, its culture and even its real history were indeed rather a mysterious and unknown world in the early seventies. The long lasting collaboration with Russian teams and the development of deep friendly relations with many of our colleagues resulted in the fact that, year after year, Russia took a larger place in our life. I know how much this evolution made Yuri happy, he who believed so much in the importance of the "human factor". Certainly the long discussions we had during night sessions and also the warm welcome by our friend's families were essential and I would take the occasion here to thank Natasha, Yuri's wife, for her role during all these years.

A bright scientist, a man of impressive culture Yuri has kept up to the very last days of his life the indefatigable spirit of a pioneer. In all possible aspects, his life brought him a lot of successes and happiness, either on the scientific and professional side or in his family life and in the many long lasting and faithful friendships that he developed not only in his country but all over the world. It is difficult for us to realize that we will no more be given the occasion to be enthusiastically told of new ideas or new projects when meeting him at conferences or in his IKI office, filled up with papers and souvenirs. But he will stay present in the memory of many since, as we know from an old Irish song, "old warriors never die they just fade away…".

Yuri’s father Ilija Romanovich Galperin

Yuri’s mother Nadezhda Michailovna

Yuri - student of Moscow university

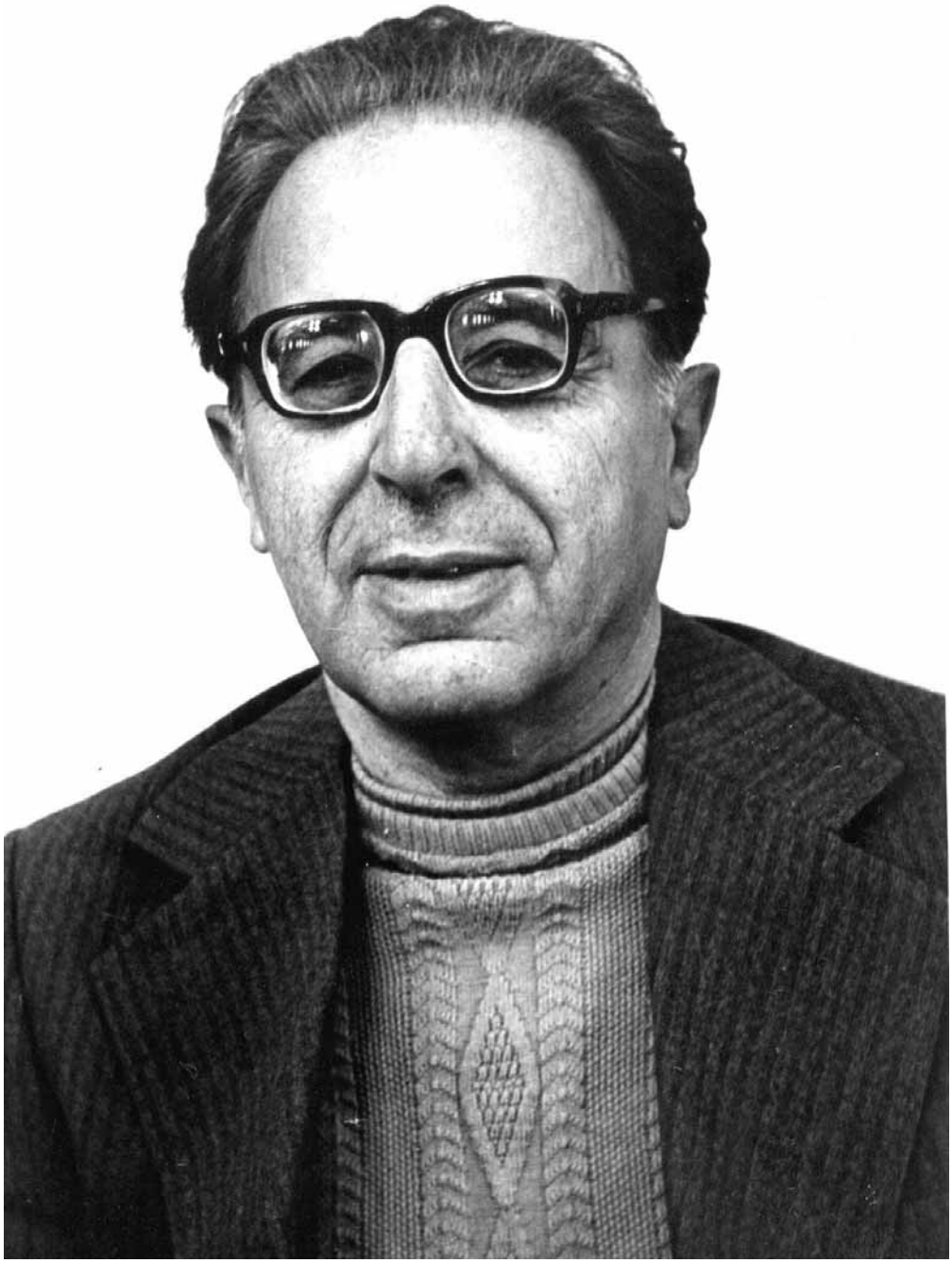

Yuri’s favorite teacher - Iosif Shklovsky

Shklovsky drawing a picture of the clouds and dragon fighting over the sun at the time of  a solar eclipse. Nevinnomysk, 1954.

Yuri with his teacher Valerian Krassovsky

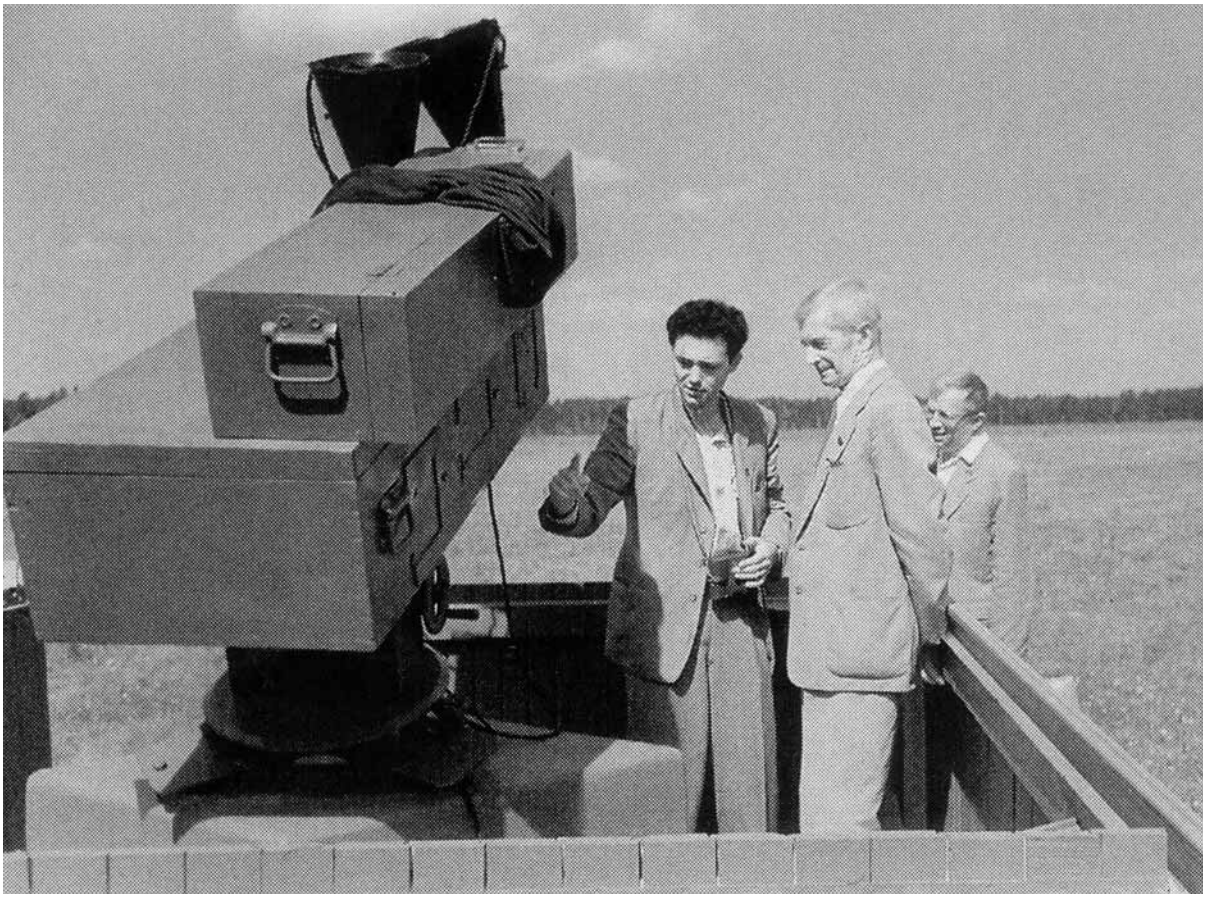

From left: Yuri Galperin, Sydney Chapman, Valerian Krasovsky
Yuri is showing Sydney Chapman a spectrograph for nightglow observations during preparation for the International Geophysical Year.

Top and bottom - International Geophysical Year, Loparskaja
Bottom, from left: Vladimir Gladyshev, Tatiana Mularchik, Yuri Galperin

P

Auroras in Loparskaya

In 1956 Yuri married Natasha Fish, student of biological faculty ot Moscow university

In 1957 their son Michael was born

Top - Natasha and Michael
Bottom - Yuri and Michael

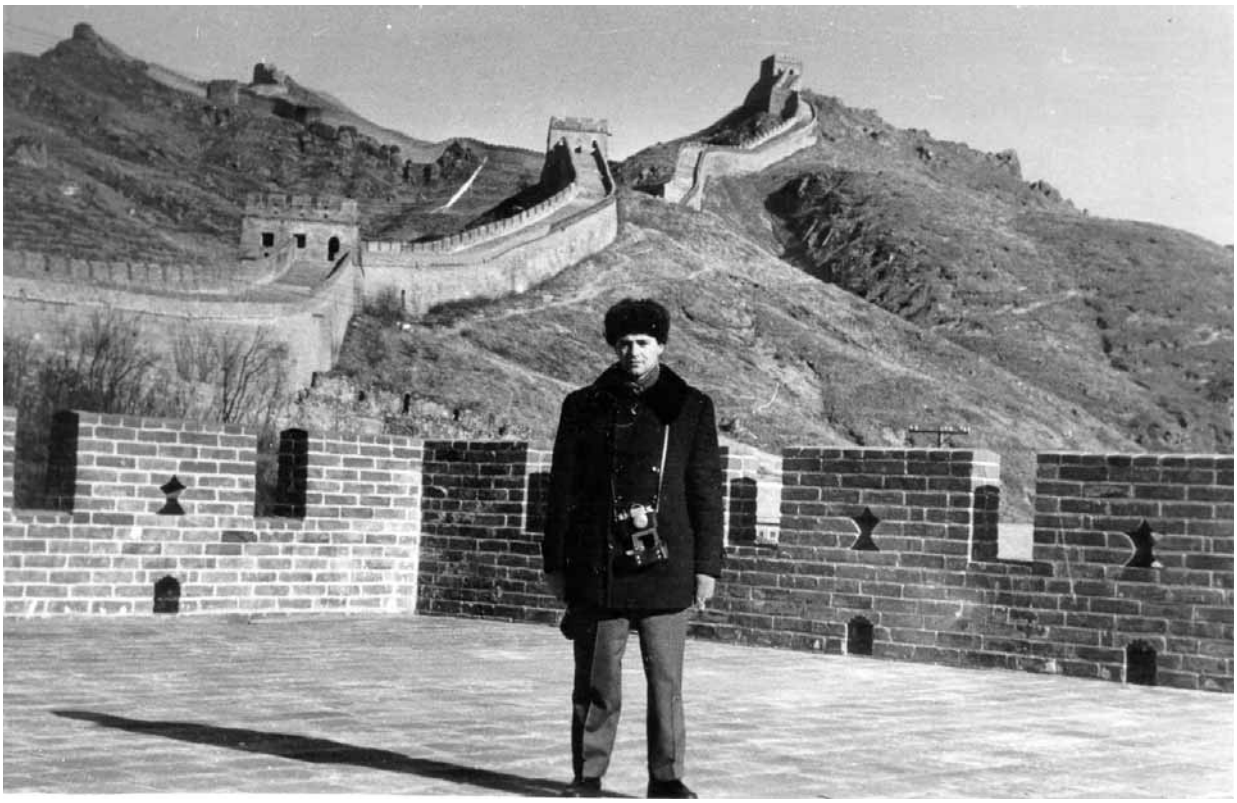

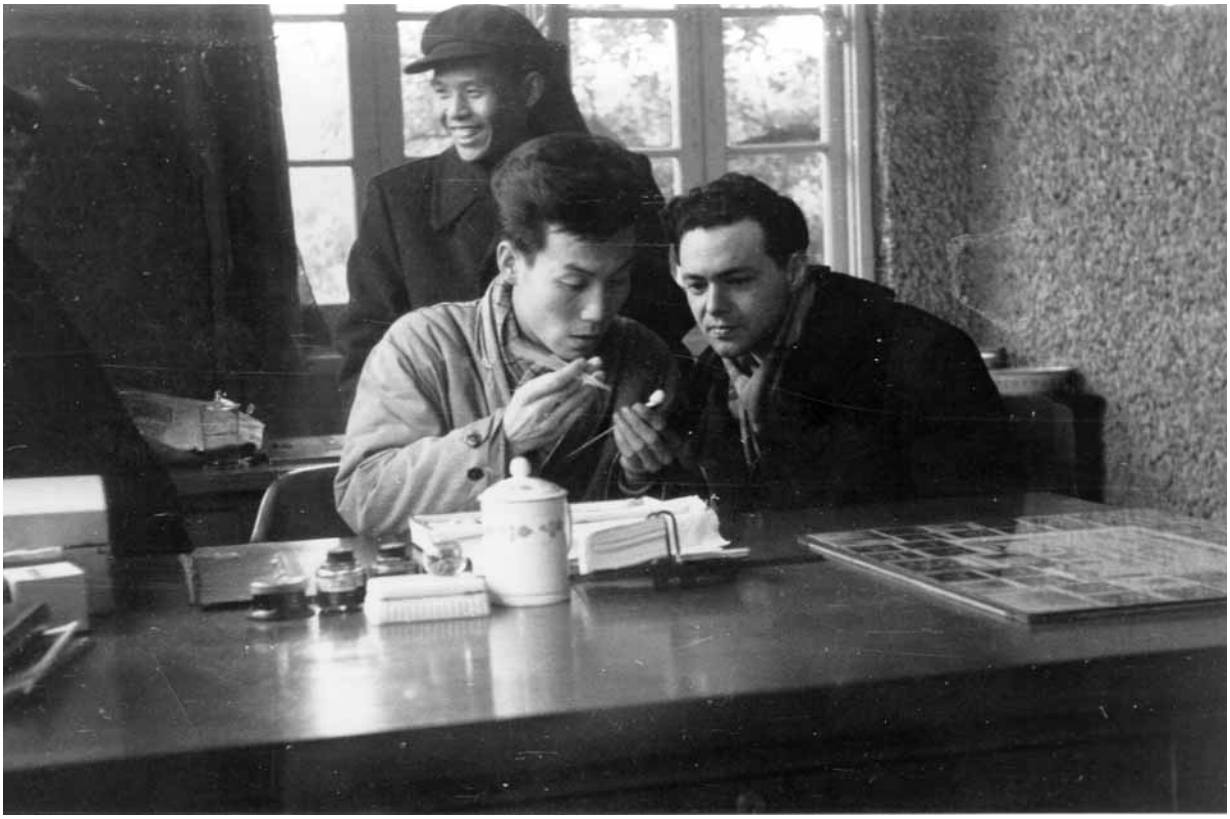

In 1959 - 1960  Yuri was sent to China where he taught chinese colleagues to use spectrographs for nightglow observations

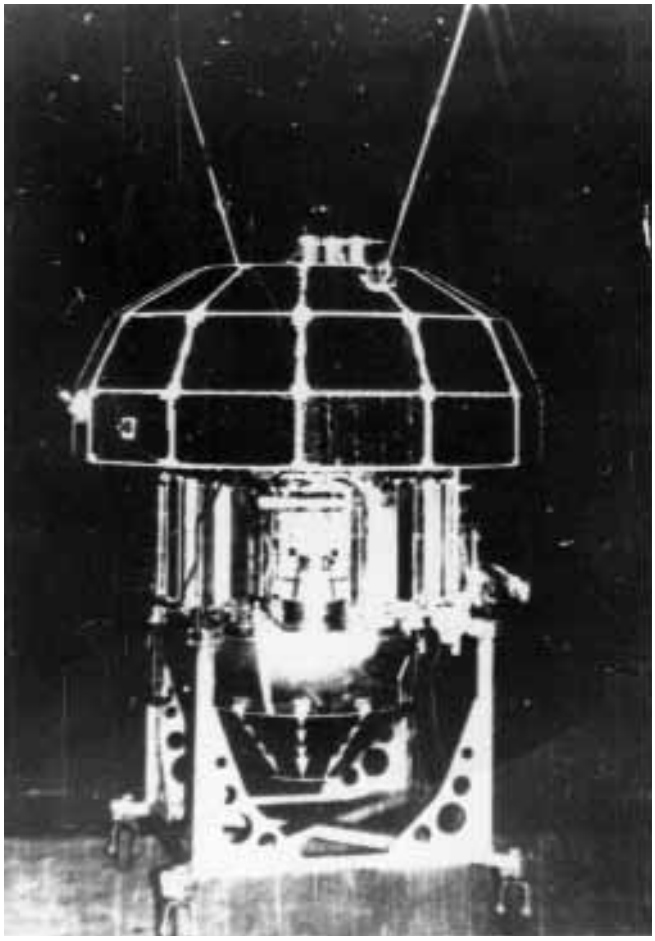

Kosmos - 5


Aureole


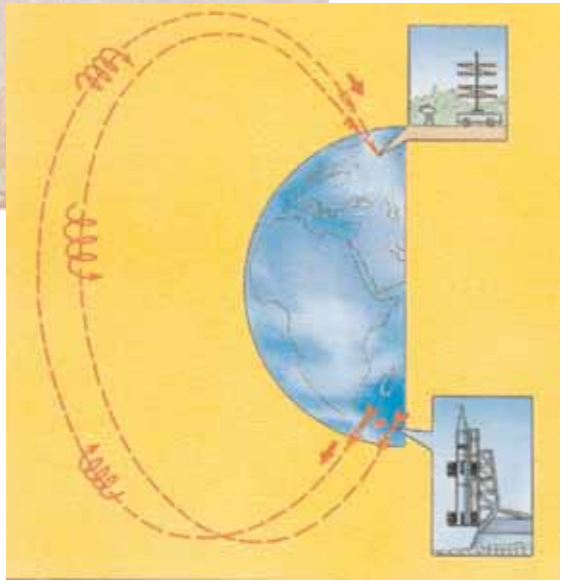

French - Soviet ARAKS project

Two french rockets were launched from Kerguelen. Electron beams injected from these rockets were registered at a conjugate point near Arkhangelsk (Sogra) by ground - based observations.

Yuri was a member of the Soviet team in Kerguelen.

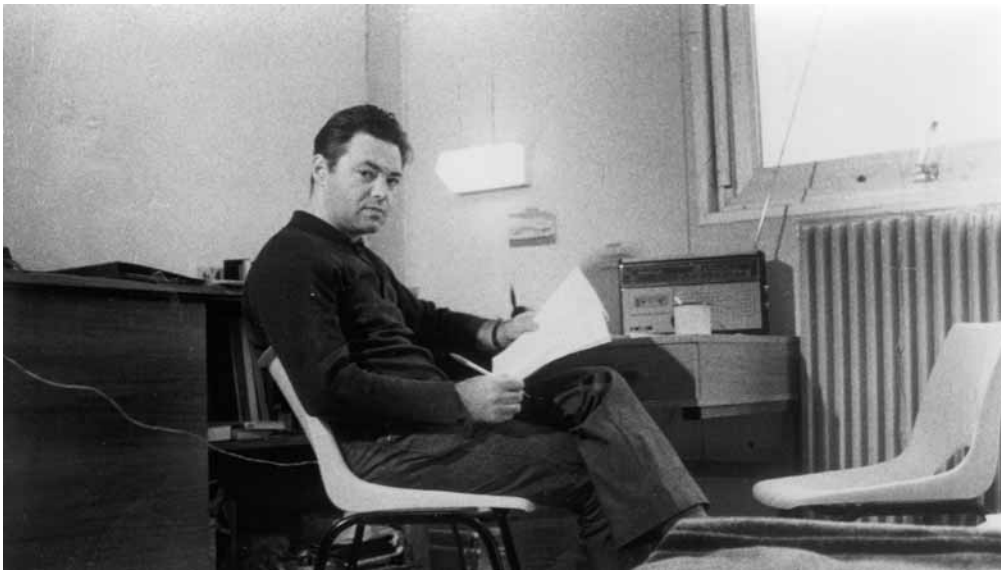

French - Soviet ARAKS team in Sogra at the time of the preparation for the experement.
Francis Cambou, project leader, is in the center, Yuri is third from the right.

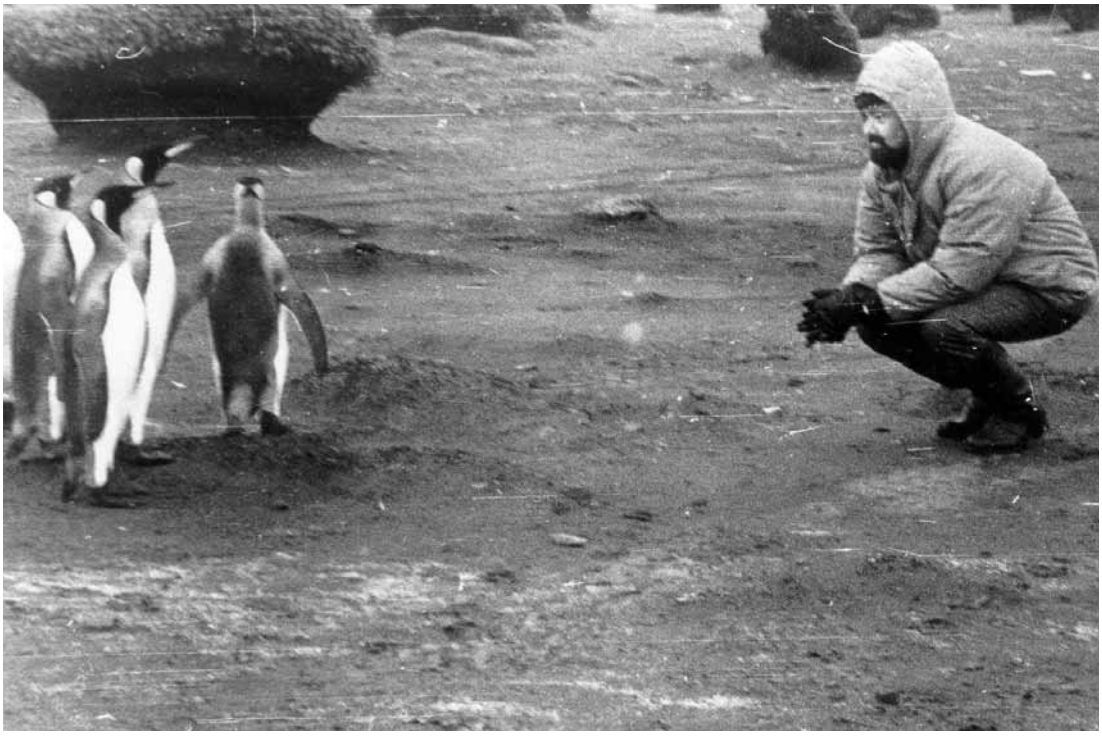

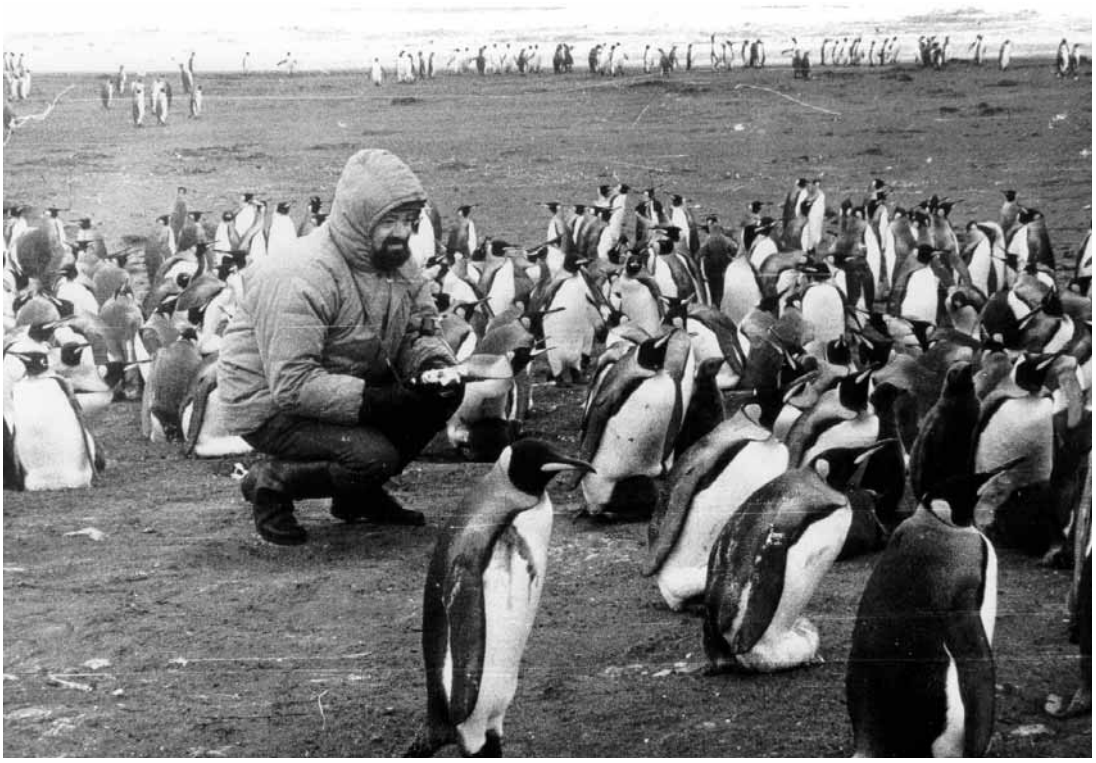

Yuri reading a lecture to the Kerguelen aborigines
Top: Yuri meets the aborigines
Bottom: at the end of the lecture

The Space Research Institute (IKI)

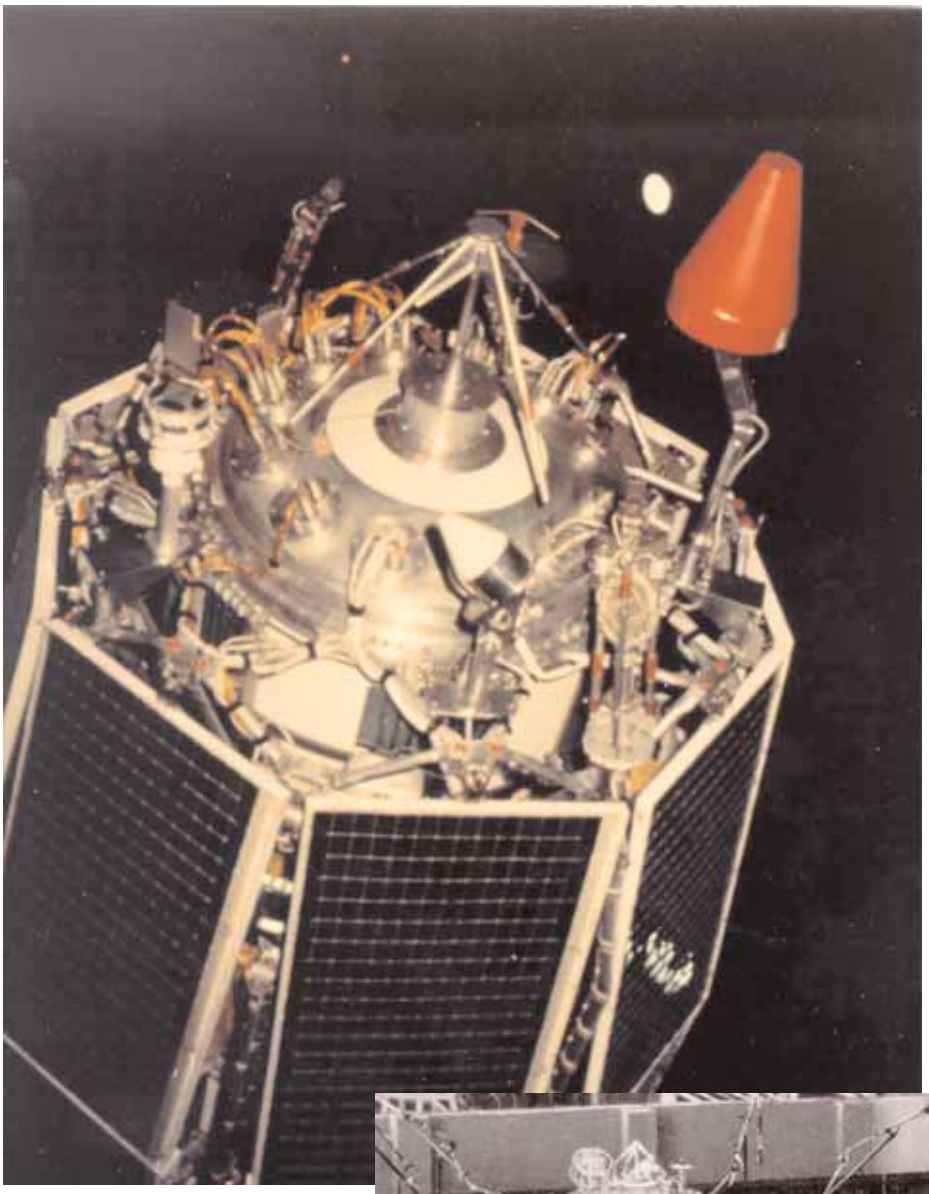

AUREOL - 3

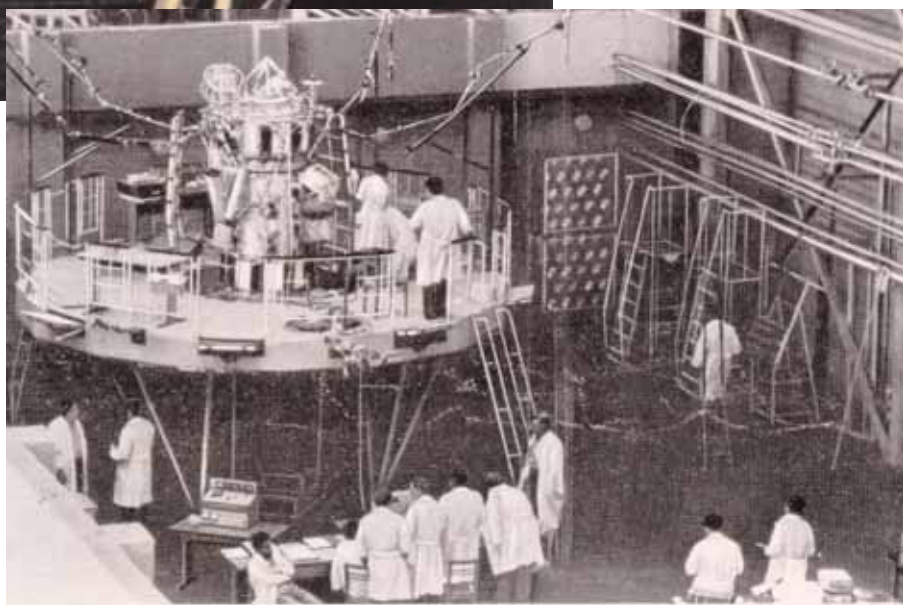

At the time of the tests


Yuri at AUREOL team meetings

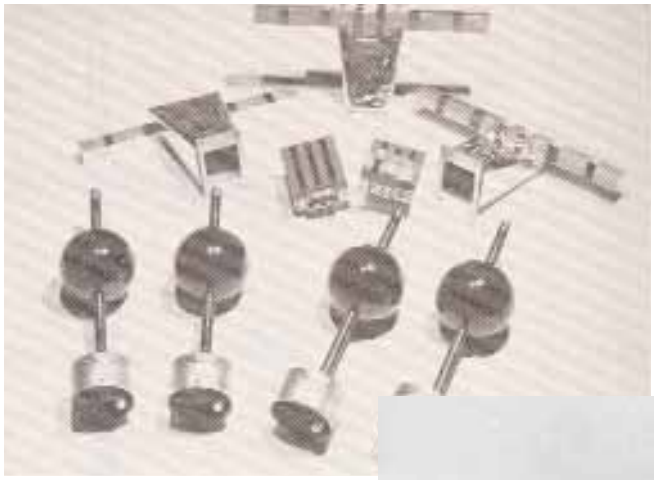

ISOPROBE sensors

Yuri at work

Yakutsk 1978
Top: Yuri Galperin, Mila Sivtseva, Ya. I. Feldstein
Bottom: Galina Nazarchuk, Liza Antonova , Yuri Galperin

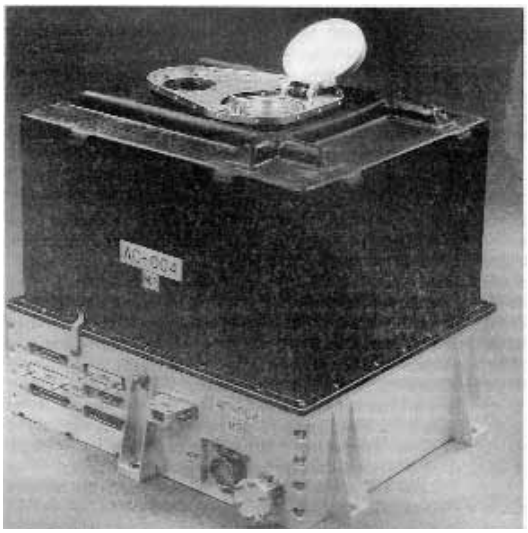

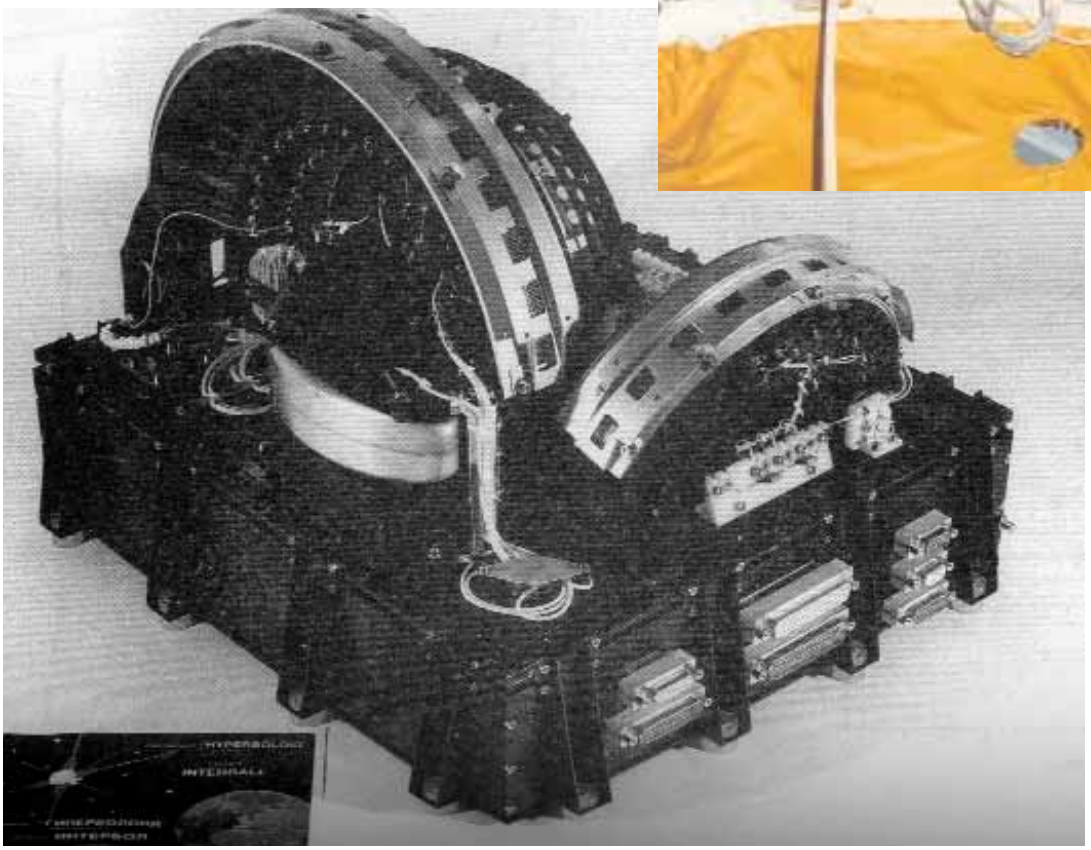

Two experiments of INTERBALL-2: Positive ions gun RON (top)
and spectrometer of superthermal ions Hyperboloid (bottom)
Hyperboloid with protective cover installed on the satellite (middle right)


In front of Geophysical institute in Alaska


Yuri and Maha Ashour - Abdalla on a sightseeing trip

Jean - Michel Bosqued and Yuri Galperin

Yuri with Odille de la Beaujardiere

At Yuri’s house
Top, from left: Yuri, Lev Zelenyi, Natasha (Yuri’s wife), Nariko and Atsuhiro Nishida
Bottom: Yuri and Natasha with journalist Slava Nechaev

Yuri with W. Hanson at Hanson’s house

Yuri having a discussion with J. Safrankova and Z. Nemecek

Yuri at C. McIlwain's lab in University San Diego, 1992

Yuri with his wife Natasha and their friend Olga Trifonova in Prague



Yuri talking at seminars

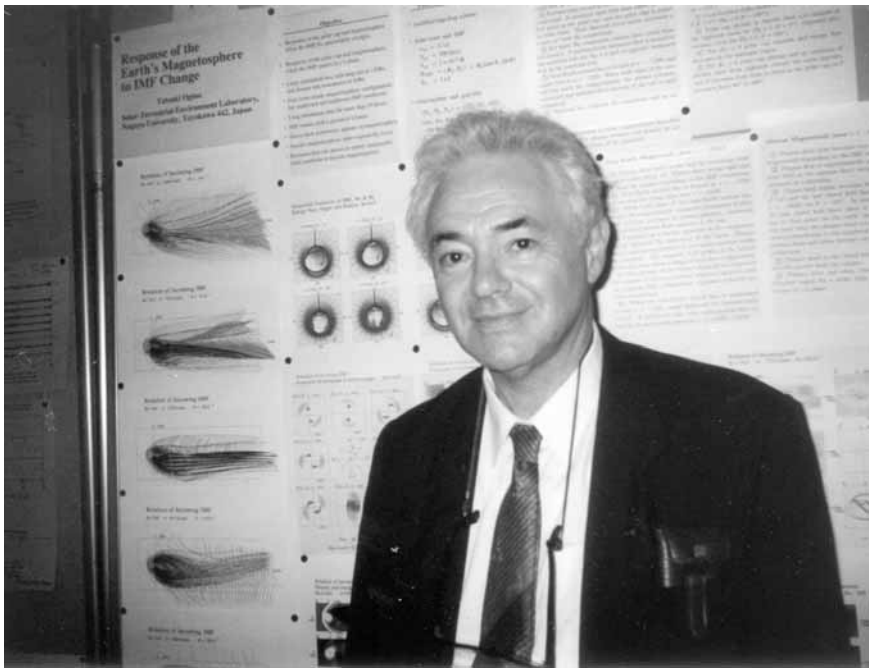


Yuri's last visit to STEL (Japan), 2001
Top: Yuri in front of T. Ogino's poster
Botttom: G. Rostoker, his wife Jilian, T. Ogino and Yuri

Yuri with IKI's postgraduates.
From left: D. Chugunin, V. Stepanov and P. Eiges

Yuri at IKI
From left: I. Afatkina,  J. Juchniewicz, L. Zelenyi, L. Gavrilova, Yu. Galperin

Yuri and Natasha in Graz

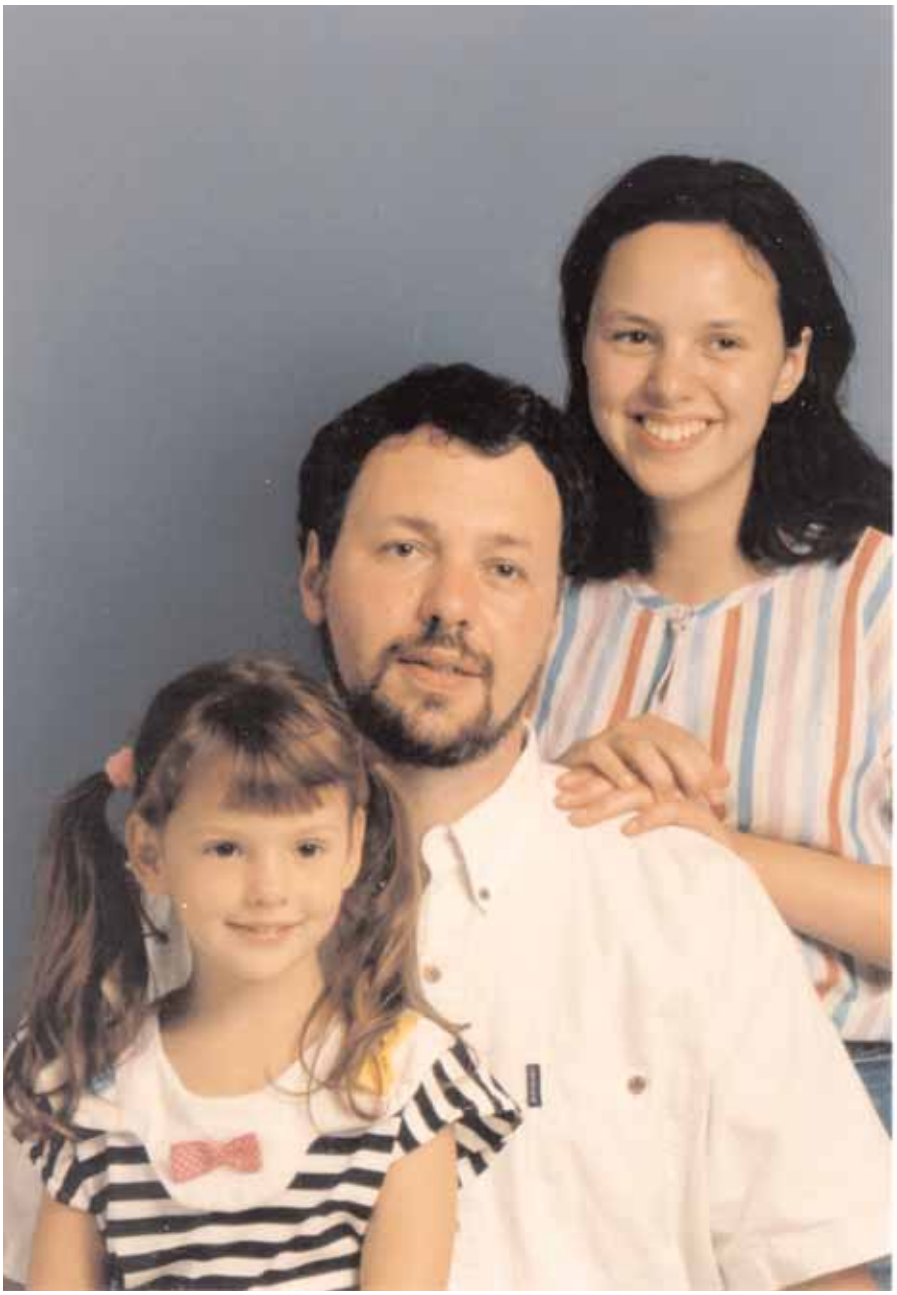

Yuri’s son Michael Galperin with daughters Natalia and Maria

# Ion escape from the cusp and cleft ionosphere. Results from AUREOL-3 and INTERBALL

J. -J. Berthelier[1], M. Bouhram[1], D. Chugunin[2], N. Dubouloz[3], V. Gladyshev[4], M. Hamelin[1], M. Malingre[1], T. Mularchik[2], and L. Zinin[5]

[1] Centre d'étude des Environnements Terrestre et Planetaries, Saint-Maur, France,
[2] Space Research Institute, Russian Academy of Sciences, Moscow, Russia,
[3] Laboratoire de Physique et Chemie de l'Environnement/Observatoire de Nancay, Orleans, France,
[4] Institute of Earth Physics, Moscow, Russia,
[5] Kaliningrad State University, Kaliningrad, Russia.

*In memory of Yuri Galperin's work on DYCTION and HYPERBOLOID experiments*.

## 1. Introduction

Coupling between the Earth's ionosphere and magnetosphere is an essential feature of the physics of the distant terrestrial environment and strongly contributes to numerous processes that control its dynamics. This coupling takes on varied forms where the ionosphere plays both a passive and an active role. The ionosphere behaves as a load in the global electrical circuit that results from interaction of the solar wind with the Earth's magnetic field, and also controls current flow along the field lines. Together with the upper atmosphere it represents a major sink for the energy released during magnetospheric substorms. But it also has a significant role as a source of magnetospheric plasma. During periods of high magnetic activity, it can even become a more important source than the solar wind [*Chappell et al*., 1987] and, in practice; all regions of the ionosphere contribute to this role. At mid-latitudes, along co-rotating magnetic lines of force, ionospheric particles are the only source of high altitude plasmaspheric plasma and plasmasphere refilling is an essential and complex process that is not yet fully understood [*Carpenter and Lemaire*, 1997]. The high latitude ionosphere appears however as the region of foremost importance and interest owing to its link with the distant magnetosphere and the tail which are key regions for magnetosphere dynamics. The ionosphere in the auroral oval and polar cap can indeed supply extremely large regions of the distant magnetosphere with plasmas of varied compositions and energy characteristics. The polar wind that mainly originates along open lines of force in the polar cap supplies cold, light ions in the tail and in the lobes. (See next paper of this issue). In the auroral zone, light and heavy ionospheric ions can interact with electromagnetic waves that accelerate them to suprathermal energies. They are ultimately injected as energetic particles in the high latitude magnetosphere [*Shelley et al*., 1982, *Yau and Andre*, 1997]. The major role of the cusp and cleft regions was discovered and fully appraised thanks to satellite missions that were flown during the last two decades [*Roux et al*., 1984; *Lockwood et al.*, 1985; *Chappell et al.*, 2000]. The main reason for the importance of this region stems from the fact that the magnetic lines of force that thread the cusp and cleft are in direct contact with the solar wind. Processes occurring at the magnetopause, such as magnetic reconnection and entry of solar wind particles, have immediate consequences on the production, transport and acceleration of ionospheric plasma at lower altitudes. Contrary to the case of auroral activity, processes occurring in the cusp and cleft regions are quasi-permanent features since they are observed almost without respect to the solar wind state except during relatively rare periods of prolonged northward-directed interplanetary magnetic field. They have thus, in the long term, a very significant role; all the more so since the energy sources, even less powerful than in auroral phenomena, have been shown to be quite effective [*Pollock et al.*, 1990]. In addition, the cusp and cleft regions directly reflect temporal variations of solar wind parameters that impact on the magnetopause. In particular, changes in the direction of the interplanetary magnetic field are known to control, with a very small time constant, the location and extent of the cusp and cleft, and the plasma convection in these regions, making the resulting phenomena extremely dynamic.

For these reasons the transport and acceleration of plasma in the cusp and cleft regions has been one of the central questions in most of the ionospheric and magnetospheric satellite missions of the last twenty years. This was particularly the case for the ARCAD and

INTERBALL projects that were realized in the framework of the French-Russian collaboration in space physics in which Yuri Galperin played a key role. We shall briefly review here some of the main results that were obtained in this domain over an altitude range encompassing the upper ionosphere and the high-altitude part of the cusp field lines. This paper will thus consist in two main parts: the first one devoted to low altitude observations provided by the AUREOL-3 satellite, flown in the frame of the ARCAD project, and the second one centred on high-altitude observations from the AURORAL PROBE of the INTERBALL mission.

## 2. Ionosphere dynamics in the low altitude cusp and cleft

Low energy plasma observations were achieved by the DYCTION ion mass spectrometer that was launched on the AUREOL-3 spacecraft with perigee at 400 km and apogee at 2000 km. The instrument measured the major ionospheric ions $H^+$, $He^+$ and $O^+$ independently. The instrument is described in *Berthelier et al.* [1982].

Typical examples of the observations are shown in Figures 1 to 3, which represent northern high latitude passes of the spacecraft (orbits 761 and 3649), and that span similar altitude ranges in both cases. The first figure provides a view of the convection velocity vector along the satellite path. It shows the rather typical convection pattern with anti-sunward convection in the polar cap, possibly tilted significantly from the Sun-Earth direction, as in the case of orbit 761, due to a large azimuthal component of the interplanetary magnetic field. In Figure 2 (orbit 761) are displayed in more details: (i) in the upper panel, low energy electron fluxes in the energy range from ~100eV to ~700 eV (3 channels) [*Bosqued et al.*, 1982]; and (ii) in the two lower panels the velocity parallel to the magnetic field (positive for upwards directed velocities) and the temperature of $O^+$, the major heavy ion of interest in this altitude and latitude range. According to the particle and electric field data, the cleft is crossed between about 7.39 UT and 7.41.30 UT. As evidenced from particle data and due to the geometry of the IMF, the satellite detected precipitations from the plasma sheet boundary layer after having crossed the cleft proper but with fluxes smaller than in the cleft. At the end of the pass the satellite reenters the auroral zone as evidenced from the direction of the electric field. The $O^+$ parallel velocity is seen to respond very quickly when the satellite enters the cleft, reaching a maximum of about 200 m/s at the end of the traversal while the $O^+$ temperature shows a moderate decrease by about 250°K in the same time interval.

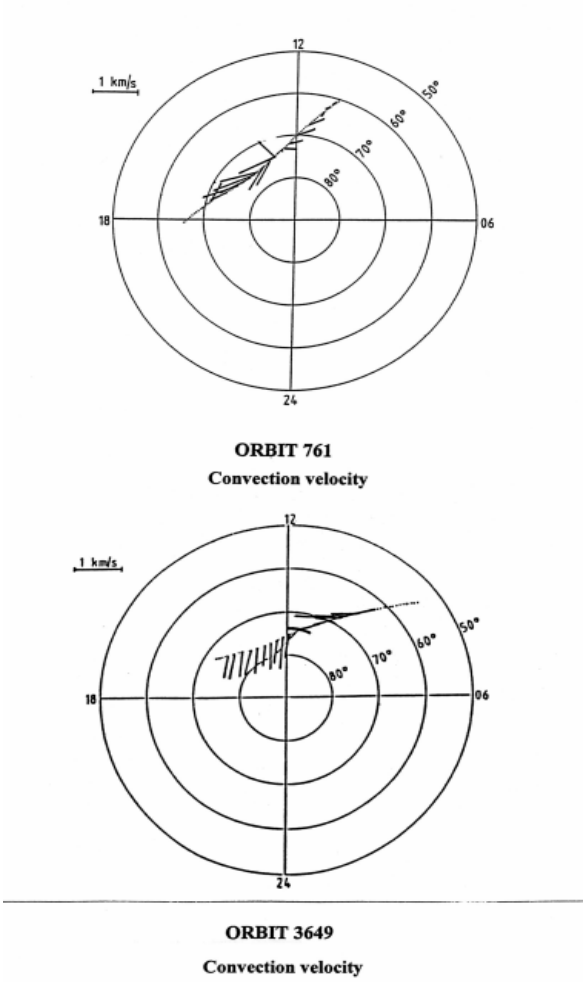


**Figure 1.** AUREOL-3 data: convection velocity for orbits 761 and 3649.

In the polar cap the parallel velocity reverses and becomes downward, reaching a maximum of ~ 500 m/s. The ion temperature increases at the end of the cleft crossing up to its original value of 2100°K, observed before the entry in the cleft, and subsequently reaches 2600°K at 7.44 UT with some time lag with respect to the corresponding variations of the parallel velocity in the polar cap. Figure 3 shows similar data in the case of orbit 3649 with a rather identical behavior of the $O^+$ parameters during and after the cleft traversal. The cusp traversal, as indicated by the soft electron precipitation, extends over a longer period than in the preceding case. This may explain why the upward velocity reaches a larger value of about 500 m/s approximately 30 s after the end of the electron precipitation. Again, as in the previous case, it decreases towards slightly negative values in the polar cap. The $O^+$ temperature decreases by 300°K during the rise of upward velocity and then

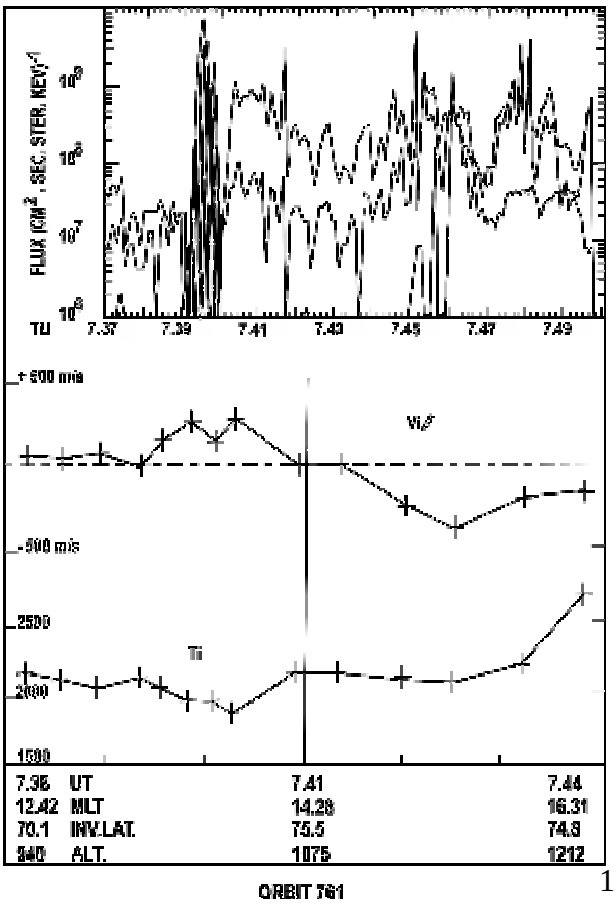


**Figure 2.** Electron precipitation and $O^+$ ion temperature and parallel velocity variations through the cusp and polar cap (AUREOL-3, orbit 761).

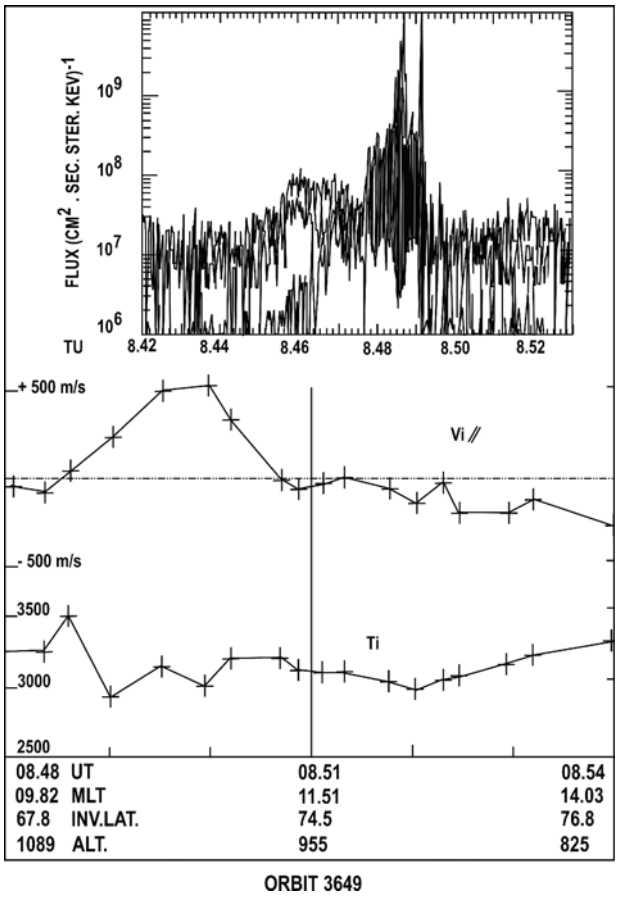


**Figure 3.** Electron precipitation and $O^+$ ion temperature and parallel velocity variations through the cusp and polar cap (AUREOL-3, orbit 3649).

increases by 200°K near the time of maximum velocity. In the polar cap the ion temperature increases by about 300°K coincident with the increases of negative (downward) values for the parallel velocity.

To summarize:

– Almost simultaneously with the soft electron precipitation, the parallel $O^+$ velocity becomes upwards and reaches maximum values of 200 to 500 m/s shortly after exit from the precipitation zone. In the polar cap the parallel velocity varies regularly from upwards to downwards values reaching maximum values of the same order of magnitude.

– The $O^+$ temperature decreases by ~200°K during the rise of upward velocities and then increases regularly to reach maximum values in the polar cap a few minutes after the cusp/cleft crossing.

Two mechanisms have been proposed to account for the upward drift of the heavy ions in the cusp. The first one is based on the direct Joule heating of ions and their subsequent upward diffusion. Some amount of Joule heating is certainly present in the cusp since intensified convection electric fields have been regularly observed there by satellite measurements together with the occurrence of small-scale structures with large gradients that may also help in heating the ions. The second one [*Whitteker*, 1977; *Schunk*, 2000] is based on heating of ionospheric thermal electrons by the magnetosheath soft-electron precipitation in the cusp and cleft. The heated electrons diffuse almost instantaneously upwards dragging the ions behind them through the ambipolar electric field and more slowly transferring their energy to the ions. The data presented above indicate that the dynamics of the thermal ionospheric $O^+$ ions in the cusp are mainly controlled by electron precipitation.

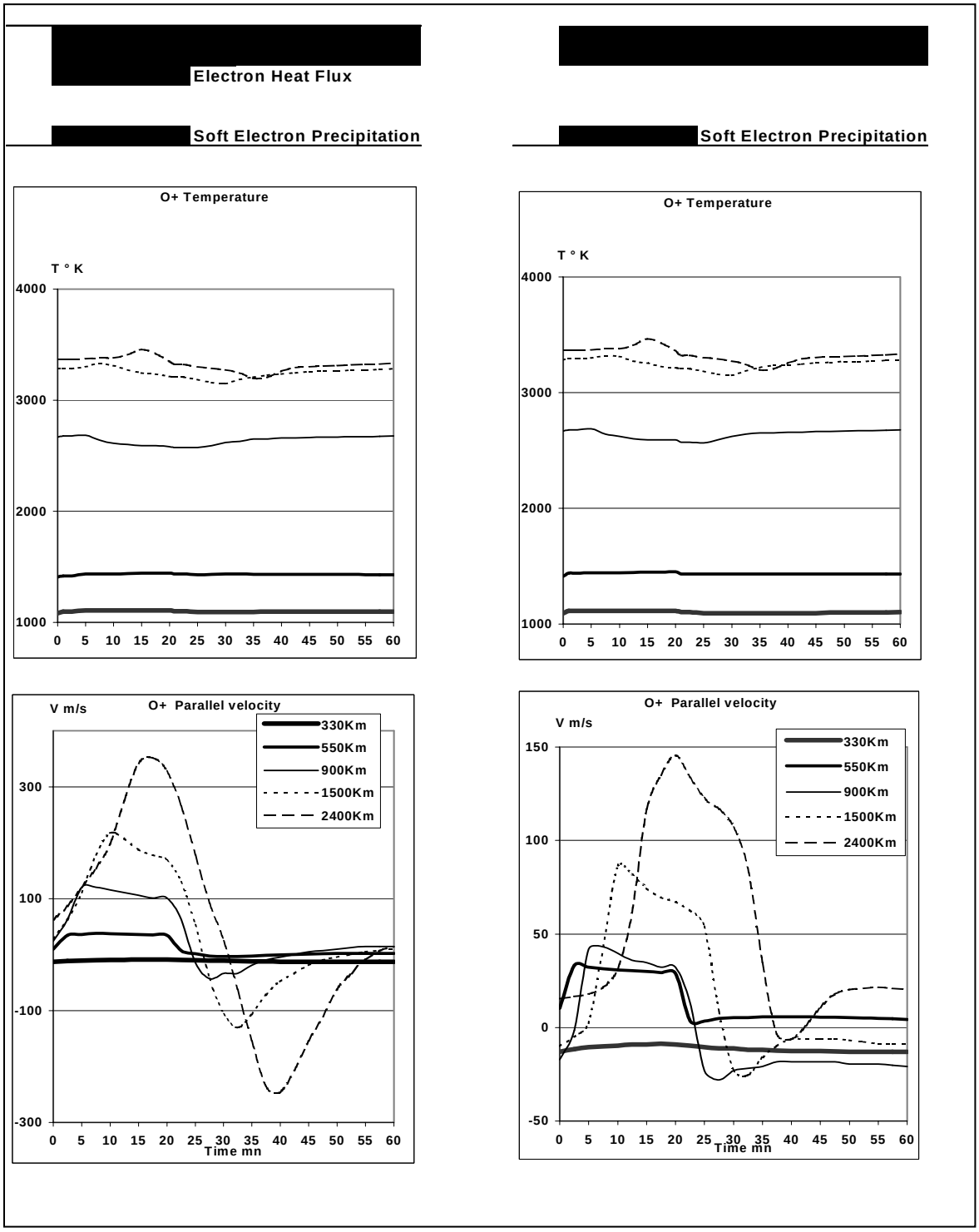


**Figure 4.** Numerical simulation of $O^+$ ion dynamics in the cusp and adjacent polar cap.

The decrease of the $O^+$ temperature with increasing upward parallel velocity is indeed a very strong argument in favour of this mechanism. In order to study in more detail the dynamics of ionospheric plasma that is convected from the dayside auroral zone to the polar cap through the cusp or cleft regions, we have developed numerical simulation models. They were run for an altitude range from ~125 km, where the local

equilibrium hypothesis is valid, to ~10,000 km where appropriate boundary conditions must be imposed. The first model is based on a 5-moment fluid description of the major ions and electrons [*Zinin*, 1985], the second one on an 8-moment description, which takes account of the electron heat flux at high altitude [*Robineau*, 1992]. During the course of this study it was shown that Joule heating is indeed of minor importance compared to energy deposition by precipitating soft electrons [*Robineau*, 1992]. Joule heating may be effective in the polar cap due to the travel time, which is much longer than the cusp traversal. An interesting result was the discovery of a rather significant influence of the downward electron heat flux at high altitude. Using a time-variable heat flux as an upper boundary condition resulted in noticeable changes in the parallel velocity variation. Introducing an intensified heat flux (from 1.0 to $1.2 \times 10^{-7}$ J/m$^2$/s) on the field lines that support the precipitating electrons gave better reproduction of the downward parallel velocities in the polar cap. This is shown in Figure 4, where model curves are displayed for the two situations. In one case, the downward electron heat flux is constant and equal to $10^{-7}$ J/m$^2$/s, corresponding to the estimated mean value at such an altitude. In the second case the heat flux has been intensified by 20% on the field lines that correspond to the cusp location and support the soft electron precipitation. Increasing the heat flux results first in larger upward $O^+$ velocities in the cusp compared to the case of a constant heat flux. The second effect is to significantly enhance the downward velocities in the polar cap, which is in very good agreement with experimental observations.

## 3. Plasma dynamics in the high-altitude cusp/cleft

### 3.1. INTERBALL-2 observations

The INTERBALL-2 satellite was launched on August 1996, into a 19,200 × 750 km orbit with 62.5° inclination. One of its main objectives was to investigate plasma dynamics and underlying energization processes occurring in the auroral regions (for a complete description of the Interball Project, see the report by *Galeev et al.* [1995]). Here, we discuss the results of HYPERBOLOID and ION experiments. The Hyperboloid ion mass spectrometer measures 3D distributions of $H^+$, $He^+$, $O^+$ and $O^{++}$ ions at 1-80 eV [*Dubouloz et al.*, 1998*a*]. It consists of two multi-directional analyzers viewing in two, almost mutually-perpendicular, half planes. The main analyzer has 16 entrance windows positioned in a plane containing the satellite spin axis 10° apart from each other (angular acceptance of each window ~13°x12.5°). The time resolution for 2-D ion distribution functions is a few seconds. At thermal energies (<10 eV), ion measurements are often shielded because of the positive value of the satellite electric potential with respect to the plasma. Therefore, a filling-in procedure has been developed in order to extend the measured distribution to low-energy [*Bouhram*, 2002]. The ION experiment provides energy spectra of $H^+$, $O^+$ ions and electrons at higher energies (30 eV–15 keV) over two view directions, which rotate in the spin plane along with the satellite [*Sauvaud et al.*, 1998]. From both experiments, ion distribution functions and moments of major species were recorded every spin period (120 s), by covering a continuous and wide energy range (1 eV-15 keV). Analysis of data acquired during the two-year satellite lifespan, combined with modeling and intensive numerical simulations, led to a better overall view of the morphology of high-latitude ionospheric ion outflow and also to improved understanding of the physical processes involved in the energization and transport of ions through the magnetosphere [*Dubouloz et al*, 2001; *Delcourt et al*., 1999; *Malingre et al*., 2000; *Bouhram*, 2002, *Bouhram et al*, 2003*a*,*b*].

*Example of observations in the polar cusp*

Figure 5 shows 40 minutes of data from a pass through the cusp around noon at about 2.5 $R_E$ altitude, during a period of moderate geomagnetic activity ($K_p$=2). At the beginning of the time interval, Interball-2 was on closed field lines, as evidenced by substantial $H^+$ flux with high energies (up to 10 keV) in Figure 5-b, accompanied by a denser, low-energy (<10 eV) component (Figure 5-c). From about 21:26 UT, a sudden onset of transverse ion heating is detected from $O^+$ measurements. Right after the onset, the $H^+$ high-energy panel (Figure 5-b) shows a background population with a time-energy dispersion, characteristic of magnetosheath injections. Such observations along with stronger, low-energy (<200 eV) electron fluxes (Figure 5-a) satisfy criteria indicating that the observed heating region is associated with the polar cusp. As INTERBALL-2 travels poleward from the cusp, the observed conical distributions fold up, i.e. become more anti-field-aligned, while their mean energy decreases. This signature may be explained by a transverse ion heating occurring in a region of finite latitudinal extent, followed by an adiabatic convective flow up to the satellite track [*Knudsen et al.*, 1994; *Dubouloz et al.*, 1998b]. During this event, the orientation of the IMF is steady and southward ($B_x$~–2 nT, $B_y$~0, and $B_z$~–4 nT), which is consistent with convection patterns that are antisunward directed in the polar cap. The out-flowing ionospheric $H^+$ component is accompanied by a background population that represents the low-energy tail of the magnetosheath component. Depending on the flux intensities and the

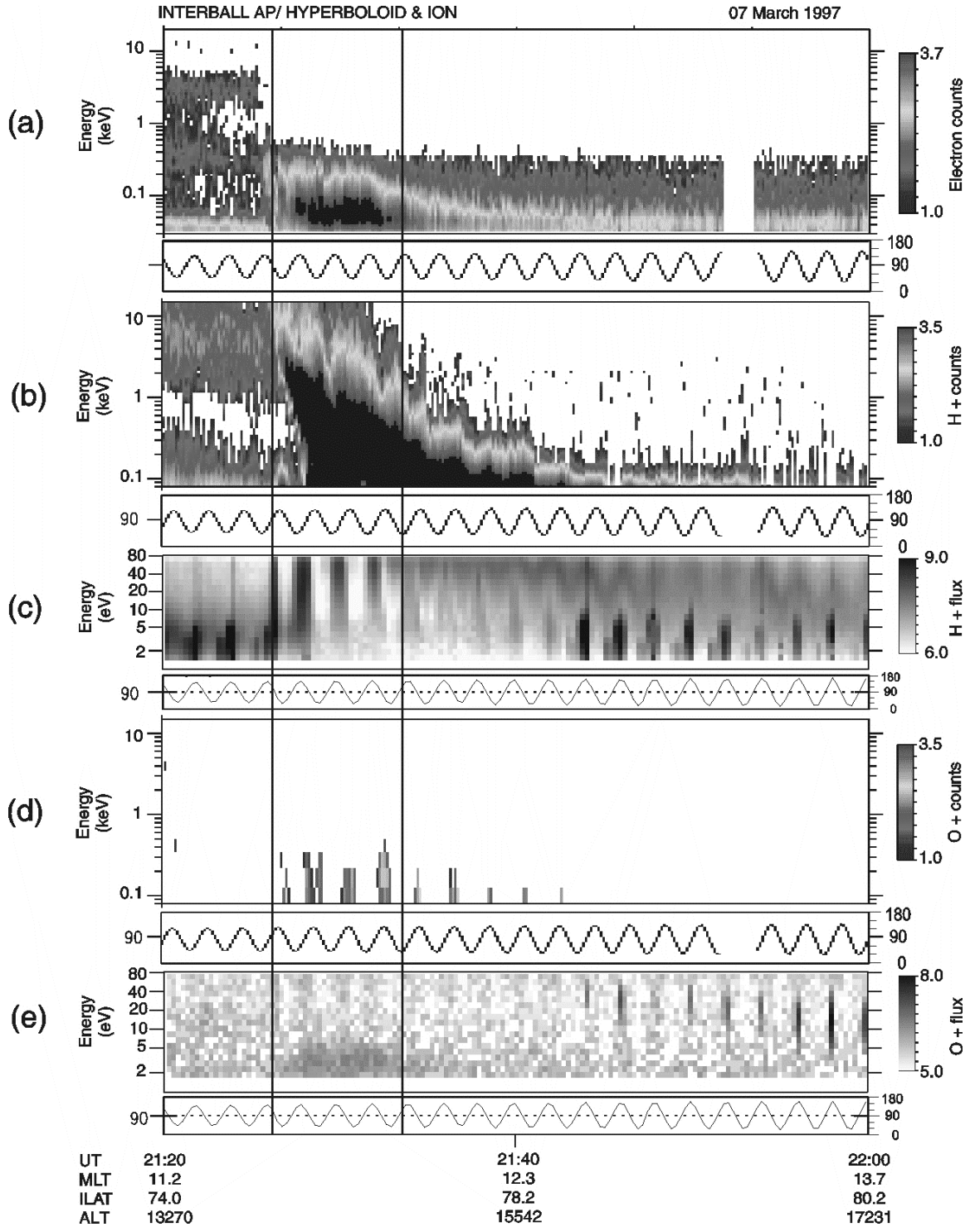


**Figure 5.** Overview of a transverse ion-heating event on March 7, 1997, between 21:20 and 22:00 UT. From top to bottom: energy-time spectrograms of (**a**) 30 eV to 15 keV electrons, (**b**) 30 eV to 15 keV $H^+$ ions, (**c**) 1 eV to 80 eV $H^+$ ions, (**d**) 30 eV to 15 keV $O^+$ ions, and (**e**) 1 eV to 80 eV $O^+$ ions. High-energy measurements in counts are from the ION experiment, while low-energy measurements in $\log[(m^2\ s\ sr\ eV)^{-1}]$ are measured by the central detector of the Hyperboloid experiment. The vertical black lines indicate the boundaries of the heating region.

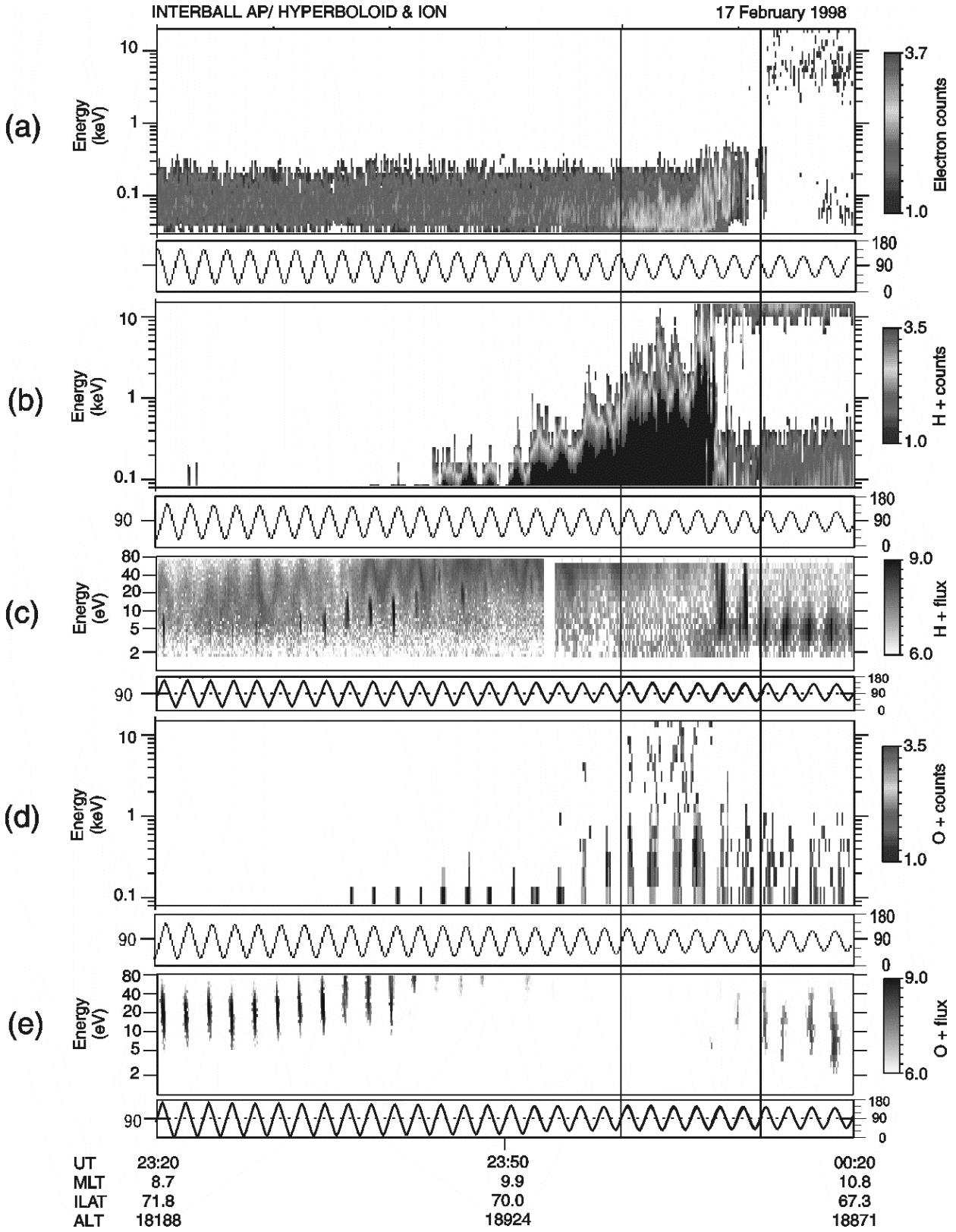


**Figure 6.** Overview of a transverse ion-heating event on February 17, 1998, between 23:20 and 00:20 UT. The format is the same as for Figure 5.

energy resolution, it is not always possible to separate the ionospheric component from the magnetosheath component.

*Example of observations in the cleft*

Figure 6 shows 1 hour of data from a pass through the dawn polar cap and cleft at about 3 $R_E$ altitude, during a period of high geomagnetic activity ($K_p$=6). At the beginning of the time interval, INTERBALL-2 was in the polar cap and low-energy out-flowing ions were detected. During this event, the orientation of the IMF is steady and strongly southward ($B_x$~$B_y$~2 nT, and $B_z$~ −14 nT), which is consistent with convection patterns that are anti-sunward directed in the polar cap. This suggests that the ion heating, responsible for the observed outflow, occurs at lower latitude on the dawn side (8.5–10.5 MLT) of the cleft region, where ions are drifting into the dawn polar cap. As a result of the velocity-filtering effect due to convection drift, the mean energy of up-flowing ion species increases nearby as the satellite enters the poleward boundary of the cusp near 00:00 (UT). Once again, the cusp region may be detected from high-energy proton injections and intense low-energy isotropic electron fluxes. The region is also correlated with elevated $O^+$ conics with energies extending up to a few KeV. Figure 7 shows an example of such velocity distributions recorded by the ION

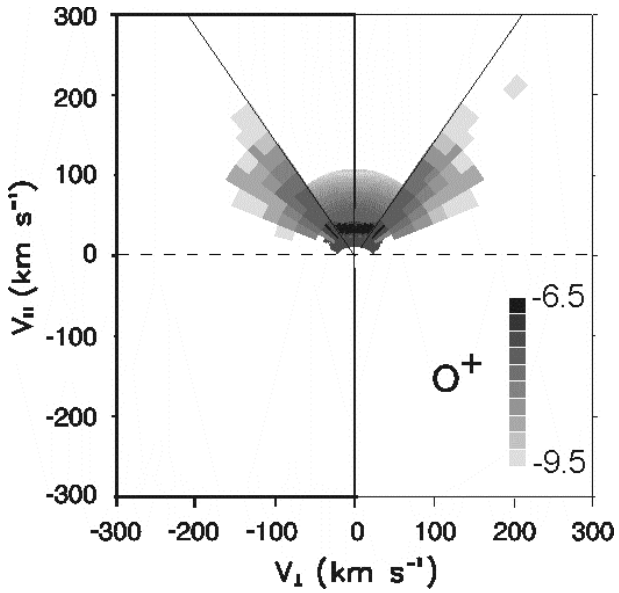


**Figure 7.** Ion distribution function in log(cm$^{-3}$ km$^{-3}$ s$^3$) recorded near the poleward heating boundary at 23:59 UT on February 18, 1997.

experiment near the poleward edge of the heating region. In this plot, we observe ion conics with a net upward velocity component and more extended at high energies in an oblique direction corresponding to an apex angle of 40–50°. This shape is consistent with height-integrated transverse ion-energization in combination with the mirror force up to the satellite orbit, weakly heated ions (i.e. those of lower energies) being spread out poleward from the heating region by the convection drift.

### 3.2. Review of the physical processes involved

The energization and outflow of ionospheric ions at auroral latitudes have been an area of active research over the past three decades. Some recent reviews can be found in *André and Yau* [1997] and *Moore et al.* [1999]. Inside the dayside cusp/cleft, the energetic, or non-thermal, ion outflow is classified into beams and conics. Beams have a strongly field-aligned flux, and tend to be associated with acceleration through structures of field-aligned potential drops. Conics have a peak flux in a direction oblique to the upward direction and are caused by transverse ion heating. The energized ions can then move up to the magnetic field lines and form conics in velocity space. Statistical studies on dayside ion conics pointed out that their temperature increases versus

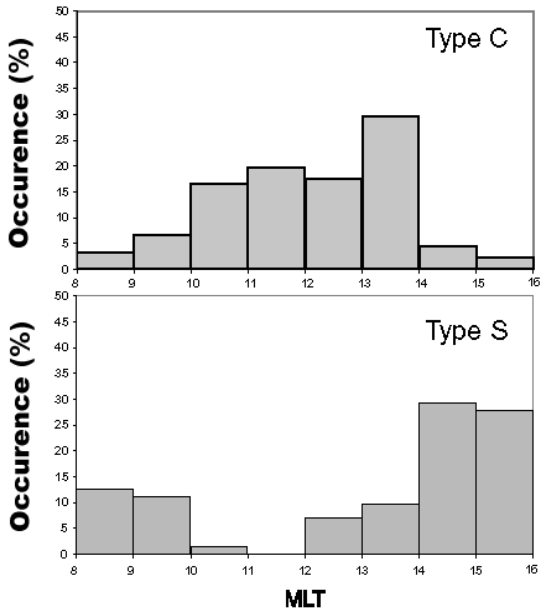


**Figure 8.** Occurrence frequencies of (**top**) transverse heating events, and (**bottom**) events associated with structures of field-aligned potential drops as a function of MLT (from *Bouhram et al.* [2003b]).

altitude, while their angle with respect to the upward direction (apex) decreases more slowly than expected from adiabatic folding [*Peterson et al.*, 1992; *Miyake at al.*, 1993]. Such results are consistent with a height-

integrated heating of ions along the geomagnetic field lines. Figure 8 shows a study from *Bouhram et al*. [2003b] using INTERBALL-2 observations of the occurrence versus magnetic local time (MLT) of events related to transverse heating and field-aligned potential drops. According to previous statistical studies [*Gorney et al*., 1981; *Kondo et al*., 1990, *Miyake et al*., 1996], such structures are not common in the cusp and tend to be associated with the cleft region.

Much of the ion outflow observed in the cusp/cleft region is associated with transverse heating. The energization is caused by the perpendicular component of electric fields oscillating within some frequency range. Recent statistical studies based on observations from the FREJA and FAST satellites pointed out that most ion transverse-heating events are associated with an enhancement of broadband extremely low frequency (BBELF) wave turbulence. The BBELF turbulence covers frequencies from less than 1 Hz up to several hundred Hz, thus including the $H^+$ and $O^+$ gyrofrequencies at altitudes from about 1,000 km up to a

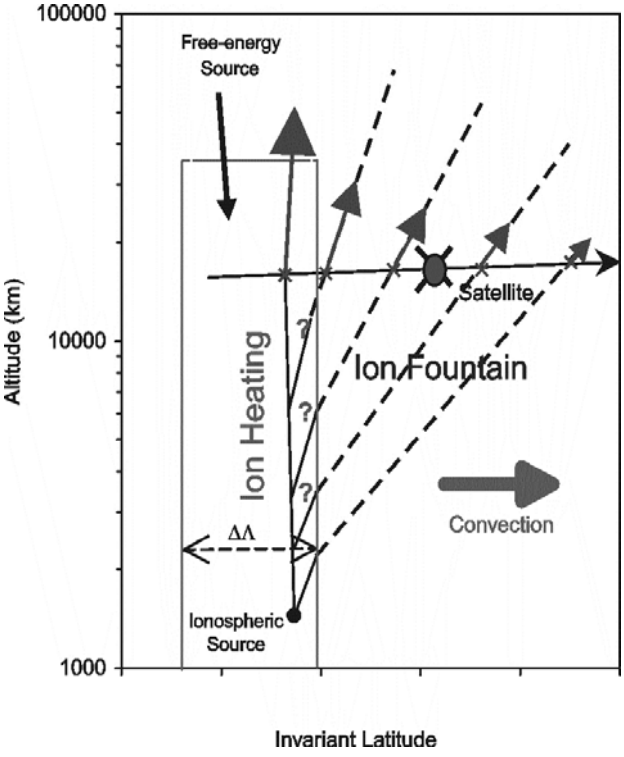


**Figure 9.** Sketch illustrating the transport pattern of ion outflows from the cusp/cleft in conjunction with a satellite crossing. The trajectories are projected in a meridian plane.

few $R_E$. Its profile versus frequency generally exhibits a power law spectrum, which may be characterized by an index $\alpha$. Many wave modes may be contained in the BBELF turbulence, such as narrow-band electromagnetic ion cyclotron waves, electrostatic ion cyclotron waves, slow ion acoustic waves, and inertial Alfvén waves that are Doppler-shifted by the satellite's motion. However, in terms of ion energization, the theory of ion cyclotron resonance (ICR) heating by the electromagnetic left-hand circular polarized component around the ion gyrofrequencies [*Chang et al.*, 1986] seems the most plausible mechanism and only a small fraction of the observed turbulence is responsible for ICR heating to produce the observed ion energies, as confirmed by numerical simulation studies [*André et al*., 1990; *Norqvist et al*., 1996; *Bouhram et al*., 2003*a*,*b*].

### 3.3. Modeling of transverse heating and large-scale transport

*Bouhram et al*. [2003*a*] developed a two-dimensional, trajectory-based code based on a steady-state, to investigate the transport patterns of non-thermal $H^+$ and $O^+$ field-aligned flows from the dayside cusp/cleft that are associated with small-scale processes such as transverse heating by means of wave-particle interactions and combined with poleward motion due to magnetospheric convection,

The scheme of the model geometry is given in Figure 9. According to the scheme, the coordinate system is defined by two spatial dimensions: *s* and *X*, where s denotes the length of the geomagnetic field line from its footprint, plus the earth's radius. The ion heating is modeled by means of a Monte Carlo technique, via the ICR process with the electromagnetic left-hand circular polarized component of the BBELF turbulence. The altitude dependence of ICR heating from 1000 km to 3 Earth radii ($R_E$) is modeled by a power law spectrum, with an index $\alpha$, and a parameter $w_0$ that is proportional to the spectral density at a reference gyrofrequency. Because of the finite latitudinal extent of the cusp/cleft, incorporation of the horizontal convection drift leads to a maximum residence time $t_D$ of the ions when they are being energized. A large set of simulations has been computed to study the transport patterns of $H^+$ and $O^+$ bulk parameters as a function of $t_D$, $\alpha$, and $w_0$. Residence time effects were found to be significant in $O^+$ density patterns while negligible for $H^+$. When comparing the results with analytical one-dimensional theories [*Chang et al*., 1986, *Crew et al*., 1990], we find that mean ion energies and pitch angles at the poleward edge of the heating region are slightly influenced by $t_D$ and may be used as a probe of ICR parameters ($\alpha$, $w_0$). Conversely, poleward of the heating region, upward velocity and mean energy dispersive patterns depend mainly on $t_D$ (e.g. the magnitude of the convection drift) with latitudinal profiles varying versus $t_D$. In short, the main conclusion of the study is that any triplet ($t_D$, $\alpha$, $w_0$) leads to a unique transport-pattern feature of ion flows associated with a cusp/cleft ionospheric source.

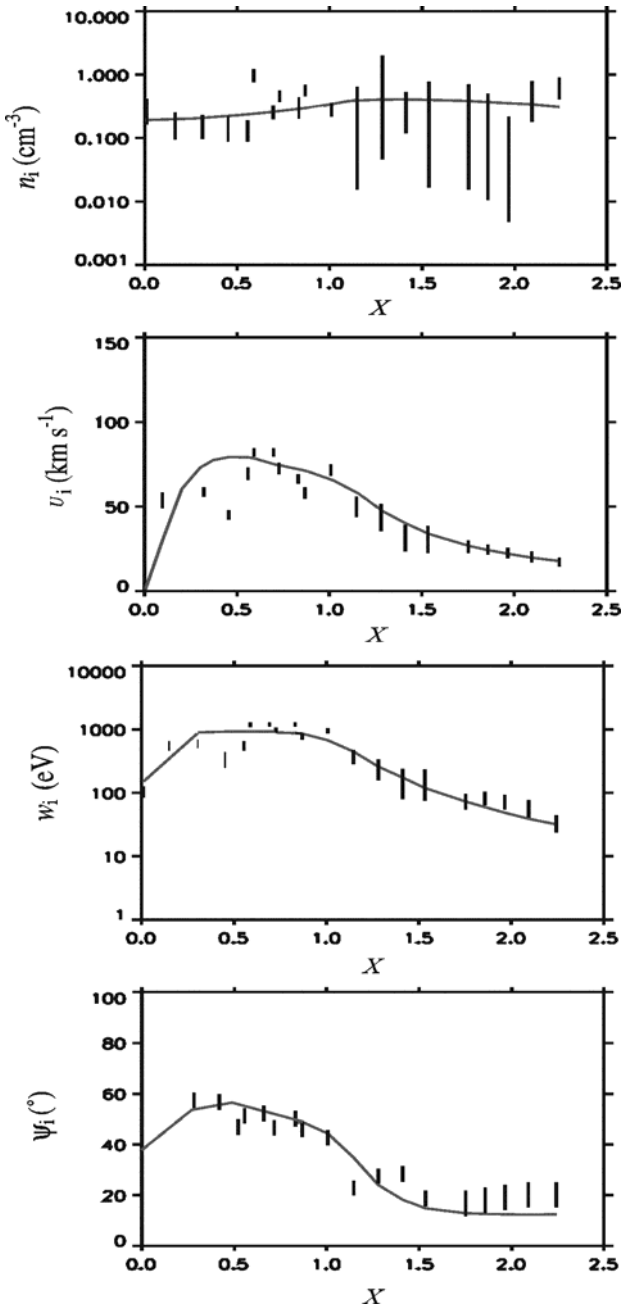


**Figure 10**. Comparisons for one event of experimental ion moments along the satellite track with those from a numerical simulation (solid curves) for $O^+$ ions. From top to bottom, ion density in $cm^{-3}$, upward mean velocity in km $s^{-1}$, ion mean energy in eV and apex angle in deg. The distance $X$ denotes the poleward distance from the downstream border of the heating region and is normalized with respect to the thickness of the region.

### 3.4. Comparison between modeling results and observations

Providing high-altitude (1.5–3$R_E$) ion observations are available, the results from the parametric study by *Bouhram et al*. [2003*a*] were used to determine the altitude dependence of transverse ion heating during a significant number of passes of the INTERBALL-2 satellite [*Bouhram et al*., 2003*b*]. Figure 10 shows the moment profiles along the satellite track for the event of Figure 2. A solution for the altitude heating profile is tested here by being introduced as input to a numerical simulation. As onset to a simulation, we introduced an ionospheric ion source $S_{i0}$ at $z$=1000 km, characterized by a density $n_{i0}$ and a flux $J_{i0}$, and a component $S_{ie}$ along the equatorward edge of the heating region with a density $n_{ie}$ at INTERBALL-2 altitude. This latest component allows us to reproduce the patterns of ion moments near the equatorward heating-boundary. The value of $n_{ie}$ is inferred from Hyperboloid measurements just equatorward from the heating region. Because equatorward from the heating region, energization processes are less important, it is reasonable to assume that the density is inversely proportional to the cross-section area $A(s) = (s/s_0)^3$ of a magnetic flux tube, so as to satisfy the particle conservation law. The values of $n_{i0}$ and $J_{i0}$ are adjusted so as to reproduce the densities and fluxes observed at INTERBALL-2 altitude poleward from the heating region. We can see in Figure 10 that the simulated ion moments follow the tendencies of those observed. A few disagreements are observed locally and may be explained by the assumption of a steady-state model associated with a finite number of parameters. In the simulations, the heating region is assumed to be uniform versus $X$ (latitude). Therefore, non-monotonic variations in the observed ion moments cannot be reproduced without introducing inhomogeneous structures versus $X$. In the same way, spatial and time variations of the ionospheric ion flux and density convection-drift may be expected to occur. However, observations by a single satellite do not provide enough information to include these effects.

This procedure was applied and tested successfully for 25 cusp/cleft crossings associated with steady IMF conditions, where isolated ICR heating is expected to occur. It was pointed out that ICR heating increases gradually versus geocentric distance as $s^{3.3\pm1.8}$. We compared such dependence and the values of the wave power responsible for ICR heating with those of the BBELF spectra as usually observed in the cusp/cleft. The results are consistent in such a way that the wave-mode responsible for ICR heating acts as a minor component in the BBELF spectrum since the inferred wave power values correspond to less than a few % of those usually observed by wave experiments. We also

noticed that the inferred power-law altitude dependence is consistent with previous statistical studies on the evolution of ion conics along the geomagnetic field lines up to $s$=5 $R_E$ [*Peterson et al*., 1992; *Miyake et al*., 1993].

## 4. Conclusions and perspectives

The global set of measurements performed first at low altitude with the AUREOL-3 satellite and then at high altitude with INTERBALL-2 produced a rather detailed view of the complex chain of processes that are active along a wide range of altitudes for the lines of force of the cusp and cleft regions.

Analysis of thermal plasma measurements in the upper ionosphere below 2000 km has shown that electron heating by soft electron precipitation is the basic mechanism that controls plasma dynamics along the lines of force. Thermal electrons that are heated in the cusp by soft-electron energy deposition diffuse upwards, almost immediately dragging along the ions and more slowly exchanging their energy with them. In the polar cap the plasma settles down and parallel $O^+$ velocities are downward while the ion temperature is increased. The effect of a high altitude enhanced downward electron heat flux along cusp field lines is significant down to rather low altitudes.

Thermal and low energy suprathermal ion measurements performed at high altitudes by the INTERBALL-2 were interpreted through a model of altitude-dependent transverse ion heating by resonant interaction at the ion gyrofrequency with BBELF waves. It has been shown that only a small fraction (typically a few percent) of the BBELF turbulence usually observed in the cusp/cleft is needed to obtain the observed ion energies. Transverse heating by lower hybrid waves generated by precipitating magnetosheath ions can also occur in the cusp, but this is a mechanism of lesser importance. In the cleft, acceleration by field-aligned potential drops may provide additional acceleration.

These studies have shown that the processes that are active in the cusp and cleft regions have a great importance for coupling between the ionosphere and magnetosphere and for escape of plasma from the high latitude ionosphere. Owing to the wide variety of physical processes that have to be taken into account, data analysis must combine a global set of measurements from both spacecraft and from ground-based instruments, which is now possible thanks to the magnetospheric and ionospheric missions that are in operation and to the Super Darn network. A complete understanding of plasma transport and acceleration requires a large effort in numerical modeling which is a major goal of the Space Weather programs. Very significant progress can be made when and if models are able to describe in a unified way fluid similar processes and microscopic physics which are operating simultaneously over a wide altitude range in the upper ionosphere. Progress in numerical algorithms and in computing power should make this possible in the coming years.

## References

André, M., G. B. Crew, W. K. Peterson, A. M. Persoon, C. J. Pollock, and M. J. Engebretson, Ion heating by broadband low-frequency waves in the cusp/cleft, *J. Geophys. Res.*, *95*, 20809, 1990.

André, M., and A. W. Yau, Theories and observations of ion energization and outflow in the high latitude magnetosphere, *Space Sci. Rev.*, *80*, 27-48, 1997.

Berthelier, J. J., J. Covinhes, M. Godefroy, G. Gogly, C. Guerin, D. Roux, P. Thevenet and V. A. Gladyushev, The thermal ion mass spectrometer on board AUREOL-3: the DYCTION experiment, *Ann. Geophys*., *38*, 5, 591-614,1982.

Bosqued, J. M., H. Barthe, J. Coutelier, J. Crasnier, J. Cuvilo, J. M. Medale, H. Reme, J. A. Sauvaud and R. A. Kovrazhkin, The low energy electron and ion spectrometers on the AUREOL-3 satellite: the SPECTRO experiment, *Ann. Geophys.*, *38*, 5, 567-582, 1982.

Bouhram, M., Etude des échappements d'ions du côté jour des zones aurorales, PHD thesis, Univ. Pierre and Marie Curie, Paris, France, 2002.

Bouhram, M., M. Malingre, J. R. Jasperse, N. Dubouloz, and J. -A. Sauvaud, Modelling transverse heating and outflow of ionospheric ions from the dayside cusp/cleft. 1 A parametric study, *Ann. Geophys*., *21*, 1753, 2003*a*.

Bouhram, M., M. Malingre, J. R. Jasperse, N. Dubouloz, and J. -A. Sauvaud, Modeling transverse heating and outflow of ionospheric ions from the dayside cusp/cleft: 2 Applications, *Ann. Geophys*., *21*, 1773,2003*b*.

Carpenter, D. L. and J. Lemaire, Erosion and recovery of the plasmasphere in the plasmapause region, *Space Sci. Rev.*, *80*, 153-179, 1997

Chang, T., G. B. Crew, N. Hershkowitz, J. R. Jasperse, J. M. Retterer, and J. D. Winningham, Transverse acceleration of oxygen ions by electromagnetic ion cyclotron resonance with broadband left-hand-polarized waves, *Geophys. Res. Lett.*, *13*, 636-639, 1986.

Chappell, C. R., B. L. Giles, T. E. Moore, D. C. Delcourt, P. D. Craven, M. O. Chandler, The adequacy of the ionospheric source in supplying magnetospheric plasma, *JASTP, 62*, 421-436, 2000.

Crew, G. B., T. Chang, J. M. Retterer, W. K. Peterson, D. A. Gurnett, and R. L. Huff, Ion cyclotron resonance heated conics: theory and observations, *J. Geophys. Res.*, *95*, 3959, 1990.

Delcourt, D. C., N. Dubouloz, J. A. Sauvaud and M. Malingre, On the origin of sporadic keV ion injections observed by Interball-Auroral during the expansion phase of a substorm, *J. Geophys. Res.*, *104*, 24929, 1999.

Dubouloz, N., J. -J. Berthelier, M. Malingre, L. Girard, Y. Galperin, J. Covinhes, D. Chugunin, M. Godefroy, G. Gogly, C. Guérin, J. -M. Illiano, P. Kossa, F. Leblanc, F. Legoff, T. Mularchik, J. Paris, W. Stzepourginski, F. Vivat, and L. Zinin, Thermal ion measurements on board Interball Auroral Probe by the Hyperboloid experiment, *Ann. Geophys.*, *16*, 1070-1086, 1998*a*.

Dubouloz, N., D. Delcourt, M. Malingre, J. -J. Berthelier, and D. Chugunin, Remote analysis of cleft ion acceleration using thermal plasma measurements from Interball Auroral Probe, *Geophys. Res. Lett.*, *25*, 2925, 1998*b*.

Dubouloz N., M. Bouhram, C. Senior, D. Delcourt, M. Malingre, and J. A. Sauvaud, Spatial structure of the cusp/cleft ion fountain: a case study using a magnetic conjugation between Interball AP and the Saskatoon-Kapuskasing pair of SUPERDARN radars, *J. Geophys. Res.*, *106*, (A1), 261, 2001.

Galeev, A. A., Y. I. Galperin and L. Zelenyi, The INTERBALL project to study solar-terrestrial physics, in *Interball Mission and Payload*, edited by RKA, IKI and CNES, p. 11,Toulouse, 1995.

Gorney, D. J., A. Clarke, D. R. Croley, J. Fennell, J. Luhmann, and P. Mizera, The distribution of ion beams and conics below 8000 km, *J. Geophys. Res.*, *86*, 83, 1981.

Knudsen, D. J., B. A. Whalen, T. Abe, and A. Yau, Temporal evolution and spatial dispersion of ion conics: evidence of a polar cusp heating wall, in Solar System Plasmas in Space and Time, Geophys. Monogr. Ser., vol. 84, edited by J. L. Burch and J. H. Waite Jr., pp 163-169, AGU, Washington D.C., 1994.

Kondo, T., B. A. Whalen, A. W. Yau, and W. K. Peterson, Statistical analysis of upflowing ion beam and conic distributions at DE 1 altitudes, *J. Geophys. Res.*, *95*, 12091, 1990.

Lockwood, M., M. O. Chandler, J. L. Horwitz, J. H. Waite, T. E. Moore and C. R. Chappell, The cleft ion fountain, *J. Geophys. Res.*, *90*, 9736, 1985.

Malingre, M., N. Dubouloz, J. J. Berthelier, Y. Galperin, D. Chugunin, S. Perraut, J. A. Sauvaud, D. Delcourt and V. Stepanov, Low energy upflowing ion events at the poleward boundary of the nightside auroral oval: high altitude INTERBALL Auroral Probe observations, *J. Geophys. Res.*, *105*, 18,693, 2000.

Miyake, W., T. Mukai, and N. Kaya, On the evolution of ion conics along the field line from EXOS-D observations, *J. Geophys. Res.*, *98*, 11127, 1993.

Miyake, W., T. Mukai, and N. Kaya, On the origins of the upward shift of elevated (bimodal) ion conics in velocity space, *J. Geophys. Res.*, *101*, 26961, 1996.

Moore, T. E., R. Lundin, D. Alcayde, M. André, S. B. Ganguli, M. Temerin, and A. Yau, Source processes in the high-altitude ionosphere, *Space Sci. Rev.*, *88*, 7-84, 1999.

Norqvist, P., M. André, L. Eliasson, A. I. Eriksson, L. Blomberg, H. Lühr, and J. H. Clemmons, Ion cyclotron heating in the dayside magnetosphere, *J. Geophys. Res.*, *101*, 13179, 1996.

Peterson, W. K., H. L. Collin, M. F. Doherty, and C. M. Bjorklund, $O^+$ and $He^+$ restricted and extended (bi-modal) ion conic distributions, *Geophys. Res. Lett.*, *19*, 1439-1442, 1992.

Pollock, C. J., M. O. Chandler, T. E. Moore, J. H. Waite, C. R. Chappell and D. A. Gurnett, A survey of upwelling ion event characteristics, *J. Geophys. Res.*, *95*, 18,969, 1990.

Robineau, A., Modélisation du transport parallèle du plasma ionosphérique: etude de mécanismes d'extraction à haute altitude, *Thèse Université Paris 6*, 1992

Roux, D., J. J. Berthelier, V. A. Gladyshev, L. V. Zinin, V. D. Maslov and M. L. Pivovarov, in *Proceedings of the results of Project ARCAD-3*, 381-390, ed. Cepadues, 1984.

Sauvaud, J. -A., H. Barthe, C. Aoustin, J. -J. Thocaven, J. Rouzaud, E. Penou, D. Popescu, R. A. Kovrazhkin, and K. G. Afanasiev, The ion experiment onboard the Interball-Aurora satellite; initial results on velocity-dispersed structures in the cleft and inside the auroral oval, *Ann. Geophys.*, *16*, 1056-1069, 1998.

Schunk, R. W., Theoretical developments on the causes of ionospheric outflow, *JASTP, 62*, 399-420, 2000.

Shelley, E. G., W. K. Peterson, A. G. Ghielmetti and J. Geiss, The polar ionosphere as a source of energetic magnetospheric plasma, *Geophys. Res. Lett.*, *9*, 941-944, 1982.

Whitteker, J. H., The transient response of the topside ionosphere to precipitation, *Planet. Space Sci.*, 25, 773, 1977.

Zinin, L. V., Yu. I. Galperin and K. S. Latyshev, Field-aligned motions of $O^+$ and $H^+$ thermal ions in a magnetic fild tube convected across the dayside polar cusp: model calculations, In: Results of the ARCAD–3 project, CNES, CEPADUES-EDITIONS, Toulouse, France, 1985, p. 409-416.

# Polar wind observations on the INTERBALL-2 satellite

D. V. Chugunin[1], L. V. Zinin[2], and N. Dubouloz[3]

[1] Space Research Institute, Russian Academy of Sciences,
Profsoyuznaya ul. 84/32, Moscow, 117810 Russia,
[2] Kaliningrad State University, Kaliningrad, Russia,
[3] Laboratoire de Physique et Chemie de l'Enviroment/Observatoire de Nancay, Orleans, France.

**Abstract.** Results of measurements are presented of ionospheric ions fluxes in the nightside polar cap at an altitude of about 20,000 km. The data were obtained with the HYPERBOLOID instrument onboard the INTERBALL-2 satellite. Passages without intense precipitation of magnetospheric ions and electrons were selected using the ION instrument data, so observations of ionospheric ion fluxes caused by heating in the auroral region were excluded. In addition, an attempt was made to exclude observations of the "cleft ion fountain" from the analysis. Measurements in the summer and winter seasons (when the ionosphere was totally sunlit and completely shadowed, respectively) are considered separately. By analyzing the distribution functions of the measured fluxes, we have separated six different types of ionospheric plasma outflows in the polar cap. A strong distinction is revealed between summer and winter flows. In winter, only weak flows of $H^+$ ions were detected. In the summer period, we detected both $H^+$ and $O^+$ ions. Flux values of ionospheric ions are found to be strongly dependent on the intensity of the polar rain. The measurements are compared to existing models of the polar wind. The best models (for the description of our measurements) are indicated. After the choice of measurement periods, the resulting region coincides with the ion depletion zone (IDZ). Based on earlier measurements by the Akebono satellite, nothing could be said about the fluxes of the thermal ions in this zone, either because of the sensitivity of the instrument aboard this satellite, or because of the positive satellite potential.

## 1. Introduction.

The process known as the polar wind consists of plasma flowing out of the ionosphere (where the plasma pressure is sufficiently high) and up along high-latitude magnetic field lines into the magnetosphere (where plasma pressure is extremely low). According to the classical theory [*Dessler and Michel*, 1966; *Banks and Holzer*, 1968], the thermal energy of ions and electrons in the ionosphere is the source of energy for the polar wind. This means that ions move upwards, solely due to the pressure gradient, along a magnetic flux tube. This gradient acts against the gravity force. When the ionosphere temperature is about 1,000º K, only light ions, such as $H^+$ and $He^+$, are capable of overcoming the gravity barrier and escaping from the ionosphere (this process is similar to the gas-dynamic acceleration of particles in the Laval nozzle). As for heavier ions ($O^+$ and others), the particles forming the core of their velocity distribution function remain in the ionosphere and only the ions from the distribution function tail or the ions heated (accelerated) by some additional energy sources can overcome the gravity barrier [*Dessler and Michel*, 1966]. Next, it was shown that light ions reach supersonic velocities at sufficiently low altitudes [*Banks and Holzer*, 1968].

However, the thermal plasma measurements carried out mainly by the DE-1 and AKEBONO satellites showed a large number of $O^+$ ions at high altitudes above the polar cap [*Gurgiolo and Burch*, 1982; *Abe et al.*, 1993], the density of $O^+$ ions being sometimes even higher than that of $H^+$ ions.

This fact contradicted the classical theory of the polar wind. Some attempts were made to find ways of heating or accelerating heavy ions (such as $O^+$) and molecular ions. In order to describe this phenomenon, various hydrodynamic and semi-kinetic models were constructed, as were models of the "particle in a cell" type. They took into consideration such mechanisms as centrifugal acceleration of ions, parallel acceleration due to the curvature of magnetic field lines and convection, and the growth of the ambipolar electric field when suprathermal electrons appear in a field tube [*Tam et al.*, 1995; *Wilson et al.*, 1997; *Khazanov et al.*, 1997; *Su et al.*, 1998*a*].

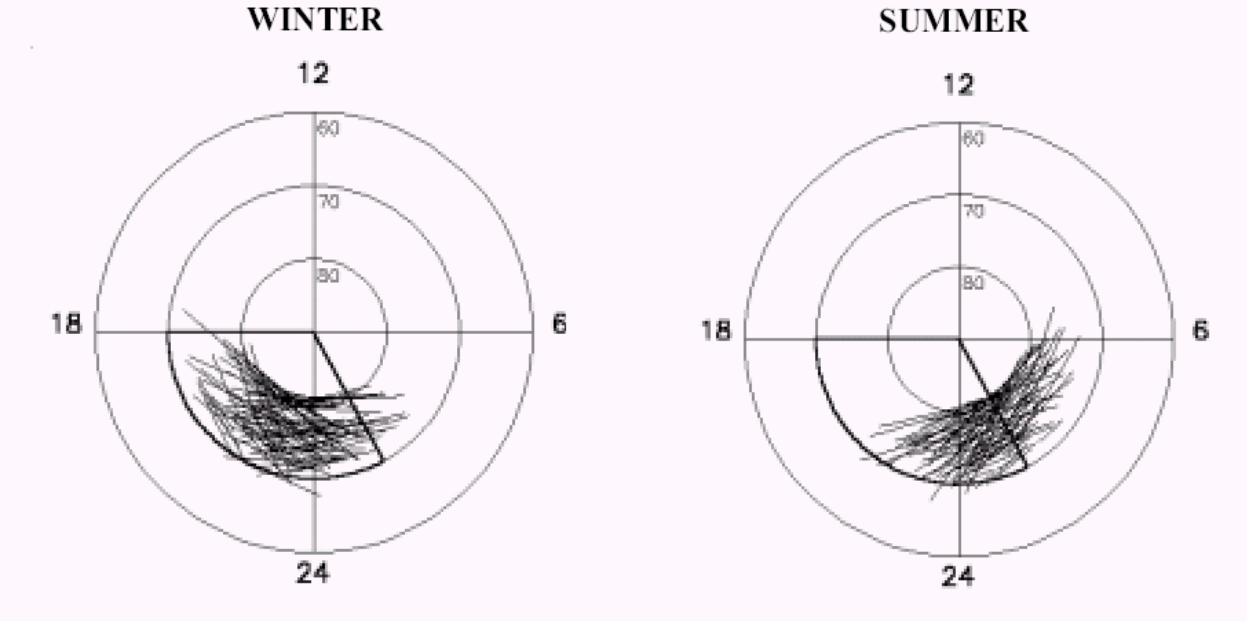


**Figure 1.** Projections of trajectories of the INTERBALL-2 satellite orbits for time intervals selected for the analysis in coordinates of invariant latitude–MLT. The sector traced by a heavy line corresponds to the ion depletion zone as measured by the AKEBONO satellite.

Recent measurements with the POLAR satellite have also shown the $O^+$ ions to be almost permanently present at altitudes of up to $8R_E$ over the polar cap (see [*Su et al*., 1998b; *Elliott et al*., 2001]).

After analysis of measurements of ascending flows of $O^+$ ions it was found that $O^+$ ions measured by the POLAR satellite in the polar cap most likely have the cusp/cleft as a source. In other words, they are not produced by the polar wind effect in the polar cap topside ionosphere.

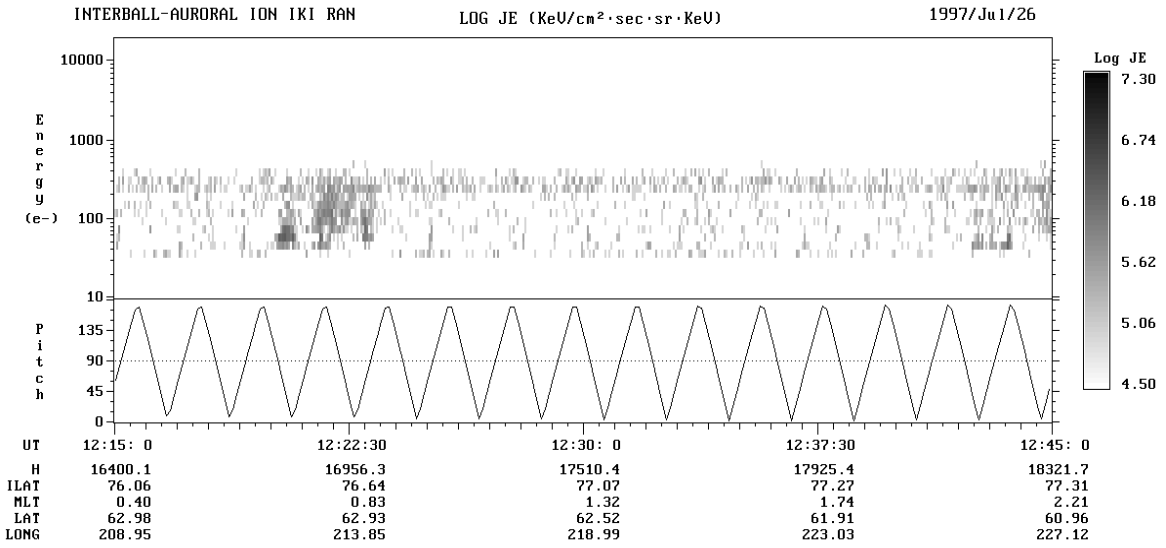


**Figure 2.** Electron measurements by the ION instrument on July 26, 1997. The scale of gray represents the measured flux. One can see that the measurements correspond to the polar cap.

One can distinguish several types of ionospheric ion outflow, and only one of them is caused solely by the polar wind mechanism. First, this is an outflow in the region of auroral currents and fields (mainly, in the auroral oval), where the bulk of the kinetic energy of suprathermal $O^+$ and other ions is transformed from the field-aligned currents of a magnetospheric origin by way of wave–particle interactions. This energy can also be provided by the electric potential difference along a magnetic flux tube, which, in turn, is caused by the field-aligned current.

The second mechanism is the "cleft ion fountain," where small-scale field-aligned currents are observed, as well as a direct penetration of energetic particles from the magnetosheath. This leads to generation of intense conical beams (conics), which are heated in the transverse velocity component by wave–particle interactions. Suprathermal ions of the "ion fountain" drift to the polar cap due to magnetospheric convection, if the $B_z$ component of the interplanetary magnetic field (IMF) is negative or is less than a few nanotesla. It is a mechanism that was considered to interpret the *POLAR* satellite measurements [*Su et al*., 1998*b*; *Elliott et al*., 2001].

Finally, the third mechanism is the polar wind mechanism proper, by which we mean, as in [*Dessler and Michel*, 1996], an outflow of thermal ionospheric ions along open field lines over the polar cap. This process is supported only by the thermal energy of the ionospheric ions and electrons; i.e., it proceeds without field aligned currents and particle precipitation, except for photoelectrons and polar rain electrons (if this rain takes place). Some use terminology in which different types of ion outflow from the polar ionosphere are not distinguished. In such cases, any outflow of the ionospheric ions upward to the polar cap is referred to as the polar wind, although the underlying processes are physically different and have different sources of energy. Hence, the ion composition, altitude behavior, and localization of sources are also different for these processes. This mixture of physically different ion fluxes with different morphology is not always justified, but it can occur at any observation point, so that the experimental separation of these fluxes is a considerable problem. In this paper, an attempt is made to separate these different types of measured ascending ion flows to determine the conditions and events of measuring the "pure" polar wind, and then to carry out an analysis of the action of this mechanism.

For studying the polar wind, it is necessary to separate the above-described different sources of suprathermal ionospheric ions at high altitudes. In previous studies of the polar wind, no attempts were made to clearly distinguish the ions accelerated in the "cleft ion fountain" from the polar wind effect. The main reason is the criteria selected for isolating the area in space where the polar wind can be observed. Usually, all types of high-latitude ion flows (invariant latitudes >~75°–80°) have been considered together [*Chandler et al*., 1991; *Abe et al*., 1996]. The data were not classified according to presence or absence at a given point of field-aligned currents and/or energetic particles, using the results of simultaneous measurements.

In this case, studying the fluxes of ionospheric ions one can easily mistake the auroral flows of suprathermal ionospheric ions for polar wind effects. Another problem is to take account of the conditions of ion transport by convection through the polar cap from their source in the cusp/cleft at high latitudes (over 75°). This process is a source of intense flows of ionospheric ions (in particular, $O^+$ ions), but the IMF vector determines it.

The confusion of fluxes of the "ion fountain in the cusp" and conics with the polar wind effects takes place especially often for high-altitude measurements on the dayside. The data presented in *Gurgiolo and Burch* [1982] give an example of this. The authors presented the first observation of the supersonic polar wind. Then, in *Nagai et al*., [1984] and *Horwitz* [1984] it was supposed that they measured mainly ion streams from the cusp that drifted by convection into the polar cap. At the same time, in *Green and Waite* [1985] an attempt was made to show that in both the cases the "cleft ion fountain" was measured. However, it is fairly possible that the polar wind effects were also present in these measurements.

As a result of more detailed analysis of outflowing thermal ions measured by the *AKEBONO* satellite [*Yau et al*., 1984; *Abe et al*., 1996], it was found that ion streams drifting from the cusp could influence derived characteristics of the polar wind, but it was suggested that the polar wind ions dominate at high latitudes. It should be emphasized that, since the SMS spectrometer onboard AKEBONO measured ions up to an energy of 3 KeV, the appearance of strongly accelerated or heated ions was taken into account in the data analysis.

From the above short review of the problems of measuring ions ouflowing from the polar ionosphere, it is clear that it is necessary to analyze the measurements of polar wind effects, comparing simultaneous measurements of energetic particles and thermal plasma, so that ions transported by convection to the polar cap from the "cleft ion fountain" and the suprathermal ions accelerated in the auroral oval can be separated from the polar wind effects. This paper is our step in a detailed analysis of ionospheric ion fluxes in the polar cap.

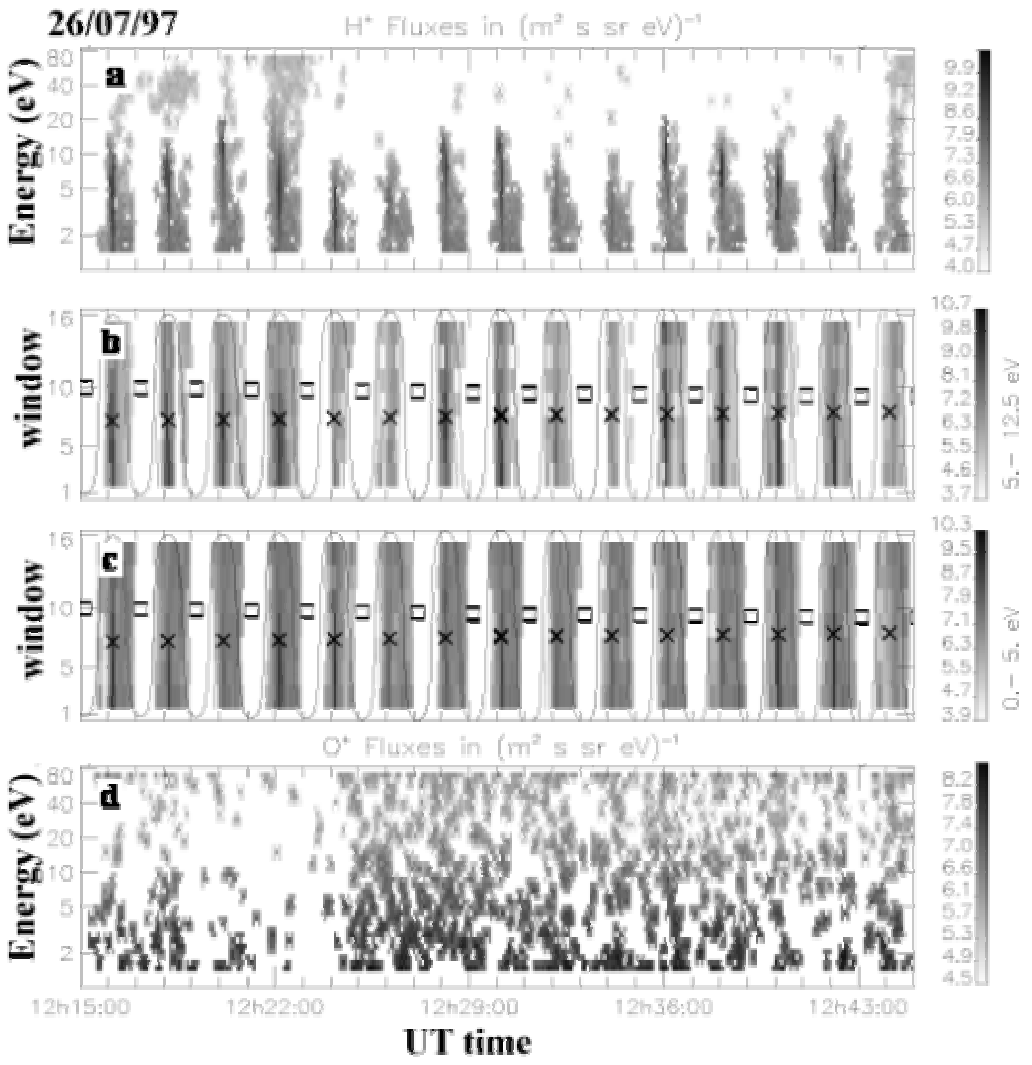


**Figure 3.** Measurements by the HYPERBOLOID instrument on July 26, 1997. Panels (a) and (d) present energy–time spectrograms of $H^+$ and $O^+$ ions, respectively. The data were averaged over all angular detectors. One can see that the measurements of $O^+$ ions contain only background noise. Panels (b) and (c) present the pitch-angle distribution of $H^+$ ions averaged over two energy ranges. The intensity of gray represents the ion flux $F$ ($cm^2$ s sr eV)$^{-1}$. A two-minute modulation caused by the satellite rotation is clearly seen. The beams of $H^+$ ions are narrow (low temperature) and directed away from the Earth. These fluxes are classified as type 1.

## 2. Data analysis

For studying the polar wind, we used data from the energy-mass-angle spectrometer HYPERBOLOID installed onboard the INTERBALL-2 (Auroral Probe) satellite. One can find a description of the experiment in [*Dubouloz et al.,* 1998]. The HYPERBOLOID instrument allows the three-dimensional distribution function to be measured for basic ions $H^+$, $He^+$, $O^{++}$, and $O^+$ in the energy range from ~1 to 80 eV (evidently, the lower energy threshold is determined by the satellite potential, which usually did not exceed +10 V). A complete 3D distribution function was measured for one period of revolution equal to 2 min. The INTERBALL-2 orbit with an apogee at altitudes of about $3R_E$ and an angle of inclination of 62.8° allowed it to reach the maximum invariant longitude of ~81°. The summer and winter seasons of 1996/1997 were chosen for the analysis. The periods of measurements were classified according to the zenith angle of the Sun at the altitude of

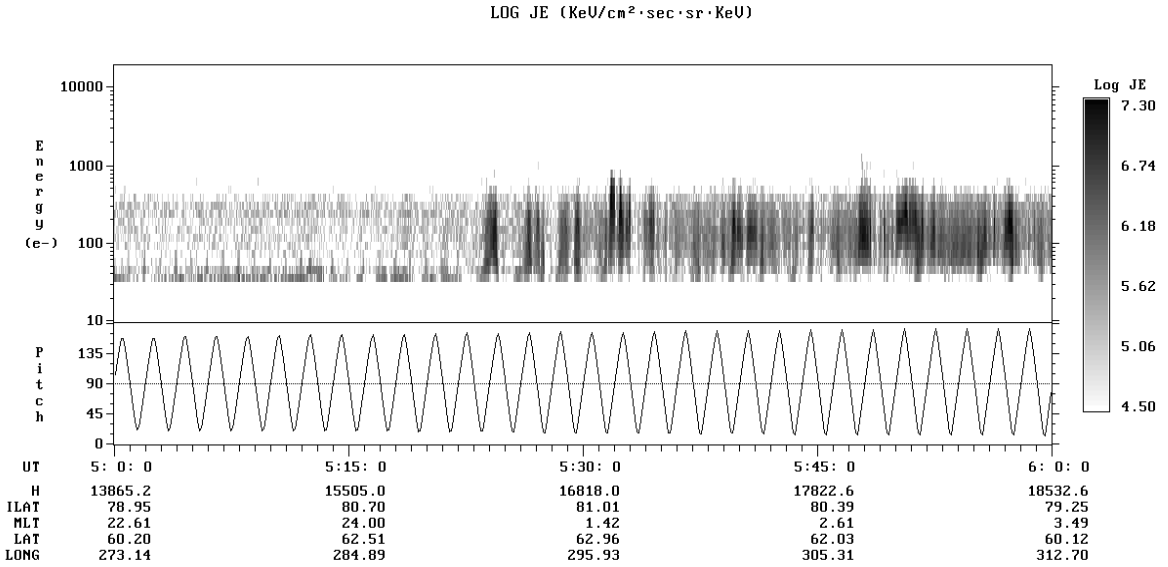


**Figure 4.** Electron measurements by the ION instrument on August 10, 1997. One can see that at 05:24 UT the flux of electrons increased ("electron rain" turned into "electron shower").

the underlying F-layer. Thus, we selected measurement intervals when the northern polar ionosphere was either completely sunlit or totally shadowed. This corresponds to two different situations in the ionosphere, which is the source of the polar wind. In one case, suprathermal photoelectrons are present in magnetic flux tubes, which considerably amplify the ambipolar electric field, the density of ions in the F-layer being large and their temperature being higher than in winter. In the second case, photoelectrons are practically absent and the density and temperature of ions in the F-layer are significantly lower. These factors are of key importance for the polar wind mechanism.

For the analysis, we have selected orbits when the satellite crossed "open" field lines above the polar cap. "Open" lines here mean that they have no intense precipitation of particles from the plasma sheet, so that only small intensities of electrons with energies not exceeding 400 eV can be observed (thus, the cusp/cleft flux tubes were excluded from the analysis). According to [*Winningham and Heikkila*, 1974], such weak streams of electrons over the polar cap correspond to the "polar rain" or "polar showers" with a source in the distant magnetotail or in the interplanetary space. This was done in order to exclude the ionosphere ions produced by other physical mechanisms from the analysis and to separate the polar wind effects from the ionosphere ions heated and/or accelerated by wave–particle interactions, which are related to the presence of energetic ions and electrons in the regions of the auroral zone with field-aligned currents. To this end, we have analyzed the data of the ION particle spectrometer [*Sauvaud et al*., 1998] for all selected orbits. Only those time intervals when either there were no energetic particles or when only electrons with energies of no more than 400 eV were detected were selected for the analysis.

In addition, we also tried to exclude intervals with overlapped thermal and suprathermal ions that convected into the polar cap from the region of the "cusp/cleft ion fountain".

All time intervals when crossing the cusp/cleft that had a typical velocity ion-dispersion with low energies propagating into the polar cap were excluded. Of course, in this case one cannot be sure that ion fluxes in the polar cap produced by various mechanisms of additional heating and acceleration were completely eliminated from the dataset. However, the data were at least substantially cleaned, which is important for more reliable isolation of the ionospheric flows in the polar cap caused by the polar wind effects.

We have used the data from measurements for the period of October 1996 to November 1997. The numbers of intervals selected by the method described above are, respectively, 141 and 90 for the winter and summer periods. The difference is caused by the fact that in the summer season the number of orbits crossing the cusp region was much larger. Projections onto the ionosphere of orbit segments for the selected intervals are shown for the winter and summer periods in Figures 1*a* and 1*b*, respectively.

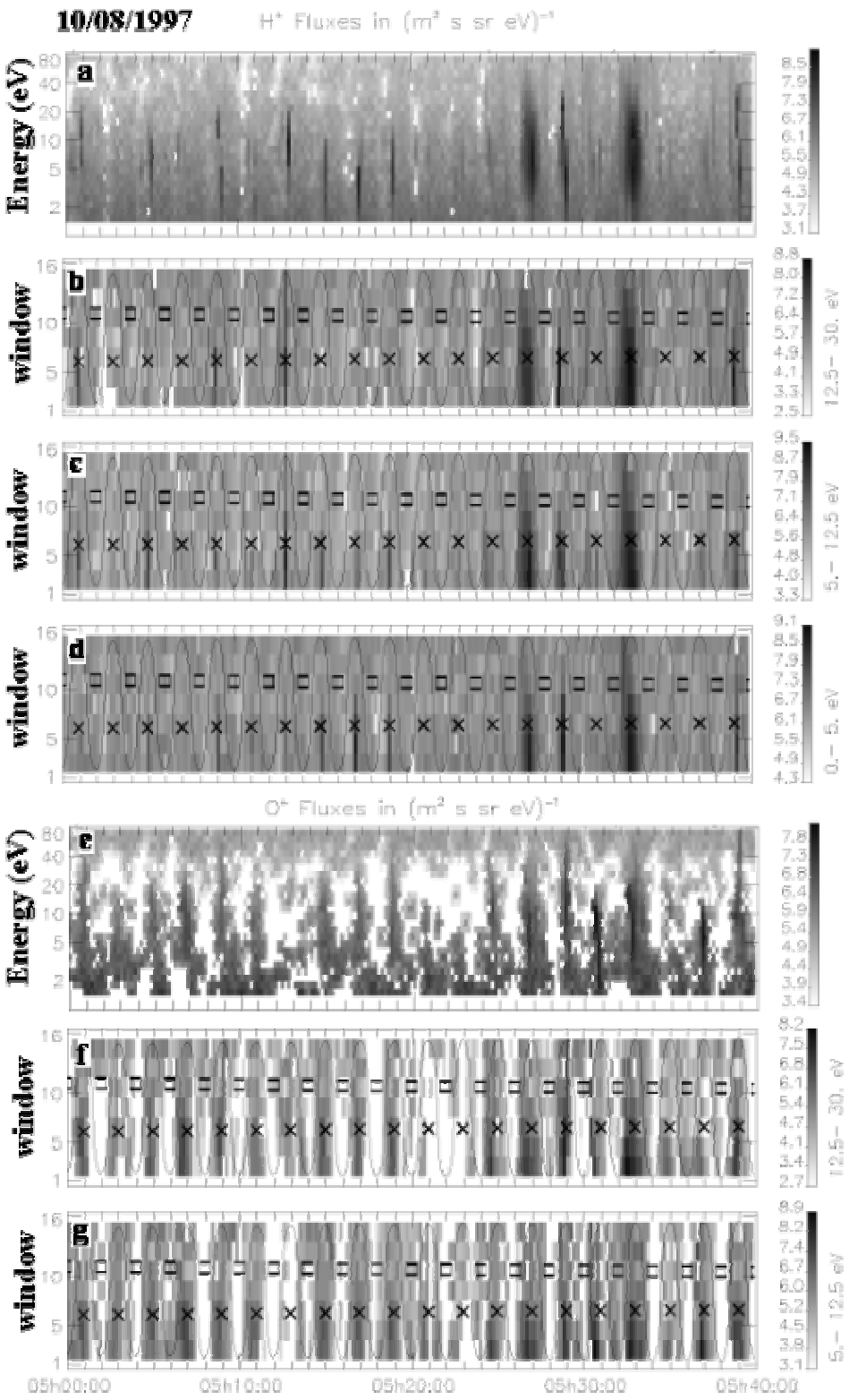


**Figure 5.** Measurements by the HYPERBOLOID instrument on August 10, 1997. Panels (a) and (e) present energy–time spectrograms of $H^+$ and $O^+$ ions, respectively. Panels (b), (c), and (d) present the pitch-angle distribution of $H^+$ ions averaged over three energy ranges. Panels (f) and (g) show the pith-angle distribution of $O^+$ ions averaged over two energy ranges. Before 05:24 UT the fluxes of ions are classified as type 2 and after that as type 6.

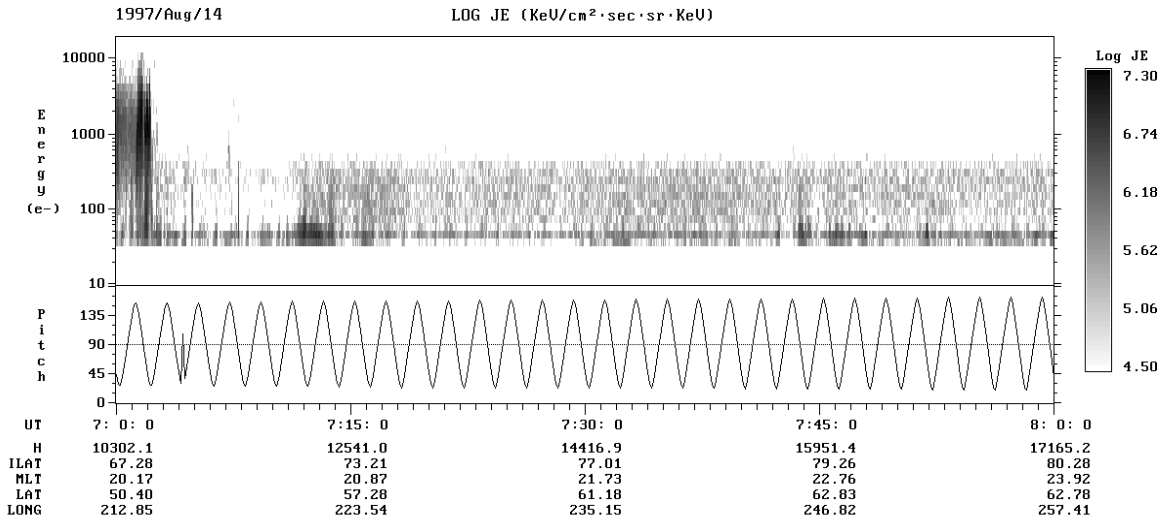


**Figure 6.** Measurements of electrons by the ION instrument on August 14, 1997.

As expected, the selected orbit segments turned out to be located on the nightside of the polar cap. Unfortunately, the polar cap coverage by satellite passages is not identical in summer and winter: the summer region observation is somewhat displaced to the morning sector as compared to the winter region. Nevertheless, there is a considerable overlapping of these regions in the near-midnight sector. We assume that this circumstance has introduced no significant errors into the results of our investigation.

As said above, the HYPERBOLOID instrument measured $H^+$, $He^+$, $O^{++}$, and $O^+$ ions. We consider here only the $H^+$ and $O^+$ ions, since the $He^+$ and $O^{++}$ ions were not measured permanently. As a result of our analysis, all measurements were classified into six characteristic types of ion streams measured in the polar cap. They are described below.

***Type 1.*** The first type corresponds to relatively cold, ascending fluxes of $H^+$ without any presence of $O^+$ ions. An example of measurements of this type is shown in Figures 2 and 3. Figure 2 shows the simultaneous measurements of energetic electrons (the ION instrument). One can see from the data that the time of measurements corresponds to polar cap passage. The energy–time spectrogram for $H^+$ ions averaged over all directions of measurements of the HYPERBOLOID spectrometer (160° × 5°) is shown in panel 3a. Panel 3d gives the same spectrogram for $O^+$ ions. It is obvious from these two spectrograms that only $H^+$ ions are detected. Panels 3b and 3c present the pitch-angle distribution of $H^+$ ions averaged over two energy intervals. The window number (direction of measurement) is plotted along the ordinate axis, reckoned from the window nearest to the solar direction. Crosses show the direction antiparallel to the magnetic field vector, i.e., the direction where the detected ion flux propagates upward from the Earth (in the northern hemisphere, where the measurements were carried out). Squares show the direction parallel to the magnetic field vector, i.e., the direction where the detected flux moves toward the Earth in the northern hemisphere.

The solid line shows where the inlet aperture of the window is directed perpendicular to the magnetic field; i.e., the pitch-angle is equal to 90°. A two-minute modulation clearly seen in the measurements is due to the satellite's rotation about its axis. Thus, the narrower the beam, the colder it is in the transverse component. The density of hydrogen ions derived from the moments of the distribution function varies from 0.2 to 1.5 $cm^{-3}$. Their directional velocity $V_\parallel$ changes from 26 to 40 km/s, the temperature $T_\parallel \sim$ 2000–6000 K, and $T_\perp$ is, as a rule, less than $T_\parallel$. It should be noted that the measurement of ions with such low energies is very difficult at low densities. The satellite, when illuminated by the Sun, is always charged positively in rarefied plasma due to the outflow of suprathermal photoelectrons. This prevents low energy ions from the reaching a detector. Trajectories of ions that overcame the potential barrier are changed, and corresponding corrections to measurement data are especially significant for ions with energies close to the satellite potential. This potential is higher in the regions with low plasma density, i.e., precisely over the polar cap, where the measurements in which we are interested were made.

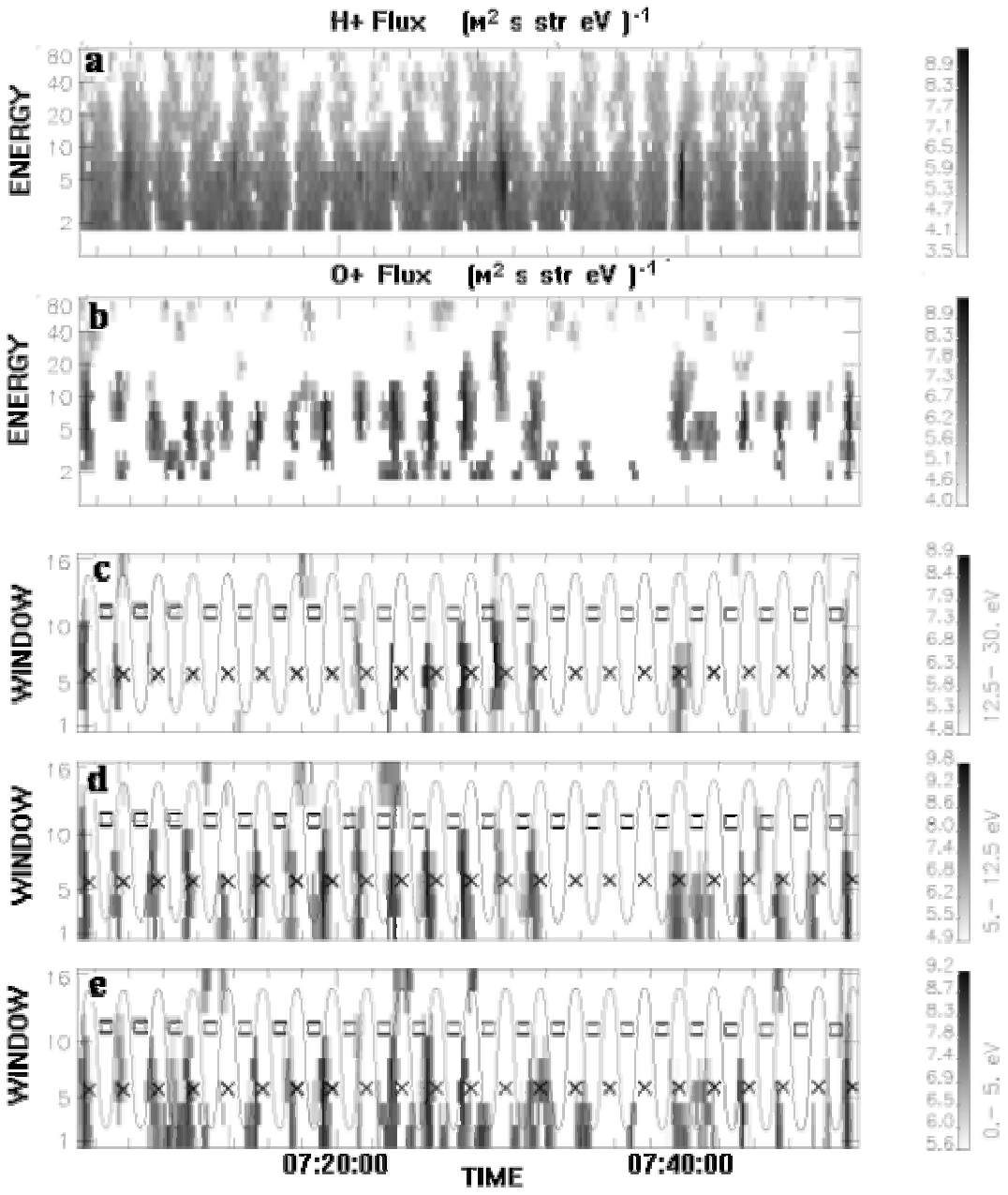


**Figure 7.** Measurements of the HYPERBOLOID instrument on August 14, 1997. Panels (a) and (e) present energy–time spectrograms of $H^+$ and $O^+$ ions, respectively. Lower, the pitch-angle distribution of $O^+$ ions are presented averaged over three energy ranges. At 07:30 UT one can see the dispersion of $H^+$ and $O^+$ ions in velocities. These streams are classified as type 3.

Sometimes, it reached 8–10 V here. Therefore, the density values given below and especially the higher moments of the distribution function are very preliminary estimations. In *Zinin et al*. [1998] and *Hamelin et al*. [2002] some calculations of the distribution functions modified by the electric field of the Langmuir layer around the spacecraft were made, but the technique for correcting distribution functions using these calculations is not elaborated sufficiently.

***Type 2.*** We classified as type 2 those measurements in which $H^+$ ions have the same characteristics as for type 1, but in which ascending fluxes of $O^+$ ions are also present. Figure 5 presents measurements that correspond to type 2 in the time interval from 05:00–05:25 UT.

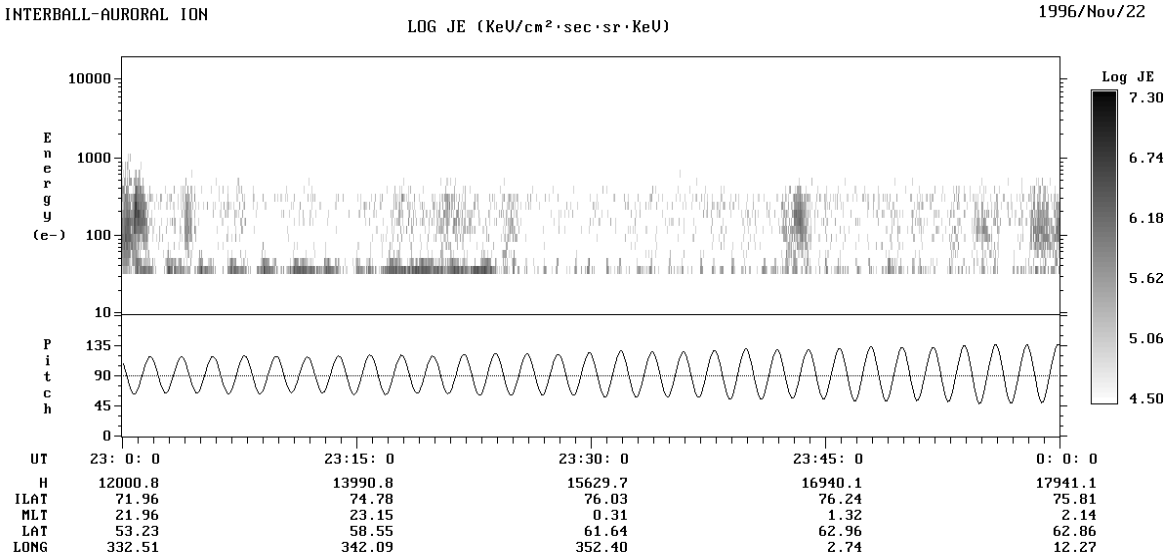


**Figure 8.** Measurements of electrons by the ION instrument on November 22, 1996.

Simultaneous measurements of energetic electrons are presented in Figure 4. Panel 5a shows the energy–time spectrogram for $H^+$ ions averaged over all 16 windows of the HYPERBOLOID spectrometer. Panels 5b–5d demonstrate the pitch-angle distribution of $H^+$ ions averaged for three energy ranges. Panel 5e presents the energy–time spectrogram for measurements of $O^+$ ions. Spectrograms 5f and 5g show the pitch-angle distribution of $O^+$ ions for two energy ranges. The density of $O^+$ ions is estimated as 0.1 $cm^{-3}$ and lower, the parallel velocity varies from 5 to 9 km/s, and the temperature of $O^+$ ions is higher than the hydrogen ions.

***Type 3.*** Examples of measurements that were classified as type 3 are presented in Figures 6 and 7. As in previous cases, Figure 6 shows the measurements of energetic electrons. Panels 7a and 7b give the energy–time spectrograms for measurements of $H^+$ and $O^+$ ions, respectively. Other spectrograms (**c – e**) present the pitch-angle distribution for $O^+$ ions. This type of ion flux is characterized by the fact that the density of $O^+$ ions is larger than that of $H^+$ ions. Rather often, the measured fluxes of $H^+$ ions are very weak and even disappear in the background noise. In cases when the fluxes of $H^+$ ions are clearly detected, ion velocity dispersion is observed. The $H^+$ ions appear with an increase of the mean energy of the $O^+$ ions, the energy of $H^+$ being less than that of $O^+$ (see, for example, 07:30 UT). In comparison with type 2 fluxes, $O^+$ ions of type 3 have a larger velocity perpendicular to the magnetic field; i.e., the velocity of convection is pretty high in this case. One can easily see this by comparing Figures 7*c*–7*e* and Figures 5*f* and 5*g*. In Figure 7, the beams of $O^+$ ions are strongly displaced from the field-aligned motion (×), which is indicative of fast convection. Fluxes of ions of type 3 are often observed in these regions with an enhanced flux of electrons (see Figure 6).

***Type 4.*** There are many intervals of measurements when only $H^+$ ions were observed, but their densities were very low and the temperature was much higher than in the type 1 fluxes. An example of measuring a type 4 flux is shown in Figure 9 (23:05–23:25 UT). Panels 9b–9d present pitch-angle spectrograms of $H^+$ ions for various energy ranges. Panels 9d and 9b demonstrate energy–time spectrograms for $H^+$ and $O^+$ ions. Figure 8 gives simultaneous measurements of electrons.

***Type 5.*** In Figure 9, beginning from 23:24 UT the data contain only noise, while the electron density calculated through the dependence of a satellite potential on density [*Torkar et al.*, 1999] would be above the threshold of detection for the HYPERBOLOID instrument if the satellite potential were equal to zero. We have classified such measurements as type 5. Nevertheless, a two-minute modulation of the noise is observed very frequently. One possible cause of this modulated noise could be UV emission.

A satellite always has some nutation; and at large angles of deviation of its rotation axis from the Sun's direction, UV emission can hit an edge of the instrument aperture. However, its sensitive detecting part is very well-protected against such illumination.

To check this hypothesis, we have compared the measurements at large and small amplitudes of nutation. No direct dependence of the noise modulation on the

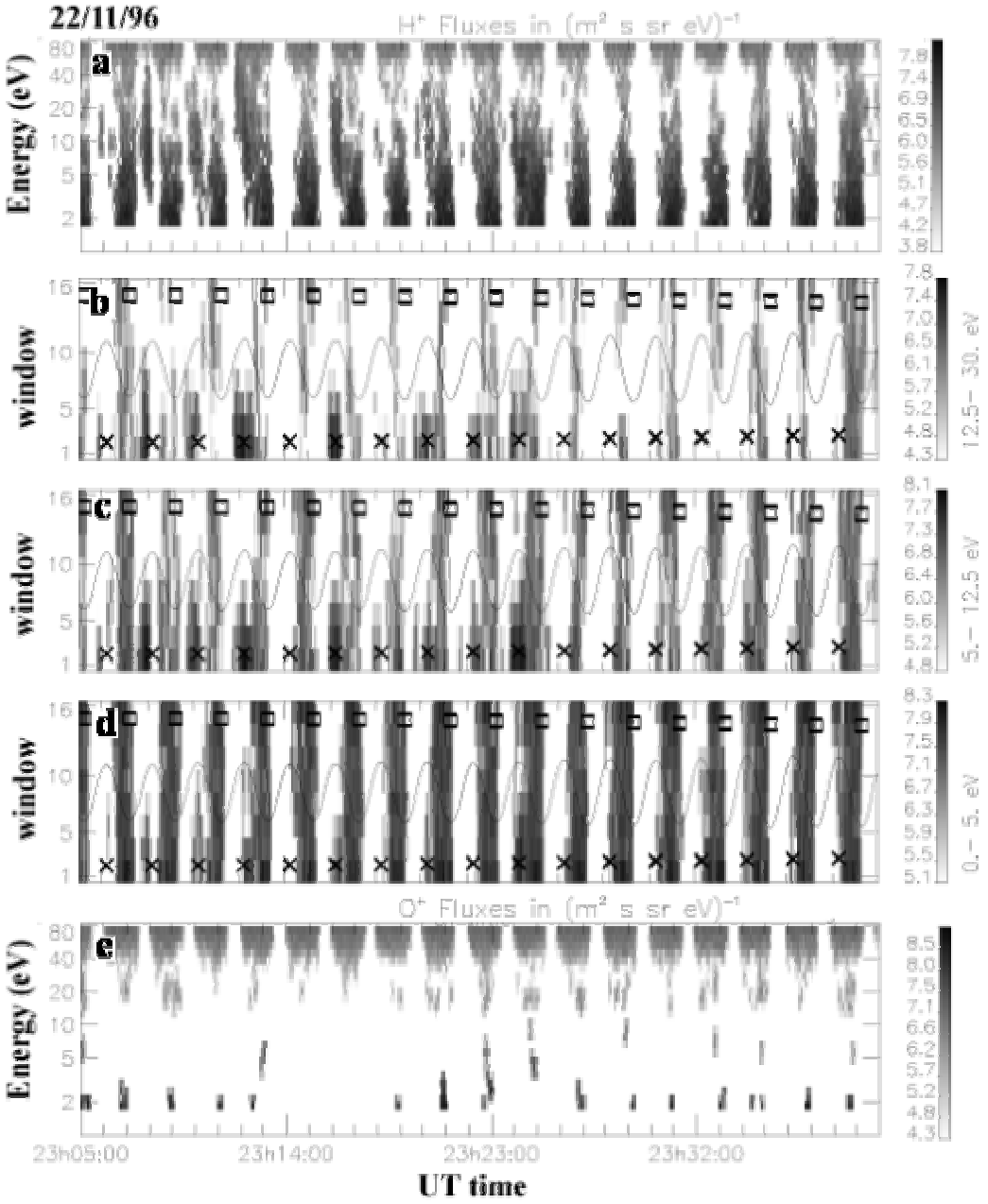


**Figure 9.** Measurements of the HYPERBOLOID instrument on November 22, 1997. Panels (a) and (e) present energy–time spectrograms of $H^+$ and $O^+$ ions, respectively. Panels (b), (c), and (d) present the pitch-angle distribution of $H^+$ ions averaged over three energy ranges. At the time interval 23:05–23:25 UT the streams of ions are classified as type 4 (weak fluxes of $H^+$ ions). After 23:05 UT only the instrument noise is observed; these streams are classified as type 5.

satellite axis' angle of deviation from the Sun's direction was found; i.e., the above hypothesis was rejected. Penetrating high-energy particles and cosmic rays are another possible cause of the noise. However, when the instrument was designed and installed, all necessary measures were taken to reduce the role of this factor.

All the above events were accompanied by a relatively high positive potential of the satellite (~5–10 V) and, hence, by a low plasma density. Therefore, the most plausible explanation presents a combination of the effect of a satellite potential and the asymmetry of the Langmuir layer at low temperature on the intensity of

ions reaching the instrument. In *Hamelin et al*. [2002], possible trajectories of the ions that can hit the HYPERBOLOID detector at a large Debye-length were calculated taking the satellite potential into account. In these calculations, a model electric field around the satellite in a vacuum was taken with the model of an equipotential satellite being close to reality. It was found that the particles that could not reach the detector for a spherical geometry of the electric field are able to hit the detectors. The low energy background of the instrument and its two-minute modulation are explained by this effect.

***Type 6.*** An example of this last type of ion fluxes is shown in Fig. 5 from 05:25 UT. A relatively high energy and high temperatures of ion beams characterize this type. The characteristics of suprathermal ions are similar to those observed in the auroral region except for the absence of energetic particles. It is obvious that these ions must have previously endured considerable heating/acceleration at lower altitudes.

All measurements of ascending ion fluxes at selected orbit segments were classified into the above six types. The events when, in addition to noise, well pronounced fluxes were observed for less than 3 min were qualified as type 5.

## 3. Discussion

Figures 10*a* and 10*b* present the number of selected passages at various levels of magnetic activity (*Kp* index) separately for winter and summer seasons. It follows from these statistics that almost all of the selected events are related to low levels of magnetic activity. Most likely, this is due to the fact that the probability of crossing the polar cap at a high magnetic activity level was small for the INTERBALL-2 satellite. During magnetic disturbances, precipitation of energetic particles was often observed in the polar cap up to 80° of invariant latitude and such passages were excluded from the analysis. Therefore, Figures 10*c* and 10*d* present the number of intervals of measuring various types of fluxes summarized over all *Kp* values.

A fundamental difference between winter and summer seasons is seen from Figures 10*c* and 10*d*. In the summer time, most measured fluxes belong to type 2, while for more than 50% of the events in the winter period one cannot find in the data any ion fluxes above background. This can probably be explained by the fact that in the dark and cold polar cap there are no photoelectrons at ionospheric altitudes. As a result, the ambipolar electric field is much weaker than over the sunlit ionosphere (in summer). In addition, there are significantly fewer particles in the distribution function tail that are capable of overcoming the potential barrier of the Langmuir layer. Both these factors reduce the plasma density at satellite altitudes and the velocities of the polar wind flux. Thus, the plasma density and ion energy at altitudes of ~20,000 km over the polar cap turn out to be so small that the satellite potential (equal to approximately 8 V) prevents one from measuring this low-energy ion flux. Therefore, in the winter period the plasma density at altitudes of ~3$R_E$ is small, the satellite potential is high, and only a small part of the ion distribution function can reach the detector.

Indeed, in cases when one observes fluxes of $H^+$ ions in the detector, their density, calculated by using the zero moment of the distribution function for ions having reached the detector, turns out to be very small, on the order of 0.01 $cm^{-3}$ (while, according to *Torkar et al.* [1999], the electron density corresponding to a potential of 8 V is equal to ~1 $cm^{-3}$) and the temperature of ions is higher than that obtained in summer measurements. Simultaneous wave measurements [*Burinskaya et al*., 2000] show the plasma frequency to be equal to approximately 10 kHz, which corresponds to a density of ~1 $cm^{-3}$. This confirms that the main part of the ion distribution function cannot reach the detector so that the instrument measures only ions from the distribution function tail. An analysis was made of the potential difference measured between the satellite and a probe placed at a distance of 15 m from the spacecraft. This potential difference was found to be equal to about 6 V. Under these conditions, the order of the Debye length is estimated as 10 m. Thus, the measurements with the RON-IESP-2 instrument [*Torkar et al*., 1998] give no total value of the satellite potential with respect to the ambient plasma. However, even at a potential of 6 V, the velocity of $H^+$ ions, with which they can overcome the potential barrier, should exceed 35 km/s. One can conclude from all the above that in the dark (winter) polar cap, according to HYPERBOLOID measurements corresponding mostly to type 5 fluxes, the polar wind density is about 1 $cm^{-3}$ and the velocity along the magnetic field is less than 30 km/s. Thus, all available data confirm the conclusion that, under these conditions, the bulk of the polar wind ions cannot reach the detector mounted aboard the satellite.

For the summer season, there are no wave measurements available to independently derive the plasma density. Therefore, thus far we cannot compare the plasma density calculated from the HYPERBOLOID data with the density derived from plasma frequency measurements. The potential difference between the probe and the satellite was ~2–4 V, which correspond to larger plasma densities, ~1.5–2 $cm^{-3}$, as follows from the calculated dependence of the spacecraft potential on the surrounding plasma density by *Torkar et al*. [1999].

In order to verify the above ideas about the seasonal difference in measurements, we used a model of measurements with the HYPERBOLOID instrument depending on the potential of its body with respect to the

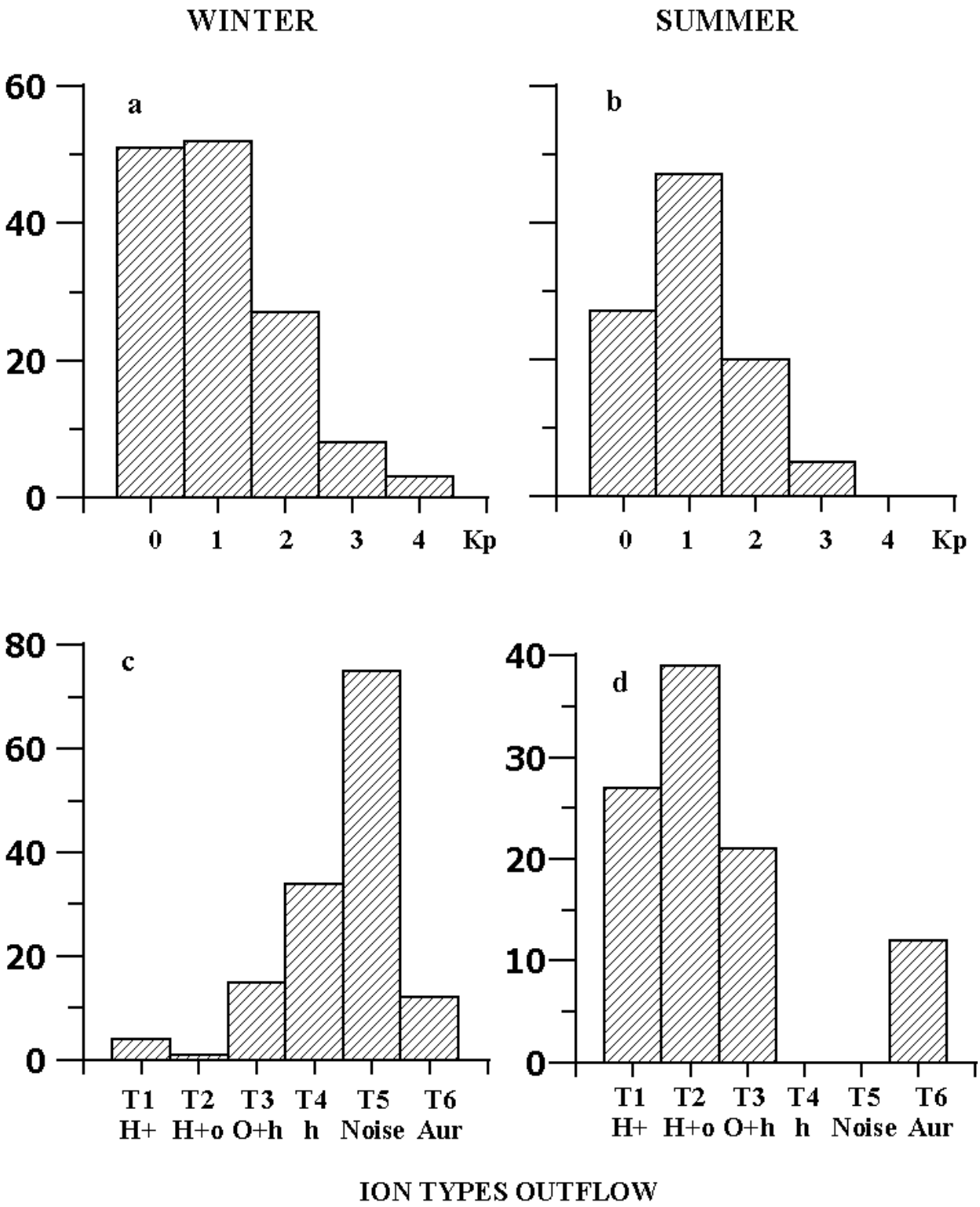


**Figure 10.** a) and b) present the number of selected passages at various levels of magnetic activity (*Kp* index) separately for the winter and summer seasons. c) and d) present the number of intervals of measuring various types of fluxes summarized over all *Kp* values. For clarity the flux types were also marked by letters. **H** and **h** are intense and weak $H^+$ flux, the same is for $O^+$. **Aur** is auroral-like outflow. **Noise** is fluxes under the sensitivity threshold.

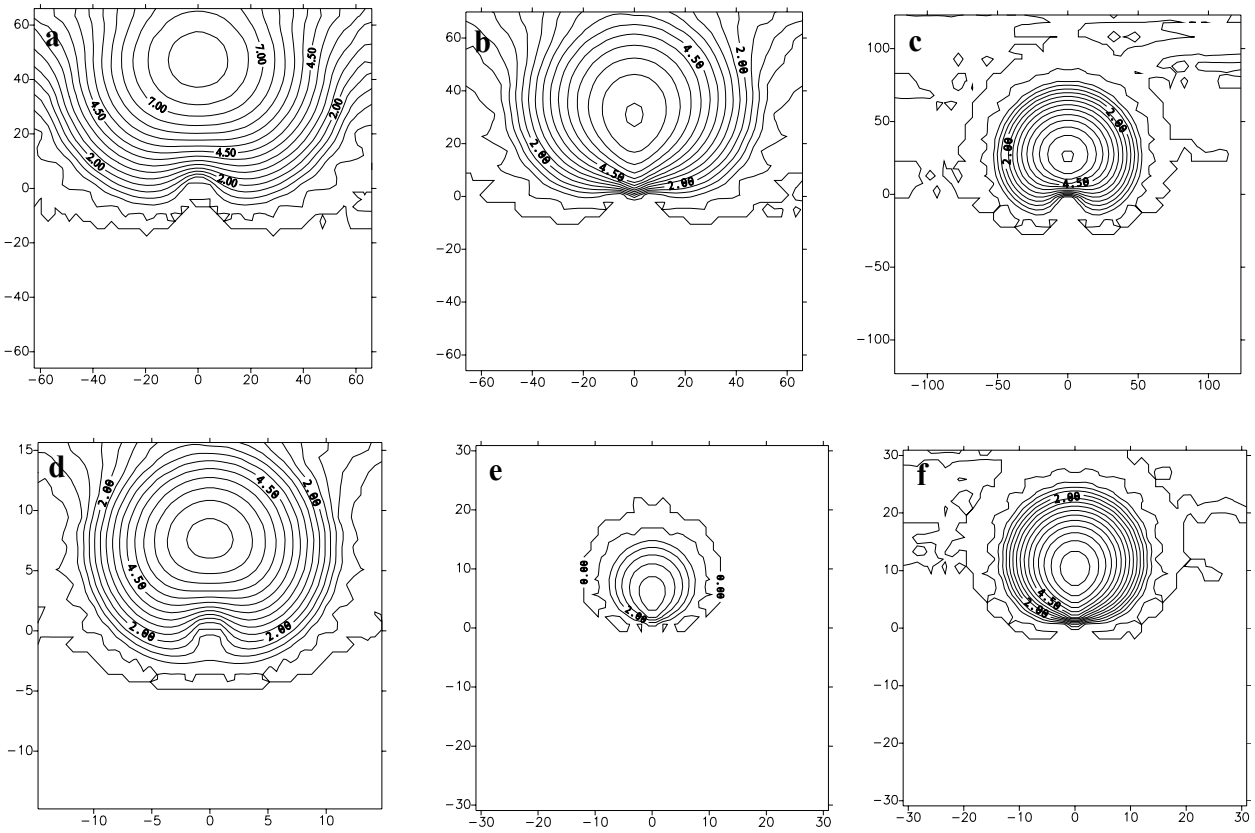


**Figure 11.** Calculation of the distribution functions for $H^+$ and $O^+$ ions measured by the HYPERBOLOID instrument. The following conditions were simulated for $H^+$ ions: (a) $U$s =0 V, $V_{\parallel}$= 40 km/s, T = 10 000 K; (b) $U$s = 6 V, $V_{\parallel}$= 30 km/s; (c) $U$s = 4 V, $V_{\parallel}$= 20 km/s; for $O^+$ ions: (d) $U$s = 0 V, $V_{\parallel}$= 6 km/s, T = 6000 K; (e) $U$s = 6 V, $V_{\parallel}$= 6 km/s; (f) $U$s = 4 V, $V_{\parallel}$= 10 km/s, T = 10 000 K.

plasma [*Zinin et al.*, 1998]. This model calculates the distribution function of ions measured by the HYPERBOLOID taking into account the electric field on the surface of the instrument and the real distribution function of the ions. Figure 11 presents some calculations of distribution function for $H^+$ and $O^+$ ions "measured" by the HYPERBOLOID instrument for various potentials of the satellite with respect to the ambient plasma. It must be emphasized that during measurements a negative potential of –6 or –8 V was applied to the grid of the instrument at its input aperture. As was shown by calculations of the electric field distribution around the satellite [*Hamelin et al.*, 2002, *Torkar et al.*, 1998], the negative potential region at a large Debye length does not extend to distances more than 1 m from the instrument. Therefore, practically it does not change the barrier formed by the positive potential of the satellite. In this case, the negative potential on the instrument does not increase the total number of detected ions; it only modifies their distribution function that is displaced to higher energies. Isolines in Figure 11 represent the ion flux on the detector. Figures 11*a* and 11*b* present the model distribution function for measurements of $H^+$ ions at $U_s$ = 0, $V_{\parallel}$= 40 km/s and $U_s$ = 6 V, $V_{\parallel}$= 30 km/s, respectively. If we compare these two distribution functions, we can see that in the latter case the flux is an order of magnitude less than in the former case. This explains why the density derived by calculating moments of the measured distribution function turns out to be so low in the winter period. Figure 11*c* presents the simulated distribution function for $U_s$ = 4 V and $V_{\parallel}$= 20 km/s. In this case, the flux is not so small as in the previous case. The parameters of the latter case satisfy the situation in the summer period, when the rate of detection of type 1 and type 2 fluxes is high. Figures 11*d* – 11*f* present simulated measurements of $O^+$ ions. Again, at a high satellite potential with respect to the plasma, the instrument detects very small flux; hence, an improved sensitivity is necessary for measuring the ions. At $U_s$ = 4 V and $V_{\parallel}$= 10 km/s the number of $O^+$ ions falling onto the detector is sufficient for the instrument sensitivity. This corresponds to type 2 fluxes, when both $H^+$ and $O^+$ ions are detected. Thus, the simulated measurements are

in qualitative agreement with the observed differences of measured fluxes in the summer and winter periods, and allow one to explain them.

Another result concerns ion fluxes that we classified as type 3. Most likely, they do not represent the polar wind. This type has a clearly pronounced dispersion in velocities. One can assume that the source of heating/acceleration for these ions was located at some altitudes below the satellite trajectory, and at the moment of measurement the major part of the $H^+$ ions turn out already to be above the satellite in its passage, so that only the heavy and slower $O^+$ ions are detected, as well as a remainder of $H^+$ ions with a velocity approximately equal to that of the $O^+$ ions. The polar edge of the auroral oval, where enhanced fluxes of heated $H^+$ and $O^+$ ions were observed by the INTERBALL-2 satellite [*Dubouloz et al*., 1998; *Malingre et al*., 2000], can be a possible source of these ion fluxes. At the instant (07:30 UT) when a flux of $H^+$ ions is seen in Figure 3, the energy of $O^+$ ions is the highest, consequently, the time from the beginning of ion motion from a source (presumably, the auroral oval edge) is minimal, and not all $H^+$ ions have managed to ascend above the point of measurement.

The next result is related to ion fluxes of type 2. Along with type 1, these fluxes were detected only in the summer period, being observed more frequently (by 10%) than type 1 fluxes. The question now arises as to why sometimes both $H^+$ and $O^+$ ion fluxes reach altitudes of 20,000 km, while at other times only $H^+$ ions are observed. The possibility for these fluxes to come from the cusp by way of convection through the cap is excluded, since in this case a very large velocity of convection from the cusp should exist in the polar cap during measurements over a long time. The time intervals selected by us belong to very quiet periods, which contradicts a large velocity of convection through the polar cap. Using the HYPERBOLOID data, the mean velocity of convection was calculated to be equal to about 2 km/s. If one projects this velocity to ionospheric altitudes, it turns out to equal 0.25 km/s. The time of motion for $H^+$ ions from the ionosphere to the altitudes of the INTERBALL-2 orbit (~20,000 km) is about 30 min. At so low a velocity of convection, $O^+$ ions will enter the cap to only 4° from the cusp, while the selected region of observation lies at a distance of about 20° from the cusp. This shows that only at a very high mean velocity of convection can the cusp serve as a source of ions for the near-midnight sector of the polar cap. The auroral oval also cannot be such a source, first, because of the adopted criterion for selecting the measurements and, second, because the temperature of the measured ions is not so high here as in the fluxes of suprathermal ions accelerated in the auroral oval. Thus, the origin of this type of ion fluxes is still unclear. It is likely that this type is caused by a more intense (maybe localized and/or burst-like) flux of electrons of the polar rain or photoelectrons in the polar cap, which increases the ambipolar electric field and, hence, amplifies ascending ion streams without significantly heating them.

In addition to ascending flows of ionospheric ions, there are magnetospheric fluxes of ions and electrons in the polar cap that have, usually but not always, a fairly low intensity. The first classification of these fluxes is given in *Winningham and Heikkila* [1974]. They were subdivided into the following three types according to their intensity, composition, mean energy, and the structure: (a) polar rain, (b) polar shower, and (c) polar squall. In this classification, the polar shower is distinct from the polar rain by being structured and by the occurrence of short-lived electron beams. Due to our criteria of selection, passages with polar squalls were excluded from the analysis. However, passages with polar rains and polar showers remained. We have studied the occurrence of different types of ionospheric streams as a function of the intensity of magnetospheric electrons. The polar rains and polar showers were classified in several groups according to the level of the flux intensity. The level S5 is the maximum flux of electrons with energy <400 eV equal to $\sim 10^6$ /(cm$^2$ s sr); the minimum flux level is S1 $\sim 2 \times 10^5$ (cm$^2$ s sr)$^{-1}$. Figure 12 presents the number of events (classified in the above six types) of measuring fluxes of ionospheric ions over the polar cap versus the flux of electrons in the polar rain or polar shower. The number of events is represented by the intensity of the black color. A considerable difference is seen in this figure between the winter and summer periods. It is also seen that the occurrence of different types of ion fluxes depends on the intensity of electrons over the polar cap. When a weak polar rain is observed above the polar cap or the electron fluxes are below the threshold of sensitivity of the ION instrument (level S1), the fluxes of type 1 are the most frequently detected upward fluxes of ions in the summer time (only rather cold $H^+$ ions are observed). In winter, the fluxes of type 5 are the most frequent. They are weak fluxes unable to overcome the satellite potential barrier so that only a very weak flux near the threshold of sensitivity can reach the HYPERBOLOID instrument.

In our opinion, these two types, type 1 and type 5, most likely represent the "classic" polar wind, in which there are practically no $O^+$ ions. The ion fluxes of type 2, observed only in summer time, correlate with an enhanced intensity of electrons (mainly, S2 level), i.e., with a more intense polar rain. This can be seen by comparing Figures 2 and 3 with Figures 4 and 5. Thus, the enhanced flux of the polar rain increases the outflow of $O^+$ ions from the ionosphere into the magnetosphere. Fluxes of type 6 correlate with the intense polar rain in both winter and summer seasons. One can clearly see in Figures 4 and 5 that $H^+$ ions (presumably heated by wave–particle interactions) appear together with the

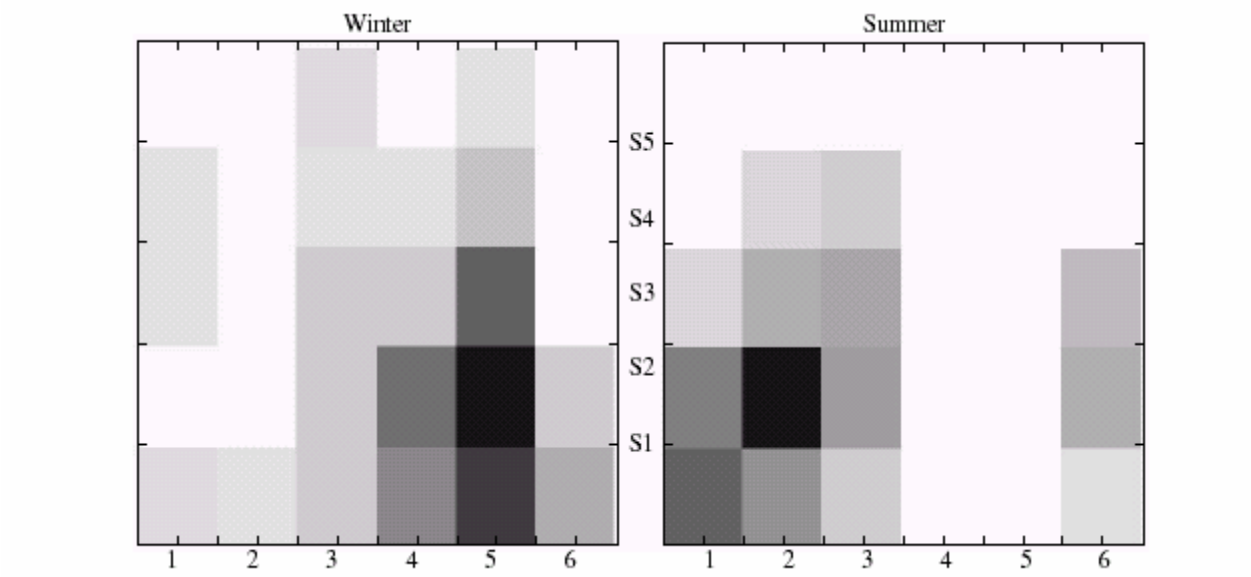


**Figure 12.** The number of occurrence of six types of outflow of the ionosphere plasma in the nighttime polar cap versus the "polar rain" intensity for winter and summer seasons.

"fine" structure of the polar rain. This polar rain influence on ion outflow can possibly be explained by interaction of energetic electrons with low-energy ions through a wave interaction at lower altitudes. In addition, polar rain electrons collide with ionospheric electrons and heat them, which also results in an increasing ambipolar electric field. In winter, the fluxes of type 4 also occur as an enhanced polar rain. Thus, one can conclude that even such a weak isotropic background of low-energy electrons as the polar rain has an effect on the dynamics of the polar wind, increasing the ascending fluxes of ions. So far, the polar rain influence on the polar wind fluxes has not yet been studied experimentally; therefore, we cannot compare our result with earlier works. In numerical models, the influence of the polar rain on the outflow of the polar wind has also not been analyzed in detail, though papers [*Tam et al*., 1995; *Su et al*., 1998*a*] mark the beginning of such an analysis. In these models, the polar rain influence is restricted to restoration of charge neutrality, and compensation for electron outflow from the ionosphere, which does not change the ion outflow from the ionosphere. For example, according to Su et al. [1998a], the ambipolar electric field has an abrupt change (sudden increase) at altitudes of ~3–4$R_E$. In the presence of an enhanced flux of the polar rain this change descends lower, but this has no effect on the global ion outflow from the ionosphere. Therefore, the above results of the HYPERBOLOID instrument make one reconsider model calculations of the polar wind.

The results of measurements onboard the INTERBALL-2 satellite show that at altitudes of 2–3$R_E$ in the winter period the HYPERBOLOID instrument cannot measure the pure polar wind for more than 50% of the events, because of the positive potential (~5–10 V) of the satellite and the low velocity of $H^+$ and $He^+$ ions parallel to the magnetic field.

In studies of the polar wind by other high-orbit satellites (DE-1, AKEBONO, and POLAR), a large content of suprathermal $O^+$ ions was also found at high altitudes. The measurements of the AKEBONO satellite at altitudes of 5,000–10,000 km above the polar cap showed that $O^+$ ions often dominate over $H^+$ ions. It is significant that analysis of AKEBONO data discovered a zone in the polar cap where the mass-s pectrometer of suprathermal ions (SMS) could not detect any ion fluxes above the threshold of its sensitivity. *Horita et al*. [1993] referred to this zone as the ion depletion zone. In Figure 1, this zone is shown as a sector with a boundary marked by a thick line. It is seen from the figure that the ion depletion zone almost coincides with segments of INTERBALL-2 orbits where, according to our concept, one could expect to observe the fluxes of ionospheric ions that most closely correspond to the polar wind. Thus, the results of INTERBALL-2 measurements are consistent with the AKEBONO data in the nightside of the polar cap. They show the ion depletion zone to be a zone of ionospheric ion fluxes with low temperature and small parallel bulk velocity that correspond to the polar wind in their characteristics. These fluxes, apparently, could not be measured because of insufficient sensitivity of the SMS spectrometer and the satellite potential. In winter time the HYPERBOLOID instrument under these conditions also could not detect ions from the velocity distribution tail due to the high satellite potential and insufficient sensitivity. However, in summer time the ion

density was larger and the potential was lower. At the same time, parallel velocities of ions were also larger and, as a result, the instrument reliably measured polar wind fluxes.

When the region of measurements from the AKEBONO satellite was much closer to the cusp/cleft, the SMS instrument measured a large density of $O^+$ ions. In *Abe et al.*[1993]; *Abe et al*., [1996]; and *Yau et al*., [1984], no detailed analysis of passages was made taking energetic particles into account nor was the possibility for particles to find the way from the "cleft ion fountain" into this region of the polar cap explored. Most likely, the published characteristics of the polar wind as measured by the SMS instrument include a mixture of ions from the polar wind and from the "cleft ion fountain," which explains the large content of $O^+$ ions obtained.

Measurements with the TIDE instrument onboard the *POLAR* satellite also showed a regular detection of $O^+$ ions over the polar cap [*Su et al*., 1998b; *Elliott et al*., 2001]. But the POLAR satellite reaches $8R_E$ in apogee; therefore, the ions, drifting by convection into the polar cap, in order to reach such altitudes near the cusp in a short time, already should be accelerated up to considerable velocities at low altitudes. Thus, these measurements also may contain a large part of ions from the "cleft ion fountain." A direct dependence of the concentration of $O^+$ ions on the IMF strength was established in these works. The authors had to suggest that the $O^+$ ion fluxes detected by them on the POLAR satellite had the cusp or cleft as a source. Our measurements confirmed this suggestion in general, excluding the summer time conditions. In summer, the fluxes of type 2 are detected very often and most likely the polar cap is their source. In winter, the HYPERBOLOID instrument detected no $O^+$ fluxes. The polar wind characteristics measured by the HYPERBOLOID instrument are compared with published model calculations [*Tam et al*., 1995; *Wilson et al*.; 1997, *Su et al*., 1998a; *Grigoriev et al*., 1999] in the table. The last row presents the averaged data of measurements with the INTERBALL-2 satellite in summer time. The data comparison was made only for the sunlit ionosphere, because no model calculations for the dark ionosphere are available in the literature. Furthermore, where it was possible, we took for our comparisons the calculations made for the solar minimum, since 1997 was a year of minimum solar activity.

| **MODEL CALCULATION FOR 20000 km** | $N_{H^+}$, $cm^{-3}$ | $N_{O^+}$, $cm^{-3}$ | $V_{par}$, $H^+$, km/s | $V_{par}$, $O^+$, km/s |
|---|---|---|---|---|
| Tam et al., 1995 | 2 | 100 | ~50 | ~10 |
| Su et al., 1998a. Minimum solar activity | ~1 | 0.05 | 28 | ~2 |
| Grigoriev et al., 1999. Minimum solar activity | 0.6 | 0.4 | 21 | 1 |
| Wilson et al., 1997. Minimum solar activity | 0.1 | 0.01 | 100 | 20 |
| **INTERBALL-2 measurements. Summer (this work)** | **0.5–1** | **0.01** | **25–40** | **5–9** |

The mean parallel velocity of $H^+$ ions as measured by the HYPERBOLOID instrument at altitudes of $2–3R_E$ is about 30 km/s for fluxes of types 1 and 2 that are detected in the sunlit ionosphere. This is in fairly good agreement with the polar wind model [*Su et al*., 1998*a*] that gives 28 km/s for an altitude of 20,000 km. The correspondence to the model of *Grigoriev et al*. [1999] that gives 21 km/s is also rather good. The model concentration of $H^+$ ions in these two models is 1 and 0.6 $cm^{-3}$, respectively. As has already been noted, the HYPERBOLOID measurements relate to the tail of the ion distribution function, which comprises a small fraction of the total ion concentration above the polar cap. Unfortunately, we have no simultaneous measurements of the plasma frequency for these conditions, so the plasma density can be estimated only from the satellite potential (5–10 V), which yields a close value of ~1 $cm^{-3}$, but to an accuracy of a factor of ~3–5. Nevertheless, in winter the results of wave measurements of the plasma frequency are available and they also yield a concentration of about 1 $cm^{-3}$. Therefore, one should expect a larger value in the summer time.

For $O^+$ ions, the difference between measurements and models is more significant. In models [*Su et al*., 1998*a*; *Grigoriev et al*., 1999], the velocities of $O^+$ ions are less than 2 km/s, while measurements of the type 2 fluxes yield a mean velocity of 7 km/s. Most likely, the fluxes of $O^+$ ions with such low velocities cannot be detected by a satellite instrument without artificial reduction of the positive potential of the spacecraft. It well may be that such $O^+$ fluxes exist in the fluxes of type 1, but were not detected by the HYPERBOLOID instrument. The density of $O^+$ ions measured by the HYPERBOLOID instrument is, on average, 0.01 $cm^{-3}$, but this also represents a part of the distribution function of these ions. The corresponding densities are equal to 0.05, 0.4, and 0.01 $cm^{-3}$ in models of *Su et al*. [1998*a*],

*Grigoriev et al.* [1999], and *Wilson et al.* [1997], respectively, but in our opinion this difference from the measurements is within experimental errors.

There are practically no fluxes of $O^+$ ions in the winter season, while the density of plasma (mainly $H^+$ ions) derived from the plasma frequency is approximately equal to 1 $cm^{-3}$ at altitudes of about 20,000 km. The parallel velocity of $H^+$ ions is not a very well-determined parameter for the winter period, since variations of the distribution function are extremely large. On average, an estimate gives 20 km/s, again in good agreement with models *Su et al*. [1998*a*] and *Grigoriev et al*. [1999]. However, these models do not predict an increase of the polar wind with increasing polar rain flux. Interestingly, the model of *Su et al*., [1998*a*] is kinetic, while the model of *Grigoriev et al*. [1999] is hydrodynamic.

Differences between measurements and the model predictions of *Tam et al*. [1995] are much more substantial. This model was constructed for comparison with polar wind measurements on the AKEBONO satellite, but we already noted above that these data were strongly biased by fluxes of the "cleft ion fountain." Thus, a significant difference appears to exist between modern models of the polar wind and measurements at altitudes of ~3$R_E$.

One can see that not all physical mechanisms resulting in the outflow of ionospheric plasma into the magnetosphere are taken into account in existing models. In addition, unfortunately, all simulations are carried out for equilibrium conditions, which very rarely are the case in physics of the magnetosphere. This also can explain differences between models and measurements.

## 4. Conclusions

We carried out an investigation of the polar wind based on measurements of thermal and suprathermal ions by the HYPERBOLOID mass-spectrometer installed on the INTERBALL-2 satellite. Passages through the polar cap in the period of 1996–1997 were analyzed. These passages were selected taking into account simultaneous measurements of electrons in the range 100 eV – 22 keV by the ION instrument. We have isolated six different types of fluxes of ionospheric ions in the polar cap: (1) cold and fairly intense fluxes of $H^+$ ions without accompanying $O^+$ ions; (2) the same fluxes of $H^+$ ions but together with $O^+$ ions; (3) sufficiently intense fluxes of $O^+$ ions with weak fluxes of $H^+$ ions; (4) very weak fluxes of $H^+$ ions without $O^+$ ions; (5) only the instrument noise is detected; i.e., measurable intensities of ions are below the threshold of detection; and (6) fluxes in the polar cap similar to those observed in auroral precipitation. As a result, conditions were determined under which there was minimal probability for fluxes from regions of auroral precipitation and the cusp/cleft (from the so-called "ion fountain") to be included in the analysis. The following results are obtained:

(1) In the summer period (when the underlying F-layer is sunlit), when only background or weak polar rain (S1) is detected in measurements of low-energy electrons by the ION instrument, only fluxes of $H^+$ ions (type 1) are observed. However, when an enhanced polar rain or polar shower is detected, then type 2, when both $H^+$ and $O^+$ ions are observed, becomes the main type of fluxes.

(2) In the winter period, the HYPERBOLOID instrument background accounts for about 80% of the measurement intervals. In this case, bulk ion flux cannot reach the detector because of the positive potential of the satellite and the low velocity of the ions.

(3) It is shown that the increasing intensity of electrons of the polar rain or shower strongly affects the value of the ascending flow of ionospheric $O^+$ ions. It is necessary to construct a model describing this phenomenon. From consideration of already published model calculations it follows that the model of *Su et al*. [1998*a*] describes the polar wind better than other models. More precisely, it describes the characteristics of $H^+$ ions at altitudes of 20,000 km. At the same time, the difference between measurements and calculations for $O^+$ ions remains significant. Most likely, in spite of our selection criteria, we did not succeed in complete elimination of overlapping additional mechanisms of heating/acceleration of $O^+$ ions under these conditions.

(4) The ion depletion zone (IDZ) that was isolated in measurements made by the AKEBONO satellite almost coincides with the region selected by us as a region where most probably the polar wind measurements have no admixture of ions drifting by convection from the "cleft ion fountain." Thus, on one hand INTERBALL-2 measurements confirm the results of AKEBONO. On the other, most likely published polar wind characteristics for high altitudes based on SMS data are disturbed by the considerable presence of ion fluxes arriving from the cusp. No characteristics of ion fluxes in the IDZ were published based on the AKEBONO data (the combination of the positive potential of the satellite with insufficient sensitivity of the instrument is a possible reason for this).

Thus, in this paper we present for the first time the mean characteristics of fluxes of ionospheric ions in the IDZ, as measured by the HYPERBOLOID instrument.,

They represent, better than other measurements, the properties of the "pure" polar wind at altitudes of 2–3$R_E$. Dependence of the polar wind intensity over the polar cap on the intensity of low-energy electrons (polar rain) is also investigated for the first time.

**Acknowledgments.** The paper is dedicated to the memory of Yu. I. Galperin who inspired this work. The authors thank him for his attention and many fruitful discussions.

This work was supported by the Russian Foundation for Basic Research (grant 03-02-16749) and by the ussian Ministry of Industry, Science and Technology grant HIII–1739.2003.2. We thank J. -A. Sauvaud and R. A. Kovrazhkin who made the ION instrument data available for us and A. Glazunov who processed these data.

## References

Abe, T., B. A. Whalen, A. W. Yau *et al.*, EXOS D (AKEBONO) Suprathermal mass spectrometer observations of the polar wind, *J. Geophys. Res.*, *98*, 11191–11203, 1993.

Abe, T., S. Watanabe, B. A. Whalen *et al.*, Observation of polar wind and thermal ion outflow by AKEBONO/SMS, *J. Geomagn. Geoelectr.*, *48*, 319–325, 1996.

Banks, P. M. and E. N. Holzer, The polar wind, *J. Geophys. Res.*, *73*, 6846–6854, 1968.

Burinskaya, T. M., A. A. Rusanov, and M. M. Mogilevsky, Small-scale bursts of the langmuir oscillations in the polar cap, *Kosm. Issled.*, *38*, 5, 507–514, 2000.

Chandler, M. O., J. H. Waite, Jr., and T. E. Moore, Observations of the polar wind, *J. Geophys. Res.*, *96*, 1421–1428, 1991.

Dessler, A. J. and F. C. Michel, Plasma in the geomagnetic tail, *J. Geophys. Res.*, *71*, 1421–1426, 1966.

Dubouloz, N., J. –J. Berthelier, M. Malingre *et al.*, Thermal ion measurements on board INTERBALL Auroral probe by the HYPERBOLOID experiment, *Ann. Geophys.*, *16*, 1070–1085, 1998.

Elliott, H. A., R. H. Comfort, P. D. Craven *et al.*, Solar wind influence on the oxygen content of ion outflow in the high-altitude polar cap during solar minimum Conditions, *J. Geophys. Res.*, *106*, 6067–6084, 2001.

Green, J. L. and J. H. Waite Jr., On the origin of the polar ion streams, *Geophys. Res. Lett.*, *12*, 149–152, 1985.

Grigoriev, S. A., L. V. Zinin, I. Yu. Vasilenko, and V. E. Lynovsky, Multi-ion one-dimensional MHD models of upper ionosphere dynamics: 1. A mathematical ionosphere model with seven positive ion species, *Kosm. Issled.*, *37*, 5, 451–462, 1999.

Gurgiolo, C. and J. L. Burch, DE-1 Observations of the polar wind − A heated and an unheated component, *Geophys. Res. Lett.*, *9*, 945–948, 1982.

Hamelin, M., M. Bouhram, N. Dubouloz *et al.*, Electrostatic interaction between INTERBALL-2 and the ambient plasma. 2. Influence on the low energy ion measurements with HYPERBOLOID, *Ann. Geophys.*, *3*, 377–390, 2002.

Horita, R. E., A. W. Yau, B. A. Whalen, T. Abe, and S. Watanabe, Ion depletion zones in the polar wind: EXOS D suprathermal ion mass spectrometer observations in the polar cap, *J. Geophys. Res.*, *98*, 11439–11448, 1993.

Horwitz, J. L., Features of Ion Trajectories in the Polar Magnetosphere, *Geophys. Res. Lett.*, *11*, 1111, 1984.

Khazanov, G., M. W. Liemohn, and T. E. Moore, Photoelectron effects on the self-consistent potential in the collisionless polar wind, *J. Geophys. Res.*, *102*, 7509–7521, 1997.

Malingre, M., N. Dubouloz, J. -J. Berthelier *et al.*, Low-energy upflowing ion events at the poleward boundary of the nightside auroral oval: high-altitude INTERBALL-Auroral probe observations, *J. Geophys. Res.*, *105*, 18693–18708, 2000.

Nagai, T., J. H. Waite, Jr., J. L. Green, and C. R. Chappell, First measurements of supersonic polar wind in the polar magnetosphere, *J. Geophys. Res.*, *11*, 669–672, 1984.

Sauvaud, J. A., H. Barthe, C. Aoustin *et al.*, The ion experiment onboard the INTERBALL-Aurora satellite; initial results on velocity-dispersed structures in the cleft and Inside the auroral oval, *Ann. Geophys.*, *16*, 1056–1069, 1998.

Su, Y. -J., J. L. Horwitz, G. R. Wilson *et al.*, Self-consistent simulation of the photoelectron-driven polar wind from 120 km to 9$R_E$ altitude, *J. Geophys. Res.*, *103*, 2279–2296, 1998*a*.

Su, Y. -J., J. L. Horwitz, T. E. Moore, *et al.*, Polar wind survey with the thermal ion dynamics experiment/plasma source instrument suite aboard POLAR, *J. Geophys. Res.*, *103*, 29305–29337, 1998*b*.

Tam, S. W. Y., F. Yasseen, T. Chang, and S. B. Ganguli, Self-consistent kinetic photoelectron effects on the polar wind, *Geophys. Res. Lett.*, *22*, 2107–2110, 1995.

Torkar, K., H. Jeszenszky, M. V. Veselov *et al.*, Spacecraft potential measurements on board INTERBALL-2 and derived plasma densities, *Kosm. Issled.*, *37*, 6, 644–653, 1999.

Torkar, K., M. V. Veselov, V. V. Afonin *et al.*, An experiment to study and control the langmuir sheath around INTERBALL-2, *Ann. Geophys.*, *16*, 1086 1998.

Wilson, G. R., G. Khazanov, and J. L. Horwitz, Achieving zero current for polar wind outflow on open flux tubes subjected to large photoelectron fluxes, *Geophys. Ress. Lett.*, *24*, 1183–1186, 1997.

Winningham, J. D. and W. J. Heikkila, Polar cap Auroral electron fluxes observed with isis 1, *J. Geophys. Res.*, *79*, 949, 1974.

Yau, A. W., B. A. Whalen, W. K. Peterson, and E. G. Shelley, Distribution of upflowing ionospheric ions in the high-altitude polar cap and auroral ionosphere, *J. Geophys. Res.*, *89*, 5507–5522, 1984.

Zinin, L. V., Yu. I. Galperin, S. A. Grigoriev, and T. M. Mularchik, On measurements of polarization jet effects in the outer plasmasphere, *Kosm. Issled.*, *36*, 1, 39–48, 1998.

# Models of electric field distribution near a satellite

L. Zinin[1,2], S. Grigoriev[2], and I. Rylina[2]

[1] Space Research Institute, Russian Academy of Sciences, Moscow, Russia
[2] Kaliningrad State University, Kaliningrad, Russia

**Abstract.** The electric field distribution around a charged satellite in rarified magnetospheric plasma greatly influences the densities and trajectories of particles measured by onboard instruments. The simulation of macro-parameters of thermal plasma near a moving charged satellite, which is necessary for correction of experimental measurements, encounters considerable computational difficulties. In this work, two three-dimensional models of the electric field distribution around a satellite are considered under conditions when the Debye length is comparable to the geometrical size of the spacecraft. In the first model a system of hydrodynamic equations of continuity and motion was used, which was solved jointly with the Poisson equation. In the second model the hydrodynamic equation of motion was used for analyzing motion of large particles by means of the method of particles in a cell. The results of calculations of potential near the satellite, as well as distributions of densities of electrons and ions and of volume charge, are considered for two magnetic field orientations. Results of test calculations for some situations in ambient plasma are presented, and the influence of the spatial electric field distribution on thermal plasma measurements is considered.

## 1. Introduction

Performance and interpretation of many spacecraft-based experiments require analysis of the spatial electric field distribution near a charged satellite. For example, a positive satellite potential of some volts relative to the ambient plasma results in essential distortion of mass-spectrometric measurements of the thermal plasma and, especially, of light ions, such as $H^+$, and under some conditions a determination of characteristics of the distribution function becomes impossible [*Olsen*, 1982; *Olsen et al.,* 1985; *Parker and Whipple*, 1970]. On the other hand, even if satellite potentials are low, in order to analyze experimental measurements it is necessary to know the electric field distribution near the satellite to evaluate its influence on trajectories of particles, as well as on the extent and character of the distortion of the distribution function of ions [*Parker and Whipple*, 1970; *Berthelier et al*., 1982]. The value of the Debye length ($\lambda_D$) plays an important role as the characteristic spatial size of interactions in the plasma. The problem becomes especially complicated in the case when $\lambda_D$ is comparable with the characteristic size of a satellite.

In the case of thin-sheet approximations, the value of the relative velocity of motion of the plasma and satellite and the corresponding value of thermal velocities of particles become decisive factors. A second extreme case can be reduced to the problem of finding the electric field distribution in a vacuum. The main difficulty in this problem is related to the fact that a majority of satellites have rather complicated shapes, with different antennas and booms. In addition, the spacecraft as a whole can have rather large spatial dimensions while, for analyzing operation of some instruments, the potential distribution near the surface must be known with a rather high accuracy. Nevertheless, this problem has been solved to date [*Galperin et al*., 1993; *Zinin et al*., 1998; *Riedler et al*., 1998; *Torkar et al.*, 1998] and was already used successfully to analyze measurement data from the HYPERBOLOID instrument on the INTERBALL-2 satellite [*Zinin et al*., 1998; *Bouhram et al*., 2001; *Hamelin et al.*, 2001].

The problem with a finite Debye length can be considered at present to be the most difficult and important. Progress in solving problems of this class is associated both with the development of the theory of numerical methods [*Elizarova and Chetverushkin*, 1989; *Graur et al*., 1985] and with the greatly increased powers of computers, which has made it possible to calculate plasma parameters, although with some limitations. Difficulties arise here in connection with the multidimensional character of the problem and the requirements for high temporal and spatial resolution.

Some attempts to solve this problem have been undertaken thus far, although only for the simplest geometrical interpretation. For example, in recent years non-stationary models of body-plasma interaction have been developed which provide a self-consistent solution

for the electric field and plasma distribution, as well as for associated currents. One of them is a three-dimensional model based on the method of particles in cells (referred to below as the Particle In Cell or PIC method) and on the Poisson equation [*Singh et al*., 1994; *Singh et al.,* 1997]. *Ma and Schunk* [1989] first considered a similar problem using a hydrodynamic approach for a small sphere. *Zinin et al*. [1999] and *Rylina et al.* [2002] considered the cases of a cylinder and a cube. Subsequently, theoretical aspects of satellite–plasma interaction were presented in detail in a paper by *Roussel* [2001] and preliminary results based on two-dimensional [*Okada and Matsumoto*, 2001] and three-dimensional [*Forest et al*., 2001; *Usui et al*., 2001] kinetic models were considered in *Afonin et al*. [2001]. A majority of the models presented there used the PIC method of numerical solution.

This work is devoted to two ways of modeling the electric field around a satellite by using a hydrodynamic approach for a simplified cylindrical shape moving in plasma. Conditions in the ambient plasma are identical for the first and second cases and are close to real conditions of measured thermal plasma. Both versions of the model considered are isothermal.

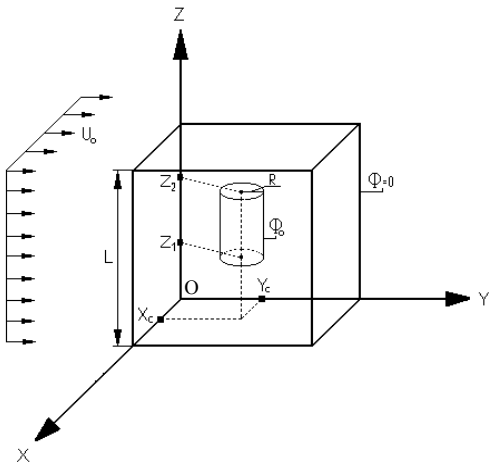


**Figure 1.** Simulation region geometry: The satellite is represented as a cylinder situated at the center of a cube. Both diameter and height of the cylinder equal 2 m. The length of the calculation region is L=24 m. The relative velocity $V_O$ of the plasma and satellite is 20 km·s$^{-1}$. The magnetic field is directed along the *OY* axis.

## 2. Model geometry

We replace the real situation of plasma interaction with a charged body (a satellite) moving in plasma with the following model situation. Let the interaction of plasma with a charged body be isothermal. Represent the body by a cylinder. It is supposed to be conductive and have positive potential $\Phi_0$ at the boundary. Undisturbed plasma moves relative to the body at a constant velocity $V_0$. This positively charged cylinder is the only electrode (anode) in the model.

Thus, we neglect the internal turnover of plasma between two electrodes, supposing the cathode to be at an infinite distance from the anode.

We make use of an electrostatic approximation, the important consequence of which is ignorance of the magnetic field formed by the moving charged particles.

The geometry of the problem considered is presented in Figure 1. Mathematical modeling is accomplished in the Cartesian coordinate system *XYZ*. We consider a cube with the side *L*, one of whose vortices has the coordinates (0, 0, 0), and whose three edges lie on the coordinate axes. This cube represents the environment for a charged body (cylinder) situated at its center. It is chosen so that the influence of a charged body outside this environment could be considered as negligible. The charged body in the form of a circular cylinder is specified as follows: the cylinder axis is parallel to the *Z*-axis, its bases are the circles with a center at the point (*Xc*, *Yc*) and radius R, and the height is equal to $Z_2 - Z_1$. A constant positive potential $\Phi_O$ is maintained at the boundary of the cylinder. The undisturbed plasma moves relative to this body at a velocity $V_0$ along the ordinate axis. The electric potential of the undisturbed plasma is equal to zero.

## 3. Hydrodynamic approach: the kinetic algorithm

The hydrodynamic approach to the problem of a charged body's interaction with plasma is as follows. The plasma in the given model is considered to be a continuous medium composed of electrically charged particles: electrons and ions. Its state is described by the following functions: velocity components *Vx*(*t, x, y, z*), *V*y(*t, x, y, z*), and *V*z(*t, x, y, z*); density *N(t, x, y, z)*; constant temperature $T_0$; and pressure *P(t, x, y, z)*. These quantities satisfy the equations of gas dynamics: the continuity equation

$$\frac{\partial N}{\partial t} + \nabla(N \cdot \vec{V}) = 0 \qquad (1)$$

where $\vec{V} = (V_x, V_y, V_z)$; and the equation of motion

$$\frac{\partial (N \cdot \vec{V})}{\partial t} + \vec{V} \cdot \nabla(N \cdot \vec{V}) + N \cdot (\vec{V} \cdot \nabla) \cdot \vec{V} = -\frac{\nabla P}{m} + \frac{N \cdot \vec{F}}{m} \pm \frac{N \cdot e}{m}(\vec{E} + \frac{1}{c} \cdot \vec{V} \times \vec{H}) \qquad (2)$$

where *m* is the mass of an ion or electron, *e* is the electron charge, *c* is the velocity of light in a vacuum, $\vec{E}$

is the electric field, $\vec{F}$ is the external force, and $\vec{H}$ is the geomagnetic field. In the equation of motion used in this model, we neglected the term containing viscosity, as well as the terms that take friction into account, by virtue of their insignificant contribution to the final result over the time typical for the given model.

System (1), (2) is closed by the final relationship. This is the equation of state $P = NkT_0$, which connects the thermodynamic characteristics of the medium $P$, $N$, and $T_0$ at each point $(t, x, y, z)$. Equations (1), (2) are supplemented by the initial data specified by functions $V_x$, $V_y$, $V_z$, $P$, $N$ at the instant when $t = 0$ and by the boundary conditions at the inner and outer boundaries of the environment. At the outer boundary all unknown functions have a boundary condition of the first kind, coordinated with initial data, and at the inner boundary the conditions can be of the first or second kind, depending on the direction of the velocity vector.

The corresponding differential difference system of equations for describing the gas dynamic flow, called the kinetic algorithm [*Elizarova and Chetverushkin,* 1989], was described in *Rylina et al*. [2002].

At each time step, the Poisson equation

$$\nabla^2\Phi = -\frac{\rho}{\varepsilon_0} \qquad (3)$$

for electric fields and gas dynamic equations (1)–(2) are solved in a self-consistent manner. The electric field $\vec{E}$ in gas dynamic equation of motion (2) has two components: $\vec{E} = \vec{E}_0 + \vec{E}_1$, where $\vec{E}_0$ is the convection field, which is spatially homogeneous, and $\vec{E}_1$ is the electric field of a volume charge, which satisfies the equation

$$\vec{E}_1 = -\nabla\Phi \qquad (4)$$

where $\Phi$ is the electrostatic potential.

The electric field $\vec{E}$ is found from Poisson equation with $\rho = e\,(N_i - N_e)$, then hydrodynamic equations are solved for this $\vec{E}$ to find $N_i$ and $N_e$. Time evolution of the plasma and fields should proceed until the plasma and the field distribution inside the system reach a quasi-stationary state. However, because of computational difficulties the calculation is limited by characteristic plasma times.

In the given mathematical model this equation is solved by the alternately triangular method.

### 4. Hydrodynamic approach: the PIC method

The second isothermal model considered here is based on the PIC method (see, e.g., *Hockney and Eastwood* [1984; *Fedorenko* [1994]), and for this reason the model represents a combination of the hydrodynamic and kinetic approaches to plasma modeling. For example, a great number of charged particles take part in the calculations, but, on the other hand, the hydrodynamic equation of motion is solved. The given model is also based on the method of heavy electrons (in this case, for a greater stability of numerical schemes the electron mass is multiplied by 100), as well as on the method of charged clouds [*Sigov and Khodyrev*, 1976] (where a particle "distributes" its charge between 64 neighboring nodes adjacent to it). The given model operates with so-called macroscopic particles, which represent a combination of a great number of real particles of the same type.

The geometry of this model coincides with the geometry of the previous model, the charged satellite represents a cylinder and is illustrated by Figure 1. The cubic environment is covered with a grid with constant step h, which is identical in $x$, $y$, and $z$. The cube is filled with particles characterized by the following quantities: $X_n$ , $Y_n$ , and $Z_n$ , the coordinates of the position of a particle; m, the mass of a particle; and $\alpha = e$ or $I$, is the type of particle (electron or ion). The superscript $n$ indicates that these quantities are related to the time $t_n$. The set of numbers $t_0, t_1, \ldots, t_n, \ldots$, forms a time grid with step $\tau$. Cells of the grid are numbered by triples of subscripts $i$, $j$, and $k$. Quantities, $V_{x_\alpha\,ijk}^{\;n}, V_{y_\alpha\,ijk}^{\;n}, V_{z_\alpha\,ijk}^{\;n}$ are determined at centers of computing cells as the components of velocity of the plasma of the type $\alpha$ at the time instant $t_n$.

At the time $t = 0$ the modeled system is filled with particles in accordance with density $N_0$ and temperature $T_0$. At each subsequent time step, electrons and ions are supposed to flow from the plasma reservoir, which encloses the modeled region, inside the system. The charged particles are injected to the plane $y = 0$ at an initial velocity $V_0$ along the ordinate axis. Such a method of injection corresponds, more probably, to the hydrodynamic approach. Note that the velocity distribution of particles is ignored at injection (which proceeds at a constant speed along the selected direction $OY$) and is reflected only in the presence of the isotropic temperature $T_0$. Further on, the particles move in accordance with the equation of motion (2), which is solved by the PIC method. In this method, the transition from quantities on a temporal layer $n$ to quantities on a layer $n + 1$ is accomplished for some small time $\tau$ in two stages, at each of which the basic physical quantities change due to a process of only one type. Therefore, in solving the equation of motion, account is taken of, at first, the change of momentum due to pressure gradients and electromagnetic forces and, then, due to the transport processes. This numerical scheme and the equations are described in *Rylina et al*. [2002].

The electric field $\vec{E}$ is found from the Poisson equation at which we arrive by the same method as in the previous Section. The only exception is the volume charge density *r*, which is determined in a different manner in this model. Namely, the method of charged clouds [*Sigov and Khodyrev*, 1976] is used in this model. The concept is essentially that a particle "distributes" its charge between several (namely, 64) neighboring cells. Thus, the volume charge density at each computation cell is determined as the sum of the parts of charges of particles "acting" upon this cell divided by $h^3$. At each time-step the Poisson equation for electric fields and the equations of motion for all charged particles inside the system are solved in a self-consistent manner.

The assumption made above of a constant potential leads to a necessity for the electrons absorbed by a body to be newly injected into the calculation region. In the given model they are injected into the calculation region randomly at the velocity $V_O$ along the ordinate axis.

Temporal evolution of the plasma and fields proceeds until the calculation time exceeds the characteristic times for the corresponding plasma parameters.

## 5. Results of numerical simulation

The following physical parameters were chosen for model calculations. The satellite was supposed to be a cylinder with a diameter of 2 m and a height of 2 m as well. The calculation region was a cube with a side of 24 m. The potential of the satellite was +10 *V*. The density of electrons and ions $H^+$ in the undisturbed region was 10 $cm^{-3}$. The relative velocity of the plasma and the satellite was chosen from typical conditions of polar wind measurements as 20 km $s^{-1}$. It was directed along the *OY* axis parallel to the magnetic field. The temperatures of electrons and ions were 5000 K. The Debye length for the selected conditions was about 1 m. Each time step is $10^{-10}$ s. for the hydrodynamic model and $10^{-8}$ s for the PIC model. Final times are $2x10^{-4}$ s. (hydrodynamic) and $10^{-3}$ s. (PIC).

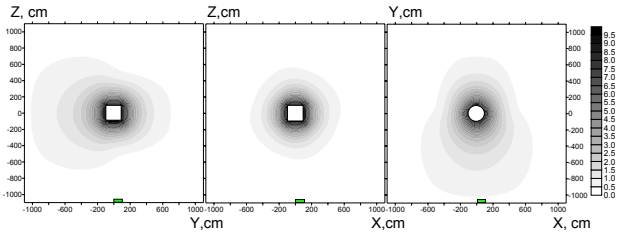


**Figure 2.** Spatial distribution of the electric field around the satellite calculated by a hydrodynamic model. The satellite potential is 10 V; the undisturbed plasma density is 10 $cm^{-1}$. The relative velocity is co-directed with the magnetic field along the *OY* axis and has a value of 20 km $s^{-1}$. The intensity of gray color indicates the potential value in volts, in accordance with the scale.

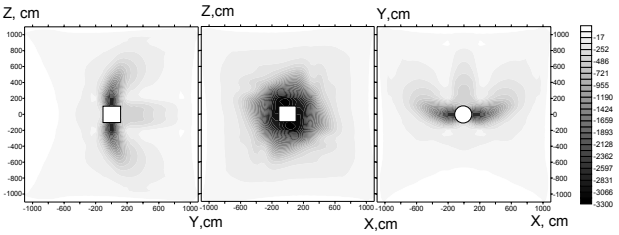


**Figure 3.** The volume charge density in arbitrary units. The scale of relative units is shown on the right. The charge sign is observed. Model conditions are the same as for Figure 2.

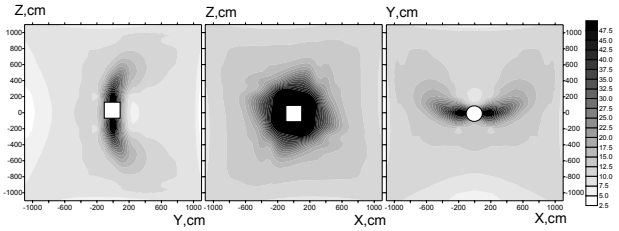


**Figure 4.** Electron density distribution near the satellite.

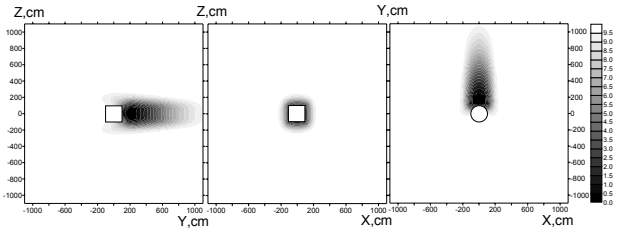


**Figure 5.** The density distribution of $H^+$ ions.

There are two types of calculation for both models. In the first case the magnetic field and plasma velocity are parallel to *OY* axis. In the second case the magnetic field is parallel to *OZ* axis and plasma velocity is parallel to *OY* axis.

Figures 2–5 present results of numerical simulations with a model based on the kinetic algorithm and the magnetic field directed along the *OY* axis. All figures present the spatial distribution of the basic plasma parameters in the plane $X = 0$. Figure 2 gives the spatial distribution of the electric field near the satellite.

The potential near the surface drops rapidly, which corresponds to the exponential dependence on the distance to a charged body. At the same time, no spherical symmetry is observed. This is revealed especially strongly at a distance of a few Debye lengths. Obviously, the volume density of the electric charge determines the form of the spatial distribution of the potential. This volume density is presented in arbitrary units in Figure 3. We distinguish two regions of negative charge near the satellite: the region localized near $Y = 0$ around the whole satellite, and the region immediately

behind the satellite. It is seen from the distributions of electron density (Figure 4) and ions (Figure 5) that the first region arises as a result of an excess of electrons drifting in the magnetic field, while the second region is a consequence of the deficiency of ions behind the satellite, or the so-called "ion shadow." A different situation corresponds to when the magnetic field is directed along the *OZ* axis and the plasma velocity is directed along the *OY* axis (Figures 6–9). Figure 2 and Figure 6 show different space distributions of the electric field near the model satellite. In both cases the electric field is elongated along the magnetic field and is asymmetric.

Electric field values decrease faster for the case of an *OZ*-oriented magnetic field. Distributions of charge and electrons show a strong dependence on magnetic field directions and the both elongate along the magnetic field. Ion shadows exist in both cases, but they are shorter in the second case.

By virtue of the fully "hydrodynamic nature" of the model considered above, the solutions obtained are rather smooth; there are no statistical fluctuations.

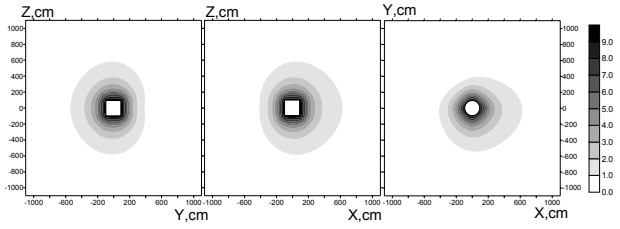


**Figure 6.** The same as in Figure 2, but with the magnetic field oriented along the *OZ* axis.

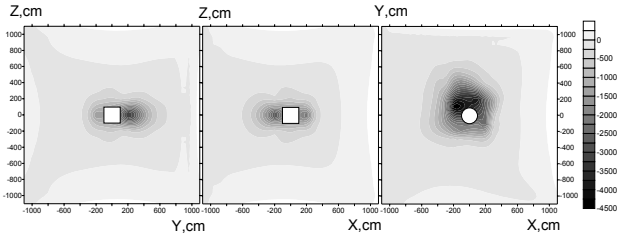


**Figure 7.** The same as in Figure 3, but with the magnetic field direction along OZ.

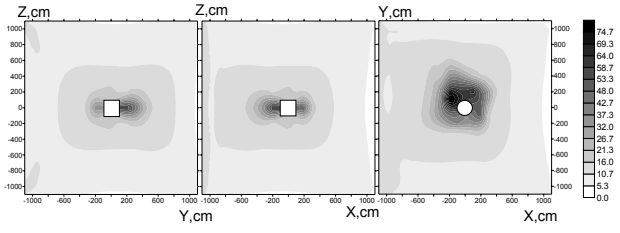


**Figure 8.** The same as in Figure 4, but with the magnetic field direction along OZ.

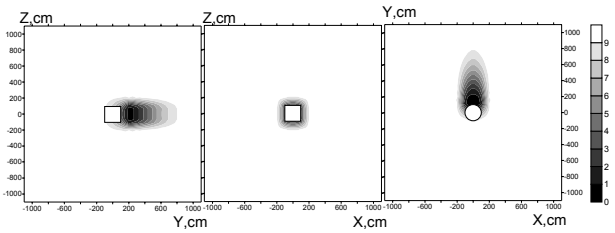


**Figure 9.** Ion space distribution with parameters similar to Figure 5, and magnetic field direction along *OZ*.

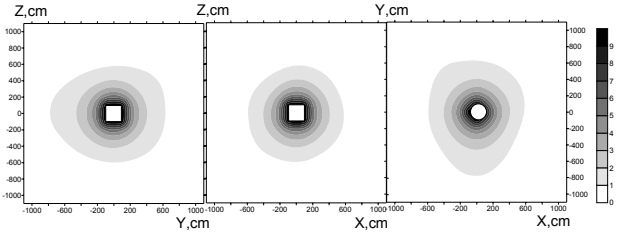


**Figure 10.** Spatial distribution of the electric field around the satellite model, calculated by the particles in a cell (PIC) method. The satellite potential is 10 V, and the undisturbed plasma density is 10 cm $^{-3}$. The relative velocity is directed along the magnetic field oriented on the *OY* axis and has a value of 20 km s$^{-1}$. The $X = 0$ cross section in the *YZ* plane is presented. The intensity of gray color indicates the potential value in volts, in accordance with the scale.

A slightly different picture arises from calculations using the PIC-method model. As has already been mentioned, this method is based on analysis of the motion of "large" particles. Our approach uses the equation of motion from a system of hydrodynamic equations with particle injection into the plane along the plasma velocity direction. The velocity distribution of particles is ignored in this case. Also ignored is the existence of "catching-up" electrons having thermal velocities an order of magnitude higher than the relative velocity of the satellite and the plasma.

Spatial distribution of the electric field potential is presented in Figure 10 for a case when the magnetic field is directed along the *OY* axis. In general, the electric field distribution has the same features as in Figure 2 with a more rapid decrease across the magnetic field. The space distribution of charge (Figure 11), by virtue of the other simulation technique, is essentially inhomogeneous. However, even in this case the negative charge is situated behind the satellite and around it in the plane near $Y = 0$; its localization depends on the magnetic field direction. An intensive ion shadow is situated behind the satellite, and in this case the ion density inside it drops virtually down to zero (Figure 12). The spatial distribution of electron density (Figure 13)

indicates a great number of irregularities, but even in this case electrons are localized in the plane $Y = 0$.

The next set of calculations corresponds to a magnetic field orientation along the *OZ* axis. Figures 14-17 show the results according to the PIC model.

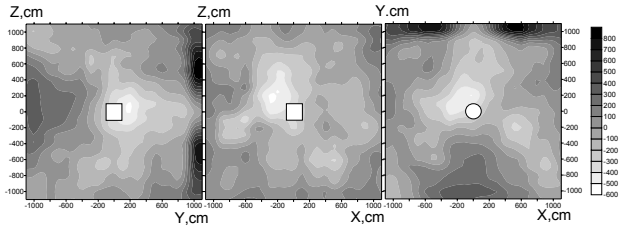


**Figure 11.** Volume charge density in arbitrary units, calculated by the PIC model. The scale of units is shown on the right. The sign of the charge is observed. Model conditions are the same as for Figure 6.

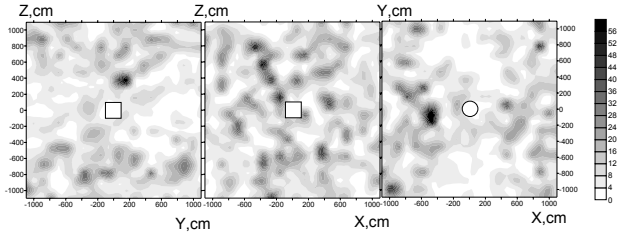


**Figure 12.** Density distribution of $H^+$ ions calculated by the PIC model.

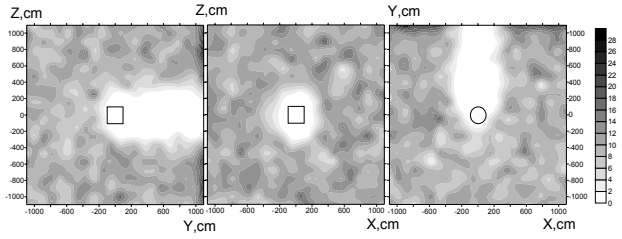


**Figure 13.** Distribution of the electron density near a satellite model calculated by the PIC model.

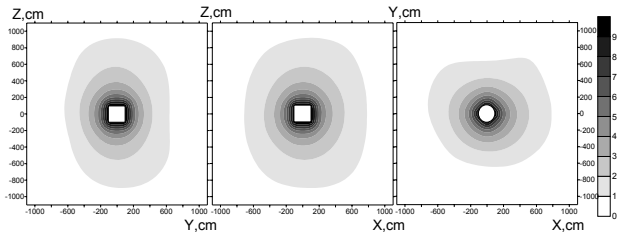


**Figure 14.** Electric field distribution for the PIC model and *OZ*-oriented magnetic field.

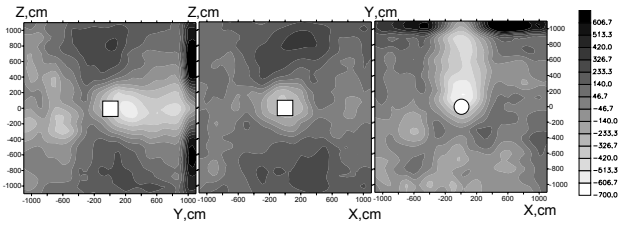


**Figure 15.** Distribution of charge in relative units for the PIC model and with *OZ*-oriented magnetic field.

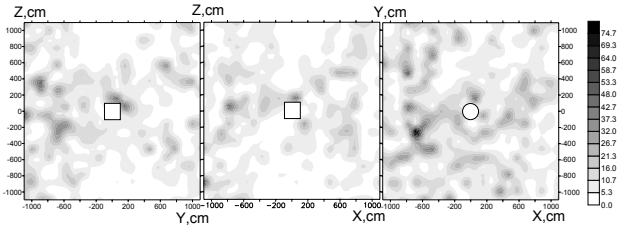


**Figure 16.** Electron distribution ($cm^{-3}$) for the PIC model and with OZ-oriented magnetic field.

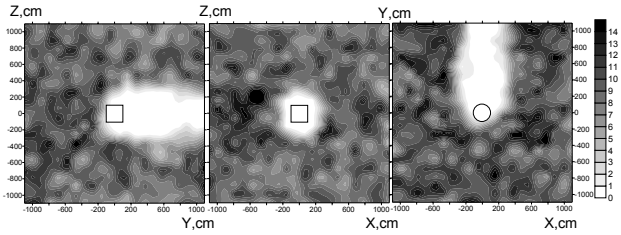


**Figure 17.** $H^+$ distribution ($cm^{-3}$) for the PIC model and with *OZ*-oriented magnetic field.

The next set of calculations corresponds to a magnetic field orientation along the *OZ* axis. Figures 14-17 show results according to the PIC model.

## 6. Conclusion

On the basis of these reported results of numerical simulations, it is possible to determine some features of plasma distribution near a charged satellite. Both numerical models indicate the presence of a deep ion shadow behind the satellite. The length of this trace exceeds 10 Debye lengths, and the ion density in this region drops from 10 particles in a cubic centimeter virtually down to zero. Such a peculiarity of the spatial distribution of thermal ions considerably distorts the angular distribution and, in some cases, can even make experimental measurements impossible. The volume charge distribution is determined, among other things, by the magnetic field direction, or more correctly, by the angle between the direction of a relative velocity and the magnetic field. The arising volume charge greatly

influences the form of equipotentials at a distance of a few Debye lengths from the satellite, and, hence, it results in distortion of the trajectories of the measured particles. An even more complicated picture should be expected in the case when the shape of the satellite is closer to a real one.

Comparison of two orientations of the magnetic field show great dependences of the electric field, electron density and charge distributions on the magnetic field for both numerical models.

**Acknowledgments.** This paper is dedicated to the memory of Yu. I. Galperin. The authors thank Yu. I. Galperin for initiating this work and for discussion of the results.

The authors thank N. Yu. Buzulukova, V. V. Vovchenko, and D. V. Chugunin for valuable discussions. This work was supported in part by the Russian Foundation for Basic Research, projects No. 01-01-00718-a, 03-02-16749-a, by the JURRISS NAG5-8638 grant and by INTAS 2000-465 grant.

## References

Afonin, V., N. Smirnova, Ja. Smilauer, and J. Stanev, INTERBALL-2 thermal plasma measurements. 2. spacecraft potential in magnetospheric auroral region at altitudes 2–3$R_E$, in *2001: A Spacecraft Charging Odyssey. Proceed. of the 7th Spacecraft Charging Technology Conf., 23–27 April, 200*1, ESTEC, Noordwijk, The Netherlands, ESA SP-476, pp. 351–356.

Berthelier, J. J., J. Covinhes, M. Godefroy, *et al*., The thermal ion mass spectrometer on board AUREOL-3: the DYCTION experiment, *Ann. Geophys*., *38*, 591–614, 1982.

Bouhram, M., N. Dubouloz, M. Hamelin, *et al*., Plasma sheath analysis and current calculations from the potential distribution around INTERBALL auroral probe, *2001: A Spacecraft Charging Odyssey. Proceed. of the 7th Spacecraft Charging Technology Conf., 23–27 April, 200*1, ESTEC, Noordwijk, The Netherlands, ESA SP-476, pp. 557–561.

Elizarova, T. G. and B. N. Chetverushkin, One computational algorithm for calculating gas-dynamic flows, *Dokl. Akad. Nauk SSS*R, *279*, 1989.

Fedorenko, R. P., *Vvedenie v vychislitel'nuyu fiziku* (Introduction to Computational Physics), Moscow: MFTI, 1994.

Forest, J., L. Eliasson, and A. Hilgers, A new spacecraft plasma interactions simulation software PicUp3D/SPIS, in *2001: A Spacecraft Charging Odys-sey. Proceed. of the 7th Spacecraft Charging Technology Conf., 23–27 April, 200*1, ESTEC, Noordwijk, The Netherlands, ESA SP-476, pp.515-520.

Galperin, Yu. I., S. A. Grigoriev, L. V. Zinin, and V. A. Gladyshev, Calculations of electric potential distribution around the auroral probe satellite of the INTERBALL Project, *Preprint of Space Res. Ins*t., Russ. Acad. Sci., Moscow, 1993, no. Pr-1879.

Graur, I. A., T. G. Elizarova, and B. N. Chetverushkin, The use of kinetic algorithms for calculations in gas-dynamic problems modeling viscous flows, *Preprint of Keldysh Inst. of Applied Math*., Moscow, *85*, 1985.

Hamelin, M., M. Bouhram, N. Dubouloz, *et al*., Combined effects of satellite and ion detector geometries and potentials on the measurements of thermal ions. The Hyperboloid Instrument on Interball, in *2001: A Spacecraft Charging Odyssey. Proceed. of the 7th Spacecraft Charging Technology Conf., 23–27 April, 200*1, ESTEC, Noordwijk, The Netherlands, ESA SP-476, pp. 569–574.

Hockney, R. and J. Eastwood, *Computer Simulation Using Particle*s, New York: McGraw-Hill, 1984.

Ma, T. -Z. and R. W. Schunk, A fluid model of high voltage spheres in the ionosphere, *Planet. Space Sci*., *37*, 21–47, 1989.

Olsen, R. C., The hidden ion population of the magnetosphere, *J. Geophys. Res., 87*, 3481–3488, 1982.

Olsen, R. C., C. R. Chappell, D. L. Gallagher, *et al*., The hidden ion population: revisited, *J. Geophys. Res*., *90*, 12121–12132, 1985.

Okada, M. and H. Matsumoto, Electromagnetic particle simulations with unstructured-grid Model, in *2001: A Spacecraft Charging Odyssey. Proceed. of the 7th Spacecraft Charging Technology Conf., 23–27 April, 200*1, ESTEC, Noordwijk, The Netherlands, ESA SP-476, pp. 521–524.

Parker, L. W. and E. C. Whipple, Theory of spacecraft sheath structure, potential and velocity effects on ion measurements by traps and mass spectrometers, *J. Geophys. Res*., *75*, 4720–4733, 1970.

Riedler, V., K. Torkar, M. V. Veselov, *et al*., Experiment RON for active control of spacecraft electric potential, *Kosm. Issled*., *36*, 1, 53–62, 1998.

Roussel, J. -F., Modeling of spacecraft plasma environment interactions, *2001: A Spacecraft Charging Odyssey. Proceed. of the 7th Spacecraft Charging Technology Conf., 23–27 April, 200*1, ESTEC, Noordwijk, The Netherlands, ESA SP-476, pp. 45–59.

Rylina, I. V., L. V. Zinin , S. A. Grigoriev , and M. V. Veselov, Hydrodynamic approach to modeling the thermal plasma distribution around a moving charged satellite *Cosmic Research,* Vol. 40, No. 4, 2002, pp. 367–377. *Translated from Kosmicheskie Issledovaniya, 40,* 4, 395–405, 2002.

Singh, N., B. I. Vashi, and W. C. Leung, Three-dimensional numerical simulation of current collection by a probe in a magnetized plasma, *Geophys. Res. Lett*., *21*, 833, 1994.

Singh, N., W. C. Leung, and B. I. Vashi, Potential structure near a probe in a flowing magnetoplasma and current collection, *J. Geophys. Res*., *102*, 195, 1997.

Sigov, Yu. S. and Yu. V. Khodyrev, The theory of discrete plasma models, in *Chislennye metody mekhaniki sploshnoi sredy* (Numerical Methods of Mechanics of Continua), *7*, 1976.

Torkar, K., M. V. Veselov, V. V., Afonin, *et al*., An experiment to study and control the langmuir sheath around INTERBALL-2, *Ann. Geophys*., *16*, 1086–1096, 1998.

Usui, H., M. Yasugi, and Y. Omura, PIC simulation of the space environment effects of plasma contactor, in *2001: A Spacecraft Charging Odyssey. Proceed. of the 7th Spacecraft Charging Technology Conf., 23-27 April, 200*1, ESTEC, Noordwijk, The Netherlands, ESA SP-476, pp. 535–538.

Zinin, L. V., Yu. I. Galperin, S. A. Grigoriev, and T. M. Mulyarchik, On measurements of polarization jet effects in the outer plasmasphere, *Kosm. Issled*., *36*, 1, 42–52, 1998.

Zinin, L. V., S. A. Grigoriev, I. A. Rylina, and M. V. Veselov, The model of electric field distribution near the INTERBALL-2 satellite, in *Dynamics of the Magnetosphere and Its Coupling to the Ionosphere on Multiple Scales from INTERBALL, ISTP Satellites, and Ground-Based Observations, Zvenigorod, Russia, February 8–1*3, 1999, p. 79.

# Modeling plasma density for the dayside of Earth's magnetosphere

V. V. Domrachev and D. V. Chugunin

Space Research Institute, Russian Academy of Sciences, Moscow, Russia

**Abstract.** Results from comparison of density profiles obtained using the CDPDM model and ISEE-1 experimental data for years 1977–1983. A hypothesis about the validity of mirror mapping of the convection boundary relative to the dawn-dusk direction is verified. An attempt is made to improve the CDPDM model for the dayside.

.

## 1. Introduction

The plasmasphere represents the magnetospheric region filled with ions and electrons of energy lower than 1–2 eV, which came from the ionosphere. These charged particles, trapped by the geomagnetic field, form a cloud of cold thermal plasma around the Earth, which extends to equatorial geocentric distances of 4–5 Earth radii. The outer plasmasphere boundary forms a characteristic "knee" in the equatorial density profile. This region is called the plasmapause.

*Gringauz, et al* [1960] discovered the plasmapause as a sharp decrease of the positive current in the ion trap on the satellite. According to *Nishida* [1966], and *Brice* [1967], the plasmapause originates as a result of the rapid depletion of field tubes due to growing convection onto the magnetopause. This implies that it is the convection boundary that can be called the plasmapause [*Galperin et al.,* 1975].

Filling of field tubes with plasma in the outer plasmasphere is a result of plasma outflow from the subauroral *F*-layer. Thus, the radial profile of the thermal plasma density is primarily associated with dynamics of the plasma escape due to convection penetrating to low latitudes and with gradual plasma tube-filling from the *F*-layer. The density profile contains information on the prehistory of convection and filling of *L*-shells in the outer plasmasphere. A comprehensive review of the plasmasphere is given in the monograph of *Lemaire* and *Gringauz* [1998]. The plasma density distribution in the plasmasphere and the plasmapause position depend on various factors, such as magnetic field disturbance (the $K_p$ index), the convection rate, illumination by the Sun, and the intensity of plasma outflow from the ionosphere. Taking into account these factors, one can model the plasma density distribution. One such model is the semi-empirical CDPDM [*Galperin et al*., 1997], which makes it possible to obtain reliable results for the nightside MLT sector.

## 2. Description of measurements

The plasma density in the Earth's magnetosphere is obtained by direct measurement of particles or by means of more accurate active and passive wave methods. Both active and passive wave methods were used for measuring the electron density onboard the ISEE-1 satellite and its data are used in this paper. Over time, the Sweep Frequency Receiver (SFR) provided almost continuous determination of electron density with a high resolution in almost all domains of the Earth's magnetosphere. Emission rise at a frequency close to the upper hybrid resonance frequency or cut-offs at the electron plasma frequency were investigated. These data allow us to make quite accurate measurements of the plasma density, which do not depend on the satellite's potential.

## 3. The CDPDM model

*Soloviev et al*. [1989] developed the CDPDM model. This is a three-dimensional quantitative model of cold plasma distribution in the nightside outer plasmasphere, which gives plasma density values at a particular instant. It is based on calculations of the prehistory of the processes of plasma outflow and filling for a particular magnetic field-tube and on the prediction of its convection in the large-scale electric field, which varies in time. This model uses the electric field, which depends on $K_p$, with a specified empirical model of the equatorial boundary of large-scale convection (CB), and the $K_p$ indices known for preceding time periods. The instantaneous position of the magnetic tube is transferred (traced according to the convection model) back in time, and, in accordance with the accepted rate of filling, ions are added into the tube volume. It is supposed that if the magnetic tube trajectory goes beyond the CB into the

rapid convection region (auroral oval, or polar cap) and stays there for more than three hours, then its contents are depleted on the dayside of the magnetopause. Thus, the filling of a tube with plasma begins anew after its last excursion beyond the CB. This filling with plasma can continue until equilibrium is reached or up to a given time (in which case, the filling is incomplete). At distances greater than $2R_E$ the plasma is considered to be isotropic. To derive the plasma density, the calculated number of particles in a tube is divided by its volume. The lower limit in altitude is estimated as ~1–2 $R_E$. These are altitudes at which isotropy is supposed to be achieved, and at which the analytical solution for the plasma density with the gravitation effect is applicable.

The empirical SEB (soft electron boundary) model [*Galperin et al*., 1977] for the 18:00–01:00 MLT sector and the model of *Val'chuk et al*. [1986] for the 00:00–07:00 MLT sector were taken as a CB in the model, with interpolation between these models in the 00:00–01:00 MLT sector. These boundaries are calculated by the following formulas:

$$G77 = 71.48 - 1.25K_{ps} - 0.18K_{ps}^2 - \\ -(2.84 + 1.24K_{ps} - 0.076K_{ps}^2)\times \\ \times(MLT/6 - 3) \quad (1)$$

$$V86 = 65.646 - 2.719K_{ps} + 0.203K_{ps}^2 - \\ -(0.753K_{ps} - 1.698)\,MLT/6 + \\ + 6.304(MLT/6 - 0.5)^2 \quad (2)$$

where $K_{ps}$ is the mean value between two values of $K_p$ for the preceding 3-hour interval, if the moment of time falls into the first hour of a 3-hour interval. In the opposite case, the $K_p$ values for the current and preceding intervals are used. To simplify the calculations, the analytical Stern–Volland convection model was accepted toward the polar side from the SEB [*Stern*, 1974; *Volland*, 1973]. The total electric field potential (in kV) is specified in the form

$$\Phi_\Sigma = A(Kps, MLT)L^2 \sin(MLT) - 91{,}5/L \quad (3)$$

The value of the $A(K_{ps}$, MLT) parameter was selected in each case in such a way that, in the MLT sector considered, the invariant latitude of the last closed equipotential, calculated by formula (3), would coincide with the one calculated for the given time instant by formulas (1) and (2).

The model of the process of field tubes filling with thermal plasma is taken in its simplest form, which was obtained in [*Krinberg and Tashchilin*, 1984] by approximating calculations in the polar wind model. In this case, the flux of ions directed upwards from the ionosphere is supposed to be independent of the after-storm time and of the $L$–shell and the plasma isotropization process is supposed to be continuous, so that the plasma density does not change throughout the entire tube length and proportionally increases as the filling proceeds. Under these assumptions, the plasma density in the equatorial plane on the shells $L \ge L_{\min}$ (where $L_{\min}$ is the greatest depth of tube penetration into the plasmasphere, into which these tubes have drifted by convection from the magnetotail during the considered period of geophysical activity prehistory) has the following form [*Krinberg and Tashchilin*, 1984]:

$$N_{eq}(L \ge L_{\min}, t) = N_\infty(1 - e^{-t/\tau})$$

where $\tau = \tau_* L^4$ is the characteristic time of tube filling up to the equilibrium value of $N_\infty$ ($\tau_* = 0{,}2$ days, $N_\infty = 4 \cdot 10^3\, см^{-3}$ [*Moore et al*., 1987]). For $L < L_{\min}$, according to [*Moore et al*., 1987], we have $N_{eq}(L < L_{\min}, MLT) = N_0 L^{-\alpha}$, where $\alpha = 3.5 + 0.5\sin(2\pi\, MLT/24)$ and the value of $N_0$ is determined from the condition $N_{eq}(L = 2) = N_\infty$.

**4. The nightside**

Now we present a comparison of density profiles constructed by means of the CDPDM model with measurements onboard the ISEE-1 satellite in the nightside of the plasmasphere. The heavy and thin lines represent the experimental and model profiles, respectively. The first three profiles are taken from the 4–6 MLT regions. They are indicated in Figures 1*a*–1*c*. These three profiles represent quiet, moderately disturbed, and active periods. In Figure 1a we can see the first plasmapause, when the satellite was at $L$ = 4.5 and 5.4 MLT. The second plasmapause was found to be present at $L$ =5.4. In addition to a smooth profile drop at $L$ = 3.3, inside the plasmasphere the profile drops as $L^{-4}$. The $K_p$ indices for the elapsed 24*h* were as follows: 1; 2+; 1+; 0+; 2–; 1; 1, and 0+. The current $K_p$ was 0+.

Profile 1*b* presents measurements for a moderately disturbed period preceded by the very quiet period. On this profile the plasmapause is seen at $L$ = 4.2 at 5.1 MLT. Inside the plasmasphere the density drops as $L^{-2}$.

The $K_p$ indices for the previous 24*h* were as follows: 0; 0+; 0+; 2–; 1+; 3; 3+; and 2. The current value was $K_p = 2$. Though the period for profile 1a is quieter than that for 1b and the plasmapause is located at a greater distance, the density in the plasmasphere for profile 1*b* is greater for the same *L* values. This can be explained by the fact that the geomagnetic conditions were quieter for several hours in Figure 1*b* than in Figure 1*a*.

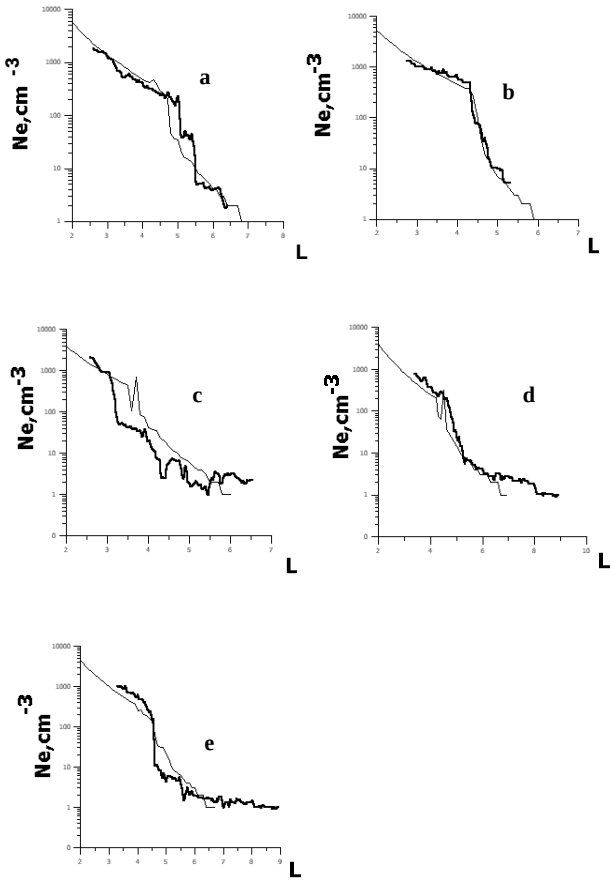


**Figure 1:** Comparison of the experimental density profiles obtained by the ISEE-1 satellite with profiles derived by means of the CDPDM model for the nightside of the plasmasphere. The heavy and thin lines show the experimental and model profiles, respectively.

(a) November 3, 1977, UT = 14:45, MLT = 5.4;
(b) November 10, 1977, UT = 19:00, MLT = 5.1;
(c) November 13, 1977, UT = 03:50, MLT = 4.1;
(d) November 6, 1977, UT = 00:16, MLT = 5.9;
(e) November 29, 1977, UT = 21:56, MLT = 4.0.

Profile 1c represents an active period. On this profile the plasmapause at $L = 3.0$ and a sharp density drop as $L^{-8}$ are seen. The $K_p$ indices for the elapsed 24 h were as follows: 3+; 3+; 3–; 3; 3–; 4–; 4, and 4+. The current value was $K_p = 4+$.

For the three cases in Figures 1*a*–1*c* the position of the plasmapause was displaced to lower *L* values with growing magnetic activity as determined from the current $K_p$ or from the prehistory.

Let us consider two more profiles. In Figure 1*d* we see a very sharp drop of density, i.e., the plasmapause at $L = 4.54$ and 4.0 MLT. The $K_p$ indices for the elapsed 24*h* were as follows: 2+; 2; 1; 1; 1+; 1; 1, and 2+. The current value was $K_p = 2+$. On profile 1e, one can see a smoother density drop, which began at $L = 4.59$ and 5.9 MLT. The $K_p$ indices for the elapsed 24*h* were, respectively, 3–; 2; 2; 1; 2; 1; 2–, and 2+. The current value was $K_p = 2+$. Comparison of these two profiles shows that for quiet periods the density drop is smoother at 4 MLT than at 6 MLT. It is interesting that on the 1*b* profile, which was constructed for a slightly more disturbed period, the plasmapause is observed at higher latitudes than on the 1*d* and 1*e* profiles and the density drop is smoother than on 1e, but sharper than on 1*d*. Though the 9-h sum of $K_p$ and the initial position of the plasmapause are approximately the same for the 1*d* and 1e profiles, the density in the plasmasphere is slightly lower for 1*e* than for 1*d*. This can be explained by the fact that on the 1e profile the geomagnetic disturbances for the past 24*h* were slightly greater, 12 and 17, respectively.

These comparisons of experimental plasma density profiles obtained from the high-apogee ISEE-1 satellite in the nightside MLT sector with model calculations have shown, in general, a good correspondence between the model and experiment concerning localization of the electron density gradients in the radial profile in the outer plasmasphere, though in Figure 1*c* one can see a slight difference between the experiment and the model. A second plasmapause is seen in the experimental data, which is absent in the CDPDM model. This can be explained by the fact that the CDPDM uses the $K_p$ index representing the average activity for 3*h*. If a strong short disturbance takes place, it can cause plasmapause displacement to lower latitudes. Therefore, in the CDPDM model the plasmapause appears to be located more poleward than its real position. In the remaining cases the model plasmasphere coincides well with the measurements, and in Figure 1*a* the model even predicts a double plasmapause.

## 5. The dayside. Symmetry

In the nightside, the convection boundary is determined from SEB. In *Galperin et al*., [1977] it was shown that the SEB, at least in the pre-midnight and near-midnight sectors, represents the "convection boundary." Electrons that form the SEB in the nightside do not reach the dayside; as a result, this scenario is not valid there. Thus, the "convection boundary" cannot be determined from the satellite measurements of electron precipitation in the dayside sector. But, it could be supposed that the plasmapause is symmetric relative to the dawn-dusk direction. We have verified this hypothesis by comparing experimental profiles with the profiles obtained by means of the CDPDM model, in which the convection boundary in the dayside is symmetric with respect to the boundary in the nightside (the SEB).

Consider three density profiles for MLT of 12:50, 09:32, and 13:00, respectively, and for various $K_p$ values.

The first profile is shown in Figure 2*a* and represents a very quiet period. The preceding $K_p$ values for 3, 6, 12, 24, and 48 hours before were, respectively, 0+; 1–; 2–; 4, and 12. The density on this profile drops as *L*–3. The plasmapause is seen at *L* = 7.2. The $K_p$ indices 12*h* prior to the observation were as follows: 2–; 1+; 3, and 3+. These $K_p$ indices correspond to a slightly disturbed period, and it could be supposed that the plasmapause should be located deeper than in reality. So, the previous rather than current $K_p$ indices should be taken into consideration.

The density profiles can often be rather complex and have diverse structures. While some parts of the structure of profiles can change rapidly, others are conserved for some days. Figure 2*b* shows the density profile in which the structures caused both by rapid changes and by longer, almost stationary processes are seen simultaneously. The preceding $K_p$ indices for 3, 6, 12, 24, and 48 h before were as follows: 1–; 1; 3+; 11–; and 30–. No classical plasmapause is seen on this profile. However, there are two possible plasmapauses at *L* = 6.5 and *L* = 6.7.

The third profile is taken for a disturbed period. It is shown in Figure 3*c*. The preceding $K_p$ indices for 3, 6, 12, 24, and 48*h* before were as follows: 6–, 10, 20, 38–, and 69–. The plasmapause is seen at *L* = 3.2. ***

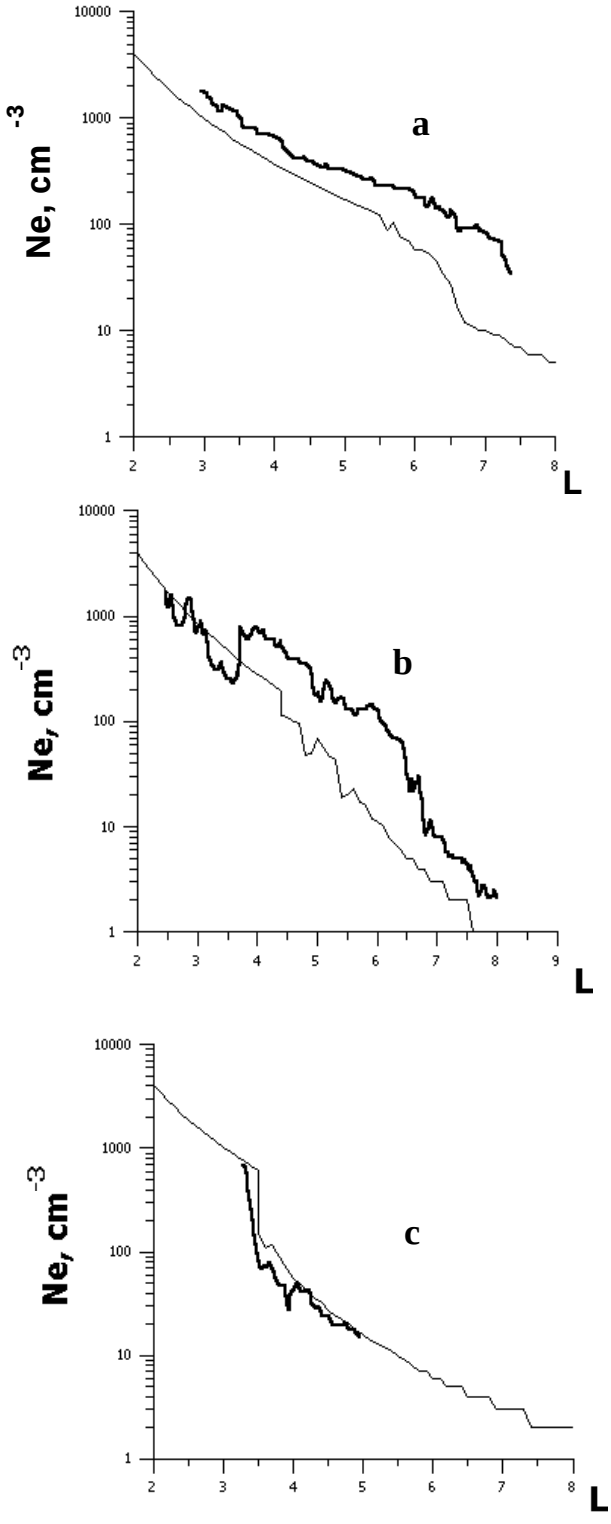


**Figure 2:** As in Figure 1, but on the dayside of the plasmasphere.
(a) November 10, 1977, UT = 16:12, MLT =12.50;
(b) November 28, 1977, UT = 11:00, MLT = 09.32;
(c) November 5, 1977, UT = 11:12, MLT = 13.0.

The constructed profiles demonstrate a good correspondence to the experiment. For a quiet period the structure of the profiles is quite similar, but the experimental density profile is higher than the model. For an active period, the model calculations coincide well with the experimental data. This is explained by the fact that, for a disturbed period, the plasmapause is displaced toward lower latitudes and only the very beginning of filling of outer shells of the plasmasphere can be seen. Thus, at this initial stage the density profile still depends poorly on the magnetic tube filling rates; it is determined by the convection boundary only. This is precisely the reason for the good correspondence to the model.

The fine agreement of the profiles constructed by means of the CDPDM model with the experimental profiles proves the validity of a mirror-like mapping of the convection boundary relative to the dawn–dusk direction.

The dayside plasmapause has not been explored adequately. Thermal plasma measurements are hampered because of the influence of the satellite's potential on the trajectories of charged particles. For this reason, the most reliable measurements are those of plasma frequency. It is clear that the density should be greater in the daytime than at night, because of the greater illumination of the plasmasphere by the Sun, since the ionosphere is mainly formed due to the production of ions through ionization by ultraviolet radiation. In addition, in the sunlit ionosphere the temperature of ions and electrons is higher than in the dark one. Electrons, possessing a greater temperature, produce a greater ambipolar field, which augments the outflow of ions with higher velocities upwards; as a result, the flux is also augmented. The CDPDM model makes no provision for all these factors, however.

## 6. Empirical curve

More than 25 density profiles were analyzed for the dayside, and, with allowance made for the above considerations, an empirical curve of the MLT dependence of the electron density of saturation in the inner plasmasphere (i.e., the dependence of $N_\infty$ on MLT in the tube filling model) was constructed. This curve was constructed for a quiet period (i.e., for small $K_p$ indices), because for the disturbed period the model agrees well with the experiment.

For the nightside MLT sector, $0 \le MLT \le 4$, $N_\infty$ remained unchanged, independent of MLT, and equal to $4 \cdot 10^3\, см^{-3}$; for the $4 < MLT < 9$ sector,

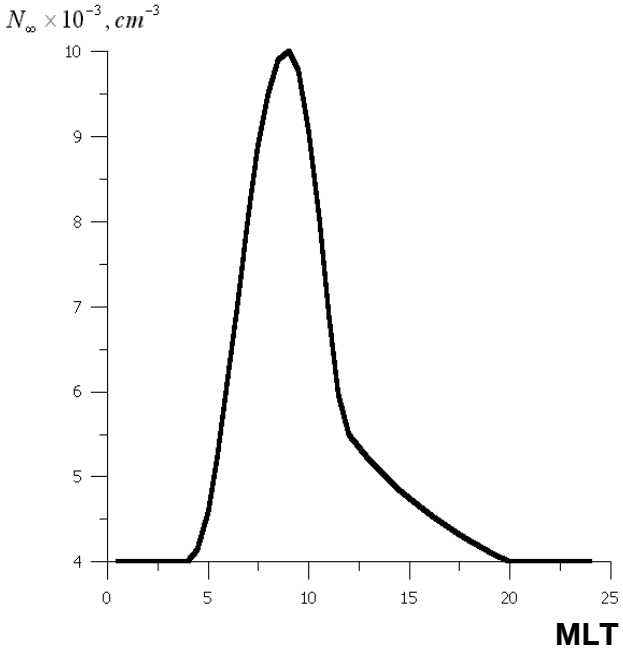


**Figure 3:** Empirical curve of the MLT dependence of saturation density obtained by analyzing experimental data of ISEE-1 (1977–1983).

$$N_\infty = ((\sin(\frac{MLT}{1.55} + 2.12) + 1) \cdot 3 + 4)) \cdot 10^3\, см^{-3}.$$

For $9 \le MLT < 12$,

$$N_\infty = \frac{1}{2} \cdot$$
$$\cdot ((\sin(\frac{MLT^2}{20.7} + 22.8) + 1) \cdot 4.5 + 5.5) \cdot 10^3;$$

for $12 \le MLT < 20$

$$N_\infty = ((\frac{1}{MLT} - 0.05) \cdot 45 + 4) \cdot 10^3\, см^{-3};$$

and for $20 \le MLT \le 24$ $N_\infty = 4 \cdot 10^3\, см^{-3}$.

This empirical curve is shown in Figure 3. The CDPDM model was improved on the basis of this curve.

A comparison of density profiles constructed by means of the improved CDPDM model with ISEE-1 experimental data is shown in Figure 4. For the profiles processed using this curve, the model provides a better agreement with the experiment.

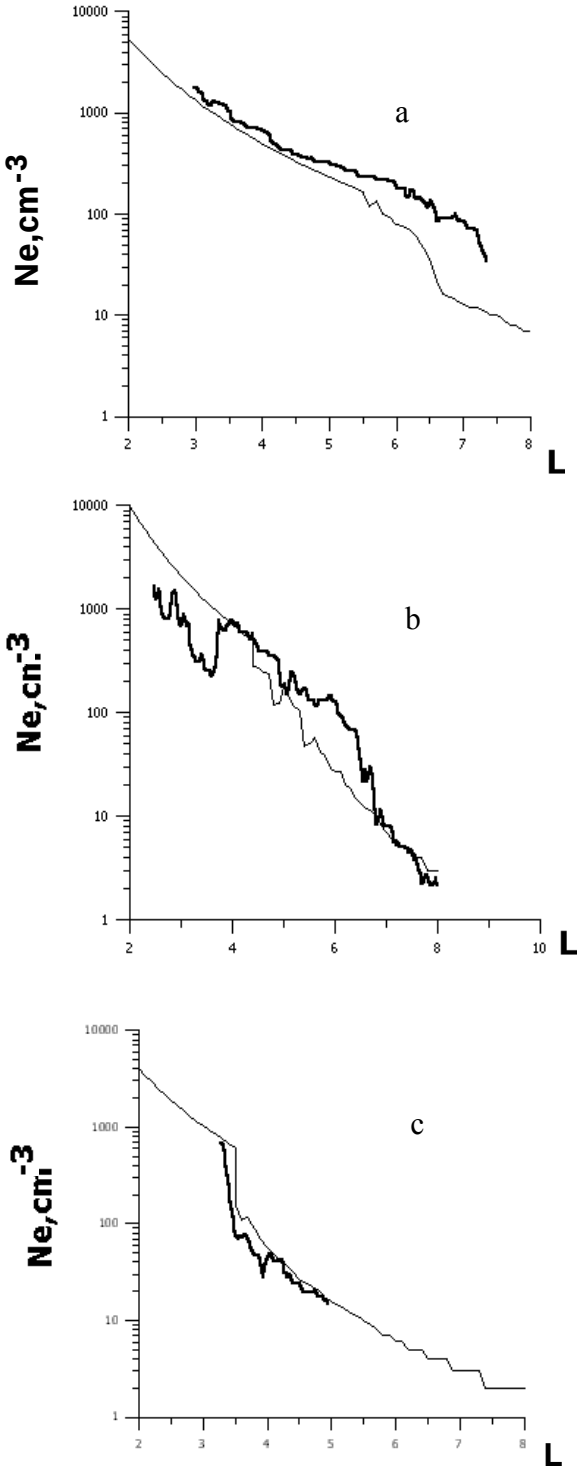


**Figure 4:** Comparison of experimental density profiles obtained by the ISEE-1 satellite with profiles derived by means of the improved CDPDM model in the dayside of the plasmasphere.
(a) November 10, 1977, UT = 16:12, MLT = 12.50;
(b) November 28, 1977, UT = 11:00, MLT = 09.32;
(c) November 5, 1977, UT = 11:12, MLT = 13.0.

## 7. Conclusion

We have compared daytime-measured profiles of the outer plasmasphere density with the CDPDM model.

The model employs the idea of convection boundary symmetry relative to the dawn–dusk direction. The convection boundary in the nightside was taken from the SEB. The fine correspondence of the experimental profiles with the model has shown that the simple idea of nighttime convection mapping to the dayside is adequate. Certainly, the small set of 25 dayside profiles that was used in this paper does not provide a complete picture of the plasmasphere. Furthermore, because of the deficiency of the data, no comparison of experimental and model density profiles was carried out in the 15–24 MLT regions. For this reason, we cannot say anything about the CDPDM model prediction of the evening bulge in the plasmasphere, which, according to the data of *Carpenter* [1966], is not symmetric relative to the dawn–dusk direction. The experimental data on the shape of the plasmasphere have a certain drawback. Namely, each satellite passage, when the measurements are carried out, falls at a time that differs from the time of the other passage. As a result, the measured shape of the plasmasphere is averaged over long time intervals, while the model yields an instantaneous picture. Most likely, because of these considerations the plasmasphere asymmetry is not so great. This is why the CDPDM agrees well with the experiment.

On the basis of comparison of dayside passages of ISEE-1 with the CDPDM model, the dependence of $N_\infty$ on MLT was included in our model, which improved its correspondence to the experimental density profiles. As a result, an improved CDPDM model has been developed.

**Acknowledgements** The authors thank R. R. Anderson, for the experimental density profiles obtained by the ISEE-1 satellite, and Yu. I. Galperin for the proposed subject, continuous attention to our work, and useful discussions. This work was supported by the Russian Foundation for Basic Research (project No. 03–02–16749), by the JURRISS NAG5-8638 grant and by the Russian Ministry of Industry, Science and Technology grant HIII – 1739.2003.2.

## References

Brice, N. M., Bulk Motion of the Magnetosphere, *J. Geophys. Res.*, *72*, 5193–5211, 1967.

Carpenter, D. L., Whistler Study of the Plasmapause in the Magnetosphere. I. Temporal Variations in the Position of the Knee and Some Evidence on Plasma

Motions Near the Knee, *J. Geophys. Res.*, *71*, 693-709, 1966.

Galperin, Yu .I., V. N. Ponomarev, Yu. N. Ponomarev, and A. G. Zosimova, Plasma Convection in the Evening Sector of the Magnetosphere and the Plasmapause Nature, *Kosm. issled.*, *13*, 5, 669–686, 1975.

Galperin, Yu. I., J. Crasnier, Yu. V. Lisakov *et al.*, Diffused Auroral Zone. I. A Model of Equatorial Boundary of the Diffused Zone of Precipitation of Auroral Electrons in the Evening and Near-Midnight Sectors, *Kosm. issled.*, *15*, 3, 421–434, 1977.

Galperin, Yu. I., V. S. Soloviev, K. Torkar *et al.*, Predicting the Plasmaspheric Density Radial Profiles, *J. Geophys. Res.*, *102*, 2079–2091, 1997.

Gringauz, K. I., V. V. Bezrukikh, V. D. Ozerov, and R. E. Rybchinskii, Investigation of Interplanetary Ionized Gas, Energetic Electrons, and Corpuscular Solar Radiation Using Three-Electrode Traps of Charged Particles onboard the Second Space Rocket, *dokl. akad. nauk SSSR*, *131*, 6, 1301–1304, 1960.

Krinberg, I. A. and A. V. Tashchilin, *Ionosfera i plazmosfera* (Ionosphere and Plasmasphere), Moscow: *Nauka*, 1984.

Lemaire, J. F. and K. I. Gringauz, *The Earth's Plasmasphere*, Cambridge Univ. Press, 1998.

Moore, T. E., D. L. Gallagher, J. L. Horwits, and R. H. Comfort, MHD Wave Breaking in the Outer Plasmasphere, *Geophys. Res. Lett.*, *14*, 10, 1007-1010, 1987.

Nishida, A., Formation of Plasmapause, or Magnetospheric Knee, by the Combined Action of Magnetospheric Convection and Plasma Escape from the Tail, *J. Geophys. Res.*, *71*, 5669–5679, 1966.

Soloviev, V. S., Yu. I. Galperin, L. V. Zinin *et al.*, Equatorial Boundary of Diffused Precipitation of Electrons from the Plasma Sheet as a Boundary of Large-Scale Convection in the Magnetosphere (Plasmapause), *Kosm. iIssled.*, *27*, 232–247, 1989.

Stern, D. P., Models of the Earth's Field, NASA/GSFCX Doc. 602-74-159, May 1974.

Val'chuk, T. E., Yu. I. Galperin, L. M. Nikolaenko *et al.*, Diffused Auroral Zone. VIII. Equatorial Boundary of the Zone of Diffused Precipitation of Auroral Electrons in the Morning Sector, *Kosm. issled.*, *24*, 6, 875–883, 1986.

Volland, H. A., Semiempirical Model of Large-Scale Magnetospheric Electric Fields, *J. Geophys. Res.*, *78*, 1, 171–180, 1973.

# Solar wind-magnetosphere effects in the middle and low latitude ionosphere

B. G. Fejer

Center for Atmospheric and Space Science, Utah State University,
Logan, UT 94322-4405, USA

**Abstract.** Ionospheric electric fields play fundamental roles in the dynamics of the Earth's ionosphere and thermosphere. Enhanced geomagnetic activity has long been known to cause large ionospheric electric field and current perturbations from high to equatorial latitudes. These electrodynamic disturbances can affect strongly the altitudinal and latitudinal distribution of ionization and the generation of plasma irregularities over a large area of the Earth. Over the last decade, experimental and global convection modeling studies have significantly improved our understanding of the electrodynamic response of the middle and low latitude ionosphere to enhanced geomagnetic activity. The dominant electric field disturbance processes have been identified as due to the prompt penetration of high latitude electric fields to lower latitudes, and to ionospheric disturbance dynamo electric fields driven by enhanced energy input into the high latitude ionosphere. The typical latitudinal, local time, and storm time dependence of these electric field disturbances do not depend on the details of magnetospheric physics, and are now reasonably well explained by global convection and ionospheric dynamo models. On the other hand, the mechanisms responsible for the large spatial and temporal variability of these perturbation electric fields, particularly during and shortly after strong geomagnetic activity, are not well understood. In this work, we first review the recent progress in the study of the middle and low latitude disturbance electric fields, focusing on prompt penetration electric fields. Then we discuss some of the solar wind-magnetosphere-ionosphere processes responsible for their large variability. These include magnetic field line stretching, dipolarization, and ionospheric conductivity effects.

## 1. Introduction

Numerous studies have documented large and complex geomagnetic storm effects in the density, composition and dynamics of the subauroral middle- and low-latitude ionosphere and thermosphere [e.g. *Kelley*, 1989; *Fuller-Rowell et al*., 1994; *Buonsanto*, 1999; *Basu et al*., 2001]. Ionospheric plasma density can be affected significantly by high latitude thermospheric winds and composition changes during and shortly after geomagnetic disturbed periods, but the most severe ionospheric effects result from electrodynamic disturbances. At subauroral latitudes there are often very strong and highly localized polarization electric fields during large magnetic storms. These electric fields generate large and highly structured storm-enhanced plasma densities, steep spatial gradients in plasma parameters, strong radio wave scintillations, and also control the erosion and reconfiguration of the outer plasmasphere [e.g., *Foster et al*., 2002]. At low latitudes, storm-driven electrodynamic effects can severely change the distribution of ionization over a large area of the globe and control the generation of ionospheric plasma irregularities [*Fejer*, 1996], which disrupt the performance of communication, navigation, and surveillance systems.

Satellite and incoherent scatter observations have shown that during enhanced geomagnetic conditions, significant subauroral, middle and low latitude electric fields and currents result from the interaction of the high latitude electric fields of solar wind dynamo origin and the coupled magnetosphere-ionosphere system [e.g., *Yeh et al*., 1991; *Galperin et al*., 1997; *Burke et al*., 2000; *Anderson et al.*, 2001]. These electrodynamic disturbances are basically due to extension of the auroral zone to lower latitudes, formation of very large (over 100 mV/m) polarization electric fields near the equatorward edge of the pre-midnight sunward convection [e.g., *Galperin*, 1974], penetration of magnetospheric electric fields into the plasmasphere [e.g., *Jaggi and Wolf*, 1973], and auroral zone driven ionospheric dynamo electric fields [*Blanc and*

*Richmond*, 1980]. The first two processes are dominant at subauroral and upper midlatitudes (above about 50˚) during large magnetic storms. Prompt penetration and disturbance dynamo electric fields have much smaller magnitudes (< 10 mV/m), but they are the most important sources of low latitude ionospheric electrodynamic disturbances.

Several experimental studies have determined the characteristics of subauroral ionospheric convection electric fields [e.g., *Holt et al*., 1987; *Yeh et al., 1991*; *Foster and Rich*, 1998; *Buonsanto*, 1999]. Subauroral observations often show narrow (≤ 1˚) latitudinal regions of very large (> 1000 m/s) westward plasma drifts and very low plasma densities during the initial phases of large magnetic storms. These high speed westward flows, called polarization jets [*Galperin et al*., 1974] or subauroral ion drifts [e.g., *Spiro et al*., 1979; *Anderson et al*., 1991; 2001], are driven by polarization electric fields resulting from the separation of the equatorward boundaries of electron and ion precipitation [*Southwood and Wolf*, 1978]. There are also broader (~5˚) subauroral regions of large (> 500 m/s) westward convection during strongly disturbed times. The entire region of largely enhanced westward plasma drifts has recently been termed Subauroral Polarization Streams (SAPS) [*Foster and Burke*, 2002].

In this work, we review the present understanding and recent results and outstanding problems in the study of middle and low latitude ionospheric disturbance electric fields. We focus on short-lived prompt penetration electric field perturbations, which nearly simultaneously affect the ionosphere from middle to equatorial latitudes, but we also briefly discuss ionospheric disturbance dynamo electric fields. In the following sections, we first describe the general properties of these electric field perturbations, using mostly equatorial electrodynamic plasma drift measurements, and their relationship to higher latitude electric fields and currents. Then, we compare these observations with predictions from recent global convection and disturbance dynamo models. Finally, we examine the latest results and outstanding questions in this field.

## 2. Experimental studies

Low latitude and equatorial ionospheric electric fields and currents have been studied in detail using incoherent and coherent scatter radar and satellite electrodynamic plasma drift observations [e.g., *Kelley*, 1989; *Fejer*, 1997; *Su et al*., 2003], and extensive ionosonde and magnetometer measurements [e.g.; *Abdu et al*., 1995; *Sastri*, 1997; 2002]. The most detailed equatorial electric field studies were performed using radar observations of *F* region vertical plasma drifts at

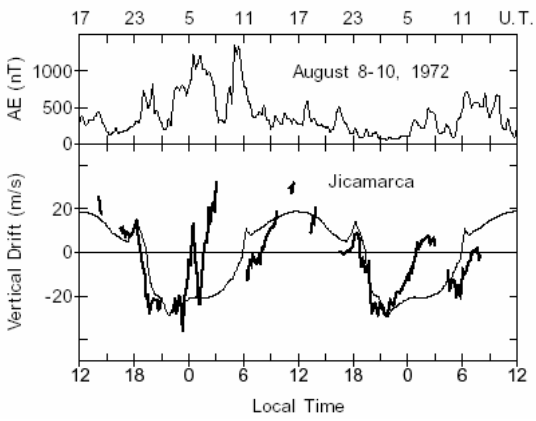


**Figure 1.** Auroral electrojet indices and equatorial vertical (positive upward) plasma drifts over Jicamarca, Peru during a strongly disturbed period. The thin curve denotes the average quiet time drift pattern (after *Scherliess and Fejer* [1987]).

the Jicamarca Radio Observatory (11.9˚ S, 76.8˚ W, dip latitude 1˚ N) near Lima, Peru. Figure 1 shows the auroral electrojet (*AE*) indices and vertical plasma drift velocities measured with the Jicamarca radar during and shortly after the large magnetic storm of August 8-9, 1972. Over Jicamarca, an *F* region upward plasma drift velocity of 40 m/s corresponds to an eastward electric field of 1 mV/m. These vertical drifts measurements have a typical integration time of about 5 min and an uncertainty of 1–2 m/s. Figure 1 provides examples of strong vertical perturbation drifts, relative to the quiet time values, lasting several hours after large changes in the high latitude current systems, as indicated by the *AE* indices.

The equatorial perturbation electric fields (electrodynamic plasma drifts) associated with geomagnetic disturbances occur globally and cover a broad range of time scales [e.g., *Fejer*, 1986; *Abdu*, 1997]. Sharp electric field perturbations with time scales typically shorter than about an hour are due mostly to the prompt penetration of solar-wind/magnetospheric electric fields to middle, low, and equatorial latitudes [e.g., *Kelley et al*., 1979; *Fejer*, 1986; *Fejer et al*., 1990a; *Kikuchi et al*., 1996, 2003; *Abdu*, 1997; *Sastri et al*., 1997, 2002]. These prompt penetration electric fields occur during periods of large and rapid changes in magnetospheric convection, when the inner edge of the plasma sheet and the region-2 Birkeland currents are temporarily configured to shield out a weaker (undershielding) or stronger (overshielding) cross-tail electric field [e.g., *Wolf*, 1983; *Senior and Blanc*, 1984; *Spiro et al*., 1988; *Peymirat et al*., 2000]. Figure 2 shows examples of correlated rapid temporal variations in IMF $B_z$, *AE* indices, auroral and equatorial zonal electric

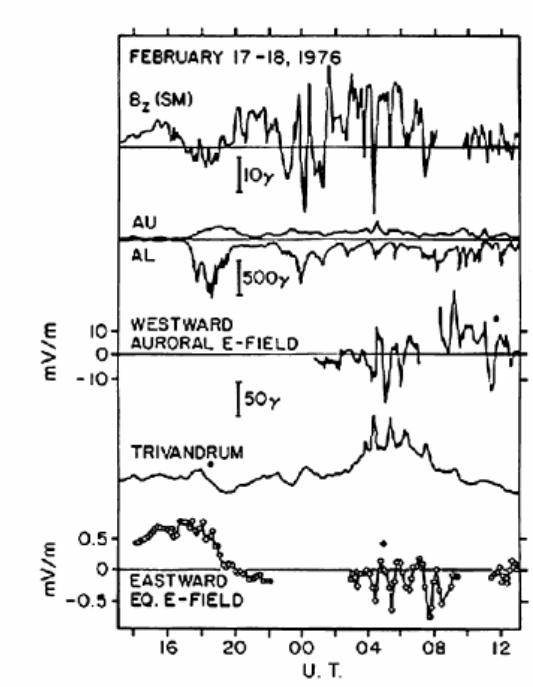


**Figure 2**. IMF *Bz* component, auroral indices, zonal electric field at Chatanika, Alaska, horizontal component of the magnetic field at Trivandrum, India, and zonal electric field over Jicamarca during a disturbed period. The dots denote local magnetic midnight (after *Gonzales et al*. [1979]).

fields, and in the horizontal component of the Earth's magnetic field over the Indian equatorial region during a disturbed period. The equatorial prompt penetration electric fields associated with a sudden increase (decrease) in the high latitude convection are westward (eastward) at night with largest magnitudes near dawn, and eastward (westward) with typically smaller magnitudes during the day. Equatorial prompt penetration zonal plasma drifts, driven by vertical perturbation electric fields, are not easily observed and have been detected only recently at Jicamarca [*Fejer and Emmert*, 2003].

High time-resolution magnetic field observations near the dip equator also have been used extensively to study the effect of penetration of convection electric fields [e.g., *Nishida et al*. 1966; *Kikuchi et al*., 1996, 2000, 2003]. Quasi-periodic so-called *DP2* magnetic field fluctuations, with time scales from about half an hour to several hours at high latitudes and in the dayside magnetic equator, are signatures of convection electric fields controlled by the southward IMF [*Nishida*, 1968]. *Kikuchi et al*. [1996] pointed out that convection driven Hall currents cause high latitude DP2 effects and that they propagate nearly instantaneously (within a temporal resolution of 25 s) to the equator, where the Hall effect then amplifies the corresponding Pedersen current magnetic field fluctuations. The shielding time constant, inferred from magnetometer measurements, is about 20 min [e.g., *Kikuchi et al*., 2000], which is consistent with theoretical values. *Kikuchi and Araki* [1979] and *Kikuchi et al*. [2003] suggested that the polar electric fields are transmitted to low latitudes by the zero-order TM mode in the Earth-ionosphere waveguide and transported upward along the magnetic field lines by Alfven waves. Recent magnetometer studies have examined the conditions required for daytime geomagnetic field perturbations resulting from magnetospheric substorms. *Sastri et al*. [2003] reported a weak response in the daytime equatorial horizontal magnetic field component to a substorm occurring during steady southward IMF and increasing polar cap potential drop. On the other hand, they observed a strong bay-like equatorial magnetic field perturbation, which was interpreted as due to a westward overshielding electric field, following a fully developed substorm associated with a northward IMF turning and a rapid reduction of the cross polar cap potential. *Kikuchi et al*. [2003] also reported noticeable short-lived substorm-associated equatorial counter-elecrojet (westward daytime electric field and current perturbations) events following region-1 magnetic field-aligned current decreases associated with northward IMF turnings.

*Sibeck et al*. [1998] studied the source of small north/south fluctuations in dayside magnetic field measurements using ground-based magnetometers and satellite IMF and particle data. They explained the large majority of daytime equatorial magnetic field perturbations with magnitudes between 10 and 40 nT in terms of either substorm onsets or changes in the solar wind dynamic pressure, and pointed out that many southward IMF turnings produced no observable magnetic field effects. However, large fluctuations in the solar wind electric field can produce significant ionospheric electric field and current disturbances from high to equatorial latitudes [e.g., *Gonzales et al*., 1979; *Kelley et al*., 2003], as illustrated in Figure 2. IMF $B_y$ changes have also been proposed as a source of equatorial prompt penetration electric fields [*Galperin et al*. [1974] and *Kelley et al*., [2002].

Incoherent scatter radar and whistler studies [*Gonzales et al*., 1980; *Kelley*, 1989; *Fejer et al*., 1990a] indicate that latitudinal variation of the zonal prompt penetration electric fields approximately follows the $L^{3/2}$ theoretical prescription derived by *Mozer* [1970], which is based on the assumption that the zonal electric field component is constant in the equatorial plane. The meridional prompt penetration electric fields increase more strongly with latitude than the zonal electric fields and have larger magnitudes at middle and subauroral

latitudes. As mentioned earlier, during large storms, the upper middle latitude and subauroral SAPS electric fields have much larger magnitudes than the prompt penetration electric fields.

Slower varying electric field disturbances with time scales typically ranging from a few to tens of hours are generally identified as ionospheric disturbance dynamo electric fields caused by enhanced energy deposition (mostly through Joule heating) into the auroral ionosphere [*Blanc and Richmond*, 1980; *Mazaudier and Venkateswaran*, 1990]. Ionospheric disturbance dynamo drifts play important roles in storm-time ionospheric dynamics at low and equatorial latitudes; at higher latitudes their magnitudes are much smaller than those generated by other processes. The equatorial ionospheric disturbance dynamo drifts are westward during the day and eastward at night, with largest magnitudes near dawn. Figure 1 shows an example of strong nighttime disturbance dynamo drifts between about 0500 and 1000 UT on August 10, 1972, when the auroral currents, as indicated by the *AE* indices, were relatively small. These drifts were due to disturbance dynamo electric fields associated with the large enhancements in the auroral currents about a day earlier [*Scherliess and Fejer*, 1997].

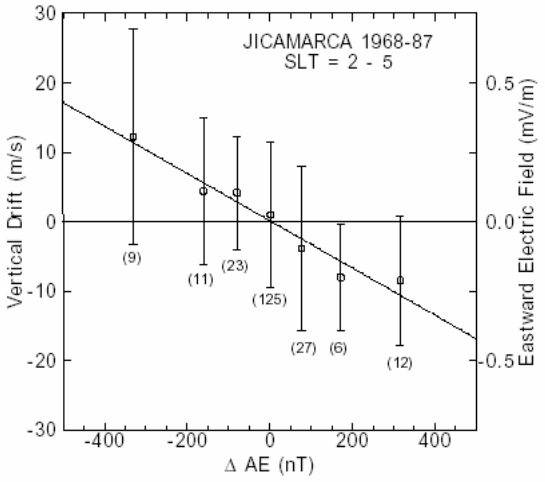


**Figure 3.** Variation of the hourly averaged Jicamarca vertical disturbance drifts for changes in the *AE* index in the 0200–0500 local time sector. The number of measurements in each binned average is also shown (after *Fejer and Scherliess* [1995]).

## 3. Storm-time dependent empirical models

*Fejer and Scherliess* [1995, 1997] and *Scherliess and Fejer* [1997] used a large database of Jicamarca vertical plasma drift measurements to study and empirically model the storm-time dependence of equatorial vertical disturbance plasma drifts (zonal electric fields) as a function of the time history of geomagnetic activity, as represented by the *AE* index. In these studies the local time, season, and solar cycle dependent average quiet time drift values were subtracted from the drift measurements and the residuals were analyzed using linear regression, multi-parameter fitting, and storm-time dependent binning. *Fejer and Scherliess* [1995] showed that, on average, identical sudden increases and decreases in *AE* lead to vertical perturbation drifts with about the same magnitude but opposite polarities. This is illustrated in Figure 3 for the post-midnight sector.

The local time variation of the disturbance drifts was empirically modeled using nine normalized cubic-B splines of order 4, and the magnetic activity variation is accounted for by five storm-time parameters. The 45 coefficients were determined by a least square fit to a data set of over 15,000 quarter-hourly averaged drift values. The model inputs are changes in *AE* index and time averaged values of *AE* over the preceding periods of 1-6, 7-12, and 22-28 hours, which account for prompt penetration and disturbance dynamo electric fields, respectively [*Fejer and Scherliess*, 1997].

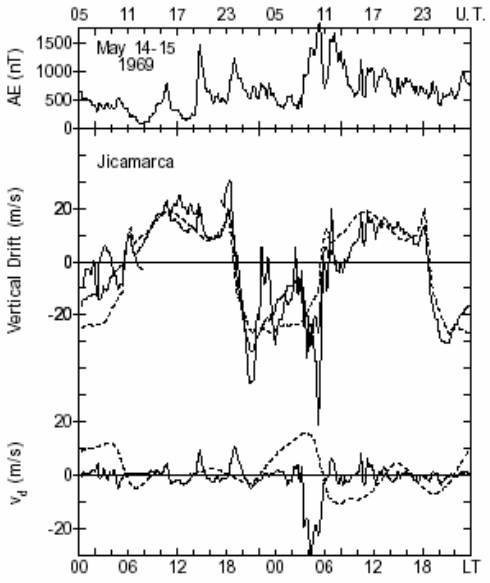


**Figure 4**. Auroral electrojet indices; measured (thin solid line), average quiet (dashed line) and model (thick solid line) equatorial vertical drifts; and calculated prompt penetration (solid line) and disturbance dynamo (dashed line) drifts for a disturbed period during May 1969. The model drifts in the center panel were obtained by adding the average quiet time and the calculated disturbance drift (after *Fejer and Scherliess* [1997]).

This empirical drift model can effectively determine the contributions of prompt penetration electric fields and short-term (1–12 h) and long-term (20–36 h) disturbance dynamo electric fields, and it allows for quantitative testing of global convection and disturbance dynamo models. These empirical studies also showed that the lifetimes of the disturbance drifts following sudden decreases in convection are longer than after convection increases, due to short-term disturbance dynamo electric fields.

Figure 4 shows the *AE* indices, the vertical drift data, the average quiet time drift pattern, and the prompt penetration and disturbance drift components obtained using the *AE* indices as input in the model, during an extended period of high geomagnetic activity. The large upward and downward velocity perturbations observed in the postmidnight sector (about 0100–1200 UT) on May 15 are generally consistent with the model results, but the upward velocity perturbations between 0300-0500 UT were not reproduced by the model. Sharp eastward electric field perturbations occasionally observed in the midnight sector during disturbed periods are probably due to substorms triggered by sudden northward IMF changes. These results highlight the fact that this climatological empirical model, which uses the *AE* index as the high-latitude disturbance parameter, can generally explain prompt penetration electric fields resulting from changes in the high latitude convection, but not prompt penetration electric fields due from other magnetospheric processes (e.g., substorms). Recently, *Su et al*. [2003] reported good agreement between plasma drift measurements on board ROCSAT during a storm and the predictions from the empirical Scherliess-Fejer disturbance dynamo model.

The methodology introduced by *Fejer and Scherliess* [1997] was also used to study and empirically model the storm-time dependence of low and midlatitude disturbance zonal drifts measured by the DE-2 satellite [*Scherliess and Fejer*, 1998; *Fejer and Scherliess*, 1998], and meridional and zonal drifts over Saint-Santin (45˚ N, 2˚ E; magnetic latitude 40˚) and Millstone Hill (42.6˚ N, 66.5˚ W; apex magnetic latitude 54˚) [*Scherliess et al*., 2001]. The midlatitude meridional/perpendicular disturbance drifts are upward during the day and downward at night. The zonal disturbance drifts are predominantly westward, have largest magnitudes in the dusk-midnight sector, and decay more slowly than the meridional drifts. These polarities are reversed following a sudden decrease in the high latitude convection. *Scherliess et al*. [2001] showed that disturbance drift patterns derived from Millstone Hill and Saint-Santin zonal drift measurements are in good agreement with the corresponding results from the DE-2 satellite. In the next section, we will compare these empirical drift patterns with results from global convection and disturbance dynamo models.

## 4. Theoretical model results and comparisons with observations

Several global convection models have been used to study effects of the prompt penetration of polar cap electric fields to lower latitudes [e.g., *Senior and Blanc*, 1984; *Spiro et al*., 1988, *Tsunomura*, 1999; *Peymirat et al*., 2000; *Sazykin*, 2000]. This penetration, resulting from sudden changes in magnetospheric convection, is controlled by the region-2 field-aligned currents, which are driven by interaction of hot magnetospheric plasma and the ionosphere. The various convection models predict generally similar perturbation electric field patterns, which depend mainly on the high-latitude potential drop and the distribution of magnetospheric and ionospheric conductances but are largely independent of the details of magnetospheric physics.

*Tsunomura* [1999] studied the local time variation of transient middle and low latitude equatorial perturbation electric fields and current changes for given high latitude field-aligned current distributions by solving the current conservation equation, which accounts for the drift physics in the inner magnetosphere, and using a realistic two-dimensional thin shell ionospheric conductivity model. The model reproduces well the electric and magnetic field signatures associated with geomagnetic sudden commencements, and also the climatological prompt penetration equatorial zonal electric fields of *Fejer and Scherliess* [1997].

*Peymirat et al*. [1998] presented the Magnetosphere-Thermosphere-Electrodynamics General Circulation Model (MTIE-GCM), which coupled a two-fluid self-consistent time dependent inner magnetospheric convection model with the Thermosphere-Ionosphere-Electrodynamics General Circulation Model (TIEGCM). This model self-consistently includes the electrodynamic coupling due to auroral particle precipitation, region 2 field aligned currents, and thermospheric neutral winds. The potential along the polar cap is assumed to have a sinusoidal shape with a maximum and a minimum at 0600 and 1800 magnetic local time (MLT) [*Heelis et al*., 1992], respectively. The MTIE-GCM predicts the magnitude of prompt penetration electric fields fairly accurately, but cannot simulate specific events since it uses a simple dipole magnetic field in the magnetosphere and therefore does not account for the magnetospheric reconfiguration effects discussed by *Fejer et al*. [1990*b*]. On the other hand, it allows for realistic studies of ionospheric wind dynamo effects during and shortly after magnetic storms. *Peymirat et al*. [1998] used this model to show that neutral winds enhance the shielding effect by about 10%, which results in an increase (decrease) of the north-south (east-west) component of the ionospheric electric field. *Peymirat et al*., [2000] pointed out that fluctuating electric and magnetic field disturbances poleward and equatorward of the region-2

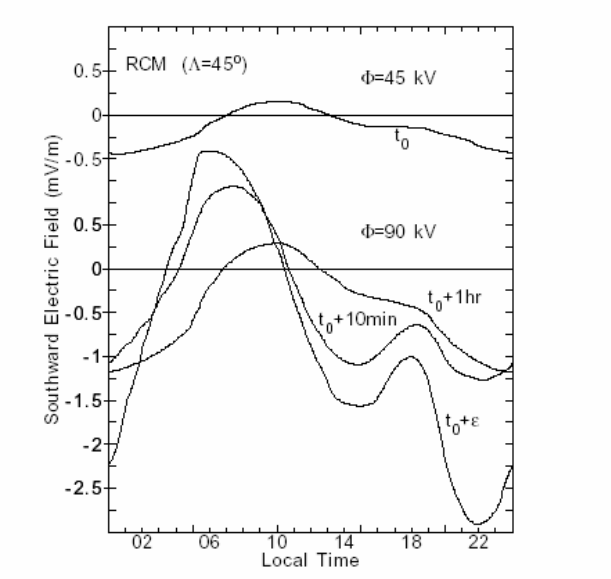


**Figure 5**. Meridional disturbance electric fields for average plasma sheet conditions obtained from the RCM for quasi-equilibrium conditions and a polar cap potential drop of 45 kV (upper panel), and prompt penetration electric fields after a step function increase in the polar cap potential drop to 90 kV (after *Fejer and Scherliess* [1998]).

currents are not exactly simultaneous fields, due to the time delay associated with the re-establishment of shielding, which increases with plasma sheet pressure. Recently, *Richmond et al.* [2003] used the MTIE-GCM to study long-lasting equatorial disturbance electric fields resulting from disturbance dynamo [*Blanc and Richmond*, 1980] and fossil wind effects [*Spiro et* al., 1988; *Fejer et al*., 1990*b*].

The Rice Convection Model provides a detailed, self-consistent description of the time-dependent inner magnetospheric particle distribution, region-2 field aligned currents, and resulting ionospheric electric fields [e.g., *Wolf et al*., 1982; *Wolf*, 1983; *Toffoletto et al*., 2003] by solving the fundamental equations of magnetosphere-ionosphere coupling [*Vasyliunas*, 1970]. The time-dependent plasma densities and drifts in the inner and middle magnetosphere (within about 20 Earth radii) are computed for given electric field distributions along the polar cap boundary, particle populations along the outer magnetosphere, and ionospheric conductivities. This is the only global convection model that can give predictions for specific events, since it allows for magnetospheric reconfiguration effects.

RCM predictions are in good agreement with measured ion and electron plasma sheet locations and electric field magnitudes during SAPS events. However, the model is not fully self-consistent, because the magnetic field is assumed and the magnetic field generated by the field-aligned currents is not computed. Recently, several upgrades have been made to the RCM [e.g., *Sazykin*, 2000; *Toffoletto et al*., 2003]. However, because the basic middle and low latitude ionospheric electric field results have not changed significantly, we show a comparison of the empirical prompt penetration patterns presented earlier with results from the computer runs described by *Spiro et al*. [1988], and discussed in more detail by *Fejer et al*. [1990b]. Some results obtained using newer versions of the RCM will be discussed later.

The top panel of Figure 5 presents the typical meridional prompt penetration electric fields (zonal plasma drifts) obtained from the RCM for approximate equilibrium conditions at average plasma sheet conditions with a cross polar cap potential of 45 kV. The bottom panel depicts the transient electric fields after a sudden increase in the potential to 90 kV. These RCM results were obtained assuming a sinusoidal shape for the potential along the poleward boundary with maximum at 0600 MLT and a minimum at 1800 MLT. The results for t+ε are not realistic since it is unlikely that significant polar cap potential changes can occur on time scales shorter than about 10 min, as assumed in the simulation. Figure 5 indicates that, following the increase in the potential, there are large transient poleward electric fields in the dusk-midnight sector, and smaller equatorward electric fields in the late-night to noon period. These transient electric fields decay with a time constant of about 15-20 min, and shift to later local times as the inner edge of the plasma sheet reacts to the new polar cap potential drop. After one hour, the convection pattern essentially reaches a new equilibrium maintained by the quasi-steady state leakage of high latitude electric fields for the higher cross polar cap potential.

Figure 6 presents comparisons of the DE-2 initial perturbation drifts for $\Delta AE$ = +400 nT, and the response predicted by the RCM [*Fejer et al*., 1990b] for the corresponding increase of the polar cap potential drop by 33 kV. In this case, these two parameters are related by $\Phi$(kV) = 36 + 0.082 *AE*(nT) [*Ahn et al*, 1992]. Figure 6 indicates that the RCM prompt penetration zonal drift patterns are generally in good agreement with the DE-2 model drifts. The empirical perturbation drifts have larger amplitudes, particularly near dusk, and they decay more slowly than the theoretical values. Near steady state (i.e., after about 90 minutes; not shown) the DE-2 and the RCM disturbance drifts have the same local time dependence. The magnitudes of the RCM steady-state perturbation drifts for invariant latitudes of 45˚ and 35˚ are smaller than the empirical values. *Scherliess et al.* [2001] showed that the zonal and meridional prompt penetration electric field patterns derived from the Millstone Hill and Saint-Santin drift data are also in good agreement with RCM results. As mentioned earlier,

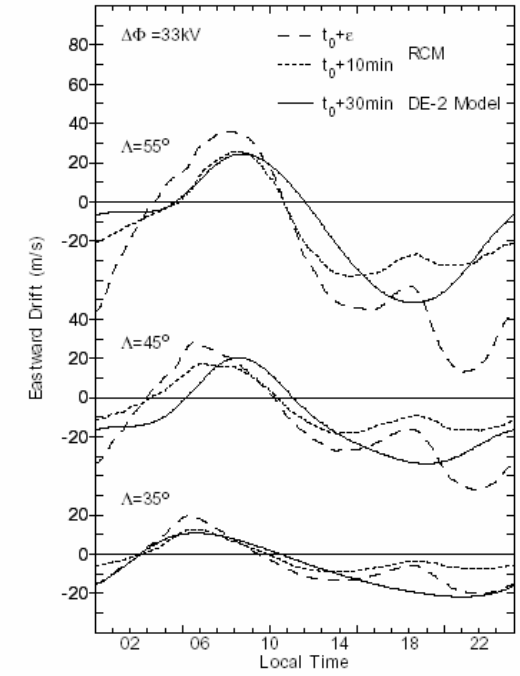


**Figure 6**. Comparison of initial time DE-2 empirical and RCM prompt penetration zonal disturbance drifts resulting from a step function increase in the cross polar cap potential by 33 kV (after *Fejer and Scherliess* [1998]).

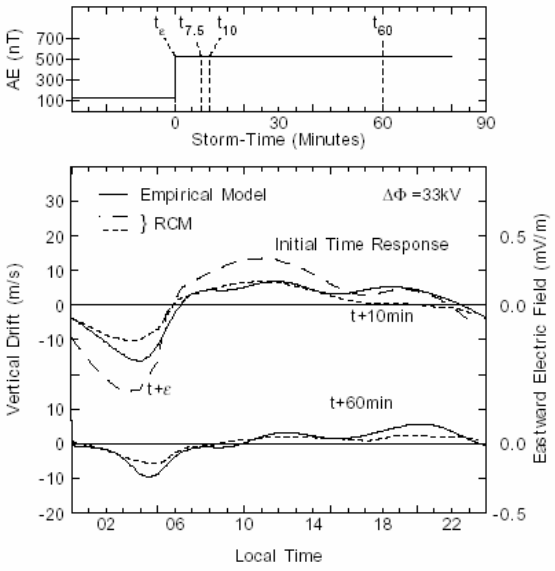


**Figure 7.** Comparison of empirical equatorial prompt penetration vertical drifts and RCM drifts following an idealized increase in the polar cap potential drop by 33 kV (after *Fejer and Scherliess* [1997].

prompt penetration electric fields over Millstone Hill are only detected under moderate geomagnetic conditions; during highly active times they are masked by much stronger auroral zone or SAPS electric fields.

Figure 7 shows a comparison of the equatorial vertical perturbation drifts from the Fejer-Scherliess [1997] empirical model 7.5 min and 60 min after an idealized 400 nT increase in *AE*, and the RCM disturbance drifts following a 33 kV increase in the cross polar cap potential. Figure 7 indicates that the local time dependence, storm time dependence, and the amplitudes of the disturbance drifts predicted by the RCM are in excellent agreement with the results from the empirical model. These equatorial zonal perturbation electric field patterns are also in good agreement with results from other convection models [e.g., *Senior and Blanc*, 1984; *Tsunomura*; 1999; *Peymirat et al*., 2000]; the small differences are mostly due to different assumptions about the plasma sheet and ring current plasmas, and ionospheric conductivities. Cases studies suggest that upward prompt penetration drifts near dusk can be much larger than shown in Figure 7. Recent convection model results [e.g., *Peymirat et al*., 2000, *Tsunomura*, 1999; *Sazykin*, 2000], using more realistic low latitude evening conductivities, predict larger equatorial zonal prompt penetration electric fields near dusk, in better agreement with these observations.

Prompt penetration zonal drifts (driven by vertical electric fields) are not easily detected at equatorial latitudes since they usually have much smaller magnitudes than the quiet time values.

Therefore, the observation of these relatively small drift perturbations requires accurate measurements with high temporal resolution. *Fejer and Emmert* [2003] recently presented evidence for short-lived daytime westward prompt penetration drifts over Jicamarca. These disturbance zonal drifts, probably driven by a sudden increase in the solar wind dynamic wind pressure, were fully consistent with RCM results.

*Blanc and Richmond* [1980] pointed out that enhanced energy deposition into the auroral zone during disturbed periods generates a meridional circulation with equatorward thermospheric winds above 120 km. Coriolis forcing on this circulation induces westward perturbation winds and plasma drifts at midlatitudes. The disturbance winds do not attain significant magnitudes near the equator. The westward plasma drifts generate equatorward Pedersen currents above about 150 km. These set up polarization charges at the equator and a poleward electric field, which eventually cancels the equatorward Pedersen current and produces eastward Hall currents that are largest at midlatitudes. Finally, the Hall currents set up polarization charges at the terminators and dusk-to-dawn electric fields.

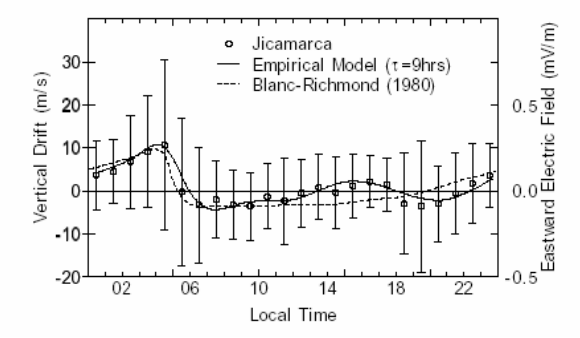


**Figure 8**. Equatorial disturbance dynamo drifts obtained from the Jicamarca empirical model (solid curve), the Blanc-Richmond model (dashed curve), and from the binned Jicamarca data (dots) all for the same increase in the hemispheric power input corresponding to $\Delta AE$ = 400 nT. The scatter bars illustrate the variability of the data (after *Scherliess and Fejer* [1997]).

Disturbance dynamo electric fields have opposite polarity to quiet time dynamo electric fields from middle to equatorial latitudes. They generally have smaller amplitudes, but considerably longer lifetimes, than the prompt penetration drifts. Recent simulations using the MTIE-GCM model of *Peymirat et al.* [1998] confirmed the general results of the Blanc-Richmond disturbance dynamo model, but suggested stronger MLT effects [*Richmond et al*., 2003].

*Scherliess and Fejer* [1997] showed that the short-term Jicamarca vertical disturbance dynamo drifts are in good agreement with results from the Blanc-Richmond model. This is illustrated in Figure 8; the scatter bars indicate the large variability of the equatorial disturbance dynamo drifts. In the evening sector the short-term downward disturbance dynamo drifts near dusk have largest magnitudes during equinox solar maximum conditions, and very small values during solar minimum June solstice periods [*Fejer*, 2002].

The low latitude zonal disturbance dynamo drifts are westward at night with largest values near midnight; the daytime perturbation drifts are slightly eastward over Jicamarca, and close to zero over Arecibo [*Fejer*, 1997], in good agreement with the results from the Blanc-Richmond model. At present, there is no theoretical model for the long-term equatorial disturbance dynamo drifts, which occur about a day after large increases in the high latitude currents. *Scherliess and Fejer* [1997] showed that long-term disturbance dynamo drifts are upward at nighttime with largest values near midnight; the daytime drifts are downward and have largest magnitudes in the morning.

During the recovery phase of a storm, middle and low latitude electric fields can also be affected by magnetosphere-driven neutral fossil winds [*Spiro et al*., 1998, *Fejer et al*., 1990b; *Richmond et al*., 2003]. In this process, as convection lessens and the shielding layer moves poleward, part of the winds accelerated earlier by strong ion convection are left equatorward of the plasma sheet shielding layer and are therefore able to generate electric fields which are unshielded from lower latitudes. *Spiro et al.* [1988] *and Fejer et al.* [1990] examined these fossil wind effects with RCM runs in which ion-drag-accelerated neutral winds were displaced equatorward of the shielding layer. They suggested that this process could explain the relatively long lifetimes of equatorial vertical drift perturbations following northward IMF turnings. *Fejer* [1997] pointed out, however, that since equatorial vertical drifts associated with undershielding and overshielding effects have generally comparable amplitudes (see Figure 3), this process is probably not important except perhaps after very large storms. *Richmond et al*. [2003] conclusively showed that the influence of the disturbance winds on equatorial electric fields, following sudden decreases in convection, depends very little on polar cap contraction.

## 5. Variability of disturbance electric fields

We have seen that present convection and disturbance dynamo models provide good understanding of several aspects of magnetospherically generated middle and low latitude ionospheric electric fields. Specifically, there is good agreement between model predictions and observations of the local time and latitudinal dependence of the middle and low latitude potential distributions following changes in the magnetospheric convection. These global-scale features primarily depend on the perturbation potential penetrating from high to low latitudes, on the disturbance winds, and on the distribution of ionospheric conductance, but they are relatively insensitive to the details of magnetospheric physics.

Although the understanding of processes that determine the general form of perturbation potential distributions is fairly straightforward, the same is not true of the mechanisms that control the strength and duration of these perturbations, particularly in the case of the prompt penetration effects, which involve subtle points of magnetospheric physics and details of solar wind-magnetosphere-ionosphere coupling. In this section, we describe results from the most recent studies of the variability of prompt penetration electric fields; disturbance dynamo electric fields will not be discussed since, except for the recent study by *Richmond et al.* [2003], very little new work has been done on their variability.

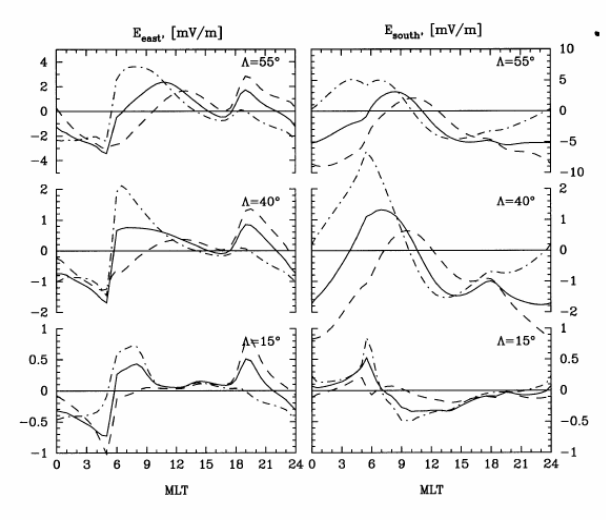


**Figure 9**. Comparison of prompt penetration electric fields, predicted by the RCM 10 min after a convection increase, for 3 polar cap boundary conditions. These patterns correspond to a polar cap potential centered on the noon-midnight meridian (solid lines), and to potential distributions rotated by 2 hours toward earlier (dash-dotted lines) and later (dashed lines) local times (after *Sazykin* [2000]).

*Polar cap potential distribution effects*. The potential distribution along the high latitude boundary is a fundamental parameter for the high latitude convection and its lower latitude electrodynamic effects. This potential distribution accounts for high latitude processes at the magnetopause, where the slow-flow approximation (drift velocities much smaller than the thermal speeds) of the convection models breaks down, and is the Dirichlet boundary condition for the current-conservation partial differential equation. The potential distribution imposed on the subauroral and midlatitude ionosphere is determined by the polar cap potential, the divergence-free current condition, and the enhancement of auroral conductivities. This last effect produces an eastward rotation of the potential distribution, which is a function of the ratio of the Hall to Pedersen conductivities [e.g., *Riley*, 1994].

There is experimental evidence for systematic season- and solar-cycle-dependent rotations, and more random IMF $B_y$–controlled rotations of the potential distribution of the polar cap. The present convection models (e.g., RCM, MTIE-GCM) generally assume a sinusoidal shape for the polar cap potential distribution with a maximum and a minimum at 0600 and 1800 MLT, respectively.

However, most recent studies suggest that a rotation of 1 h toward earlier local times generally gives better agreement with observations [e.g., *Peymirat et al.*, 2000]. *Senior and Blanc* [1984] showed that ±2 h phase shifts of this sinusoidal potential causes large changes in the southward/perpendicular penetration electric fields near dawn and dusk. *Sazykin* [2000] performed computer experiments using the RCM to examine the effects of these phase shifts on both the zonal and meridional prompt penetration electric fields. Figure 9 illustrates the changes in the RCM prompt penetration electric field patterns, following a 45 kV increase in the polar cap potential drop, when the polar cap potential is rotated by ±2 h relative to the dawn-dusk potential. These results indicate increased eastward (westward) electric field perturbations near dusk (dawn) when the pattern is rotated toward later (earlier) local times. The meridional electric fields show equatorward and poleward nighttime electric field changes for shifts toward earlier and later local times, respectively. These meridional electric field results are similar to previous calculations presented by *Senior and Blanc* [1987].

*Shielding and magnetospheric reconfiguration.* RCM simulations presented by *Spiro et al*, [1988] showed that, following identical rapid increases and decreases in the cap potential, the magnitudes of undershielding and overshielding prompt penetration electric fields are essentially identical. This is consistent with the results presented in Figure 3. On the other hand, recent RCM simulations presented by *Sazykin* [2000] suggest larger magnitudes and longer lifetimes for prompt penetration electric fields following convection increases than following decreases, and that a symmetrical response would require the formation of a preexisting ring current of shielding particles (protons). The possible occurrence of larger and longer lasting prompt penetration electric fields during periods of asymmetric ring currents has not been verified experimentally. Another interesting question is whether the occurrence of substorms following northward IMF changes and sudden decreases in the polar cap potential drop increases the magnitudes and lifetimes of overshielding electric fields. Unfortunately, substorm effects cannot be modeled with present convection models.

The shielding time constant is generally of the order of 20 min, but it can have values between about 5 and 200 min, depending on magnetospheric plasma properties and ionospheric conductivities [e.g., *Jaggi and Wolf*, 1973; *Wolf et al., 1983*; *Senior and Blanc*, 1984]. RCM simulations suggest that the shielding is strong when the plasma sheet is cold and dense, and strong when it is hot and rarefied [*Spiro et al*., 1988; *Garner*, 2003]. These simulation studies also indicate that the shielding time constant increases with the plasma sheet temperature from about 15–20 minutes to about 1 hour, but the duration of overshielding electric fields does not appear to increase with the plasma sheet temperature [*Spiro et al*, 1988].

Lifetimes of undershielding and overshielding electric fields can undergo large increases as a result of

changes in the magnetic field geometry in the magnetotail, which is controlled by the cross tail current [*Wolf et al*., 1982; *Fejer et al*., 1990b]. When the convection increases, the cross tail current increases, which causes stretching of the magnetic field lines in the magnetotail. The motion of the equatorial crossing point of these field lines can be considered as resulting from a dusk-to-dawn induction electric field. This inductive electric field should have largest effects near midnight, where the magnetic field lines move the most. The electrodynamics of the shielding layer produces a secondary effect, associated with the increase in convection, consisting of an inward motion of the shielding layer and a dawn-to-dusk potential electric field. Since the induction field involves no ionospheric electric field, the net ionospheric effect is a dawn–to–dusk electric field and a longer shielding time constant that is proportional to the rate of latitudinal motion of the shielding layer. During dipolarization events, following sudden decreases in convection, the directions of these electric fields are reversed, but the shielding time constant is increased again. When magnetic field line stretching and dipolarization stop, the induction electric fields vanish and the prompt penetration fields decay as in the constant magnetic field cases. Recent RCM simulations confirmed that magnetic field configuration effects can largely increase the time constants of prompt penetration electric fields during both undershielding and overshielding conditions [*Sazykin*, 2000], and can produce stronger SAPS structures [*Garner*, 2003]. It is also quite likely that magnetospheric reconfiguration effects play an important role on the prompt penetration electric fields associated with substorms.

*Conductivity effects*. The general effects of the equivalent ring current conductivity (proportional to the plasma sheet temperature and density), precipitation-produced auroral conductivities, and (at high and low latitudes) solar EUV-produced conductivities on prompt penetration electric fields are fairly well understood and accounted for in global convection models [e.g. *Jaggi and Wolf*, 1973; *Senior and Blanc*, 1984, 1987; *Peymirat et al*., 2000; *Sazykin*, 2000; *Garner*, 2003]. Different assumptions of the values of these parameters are responsible for most of the relatively small differences in the climatological electric field patterns and shielding time constants predicted by different models.

*Sazykin* [2000] made a detailed study of magnetospheric and ionospheric conductivity effects on prompt penetration electric fields. This study showed that sharper boundaries of precipitation-produced auroral conductivities produce stronger shielding and weaker penetration electric fields, and that overshielding electric fields are less sensitive to the auroral conductivities than undershielding fields. These simulations also indicated that dayside prompt penetration patterns and meridional electric fields at low latitudes are controlled to a large extent by solar EUV-produced conductivities, and are independent of the precipitation-produced high-latitude conductivities.

We have seen that middle and low latitude perturbation electric fields are essentially inversely proportional to the ionospheric conductivity. *Tsunomura* [1999] showed that the undeshielding eastward (westward) prompt penetration electric fields in the dusk-premidnight (late night-dawn) period are larger during solar minimum than during solar maximum; the daytime electric fields are essentially independent of solar flux. This is consistent with Jicamarca evening and nighttime drift observations presented by *Fejer* [1986], which indicated vertical disturbance drifts at lower levels of magnetic activity near solar minimum than near solar maximum. *Sazykin* [2000] showed that the RCM predicts larger zonal and meridional electric fields during solar minimum than near solar maximum during both undershielding and overshielding conditions.

Satellite studies during highly disturbed conditions have recently shown very large increases in the strength of the Appleton anomaly and very large poleward excursions of its northern and southern peaks during daytime and evening periods [e.g., *Basu et al*., 2002]. These events, which often are correlated with the plasmaspheric tail events, predominantly occur near June solstice and in the Atlantic sector. Because large equatorial upward drift perturbations are required for these phenomena, it has been suggested that daytime and evening eastward prompt penetration electric fields should have largest magnitudes in the Atlantic sector and near June solstice. The low latitude ionospheric conductivities exhibit strong and well-known seasonal/longitudinal variations, which should produce noticeable seasonal and UT effects on the global low latitude ionospheric conductivities and also on the equatorial prompt penetration electric fields, which could explain the above observations.

## 6. Summary

We have seen that over the last decade, extensive experimental, theoretical and simulation studies have provided a great deal of information on the general properties of ionospheric electrodynamic disturbances driven by solar wind-magnetosphere and ionospheric disturbance dynamo electric fields. The main characteristics of middle and low latitude ionospheric electric fields, including their local and storm-time dependence, lifetimes, and latitudinal variations, are fairly well understood and in good agreement results from various global models. Recent studies determined the effects of ionospheric and magnetospheric processes that could potentially explain the large variability of the disturbance electric fields, particularly during large

magnetic storms. Given the large expected increase in the database of global ionospheric plasma drift and electric fields observations (mostly from satellite probes), the rapid development of more powerful and sophisticated coupled numerical models, and the ever-increasing need for more realistic ionospheric predictions, storm time electrodynamics should remain a thriving area of space research for many years to come.

**Acknowledgements.** I thank R. Wolf and S. Sazykin, L. Scherliess, and J. Emmert for helpful discussions. This work was supported by the National Aeronautics and Space Administration JURRIS grant NAG5-8638, and by the Aeronomy Program, Division of Atmospheric Sciences, National Science Foundation through grant ATM-0004380.

**References**

Abdu, M. A., Major phenomena of the equatorial ionosphere-thermosphere system under disturbed conditions, *J. Atmos. Solar-Terr. Phys.*, *59*, 1505, 1997.

Abdu, M. A., I. S. Batista, G. O. Walker, J. H. A. Sobral, N. B. Trivedi, and E. R. de Paula, Equatorial ionospheric electric fields during magnetospheric disturbances: local/longitudinal dependencies from recent EITS campaigns, *J. Atmos. Terr. Phys.*, *57*, 1065, 1995.

Ahn, B., Y. Kamide, H. W. Kroehl, and D. J. Gorney, Cross polar cap potential difference, auroral electrojet indices, and solar wind parameters, *J. Geophys. Res.*, *97*, 1345, 1992.

Anderson, P. C., R. A. Heelis, and W. B. Hanson, The ionospheric signatures of rapid subauroral ion drifts, *J. Geophys. Res.*, *96*, 5785, 1991.

Anderson, P. C., et al., Multisatellite observations of rapid subauroral ion drifts (SAID), *J. Geophys. Res.*, *106*, 29585, 22001.

Basu, S., Su Basu, K. M. Groves, H.-C. Yeh, S.-Y. Su, F. J. Rich, P. J. Sultan, and M. J. Keskinen, Response of the equatorial ionosphere in the South Atlantic region to the magnetic storm of July 15, 2000, *Geophys. Res. Letts.*, *18*, 3577, 2001.

Blanc, M., and A. D. Richmond, The ionospheric disturbance dynamo, *J. Geophys. Res.*, *85*, 1669, 1980.

Buonsanto, M. J., Ionospheric storms: A review, *Space Sci. Rev.*, *88*, 563, 1999.

Burke, W. J., A. G. Rubin, N. C. Maynard, L. C. Gentile, P. J. Sultan, F. J. Rich, O. de la Beaujardiere, C. Y. Young, and G. R. Wilson, Ionospheric disturbances observed by DMSP at middle to low latitudes during the magnetic storm of June 4-6, 1991, *J. Geophys. Res.*, *105*, 18391, 2000.

Fejer, B. G., Equatorial ionospheric electric fields associated with magnetospheric disturbances, in *Solar Wind Magnetosphere Coupling*, Y. Kamide and J. A. Slavin (Eds.), pp. 519-545, Terra Sci., Tokyo, Japan, 1986.

Fejer, B. G., Natural ionospheric plasma waves, in *Modern Ionospheric Science*, H. Kohl, R. Ruster, and K. Schlegel (Eds.), pp. 216-273, EGS, Katlenburg-Lindau, 1996.

Fejer, B. G. The electrodynamics of the low-latitude ionosphere: recent results and future challenges, *J. Atmos. Solar-Terr. Phys.*, *59*, 1465, 1997.

Fejer, B. G., Low latitude storm time ionospheric electrodynamics, *J. Atmos. Solar-Terr. Phys.*, *64*, 1401, 2002.

Fejer, B. G., and L. Scherliess, Time dependent response of equatorial ionospheric electric fields to magnetospheric disturbances, *Geophys. Res. Lett.*, *22*, 851, 1997.

Fejer, B. G., and L. Scherliess, Empirical models of storm time equatorial electric fields, *J. Geophys. Res.*, *102*, 24047, 1997.

Fejer, B. G., and L. Scherliess, Mid- and low-latitude prompt penetration ionospheric zonal plasma drifts, *Geophys. Res. Lett.*, *25*, 3071, 1998.

Fejer, B. G., and J. T. Emmert, Low-latitude ionospheric disturbance electric field effects during the recovery phase of the 19–21 October 1998 magnetic storm, *J. Geophys. Res.*, *108* (A12), 1454, doi:10.1029/2003JA010190, 2003.

Fejer, B. G., et al., Low- and Mid-latitude ionospheric electric fields during the January 1984 GISMOS campaign, *J. Geophys. Res.*, *95*, 2367, 1990*a*.

Fejer, B. G., R. W. Spiro, R. A. Wolf, and J. C. Foster, Latitudinal variation of perturbation electric fields during magnetically disturbed periods: 1986 SUNDIAL observation and model results, *Ann. Geophys.*, *8*, 441, 1990*b*.

Foster, J. C., and F. J. Rich., Prompt penetration electric field effects during severe geomagnetic storms, *J. Geophys. Res.*, *103*, 26359, 1998.

Foster, J. C., and W. J. Burke, SAPS: A new characterization for subauroral electric fields, *EOS Trans. AGU*, *83*, 393, 2002.

Foster, J. C., P. J. Erickson, A. J. Coster, J. Goldstein, and F. J. Rich, Ionospheric signatures of plasmaspheric tails, *Geophys. Res. Lett*, *29*, doi:10.1029/2002JA009409, 2002.

Fuller-Rowell, T. J., M. V. Codrescu, R. J. Moffet, and S. Quegan, Response of the thermosphere and ionosphere to geomagnetic storms, *J. Geophys. Res.*, *99*, 3893, 1994.

Galperin, Y., V. N. Ponomarev, and A. G. Zosimova, Plasma convection in the polar ionosphere, *Ann. Geophys.*, *30*, 1, 1974.

Galperin, Y., V. N. Ponomarev, and A. G. Zosimova, Equatorial ionospheric anomaly and the interplanetary magnetic field, *J. Geophys. Res*., 83, 4265, 1978.

Galperin, Y. I., V. S. Soloviev, K. Torkar, J. C. Foster, and M. V. Veselov, Predicting plasmaspheric radial density profiles, *J. Geophys. Res*., *102*, 2079, 1997.

Garner, T. W., Numerical experiments on the inner magnetospheric electric field, *J. Geophys. Res*., *108*(A10), 1373, doi:10.1029/2003JA010039, 2003.

Gonzales, C. A., M. C. Kelley, B. G. Fejer, J. F. Vickrey, and R. F., Woodman, Equatorial electric fields during magnetically disturbed conditions 2. Implications of simultaneous auroral and equatorial measurements, *J. Geophys. Res*., *84*, 5803, 1979.

Gonzales, C. A., M. C. Kelley, D. L. Carpenter, T. R. Miller, and R. H. Wand, Simultaneous measurements of ionospheric and magnetospheric electric fields in the outer plasmasphere, *Geophys. Res*. *Lett*, *7*, , 517, 1980.

Heelis, R. A., J. K. Lowell, and R. W. Spiro, A model of high-latitude ionospheric convection pattern, *J. Geophys. Res*., *87*, 6339, 1992.

Holt, J. M., R. H. Wand, J. V. Evans, and W. L. Oliver, Empirical models of plasma convection at high latitudes from Millstone Hill observations, *J. Geophys. Res*., *92*, 203, 1987.

Jaggi, R. K., and R. A. Wolf, Self-consistent calculation of the motion of a plasma sheet of ions in the magnetosphere, *J. Geophys. Res*., *78*, 2852, 1973.

Kelley, M. C., *The Earth's Ionosphere, Plasma Physics and Electrodynamics*, Academic, San Diego, Calif., 1989.

Kelley, M. C., B. G. Fejer, and C. A. Gonzales, An explanation for anomalous ionospheric electric fields associated with a northward turning of the interplanetary magnetic field, *Geophys. res. Lett*., *6*, 301, 1979.

Kelley, M. C., and J. J. Makela, By-dependent prompt penetration electric fields at the magnetic equator, *Geophys. Res. Lett*., *29*(7), 1158, doi: 10.1029/2001GL014468, 2002.

Kelley, M. C., J. J. Makela, J. L. Chau, and M. J. Nicholls, Penetration of the solar wind electric field into the magnetosphere/ionosphere system, *Geophys. Res. Lett*., *30*(4), 1158, doi: 10.1029/2002GL016321, 2003.

Kikuchi, T. and T. Araki, Horizontal transmission of the polar electric field to the equator, *J. Atmos. Terr. Phys*., *41*, 917, 1979.

Kikuchi, T., H. Luhr, T. Kitamura, O. Saka, and K. Schlegel, Direct penetration of the polar electric field to the equator during a DP2 event as detected by the auroral and equatorial magnetometer chains and the EISCAT radar, *J. Geophys. Res*., *101*, 19643, 1996.

Kikuchi, T., H. Luhr, K Schlegel, H. Tachihara, M. Shinohara, and T.-I. Kitamura, Penetration of auroral electric fields to the equator during a substorm, *J. Geophys. Res*., *105*, 23251, 2000.

Kikuchi, T., K. K. Hashimoto, T.-I. Kitamura, H. Tachihara, and B. Fejer, Equatorial counterelectrojets during substorms, *J. Geophys. Res*., *108*(A11), 1406, doi: 10.1029/ 2003JA009915, 2003.

Mazaudier, C., and S. V. Venkateswaran, Delayed ionospheric effects of the geomagnetic storms of March 22, 1979, studied by the sixth coordinated data analysis workshop (CDAW-6), *Ann. Geophys*., *8*, 511, 1990.

Mozer, F. S., Electric field mapping from the magnetosphere to the equatorial plane, *Planet. Space Sci*., *18*, 259, 1970.

Nishida, A., N. Iwasaki, and T, Nagata, The origin of fluctuations in the equatorial electrojet; A new type of geomagnetic variation, *Ann. Geophys*., *22*, 178, 1966.

Nishida, A., Geomagnetic DP2 fluctuations and associated geomagnetic phenomena, *J. Geophys. Res*., *73*, 1795-1803, 1968.

Peymirat, C., A. D. Richmond, B. A. Emery, and R. G. Roble, A., A magnetosphere thermosphere ionosphere electrodynamics general circulation model, *J. Geophys. Res*., *103*, 17467, 1998.

Peymirat, C., A. D. Richmond, and A. T. Kobea, Electrodynamic coupling of high and low latitudes: Simulations of shielding/overshielding effects, *J. Geophys. Res*., *105*, 22991, 2000.

Richmond, A. D., C. Peymirat, and R. G. Roble, Long-lasting disturbances in the equatorial ionospheric electric field simulated with a coupled magnetosphere-ionosphere-thermosphere model, *J. Geophys. Res*., *108* (A3), 1118, doi:10.1029/2002JA009758, 2003.

Riley, P. Electrodynamics of the low latitude ionosphere, PhD thesis, Rice Univ., Houston, TX, 1994.

Sastri, J. H., M. A. Abdu, and J. H. A. Sobral, Response of equatorial ionosphere to episodes of asymmetric ring current activity, Ann. Geophys., 15, 1316-1323, 1997.

Sastri, J. H., K. Niranjan, and K. S. V. Subbarao, Response of the equatorial ionosphere in the Indian (midnight) sector to the severe magnetic storm of July 15, 2000, *Geophys. Res. Lett*., *29*(13), doi:10.1029/2002GL015133, 2002.

Sastri, J. H., Y. Kamide, and K. Yumoto, Signatures from magnetospheric substorms in the geomagnetic field of dayside equatorial region: Origin of the ionospheric component, *J. Geophys. Res*., *108* (A10), 1375, doi:10.1029/2003JA009962, 2003.

Sazykin, S., Theoretical studies of penetration of magnetospheric electric fields to the ionosphere, PhD dissertation, 292 pp., Utah State Univ., Logan, 2000.

Scherliess, L., and B. G. Fejer, Storm time dependence of equatorial disturbance dynamo zonal electric fields, *J. Geophys. Res*., *102*, 24037-24046, 1997.

Scherliess, L., and B. G. Fejer, Satellite studies of mid- and low-latitude ionospheric disturbance zonal plasma drifts, *Geophys. Res. Lett*, *25*, 1503-1506, 1998

Scherliess, L., and B. G. Fejer, J. Holt, L. Goncharenko, C. Amory-Mazaudier, and M. J. Buonsanto, Radar studies of midlatitude ionospheric plasma drifts, *J. Geophys. Res*., *106*, 1771-1783, 2001.

Senior, C., and M. Blanc, On the control of magnetopsheric convection by the spatial distribution of ionospheric conductivities, *J. Geophys. Res*., *89*, 261, 1984.

Senior, C., and M. Blanc, Convection in the inner magnetosphere: model predictions and data, *Ann. Geophysicae*, *5*, 405, 1987.

Sibeck, D. G., K. Takahashi, K. Yumoto, and G. D. Reeves, Concerning the origin of signatures in dayside equatorial magnetograms, *J. Geophys. Res*., *103*, 6763-6769, 1998.

Southwood, D., and R. A. Wolf, An Assessment of the role of precipitation in magnetospheric convection, *J. Geophys. Res*., *83*, 5227, 1978.

Spiro, R. W., R. A. Heelis, and W. B. Hanson, Rapid subauroral ion drifts observed by Atmospheric Explorer C, *Geophys. Res. Lett*, *6*, 657, 1979.

Spiro, R. W., R. A. Wolf, and B. G. Fejer, Penetration of high-latitude electric fields effects to low latitudes during SUNDIAL 1984, *Ann. Geophys*., *6*, 39-50, 1988.

Su, S. -Y., C. K. Chao, H. C. Yeh, and R. A. Heelis, Observations of shock impact, disturbance dynamo, and a midlatitude large-density depletion at 600 km altitude on the 17 April 2002 storm, J. Geophys. Res., *108*(A8), 1310, doi:10.1029/2002JA009752, 2003.

Toffoletto, F. R., S. Sazykin, R. W. Spiro, and R. A. Wolf, Inner magnetospheric modeling with the Rice Convection Model, *Space Sci. Rev*., *107*, 175, 2003.

Tsunomura, S., Numerical analysis of global ionospheric current system including the effect of the equatorial enhancement, *Ann. Geophysicae*, *17*, 692, 1999.

Vasyliunas, V. M., Mathematical models of magnetospheric convection and its coupling to the ionosphere, in Particles and Fields in the Magnetosphere, pp. 60-71, B. M. McCormac (Ed.), Reidel, Norwell, MA, 1970.

Wolf, R. A., The quasi-static (slow flow) region of the magnetosphere, in *Solar Terrestrial Physics*, R. L. Carovilano and J. M. Forbes (Eds.), D. Reidel, Hingahm, MA., pp. 303-368, 1983.

Wolf, R. A., R. W. Spiro, G. -H. Voigt, P. H. Reiff, C. K. Chen, and M. Hare, Computer simulation of inner magnetospheric dynamics for the magnetic storm of July 29, 1977, *J. Geophys. Res., 87*, 5949-5962, 1982.

Yeh, H.-C, J. C. Foster, F. J. Rich, and W. Swider, Storm-time electric field penetration observed at mid-latitude, *J. Geophys. Res*., *96*, 5707, 1991.

# Magnetotail turbulence and the "MATRESHKA" model of field-aligned currents

E. E. Antonova[1,2], and I. L. Ovchinnikov[1]

[1] Skobeltsyn Institute of Nuclear physics Moscow State University,
[2] Space Research Institute, Russian Academy of Sciences, Moscow, Russia

**Abstract.** A plasma flow with high Reynolds number produces a turbulent wake behind an obstacle. The magnetosphere of Earth is formed in the process of turbulent solar wind flow around the geomagnetic field. Turbulent fluctuations are observed in magnetospheric regions with high plasma parameters. The most powerful contribution to plasma transport is produced by medium-scale harmonics. Results of auroral observations lead to the "MATRESHKA" model of field-aligned currents. This model reproduces the multi-scale character of observed fields, currents and particle precipitation. According to this model, electric fields are formed due to field-aligned current closing in the auroral ionosphere. Properties of medium-scale magnetotail turbulence are discussed in connection with problems of plasma sheet stability and the inner magnetospheric substorm expansion phase onset.

## 1. Introduction

Multiple results of experimental observations demonstrate a constant presence of strong turbulence inside the plasma sheet (see, for example, reviews of *Antonova and Tverskoy* [1998], *Antonova* [2002]). The existence of such turbulence requires reanalysis of many aspects of the physics of magnetospheric dynamics, including the nature of the dawn-dusk electric field, the formation of the plasma sheet, and the localization and mechanisms of substorm onset. Investigation of medium-scale harmonics of magnetospheric turbulence continues to be one of the most difficult problems. The "MATRESHKA" model of field-aligned currents of Yuri Galperin and his colleagues can be considered as an example of investigation of some properties of medium-scale harmonics of turbulence. In this paper we discuss aspects of turbulence spectra formation. We try to explain the nature of Earth's magnetospheric plasma sheet as a turbulent wake compressed in one direction. We also dwell on the main features of substorm dynamics, including substorm expansion-phase onset deep inside the magnetosphere.

## 2. Earth's turbulent wake

Formation of a turbulent wake behind an obstacle is a natural property of gas or liquid flow. The turbulent wake appears when a liquid or gas with high Reynolds number flows past an obstacle. Figure 1 presents one of the first observed examples of such a wake – a photo of a brass bullet produced by E. Mach in 1893 [*Van-Dyke*, 1982]. The Coulomb collision frequency of the solar wind and magnetospheric plasma is very low. Therefore the suggestion of existence of a turbulent wake for Earth seems very natural. But the picture of plasma and magnetic field distribution observed in the first stages of investigation of the magnetospheric tail seems quite different from the picture of a turbulent wake behind an obstacle. The scale of the turbulent wake in the direction transverse to the flow is the same as that of the obstacle. In most cases, the plasma sheet, a structure that is quite anisotropic in *Y*- and *Z*-directions, fills the space of the nighttime magnetosphere. A *Y*-directed current is concentrated in the plasma sheet. The scale of the plasma sheet in the *Z*-direction ($\sim 1-5R_E$) is much smaller than its scale in the *Y*-direction ($\sim 40R_E$). Near empty tail lobes with the regular structure of the magnetic field separate the plasma sheet from the plasma mantle. The magnetic field inside the plasma sheet is more variable than the magnetic field in the tail lobes and it shows changes in the $B_Z$ component. Such events were attributed to the effect of current sheet instabilities (mainly to tearing mode development). Comparatively rare events of the lobes filling with plasma sheet particles are observed but do not attract real attention.

The most popular point of view in space plasma studies was the validity of the concept of a frozen-in condition, destroyed only in certain small regions. Therefore the concept of turbulent wake formation had no chance to become a dominant point of view. However, experimental observations display a structure of magnetotail plasma flow that can be understood only as a turbulent wake.

Since the start of auroral observations, it has been known that the distribution of plasma precipitation (the discrete auroral oval) is very structural. Such precipitations appear as a result of the plasma sheet and its dayside continuation mapping down to ionospheric altitudes. Effects of field-aligned acceleration processes make the plasma sheet structures more distinguishable. Some structures are comparatively stable (auroral bands and stable arcs). Others (for example rayed arcs) move rapidly. A review by *Galperin* [2002] summarized the results of observations of auroral features ranging from the entire auroral oval of bright discrete forms down to moving solitary structures throughout the observed space scales. Yuri Galperin stressed that the Earth's magnetosphere/ionosphere/aurora is a unified multi-scale system which seems to be ordered at large scales, but sometimes looks to be nearly non-deterministic, or chaotic, at small scales.

Observations of the electric field on auroral field lines and inside the plasma sheet (see *Mozer et al*. [1980], *Maynard et al*. [1982]; *Weimer et al*. [1985] and later results of *Viking, Freja,* and *Fast* satellites) show the constant existence of high levels of electrostatic fluctuations. Such observations lead to the suggestion [*Antonova*, 1985] that the plasma sheet is a turbulent structure and that plasma sheet turbulence produces intense plasma sheet mixing. Experimental proofs of the existence of field-aligned electrostatic potential drops (electric field measurements and observations of electron and ion beams) were real contradictions to the suggestion of the validity of a frozen-in condition. But observation of electric fields in rarified magnetospheric plasma is a very complicated problem (see, for example, *Sopruniuk et al.* [1994]) due to large values of the Debye radius. Therefore observations of turbulent electric fields inside the plasma sheet were not considered as proof of the existence of a turbulent Earth-wake for a long time.

Motion of most particles in the plasma sheet is non-adiabatic. The non-adiabatic motion of ions appears when the Larmor radius of particle is comparable to the radius of the magnetic field line curvature [*Sergeev et al.* [1983], *Chen and Palmadesso*, 1986; *Büchner and Zelenyi*, 1989]. The Larmor radii of electrons are much smaller, in most cases, then that of the magnetic field line curvature. But the distribution of electron temperature across the plasma sheet can be explained under the assumption of the non-conservation of adiabatic invariants of electrons [*Antonova et al.,* 1999]. *Antonova et al.* [1999] discussed such non-conservation as a result of particle motion in the inhomogeneous electric field when the Larmor radius of a particle is comparable to the electric field inhomogeneity. Therefore observations of electron particle fluxes can be considered as indirect proof of the existence of very structured electric fields inside the plasma sheet.

Real proof of the existence of a high level of plasma sheet turbulence appears when it is possible to measure a plasma sheet distribution function with comparatively high temporal and spatial resolution and to restore hydrodynamic velocity fluctuations. *Angelopoulos et al.* [1992, 1993, 1996, 1999]; *Borovsky et al.* [1997, 1998]; *Antonova* [2002]; *Troshichev et al.* [2000, 2002]; *Ovchinnikov et al*. [2000, 2002] have shown that the amplitudes of bulk velocity fluctuations are much larger then the averaged velocities. *Borovsky et al.* [1997, 1998] obtained velocity fluctuation results in the ($X$, $Y$) plane from ISEE observations. Results from the INTERBALL/Tail Probe and Geotail observations make it possible to obtain velocity fluctuations in the ($Y$, $Z$) plain. *Antonova* [2002] summarizes the results of observations and shows that in spite of different temporal resolution, the velocity hodograms obtained during various time periods by various satellites are very similar. The level of fluctuations depends on the phase of a magnetospheric substorm. It increases after the substorm expansion phase onset. *Antonova et al*. [2000]; *Ovchinnikov et al.* [2002]. *Angelopoulos et al,* [1999] argue that the magnetotail is a system that exhibits sporadic variability and has properties of intermittent turbulence.

The observed turbulence is asymmetric. The main difference of velocity fluctuations in ($X$, $Y$) and ($Y$, $Z$) planes is connected with fast flows, termed bursty bulk flow (BBF) events. BBF events are ~10 min time scale, directed mainly toward the Earth at geocentric distances smaller than $20R_E$, and have flow intervals with peaks 10 times larger than the average ~20–30 km/s convection speed. They are composed of flow bursts lasting ~1 min and are observed at substorm growth, expansion and recovery phases. Many BBF events occur without classical substorm signatures (during pseudo-breakups and auroral brightening). BBF typically cover 10–20% of all measurements (see *Baumjohann* [2000]). In accordance with *Borovsky et al.* [1997], and *Angelopoulos et al.* [1999], the presence of BBF produces asymmetry in the probability density function of the $X$ component of the inner plasma sheet flows. In accordance with *Angelopoulos et al*. [1999], when BBFs are removed from plasma sheet observational databases, flow state has an average convection that is small and a flow variance that is many times larger than its average level.

Properties of observed turbulence at all scales and frequencies are not very well known yet. Turbulence in most cases has an intermittent character. Sources of the instabilities leading to plasma turbulization have been investigated intensively. The most fruitful approach to turbulence investigation, in addition to in-situ observations of electric and magnetic fields, and velocity fluctuations, is the work on Self Organized Criticality (SOC). It becomes possible, for example, to show (see

*Uritsky and Pudovkin* [1998]) that the properties of magnetospheric turbulence do not coincide with the properties of solar wind turbulence. The most important harmonics for solution of plasma transport problems are the large- (~500–1000 km mapping at the ionosphere) and medium-scale (~50–200 km mapping at the ionosphere) harmonics. Very important results in the investigation of such harmonics are connected with "MATRESHKA" model of field-aligned currents.

## 3. Large and medium-scale harmonics of turbulence and the "MATRESHKA" model

Investigation of properties of medium-scale turbulence can be based on the "MATRESHKA" scheme of auroral field-aligned currents and particle precipitation suggested by *Galperin et al.* [1985]; *Timofeev et al.* [1985] (see also *Timofeev et al.* [1988]; *Timofeev and Galperin* [1991]; *Galperin* [2002]). Figure 2 from the paper *Galperin* [2002] shows the main features of this model. A Russian matreshka doll is a series of similar wooden dolls enclosed one within another. The "MATRESHKA" scheme illustrates the hierarchy of aurora-encircled Birkeland current loops. .

A smaller field-aligned two-sheet current loop (or several loops) is encircled by a larger-scale one but similar in form and with the same direction as the closing Pedersen current in the ionosphere. *Galperin* [2002] stressed that medium-scale auroral regions (~hundreds of kilometers) split to discrete auroral forms with scales one-two orders of magnitude lower (~10 km). Discrete auroral forms can split to smaller scales (~tens to hundreds of meters). The "MATRESHKA" scheme gives a proper presentation of the fractal nature of the observed phenomena, including their self-similarity. A specific feature of the imbedded structure of the field-aligned current loops is the hierarchy of their intensities.

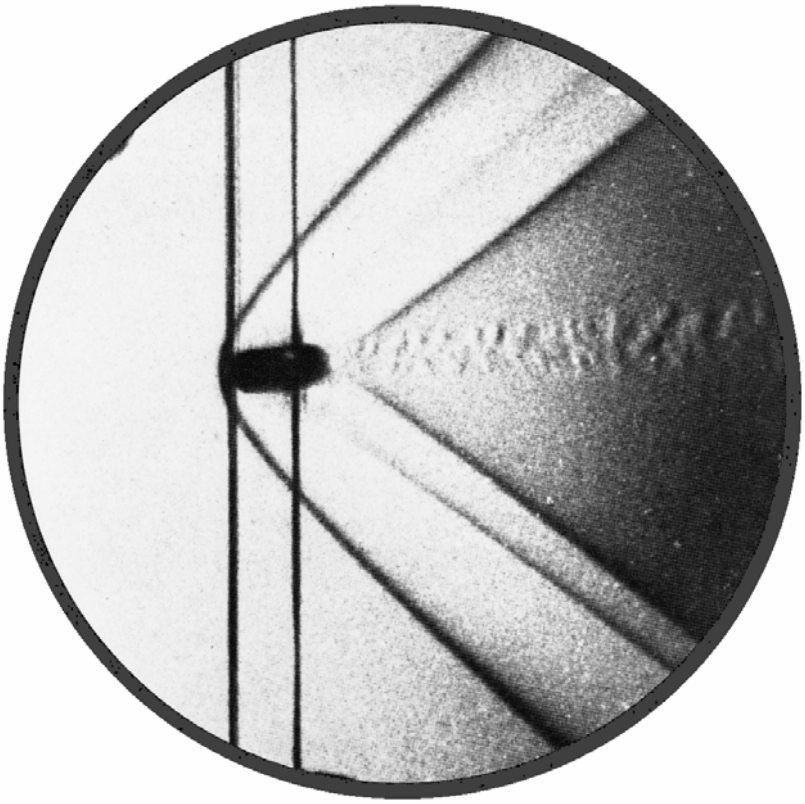

**Figure 1.** Photograph of a brass bullet produced by E. Mach in 1893 using an interferometric technique [*Van Dyke*, 1982]. We can see the shock wave and the turbulent wake (vertical lines are wire fastenings).

Intensity of the field-aligned current in the loop increases with a decrease of scale. This idea is supported by the multiple results of auroral electric field observations at high altitudes.

The "MATRESHKA" scheme allows one to understand why it is possible to see very structural electric fields inside the auroral oval and rather regular electric fields at lower latitudes and in the polar cap. The small-scale electric fields are concentrated between nearly equal upward and downward small-scale field-aligned currents in regions of high conductivity. Therefore such fields do not penetrate far from the

regions of small-scale current loops. *Iijima and Potemra* [1976] showed that the integral current in the dawn and dusk sheets of Region-1 is, as a rule, two times larger then the integral current in the corresponding sheet of Region-2. Therefore the current loop connected with Region 1/Region 2 currents comprises the integral downward current on the dawn side of the auroral oval and the integral upward current on the dusk side (see Figure 3). Closing of these concentrated currents in the polar cap and low latitudes, as shown by many calculations (see, for example, *Troshichev* [1982]), produces the observed picture of a large-scale distribution of electric fields at ionospheric altitudes, i.e. the large-scale picture of magnetospheric convection.

This picture does not agree with the most popular points of view about the nature of large-scale magnetospheric convection. Such points of view are based on suggestions of penetration of the electric field from the solar wind (*Dungey* [1961]), a quasiviscous interaction of the solar wind with the magnetosphere (*Axford and Hines* [1961]), or the generation of large-scale Region-1 currents of *Iijima and Potemra* [1976] in the magnetospheric boundary layers by an MHD dynamo mechanism. The first two points of view are not connected to magnetospheric plasma pressure gradients and do not require coincidence of the regions of field-aligned currents with the regions of intense ion precipitations. Multiple results of field-aligned current observations show the coincidence of their appearance with the regions of intense plasma precipitations and plasma pressure gradients (see, for example, *Iijima et al.* [1997]). Generation of Region-1 currents in the magnetospheric boundary layers has difficulties due to a different plasma domain mapping (see *Antonova* [2002]) as a maxima of the integral on the bend, Region-1 currents are concentrated near dawn and dusk meridians (see *Foster et al.* [1989]). *Antonova and Ganushkina* [1996, 1997] developed a "topological mechanism" for generation of field-aligned currents. They showed that the existence of a necessary plasma pressure gradient can be connected to a noncoincidence of flux tube volume isolines with transition region current lines from the dipole until they become tailward-stretched field lines, i.e. with the magnetospheric topology. Therefore the hypothesis of the generation of large-scale currents and the dawn-dusk electric field by magnetospheric plasma pressure gradients has real experimental and theoretical support.

Verification of the hypothesis of generation of field-aligned currents and the dawn-dusk electric field by plasma pressure gradients requires measurement of the pressure gradients. *Antonova* [2002] summarized results of plasma pressure gradient observations. It is possible to select from experimental observations, results obtained by low altitude satellites. Satellites such as DMSP (*Wing and Newell* [1998, 2000]) and AUREOL-3 (*Stepanova et al.* [2002]) can provide a footprint of the plasma sheet pressure distribution in the equatorial plane for a very short time interval (minutes), which is impossible with high-altitude satellites. Low-altitude observations were used to reconstruct plasma pressure profiles and map them to the equatorial plane. The magnetic field model used to map the low-altitude observations to the equatorial plane provides the main uncertainty in this method. The modified Tsyganenko-89 [*Tsyganenko*, 1989] geomagnetic field model was used by *Wing and Newell* [1998, 2000] and the Tsyganenko–96 [*Tsyganenko and Stern*, 1996] model was used by *Stepanova et al*. [2002]. The statistical results of *Wing and Newell* [2000] provide direct evidence of the production of the Region 1 currents by magnetospheric plasma pressure gradients. This means that inside the magnetosphere there is a source of dawn-dusk electric field constantly observed in the polar cap.

The resulting proofs of two-vortex magnetospheric convection by plasma pressure gradients inside the magnetosphere and multiple results demonstrating the existence of plasma sheet turbulence throughout all the scales produces a picture of magnetospheric dynamics that much more resembles a turbulent wake then the traditional picture of magnetospheric flows. The harmonics of different scales can be generated due to one or many instabilities and the strong interaction between different harmonics. Energy cascades between the harmonics of different scales leads to the formation of observed turbulence spectra. In accord with the theoretical approach suggested by *Tverskoy* [1969, 1972], generation of large-scale harmonics of magnetospheric convection including the dawn-dusk electric field take place due to the existence of inner magnetospheric plasma pressure gradients (see also *Antonova and Tverskoy* [1998]; *Antonova* [2002]) as a result of the magnetosphere-ionosphere interactions (see the review of *Antonova and Tverskoy* [1998]). According to *Tverskoy* [1969], two-vortex, four-vortex etc. types of magnetospheric convection are intrinsic modes of inner-magnetospheric plasma turbulence connected with the existence of plasma pressure gradients. The observed large and middle-scale harmonics (two-vortex convection, four–vortex convection, and fields of inverted-V structures) have discrete characters determined by the boundary conditions. The large-scale field-aligned currents are generated only in regions of large plasma pressure gradients. Two-vortex convection (zero harmonic of the turbulence) is supported by field-aligned currents with maxima near dawn and dusk, four–vortex convection (first harmonic of the turbulence) is supported by two sheets of current. The predicted distribution and amplitude of large-scale field-aligned currents are very close those measured later by *Iijima and Potemra* [1976]. Dissipation of the flow energy takes place in the ionosphere (dissipation of

ionospheric currents) and the magnetosphere (particle acceleration). Amplitudes of the main harmonics of the turbulent wake are determined by the boundary conditions and changes of magnetospheric geometry due to the solar wind flow and interplanetary magnetic field (IMF). The flux of solar wind electromagnetic energy and the angle between the direction of the magnetic field of Earth's dipole and the IMF are the main parameters determining magnetospheric turbulence pumping. The energy can be pumped into magnetospheric turbulence at different scales and, then, it is distributed between the different scale harmonics. This approach makes it possible to understand the multiple results from investigation of the spectra of fluctuations of the AE index and the validity of Self-Organized Criticality (SOC) models of magnetospheric activity.

## 4. Geometry of the turbulent wake

This interpretation explains the geometry of the turbulent wake of the magnetosphere of Earth – the formation of the sheet structure during periods of southward IMF orientation and tail lobe filling by the plasma sheet plasma during the periods of northward IMF orientation. *Antonova and Ovchinnikov* [1998] explain such a feature by means of turbulent mode interactions. A large-scale dawn-dusk electric field, considered as the zero mode of magnetospheric turbulence (see *Antonova and Tverskoy* [1998]), acts to compress the plasma sheet and medium-scale modes act to expel it. Equilibrium of the compression and expansion processes determines the scale of the plasma sheet in the *Z*-direction. Weakening of the dawn-dusk electric field under IMF $B_Z > 0$ conditions leads to filling of the tail lobe by plasma from the plasma sheet according to observations of *Huang et al.* [1989]. In such a case the scale of the magnetospheric turbulent wake becomes the same in *Y*- and *Z*-directions.

The model of *Antonova and Ovchinnikov* [1996, 1999] is developed under the assumption that the regular plasma transport related to the dawn-dusk electric field is compensated by the quasi-diffusive transport related to the existence of turbulent fluctuations. The integral flux in the conditions of existence of turbulent fluctuations is equal to

$$\mathbf{j} = n\langle \mathbf{V} \rangle - D\nabla n \,, \qquad (1)$$

where $n$ is the averaged plasma concentration of the turbulent fluctuations, <V> is the averaged velocity, and $D$ is the coefficient of quasi-diffusion. In quasi-stationary conditions the integral flux is equal to zero. Turbulent fluctuations try to destroy the plasma sheet. Its thickness is constantly increased. The large-scale electrostatic dawn-dusk electric field tries to compress the sheet just as in a laboratory pinch compressed by an induction electric field. If the velocity of destruction and compression are equal, a stationary structure is formed. Quick plasma sheet mixing equalizes the temperature across the sheet. So we can use approximation of constant temperature, $T$=*const*, that is supported by experimental data. The equilibrium distribution of concentration across the plasma sheet gives the equilibrium distribution of plasma pressure $p = nT$. If the dependence of the regular velocity and the quasi-diffusion coefficient from the magnetic field value is known, the condition j = 0 determines the dependence of the plasma pressure on the magnetic field. The validity of the pressure balance condition across the plasma sheet, supported by multiple experimental observations including GEOTAIL data [*Tsyganenko and Mukai*, 2003], makes it possible to solve the Grad-Shafranov equation and to determine the distribution of plasma concentration and plasma pressure across the sheet. The relation between the plasma pressure and the magnetic field can be generalized in two– and three–dimensional cases in the tail approximation developed by *Schindler and Birn* [1986] if the plasma sheet half thickness $L$ is much smaller than the plasma sheet characteristic length. The local thickness of the plasma sheet in this theoretical approach is determined by the local value of the dawn-dusk electric field and local value of the coefficient of the quasi-diffusion. The increase of the large-scale field causes plasma sheet thinning, whereas the increase of the coefficient of the quasi-diffusion causes plasma sheet thickening. The term diffusion is changed to quasi-diffusion, as the condition of the smallness of the turbulent vortex (inverted-*V* scale in the ionospheric mapping) as compared to the width of the plasma sheet (its scale can constitute 0.1–0.2 $L$) is not complete. If the large-scale electric field becomes zero or changes sign, an equilibrium solution cannot be obtained and the plasma sheet configuration cannot be formed.

These results can be used for analysis of changes of the turbulent wake configuration under the influence of IMF conditions.

When the IMF is northward, the size of the auroral oval is decreased (the oval contracts toward the pole) and polar cap arcs appear. It has been shown experimentally that during northward IMF orientation, auroral arcs appear in the polar cap. Characteristics of these arcs are close to the characteristics of arcs in the auroral oval. Single, double and triple arcs are observed. Theta–aurora is observed by the satellite imagers. Theta-aurora is a comparatively wide band of luminosity crossing the polar cap from midnight to midday [Frank et al., 1986]. Ground observations [*Gusev and Troshichev*, 1990] have shown that polar cap arcs are the structural elements of theta-aurora. Horse-collar aurora also can be observed [*Hones et al.*, 1989] in the polar cap under northward IMF orientation. The polar cap in such a case is observed in the form of a horse-collar.

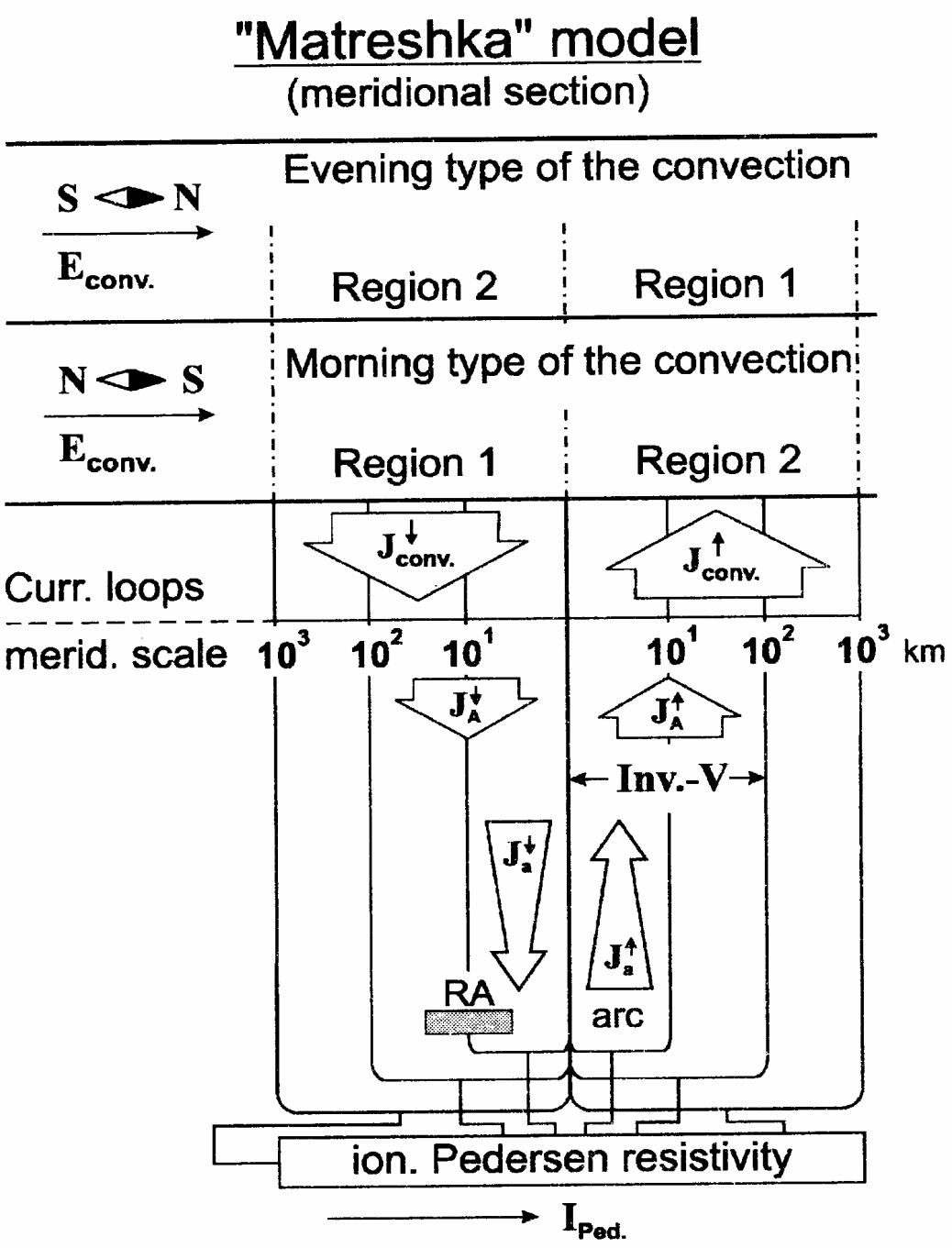


**Figure 2.** Schematics of the auroral encircled Birkeland current loops hierarchy, the "MATRESHKA" model [*Galperin*, 2002]. RA – radar arc, arc– steady homogeneous arc, index A for the arc's field-aligned currents, index a for arc's filaments.

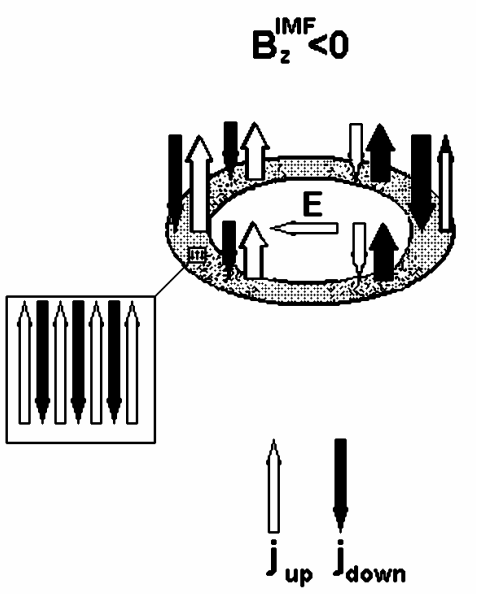


**Figure 3:** Schematic illustration of field-aligned current configuration when IMF $B_Z < 0$. White arrows show upward currents, black arrows downward currents. The horizontal white arrow in the polar cap shows the direction of dawn-dusk electric field.

Electron spectra in polar cap arcs coincide with spectra in the plasma sheet and with electron spectra on the polar boundary of the auroral oval. The ion composition of precipitating particle fluxes is the same as that of the plasma sheet in which ions and electrons with energies 1–10 KeV are observed. The pitch angle distribution of the precipitating electrons shows the appearance of polar cap arcs are on closed field lines. Differential fluxes of electrons at the conjugate points are nearly the same. The polar cap arcs are conjugate [*Feldstein, et al*., 1995].

Observations support the viewpoint that theta-aurora and polar cap arcs form due to plasma sheet bifurcation and polar cap filling. The polar cap potential drop decreases up to 10–30 kV when the IMF changes its sign from southward to northward and a dusk–to–dawn electric field is formed in the center of the polar cap [*Taguchi et al.* 1995; *Knipp et al*. 1993]. The convection is highly structural [*Burke et al*., 1979, *Burke et al.* 1982; *Bythrow et al.,* 1985; *Hoffman et al*., 1988]. The high latitude system of field-aligned currents when the IMF $B_z > 0$, named the NBZ current system according to *Iijima and Shibaji* [1987], consists of two sheets of field-aligned currents with a sign which is inverse to the sign of the *Iijima and Potemra* [1976] Region-1 current system. NBZ and Region-1 currents support the four-vortex convection. The direction of convection in the polar cap vortices is reversed to the direction of large-scale convection supported by the Region-1 of the Iijima and Potemra current system [*Cumnock et al*., 1995]. A four-vortex convection is formed if IMF $B_y$ is small.

Three-dimensional modeling of *Antonova and Ovchinnikov* [1999] shows that the form of the plasma sheet when IMF $B_z < 0$ is concave: the plasma sheet is thinner near its center (plane $y = 0$) and becomes thicker near the magnetospheric flanks. The plasma sheet becomes thicker in its center and thinner on the flanks when $B_z > 0$. If $B_z > 0$ we can see the bulge in the center of the structure. If the small plasma bulge is formed in the first stage of the process, the drift motion of ions and electrons results in the appearance of polarization charges on the borders of the plasma bulge. The charges produce a dusk–to–dawn polarization electric field. Hence, the dawn-to-dusk electric field in the bulge region decreases and may even change its sign. Such a decrease produces a local plasma sheet thickening, and the bulge increases in size. If the electric field changes its sign, the plasma sheet structure acquires the form of the "Malthusian cross" (see Figure 4). When this structure is mapped to the ionosphere, it resembles a tongue that originates near midnight and crosses the polar cap. The electric field in the tongue has the dusk-to-dawn direction (which corresponds to sunward convection in the polar cap). Thus, in accordance *with Antonova and Ovchinnikov* [1999] the plasma sheet can be stable if IMF $B_z < 0$. If IMF $B_z > 0$, the plasma sheet becomes unstable, the magnetospheric lobes are filled by plasma sheet plasma, and a theta-aurora is formed. The condition of magnetospheric configuration instability when IMF $B_z > 0$ exists for a long time period (~10 hours) results in the disappearance of high-latitude magnetospheric gradients and the auroral oval. When IMF $B_z > 0$, the stable magnetosphere will have no plasma sheet and tail lobes. In such conditions the auroral oval should transform into a circle filled with precipitation (see Figure 5). Such a case was observed on 11 January 1997 and was analyzed by *Koshkinen et al.* [2000]. The generation of field-aligned currents directed upward on the morning side of the bulge structure and dawnward on the evening side is discussed by *Antonova and Ganushkina* [1996].

*Antonova and Ovchinnikov* [2001] model the process of plasma sheet bifurcation under the condition of changes of the dawn-dusk electric field distribution. The model developed can describe only the magnetostatic equilibrium configurations when the electric field distribution in the polar cap is known. The process of plasma sheet bifurcation and the formation of the Malthusian cross structure are modeled by the changing of the electric field distribution in the center of the plasma sheet. If the time needed for the electric field to change in the bulge region is much smaller than the time when the plasma configuration changes, we can model the form of the bulge at any specific moment as a quasi-equilibrium configuration corresponding to the specific

large-scale electric field distribution. The results of such modeling are shown in Figure 6. It was assumed that the electric field changes in accordance with the relations

$$\Phi = \Phi_{VS} + \phi_0 \tanh(y / y_0), \qquad (2)$$

$$\Phi_{VS} = \frac{1}{2}\Phi_0 \left( \frac{\sin\theta_0}{\sin\theta} \right)^{2\gamma} \sin\varphi \quad \text{при } \theta > \theta_0$$

$$\Phi_{VS} = \frac{1}{2}\Phi_0 \frac{\sin\theta_0}{\sin\theta} \sin\varphi \qquad \text{при } \theta \le \theta \qquad (3)$$

where $\Phi_{VS}$ is the Volland-Stern potential [*Stern*, 1977, *Volland,* 1973; *Volland*, 1978], $\Phi_0$ is the potential drop across the polar cap, $\theta$ is the geomagnetic colatitude, $\varphi$ is the geomagnetic longitude, the parameter $\theta_0$ determines the boundary of the screening by the dawn–dusk electric field inside the magnetosphere. It was suggested that $\gamma = 1$. $y_0$ determines the value of the plasma bulge, $\phi_0$ is the potential drop across the bulge. Values $\Phi_0$ = 20 kV and $\theta_0$ = 12° were used. Tracing of ionospheric potential into the tail was performed using the Tsyganenko T87W model [*Peredo et al.,* 1993] for the case of IMF $B_z$ = +4 nT. Dependence of the plasma large-scale (average) velocity on the magnetic field was taken in the form $v = E/B$ and dependence of the coefficient of diffusion on the magnetic field was assumed to be $D \sim B^{-1}$. Parameters of the potential disturbance constitute $y_0 = 0.2R_E$; $\phi_0$ = 0; 0.25 kV; 0.5 kV; 0.75 kV (Figure 6 *a, b, c, d*).

## 5. Plasma sheet coefficient of quasi-diffusion

The theory of a plasma sheet with medium scale turbulence, as developed by *Antonova and Ovchinnikov* [1996], predicts the value of the coefficient of diffusion across the sheet $D_{zz}$ (GSM frame of reference is used). The order of magnitude of $D_{zz}$ was determined by the layer half thickness $L_z$ and the velocity of regular convection to the neutral sheet $\langle V_z \rangle$, so $D_{zz} \sim \langle V_z \rangle L_z$. The distribution of $D_{zz}$ across the sheet was determined by the selected dependence of the regular velocity and quasi-diffusion coefficient on the magnetic field. Solid lines on the Figure 7 show quasi-diffusion coefficients predicted by *Antonova and Ovchinnikov* [1996] for a substorm growth phase (lower curve) and substorm expansion phase (upper curve). ISEE-2 velocity fluctuation measurements provide the first published values of the quasi-diffusion coefficient [*Borovsky et al*., 1998]. Statistical analysis of the flow velocities $V_x$ and $V_y$ in the magnetotail plasma sheet presents two populations: a population of fast flows in the $X$ directions (burst bulk flows) and a population of slower turbulent flows that are close to isotropic in $X$ and $Y$ directions. Flows in the $Z$ direction were not measured in that study. For evaluation of $D_{zz}$ [*Borovsky et al.,* 1998] suggested that turbulent flows are quasi-isotropic and measured statistical properties of the $V_y$ have been used for $V_z$ flows. For calculation, a fluctuating velocity 60.8 km/s and an autocorrelation time of flow velocity 140s, gives $D_{zz}$=2.6 × $10^5$ km$^2$/s. This value is in rather good agreement with the predictions of *Antonova and Ovchinnikov* [1996]. *Borovsky et al*. [1998] have suggested that $D_z$ reduced to zero near the plasma sheet boundary layer in accordance with the relation

$$D_{zz} = 2.6\times10^5 \text{ км}^2/\text{с} \times \left[ 1 - 3.86\times10^{-3} \cosh\left( \frac{z}{0.48R_E} \right) \right].$$

This relation was used also by *Ovchinnikov et al*. [2000] for the approximation of $Z$-dependence of $D_{zz}$. INTERBALL/Tail observations (see *Ovchinnikov et al.* [2000]; *Antonova et al.* [2002]), provided plasma sheet distribution functions measured every 2 minutes in $Y$ and $Z$ directions and $D_{zz}$, which later was compared to the theoretical predictions. Figure 7 shows a comparison of calculated $D_{zz}$ (dashed dotted line) with the theoretical predictions by *Antonova and Ovchinnikov* [1996] (solid line). As can be seen, evaluations of $D_{zz}$ based on the theory of a plasma sheet with medium scale turbulence provide values very close to the experimental ones.

*Troschivev et al*. [2002] compare predicted plasma sheet quasi-diffusion coefficients with observations of the GEOTAIL satellite. The 12-seconds averages of magnetic field and particle measurements produced by GEOTAIL in the far-distant plasma sheet, $X$ = –130–200$R_E$ and medium-distance, $X$ = – 40–80$R_E$, were used in the analysis. The following criteria were used to identify two plasma regions: tail lobes with a large magnetic $B_X$ component, $B_X$ >5 nT, and low ion temperature $T_i$ <3 00 eV; and a plasma sheet region with a low magnetic $B_X$ component, $B_X$ <5 nT and large ion temperature $T_i$ > 300 eV. Periods in the plasma sheet boundary layer (PSBL), as well as periods of "empty" tail lobes, were intentionally excluded from the lobe analysis. Intervals of a quiet magnetospheric state ($PC$ < 1.5, $AE$ < 200 nT) were examined from October 1993 through December 1994. 64 solar wind events, 56 distant plasma sheet events ($-X > 100R_E$), 48 middle plasma sheet events ($-20 < X < 100R_E$), and 28 distant tail lobes events were selected. It was found that high changeability of plasma parameters and magnetic field is typical of the middle and distant plasma sheet even during the selected quiet intervals. Fluctuations with periods from 30*s* to few minutes are quite common for all events examined. An autocorrelation function was used to estimate the variability of the plasma and magnetic field in the plasma sheet. This produced values

of diffusion coefficients $D_{zz}$ lying in a range from $3 \times 10^4$ to $1.2 \times 10^5$ km$^2$/s. Values of $D_{zz}$ that resulted are shown on Figure 7 by the gray band.

The data from satellites ISEE-2, INTERBALL/Tail probe and GEOTAIL were obtained by different devices with different time resolutions. The agreement of the calculations of $D_{zz}$ resulting from the ISEE-2, INTERBALL/Tail probe and GEOTAIL (see Figure 7) measurements with the predictions of *Antonova and Ovchinnikov* [1996] therefore can be considered as the first real support of the main suggestions of their theory.

## 6. Mechanisms of substorm expansion phase onset and plasma sheet turbulence

At the early stage of studies of auroral morphology *Akasofu* [1964] showed that substorm onset is characterized by brightening of the equatorward auroral arc. Subsequent studies (see the discussion in *Stepanova et al.* [2002]) confirmed these results. The substorm expansion phase onset is traditionally explained as a result of the development of some kind of instability, but the development of such instability near the equatorial boundary of the auroral oval was a problem for multiple scenarios of substorm expansion phase onset. The existence of a high level of plasma sheet turbulence can explain such localization. Only that plasma region which is stable before a substorm expansion phase onset can become unstable. The plasma between the equator and the equatorial boundary is more stable then that of the plasma sheet. Therefore the substorm expansion phase onset near the equatorial boundary of the auroral oval on the quasi-dipole magnetic field lines is localized more clearly.

Another factor which explains the brightening of the equatorward auroral arc is the observed asymmetry of inverted *V* structures during substorm growth phase (see *Stepanova et al.* [2000, 2002]). The lower part of Figure 8 schematically illustrates results of observations during substorm growth. The most-equatorial inverted-*V* structure is the most powerful one. This means that the maximal upward field-aligned current is concentrated along the equatorial boundary of the discrete precipitation during substorm growth phase. In the region of maximal field-aligned current the maximal field-aligned potential drop takes place and therefore the maximal magnetosphere/ionosphere decoupling occurs. This means that ionospheric damping of magnetospheric instabilities is considerably decreased.

It was found (see *Liou et al*. [1999]) that Pi-2 bursts often can lag behind the brightening of the onset arc. This experimental observation shows that development of electrostatic instability is the cause of substorm expansion phase onset. Magnetic field disturbances including tail current disruption take place ≤1 min later. Development of the flute (interchange) instability in the dipole magnetic trap (see *Kadomtsev* [1963]) requires a decrease in the plasma pressure that is faster than $L^{-20/3}$. An analysis of the radial distribution of plasma pressure produced by *Stepanova et al.* [2002] shows that the pressure distribution is stable for traditional interchange disturbances. The magnetic field model Tsyganenko-96 [*Tsyganenko and Stern*, 1996] was used for mapping the ARCAD pressure measurements onto the equatorial plane. The properties of the region of strong field-aligned currents in the most equatorial inverted-V structure can be considered as the proof of the existence of an azimuthal plasma pressure gradient. Therefore the modified interchange instability which is caused by the azimuthal gradient of plasma pressure can be considered. The field-aligned current determining the instability threshold in accordance with *Stepanova et al.* [2002] is given by the expression

$$\left| j_{II}^0 \right| = \frac{c}{2g^{1/2}} \frac{dW}{d\alpha} \left| \frac{k_\beta}{k_\alpha} \right| \frac{1}{W^\chi} \frac{\partial}{\partial \alpha} \left( p^0 W^\chi \right) \qquad (4)$$

where $W$ is the flux tube volume, $k_\alpha$ and $k_\beta$ are coordinates of the wave vector (the Euler coordinate system ($\alpha$, $\beta$, $l$), in which the magnetic field $\mathbf{B} = [\nabla\alpha \times \nabla\beta]$, $l$ is the coordinate along the field line, was used), $p^0$ is the undisturbed plasma pressure, $\chi$ is the polytropic index, then

$$g = \det[g_{i,k}] = \left[ \frac{\partial(x, y, z)}{\partial(\alpha, \beta, l)} \right]$$

is the determinant of the metric tensor. The relation of instability increments in the regions of upward and downward current is

$$\frac{\gamma^{up}}{\gamma^{dawn}} = 1 + \frac{\Sigma_P T_e^{mag} k_\perp^2}{j^* e}, \qquad (5)$$

where $k_\perp^2 = G_{\alpha\alpha} k_\alpha^2 + G_{\beta\beta} k_\beta^2$, $G^{ik} = \int g^{ik} g^{1/2} dl$, $e$ is the electron charge, $\Sigma_P$ is the integral ionospheric Pedersen conductivity, $j^* = e n_e^{mag} \left( T_e^{mag} \right)^{1/2} / 2\pi m_e^{1/2}$, $n_e^{mag}$ is the concentration of hot magnetospheric electrons, $m_e$ and $T_e^{mag}$ are the electron mass and temperature, respectively. The instability increment is higher when the field-aligned current is directed upward [*Antonova,* 1993]. Instability development can lead to the electrostatic field disturbance. We note that electrostatic field bursts during substorm onsets were experimentally observed (see *Aggson et al* [1983], *Maynard et al.*, [1996].

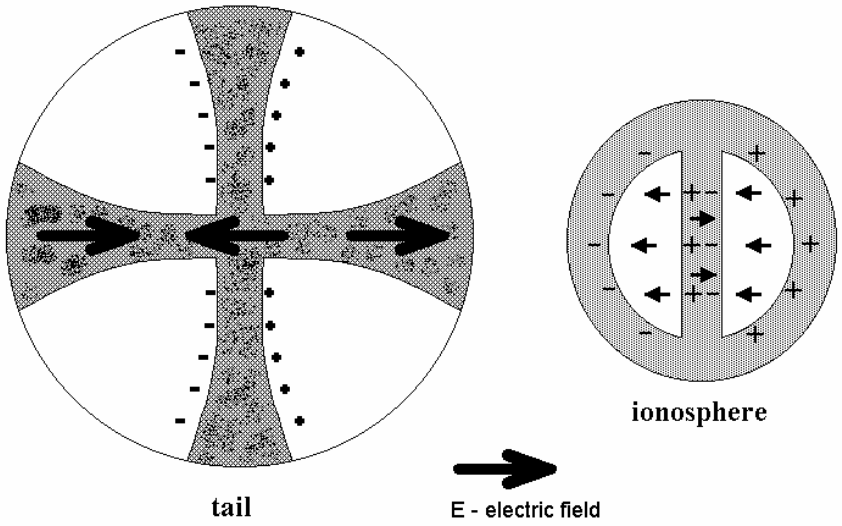


**Figure 4.** Schematic picture of the plasma sheet ("Malthusian cross" plasma sheet structure) and auroral oval precipitations during theta-aurora.

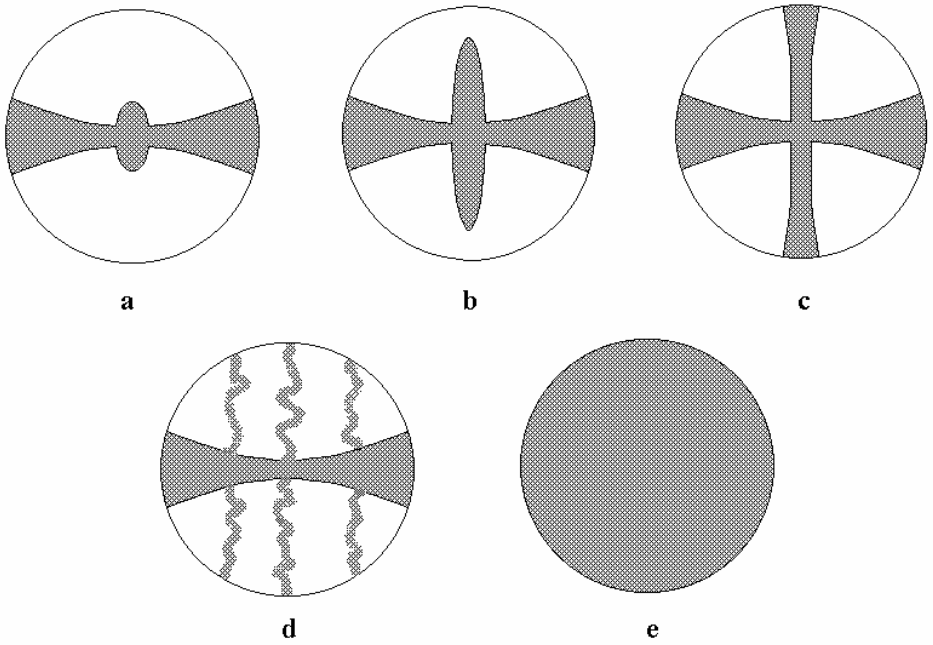


**Figure 5.** Schematic picture illustrating plasma sheet evolution during IMF $B_Z > 0$. a, b, c – the stages of theta-aurora formation, d – the appearance of multiple arcs, e – tail lobes filling.

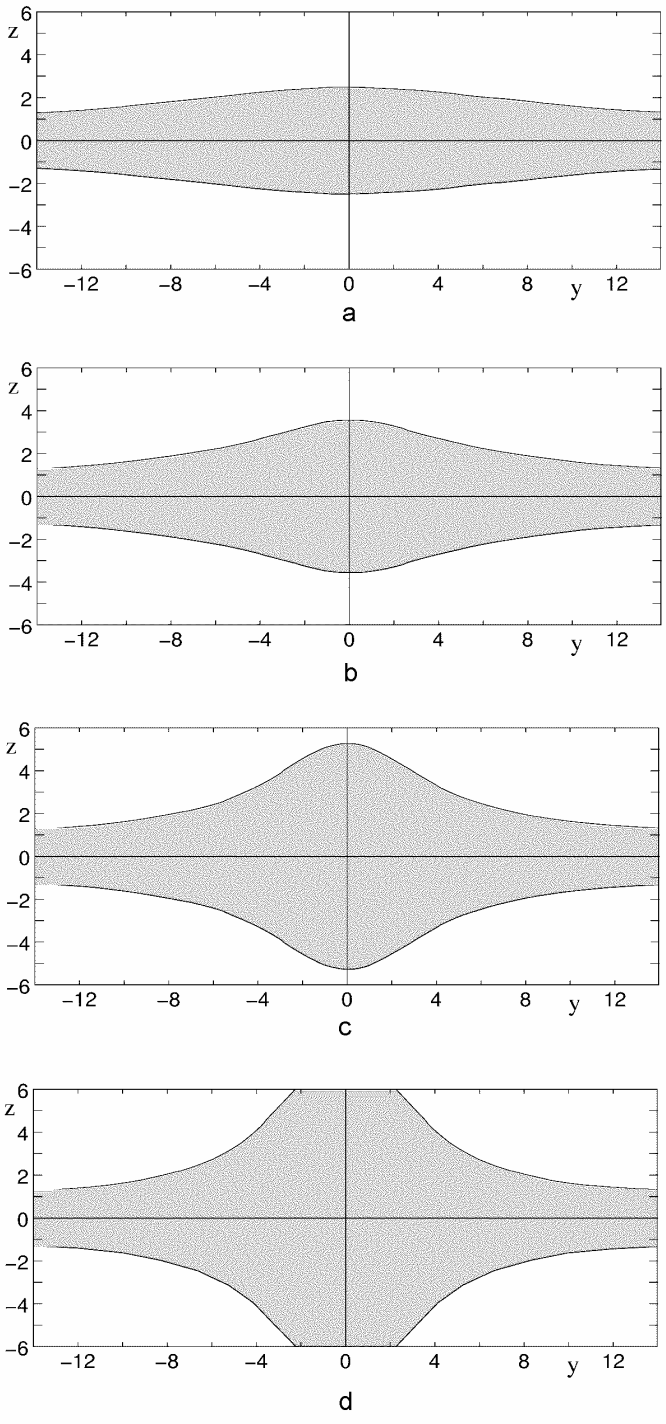


**Figure 6:** Evolution of the modeled structure of the plasma sheet caused by dawn-to-dusk electric field decrease. Regions where plasma pressure $p \geq e^{-1} p\big|_{Z=0}$ are shown for parameters: (a) – $\phi_0$=0, (b) – $\phi_0$=0.25 kV, (c) – $\phi_0$= 0.5kV, and (d) – $\phi_0$=0.75 kV.

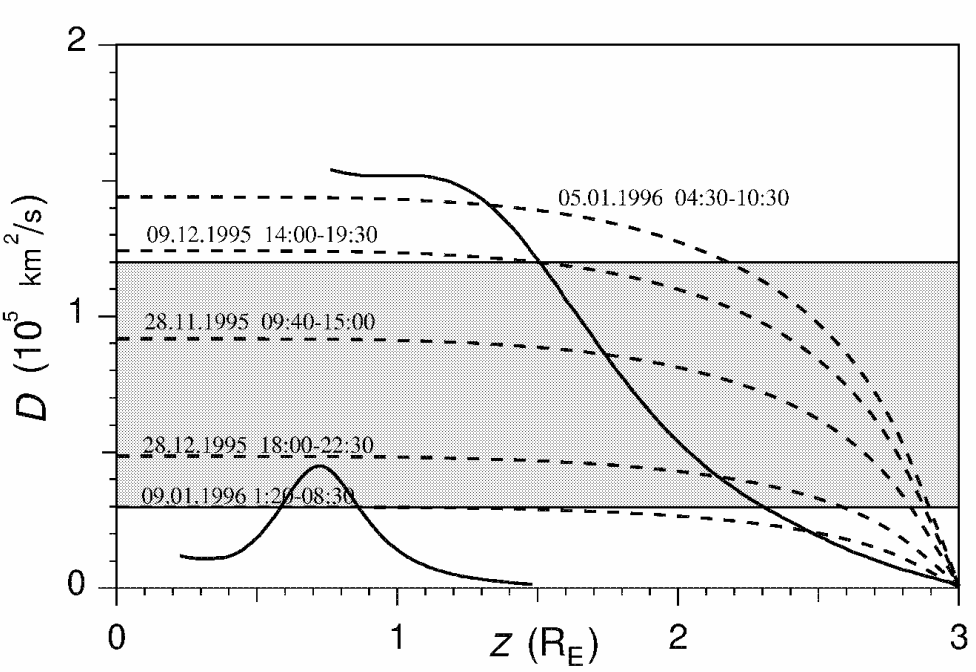


**Figure 7:** Comparison of the medium-scale turbulence plasma sheet theory (solid lines) with experimental observations (dashed lines – INTERBALL/Tail probe observations, gray band – GEOTAIL observations).

is the determinant of the metric tensor. The relation of the instability increments in the regions of upward and downward current is

$$\frac{\gamma^{up}}{\gamma^{dawn}} = 1 + \frac{\Sigma_P T_e^{mag} k_\perp^2}{j^* e}, \qquad (5)$$

where $k_\perp^2 = G_{\alpha\alpha}k_\alpha^2 + G_{\beta\beta}k_\beta^2$, $G^{ik} = \int g^{ik} g^{1/2} dl$, $e$ is the electron charge, $\Sigma_P$ is the integral ionospheric Pedersen conductivity, $j^* = en_e^{mag}\left(T_e^{mag}\right)^{1/2} / 2\pi m_e^{1/2}$, $n_e^{mag}$ is the concentration of hot magnetospheric electrons, $m_e$ and $T_e^{mag}$ are the electron mass and temperature, respectively. The increment of instability is higher when the field-aligned current is directed upward [*Antonova,* 1993]. An instability development can lead to an electrostatic field disturbance. We note that electrostatic field bursts during substorm onsets were experimentally observed (see *Aggson et al* [1983], *Maynard et al.*, [1996].

The appearance of a localized electric field will lead to the penetration of cold plasma inside the inverted-*V* structure (see the upper part of Figure 8) and the formation of a cold field-aligned electron beam. The flux in such a beam is 1–2 orders of magnitude larger than the flux of accelerated magnetospheric electrons. The time scale of the process is less then 20s. Cold beam electrons produce a thin rayed arc, intense bursts of *X-rays* and auroral kilometric radiation. Currents of precipitating electrons and upward accelerated ions distort the magnetic field, lead to local transverse current disruption, dipolarization of the magnetic field lines and therefore particle acceleration and injection inside the magnetosphere. Change of the magnetic configuration will lead to the appearance of the reconnection region in the near Earth tail and plasmoid formation. The appearance of very high values of high frequency oscillations can produce acceleration of particles up to very high energies (turbulent acceleration). Such a mechanism of acceleration can explain the appearance of relativistic electrons deep inside the magnetosphere or a seed population of electrons with energies ~50–100 keV during a magnetospheric substorm. This problem requires more careful investigation because the problem of acceleration of relativistic electrons is now one of the "hottest" in Space Weather investigations.

## 7. Conclusions and discussion

These results show that the turbulent wake model of magnetospheric tail formation explains multiple experimental observations of fluctuating auroral indexes, electric and magnetic fields, and plasma velocity. The "MATRESHKA" model of field-aligned currents developed by Yuri Galperin and his colleagues reproduces the multi–scale character of the observed fields, currents and particle precipitation.

According to the model, electric fields are formed due to field-aligned currents closing in the auroral ionosphere. The nature of this turbulence has not been clear till now. It can include large–, middle– and small–scale vortexes (eddies), bursty bulk flows, particle beams etc. The mechanisms of turbulence generation are not clear either. Possible sources of turbulent fluctuations are plasma pressure gradients, velocity shears, unstable current sheets, non-equilibrium features of the distribution functions. Observed turbulence has an intermittent character and fractal structure. The SOC approach allows development of a sand-pile cellular automation model adequately reproducing the observed fluctuation spectra.

Medium-scale turbulence plasma sheet theory explains the highly anisotropic (if the scale in the $Z$ direction is much smaller then the scale in the $Y$ direction) form of the magnetospheric turbulent wake when IMF $B_Z < 0$. Formation of a turbulent electrostatic pinch compressed by the dawn-dusk large-scale electrostatic field produces such anisotropy. Theory predicts the disappearance of the anisotropy during prolonged IMF $B_Z > 0$. The turbulent wake in such a case will have a cylinder-like shape and the auroral oval will transform into the circle filled with plasmasheet-like precipitations. Medium scale turbulence plasmasheet theory suggests a simple explanation of plasmasheet thinning during a substorm growth phase (due to a dawn-dusk electric field increase) and plasma sheet thickening during a substorm expansion phase (due to amplitude increase of fluctuations). The value of the quasi-diffusion coefficient was theoretically predicted (see Antonova and Ovchinnikov [1996]) 2 years before the first value of such a coefficient was published (Borovsky, et al. [1998]) and it is in a rather good agreement with the results of ISEE-2, INTERBALL/Tail probe and GEOTAIL observations.

The existence of intense plasma sheet turbulence offers a very simple explanation for the onset of a substorm expansion phase (brightening of the most equatorial aurora) deep inside the magnetosphere on the quasi-dipole magnetic field lines. It is natural to argue that only the region, which was stable before the substorm expansion phase onset, can become unstable. In accordance with data from experimental observations, this region is situated near the inner plasma sheet boundary. The scenario developed here predicts the appearance of a localized electric field near the equatorial boundary of the most equatorward inverted-$V$ (pre-onset quiet auroral arc) and the formation of a thin rayed arc at the moment of onset, and explains the intense particle acceleration before the beginning of tail current disruption and magnetic field dipolarization.

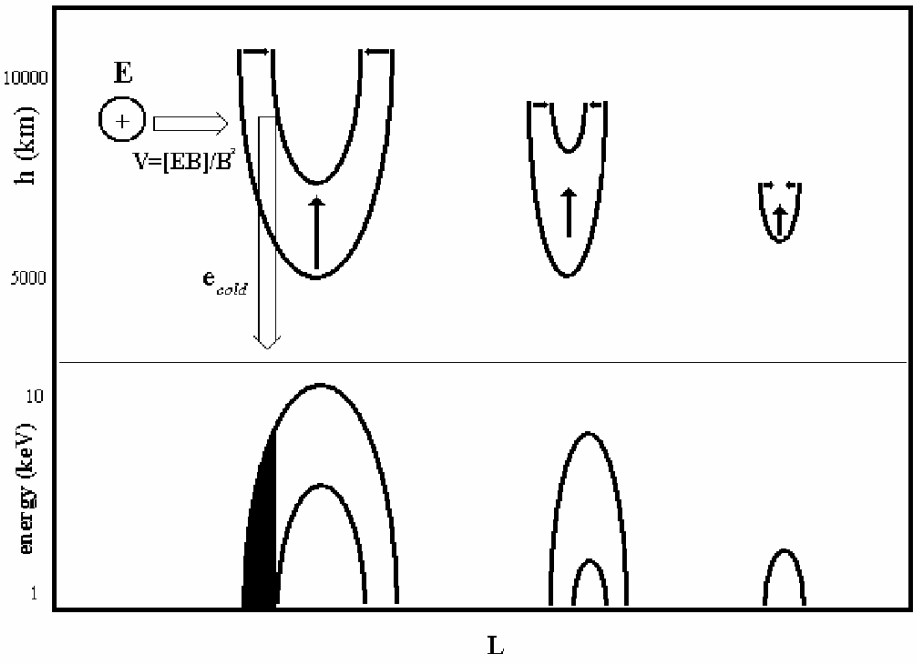


**Figure 8: A** schematic picture of the distribution of multiple inverted V structures during the substorm growth phase and the penetration of a cold plasma inside the boundary of the most equatorward auroral structure and the formation of cold particle beam.

This analysis can be considered only as one of the first steps in creating a picture of magnetospheric processes to adequately describe magnetospheric turbulent wake formation. It explains some features of observed phenomena and predictions based on it have been verified experimentally. This concept offers a possibility for further direct verification. It is based on rather simple relations that contain measurable parameters and that can be verified on the basis of simultaneous ground-based and satellite observations.

**Acknowledgements**

RFBR grants and the program Universities of Russia supported the research.

**References**

Aggson, T. L., J. P. Heppner, and N. C. Maynard, Observations of large magnetospheric electric fields during the onset phase of a substorm, *J. Geophys. Res., 88*(A5), 3981-3990, 1983.

Akasofu, S. I., The development of the auroral substorm, *Planet. Space Sci., 12*(2), 273-282, 1964.

Angelopoulos, V., W. Baumjohann, C. F. Kennel, F. V. Coroniti, R. Pellat, R. J. Walker, H. Luhr H., G. Pashmann, Bursty bulk flows in the inner central plasma sheet. *J. Geophys. Res.,* **97**(A4)**,** 4027-4039, 1992.

Angelopoulos, V., C. F. Kennel, F. V. Coroniti, R. Pellat, H. E. Spence, M. G. Kivelson, R. J. Walker, W. Baumjohann, W. C. Feldman, J. T. Gosling, C. T. Russell, Characteristics of ion flow in the quiet state of the inner plasma sheet. *Geophys. Res. Lett., 20*(16), 1711-1714, 1993.

Angelopoulos, V., F. V. Coroniti, C. F. Kennel, M. G. Kivelson, R. J. Walker, C. T. Russell, R. L. McPherron, E. Sanchez, C.-I. Meng, W. Baumjohann, G. D. Reeves, R. D. Belian, N. Sato, E. Friis-Christensen, P. R. Sutcliffe, K. Yumoto, and T. Harris, Multipoint analysis of a bursty bulk flow event on April 11, 1985. *J. Geophys. Res., 101*(A5)**,** 4967-4989, 1996.

Angelopoulos, V., T. Mukai, and S. Kokubun, Evidence for intermittency in Earth's plasma sheet and implications for self-organized criticality, *Physics of Plasmas, 6*(11), 4161-4168, 1999.

Antonova, E. E., Nonadiabatic diffusion and equalization of concentration and temperature in the plasma sheet of the magnetosphere of the Earth, *Geomagn. Aeron. (Engl. Transl.), 25*(4), 517-520, 1985.

Antonova, E. E., The development of initial substorm expansion phase disturbance due to generation of localized electric fields in the region of maximum upward field-aligned current, *Adv. Space Res., 13*(4), 261-264, 1993.

Antonova, E. E., and I. L.Ovchinnikov, The equilibrium of turbulent current sheet and the current sheet of the Earth's magnetotail, *Geomagnetism and Aeronomia (in Russian), 36*(5), 7-14, 1996.

Antonova, E. E., and N. Yu. Ganushkina. Geometry of the magnetic field of the Earth's magnetosphere and generation of field-aligned currents, *Geomagn. Aeron. (Engl. Transl.), 35*(5), 605-609, 1996.

Antonova, E. E., and N. Yu. Ganushkina, Azimuthal hot plasma pressure gradients and dawn-dusk electric field formation, *J. Atmos. Solar-Terr. Phys., 59*(11), 1343-1354, 1997.

Antonova, E. E., and B. A. Tverskoy, On the nature of electric fields in the Earth's inner magnetosphere (a review), *International Journal of Geomagn. Aeron., 1*(1), 9-21, 1998.

Antonova, E.E., and I.L. Ovchinnikov, Magnetostatically equilibrated plasma sheet with developed medium scale turbulence: Structure and implications for substorm dynamics, *J. Geophys.Res., 104(*A8), 17289-17297, 1999.

Antonova, E. E., M. V. Stepanova, E. A. Vikhreva, I. L. Ovchinnikov, and M. V. Teltsov, Generation of unmagnetized motion of plasma sheet electrons and its possible causes, *J. Geophys. Res., 104*(A9)**,** 19941-19953, 1999.

Antonova, E.E., I.L.Ovchinnikov, and Yu. I. Yermolaev, The coefficient of the diffusion in the plasma sheet during substorm: INTERBALL/Tail observations, Proc, *5th International Conference on Substorms*, St. Petersburg, Russia, 16-20 May 2000 (ESA SP-443, July 2000), p. 141-144, 2000.

Antonova, E. E., and I. L. Ovchinnikov, The model of turbulent plasma sheet during IMF $B_z > 0$, *Adv. Space Res., 28*(12), 1747-1752, 2001.

Antonova, E. E., Magnetostatic equilibrium and turbulent transport in Earth's magnetosphere: A review of experimental observation data and theoretical approach, *International Journal* of *Geom. and Aeronomy*, *3*(2), 117-130, 2002.

Antonova,E.E., I.L. Ovchinnikov, and Yu. I. Yermolaev, Plasma sheet coefficient of diffusion: Predictions and observations, *Adv. Space Res., 30*(12), 2689-2694, 2002.

Axford, W. C., and C. O. Hines, A unifying theory of high latitude geophysical phenomena and geomagnetic storms, *Can. J. Phys., 39*(10), 1433-1464, 1961.

Borovsky, J. E., R. C. Elphic, H. O. Funsten, and M. F. Thomsen, The Earth's plasma sheet as a laboratory for turbulence in high-β MHD, *J .Plasma Phys., 57*(1), 1-34, 1997.

Borovsky, J. E., M. F. Thomsen, and R. C. Elphic, The driving of the plasma sheet by the solar wind, *J. Geophys. Res., 103*(A8), 17617-17639, 1998.

Burke, W. J., M. C. Kelly, R. C. Sagalyn, M. Smiddy, and S. T Lai, Polar cap electric field structures with a northward interplanetary magnetic field, *Geophys. Res. Lett*., *6*(1), 21-24, 1979.

Burke, W. J., M. S. Gussenhoven, M. C. Kelly, D. A. Hardy, and F. J. Rich, Electric and magnetic field characteristics of discrete arcs in the polar cap, *J. Geophys. Res., 87*, 2431, 1982.

Büchner, J., and L. M. Zelenyi, Regular and chaotic charged particle motion in magnetotail like field reversals. 1. Basic theory of trapped motion, *J. Geophys. Res., 94*(A9), 11821-11842, 1989.

Bythrow, P. F., W. J. Burke, T. A. Potemra, L. J. Zanetti, and A. T. Y. Lui, onospheric evidence for irregular reconnection and turbulent plasma flows in the magnetotail during period of northward interplanetary magnetic field, *J. Geophys. Res., 90*(A6), 5319-5322, 1985.

Chen, J., and P. J. Palmadesso, Chaos and nonlinear dynamics of single-particle orbits in a magnetotaillike magnetic field, *J. Geophys. Res., 91*(A2)**,** 1499-1508, 1986.

Cumnock, J. A., R. A. Heelis, M. R. Hairston, and P. T. Newell, High-latitude ionospheric convection pattern during steady nortward interplanetary magnetic field, *J. Geophys. Res., 100*(A8), 14537-14555, 1995.

Dungey, J. W., Interplanetary magnetic field and auroral zone, *Phys. Rev. Lett., 6*(1), 47-49, 1961.

Feldstein, Y. I., P. T. Newell, I. Sandahl, J. Woch, S. V. Leontjev, and V. G. Vorobjev, Structure of auroral precipitation during a theta aurora from multisatellite observations, *J. Geophys. Res., 100*(A9), 17429-17442, 1995.

Foster, J. C., T. Fuller-Rowell, and D. S. Evans. Quantitative patterns of large-scale field-aligned currents in the auroral ionosphere, *J. Geophys. Res., 94*(A3), 2555-2564, 1989.

Frank, L. A., J. D. Craven, D. A. Gurnett, S. D. Shawhen., D. R. Weimer, J. L. Burch, J. D. Winningham, C. R. Chappell, J. H. Waite, R. A Heelis, N. C. Maynard, M. Sugiura, W. H. Peterson., and E. J. Shelley, The theta aurora, *J. Geophys. Res., 91*(A3), 3177-3224, 1986.

Galperin, Yu. I., E. E. Timofeev, M. A. Volkov, and A. V. Volosevich, Models of electric potential and current distribution in stable discrete auroral forms, Results of the ARCAD-3 project and the recent programmes in magnetospheric and ionospheric physics, ed. By CNES, CEPADUES – EDITIONS, Toulouse, France, 153-176, 1985.

Galperin, Yu. I., Multiple scales in auroral plasmas, *J. Atmosph. Solar-Terr. Physics, 64*(2), 211-229, 2002.

Gusev, M. G., and O. A. Troshichev, Relation of Sun-aligned arcs to polar cap convection and magnetic disturbances, *Planet. Space Sci*., *38*(1), 1-11, 1990.

Hoffman, R. A., M. Sugiura, N. C. Maynard, R. M. Candey, J. D. Craven, and L. A. Frank, Electrodynamic pattern in the polar region during periods of extreme magnetic quiescence, *J. Geophys. Res., 93*(A12), 14515-14541, 1988.

Hones, E. W., J. D. Craven, L. A. Frank, D. S. Evans, and P. T. Newell, The horse-collar aurora: A freguent pattern of the aurora in quite times, *Geophys. Res. Lett., 16*(1), 37-40, 1989.

Huang, C. Y., J. D. Craven., and L. A. Frank, Simultaneous observations of a theta aurora and associated magnetotail plasmas, *J. Geophys. Res., 94*(A8), 10137-10143, 1989.

Iijima, T., and T. A. Potemra, The amplitude distribution of field-aligned currents at northern high latitudes observed by Triad, *J. Geophys. Res*., *81*(13), 2165-2174, 1976.

Iijima, T., and T. Shibaji, Global characteristics of northward IMF-associated NBZ field-aligned currents, *J. Geophys. Res., 92*, 2408-, 1987.

Iijima, T., T. A. Potemra, and L J. Zanetti, Contribution of pressure gradients to the generation of dawnside region 1 and region 2 currents, *J. Geophys. Res., 102*(A12), 27069-27081, 1997.

Kadomtsev, B. B., Collective events in plasma, Moscow, Nauka, 1976.

Knipp, D. J., B. A. Emery, A. D. Richmond, N. U. Croorer, M. R. Kairstone, J. A. Cumnock, W. F. Denig, F. J. Rich, O. de la Beaujardiero, J. M. Ruohoniemi, A. S. Rodger, G. Growley, B. -H. Ahn, D. S. Evans, T. J. Fuller-Rowell, E. Friis-Christensen, M. Lockwod, H. W. Kroehl, C. G. Maclennan, A. McEwin, R. J. Pellinen, R. J. Morris, G. B. Burcs, V. Papitashvili, A. Zaitzev, O. Troshichev, N. Sato, P. Sutcliffe, and L. Tomlinson, Ionospheric convection response to slow, strong variations in the northward interplanetary magnetic field: A case study for January 14, 1988, *J. Geophys. Res., 98*(A11), 19273-19292. 1993.

Koshkinen, H. E. J., A. M. Malkki, T. I. Pulkkinen, I. Sandahl, E. Yu. Budnik, A. O. Fedorov, R. A. Greenwald, K. B. Baker, L. A. Frank, J. B. Sigwarth, and W. K. Peterson. Observations of plasma entry into the magnetosphere at late magnetic local times, *Adv. Space Res*., *25*(7/8), 1617-1622, 2000.

Liou, K., C. -I. Meng, A. T. Y. Lui, P. T. Newell, M. Brittnacher, G. Parks, G. D. Reeves, R. R. Anderson and K. Yumoto, On relative timing in substorm onset signatures, *J. Geophys. Res., 104*(A10), 22807-22817, 1999.

Maynard, N. C., J. P Heppner,. and T. L. Aggson, Turbulent electric fields in the nightside

magnetosphere, *J. Geophys. Res., 87*(A3), 1445-1454, 1982.

Maynard, N. C., W. J. Burke, E. M. Basinska, G. M. Erickson, W. J. Hughes, H. J. Singer, A. G. Yahnin, D. A. Hardy, and F. S. Mozer, Dynamics of the inner magnetosphere near times of substorm onset, *J. Geophys. Res., 101*(A4), 7705-7736, 1996.

Mozer, F. S., C. A. Cattell, M. K. Hudson, R. L. Lysak, M. Temerin, and R. B. Torbert, Satellite measurements and theories of low altitude auroral particle acceleration, *Space Science Reviews*, *27*(1), 153-213, 1980.

Ovchinnikov, I. L., E. E. Antnova, and Yu. I. Yermolaev, Determination of the turbulent diffusion coefficient in the plasma sheet using the project Interball data, *Cosmic Research, 38*(6), 596-601, 2000.

Ovchinnikov, I. L., E. E.Antnova, and Yu. I. Yermolaev, Plasma sheet heating during substorm and the values of the plasma sheet diffusion coefficient obtained on the base of Interball/Tail probe observations, *Adv. Space res., 30*(7), 1821-1824, 2002.

Ovchinnikov, I. L., E. E.Antnova, and Yu. I. Yermolaev, Turbulence in the plasma sheet during substorm: A case study for three events observed by the Interball Tail probe, *Cosmic Research, 40*(6), 521-528, 2002.

Peredo, M., D. P. Stern, and N. A. Tsyganenko, Are existing magnetospheric models excessively stretched? *J. Geophys. Res*., *98*(A9), 15343-15354, 1993.

Sergeev, V. A., E. M. Sazhina, N. A. Tsyganenko, J. A. Lundblad, and F. Soraas, Pitch angle scattering of energetic protons in the magnetotail current sheet as the dominant source of their isotropic precipitation into the ionosphere, *Planet. Space Sci., 31*, 1147-1155, 1983.

Schindler, K., and J. Birn, Magnetotail theory, *Space Sci. Rev., 44*(3/4), 191-240, 1986.

Sopruniuk, P. M., S. I. Klimov, and V. E. Korepanov, Electric fields in Space plasma, Kyiv, Naukova dumka, 1994. 189 p.

Stepanova, M., O. Luizar, E. E. Antonova, J. M. Bosqued, and R. A. Kovrazhkin, Asummetry of auroral inverted V structures and substorm expansion phase onset, Proc. 5th International Conference on Substorms, St. Peterburg, Russia, 16-20 May 2000, 333-336, 2000.

Stepanova, M. V., E. E. Antonova, J. M. Bosqued, R. A. Kovrazhkin, and K. R. Aubel, Asymmetry of auroral electron precipitations and its relationship to the substorm expansion phase onset, *J. Geophys. Res., 107*(A7), 10.1029/2001JA003503, 25-1 – 25-12, 2002.

Stern, D. P., Large-scale electric fields in the earth's magnetosphere, *Rev. Geophys. Space Phys., 15*(5), 156-194, 1977.

Taguchi S., M. Sugiura, T. Iyemiri, J.D. Winningham, and J.A.Slavin, Highly structured ionospheric convection for northward interplanetary magnetic field: a case study with DE-2 observations, *J. Geophys. Res.*, *100*(A8), 14743-14757, 1995.

Timofeev, E. E., V. M. Smyshliaev, N. V. Jorjio, Yu. I. Galperin, J. M. Bosqued, J. J. Berthelier, M. K. Vallinkoski, and R. J. Pellinen, Coordinated data on auroral electrodynamics from ground-based radar diagnostics and AUREOL-3 satellite, Results of the ARCAD-3 project and the recent programmes in magnetospheric and ionospheric physics, Ed. By CNES, CEPADUES – EDITIONS, Toulouse, France, 949-971, 1985.

Timofeev, E. E., O. M. Raspopov, Yu. I. Galperin, N. V. Jorjio, A. Berthelier, J. J. Berthelier, J. M. Bosqued, M. K. Vallinkoski, and R. J. Pellinen, The lows of the stratification of Birkeland current systems (Coordinated experiments in the ARCAD project), *Cosmic Research, 26*(5), 709-724, 1988.

Timofeev, E. E., and Yu. I. Galperin, Convection and currents in stable auroral arcs and inverted-V's, Journal of *Geomagnetism and Geoelectricity*, 43(Suppl.), 259-274, 1991.

Troshichev, O. A., Polar magnetic disturbances and field-aligned currents. *Space Sci. Rev*., *33*(3), 275-315, 1982.

Troshichev, O. A., E. E. Antonova, and Y. Kamide, Inconsistency of magnetic field and plasma velocity variations in the distant plasma sheet: A criterion for MHD approximation? *Proc. 5-th International conference on Substorms,* St. Petersburg, Russia, 16-20 May 2000, p. 209-212, 2000.

Troshichev, O. A., E. E. Antonova, and Y. Kamide, Inconsistence of magnetic field and plasma velocity variations in the distant plasma sheet: violation of the "frozen-in" criterion? *Adv. Space Res., 30*(12), 2683-2687, 2002.

Tsyganenko, N. A., A magnetospheric magnetic field model with a warped tail current sheet, *Planet. Space Sci*., *37(*1), 5-20, 1989.

Tsyganenko, N. A., and D. P. Stern, A new generation global magnetosphere field model, based on spacecraft magnetometer data, *ISTP newsletter, 6*(1), 21, 1996.

Tsyganenko, N. A., and T. Mukai, Tail plasma sheet models derived from Geotail data*, J. Geophys. Res., 108*(A3), 10.1029/2002JA009707, 23-1 – 23-15, 2003.

Tverskoy, B. A., On electric fields in the Earth's magnetosphere, *Dokl. Akad. Nauk SSSR, 188*(3) 575-578, 1969.

Tverskoy, B. A., Electric fields in the magnetosphere and the origin of trapped radiation, *Solar-Terrestrial Physics,* edited by E. R. Dyer, Dordrecht, Holland, 297-317, 1972.

Uritsky, V. M., and M. I. Pudovkin, Low frequency 1/*f*-like fluctuations of the AE-index as a possible manifistation of self-organized criticality in the magnetosphere, *Ann. Geophysicae, 16*, 1580-1588, 1998.

Van, Dyke M., An album of fluid motion assembled by Milton Van Dyke, Department of Mechanical Engineering, Stanford University, Stanford, California, The parabolic press, Stanford, California, 1982.

Volland, H. A., A semi-empirical model of large-scale magnetospheric electric fields, *J. Geophys. Res., 78*(1). 171-180, 1973.

Volland, H. A., A model of the magnetospheric electric convection fields, *J. Geophys. Res., 83*(A6), 2695-2699, 1978.

Weimer, D. R., C. Goerts, D. A. Curnett, N. C. Maynard, and J. L. Burch, Auroral zone electric fields from DE-1 and 2 at magnetic conjunctions, *J. Geophys. Res*., *90*(A8), 7479-7494, 1985.

Wing, S., and P. T. Newell, Central plasma sheet ion properties as inferred from ionospheric observations. *J. Geophys. Res., 103*(A4)**,** 6785-6800, 1998.

Wing, S., and P. T. Newell, Quite time plasma sheet ion pressure contribution to Birkeland currents, *J. Geophys. Res., 105*(A4)**,** 7793-7802, 2000.

_____

Antonova Elizaveta, antonova@taspd.npi.msu.su.
Ovchinnikov Ilya, ilya@psn.ru.

# Field-aligned currents of Region 0 as an electric shield of the polar cap ionosphere

V. M. Mishin[1], D. Sh. Shirapov[2], V. P. Golovkov[3], and M. Főrster[4]

[1] Institute of Solar-Terrestrial Physics Russian Academy of Science, Russia
[2] East Siberia State University of Technology, Russia
[3] Institute of Terrestrial Magnetism, Ionosphere and Radio propagation Russian Academy of Science, Russia
[4] Max Planck Institute of Extraterrestrial Physics, Garching, Germany

**Abstract.** [1]. It is shown that field-aligned currents (FAC) of the Region 0 (R0) of Iijima and Potemra create an electric shielding of the polar cap ionosphere just as Region 2 currents shield the mid-latitude ionosphere. Some significant consequences of this effect are considered.

## 1. Introduction

[2]. It is known that intense FAC, having the direction and location of R0 FAC, appear in the course of substorms under the conditions of both northern and southern IMF. They are not only present near the dayside cusp but also in the nightside sector. Therefore, the terms "cusp currents" and "NBZ currents", often applied as synonyms of R0 FAC, are not adequate. The same conclusion can also be made from data by, e.g., *Weimer* [2001] and *Eriksson et al* [2002].

It is also known that the dawn-dusk electric field is produced in the ionosphere of the polar cap (PC) by the Region 1 field-aligned currents (R1 FACs) of Iijima and Potemra. These currents flow on the equatorial side of the PC. In turn, R1 FACs are encircled by R2 FACs from the equatorial side. As the R2 currents are directed opposite to the R1 currents, the mid-latitude ionosphere equatorward of the Region 2 is shielded from penetration of the dawn-dusk electric field. As far as the R0 FACs are concerned, those adjoin to the Region 1 at the poleward side and are directed as the R2 FACs [*Iijima and Potemra*, 1976; *Potemra*, 1994]. Thus, it is anticipated that the R0 FACs may shield the polar cap ionosphere as the R2 FACs shield the mid-latitude ionosphere. The present paper is aimed at a quantitative description of this observed shielding effect.

[3]. This problem is solved as applied to the substorm load stage. We divide the polar cap (PC) into two parts of comparable areas because the observed amplitudes of the convection electric field in those parts significantly differ. One part, termed the "old PC", is observed before substorms and is partly preserved during substorms. The other one, the "new PC", appears and expands in the course of the substorm load phase, expanding the total PC area, according to our data [see also, e.g., *Stern and Alexeev*, 1988; *Cowley and Lockwood,* 1992]. It is demonstrated in the present paper that the ionospheric convection dawn-dusk electric field, created by the dayside magnetopause reconnection, is transferred by R1 FAC in the new PC but it does not penetrate into the old PC at the beginning of the load stage. This shielding decreases or disappears by the end of this stage, and recovers during the unloading stage. Correspondingly, it is assumed that the "old open tail" and "new open tail" (mantle) are separated in the open magnetotail. If it is correct, low-velocity plasma convection is characteristic of the former, while the latter is related to greatly enhanced convection velocities near the magnetosheath drift velocity. In such a model, it follows from our data that the open magnetic flux in the old open tail reduces or disappears being superseded by that in the new open tail in the course of the load phase. During the unloading phase, the old open tail recovers. Thus the R0 FACs and their shielding effect control the plasma convection systems in the mantle and in the ionosphere.

[4]. Experimental results were obtained applying the magnetogram inversion technique, MIT2, to ground magnetometer observations during 12 substorms. In addition, solar wind data from the ISEE-3, IMP-8, and Wind satellites were used. The electrodynamic parameters of these events were averaged by the method of superimposed epochs to obtain characteristics of a statistical substorm. The MIT2 and statistical substorm are described in detail by [*Mishin et al*., 2001]. A comprehensive description of the MIT2 can also be found in [e.g., *Glassmeier*, 1987; *Kamide and Baumjohann*, 1993]. A short description of some details of the MIT2, relevant to this paper, is given below.

## 2. Some MIT-2 parameters

[5]. The Magnetogram Inversion Technique (MIT) uses as inputs: (1) data of the world array of ground based magnetometers and (2) a model of the ionospheric height-integrated conductivity. The primary output data are the 2D spatial distribution of the electric potential in the ionosphere, horizontal (Hall and Pedersen) currents, and FAC densities. Additionally, in the MIT2 the PC boundary is determined from a map of the FAC's density distribution, assuming that the boundary of the total PC coincides with the high-latitude boundary of the R1 FACs. To check and correct this result, a map of the ionospheric electric potential is used to compare the initial boundary of the total PC to the boundary of the reversal of the ionospheric plasma convection.

[6]. In the MIT2, the boundary between the R0 and R1 FACs coincides with the convection reversal. A remark is in order. The MIT2 convection system is calculated from three components of geomagnetic variations $\delta X_k = X_k - X_{0k}$, k=1, 2, and 3. Here $X_{0k}$ and $X_k$ are the reference level (background) and observed variations of the geomagnetic field, respectively. $X_{0k}$ is measured during the quiet period before a substorm when quasi-viscous drag is the major contributor to the total convection system. Thus, the MIT2 describes the convection system created by the dayside merging in the course of substorms.

[7]. In such a way, the PC's area S and the total magnetic flux $\Psi = BS$ piercing the northern PC are determined. Here B is the mean value of the magnetic field in the northern PC. Thereafter, $\Psi$, $\Psi_1$, and $\Psi_2$ designate the open magnetic flux through the total, new, and old PC, respectively. Some precautions should be taken after *Brittnacher et al.'s* [1999] results. As the MIT2 method does not account for the polar cap auroras, $\Psi$ seems to be slightly overestimated. However, comparing Figures 1 to 3 [*Brittnacher et al.,* 1999] to the statistical substorm data in *Mishin et al.'s* [2001], in Figure 1, one can see that the main trends during the substorm are practically the same. The most significant of those is the anti-correlation between the PC area and the global power of particle precipitations following the expansion onset.

[8]. Based upon our many-years experience, the PC boundaries appear to be accurately determined by the MIT2 practically regardless of the ionospheric conductance model used. *Mishin et al*. [1997]; and references therein tested the MIT2 accuracy comparing the polar cap areas and values of $\Psi$ from the MIT2 against the results from *Holzer et al.* [1986], *Elphinstone et al.* [1990, 1991], *Birn et al*. [1991], and *Baker et al*. [1994]. The characteristic difference between the MIT2 values of $\Psi$ and those of the other methods was found to be less than 20%. Thus, we believe that the anticipated errors of MIT2 do not affect the results of this paper.

[9]. The main parameters of MIT2 are the PC electric potential drop, open magnetic fluxes $\Psi$, $\Psi_1$, and $\Psi_2$, and the Poynting flux $\varepsilon$' from the solar wind into the magnetosphere. Intensities of the R1 and R0 FACs are used as well. According to *Newell et al*. [1997], a typical short-lasting (~15 min) pulse of southward IMF produces an open magnetic flux with the lifetime of a few hours. This flux is transferred by the solar wind along distances up to $1000R_E$ creating the "old PC" and "old open magnetotail" (Figure 1, top). This part of Figure 1 pertains to the period when the magnetopause reconnection is not present for several hours. Figure 1 (bottom) illustrates the case where the reconnection has recently created the "new PC" and "new open magnetotail". Thus we have the following.

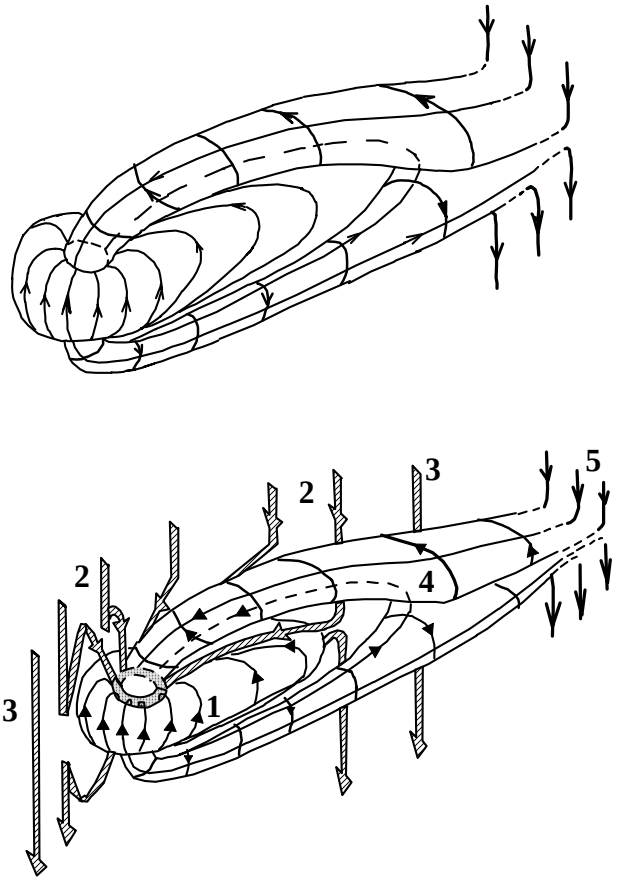


**Figure 1:** Top: The "old PC" and "old open magnetotail" created by dayside merging a few hours before the period considered. Bottom: The new open magnetotail recently created by dayside merging, which is continuing at the time considered; 2 to 5 designate the magnetic field lines of the new and old open magnetotails, respectively.

[10]. *The Poynting vector flux* $\varepsilon'$ of the solar wind into the magnetosphere can be approximately expressed as follows

$$\varepsilon' = \Psi_1^2 V/(\mu_0 S_T) \quad (1).$$

Here $\mu_o = 4\pi 10^{-7}$ H/m, V is the solar wind speed, $S_T$ is the sectional area of the magnetotail lobes, containing the total variable open flux $\Psi_1$ of the new PC, which is created immediately by the dayside magnetopause reconnection [e.g., *Mishin and Falthammar*, 1998].

[11]. *The open magnetic flux* $\Psi$ is the sum of two parts, $\Psi_1$ through the new PC, and $\Psi_2$ through the old PC:

$$\Psi = \Psi_1 + \Psi_2 \quad (2).$$

$\Psi_2$ can also be a variable parameter but it is assumed not to participate in the transport of the Poynting flux. To ensure the afore-named requirements to $\Psi_1$ and $\Psi_2$, the following definitions will be used. The first is

$$\Psi_2 = \beta \Psi_{02} \quad (3),$$

where $\Psi_{02}$ is an initial value of $\Psi_2$, which ($\Psi_{02}$) is determined just prior to the substorm growth phase. $\Psi_2$ is conserved within the old PC during substorms indicating that it does not transport the Poynting flux. The other part of $\Psi_{02}$ that may transport the Poynting flux (and is deleted from old PC) is denoted as

$$\delta\Psi_2 = k \cdot \Psi_{02} \quad (4)$$

with a time-dependent coefficient k≤1. From (2)-(4) one gets

$$\beta = 1-k \quad (5)$$
$$\Psi_1 = \Psi - \beta \cdot \Psi_{02} \quad (6).$$

The parameters $\Psi$ and $\Psi_{02}$ are determined from the MIT2 output data described below.

## 3. Method

[12]. To calculate the coefficients $k$ and $\beta$, one can rewrite (1) as follows:

$$\varepsilon' = \frac{\psi_1^2 V}{\mu_0 S_T} + \frac{\psi_{02}^2 V_i}{\mu_0 S_T} \quad (7)$$

$$\varepsilon' = \frac{\Psi_1^2 V}{\mu_0 S_T} + \frac{\delta\Psi_2^2 V}{\mu_0 S_T} \quad (8)$$

In (7), V and $V_i$ are, respectively, the average velocities of anti-sunward transport of $\Psi_1$ and $\Psi_{02}$ through the tail lobes. Equation (8) explicitly states that $\delta\Psi_2$ transports the Poynting flux with the velocity $V$. Thus, $\delta\Psi_2$ is removed from the old PC consistent with (4) for $k > 0$. In (8), the Poynting flux is transported with the same rate $V$ by fluxes $\Psi_1$ and $\delta\Psi_2$ indicating that the magnetic flux $\delta\Psi_2$ is replaced by the new open flux. As (7) is equivalent to (8), and $\delta\Psi_2/\Psi_{02} = k$, (7) and (8) yield

$$k^2 = V_i/V \quad (9).$$

[13]. The difference $1-k = \beta$ (5) defines the quota of $\Psi_{02}$, which does not contribute to $\varepsilon'$. According to (6), $\Psi = \Psi_1$ for $\beta = 0$. That is, the total open flux, including the magnetic flux within the old PC, transports the Poynting flux. As $\Psi_2 = 0$, there is no shielding. To the contrary, when $\beta = 1$ one has $\Psi_2 = \Psi_{02}$ and $\Psi_1 = \Psi - \Psi_{02}$ according to (3) and (6). In this case the total variable open flux, which transports $\varepsilon'$, flows around the old PC. That means that the old PC is perfectly shielded. We will refer to the parameter $\beta$ as a measure of the electric shielding of the old PC, or of the ionospheric plasma flow around the old PC.

[14]. To find the equations for $k$ and $\beta$, we suppose that

$$V_i/V = V_{id}/V_d \quad (10),$$
$$V_{id} = E_i/B \quad (11),$$
$$V_d = E/B \quad (12),$$

where $V_{id}$ ($V_d$) and $E$ ($E_i$) are the ionospheric plasma convection speed and electric field in the new (old) PC, respectively. Assuming for simplicity a circular boundary of the polar cap and a homogeneous ionospheric conductance, one gets

$$E_i = \frac{U_i - U_{i0}}{D_0}, \quad E = \frac{U - U_i + \delta U_{i0}}{D - D_0} \quad (13)$$

Here $U$ ($U_i$) designates the potential drop on the boundary of the new (old) PC; $D$ ($D_0$) stands for the diameter of the new (old) PC. The value of the potential drop $U_i$ taken just before the beginning of the dayside merging is named $U_{i0}$. Finally, $\delta U_{i0}$ is the potential difference between the boundaries of the old and new polar caps in the potential distribution map taken just before the beginning of the growth phase. Thus, one has

$$BV_{id} = \frac{U_i - U_{i0}}{D_0},\ BV_d = \frac{U - U_i + \delta U_{i0}}{D - D_0} \qquad (14)$$

Denoting

$$\gamma = V_{id}/V_d = E_i/E \qquad (15)$$

and recalling that the open magnetic flux in a circular homogeneous model is defined by the following expressions

$$\Psi = B\pi(D/2)^2 \qquad (16),$$

$$\Psi_2 = B\pi(D_0/2)^2 \qquad (17)$$

one arrives at

$$\gamma = \left(\frac{U_i - U_{i0}}{U - U_i + \delta U_{i0}}\right)\left(\sqrt{\frac{\Psi}{\Psi_{02}}} - 1\right) \qquad (18),$$

Making use of the equalities $\delta\Psi_2 = k\Psi_{02}$, $(\delta\Psi_2/\Psi_{02})^2 = V_i/V$, and (14) – (15), one obtains

$$\gamma = k^2 \qquad (19).$$

Note that the values of γ, calculated by using the MIT, all depend on the model of the ionosphere.

Substorm time $T$ (in minutes) is the following: $T$= 0 is the expansion onset and $T$= –90 is the start of the substorm. New polar cap boundaries are displayed on these maps for $T$= –60 in the left column and for $T$= 0 in the right column (they are the same in the top and bottom panels). The old polar cap boundary (thick dashed line) is determined at $T$= –90, and it is the same in all of the maps. The data represent the statistical substorm. Coordinates: geomagnetic latitude and MLT conductance are used, but only slightly, because the errors of determining the ionospheric electric field in the numerator and denominator of the right part of (18) partly compensate each other.

[15]. In equation (18), $U$ is the electric potential drop on the total PC boundary at an arbitrary instant $T$, $U_i$ is the same on the old PC boundary; $U_{i0}$ – the value of $U_i$ at $T$= –90 min (start of the statistical substorm); $\delta U_{i0}$ is the potential drop between the boundaries of the old and new polar caps for an arbitrary $T$ but in the map of the potential distribution at $T$ = –90 min. Figure 2 demonstrates as an example, how the parameters $U$, $U_i$, $U_{i0}$, and $\delta U_{i0}$ were determined from the MIT2 data of the abovementioned statistical substorm. These parameters, determined for $T$= –90, –60, and 0, are, respectively, the following: $U$=30, 46, and 65 kV, $U_i$=26, 37, and 48 kV, $\delta U_{i0}$=0, 9, and 5 kV, and $U_{i0}$=26 kV. These results can be verified using the data of Figure 2.

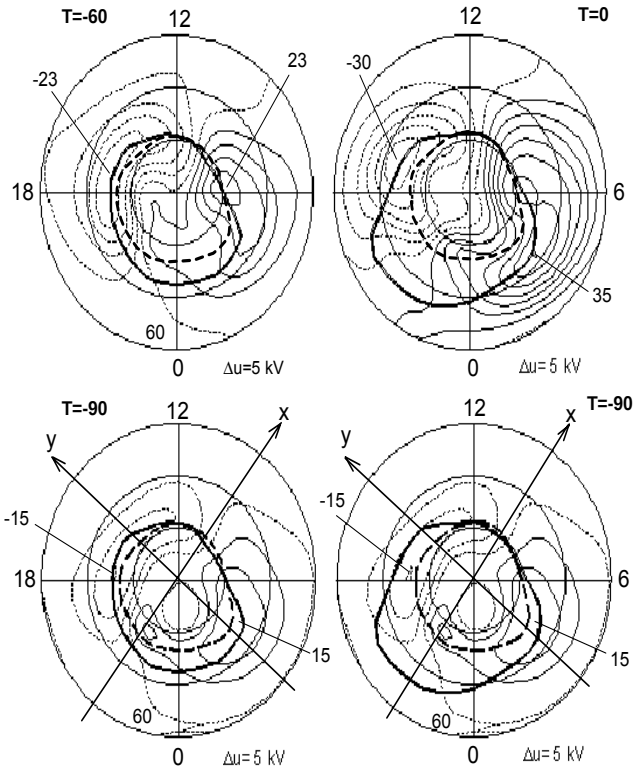


**Figure 2:** Isocontours of electric potential, U (thin lines), with superimposed boundaries of the new polar cap (thick solid lines), and the old polar cap (thick dashed line).

## 4. Results

[16]. It was mentioned that β is an indicator of the electric shielding of the old PC. When β=1, the ratio $E_i/E$=0, indicating perfect shielding. When β=0, the ratio $E_i/E$=1, i.e., no shielding is present. Calculations of the above-mentioned parameters have been performed using the statistical substorm data [*Mishin et al*., 2001]. The calculation results are shown in Figure 3, including the variation of β with time. The shielding is almost perfect at the substorm's beginning, but disappears during the load stage, and is restored during the unloading.

[17]. The expected cause of the shielding effect under consideration is an influence of R0 FACs that take place if the ratio α, of the R0 FAC to the R1 FAC intensity, is large enough. The temporal variation of α is also given in Figure 3. The expected positive correlation between α and $\beta$ can be seen. Their correlation coefficient is 0.82.

[18]. Further, the ionospheric convection systems created by different given systems of FACs have been calculated making use of the Ohm law in the form

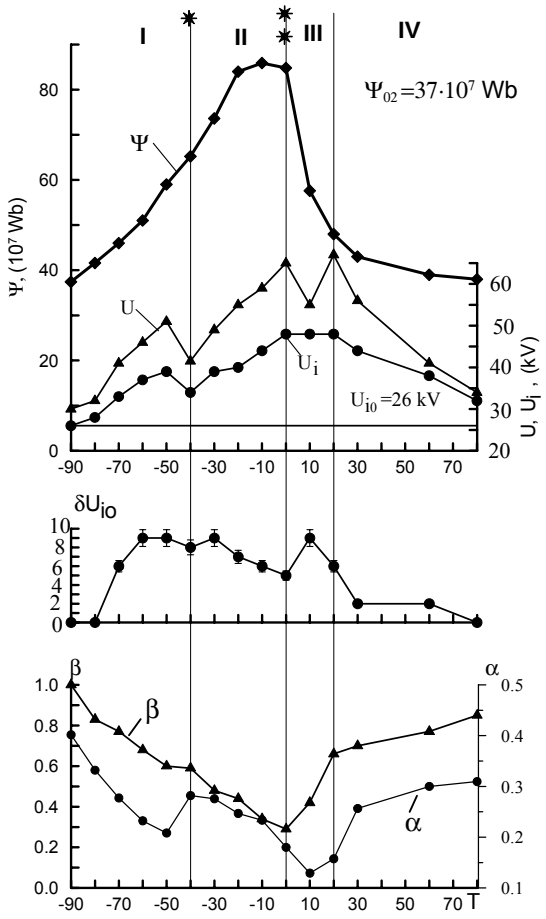


**Figure 3:** Parameters $\Psi$, $U$, $U_i$, $U_{i0}$, $\delta U_{i0}$, $\beta$, and $\alpha$ for a statistical substorm.

Div($\widehat{\sum}\cdot\nabla_\perp\mathbf{u}$) = $\mathbf{j}_{II}$, where $\widehat{\sum}$ is the height-integrated tensor of ionospheric conductivity, **u** is electric potential, and Div is a 2D-operator. Three models of FAC-density $\mathbf{j}_{II}$ spatial distribution in central dipole coordinates, latitude (Φ) and MLT (t), have been used: (1) the model by *Iijima and Potemra* [1976] without R0 FAC, (2) the same with R0 FAC, and (3) the model by *Watanabe et al*. [1998] taken from their Table 2. The first two models are true for quiet conditions, AL<100 nT (Figure 4*a*,*b*). The third one is true for the magnetospheric ground state with extremely low values of the IMF $|B_y|$ and $|B_z|$ which do not exceed 1.5 nT (Figure 4*c*).

The solutions of the current continuity equation Div($\widehat{\sum}\cdot\nabla_\perp$u)=$j_{II}$ are given in Figures 4*a* to 4*c* as the systems of isolines u(Φ,t) = *const*; the values of $\beta$ are designated, as well. The boundary of the old polar cap, shown as the solid line, is taken from *Elphinstone et al*. [1990]. One can see that the azimuthal size (longitudinal range) of the R0 FACs increases from zero in the top panel of Figure 4 to ~90° in the bottom panel.

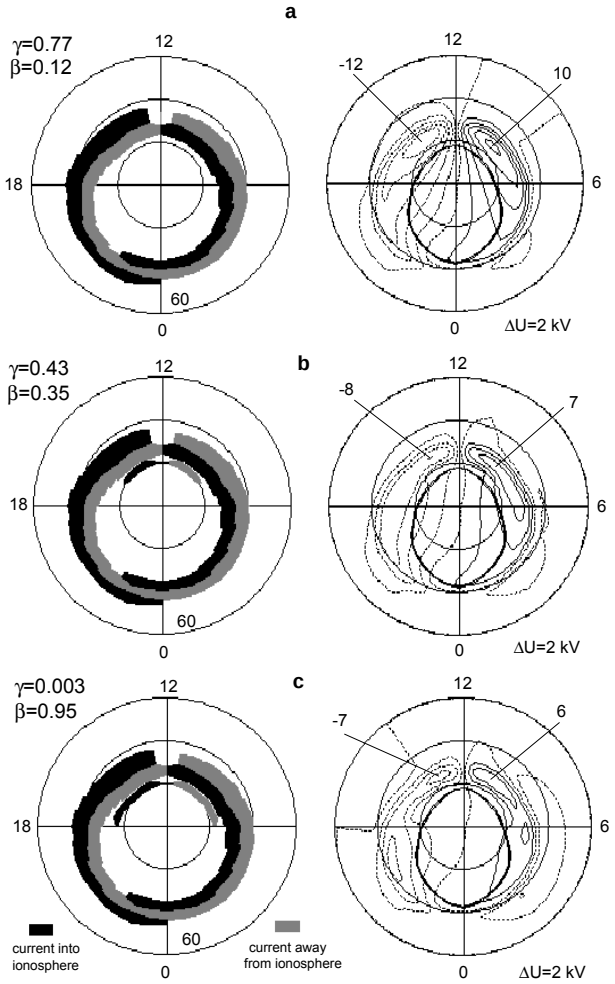


**Figure 4:** Distribution in the ionosphere of the FACs density (on the left), and electric potential (on the right). Model by *Ijima and Potemra* [1976], without (*a*) and with (*b*) the R0 FACs. Model by *Watanabe et al*. [1998] (*c*). The polar cap boundary is taken from *Elphinstone et al*. [1990] for IMF $B_z$ = 0. Coordinates: geomagnetic latitude and MLT.

Accordingly, in the right column one can see that the flow around the old PC has appeared and enhances gradually following the R0 FACs. When the azimuthal size is close to ~90°, the value of $\beta$ is close to unity. The observed increase of the R0 azimuthal size is followed by an increase of $\beta$. This is an unambiguous indication that the R0 FACs ensure the shielding of the old PC.

## 5. Summary

[19]. The polar cap is divided into two parts by the different strength convection electric fields created by dayside merging. Of them, the old PC is observed before the substorm, and the new PC appears and expands in the course of the substorm load phase. It is shown that during the substorm load phase, the R0 FACs shield the old PC ionosphere from penetrating electric fields created by the dayside magnetopause reconnection. This shielding effect is as effective for the polar ionosphere as is the similar effect of the R2 FACs for the mid-latitude ionosphere.

[20]. The shielding of the PC decreases or disappears by the end of the load stage and recovers during the unloading stage. The two different regions of the open magnetotail correspond to the aforementioned parts of the polar cap. These are the "old open tail" with low plasma convection velocities and the "new open tail" (mantle) where the convection velocities are much larger. In the course of the load stage, the open magnetic flux of the old open tail disappears partly or totally, being superseded by the new open magnetic flux. During the unloading stage, the old open tail recovers. Thus the R0 FACs and their shielding effect control the global plasma convection systems in the mantle and ionosphere.

[21]. An observed decrease of the old PC area is accounted for as the replacement of field lines of the old open tail by the new open tail field lines.

[22]. The shielding effect considered suggests that the R1 and R0 FACs are connected in-series in the circuit of a common MHD generator. A model of this generator is the subject of the associated paper [*Mishin et al.,* Electric field and field-aligned currents of Region 1 and Region 0 generators during the substorm load phase, this issue].

**Acknowledgements:** [23]. This work was supported under grant INTAS 01-01142, grant RFBR 02-05-64159, and grant RFBR-DFG 02-05-04002. V. M. M. thanks S. W. H. Cowley for stimulating discussions, V. M .M. and M. F. thank G. Haerendal, G. Paschmann, and W. Baumjohann in MPE (Garching), L. Zeleny in IKI RAS for seminars and discussions which helped to develop this work. The authors from ISTP (Irkutsk) and Ulan-Ude University are also grateful to the colleagues from the ISTP MIT group, A. Bazarzhapov, T. Saifudinova, L. Sapronova , L. Gazhelova, M. Smekhnova, and M. Tolochko for their technical help and discussions.

## References

Baker, D. N., T. I. Pulkkinen, R. L. McPherron, and C. R. Clauer, Multi spacecraft study of a substorm growth and expansion phase features using a time-evolving field model, in *Geophys. Monograph. Ser., vol 84,* edited by J. L. Burch and J. H. Waite, Jr., pp. 101-110, AGU, Washington, 1994.

Birn, J. E., E. W. Hones, Jr., J. D. Craven, L. A. Frank, et al., On open and close field line region in Tsyganenko's field model and their possible associations with horse collar auroras, *J. Geophys. Res., 96*, 3811, 1991.

Brittnacher, M., M. Fillingim, G. Parks, G. Germany, and J. Spann, Polar cap area and boundary motion during substorms, *J. Geophys. Res. 104*, 12251, 1999.

Cowley, S. W. H. and M. Lockwood, Excitation and decay of solar wind-driven flows in the magnetosphere-ionosphere system, *Ann. Geophys., 10*, 103, 1992.

Elphinstone, R. D., K. Jankowska, J. S. Murphree, and L. L. Cogger, The configuration of the auroral distribution for the northward IMF 1. $B_x$ and $B_y$ dependencies as observed by the Viking satellite, *J. Geophys. Res. 95*, 5791, 1990.

Elphinstone, R .D., D. D. Hearn, J. S. Murphree, and L. L. Cogger, Mapping using the Tsyganenko long magnetospheric model and its relationship to Viking auroral images, *J. Geophys. Res., 96*, 1467, 1991.

Eriksson, S., J. W. Bonnell, L. G. Blomberg, R. E. Ergun, G. T. Marklund, and C. W. Carlson, Lobe cell convection and field-aligned currents poleward of the region 1 current system, *J. Geophys. Res., 107*, SMP 16-(1-15), 2002.

Glassmeier, K. -H. Ground-based observations of field-aligned currents in the auroral zone: Methods and results, *Annales Geophysicae*, *5A***,** (3), 115-126, 1987.

Holzer, R. E., R. L. McPherron, and D. A. Hardy, A quantitative empirical model of the magnetospheric flux transfer process, *J. Geophys. Res., 91*, 3287, 1986.

Iijima T., and Potemra T. A., Field-aligned currents in the dayside cusp observed by TRIAD, *J. Geophys. Res., 81,* 5971-5979, 1976.

Kamide, Y. and W. Baumjohann, Magnetosphere-Ionosphere Coupling, Springer-Verlag, Berlin Heidelberg, 1993.

Mishin, V. M., L. P. Block, A. D. Bazarzhapov, T. I. Saifudinova, S. B. Lunyushkin, D. Sh. Shirapov, J. Woch, L. Eliasson, G. T. Marklund, L. G. Blomberg, and H. Opgenoorth, A Study of the CDAW9C Substorm, May 3, 1986 using magnetogram inversion technique 2, and a substorm scenario with two active phases, *J. Geophys. Res., 102,* 18425, 1997.

Mishin, V. M., C. -G. Falthammar, Pseudo- and true substorm onsets within framework of the analogy "magnetospheric substorms-solar flares", Substorms-4, S. Kokubun and Y. Kamide (Eds), 319-322, 1998.

Mishin, V. M., T. I. Saifudinova, A. D. Bazarzhapov, C. T. Russell, W. Baumjohann, R. Nakamura, M. Kubyshkina, Two distinct substorm onsets, *J. Geophys. Res., 106,* 13105-13118, 2001.

Newell, P. T., D. Xu, Meng C. -I., and Kivelson M. G., Dynamical Polar Cap; A Unifying approach, *J. Geophys. Res., 102,* 127-139, 1997.

Potemra, T. A., Sources of Large-Scale Birkeland Currents, *Physical Signatures of Magnetospheric Boundary Layer Processes*, J. A. Holter and A. Egeland (eds.), 3-27, 1994.

Shirapov, D. Sh. and V. M. Mishin, Some problems of the polar cap and geomagnetic tail dynamics, Substorms-4, S. Kokubun and Y. Kamide (Eds), 413-417, 1998.

Stern, D. P., and I. I. Alexeev, Where do field lines go in the quiet magnetosphere, *Rev. Geophys*., *26*, 782-791, 1988.

Watanabe, M., T. Iijima, M. Nakagawa, T. A. Potemra, L.J. Zanetti, SW.-I. Ohtani, and P. Newell, Field-aligned current system in the magnetospheric ground state, *J. Geophys. Res., 103*, 6853, 1998.

Weimer, D. R., Maps of ionospheric field-aligned currents as a function of the interplanetary magnetic field derived from Dynamic Explorer 2 Data, *J. Geophys. Res., 106,* No A7, 12,8889-12,902, 2001.

# Generators of electric field and field-aligned currents of Region 1 and Region 0 during the substorm load phase

V. M. Mishin[1], V. V. Mishin[1], D. Sh. Shirapov[2],
V. P.Golovkov[3], and M. Főrster[4]

[1] Institute of Solar-Terrestrial Physics Russian Academy of Science, Russia
[2] East Siberia State University of Technology, Russia
[3] Institute of Terrestrial Magnetism, Ionosphere and Radio propagation
Russian Academy of Science, Russia
[4] Max Planck Institute of Extraterrestrial Physics, Garching, Germany

**Abstract.** [1]. The terms "Cusp Currents" or "NBZ Currents", often used for the Region 0 field-aligned currents (R0 FAC) of Iijima and Potemra, are not adequate because the intense currents, having the direction and location of the R0 FAC, are not only observed during IMF NBZ and near the cusp, but during substorms with southward IMF and in the night sector as well. In the associated Paper 1 [*Mishin et al*., this issue], it is revealed that such R0 FAC effectively screen the polar cap (PC) ionosphere by dividing it in two parts, the "old PC", existed before substorms, and the "new PC", formed during substorms. The areas of the two parts are comparable, but their electric field strength differ, since the electric field, created by dayside magnetopause reconnection, does not penetrate into the old PC due to the shielding effect of the R0 FAC. There is a correspondence between these two parts of the total PC, on one hand, and two separate regions of open magnetotail, on the other hand: the "new open tail" (mantle) corresponds to the new PC, and the "old open tail" (that is located inside of the generator's region but does not belong to it) corresponds to the old PC. A conceptual model of an electric field and current (R1 and R0) generator has been constructed for the load stage of a substorm. The generator consists of 5 components. One, located in the region of dayside reconnection, is mainly the "starting generator" in the proposed model, whose function is to create an open magnetic flux (though it also creates the noon parts of both R1 and R0 FACs). The next one is a generator in the total volume of the new open tail. The model values of the EMF of this volumetric generator turned out to be compatible with the observed values of the polar cap potential drop, *U*. The proposed model also explains the shielding effect of R0 FAC, and accounts for the observed slow (~1 hour) increasing of the U values during the load stage of substorms even at fast (~1 min) southward turnings of IMF. It is argued that the shielding effect of R0 FAC is an important factor, coordinating plasma convection systems in the tail and the ionosphere.

## 1. Introduction

[2]. Three large-scale regions of field-aligned currents exist in the polar ionosphere: Regions 2, 1, and 0 of Iijima and Potemra [*Potemra,* 1994; *Iijima and Potemra,* 1976]. We denote them, respectively, R2 FAC, R1 FAC, and R0 FAC. The R1 FAC flows into the ionosphere in the dawn sector and flows out of it in the dusk. That is opposite to the current directions of the adjacent R2 FAC and R0 FAC, which adjoin the R1 FAC at lower and higher latitudes, respectively. The R1 FAC creates the dawn-dusk electric field at latitudes above Region 1, however, the R2 FAC shields the lower latitudes, as was predicted by *Vasyliunas* [1984]. This shielding effect means that the R1 and R2 FACs flow in series in the circuit of the common magnetospheric generator. This paper is based on data of the statistical substorm, and is associated with Paper 1 [*Mishin et al.,* this issue]. It is shown there that the R0 FAC screens the ionosphere above Region 1, as the R2 FAC screens the ionosphere below Region 1. In the course of the substorm load stage, the shielding effect weakens and, sometimes even disappears, to be restored during substorm unloading and recovery. The task of the present paper is to present a simple ("wire") model of the common generator of both R1 and R0 FACs for the load phase of the statistical substorm, one that is able to account for the aforesaid shielding effect, with its variable nature, and to shed a new light on some other outstanding questions, see Abstract. For this purpose, new observational data from [Paper 1; *Weimer*, 2001; and *Maltsev and Ostapenko*, this issue], and some results from MHD – models [*Siscoe et al*., 1991; *Siebert and Siscoe*, 2002], are used. For the substorm load stage, created by dayside magnetopause reconnection, a new approach is realized.

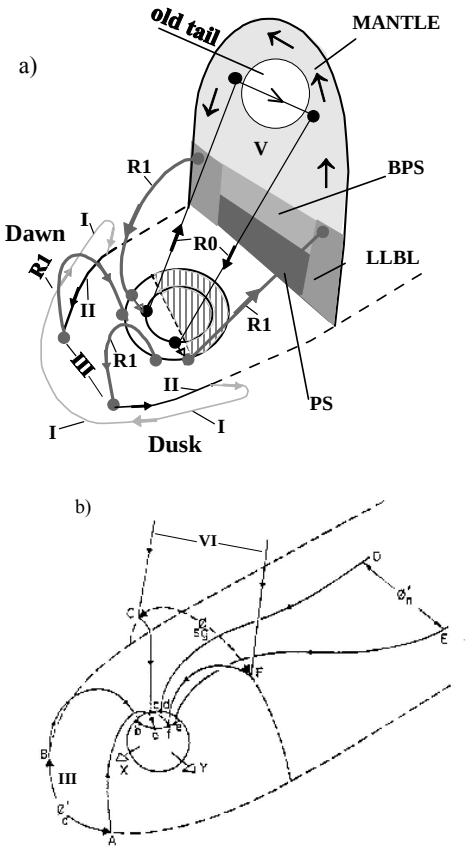


**Figure 1:** Top: Model of the generators, feeding the dayside ionosphere at IMF B = $B_Z$ < 0. Shown are two sections of the tail, and the Region 1 (thick lines) and Region 0 (thin lines) field-aligned currents. The Roman numerals I to V mark the generators and their currents, see paragraph [13] for more details.

Bottom: The magnetosphere showing the dayside magnetopause X-line, AB, the nightside neutral sheet X-line, DE, and the "Stern Gap", CF. Solid lines are magnetic field lines, dashed lines lie in the magnetopause. Field lines map to the polar cap ionosphere. The dayside merging gap (the ionospheric projection of AB) is *ab*, the nightside merging gap (projection of DE) is *de* and the dawn-dusk diameter of the polar cap is *cf*. (From [*Lockwood and Cowley*, 1992]).

Along with the solar wind dynamo and the generator, located in the magnetopause (which are traditionally the principal generators [e.g., *Heikkila,* 1984; *Stern*, 1984; *Lockwood and Cowley*, 1992; and references therein]), the other generator, occupying the total volume of the new open tail, plays an essential role in the proposed model.

## 2. The volumetric generator

[3]. The scheme of the proposed generator's model is shown in Figure 1*a*, which corresponds to the load stage of the substorm. It is a view from the dusk side on the northern half of the magnetosphere. The equatorial and meridional sections are shown. In the meridional section, the projections of LLBL, mantle, old open tail, central plasma sheet (PS), and boundary plasma sheet (BPS) are marked. In this scheme, the mantle is the region of high-speed plasma convection, created by dayside merging in the open tail.

In contrast the old open tail is the region, where plasma convection, created by a recent dayside merging, is absent due to the above-mentioned shielding effect by R0 FAC. The two rings on the projection on Earth are the boundaries of the old and new polar cap, where the first (old PC) was observed before the substorm, and the second, the new PC, is formed during the substorm. The mantle and old open tail, respectively, are projected on the areas of the new and old polar cap. The two rings coincide with the high-latitude boundary of the R1 FAC: the inner ring - before the substorm, and the external one – during the substorm.

[4]. Although not comprehensive, and not in scale, the structure of the tail in the meridional section in Figure 1*a* corresponds to that of *Potemra* [1994, Figure 5.1]. The term "lobe" in Potemra's figure has been replaced by the term "old open tail" in Figure 1*a* because, to account for the above-mentioned shielding effect, it was necessary to separate the two parts of the polar cap and the corresponding two parts of the open tail. Potemra's diagram was derived from many earlier examples [e.g., *Siscoe et al*., 1991]. For the most comprehensive view from the side of the particle's characteristics see *Newell and Meng* [1994].

[5]. Two regions of the meridional section in Figure 1*a*, the mantle and the LLBL, constitute the elementary generator. It is supposed, that magnetic field lines of the LLBL are closed but the mantle is pierced by open magnetic flux. The loop with a magnetic field enveloping the mantle and LLBL moves in an antisunward direction, and is carried away by the solar wind. According to Faraday's law, an emf is generated in the loop, as will be discussed in the following section. Elementary generators inside the total tail-volume are parallel-connected and this constitutes the volumetric generator as a whole. The current in this generator (**J**) flows in the mantle from dusk to dawn, and in the opposite direction within the LLBL. Polarization electric fields (**E**) have an opposite direction, so that $\mathbf{E}\cdot\mathbf{J}<0$ is fulfilled, where $\mathbf{E} = -\mathbf{V}\times\mathbf{B}$ and $B = B_S$ or $B = B_N$, accordingly, in the mantle and LLBL.

[6]. The R1 FAC flows out from the LLBL [*Siscoe et al*., 1991]. The projection of the LLBL adjoins the boundary of the new PC on the lower latitude side. In Figure 1*a*, the R1 (R0) FAC is shown by a thick (thin)

solid line. The R1 FAC (by excluding its noon part) flows into the ionosphere from the LLBL on the dawn side, then flows from there to higher latitudes, and finally flows out from the ionosphere into the old PC as the R0 FAC. Further, the R0 FAC flows along field lines of the tail lobe, where it is closed in the dawn-dusk direction through, mainly, the old tail. Any other R0 FAC closure seems to be impossible. It is impossible to draw a continuation of the R0 FAC in the ionosphere on lower latitudes than the lobe's projection, i.e. in the BPS, because its latitude is not at higher latitudes with respect to the LLBL. Therefore it is shown in Figure 1*a* that the R0 FAC is closed mainly through the old open tail.

[7]. The R0 FAC flows into the ionosphere on the dusk side of the old PC, flows there toward lower latitudes, and then it flows out of the ionosphere as the R1 FAC on the low-latitude side of the new PC boundary. The closure of the R1 FAC is completed in the mantle, where the current flows from dusk to dawn.

[8]. The volumetric generator is designated by the Roman numeral V in Figure 1*a*. This is the end of a chain of generators as shown in Figure 1. The chain as the whole will be discussed briefly in paragraph [13].

### 3. Test of the volumetric generator model: estimation of the EMF

[9]. We estimate the EMF of the volumetric generator (U′) by using the model of Figure 1*a*, and compare it with the PC potential drop values, U, obtained from observations with help of the magnetogram inversion technique MIT2 [*Mishin et al*, 2000]. As shown in Paper 1 (this issue), the open magnetic flux of the tail is the sum

$$\Psi = \Psi_1 + \Psi_2, \qquad (1)$$

Here, $\Psi_1$ – is the open magnetic flux piercing the mantle that is carried away by the antisunward plasma convection with some velocity V; $\Psi_2$ is the old open tail magnetic flux, which does not participate in the plasma convection, created by the recent dayside merging. We assume that $V = V_{SW}$ on the boundary between the mantle and magnetosheath, and $V = 0$ on the boundary of the mantle and plasma sheet, and assume an average value $V = \langle V \rangle = 0{,}5V_{SW}$.

Thus we have:

$$d\Psi_1/dt = \partial\Psi_1/\partial t + \mathbf{V}\cdot\nabla\Psi_1, \qquad (2)$$

$$U' = -\, d\Psi_1/dt\,, \qquad (3)$$

$$|\nabla\Psi_1| = \Psi_1/L_T, \qquad (4)$$

$$L_T = V_{sw}\cdot(t - t_0). \qquad (5)$$

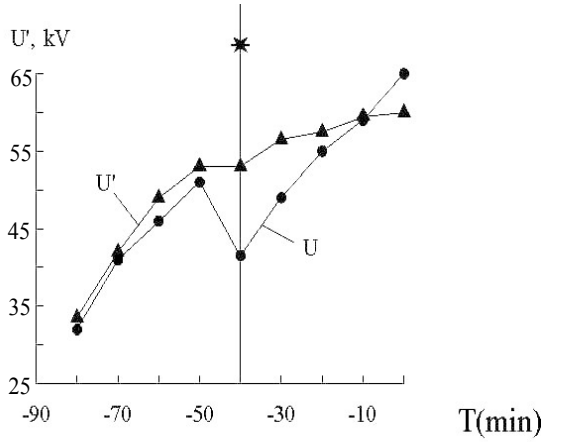


**Figure 2:** Time variations of the polar cap potential drop for the load stage of the statistical substorm: U′ – model values, U – observations (MIT2, [*Mishin et al*., 2001]). The asterisk marks the start of the 1st active phase, T = 0 is the expansion onset.

Here, $t_0$ is the beginning time of the substorm load-stage; $L_T$ is the length of the new open tail at instant t. To compare this with observations, we use the data of the statistical substorm [*Mishin et al*., 2001], supposing $\partial\Psi_1/\partial t = 0$ (that is true for the volumetric but not for the starting generator, see below). From such an approach we have

$$U' = 0{,}5\Psi_1/(t - t_0), \qquad (6)$$

where it is taken into account that the vectors $\mathbf{V}$ and $\nabla\Psi_1$ have opposite directions. The plots of the U' and U variations are given in Figure 2.

One can see a reasonable coincidence of the two curves, and the characteristic time of both variations is ~1.5 hours. These results are both important, and they will be discussed in section 5.

### 4. Region 0 FAC as the coordinator of the plasma convection systems in the tail and ionosphere

[10]. *Shirapov and Mishin* [1998] introduced the notations $t_1$ and $t_2$ as the durations of plasma flow in the ionosphere from the midday boundary of the PC up to the midnight boundary, and also the notation $t_3$ for the time that plasma on the mantle-magnetosheath boundary spends on its way from the dayside magnetopause up to the turning point in the distant tail. The values of $t_1$ and $t_2$ have been evaluated based on two different models. In the first model, for $t_1$, the shielding effect of R0 FAC has been taken into account, but in the second model (for $t_2$) the shielding effect was absent. The characteristic ratios

are the following: $t_3/t_1 \sim 1$, and $t_3/t_2 \sim 0.2$. Therefore it was concluded that the shielding effect of the R0 FAC provides a synchronization (coordination) of the two plasma convection systems, in the mantle and the ionosphere, and also of the convection systems at intermediate heights of the magnetosphere. The term "coordination" means that the plasma with open magnetic flux, which moves in the polar cap ionosphere in the antisunward direction, reaches the reversal point at the same instant when plasma in the mantle reaches the reversal point in distant tail. Observed regular variation of the shielding indicator, $\beta$, shows (see Figure 3 in Paper 1) that the coordination disappears in the course of the loading stage and is restored during unloading. Thus the shielding effect accelerates the plasma flow in the new PC ionosphere, and it promotes coordination of the convection systems at different heights in the magnetosphere. Further considerations are given next in paragraph [16].

## 5. Discussion and conclusions

[11]. Solar wind-magnetosphere coupling comprises a distributed (not wire) web of MHD–generators, converting solar wind energy into substorm energy. This web is complicated, and the wire approach makes it easier to discriminate between separate processes [*Siebert and Siscoe*, 2002]. This paper is concentrated on the final element of the afore-named web, operating under the condition of southward IMF during the substorm load stage, without unloading processes being taken into account. This is the volumetric generator, which consists of elementary generators that have already been known [*Stern*, 1984; *Siscoe*, 1991; and references therein]. However, as seen from the earlier publications, this paper is devoted to the initial stage of a substorm, and describes some new features of elementary generators; in particular, the existence of an "old" and "new" PC. And, respectively, two parts of the open magnetospheric tail, which were taken into account as shown in Figure 1*a*: the passive old open tail (that existed before the substorm) and the active new open tail (that was formed during the substorm). The R0 FAC during southward IMF, and its region of closure through the old open tail, are not trivial details.

[12]. Principal new results are the following:

a) the sum of the elementary generators, connected in parallel, makes up a volumetric generator;
b) that accounts for the polar cap potential drop variation, observed during the statistical substorm load stage;
c) the EMF of the volumetric generator and the polar cap potential drop, both grow slowly during the substorm load stage, with characteristic time scales of $\sim 5 \cdot 10^3$ s, by attaining the level of the dayside magnetopause reconnection rate.

It should be noted that this delay time is characteristic of an isolated moderate substorm with a maximum value of the AE-index of ~800 nT.

[13]. In the model considered, during southward IMF, the load generator as a whole consists of 5 generators marked by the Roman numerals I to V in Figure 1. The currents of the first two generators, i.e. those on the bow shock and on the magnetopause, are marked by the Roman numerals I and II and by thin and thick lines, respectively. During southward IMF, the currents of these two generators constitute a closed circuit as shown in Figure 1*a* according to the results of MHD modeling [*Siebert and Siscoe*, 2002]. The starting generator III is located in the region of disruption of the common current circuit of the generators I and II. Further, generator IV is the solar wind dynamo, and the volumetric generator is marked by the numeral V.

The functions of each of these 5 generators differ in the proposed model. Disruption of the common current circuit of generators I and II is the anticipated reason for dayside merging, which creates the starting generator III. The principal role of the starting generator is to create the observed open magnetic flux $\Psi_1$, although it also creates the noon part of the R1 FAC. The function of the solar wind dynamo is to ensure the observed open magnetic flux $\Psi_1$ convection. The volumetric generator provided by such preconditions produces the observed R1 and R0 FACs and the observed polar cap potential drop. A self-consistent description of the work of the load generator as a whole is the task of MHD-modeling.

[14]. An estimate of the effective values of the inductance and resistance of the chain of generators is given below, based on the characteristic time, $\sim 5 \cdot 10^3$ s, mentioned above, and some simplifying assumptions.

We denote: U* – the rate of dayside reconnection, i.e. the emf of the starting generator; U – the polar cap potential drop; I – the total current intensity in the common load of the starting and volumetric generators, connected in parallel; L and R, respectively, are the inductance and resistance of the aforesaid load; $-L(dI/dt)$ – the inductive emf; $I = U/R$; and $R = const$. Then we have the equation $U = U^* - (L/R)(dU/dt)$ and its solution $U = U^*\{1 - k \cdot \exp[-t/(L/R)]\}$.

Taking into account the above-mentioned characteristic time, we obtain $L/R = 5 \cdot 10^3$ s. The effective resistance can be determined as $R = U/I$. By assuming that for the end of the substorm load stage $U = 1 \cdot 10^5$ V; $I = 10^7$ Ampere (this is an underestimate of the total intensity of the R1 FAC and the cross-tail current), we have $R = 10^{-2}$ Ohm, and $L = 50$ H. Then, the total energy stored in the magnetic field of the current system is, at the end of the load stage, $W = 0.5LI^2 = 2.5 \cdot 10^{15}$ Joule which is consistent with known estimations that were obtained independently.

[15]. Now, let us try to interpret the shielding effect and its variable nature, mentioned in the Introduction, in the framework of this proposed model. This effect prohibits flow of the R1 FAC, generated in the LLBL, into the ionosphere of the old PC. This is a necessary condition, due to which the R1 FAC continues on its way in the form of the R0 FAC and further, through the tail lobe, where the R0 FAC closes mainly in the region of the old tail, but not in the high-speed mantle. Hence, an additional necessary condition is a high conductance in the volume of the old tail, which should be much larger than that in the ionosphere of the old PC. We assume that the conductance is proportional to the volume of the old tail region outside of the high-speed mantle, because the plasma flow is much faster and more turbulent in the mantle, than in the old tail. We found that the field lines of the old open tail are replaced by those of the new open tail in the course of the substorm load stage (Figure 3 in Paper 1). The volume of the old tail is therefore diminished during this stage, concurrently with an increase of the R1 FAC intensity, thereby providing a decrease of the relative intensity of R0 FAC. The volume is restored again during the substorm unloading and recovery phases, after dayside reconnection is turned off and the mantle's volume is diminished, which leads to an increase of the relative intensity of the R0 FAC.

[16]. Variations in the strength of the shielding effect have been quantified and are shown in the plot of $\beta$ [Figure 3 in Paper1]. On the other hand, it follows from section 4 that $\beta$ is also an index for the coordination of the convection systems in the tail and the ionosphere. This coordination disappears in the course of the loading stage and is restored during unloading. In our interpretation, a diminishing of the coordination at loading is a signature of the development of a turbulence and plasma-stagnation region forming in the distant tail. The turbulence and stagnation are promoted (during the load stage) by increasing the difference between dayside and nightside magnetic merging rates. This difference disappears or even changes its sign after a northward turning of the IMF, and coordination is restored in the course of substorm unloading and recovery, as can be seen in the plots of $\beta$ in Paper 1 and the ratios $t_3/t_1$ and $t_3/t_2$ in [*Shirapov and Mishin*, 1998].

[17]. First results of an interpretation of the shielding effect of the R0 FAC were described in terms of the generators of the FACs and the electric fields during a substorm load stage. These results do not contradict the conventional knowledge about substorm processes, but they supplement its base and affect a set of unsolved questions. Further studies are necessary. We plan to check and develop the initial results. More comprehensive studies are required based on both *in situ* measurements and MHD-modeling.

**Acknowledgements:** [18]. This work was supported by the grants: INTAS 01-01140, RFBR 02-05-64159, and RFBR-DFG 02-05-04002.

V. M. M. and M. F. thank G. Haerendal, G. Paschmann, W. Baumjohann, and R. Nakamura in MPE (Garching), L. Zelenyi in IKI RAS for seminars and discussions, which helped to develop this work. The authors from ISTP (Irkutsk) and Ulan-Ude University also are grateful to their colleagues from the ISTP MIT group: A. Bazarzhapov, T. Saifudinova, L. Sapronova, L. Gazhelova, M. Smekhnova, and M. Tolochko for their technical help and discussions, and to members of the seminars in ISTP, where discussions of this work took place, specially Drs G. Kichigin, A. Altyntsev, and A. Leonovich.

**References**

Heikkila, W., Magnetospheric topology of fields and currents, Magnetospheric currents, *Geophysical Monograph, 28,* 208-221, 1984.

Iijima T., and T. A. Potemra, Field-aligned currents in the dayside cusp observed by TRIAD, *J. Geophys. Res., 81,* 5971-5979, 1976.

Iijima, T., Field-Aligned Currents in the Geospace: Substance and Significance, Magnetospheric Current Systems, *Geophysical Monograph, 118*, 107-129, 2000.

Lockwood, M., and S. W. H. Cowley, Ionospheric convection and the substorm cycle, Proceedings of the ICS-1, ESA SP-335, 99-109, 1992.

Maltsev, Y. P., A. A. Ostapenko, Field-aligned currents in the ionosphere and magnetosphere, *this issue*.

Mishin, V. M., D. Sh. Shirapov, V. P. Golovkov, and M. Főrster, Field-aligned currents of Region 0 as electric shield of the polar cap ionosphere, *this issue*.

Mishin, V. M., C. T. Russell, T. I. Saifudinova, A. D. Bazarzhapov, Study of weak substorms observed during December 8, 1990, Geospace Environment modeling campaign: timing of different types of substorm onsets, *J. Geophys. Res., 105*, 10, 23,263-23,276, 2000.

Mishin, V. M., T. I. Saifudinova, A. D. Bazarzhapov, C. T. Russell, W. Baumjohann, R Nakamura, M. Kubyshkina, Two distinct substorm onsets, *J. Geophys. Res., 106*, 7, 13105, 2001.

Newell, P. T. and C. -I. Meng, Ionospheric projections of magnetospheric regions under low and high solar wind pressure conditions, *J. Geophys. Res., 99,* A1, 273-286, 1994.

Potemra, T. A., Sources of Large-Scale Birkeland Currents, Physical Signatures of Magnetospheric Boundary Layer Processes, J. A. Holtet and A. Egeland (eds.), 3-27, 1994, Dordrecht, Boston, Kluwer pub.

Shirapov, D. Sh. and V.M. Mishin, Some problems of the polar cap and geomagnetic tail dynamics, Substorms-4, S. Kokubun and Y. Kamide (eds.), 413-417, 1998.

Siscoe G.L., W. Lotko, And B.U.O. Sonnerup, A high-latitude, low-latitude boundary layer model of the convection system, *J. Geophys. Res., 96,* 3487, 1991.

Siebert, K.E., G.L. Siscoe, Dynamo circuits for magnetopause reconnection, *J. Geophys. Res., 107,* No A7, SMP-6, 10.1029/2001JA000.237. 2002.

Stern, D. P., Magnetospheric dynamo processes, *Geophysical Monograph, 28,* 200-207, 1984.

Vasyliunas, V. M., Steady state aspects of magnetic field line merging, *Geophysical Monograph, 28,* 63, 1984.

Weimer, D. R., Maps of ionospheric field-aligned currents as a function of the interplanetary magnetic field derived from Dynamic Explorer 2 Data, *J. Geophys. Res., 106,* A7, 12,8889-12,902, 2001.

# The IMF $B_z$-variability and high-latitude magnetic activity index relationship

M. Yu. Goncharova[1], and V. A. Pilipenko[2]

[1] Polar Geophysical Institute, 14 Fersmann, 184209 Apatity, Russia
[2] Institute of the Earth Physics, 10 Bolshaya Gruzinskaya, 123995 Moscow, Russia

**Abstract.** We attempt to reveal statistically the possible influence of IMF variability, as measured by the standard deviation of IMF $B_z$, on the ground effect of auroral disturbances, as measured by the AE index. It has been discovered that the AE level, on average, is higher for the higher current-hour $B_z$ variance values. Being compared for stable and variable hourly $B_z$ values, separately for positive and negative polarities, the AE index is shown to be suppressed/to grow larger under a stable preceding field. Since the $B_z$ variance occurrence subsides rapidly as its value increases, it is highly possible that AE growth with increasing $B_z$ variance is due to the effectiveness of $B_z$ "stairs". A new index is needed to characterize IMF variability in solar-terrestrial studies and is proposed here.

## 1. Introduction

The influence of solar wind turbulence on solar wind and magnetosphere coupling is commonly ignored. However, theory predicts [*Baranov and Krasnobayev*, 1977] that developing of magnetic viscosity in the presence of collisionless shock and MHD waves (in transition layers and other thin regions), significantly affects solar wind radial bulk flow. The solar wind velocity enters the solar wind-induced electric field, being the source of Dungey convection in the polar ionosphere. The same velocity determines the efficiency of solar wind momentum transfer to the magnetosphere in the course of a quasi-viscous interaction. In theoretical modeling, with magnetic viscosity taken into account, the radial bulk flow velocity has been always found lower than its experimental values, both for B=0 and B≠0 situations.

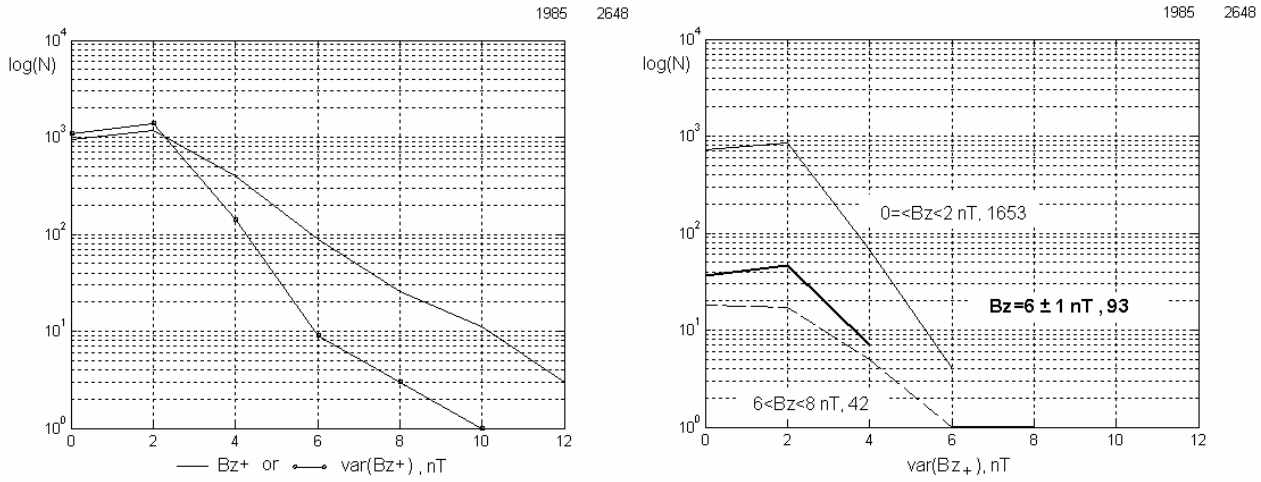


**Figure 1:** Left panel: data amount (log scale) in bins of 2 nT width for northward $B_z$ (solid line) and var ($B_z$) (marked line). Right panel: occurrence distribution of var ($B_z$) for $B_z$ = 0.2 nT (solid line), 6–8 nT (dashed line), and 6±1 nT (heavy solid line).

Turbulence may have different impacts on solar wind and magnetosphere coupling. Laboratory experiments showed that the viscous interaction of a fluid and an obstacle is drastically different between laminar and turbulent flows [*Borovsky et al.,* 1997]. Thus, the external turbulent viscosity of the solar wind upstream to the Earth must control the degree of quasi-viscous interaction at the dayside magnetopause. Besides, turbulent plasma convection inside the current sheet on the nightside also might depend on the external turbulence level [*Antonova and Ovchinnikov*, 1999]. IMF variability may control fast processes as well, such as reconnection, since the magnetic field penetration time into the magnetosphere depends on the magnetic Reynolds number. In [*Maltsev and Ryzhova,* 2002], the characteristic time corresponding to usually-assumed high Reynolds numbers was found to be too long to provide fast process efficiency.

Correspondence between theory and experiment improved when magnetic field fluctuations were added. However, the solar wind velocity growth in the presence of IMF variability was theoretically found under some special limitations and thus the turbulence-viscosity-velocity-magnetosphere coupling problem is not yet completely solved.

In early studies of ring current dynamics, IMF variance was used as one of the governing parameters for Dst-modelling [*Feldstein,* 1992]. The IMF partial variances, being standard deviations of $|B|$, $B_x$, $B_y$ and $B_z$, reflect magnetic field variability, but possess a drawback in that they give information only on average amplitude, with no distinction for sudden B direction or magnitude changes and permanent wave activity. However, the maximum magnetic field fluctuation amplitude is known as related to the maximum magnetosonic wave phase velocity determining the moment of wave front capsizing and laminar-to-turbulent plasma flow regime transition [*Baranov and Krasnobayev*, 1977]. So far, one may expect that variance includes plasma turbulence, though not directly and not completely.

Recently it was found that solar wind low-frequency waves can modulate high-latitude electrodynamics [*Pilipenko et al*., 2000]. Moreover, according to the model of Goertz and Smith [1989], pre-heating of plasmasheet plasma by MHD waves may be a significant factor in substorm development. On the other hand, steady northward magnetic fields of 8÷10 nT hourly mean values were found to be most effective in constructing conditions preceding AE growth after the $B_z$ polarity changes to southward [*Goncharova,* 2002]. Isolated within a characteristic time scale of AE-to-$B_z$ response of ~40 min, these events are commonly named "stairs" and are known to be substorm activity triggers. $B_z$ stairs originate from MHD discontinuities, when the entire fluctuation viscosity is concentrated within a thin transition layer, and at either side of the layer fluctuations are small.

The comparative efficiency of the external solar wind turbulence impact on the Dungey or Axford-Hines solar-wind – magnetosphere interaction has not been clarified yet, nor has the solar wind velocity response. That depends on a number of factors related to the thermal properties of plasma components and the energy exchange between them. However, there are no indices that describe the extended characteristics of solar wind turbulence.

Here we present preliminary results of a direct comparison of IMF variability amplitude, as measured by $B_z$ variance (standard deviation), with the high-latitude geomagnetic activity level, as measured by the AE index.

## 2. Basic statistical features of the IMF $B_z$ variance

For statistical analysis we used hourly IMF and solar wind data from the OMNI database and hourly AE index values for 1985. As the simplest indicator of IMF variability, the standard deviation of the IMF $B_z$ component, var ($B_z$) from the OMNI database has been used.

Figure 1 shows the basic statistical properties of the IMF $B_z$. The IMF is directed northward ($B_z > 0$) during 2570 of 8760 hours. Independent distributions of $B_z > 0$ and var ($B_z$) are shown on the left panel of Figure 1, bin width is chosen as 2 nT. The distributions show that for $B_z > 2$ nT, IMF variance (marked line) subsides more rapidly than $B_z$ itself (solid line). This provides indirect evidence that the IMF is stronger when $B_z$ conditions are quieter; the relative IMF fluctuation level, w = var($B_z$)/$B_z$, also becomes lower for stronger northward IMF $B_z$.

Cases with variances >8nT are very rare. The distributions are peaked at $B_z$ = 2nT and var($B_z$) = 2 nT too. For hourly $B_z$ ~ 6 nT one expects ~100 events of northward $B_z$ per year, with ~10% of them having comparable and greater variances. Selection of events satisfying the condition $B_z = 6\pm1$ nT (heavy solid line in Figure 1, right panel) gave 93 events in 1985, with their var($B_z$) staying within 2-4 nT range. 90 of 93 events have their var($B_z$) less than 5 nT (NB: the lower limit of the chosen northward $B_z$ strength). Weak northward IMF, $B_z$ = 0–2 nT, appears to be associated with var($B_z$) that can vary in the 0-6 nT range. Thus, for these events the $B_z$ variance most often cancels the $B_z$ polarity importance. Strongest northward IMFs, $B_z$ = 6–8 nT, are associated with var($B_z$) ≤ 8 nT and therefore support an unchanged IMF polarity.

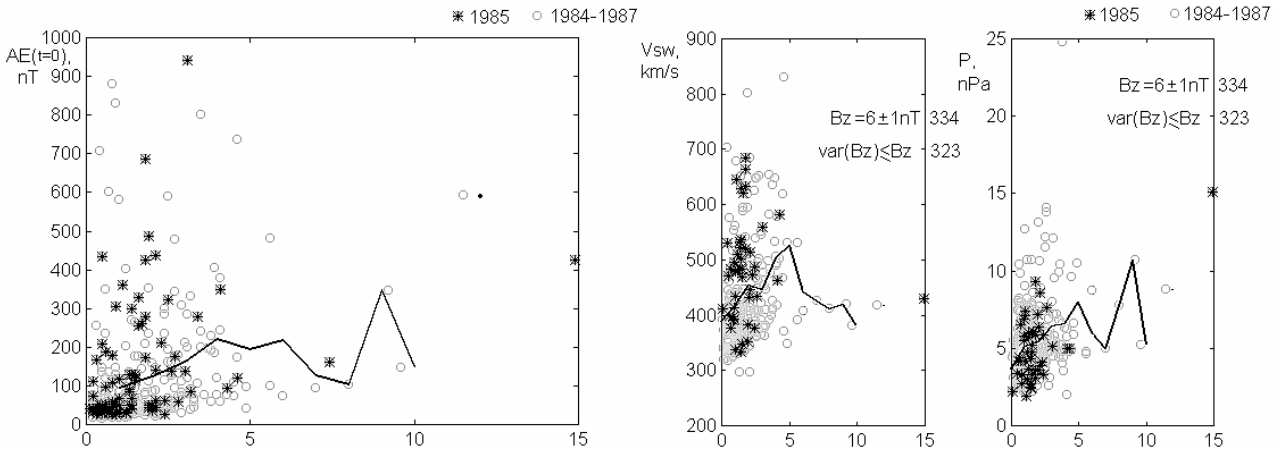


**Figure 2:** Relationship of the AE index, solar wind velocity $V_{SW}$ (km/s) and dynamic pressure P (nPa) to IMF $B_z$ variance, var($B_z$)

.

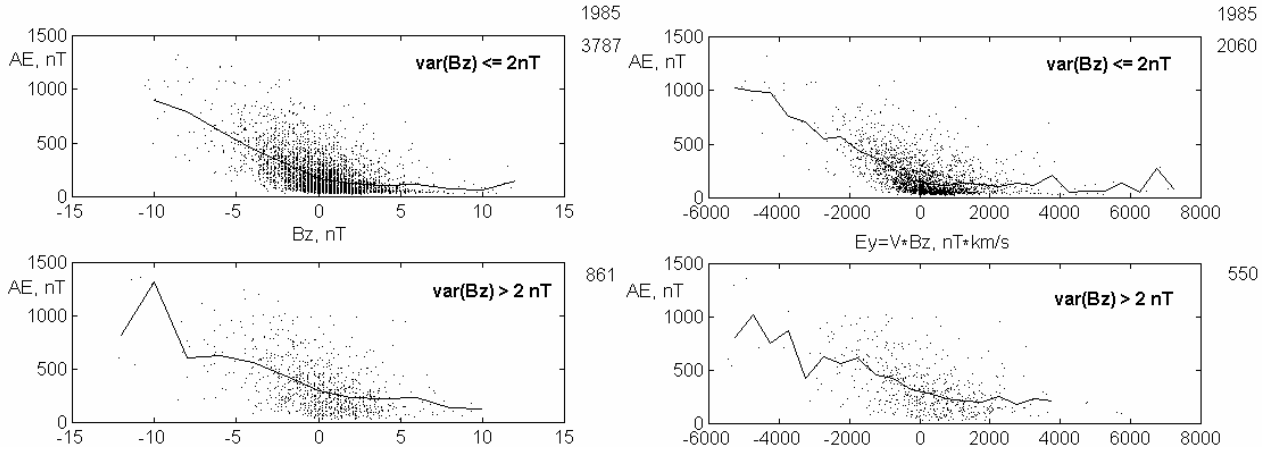


**Figure 3:** Relationship between AE and $B_z$ (nT), and between AE and $E_y$ (nT km c-1) (right panel) for weak (≤ 2 nT) and strong (> 2 nT), variances of $B_z$.

In Figure 2 the AE index, nT (left panel), solar wind velocity Vsw, km/s, and dynamic pressure $P = m_p n_p (Vsw)^2$, nPa (right panel), versus var($B_z > 0$) are given. $B_z$ is fixed around 6 nT within ±1 nT. Since a majority of the data has lower variances, to avoid ambiguities, the lack of data in the enhanced variances' area was overcome by extending the data set. Data from years 1984–1987 are also used (here only), and denoted in the figure by gray circles. Data from 1985 are marked with asterisks. The AE index evidently grows in bin-averaged value towards higher var($B_z$) unless the variance begins to exceed the $B_z$ mean value, e.g., excursions into the opposite polarity occur. Then AE subsides down to ~100 nT at var($B_z$) ~ 8 nT, and slowly increases again towards higher var($B_z$). AE grows slightly non-linearly in its first interval of growth, whereas it goes up quasi-linearly in its second one. Looking at the right panel of Figure 2, we see that the variance growth is followed by a solar wind velocity and pressure increase until the same point of the $B_z$ – var ($B_z$) equilibrium is reached. Maximum Vsw (and AE) values correspond to variances of 2.4 nT, whereas the bin-averaged curves of Vsw, and P peak at 5 nT. Then each parameter drops. The velocity stabilizes near its mean level, and the pressure starts to grow again quasi-linearly, as the number density does also. AE index variation seems to be more like that of the solar wind dynamic pressure.

This relationship may be considered as an indication that, for low variance amplitudes, solar wind flow is quasi-laminar in spite of any increase in fluctuation amplitudes, unless polarity changes occur. Meanwhile, fluctuation-effects enhance flow velocity, as theoretical modeling predicts [[Baranov and Krasnobayev, 1977]. Further increase of fluctuation amplitude and flow

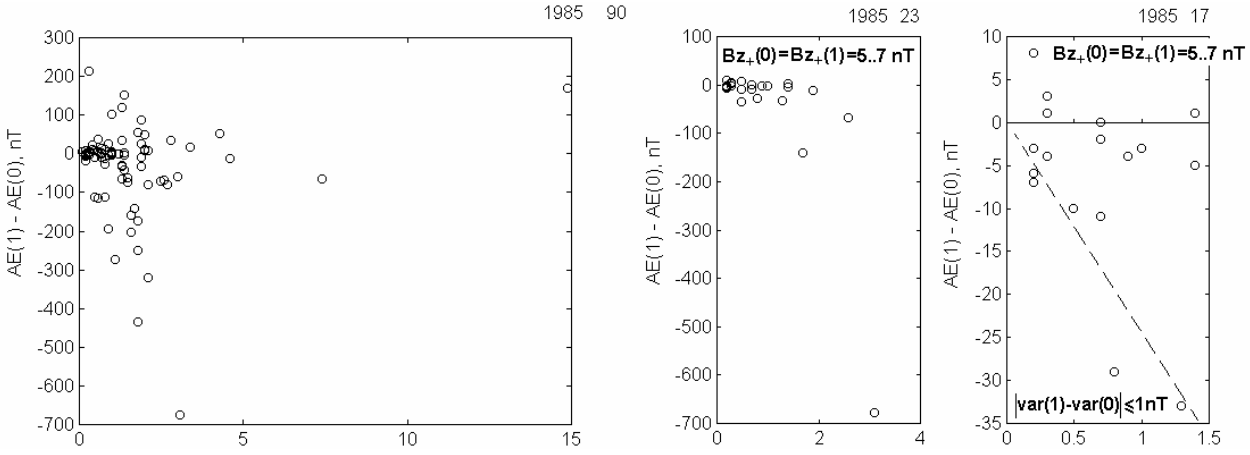


**Figure 4:** Relationship between dAE/dt and var($B_z$) for $B_z$ (0) = 5-7 nT (left panel), for $B_z$ (0-1) = 5-7 nT (middle panel) and |d(var($B_z$(0)))/dt| ≤ 1 nT/hr (right panel).

velocity results in collisionless shock waves forming, with the turbulence concentrating within a thin layer of MHD discontinuity [*Kleymenova and Kosyreva*, 2002; this issue as well], being small on either side of it and thus weakly affecting bulk flow. As signatures, sudden polarity changes of IMF components occur, and the solar wind begins to drive the magnetosphere via reconnection processes. Thus, large-amplitude $B_z$ fluctuations (var($B_z$)>, ~$B_z$) affect not only the quasi-viscous interaction efficiency, but also reconnection processes as well.

## 3. The AE index and its hourly derivative response to IMF $B_z$, $E_y$ and $B_z$ variance

The impact of IMF variability on high-latitude magnetic activity may be inferred from comparison of the AE index's static and dynamic response to quiet and noisy IMF of similar mean strengths. Though the linear correlation between AE and $B_z$ is best when there is ~40 min delay between them [Carbary and Meng, 1986], this might be wrong for transient IMF fields. Therefore we set no delay between the compared $B_z$ and $E_y = V \cdot B_z$ time series. We also note, that $B_z$ polarity can be assumed unchanged only for $|B_z| > 2$ nT, var($B_z$) ≤ 2 nT conditions.

In Figure 3 the AE index is plotted versus $B_z$ (left) and $E_y = B_z \cdot Vsw$ (right panel) for the weak and strong (≤ or >2 nT respectively) variances of $B_z$. It is well seen, that the bin-averaged AE values (solid curves) under var($B_z$) > 2 nT are higher than under var($B_z$) < 2 nT. The difference is most significant in –8…+8 nT range. Thus, variable IMF produces, on average, a higher AE level than quiet IMF for the same bulk parameters. But here we do not address the behavior of the AE derivative because no delay is suggested between var($B_z$) and AE. Figure 4 accounts for this.

The hourly derivative of AE, taken between the current and the next hour with respect to the var($B_z$) hourly value, when compared with the $B_z$ variance for the current hour, $B_z$(0) = 5..7 nT (fixed), is shown in Figure 4, left panel. Two kinds of AE derivative behavior are observed: growth in negative value and non-monotonic variation with increasing variance. In the latter case, dAE/dt is initially positive, slowly diminishing in value towards higher variances, until the variance exceeds ~8nT, then rising up again. The right panels represent AE derivative response to $B_z$ variance under the $B_z$ (0-1) = 5...7 nT during the two subsequent hours, the current and the next one (steady $B_z$). The variances reduce in amplitude, but within 0…4nT one can observe the same two sorts of dAE/dt behavior, with very small positive increments by smallest var($B_z$). If we want to check whether the variance causes this separation, var($B_z$) must be invariant during the same two hours as well. As is seen in the right panel of Figure 4, the separation dAE/dt in response to $B_z$ variance under steady $B_z > 0$ remains after two proportional divisions of the data. One possible explanation is that the $B_z$ variance participates twice in the solar wind–magnetosphere coupling: via the quasi-viscous interaction efficiency and $B_z$ polarity variations. Another is the AE index pre-history, since the enhanced AE (>400 nT) tends to subside in response to a $B_z$ polarity change from + to – [*Goncharova*, 2002] .

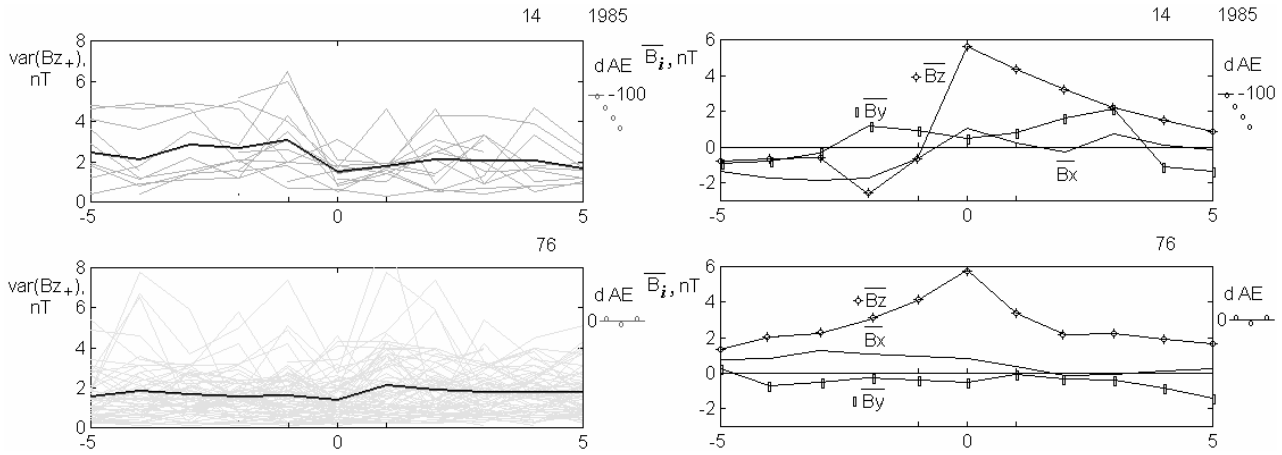


**Figure 5:** SPE temporal profiles of the var ($B_z$) and IMF components, under $B_z(0)$ = 5-7 nT ($B_z(0)$) < 5 nT condition, for two subsets of AE responses shown in Figure 4: dAE/dt ~ 0 and dAE/dt < 0 (followed with sketches).

Thus, the plots of Figure 4 reveal two kinds of AE dynamic response: The AE time dynamics depend weakly and non-monotonically on an increase in IMF variance; roughly dAE/dt ~ 0 when northward $B_z$ is fixed in value. Acceleration toward higher IMF variance occurs when d(AE)/dt <0.

An assumption of acceleration in AE drop follows from comparison of the descending branch inclinations (~–350 and ~–23 nT/hr of AE per 1 $B_z$ nT ).

For the 2nd group of events, the AE index is as likely to be suppressed by IMF variability, based on the dAE/dt<0 proportionally diminishing in modulus with var($B_z$) automatically reducing in amplitude, when $B_z$ is fixed (for one hour) and steady (for two hours), being of ~6 nT. Note the $B_z$ variances remain less than the chosen northward $B_z$ value for this group of events.

So far, though for greater $B_z$ variances of the current hour, the solar wind velocity is higher and AE level is higher too, but its derivative, controlled by the preceding IMF $B_z$ (or rather $E_y$) factor, is hardly expected to be found positive and increasing.

## 4. Epoch-matching technique (EMT) analysis

We now try to show the IMF features that may cause the AE response to split into two groups of events. In Figure 5, results are shown of searching for effects on IMF $B_x$, $B_y$, *and* $B_z$ components with the epoch-matching technique (EMT). The data set (90 events) is determined by the condition $B_z$ = 5–7 nT and var($B_z$) < 5 nT, held at zero moment, that is $B_z$ is assumed fixed in polarity. Otherwise, the averaging amongst fixed and non-fixed in $B_z$ polarity events would be incorrect. Two kinds of AE responses, AE(1) < AE(0) (14 events) and AE(1) ~ AE(0) (76 events) are analyzed separately (top and bottom plots, respectively).

In Figure 5, the $B_z$ variance (left panel) is given by both individual time series (left panel) and case-averaged curve, the IMF components $B_x$, $B_y$, $B_z$ (right panel) are given by case-averaged curves only, for each hour within the –5 – +5 hr interval, separately for two kinds of AE(t) responses. In the second subset, where d(AE)/dt < 0, the $B_z$ temporal profile manifests a positive stair, with small negative $B_z$ during preceding hours, and with $B_z$ (–1) ~ 0. In the 1st subset (where d(AE)/dt~0) the preceding IMF $B_z$ is positive. The $B_x$ temporal profiles are identical for t = 0–2 hours and differ strongly for t < 0. In the 1st subset a positive stair in $B_x$ is associated with dAE/dt < 0 as well. The $B_y$ temporal profile is symmetric about zero, but is of opposite sign in the 1st and 2nd dAE/dt subsets.

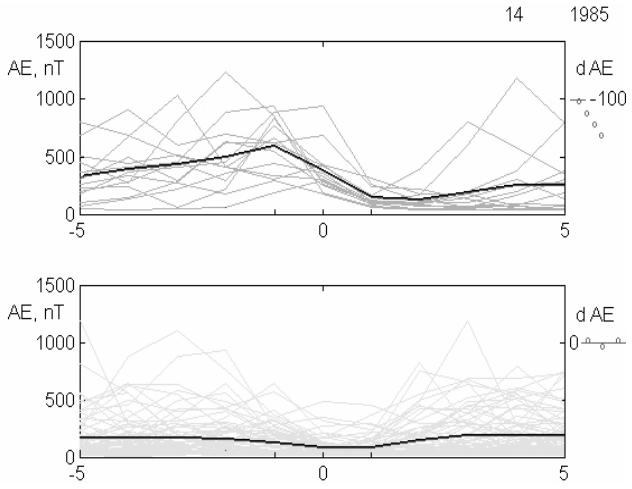


**Figure 6:** Temporal profiles of AE index under the same conditions as in Figure 5.

In Figure 6, the EMT temporal profile of AE under the same conditions as in Figure 5 is given both by individual and case-averaged curves. As seen, the $B_z$ variance in the 2nd subset and the AE index both subside at the t=0 moment ($B_z(0)>0$). The averaged value of AE(-1) is much larger than the natural fluctuations level at auroral latitudes (~300nT), whereas AE(1)-AE(0)<0. In the 1st subset the tendency is inverse and the AE level is strongly suppressed, with the case-averaged AE being < 300nT. The average AE in individual time series mostly decreases weakly when passing through the instant of fixed $B_z$ and limited variance value (t = 0). The variance increases slightly just as the condition is passed, and ~1/3 of the subset increases significantly, resulting in the case-averaged value growth of 1nT. However, it doesn't result in AE growth. From comparison of var($B_z$) and AE temporal profiles it follows that a small increase in var($B_z$) is associated with both invariant and subsiding AE, but the pre-history of the AE dynamics is drastically different. However, one can not ignore distinctions in var($B_z$) pre-history. As Figures 5-6 show, diminishing in var($B_z$) amplitude after a positive $B_z$ stair appears to be favorable for subsequent diminishing of AE in value.

Thus, a question arises, which of the two AE controlling factors is most important – the $B_z$ variance (based on results of Figure 4) or $B_z$ polarity (based on results of Figures 5-6)? Below we examine this problem with another statistical method.

## 5. Relationship reliability analysis

The relationship reliability function F verifies the causal relationship between the two variables. It is the conditional-to-neutral ratio of their occurrence probability, (dn/n)/(dN/N), where n is the number of events associated with a given condition, N is the number of events in the total data set, dn and dN are the numbers of favorable events in the two data sets [*Goncharova*, 2002].

The relationship reliability technique has been applied to analysis of relative variance, $w$=var*(Bz)/Bz*. The parameter $w$ comprises information both on polarity of IMF $B_z$ and the balance between var($B_z$) and $B_z$. The current hour AE(0) was compared with the preceding hour $B_z(-1)$, taken together with the variance of the preceding hour, var($B_z(-1)$), because it is known that AE correlates best with the preceding hour $B_z$ (even for hourly data). The relative variance is taken thus for the t = –1 hr moment (with reference to SPE technique). Observation of w(–1) values within the bins of 0–0.5, 0.5–1, 1–2, 2–5, 2–10 (times) width (between those, the AE response is fairly distinctive) is chosen as *a condition*, and the AE index is taken for the current moment, t = 0, and the occurrence distribution of AE(0) over the 0...1600 nT range (divided into bins of 100 nT width), is considered inside any of $w(-1)$ bins.

Figure 7 shows that the deviation of AE conditional probability from the neutral probability (solid line) is maximal for the lowest $w$ values. The $B_z(-1)$ polarity importance can be inferred from the comparison of $w$(-1) of different signs. For $w(-1) > 0$, the forthcoming AE(0) level is better suppressed by the smaller $|w(-1)|$ values; whereas for $w(-1) < 0$, the AE(0) level is better amplified by the smaller $|w(-1)|$ values.

Thus, at very low relative variances, not unexpected, AE is suppressed by northward IMF and stimulated by southward IMF, with the usual delay < ~1 hour. But, the growth in IMF variability as compared to the mean $B_z$ value reduces the significance of $B_z$ and its polarity.

Besides, for AE reaction to the IMF $B_z$ variance, perhaps, not only its amplitude is important but also the proper characteristic time of response, corresponding to the decreased/enhanced variance' amplitude.

## 6. Discussion and conclusions

It is now recognized that long-term steady southward IMF $B_z$ produces enhanced magnetospheric convection [*Pytt et al.,* 1978; *Yahnin et al.,* 1994], but not yet a substorm, whereas steady northward IMF $B_z$ practically suppresses AE to very low values. The substorm occurrence might be related to rapid changes of IMF $B_z$, isolated at a characteristic time scale of magnetospheric response (stairs), under favorable IMF polarity [*Kamide*, 2001]. Magnetospheric plasma convection can be driven by the solar wind by transferred momentum (quasi-viscous interaction) and by induced electric field across the magnetosphere (reconnection). Southward (northward) IMF stimulates convection in the same (opposite) direction as a convection driven by quasi-viscous interaction. Hence, northward IMF may provide a misbalance of these two convections, which could result in energy accumulation and its subsequent release (substorm). The threshold ~8nT of an hour preceding $B_z > 0$, as revealed by *Goncharova* [2002], is a pre-condition of AE growth after a change of IMF polarity to southward. It may correspond to an unstable equilibrium between opposing convections. When the magneto-spheric system is unable to release an accumulated amount of energy in a short time to adjust to the quasi-steady condition, a substorm becomes inevitable.

Our statistical analysis has shown that substorm activity, as measured by AE index, is sensitive not only to the bulk IMF and solar wind parameters, but to the level of IMF variability as well. Disturbed IMF $B_z$ causes a larger response, especially for small and moderate fields, than a quiet IMF $B_z$.

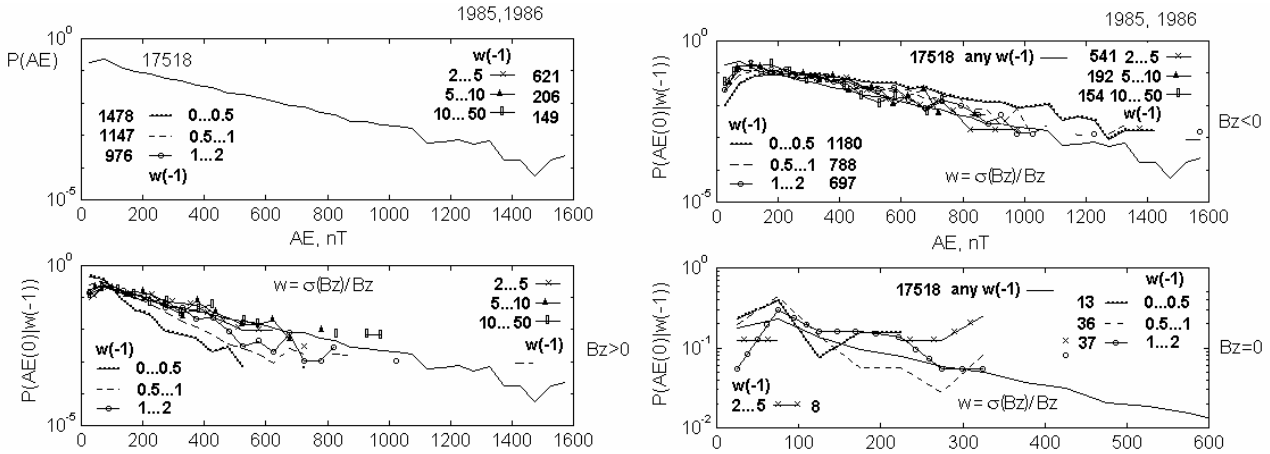


**Figure 7:** The probability of observing the current hour-related AE(0) under the arbitrary $B_z$ (−1) polarity of the preceding hour is compared with the one defined by the different relative variance level $w$ (−1) of the preceding hour (for $B_z$ (−1) >, < ~0 separately).

Examination of the influence of IMF variance on the time history of auroral disturbances reveals two kinds of AE responses:

1) AE time derivative weakly and non-monotonically depends on increasing IMF variance; and
2) Non-linear decrease in the AE time derivative with enhancement of the northward IMF $B_z$ variance.

Non-monotonic dependence of solar wind velocity and pressure on IMF variability, with maximum values observed around 2–4 nT, was found. SPE shows that enhanced decrease of AE is associated with a clear positive stair in $B_z$, whereas slow variations of AE level are related to fluctuations of northern IMF. Possible physical mechanisms for IMF variability impacting the solar wind-magnetosphere interaction have not been fully identified yet.

Quasi-viscous interaction enhancements at the dayside magnetopause might be an effective cause of substorm activity, especially under IMF $B_z > 0$ conditions. Quasi-viscous interaction on the flanks of the magnetosphere's tail is theoretically shown to increase cross-polar cap potential drop up to 30 kV [*Denissenko et al.,* 2002]. Laboratory experiments showed that the coupling of a fluid with an obstacle is mainly determined by the Reynolds number $R_e$, constructed with the turbulent rather than molecular viscosity. According to this turbulent viscosity concept, one would expect the coupling of the solar wind with the magnetosphere to be increased when the level of upstream solar-wind turbulence is enhanced.

On the other hand, a turbulent viscosity superimposed on rapid changes in IMF orientation might diminish the rapid change of convection, which is one of the mechanisms of substorm triggering. Rapid variations of IMF orientation on a time scale less than the characteristic time of global convection response may prevent accumulation of energy provided by positive $B_z$ as well. This follows from a comparison of neutral and conditional probabilities of enhanced AE for the steady and highly variable IMF $B_z$ during the preceding hour.

The cause of AE-level enhancement by higher IMF variability might be as follows. The IMF variance incorporates not only turbulent fluctuations and low-frequency waves, but also, the rotational discontinuities that generate $B_z$ stairs. Specific stair amplitudes are less frequently observed as they become higher. Higher AE index values corresponding to the var($B_z$) > 2 nT can be explained by an increased occurrence of $B_z$ stairs. The rarefaction of dots in Figure 3, lower panels, favors this suggestion.

The quasi-viscous interaction efficiency may depend non-linearly on the external turbulence level in the solar wind. One can not exclude that the importance of IMF variability for quasi-viscous interaction and reconnection should be estimated at different proper time scales: in the latter case the overtaking fields, with no regard for whether they are steady or variable, ought to be used.

Our consideration supports the necessity to incorporate a new index into the study of solar-terrestrial relationships, to characterize the variability of the solar wind flow more concretely. For instance, it would provide information on a specific sort of viscosity. However, the time scale of IMF variations and the relevant magnetospheric response is about 10 min, much less than the averaging interval (1 hour) of the OMNI database. Further development and verification of the turbulent phenomenology of the magnetosphere should employ long-term time series of solar wind satellite data and auroral indices with higher time resolution (up to 1 min). The future index also should be based on some algorithm discriminating recurrent turbulence from discontinuities in the IMF.

**Acknowledgement.** This research is partly supported by the NATO grant PST.CLG.978252.

**References**

Antonova, E. E., and I. L. Ovchinnikov, Magnetostatically equilibrated plasma sheet with developed medium scale turbulence: Structure and implications for substorm dynamics. *J. Geophys. Res., 104* (A8), 17289-17298, 1999.

Baranov, V. B., and K. V. Krasnobaev, Hydrodynamic theory of space plasma, *ed. by Nauka, Moscow*, 1977. (*in Russian*).

Borovsky, J. E., R. C. Elphic, H. O. Funsten, and M. F. Thomsen, The Earth's plasma sheet as a laboratory for flow turbulence in high-$\beta$ MHD, *J. Plasma Phys., 57*, 1, 1997.

Cowling, T. G., Magnetohydrodynamics, Reports on Progress in Physics, XXV, 1962 (*translated in Russian,) ed. by Mir, Moscow*, 1964.

Denissenko, V. V., A. V. Kitaev, S. S. Zamay, Influence of the viscous interaction at the flanks of the magnetospheric tail on the ionospheric electric field, *Proc. of the International conference Problems of Geocosmos, June 3-7, 2002, St.-Petersburg, Russia;* p.150-153.

Feldstein, Y. I., Modeling of the magnetic field of magnetospheric current as a function of interplanetary medium parameters, *Space Sci. Rev*., *59*, 83-165, 1992.

Goertz, C. K., and R. A. Smith, The thermal catastrophe model of substorms, *J. Geophys. Res., 94*, 6581-6596, 1989.

Goncharova, M. Yu., On AE index rising and subsiding after a negative stair in Bz IMF, *Proc. of the International conference Problems of Geocosmos, June 3-7, 2002, St.-Petersburg, Russia;* p.112-115.

Kamide, Y., Interplanetary and magnetospheric electric fields during geomagnetic storms: what is more important, steady-state fields or fluctuating fields? *J. Atmos. & Solar-Terr.Phys., 63,* 413-420, 2001.

Kleimenova, N. G., and O. V. Kozyreva, Daytime high-latitude geomagnetic pulsation response to the front edge of the magnetic clouds, *Physics of Auroral Phenomena, 25 Annual Seminar, Apatity, Abstracts,* 46, 2002

Maltzev, Yu. P., and O. A. Ryzhova, Very low magnetosheath conductivity deduced from fast magnetospheric response to the IMF changes, *Proc. of the International conference Problems of Geocosmos, June 3-7, 2002, St.-Petersburg, Russia;* p.112-115

Pilipenko, V. A., E. N. Fedorov, M. J. Engebretson, V. O. Papitashvili, and J. Watermann, Poleward progressing quasi-periodic disturbances at cusp latitudes: The role of wave processes, *J. Geophys. Res., 105*, A12, 27,569-27,588, 2000.

Pytte, T., R. L. McPherron, E. W. Hones Jr., and H. I. West Jr., Multiple-satellite studies of magnetospheric substorms: Distinction between polar magnetic substorms and convection-driven magnetic bays, *J. Geophys. Res., 83*, 663-679, 1978.

Yahnin, A. G., M. V. Malkov, V. A. Sergeev, R. J. Pellinen, O. Aulamo, S. Vennerström, E. Friis-Christensen, K. Lassen, C. Danielsen, J. D. Craven, C. Deehr, and L. A. Frank, Features of steady magnetospheric convection, *J. Geopys. Res*., *99*, 4039-4051, 1994.

# Influence of the IMF $B_Y$-component on a substorm current wedge

V.A. Velichko, R.N. Boroyev, I.Ya. Plotnikov, and D. G. Baishev

Yu. G. Shafer Institute of Cosmophysical Research and Aeronomy, Yakutsk, Russia

**Abstract.** Magnetospheric field-aligned currents associated with substorm development under the condition of a southward interplanetary magnetic field have been studied by using data from the longitudinal mid-latitude station chain in Earth's northern hemisphere. Variations of IMF components and characteristics of field-aligned current sheets in substorm centers are compared. It is found that a ratio of values of Birkeland currents flowing into the ionosphere and flowing out of it depends on the IMF $B_Y$–component. In this connection, the polar ionosphere conditions, at which currents flow between the regions of the dayside cusp and auroral oval in the midnight sector, are discussed. The essential differences found between sheet structures of the substorm current wedge are explained by their redistribution.

## 1. Introduction

The substorm current wedge (SCW) is the activization of a magnetosphere-ionosphere current system which flows over the auroral oval in the midnight sector. It is assumed to originate from the nonstationary generation of the electric field in the magnetospheric plasma sheet [*Semyenov and Sergeev,* 1979]. In this case, it remains unknown why currents flowing across the magnetotail from the dawn side to dusk generate the field-aligned currents closed by ionospheric currents at their branching. There are difficulties in representing the currents directed perpendicular to the current sheet that separates the lobes of the magnetotail. At the same time, *Sergeev* [1987] gives strong arguments in favor of the existence of such currents under stationary conditions. Apparently, the noted difficulties are of common basis and they are part of the physics of the magnetopause current layer. According to *Sonnerup* [1980], *Plotnikov* [1989] and *Plotnikov* [1996], the flow of currents transverse to the magnetopause is a key element in the nature of electrodynamic connection of a boundary layer and the ionosphere. Summarizing the stationary and nonstationary cases, we reason that the branching of currents is a widespread magnetospheric phenomenon that is probably caused by the generation of field-aligned electric fields of static and induction origin.

In the present work conditions are studied of SCW formation in which explosive reconstruction of plasma sheet current is controlled by the induction electric field. This situation allows one to associate correctly the electric field with a current and but not yet to consider the anomalous resistivity in space plasma which is essential for electrostatics. Taking into account that substorms are mainly triggered by southward IMF, the cases considered by us for a large azimuth component are of special interest. It is particularly important that a substorm onset occurs under conditions associated with the electric field generated by the structure of the IMF sector in a certain way [*Krymsky,* 1994].

Note that at $|B_Y/B_Z| > 1$ according to *Leontyev and Lyatsky* [1974], the electric field $E_Z \sim -V_0 B_Y$ ($V_0$ is the solar wind speed, $B_Y$, and $B_Z$ are IMF components in the GSM system) is most effectively transferred from the solar wind to the magnetosphere and to the polar cap region. Then, in correspondence with the concepts of *Krymsky* [1994]; *and Kozlov and Krymsky* [1994], the field with a component perpendicular to the neutral line surface penetrates to the plasma sheet. The task of experimentally finding the influence of components of such a field upon substorm wedge currents, and describing the consequences of the process of current branching in the current sheets qualitatively is set for checking the above mentioned concepts.

At present, there are methods [*Weimer*, 2001] to solve similar problems of magnetic field variations measured by spacecraft. It is advisable to begin the search for the solution of such tasks with analysis of ground-based magnetic observations. We have studied ground magnetic effects for differing directions of the IMF azimuth component on the basis of *Sergeev and Tsyganenko* [1980] where the method for distance control over the field-aligned currents in the SCW was suggested.

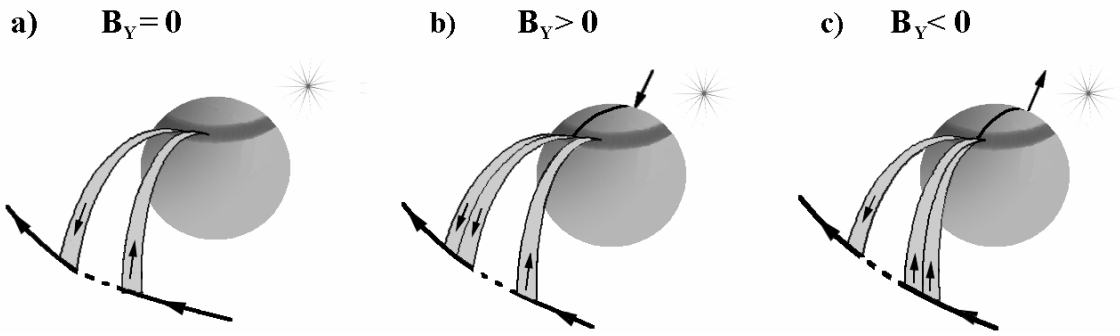


**Figure 1:** Systems of SCW field-aligned currents: (a) antisymmetric system for IMF $B_Y = 0$ and (b) and (c) asymmetric ones for IMF $B_Y > 0$ and IMF $B_Y < 0$.

## 2. Analysis of experimental data

Here analysis results for six isolated substorm disturbances are presented. They develop when $B_Z < 0$ and under the condition when $|B_Y/B_Z| > 1$ which is typical for the class of events discussed by *Leontyev and Lyatsky* [1974]; *Lu et al*. [1994]. The onset of expansion phase $T_0$ has been determined by the H-component at magnetic stations of the auroral zone.

*McPherron et al*. [1973] and *Sergeev* [1978] have shown that one can use the longitudinal distribution of amplitude increments (magnetic field D- component)

$$\Delta D(t,\lambda) = D(t,\lambda) - D(T_0,\lambda)$$

in order to determine the longitudinal scale of the substorm expansion phase field-aligned currents.

*Velichko et al.* [2002*a*] have used such a method for the determination of field-aligned current sheet sizes by a mid-latitudinal chain of magnetic stations. The approximation (1) by a cubic polynomial $\Delta D3$ from $\lambda$ is used in the equation:

$$\Delta D3(T_0 + \Delta t, \lambda) = 0$$

$\lambda_W$, $\lambda_E$ and $\lambda_0$ are three roots ($\Delta t$ are fixed time interval of 5, 10 and 15 min, $\lambda_W$ and $\lambda_E$ are the longitudes of magnetic effect boundaries of inflowing and out-flowing field-aligned currents, respectively, $\lambda_0$ is the substorm center longitude). The bandwidth of the current flowing into the ionosphere is given by the expression

$$\Lambda_W = \lambda_W - \lambda_0$$

and the band width of the current flowing out of the ionosphere is determined in the following way:

$$\Lambda_E = \lambda_E - \lambda_0$$

From our calculations of these field-aligned current sheet sizes, we suggest a scheme for the distribution of field-aligned currents in the substorm current wedge (Figure 1).

We explain the observed picture as the superposition of two systems of field-aligned currents: a) the antisymmetric part of SCW and b) the additional field-aligned current whose direction is controlled by the IMF azimuth component (shown by the arrow).

In addition, *Velichko et al*. [2002*b*] have shown that substorms in the northern and southern hemispheres do not develop symmetrically. The ratios of substorm disturbance amplitudes in the northern and southern hemispheres $|\Delta H|_{\max N} / |\Delta H|_{\max S}$ depend on the $B_Y$ IMF sign.

Taking this fact into account and analogously to *Watanabe and Iijima* [1996], Figure 2 presents the longitudinal distribution obtained by superposition of these field-aligned current systems for the northern and southern hemispheres depending on the IMF $B_Y$-component sign.

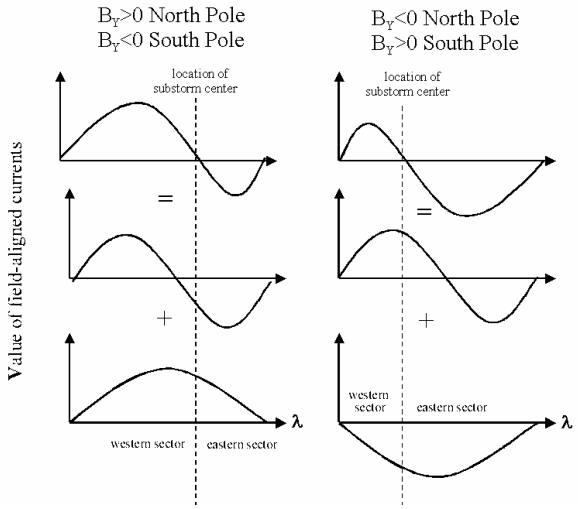


**Figure 2:** Longitudinal distribution of field-aligned currents in the SCW depending on the IMF $B_Y$-component

This evidence makes it possible to construct the full picture of substorm currents in their passage through the IMF sectoral structure in comparison with Figure 1. Figure 3 presents the generalized scheme taking into account the additional source, tail currents during a substorm and distribution of intensity of auroral electrojets of northern and southern hemispheres depending on the IMF azimuth component sign. The boundary of direction change of the field-aligned current is shown by the dashed line. On the level of the plasma sheet there is a part of a line connecting the substorm centers separated in space for the northern and southern hemispheres. A detailed experimental check is required of this circumstance that is not provided in the known substorm models.

## 3. Discussion

In the previous sections we demonstrated the effect of the IMF $B_Y$ component on the distribution of SCW-associated FACs (field-aligned currents), leading to both pre-midnight/post-midnight and northern hemisphere/southern hemisphere asymmetry in substorm development. We note, that the manner in which the northern/southern asymmetry matches the pre-midnight/post-midnight asymmetry in the present study differs from [*Danilov*, 1998; and *Shelementsov*, 1974], where the effect of the IMF $B_Y$ component on auroral magnetic activity also was treated. This inconsistency can be understood, because the geomagnetic indexes indicate Hall current behavior rather than that of magnetospheric FACs. This point makes ground-based distant diagnostics of FAC intensities to be preferred [*Sergeev* and *Tsyganenko*, 1980].

Further, let us take into account that the current generator governed by the IMF sectoral structure is located in the magnetopause in the dayside cusp region. In accordance with the distribution of ionospheric conductivity it provides the transfer of the electric field in polar caps. Hence one can estimate the ratio of amplitudes of the electric fields

$$E_M / E_E \approx (r-d) / (r+d)$$

in the morning and evening sectors of the ionosphere where $r$ is the polar cap radius and $d$ is the shift of cusp relatively the plane of the noon-midnight meridian. For the simplicity we neglect the shift of cusp on this plane and if it is shifted to the morning sector, we consider $d > 0$.

Because of the fact that at $B_Y > 0$ ($B_Y < 0$) according to *Newell et al*. [1995] the cusp is located in the evening (morning) sector in the northern (southern) hemisphere then the parameter used by us is $d < 0$ ($d > 0$). Consequently, we find $E_M / E_E > 1$ ($E_M / E_E < 1$) in the northern (southern) hemisphere which is in agreement with the results obtained by *Danilov* [1998] and *Shelomentsev* [1974].

Obviously the magnetospheric generator of current system additional to the SCW (Figure 3) which is governed by the IMF sectoral structure does not contrast to these facts established reliably. Defining the current direction from [*Krymsky,* 1994] one can conclude that at $B_Y > 0$ ($B_Y < 0$) it flows into (flows out of) the magnetosphere in the evening (morning) sector of the northern (southern) hemisphere and in this case the quantity of current equal to it flows out of (flows into) the magnetosphere in the morning (evening) sector of southern (northern) hemisphere. Naturally, it is necessary to check the assumed equality, for example, excluding the contributions from other possible sources of currents. Without going into details of this difficult task just now, a preliminary simplified determination of current direction is worth discussing.

The directions of field-aligned currents in dayside cusps are determined by their relationship of

$$J_{/\!/} \sim [\boldsymbol{V}\, \boldsymbol{B}_Y]_{\perp}$$

to the Lorentz force component perpendicular to the magnetosphere′s boundary. It is considered that it acts from the side of solar wind fixed in a magnetic field which flows around the magnetopause with different speeds $V$ in the regions of northern and southern cusps. In Figure 3 the current directions in cusps during the passage of IMF sectors different in sign are shown by arrows near the *N* and *S* poles.

The change of magnetospheric current direction (Figure 3) corresponds to the change of field-aligned current distributions in models of *Watanabe and Iijima* [1996], taking into account the IMF $B_Y$ effects. The definite consistency gives a possibility to discuss quantitative characteristics of dynamical association between distributions of field-aligned currents and branchings of the diamagnetic or inertial currents in the ionosphere – magnetosphere plasma and in the solar wind of the transient region. Using the relationships from [*Watanabe and Iijima*, 1996], for the full current flowing into the magnetosphere in one of the cusps and flowing out it in another one, we obtain the estimation

$$J \approx B_n\, d_j / \mu \approx 200\text{A},$$

where $B_n \approx 1$nT is the magnetic field perpendicular to the magnetopause in the region of the open magnetosphere, $d_j \approx 200$ km is a thickness of current sheet and $\mu = 4\pi \cdot 10^{-7}$ H/m – is the magnetic penetrability of vacuum. The order of value of the given estimation is considerably less than it is necessary to explain the influence of the

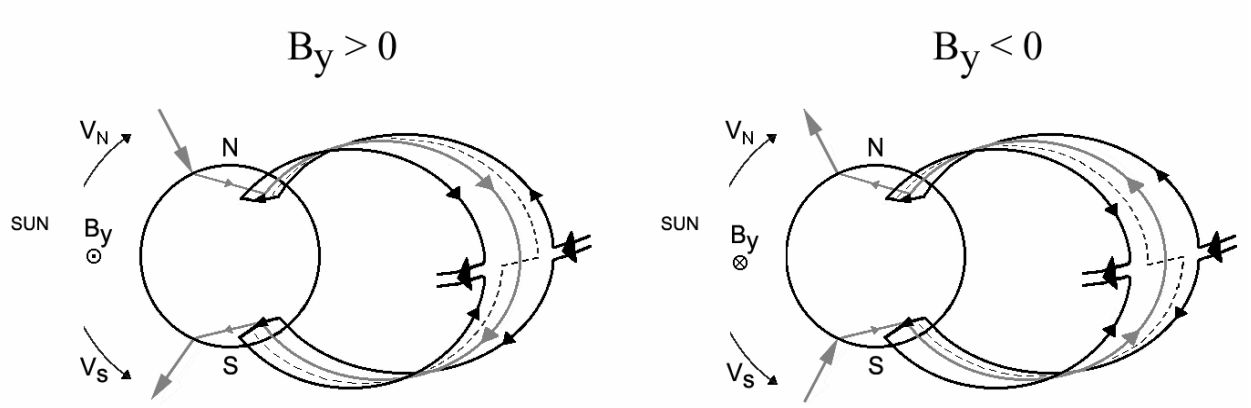


**Figure 3:** Current superposition from the passage of the IMF sectoral structure and substorm current wedge in the northern and southern hemispheres at different directions of the IMF azimuth component.

IMF $B_Y$ on SCW which contains the current $\geq 10^6$ A [*Semyenov and Sergeev*, 1979].

On the basis of generalized Ohm′s law one can consider the MHD-approach to the description of influence of the IMF $B_Y$ on the magnetospheric boundary layer. It is taken into account that in the cusp region the conductivity currents transverse to the magnetopause mainly flow in parallel to the intra-magnetospheric magnetic field. For the high-latitude region (mantle) let us estimate the upper limit

$$J_{//} < V B_Y d_V / R$$

of the value of full current $\approx 10^6$ A, where the values of velocity V ≈ 200 km/s, magnetic induction $B_Y \approx 10$ nT, thickness $d_V \approx 6 \cdot 10^3$ km of the shift flow [*Sckopke and Paschman*, 1978] and effective resistance $R = 10^{-2}$ Ohm are used.

In a calculation the value of $R \approx R_I$ is substituted into the right part of the inequality, i.e. comparable with the ionospheric resistance which was estimated for SCW by data of the work [*Semyenov and Sergeev*, 1979]. Note that similarly to the usual electric chain under the condition $R = R_I$ the limiting conductivity current in the mantle – ionosphere contour is equal to the self-charge current in value $\boldsymbol{J}_c = \boldsymbol{E} / \boldsymbol{R}$ in the electrostatic field of plasma flowing around the magnetopause.

$$\boldsymbol{E} \sim -[\boldsymbol{V}\, \boldsymbol{B}_Y]$$

Besides $\boldsymbol{J}_{\|} = \boldsymbol{J}_c$ it is known in this connection that their sum precisely coincides with the upper limit of the value of full current. With the account of these relationships we obtain $\boldsymbol{J}_{\|} \approx 0.5 * 10^6$ A.

Thus, on the assumption of the penetration of the IMF $B_Y$ into the mantle the estimation of conductivity current is near the value required for the explanation of their contribution into the substorm currents.

## 4. Conclusions.

1. The influence of the IMF $B_Y$–component on the substorm current wedge is determined by currents connected with the passage of the IMF sectoral structure.
2. During substorms the IMF sectoral structure adds the north-southern anti-symmetry to the morning-evening one in the distribution of field-aligned currents.
3. Asymmetric distributions of ionospheric and field-aligned currents of the substorm form the particular class of planetary – antisymmetric geomagnetic activity.

## References

Danilov, A. A., The north-southern asymmetry of geomagnetic activity, *Geomagn. Aeron*., *(in Russian)*, 39, 3, 39-46, 1998.

Kozlov, V. I. and P. F. Krymsky, Physical bases for the forecast of catastrophic geophysical phenomena, *Yakutsk: YaNTs SO RAN*, *(in Russian)*, 164, 1993.

Krymsky, P. F., Possible mechanism of the influence of solar wind on atmospheric and geophysical processes and the rotation of the Earth, *Preprint of IKFIA, 94-2(42). Yakutsk: YaNTs SO RAN*, *(in Russian)*, 64, 1994.

Leontyev, S. V. and W. B. Lyatsky, Electric field and currents connected with Y-component of interplanetary magnetic field, *Planet. Space Sci*., *22*, 811-819, 1974.

Lu, G., A. D. Richmond, B. A. Emery, P. H. Reiff, de la. Beaujardiere, F. J. Rich, W. F. Denig, H. W. Kroehl, L. R. Lyons, J. M. Ruohoniemi, E. Friss-Christensen, H. Opgenorth, M. A. L Person, R. P. Lepping, A. S. Rodger, T. Hughes, A. McEwin, S. Dennis, R. Morris, J. Burns, and L. Tomlinson, Interhemispheric asymmetry of the high-latitude ionospheric convection pattern, *J. Geophys. Res*., *99*, A4, 6491-6510, 1994.

McDiarmid, I. B., J. R. Burrows, M. D. Wilson, Large-scale magnetic field perturbations and particle measurements, *J. Geophys. Res*., *84*, 1431, 1979.

McPherron, R. L., C. T. Russell, M. P. Aubry, Satellite studies of magnetospheric substorm on August 15, 1968. 9. Phenomenological model for substorms, *J. Geophys. Res*., *78*, 16, 3131-314, 1973.

Newell, P. T., D. G. Sibeck, C. -I. Meng, Penetration of the interplanetary magnetic field $B_Y$ and magnetosheath plasma into the magnetosphere: implications for the predominant magnetopause merging site, *J. Geophys. Res*., *100*, A1, 235-243, 1995.

Plotnikov, I. Ya., The viscous flow in the boundary layer of the magnetosphere, *Geomagn. Aeron*., *(in Russian)*, *29*, 5, 843-846, 1989.

Plotnikov, I. Ya., Hydromagnetic model of the dayside cusp of the Earth´s magnetosphere, *Geomagn. Aeron., (in Russian)*, *36*, 3, 50-58, 1996.

Sckopke, N. and G. Paschman, The plasma mantle. A survey of magnetotail boundary layer observations, *J. Atmos. Terr. Phys*., *40*, 3, 261-278, 1978.

Semyenov, V. S. and V. A. Sergeev, The electric field and energy isolation during a substorm, *Geomagnetize Issledovaniya, M.: Sov. Radio*, *(in Russian)*, *26*, 49-61, 1979.

Sergeev, V. A., On the relationship of the field-aligned currents Birkeland´s system to the geometry of invasion of the auroral plasma, *Geomag. Res*. *(in Russian)*, *23*, 52-58, 1978.

Sergeev, V. A., On penetration of the IMF $B_Y$-component into the magnetotail, *Geomagn. Aeron., (in Russian)*, *27*, 4, 612-615, 1987.

Sergeev, V. A. and N. A. Tsyganenko, The Earth's magnetosphere, *Nauka*, *(in Russian)*, *175*, 1980.

Shelomentsev, V. V., Modulation of auroral electrojets, Issled. *Geomagn. Aaeron Fiz. Solntsa, (in Russian)*, *30*, 95-106, 1974.

Sonnerup, B. U. O., Theory of the low-latitude boundary layer, *J. Geophys. Res*., *85*, A5, 2017-2035, 1980.

Velichko, V. A., R. N. Boroyev, M. G. Gelberg, Azimuthal asymmetry of the regions of field-aligned currents flowing in to and out of the ionosphere in the substorm current wedge, *Geomagn. Aeron*., *42*, 5, 588-592, 2002*a*.

Velichko, V. A., R. N. Boroyev, M. G. Gelberg, D. G. Baishev, J. V. Olson, R. J. Morris, K. Yumoto, North-south asymmetry of the substorm intensity depending on the IMF $B_Y$–component, *Earth Planets Space*, *54*, 10, 955-961, 2002*b*.

Watanabe, M. and T. Iijima, Synthesis models of dayside field-aligned currents for strong interplanetary magnetic field $B_Y$, *J. Geophys. Res*., *101*, A6, 13,303-13,319, 1996.

Weimer, D. R., Maps of ionospheric field-aligned currents as a function of the interplanetary magnetic field derived from Dynamics Explorer 2 data, *J. Geophys. Res*, *106*, 7, 12,889-12,902, 2001.

# Field-aligned currents in the ionosphere and magnetosphere

Yu. P. Maltsev, and A. A. Ostapenko

Polar Geophysical Institute, Apatity, Russia

**Abstract**. Based on magnetic data of the Dynamics Explorer 2 satellite we defined field-aligned current distribution above the ionosphere as a function of geomagnetic activity and solar wind parameters. We found that the Region 1, 2, and 0 currents exist permanently. Their intensity grows and the latitude falls with the enhancement of the southward IMF and solar wind dynamic pressure. We also used the database by *Fairfield et al.* [1994] to study the magnetospheric partial ring current closed to the Region 2 field-aligned currents. Maximuma of the Region 2 FACs at $z = 3R_E$ are located at ~05 and 16 LT at radial distances of ~$5R_E$, the location being practically independent of geomagnetic activity.

## 1. Introduction

Large-scale sunward magnetospheric convection generates the magnetosphere-ionosphere electric current system shown schematically in Figure 1. The system consists of three parts:

1) Region 1 field-aligned currents (FACs) connected with the centers of the convection vortices in the ionosphere,
2) Region 2 field-aligned currents closed to the partial ring current arising due to polarization of the drifting plasma, and
3) Region 0 currents located inside of region 1.

The Region 1 current flows into the ionosphere at dawn and flows out at dusk. The Region 2 and 0 currents have the opposite direction. The Region 1 and 2 FACs were predicted by [*Schield et al*., 1969; *Jaggi and Wolf*, 1973; *Lyatsky et al*., 1974] and experimentally obtained by *Iijima and Potemra* [1976*a*]. The Region 0 FACs found by *Iijima and Potemra* [1976*b*] may be caused by an antisunward convection caused in the polar cap by the quasi-viscous interaction of the solar wind with the magnetotail lobes [*Lyatsky et al*., 1985].

Statistical investigations of FACs are not numerous. *Iijima and Potemra* [1976*a*] studied them at the altitude of 1000 km for two ranges of the *AL* index. *Mishin et al*. [2001, 2003], applying the magnetogram inversion technique, used ground observations to obtain the characteristics (FACs and electric potential) of a statistical substorm. Region-1 FACs in the magnetotail were examined by *Tsyganenko et al*. [1993].

In this paper we statistically study the field-aligned currents over the ionosphere and in the distant magnetosphere under various geophysical conditions.

## 2. Field-aligned currents above the ionosphere

We used data of the Dynamic Explorer-2 satellite obtained from August, 1981 to February, 1983. DE-2 was launched into a polar orbit, 300–1000 km altitude, and measured three magnetic components with half-second resolution. Data supplied by the model inner field and values of invariant latitudes calculated below 84° are taken from the CD-ROM-NSSDC. The horizontal magnetic disturbance determined as a difference between the measured and model fields was averaged in spatial bins with the size of 1 degree of invariant latitude and 2 hours of MLT. Magnetic field lines in high latitudes are almost vertical, so that the FAC density can be calculated from the following equation

$$j_z = \frac{1}{\mu_o}\left(\frac{\partial B_y}{\partial x} - \frac{\partial B_x}{\partial y}\right),$$

where the *y* axis is directed eastward, and the *z* axis is downward.

Figure 2 shows the distribution of $B_y$ and $j_z$ for two ranges of the *AL* index considered earlier by *Iijima and Potemra* [1976a]. The maximum magnetic disturbances achieve values of ~100 nT and ~400 nT for the average $AL = -42$ nT and $AL = -313$ nT, respectively. Thus the ground disturbance is smaller than the disturbance above the ionosphere. The maximum FAC density is ~0.2 and 0.4 A/km$^2$, respectively.

One can see three regions of FACs. Averaging over the whole observation period yields the total FAC intensities $I_1 = 0.75$ MA, $I_2 = 0.62$ MA, $I_0 = 0.054$ MA. The latitudes of the maximum FAC surface density are $\Lambda_1 = 74°$, $\Lambda_2 = 61°$, $\Lambda_0 = 76°$. The average geophysical parameters are *Dst* = -24 nT, *AL* = -180 nT, *Kp* = 2.9, $B_z$ IMF = 0, $P_{sw} = 3.3$ nPa. Enhancement of the geomagnetic activity gives rise to a growth in intensity of the Region-1 and -2 FACs and to their equatorward shift.

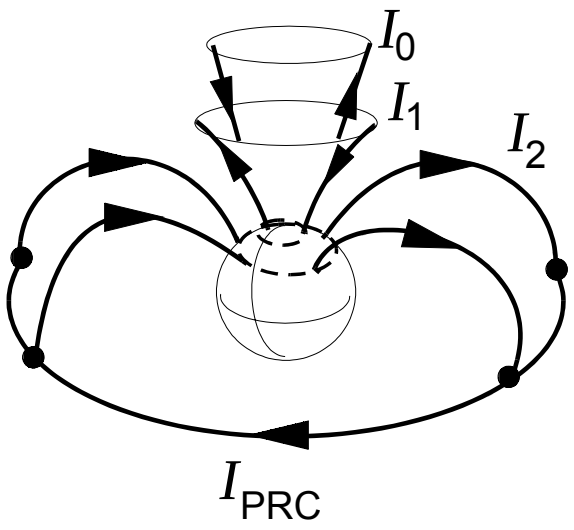


**Figure 1**: The field-aligned currents of Region 0 ($I_0$), Region 1 ($I_1$), and Region 2 ($I_2$) as well as the partial ring current $I_{PRC}$ closed to the Region 2 currents.

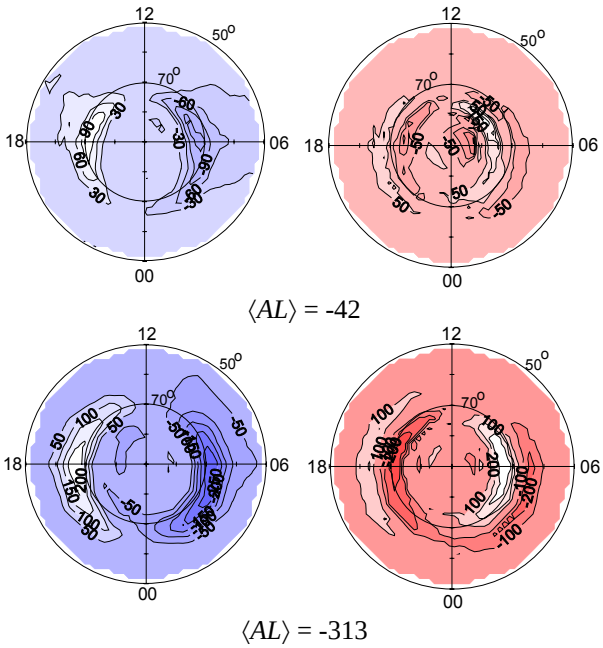


**Figure 2**: Spatial distribution of (left) azimuthal magnetic disturbances in nT and (right) field-aligned currents in mA/km$^2$ for (top) $|AL| < 100$ and (bottom) $|AL| > 100$. The downward currents are shown by white; the upward currents are shadowed.

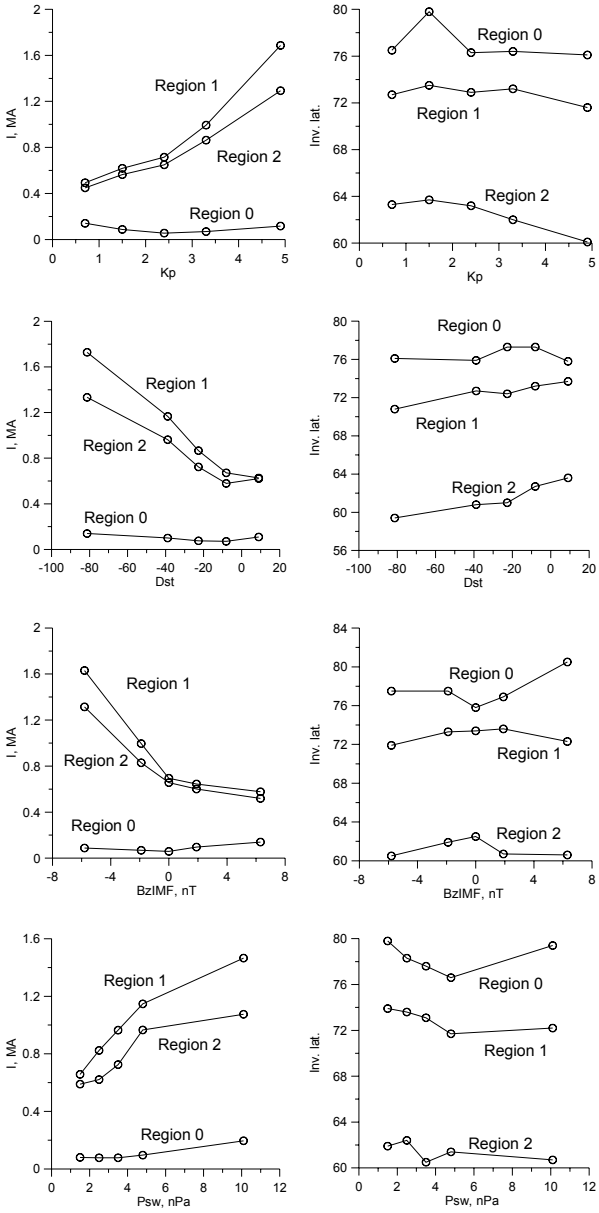


**Figure 3:** Effect of various geophysical parameters on (left) the total electric current and latitude of different FAC regions.

To study the behavior of the FACs we divided the data set into five subsets differing by one of the geophysical parameters such as *Kp*, *Dst* indices, the solar wind dynamic pressure, and $B_z$ IMF. The spatial distribution of FAC density was obtained for each of subset. We calculated the total electric current in each region as well as the average latitude where the surface current density is a maximum. Results are shown in Figure 3. One can see that the Region 1 and 2 currents grow with increasing activity. Region 0 current grows monotonically only

with the solar wind dynamic pressure. The latitudes of Region 1 and 2 currents decrease with rising activity.

Since there is a correlation between geophysical parameters, we found the following three-parameter dependence for the total current intensity in each region

$$I_1 = (32 - 1.0\,Dst - 10\,B_s\text{IMF} + 8.3\,P_{sw})/100 \quad (1)$$
$$I_2 = (38 - 0.64\,Dst - 8.5\,B_s\text{IMF} + 5.2\,P_{sw})/100 \quad (2)$$
$$I_0 = (3 - 0.047\,Dst - 0.36\,B_s\text{IMF} + 1.5\,P_{sw})/100, \quad (3)$$

where $I_k$ are expressed in MA, $P_{sw}$ in nPa, and $Dst$ and $B_s$IMF in nT. The relative residual error of the fitting is 7% for Region 1, 8% for Region 2, and 21% for Region 0. Here $B_s$IMF is the IMF southward component ($B_s = 0$ for $B_z > 0$ and $B_s = B_z$ for $B_z < 0$).

### 3. Field-aligned currents in the magnetosphere

The database of *Fairfield et al.* [1994] contains about 70,000 three-component magnetic field measurements obtained from 11 satellites at distances from 3 to 60$R_E$ during 20 years. All data are supplied with $Dst$ indices. About 60% of data are supplied with the hourly solar wind parameters. We studied Region 2 FACs only. The data in the layer of $|z_{SM}| < 4R_E$ were utilized. We divided the whole data array into five ranges of $Dst$, five ranges of $B_z$IMF, and five ranges of solar wind dynamic pressure $P_{sw}$.

For each subset the electric current surface density inside the layer of width of ±3 $R_E$ near the equatorial plane was calculated from the following formula

$$J_\perp = \int_{-z_0}^{z_0} j_\perp dz = \frac{1}{\mu_0}\oint [B \times dl]. \quad (4)$$

As an integration contour we adopt a rectangle with a vertical side of $-z_0 < z < z_0$ where $z_0 = 3R_E$ and with the horizontal size of $1R_E$. The external magnetic field was computed as a running average in bins with horizontal sizes of $3R_E$. The vertical size of averaging was $2R_E < |z| < 4R_E$ for the horizontal magnetic components ($B_x$ and $B_y$) and $-3R_E < z < 3R_E$ for the vertical magnetic component $B_z$. North-south symmetry was assumed.

The left panel of Figure 4 shows the distribution of the azimuthal electric current flowing in the layer $-3R_E < z_{SM} < 3R_E$ averaged for the whole data array. The average geophysical parameters are $Dst = -16$ nT, $AL = -118$ nT, $Kp = 2.2$, $B_z\text{IMF} = 0$, $P_{sw} = 2.2$ nPa. Strong day-night asymmetry is evident; the nightside current density is several times greater than the dayside one. Current is a maximum at $L \approx 6$–8 near midnight. The currents grow with the enhancement of the storm time activity, southward IMF, and solar wind dynamic pressure. There is no pronounced dependence of the maximum position on geomagnetic activity. The radial component of the electric current is small as compared to the azimuthal one.

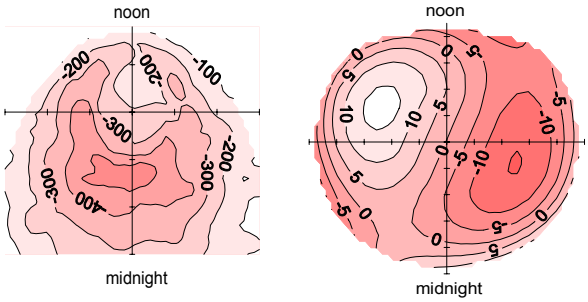


**Figure 4**: Distribution of azimuthal (left) and field-aligned (right) currents in the magnetosphere under average conditions. The transverse current is expressed in kA/$R_E$, the field-aligned current is in kA/$R_E^2$. The FAC flowing into the ionosphere is shown by white; the FAC flowing out is shaded.

The day-night asymmetry of the magnetospheric current means that a part of the current deviates to field-aligned current for which a density can be calculated as follows:

$$j_z(z=3) = -\frac{1}{2} divJ_\perp = -\frac{1}{2}\left(\frac{\partial J_x}{\partial x} + \frac{\partial J_y}{\partial y}\right), \quad (5)$$

where the coefficient 1/2 is due to FACs flowing in both northern and southern hemispheres. Unfortunately, the direct calculation of $j_z$ from experimental $J_x$ and $J_y$ fails due to a large scattering of the data. So we preliminarily approximated $J_x$ and $J_y$ by polynomials of the fourth order of $x$ and $y$ in the disk of $4R_E < (x^2 + y^2)^{1/2} < 10R_E$. The relative residual error of the fitting varied from 2% to 24% in different subsets. Then FACs were calculated using expression (5). The right panel of Figure 4 shows the distribution of $j_z$ averaged for the whole data array. One can see that the FACs flow out from the magnetospheric current sheet in the dusk and flow into the sheet in the dawn. At the ionosphere level the FACs flow correspondingly into the ionosphere in the dusk and flow out in the dawn, i.e. they behave as region 2 currents. The maximums of the Region 2 FACs are located at ~05 and ~16 LT at radial distances of ~5$R_E$. We did not find any pronounced dependence of the FAC maximum location on geophysical activity.

Dependence of the total FAC on various parameters is shown in Figure 5 (on the left). The dependence on $P_{sw}$ is almost linear. The dependence on $Dst$ is not monotonic and reveals a minimum at $Dst \approx -10$ nT. The dependence on $B_z$IMF also reveals a very deep minimum at $B_z\text{IMF} \approx 0$. Similar minima are seen in Figure 5 (on the

right) showing the dependence of $P_{sw}$ on *Dst* and $B_z$IMF. Since the FAC depends on both *Dst* and $P_{sw}$, and these values are statistically related we found the three-parameter dependence $I_2$ (*Dst*, $B_z$IMF, $P_{sw}$) by the least square technique. The following expression is obtained

$$I_2 = (13 - 1.1\ Dst - 7.5\ B_s\text{IMF} + 27\ P_{sw})/100. \qquad (6)$$

The relative residual error of the fit is 3.6%.

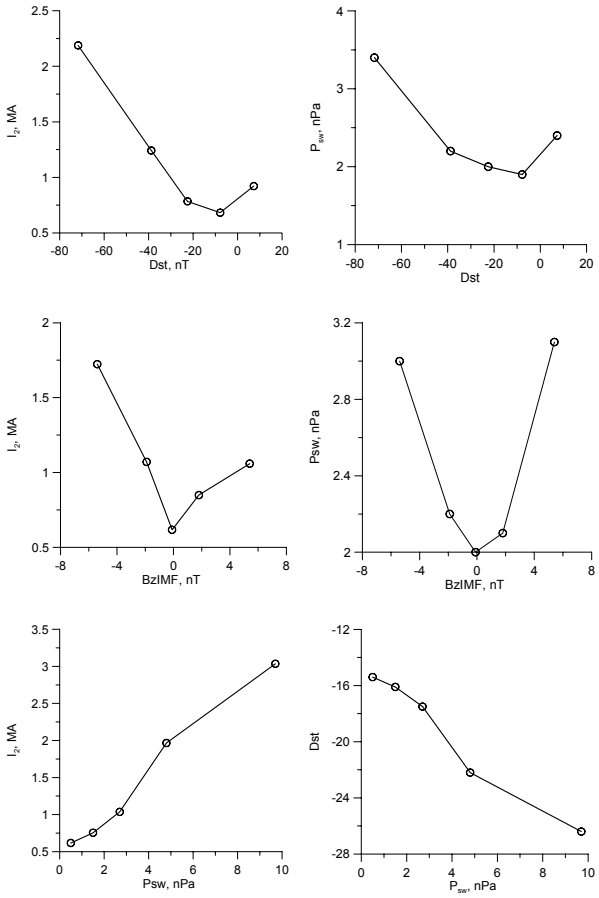


**Figure 5:** Left: dependence of Region 2 FAC in the magnetosphere on some geophysical parameters. Right: relations between the geophysical parameters.

## 4. Discussion

As seen from Figure 3 (on the left) and expressions (1) and (2), the Region 1 and 2 currents grow with rising geomagnetic activity. Dependence of the Region 0 current on geomagnetic indices and $B_z$ IMF is more complicated. *Iijima and Potemra* [1976b] supposed that these FACs exist during northward IMF. Our results agree with those of *Mishin et al.* [2003] who found that the Region 0 FACs exist under any type of activity. According to (3), the Region 0 FAC is mainly controlled by the solar wind dynamic pressure.

Magnetospheric and ionospheric data yield the same locations for Region 2 FACs. As seen in Figure 3 (on the right), the latitude under average conditions is ~61°. The right panel of Figure 4 shows the maximum of the FAC at $L = 5R_E$. Dependence of Region 2 FAC intensity as derived from two databases of various geophysical parameters is also rather similar. The FAC obtained from the magnetospheric data is somewhat larger and its dependence on solar wind dynamic pressure is more pronounced. It is possible that the fourth order of the polynomial is insufficient for approximation of the magnetospheric current in the $-3R_E < z < 3R_E$ sheet.

The asymmetric current distribution shown in Figure 4 (on the left) is in agreement with observations of *Iijima et al*. [1990] who found that the nightside ring current is 2–3 times larger than the dayside one. Energetic particle measurements [*Daglis et al*., 1999; *Greenspan and Hamilton*, 2000; *Turner et al*., 2001] also reveal the strong day-night asymmetry of the ring current. Moreover, *Greenspan and Hamilton* [2000] revealed no essential correlation between *Dst* and the dayside ring current.

The magnetic field model by *Tsyganenko* [1996] predicts an almost symmetric ring current. The last model by *Tsyganenko* [2002*a*,*b*] yields a strong day-night asymmetry. We calculated the FAC intensity from the *Tsyganenko* [2002*a*,*b*] model using the same method as that utilized for building Figures 4 and 5. We obtained the following approximation for the Region 2 FAC intensity $I_2 = -0.44 + 0.34\ P_{sw} - 0.025\ B_s\text{IMF} - 0.013\ Dst$, which is rather close to our expression (6). In contrast to the *Tsyganenko* [2002*a*,*b*] model, our calculations did not find any growth of dawn-dusk asymmetry in the partial ring current with increasing geomagnetic activity.

## 5. Conclusions

Three regions of FAC exist permanently above the ionosphere. The latitudes of the maximum FAC surface density averaged from August, 1981 till February, 1983 are $\Lambda_1 = 74°$, $\Lambda_2 = 61°$, $\Lambda_0 = 76°$. The Region-1 and -2 FAC intensity and latitude are controlled both by the IMF southward component and solar wind dynamic pressure. The Region-0 current is affected predominantly by the solar wind dynamic pressure. The processing of magnetospheric measurements over 20 years revealed the maxima of the Region 2 FACs to be located at ~05 and ~16 LT at radial distances of ~$5R_E$, the location was practically independent of geomagnetic activity.

**Acknowledgments** This work was supported by the Russian Basic Research Foundation (grant 03-05-65379) and by the Division of Physical Sciences of the Russian Academy of Sciences (program DPS-16). The Dynamics Explorer-2 as well as solar wind and IMF data have been taken from NSSDC CD-ROMs. We are obliged to J. King and N. Papitashvili for providing us with the data.

**References**


De Michelis, P., I. A. Daglis, and G. Consolini, An average image of proton plasma pressure and of current systems in the equatorial plane derived from AMTE/CCE-CHEM measurements, *J. Geophys. Res*., *104*, No A12, 28,615-28,624, 1999.

Fairfield, D. H., N. A. Tsyganenko, A. V. Usmanov, and M. V. Malkov, A large magnetosphere magnetic field database, *J. Geophys. Res.*, *99*, No A6, 11,319-11,326, 1994.

Greenspan, M. E., and D. C. Hamilton, A test of the Dessler-Parker-Sckopke relation during magnetic storms, *J. Geophys. Res*., *105*, No A3, 5419-5430, 2000.

Iijima, T., and T. A. Potemra, The amplitude distribution of field-aligned currents at northern high latitudes observed by TRIAD, *J. Geophys. Res.*, *81*, 2165-2174, 1976a.

Iijima, T., and T. A. Potemra, Field-aligned currents in the dayside cusp observed by TRIAD, *J. Geophys. Res.*, *81*, 5971-5979, 1976.

Iijima, T., T. A. Potemra, and L. J. Zanetti, Large-scale characteristics of magnetospheric equatorial currents, *J. Geophys. Res.*, *95*, No A2, 991-999, 1990.

Jaggi, R. V., and R. A. Wolf, Self-consistent calculation of the motion of a sheet of ions in the magnetosphere, *J. Geophys. Res*., *78*, No 16, 2852-2866, 1973.

Lyatsky, W. B., Y. P. Maltsev, and S. V. Leontyev, Three-dimensional current system in the different phases of a substorm, *Planet. Space Sci., 22*, No 8, 1231-1247, 1974.

Lyatsky, W. B., B. V. Rezhenov, and Y. P. Maltsev, Ionospheric convection caused by quasi-viscous interaction of the solar wind with magnetosphere (in Russian), *Geomagnetism and Aeronomy*, *25* (4), 566-570, 1985.

Mishin, V. M., T. I. Saifudinova, A. D. Bazarzhapov, C. T. Russell, W. Baumjohann, R. Nakamura, and M. Kubyshkina, Two distinct substorm onsets, *J. Geophys. Res.*, *106*, 13,105-13,118, 2001.

Mishin, V. M., V. V. Mishin, D. Sh. Shirapov, V. P. Golovkov, and M Förster, Electric field and field-aligned currents of Region 1 and Region 0 generators during the substorm load phase, this issue, 2003.

Schield, M. A., J. W. Freeman, and A. J. Dessler, A source for field-aligned currents at auroral latitudes, *J. Geophys. Res.*, *74*, No 1, 247, 1969.

Turner, N. E., D. N. Baker, T. I. Pulkkinen, J. L. Roeder, J. F. Fennell, and V. K. Jordanova, Energy content in the storm time ring current, *J. Geophys. Res*., *106*, No A9, 19,149-19,156, 2001.

Tsyganenko, N. A., Effects of the solar wind conditions on the global magnetospheric configuration as deduced from data-based field models, *Proc. of the Third International Conference on Substorms (ICS-3)*, ESA SP-389, pp. 181-185, Versailles, France, 1996.

Tsyganenko, N. A., A model of the near magnetosphere with a dawn-dusk asymmetry, 1, Mathematical structure, *J. Geophys. Res*., *107*, No A8, 10.1029/2001JA000219, 2002a.

Tsyganenko, N. A., A model of the near magnetosphere with a dawn-dusk asymmetry, 2, Parameterization and fitting to observations, *J. Geophys. Res.*, *107*, No A8, 10.1029/2001JA000220, 2002b.

Tsyganenko, N. A., D. P. Stern, and Z. Kaymaz, Birkeland currents in the plasma sheet, *J. Geophys. Res*., *98*, No A11, 19,455-19,464, 1993.


---

Y. P. Maltsev and A. A. Ostapenko, Polar Geophysical Institute, Apatity, Murmansk region, 184209, 14 Fersman Str., Russia. (maltsev@pgi.kolasc.net.ru; ostap@pgi.kolasc.net.ru)

# Numerical modeling of magnetospheric Pc 1 emissions modulated by Pc 3–4 waves

A. G. Demekhov[1], S. V. Isaev[2], and V. Y. Trakhtengerts[1]

[1] Institute of Applied Physics, Nizhny Novgorod, Russia
[2] Radiophysical Research Institute, Nizhny Novgorod, Russia

**Abstract.** We study the joint influence of intrinsic feedback and external modulation (by Pc3/4 oscillations) on the formation of dynamic spectra of Pc 1 emissions in the Earth's magnetosphere using the self-consistent model known as Alfven sweep maser, which takes into account the nonlinear coupling between the magnetospheric and ionospheric resonators for Alfven ion-cyclotron waves. We consider the cases of antisymmetric and symmetric spatial structure of the hydromagnetic oscillations with respect to the geomagnetic equator. We think that the modulation by Pc3/4 waves is unlikely to be the dominant mechanism for formation of Pc 1 pearls, since it is very sensitive to the mismatch between the modulation period and the intrinsic period of the system, related to the propagation of wave packet between the reflection points. Moreover, the external modulation alone leads to unrealistically narrow spectrum of Pc 1 pulsations. However, it can speed up significantly the development of the dynamic regime related to the magnetosphere-ionosphere interaction.

## 1. Introduction

Despite many years of studies of magnetospheric Pc 1 pearl emissions, a detailed theory describing formation of their spectral forms is still absent. Even the basic question concerning the influence of the ionospheric reflection on Pc 1 generation remains open and causes controversial opinions. At present, there is a great interest to this problem [e.g., *Trakhtengerts et al*., 2000; *Prikner et al*., 2000; *Demekhov et al*., 2000; *Mursula et al*., 2001]), because much more precise and detailed ground-based and satellite data about Pc 1 waves as well as precipitation of energetic particles have been accumulated recently. The conventional scheme of Pc 1 formation is based on the concept of bouncing Alfven-wave packets which are amplified near the equatorial plane due to the cyclotron resonant interaction with energetic protons and loose part of their energy due to refraction and nonideal reflection from the ionosphere (Figure 1). A detailed study of this concept was performed by *Gendrin et al*. [1971].

[*Polyakov et al*., 1983] introduced into this scheme the magnetosphere-ionosphere (M-I) feedback related to the influence of precipitated energetic protons on the ionospheric reflection. This model called Alfven sweep maser (ASM) explains formation of a single Pc 1 wave packet oscillating between the reflection points. Analytical studies of this model [*Belyaev et al*., 1987; *Trakhtengerts et al*., 2000] have been confirmed by numerical simulations [*Demekhov et al*., 2002*a*], which showed that pearl-type pulsations are formed in the ASM model even if the reflective properties of conjugate parts of ionosphere are strongly different and vary in time.

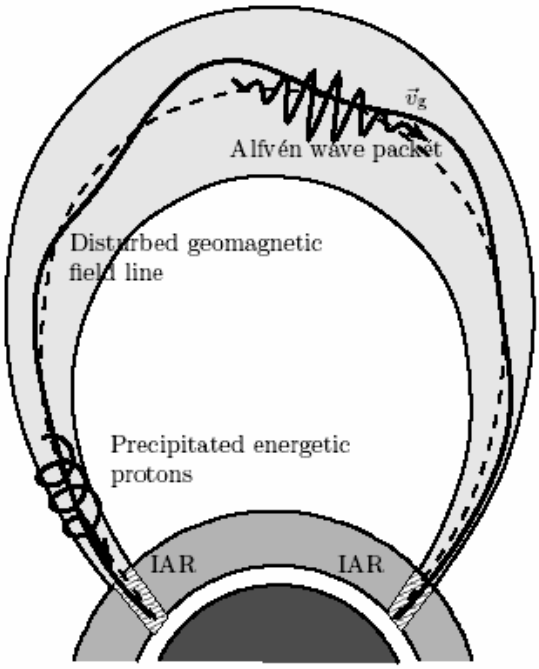


**Figure 1.** Qualitative model of Pc 1 generation.

Some new satellite and ground-based observations [*Mursula et al*., 2001] are interpreted in terms of an alternative scheme in which the ionospheric reflection does not play a significant role in wave generation. This scheme attributes formation of Pc 1 pearl elements only to the external modulation of the growth rate by large-period (Pc 3–4) hydromagnetic waves.

First numerical results for Pc 1 modulation by Pc 3/4 were presented by *Demekhov et al*. [2002*a*], who assumed the fundamental eigenmode of _field-line oscillations. *Demekhov et al*. [2002*b*] extended the study to the case of higher modes, which can have larger compressional components in the equatorial plane. In both of those papers, the pure influence of the modulation was studied, i.e., the ionospheric reflection was assumed constant and independent of frequency. Here, we compare how the Alfven maser operates in the following cases:

1. the magnetosphere/ionosphere feedback is present, and an external growthrate modulation is absent;
2. the magnetosphere/ionosphere feedback is absent but the growth rate is modulated by an external factor;
3. the effects of resonant ionospheric reflection and external modulation are combined in the presence of the diurnal variation in the properties of the ionospheres.

## 2. Basic equations

### 2.1. Original ASM model

Our basic model is the same as used by *Belyaev et al*. [1987]; *Demekhov et al*. [2002*a*]. It is based on the quasilinear plasma theory. The wave energy transfer is described by the equation

$$\frac{\partial \varepsilon_\omega^\pm}{\partial t} \pm v_g \frac{\partial \varepsilon_\omega^\pm}{\partial z} = N\gamma(\omega, z, t)\varepsilon_\omega^\pm + a_\omega \qquad (1)$$

Here, $\varepsilon_\omega^\pm$ is the spectral energy density of ion-cyclotron waves propagating in $\pm z$ directions, $z \in [-l, l]$ is the coordinate along the magnetic field, $v_g$ is the Alfven wave group velocity, $a_\omega$ is the background source of Alfven waves, the function $\gamma(\omega, z, t)$ describes the frequency and space dependence of the growth rate, as well as its temporal evolution due to the external modulation, and $N$ is the number of energetic protons in a magnetic flux tube with the unit cross-section at the ionospheric level. The evolution of energetic protons is described using the balance approximation valid for the weak pitch-angle diffusion [*Bespalov and Trakhtengerts*, 1986]:

$$\frac{dN}{dt} = -\left(S^+ + S^-\right) + J - \frac{N}{T_N} \qquad (2)$$

where $S^\pm$ are the fluxes of energetic protons precipitated into the conjugate ionospheres, $J(t)$ is the source of energetic-protons, and $T_N$ is their loss time due to the pair processes (mostly charge exchange). The precipitated fluxes are determined by the relation.

$$S_z = DN \int \phi(\omega, z)\varepsilon_\omega^\pm \, dz \, d\omega \qquad (3)$$

where $D$ is the known coefficient providing the energy conservation for wave-particle interactions. Reflection of waves from the ionosphere is described by the boundary conditions

$$\varepsilon_\omega^\pm(\mp l) = R_\mp \varepsilon_\omega^\mp(\mp l) \qquad (4)$$

where $R_\mp$ is the reflection coefficient from the ionosphere at $z = \mp l$. The ionospheric reflection depends on the electron density profile, which can vary in time due to any change in the background ionization or loss rates and is modified by the energetic proton precipitation. The latter factor influences mainly the E-layer, since the proton energy is several tens of keV. Therefore, we need the ionization balance equation for the E-layer:

$$\frac{dn_\pm}{dt} = \eta\left(S_O^\pm + S^\pm\right) - \chi n_\pm^2 \qquad (5)$$

where $n_\mp$ are electron plasma densities in the conjugate ionospheres, $\chi$ is the recombination coefficient, $\eta$ is the ionization efficiency, and $\eta S_{O\pm}$ is the background ionization rate.

### 2.2. Influence of the modulation

We take into account the influence of a hydromagnetic Pc 3/4 oscillation by adding external modulation of the Pc 1-wave growth rate. To model the finite spectral width of the Pc 3/4 pulsations, we can assume that several harmonic components with close frequencies are present. In this case, the growth-rate function can be represented in the form

$$\gamma(\omega, z, t) = \gamma_O(\omega, z)\left[1 + \varphi(z)\sum_{i=1}^{m}\delta_i \sin\left(\Omega_h^i t\right)\right] \quad (6)$$

where $\Omega_h^i$ are the frequencies of the spectral components and $\delta_i$ are weight coefficients satisfying the normalization condition $\delta = \sum_{i=1}^{m}\delta_i$, $\delta$ has the meaning of the effective modulation depth, and $\varphi(z)$ is the spatial profile of the modulation function, which is assumed to be constant.

### 3. Results of numerical modeling

3.1. M-I interaction; no external modulation

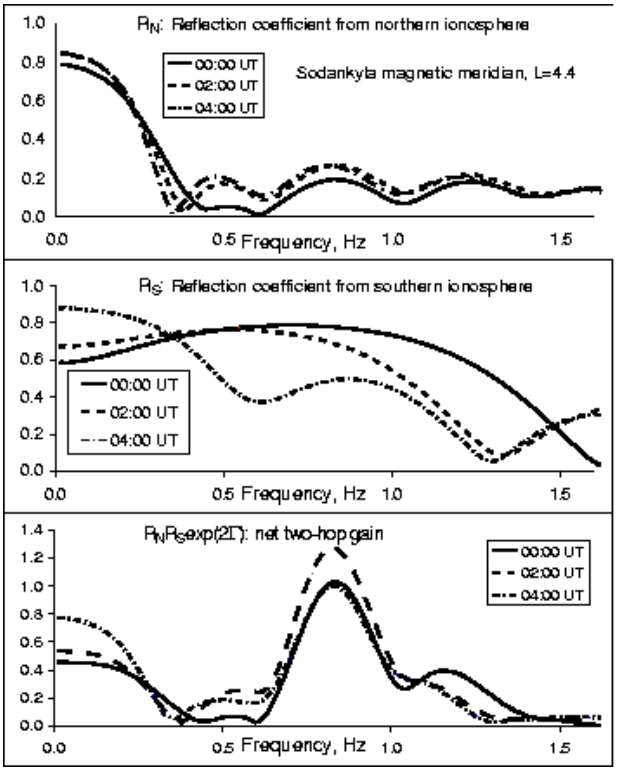


**Figure 2.** Reflection coefficients of conjugate ionospheres for June 06, 1999 at $L$ = 4.4, Sodankylä magnetic meridian, calculated using the IRI profile (upper and middle panels), and total two-hop gain of Pc 1 waves (bottom panel), calculated using the bi-Maxwellian hot protons with the mean parallel energy $W_0$ = 100 keV, the anisotropy $W_\perp = W_0$ = 1.3, geomagnetic shell $L$ = 4.4, and cold plasma density $N_c$ = 100 cm$^{-3}$.

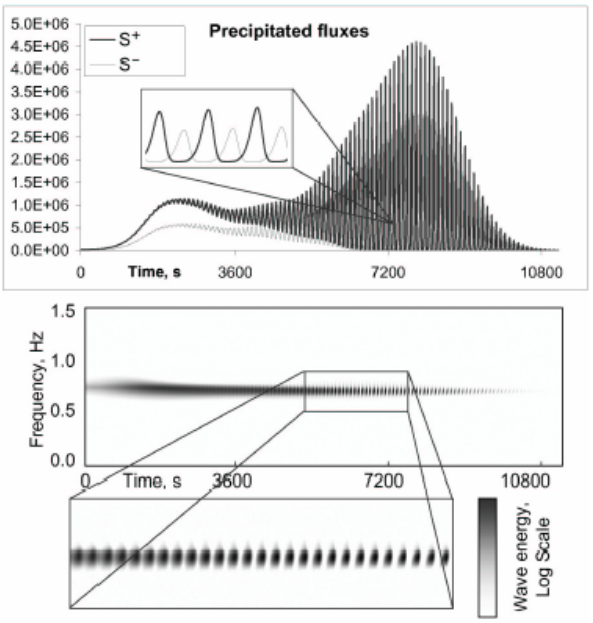


**Figure 3.** Precipitated fluxes of energetic particles (upper panel) and dynamic spectrum of Pc 1 waves, obtained in the simulation with the reflection coefficients and total gain shown in Figure 2.

First we consider the case for which the ionospheric reflection coefficients are calculated using the program based on the code by A. A. Ostapenko [*Ostapenko and Polyakov*, 1990].

The ionospheric parameters are specified using the IRI model; particular case presented here corresponds to the geomagnetic meridian of Sodankylä and $L$ = 4.4, for June 22, 1999. The date near solstice is chosen intentionally, to simulate the conditions when the difference between the conjugate ionospheres can be most pronounced. This is seen in Figure 2, where the reflection coefficients are shown. The nonlinearity of the ionospheric reflection was chosen in the simplest parametric way consistently with calculations by *Ostapenko and Polyakov* [1990]. Specifically, we use the shift of the $R_\pm(f)$ profile along the frequency axis with the rate $df_m/dn_+ = -10^{-6}$ and $df_m/dn_- = -0.9 \cdot 10^{-6}$.

As a result we can see the following. First of all, a single wave packet with stable frequency drift is formed. This is indicated by the antiphase variation of the precipitated particle fluxes in conjugate hemispheres. The pearl-type pulsation can appear even if the reflective properties of conjugate parts of ionosphere are strongly different (Figure 2). The time scales of pearl formation and diurnal variation are close to each other. The formation of pearl-type pulsation takes place if the

condition $R_+R_- \exp(2\Gamma) > 1$ is realized and doesn't occur in the opposite case, where $R_+$ and $R_-$ are the reflection coefficients and $\Gamma = \int (\gamma / v_g) dz$ is the Alfvén-wave one-hop amplification. The pearl-type pulsation can be generated even if the reflection from the ionosphere is rather low.

3.2. External modulation; no M-I interaction

In this section, we neglect the presence of the ionospheric Alfven resonator and consider the model where reflection coefficients are independent of frequency, daytime and electron density of ionospheres, $R_\pm = 0.3$. It allows us to study the pure influence of the modulation on the processes in the Alfvén maser and, therefore, to consider this influence as an alternative mechanism of pearl formation. The active proton concentration in the magnetic flux tube is chosen according to the condition

$$R_+R_- \exp(2\Gamma(\omega_m)) = 1 \qquad (7)$$

where $\omega_m$ is the frequency of the maximum amplification. It is important to consider the cases of the asymmetric and symmetric spatial structure of the modulation with respect to the geomagnetic equator. Indeed, the asymmetric modulation represents the field-line resonance harmonic, which has zero compressional component at the equator, while a symmetric disturbance corresponds to the maximum compressional component in the equatorial plane. According to *Woch et al*. [1990], both types of ULF pulsations are observed by geosynchronous satellites, so their influence on the Pc 1 generation should be studied.

The case of antisymmmetric modulation was considered in detail by [*Demekhov et al*., 2002*a*]. Here, we show only one example of simulation (Figure 4), which indicates the main properties of the solution. First of all, the temporal behavior of the precipitated fluxes demonstrates the formation of the single wave packet, similar to the case where the magnetosphere-ionosphere interaction is taken into account. However, the resulting wave spectrum is seen to be extremely narrow in the case of pure external modulation. Moreover, the influence of the modulation is rather weak, which is related to the absence of the compressional component at the equator. i.e., at the region of the largest cyclotron amplification. A considerable effect is obtained if the Pc4 ULF pulsation has the extraordinary large amplitude of about 50–100 nT. Simulations which we do not present here for brevity could demonstrate that this influence is very sensitive to the mismatch between the

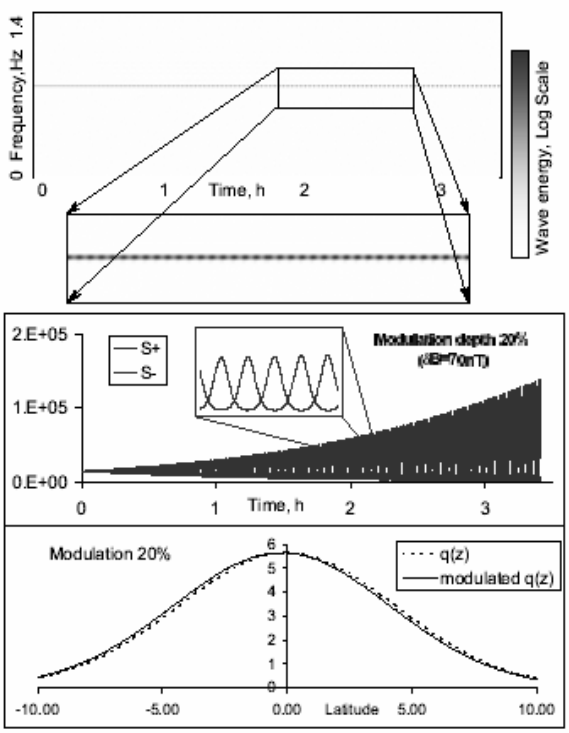


**Figure 4.** Alfvén maser modulated by an antisymmetric monochromatic disturbance. Here, $R_+ = R_- = 0.3$, and the magnetospheric parameters correspond to those in Figure 2. Upper, middle, and lower panels show the dynamic frequency spectrum, precipitated proton fluxes and the cyclotron interaction efficiency $q(z)$, which represents the *z*-dependence of the growth rate $\gamma$.

modulation period and the period of Pc 1 wave bouncing. Numerical results for the symmetric modulation are shown in Figure 5. Two main differences as compared to the antisymmetric case are that (i) the symmetric mode favors formation of Pc 1 wave packets propagating in both directions and (ii) its effect is much stronger. Indeed, the precipitated fluxes shown in Figure 5 are very large, while the modulation amplitude is significantly (10 times) smaller than in Figure 4. Other properties, such as the narrow spectrum, and the large sensitivity to the mismatch between the modulation and Pc 1 propagation periodsare also characteristic of the symmetric mode. Actually for such large fluxes the weak pitch-angle diffusion regime is changed by the strong diffusion, and the balance approximation used here is violated. In this case, one must take (*into account)*, the evolution of the pitch-angle distribution of energetic protons and its influence on the spectrum, which will be the subject of future studies.

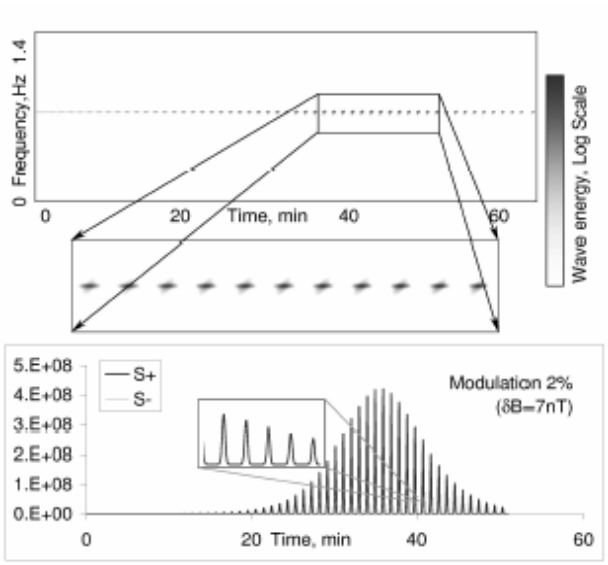


**Figure 5.** Alfvén maser modulated by a symmetric monochromatic disturbance. Here, $R_+ = R_- = 0.1$, and the magnetospheric parameters correspond to those in Figure 2.

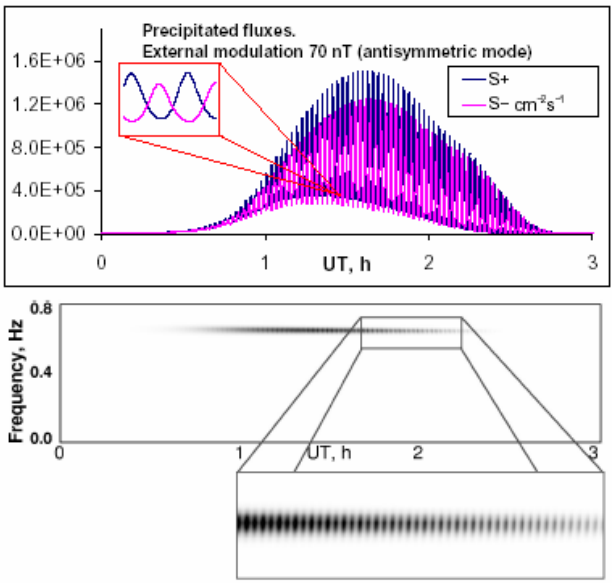


**Figure 6.** The joint effect of the magnetosphere-ionosphere interaction and antisymmetric monochromatic modulation on the dynamics of the magnetospheric Alfvén maser.

### 3.3. Joint action of M-I interaction and external modulation

Figure 6 shows the dynamics of particles and waves in Alfvén maser with both M-I interaction and external modulation taken into account. The modulation was chosen to be antisymmetric, with the same parameters as for Figure 4. This choice was made to obtain the single wave packet instead of two symmetric ones, which corresponds better to observations. The basic input parameters here are mostly the same as in Figure 3, including the diurnal variation of the ionospheric reflection. The difference is that the energetic proton flux was chosen smaller than the threshold one, so that the instability condition (7) is not satisfied at any time in the absence of modulation. The modulation ensures formation of the Pc 1 emissions in spite of low energetic proton flux; in other cases not shown here, it leads to a decrease in the formation time of the Pc 1 wave packet. If the symmetric modulation is added to the simulations corresponding to Figure 3, then the wave packet is not formed. This fact is probably explained by mismatching structures of the modulation and the wave packet arising due to the M-I interaction.

## 4. Conclusions

1. As it could be expected, symmetric modulation of the cyclotron amplification has much stronger effect on the Alfvén maser dynamics than the antisymmetric one. In particular, the latter causes maximum precipitation fluxes $S \sim 10^6$ cm$^{-2}$ s$^{-1}$ for the modulation depth $\delta = 20\%$ [*Demekhov et al.*, 2002*a*], while the former results in the maximum flux $S \geq 10^8$ cm$^{-2}$ s$^{-1}$ for $\delta = 2\%$ (all other calculation parameters being the same).
2. For both types of modulation, the Pc 1 waves generated in our simulation model have very narrow frequency spectrum (i.e., much narrower than a typical pearl event), if the influence of the ionospheric Alfvén resonator modulated by precipitated energetic protons on the Pc1 reflection is neglected.
3. The influence of both symmetric and antisymmetric modulation is very sensitive to the mismatch of the modulation period and the bounce period of Pc 1-wave packet. Note that taking into account finite spectral width of the Pc3/4 pulsation also leads to a significant decrease in the modulation effect [*Demekhov et al.*, 2002*a*].
4. Formation of the pearl-like wave packet related to the magnetosphere-ionosphere interaction (or Alfvén sweep-maser mechanism) can be accelerated significantly in the presence of the Pc3/4 pulsations with suitable period.

This study shows that a hydromagnetic Pc3/4 oscillation having significant compressional component in the equatorial plane can produce rather strong

modulation of Pc 1 wave activity and related energetic ion precipitation. However, this mechanism alone leads to unrealistically narrow spectrum of Pc 1 pulsations; moreover, it requires almost exact coincidence of the modulation and Pc 1 bounce period. We conclude that the modulation of the cyclotron amplification by Pc3/4 waves is unlikely to be the dominant mechanism for formation of Pc 1 pearls by itself but still it can influence this process and either speed it up or slow it down, depending on the match between the structures of the Pc3/4 pulsation and the Pc 1 wave packet.

**Acknowledgments.** This work was supported by the Russian Foundation for Basic Research (grant 02-02-17109), INTAS (grant No. 99-0335), and the General Physics Division of the Russian Academy of Sciences (Program No.16 for Basic Research).

**References**

Belyaev, P. P., S. V. Polyakov, V. O. Rapoport, and V. Y. Trakhtengerts, Dynamic frequency spectrum formation of the Pc-1 pulsations, *Geomagn. Aeron., 27*, 652-656, 1987.

Bespalov, P. A., and V. Y. Trakhtengerts, The cyclotron instability in the Earth radiation belts, in Reviews of Plasma Physics, edited by M. A. Leontovich, vol.10, pp.155-192, Plenum, New York, 1986.

Demekhov, A. G., V. Y. Trakhtengerts, and T. Bösinger, Pc 1 waves and ionospheric Alfvén resonator: generation or filtration? *Geophys. Res. Lett., 27*, 3805-3808, 2000.

Demekhov, A. G., S. V. Isaev, and V. Y. Trakhtengerts, Selfconsistent modeling of Pc 1 emissions in the Earth's magnetosphere, in *Proc. of XXV Apatity Seminar "Physics of Auroral Phenomena"*, pp.69-72, Polar Geophysical Institute, Apatity, Russia, 2002*a*.

Demekhov, A. G., S. V. Isaev, and V. Y. Trakhtengerts, Numerical modeling of Pc 1 emissions modulated by Pc3-4 waves, in *Proc. of 4-th Int Conf. "Problems of Geocosmos"*, pp.184-187, St. Petersburg State University, St. Petersburg, Russia, 2002*b*.

Gendrin, R., S. Lacourly, A. Roux, J. Solomon, F. Z. Feigin, M. V. Gokhberg, V. A. Troitskaya, and V. L. Yakimenko, Wave packet propagation in an amplifying medium and its application to the dispersion characteristics and to the generation mechanisms of Pc 1 events, *Planet. Space Sci., 19*, 165-194, 1971.

Mursula, K., T. Bräysy, K. Niskala, and C. T. Russell, Pc 1 pearls revisited: Structured electromagnetic ion cyclotron waves on Polar satellite and on ground, *J. Geophys. Res., 106*, 29,543-29,553, 2001.

Ostapenko, A. A., and S. V. Polyakov, The dynamics of the reection coe_cient of Alfvén waves in Pc 1 range from ionosphere under variations of electron concentration of the lower ionosphere, *Geomagn. Aeron., 30*, 50-56, 1990.

Polyakov, S. V., V. O. Rapoport, and V. Y. Trakhtengerts, Alfvén sweep maser, *Fizika Plazmy, 9*, 371-378, 1983.

Prikner, K., K. Mursula, F. Z. Feygin, J. Kangas, R. Kerttula, T. Pikkarainen, O. A. Pokhotelov, and V. Vagner, Nonstationary Alfvén resonator: vertical profiles of wave characteristics, *J. Atmos. Sol.-Terr. Phys., 62*, 311-322, 2000.

Trakhtengerts, V. Y., A. G. Demekhov, S. V. Polyakov, P. P. Belyaev, and V. O. Rapoport, A mechanism of Pc 1 pearl formation based on Alfvén sweep maser, *J. Atmos. Sol.-Terr. Phys., 62*, 231-238, 2000.

Woch, J., G. Kremser, and A. Korth, A Comprehensive investigation of compressional ULF waves observed in the ring current, *J. Geophys. Res., 95*, 15,113-15,132, 1990.

---

A. G. Demekhov and V. Y. Trakhtengerts, Institute of Applied Physics of the Russian Academy of Sciences, 46 Ulyanov st., 603950 Nizhny Novgorod, Russia (andrei@appl.sci-nnov.ru, vyt@appl.sci-nnov.ru).

S. V. Isaev, Radiophysical Research Institute, 25 B.Pecherskaya st., 603950 Nizhny Novgorod, Russia (serg@nirfi.sci-nnov.ru).

# Particle precipitation, noon cusp and positive ionospheric disturbances

D. V. Blagoveshchensky

St. Petersburg University of Aerospace Instrumentation

**Abstract.** The following scenario of the positive phase of an ionospheric storm is considered. Precipitation of soft particles begins in the noon cusps. The energy of these particles is absorbed near the heights 200–300 km. The absorption and currents caused by these particles must provide the heating of F-region in the cusp. Disturbed wind from the cusp can provide an increase of $\Delta f_oF2$. It corresponds to the positive ionospheric disturbance ($\Delta f_oF2 > 0$) before a magnetic storm. The latter is connected with the precipitation of soft particles in the cusp from the boundary layer regions before the precipitation of auroral particles and with a development of a ring current that is registered on the Earth as a beginning of the magnetic disturbance. That's why this process can forerun the traditional channel of the energy transfer connected with currents caused by Joule heating (magnetospheric tail – plasma sheet – field aligned currents – Joule heating – variations of circulation and composition of neutrals). Hence, while the positive disturbance and the subsequent negative disturbance can exist as a united process of an ionospheric storm they can be connected with absolutely different channels of solar wind energy penetration into the polar ionosphere. The channel connected with the particle precipitation and heating in cusp brings to the positive phase of ionospheric disturbances ($\Delta f_oF2 > 0$). The channel connected with Joule heating through processes in the tail brings to the negative phase of disturbances ($\Delta f_oF2 < 0$).

## 1. Introduction

In this paper, the main attention will be given to the Earth's ionosphere processes preceding to the onset of the active phase of an isolated substorm (moment $T_o$), in particular, to positive enhancements of the critical frequency $f_oF2$ ($\Delta f_oF2 > 0$) 6–8 hours before $T_o$ [*Blagoveshchensky et al.,* 1992; 1996; 2000; 2003] which have been observed by ionosondes in Europe irrespective of the polarity of substorms (positive or negative) [*Blagoveshchensky et al.,* 2003]. Results of such analysis can be useful and important for development of algorithms of substorm onset forecasting with 2–3 hours ahead $T_o$. It is very necessary for problems of wave propagation, space weather and so on.

## 2. General analysis of physical mechanisms of positive phase of ionospheric storm ($\Delta f_oF2 > 0$) before SSC

2.1. A magnetospheric disturbance arises as a result of an interaction of the magnetosphere with the inhomogeneous flow of the solar wind plasma. When the front of interplanetary shock from the Sun contacts with the Earth's magnetosphere, the storm sudden commencement (SSC) or the sudden magnetic impulse (SI) appears. The magnetosphere compression takes place. The compression can result, among other factors, in the Pc1 electromagnetic waves appearing in the range of 0.2–5 Hz. According to *Gulielmi et al.* [2001]; *Kangas et al.* [2001], the Pc1 excitation may occur not only after SI but prior to SI as well. Before the interplanetary shock waves propagates in the collision-free plasma, there exist regions known as foreshocks. An example of this type of region is a plasma-wave turbulence formed in front of near-Earth shock or turbulence prior to the interplanetary shock. The latter one will influence the magnetosphere *several hours* before SI causing Pc1 wave appearance. According to [*Kangas et al.,* 2001], these preshock Pc1 pulsations, observed before SSC, are generated due to magnetospheric interaction with upstream turbulence of an interplanetary shock wave. Figure 1a, taken from the paper [*Kangas et al.,* 2001], illustrates an appearance of the Pc1 pulsations excited by the upstream 04 hours before SSC.

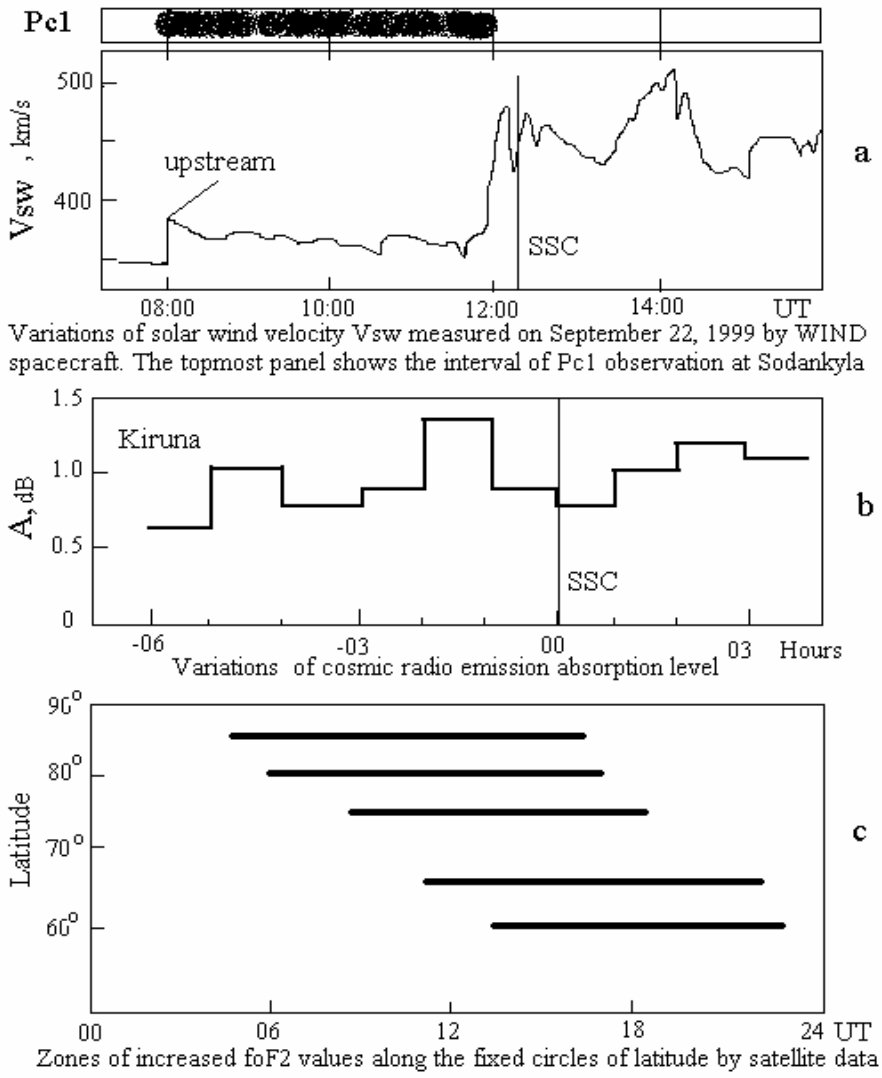


**Figure 1.** Examples of solar wind effects.

There is another phenomenon due to the interplanetary foreshock regions apart from the Pc1 pulsations. The foreshock regions are known to contain the beams of particles reflected from the front, which are flying from the Sun with velocities higher than that of the shock. One can see from papers *Gulielmi et al.* [2001]; *Zolotukhina et al.* [1983] that solar wind regions in front of the shock wave (from the Sun), being connected with the latter by magnetic field, are disturbed by shock front (near the Earth). For the near-Earth wave, these disturbances are the beams of reflected ions and electrons, as they are called, the diffuse and intermediate particles as well as electromagnetic waves the part of which is registered on the Earth's surface. Such corpuscular and wave phenomena are observed by spacecraft before the interplanetary shock waves during *several hours* preceding a passage of the interplanetary shock front. Going to the moment SI, repeated reflections of the solar wind particles in a gap between the fronts of the interplanetary and the near-Earth shocks increase and an acceleration of the reflected particles takes place additionally. As a result, prior to SI there is an intensification of the flow with high energetic particles immediately before the magnetospheric front. It

is safe to assume that *several hours* before SSC (5 –6 hours), near the Earth's locality, for the morning and noon sectors of the magnetosphere (LT ≤ 14h), there will be an increase of the intensity of fluctuated flows of ions and electrons with energies up to 40 –50 keV. Further the accelerated particles of solar wind are precipitated into the Earth's ionosphere. This precipitation causes the following geophysical effects: additional ionization, heating and increased absorption *a few hours* before SI. The most probable region of these effects is the ionospheric projection of the noon cusp. Another region is the auroral oval where precipitation from the entry layer of the magnetosphere is possible. The mentioned effects of ionization, heating and absorption can be used as ionospheric precursors of SI.

2.2. In the papers [*Gulielmi et al.,* 2001; *Zolotukhina et al.,* 1983], behavior of a riometer absorption during the day-time sector of the magnetosphere on Kiruna and Sodankyla observatories was studied *several hours* before SI (SSC). The riometer absorption is caused usually by protons with energy 1–10 MeV. Although Kiruna and Sodankyla are located significantly southward from the cusp, nevertheless an enhancement of the riometer absorption level before SSC was discovered. The main cause is an enlargement of flows of the reflected particles moving before the front of flare stream. In [*Zolotukhina et al.,* 1983] it was shown that a riometer absorption level had maximum and ensuing minimum before SSC. Therefore, the absorption has the form of a positive bay. This can be seen from Figure 1b taken from [*Zolotukhina et al.,*1983], where the riometer absorption level before and after SSC is presented. Here the method of superimposed epochs was used. Hence, one might think that in the tail part of an interplanetary foreshock, the particles having induced the riometer absorption are absent and they are all shaped like the bay-like precursor [*Gulielmi et al.,* 2001; *Zolotukhina et al.,* 1983].

2.3. Recently the following nontraditional scenario of formation of the positive phase of an ionospheric storm before the onset of a magnetospheric disturbance was proposed [*Danilov et al.,* 1985; 1991]. Precipitation of the soft particlesoccurs in the noon cusp. The energy of these particles is absorbed at the heights of 200–300 km. The absorption and currents caused by these particles must provide the heating of the ionospheric F–region in the cusp and the meridional neutral circulation. According to convection, the disturbed wind carries a gas enriched by the atomic oxygen from the cusp through the polar cap, equatorward, with velocity $V$ = 50–100 m/s. This gas provides an enhancement of the F-layer ionization. Under these conditions, before a magnetic storm considered above in the point 2.1, an increased ionization causes the positive ionospheric disturbance ($\Delta f_oF2 > 0$) in the evening and at night. This situation was confirmed by the following observational facts.

1. There is an enlargement of the electron concentration in the cusp region during the period of particle precipitation.
2. An appearance of the equatorward wind moving through the polar cap takes place. The wind is absent under quiet conditions. The 20–40% enhancement of the concentration could be observed equatorward the cusp (an example is presented on Figure 1c taken from [*Danilov et al.,* 1991]).
3. The positive $\Delta f_oF2$ values are often observed *several hours* before the storm onset [*Blagoveshchensky et al.,* 1992; *Danilov et al.,* 1985; 1991; *Ondoh et al.,* 1980].

These positive $\Delta f_oF2$ values are connected with precipitation of the soft particles in the cusp before precipitation of the auroral particles and development of the ring current which is registered on the Earth's surface as a beginning of magnetic disturbance [*Gonzales et al.,* 1994]. The mentioned precipitations in the cusp are connected with the boundary layers of magnetosphere. The currents causing the Joule heating in the ionospheric E–region are connected with other regions (magnetospheric tail–plasma sheet–field aligned currents–Joule heating–change of composition and circulation). Therefore, the considered hypothesis explains why positive phase of ionospheric storm can appear before a magnetic disturbance. According to *Danilov et al*. [1985], for the positive phase (as opposed to the negative phase) an essential dependence on indexes of magnetic activity was not revealed, but there is a clear connection with parameters of the IMF which are known to define the character of interaction between the solar wind and the Earth's magnetosphere.

Hence, while the positive disturbance and the subsequent negative disturbance can exist as a united process of an ionospheric storm they can be connected with absolutely different channels of the solar wind energy penetration into the polar ionosphere. The channel connected with particle precipitation and heating in the cusp forms the positive ionospheric disturbances ($\Delta f_oF2 > 0$) at night. Another channel connected with Joule heating in the ionospheric E–region (magnetospheric tail, plasma sheet and so on) causes the negative phase of disturbances ($\Delta f_oF2 < 0$) at night too. If both channels (heating in the cusp and auroral Joule heating) act simultaneously, the total effect in the electron concentration depends on the sum of these two processes acting in the opposite way on composition variations.

2.4. Authors of paper [*Ondoh et al.,* 1980] studied magnetic and ionospheric conditions of the HF radio

propagation (f = 20 and 25 MHz) on the polar path crossing the auroral oval and the noon polar cusp during 50 moderate geomagnetic storms. Increases of signal amplitude at the receiving center were observed ~10 hours before SSC. These pre-SSC increases are accompanied with the ionospheric $f_oF2$ increases ($\Delta f_oF2 \leq 5.5$ MHz) in the polar cusp region ~17 hours before SSC. It was shown that the pre-SSC $f_oF2$ increase occurred at the invariant latitudes between 83° N and 57° N around the local noon (LT ≈ 12h). An additional ionization is created by precipitation of electrons with energies 1–2 keV in the cusp. Fluxes of such electrons begin to grow 16–20 hours before SSC.

These data correspond to the ideas mentioned in the points 2.1 and 2.3 as well as to results obtained in papers [*Blagoveshchensky et al.,* 1992; 1996; 2000].

2.5. Let us consider all existing mechanisms [*Blagoveshchensky et al.,* 1996; *Chao-Song Huang et al.*, 2002; *Danilov et al.,* 1985; 1991; *Pirog et al.,* 2000].

*Day-time conditions*

There are some possible mechanisms of the $f_oF2$ increase ($\Delta f_oF2 > 0$) during a few hours before the onset of a magnetic disturbance.

a) Enlargement of $\Delta f_oF2$ values at high and middle latitudes before storm onset is stipulated by lifting the F2 layer (or $h_mF2$) caused by the vertical drift. The latter arises, firstly, due to electric field origin (although the positive $B_z$ before a storm is not favorable to this) and, secondly, due to the meridional winds directed southward [*Danilov et al.,* 1991].
b) An additional source of ionization enlargement is, firstly, the particle precipitation from the plasmasphere due to its compression as a result of the magnetosphere compression and, secondly, downward flow of plasmaspheric plasma into the underlying ionosphere induced by westward electric fields [*Park*, 1974]. These particles and flow of plasma ionize the ionospheric F2 layer and the mechanism of the considered ionization is likely to be close to that of the SAR arcs origin. The most probable region of precipitation extends from middle latitudes to $\Phi_L \sim 70^o$ where maximum is located on $\Phi_L \sim 50^o$ [*Blagoveshchensky et al.,* 2003; *Chao-Song Huang et al.*, 2002; *Park*, 1974].
c) As discussed above, in the auroral oval an extra source of the increased ionization before SSC is particle precipitation from the entry layer of the magnetosphere.

*Night conditions*

There are also some possible mechanisms of the $f_oF2$ increase ($\Delta f_oF2 > 0$).

a) Drift of the thermospheric gas from the day-time cusp through the pole to the night side [*Danilov et al.,* 1985]. According to [*Blagoveshchensky et al.,* 2003;] this mechanism results in the ionization enhancement and the positive $\Delta f_oF2$ values.
b) Impact of the electric fields [*Chao-Song Huang et al.*, 2002;]. Specifically, the electric fields from the noon cusp can penetrate to the night side.
c) Night precipitation of the cold plasma from the plasmasphere that can provide the $\Delta f_oF2$ values growing at pre-dawn hours [*Danilov et al.,* 1991].
d) Particle flows (ions), precipitated from the protonosphere into ionosphere during disturbances preceding the SSC, influence the F2 layer result in positive $\Delta f_oF2$ mainly at night [*Danilov et al.,* 1991].
e) Particle precipitation from the magnetosphere tail, more exactly from the plasma sheet, due to the magnetosphere compression before SSC. Besides growing the $\Delta f_oF2$, this precipitation leads to formation of sporadic $E_{sr}$ layers a few hours before the moment $T_o$ at high latitudes [*Pirog et al.,* 2000].

2.6. The positive phase of ionospheric storms ($\Delta f_oF2 > 0$), as a rule [*Buonsanto*, 1999; *Danilov et al.,* 1985; 1991; *Prölss et al.,* 1991; 1993; *Rodger et al.,* 1989], is observed before the negative phase ($\Delta f_oF2 < 0$). Moreover, the positive phase can occur both before SSC and after it. The first case was considered right above. Possible causes of the positive phase production after SSC are as follows: changes of the large-scale circulation of the thermospheric wind, traveling atmospheric disturbances, displacement of the auroral oval equatorward and so on.

## 3. Charater of the $\Delta f_oF2$ variations during periods of positive and negative substorms

Some conditions and phenomena in the magnetosphere were considered above for the magnetic storms. In accordance with [*Gonzales et al.,* 1994], we believe that as to the substorms these conditions and phenomena do not differ much from the physical point of view, of course, qualitatively but not quantitatively.

Let us start with the mentioned above assumption that there are diffuse and intermediate particles with $V > V_{sw}$ before the interplanetary shock. These particles can occur in the regions of cusps and entry layer of the magnetosphere ~6 hours before the moment $T_o$. The latter is the onset of the expansion phase of substorm and it is equivalent to the moment SSC for storms. The moment of the beginning of interaction of accelerated particles of the solar wind with the Earth's magnetosphere is the onset of the $\Delta f_oF2$ growing. The

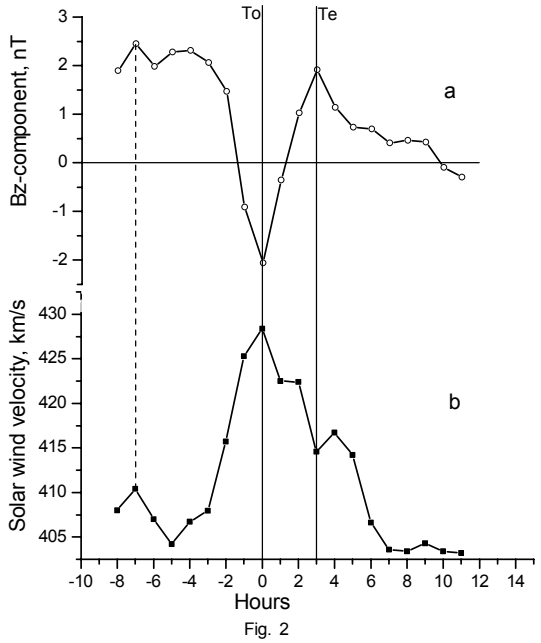


**Figure 2.** Variations of $B_z$ and $V_{sw}$ values received by superimposed epochs method (OMNIWeb data, 20 isolated substorms). $T_o$ – onset of substorm expansion phase, $T_e$ – ending of expansion phase.

possible mechanisms of the ionization increase in the F2 region before SSC were considered above, in the point 2.5. There is a good reason to believe that these mechanisms for storms are similar to mechanisms for substorms before $T_o$. Let us show that this suggestion may be tolerated by means of the satellite data NSSDC OMNIWeb.

First we emphasize that the isolated substorms (close to ideal ones) are considered here. Isolated substorms afford better opportunities to study the spatial extent of the effects and to separate temporal and spatial variations [*Park,* 1974]. They were studied during period 8h < $T_o$ < 11h on the quiet background of the magnetic field. From all amount 41 substorms used in the paper [*Blagoveshchensky et al.,* 2003] only 20 substorms were selected for the further analysis. These 20 substorms, firstly, are in the best accordance with the conditions of isolation to exclude the effects of any preceding disturbances. Secondly, they all have nearly equal durations for the convenience of averaging. The graphical displays in Figure 2 and 3 were constructed using the method of the superimposed epochs. Figure 2 illustrates the variations of two parameters: $B_z$ – component of the IMF and velocity of the solar wind $V_{SW}$ by the OMNIWeb data. From Figure 2*a* it follows that $B_z$ variations have the classical character. Moment $T_o$ is the onset of substorm expansion phase, $T_e$ – is the moment of ending the expansion phase. The moment $T_o$ was determined as a sharp growing of the AE–index of geomagnetic activity. Additionally, this moment was found as the bay onset of the X-component of magnetic field by the IMAGE chain data in accordance with recommendations presented in [*Rostoker et al.,* 1980]. For selected 20 substorms, essential discrepancies in $T_o$ values determined by the first and second methods were not revealed. One can see from Figure 2*b* that $V_{SW}$ maximum takes place at t = $T_o$. At this moment, there is contact of the main flow of solar wind with the Earth's magnetosphere and the onset of the substorm expansion phase takes place. At t = –7h (dotted line) one can see also a weak maximum of $V_{SW}$ value evidently due to the upstream impact on the Earth's magnetosphere. Referring to Figure 1*a* and Figure 2*b*, the similarity of $V_{SW}$ behavior can be seen as well as the SSC and $T_o$ values correspond to $V_{SW}$ maximum. In Figure 3 variations of the proton flux > 1 MeV and proton density by the OMNIWeb data are presented. Proton flux values grow in Figure 3 starting from t = –3h up to t = $T_e$. Character of behavior of this parameter through the time interval from –7h to $T_o$ corresponds to that of $V_{SW}$ on the same interval. As for the proton density parameter in Figure 3*b*, it correlates very good with the level of riometer absorption presented in Figure 1*b*. Therefore, the considered mechanisms of geophysical phenomena before SSC of a storm and before $T_o$ of a substorm accordingly are not different in principle by physical processes and coincide one with another by the temporal character of behavior.

After turning $B_z$ southward, 1–1.5h before $T_o$, the growth phase of a substorm begins. Signs of the growth phase under $B_z$ < 0 are as follows: day-time part of magnetosphere approaches to the Earth; flow of magnetic field in the magnetosphere tail increases; plasma sheet approaches to the Earth and gets thin; electric field from the day-time side to night one increases in the polar cap; precipitation of the soft particles intensifies and so on.

Further, the main (or expansion) phase of a substorm develops starting from the moment $T_o$ to $T_e$. There are bay-like variations of the magnetic field. While the H-component has positive deviation the substorm is positive. If the bay is negative so a substorm is negative too. By virtue of this difference, let us consider each type of substorms separately. Here are some results.

- The $\Delta f_oF2$ variations for negative substorm differ from the ones for positive substorm most essentially at high latitudes (geomagnetic latitude $\Phi_L > 50^o$).
- At middle and low latitudes ($\Phi_L < 50^o$) ionospheric responses to both negative and positive substorms are approximately equal.

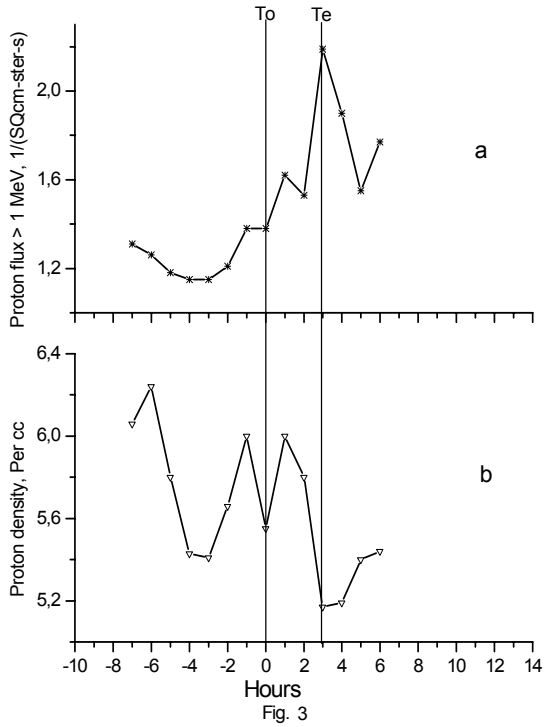


**Figuire 3.** Variations of proton flux and proton density values received by superimposed epochs method (OMNIWeb data, 20 isolated substorms). $T_o$ – onset of substorm expansion phase, $T_e$ – ending of expansion phase.

– Substorm effects is better expressed for negative substorms than for positive ones. Here the substorm effect is considered as the following.

*Negative substorms*

The $\Delta f_oF2$ values 6–8 hours before the moment $T_o$, the onset of the expansion phase, increase up to maximum located 2–3 hours before $T_o$. To the moment $T_o$ the sharp drop of the $\Delta f_oF2$ values till minimum and further their rising during period of the expansion phase take place. The second maximum happens in 1–2 hours after the end of the expansion phase. Then dropping the $\Delta f_oF2$ values during 3–4 hours after the second maximum and rising occur again. An example of the substorm effect is presented on Figure 4, where the substorm is the same as on Figure 1*a*.

*Positive substorms*

Here the position of the first maximum of the $\Delta f_oF2$

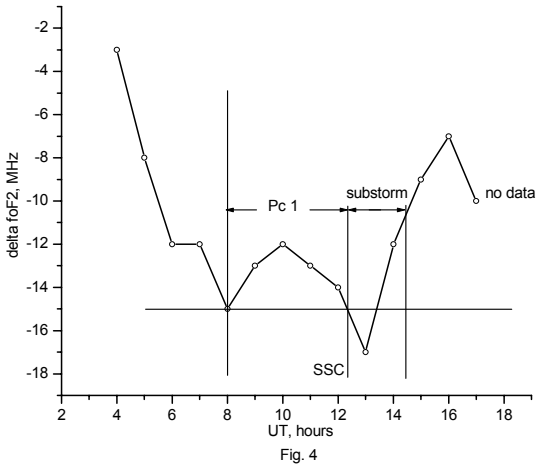


**Figure 4.** Variations of $\Delta f_oF2$ values during substorm on September 22, 1999 by Sodankyla.

values depends of a substorm duration – if it is longer, the position is closer to the moment $T_o$.

## 4. Conclusion

Little-known mechanisms of formation of $\Delta f_oF2$ ionospheric positive peaks during 6–8 hours before $T_o$ (onset of the expansion phase of an isolated substorm) are considered in detail. They are connected with an impact of the high-speed particles in the foreshock region of solar wind on the Earth's magnetosphere. Here, the main feature is an entirely different channel of solar wind penetration in the ionosphere. This channel realizes the transmission of energy through the entry layer into the inner magnetosphere and through the day-time cusp into the ionosphere, unlike the classical channel which describes all three substorm phases, namely, through the magnetospheric tail, plasma sheet and auroral ionosphere. The ionospheric effect due to cusp and magnetospheric entry layer manifests most likely at high latitudes (polar cap and auroral oval). Enhancement of $\Delta f_oF2$ values can be used for prediction of the ionospheric disturbance onset and, in its turn, of space weather problems, radio propagation and so on.

## References

Bauske, R., S. Noel, and G. W. Prölss, Ionospheric storm effects in the nighttime E region caused by neutralized ring current particles, *Ann. Geophys. 15*, 300–305, 1997.

Blagoveshchensky, D. V., T. D. Borisova, Substorm effects of ionosphere and HF propagation, *Radio Sci*. *35*, 5, 1165-1171, 2000.

Blagoveshchensky, D. V., T. D. Borisova, and L. V. Egorova, Pre- and after substorm situations in the ionosphere and decameter radio wave propagation, *Geomagn. Aeron, 96*, 4, 125–134, 1996 (in Russian).

Blagoveshchensky, D. V., L. V. Egorova and V. M. Lukashkin, High-latitude ionospheric phenomena diagnostics by high-frequency radio wave propagation observations, *Radio Sci*. *27*, 267-274, 1992.

Blagoveshchensky, D. V., O. A. Maltseva and A. S. Rodger, Ionosphere dynamics over Europe and Western Asia during magnetospheric substorms 1998-99, *Ann. Geophys*. *11*, 1–11, 2003.

Buonsanto, M. J., Ionospheric storms – a review, *Space Science Reviews. 88*, 563–601, 1999.

Chao-Song Huang, J. C. Foster, Prompt effects of solar wind variations on the inner magnetosphere and midlatitude ionosphere, *Space Weather Week, April 16-19, Boulder, Colorado, Abstracts*, p.17, 2002.

Danilov, A. D., L. D. Morozova, Thermosphere-ionosphere interaction during ionospheric storms (review), *Geomagn. Aeron. 31*, 2, 209-222, 1991 (in Russian).

Danilov, A. D., L. D. Morozova, E. G. Mirmovich, About a possible nature of the positive phase of ionospheric storms. *Geomagn. Aeron, 25*, 5, 768-772, 1985 (in Russian).

Foster, J. C., Radar observations of magnetosphere-ionosphere coupling at mid and high latitudes, *J. Geom. Geoelectr. 47*, 801–812, 1995.

Gonzales, W. D., J. A. Joselyn, Y. Kamide et al., What is a geomagnetic storm? *J. Geom. Res. 99*, A4, 5771-5792, 1994.

Gulielmi, A. V., N. A. Zolotukhina, J. Kangas et al., The build-up of Pc1 wave activity prior to sudden magnetic impulses SI, *Issl. po geom., aeronom. i phys. Solntsa*, Issue *112*, Irkutsk, Siberian Branch of RAS, 115–123, 2001 (in Russian).

Kangas, J., J. Kultima, A. Guglielmi, A. Potapov, and K. Hayashi, Impact of interplanetary shock on the ULF wave activity: A case study of the storm sudden commencement on September 22, 1999, *Earth Planets Space*, *53*, 1173–1182, 2001.

Kozyra, J. U., M. O. Chandler, D. C. Hamilton, W. K. Peterson, D. M. Klumpar, D. W. Slater, M. J. Buonsanto, and H. C. Carlson, The role of ring current nose events in producing stable auroral red arc intensifications during the main phase: observations during the September 19-24, 1984, equinox transition study, *J. Geophys. Res*., *98*, 9267-9283, 1993.

Lyons, L. R., Substorms: Fundamental observational features, distinction from other disturbances and external triggering, *J. Geophys. Res*., *101*, 13,011-13,025, 1996.

Tinsley, B. A., Energetic neutral atom precipitation as a possible source of midlatitude F region winds. *Geophys. Res. Lett., 6*, 291–293, 1979.

Ondoh, T., K. Obu, Prediction of HF communications disturbances by pre-SC HF field increase on polar paths crossing the auroral zone, *Solar-Terr. Predict. Proc*., *4*, D2-21–D2-30, 1980.

Park, C. G., A morphological study of substorm-associated disturbances in the ionosphere, *J. Geophys. Res*., *79*, 2821–2827, 1974.

Pirog, O. M., V. D. Urbanovich, G. A. Zherebtsov, Effects of substorms in the night auroral E-region, *5th International Conference on Substorms. Book of abstracts*, St.-Petersburg, 545–547, 2000.

Prölss, G.W., On explaining the local time variation of ionospheric storm effects, *Ann. Geophysicae*, *11*, 1-9, 1993.

Prölss, G.W., L. H. Brace, H. G. Mayer et al., Ionospheric storm effects at subauroral latitudes: a case study, *J. Geophys. Res*., *96*, 2, 1275–1288, 1991.

Pudovkin, M. I., O. M. Raspopov, N. G. Kleimenova, Disturbances of the Earth's electromagnetic field. Part 2. Short periodic oscillations of the geomagnetic field, *LGU*, Leningrad, p.270, 1976.

Rodger, A. S., G. L. Wrenn, H. Rishbeth, Geomagnetic storms in the Antarctic F-region. 2. Physical interpretation, *J. Atmos. Terrest. Phys*., *51*, 851–866, 1989.

Rostoker, G., S. –I. Akasofu, J. Foster et al., Magnetospheric substorms – definition and signatures, *J. Geophys. Res*., *85*, 1663–1668, 1980.

Zolotukhina, N. A., About geophysical precursors of the SSC. *Issl. po geom., aeronom. i phys. Solntsa*, Issue *66*, Moscow, Nauka, 51–54, 1983 (in Russian).

Yeh, K. C., S. Y. Ma, K. H. Lin and Conkright, Global ionospheric effects of the October 1989 geomagnetic storm, *J. Geophys. Res., 99*, 6201–6218, 1994.

# Energy dispersed auroral structures from magnetotail ion beams

R. A. Kovrazhkin[1] and J. -A. Sauvaud[2]

[1] Space Research Institute of Russian Academy of Sciences, Moscow, Russia
[2] Centre d'Etude Spatiale des Rayonnements, Toulouse, France

**Abstract.** This paper analyses the characteristics of proton energy-dispersed structures near the poleward edge of the nightside auroral zone. Using data from the INTERBALL-Auroral satellite at geocentric distances ~2.8 – 3.0 $R_E$ and from CLUSTER at geocentric distances ~4.4 – 4.6 $R_E$, we show that the structures, known as Velocity Dispersed Ion Structures (VDIS), consist of several substructures lasting ~1 – 4 min. Each substructures displays an inverse energy-time dependence, i.e., the higher-energy protons reach the altitudes of the INTERBALL-Auroral and CLUSTER satellites earlier than lower-energy protons. VDIS are observed mainly during magnetically quiet times and during substorm recovery phases. They are accompanied by electron populations with an average energy ≤ 1 keV, typical for PSBL in the magnetotail. Main properties of VDIS substructures allow us to conclude that they are the auroral signatures of ion beams generated in the equatorial plane of the magnetotail. Estimations show that the ion beams, forming the VDIS substructures, can be ejected from different parts of the extended tail current sheet between ~15 and 47 $R_E$. Dispersion properties of these auroral structures show that time-of-flight effect dominate the propagation of ion beams from the tail down to the Earth.

*The authors dedicate this paper to the memory of their Teacher - Yuri Galperin. The most of all, Yuri valued the real knowledge of the Nature. Space Physics was for him as a precious vessel, which he filled with bright ideas and experimental results during all his life. We have had the chance to travel along this difficult way for a time with him and to benefit from his brilliant work.*

## 1. Introduction

The region between the tail lobes and the plasmasheet is very dynamical and plays a crucial role in the dynamics of magnetotail. Field aligned plasma flows with energies up to a few tens of keV were observed in external part of plasmasheet (PSBL) on high-apogee spacecraft [e.g., *DeCoster and Frank*, 1979; *Parks et al*., 1979; *Eastman et al*., 1984; *Takahashi and Hones*, 1988, *Baumjohann et al*., 1990]. Direct measurements showed that ions are often observed as earthward beams with velocities of > 400 km/s, although tailward beams have sometimes been measured [*Takahashi and Hones*, 1988 and references therein].

It is evident that beams observed in distant magnetotail should constitute a source of ion populations for the nighttime auroral zone. Indeed, precipitations in the form of energy-dispersed ion structures in the energy range ~1–20 keV were detected from low-apogee satellites near the polar boundary of auroral oval [*Kovrazhkin et al*., 1987; *Bosqued*, 1987; *Zelenyi et al*., 1990; *Saito et al*., 1992; *Bosqued et al*., 1993; *Onsager and Mukai*, 1995]. Such structures were called Velocity Dispersed Ion Structures (VDIS). It was first indeed considered that the mechanism responsible for their formation was the velocity filter drift **E×B.** This effect, induced by the large-scale dawn-dusk electric field, is operative during the propagation of the ions of different energies toward the Earth.

A different type of $H^+$ and $O^+$ ion dispersed injections, with energies up to 14 keV was detected for the first time onboard the INTERBALL-Auroral satellite at altitudes 2–3$R_E$ near the polar edge of the auroral oval [*Sauvaud et al*., 1999]. Such structures called Time of flight Dispersed Ion Structures (TDIS), were explained in terms of time-of-flight dispersion of ions with different mass and energies during their propagation from the tail to the Earth. Such injections are clearly associated with substorms and have been observed inside the poleward part of the auroral bulge [*Sauvaud et al*., 1999; *Sergeev et al*., 2000; *Popescu et al*., 2002].

Proton dispersed structures have been observed also at altitudes 4–7$R_E$ with the TIMAS mass-spectrometer onboard the POLAR satellite [*Lennartsson et al*., 2001].

The energy-dispersed structures were called by the authors "blast-like" structures. The POLAR satellite data indicate that those structures are most likely of temporal nature, as attempts to reveal their spatial dispersion, i.e., dependence on the latitude, have failed.

Thus, direct measurements of dispersed ion structures illustrate their different properties, although all of them are observed near the polar edge of the auroral oval. However, the classification of such structures is far from being complete as a large statistical data base is still under construction.

In this paper we analyze dispersed ion structures of the VDIS type using passes of INTERBALL-Auroral at geocentric distances ~ 2.8 – 3.0$R_E$ and of CLUSTER at geocentric distances ~ 4.4 – 4.6$R_E$. The main objectives of this paper is to investigate the properties of the ion structures and to identify the magnetotail sources, where the ion beams are generated and accelerated.

## 2. Instrumentation

In this study we use data from the ION experiment flown onboard the INTERBALL-Auroral satellite (IA) and the CIS experiment flown aboard the CLUSTER spacecraft (we use the data from SC-1, SC-3, and SC-4). The IA apogee was ~3$R_E$ and the orbital period was 6 hours; the CLUSTER apogee is ~19.6$R_E$, perigee ~4$R_E$, and the orbital period reaches 57 hours.

The ION experiment comprised two sets of instruments: two ion mass spectrometers to measure fluxes of $H^+$, $He^{++}$, $He^+$ and $O^+$ in the energy range ~5 – 14,000 eV/Q and two electron spectrometers to measure electron fluxes in the energy range ~10 – 22,000 eV/Q [*Sauvaud et al*., 1998]. In this study we used the ION/IA

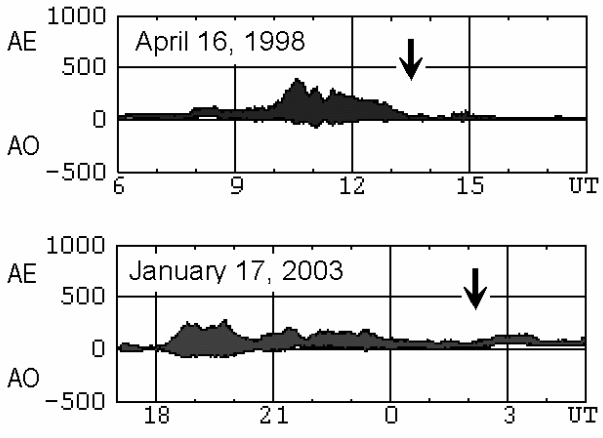


**Figure 1**. The variations of the AE and AO magnetic indices during passes of INTERBALL-Auroral (upper panel) and CLUSTER (lower panel). The time when VDIS are observed is indicated by arrows.

energy spectra of $H^+$ measured each 7.5 s and the electron energy spectra measured each 3.75 s.

The CIS experiment comprises two sensors: the Hot Ion Analyzes (HIA) without mass selection for the analysis of the ions in the energy range from ~5 to 34,000 eV/Q and the Composition and Distribution Function (CODIF) analyzer designed to measure the $H^+$, $He^{++}$, $He^+$, and $O^+$ ions in the energy range from ~5 to 40,000 eV/Q [*Rème et al*., 1997]. The three-dimensional ion distributions were measured with a time resolution of 4 s (one spin period of a CLUSTER satellite).

We used also preliminary values of the AE and AO indices, obtained from the WDC-C2 (Kyoto) to characterize the geomagnetic activity during IA and CLUSTER measurements.

## 3. Observations

### 3.1. IA and CLUSTER examples of VDIS

In this section we present two typical example of energy-dispersed structures. They were separately detected by the ION/IA and by the HIA/CLUSTER experiments at different altitudes. During the measurements presented here, the satellites moved poleward, i.e., from the auroral zone to the polar cap. For both passes the magnetic conditions in the magnetosphere were about the same: Kp was 2- during IA observations on April 16, 1998, and Kp was 1 when CLUSTER passed the auroral zone on January 17, 2003. Preliminary AE and AO indices during these observations are shown in Figure 1. The arrows indicate the time when the satellite crossed the dispersed structures. These were detected after small substorms during magnetically quiet time, what enables the comparison of measurements made onboard different satellites.

Proton VDIS dispersed structure was observed by IA from 13:33 to 13:37 UT at altitudes 11,600 – 12,200 km (2.9$R_E$ geocentric distance) in the energy range 1–10 keV. The corresponding energy-time spectrogram is shown in upper panel of Figure 2. The differential energy flux (JE) shows a few well-defined maxima, indicating that the VDIS structure contains several substructures denoted in the lower panel by A1, A2, A3, and A4. The duration of each substructure is ~0.8 – 1.0 min. Inside the A1 – A4 substructures high-energy protons arrive first to the satellite altitude, followed by low-energy protons. On the contrary, the VDIS structure as a whole displays an energy-latitude "dispersion", where the average energy increases with latitude. It is that overall feature that led previous authors to conclude that VDIS have a spatial nature, based on earlier measurements from low-altitude satellites [*Zelenyi et al*., 1990; *Saito et al*., 1992; *Bosqued et al*., 1993]. The

spatial-temporal resolution of the data taken onboard these satellites did not allow to reveal the dispersion properties of individual substructures within VDIS, although substructures (beamlets) were observed earlier aboard AUREOL-3 [*Ashour-Abdalla et al*., 1992; *Bosqued et al*., 1993]. Thus the energy-time dispersion inside each small-scale substructures may be considered as a fundamental characteristic of VDIS. This evidences the fact that ion beams are generated in the magnetotail and dispersed by time of flight effects.

Note that during this pass near the poleward edge of the auroral zone, the average energy of the electron population coinciding with the VDIS structure is ~0.5 – 0.8 keV. This energy is a characteristics of the PSBL. Equatorwards of VDIS, the electron average energy reaches ~3 – 5 keV (not shown here). Electron with this energy are probably coming from the CPS [e.g., *Eastman et al*., 1984; 1985]. Therefore we may conclude that ion beams, observed here, are formed near the equatorial plane of the magnetotail, in the PSBL.

The slope of substructures A1 – A4 (in inverse velocity – time spectrogram) allows an estimation of the distance of the source of the ion beam, if one assume that time of flight is the main mechanism leading to the energy dispersion during the beam propagation in the

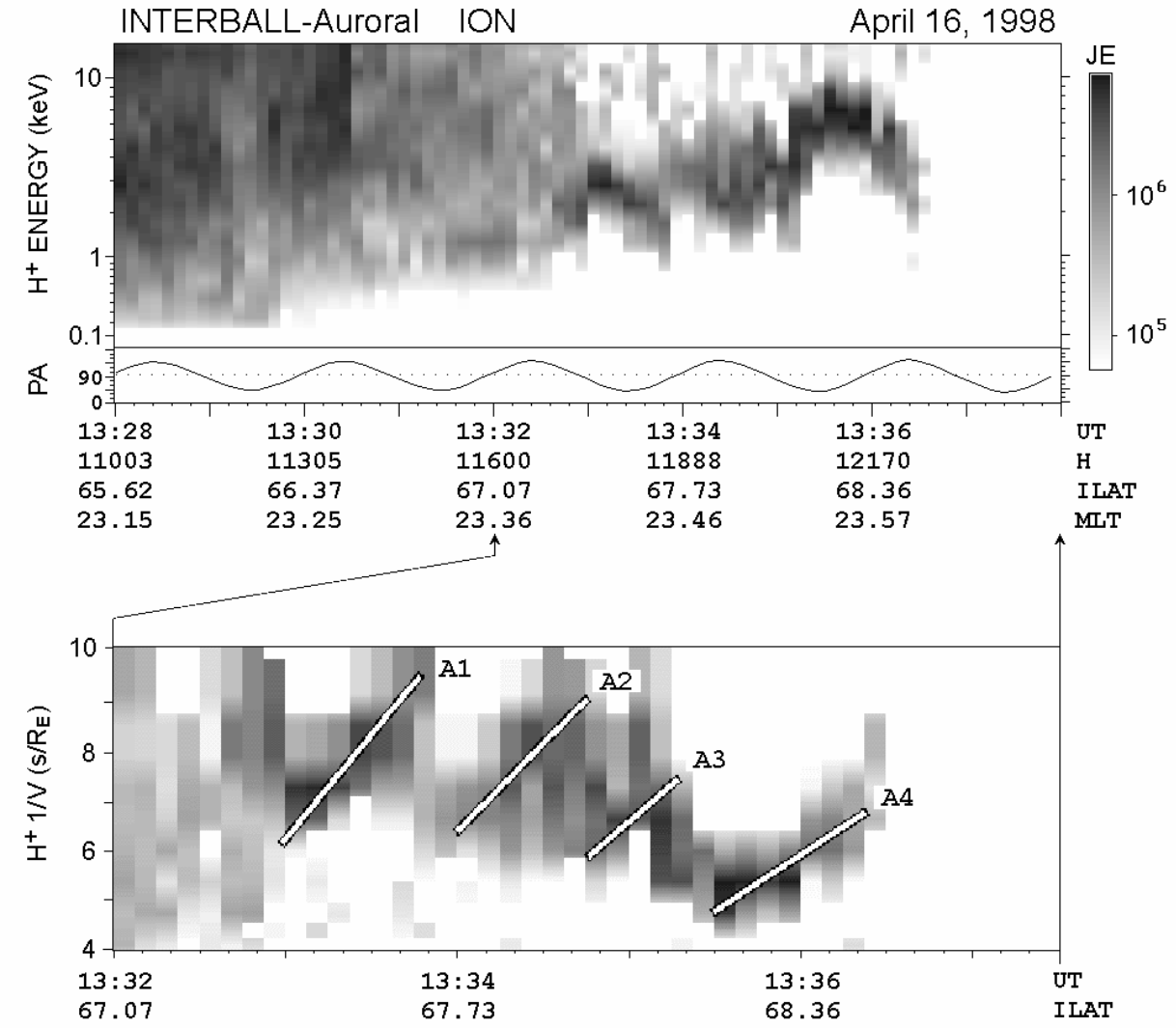


**Figure 2**. VDIS event measured onboard INTERBALL-Auroral on April 16, 1998 during a poleward crossing of the auroral zone – polar cap boundary. The upper panel displays the energy time spectrogram of ions. The lower panel displays their $(\text{velocity})^{-1}$ – time spectrogram. Differential energy fluxes expressed in keV/[$\text{cm}^2$.s.sr.keV] are color-coded. Lines on the lower panel give an estimation of the ion beam dispersion.

magnetosphere. Such a method was used in *Sauvaud et al*., [1999]; and in *Popescu et al*., [2002]. Here, the source distance of the A1 – A4 beams are found to be in the range 15.0$R_E$ to 28.4$R_E$.

A VDIS energy-dispersed ion structure detected by HIA/CLUSTER between 01:58 and 02:12 UT on January 17, 2003 is shown in Figure 3. Similarly to the previous case (Figure 2) the structure contains individual substructures (ion beams), labeled B1, B2, B3, and B4, in the lower spectrogram. Inside each substructure, high energy protons arrive first. These beams were observed at altitudes 22,000 – 23,100 km (R ≈ 4.5$R_E$) in the energy range 0.8 – 10 keV. The distance of the source of the beam, estimated from the time-inverse velocity slope (shown in lower panel of Figure 3), for beams B1 – B4 ranges from 36$R_E$ to 47$R_E$.

### 3.2. Relation of dispersed structures to geomagnetic activity

Figure 4 is an attempt to present the magnetic conditions related to the measurements of ion beams performed onboard INTERBALL-Auroral during a 18 day interval in January 1997. The arrows indicate the times when ion beams are observed. Numbers denote the IA orbit number. The symbols "V" and "T" indicate respectively that a VDIS or a TDIS structure is observed.

The data presented in Figure 4 show that VDIS are

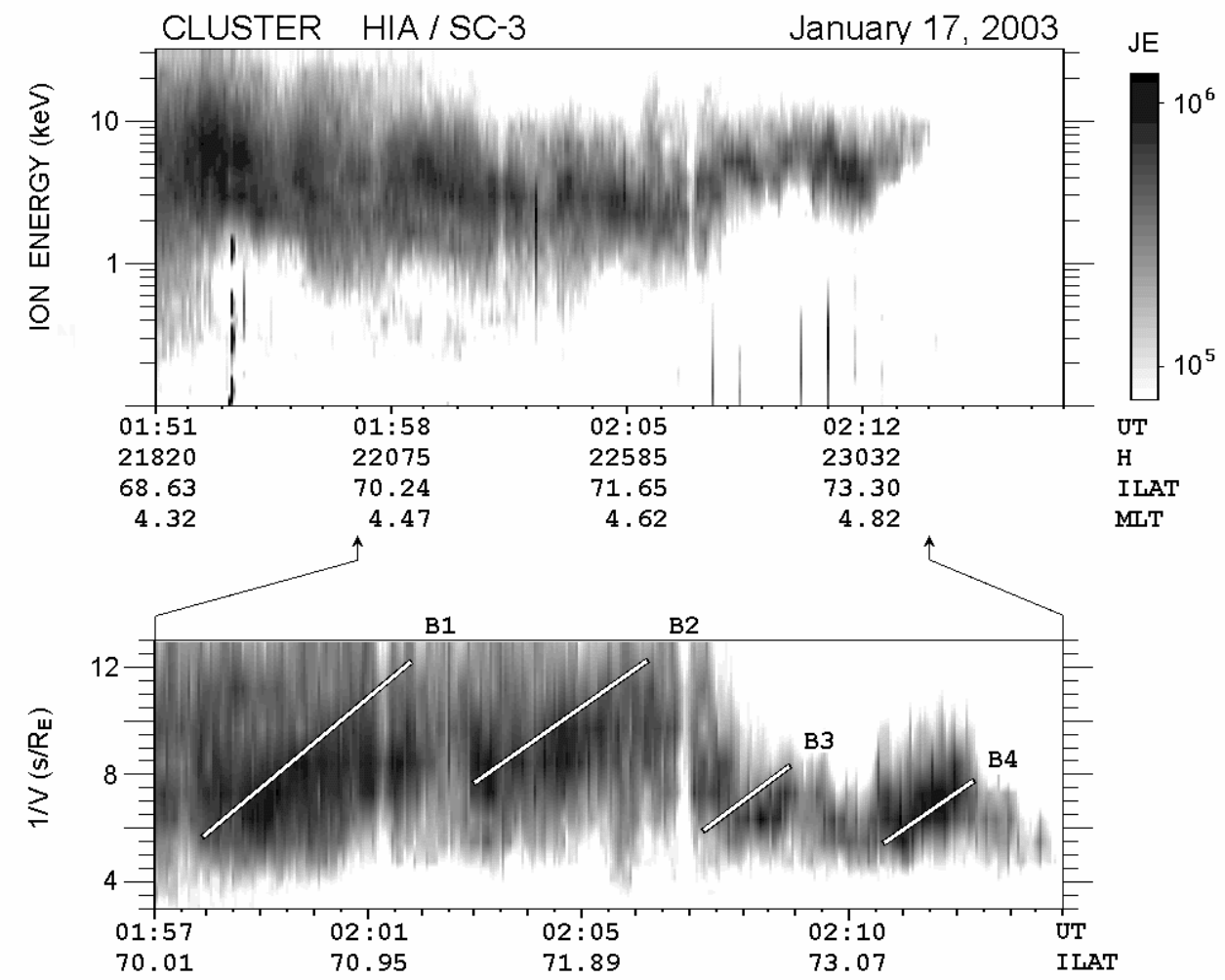


**Figure 3**. VDIS event measured onboard CLUSTER on January 17, 2003 during a poleward crossing of the auroral zone – polar cap boundary. Same presentation as Figure 2.

most frequently observed either during magnetically quiet time (8 events), or during a substorm recovery phase (7 events), although 2 events are observed during the main phase of a substorm. In contrast to VDIS, TDIS are recorded mainly during the onset and main phases of substorms.

## 4. Summary and conclusions

The main experimental results pertaining to the observations of energy-dispersed structures of the VDIS type onboard IA and CLUSTER near the polar edge of the auroral zone can be summarized as follows.

(1) The structures, referred earlier as VDIS, contain substructures lasting ~1–4 min. Therefore the formation of individual ion beams is a key feature of the observed VDIS. The average energy of the ion beams depends strongly on the latitude: the beams measured at the polar edge of VDIS are formed by more energetic protons than the beams measured equatorward.

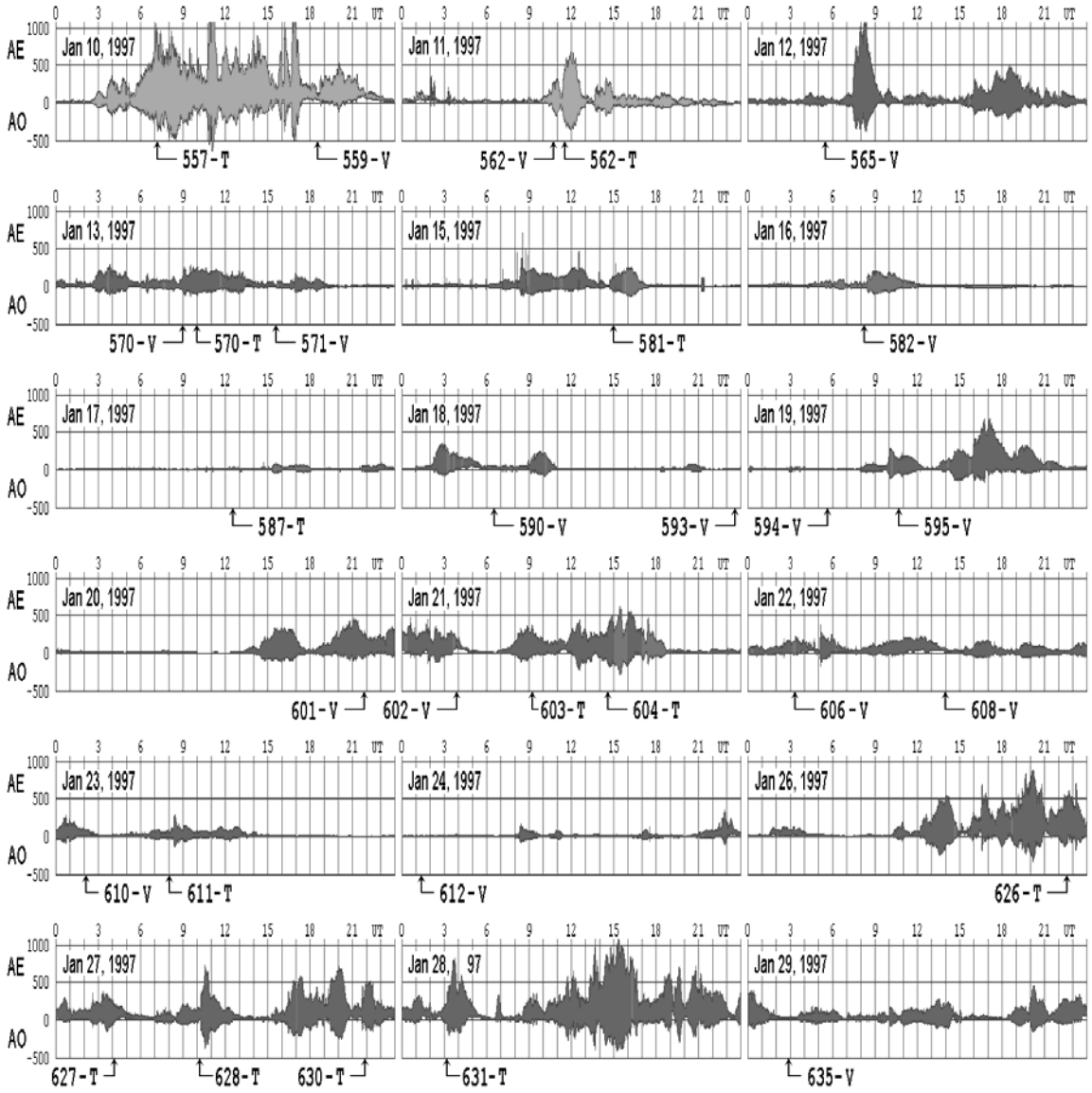


**Figure 4**. The variations of the AE and AO indices during a 18 day interval on January 1997. The arrows indicate the measurement times of VDIS (V) and TDIS (T) structures (see text). The numbers give the orbits number of INTERBALL-Auroral.

(2) The electron precipitation accompanying VDIS are characterized by a rather low energy ≤ 1 keV, typical for the PSBL. Thus we can conclude that the ion beams are formed in successive parts of the magnetotail at distances ranging 15–47$R_E$.
(3) The ion beams observed within VDIS are generated mainly in magnetically quiet time and during recovery phases of substorms.

The ejection of these beams from the magnetotail occurs when plasma acceleration can take place in the distant tail. The model calculations made by *Ashour-Abdalla et al*., [1991] have shown that along the tail X-direction several zones can be formed, within which the ions are ejected along Speiser-orbits [*Speiser*, 1965; 1967]. Between these zones in the tail there are the regions where the ions are on trapped orbits and can not be ejected towards the Earth. The ion acceleration probably result from the mechanism described by *Lyons and Speiser* [1982]. The presence of a small normal component of the geomagnetic field $B_z$ in the current sheet leads to particle acceleration in the large-scale dawn-dusk electric field followed by ejection along the B field. As described by [*Delcourt and Martin*, 1999], it is likely that ions undergo pitch angle scattering near energy resonances where particles escape after transient oscillations inside the sharp field reversal. However, the models of Lyons and *Speiser* [1982] and of *Delcourt and Martin* [1999] are strictly applicable in stationary conditions only, while our experimental results lead to the conclusion that the beams should leave the current layer in the form of ion bursts ("packets") with a quasi-period ≤ 4 min. The "packet" injection seem to be related to the non-adiabatic particle dynamics in the process of the self-adjustment of the magnetotail itself. It is appropriate to mention here that the large-scale kinetic (LSK) simulation of the magnetotail variability in increasing convection electric field shows, that strong magnetic field perturbation can develop [*Peroomian et al*., 2000; 2002]. As a result, fewer magnetic islands form in the tail. In addition, the X-line experiences oscillations with characteristic period ~ 3–4 min. Under these conditions the period of the cycle of ion loss and replenishment becomes governed by the duration of the replenishment process.

Finally, the dispersed properties of substructures in VDIS, as observed onboard the IA and CLUSTER satellites, allow us to assume that the main mechanism of dispersed structure formation is the different time of flight of ions with different energies, moving from their source down to auroral altitudes. Thus a **E×B** velocity filter effect may be of secondary importance in comparison with the TOF effect even if this drift undeniably plays a role during the ion flight to the Earth.

**Acknowledgements.** The CIS/CLUSTER data has been kindly provided by H. Rème. AE- and AO-indices were provided by WDC-2 in Kyoto. This research program was supported by the French-Russian program PICS (grant APIC0090) and RFBR (grant 00-02-22001). Thank are due to E. Penou (CESR) and A. L. Glazunov (IKI) for the visualization software of the ION/IA and CIS/CLUSTER experimental data.

## References

Ashour-Abdalla, M., J. Berchem, J. Buchner, and L. M. Zelenyi, Large and small scale structures in the plasma sheet: A signature of chaotic motion and resonance effects, *Geophys. Res., Lett. 18*, 1603, 1991.

Ashour-Abdalla, M., L. M. Zelenyi, J. M. Bosqued, and R. A. Kovrazhkin, Precipitation of fast ion beams from the plasma sheet boundary layer, *Geophys. Res. Lett., 19*, 617, 1992.

Baumjohann, W., G. Paschmann, and H. Lühr, Caracteristics of high speed flow in the plasma sheet, *J. Geophys. Res., 95*, 3801, 1990.

Bosqued, J. M., AUREOL-3 results on ion precipitation, *Phys. Scr., 18*, 158, 1987.

Bosqued, J. M., M. Ashour-Abdalla, M. El Alaoui, V. Peroomian, L. M. Zelenyi, and C. P. Escoubet, Dispersed ion structures at the poleward edge of the auroral oval: Low latitude observations and numerical modeling, *J. Geophys. Res., 98*, 19181, 1993.

DeCoster, R. J., and L. A. Frank, Observation pertaining to the dynamics of the plasma sheet, *J. Geophys. Res., 84*, 5099, 1979.

Delcourt, D. C., and R. F. Martin Jr., Pitch angle scattering near energy resonances in the geomagnetic tail, *J. Geophys. Res., 104*, 383, 1999.

Eastman, T. E., L. A. Frank, W. K. Peterson, and W. Lennartsson, The plasma sheet boundary layer, *J. Geophys. Res., 89*, 1553, 1984.

Eastman, T. E., L. A. Frank, and C. Y. Huang, The boundary layers as a primary transport regions of the Earth's magnetotail, *J. Geophys. Res., 90*, 9541, 1985.

Kovrazhkin, R. A., J. M. Bosqued, L. M. Zelenyi, and N. V. Jorjio, Observation of evidence of reconnection and plasma acceleration at a distance of about $5 \times 10^5$ km in the tail of Earth's magnetosphere, *JETP Lett.*, Engl. Transl., *45*(8), 479, 1987.

Lennartsson, O. W., K. J. Trattner, H. L. Collin, and W. K. Peterson, Polar/Toroidal Imaging Mass – Angle Spectrograph survey of earthward field-aligned proton flows from the near – midnight tail, *J. Geophys. Res., 106*, 5859, 2001.

Lyons, L. R., and T. W. Speiser, Evidence for current sheet acceleration in the geomagnetic tail, *J. Geophys. Res*., *87*, 2276, 1982.

Onsager, T. G., T. Mukai, Low altitude signature of the plasma sheet boundary layer: Observations and model, *Geophys. Res. Lett.*, *22*, 855, 1995.

Parks, G. K., C. S. Lin, K. A. Anderson, R. P. Lin, and H. Reme, ISEE-1 and 2 particle observations of outer plasma sheet boundary, *J. Geophys. Res., 84*, 6471, 1979.

Peroomian, V., M. Ashour-Abdalla, Zelenyi, L. M., and Petrukovich A. A., Intrinsic self-adjustment and variability of the magnetotail, *Procedings of the Fifth Internationale Conference on Substorms (ICS-5)*, SP-443, pp. 121-126, July 2000.

Peroomian, V., L. M. Zelenyi, and D. Schriver, Imprints of small-scale nonadiabatic particle dynamics on large-scale properties of dynamical magnetotail equilibria, *Adv. Space Res.*, *30*, 2657, 2002.

Popescu, D., J. -A. Sauvaud, H. Stenuit, D. C. Delcourt, V. A. Sergeev, M. Brittnacher, G. K. Parks, T. Mukai, S. Kokubun, and R. A. Kovrazhkin, Auroral signatures of transient processes in the outer magnetosphere, *Adv. Space Res.*, *30*, 2701, 2002.

Rème, H., J. -M. Bosqued, J. -A. Sauvaud, A. Cros, J. Dandouras, C. Aoustin, J. Bouyssou, Th. Camus, J. Cuvilo, C. Martz, H. Perrier, D. Romefort, J. Rouzaud, C. d'Uston, E. Moebius et al., The Cluster Ion Spectrometry (CIS) Experimentt, *Space Science Reviews*, *79*, 303, 1997.

Saito, Y., T. Mukai, M. Hirahara, S. Machida, and N. Kaya, Distribution function of precipitating ion beams with velocity dispersion observed near the poleward edge of the nightside auroral oval, *Geophys. Res. Lett.*, *19*, 2155, 1992.

Sauvaud, J. -A., H. Barthe, C. Aoustin, J. J. Thocaven, J. Rouzaud, E. Penou, R. A. Kovrazhkin, and K. G. Afanasiev, The ION experiment onboard the INTERBALL-Auroral satellite: initial results on velocity dispersed structures in the cleft and inside the auroral oval, *Ann. Geophys.*, *16*, 1056, 1998.

Sauvaud, J. -A., D. Popescu, D. C. Delcourt, G. K. Parks, M. Brittnacher, V. A. Sergeev, R. A. Kovrazhkin, T. Mukai, and S. Kokubun, Sporadic plasma sheet ion injections into the high altitude auroral bulge – satellite observations, *J. Geophys. Res.*, *104*, 28565, 1999.

Sergeev, V. A., J. -A. Sauvaud, D. Popescu, R. A. Kovrazhkin, V. N. Lutsenko, L. M. Zelenyi, M. Syrjasuo, A. Viljanen, T. I. Pulkkinen, K. Kudela, S. Kokubun, and T. Mukai, Plasma sheet ion injections into the auroral bulge: correlative study of spacecraft and ground observations, *J. Geophys. Res.*, *105*, 18465, 2000.

Speiser, T. W., Particle trajectories in the model current sheets, 1. Analytical solutions, *J. Geophys. Res., 70*, 4219. 1965.

Speiser, T. W., Particle trajectories in model current sheets, 2, Applications to auroras using a geomagnetic tail model, *J. Geophys. Res., 72*, 3919, 1967.

Takahashi, K., and E. W. Hones, Jr., ISEE-1 and 2 observations of ion distribution at the plasma sheet-tail lobe boundary, *J. Geophys. Res.*, *93*, 8558, 1988.

Zelenyi, L. M., R. A. Kovrazhkin and J. M. Bosqued, Velocity-dispersed ion beams in the nightside auroral zone: AUREOL 3 observations, *J. Geophys. Res.*, *95*, 12119, 1990.

# Fine details of space, time and spectral structure of aurora, VLF emissions and magnetic pulsations.

I. A. Kornilov[1], T. A. Kornilova[1], and O. I. Kornilov[2]

[1] Polar Geophysical Institute, Apatity, Russia.
[2] Institute of Physics, St.Petersburg State University, St.Petersburg, Petrodvorets, Russia.

**Abstract.** Wide use of modern computers gives essentially new opportunities in processing various experimental data. Some examples of nowadays capabilities in geophysical investigations are presented in our report. Using different methods of image enhancement and filtering (gradient, convolution, based on FFT and Wavelet transforms, SVD and others) for TV frames and keograms processing demonstrates surprising improvement of experimental material. Auroral luminosity variations as small as 0.0001 of the average signal amplitude can be revealed and studied, potentially providing a completely new insight into the aurora and hence to the related magnetospheric dynamics. Applying modified FFT and AR-models methods of spectral analyses to VLF emissions study revealed, for example, extremely fine time and spectral structure of VLF chorus. Ground-based and satellite data demonstrate, that chorus is structured initially, in the region of generation and characteristic scales are about 10-20 Hz and 10-30 milliseconds correspondingly. Probably a fine chorus structure is the key to understanding their physical nature. Traditional spectrograms of magnetic pulsations can be essentially improved by using different methods of image filtering. Some examples of Alfven resonance structures processing are presented. In the modern interferometric investigations high-sensitivity CCD-TV cameras are widely used. Using two-dimensional Wavelet Transform for the interferometer data compression happened to be very effective. The resulting image can be as small as 0.25 Kbytes (about 1.5 percents from initial 16 Kbytes) and contain most of the important information of initial non-compressed frame.

## 1. Auroral TV data processing

During the recent decades a lot of different methods of image processing and filtering were developed (robotics, machine vision, radars and sonars, satellites imaginary, *X-rays*, computer tomography and many others) for various areas of science and engineering. Some of these methods can be successfully used for auroral TV data processing, and many weak details of aurora, invisible at initial frames and keograms, can be revealed. Image defects caused by difficult observational conditions can be corrected as well (fog, clouds, city lights, etc).

The list of procedures that can be applied to processing of the auroral TV information [*Fu*, 1981] is given below. Many of them are in-built into advanced programming languages, such as, for example, IDL, MatLab and LabView [*IDL User's Guide*, 1995].

1. Various arithmetic and nonlinear operations (sum and difference of frames, addition of various compensating signals for suppression of a non-uniform camera sensitivity along the field of view. Parasitic background from urban illumination, fog, clouds, and different geometric image distortions can also be compensated.
2. Smoothing and sharpening of image, using different gradient and convolution filters, and also filters, based on FFT (Fast Fourier Transform), WTN (Wave-let Transform), SVD (Singular Value Decomposition), local contrast intensification, histogram equalization, and image transformation on a given histogram pattern.
3. Motion detection and moving objects tracing (various differential methods, calculation of accumulative difference, using of integral projection functions). This method in particular allows constructing vector field of auroral form velocities for the analysis of magnetospheric electric fields and the study of auroral forms vorticity.

4. Segmentation of the image, contour detection, constriction of the borders between image fragments, global analysis using the Hough transform (lines connection, association of boundary points).
5. Description of object borders, and contours recognition applying Fourier descriptors and chain codes.
6. Object skeleton construction and schematization of object (so called average axis transformation). This procedure allows, for example, to localize bright bottom edge of auroral arc, ignoring extended vertical structure.
7. Various pattern recognition procedures. Two-dimensional correlation analysis and comparison of different parts of image with the reference object, application of decision functions, etc.

The items 4, 5, 6 and 7 provide for automatic selection and preliminary analysis of interesting auroral events. Some of these methods are in-build in many graphic processors (Adobe PhotoShop, etc.) However all these processors work with the ready image, where interesting details can be absent because of a small dynamic range of the data (for example, Adobe PhotoShop has one-byte presentation for the black-and-white image). Image manipulations prior to the image display, i.e., work with initial file, are much more effective.

It is important to note that methods of image improvement can be applied to not only the TV information, but also many others. Scanning photometers data, VLF and magnetic pulsations spectra and in general any other information, which can be presented in a two-dimensional form, i.e., as an image, can be successfully processed.

For demonstration of processing opportunities we shall consider just several examples, such as frame arithmetic operations and some simple methods of image filtering. Difference between frames reveals moving and varying details of the image. Gradient image filtering, operating as a high-pass space filter, emphasizes weak and thin image details. Gradient filtering is a result of simple subtraction of the initial matrix of TV frame or keogram, and a matrix, shifted in vertical or horizontal direction on desired number of pixels.

Despite the primitiveness, gradient filtering is very effective for revealing fine details of keogram, invisible in initial data because of TV camera defects or bad observational conditions, Figure 1 presents an example. Low stability of the camera's "level of black" results in strong and chaotic modulation of brightness. Besides, rather heavy fog accompanies the presented interval of time, especially after 21.50. Nevertheless, the application of gradient filtering allows revealing many

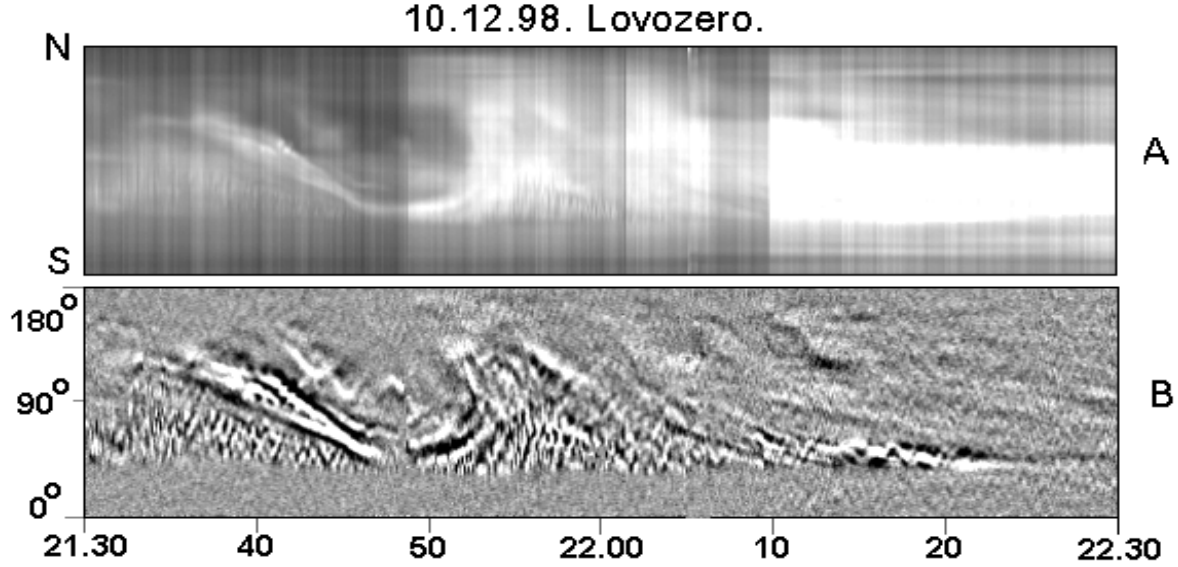


**Figure 1**. Suppression of TV camera technical defects and fog. (a) ordinary keogram, (b) gradient filtered keogram.

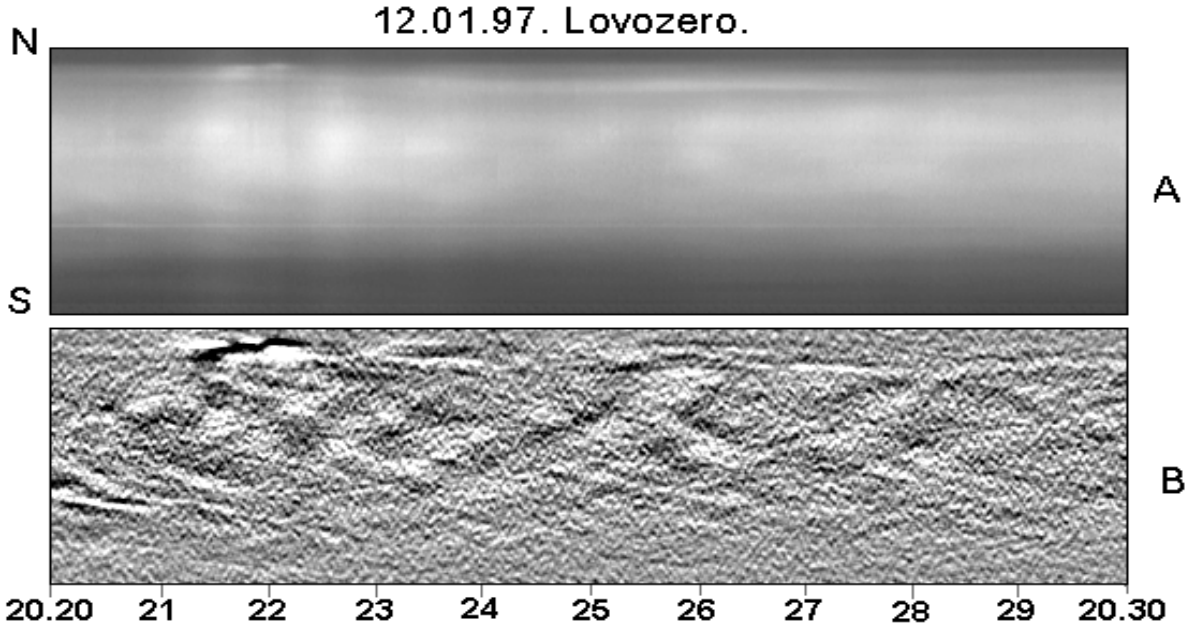


**Figure 2**. Revealing subvisual waves and pulsations inside diffuse luminosity band**.**

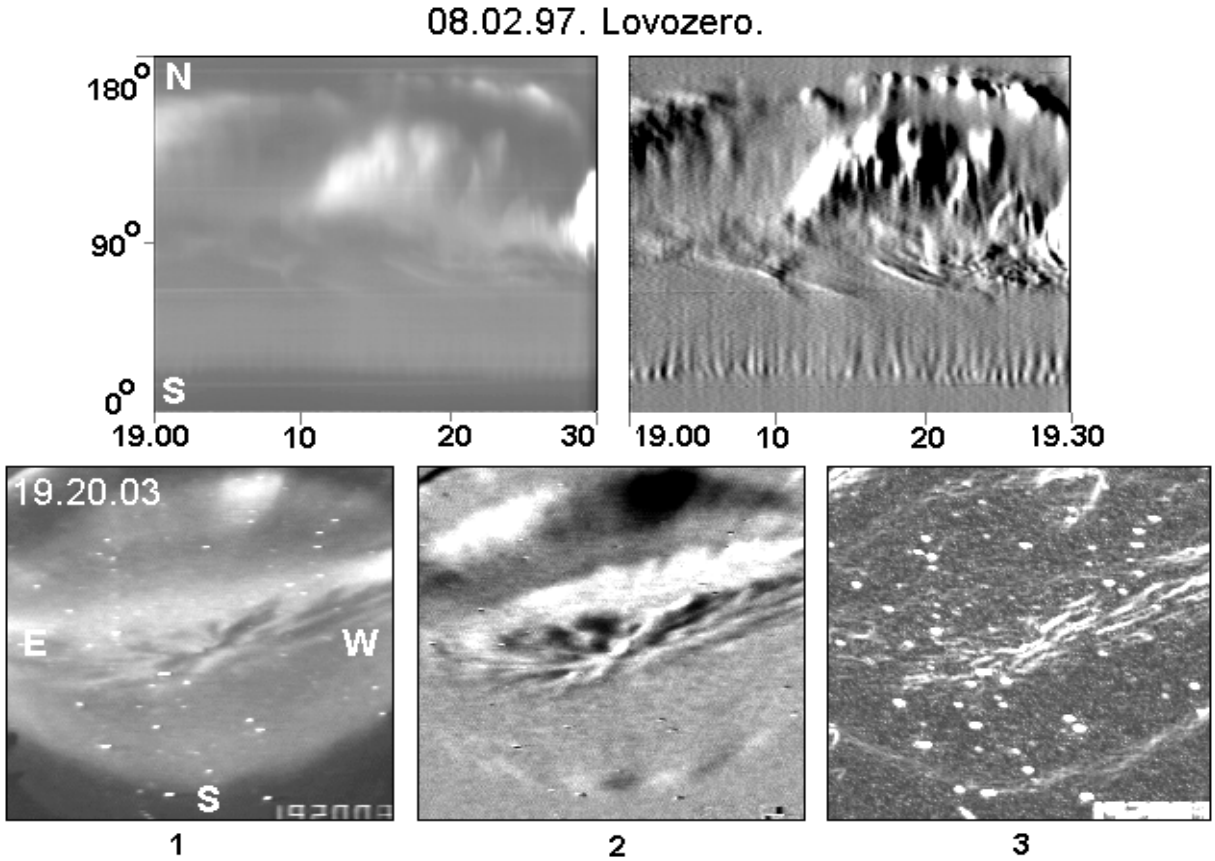


**Figure 3**. Auroral pulsations at the southern border of diffuse luminosity. Top panel shows a pair of normal and filtered keograms. Bottom panel presents an example of TV frame processing for this time interval. (1) 10-seconds integrated frame; (2) time gradient filtering; (3) wavelet filtering.

details, especially, intense auroral pulsations (period about 10−20s). These pulsations occur southward of the diffuse band and are practically invisible in initial data. Figure 2 shows an example of revealing fine structures inside diffuse luminosity band. Subvisual auroral waves move between North and South with characteristic velocities of 400–600 m/s, and periods of about 40–60s.

We can probably see auroral manifestation of MHD-waves, captured in the resonator, formed by plasma gradients at diffuse luminosity borders.

Figure 3 presents an example of frames filtering. The top panel shows two keograms for 30 minutes time interval. At the bottom part of left plot we can see the southern border of diffuse luminosity, coinciding, according to satellite data, with a border of 30−40 keV proton precipitation. Filtered keogram at the right plot reveals time variations of border brightness with the period of 40−60 seconds. The spatial structure of these pulsations is completely invisible in ordinary TV frames, even after 10 seconds integration. The result of time gradient filtering, presented in the middle frame, suggests that the observed pulsations is a non-spreading standing wave on the border, while wavelet filtering reveals a very fine plasma spatial structure at the luminosity border.

## 2. Fine structure of VLF chorus

For many years FFT has been used in spectral analysis of VLF emissions. Though FFT gives correct spectral amplitudes and almost no artifacts (false spectral details), it has a fundamental limitation. The product of spectral and time resolution is a constant; in other words, it is impossible to have high spectral and time resolution simultaneously. More advanced methods of spectral estimations were developed [*Lawrence*, 1979; *Oppenheim*, 1978], using a prior information and the modeling of time series internal structure (method of Prony, Pisarenko method, Maximum Entropy and others).

The spectral image can often be noticeably improved by using a simple procedure of spectra interpolation. The size of the data block is artificially increased by adding zeros to both ends; thus spectral resolution can be improved without losing time resolution. Though it looks somewhat strange, as if extra information comes from nowhere, but the spectral image, at least for some types of data, really becomes much better, with a lot of new details. The idea of an artificial data block spreading was further developed in different methods of time series forecasting and backcasting outside the block. Because of special waveform, for VLF chorus spectral analyzes with autoregression model-base forecasting happened to be very effective. Changing the number of model, i.e., length of forecasting, one can get different spectra from ordinary FFT to high resolution ones, and so, can control the appearance of false spectral details. Another useful recommendation is the noise addition to initial data with the following smoothing. This procedure allows reducing the “quantum effect” of small dynamic range of initial information (8 bits for the satellite VLF data).

Figure 4 demonstrates the usefulness of AR-model-based spectral analysis. VLF data were recorded at ground-based station, so horizontal lines are power lines harmonics. Figure 4(a) presents ordinary FFT spectra (no interpolation). VLF chorus can be seen in the frequency band 1.5–3.0 kHz. An attempt to improve time and frequency resolution of spectra shown in Figure 4(b), (b1), has no success. The results of autoregression model spectra analysis presented in Figure 4(c) are radically different. Very fine internal structure of chorus element, with complicated

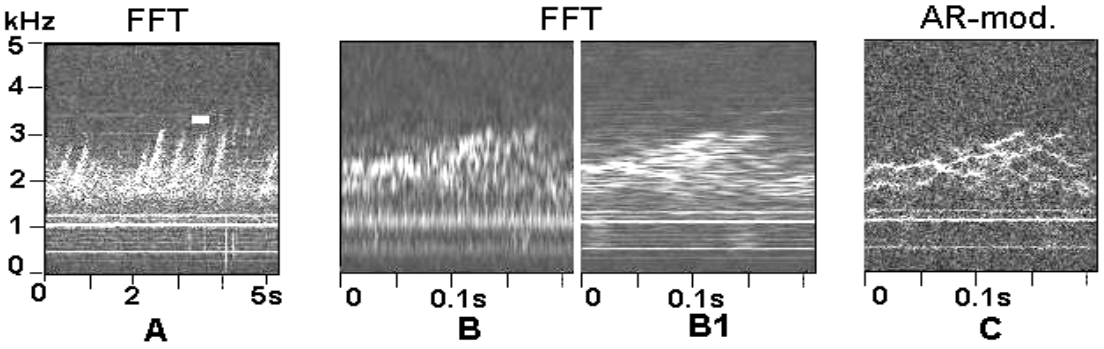


**Figure 4.** Benefits of autoregression spectral analysis. (a) Spectrogram of 5-seconds time interval. Ground-based VLF chorus data from Lovozero; (b) and (b1) Results of ordinary FFT for 0.2 seconds fragment, marked by short white line in plot (a); (c) fine spectral and time chorus structure, revealed by autoregression model spectral analyses.

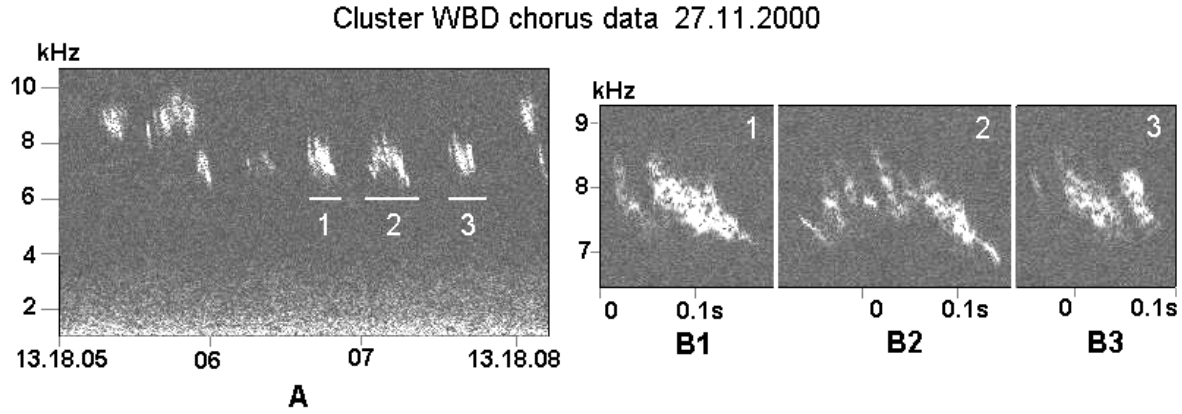


**Figure 5**. Spectrograms of Cluster satellite chorus data. (a) Result of FFT with spectra interpolation, 4-times data block spreading. (b1), (b2), (b3) AR–model spectra of three fragments, marked by white horizontal lines in (a). Satellite is near the equator, in the chorus generation region.

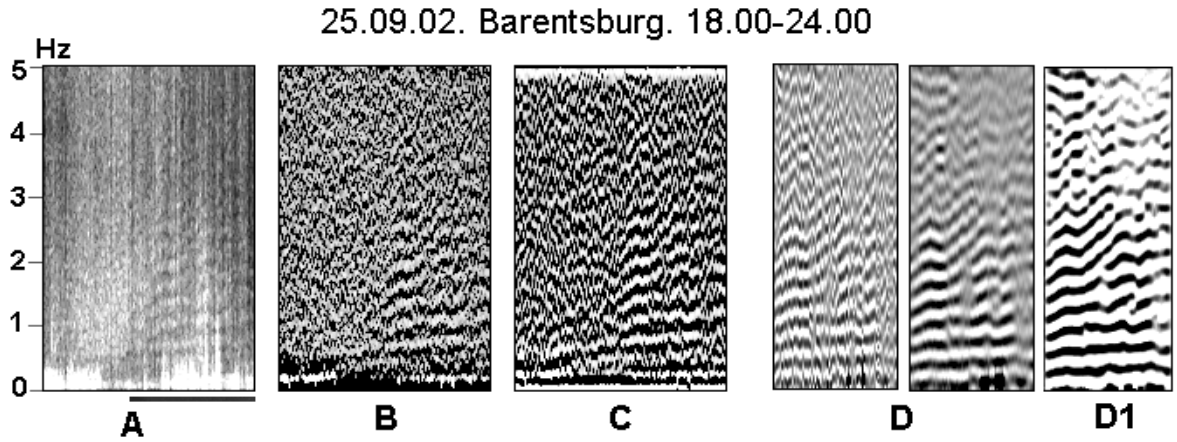


**Figure 6**. Magnetic pulsations spectrogram with Alfven resonator signatures. (a) ordinary FFT-spectrogram; (b) gradient, and (c) wavelet spectrogram filtering; (d) and (d1) examples of SVD-based spectrogram filtering.

interconnection of different frequencies is well visible.

To prove that fine chorus structure is not a chorus propagation effect, in Figure 5 we present satellite chorus data recorded directly inside chorus generation region. Figure 5(a) shows 3-seconds spectrogram, constructed by FFT with spectra interpolation (ordinary FFT give approximately the same picture, as in Figure 4(b), (b1)). High-resolution AR-model spectra fragments can be seen in Figure 5(b1), (b2), (b3). Extremely fine structure at the time scale of milliseconds is distinguishable. Chorus looks as a “chain reaction” of short activations.

### 3. Magnetic pulsations

The study of Alfven resonator (IAR) is an important part of modern ionospheric investigations [*Belyaev et al.*, 1990; *Belyaev et al.*, 1990] At high latitudes, for example, at Spitsbergen, it is rather difficult to do them. Resonance structure on magnetic pulsations spectrograms is very weak and masked by strong natural pulsations of magnetospheric origin, so various methods of spectrogram-image filtering are very useful. Figure 6 presents some typical examples. Non-filtered

spectrogram of N-S component of magnetic pulsations for the time interval of 18.00-24.00UT in the frequency range of 0–5 Hz are shown in Figure 6*a*. Weak quasi-parallel lines are Alfven resonator structures, and they are hardly visible in initial spectra. Figure 6*b* and 6*c* are the results of gradient and wavelet filtering correspondingly. Filtering is one- dimensional, applied to every vertical line of spectra separately. As a result of filtering, natural pulsations are strongly suppressed, resonance structure becomes much more contrast, and some important physical information is pointed out. One can see, that the resonator was switched on off rather quickly, and high frequencies are separated from the low ones. Time variations of resonance structure are obvious as well. Figure 6 (d) and (d1) show the results of another method of filtering, basing on SVD (Singular Value Decomposition). In Figure 6 (d) SVD filtering is applied to every single spectral line, and in Figure 6 (d1) to the whole matrix. The filtered fragment is marked by horizontal line at the bottom of Figure 6 (a). SVD filtering reveals an interesting detail, i.e. in the middle of the interval the number of resonance lines suddenly increments.

## 4. Fabry-Perot interferometer data

Since their introduction in the 1980's, wavelets have become a powerful tool in mathematical analysis, with applications such as image compression, statistical estimation and numerical simulation of partial differential equations. One of their main attractive features is the ability to accurately represent the whole spectra of analytical and numerical one- and multidimensional functions with a small number of adaptively chosen wavelet coefficients. Wavelets have a very broad range of applications, and can be very useful for the large variety of data and images filtering and compression. Many interesting papers and references can be found in Internet (*wavelet.org*, Russian site *wavelet narod.ru*).

In modern interferometric investigations high-sensitivity CCD-TV cameras are widely used [*Batten and Rees*, 1990; *Leontyev*, 2000]. As the camera creates high-resolution image (typical size is 512*512 pixels, or 256 Kbytes) every 1–3 minutes, there are serious problems of data storage and acquisition. Even after 16-points image averaging, the size of the digital frame is 16 Kbytes. A special procedure of frame scanning is usually used, and only the resulting information about Doppler profile is recorded into the computer memory (file size is about 1–2 Kbytes). But in this case all initial frame information is lost, and, for example, the control of the CCD-matrix dark current (that is important for correct detection of Doppler profile maximum) becomes difficult (dark current is non-uniform along the frame and unstable in time). Using two-dimensional wavelet transform (WTN) provides a simple, fast and effective method of direct interferometric image data compression. Because of the special image geometry (concentric rings plus strong noise), WTN compression happened to be very effective, the resulting image can be as small as 0.25 Kbytes (about 1.5 percents from initial 16 Kbytes) and contains most of the non-compressed frame important information. Another positive effect of WTN compression is a good image filtering and improving of S/N ratio. Figure 7 shows an example of WTN compression for interferometric data. One can see, that after wavelet compression the frame looks much better, with less noise, than even a smoothed one, though it was reconstructed from only 1.5 percents of initial information. In contrast with the simple averaging presented in Figure 7 (c), details of interferometric rings are conserved.

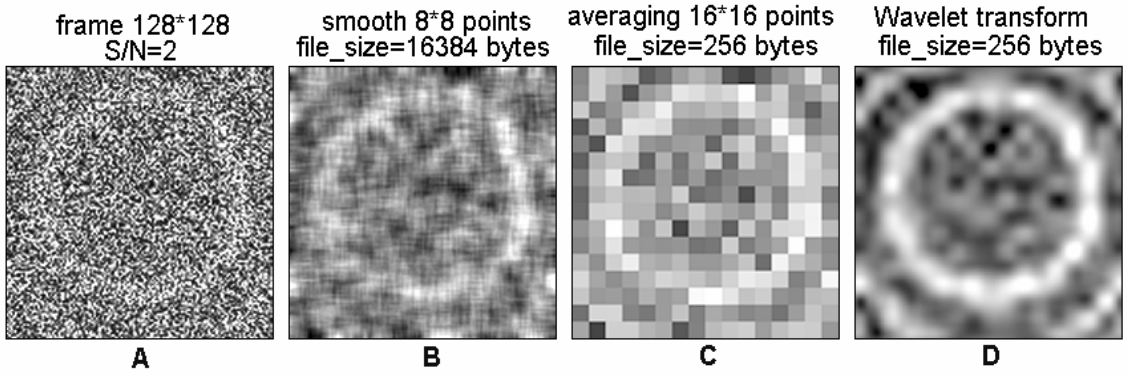


**Figure 7**. Example of using two-dimensional Wavelet Transform (WTN) for Fabry-Perot interferometer data compression. (a) Initial image with noise addition. (b) Result of 8*8 points box sliding smoothing. (c) Averaging 16*16 points. (d) Reconstructed image after wavelet compression.

## 5. Conclusions

Only a small amount of the modern data processing procedures were presented here and they demonstrate, that routine experimental data that have been studied for many years can yield considerable amount of new information. Many TV camera defects, results of bad observational conditions can be compensated, and data not used for a long time can be successfully processed. TV frames and keograms filtering can potentially provide a totally new insight into the aurora and hence to the related magnetospheric dynamics. A lot of new opportunities for VLF emissions and magnetic pulsation investigations can be found as well. Autoregression model-based spectral analysis reveals very fine details of VLF chorus spectral and time structure, and can be compared only to direct chorus waveforms study. Using wavelet transform for image compression and filtering (that is a fundamental part of modern JPEG-2000 standard) is rather useful for Fabry-Perot interferometer data processing.

**Acknowledgments**. The authors thank Prof. D. A. Gurnett and J. S. Pickett for preparing the fragments of Cluster WBD chorus data and S. V. Leontyev for Fabry-Perot interferometer images.

## References

Allan, V. Oppenheim, editor, Applications of digital signal processing. *Jr. Prentice – Hall, Inc., Englewood Cliffs, New Jersey*, 1978

Batten, S. and Rees D., Thermospheric winds in the auroral oval observations of small-scale structures and rapid fluctuations by a Doppler Imaging System, *J. Geophys. Res., 38*, 675, 1990.

Belyaev, P. P., S. V Polyakov, V. O. Rapoport. and V. Y. Trakhtengerts, Ionospheric Alvfen resonator. *J. Atmos. Terr. Phys., 52*. 781, 1990.

Belyaev, P. P., S. V. Isaev, V. Yu. Trakhtengerts, T. Bosinger, and J. Kangas, First evidence at high latitudes for the ionospheric Alfven resonator, *University of Oulu. Report series in physical sciences. Rep. No 11*, 1997.

Fu, K. S., and C. S. G. Lee, Robotics: Control, Sensing, Vision and Intelligence. *McGraw-Hill-Book Company*, 1981.

IDL User's Guide. *Research Systems, Inc. Boulder, Colorado*. 1995.

Lawrence, S. Marple. Digital spectral analysis with applications, *Jr. Prentice – Hall, Inc., Englewood Cliffs, New Jersey*. 1979.

Leontiev, S. V., and N. N. Bogdanov, Vertical winds in the auroral zone in quiet and disturbed conditions, *"Physics of auroral phenomena", Proc. 23 Annual Seminar, Apatity*, 93, 20.

# Characteristics of auroral pulsations in diffuse luminosity during a substorm

T. A. Kornilova [1], I. A. Kornilov [1], and O. I. Kornilov [2]

[1] Polar Geophysical Institute, Apatity, Murmansk region, Russia
[2] Institute of Physics, St.Petersburg State University, St. Petersburg, Russia

**Abstract**. Using the method of TV image filtering, characteristics of auroral pulsations in diffuse luminosity situated southward of the discrete auroral form oval during a substorm were investigated. It was shown that three types of auroral pulsations may occur: (A) – arc-like filaments pulsating with the period of ~3–10s, (B) – auroral pulsations of the southern boundary of diffuse luminosity with the period of ~30–40s, (C) – auroral arc-like filaments pulsating with the period of 30–50s appearing in 30-70 s at the southern boundary of the localised region and spreading northward at the velocity of ~0.2–0.8 km/s simultaneously with the same structures appearing at the northern boundary while spreading southward. The regime of auroral pulsations could change in the course of the growth phase. Auroral activations inside discrete forms oval (breakup or pseudobreakup) result in the pulsating regime change or disappearance of auroral pulsations at the diffuse luminosity boundary. All three types of auroral pulsations are accompanied by geomagnetic ones of the same periods. Magnetospheric footprint of the auroral pulsation band with the average period of about 40s at the southern boundary of diffuse luminosity is located near the isotropy boundary (b2i) which is projected to the equatorward edge of the magnetotail current sheet. The period of auroral pulsations at the southern boundary changes synchronously with the movement of the boundary. The substorm expansive phase represented by extension of bright diffuse region having internal structure as patches and arc fragments is more often preceded by the auroral pulsations of (A) type. (B) and (C) types precede the expansive phase when poleward expansion looks like arc jumps into more polar latitudes.

## 1. Introduction

As it is known the diffuse luminosity is connected with unstructured precipitation of electrons and protons and it makes the main contribution to the energy balance of atmospheric radiation in the auroral zone [*Ponomarev*, 1985]. Energy characteristics of diffuse luminosity, its dynamics and relationship with electrojets and geomagnetic pulsations were investigated, for example, in [*Winningham et al*., 1975; *Lui et al.*, 1977; *Oguti*, 1980; *Galperin and Feldstein*, 1989; *Solovjev*, 1991; *Yamamoto et al.*, 1991; *Tagirov*, 1993]. One of the most important questions yet discussed is what regions of the magnetosphere are projected to the polar aurora oval and diffuse luminosity region [*Galperin and Feldstein*, 1989; *Yahnin et al.*, 1977; *Vorobjev et al*, 2000]. However, independently of the region where the diffuse luminosity is mapped, the processes occurring inside the diffuse luminosity surely are connected with the substorm development. In this paper using TV auroral data we investigate the behaviour of auroral pulsations during the growth phase of substorm and its relationship with the explosive phase onset.

## 2. Experimental data and analysis

Experimental data used in this study were the following:

1. TV auroral data from Porojarvi (65.6°N, 105.9°E), Kalkkoaivi (65.6°N, 105.4°E), Lovozero (64.07°N, 114.7°E) and Loparskaya (64.7°N, 116.3°E) during Russian-Finnish experiments in 1993–1995, 1997 as well as during continuous observations in 1996–1998 at Lovozero and Loparskaya.
2. Geomagnetic pulsations data of Sodankyla and Lovozero observatories.
3. Scandinavian IMAGE Magnetometer Network data.

4. The DMSP satellites data on the precipitation boundary of auroral particles.

TV data discussed in this paper were processed by a very simple and efficient gradient filtering [*Kornilov I. and Kornilov O.*, 1997] which allowed to reveal fine effects in the dynamics and structure of diffuse luminosity.

The advantage of the gradient filtering method can be seen in Figure 1, where (a) is a standard keogram, (b) and (c) are space and time gradient keograms respectively. Keograms demonstrate a fragment of aurora development at Lovozero on February 8, 1997. Vertical scale is given in zenith angles. Arrow $T_o$ marks the breakup onset. Space gradient filtering (Figure 1b) allows us to reveal fine effects in the northern-southern aurora motion and to notice the stable south boundary of diffuse luminosity, which is hardly visible in a standard keogram.

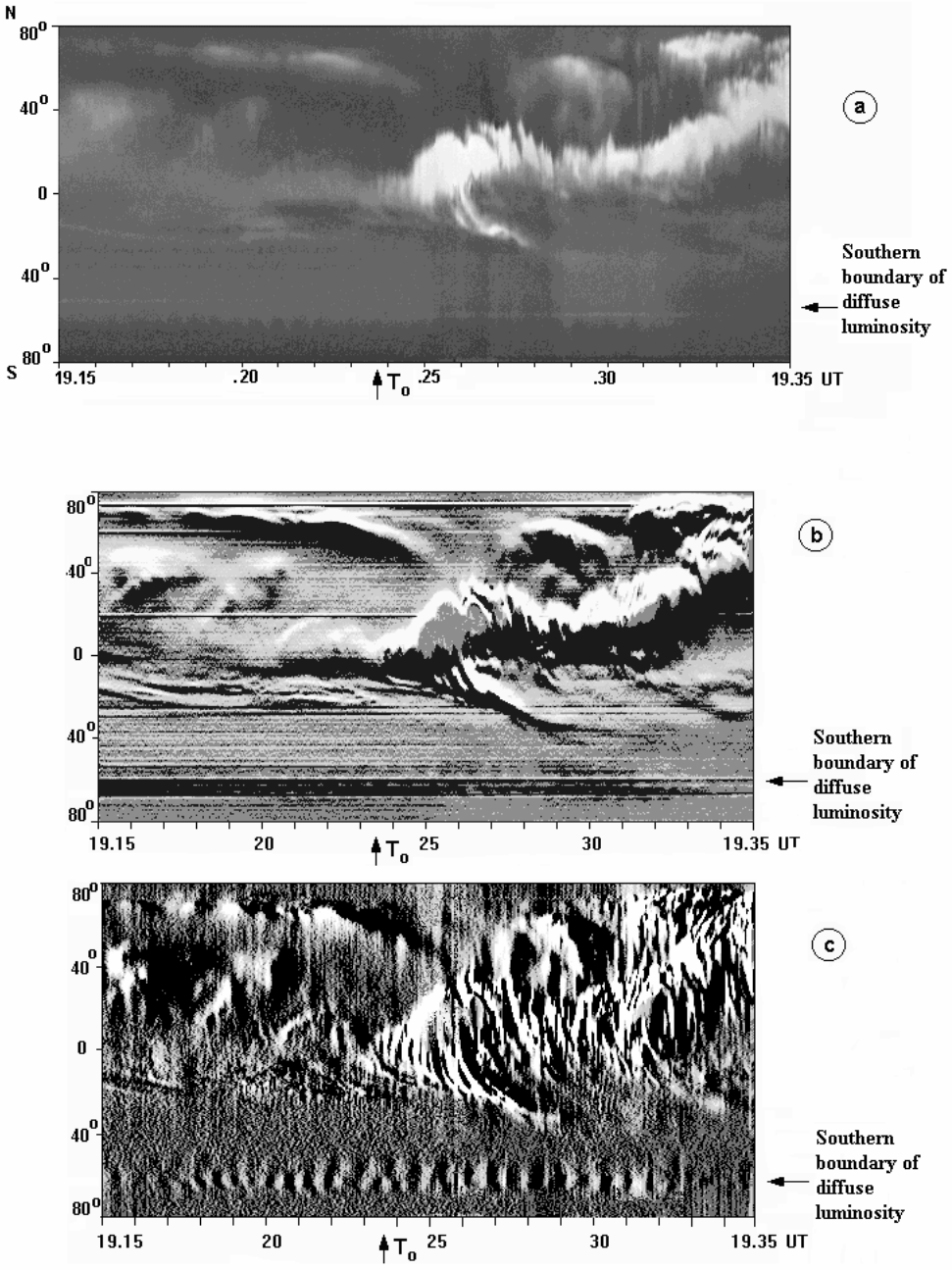


**Figure 1.** Substorm development on February 8, 1997 in Lovozero. (a) is a standard keogram, (b) is a space gradient keogram, (c) is a time gradient keogram.

The time gradient keogram (Figure 1c) shows luminosity pulsations of auroral structures inside the discrete forms oval as well as in the diffuse luminosity. Auroral pulsations are clearly seen at the immovable southern boundary of diffuse luminosity. Data analysis of 18 substorms reveals three types (A, B, C) of auroral pulsations occurring in diffuse luminosity in the course of the growth phase.

### 3. Auroral pulsation types

Pulsations of (A) type represent arc-like filaments pulsating with the period of ~3–10s, moving (northward/southward) or motionless inside diffuse luminosity. One can see pulsations of (A) types in Figure 2, which shows standard keogram of aurora development on November 19, 1995 at Porojarvi (a) and three consecutive time gradient keograms for interval 2020–2050 UT (b). Southern boundary of diffuse luminosity is marked by horizontal arrows on the right. As it can be seen from time gradient keograms there are a lot of auroral pulsations of different periods in various auroral regions. Pulsations of (A) type are situated between the auroral arc and the southern boundary of diffuse luminosity. They disappear after breakup onset $T_o$.

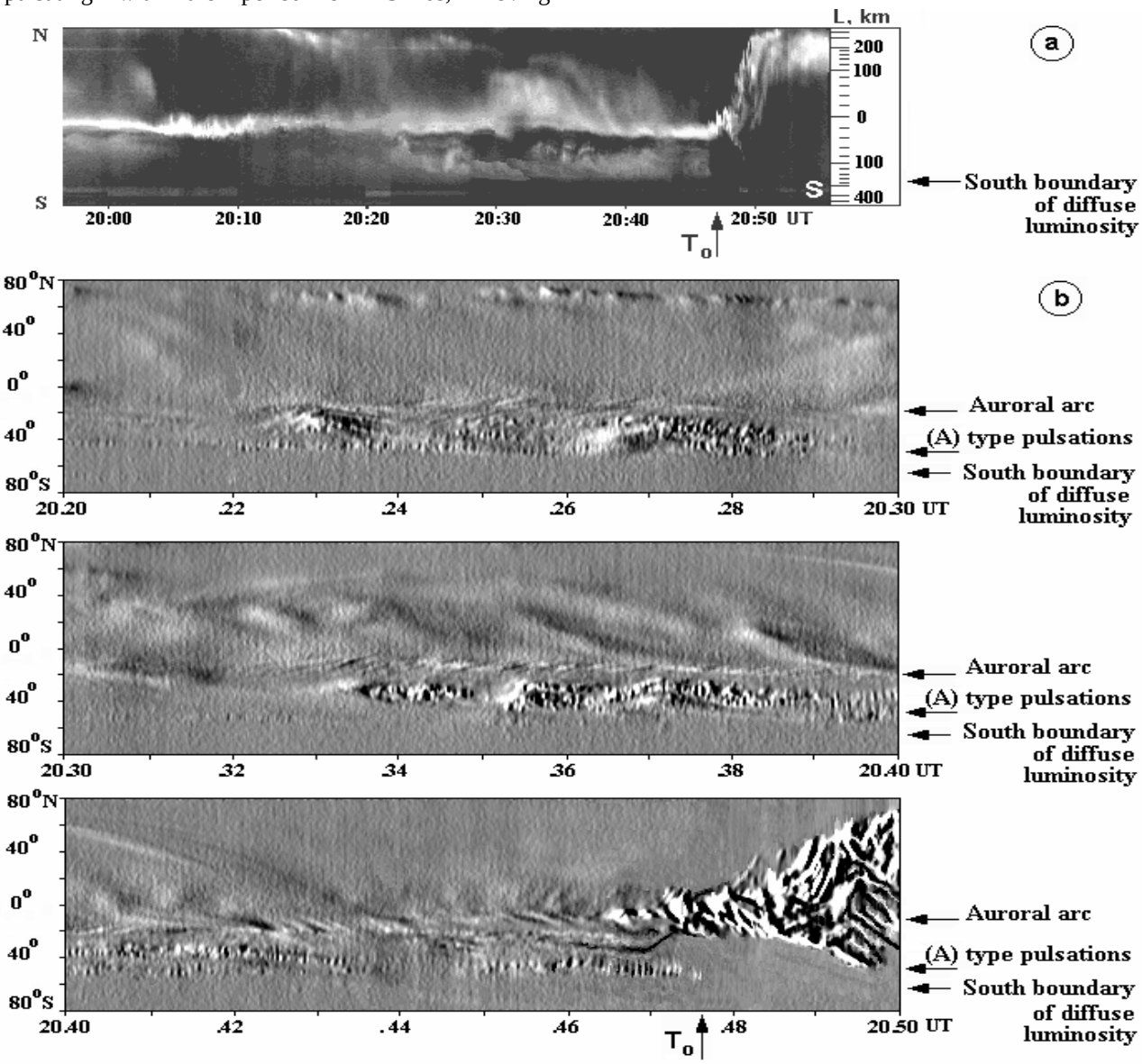


**Figure 2.** Substorm development on November 19, 1995 in Porojarvi. (a) is a standard keogram, (b) is time gradient keograms for three consecutive time intervals.

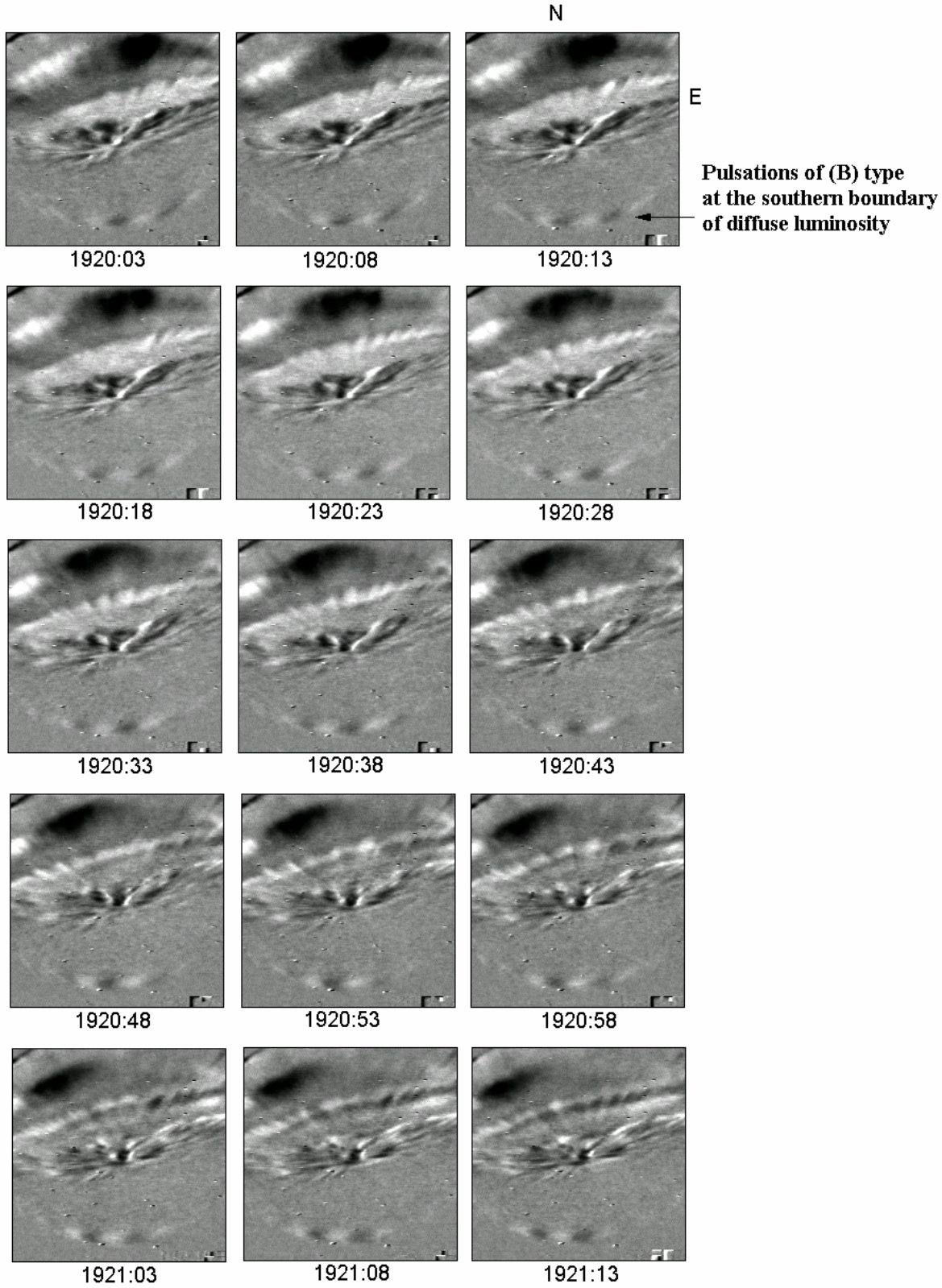


**Figure 3.** Filtered frames for time interval 1920:03–1921:13UT on February 8, 1997 at Lovozero.

Pulsations of (B) type are auroral pulsations of the southern boundary of diffuse luminosity with the period of ~ 30–40s. An example of (B) type pulsations can be seen in Figure 1*c*. They represent the change of luminosity brightness of the southern boundary. Filtered frames for time interval 1920:03 – 1921:13UT on February 8, 1997 at Lovozero are shown in Figure 3. The position of the southern boundary is marked by a horizontal black arrow (top right frame).

On the frames one can see the periodical variations of luminosity at the diffuse aurora south boundary. One can see no spatial motion, only temporal variations of brightness (some kind of standing waves).

Pulsations of (C) type are auroral arc-like filaments pulsating with the period of 30–50*s* inside a well localised region inside diffuse luminosity. This region usually represents a band with the width of 100–200 km stretched along the geomagnetic latitude. Pulsating with the period of 30–50*s* arc-like filaments emerge in 30-70*s* at the southern boundary of the region localised in the diffuse luminosity and move to the northern boundary at the velocity of 0.2–0.8 km/s. Simultaneously, the same pulsating filaments appear at the northern boundary of the localised region and move southward. As a result, an intricate interference picture is formed looking like waves moving behind the ship and reflected from the walls of the channel. An example of (C) type pulsations is given in Figure 4. It shows the substorm development on March 26, 1998 in Lovozero, where (a) is a standard keogram, (b) is the time gradient keogram. Figure 4*b* shows pulsations occurring before the breakup onset in the time interval of 2000:00-2017:40UT in diffuse band (its position is marked by the vertical bar on the left in Figure 4b) situated at the distance of 17–47° of zenith angle southward of zenith. These pulsations look like waves simultaneously emerging in ~50*s* at the northern and southern boundaries of the diffuse band and moving toward the opposite boundary of it. The period of brightness luminosity changes in the waves is about 30*s*.

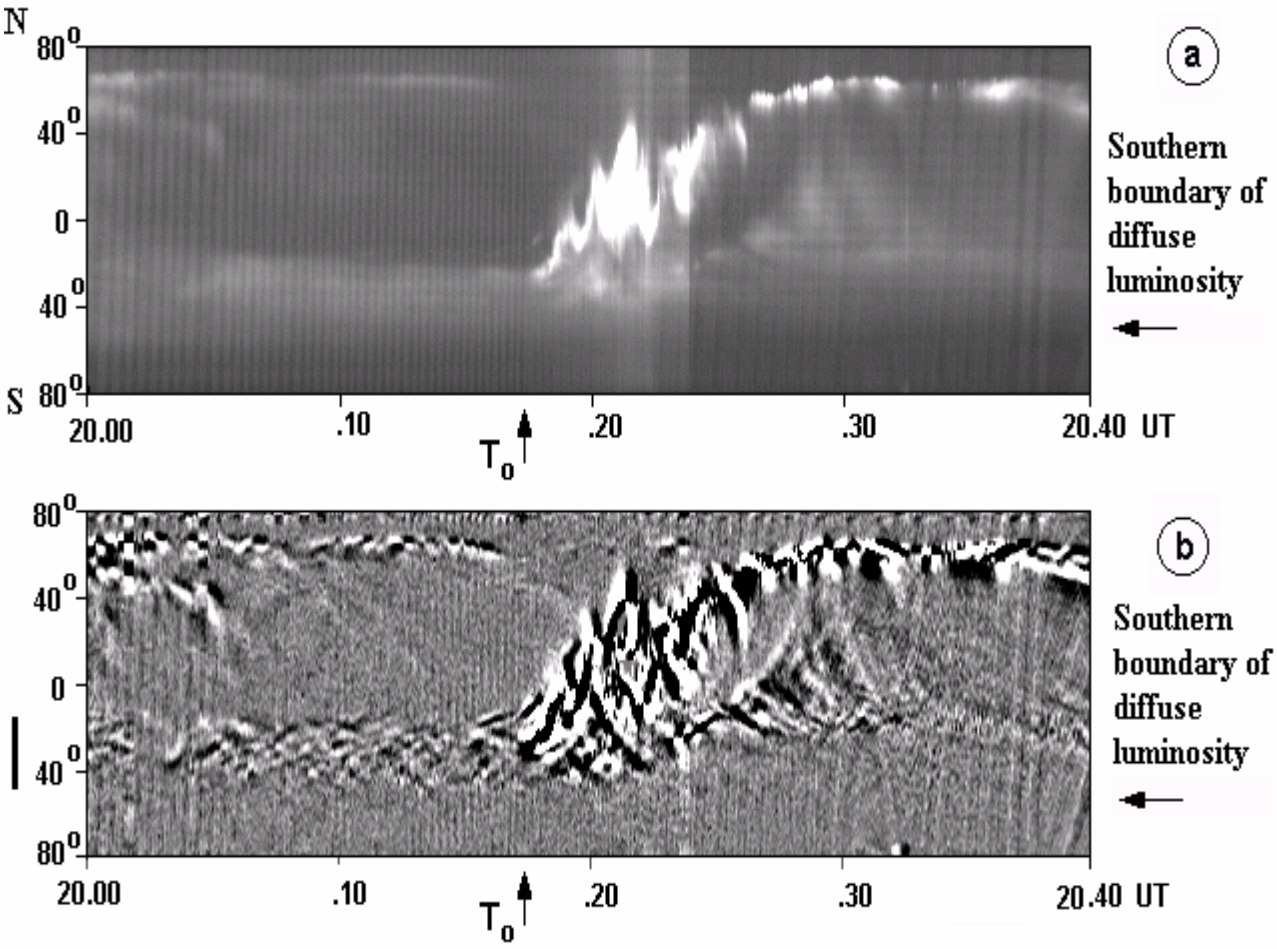


**Figure 4.** Substorm development on March 26, 1998 in Lovozero. (a) is a standard keogram, (b) is a time gradient keogram.

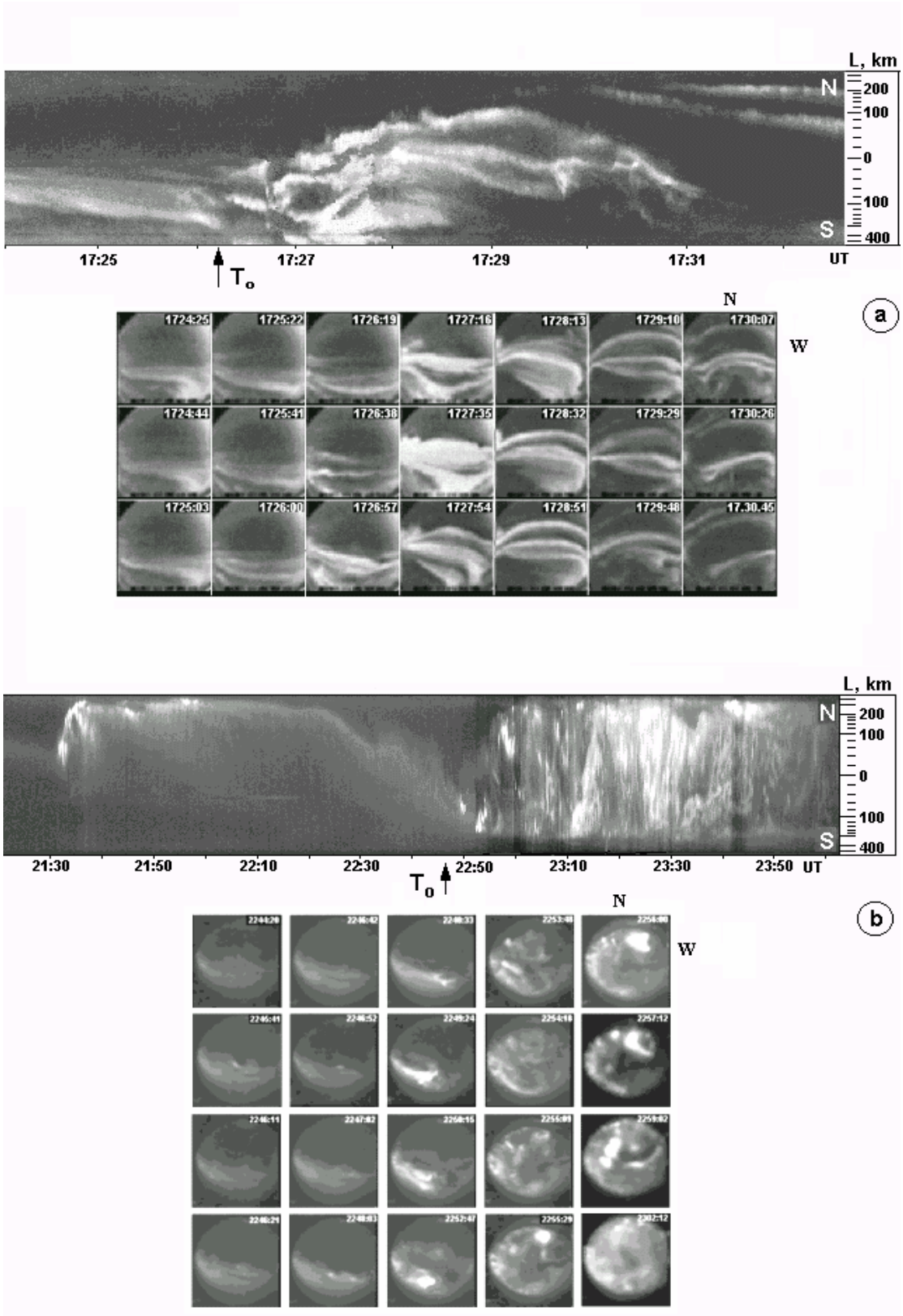


**Figure 5.** Two examples of the poleward expansion. a – Poleward expansion of the first type observed on October 7, 1994 at Kalkkoaivi. b – Poleward expansion of the second type observed on December 9, 1996 at Loparskaya.

**4. Peculiarities of pulsations behaviour**

1. The characteristic feature of auroral pulsations in the diffuse luminosity is the change of pulsation type during the growth phase.
2. During the growth phase the period of auroral pulsations at the southern boundary of diffuse luminosity changes synchronously with the boundary movement: The southward motion of the boundary accompanied by a shortening of the period, during the northward drift period increases.
3. Auroral pulsations at the southern boundary of diffuse luminosity usually disappear after the breakup onset.
4. The comparison of auroral pulsations in diffuse luminosity with geomagnetic ones with the help of the wavelet analysis of spectrum-time structure of geomagnetic pulsations showed that in the spectrum of geomagnetic pulsations there are pulsations of the same period as auroral ones.
5. In all cases under consideration the band of auroral pulsations of (B) type with the average period of about 40*s* was registered just equatorward the isotropy boundary (b2i). According to the nightside boundary identifications given in [*Feldstein and Galperin*, 1996; *Newell et al.*, 1998], (b2i) boundary is the best for the location of the equatorward edge of the current sheet.

Some attempt to reveal the relationship between types of auroral pulsations in diffuse luminosity during the growth phase and types of aurora poleward expansion during the active phase was done. Two types of auroral poleward expansion during substorm explosive phase are described in [*Kornilova et al.*, 2003]. *The first type* of poleward expansion representing leaps of arcs into higher latitudes is shown in Figure 5*a* (top panel is a standard keogram, the next panel is TV frames of the same time interval on October 7, 1994 at Kalkkoaivi). *The second type* of expansion is shown in Figure 5*b* (plots are the same as in Figure 5*a* but for December 9, 1996, Loparskaya). It looks like the spread of bright diffuse region with internal structure consisting of patches and rotating arc fragments.

Data analysis has shown that poleward expansion of *the first typers* usually preceded by pulsations of (B) and (C) types, poleward expansion of *the second type* is preceded by pulsations of (A) type.

**3. Summary and conclusions**

The auroral pulsations in diffuse luminosity situated southward of the discrete auroral form oval were studied using the methods of TV images filtering. This method allowed to reveal earlier unknown fine effects in the dynamics and brightness variations of diffuse luminosity. Results of these studies can be summarised as follows:

1. During the growth phase one of the three types of auroral pulsations (A, B, or C) may occur. (A) – arc-like filaments pulsating with the period of ~3–10*s* inside diffuse luminosity, (B) – auroral pulsations of the southern boundary of diffuse luminosity with the period of ~30–40*s*, (C) – auroral arc-like filaments pulsating with the period of 30–50*s* and appearing in 30–70*s* at the south boundary of the region localised inside diffuse luminosity and spreading northward simultaneously with the same structures appearing at the north boundary and drifting southward.
2. The type of auroral pulsations could change in the course of the substorm growth phase. Auroral activations (breakup or pseudobreakup) inside discrete forms oval result in the pulsating regime change or disappearance of auroral pulsations at the diffuse luminosity boundary. All three types of auroral pulsations may be accompanied by geomagnetic ones of the same periods. The band of auroral pulsations with the period of 30–40*s* at the southern boundary of diffuse luminosity is located near the isotropy boundary (b2i) which is projected to the equatorward edge of the magnetotail current sheet. The period of auroral pulsations at the southern boundary changes synchronously with the movement of the boundary.
3. Different types of poleward expansion during substorm explosive phase are preceded by different types of pulsations at the growth phase. Poleward expansion represented by leaps of arcs into more high latitudes is usually preceded by pulsations of (B) and (C) types, poleward expansion looking like the spreading of bright diffuse region with internal structure is preceded by pulsations of (A) type.

**Acknowledgements.** The IMAGE magnetometer data were collected as a Finnish-German-Norwegian-Polish-Russian-Swedish project conducted by the Technical University of Braunschweig. We thank Sodankyla Geophysical observatory and Johannes Kultima for geomagnetic pulsations data. The DMSP particle detectors were designed by Dave Hardy of AFRL and data obtained from JHU/APL. We thank Dave Hardy, Fred Rich and Patrick Newell for their use. This paper was supported by the Russian Foundation for Fundamental Research by grant 02-05-64807.

**References**


Feldstein, Ya. I., and Yu. I. Galperin, Structure of the auroral precipitations in the nightside sector of the magnetosphere, *Cosmic research*, *34*, 227, 1996.

Galperin, Yu. I., Ya. I. Feldstein, Diffuse auroral zone. X. The nightside diffuse auroral zone, auroral oval of discrete forms and diffuse luminosity poleward from the oval, as the projections of the plasma domains of the magnetospheric tail, *Cosmic investigations*, *27*, 6, 890, 1989.

Kornilov, I. A., O. I. Kornilov, Computer-based equipment for TV, VLF, magnetic and other videotape recorded data processing, in *Instruments and methods of geophysical experiment*, Edited in PGI, Apatity, 91, 1997.

Kornilova, T. A., I. A. Kornilov, M. I. Pudovkin, O. Kornilov, Two types of auroral development during substorm explosive phase, *Geomagnetism and aeronomy*,. *43*, 1, 40, 2003.

Lui, A. T. Y., D. Venkatesan, C. D. Anger et al., Simultaneous observations of particle precipitation and auroral emission by the ISIS-2 satellite, *J. Geophys. Res*., *82*, 2210, 1977.

Newell, P. T., V. A. Sergeev, G. R. Bikkuzina, S. Wing, Characterizing the state of the magnetosphere: testing the ion precipitation maxima latitude (b2i) and the ion isotropy boundary, *J. Geophys. Res.*, *103*, 4739, 1998.

Oguti, T., S. Kokubun, K. Hayashi, K. Tsuruda, S. Mschida, T. Kitamara, O. Saka, T. Watanabe, Statistics of pulsating auroras on the basis of all-sky TV data from five stations. I. Occurrence frequency, in *Pulsating Aurora Campaign 1980*, spesial issue of the *Canadian Journal of Physics*, August 1980, 1150, 1980.

Ponomarev, E. A., Mechanisms of the magnetospheric substorms, M.: *Nauka*, 159 p., 1985.

Solovjev, S. I., E. S. Barkova, N. E. Molochushkin, S. N. Samsonov, Formation of undulation structures at the high latitude boundary of diffuse aurora of Ps6, Pc5 pulsation during the magnetic storm of January 31, 1989, *XX General Assembly IUGG, Vienna, Austria, August*, 248, 1991.

Tagirov, V. R., Auroral torch structures: results of optical observations, *Journ. Atmosph. Terrestr. Physics*., *55*, 1775, 1993.

Vorobjev, V. G., L. I. Gromova, B. V. Rezhenov, G. V. Starkov, Ya. I. Feldstein, Variations of location of plasma penetration boundary and auroral luminosity in the night sector, *Geomagnetism & Aeronomy*, *40*, 3, 79, 2000.

Winningham, J. D., F. Yasuhara, S. -I. Akasofu, W. J. Heikkila, The latitudinal morphology of 10 eV to 10 KeV electron fluxes during magnetically quiet and disturbed times in the 2100−0300 MLT sector, *J. Geophys. Res., 80*, 3148, 1975.

Yahnin, A. G., V. A. Sergeev, B. B. Gvozdevsky, S. Vennerstrom, Magnetospheric source region of discrete auroras inferred from their relationship with isotropy boundaries of energetic particles, *Ann. Geophys., 15*, 943, 1997.

Yamamoto, T., K. Makita, C. -I. Meng, A particle simulation of large-amplitude undulations on the evening diffuse auroral boundary, *J. Geophys. Res.*, *96*, 1439, 1991.

# Three-dimensional direction and location determination of AKR sources

M. Panchenko

Space Research Center PAS, Toruń, Poland

**Abstract.** The method of AKR (auroral kilometric radiation) direction determination onboard spinning satellite is proposed. It is based on the measurements of radiation power density registered by three orthogonal antennas with the assumption that the AKR is circularly polarized. This method is applied for determination of AKR source locations with Polrad spectro-polarization measurements onboard INTERBALL-2 satellite. The obtained source locations projected along the magnetic field lines onto the ionosphere correlate with the locations of active auroral arcs observed by Polar UV imager.

## 1. Introduction

The aim of this paper is to present the method of the AKR source direction determination.

One of the first measurements of the AKR's origin location were provided by *Kurth et al.* [1975] from HAWKEYE-1 and IMP-8 data. Their direction-finding method was based on the analysis of spin-modulated electric field intensities. This method was also applied to the data from lunar-orbiting RAE-2 [*Kaiser and Alexander*, 1977] and from ISIS-1 spacecraft [*James*, 1980]. *Huff* et al. [1988] provided more precise measurements of AKR source locations, performed by DE-1 satellite. They used the method proposed by *Calvert* [1985], which was based on the measurements of relative phases of the signals, received by two orthogonal antennas.

However, these methods need more than one spin period of observations and can be used only when spin axis of the antenna system is approximately orthogonal to the presumed source direction.

Polarization measurements of the AKR with two spinning orthogonal antennas [*Manning and Fainberg*, 1980] provide a method, which does not have these limitations. More reliable measurements of the wave direction can be obtained from analysis of the wave distribution function (WDF), which is calculated from simultaneous waveforms of magnetic and electric wave field components [*Morioka et al.*, 1998; *Lefeuvre et al*., 1990; *Parrot et al.* 2001; *Schreiber et al.,* 2002]. This method however needs transmission of a huge stream of data, and therefore is usually limited to very short time intervals of observations.

The method proposed in this paper is based only on three simultaneous measurements of intensities of the AKR electric field components received by three orthogonal antennas. The main assumption is that the AKR is fully circularly polarized. This method has time resolution of a single measurement. It has been applied to AKR observations provided by Polrad experiment onboard INTERBALL-2 (Auroral Probe) satellite.

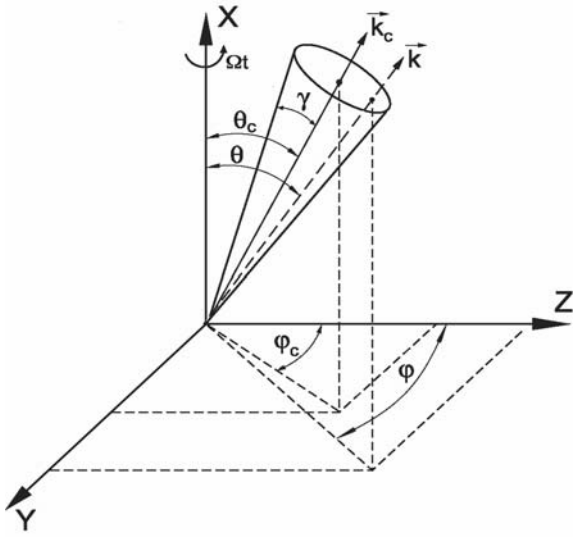


**Figure 1.** A conical uniform source of emission with half angular width $\gamma$ in the spacecraft coordinates. $\theta_c$ and $\varphi_c$ – direction angles of the source center vector $\mathbf{k}_c$; $\theta$ and $\varphi$ – direction angles of the given source point vector $\mathbf{k}$; the antennas are deployed along axes *X*, *Y* and *Z*; axes *Y* and *Z* rotate around *X* with an angular frequency $\Omega$.

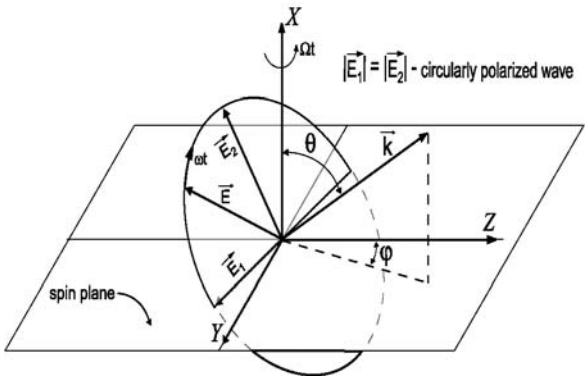


**Figure 2.** Geometry of a circularly polarized wave in the antenna coordinates.
**k** – direction vector of a given source point; $\mathbf{E} = \mathbf{E}_1 \cos(\omega t + \phi) + \mathbf{E}_2 \sin(\omega t + \phi)$, $\omega$ – wave angular frequency; $\theta$ and $\varphi$ – wave direction angles.

Polrad was a step-frequency analyzer operating in a frequency range from 4 to 1000 kHz with resolution of 4 kHz and sweep period 6 or 12 s [*Hanasz, et al*., 1998]. The antenna system of Polrad consists of three short electric antennas (X, Y, Z) orthogonal to each other. It is spinning around X antenna with angular frequency $\Omega$ (spin period 120s). Polrad was operated only in the northern hemisphere, in all magnetic local times (MLT), invariant latitudes (invLat) between 60º and 82º, and at the altitudes between 15000 km and 19000 km, so that the AKR sources were located at altitudes below the spacecraft.

## 2. Theory

In a spacecraft coordinate system (Figure 1) three antennas are deployed along *X, Y* and *Z* coordinate axes. A normalized vector **A** represents these antennas and is defined as $\mathbf{A} = a_1\mathbf{i} + a_2\mathbf{j} + a_3\mathbf{k}$, where $a_1$, $a_2$ and $a_3$ are effective antenna lengths. In our case $a_1 = a_2 = a_3 = 1$.

Let the antenna system receive a circularly polarized wave from a given point of the uniform conical source with a half angular width $\gamma$. The vector $\mathbf{k}_c(\theta_c, \varphi_c)$ represents the source center. $\mathbf{k}(\theta, \varphi)$ is the direction vector of the wave emitted from a given point of the source $(\theta, \varphi)$. Then, the electric vector **E** traces out a circle in a plane $\perp\mathbf{k}$ and can be described by two orthogonal components (see Figure .2):

$$\mathbf{E} = \mathbf{E}_1 \cos(\omega t + \phi) + \mathbf{E}_2 \sin(\omega t + \phi) \qquad (1)$$

For a circularly polarized wave $|\mathbf{E}_1| = |\mathbf{E}_2|$.

In the antenna coordinate system the vectors $\mathbf{E}_1$ and $\mathbf{E}_2$ can be expressed by angles $\theta$ and $\varphi$:

$$\mathbf{E}_1 = E_0\,[0,\ \cos\varphi,\ -\sin\varphi] \qquad (2)$$
$$\mathbf{E}_2 = E_0\,[\sin\theta,\ \cos\theta\sin\varphi,\ \cos\theta\cos\varphi]$$

The open-circuit voltage on antennas from a given point of the source $(\theta, \varphi)$ is:

$$dV = \mathbf{E}\ \mathbf{A} \qquad (3)$$

The instantaneous power density of the wave is:

$$dP_{ins} = Z_0\,(dV)^2 \qquad (4)$$

where $Z_0$ is impedance of vacuum.

The time-averaged $dP_i$ will be:

$$dP = \langle dP_{ins} \rangle =$$
$$= \frac{1}{T}\int_{-T}^{T} dP_i\,dt = \frac{1}{2} Z_0\,((\mathbf{E_1}\ \mathbf{A})^2 + (\mathbf{E_2}\ \mathbf{A})^2) \qquad (5)$$

The total power density of the source can be expressed as the integral over the source surface:

$$P = \frac{1}{2\pi(1-\cos\gamma)} \int\int_S dP\,d\varphi \sin\theta\,d\theta \qquad (6)$$

where S - means an angular surface of the source.

In order to evaluate the integral (eq.6) we rotate the coordinate system in two steps: 1) around $X$ axis by an angle $\varphi_c$, 2) around $Y$ axis by an angle $\theta_c$. These rotations will be described by $\hat{M}_x$ and $\hat{M}_y$ matrixes. In the new coordinate system the integral (eq.6) is:

$$P = \frac{Z_0}{4\pi(1-\cos\gamma)} \int_0^{\gamma}\int_0^{2\pi} \left(\left(\hat{M}_y \hat{M}_x E_1 A\right)^2 + \right. \qquad (7)$$
$$\left. + \left(\hat{M}_y \hat{M}_x E_2 A\right)^2 d\,\varphi \sin\theta\,d\theta \right.$$

The total power densities received by the antennas are:

$$P_x = \frac{1}{4} Z_0 E_0^2 \times \qquad (8)$$
$$\times \left[\sin^2\theta_c (1+D) + 2\cos^2\theta_c (1-D)\right]$$

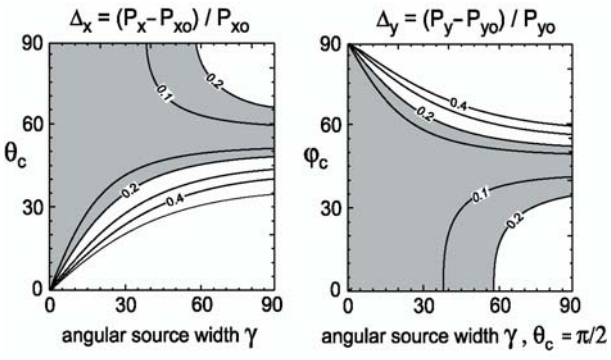


**Figure 3.** Relative differences between power densities for approximation of an extended source (eq.8) and a point source (eq.9). The shaded regions represent the range of the angles $\theta_c$, $\varphi_c$, $\gamma$ where $\Delta_x$ and $\Delta_y$ are less than the relative power fluctuation for a single measurement ($\Delta_{x,y} < \Delta P/P \approx 0.2$) and point source approximation can be applied.

$$P_x = \frac{1}{4} Z_0 E_0^2 \left[ \left( \cos^2 \varphi_c + \cos^2 \theta_c \sin^2 \varphi_c \right)(1+D) + \right.$$
$$\left. + 2 \sin^2 \varphi_c \sin^2 \theta_c (1-D) \right]$$

$$P_x = \frac{1}{4} Z_0 E_0^2 \left[ \left( \sin^2 \varphi_c + \cos^2 \theta_c \cos^2 \varphi_c \right)(1+D) + \right.$$
$$\left. + 2 \cos^2 \varphi_c \sin^2 \theta_c (1-D) \right]$$

where $D = (1-\cos^3 \gamma)/(3-3\cos\gamma)$.

For the point source approximation $\gamma = 0 \rightarrow$ D=1 the eq.8 will be:

$$P_x = \frac{1}{4} Z_0 E_0^2 \sin^2 \theta_c$$
$$P_x = \frac{1}{4} Z_0 E_0^2 \left( \cos^2 \varphi_c + \cos^2 \theta_c \sin^2 \varphi_c \right) \quad (9)$$
$$P_x = \frac{1}{4} Z_0 E_0^2 \left( \sin^2 \varphi_c + \cos^2 \theta_c \cos^2 \varphi_c \right)$$

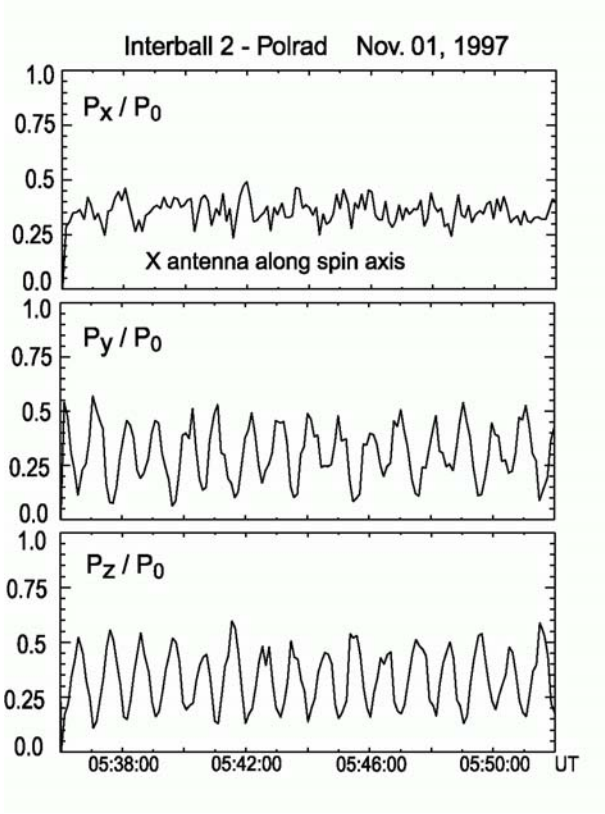


**Figure 4.** The normalized power densities averaged over frequency range 340-360 kHz. $P_0$ is the total power density: $P_0=P_x+P_y+P_z$; $P_y/P_0$ and $P_z/P_0$ are modulated due to spacecraft spin.

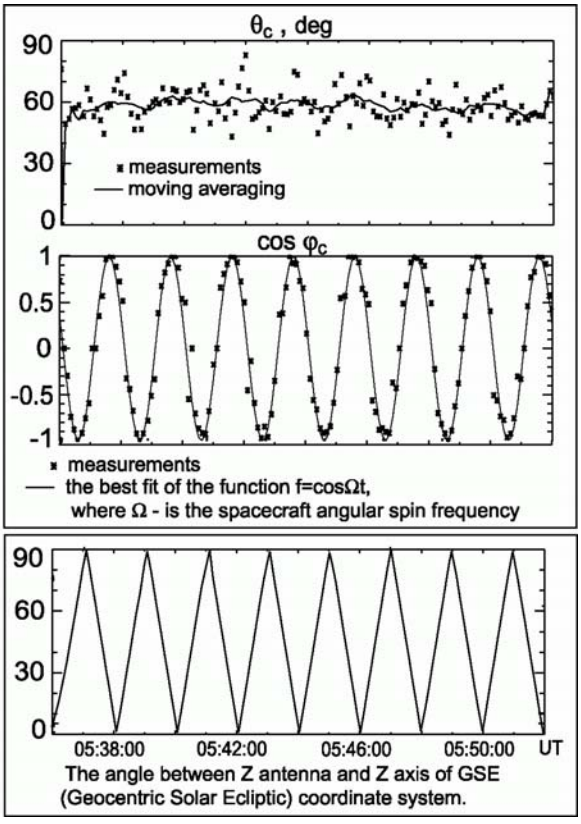


**Figure 5.** Determination of direction angles $\theta_c$ and $\varphi_c$ in the spacecraft frame. The bottom panel shows the attitude of the Z antenna in GSE coordinates.

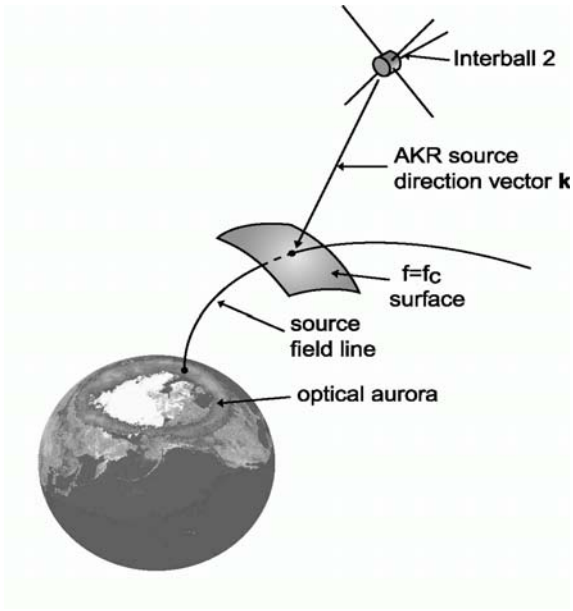


**Figure 6.** Principle of AKR source location [*after Huff et al.,* 1988]. The source field line is found by means of intersection of the AKR source direction **k** and the plane where the local gyro-frequency is equal to the frequency of the observed wave.

In order to decide when we can assume the point source approximation (eq.9) we define a fluctuation of the received signal $P$ as $\Delta P / P = 1/\sqrt{\Delta f \tau}$, where $\Delta f$ is the receiver bandwidth and $\tau$ its time constant. For a single measurement of the Polrad spectro-polarimeter they are: $\Delta f$ = 4096 Hz, $\tau$ = 0.006s and $\Delta P / P \approx 0.2$. Applicability of the point source approximation can be described by the parameter $\Delta_i = (P_i - P_{i0}) / P_{i0}$ ($P_i$ is the power density of the signal from the extended source (equation 8), $P_{i0}$ is the power density for the point source approximation (equation 9) and *I=X, Y, Z*). For the $X$ antenna $\Delta_x$ depends only on elevation of the source center $\theta_c$ and half angular source width $\gamma$. This dependence is shown in the left panel of Figure 3. For the $Y$ antenna the parameter $\Delta_y$ is a function of three angles: $\theta_c, \varphi_c, \gamma$. For value of $\theta_c = \pi/2$ this dependence is shown in right panel of Figure 3. The shaded regions in these plots represent the ranges of angles $\theta_c, \varphi_c$ and $\gamma$ where $\Delta_i$ parameters are less than fluctuation level of the single measurement of Polrad receiver, $\Delta P / P \approx 0.2$. Point source approximation can be applied to these ranges.

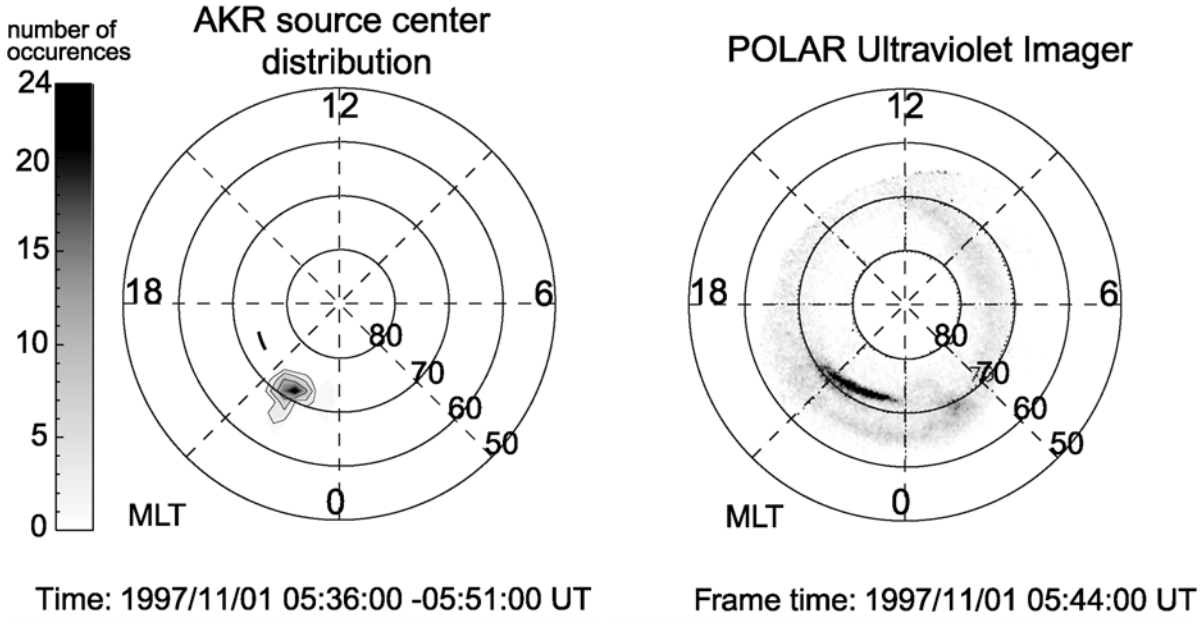


**Figure 7.** Occurrence frequency of AKR source center position projected along magnetic field lines onto the ionosphere (left panel) for the event of November 1, 1997. The solid line indicates the segment of the INTERBALL–2 orbit in a period of measurement. The source center distribution is compared with ultraviolet auroral observations, provided by Polar satellite (right panel).

### 3. Determination of the AKR source location

Application of the method is illustrated by the AKR event on November 1, 1997, 05:36 – 05:51 UT. Assuming that the AKR is circularly polarized and originates from a point source the response of the Polrad antenna system to AKR is described by equation 9. Figure 4 shows normalized power densities of AKR ($P_x / P_0$, $P_y / P_0$, $P_z / P_0$) averaged over frequency range 340–360 kHz.

From equation 9 the direction of the source center ($\theta_c, \varphi_c$) is determined in the spacecraft coordinates for each measurement of the AKR ($P_x$, $P_y$, $P_z$):

$$\begin{aligned} \cos^2\theta_c &= (P_0 - 2P_x)/P_0 \\ \cos^2\varphi_c &= (P_0 - 2P_z)/2P_x \\ P_0 &= P_x + P_y + P_z = Z_0 E_0^2 \end{aligned} \qquad (10)$$

From eq.10 four solutions of the source center vector are obtained: $\mathbf{k}(\theta_c, \varphi_c)$, $\mathbf{k}(\theta_c, -\varphi_c)$, $\mathbf{k}(-\theta_c, \varphi_c)$ and $\mathbf{k}(-\theta_c, -\varphi_c)$. We choose two downgoing ones since the AKR propagates only upwards. From these two vectors we select only that one which points towards the auroral invariant latitudes. The direction angles ($\theta_c, \varphi_c$) of that vector are shown in top and middle panels of Figure 5.

For a given spacecraft attitude (bottom panel of Figure 5) we determine the direction vector of the source center $\mathbf{k}_c$ in GSE (Geocentric Solar Ecliptic) coordinate system.

Assuming that the AKR is originated at the altitudes where the local electron gyro-frequency $f_c$ is equal to the wave frequency, a source field line is found by means of intersection of the vector $\mathbf{k}_c$ with the model surface $f=f_c$. Then, the source field line is traced down to auroral altitudes (Figure 6). Gray scale in Figure 7 (left panel) indicates a number of source center footprints in a given bin (1° inv Lat × 4 m MLT) for the time interval of observation.

The obtained occurrence distribution of the source center footprints coincides with the active UV auroral arc observed by Polar (Figure 7 right panel). For several other cases the results are similar. However the method has some limitations. In some AKR events the determined source footprints do not coincide with the auroral arcs. One cause of errors is the source extension. The method cannot be applied when the extended AKR source is located close to the YZ antenna plane ($\theta_c \to \pi/2$) or along the antenna X ($\theta_c \to 0$) (Figure 3). Moreover, the errors strongly depend on the distance between the satellite and the source and also on their relative geometry. The deviation between radio and UV structures can be sometimes of the order of 10°.

### 4. Summary

1. The advantage of the presented method is that the source location can be determined at any time of observation by means of simultaneous measurements of the wave intensities by three orthogonal antennas. The basic assumption of the method is that the radiation is circularly polarized.
2. Footprints along magnetic field lines of the determined AKR source locations roughly coincide with active UV arcs.
3. The limitation of the method is that for some source positions (see Figure 2) the application of the point source approximation (equation 9) can lead to large errors.

**Acknowledgments.** The author thanks G. Parks and M. Brittnacher for being allowed to use the Polar imager UV data. N. Eismont and I. Belova from Space Research Institute RAN Moscow are gratefully acknowledged for providing attitude data for INTERBALL-2. The author wishes to extend special thanks to J. Hanasz for many helpful discussions and assistance in editing this paper.

This work was supported by the Polish Committee on Scientific Research, grant no. 5T12E 001 22.

### References

Calvert, W., DE-1 measurements of AKR wave direction, *Geophys. Res Lett., 12*, 381, 1985.

Hanasz, J., Z. Krawczyk, M. M. Mogilevsky et al., Observations of auroral kilometric radiation on the INTERBALL-2 satellite: The Polrad experiment, *Cosmic Res. (English transl.), 36*, 576, 1998.

Huff, R. L, W. Calvert, J. D. Craven, L. A. Frank, and D. A. Gurnett, Mapping of Auroral Kilometric Radiation sources to the aurora, *J. Geophys. Res., 93*, 11445, 1988.

James, H. G. Direction-of-arrival measurements of auroral kilometric radiation and associated ELF data from Isis 1, *J. Geophys. Res., 85*, 3367, 1980.

Kaiser, M. L., and J. K. Alexander, Source location measurements of terrestrial kilometric radiation obtained from lunar orbit, *Geophys. Res Lett., 3*, 37, 1976.

Kurth, W. S., M. M. Baumback, and D. A. Gurnett, Direction-finding measurements of auroral kilometric radiation, *J. Geophys. Res., 80*, 2764, 1975.

Lefeuvre, F., M. Parrot, J. L. Rauch, B. Poirier, A. Masson, M. Mogilevsky, Preliminary results from the MEMO multicomponent measurements of waves on-board INTERBALL 2, *Ann. Geophys., 16,* 1117, 1998.

Manning, R., J. Fainberg, A new method of measuring radio source parameters of a partially polarized distributed source from spacecraft observations, *Space Science Instrumentation., 5,* 161, 1980.

Morioka, A., H. Oya, K. Kobayashi, Polarization and mode identification of auroral kilometric radiation by PWS system onboard the Akebono (EXOS-D) satellite, *J. Geomagn. Geoelect., 42,* 443, 1990.

Parrot, M., F. Lefeuvre, J. L. Rauch, O. Santolik, M. M. Mogilevsky, Propagation characteristics of auroral kilometric radiation observed by the MEMO experiment on INTERBALL 2, *J. Geophys. Res., 106*, 315, 2001.

Schreiber, R., O. Santolik, M. Parrot, F. Lefeuvre, J. Hanasz, M. Brittnacher, and G. Parks, Auroral kilometric radiation source characteristics using ray tracing techniques, *J.Geophys. Res., 107*, 1381, 2002.

# ULF waves at very high latitudes

V. A. Pilipenko[1], N. V. Yagova[1], O. M. Chugunova[1], M. J. Engebretson[2], A. Rodger[3], and L. Lanzerotti[4]

[1] Institute of the Physics of the Earth, Moscow[2] Augsburg College, Minneapolis, MN
[3] British Antarctic Survey, Cambridge, UK
[4] AT&T Bell Laboratories, NJ

**Abstract.** Two new classes of ULF pulsations specific for the polar cap and still having no established physical understanding are analyzed using the data of magnetometer array in Antarctica. The first class comprises the polar geomagnetic variations in the period range 4–20 min, that have been designated as the cap associated Pi3 pulsations. Statistical 1D and 2D patterns of spectral power and coherence show an occurrence of intense, but low spatial coherent variations near the cusp projection and in the night side auroral region. At the same time, low amplitude Pi3 pulsations are very coherent throughout the polar cap and are decoupled from the auroral and cusp ULF activity. The primary sources of long-period polar pulsations are probably related to the magnetosheath turbulence or tail lobe oscillations. The search using the trans-Antarctic profile of magnetometers unexpectedly revealed additional region of the high Pc3–4 activity (~10–50 mHz) in the polar cap. This region corresponds to the morning flank of the magnetotail lobe. The groups of Pc3–4 emissions, related to the polar cap and to the cusp, have different characteristics, and, probably, are related to different mechanisms. Statistical diurnal variations confirm the occurrence of two sources of Pc3–4 activity. Thus, besides traditional channels of propagation of upstream turbulence to the ground (via the equatorial magnetosphere and the cusp), additional path - via the lobe/mantle may be possible.

## 1. Introduction: ULF pulsations at polar latitudes in Antarctica

The paucity of ULF studies at very high geomagnetic latitudes was partly due to a dominating view that the polar cap is a relatively quiet area and thus ULF variations in this region are merely a combination of residual cusp and auroral activity. However, the disturbances/waves in the turbulent flow in the magnetospheric boundary regions and magnetotail can be transported along stretched field lines into the polar ionosphere. The variations of boundary regions and magnetotail can be monitored with ground-based magnetic observations at polar latitudes.

Most studies of long-period ULF waves at the polar latitudes assumed that this ULF activity observed in the polar cap is a result of substorm/auroral activity extension poleward. However, the recent study of ULF disturbances at very high latitudes in the night time sector [*Yagova et al.,* 2002] indeed indicated the occurrence of pulsations specific for the polar cap. These quasi-periodic short-lived irregular variations have typical periods about 4–20 min, and because of their frequency range and waveforms they should be classified as Pi3 according to the ULF nomenclature. In the night time hours the cap pulsations were decoupled from the auroral activity in the same MLT sector.

The prevailing viewpoint is that the primary source of the Pc3–4 pulsations (10–100 mHz) is the turbulence upstream of the magnetospheric bow shock. This turbulence is assumed to be convected with solar wind plasma flow in the magnetosheath. Then, broadband waves from the turbulent magnetosheath penetrate in the equatorial magnetosphere and resonantly convert into Alfven field line oscillations. This resonant conversion mechanism acts as a natural band-pass filter producing narrow-band signals at low and middle latitudes. Additional source of broadband Pc3–4 activity is related to the dayside cusp/cleft projection. Thus, according to existing notions, narrow-band Pc3 pulsations cannot be formed in regions with open field lines, that is in the polar cap, where no field line Alfven resonances exist.

Nevertheless, in a case study of ULF pulsations at very high latitudes [*Chugunova et al.,* 2002] the events were found that revealed narrow-band Pc3-4 waves at geomagnetic latitudes up to 80°, deep in the polar cap. Narrowband Pc3 pulsations were found to be high not only in the dayside adjacent to the magnetopause, but even in the regions of magnetotail lobe. It was suggested that different channels of propagation of upstream

turbulence to the ground are possible: via the equatorial magnetosphere, the cusp (LLBL), and the lobe flanks.

In this paper we propose a technique, based on the cross-spectral analysis of 2D distributions of wave parameters from Antarctic stations, to distinguish unambiguously the specific polar cap Pi3 pulsations. Additionally, we verify the conclusions about two sources of Pc3–4 pulsations at very high latitudes made earlier on the basis of case study with the statistical analysis.

## 2. Observational facilities in Antarctica

The unique feature of the Antarctic array, not available in the Northern hemisphere, is the possibility to monitor simultaneously processes in the polar cap, auroral oval, and cusp.

To discriminate the specific cap Pi3 pulsations, we have compiled the comprehensive database of magnetic data from the 2D array of 16 available stations with flux-gate magnetometers at geomagnetic latitudes from –87° to –70° in Antarctica.

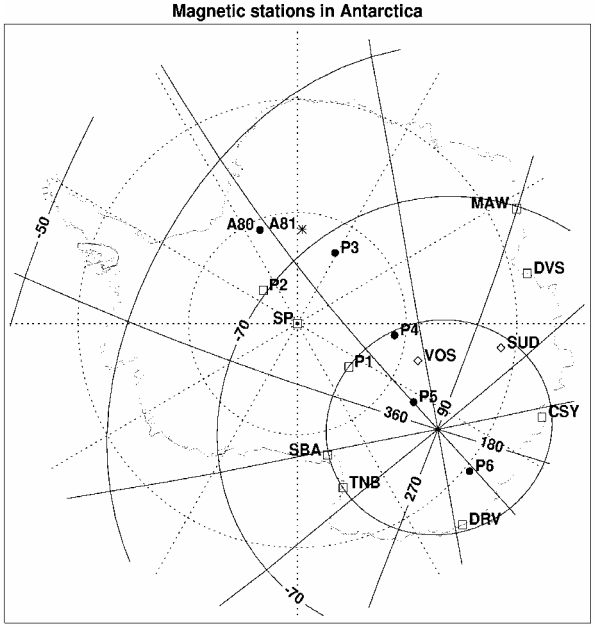


**Figure 1.** Antarctic array of magnetic stations.

The stations, shown in Figure 1, can be classified into 4 latitudinal groups: *polar* (Φ > 80°): P5, VOS, P6; *longitudinal profile along CGM latitude 80°*: P1, P4, SUD, CSY, DRV, TNB, SBA; *polar auroral* (74°–77°): MIR, SP, DVS; and *auroral* (~70°): A80, A81, MAW.

For Pc3–4 studies the *trans-Antarctic meridional array* of search-coil magnetometers (depicted by dark circles in Figure 1) along the CGM longitude ~40°: A80, P3, P4, P5, (MLT noon ~1400 UT), and continued by P6 across the pole, has been formed. Station A80 is mapped to the inner magnetosphere, P3 is mapped to the closed field line region adjacent to the magnetopause in the dayside sector, whereas P4, P5 are mostly on the open field lines.

## 3. Quasi-periodic long-period variations at polar latitudes: Pi3 pulsations

An example of long-period magnetic variations, detected on February 16, 1998 (DOY = 047) along the latitudinal array of flux-gate magnetometers A81–P4–P5–P6–DRV is shown in Figure 2. The quasi-periodic variations at ~04–08 UT we designate as Pi3 pulsations.

## 4. Spatial distribution of Pi3 power and invariant coherency in polar region

For estimate of coherency an advanced approach based on the use of cross-spectral matrix $\hat{C}$ of multi-component time series has been applied. The coordinate-

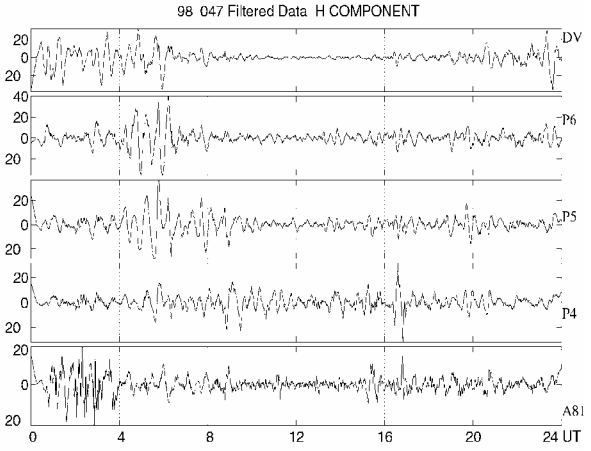


**Figure 2.** Example of Pi3 pulsations recorded along the Antarctic latitudinal array. Magnetograms have been detrended with cut-off period 30 min.

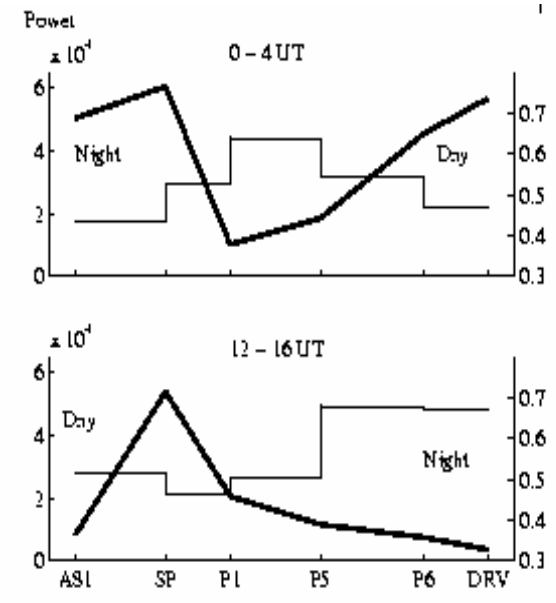


**Figure 3.** Variations of spectral power and inter-station coherency along the trans-Antarctic latitudinal profile.

invariant coherency $\gamma$ is introduced as a ratio of the intensity of the coherent part to the total intensity as follows $\gamma^2 = 1 - 4|\hat{C}|/Tr^2\hat{C}$, where $|\hat{C}|$ is the determinant and $Tr(\hat{C})$ is the trace of the cross-spectral matrix.

The main features of Pi3 distribution can be evidently shown a trans-Antarctic 1D latitudinal profile A81–SP–P1–P5–P6–DRV (Figure 3). The month-averaged (February, 1998) total horizontal spectral wave power $P_f$ in the band 0.7–7.0 mHz and inter-station coherence $\gamma$ along this quasi-meridional profile are shown for two UT intervals when the profile is directed along the noon-midnight meridian.

The *00-04 UT* interval is characterized by the amplitude maxima at nightside auroral zone (A81, SP) and at dayside at 80° (DRV). However, $\gamma$ between nearby stations in these regions is low (<0.5), and it reaches higher values (~0.65) deep in the polar cap, at P5–P1 pair (nightside, 80° – 86°).

For *12-16 UT*, the profile goes only till 80° at nightside (DRV) while at the dayside it reaches 68° (A81). The peak of $P_f$ at the nighside is beyond the profile and at the dayside it is at SP (75°). Coherency is again maximal (~0.7) between stations in the polar cap: P5 (dayside) and P6 (nighside).

2D patterns of the ULF spatial structure (month-averaged for time intervals 0–6, 6–12, 12–18, and 18–24 UT) are shown in Figure 4 combining information about the power $P_f$ and coherence $\gamma$, where $P_f$ is denoted by empty circles with radii proportional to $\log P_f$ and $\gamma$ is shown by the connecting lines with two grades in thickness. The examination of Figure 4 shows that the power of long-period pulsations at high latitudes is maximal in the nominal dayside cusp/cleft projection and nightside auroral zone (largest circles), but maximal coherence is found at polar cap latitudes. Inter-station "coherency net" shows that the ULF activity at the cap stations (with center at P5) is decoupled from that at the auroral stations. The coherent spot of long-period pulsations is shifted from the geomagnetic pole towards night side and indicates the "cap in pulsations".

## 5. Possible mechanisms of $Pi_{cap}3$ pulsations

Analysis of the spectral coherence and $P_f(t)$ variations enables us to group all high-latitude stations into 3 classes with specific ULF disturbances according to their probable magnetospheric sources:

- In the ***cusp region,*** the oscillations are intense, but spatially incoherent and decay fast towards the polar cap. Minimum of coherence between nearby dayside stations may correspond to a separatrix between tailward and sunward field lines, and can be used as an additional indicator of the poleward cusp boundary. Primary source of intense cusp-associated ULF activity is, probably, the magnetosheath turbulence, though its specific excitation mechanism has not been identified yet.
- The source of the ***auroral-related fraction*** of polar pulsations is most probably related to the sporadic extension of the auroral activity to very high latitudes.
- The occurrence of fraction of $Pi_{cap}3$ variations, that is linearly independent on the cusp and auroral pulsations, proves that a specific source of the ***cap pulsations*** does exist. The cap-associated pulsations are coherent within the polar night hemi-circle and low $\gamma$ is found between them and auroral/cusp disturbances. The location of the "coherent spot" of these pulsations is similar to that of the polar cap.

Probably, polar cap component of $Pi_{cap}3$ signals is related to the wave/transients in the tail lobes due to penetration and conversion of magnetosheath turbulence inside these regions. According to this scenario, $Pi_{cap}3$ oscillations can be stimulated by bursts of the magnetosheath turbulence, caused either by solar wind pressure pulses or internal turbulence intermittency. The polar cap fraction of $Pi_{cap}3$ pulsations may be caused also

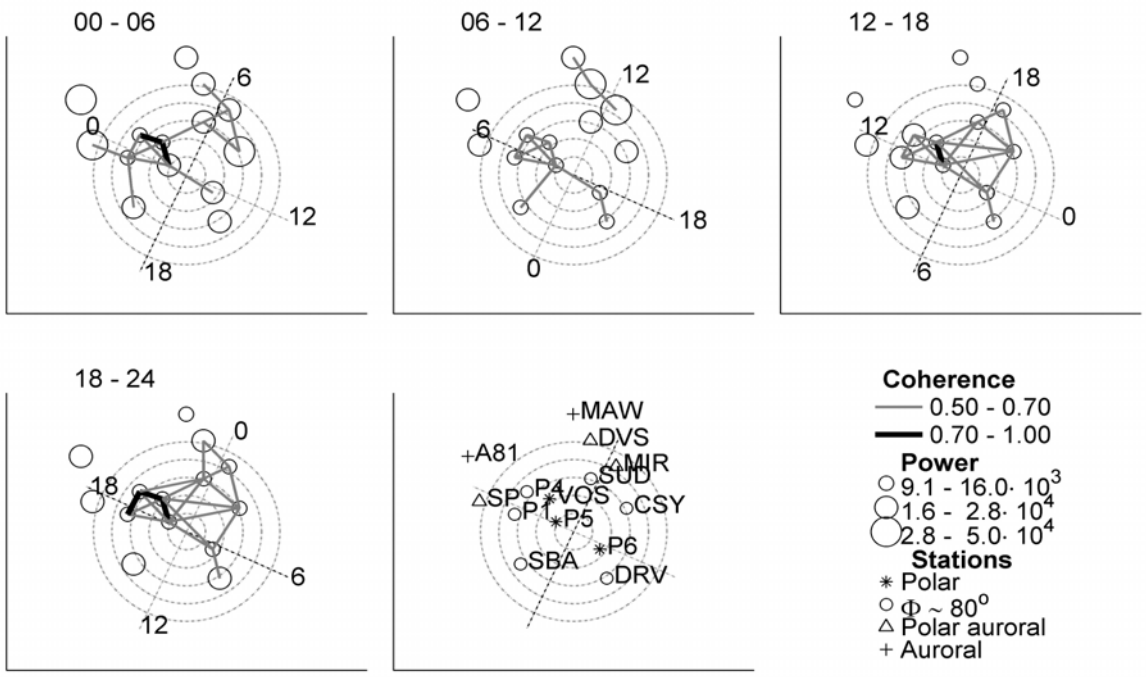


**Figure 4**. Statistical 2D spatial structure (in geomagnetic coordinates) of ULF pulsations intensity in the bandwidth 1.0–1.5 mHz and inter-station coherency over Antarctica in various MLT intervals. Four latitudinal groups of stations are indicated by different symbols in the right bottom panel.

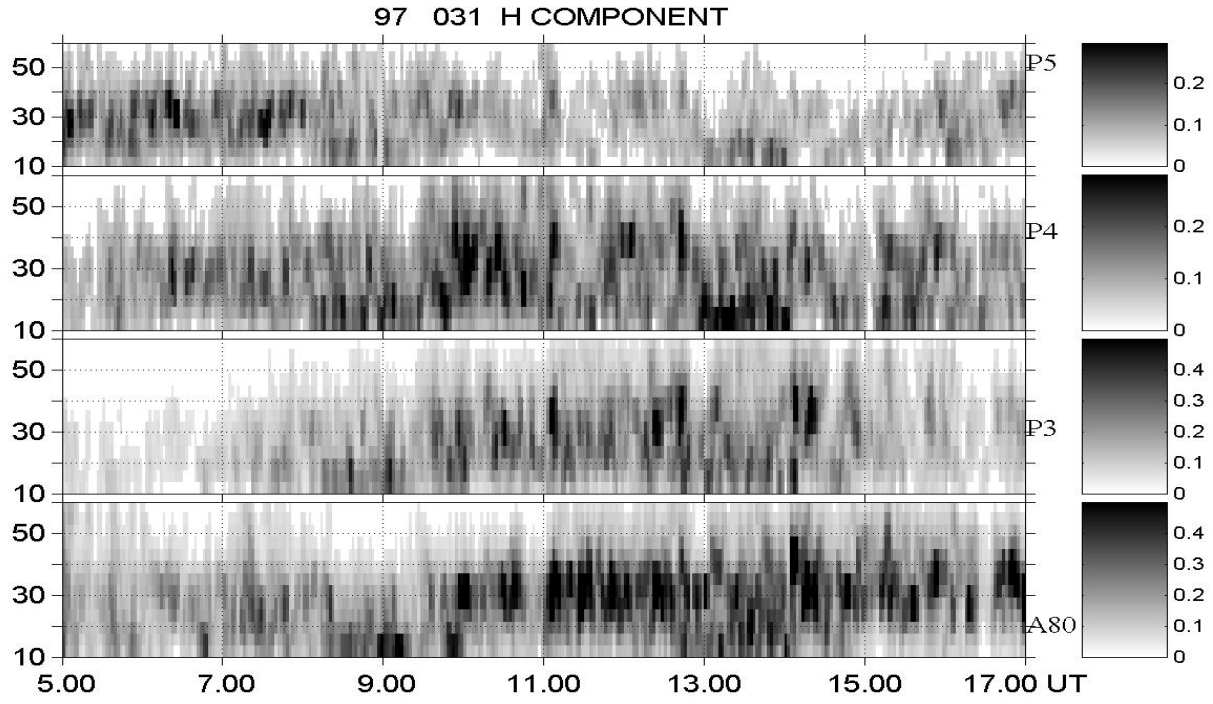


**Figure 5.** Dynamic spectrograms of H components from Antarctic latitudinal profile of search-coil magnetometers produced using a Yule-Walker maximum entropy method.

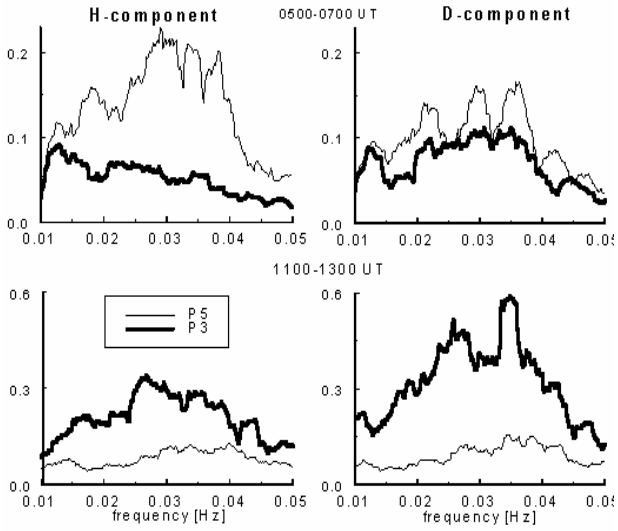


**Figure 6**. Spectra of horizontal components of waves in the Pc3-4 band detected in early morning (upper panels) and daytime (bottom panels) hours.

by global oscillations of tail lobes, excited by magnetosheath turbulence and bursty processes in the plasmasheet. Crude estimates of the expected periods, simulating tail lobe as a half-cylinder, give values $T \cong R/V_A \cong 9$ min, min, corresponding to the typical time scale of these pulsations.

## 6. Example of high-latitude Pc3-4 waves

We present as a typical example the Pc3–4 event on January 31, 1997. Figure 5 shows the dynamic January 31, 1997. Figure 5 shows the dynamic spectrograms (05–17 UT) of H components from trans-Antarctic latitudinal profile. At early morning hours (~05–08 UT), the maximum of narrow-band Pc3 activity at frequency around 30 mHz occurs at polar stations P4 and P5. But, at pre-noon hours (~11–16 UT), the Pc3 activity is shifted to the auroral stations P3 and A80.

The spectral structure of early morning (05–07 UT) and near-noon (11–13 UT) waves are different, as evident from the corresponding spectra (Figure 6). In the band 25–40 mHz the early morning Pc3 pulsations are polarized mainly along the geomagnetic meridian, $H>>D$, whereas the near-noon Pc3 pulsations have $D>H$.

The diurnal variation of the spatial distribution of Pc3 waves along a meridian can be evidently seen in the latitudinal profile of time-integrated spectral power of Pc3 wave packets detected during the early morning

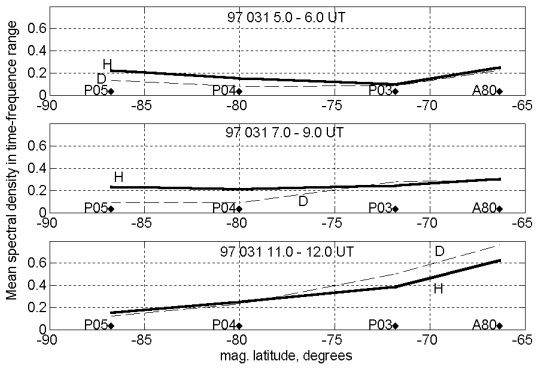


**Figure 7.** Latitudinal distribution of the power of Pc3 wave packets at different LT during the January 31, 1997 event.

(05–06 UT), morning (07–09 UT) and daytime (11–12 UT) hours.

Total ULF wave intensity at sub-auroral station A80 is always the highest. At the higher latitudes the peak wave power gradually shifts from the polar cap (P5) in early morning hours to the auroral latitude (A80, P3) in pre-noon hours. The change of the polarization also occurs: Pc3 waves in the polar cap have $H>>D$, whereas at auroral/cusp latitudes $H \leq D$.

## 7. Diurnal variations of the wave events characteristics

In contrast with previous statistical studies, where the wave and IMF/solar wind parameters averaged over

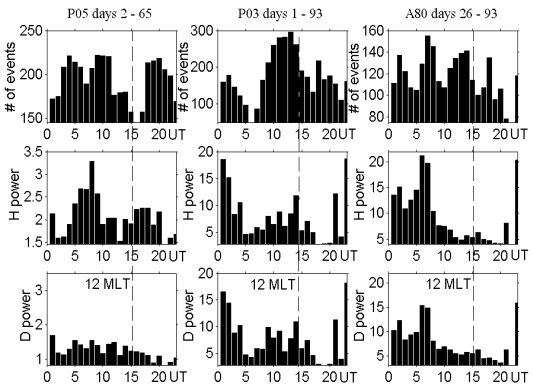


**Figure 8.** Diurnal variations of number of wave events, power of H and D components for the polar cap station P5, cusp station P3, and sub-auroral station A80. For visual guidance a vertical lines denoting the MLT noon are indicated.

a fixed lengthy interval (commonly, 1 hour) had been used, here the following technique of more detailed event selection is applied. Data have been de-spiked and band-pass filtered in range 0.008–0.1 Hz. At first, FFT dynamic spectrograms in the frequency band 10–60 mHz for every station in night 00-05, morning-noon (05–17 UT) and evening (17–24 UT) time intervals are calculated. Then, averaged spectral power and standard deviations for every frequency band are estimated for these time intervals. In dynamic spectrograms the values less than a threshold – mean power +3 standard deviations, are omitted. Two and more adjacent values above a threshold in a spectrogram are considered to be a wave packet. For each wave packet the onset and end times, total energy, peak amplitude of the *H* and *D* components and its frequency are calculated. Finally, the propagation time-shifted and averaged over the wave event duration values of the IMF components and solar wind velocity, as measured at the Wind spacecraft, have been calculated. Thus, this new statistical approach operates not just with the time-averaged characteristics of wave activity, but with isolated wave packets and corresponding IMF/solar wind parameters.

The statistical features of Pc3–4 pulsations are examined with the data from 3 characteristic stations: A80 at sub-auroral latitude ($-66^0$, MLT midnight 0250 UT), P3 located near the nominal latitude of dayside cusp/cleft ($-72^0$, midnight 02 UT), and P5 located deep in the polar cap ($-87^0$, midnight 0250 UT). Diurnal variations of basic ULF wave parameters for these stations are shown in Figure 8. The number (top panel), total power of H (middle panel) and D components (bottom panel) of wave packets are given.

At the equatorward auroral boundary (station P3) diurnal variations of the number of events and their power have two maxima. The night side peak between 22 and 04 UT evidently corresponds to the influence of the substorm activity. Another broad maximum at the near-noon hours, 10–15 UT, may be associated to the dayside cusp/cleft. The power of the *H* component is comparable to the power of *D* component.

In the polar cap (station P5) the peak in the diurnal variations of the Pc3–4 power in the nighttime related to substorm activity, is absent. Also, the near-noon maximum of the ULF power is much weaker at P5 than that at P3. At the same time, there is a spectacular broad maximum of the number of events and their power at early morning hours, 06–10 UT. Polarization of this peak at P5 is different from the near-noon peak at P3: the power of H component is bigger than power of D component. Besides early morning maximum, there is another, but weaker, maximum of H component power in the evening hours, 18–20 UT.

At sub-auroral latitudes (A80), besides the nighttime peak, the maximum Pc3–4 intensity is observed in the morning hours. Though, weak traces of the near-noon activity can be seen in the distribution of the amounts of wave events.

Diurnal variations of wave power are different at cusp latitudes and in the polar cap:

- at 70° – 80° CGM there are near-noon and mid-night maxima, related to the cusp and substorm activities;
- at >85° there are the morning maximum and weaker evening maximum, possibly, conjugate to the lobe flanks. Influence of the nightside substorm activity is hardly noticeable at these latitudes.

## 8. Possible channels of Pc3 penetration to polar latitudes

Unexpectedly, the narrow-band Pc3 activity was found to be high not only in the regions corresponding to the dayside closed field lines adjacent to the cusp/LLBL, but even to the magnetotail lobe. The statistical dependences of the wave powers and frequency at both high-latitude stations P3 and P5 on *V* and *B* [*Chugunova et al.,* 2003] are similar to the relationships commonly found for ULF waves related to the upstream turbulence. Thus, the common primary source of both dayside cusp Pc3–4 waves and morning Pc3-4 cap waves is, probably, the upstream ULF turbulence.

Comparison of the diurnal variations at the cusp latitudes and in the polar cap confirms the occurrence of two sources of Pc3 wave activity at very high latitudes, proposed on the basis of case study [*Chugunova et al.,* 2002]. The occurence of the cusp-associated intensification of Pc3 activity at near-noon hours was known from previous studies [*Bolshakova and Troitskaya,* 1984; *Engebretson et al.,* 1990]. The difference of the ratio between the horizontal magnetic components of the morning and near-noon Pc3 pulsations may be related to the difference between their spatial structures, corresponding to large-scale (small zimuthal wave numbers *m*) waves on the morning/evening magnetotail flanks, and small-scale (large *m*) waves in the cusp area.

Both the case study of January 31, 1997 event and statistical analysis indicate the occurrence of an additional source of the Pc3–4 wave activity in the polar cap, probably related to the penetration and conversion of waves at the lobe flanks. The mechanism of narrow-band filtering/amplification of Pc3 waves on the open field lines has not been identified yet.

## 9. Conclusion: Prospects of further studies

The presence of the flow turbulence in the magnetospheric boundary regions has profound effect on the large-scale electrodynamics of near-Earth environment. Geomagnetic disturbances/waves from the boundary regions and magnetotail can be transported along stretched field lines into the polar ionosphere, thus, the dynamics of boundary regions and magnetotail can be monitored with ground-based magnetic observations at polar latitudes. This study indicate the polar cap is not so quiet place as it was thought to be: it is occupied by global long-period variations (Pi3 pulsations), possibly related to the background tail activity, and it is often invaded by narrow-band waves (Pc3–4 pulsations), probably due to the penetration and conversion of waves at the lobe flanks.

Yu. I. Galperin used to say that "theoreticians should not just demonstrate their education, but they must try to get insight into real physics of space phenomena". The occurrence of new types of ULF wave phenomena in the polar cap (Pi3 pulsations and narrow-band Pc3-4 waves) provides a challenge to the space physics, because so far a conversion/filtering mechanism from the magnetosheath ULF turbulence into the waves on the ground on the open field lines has not been identified yet.

**Acknowledgements.** This research is supported by the grants from RFBR 01–05–64710 (N.V.Y.), from the RFBR 03-05-64670 (O.M.C.), from the NSF OPP–9909212 (M.J.E), and by a supplement from the NSF Office of International Programs (V.A.P.).

## References

Bolshakova, O. V., and V. A. Troitskaya, The relation of the high latitude Pc3 intensity to the dayside cusp, *Geomagn. and Aeronomy, 24,* 663, 1984.

Chugunova, O. V., V. A. Pilipenko, M. J. Engebretson, and H. Fukunishi, Pc3 pulsations deep in the polar cap: A study using Antarctic search-coil magnetometers, *in: "Problems of Geocosmos", Proc. of 4-th International Conference,* Saint-Petersburg, Russia, 111, 2002.

Chugunova, O. M., V. A. Pilipenko, and M. J. Engebretson, Statistical features of Pc3-4 pulsations at very high latitudes, *in "Physics of the Auroral Phenomena", Proc. of the 26-nd annual seminar*, Apatity, Russia, 2003.

Engebretson,. M. J., B. J. Anderson, et al., Ionospheric signatures of cusp latitude Pc 3 pulsations, *J. Geophys. Res., 95,* 2447, 1990.

Yagova, N., L. Lanzerotti, U. Villante, V. Pilipenko, S. Lepidi, P. Francia, V. Papitashvili, and A. Rodger, Magnetic activity in the ULF Pc5-6 band at very high latitudes in Antarctica, *J. Geophys. Res., 107*, N8, SMP 22, 1-12, 2002.

---

V. Pilipenko, N. Yagova, O. Chugunova, Institute of the Physics of the Earth, B. Gruzinskaya 10, 123995, Moscow, RF *(pilipenk@augsburg.edu)*

M. J. Engebretson, Augsburg College, Minneapolis, MN 554546, USA *(engebret@augsburg.edu)*

A. Rodger, British Antarctic Survey, Cambridge CB3 OET, UK (a.rodger@bas.ac.uk)

L. Lanzerotti AT&T Bell Laboratories, NJ 07974, USA (ljl@bell-labs.com)

# Pc5 range ground geomagnetic pulsations as a result of the magnetic cloud impact

N. G. Kleimenova[1], O. V. Kozyreva[1], J. -J. Schott[2], and J. Manninen[3]

[1] Institute of the Earth Physics, Bolshaya Gruzinskaya, Moscow, Russia
[2] Ecole et Observatoire des Sciences de la Terre, Strasbourg, France
[3] Sodankylä Geophysical Observatory, Finland

**Abstract.** The interaction of an interplanetary magnetic cloud with the Earth's magnetosphere has been analysed using the ground geomagnetic data. A magnetic cloud impact leads to a magnetic storm development. The analysis of several intense magnetic storms has been done. It was shown, that the bow shock and a compressional region (sheath region) with strong IMF variations on the front edge of a magnetic cloud triggers a burst of geomagnetic Pc5−6 (1−3 mHz) pulsations as well as a magnetic substorm at the polar cap near the open/closed magnetosphere boundary. In many cases the temporal, spectral structure of ground high latitude Pc5−6 pulsations and variations in IMF was rather similar. The ground Pc5−6 pulsations, associated with the front edge of magnetic cloud passage, could be a result of a wave generation at the ionosphere altitudes near a foot print of the field aligned currents, modulated by interplanetary waves or by a quasi-periodical reconnection at the low latitude magnetopause. The second possibility would be a direct penetration and transformation of solar wind hydromagnetic waves guided along the magnetopause. A cloud leading edge arrival and magnetic storm main phase onset shifted the Pc5−6 geomagnetic pulsation activity into inner magnetosphere. The daytime pulsations may be attributed to the well-known field line resonance and the evening – morning pulsations – to wave processes associated with a substorm development.

## 1. Introduction

The interplanetary magnetic cloud represents a special type of a large-scale structure of the interplanetary magnetic field loop-like configuration with a strong magnetic field strength, low ion density and temperature inside of the loop [*Burlaga et al.*, 1981]. Until recently these fast moving plasma volumes were called "plasma clouds", "turbulent clouds", "flare streams", "magnetic tongues", "magnetic bubbles". Large-scale solar wind structures are currently of great interest, because their magnetospheric impact triggers an intense geomagnetic activity [e.g., *Burlaga et al*., 1987; *Gosling et al.*, 1991; *Farrugia et al.*, 1993; *Bothmer and Schwenn,* 1995; *Farrugia et al*., 1998; *Tsurutani et al.*, 1999 and many others]. The magnetic cloud typically originates from a fast coronal mass ejection (CME) at the Sun.

The large-scale geometry of the magnetic cloud according to *Tsurutani et al.* [1999] is shown in Figure 1. The boundary of the cloud (so called a leading edge) is usually identified by a sharp increase in the magnetic field strength (*B* IMF), a sudden change of $B_z$ IMF sign, and an abrupt drop of proton density and temperature. The turbulent region, which is located between the front shock and the leading edge of the magnetic cloud, is characterised byhigh dynamic pressure and strong variations of all IMF parameters.

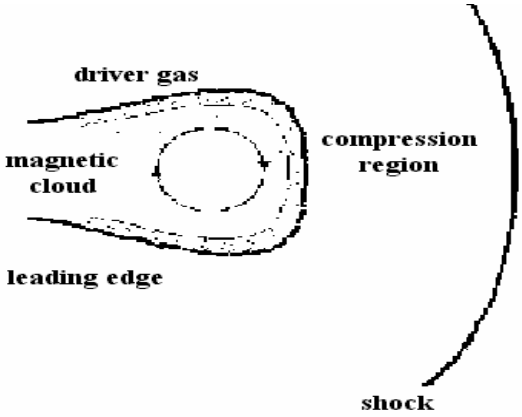


**Figure 1.** An interplanetary magnetic cloud schema from *Tsurutani et al*. [1999].

The impact of the magnetic cloud with the Earth's magnetosphere causes a magnetic storm, a front shock triggers a storm sudden commencement (ssc), and a leading edge arrival leads to a storm main phase onset.

The aim of this paper is to study the behaviour and the space- time distribution of long period (Pc5–6 range) geomagnetic wave as a response to the arrival of the magnetic cloud.

## 2. Results of observations

The ground-based magnetic measurements at 78 INTERMAGNET and 21 IMAGE stations have been studied for several selected magnetic storms associated with magnetic cloud arrival. The spectral analysis of these ground geomagnetic data showed that the maximum of the pulsations intensity was similar at different latitudes and, as a rule, was observed at the frequency range (1–3) mHz, i.e. Pc5–6 (or Pi3) range, as it has been reported by *Kleimenova and Kozyreva* [2002].

In this paper we present some examples of such scenario. Below the wave signature of two typical magnetic clouds passages is given (October 18, 1995 and January 10, 1997. The geoeffectiveness of these clouds was discussed in a number of papers, e.g., [*Farrugia et al.*, 1998; *Manninen et al*, 2002 and many others]. Figure 2 shows the the solar wind and IMF parameters variations measured by WIND. The temporal profiles of solar wind and IMF parameters resemble one another closely with similar values of solar wind speed.

On October 18, 1995 the WIND spacecraft was close to the Sun-Earth line and at the average radial distance of 176 $R_e$. The estimation gives a time delay of ~44 min. The 8-hour-long passage (~11–19 UT) of the turbulent front edge of this cloud displaced the subsolar magnetopause earthward by ~4 $R_e$ [*Farrugia et al.*, 1998]. At the leading edge of the cloud (~19 UT) there was a jump of $B$ IMF from ~5 nT to ~20 nT and a drop of solar wind density as large as about 50 times of its value.

On January 10, 1997 the WIND spacecraft was at X ~90 $R_e$, and the estimated time lag on ground measurements was ~20 min. There was the shock detected near 01 UT on the front edge of the magnetic cloud. At ~05 UT the density dropped by a factor of ~3, the $B$ IMF increased, the $B_z$ changed the sign, however the solar wind speed remained as strong as before. It is the typical picture of the leading edge of the magnetic cloud. Thus, the WIND data showed the compressional sheath, which lasted from ~01 UT to ~05 UT.

Previously *Kleimenova et al.* [2000] showed that during the initial phase of magnetic storm on February 21, 1994 the strongest Pc5–6 geomagnetic pulsations activity was observed at polar cap latitudes. Following this result we calculated the global MLT–UT plots of the Pc5–6 amplitude distribution separately for the polar and lower latitudes using the North hemisphere INTERMAGNET and IMAGE magnetic data.

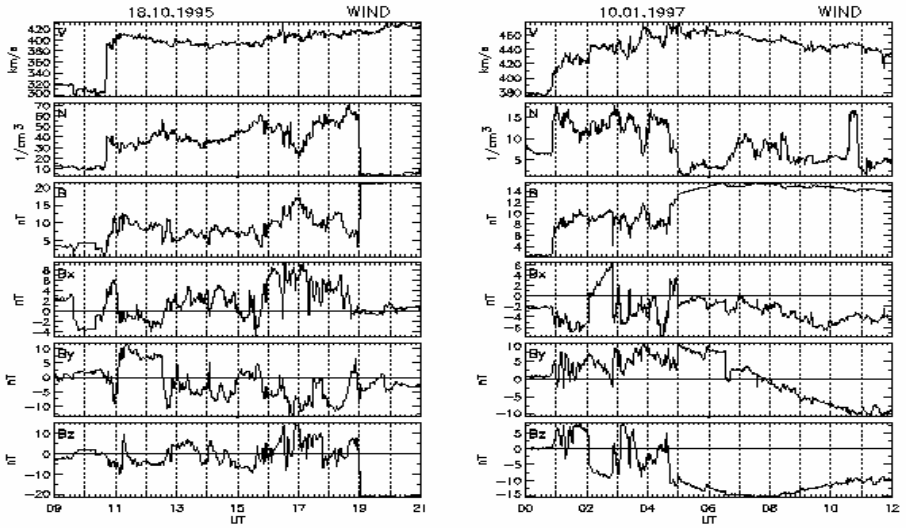


**Figure 2.** Variations of IMF and solar wind parameters on the front edges of the magnetic clouds on October 18, 1995 and on January 10, 1997.

The border between these regions was accepted as 67° on October 18, 1995 and as 73° on January 10, 1997 in accordance with the solar wind dynamic pressure, measured by WIND. The global MLT-UT plots are presented in Figure 3. The shock (see Figure 2 at ~11 UT on October 18, 1995 and at ~01 UT on January 10, 1997) was about three times stronger in the first event than in the second one (Figure 2). Accordingly, the Pc5–6 response was also much stronger in the first event. Figure 3 showed that the burst of geomagnetic pulsations was observed near 11 UT simultaneously at different latitudes. The shock on January 10, 1997 was marked as the morning burst of Pc5–6 at the polar latitudes.

The plots in Figure 3 demonstrate that both cloud turbulent front edge passages (17-19 UT on October 18, 1995 and 04–05 UT on January 10, 1997) were accompanied by bursts of Pc5–6 activity with strongest amplitudes at the morning side (~02–08 MLT) of the polar cap/cusp (upper panels in Figure 3). In both cases under consideration the cloud leading edge arrival suppresses the polar wave excitation.

After the cloud leading edge passage the Pc5–6 activity was shifted into the inner magnetosphere (bottom panels in Figure 3). Near 20 UT on October 18, 1995 and near 07-08 UT on January 10, 1997 there were several locations of the Pc5–6 amplitude enhancements observed in the inner magnetosphere. The minimum of pulsations activity was noticed in the local noon time. In both considered events the morning "Pc5–6 enhancements spots" latitude size was so large so that pulsations were measured even at high latitudes. The morning as well as the evening pulsations activities were associated with simultaneous substorms developments. However, the evening Pc5–6 range waves as well as substorm activity were observed at the polar latitudes, even on October 18, 1995, when the] energy inputs to magnetosphere (Akasofu parameter) estimated by *Farrugia et al*., [1998 was twice as large as the one on January 10, 1997. It may suggest that the latitude shift of the open/closed magnetosphere boundary in the evening sector was stronger than in the morning.

With the aim of detailed Pc5–6 latitude distribution study we calculated the Φ–Λ (geomagnetic latitude – longitude) plots of their amplitudes at Scandinavia by using the data elicited by IMAGE magnetometer measurements. Figure 4 shows the obtained results. The upper panels present the geomagnetic pulsations associated with the passage of compressional sheath on the front edge of three magnetic clouds, the bottom panels- the same after the cloud leading edge arrival. Figure 4 confirms, that the passage of the front turbulent edge of all considered clouds caused the 1–3 mHz geomagnetic pulsations generation at the geomagnetic

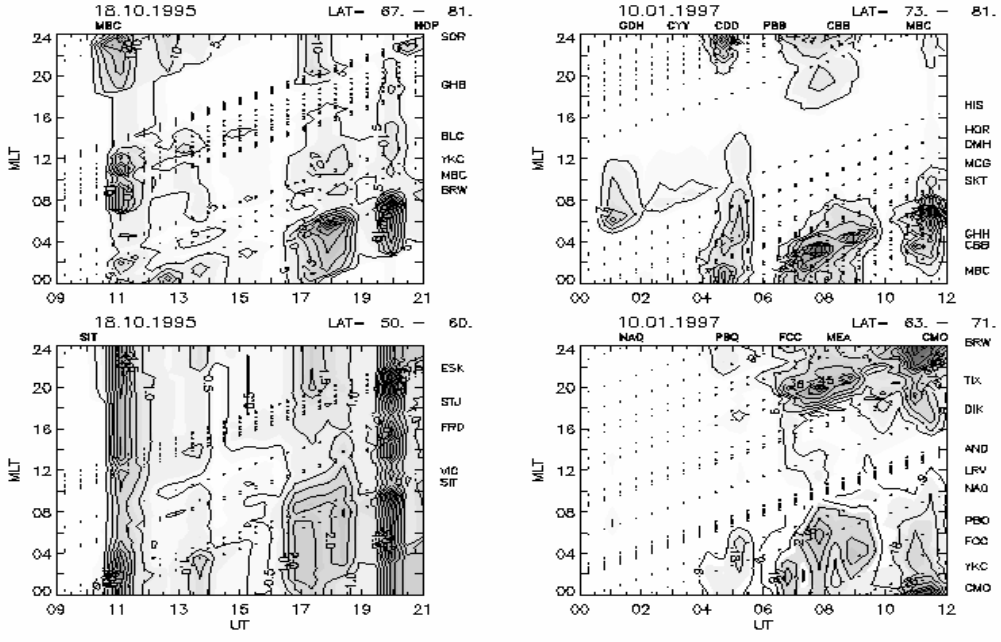


**Figure 3.** MLT-UT plots of Pc5-6 geomagnetic pulsations distributions on October 18, 1995 and on January 10, 1997.

latitudes higher than 70°. After the arrival of the cloud leading edge, geomagnetic pulsations activity shifted to the lower latitudes, into inner magnetosphere.

Thus, despite some of the individual distinctions between storms under consideration, the remarkable similarity of the space-time variations of Pc5–6 range geomagnetic pulsations has been seen. The wave signature of the passage of a front compressional edge (sheath region) of a cloud was defined as an appearance of the pulsation activity mostly at the polar cap and cusp latitudes with the largest amplitudes near the open/closed magnetosphere boundary. A cloud leading edge arrival suppressed the polar cap geomagnetic pulsations and shifted the Pc5–6 activity to the lower latitudes, i.e., into the inner magnetosphere. A similar long period geomagnetic pulsation response to the front and leading edges of magnetic cloud arrivals was observed in general terms during the passages several others clouds, which we analyzed, e.g., February 21, 1994; May 15, 1997; November 22, 1997; September 24, 1998; October 19, 1998; November 08, 1998; February 19, 1999; July 15, 2000; November 24, 2001.

Our analysis showed that strong fluctuations were also observed in IMF and solar wind density mostly in the cloud front sheath just before the leading edge border. These hydromagnetic waves probably penetrate into polar cap along the magnetopause. We compared the wavelet spectra (periods shorter than 15 min) of the pulsations in the interplanetary and ground data. Figure 5 demonstrates the results of wavelet analysis of ($B_x$, $B_y$, $B_z$) IMF and of solar wind density (N) as well as of the ground geomagnetic pulsations at polar latitudes during the passage of the front edge of the two magnetic clouds being discussed. In this Figure the IMF data are shifted to the lag time, corresponding to the estimated spacecraft – subsolar magnetopause delay. For each event we selected two polar stations at North hemisphere, located near maximum of the pulsations occurrence (Figure 3) and DRV polar antarctic station. The geomagnetic latitudes of those stations are marked on Figure 5. The magnetic noon at DRV is ~01 UT.

The calculated wavelets of October 18, 1995 data show the similarity between the temporal structure of the waves in the solar wind and the high latitude ground

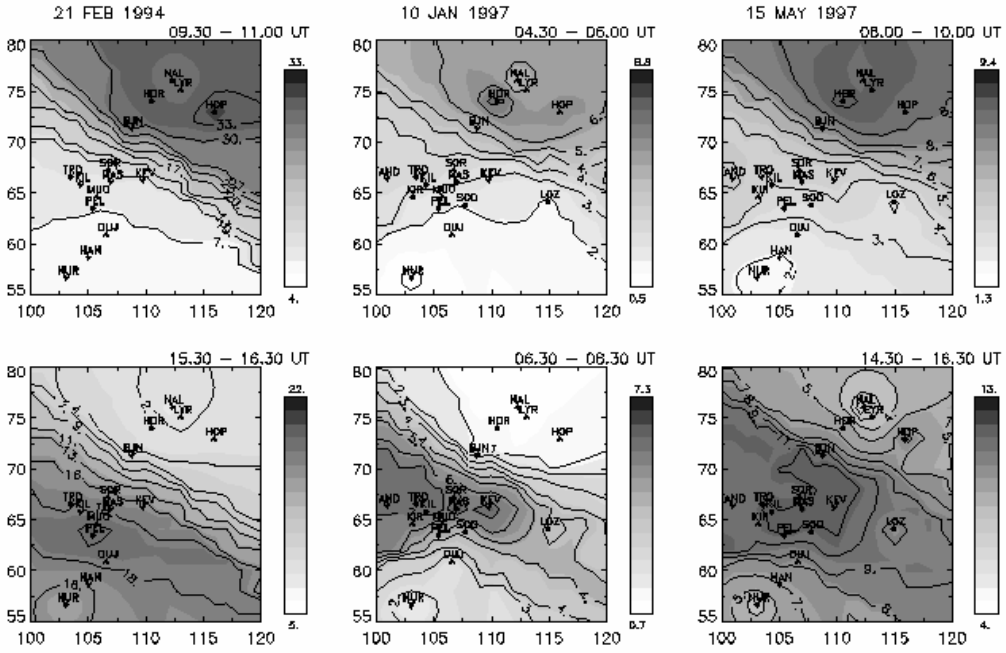


**Figure 4.** Plots of the 1–3 mHz geomagnetic pulsations distribution at the dayside magnetosphere (Scandinavia, IMAGE data) in geomagnetic coordinates. The upper panels-the response to the passage of the magnetic cloud front edge, the bottom panels- after the cloud leading edge arrival of the magnetic clouds (a – February 21, 1994; b – January 10, 1997; c – May 15, 1997).

geomagnetic Pc5–6 pulsations between 17 UT and 19 UT, i.e. in vicinity of the outside border of the cloud leading edge (Figure 2). The strongest ground bursts of Pc5–6 pulsations were observed near the morning side of the polar cusp (obs. BRW, 05–07 MLT). The best consistency was noted between the pulsations at BRW and in the $B_z$ and $B_x$ IMF accompanied by similar burst in the solar wind density (N). The spectra of waves did not coincide in details. However, they showed the similarity in the temporal variations, which may suggest their close relationship. At the North hemisphere, the polar morning Pc5–6 (BRW) and dayside (CBB, 09–11 MLT) pulsations as well as at the similar South hemisphere (DRV, 04–06 MLT) pulsations disappeared with the magnetic cloud leading edge arrival.

On January 10, 1997 the strongest fluctuations in IMF were observed at 03–04 UT. Unfortunately, there were no stations at polar latitudes, located in the morning side at that time. A little later, near 05 UT, the large burst of polar Pc5–6 pulsations was observed at HOR (~ 07 MLT) and it coincided with similar burst of IMF fluctuations measured by WIND in vicinity of the outside border of the cloud leading edge.

According to the global auroral images obtained by Ultraviolet Imager (UVI) on POLAR spacecraft [*Germany et al.,* 1998] the morning poleward boundary of the auroral oval was located at the geomagnetic latitude $\Phi \sim 70°$. At Scandinavia (Figure 3) these Pc5–6 pulsations were accompanied by substorm at the polar latitudes ($\Phi > 70°$) and by colocated pulsating particle precipitation (riometer absorption), as it has been reported by *Manninen et al.* [2002]. The substorm may be attributed to the appearance of negative values of $B_z$ IMF measured by WIND near 03.30 UT (Figure 2), and it may suggest the existence of the enhanced field aligned current. According to the observations by *Sandholt et al*. [1998] the green (557.7 nm) optical emission appeared simultaneously with the strong burst of Pc5–6 geomagnetic pulsations and moved eastward as the Pc5–6 waves at the similar speed. The geomagnetic and riometer pulsations as well as the green optical emission were suppressed by the cloud leading edge arrival. The same sharp (1–3) mHz magnetic waves disappearance with the leading edge arrival was also observed in the afternoon (~16 MLT) polar latitudes at antarctic station DRV (Figure 5).

## 3. Discussion

The analysis of the ground geomagnetic Pc5-6 range pulsations response to the interplanetary magnetic cloud impact showed that there were different wave of the auroral oval was located at the

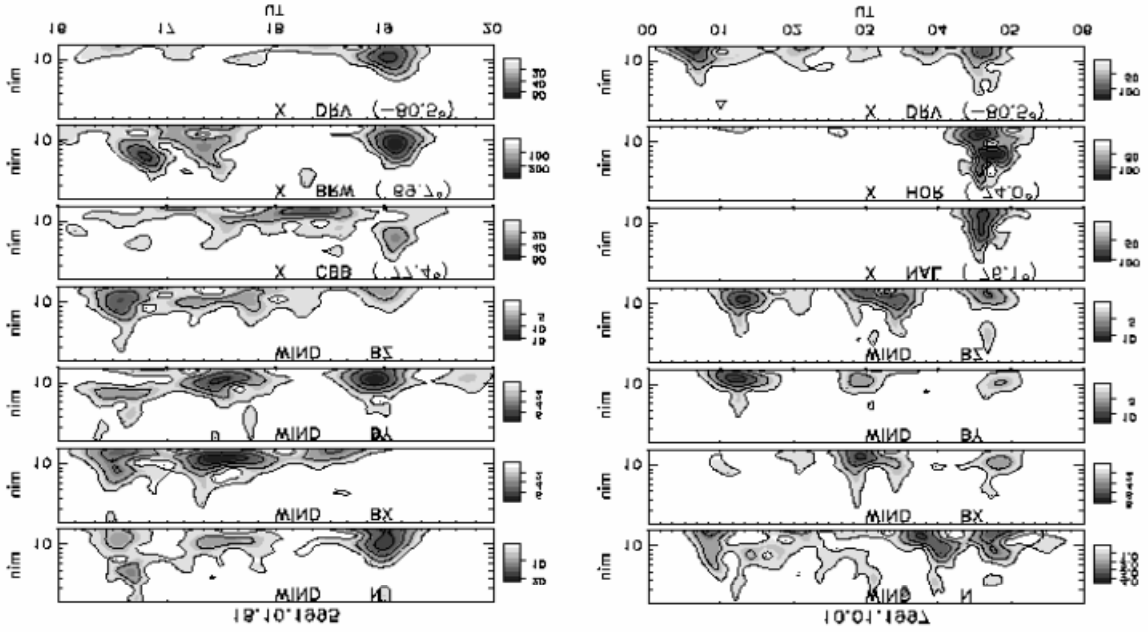

**Figure 5.** Wavelet structure of the ground polar cap geomagnetic pulsations and IMF variations on October 18, 1995 and on January 10, 1997.

geomagnetic signatures during the cloud compressional turbulent sheath and the cloud leading edge passages. A cloud turbulent sheath interaction with Earth's magnetosphere leads to Pc5–6 magnetic wave appearance at polar latitudes, and a cloud leading edge arrival leads to the Pc5–6 activity development mostly at morning and evening sides in the inner magnetosphere. Despite of the similarity of the frequency range of these ULF waves, their nature is different.

The ULF waves observed in the vicinity of the border between open and closed magnetic field lines may be referred to the ionosphere traveling convection vortices (TCVs) [*Friis-Christensen et al.,* 1988; *Glassmeir and Happner,* 1992; *Yahnin et al.,* 1997]. According to *Sibeck et al.* [1989] and *Prikryl et al*. [1998], we may suggest that the fluctuations in the solar wind, observed in the cloud turbulent front region, may transform the magnetic reconnection at the dayside magnetopause or in the cusp regions into pulses. These quasi-periodic pulses may be seen on the ground as Pc5–6 (or Pi3) geomagnetic pulsations near footprint of the open/closed magnetosphere boundary.

Another source of these pulsations could be associated with pulsating upward field aligned currents near the dayside polar cusp as it was discussed by *McHarg and Olson* [1992]. Their conclusion was based on the correlation between ground ULF magnetic and optical measurements near the footprint of the dayside polar cusp. Recently *Pilipenko et al.* [2003] published the result that confirmed the relationship between daytime ULF waves at geomagnetic latitudes 75° – 79° and upward field aligned currents. The Pc5–6 geomagnetic pulsations may represent the ionosphere signatures of the enhanced ionosphere conductivity due to the pulsating electrons precipitation of field aligned currents [*Manninen et al*., 2002]. The electron precipitation may be modulated by interplanetary waves or by a quasi-periodical reconnection at the low latitude magnetopause.

One more possible source of polar Pc5–6 range geomagnetic pulsations could be attributed to the direct penetration (and transformation) of MHD solar wind waves into the dayside polar cap/cusp under a high solar wind dynamic pressure. In many cases pulsations in the solar wind density and in the $B_x$ IMF appeared from phase wave structure, which may indicate the presence of a strong wave compressional component. We found a rather good agreement between the spectral structure and the temporal coincidence of pulsation bursts in space (on the WIND spacecraft) and on the ground in the vicinity of polar cusp/cap border. It could be some evidence of the possibility of the direct wave penetration from the solar wind.

All mechanisms listed above may appear separately as well as simultaneously in different magnetic cloud impact, and sometimes they present a very complicated pattern.

The cloud leading edge arrival, marked by an abrupt drop of the solar wind dynamic pressure, large negative $B_y$ IMF appearance and strong near continuous values of $B$ IMF, suddenly suppress the Pc5–6 pulsations at the polar latitudes.

The new ULF activity in the inner magnetosphere may be attributed to the well known field line resonances (FLR) with polarization rotation at local noon and amplitude enhancement to the morning side direction. Sometimes (as an example, May 15, 1997) ULF pulsations may show another source attribution because they may be accompanied by ring current proton injection [*Pilipenko et al.,* 2001].

Often the morning and evening Pc5-6 range geomagnetic pulsations were associated with strong negative $B_z$ IMF appearance and magnetosphere substorm development. Their source is probably related to the quasi-periodical substorm processes in the magnetosphere tail or in vicinity of the dipolarization region. Besides, the nature of the evening and the morning Pc5–6 range pulsations may be different.

## 4. Conclusion

The geomagnetic wave response of the interaction of a front edge of an interplanetary magnetic cloud with the Earth's magnetosphere represents Pc5–6 (1–3 mHz) geomagnetic pulsations generation at the polar cap with the highest intensity near dayside polar cusp.

The existence of strong wave IMF fluctuations under high and variable solar wind dynamic pressure plays critical role in this process. The time of the appearance and main spectral and wavelet structure of geomagnetic pulsations on the ground and IMF fluctuations on the front edge of the magnetic cloud were sometimes roughly similar. We assume that the ground polar Pc5–6 pulsations, associated with the front edge of magnetic cloud passage could be a result of wave generation at ionosphere altitudes near a foot-print of the field aligned currents. The interplanetary waves or the quasi-periodical reconnection at low latitude magnetopause may modulate the current intensity. Ground polar pulsations may be also a result of a direct penetration and transformation of turbulent solar wind hydromagnetic waves into the Earth polar cap.

The cloud leading edge arrival and magnetic storm main phase onset shifts the Pc5–6 geomagnetic pulsation activity into the inner magnetosphere. Daytime pulsations can be attributed to the well-known field of line resonances and the evening – morning pulsations – to waves associated with a substorm development.

**Acknowledgements.** The ground-based magnetic data from IMAGE network are collected as a Finnish-German-Norwegian-Polish-Russian-Swedish project.

## References

Bothmer, V., and R. Schwenn, The interplanetary and solar causes of major geomagnetic storms, *J. Geomag. Geoelectr., 47*, 1127, 1995.

Burlaga, L. F., E. Sittler, F. Mariani, and R. Schwenn, Magnetic loop behind an interplanetary shock: Voyager, Helios, and IMP 8 observations. *J. Geophys. Res., 86*, 6673, 1981.

Burlaga, L. F., K. W. Behannon, and L. W. Klein, Compound streams, magnetic clouds and major magnetic storms, *J. Geophys. Res.*, *92*, 5725, 1987.

Farrugia, C. J., M. P. Freeman, L. F. Burlaga, R. P. Lepping, and K. Takahashi, The Earth`s response under continued forcing; substorm activity during the passage of an interplanetary magnetic cloud, *J. Geophys. Res., 98,* 7657, 1993.

Farrugia, C. J., J. D. Scudder, M. P. Freeman, L. Janoo, G. Lu, J. M. Quinn, R. L. Arnoldy, R. B. Torbert, L. F. Burlaga, K. W. Ogilvie, R. P. Lepping, A. J. Lazarus, J. T. Steinberg, F. T. Gratton, and G. Rostoker, Geoeffectiveness of three Wind magnetic clouds: A comparative study, *J. Geophys. Res., 103*, A8, 17,261, 1998.

Friis-Christensen, E., M. A. McHenry, C. R. Clauer, and S. Vennerstrom, Ionospheric travelling convection vortices observed near the polar cleft: a triggered response to sudden changes in the solar wind, *Geophys. Res. Lett*., *15***,** 253, 1988.

Germany, G. A., G. K. Parks, H. Ranganath, R. Elsen, P. G. Richard, W. Swift, J. F. Spann, and M. Brittnacher, Analysis of auroral morphology: Substorm precursor and onset on January 10, 1997, *Geophys. Res. Lett., 25,* 3034, 1998.

Glassmeier, K. -H., and C. Heppner, Travelling magnetospheric convection twin vortices, another case study, global characteristics, and a model, *J. Geophys. Res., 97*, 3977, 1992.

Gosling, J. T., J. McComas, J. L Phillips, and S. J. Bame, Geomagnetic activity associated with Earth passage of interplanetary shock disturbances and coronal mass injections, *J. Geophys. Res., 96,* 7831, 1991.

McHarg, M. G., and J. V. Olson, Correlated optical and ULF magnetic observations of the winter cusp-boundary layer system, *Geophys. Res. Lett., 19*, 817, 1992.

Kleimenova, N. G., O. V. Kozyreva, M. Bitterly, and J. –J. Schott, Long period (1–6 mHz) geomagnetic pulsations in the initial phase of the large magnetic storm on February 21, 1994, *Geomagnetism and Aeronomy, 40,* 4, 16, 2003.

Kleimenova, N. G., and O. V. Kozyreva, Daytime high-latitude geomagnetic pulsation response to the front edge of the magnetic clouds, *Physics of Auroral Phenomena, 25 Annual Seminar, Apatity, Abstracts,* 46, 2002.

Manninen, J., N. G. Kleimenova, O. V. Kozyreva, and A. Ranta, High-latitude geomagnetic pulsation response to the passage of the front edge of the interplanetary magnetic cloud of January 10, 1997, *J. Atm. Solar-Terr. Physics., 64,* 17, 23, 2002.

Pilipenko, V., N. Kleimenova, O. Kozyreva, M. Engebretson, and O. Rasmussen, Long-period magnetic activity during the May 15, 1997 storm, *J. Atmos. Terr. Phys.*, *63*, 489, 2001.

Pilipenko, V. A., V. A. Martines-Bedenko, M. J. Engebretson, V. O. Papitashvili, and P. Newell, High-latitude mapping of ULF activity, field-aligned currents, and DMSP-based dayside magnetosheric domains, *Earth's Low-Latitude Boundary Layer, Geophys. Monograph, 133,* AGU, 231, 2003.

Prikryl, P., R. A. Greenwald, G. J. Sofko, J. P. Villian, C. W. S. Ziesolleck, and E. Friis-Cristensen, Solar wind-driven pulsed magnetic reconnection at the dayside magnetopause, Pc5 compressional oscillations, and field line resonances, *J. Geophys. Res., 103,* 17,307, 1998.

Sandholt, P. E., C. J. Farrugia, J. Moen, O. Noraberg, B. Lybekk, T. Stenand, and T. Hansen, A classification of dayside auroral forms and activities as a function of interplanetary magnetic field orientation, *J. Geophys. Res., 103,* 23,325, 1998.

Sibeck, D. G., W. Baumjohann, R. C. Elphic, D. H. Fairfield, J. F. Fennel, W. B. Gail, L. J. Lanzerotti, R. E. Lopez, H. Luehr, A. T. Y. Lui, C. G. Maclennan, R. W. McEntire, T. A. Potemra, T. J. Rosenberg, and K. Takahashi, The magnetospheric response to 8-minute period strong amplitude upstream pressure variations, *J. Geophys. Res.*, *94***,** 2505, 1989.

Tsurutani, B. T., Y. Kamide, J. K. Arballo, W. D. Gonzales, and R. P. Lepping, Interplanetary causes of great and superintense magnetic storm, *Phys. Chem. Earth (C), 24,* 1-3, 101, 1999.

Yahnin, A. G., V. G. Vorobjev, T. Bosinger, R. Rasinkangas, D. G. Sibek, and P. T. Newell, On the source region of travelling convection vortices, *Geophys. Res. Lett*., *24,* 237, 1997.

Yamauchi M, H. Nilsson, L. Eliasson, O. Norberg, M. Boehm, J. H. Clemmons, R. P. Lepping, L. Blomberg, S. -I. Ohtani, T. Yamamoto, T. Mukai, T. Terasawa, and S. Kokobun, Dynamic response of the cusp morphology to the solar wind: A case study passage of the solar wind plasma cloud on February 21, 1994, *J. Geophys. Res., 101,* A11, 24,675, 1996.

AURORAL PHENOMENA AND SOLAR-TERRESTRIAL RELATIONS
PROCEEDINGS OF THE CONFERENCE IN MEMORY OF YURI GALPERIN, 3-7 FEBRUARY 2003

# New features of the solar wind observed by INTERBALL satellites

G. N. Zastenker

Space Research Institute, Russian Academy of Sciences, Moscow, Russia

**Abstract.** Some new features of the solar wind were found in the INTERBALL project by comparison of the multipoint observations and using high-resolution plasma measurements onboard INTERBALL-1/MAGION-4 satellites. These results presented in this paper include several points, namely, dimensions of the middle-scale structures, large and sharp plasma density changes, fast plasma and magnetic field variations in the foreshock and magnetosheath.

## 1. Introduction

One of the considerable achievements of the last decade is the launch of the unprecedented fleet of spacecraft designed for the near-Earth's space studies. By simultaneous multipoint measurements a wealth of new data was collected, detailing our understanding of the Sun-Earth relationship.

An important part of this fleet was the Interball project. INTERBALL-1 satellite and its subsatellite MAGION-4 launched in August 1995 into the elliptic orbit with the apogee of 30 Re and perigee about 0.1-3 Re were utilized investigations of the solar wind, magnetopause, cusp, magnetosheath, and magnetotail [*Galeev et al.*, 1995]. In addition to the multipoint comparisons with ACE, WIND, IMP 8, GEOTAIL, POLAR spacecraft observations at INTERBALL-1 /MAGION-4 satellites have two important advantages:

- systematic measurements both of the magnetic field and plasma fluxes with high (one second or better) time resolution;
- simultaneous plasma and field measurements onboard the spacecraft at a distance of about 1000 km.

In this paper we present several new results of the solar wind investigations based on above mentioned advantages by means of INTERBALL-1 (and other spacecraft) data analyses, namely, determination of the middle-scale structures persistence time and dimension, description of the features of large and sharp plasma fronts, observations of fast solar wind variations in the foreshock, evaluation of characteristics of low and high frequency plasma and magnetic field variations in the magnetosheath.

## 2. Correlations for the middle-scale structures.

The main aim of this investigation is the determination of characteristic dimensions and lifetime of the middle-scale structures (size about several millions km) of the solar wind and interplanetary magnetic field (IMF). It can be done by estimating the cross-correlation of measurements made by several wide-separated spacecraft.

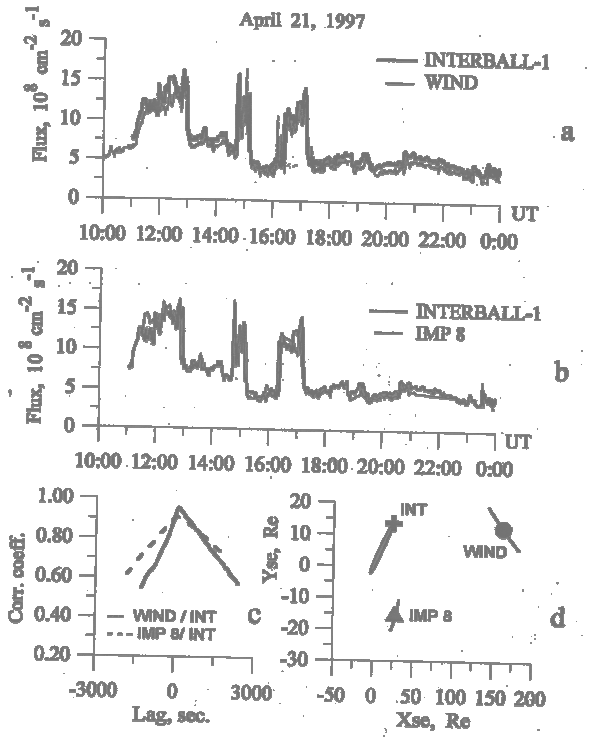


**Figure 1.** Example of good solar wind ion flux correlations by INTERBALL-1, WIND, IMP 8 data.

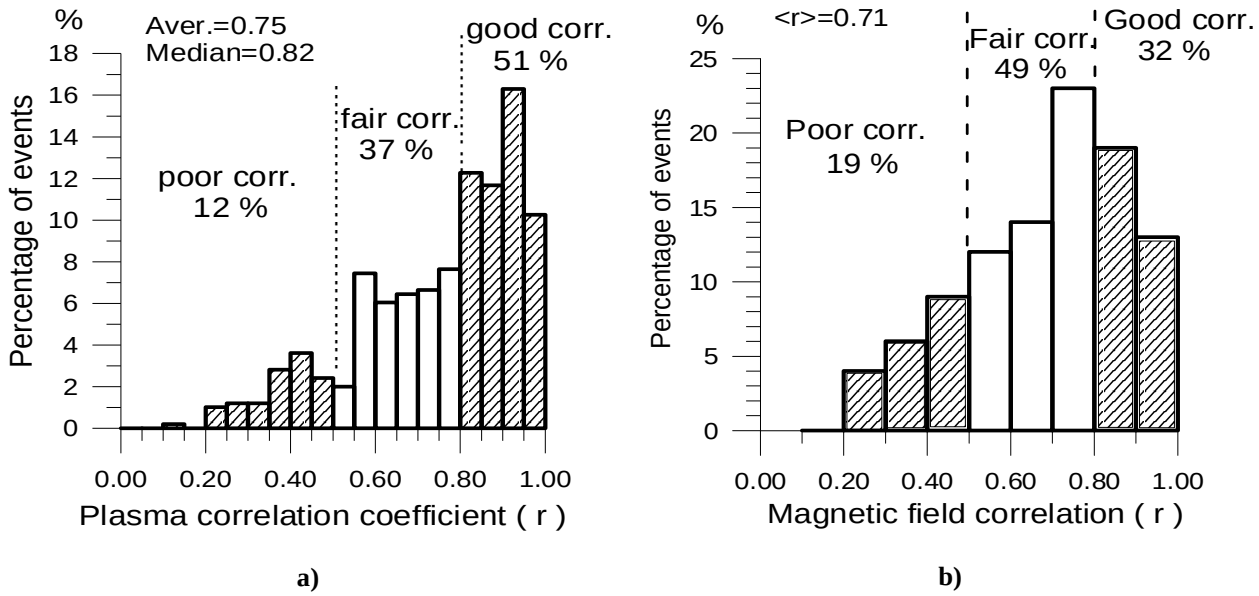


**Figure 2.** Statistics of plasma and magnetic field correlations by INTERBALL-1, IMP 8, WIND data.

Magnetic field correlations were studied in the 80s by ISEE-1,3 data [*Crooker et al*., 1982] but systematic investigation of solar wind plasma correlations was not performed before the comparison between INTERBALL-1, IMP 8 and WIND data [*Paularena* et al., 1997, *Zastenker* et al., 1998, *Paularena* et al., 1998]. In Figure 1 we present a typical example of correlations between SW ion flux measurements by INTERBALL-1, IMP 8 and WIND spacecraft separated by about 150 $R_e$ (Earth radii) along $X_{se}$ axis and about 30 $R_e$ in $Y_{se}$ direction. IMP 8 and WIND data were time-shifted by advection to INTERBALL-1 position. It can be seen that in this case the correlation level is very high (the correlation coefficient is about 0.9) for both pairs of spacecraft. But such a good level of correlations between the data from separated spacecraft does not always take place. Sufficiently large statistics calculated from the set of about 5 hundreds of 6-hours segments of measurements with 1 min resolution for the ion flux and magnetic field are shown in Figure 2a,b. It can be seen that good correlation (>0.8) takes place for only 30-50% of the segments, and for 1-19% of the segments a very poor correlation (<0.5) is observed. The average correlation coefficients are not very large and are equal to about 0.75 for the ion flux and 0.71 for the magnetic field amplitude [*Paularena et al*., 1997, *Zastenker et al*., 1998]. And from pragmatic point of view it is important that often the plasma and magnetic field correlations for the same segment are significantly different.

Investigation of the factors controlling the correlation level was done and the most important one proved to be the amplitude of the variations in a relevant parameter. As a criterion of such variations we took the value of the relative standard deviations (i.e. ratio of SD to the average value of a parameter) for plasma ion flux or density (RSD). We found that correlations became large enough if the RSD was higher than 0.2–0.3 [*Paularena et al*, 1998, 1999].

It means that the observations of a far upstream monitor are only reliable for Space Weather prediction only for large enough variations of the middle-scale solar wind structures. A possible explanation of this result is

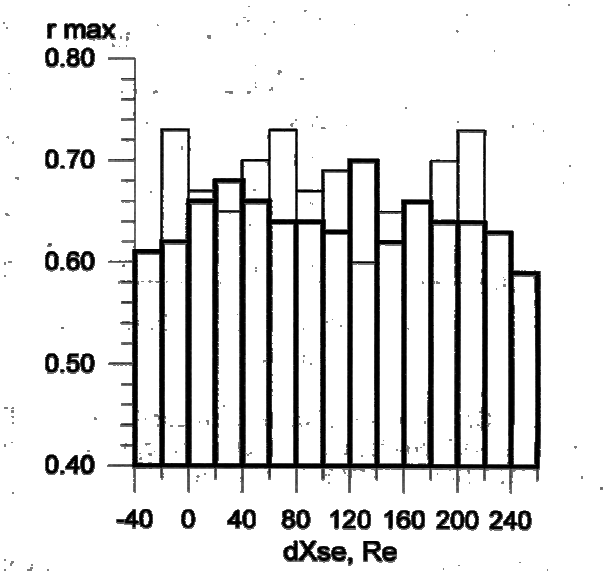


**Figure 3.** Dependence of ion flux correlations on $dX_{se}$ for $dYZ_{se} < 20R_e$ (thin line) and $>20R_e$ (thick line).

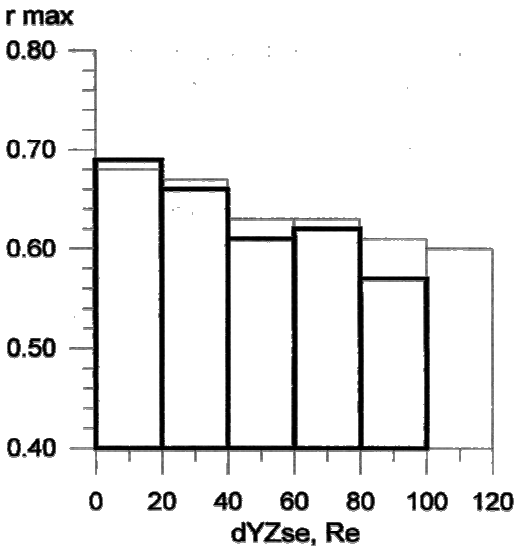


**Figure 4.** Dependence of ion flux correlations on $dYZ_{se}$ for $dX_{se}>50R_e$ (thin line) and $>200R_e$ (thick line).

that larger variations are associated with large solar wind structures giving better correlation.

We used multifactor analysis to find the dependence of correlations on spacecraft separation. We studied the influence of $dX_{se}$ (the distance along the Sun-Earth line) and $dYZ_{se}$ (the distance in the plane perpendicular to the Sun-Earth line) using large WIND/IMP 8/INTERBALL–1 dataset (2100 of 6-hours segments).

Figure 3 shows the dependence of correlation coefficients (averaged over $20R_e$ bins) on $dX_{se}$ separation for two ranges of $dYZ_{se}$ [*Zastenker et al.*, 2000*a*]. It is evident that on average the correlations do not depend on the distance along $X_{se}$ for both "small" and "large" spacecraft separations in the $YZ_{se}$ plane (slight decrease for $dX_{se} > 240R_e$ is not significant because of the small volume of measurements available for this interval). This result demonstrates that the persistence time of solar wind structures is usually longer than about 1 hour (the propagation time along 220 $R_e$ distance for the solar wind velocity equal to 400 km/s).

The dependence of correlations on the dYZse spacecraft separation (also averaged over 20 Re bins) is presented in Figure 4 for two ranges of dXse distance [*Zastenker et al*, 2000*a*]. For both subsets the correlations decrease slightly as the separation in the $YZ_{se}$ plane increases to 110 $R_e$. But this decrease is so small that we can conclude that the correlation length of the solar wind plasma inhomogeneities in the direction perpendicular to the Sun-Earth line is at least 200-500 Re [*Zastenker et al.*, 2000*b*].

**3. Sharp and large plasma fronts**.

An interesting feature of the solar wind is the sharp (from several seconds to several minutes duration) and large (from tens percents up to several times) increase or decrease of solar wind ion flux (or density). This phenomenon was not studied before mainly because of a poor time resolution of plasma measurements. Some of our recent results are published in [*Dalin et al.*, 2002*a*, 2002*b*, *Riazantseva et al.*, 2001].

A typical example of large and sharp solar wind ion flux pulse is presented in Figure 5. This pulse was observed by INTERBALL-1 satellite near the Earth ($X_{se}$ about $20R_e$) and by WIND spacecraft (data are shifted by propagation time) near the libration point L1 (about $200R_e$) and these observations are similar. Very high time resolution of INTERBALL-1 measurements (1s) allows us to show that in this event the leading front of the ion flux pulse is very short – increase in the flux by about two times during only 3s.

It is easy to calculate the width of such a narrow boundary between two plasma structures – for solar wind velocity of about 400 km/s it is equal to about 1000 km i.e. for observed conditions it is equal approximately to 10 proton giroradii.

It should be noted that the ion flux pulses under investigation are very often an increase/decrease in the plasma density only, while other solar wind parameters (velocity, temperature, magnetic field magnitude) remain almost constant [*Riazantseva et al.*, 2001].

By means of analysis of systematic solar wind observations onboard INTERBALL–1 satellite during 1996–1999, we have found a large number (several tens of thousands) of events related to this subject. Their statistics are presented in Figure 6 as the frequency observations of the sharp (less than 10 min) ion flux front dependence on their absolute (left panel) or relative (right panel) flux changes. It is seen the smooth but strong decrease of this frequency from about 90 "weak" events per day (with $dF> 0.5*10^8$ $cm^{-2}\cdot s^{-1}$) up to one "strong" event for 5 days (with $dF >8*10^8$ $cm^{-2}\cdot s^{-1}$).

It is well known that the interplanetary magnetic field in average is directed along the Parker's spiral [*Veselovskii et al.*, 2001]. But the orientation of the solar wind plasma structures is not investigated enough adequately. Some results for the orientation of middle-scale structures were obtained from the correlation study [*Richardson et al.*, 1998, *Coplan et al.*, 2001, *Dalin et al.*, 2002*c*] but for sharp plasma fronts it is necessary to use another method. We determined their orientation by means of an analysis of the time delay between observations of corresponding plasma fronts at two or more well-separated spacecraft in the solar wind [*Riazantseva et al.*, 2001].

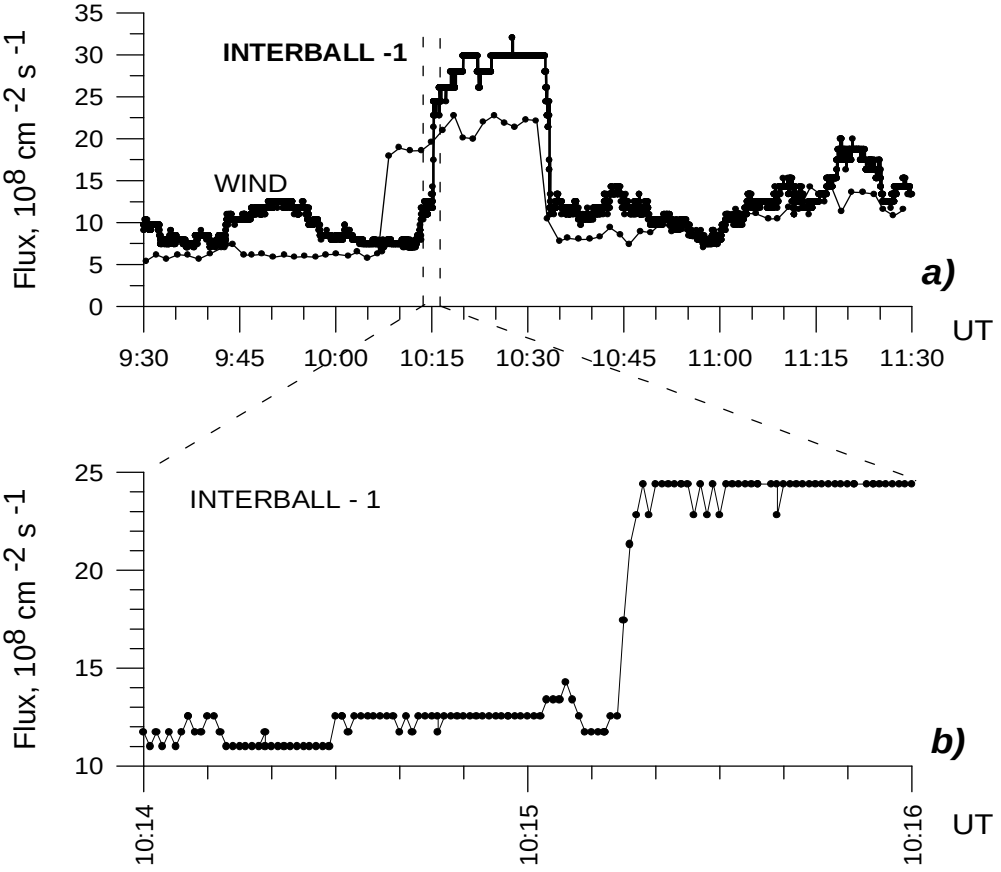


**Figure 5.** Example of the sharp and large ion flux pulse by INTERBALL-1 and WIND data. Low panel shows the detail plot of the leading front.

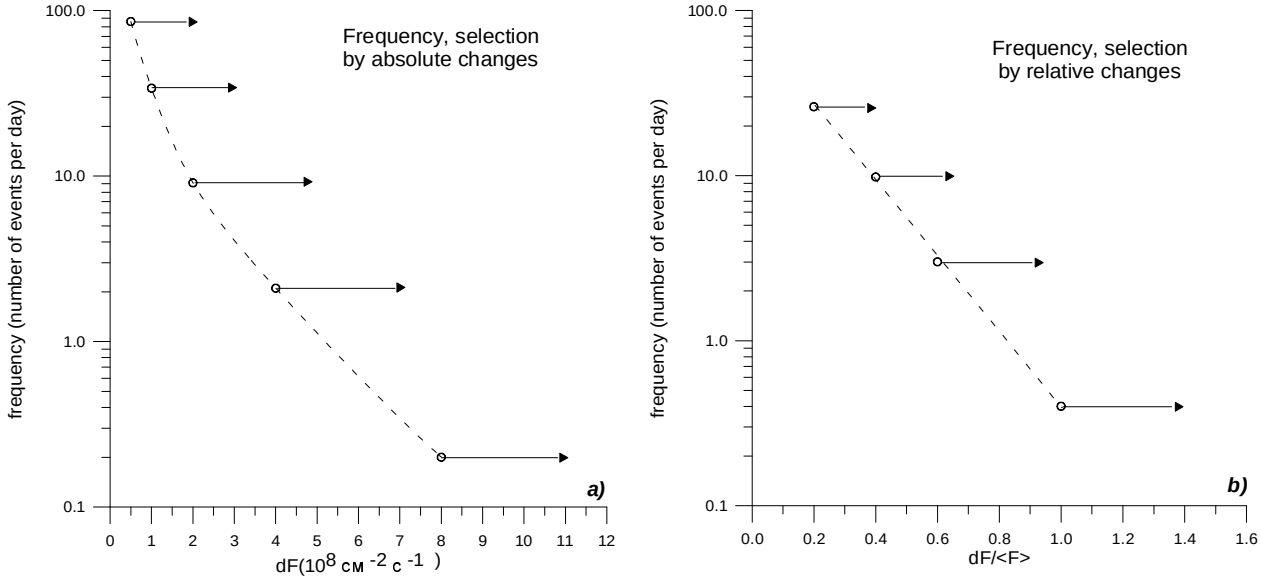


**Figure 6**. Statistics of the absolute and relative values of the sharp ion flux increase or decrease.

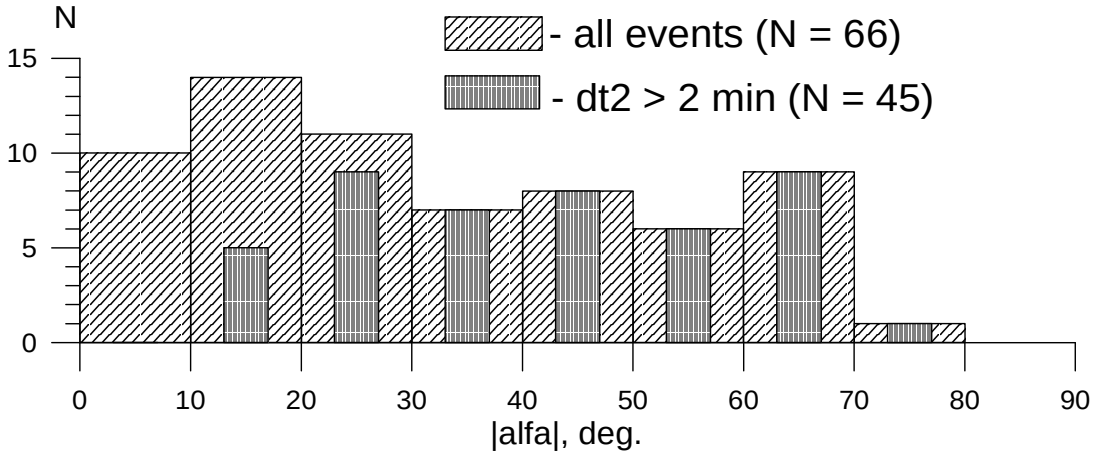


**Figure 7.** Statistics of the inclinations of the sharp ion flux fronts to the $YZ_{se}$ plane (for all delays and for delays more than 2 min.).

For this study we used simultaneous plasma measurements by ACE, INTERBALL-1, WIND, IMP-8 and GEOTAIL. Time delays of sharp fronts of ion flux changes were observed over the range of 1–20 min after advection shift of all the data to the same point by solar wind propagation time. Using these delays for two spacecraft data we calculated the inclinations of the fronts to the Sun-Earth line and for three spacecraft data - inclinations in 3D space. The key hypothesis that such fronts are plane in the scales of several tens of $R_e$ was checked by comparison between several pairs of measurements.

Results of determination of these fronts inclination to the Sun-Earth line for 66 events with "large" ion flux changes are presented in Figure 7. The distribution of the inclination angle is rather wide and for 50% of cases the angle between the plane of the front and Sun-Earth line is less than 60° (or more than 30° to the $YZ_{se}$ plane). So, these results show us that in spite of the common point of view in many cases the planes of the sharp and large plasma fronts are not perpendicular to the Sun-Earth line but are inclined to it at a significant angle.

For the study of solar-terrestrial connections it is important to recognize the influence of such sharp ion flux (or dynamic pressure) changes on the geomagnetic field. This problem yet is not investigated enough. We can mention only the paper [*Borodkova et al.*, 1995] where some fast variations in dayside magnetosphere magnetic field resulted from pressure pulses were presented.

An example of such variations in the geomagnetic field influenced by solar wind plasma pressure pulse is shown in Figure 8. This event (as it is seen in the panels “b” and “c” in Figure 8) is of special interest because neither solar wind speed, normagnitude and direction of IMF change during the pressure pulse. So, in this case geomagnetic variations are only connected with change in the plasma density.

Owing to this pressure pulse observed by WIND and INTERBALL-1 (panel “a” in Figure 8) we can see variations in the magnetic field detected by geosynchronous satellite GOES-8 and two groundbased stations – low-latitude (Tamanrasset) and high-latitude (Narsarsuaq). In the panel “d” in Figure 8 it is seen that sharp solar wind pressure changes give similar response in magnetic field behavior both in the geosynchronous orbit and at the low-latitude station. These variations are very fast (several minutes) therefore they definitely can be explained (as it was shown in [*Borodkova et al.*, 1995]) by dynamics of Chapman-Ferraro currents (DCF) on the magnetopause.

But as it is seen in panel “e” in Figure 8 at the high-latitude station the pressure pulse only creates the generation of geomagnetic pulsations with large amplitude over the frequency range of Pc 5 (T ~ 400s).

## 4. Plasma oscillations in the foreshock

The bow shock upstream region – the foreshock – ahead of the quasi-parallel shock is one of the most interesting but complicated phenomenan in space. It was widely explored in many theoretical and experimental papers (see, for example, reviews in [*Hoppe et al.*, 1981, *Fusilier S.A.*, 1994, *Song et al.*, 1994] and references therein) but many features of the foreshock are not well known so far.

Most of the previous studies concentrated to magnetic field waves and backstreaming particles, but there is no complete data based on the solar wind plasma fluctuations in the foreshock. Plasma measurements with the high-time resolution onboard INTERBALL-1 and

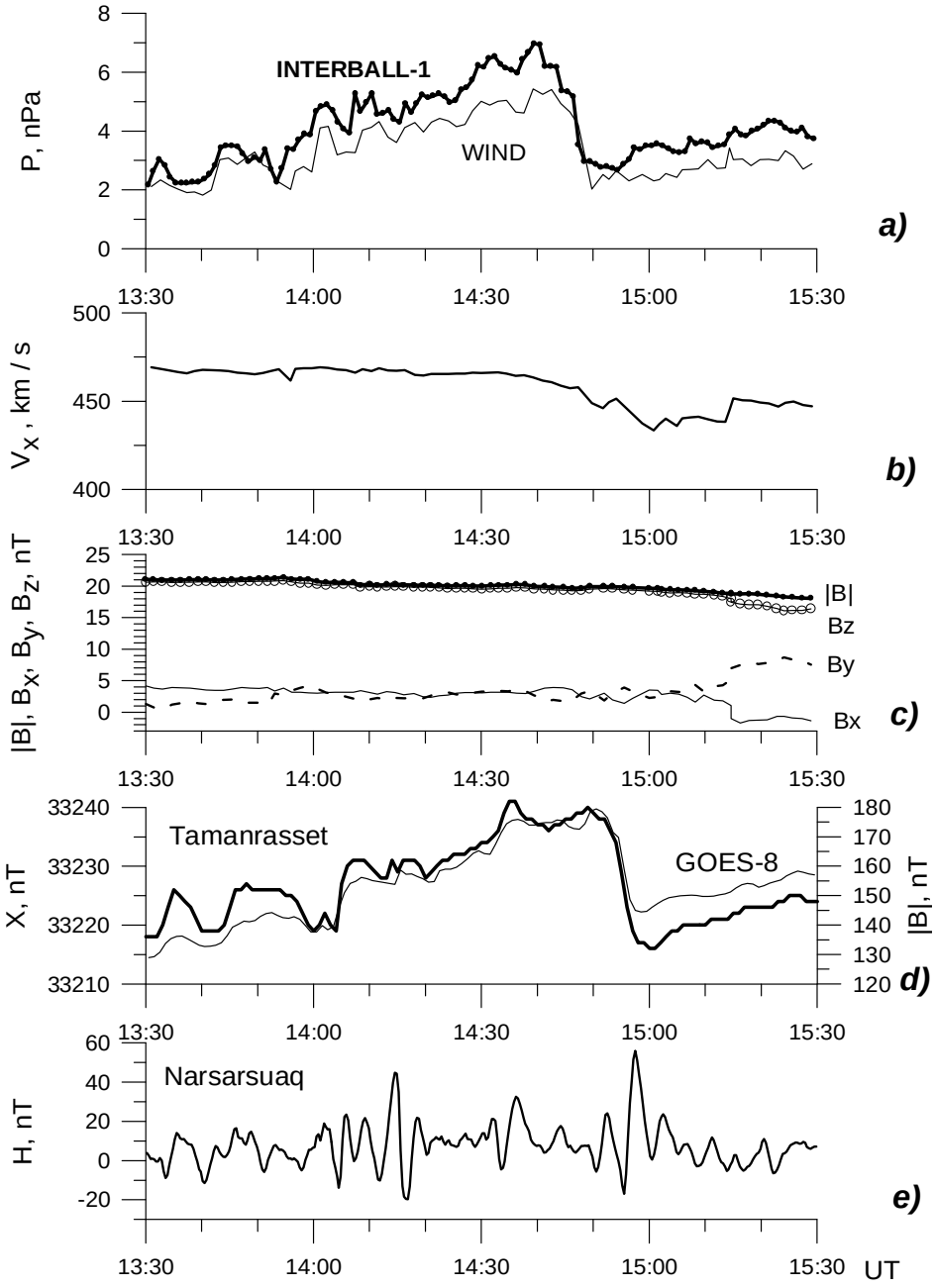


**Figure 8.** Example of geoeffectivity of the solar wind plasma pressure pulse under the almost permanent values of $V_{sw}$ and IMF. Variations of geomagnetic field by data of GOES 8 spacecraft, low latitude (Tamanrasset) and high latitude (Narsarsuaq) stations are shown.

MAGION-4 satellites allow us to observe the fast solar wind changes (modification) in the foreshock region.

Figure 9 presents an example of such kind of events from INTERBALL-1 observations during the period of several hours on April 13, 1996 [*Zastenker et al.*, 1999*a*]:

- the energy flux (in the range of 0.2–25 keV) of backstreaming particles;
- the solar wind ion flux with 1-s time resolution measured by Faraday cup detector directed to the Sun;

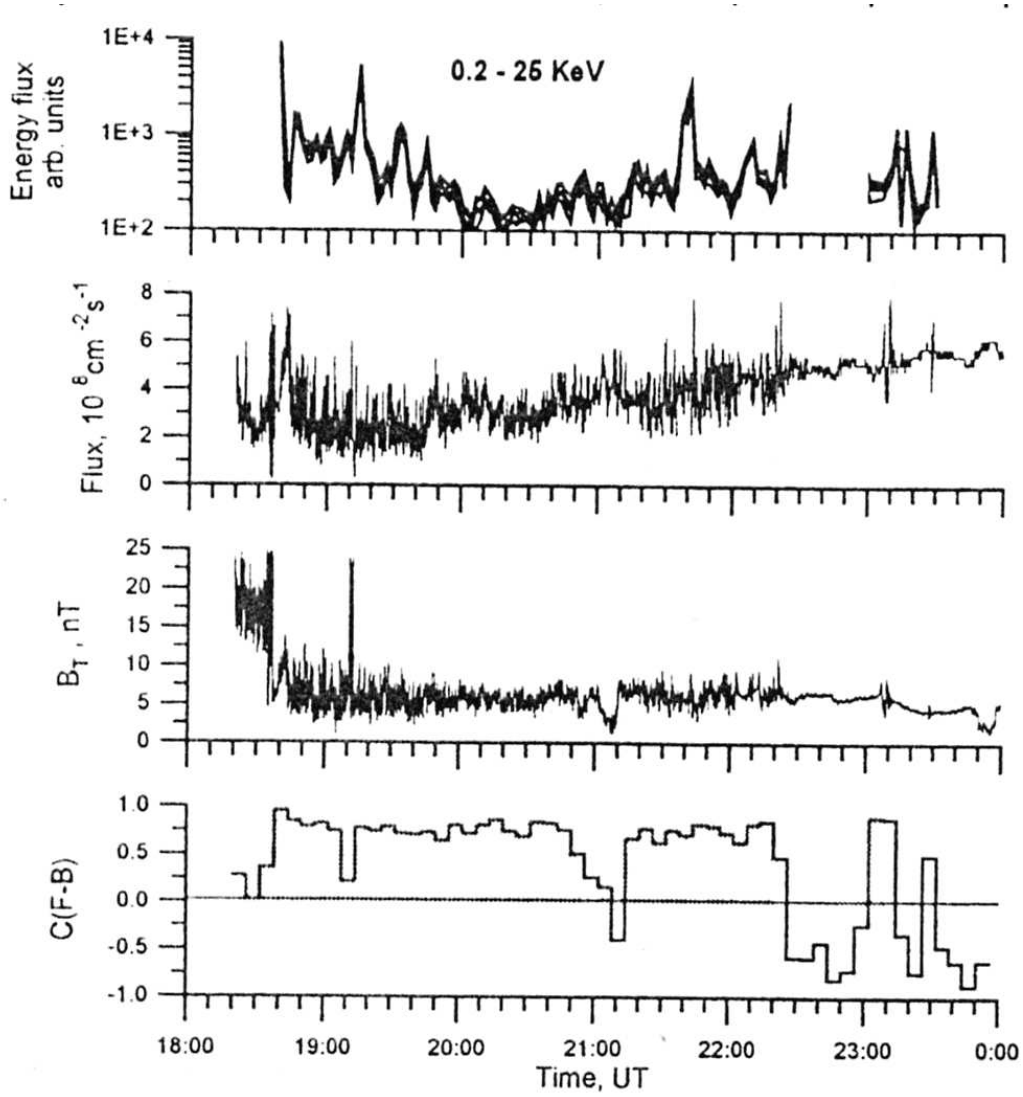


**Figure 9.** Example of backstreaming energetic particles, ion flux and magnetic field magnitude variations in the foreshock at 13.04.96. Low panel shows the cross-correlation coefficients between plasma and field variations during 10-min. intervals.

- the magnitude of the interplanetary magnetic field with the same resolution;
- windowed correlation coefficient of the solar wind ion flux and IMF values.

The interval under consideration may be clearly divided into three parts – before bow shock crossings at 18.35 UT; from 18.35 till 22.25 UT and after 22.25 UT. The first and third parts correspond to the magnetosheath and undisturbed solar wind respectively. As it can be easily seen the second interval clearly differs from the others. It allows us to identify this interval as a foreshock – a region with a large amplitude (tens percents) and fast (1–100 mHz) fluctuations of magnetic field and plasma.

This high level of solar wind ion flux variations means that the foreshock does modify the solar wind before it comes to the bow shock.

As it can be seen from Figure 9 high positive correlation (about 0.7–0.8) between plasma and field fluctuations does exist in the second interval of this event. Such phenomenon seems to be unique for the foreshock and may be interpreted as evidence of a fast mode of ion-sonic waves generated in this region [*Lacombe et al.*, 1995]. It is worth noting that the correlation between the ion flux and magnetic field strongly decreases both in the magnetosheath and in the undisturbed solar wind (see Figure 9).

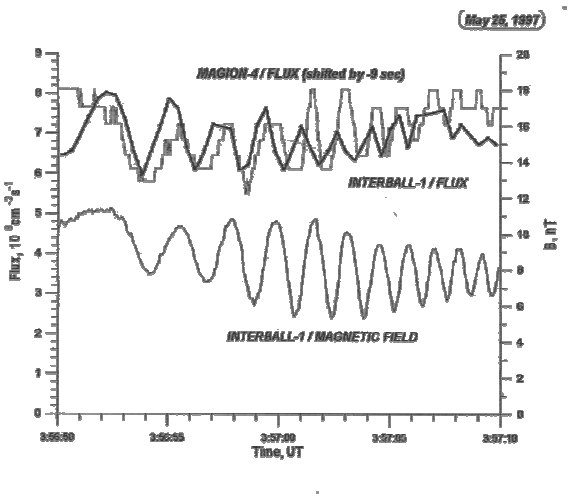


**Figure 10.** Example of the fast quasi-harmonical oscillations of the ion flux (by INTERBALL-1 and MAGION-4 data) and magnetic field (by INTERBALL-1) in the foreshock.

The comparison between the behavior of backstreaming energetic particles and the solar wind and IMF variations shows that they are very similar.

Another remarkable foreshock feature firstly found in high-time resolution measurements in the INTERBALL project is the existence of quasi-harmonic fast plasma oscillations [*Zelenyi et al*., 2000, *Eiges et al*., 2002]. Several papers described such structures in the IMF (see, for example, [*Russell C.T*., 1994]) but plasma data were never presented.

An example of such measurements is shown in Figure 10. Data on solar wind ion flux from INTERBALL-1 and MAGION-4 are compared with IMF ones from INTERBALL-1. It is seen that both values – plasma and magnetic field show almost harmonic oscillations with a period of about 2s and a duration of about 15s. A good coincidence between variations in plasma and field means that these waves are compressional.

There is also a good correlation between measurements (shifted by 9s) by INTERBALL-1 and MAGION-4 with spacecraft separation about 1200 km. The time delay between these observations can be used as an estimate of the lower limit of the "life time" of these features.

## 5. Low- and high-frequency variations in the magnetosheath

The magnetosheath (MSH), as an interface between the solar wind and the magnetosphere plays an important role in the transfer of the solar wind plasma and IMF to the magnetopause. However MSH properties have been studied less than any other region of the near-Earth space. Only recently this region received more attention (see, for example, [*Seon et al*., 1999, *Song et al*., 1999, *Zastenker et al.,* 1999*b*]).

It is commonly thought that the variability of all parameters of plasma and magnetic field in MSH is dramatically larger than in the undisturbed SW, but the quantitative comparison of their characteristics was not previously studied in detail.

From simultaneous observations of plasma and magnetic field onboard WIND spacecraft (used as a SW monitor) and INTERBALLl-1 satellite in the MSH we studied the variations in MSH [*Zastenker et al.,* 1999*b*, *Zastenker et al*., 2002]. These results were also compared with predictions of the gasdynamic model of Spreiter et al. [*Spreiter et al.,* 1966].

Figure 11 shows an example of INTERBALL-1 data on ion flux and magnetic field magnitude for a typical MSH crossing. These plots show 2.5 hours measurements with 1 min time resolution (upper panels) and 10 min of data with 1s time resolution (lower panels). The top panels also show solar wind ion flux and IMF data from WIND with 1.5 min resolution time-shifted by the plasma propagation speed from WIND to INTERBALL-1.

In accordance with the general picture of the plasma flow around the magnetosphere [*Spreiter et al*., 1966], both the ion flux and magnetic field magnitude significantly exceed values in the undisturbed SW. But the main feature of the MSH demonstrated by Figure 11 is that the ion flux and magnetic field magnitude values exhibit variations with the amplitude much larger than those in the corresponding data on solar wind.

Large variations in the ion flux and magnetic field magnitude are observed both on the time scales of several minutes (low-requency variations in the upper panels in Figure 11) and on the time scales of several seconds (high-frequency variations in the lower panels in Figure 11).

To estimate the level of variations we have used values of standard deviations (SD) and relative standard deviation (RSD). A comparison between variations of the ion flux and magnetic field magnitude in MSH and SW for low-frequency variations is presented in Figure 12, which shows histograms of the percentage of RSD values in each RSD bin. It is clearly seen that relative variations in both the ion flux and magnetic field in MSH are in average 2–2.5 times higher than those in the undisturbed SW.

The radial profile of parameters in the MSH can help to reveal a source of plasma and magnetic field variations. Nemecek *et al*. [*Nemecek et al*., 2000]

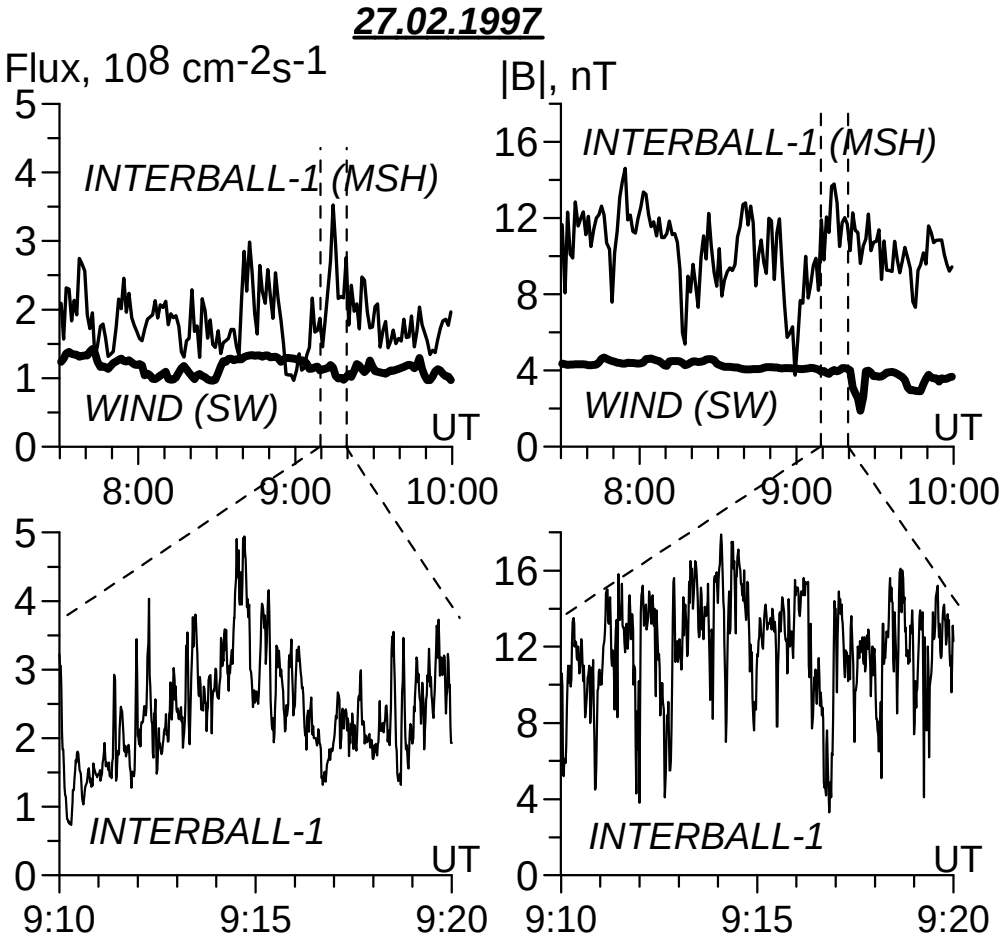


**Figure 11.** Example of ion flux and magnetic field changes in the magnetosheath (by INTERBALL-1 data) in comparison with simultaneous solar wind data (by WIND). Low panels show the high frequency variations by 1-sec. measurements.

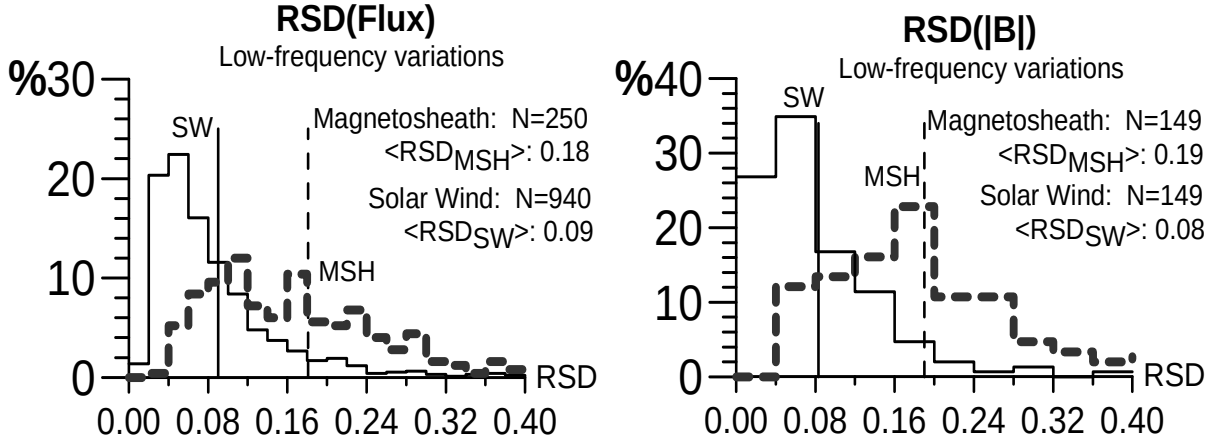


**Figure 12.** Histograms of the relative standard deviations of ion flux and IMF magnitude for high frequency variations in the solar wind and magnetosheath. Vertical lines mark the average values in SW (solid lines) and MSH (dash lines).

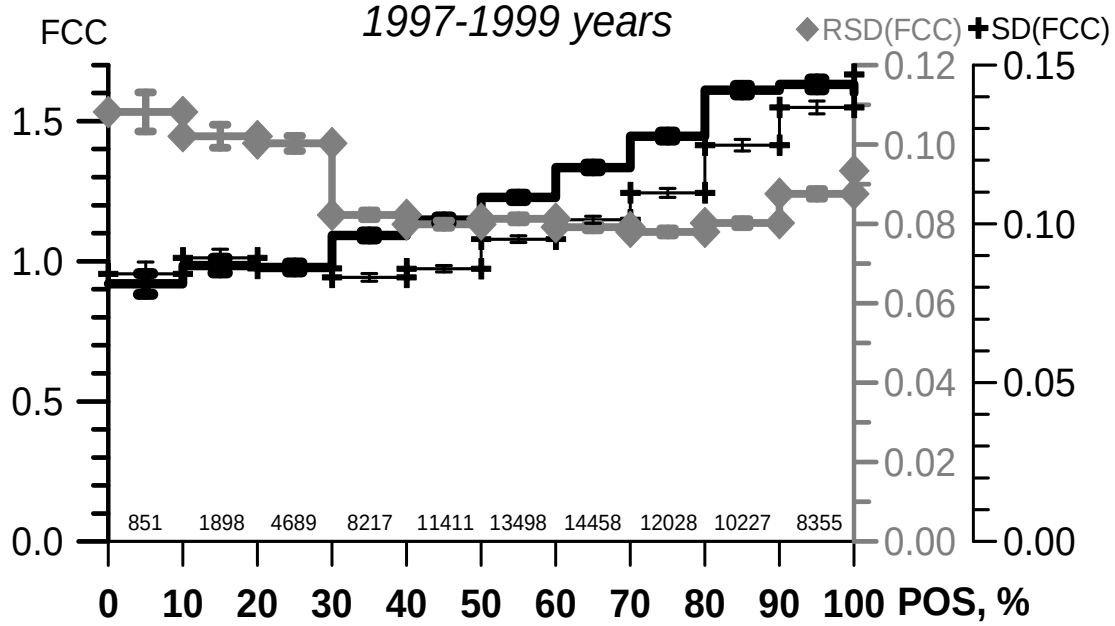


**Figure 13.** Radial dependence across the magnetosheath (0 – magnetopause, 100% – bow shock positions) of ion flux compression coefficients (FCC), standard deviations (SD) and relative standard deviations (RSD) of FCC (variations of the one second values during one minute interval).

showed that this profile could be investigated by means of the Spreiter model. A position of the satellite relative to magnetosheath boundaries (BS and MP) was determined from the Shue et al. [*Shue et al.*, 1998] model for MP locations and the MSH width determined according to the Spreiter model.

To account for simultaneous changes in SW we calculated the normalized ion flux compression coefficient FCC=(Flux)MSH/(Flux)SW (see [*Zastenker et al*., 2002]). The average radial profiles of FCC and its SD and RSD for high-frequency variations are presented in Figure 13 (see [*Shevyrev et al.*, 2003]).

FCC gradually increases from the magnetopause to the bow shock because the plasma density increases toward the bow shock in qualitative accordance with the Spreiter model. But the level of variations across the MSH remains approximately constant: the SD(FCC) is about of 0.08-0.10 for the whole distance from the magnetopause to the bow shock. Since the FCC values increase toward the shock, the average values of RSD(FCC) decrease toward the bow shock approximately from 0.1 to 0.04–0.07.

The RSD values of the low-frequency variations are about 2 times higher than for the high-frequency ones but shapes of their radial profiles are rather similar [*Nemecek et al.*, 2000]. From these results, we can conclude that the sources of high- and low-frequency variations are probably the same.

Since absolute variations in the normalized ion flux SD(FCC) are nearly constant throughout the magnetosheath from the BS to the MP, we can conclude that the source of these variations is located at the bow shock or inside the MSH but not at the magnetopause itself.

As it is well known, when the angle $\theta_{Bn}$ between the vector of the interplanetary magnetic field and the normal to the bow shock is lower than approximately $45^{o}$, very large fluctuations of plasma and magnetic field are often observed in the foreshock region ahead of the bow shock (see the chapter 4 of this paper). But effects of these foreshock fluctuations on the BS and MSH were not examined carefully. In the paper [*Luhman et al*., 1986] the effect of IMF orientation (cone angle) on the fluctuations of the magnetic field in the dayside magnetosheath was investigated, but no clear conclusions were made

To calculate the angle $\theta_{Bn}$ for our measurements, we used flow streamlines from the Spreiter model to connect a normalized satellite position to a point in the model BS. At this BS point we can determined the normal to the bow shock surface and $\theta_{Bn}$ angle using time-shifted IMF data from WIND. Of course, this procedure is correct only if the magnetosheath plasma move along the streamlines and strong waves do not propagate relative to the plasma flow. Our results suggest that these assumptions are correct, but this hypothesis needs further study.

A typical example of high-frequency fluctuations of the plasma and magnetic field in the undisturbed solar

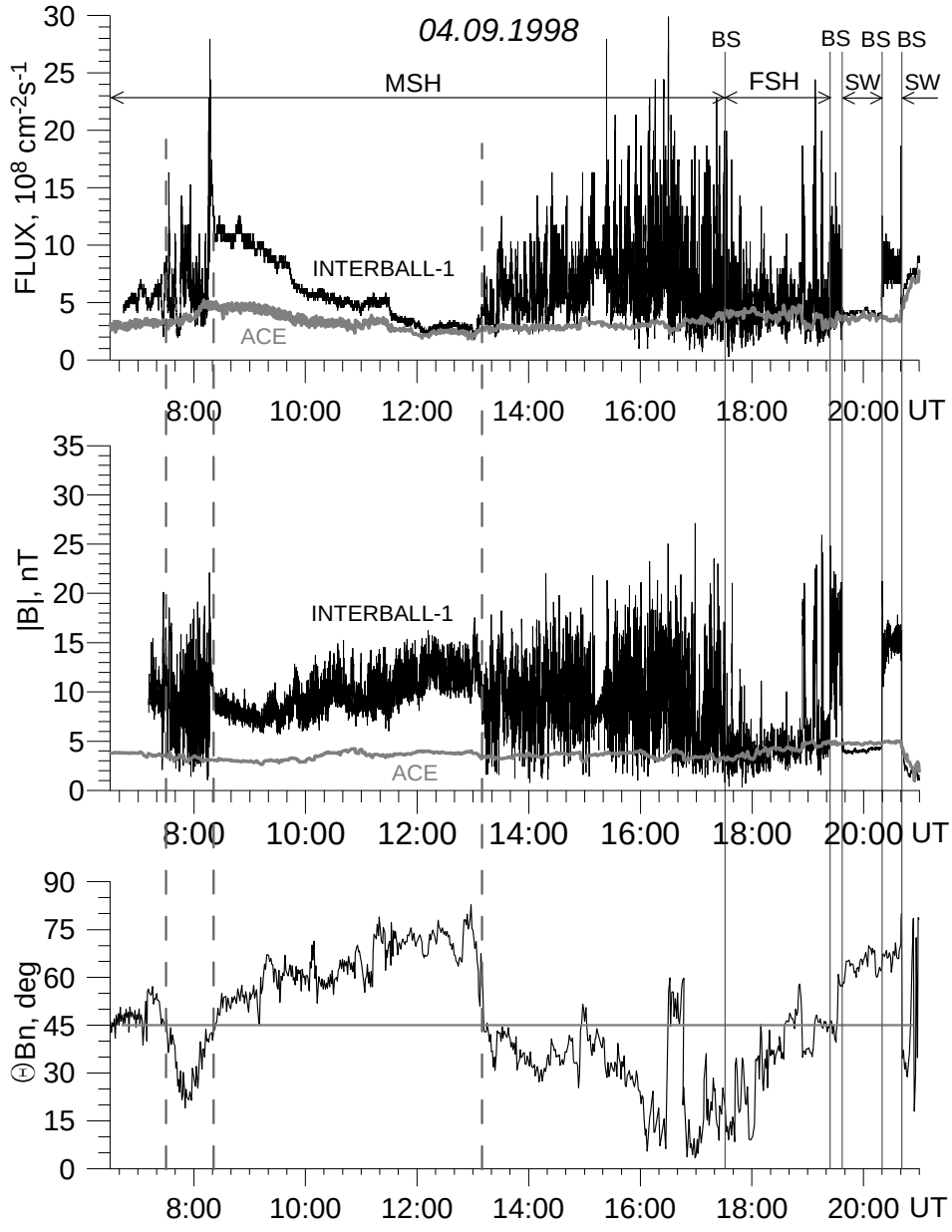


**Figure 14.** Example of ion flux and magnetic field variations in the undisturbed solar wind (SW), foreshock (FSH) and magnetosheath (MSH) under control of $\theta_{Bn}$ values. Dash lines mark the crossings of $\theta_{Bn}$ = 45° level. Solid lines mark the bow shock (BS) crossings.

wind, foreshock and magnetosheath in comparison with the $\theta_{Bn}$ angle behavior is presented in Figure 14. It is clearly seen that the amplitude of the ion flux and magnetic field fluctuations in the MSH strongly decreases when the $\theta_{Bn}$ angle became more than about 45° (for example, in the interval 8.20–13.10 UT) and increases when $\theta_{Bn}$ became less than about 45°.

As the statistical study shows (see [*Shevyrev et al.*, this issue]), plasma and magnetic field fluctuations in the MSH behind the quasi-parallel bow shocks in average are approximately two times higher than behind the quasi-perpendicular bow shocks.

These results are further evidence that the bow shock is a source of the plasma and magnetic field magnetosheath fluctuations, because their amplitudes strongly depend on bow shock features. Further study is needed to understand the mechanism of this influence in detail.

## 6. Conclusions

The new results obtained by our solar wind study can be summarized as follows:

1. For middle-scale structures (size about several millions km):

   – the average level for both the ion flux and IMF magnitude correlations between well-separated spacecraft data is about 0.7-0.75 for large statistics;
   – the level of correlation increases for large amplitudes of plasma and field variations;
   – the persistence time of these solar wind structures is usually more than about 1 hour;
   – the correlation length of these solar wind structures in the plane perpendicular to the Sun-Earth line is in average more than 200-500 Re (i.e. – significantly more than the cross-section of the magnetosphere).

2. For ion flux (density) sharp pulses:

   – in the solar wind very large (up to several times) and sharp (from several seconds to several minutes) ion flux (density) changes are observed rather often;
   – it means that the borders of the small-scale solar wind structures can be so thin as several tens of proton giroradii;
   – in about 50% of the analyzed cases phase fronts of ion flux pulses are not perpendicular to the Sun-Earth line but are inclined to it at an angle less than $60^o$;
   – these sharp ion flux (dynamic pressure) changes can be very geoeffective and can create significant disturbances of the dayside magnetic field on the geosynchronous orbit and at low latitude groundbased stations.

3. For plasma variations in the foreshock region:

   – both magnetic field magnitude and solar wind ion flux demonstrate large (about tens percents) and fast (with frequencies of 1-100 mHz) variations in the foreshock;
   – the unique foreshock feature is the large positive cross-correlation (with correlation coefficient of about 0.7-0.8) between plasma and field variations; it may be interpreted as generation of the fast ion-sonic waves;
   – sometimes in the foreshock short (about 10-15 s) bursts of quasi-harmonic ion flux oscillations (in the phase that of magnetic field) with the period of about 2s can be observed; these fluctuations are in good correlation for two rather close (<1 Re) to each other spacecraft.

4. For MSH plasma and field variations:

   – in addition to magnetic field variations large plasma variations take place in the MSH in a wide range of frequencies (1–100 mHz);
   – relative variations of both the ion flux and magnetic field in the MSH are in average 2–2.5 times higher than ones in the undisturbed solar wind;
   – the level of plasma and field variations across the MSH remains approximately constant for the whole distance from the bow shock to the magnetopause;
   – plasma and magnetic field variations in the MSH increase significantly with decreasing in the IMF $\theta_{Bn}$ angle and, on average, fluctuations behind the quasi-parallel bow shock are approximately two times higher than that behind the quasi-perpendicular shock;
   – all the features described allow us to suppose that the bow shock is the main source of the large plasma and magnetic field magnetosheath fluctuations.

It is necessary to emphasize that most of these solar wind features may be very important for the pragmatic aim - prediction of the Space Weather.

**Acknowledgement.** This paper was partly supported by RFBR grants 01-02-16182 and 01-05-64203 and NSF grants ATM-0207775, ATM-0203723.

## References

Borodkova, N. L., D. G. Sibeck, G. N. Zastenker, A case and statistical study of transient magnetic field events at geosynchronous orbit and their solar wind origin, *Journ. Geophys.Res., 100*, A4, 5643-5656, 1995.

Coplan, M. A., Ipavich F., King J., et al., Correlation of solar wind parameters between SOHO and WIND, *Journ. Geophys. Res., 106*, A9, 18615-18624. 2001.

Crooker, N. U., G. L. Siscoe, C. T. Russell, E. J. Smith, Factors controlling degree of correlation between ISEE 1 and ISEE 3 interplanetary magnetic field, *Journ. Geophys. Res., 87*, 2224-2230, 1982.

Dalin, P. A., G. N. Zastenker, K. I. Paularena, and J. D. Richardson, A Survey of large, rapid solar wind dynamic pressure changes observed by INTERBALL-1 and IMP-8, *Ann. Geoph., 20*, 3, 293-299, 2002*a*.

Dalin, P. A., G. N. Zastenker, M. N. Nozdrachev, I. S. Veselovsky, Properties of large and sharp impulses in the solar wind, *IJGA, 3*, 1, 51-56. 2002*b*.

Dalin, P. A., G. N. Zastenker, J. D. Richardson, Orientation of the solar wind plasma middle-scale structures, *Kosmich. Issled*. (in Russian), *40*, 4, 343-348, 2002*c*.

Eiges, P., G. Zastenker, M. Nozdrachev, N. Rybyeva, J. Safrankova, Z. Nemecek, Small scale solar wind ion flux and IMF quasi-harmonical structures in the Earth's foreshock: INTERBALL-1 and MAGION-4 observations, *Adv. Space Res., 30*, 12, 2725-2729, 2002.

Fusilier, S. A., Suprathermal ions upstream and downstream from the Earth's bow shock, "Solar wind sources of magnetospheric ultra-low-frequency waves", ed. by M. J. Egebretson, *Geophysical monograph, 81*, pp.107-119, 1994.

Galeev, A. A., Yu. I. Galperin, L. M. Zelenyi, The INTERBALL Project to study solar-terrestrial physics, *Cosmich. Res., 34*, 4, 339-362, 1996.

Hoppe, M. M., C. T. Russell, L. A. Frank et al., Upstream hydromagnetic waves and their assotiation with backstreaming ion populations: ISEE 1 and 2 observations, *Journ. Geophys. Res., 86*, 6, 4471-4492, 1981.

Lacombe, C., G. Belmont, D. Hubert et al., Density and magnetic field fluctuations observed by ISEE 1-2 in the quiet magnetosheath, *Ann. Geophys., 13*, 343-357, 1995.

Luhmann, J. G., C. T. Russell, R. C. Elphic, Spatial distributions of magnetic field fluctuations in the dayside magnetosheath, *Journ. Geophys. Res., 91*, 1711-1715, 1986.

Nemecek, Z., J Safrankova, G. N. Zastenker, P. Pisoft, K. I. Paularena, J. D. Richardson, Observations of the radial magnetosheath profile and a comparison with gasdynamic model predictions, *Geophys. Res. Lett., 27*, 17, 2801-2804, 2000.

Paularena, K. I., J. D. Richardson, A. J. Lazarus, G. N. Zastenker, P. A. Dalin, IMP 8, WIND, and INTERBALL observations of the solar wind, *Phys. Chem. Earth, 22*, 7-8, 629-637, 1997.

Paularena, K. I., G. N. Zastenker, A. J. Lazarus, P. A. Dalin, Solar wind plasma correlations between L1 and Earth, *Journ. Geophys. Res., 103*, A7, 14619, 1998.

Paularena, K. I., J. D. Richardson, G. N. Zastenker, P. A. Dalin, Solar wind correlations: using a solar wind monitor successfully, in book *INTERBALL in the ISTP Program*, ed. by D.G. Sibeck, K. Kudela, Kluwer Academic Publishers, 155-170, 1999.

Riazantseva, M. O., P. A. Dalin, G. N. Zastenker, Statistical study of the sharp and large solar wind ion flux changes by INTERBALL-1 satellite measurements, *Proceedings of WDS'01 Conference*, Part II. Physics of plasmas and ionized media, 233-238, 2001.

Richardson, J. D,Paularena K. I. The orientation of the plasma structure in the solar wind, *Geophys. Res. Lett., 25*, 12, 2097-2100, 1998.

Russell, C. T., Magnetospheric and SW studies with co-orbiting s/c, *AGU Geophys. Monograph 84*, Solar System Plasma in Space and Time, ed. by J. L. Burch and J. H. White, 85, 1994.

Seon, J., S. M. Parks, K. W. Min et al., Observations of the density fluctuations in Earth's magnetosheath with Geotail and Wind spacecraft, *Geoph. Res. Lett., 26*, 7, 959-962, 1999.

Shevyrev, N. N., Zastenker G. N., Nozdrachev M. N. et al., High and low frequency large amplitude variations of plasma and magnetic field in the magnetosheath: radial profile and some features, *Adv. Space Res*., *31*, 5, 1389-1394, 2003.

Shevyrev, N. N., P. E. Eiges, G. .N. Zastenker, J. D. Richardson, Comparison of ULF plasma and magnetic field waves inside the foreshock and magnetosheath, (this issue).

Shue, J. -H., P .Song, C. T. Russell, J. T.Steinberg, J. K. Chao, G. Zastenker, O. L.Vaisberg, S. Kokubun, H. J. Singer, T. R. Detman, H. Kawano, Magnetopause location under extreme solar wind conditions, *Journ. Geoph. Res., 103*, A8, 17691-17700, 1998.

Song, P., C. T. Russell, S. P. Gray, Identification of low-frequency fluctuations in the terrestrial magnetosheath, *Journ. Geophys. Res., 99*, 6011-6025, 1994.

Song, P., C. T. Russell et al., On the processes in the terrestrial magnetosheath, 1. Scheme development, *Journ. Geoph. Res., 104*, 22345, 1999; 2. Case study, *Journ. Geoph. Res., 104*, 22357, 1999.

Spreiter, J. R., A. L. Summers, A. Y. Alksne, Hydromagnetic flow around the magnetosphere, *Planet.Space. Sci., 14*, 223-253, 1966.

Veselovskii, I. S., Torsina M. V., Angular distribution of IMF vector, *Geomagn. and Aeronomie* (in Russian), *41*, 4, 471-476, 2001.

Zastenker, G. N., P. A. Dalin, A. J. Lazarus, K. I. Paularena, Comparison of the solar wind parameters measured simultaneously aboard several spacecraft, *Cosmic Research, 36*, 3, 214-226, 1998.

Zastenker, G. N., J. Safrankova, Z. Nemecek, K. I. Paularena, A. O. Fedorov, I. P. Kirpichev, N. L. Borodkova, Fast and large variations of magnetosheath parameters: variations of ion flux and other plasma characteristics, *Kosmich. Issled*., *37*, 6, 605-615, 1999*a*.

Zastenker, G. N**.**, P. E. Eiges, M. N. Nozdrachev, V. N. Lutsenko, Yu. I. Yermolaev, J. Safrankova, Z. Nemecek, K. I. Paularena, J. D. Richardson, R. P. Lepping, T. Mukai, S. Kokubun, Solar wind modifications in the foreshock, *Proceedings of the Solar Wind 9 Conference*, ed. by S.R. Habbal, Esser,

J.V. Hollweg, Ph.A. Isenberg, American Institute of Physics, 471, 555-560, 1999*b*.

Zastenker, G. N., M. Nozdrachev, J. Safrankova, Z. Nemecek, K. I. Paularena, A. J. Lazarus, R. P. Lepping, T. Mukai, Fast solar wind plasma and magnetic field variations at the magnetosheath, *Czech Journal of Physics*, *49*, 4a, 579-590, 1999*c*.

Zastenker, G. N., Dalin P. A., Paularena K. I., Richardson J. D., F. Dashevskiy, Solar wind correlation features obtained from a multi-spacecraft study, *Adv. Space Res.*, *26*, 1, 71-76, 2000*a*.

Zastenker, G. N, P. A. Dalin, A. A. Petrukovich, M. N. Nozdrachev, S. A. Romanov, K. I. Paularena, J. D. Richardson, A. J. Lazarus, R. P. Lepping, A. Szabo, Solar wind structure dynamics by multipoint observations, *Phys. Chem. Earth (C)*, *25*, No.1-2, 137-140, 2000*b*.

Zastenker, G. N., M. N. Nozdrachev, Z. Nemecek, J. Safrankova, K. I. Paularena, J. D. Richardson, R. P. Lepping, T. Mukai, Multispacecraft measurements of plasma and magnetic field variations in the magnetosheath: comparison with Spreiter models and motion of the structures, *Planet. Space Sci.*, *50*, 601-612, 2002.

Zelenyi, L., G. N. Zastenker, P. A. Dalin, P. Eiges, N. Nikolaeva, J. Safrankova, Z. Nemecek, P. Triska, K. Paularena, J. Richardson, Variability and structures in the solar wind-magnetosheath-magnetopause by multiscale multipoint observations, Proceedings of the ESA Workshop in London, *ESA SP-449*, 29-38, 2000.

# Profiles of the night-side magnetosheath

M. Hayosh[1], Z. Nemecek[1], J. Safrankova[1], and G. Zastenker[2]

[1] Faculty of Mathematics and Physics, Charles University, V Holesovickach 2, 180 00 Prague 8, Czech Republic
[2] Space Research Institute, Moscow, Russia

**Abstract.** Magnetosheath represents an interface preconditioning the solar wind prior it hits the magnetopause. The changes of the magnetic field and plasma parameters in the magnetosheath are often described by the gasdynamic model, which predicts that the velocity gradually increases down the tail but it is nearly constant across the magnetosheath, whereas the density decreases from the bow shock toward the magnetopause. The slope of the density profile would depend on the upstream Mach number, becoming steeper for higher Mach numbers. The gasdynamic model neglects the magnetic forces and thus the magnetic field strength simply follows the plasma compression/rarefaction. We summarize the statistical processing of four years of INTERBALL-1 observations in the nightside magnetosheath and discuss peculiarities of the magnetosheath radial profiles. Our investigations reveal that the magnetosheath ion flux profile is similar to but flatter than that predicted by the gasdynamic model. The most pronounced difference seen at the bow shock region is attributed to kinetic processes not involved in the model. The observed dependence of the magnetosheath flow on the Mach number is rather weak, in agreement with the model used. On the other hand, the magnetic field magnitude profile is nearly constant. It indicates that magnetic forces contribute significantly to the formation of the magnetosheath flow. According to our investigations, the size of the ion flux from the magnetopause toward the bow shock is much steeper during intervals of a radial IMF.

## 1. Introduction

The magnetosheath is the plasma region between the terrestrial bow shock and the magnetopause. The study of the physical processes in this region is important to understanding of interaction between the solar wind and the Earth's magnetosphere. The understanding of processes in this system can be also applicable to many problems in astrophysics, solar physics, space physics, and plasma physics. A simulation of the magnetosheath region in a laboratory is very difficult because the solar wind has the peculiar properties such as the superconducting solar wind matter, the supersonic flow speed, the interplanetary magnetic field frozen into the plasma flow and some other. Therefore, our knowledge about the subject is based principally on theoretical models and observations in space.

One of the first theoretical models, describing the magnetosheath plasma flows, is proposed by *Spreiter et al.* [1966]. In their model, the solar wind flows along the Sun-Earth line, strikes the subsolar magnetopause and then is diverted radially from this point. The model predicts that velocities decrease from the bow shock to the magnetopause, whereas the density and temperature increase in a vicinity of the stagnation streamline. At the flanks, the density and the velocity decrease but the temperature increases along radial profiles from the bow shock to the dayside magnetopause. Along the flanks of the near-Earth magnetotail, minimum velocities and maximum temperatures occur in the middle magnetosheath. The plasma flows radially away from the stagnation streamline. This flow accelerates up the solar wind speed and becomes increasingly like solar wind toward the flanks of the bow shock, as the shock becomes weaker.

*Zwan* and *Wolf* [1976] used the results of the *Spreiter* model at the bow shock and the magnetopause and provided formulation and numerical solution of the magnetosheath by using the MHD approach. Their model describes a magnetic flux tube moving from the bow shock to the magnetopause with two mechanisms that lead to depletion of the plasma inside the flux tube. The *Zwan* and *Wolf* theory predicts a monotonic density decrease from the bow shock to the magnetopause. Their theory also assumes a presence of a depletion layer near the subsolar magnetopause where the density drops rapidly while the field strength increases. However, a few discrepancies were found in their model later. *Southwood and Kivelson* [1992, 1995] revisited the *Zwan* and *Wolf* model and proposed a solution of these

inconsistencies by adding a compressionall front between the two depletion mechanisms of the *Zwan* and *Wolf* model. This front compresses the plasma, while rarefying the magnetic field.

*Wu* [1992] made numerical simulations for the magnetosheath profile from 3-D MHD calculation, taking into account a formation of plasma depletion layer. In this model, the magnetosphere is a solid impermeable obstacle. The density increases first and then decreases from the bow shock toward the magnetopause along the Sun-Earth line. In the inner magnetosheath, the reduction slope is larger than the rise coefficient in the outer magnetosheath.

*Spreiter and Stahara* [1980] formulated gasdynamic convected magnetic field (*GDCF*) model, and calculated magnetic-field by convecting the field lines along with the fluid. The results of simulations depend on the shape of obstacle, the Mach number of the flow, and the polytropic index. The flow is considered to be cylindrically symmetric around the Sun-Earth line and convects the three-dimensional magnetic field through the gasdynamic flow. In this model, all mass flux crossing the bow shock must flow around the obstacle. It has a minimum value near the subsolar point, and it increases toward the magnetotail. The plasma density is largest at the stagnation point, whereas the plasma velocity is small. At the magnetosheath flanks, the velocity increases more promptly than the density decreases and therefore, the flux increases. This model does well at predicting the observed magnetic field and dayside magnetopause position, somewhat less well at predicting the magnetosheath thickness, and least well at predicting plasma parameters.

*Song et al.* [1999] used observed, time-varying solar wind data to produce time-dependent predictions of the magnetosheath flux in the *GDCF* model and compared these predictions with observations. Their results showed that a nearly constant speed remains toward the magnetopause in the real magnetosheath. In *GDCF*, the predicted magnetosheath temperature is always too low and predicted magnetosheath is often thinner. *Song et al.* [1999] used an artificially elevated solar wind temperature and received the improved magnetosheath temperature and thickness predictions.

Simultaneously with an evolution of theoretical models, the magnetosheath was actively investigated on the basis of spacecraft measurements. A few studies used plasma data from the flanks. *Howe and Binsak* [1972] studied the magnetosheath 20-60 $R_E$ (Earth radii) downstream from the Earth. They found that the flow pattern agrees well with the hydrodynamic theory. *Kaymaz et al.* [1992] used IMP-8 magnetic field data to investigate the magnetic field configuration in the Earth's magnetosheath. They confirmed the draping of the magnetic field predicted by magnetohydrodynamic models and showed that the rotation of the draping patterns caused by reconnection varies with the IMF clock angle. *Petrinec et al.* [1997] looked at several GEOTAIL passes 25-45 $R_E$ downstream of the Earth and found that magnetosheath speeds near the magnetopause are larger when the magnetic field is perpendicular to the flow vector. In terms of data from the IMP 8, WIND, ISEE-1, and ISEE-3 spacecraft, *Paularena et al.* [2001] showed a significant dawn-dusk asymmetry of the plasma density in the magnetosheath near solar maximum, with larger density values on the dawn than dusk side. They used the MHD simulation to model the Parker spiral IMF case. *Nemecek et al.* [2000*a*] used measurements of the WIND, INTERBALL-1, and GEOTAIL spacecraft to investigate the magnetosheath ion fluxes. Their results displayed that the gasdynamic model can predict the magnetosheath ion flux profile with accuracy ± 40%. In another study, *Nemecek et al.* [2000*b*] showed that a difference between the averaged ion flux radial profile and its gasdynamic prediction decreases with increasing ion plasma beta and/or Alfvenic Mach number. On the other hand, *Nemecek et al.* [2002*b*] discussed the radial profile of the normalized magnetosheath magnetic field and found that it is nearly constant in the nightside magnetosheath and its value decreases with a distance from the Earth.

This paper analyzes influence of the IMF orientation on the behavior of the magnetosheath ion flux and magnetic field for both flanks of the night magnetosheath.

## 2. Data preparation

For data analysis, we used a data set of INTERBALL-1 magnetosheath ion flux and magnetic field measurements. This set contains data from both flanks during August – October and January – March from 1995 to 1999 years. We used only data from the region from $X \sim 0\ R_E$ to $X \sim -20\ R_E$. Our analysis is based on 5-min averages. We are using aberrated GSE coordinate system to account for the Earth orbital motion. Hereafter, these coordinates are denoted as *X, Y, Z*. As a solar wind monitor, we used the WIND spacecraft data to account for solar wind and IMF changes that could reach the magnetosphere. To determine both magnetopause and bow shock locations, we used following models:

1. for the magnetopause radial distance from *X* axis, $R_M$, the *Petrinec and Russell* [1996] model (it gives the best results according to *Safrankova et al.* [2002])
2. for the bow shock radial distance, $R_{BS}$, we are using following expression involving Alfvénic Mach number, $M_A$

$$R_{BS} = \frac{41.97 \cdot \sqrt{530 - 0.43 \cdot X^2}}{\sqrt[6]{\left(n \cdot V^2\right)}} \cdot \frac{0.66 \cdot M_A^2 + 2}{2.66 \cdot (M_A - 1)},$$

where $n$, $V$ is the upstream number density and velocity, respectively. This expression was obtained as the best fit to INTERBALL-1 bow shock crossings.

The parameter ordering our results is the relative position of measuring point in the magnetosheath. This position, $D$ is calculated as the ratio of the radial distance of the spacecraft from the model magnetopause to the magnetosheath thickness.

$$D = \frac{R - R_M}{R_{BS} - R_M} \cdot 100\%; \qquad R = \sqrt{Y^2 + Z^2},$$

where $R$ is the coordinate of the spacecraft perpendicular to the axis $X$, $R_M$, $R_{BS}$ are distances of the magnetopause or the bow shock from the $X$-axis at the location given by the spacecraft $X$ coordinate.

In accord with *Spreiter et al.* [1996] assumptions, we expect a linear dependence between corresponding magnetosheath and solar wind parameters. This allows us to normalize the observed values of the magnetosheath ion flux and magnetic field magnitude by computing a measured flux compression coefficient, $FCC_M$ and a measured field compression coefficient, $BCC_M$ using following ratios:

$$FCC_M = \frac{V_{Msh} \cdot n_{Msh}}{V_{SW} \cdot n_{SW}}; \qquad BCC_M = \frac{B_{Msh}}{B_{SW}},$$

where subscript *SW* denotes upstream (WIND) measurements lagged on the propagation time and *Msh* corresponds to magnetosheath values of a particular quantity.

The normalization of the bow shock position by the Mach number is very important. The left part in Figure 1 shows the magnetosheath radial profile, $FCC_M$, as a function of the distance, $D$ for different Mach number bins. $R_{BS}$ was computed using the *Formisano's* bow shock model (*Formisano et al.* [1979]), which does not include the Mach number dependence. When the influence of the Mach number on the bow shock location is taken into account (using above equation), we have received the profiles plotted in the right part of Figure 1. The Mach number dependence is now limited to the outer magnetosheath, only.

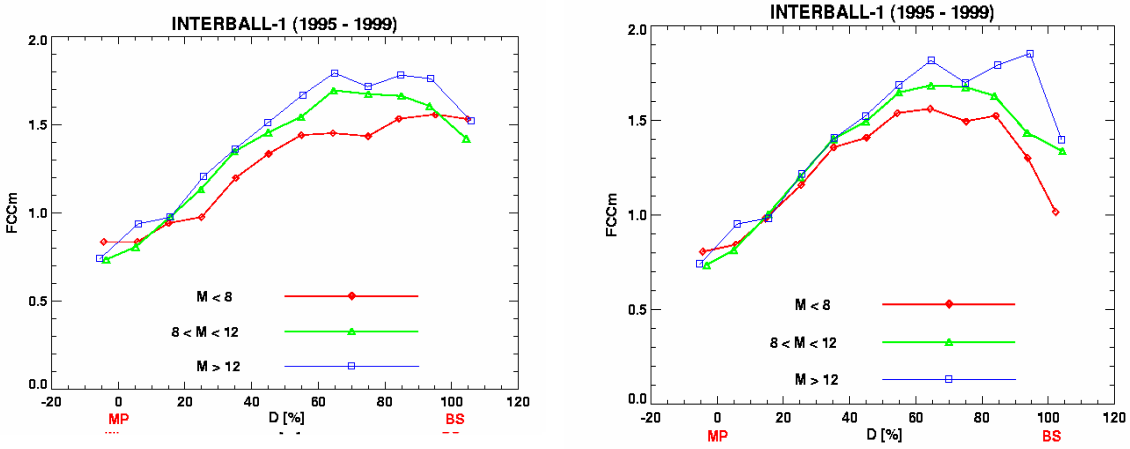


**Figure 1.** Flux compression coefficient, $FCC_M$ as a function of normalized distance for three Mach number bins. See text for explanation.

### 3. A brief summary of previous observations

As it is mentioned above, *Nemecek et al.* [2000*a*] presented a statistical study of ion fluxes in the dusk magnetosheath and showed the dependence of the magnetosheath radial profile on the upstream parameters. The authors compared experimental INTERBALL-1 results with the gasdynamic prediction by *Spreiter et al.* [1966]. Figures 2*a* and 2*b* show the comparison of the experimentally determined radial profiles of the normalized magnetosheath ion fluxes with those estimated from the gasdynamic model of *Spreiter et al.* [1966]. The normalized $FCC_M$ exhibits saturation; it never exceeds a value of 1.8, whereas the gasdynamic prediction yields a value of ~ 2.7 near the bow shock. This feature is common for both flanks. The prediction was computed for each measuring point and a mean value is presented in Figure 2. This mean value is thus

weighted by the locations of measuring points along the $X_{GSE}$ axis and these locations have different distributions at both flanks. Taking into account this peculiarity, the authors concluded that normalized ion fluxes at both magnetosheath flanks are quite similar in the bow shock region but the ion fluxes near the magnetopause differ significantly being higher than the gasdynamic prediction on the dawn flank and lower on the dusk flank. The *RSD* values reach ~ 0.3 near the dawn magnetopause and ~ 0.2 near the dusk magnetopause.

The data presented in Figure 2 are averaged in space and they represent a mean radial profile from –15 to +5 $R_E$ of the *X* coordinate. The authors have divided the data sets shown in Figure 2 into two subsets. The breakpoint was $X_{GSE}$ = -2 $R_E$ and reasonably reflected the fact that dayside and nightside magnetosheath profiles

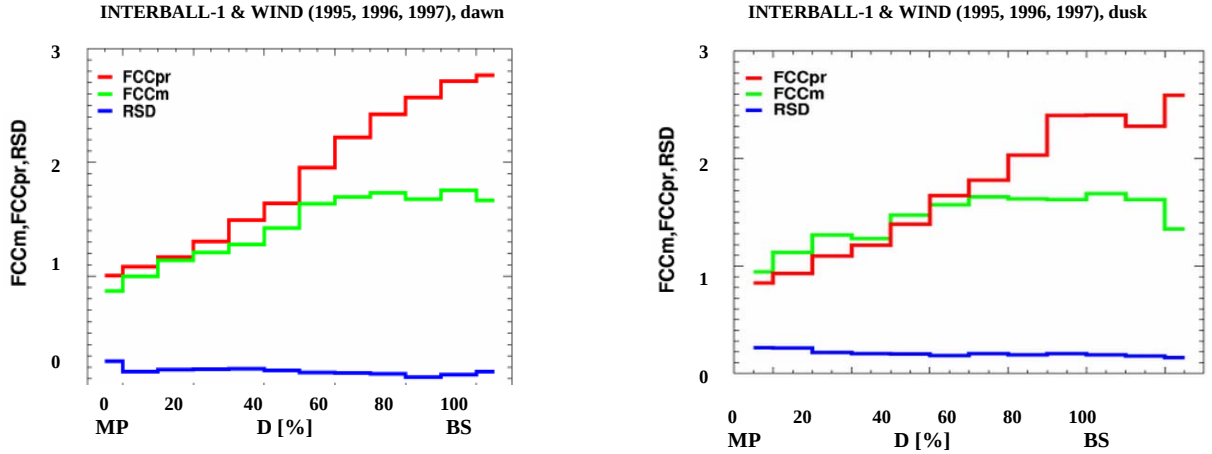


a b

**Figure 2.** 30-minute averages of $FCC_M$, corresponding relative standard deviations, *RSD*, and 30-minute averages of $FCC_{Pr}$ (predicted flux compression coefficient calculated according to *Spreiter et al.*, [1966]) along the magnetosheath thickness (dawn – a part, dusk – b part).

would be different. The results are plotted in Figure 3. One can note that "nightside" part of both dawn (a) and dusk (b) plots are qualitatively similar. A more detailed analysis shows that the rise of the dawn profile is a little steeper but that it saturates at a lower level. On the other hand, the difference between dawn and dusk "dayside" magnetosheath profiles is striking. Whereas the principal rise of the ion flux in the dawn magnetosheath is gradual and occurs from 25% to 75% of the magnetosheath thickness, the dusk profile exhibits two nearly equal steps, at the magnetopause and at ~50% of the thickness.

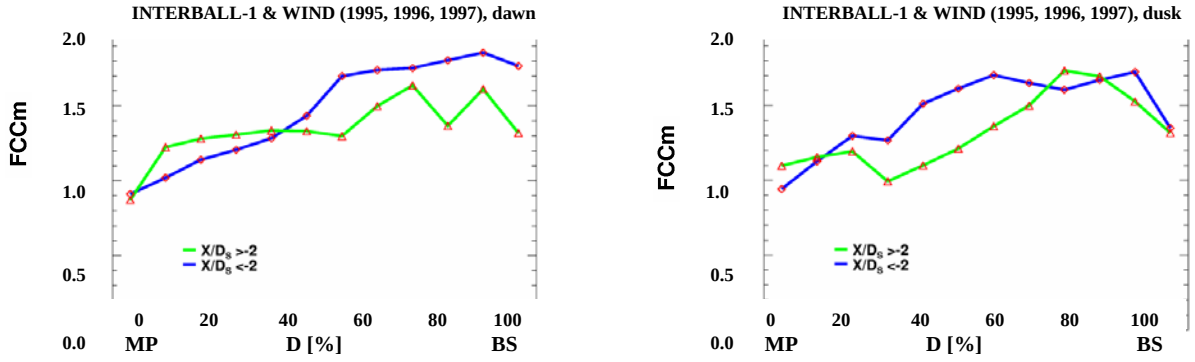


a b

**Figure 3.** A comparison of normalized ion flux profiles in the dayside ($X > -2R_E$) and nightside ($X < -2\ R_E$) magnetosheath (a - dawn profile; b - dusk profile).

## 4. Influence of alpha particles

Abovementioned investigations suffer with a systematic error – they normalized the total magnetosheath ion flux to the solar wind proton flux. Namely, the INTERBALL-1 Faraday cup provides the total ion current that is composed mainly from proton and helium contributions, whereas WIND key parameters provide proton number density. However, *Aelling et al.* [2001] investigated the helium abundance and its variations in the solar wind on a time scale of years.

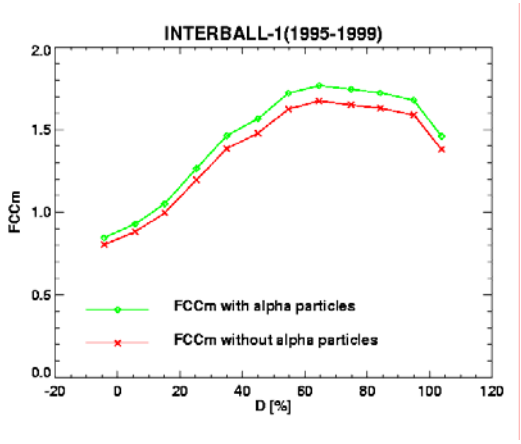


**Figure 4.** The influence of alpha particles on the flux compression coefficient value. $FCC_M$ is again a function of normalized distance.

Based on data from WIND/SWE (*Ogilvie et al.* [1995]) between the end of 1994 and early 2000, the authors found a clear dependence of the $He^{++}/H^{+}$ ratio in the solar wind on a solar cycle. We used their results and estimated INTERBALL-1 proton fluxes for $FCC_M$.

However, we should point out that the obtained differences are rather small as Figure 4 illustrates. The proton flux is lower than the total ion flux and thus the corresponding $FCC_M$ is lower too, but the difference is proportional to the $FCC_M$ value. We can conclude that the variations of the $He^{++}/H^{+}$ ratio with solar cycle and with the solar wind speed do not affect our previous results significantly. Nevertheless, we will use $FCC_M$ calculated as a ratio of proton fluxes in further presentations.

## 5. The dawn-dusk asymmetry of magnetosheath parameters

Figure 5 presents the averaged values of $FCC_M$ (Figure 5*a*) and $BCC_M$ (Figure 5*b*) as a function of the normalized distance for the dawn and dusk nightside magnetosheath. A comparison of the flanks shows that dawn $FCC_M$ is slightly lower than dusk $FCC_M$ in all points along the magnetosheath thickness. On the other hand, the normalized magnetic field, $BCC_M$ exhibits a very flat profile with a small enhancement near the magnetosheath boundaries. The difference between dawn and dusk $BCC_M$ profiles has an opposite sign than that observed between dawn and dusk $FCC_M$.

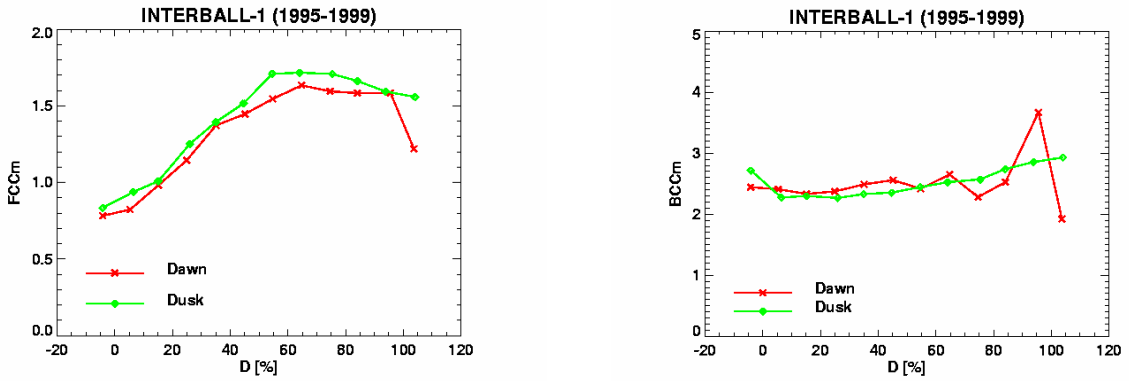


a b

**Figure 5.** Normalized magnetosheath ion flux, $FCC_M$ (a) and normalized magnetic field magnitude, $BCC_M$ (b) for the dawn and dusk flanks.

## 6. Influence of the IMF orientation

Since the dawn-dusk asymmetry can be connected with the IMF direction, we have investigated two limit cases – radial and perpendicular IMF orientations. The selection criterion was the value of upstream cone angle. As it can be seen from Figure 6, averaged $FCC_M$ profile peaks at the middle of the magnetosheath for radial IMF

(cone angle < $15^0$) but it has a maximum near the bow shock when IMF is perpendicular to the solar wind flow. However, $BCC_M$ profiles remained nearly constant for both IMF orientations but the magnetic field is less compressed when the IMF is radial.

Both investigated IMF orientations would not change the proportion between dawn and dusk ion and magnetic fluxes. Nevertheless, Figure 7 demonstrates that the dawn ion flux is larger

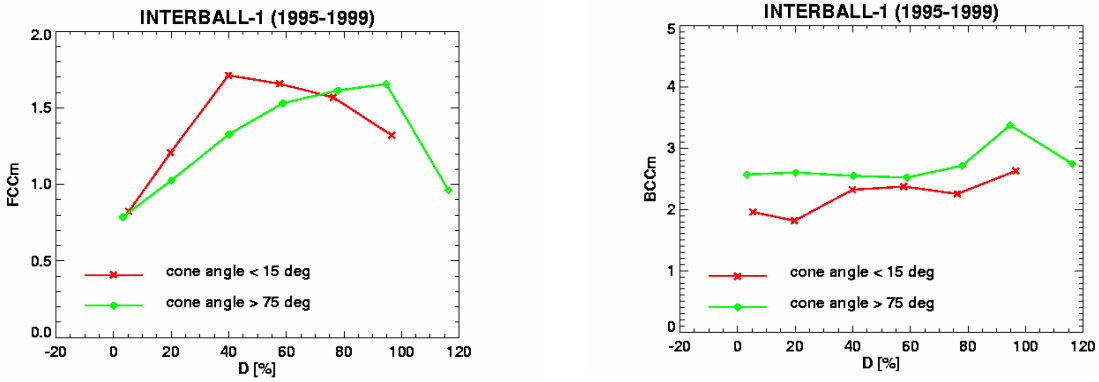


a b

**Figure 6.** Normalized ion flux (a) and magnetic field (b) profiles for radial (cone angle < 15°) and perpendicular IMF (cone angle > 75°).

during intervals of perpendicular IMF, whereas $BCC_M$ does not exhibit any dawn-dusk asymmetry. On the other hand, the situation is opposite during intervals of radial IMF, $FCC_M$ is, within statistical errors, the same on both flanks but dawn $BCC_M$ is larger as can be seen from Figure 8.

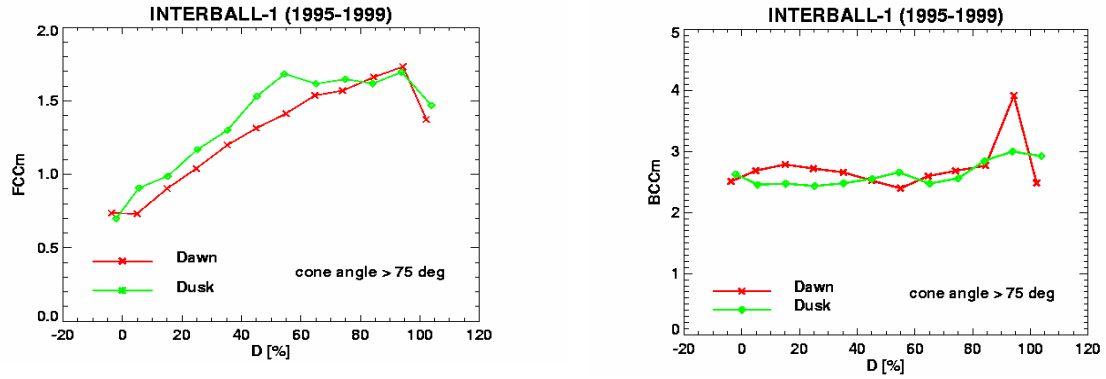


a b

**Figure 7.** The dawn-dusk difference between the same profiles as in Figure 6 (ion flux (a), magnetic field (b)) for a large cone angle.

## 7. Summary and discussion

We have investigated ion fluxes and magnetic field magnitudes in the nightside magnetosheath. Our database consists of 23927 5-minute averages of both quantities complemented with simultaneously measured solar wind and IMF data. In distinction to our previous studies, we have corrected the INTERBALL-1 ion flux data in order to receive the proton flux. However, we have found only a systematic relative difference (about 7%), which could be expected, if the mean $He^{++}$ abundance in the solar wind is taken into account.

Our investigations showed that the connection between the magnetosheath proton flux and magnetic field is rather weak. The magnetic field magnitude neither follows the plasma compression nor compensates the total pressure but it is nearly constant across the magnetosheath. On the other hand, the magnetosheath proton flux profile is strongly affected by the IMF orientation. A maximum of the plasma compression

shifts from the bow shock region toward the magnetosheath centre when IMF becomes more radial. It means that weaker plasma compression at the quasiparallel shock is compensated by a further compression in the magnetosheath. This fact can explain why the bow shock location does not depend on the angle between IMF and bow shock normal (*Safrankova et al.* [2003]) but the source of this additional compression is unknown. *Nemecek et al.* [2000*b*] attributed the difference between gasdynamic model and

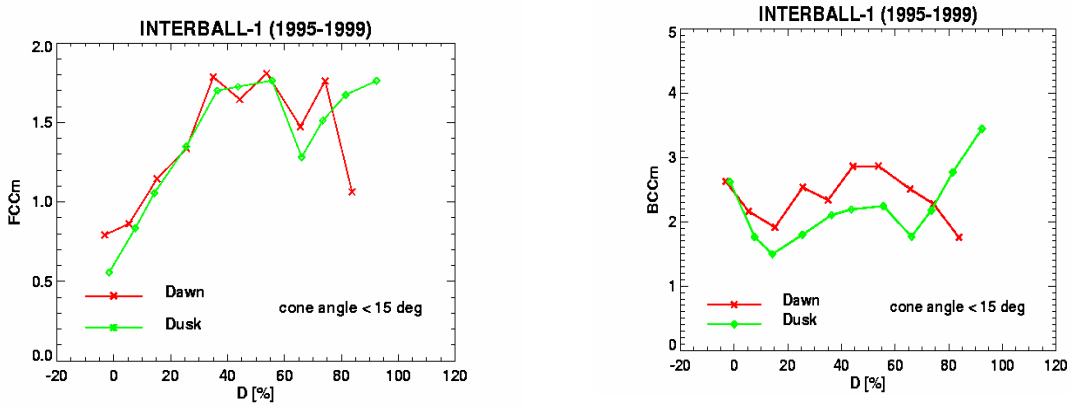


a b

**Figure 8.** *FCCm* (a) and *BCCm* (b) profiles for a small cone angle.

observations at the bow shock region to kinetic effects forming the magnetosheath flow just behind the bow shock. These effects would be more pronounced during intervals of radial IMF because nearly entire bow shock is quasiparallel and thus they can be responsible for the ion flux profile shown in Figure 6. An explanation of the observed dawn – dusk asymmetry for a perpendicular IMF orientation requires a further study. A possible source can be the tilt angle effect predicted by global MHD models in combination with a bias of our data set toward the negative tilt angles.

**Acknowledgments.** The present paper was supported by the Czech Grant Agency under contract 205/03/0953. The authors would like to thank to the reviewer of this manuscript.

## References

Aellig, M. R., A. J. Lazarus, and J. T. Steinberg, The solar wind helium abundance: Variation with wind speed and the solar cycle, *J. Geophys. Res.*, *28*, 2767, 2001.

Howe, H. C. Jr., and J. H. Binsack, Explorer 33 and 35 plasma observations of magnetosheath flow, *J. Geophys. Res.*, *85*, 2873, 1972.

Formisano, V., Orientation and shape of the Earth's bow shock in three dimensions, *Planet. Space Sci.*, *27*, 1151, 1979.

Kaymaz, Z., Siscoe, G.L., and Luhman, J. G., IMF draping around the Geotail: IMP-8 observations, *J. Geophys. Res.*, *19*, 829, 1992.

Nemecek, Z., J. Safrankova, L. Prech, G.N. Zastenker, K.I. Paularena, S. Kokubun, Magnetosheath study: Interball observation, *Adv. Space Res.*, *25*, No.7/8, 1511-1516, 2000a.

Nemecek Z., J. Safrankova, G. N. Zastenker, P. Pisoft, K.I. Paularena, J.D. Richardson, Observations of the radial magnetosheath profile and a comparison with gasdynamic model predictions, *J. Geophys. Res.*, *17*, 2801, 2000b.

Nemecek, Z., J. Safrankova, G.N. Zastenker, P. Pisoft, K.I. Paularena, Spatial distribution of the magnetosheath ion flux, *Adv. Space Res.*, *30*, 2751-2756, 2002a.

Nemecek, Z., M. Hayosh, J. Safrankova, G.N. Zastenker, J. Richardson, The dawn-dusk asymmetry of the magnetosheath: INTERBALL-1 observations, *Adv. Space. Res.*, in press, 2002b.

Ogilvie, k. W., *et al.*, SWE, a comprehensive plasma instrument for the Wind spacecraft, *Space Science Reviews*, *71*, 55-77, 1995.

Paularena, K. I., J. D. Richardson, M. A. Kolpak, C. R. Jackson, and G. L. Siscoe, A dawn-dusk density asymmetry in Earth's magnetosheath, *J. Geophys. Res.*, 106, 25,377-25,394, 2001.

Petrinec, S.M. and C.T. Russell, Near-Earth's magnetopause shape and size as determined from the magnetopause flaring angle, *J. Geophys. Res.*, *101*, 137, 1996.

Petrinec, S. M., T. Mukai, A, Nishida, Y. Yamamoto, and T. K. Nakamura, Geotail observations of magnetosheath flow near the magnetopause, using Wind as a solar wind monitor, *J. Geophys. Res.*, *102*, 26943, 1997.

Safrankova, J., Z. Nemecek, S, Dusik, L. Prech, D.G. Sibeck, and N.N. Borodkina, The magnetopause shape and location: A comparison of the Interball and Geotail observations with models, *Ann. Geophys.*, *20*, 301, 2002.

Safrankova J., K. Jelinek, and Z. Nemecek, The bow shock velocity from two-point measurements in frame of the Interball project, *Adv. Space. Res.*, in press, 2003.

Shue, J.-H., *et al.*, A new functional form to study the solar wind control of the magnetopause size and shape, *J. Geophys. Res.*, *102*, 9497, 1997.

Song, P., C. T. Russell, T. I. Combosi, J. R. Spreiter, S. S. Strahara, and X. X. Zhang, On the processes in the terrestrial magnetosheath, 1. Scheme development, *J. Geophys. Res.*, *104*, 22, 1999a.

Southwood, D.J., Kivelson, M.G, On the form of the flow in the magnetosheath, *J. Geophys. Res.*, *85*, 2873, 1992.

Southwood, D.J., Kivelson, M.G, Magnetosheath flow near the subsolar magnetopause: Zwan-Wolf and Southwood-Kivelson theories reconciled, *Geophys. Res. Lett.*, *22*, 3275, 1995.

Spreiter, J.R., and A. L. Summers, and A.Y. Alksne, Hydromagnetic flow around the magnetosphere, *Planet. Space Sci.*, *14*, 223, 1966.

Spreiter, J.R., and S. S. Strahara, A new predictive model for determining solar wind-terrestrial planet interactions, *J. Geophys. Res.*, *85*, 6769, 1980.

Wu, C.C., MHD flow past an obstacle: large scale flow in the magnetosheath, *J. Geophys. Res.*, *19*, 87, 1992.

Zwan, B.J., and R. A. Wolfe, Depletion of the solar wind plasma near a planetary boundary, *J. Geophys. Res.*, *97*, 1636, 1976.

# The scenario of substorms triggered by the IMF northward turning

I. I. Alexeev and S. Y. Bobrovnikov

Institute of Nuclear Physics, Moscow State University

**Abstract.** Substorm is described as a global magnetospheric instability. The total magnetic flux in the magnetosphere at any time is equal to its dipole value about 7,700 M Wb. This magnetic flux is shared between the closed inner magnetosphere flux, the tail plasma sheet flux, and the tail lobe flux. When tail lobe flux is too large, any steady state magnetosphere without neutral line is impossible. In this case only an unstable magnetospheric state can be realized and substorm occurs. When the IMF turns southward and energy transport into the magnetosphere increases, the subsolar magnetopause distances, and the distance to the inner plasma sheet edge, decrease and an increasing of the tail flux begins. The tail lobe magnetic flux approaches very close to the its threshold value. After the IMF turns northward, a negative contribution of Region 1 field-aligned currents to the magnetic field in the day side magnetosphere disappears, magnetic field pressure in dayside magnetosphere decreases and the magnetopause moves away from the Earth. Moreover, a positive contribution of field-aligned currents to the magnetic field in the nightside magnetosphere also disappears and the Ampere force decreases, the tail current sheet moves tailward. If during the substorm growth phase a suffcient amount of energy has been stored in the magnetospheric tail, the tail lobe magnetic flux exceed the threshold value. The tail will react to the changes in the IMF with some delay but the Region 1 field-aligned currents follow to those changes simultaneously. This is a reason of the substorm triggering by the IMF northward turning.

## 1. Introduction

Substorms are now widely accepted to be global phenomena consisting of the coherent set of processes within the magnetosphere, ionosphere and the interplanetary medium. Magnetospheric dynamics during substorms consists of the sequence of energy loading and dissipation events accompanied by well known observational phenomena such as cross-tail current and polar cap magnetic flux enhancement, field line stretching with subsequent dipolarization, Joule heating in the ionosphere, auroral particle precipitation, ring current enhancement, and plasmoid formation [*Baker et al*., 1996]. These observations support the idea that substorms are the global configurational instability of the magnetosphere [*Baker et al*., 1999; *Sitnov et al*., 2000].

In our study we used the Paraboloid model of the magnetosphere and in the present paper we try to explain why it can be used for an example of substorms which are triggered by the IMF northward turning.

Substorm triggering by the IMF northward turning is a very interesting and contradictory field of substorm physics. This problem is being investigated since 1975. *Caan et al*. [1975 made the statistical analysis of large set of substorms and showed the onset to begin at the time when the IMF $B_z$ changed from a negative value to zero, after a prolonged period of being southward directed. *Rostoker et al.* [1982] found a clear association between IMF northward turning and substorm onsets for a number of intense substorms. Later, *Rostoker et al*. [1983] found more evidence for this phenomenon. $B_z$ was shown to remain negative for a period of ~2 hours for the storm on January 20, 1978 and ~1 hour for the storm on August 19, 1978. *Lyons* [1995] noted that sudden changes in the IMF $B_y$ could also control substorm onset. It was shown by *Troshichev et al*. [1986] that a decrease of $|B_y|$ down to zero can trigger substorm onset. McPherron et al. (1986) have carried out an investigation of the IMF $B_z$ at the time of onsets and showed that 44% of 126 events were directly associated with IMF northward turning, and 29% of events occurred at a steady negative $B_z$. *Lyons* [1996] showed that taking into account changes in the IMF $B_y$ based on the investigation by McPherron revealed a clear relation between sudden IMF changes and substorm onsets. *Lyons* [1995] proposed a substorm model which explained the IMF triggering of substorm expansion by

means of a decrease of the electric field in the near-Earth magnetotail and, as a consequence, the development of field-aligned currents. *Nishida and Mukai* [1997] recently carried out a case study and did not found evidence for the Lyons' theory. They have found an increase of the electric field just before substorm expansion that contradicted the Lyons' theory. Thus, there is no widely accepted theory of the mechanism which connects changes in the IMF and substorm expansion onset.

## 2. Paraboloid model and substorm onset

Substorm onset is the most important feature of substorms. Thus, the Paraboloid model we plan to use must represent the substorm onset in terms of its

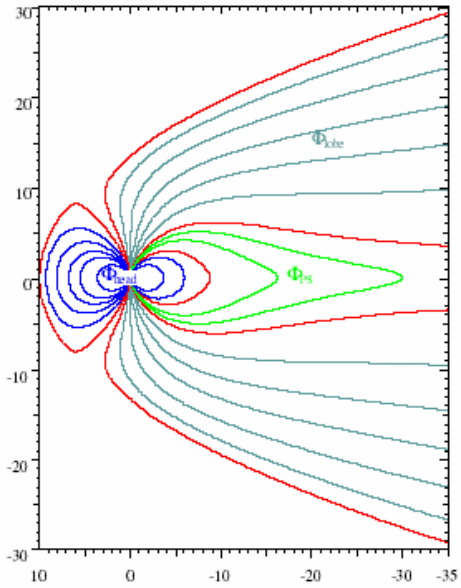


**Figure 1.** Magnetic field lines in the Paraboloid model (noon-midnight cross-section), and division in three major magnetospheric domains.

parameters. Let us consider three major parameters of the Paraboloid model: the distance to the subsolar point, $R_1$, the distance to the Earthward edge of the tail current sheet, $R_2$, the magnetic flux in the polar cap, $\Phi_{pc}$. And three sources of the magnetospheric magnetic field: the dipole, the magnetopause currents screening the dipole and the tail current system consisting of the cross-tail current and magnetopause screening (and closure) currents.

Based on Figure 1 representing the field lines in the Paraboloid model at the noon-midnight meridian we define three magnetospheric domains and their magnetic fluxes.

- Φhead is the magnetic flux in the inner magnetosphere.
- $\Phi_{lobe}$ is the magnetic flux in the tail lobe (at the infinity) equal to the polar cap magnetic flux ($\Phi_{pc}$)
- $\Phi_{PS}$ is the magnetic flux through the plasma sheet (from the inner edge of the current sheet up to the infinity), forming the auroral oval.

So, the main condition for the stability of the magnetosphere is:

$$\Phi_{dipole} = \Phi_{head} + \Phi_{lobe} + \Phi_{PS} \qquad (1)$$

$\Phi_{dipole}$ is the total magnetospheric magnetic flux which is equal to the magnetic flux of the Earth's dipole:

$$\Phi_{dipole} = \int_0^{2\pi} Rd\varphi \int_{R_E}^{\infty} B_{tz} dR = \\ = 2\pi R_E^2 B_0 \approx 7.700 \text{ Wb} \qquad (2)$$

In Equation (1) $\Phi_{PS} = \Phi_{PS\ dipole} - \Phi_{PS\ tail}$ is the magnetic flux through the plasma sheet, where $\Phi_{PS\ dipole}$ is the magnetic flux through the plasma sheet of the dipole and magnetopause screening currents and $\Phi_{PS\ tail}$ is the magnetic flux through the plasma sheet produced by the tail current system. Thus, the first order stability condition is: $\Phi_{PS} > 0$. It implies restriction on $\Phi_{PS\ tail}$ and, as a consequence, on the tail lobe magnetic flux $\Phi_{lobe} = \alpha\ (R_1, R_2)\ \Phi_{PS\ tail}$ (where avarege $\alpha$ is 1.775). In order to obtain the restriction we calculate the magnetic flux through the plasma sheet of the dipole and magnetopause screening currents in dependence on the magnetopause subsolar distance, $R_1$, and on the distance to the inner edge of the tail current sheet, $R_2$. It is shown in the Figure 2 (left panel).

The knowlege of the magnetic flux through the plasma sheet of the dipole and magnetopause screening currents in dependence on the magnetopause subsolar distance, and on the distance to the inner edge of the tail current sheet allows us to calculate the upper boundary of the tail lobe magnetic flux ($\Phi_{PS} = 0$). This values can be related to the situation where the $B_z$ component of the magnetospheric magnetic field is equal to zero in the whole plasma sheet, that is $\Phi_{PS\ tail} = \Phi_{PS\ dipole}$, or $\Phi_{lobe} = 1.775\ \Phi_{PS\ dipole}$. It is a special kind of the current sheet which demands a special configuration of the currents in the plasma sheet. Spacecraft observations do not show an evidence for such kind of current sheet to exist in the tail. Thus, it is very rough upper limit of the tail lobe magnetic flux. Therefore, we need to use the following inequation as the stability condition: $\Phi_{PS} < \Phi_{PS}$

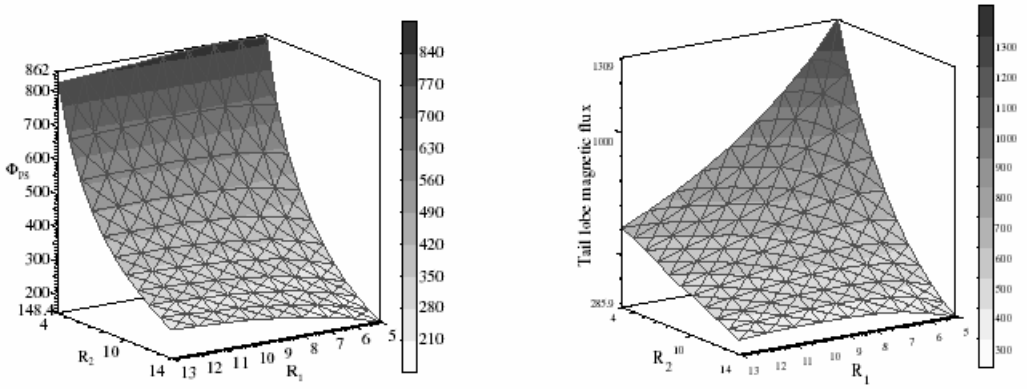


**Figure 2.** The magnetic flux through the plasma sheet of the dipole and magnetopause screening currents in dependence on the magnetopause subsolar distance, $R_1$, and on the distance to the inner edge of the tail current sheet, $R_2$ (left), and the maximal value of the tail lobe magnetic flux (right).

thr, where $\Phi_{PS}$ thr is the threshold value of the magnetic flux through the plasma sheet.

The condidtion when $\Phi_{PS} < \Phi_{PS}$ thr ($\Phi_{lobe} > \Phi_{lobe}$ thr) leads to the formation of the neutral line somewhere in the tail current sheet. This is the process which develops during substorm breakup. Thus, for more precise calculation of the upper limits of the tail lobe magnetic flux we need to find the conditions for the formation of the neutral line. The results obtained are presented in Figure 2 (right panel).

The location of the neutral point remains to be mentioned. In our model it appears at the inner edge of the tail current sheet close to the magnetopause and it can be said not to be an appropriate place for substorm onset initiation. As it was mentioned above, contradictions to the observations must correspond to some of the active magnetospheric phenomena and must be distinguished as a limit for the model application. That is the formation of the neutral point corresponding to the limit of the model applicability.

Indeed, it is most important for our research that the $B_z$ component of the magnetic field becomes zero somewhere in the magnetosphere as the cross tail current increases. It corresponds to the conditions when additional magnetic flux is needed to transform the magnetospheric configuration. This is what we call the global instability of the magnetosphere. The neutral point formation is treated as an incapability of the magnetosphere to redistribute the magnetic flux in accordance with new external or internal conditions.

Equation (1) can show that an increase of the magnetic flux in one of the defined domains leads to a decrease of fluxes in others. After the IMF turning northward the inner magnetospheric domain grows and $\Phi_{head}$ increases. At the same time the tail lobe magnetic flux $\Phi_{lobe}$ does not change. In fact, this process must be accompanied by decreasing the magnetic flux in the plasma sheet. This decrease being larger than the initial ΦPS, the neutral line must appear.

So, the final statement of this section is that all of the above reasonings are model independent, only real values of the magnetic fluxes depend on the concrete model.

### 3. The scenario of substorm

Now we would like to propose a possible scenario for substorms which are triggered by the IMF northward turning. This kind of substorm is chosen as it has the most obvious influence on the model parameters. Let us consider again three parameters of the model: $R_1$, $R_2$, and Φlobe. During the substorm growth phase stand-off distance decreases, the magnetopause shifting earthward. The subsolar distance and the magnetopause form as function of the solar wind parameters has been found in the papers by *Shue et al*. [1997] and *by Roelof and Sibeck* [1993]. It has been noted that this distance depended on the IMF $B_z$ component, decreasing when the IMF $B_z$ became negative. We think this phenomenon to have two explanations. The first reason: when the IMF turns southward the intensity of field-aligned currents increases highly. They give a negative contribution of about 10 nT to the magnetic field in the dayside magnetosphere, [*Tsyganenko et al*., 1994; *Alexeev et al*., 1997]. An other reason is an increase of the cross tail current. Its contribution to the day side magnetosphere is of the same order as that of the field-aligned currents [*Alexeev et al*., 1997; *Alexeev and Bobrovnikov*, 1997]. The magnetic pressure at the subsolar point decreases

with the enhancement of field-aligned or tail currents. The stand off distance then decreases.

Other parameters changing during substorms are the distance to the inner edge of the tail current sheet and the magnetic flux in the tail lobe. It is also well known that during substorm growth phase the magnetic flux increases and the tail current sheet moves earthward. An increase of the magnetic flux corresponds to a high level of energy transport from the solar wind to the magnetosphere, the cross tail current enhancing simultaneously. We will assume that the magnetosphere tends to develop so that the energy of the solar wind – magnetosphere interaction remains minimal. An increase of the tail lobe magnetic flux increases the flaring angle of the magnetosphere, leading to an enhancement of the magnetosphere cross section as viewed from the Sun. If the dependence of the magnetic flux on the distance to the inner edge of the tail current sheet with fixed other parameters (subsolar distances and current value at the inner edge of the current sheet) is considered, the magnetic flux is found to decrease as the cross tail current moves earthward. Taking into account this feature we can present the growth phase as a sequence of two-step processes.

1. The enhancement of the cross tail current and magnetic flux in tail lobe.
2. The earthward displacement of the current sheet.

The last step partially compensates the increasing of the magnetic flux and is limited by the conditions of MHD equilibrium in the tail. Thus, the earthward displacement of the current sheet decreases the energy of the solar wind - magnetosphere interaction. It can also be noted that $R_1$ and $R_2$ values cannot decrease without limit. Their displacement is limited by the pressure balance on the magnetopause and MHD equilibrium in the tail.

Now the scenario of substorm growth and expansion can be described as follows. When the IMF turns southward and energy transfer into the magnetosphere increases, the both above mentioned distances ($R_1$ and $R_2$) decrease and increasing of the tail flux (Φlobe) begins. This process has a low probability to reach the critical surface and thus low probability of substorm onset. The tail lobe magnetic flux comes very close to the "critical" value, but the behavior of the model parameters ($R_1$ and $R_2$) does not permit Φlobe to exceed it. When the IMF turns northward, negative contribution of the Region 1 field-aligned currents to the magnetic field in the dayside magnetosphere disappears, magnetic field pressure in the dayside magnetosphere increases and the magnetopause moves away from the Earth. Moreover, positive contribution of field-aligned currents to the magnetic field in the nightside magnetosphere also disappears, the Ampere force decreasing, the tail current sheet moving tailward. It is important to note that changes in the IMF which first appear at the subsolar point can change the current in the plasma sheet with some delay. This delay can be estimated as 5-15 minutes. During this period the following process will take place.

When the IMF turns northward, Region 1 field-aligned currents disappear, the magnetic pressure at the dayside magnetosphere (near the subsolar point) increases. The magnetopause moves away from the Earth ($R_1$ increases). The same process begins in the tail, the current sheet moves tailward, ($R_2$ increases). During this period of time the tail lobe magnetic flux Φlobe will not decrease, but the critical value will do. If during the substorm growth phase a sufficient amount of energy has been stored in the magnetospheric tail, tail lobe, the magnetic flux comes very close to the "critical" value (metastable state) and it is very possible for the Φlobe magnetic flux to reach and to exceed the critical value. It is important to note again that the tail will react to the changes in the IMF with some delay but Region 1 field-aligned currents will react to those changes almost at the same time. This is the core of the substorm triggering by the IMF northward turning (*Alexeev and Bobrovnikov* [1999]).

## 4. Substorm event of January 10, 1997

Although the scenario described in the previous section looks rather promising, it is very important to test it with a real event using the above presented calculation scheme.

There is an interesting approach to the study of the magnetospheric substorms by using nonlinear filters (for example, [*Vassiliadis et al*., 1995; *Sitnov et al*., 2000]). The basic idea of these filters is reproducing the output time series of the substorm activity, mainly AL index, based on the input time series, which are mainly the solar wind parameters and interplanetary magnetic field. This technique can also be called a forecasting of the AL index. In such methods filters represent the magnetospheric dynamics, no real magnetospheric processes being involved in the scheme. In this case the magnetosphere acts as a "black box" with an input gate for the solar wind data and an output gate for the magnetospheric indices.

Another widely used approach is a detailed investigation of the plasma processes in various domains of the magnetosphere and ionosphere. The essence of such kind of research is the study of a sequence of local processes in the magnetosphere by applying the sophisticated physical models of plasma processes based on local MHD, particle or wave simulation. When this approach is used, the substorm as a global phenomenon becomes hidden.

As it was mentioned earlier, modern study supports an idea that the substorm is a global instability of the magnetosphere. From this viewpoint the former approach seems to be more adequate but veiling the magnetosphere as a system of the magnetic field and plasma processes. In this paper we would like to present a calculation scheme which resembles the filtering approach but uses the real magnetospheric model in the core of the filter.

Now we would like to present the calculation scheme taking into account the solar wind dynamic pressure, the IMF $B_z$ component and time delay (6-8 minutes) between the changes in the IMF and the tail reaction to them.

Using the input data presented in figure 3 (left panel), let us try to satisfy the pressure balance at the subsolar point. Then the calculation scheme can be described as follows:

1. Take reasonable value of $R_1$ (the magnetopause subsolar distance) based on, e.g., *Shue et al.* [1997];

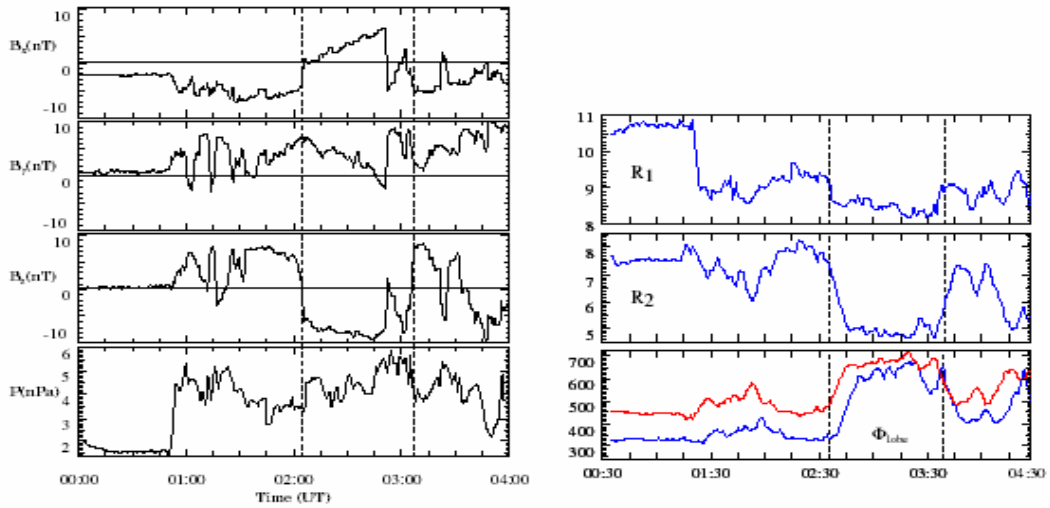


**Figure 3.** Wind spacecraft data during substorm on January 10, 1997 (left) and Dynamics of the model parameters (right).

2. Calculate $R_2$ (the distance to the earthward edge of the tail current sheet) with simple formula $R_2(t) = K\ (B_z\ (t–\Delta t))\cdot R_1(t–\Delta t)$ (taking into account the time delay);
3. Take the value of the magnetic flux $\Phi_{lobe}$ = 380 MWb as the initial value for iterations;
4. Trace the inner edge of the current sheet ($R_2$) along a magnetic field line to the ionosphere, which is very simple to be done in the Paraboloid model;
5. Calculate the new flux Φlobe through the polar cap. At this point we use the empirical relation between the auroral oval magnetic flux, which can be calculated directly and the polar cap magnetic flux. This relation depends on the IMF $B_Z$ with the same delay;
6. Compare the new value of the magnetic flux with the old one and repeat steps 4 and 5 to attain appropriate precision by changing $R_2$;
7. If the pressure balance is not attained, change $R_1$ with appropriate step and repeat the scheme from step 2 except for the initial magnetic flux to have the last calculated value.

The results of calculations are presented in Figure 3 (right panel). At the time marked by the second vertical dashed line the magnetic flux in the tail lobe exceeds its critical value. This time corresponds well to the auroral intensifications observed on-board the polar spacecraft and at the ground-based magnetometers.

Now it is time to answer the question: What can we obtain from this scheme? The answer is simple. As our scheme resembles the using of filters on the solar wind data, it enables prediction of some features of substorm. First of all the time of substorm expansion onset is predicted. It can be seen from Figure 3 (left panel) that there are two IMF northward turnings during the period of substorm development. But only the latter one produces substorm onset in reality and in our calculations.

The major advantage of our method is that we have a set of model parameters continuous in time. It enables various calculations based on the Paraboloid model. It could be calculation of Dst index, calculation of magnetic field at geostationary orbits during substorm, field line tracing which reveals the dynamics of the

magnetic field line during substorm growth phase, calculation of the auroral oval and polar cap boundaries which enables estimation of the substorm energetics. An example of results of such calculations is shown in Figure 4. This figure represents the auroral oval and polar cap boundaries for the quiet magnetosphere (left) and for the late substorm growth phase. A significant increase of the polar cap and auroral oval due to the substorm development can be seen. The equatorward edge of the auroral oval approaches 60° of latitude that provides a good correspondence to the UVI images from the polar spacecraft. Our calculations of the polar cap behavior are also in a good agreement (minimum at 02:40 UT and maximum at 03:37 UT) with the results obtained by *Brittnacher et al*. [1999].

The major advantage of our method is that we have a set of model parameters continuous in time. It enables various calculations based on the Paraboloid model.

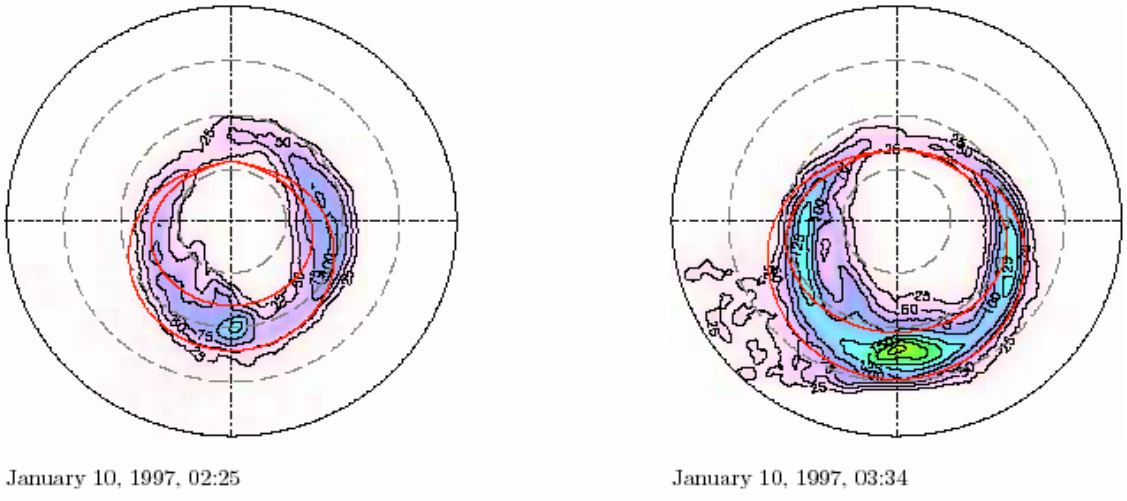


**Figure 4.** The Polar cap and auroral oval for the quiet/average magnetosphere (left) and during the late substorm growth phase (right).

It could be calculation of Dst index, calculation of magnetic field at geostationary orbits during substorm, field line tracing which reveals the dynamics of the magnetic field line during substorm growth phase, calculation of the auroral oval and polar cap boundaries which enables estimation of the substorm energetics. An example of results of such calculations is shown in Figure 4. This figure represents the auroral oval and polar cap boundaries for the quiet magnetosphere (left) and for the late substorm growth phase (right). A significant increase of the polar cap and auroral oval due to the substorm development can be seen. The equatorward edge of the auroral oval approaches 60° of latitude that provides a good correspondence to the UVI images from the polar spacecraft. Our calculations of the polar cap behavior are also in a good agreement (minimum at 02:40 UT and maximum at 03:37 UT) with the results obtained by *Brittnacher et al*. [1999].

## 5. Discussion and conclusions

In conclusion, we would like to point out the advantages and disadvantages of our study. First of all it concerns the Paraboloid model of the magnetospheric magnetic field and the appearance of the neutral point. The neutral point appears at the inner edge of the tail current sheet close to the magnetopause but measurements show that this should happen close to the Earth-Sun line at approximately 10–20$R_e$. This discrepancy can be explained by a relatively simple model of the tail current system magnetic field. For example, this model has insufficient warp of the inner edge around the Earth, so the magnetic field produced by the tail current system in the near magnetopause region at the earthward edge becomes overestimated. However, the displacement of this point will not influence the essence of our approach. Assuming the substorm to be a global instability of the magnetosphere, we would like to answer the question: why can the IMF northward turning trigger the substorm and we would not like to answer the question where the onset starts.

The presented scenario of the external triggering is based on the well examined facts. It is well known that the magnetopause moves earthward during the substorm growth phase and there exists a number of models of the stand-off distance (see, for example, *Roelof and Sibeck* [1993]; *Shue et al*. [1997]). The enhancement of the lobe magnetic flux is also well known due to measurements of the lobe magnetic field and polar cap boundaries. The

earthward displacement of the tail current sheet is also confirmed by an increase of the auroral oval size. We tried to clarify the reasons of such magnetospheric dynamics and to construct the most simple scenario of the substorm growth phase.

We have a simple scenario, and we have a simple calculation scheme based on simple assumptions of the model parameter dependences on the solar wind and interplanetary magnetic field data. In the future we plan to develop a better scenario of substorms taking into account a greater number of the input data and the model parameters.

Now, what can be inferred from our study? First of all we would like to support an idea that substorm is a global magnetospheric phenomenon comprising many different processes with different space and time scales and intensity. In order to answer the questions when and where the onset will start and what will be the intensity of the expansion phase, we need to know simultaneously the conditions in many regions of the magnetosphere, in the ionosphere and in the solar wind. We would also like to point out that it is possible to determine the time of onset and the intensity of the substorm expansion phase using the global model which yields the information about the magnetic field in every magnetospheric region, and knowing the conditions in the solar wind. Finally, the presented scenario of substorms triggered by the IMF northward turning and the calculation scheme can be described as a good approximation of real events. But it is important to improve them for investigation of a more wider range of substorms.

**References**


Alexeev, I. I., Regular magnetic field in the Earth's magnetosphere, *Geomagn. and Aeronomy*, *18*, 656, 1987 (in Russian).

Alexeev, I. I. and S. Yu. Bobrovnikov, Tail current sheet dynamics during substorm, *Geomagn. and Aeronomy*, *37*, 24, 1997 (in Russian).

Alexeev, I. I., S. Yu. Bobrovnikov, Magnetospheric dynamics during substorm: external substorm triggering, In "Problems of Geocosmos 2", Monograph. Austrian Acad. of Science. Edited by V. S. Semenov, H.K. ??

Alexeev, I. I., S. Yu. Bobrovnikov, Substorm study on the basis of the Paraboloid model of the magnetosphere, Int. Journal of *Geomag. and Aeronomy*, *3*, 1, 35-44, 2001.

Alexeev, I. I., E. S. Belenkaya, D. G. Sibeck, Comparison of effects of field-aligned and tail current on the structure of the magnetosphere, *Geomgn. and Aeronomy*, *37*, 5, 19-28, 1997 (in Russian).

Baker, D. N., T. I. Pulkkinen, V. Angelopoulos, W. Baumjohann, and R. L. McPheron, Neutral line model of substorm: Past results and present view, *J. Geophys. Res.*, *101*, 12975, 1996.

Baker, D. N., T. I. Pulkkinen, J. Buchner, and A. J. Klimas, Substorms: A global instability of the magnetosphere-ionosphere system, *J. Geophys. Res*., *104*, 14601, 1999.

Brittnacher, M., M. Fillingim, G. Parks, G. Germany, and J. Spann, Polar cap and boundary motion during substorms, *J. Geophys. Res*., *104*, 12,251, 1999.

Caan, M. N., R. L. McPherron, C. T. Russell, Substorms and interplanetary magnetic field effects on the geomagnetic tail lobes, *J. Geophys. Res*., *80*, 191, 1975.

Lyons, L. R., A new theory for magnetospheric substorms, *J. Geophys. Res*., *100*, 19065, 1995.

Lyons, L. R., Substorms: Fundamental observations features, distinction from other disturbances, and external triggering, *J. Geophys. Res*., *101*, 13011, 1996.

Lyons, L. R., G. T. Blanchard, K. B. Baker, Substorm onset: the result of IMF-driven reduction in largescale convection. Proc. Forth Int. Conf. on Substorms, Y. Kamide (ed.) Terra Sci, Tokyo, P.265, 1998.

McPherron, R. L., T. Terasawa, A. Nishida, Solar wind triggering of substorm onset, *J. Geophys. Geoelectr*., *38*, 1089, 1986.

Nishida, A., N. Mukai, Response of the near-Earth magnetotail to a northern turning of the IMF, *Geophys. Res. Lett*., *24*, 8, 943, 1997.

Roelof, E. C., D. G. Sibeck, Magnetopause shape as a bivariate function of interplanetary magnetic field Bz and solar wind dynamic pressure. J. Geophys. Res., 98, 21421, 1993 (Correction, *J. Geophys. Res*., *99*, 8787, 1993).

Rostoker, G., M. Mareschal, J. C. Samson, Response of dayside net downward field-aligned current to changes in the interplanetary magnetic field and to substorm perturbations, *J. Geophys. Res*., *87*, 3489, 1982.

Rostoker, G., Triggering of expansion phase intensifications of magnetospheric substorm by northward turning of the interplanetary magnetic field, *J. Geophys. Res*., *88*, 6981, 1983.

Sitnov, M. I., A. S. Sharma, K. Papadopoulos, D. Vassiliadis, J. A. Valdiva, A. J. Klimas, and D. N. Baker, Phase transition–like behavior of the magnetosphere during substorms, *J. Geophys. Res*, *105*, 12,955- 12,974, 2000.

Shue, J. -H., J. K. Chao, H. C. Fu, C. T. Russel, A new function form to study the solar wind control of the magnetopause size and shape, *J. Geophys. Res*., *102*, 9497, 1997.

Troshichev, O. A., A. L. Kotikov, B. D. Bolotinskaya, V. G. Andrezen, Influence of the IMF azimuthal component on magnetospheric substorm dynamics, *J. Geophys. Geoelectr.*, *38*, 1075, 1986.

Tsurutani, B. T., J. K. Arballo, G. S. Lakhina, C. M. Ho, J. M. Ajello, J. S. Pickett, A CME loop and January 10, 1997 first substorm. Proc. Forth Int. Conf. on Substorms, Y.Kamide (ed.) Terra Sci, Tokyo, P.309, 1998.

Tsyganenko, N. A., D. G. Sibeck, Concerning flux erosion from the day side magnetosphere, *J. Geophys. Res*., *99*, 113425-13436, 1994.

Vassiliadis, D. V., A. J. Klimas, D. N. Baker, D. A. Roberts, A description of solar windmagnetosphere coupling based on nonlinear filters, *J. Geophys. Res*., *100*, 3495, 1995.

# Magnetic field structure in the magnetosheath for high and low magnetic shear on the magnetopause

V. V. Kalegaev

Institute of Nuclear Physics, Moscow State University, Moscow 119992, Russia

**Abstract.** The plasma processes near the magnetopause are determined by magnetic field structure. Numerous observations in the magnetosheath give different magnetic field and plasma flow profiles near the magnetopause for high and low magnetic shear conditions. The fine-scale structure of the dayside magnetopause was investigated for different IMF orientations using the quantitative model of solar wind – Earth's magnetosphere interaction with respect to finite solar wind plasma conductivity. This model takes into account partial diffusive magnetospheric magnetic field penetration through the magnetopause. The magnetic field in the vicinity of magnetopause is determined by both the magnetosheath's magnetic field originating from solar wind and magnetic field diffused from the magnetosphere. For southward and northward IMF orientations different magnetic field structures arise. The proposed model explains unexpected magnetic field growth, plasma tangential acceleration and PDL formation for low magnetic shear. The proposed model allows explaining PDL formation for high magnetic field under disturbed conditions. The magnetic field calculated in the magnetosheath is compared with those measured by AMPTE/IRM satellite.

## 1. Introduction

The magnetic field structure in the magnetosheath region adjacent to the magnetopause depends strongly on the magnetic shear across the magnetopause, i.e. an angle between the solar wind's and magnetospheric magnetic field directions. While the magnetic shear is high (>60°), the magnetosheath is more disturbed and the magnetopause can be identified by magnetic field rotation. For the low shear the magnetic field has slow changes near the magnetopause and only discontinuities in the plasma properties characterize it. An analysis of 68 magnetosheath's passes during the AMPTE/IRM mission [*Phan et al.,* 1994] shows that reconnections are often observed on the dayside high shear magnetopause but there is no direct evidence for reconnection on the low-shear dayside magnetopause [*Phan et al.,* 1997]. In general, the magnetic field rises when we move from the bow shock to the magnetopause, but for high magnetic shear this trend often reverses in the vicinity of the magnetopause: the magnetic field decreases, indicating violation of the frozen-in magnetic field condition in this region. The plasma density is relatively constant in the dayside magnetosheath for high shear. However, plasma depletion layer with decreased values of density near the low shear magnetopause is actually detected [*Pashman et al.,* 1979; *Phan et al.,* 1997; *Phan et al.,* 1994].

We will investigate the magnetosheath magnetic field due to supersonic solar wind-Earth's magnetosphere coupling. Three regions in the Earth's environment with the different kinds of magnetic field will be considered: the region of supersonic solar wind flow, the magnetosheath, and the magnetosphere. The magnetopause is assumed to be a thin dissipative boundary layer between the magnetosheath proper and magnetosphere where the finite solar wind plasma conductivity is taken into account. The inner boundary of the magnetopause is a surface being flown past, where $V_n = 0$, the outer boundary of it is shifted at the distance $l_\varepsilon = R_1\, Re_m^{-1/2}$ (here $Re_m = 4\pi\sigma V_\infty R_1/c$ is the magnetic Reynolds number, $R_1$ is the magnetopause subsolar distance, $\sigma$ is the plasma conductivity, $V_\infty$ is the solar wind bulk velocity). The kinematical approximation will be used in the magnetosheath to calculate the magnetic field for known velocity (see [*Alexeev and Kalegaev*, 1995; 2001]).

## 2. Magnetic field and flow structure in the solar wind

We will assume the solar wind flow to be uniform in the supersonic flow and the magnetic field orthogonal to the flow. In Cartesian coordinates (X, Y, Z), where the X and Z axes are directed along the Sun-Earth line and the

IMF, $\mathbf{V} = \mathbf{V}_\infty = (-V_\infty, 0, 0)$, $\rho = \rho_1 = \rho_\infty$, $\mathbf{B} = \mathbf{B}_\infty = (0, 0, -B_\infty)$ in supersonic region.

Let us assume the magnetospheric surface to be represented as a paraboloid of revolution. In the parabolic dimensionless coordinates ($\alpha$, $\beta$, and $\varphi$), which are related to the aforementioned Cartesian coordinates by the relations

$$2x/R_1 = \beta^2 - \alpha^2 + 1; \quad y/R_1 = \alpha\beta \sin\varphi; \quad z/R_1 = \alpha\beta\cos\varphi,$$

the supersonic flow and magnetic field may be described as $\mathbf{V} = \mathbf{V}_\infty = V_\infty$ $(-\alpha/h;\ \beta/h;\ 0)$ and $\mathbf{B} = \mathbf{B}_\infty = -B_\infty$ $(\beta\cos\varphi/h,\ \alpha\cos\varphi/h,\ -\sin\varphi)$.

Let's determine the magnetospheric surface and bow shock by the $\beta = 1$ and $\beta = \beta_{bs}$ relations. In the magnetosheath region ($1 < \beta < \beta_{bs}$), where the solar wind plasma is assumed to be Ohmic conducting fluid, the kinematical approximation will be used:

$$\begin{aligned} &div\ \rho\mathbf{V} = 0, \quad \mathbf{V} = -\nabla U \\ &curl\ \mathbf{B} = Re_m\cdot(\mathbf{E} + [\mathbf{V}\times\mathbf{B}]), \\ &div\ \mathbf{B} = 0,\ curl\ \mathbf{E} = 0. \end{aligned} \qquad (1)$$

Inside the magnetosphere the magnetic field is described by paraboloid model [*Alexeev,* 1978]; [*Alexeev et al.,* 1996] as a sum of magnetic fields of the geomagnetic dipole, the ring current, the geotail current system, the Chapman-Ferraro currents, and also some part of the IMF penetrating through the magnetopause:

$$\mathbf{B}_m = \mathbf{B}_D + \mathbf{B}_R + \mathbf{B}_T + \mathbf{B}_{CF} + K_{mp}\,\mathbf{B}_\infty$$

Reconnection efficiency $K_{mp}$ will be obtained from the solution of (1).

The boundary conditions on the magnetopause

$$V_n = 0, \quad \{\mathbf{B}\} = 0,$$

and of the bow shock

$$\{V_\tau\} = 0,\ \{\rho V_n\} = 0,\ \{B_n\} = 0$$

will be taken into account.

Kinematical approximation allows to determine the magnetic field structure by known gasdynanamical flow [*Moffat,* 1978]. It is valid when the magnetic pressure is smaller than the dynamical one. There exists the partial solution inside the magnetosheath

$$\begin{aligned} U &= -V_\infty R_1\,[0.5\,(\beta^2 - \alpha^2) - \ln\beta] \\ \rho &= \rho_2 = K_{bs}(\beta_{bs})\cdot\rho_\infty, \end{aligned}$$

where $(\beta) = [(\beta^2)/(\beta^2 - 1)]$ determines the plasma compression on the bow shock.

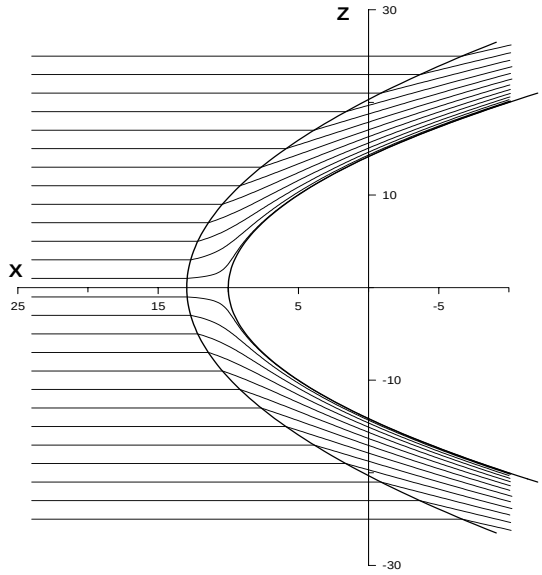


**Figure 1**. Supersonic flow past the parabolic magnetosphere.

Inside the magnetosheath the obtained solution coincides with those for a problem of non-compressible fluid flowing past a paraboloid of revolution used in [*Alexeev and Kalegaev*, 1995]. The difference is only in the plasma density magnitude, which is enhanced by $K_{bs}$ for the case of supersonic flow.

Figure 1 represents the velocity structures for the supersonic flow past the parabolic magnetosphere. The general solution of (1) is presented in [*Alexeev and Kalegaev*, 1995]. It is the superposition of the solutions of two different problems: the solar wind magnetic field coupling with non-conducting blunt body and the magnetospheric magnetic field diffusion to non-magnetized solar wind, $B_1$ and $B_2$.

The former term describes IMF penetration into the magnetosphere:

$$\begin{aligned} h\cdot B_{1\,\alpha} &= \beta f'(\beta)\cos\varphi \\ h\cdot B_{1\,\beta} &= \beta^{-1}\alpha f(\beta)\cos\varphi \\ B_{1\,\varphi} &= -f'(\beta)\sin\varphi. \end{aligned} \qquad (2)$$

(Here $f = \beta^{l+2a}\,[d_1\,M\,(a;\,b;\,z) + d_2\,U\,(a;\,b;\,z)]$; $M$ and $U$ – are confluent hypergeometrical functions; $z = -Re_m\,\beta^2/2$; $a = [(Re_m^2 + 4)^{1/2} + Re_m - 2]/4$; $b = (Re_m^2 + 4)^{1/2}/2 + 1$ (see [*Alexeev and Kalegaev*, 1995])). The constants $d_1$, $d_2$ and $K_{mp}$ are determined from the boundary conditions

$$\begin{aligned} d_1 &= \sqrt{K_{bs}(\beta_{bs})}\,[Re_m/2]^a\,\Gamma(b-a)/\Gamma(b), \\ d_2 &= -d_1\,[M(1) - M'(1)]/[U(1) - U'(1)], \\ K_{mp} &= d_1\,M(1) + d_2\,U(1). \end{aligned}$$

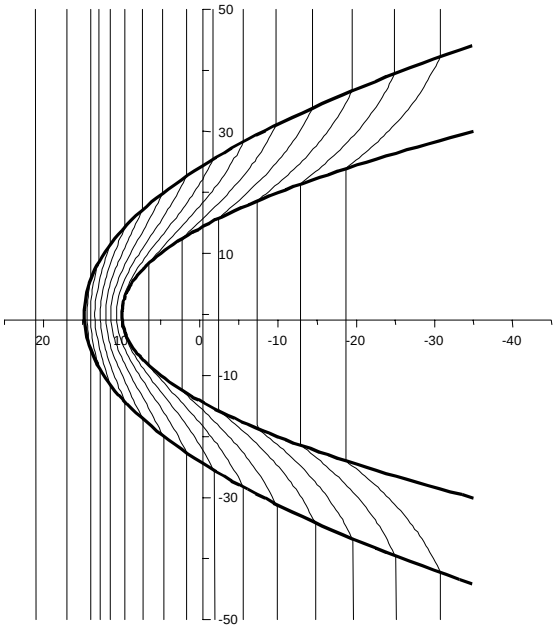


**Figure 2.** The magnetic field coupling with non-conducting blunt body in the (X, Z) plane.

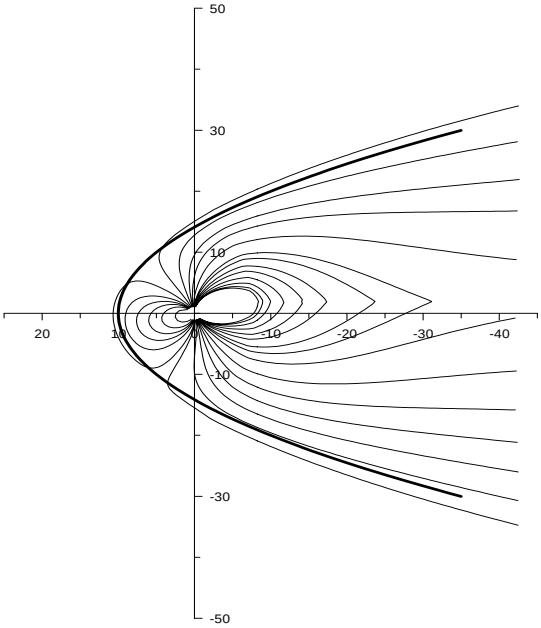


**Figure 3.** The magnetospheric magnetic field diffusion to non-magnetized solar wind flow.

The latter term describing the magnetospheric magnetic field diffusion into the magnetosheath is found by [*Alexeev and Kalegaev*, 1995] as expansion in confluent hypergeometrical functions. This solution decreases exponentially when we move from the magnetopause to the bow shock. Figures 2 and 3 represent the magnetic field $\mathbf{B}_1$ and $\mathbf{B}_2$ structures. The magnetic field $\mathbf{B}_1$ inside the magnetosheath has the same topology as in the case of subsonic flow. However the magnetic field intensity is increased. Using the boundary conditions, one can obtain that the magnetic field in the magnetosheath increases by a factor of $[(\rho_2)/(\rho_1)]^{1/2}$ times compared with the magnetic field for the subsonic flow obtained in [*Alexeev and Kalegaev*, 1995]. The solar wind velocity is decreasing but the magnetic field and solar wind density are increasing on the bow shock by the factor of $[(\beta_{bs}^2) / (\beta_{bs}^2 - 1)]$. For the large $Re_m$ the magnetopause reconnection efficiency is $K_{mp} \approx 0.9\ [(\rho_2)/(\rho_1)]^{1/2}\ Re_m^{-1/4}$. Magnetic field $\mathbf{B}_2$ is calculated under condition taken at 14:00 UT on August 29, 1984. The magnetic field diffused from magnetosphere to the magnetosheath is proportional to $\exp\{-Re_m^2(\beta^2 - 1)/2\}$.

### 3. Discussion

Let us consider the magnetic field structure for the IMF (0, 0, 7 nT) and (0, 0, 7 nT) for the same magnetospheric conditions as at UT 14:00 on August 29, 1984. Figure 4 and 5 show the magnetic field $\mathbf{B_1 + B_2}$ which is a superposition of IMF, penetrating inside the magnetosphere and magnetospheric magnetic field diffused to magnetosheath in the noon-midnight plane for the IMF $B_\infty$ = (0, 0, –7 nT) and (0, 0, –7 nT), respectively, and $Re_m = 20$. The paraboloid model of the Earth's magnetosphere [*Alexeev,* 1978; *Alexeev at al.,* 1996] was used in calculation of the magnetospheric magnetic field. The magnetic field outside the magnetosheath is uniform. Although inside the magnetosheath it has the similar topology for the both cases, the magnetospheric structures are very different (see [*Belenkaya,* 1998]). The magnetopause serves as a boundary layer matching the magnetosheath and magnetospheric magnetic fields.

Figure 6 represents the magnetic field fine structure in the magnetopause boundary layer. For the northward IMF (low magnetic shear) the solar wind magnetic field $B_{1z}$ (Figure 6*b*) in the near-magnetopause region enhances the positive $B_{2z}$ component (Figure 6*a*) of the magnetic field penetrating from the magnetosphere. For the southward IMF (high magnetic shear) the situation is opposite. The negative $B_{1z}$ component (see Figure 6*e*) reduces the diffused magnetospheric magnetic field $B_{2z}$ (see Figure 6*d*). The unexpected growth of magnetic pressure near the magnetopause for low magnetic shear, as it was by the analysis of the AMPTE/IRM magnetopause crossings, leads to the plasma density decrease (plasma depletion layer formation) near the magnetopause. Electric currents on the magnetopause associated with the IMF and diffused magnetospheric

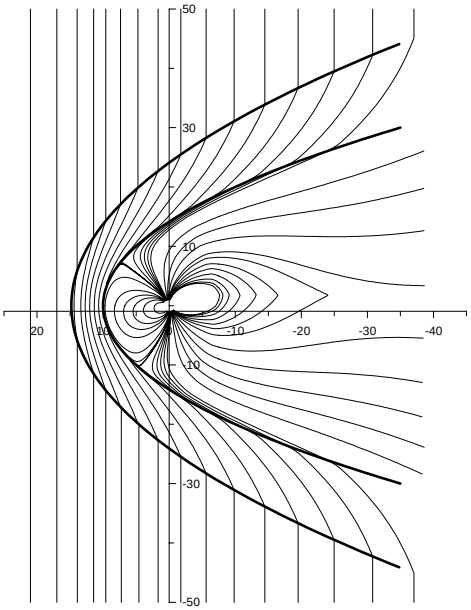


**Figure 4.** Magnetic field lying in the noon-midnight plane, calculated by open paraboloid magnetospheric model on August 29, 1984 at UT 14:00 for the IMF $B = (0, 0, -7\ \text{nT})$, $Re_m = 20$.

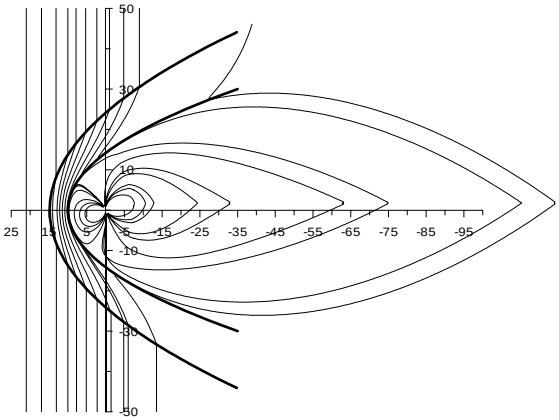


**Figure 5.** Magnetic field lying in the noon-midnight plane, calculated by open paraboloid magnetospheric model on August 29, 1984 at UT 14:00 for the IMF $B = (0, 0, 7\ \text{nT})$, $Re_m = 20$.

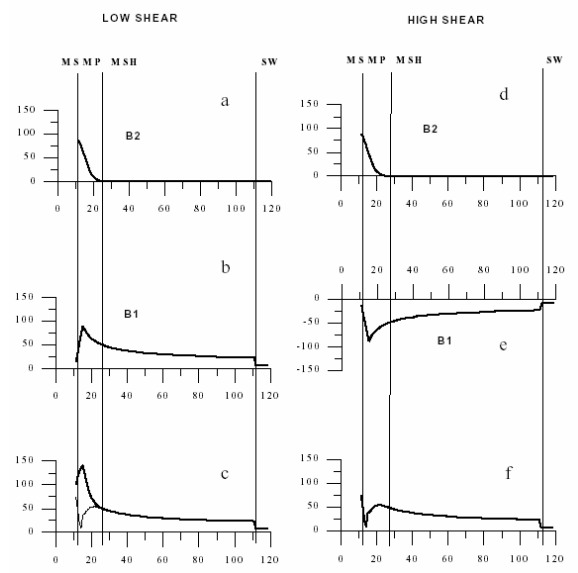


**Figure 6.** The magnetic field structure in the magnetosheath for the cases of low (a-c) and high (d-f) magnetic shear. The units along the horizontal axes are minutes, along the vertical ones are nanoteslas.

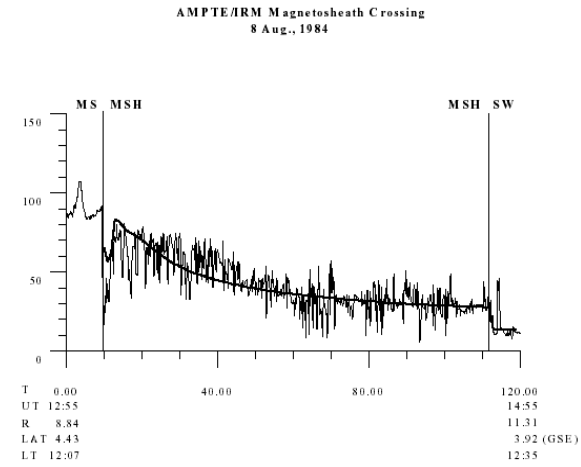


**Figure 7.** The magnetic field structure during the AMPTE/IRM magnetosheath crossing on August 28, 1984 (solid line) and calculated magnetic field (heavy solid line).

magnetic field have the same directions in the case of low magnetic shear. It leads to a drastic increase of the magnetic force near the low shear magnetopause, and hence explains the plasma tangential acceleration in this region, observed by the AMPTE/IRM and WIND spacecrafts [*Phan et al.,* 1997; *Phan et al.,* 1994]. The magnetic field decrease near the high shear magnetopause can also be explained by the influence of magnetospheric magnetic field diffusion from the magnetosphere. This simple reasoning makes it possible to explain the difference in the magnetic field behavior for low (see Figure 6*c*) and high (see Figure 6*f*) magnetic shear. It is also clear, that in the case of heavily compressed magnetosphere we can find the magnetic field enhancement and PDL formation (as was mentioned by [*Fuselier et al.,* 1991]) even near the high

shear magnetopause, because the magnetospheric magnetic field grows significantly with the decrease of magnetopause subsolar distance and the magnetic field contribution $B_{2z}$ to the total magnetic field near the magnetopause becomes rather large.

Figure 7 represents the magnetic field measurements during the AMPTE/IRM magnetosheath crossing on August 28, 1984 (high magnetic shear). The heavy solid line shows the results of calculation. The IMF and solar wind hourly averaged data were used in these calculations. We can see that in general measured magnetic field is in a good agreement with our results. The magnetic field behavior near the magnetopause is well explained by coupling between IMF and the diffused magnetospheric magnetic field. Strong plasma compression on the bow shock is responsible for high values of magnetic field near the magnetopause, and reconnection efficiency is equal to 0.28.

## 5. Conclusion

The magnetic field near the magnetopause is a sum of two terms, determined by IMF and diffusion magnetospheric magnetic field. Their superposition explains the different magnetic field structures near the magnetopause for the cases of high and low magnetic shear. The proposed model relates the reconnection efficiency with the measured solar wind parameters. Comparison with AMPTE/CCE measurement during magnetosheath passing on August 28, 1984 shows a good agreement.

**Acknowledgments.** This research was supported by RFBR grants N 00-05-65003 and N 00-07-90117.

## References

Alexeev, I. I., Regular magnetic field in the Earth's magnetosphere (in Russian), *Geomagn. Aeron., 18,* 656-662, 1978.

Alexeev, I. I., and V. V. Kalegaev, Magnetic field and the plasma flow structure near the magnetopause. *J. Geophys. Res.*, *100*, 19267-19276, 1995.

Alexeev, I. I., and V. V. Kalegaev, Magnetic field structure in the Earth's magnetosheath (in Russian), *Geomagn. Aeron., 41,* 309-316, 2001.

Alexeev, I. I., E. S. Belenkaya, V. V. Kalegaev, Ya. I. Feldstein, and A. Grafe, Magnetic storms and magnetotail currents, *J. Geophys. Res.*, *101*, 7737-7748, 1996.

Belenkaya, E. S., Reconnection modes for near-radial IMF, *J. Geophys. Res.*, *103*, 26,487-26,494, 1998.

Fuselier, S. A., D. M. Klumpar, E. G. Shelly, B. J. Anderson, and J. Coates, $He^{2+}$ and $H^{+}$ dynamics in the subsolar magnetosheath and plasma depletion layer, *J. Geophys. Res.*, *96*, 21,095-21,104, 1991.

Moffatt, H. K., Magnetic Field Generation in Electrically Conducting Fluids, 44 pp., Cambridge Univ. Press, New York, 1978.

Paschmann, G. B., U. Ö. Sonnerup, I. Papamastorakis, N. Scopke, G. Haerendel, S. J. Bame, J. R. Asbridge, J. T. Gosling, C. T. Russel, and R. C. Elphic, Plasma acceleration at the earth's magnetopause: Evidence for magnetic reconnection, *Nature*, *282*, 243-246, 1979.

Phan, T. -D., G. Paschmann, W. Baumjohann, N. Sckopke, and H. Luehr, The magnetosheath region adjacent to the dayside magnetopause: AMPTE/IRM observations, *J. Geophys. Res.*, *99*, 121-141, 1994.

Phan, T. -D., D. Larson, J. McFadden, R. P. Lin, C. Carlson, M. Moyer, K. I. Paularena, M. McCarthy, G. K. Parks, H. Réme, T. R. Sanderson, and R. P. Lepping, Low-latitude dusk flank magnetosheath, magnetopause, and boundary layer for low magnetic shear: Wind observations, *J. Geophys. Res.*, *102*, 19,883-19,895, 1997.

---

V. V. Kalegaev, Institute of Nuclear Physics, Moscow State University, Moscow 119992, Russia.

# Comparison of ULF waves of plasma and magnetic field inside the foreshock and magnetosheath

N. N. Shevyrev[1], P. E. Eiges[1], G. N. Zastenker[1], and J. D. Richardson[2]

[1] Space Research Institute Russian Academy of Sciences, Moscow, Russia.
[2] Center for Space Research, MIT, Cambridge, MA, USA

**Abstract.** Large amplitude plasma and magnetic field ULF waves (10 mHz – 1 Hz) are typical features in the foreshock and in the magnetosheath but differences and similarities of the waves in these two regions are still not well known. We investigated these waves using simultaneous measurements in the solar wind (from WIND and ACE spacecraft), in the foreshock and in the magnetosheath (from INTERBALL-1 spacecraft). The results of the case and statistical study of magnetosheath variations using a large database of high time resolution (1sec) measurements on INTERBALL-1 show that the amplitude of ULF waves in the magnetosheath strongly depends on the angle between the bow shock normal and interplanetary magnetic field direction; amplitude of variations is much larger behind quasi-parallel bow shocks.

## 1. Introduction

Consideration of the problem of Solar-Terrestrial relations will be incomplete without understanding of the processes, which occur in a layer between the magnetopause and bow shock called magnetosheath (MSH), because it is the magnetosheath plasma and magnetic field that act upon the magnetosphere, not the undisturbed solar wind (SW). The magnetosheath is a region rich of waves which in turn carry information and redistribute energy and momentum from the bow shock to the magnetopause [*Schwartz et al.,* 1996]. It is a non-uniform medium filled with anisotropic, collisionless plasma with high kinetic temperatures, particle beams and other features which are preserved unless various processes such as wave-particle scattering would bring plasma toward equilibrium. As it is also observed to be highly turbulent that is, fluctuations in ion flux and magnetic field are usually present over a broad range of frequencies, the understanding of the processes becomes extremely complicated.

The foreshock (FSH) magnetic field variations were often considered as a probable source of intensive variations in the magnetosheath layer [*Luhmann et al.,* 1986]. But lack of plasma measurements with time resolution better than 1 minute prevented comprehensive study of evolution of plasma and magnetic field fluctuations on their way from the solar wind to the magnetosheath.

In this paper fluctuations in ion flux and magnetic field magnitude in the frequency domain 10mHz – 1Hz were investigated and their relationship with orientation of the interplanetary magnetic field (IMF) with respect to the bow shock normal was considered (some results about MSH fluctuations can be found in [*Shevyrev et al.,* 2003]).

## 2. Observations

The systematic measurements in the solar wind, in the foreshock, and in the magnetosheath were performed in 1995–2000 onboard the high apogee (300,000 km) satellite INTERBALL-1 [*Galeev et al.,* 1996]. Ion flux [*Zastenker et al.,* 2000] and magnetic field [*Nozdrachev et al.,* 1998] data with time resolution of 1 second from this spacecraft have been used for our study. This high time resolution allowed to examine ULF variations of the ion flux and magnetic field in the foreshock and in the magnetosheath.

The upstream conditions in the undisturbed solar wind were taken from measurements by WIND or ACE spacecraft. Time resolution of these measurements was about 1 minute.

### 2.1. Case study

Figure 1 presents an example of the ion flux (panel a)) and magnetic field magnitude (panel b)) measurements onboard INTERBALL-1 spacecraft during a magnetosheath crossing on July 16, 1997. The spacecraft was initially in the solar wind; then near 0746 UT it crossed the bow shock; then during 3.5 hours it was inside the magnetosheath and at 1121 UT it crossed

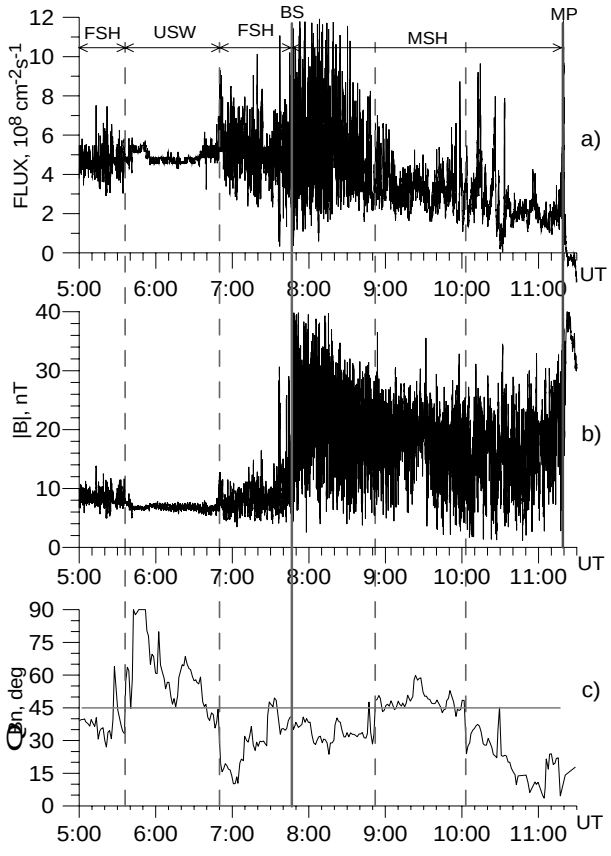


**Figure 1.** An example of INTERBALL-1 ion flux and magnetic field magnitude measurements in the FSH, SW and MSH with a time resolution of 1sec (panels a), b)) on July 16, 1997 and the $\Theta_{Bn}$ angle (panel c)) calculated using WIND data.

the magnetopause and entered the magnetosphere.

One can define by eye several regions in panels a), b), which differ from each other by the value of fluctuations. During 0535-0649 UT the spacecraft was in the undisturbed solar wind that is characterized by the small variations in the ion flux and magnetic field in frequency domain 10mHz–1Hz. During 0500–0535 UT and 0649-0746 UT it was in foreshock regions, characterized by high level of fluctuations in this frequency domain. In the magnetosheath (during 0746-1121 UT) the level of fluctuations is also high but fluctuations are different.

It is well known that for quasi-parallel orientation of the interplanetary magnetic field to the bow shock (i.e. when the angle $\Theta_{Bn}$ between the interplanetary magnetic field and the bow shock normal is less than $45^0$) some part of particles of the incident solar wind flux is reflected from the bow shock and is capable to escape far upstream the solar wind along the magnetic field lines. Also, a part of their population consists of particles of the magnetosheath and magnetosphere [*Fuselier*, 1994]. So, the extensive foreshock region is formed which is characterized by the high fluctuation level (compared with the undisturbed solar wind) of the ion flux [*Eiges et al.*, 1998] and magnetic field magnitude because of interaction of the incident solar wind flux with these reflected particles. In this study we tried to evaluate: if quasi-parallel IMF orientation controls fluctuations not only ahead (i.e. in the foreshock) but also behind (i.e. in the magnetosheath) the bow shock.

To determine $\Theta_{Bn}$ for a spacecraft inside the magnetosheath one need to have simultaneous observations of the interplanetary magnetic field in the undisturbed solar wind and to know orientation of the normal vector to the bow shock at the point, where solar wind plasma entered the magnetosheath. In this study the following procedure to determine the normal to the bow shock was applied [*Shevyrev et al.*, 2002]. As the data of solar wind monitor we used plasma and magnetic field parameters measured onboard WIND or ACE spacecraft. These data were shifted by the propagation time of plasma toward the INTERBALL-1 position. From these data distances Ds from the Earth to the subsolar point of the magnetopause were calculated using *Shue et al.* [1998] model. Then, GSE coordinates of INTERBALL-1 were normalized by Ds value and aberrated (by 5–10 degrees) for taking into account the orbital motion of the Earth around the Sun. In this relative coordinate system it is possible to compare INTERBALL-1 observations with results of the gasdynamic *Spreiter et al.* [1966] model, which provides distributions of density, temperature and velocity (normalized by upstream conditions) and also shows the streamlines of the plasma flow inside the magnetosheath and the position of the bow shock.

Having relative positions of INTERBALL-1 inside the magnetosheath and using the Spreiter model one can trace (though rather roughly) streamlines from these positions to the bow shock and to find the points of the bow shock, which are topologically connected with spacecraft. Then the model shock normal **n** at the point of intersection with the bow shock can be calculated and, hence, $\Theta_{Bn}$ angles can be obtained as a function of time for any spacecraft position in the magnetosheath.

Figure 2 provides an explanation of such a technique. Thick dots show two positions of spacecraft on different flanks of the magnetosheath. Several streamlines of the plasma flow for these positions (thick curves) are also presented therefore one can find the points of the bow shock where the plasma entered the magnetosheath and calculate normal vectors **n** to the bow shock at these points.

At this scheme the IMF is inclined at $45^0$ to the Sun-Earth line, so for spacecraft at the upper (dusk) flank of the magnetosheath $\Theta_{Bn}$ angles are $>45^0$ and the magnetosheath is behind a quasi-perpendicular bow

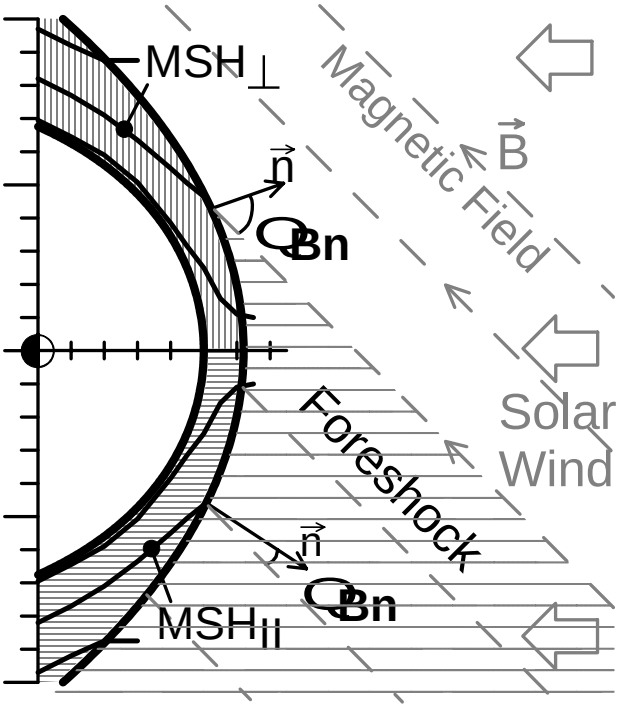


**Figure 2.** A scheme to explain various features in the solar wind and magnetosheath when the IMF vector is inclined at an angle of $45^0$ to the Sun-Earth line.

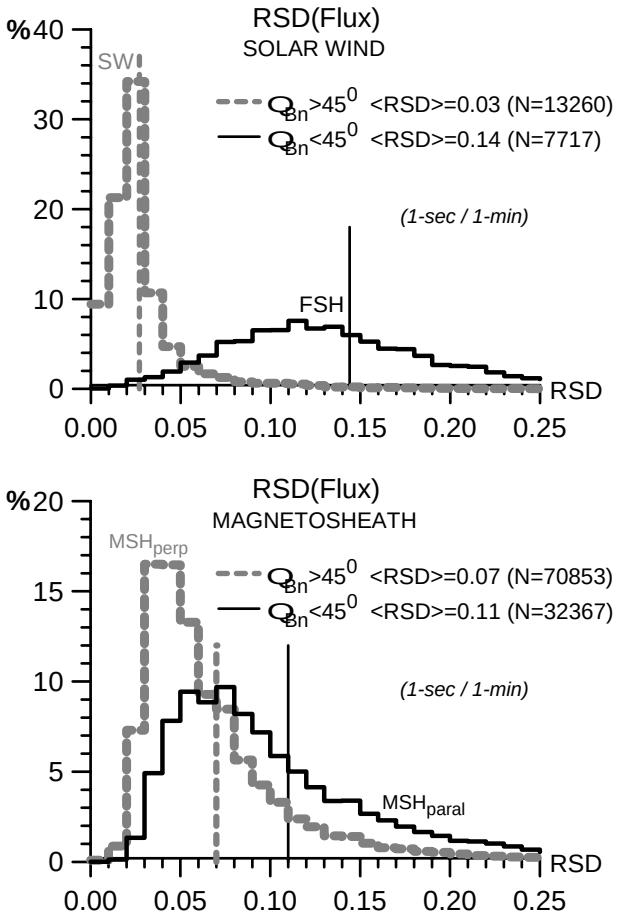


**Figure 3.** Histograms of RSD values for ion flux fluctuations in the undisturbed solar wind and foreshock (upper panel), and inside the magnetosheath for quasi-parallel and quasi-perpendicular bow shock (lower panel). N is the total number of points for calculation of the particular histogram. Vertical lines show average values of RSD in various regions.

shock (this region is indicated by vertical lines). For spacecraft at the lower (dawn) flank $\Theta_{Bn}<45^0$, the magnetosheath is behind the quasi-parallel shock (this region is indicated by horizontal lines). The foreshock region is also shown as a shaded part of the solar wind.

For the intervals when INTERBALL-1 was in the undisturbed solar wind or in foreshock $\Theta_{Bn}$ angles were calculated between the interplanetary magnetic field vectors (measured by the solar wind monitor) and normal vectors to the bow shock at points where the magnetic field vector traced through the spacecraft position crosses the bow shock.

$\Theta_{Bn}$ values calculated for July 16, 1997 are presented in the panel (c) in Figure 1. Vertical dashed lines indicate times of changes in $\Theta_{Bn}$ when it became more/less $45^0$. A very good coincidence between the intervals of foreshock observation and intervals with $\Theta_{Bn}<45^0$ is seen. But in the region of the magnetosheath the same dependence is observed: an abrupt increase in $\Theta_{Bn}$ angle at 0850 UT coincides with a decrease in the amplitude of variations in the ion flux and magnetic field which reached a minimum during 0920–0935 UT when the angle $\Theta_{Bn}$ was the highest (about $60^0$). Decrease in the $\Theta_{Bn}$ angle and return to the quasi-parallel orientation of the bow shock are accompanied by increase in the amplitude of the magnetic field variations. Ion flux data do not show any increase in fluctuation level probably because spacecraft was not far from the magnetopause [*Shevyrev et al.*, 2002].

### 2.2. Statistical study

As the measure of the fluctuations intensity in the frequency domain (0.02–1 Hz) the values of the relative standard deviation RSD were calculated from the original data with time resolution 1 second on 1 minute intervals. RSD is the standard deviation normalized by the mean value of the parameter in the appropriate interval. We considered about 220 magnetosheath crossings or about 1720 hours of observations. For comparison with other solar wind regions about 130 hours of observations in undisturbed solar wind and

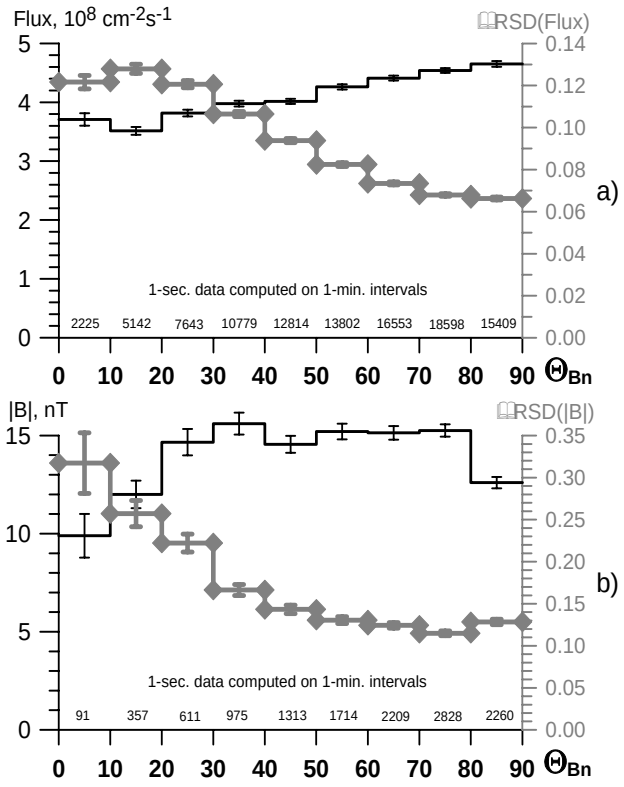


**Figure 4**. Dependencies of the averaged RSD values of variations (diamonds) in the ion flux (panel a) and magnetic field magnitude (panel b) on the $\Theta_{Bn}$ angle. Number of points in each bin is shown at the bottom of each plot.

about 220 hours of observations in foreshock were taken. Figure 3 presents histograms of RSD values for ion flux fluctuations in the undisturbed solar wind ($\Theta_{Bn} > 45^0$) and foreshock ($\Theta_{Bn} < 45^0$) (the upper panel), and inside the magnetosheath (the lower panel) – also separately for quasi-parallel and quasi-perpendicular bow shock.

From Figure 3 it is seen that the ion flux fluctuations in the solar wind are rather weak and significantly less (by about 5 times) than those ones in the foreshock for the frequency range considered. Average values of variations inside the magnetosheath are also several times exceed variations in the undisturbed solar wind, but what is of the most importance is the clear dependence of the RSD distribution on the $\Theta_{Bn}$ angle. It is seen that the maximum of the RSD distribution in the MSH when the spacecraft was behind the quasi-parallel bow shock is located at two times higher values of RSD than when the spacecraft was behind the quasi-perpendicular bow shock. Average values of RSD are also strongly differ for these two orientations of the bow shock. It is also seen, that the main part of the distribution for the case with $\Theta_{Bn} > 45^0$ is located at small RSD values, whereas for $\Theta_{Bn} < 45^0$ the distribution is wider and have an extended "tail" to RSD values more than 0.25.

Dependencies of the averaged RSD values of variations in the ion flux and magnetic field magnitude on the $\Theta_{Bn}$ angle are presented in Figure 4. RSD values are averaged inside each 10 deg. bins. It is seen that both the ion flux and magnetic field magnitude fluctuations steadily decrease with increase in the $\Theta_{Bn}$ angle and RSD values behind the quasi-parallel bow shock are about two times higher than behind the quasi-perpendicular one.

A weak dependence of distributions of the ion flux and magnetic field magnitude on the $\Theta_{Bn}$ angle is somewhat strange. For the magnetic field magnitude we can refer to an insufficient statistics of points with $\Theta_{Bn} < 20^0$, that can introduce larger error into the calculation of the average value. But this is not the case for the dependence of the ion flux, because statistics is large and sufficient.

## 3. Conclusions

As follows from both case and statistical study orientation of the interplanetary magnetic field strongly affects the character of the turbulence of the plasma flow in magnetosheath:

- during the periods of quasi-parallel orientation intensive fluctuations in ion flux and magnetic field magnitude develop in the frequency range 10mHz – 1Hz,
- on the average their amplitude is 2 times higher than the amplitude of fluctuations observed behind the quasi-perpendicular bow shock.

According to the data presented it seems that the bow shock is the dominant source of fluctuations in magnetosheath ion flux and magnetic field magnitude in the frequency range 10mHz – 1Hz, because on the average these fluctuations exceed several times those in the undisturbed solar wind and fluctuations level clearly dependent on the orientation of the bow shock with respect to the IMF direction. These results and previous ones of *Shevyrev et al.* [2003] allow us to suggest that such fluctuations are generated at the bow shock and then are convected by the plasma flow along the streamlines.

**Acknowledgements.** The present work was supported by the RFBR 01-02-16182, 03-02-06218-mac.

**References**


Eiges, P. E., G. N. Zastenker, M. N. Nozdrachev, Yu. I. Yermolaev, J. Šafránková, and Z. Němeček, Fast variations of solar wind ion flux and magnetic field in the foreshock: 1. Correlation of parameters, *Cosmic Research, 36,* 3, 235, 1998.

Fuselier, S. A., Suprathermal ions upstream and downstream from the Earth's bow shock, *Solar Wind Sources of Magnetospheric Ultra-Low-Frequency Waves, Geophys. Monogr., 81*, 107, 1994a.

Galeev A. A., Yu. I. Galperin, and L. M. Zelenyi, The INTERBALL Project to study solar-terrestrial physics, *Cosmic Research, 34*, 4, 339, 1996.

Luhmann J. G., C. T. Russell, and R. C. Elphic, Spatial distributions of magnetic field fluctuations in the dayside magnetosheath, *J. Geophys. Res., 91,* 1711, 1986.

Nozdrachev M. N., A. A. Skalsky, V. A. Styazhkin, and V. G. Petrov, Some results of Magnetic Measurements by the FM-3I flux-gate instrument onboard the INTERBALL-1 spacecraft, *Cosmic Research, 36*, 272, 1998.

Schwartz, S. J., D. Burgess, and J. J. Moses, Low-frequency waves in the Earth's magnetosheath: present status, *Ann. Geophysicae, 14,* 1134, 1996.

Shevyrev, N. N., G. N. Zastenker, J. Šafránková, Z. Němeček, M. Hayosh, and J. D. Richardson, Large and fast variations of parameters in the magnetosheath: 3. Amplitudes and transverse profiles of low and high frequency variations of the plasma and magnetic field, *Cosmic Research, 40,* 4, 335, 2002.

Shevyrev, N. N., G. N. Zastenker, M. N. Nozdrachev, Z. Němeček, J. Šafránková, and J. D. Richardson, High and low frequency large amplitude variations of plasma and magnetic field in the magnetosheath: radial profile and some features, *Advances in Space Research, 31/5,* 1389, 2003.

Shue, J.-A., J. K. Chao, H. C. Fu, C. T. Russell, P. Song, K. K. Khurana, and H. J. Singer, A new functional form to study the solar wind control of the magnetopause size and shape, *J. Geophys. Res., 102,* 9497, 1997.

Spreiter, J. R., A. L. Summers, and A. Y. Alksne., Hydromagnetic flow around the magnetosphere, *Planet. Space Sci*., *14*, 223, 1966.

Zastenker G. N., A. O. Fedorov, Yu. V. Sharko, K. A. Moldosanov, P. A Dalin, I. P. Kirpichev, L. S. Kim, and M. A. Samsonov, Peculiarities of usage of integral Faraday cups aboard the INTERBALL-1 satellite: Reduction of photocurrent and determination of incoming angles and velocities of ion flux in the solar wind and the magnetosheath, *Cosmic Research, 38*, 1, 20, 2000.

AURORAL PHENOMENA AND SOLAR-TERRESTRIAL RELATIONS
PROCEEDINGS OF THE CONFERENCE IN MEMORY OF YURI GALPERIN, 3-7 FEBRUARY 2003

# Electric currents in the solar wind – magnetosphere interacted system

A. A. Samsonov and M. I. Pudovkin

St. Petersburg State University, St. Petersburg, Russia

**Abstract.** Using results of the 3-D MHD modeling, the electric currents in the magnetosheath are calculated in the case of northward and southward IMF. The magnetosheath current concentrated mainly in the magnetic barrier is as large as the current at the bow shock and comparable with the magnetopause current for the southward IMF. There is a radial component of the magnetosheath current, therefore most part of this current reaches the magnetopause in the dayside region. Our estimations of the absolute values of the magnetosheath, bow shock and magnetopause currents are in the range of $10^6 - 10^7$ A.

## 1. Introduction

Interaction between the supersonic solar wind and the Earth's magnetosphere may be described using the MHD theory as the interaction between a supersonic flow with embedded magnetic field and an impenetrable or partly penetrable obstacle. This problem is generally three-dimensional (3-D) and can be solved only numerically. The first hydrodynamic (without magnetic field in the solar wind) solution of the problem was obtained in 60-ties of the last century by J. Spreiter and his colleagues [*Spreiter and Jones*, 1963; *Spreiter et al.*, 1966]. Later, a number of numerical isotropic and anisotropic MHD models have been developed which describe plasma flow both locally in the dayside magnetosheath (for example, [*Pudovkin et al.*, 1982; *Wu*, 1992; *Erkaev et al.*, 1999; *Samsonov and Pudovkin*, 2000]) and globally taking into account the inner magnetosphere and even the ionosphere (for example, [*Watanabe and Sato*, 1990; *Walker et al.*, 1993; *Janhunen*, 1996]).

Most of the numerical models noted above were devoted to the behavior of the MHD parameters, such as the density, the magnetic field or the bulk velocity. At the same time, they pay a little attention to configuration of the electric currents, which play an important role in the diversion of the solar wind flow near the magnetospheric obstacle. *Hannes Alfvén* [1981] presented a detailed description of the electric current system connected with the solar wind – magnetosphere interaction. He was the first who noted that the bow shock must be a current layer as well as the magnetopause. But his description is qualitative and, in our opinion, does not answer all questions arisen after careful consideration. Particularly, the assumption that the bow shock current closes on the dayside magnetopause (*Alfvén* [1981], chapter III) is not obvious.

Recently *Pudovkin et al.* [2002] noted an important role of the electric current flowing in the magnetic barrier (i.e. in the inner part of the dayside magnetosheath) in the case of a southward IMF. In their opinion, the magnetic barrier current may explain the depression of the magnetospheric magnetic field and an Earthward motion of the magnetopause during the periods of southward IMF.

In this paper, the configuration of the electric currents is shown which is formed in a steady-state numerical solution using the 3-D MHD model of the Earth's magnetosheath. For any stationary flow the electric current can be calculated easily as

$$\vec{j} = \frac{c}{4\pi}\left[\nabla \times \vec{B}\right]. \qquad (1)$$

The numerical model includes both the magnetosheath and the bow shock, but is limited in the dayside region. Using different boundary conditions on the magnetospheric obstacle, we determine the magnetosheath flow for northward and southward IMF.

We don't pretend in this brief paper to answer many questions about configuration of the magnetospheric currents, the purpose of the work is to show only relative importance of the magnetosheath currents in the whole current system.

## 2. Numerical model

The isotropic MHD equations were used in the

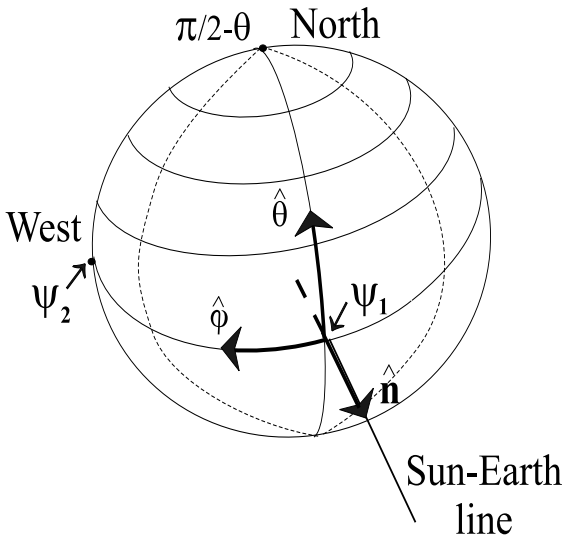


**Figure 1.** The sketch shows coordinate axes used in the numerical solution. Angles $\theta$ are measured from the equatorial plane, angles $\varphi$ are measured from the noon-meridional plane (i.e. the same spherical coordinates as the latitude and the longitude on the Earth's surface); $\psi_1$ is measured from the subsolar point, and $\psi_2$ is measured from the point with the longitude of 90° on the equatorial plane.

conservative form (see *Samsonov and Hubert* [2002]). We solve numerically the following 3-D problem using the spherical coordinates: on the outer boundary we fix boundary conditions in the supersonic solar wind, the inner boundary is an impenetrable or partly penetrable hemisphere. The solar wind conditions are determined by $M_c$ = 6.95 and $M_A$ = 8.13, the velocity is directed along the X (GSM) axis, and the IMF vector is perpendicular to the velocity. The inner boundary conditions differ for the northward and southward IMF. For a strictly northward IMF, we use the following conditions for normal components: $V_n = 0$ and $B_n = 0$; for a strictly southward IMF: $V_n = 0.15\ V_A \cos\psi_1$ and $B_n = 0.15\ B_\theta \sin\psi_2$. Here, $V_A$ is the Alfven velocity and $B_\theta$ is a corresponding component of the magnetic field in the magnetosheath close to the inner boundary (see Figure 1 for explanation of the coordinate axes $\theta$ and $\varphi$). The angles $\psi_1$ and $\psi_2$ are measured from the subsolar point (i.e. the point with $\theta$ = 0° and $\varphi$ = 0°) and from the intersection of the Y (GSM) axis with the inner sphere (i.e. $\theta = 0°$, $\varphi = 90°$), respectively.

### 3. Results and discussion

Figure 2 shows projections of the electric currents on the equatorial plane for the northward and southward IMF. There are two current systems in the calculated region: more stronger and localized system corresponds to the bow shock, and the one more extended in radial direction corresponds to the magnetic barrier near the obstacle. Inside every system the current flows in the same direction: in the eastward direction for the northward IMF, and in the westward direction for the southward IMF. There is a radial component of the electric current, which becomes bigger in the magnetic barrier at some distance from the subsolar point. Thus the bow shock and magnetosheath electric currents close on the magnetopause or somewhere inside the magnetosphere. The model is rather limited and does not include the magnetopause into consideration, but the direction of the magnetopause current is known and values of the current can be estimated using the calculated magnetosheath parameters and the pressure balance equation on the magnetopause.

Using the obtained numerical results, we calculate the total current in the radial direction near the obstacle (through the hemisphere) and the total azimuthal current $I_\varphi$ across the noon-meridianal plane which includes currents at the bow shock and in the magnetosheath. It was found that the radial current is about 70-80% of the azimuthal current, while the absolute value of the azimuthal current is around $3.5*10^6$ A for the northward IMF, and around $2.3*10^6$ A for the southward IMF. The total current for the northward IMF is bigger than for the southward IMF, because the magnetic barrier is found in this simulation to be stronger for the northward IMF. We separate the magnetosheath and bow shock currents and find that the total current inside the magnetosheath (concentrated mainly in the magnetic barrier) equals $2.2*10^6$ A for the northward IMF and $0.9*10^6$ A for the southward IMF. Of course, these estimations are approximate, because the geometry of the numerical field is simpler than the real magnetosheath-magnetopause geometry, and our simulation is limited in the dayside region.

The magnetopause current can be estimated using the numerical results obtained for the magnetosheath. We take the pressure balance condition on the magnetopause in the following form:

$$(P_d + P_g + B^2/8\pi)_{msh} = (B^2/8\pi)_{msp},$$

where on the left side there are the normal dynamic pressure, the gas thermal pressure, and the magnetic pressure in the magnetosheath, and on the right side there is the magnetospheric magnetic pressure. Knowing all parameters in the magnetosheath, we calculate easily the magnetospheric magnetic field near the magnetopause. Then, if we know the magnetic fields both inside and outside the magnetopause, we can estimate the magnetopause current for the southward IMF. It was found that the total magnetopause current (in

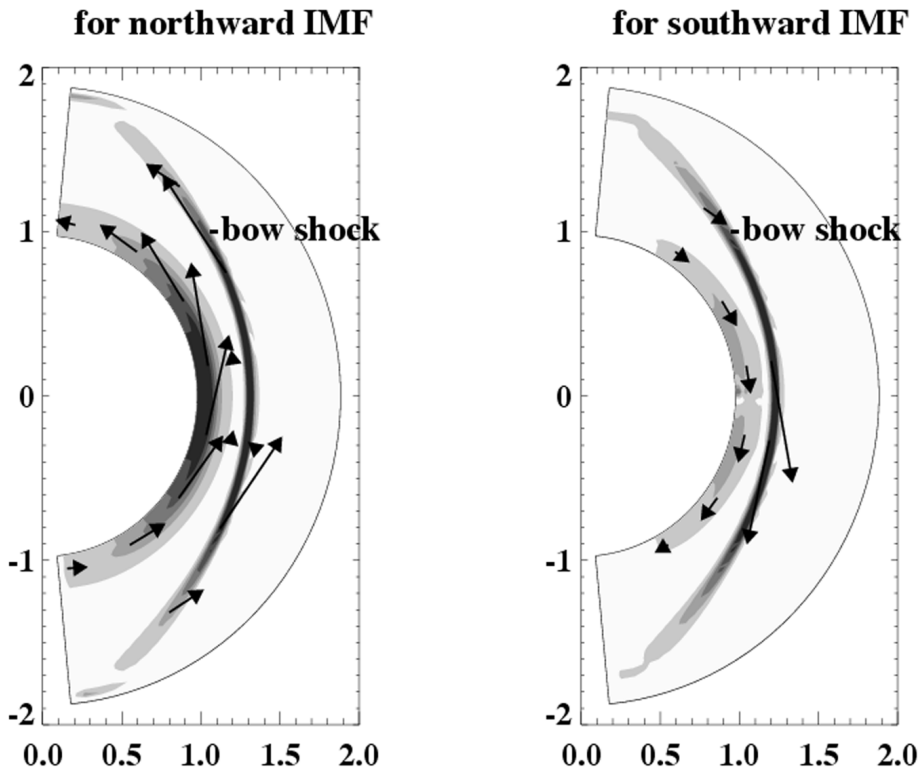


**Figure 2.** Electric currents in projection on the equatorial plane for the northward and southward IMF. Arrows show direction of the current. There are two current regions: the magnetic barrier and the bow shock. In both regions the current flows in the same direction: namely, in the eastward direction for the northward IMF and in the westward direction for the southward IMF. The total current in the magnetic barrier is bigger for the northward IMF.

the dayside region) equals $9.1*10^6$ A, which is 4.0 times bigger than the total azimuthal current for the southward IMF (and 2.6 times bigger than the current for the northward IMF). Note that this estimation is made in the case of strictly southward IMF, while for the northward IMF with the same approach we obtain that the electric current at the magnetopause is very weak (a few percents of that for the southward IMF). In any intermediate case, value of the total current will be somewhere between these two extreme states.

## 4. Conclusions

Results of the 3-D MHD modeling show that the electric current in the magnetosheath is important as well as the current at the bow shock in the whole current system connected with the solar wind – magnetosphere interaction. The absolute values of the magnetosheath and bow shock currents are comparable with the value of the magnetopause current for the southward IMF. We estimate the azimuthal current in the magnetosheath equal to $2.2*10^6$ A for the northward IMF, and equal to $0.9*10^6$ A for the southward IMF. Most part of the magnetosheath and bow shock currents reaches the magnetopause in the dayside region because of the radial current component.

**Acknowledgements.** This work is supported by grant 03-05-64865 of the Russian Foundation of Basic Research.

## References

Alfvén, H., Cosmic Plasma, D. Reidel Publishing Company, Dordrecht, Holland, 1981.

Erkaev, N. V., C. J. Farrugia, and H. K. Biernat, Three-dimensional, one-fluid, ideal MHD model of magnetosheath flow with anisotropic pressure, *J. Geophys. Res.*, *104*, 6877, 1999.

Janhunen, P., GUMICS-3 – A global ionosphere-magnetosphere coupling simulation with high

ionospheric resolution, in Proc. Environmental Modelling for Space-Based Applications, Sept 18-20, 1996 (ESTEC, The Netherlands, ESA SP-392, 1996).

Pudovkin, M. I., M. F. Heyn, and V. V. Lebedeva, Magnetosheath's parameters and their dependence on intensity and direction of the solar wind magnetic field, *J. Geophys. Res.*, *87*, 8131, 1982.

Pudovkin, M. I., S. A. Zaitseva, B. P. Besser, Magnetosheath current system and the magnetopause erosion, in Proc. of the 4th International conference Problems of Geocosmos, June 03-08, 2002 (St. Petersburg State University, 2002).

Samsonov, A. A., M. I. Pudovkin, Application of the bounded anisotropy model for the dayside magnetosheath, *J. Geophys. Res.*, *105*, 12859, 2000.

Samsonov, A. A., D. Hubert, Temporal variations in the magnetosheath: Comparison between MHD calculations and observations for one event on September 17, 1978, *Planet. Space Sci., 50,* 619, 2002.

Spreiter, J. R., W. P. Jones, On the effect of a week interplanetary magnetic field on the interaction between the solar wind and the geomagnetic field, *J. Geophys. Res.*, *68*, 3555, 1963.

Spreiter, J. R., A. L. Summers, and A. Y. Alksne, Hydrodynamic flow around the magnetosphere, *Planet. Space Sci.*, *14*, 223, 1966.

Walker, R. J., T. Ogino, J. Raeder, M. Ashour-Abdalla, A global MHD simulation of the magnetosphere when the interplanetary magnetic field is southward: the onset of magnetotail reconnection, *J. Geophys. Res.*, *98*, 17235, 1993.

Watanabe, K., T. Sato, Global simulation of the solar wind - magnetosphere interaction - The importance of its numerical validity, *J. Geophys. Res.*, *95*, 75, 1990.

Wu, C. C., MHD flow past an obstacle: Large scale flow in the magnetosheath, *Geophys. Res. Lett.*, *19*, 87, 1992.

---

A. A. Samsonov and M. I. Pudovkin, Institute of Physics, St. Petersburg State University, St. Petersburg Petrodvorets, 198504, Russia.

e-mail: samsonov@geo.phys.spbu.ru

# On the possibility of the heliospheric electric current penetration into the magnetosphere

I. S. Veselovsky

Institute of Nuclear Physics, Moscow State University, 119992, Moscow, Russia,
E-mail: veselov@dec1.sinp.msu.ru

**Abstract.** The planetary magnetospheres can intercept electric currents flowing in the heliosphere. The strongest heliospheric currents – electrojets are sufficient to produce appreciable geomagnetic perturbations in this way. Corresponding estimates are presented.

## 1. Introduction

It is well known that the geomagnetic activity is related to the solar wind and heliospheric magnetic field perturbations. Favourable heliospheric conditions are usually accompanied by strong magnetic fields and southward directions of the interplanetary magnetic field and high solar wind speeds. This leads to the increased East-West electric field penetration into the magnetosphere. As a result, electric currents increase in the geomagnetic tail, at magnetospheric boundaries, in the partial ring current. Plasma drifts and particle acceleration inside the magnetosphere are also enhanced. The geomagnetic storm ring current appears. In the current magnetospheric models it is often assumed implicitly that all important electric currents are closed inside the magnetosphere and/or on its boundaries with no external or linking currents within magnetospheric surroundings allowed (see e.g. [*Ohtani et al*., 2000] for a general review and the paper [*Siscoe et al*., 2000] for the global MHD simulation results). In reality this assumption is too restrictive [*Veselovsky et al*., 2002].

The purpose of this paper is to indicate the possibility of the heliospheric electric current penetration into the magnetosphere and to demonstrate the importance of this phenomenon for the better understanding of the origins of magnetospheric perturbations.

## 2. Electromagnetic coupling between the magnetosphere and the heliosphere

The magnetosphere is considered as an open physical system with the energy, momentum, and mass flows through it. The solar wind plasma and energetic particles partially penetrate inside the magnetospheric obstacle. External electric and magnetic fields are also strongly, but not totally, screened from the penetration. It is equally true both for quasi-stationary and wave fields. Electric currents provide an appreciable part of heliospheric perturbations and also could penetrate the magnetosphere bringing their free magnetic energy for the reversible and irreversible transformations there. The opposite processes of the feeding of the near-Earth heliosphere by the magnetospheric particles, currents, waves etc. are well known especially in the upstream regions and in the magnetospheric wake.

It is reasonable to expect that this coupling between the magnetosphere and the heliosphere via electric currents is especially important and effective during magnetic storms. Geometry conditions and electric conductivity distributions regulate this penetration process. The difficulty with its evaluation consists of the non-local character of electrodynamic and plasma processes leading to the formation of effective electric circuits in the heliosphere and the magnetosphere. Dissipative MHD and plasma kinetic equations describe these phenomena, but global problems are far from being completely solved or even correctly formulated in the qualitative manner, let alone the quantitative aspects. Because of this, the reasonable approximations for the analytical description are not easy to indicate and our knowledge is limited.

The non-local electric conductivity of the magnetosphere is inhomogeneous and anisotropic. The plasma is nearly collisionless everywhere in the solar wind and in the magnetosphere excluding the ionosphere. The plasma sheet region in the geomagnetic tail has the highest effective conductivity because plasma is denser and hotter here. Concentrated electric currents flow here inside the current sheet. The current sheet is a complicated three-dimensional structure truncated near the Earth and extending in the night side. The maximal current densities about several $pA/cm^2$ are typically attained at distances of the order of several Earth's radii. The radial distribution of the currents in the

current sheet is not monotonous and often looks complicated and perturbed. The current sheet and the ring current are morphological features mutually related in the magnetosphere, and if they are considered separately, this could lead to confusions in many ways, especially in perturbed states. In simplistic magnetospheric models they are introduced empirically as separate entities. Tail currents are traditionally assumed to be closed by Chapman-Ferraro currents on the magnetospheric boundaries and field aligned currents through the ionosphere. No electric currents are usually assumed linking the magnetosphere and the heliosphere in the known quantitative magnetospheric models

Contrary to this assumption, we consider in this paper the possibility of such coupling between the heliosphere and the magnetosphere. External currents, if they are given, can penetrate and will be concentrated mainly in the regions with the maximal conductivity as usually in parallel chains. To evaluate orders of magnitude of linking electric currents we need estimates of the heliospheric electric current densities.

### 3. Heliosperic electrojets

Electric currents in the heliosphere are not measured directly because of their low densities, but only conjectured from magnetic fields produced by them according to the equation

$$\left[\nabla \times \vec{B}\right] = \frac{4\pi}{c}\vec{j} - \frac{1}{c}\frac{\partial \vec{E}}{\partial t}.$$

The continuity equation

$$\frac{\partial \rho}{\partial t} + div\ \vec{j} = 0$$

holds because of the Coulomb condition

$$\nabla \cdot \vec{E} = 4\pi\rho.$$

The correctness of the assumption $\vec{D} = \vec{E}$; $\vec{H} = \vec{B}$; $\mu = 1,\ \varepsilon = 1$ needs careful examination. Here we used the standard electrodynamic notations [*Landau et al*., 2001].

In the quasistationary approximation, one neglects displacement currents associated with the electric charge density variations. This approximation has very limited validity in heliospheric and magnetospheric applications and will be used only for illustrative purposes. It is clear, that quasistationary approximation is not sufficient especially under perturbed conditions of magnetospheric substorms.

The electric current strength of the heliospheric electrojets associated with magnetic flux ropes during coronal mass ejection passages near the Earth can be estimated as follows. For the typical interplanetary magnetic field perturbation of interest with a duration of several hours and magnetic field perturbation amplitude *B* of the order of 10 nT at the Earth's orbit one obtains electric currents I of the order of 1*GA*. This estimate follows from the relation for the linear current

$$I = \frac{1}{2}Brc\ .$$

Here we assume $B$ ~ 10 nT, $r$ ~ Vt ~ 0,1 A.U., $c$ – light speed, $V$ ~ 400 km/s – solar wind speed.

The corresponding electric current density is equal to

$$j = \frac{I}{\pi r^2} \sim 0.3\, fA/cm^2.$$

Remember that $1 fA = 10^{-15}\ A$. We assume here the simplest cylindrical geometry of the tube with the radius $r$ for the heliospheric electrojet. The real geometry, the orientation, the intensity and other parameters of heliospheric electrojets are statistically variable with some common characteristics measured by spacecraft. The current density in the heliospheric electrojets associated with interplanetary shock waves and discontinuities can be three-to-four orders of magnitude higher, but they pass very rapidly and cross the magnetosphere only during seconds or minutes. This time is too small for the quasi-stationary response of the magnetospheric current system to this interplanetary perturbation. The characteristic time of flight of the solar wind across the magnetospheric dimensions is only about several minutes. Because of this, only electrojets associated with coronal mass ejections and therefore larger magnetic flux ropes are of interest for the discussion of their quasi-stationary impact on the magnetospheric currents.

Heliospheric electrojets associated with coronal mass ejections and magnetic flux ropes associated with them radially expand as the distance from the Sun grows. In addition to this, they tend to form a spiral pattern due to the rotation of the Sun. As a result, transient conical spirals in the field line shape appear. The total estimated electric current in heliospheric electrojets is of the order of gigaampers at the Earth's orbit according to magnetic field measurements. This value is orders of magnitude less than currents in coronal cavities associated with erupting prominences and coronal mass ejections, which

could attain teraampers near the Sun. Hence, only a small part of coronal currents is still temporarily diverted into the interplanetary medium one-to-three days after the eruption. At these time scales, the total electric currents are essentially variable and not conserved due to the boundary condition changes on the Sun.

Erupting prominences are often seen as twisted structures, which obviously mean the increased field-aligned electric currents during the coronal mass ejection process [*Veselovsky*, 1999]. The overall geometry of electrojets in the submagnetosonic corona prior to the eruption is mostly determined by force-free configurations in the low beta case and by the pressure balanced equilibria in the gravity field: long horizontal channels and pinches appear. The heliospheric electrojets transported by the supersonic solar wind plasma flow change their shape mainly due to the kinematic effects.

## 4. Linking currents between the heliosphere and magnetosphere

Let us estimate the electric current strength, which can be intercepted by the magnetosphere from the heliosphere during the coronal mass ejection passage.

In the case of appropriate mutual orientations and geometry conditions in the heliospheric electrojets and the geomagnetic tail, the lateral surface cross section of the tail $S \sim Ld$, where $L$ – the effective length of the geomagnetic tail, $d$ – its diameter, the intercepted current can be of the order of

$$I_{hm} \sim j\,S \sim 1\,MA.$$

In this estimate we accept $d \sim 40R_e$, where $R_e$ is the Earth's radius, $L \sim Md \sim 300R_e$, $M \sim 8$ is the effective Mach number in the solar wind, $j \sim 0.3$ $\mu A/cm^2$ – electric current density in the heliospheric flux rope estimated earlier. The effective length of the geomagnetic tail is equal to the "shadow" length in the supermagnetosonic flow, which is nearly the same as the magnetospheric "cavity" extension in the MHD approximation. At distances $x > L$ in the down flow region the wave-type wake develops behind the magnetosphere.

The intercepted heliospheric electric current is redistributed inside the magnetosphere and flows mainly in boundary regions, current sheets and the sites with a high electrical conductivity. The calculation of current distributions in the magnetosphere is a difficult task because of its complicated structure, but the conditions in the night side are more favourable due to the presence of the geomagnetic tail and the plasma sheath. The electric currents closest to the Earth are more effective in producing geomagnetic perturbations on the ground. The linear current of $1MA$ at the distance $r \sim 7R_e$ produces the magnetic field about 5 nT. The geometry of the circuit is important in this respect: ring currents and even partial rings around the Earth produce more concentrated magnetic perturbations than linear currents of the same strength at the given minimal distance. For example, the magnetic fields in the centre of the ring will be a factor $\pi$ stronger than from the linear current at the same distance. The night side magnetosphere has larger cross section for the collecting the heliospheric currents and the more appropriate geometry for their penetration deep inside the magnetosphere through the plasma sheet in the geomagnetic tail.

The electric current densities in the perturbed magnetospheric conditions are locally orders of magnitude higher than in the heliospheric electrojets due to better conductivity. This explains why magnetospheric perturbations are stronger in absolute and relative values if compared to heliospheric magnetic fields.

An interesting question arises about the openness degree of the magnetospheric electric circuit, which is traditionally assumed to be closed in the existing models. Our knowledge is not sufficient to answer this question quantitatively at present time. Nevertheless, we can speculate, that heliospheric electrojets bring their free magnetic energy immediately inside the magnetosphere when producing strong geomagnetic perturbations. In this respect, this energy channel is important, but not well investigated. No doubts that electrodynamic and plasma processes are tightly related both in the magnetosphere and the heliosphere. The region in the geomagnetic tail at distances around the inner edge of its current sheet is especially interesting in this respect as the place of the possible strongest current densities topologically connected to the heliosphere and the Sun.

## 5. Discussion

Heliospheric electric charges and currents are very important drivers of magnetospheric perturbations. They are non-locally connected to the Sun. The electromagnetic free energy sources outside the magnetosphere play their important roles in producing strong geomagnetic storms. This type of the energy more easily penetrates inside the magnetospheric obstacle in comparison to the more abundant kinetic energy of the solar wind which is mostly stopped and diverted by the plasma flow around the magnetosphere. Only the small part of the solar wind energy is available for the driving electric currents deep inside the magnetosphere. The magnetosphere is essentially open and connected by electric currents and electromagnetic fields to these free energy reservoirs. The free energy of electric currents in

the heliosphere is rather diluted, but can be collected, concentrated and focused in the magnetosphere due to its inhomogeneity. Heliospheric currents contribute their part to geomagnetic perturbations together with other free energy sources, but quantitative side needs further evaluations. The useful dimensionless parameters, the set of so called Trieste numbers, represents the measure of the openness degree of the magnetosphere against the energy, momentum and mass flows. In the same way, the ratio of internal (closed) electric currents to the linking (open) currents can be introduced for the magnetosphere [*Veselovsky*, 2001]. It seems quite possible, that this ratio is variable and depends on many external parameters characterising heliospheric conditions.

The magnetic storm development is associated with the solar wind and ionospheric plasma intrusion in the inner heliosphere accompanied by the acceleration and trapping of particles leading to the storm ring current formation around the Earth. This plasma process is very important. The heliospheric electric current collection by the magnetosphere also plays a role. We assume that the corresponding Trieste number characterising the ratio of closed and open currents in the magnetosphere during the first several hours of the storm initiation phase can be of the order of one or even open currents dominate. At the main phase and the recovery phase closed currents dominate and dissipate. Hence, two opposite regimes with small and large Trieste numbers are conceivable in the perturbed magnetosphere, but many important details need further investigations.

Based on these simple considerations we can interpret and better understand the well known fact that all big magnetic storms happen when the magnetic field in the near-Earth interplanetary medium is strong during several or many hours and directed to the South. The ideal geometry coupling of external heliospheric currents with the tail currents happens namely under this mutual orientation. Strong interplanetary magnetic fields mean strong heliospheric electrojets. It is remarkable that the solar wind plasma parameters could be not so extreme during big storms. This fact is also indicative of the important role of the direct electrodynamic coupling between the magnetosphere and the heliosphere via linking electric currents between them during geomagnetic storms. Strong geomagnetic storms seem to be driven not only by the strong electric currents totally closed inside the magnetosphere, which are usually assumed (the ring current, the geomagnetic tail current system, Chapman-Ferraro currects, Birkeland currents, etc.), but also by the electric currents connected immediately to the enhanced heliospheric electric currents during this time. In this sense, the geomagnetic storm can be considered as a direct consequence of the heliomagnetic storm.

The sensitivity of the CLUSTER measurements using 4 spacecraft is sufficient to observe and measure electric current densities of the order of several $pA/cm^2$. The values up to $5pA/cm^2$ were observed during short periods of time in association with the Flux Transfer Events at the magnetopause and up to $1pA/cm^2$ inside the inhomogeneous heliospheric current sheet (see e.g. Science Highlights in the ESA Report to the 34th COSPAR Meeting, ESA SP 1259, 2002, p. 40-41) These values are in a reasonable agreement with estimates presented in this paper. Currently there are quite promising perspectives for the experimental study of the openness degree of the magnetosphereand the electric currents linking it to the heliosphere under different conditions, using new CLUSTER data for this purpose.

## 6. Conclusions

The concept of linking electric currents between the magnetosphere and the heliosphere allows better qualitative understanding of the origins of the geomagnetic perturbations. Strong geomagnetic storm developments are initiated and essentially driven by strong heliomagnetic storms with only short time delays. The geomagnetic storm development depends on the heliospheric electrojet intensity and the orientation of its axis against the magnetosphere.

**Acknowledgements.** This work is partially supported by the INTAS–ESA grant 99-00727, INTAS grant 00-752, RFBR grants 01-02-16579 and 00-15-96623, State Program “Universities of Russia”, Federal Program “Astronomy”.

## References

Ohtani, S., R. Fujii, M. Hesse, and R. L. Lysak, (Eds), Magnetospheric Current Systems, AGU Geophysical Monograph Series 118, Washington, DC, 2000.

Siscoe, G. L., N. U. Crooker, G. M. Erickson, B. U. O. Sonnerup, K. D. Siebert, D. R. Weimer, W. W. White, and N. C. Maynard, Global Geometry of Magnetospheric Currents Inferred From MHD Simulations, in [1], pp.41-52, 2000.

Veselovsky, I. S., Proc. 10th European Solar Physics Meeting “Solar Variability: From Core to Outer Frontiers”, ESA SP-506, v.1, 37-41, 2002.

Landau, L. D. and E. M. Lifshits, Electrodynamics of Continuous Media, Moscow, Nauka, 2001 (in Russian).

Veselovsky, I. S., Proc. 9th European Meeting on Solar Physics “Magnetic Fields and Solar Processes”, ESA SP-448, 1217-1222, 1999.

Veselovsky, I. S., *Asrophys. and Space Sci., 234*, 219-224, 2001.

# The solar wind plasma density control of night-time auroral particle precipitation

V. G. Vorobjev, B. V. Rezhenov[1], and O. I. Yagodkina

Polar Geophysical Institute, Russian Academy of Science, Apatity,
Murmansk region, 184200, Russia

**Abstract.** DMSP F6 and F7 spacecraft observations of the average electron and ion energy and energy fluxes in different night-time precipitation regions for the whole of 1986 were used to examine the precipitation features associated with solar wind density changes. It was found that during magnetic quietness (|AL|<100 nT) the enhancement of the average ion fluxes by at least two times was observed along with the solar wind plasma density increase from 2 to 24 $cm^{-3}$. A more pronounced ion flux enhancement occurred in *b2i-b4s* and *b4s-b5* regions, which approximately correspondto the statistical auroral oval and map to magnetospheric plasma sheet tailward from the isotropy boundary. The average ion energy decrease of about 2-4 keV was registered simultaneously with this ion flux enhancement. Results testify for the effective penetration of the solar wind plasma into the magnetospheric tail plasma sheet.

## 1. Introduction

Solar wind particle penetration in the Earth's magnetosphere is one of the major problems in physics of the magnetosphere. About $10^{25}$–$10^{26}$ $part \cdot s^{-1}$ are required to support the observed particle concentration in the plasma sheet [*Hill*, 1974]. However, there is not enough experimental data about particle penetration into the magnetosphere, and the main unknown thing is either the physical mechanism responsible for this plasma transport or a place of particle penetration. It is usually assumed that during the southward interplanetary magnetic field, solar wind plasma penetrates into the magnetosphere via the magnetic reconnection of the southward interplanetary and geomagnetic field. During periods of the northward IMF a slow diffusive transport of solar wind particles into the plasma sheet is supposed.

A number of studies [*Fairfield et al.*, 1981; *Lennartsson and Shelley*, 1986; *Baumjohann et al*., 1989; *Lennartsson*, 1992] indicated that under geomagnetic quietness the plasma sheet becomes colder and denser. *Terasawa et al*. [1997] carried out a statistical study of the near Earth plasma sheet ($-15R_e > X_{GSM} > -50R_e$) properties depending on solar wind parameters. It was found out that

(1) during the northward IMF the plasma sheet becomes significantly colder and denser with the solar wind plasma density increase;

(2) temperatures diminish and densities increase more significantly near the dawn and dusk flanks of the plasma sheet than in the central region.

They suggested that the solar wind plasma penetrates into the plasma sheet across magnetospheric flanks as a result of a slow diffusion.

This paper presents the results of the statistical investigation of the relationship between the solar wind plasma density and properties (average energy and fluxes) of particles precipitating in the night-time high latitudes under quiet geomagnetic condition.

## 2. Data used and results of observations

Characteristics of precipitating ions and electrons in different auroral precipitation regions acquired by polar orbiting DMSP F6 and F7 satellites in the night sector for the whole of 1986 are examined. The notation of precipitation boundaries suggested by *Newell et al.* [1996] is used for the investigation. The average energy and the number flux of particles between the adjacent precipitation boundaries in three magnetic local time sectors (03 – 06, 18 – 21 and 21 – 24 MLT) were determined. The 00-03 MLT sector was not investigated because of insufficient statistics owing to the orbit peculiarity of DMSP F6 and F7 satellites. The average energy and the number flux of precipitating particles were calculated within $\Delta n_{sw}$=2 $cm^{-3}$ solar wind density bins. Only satellite passes, when the one hour averaged

value of the AL index at the hour of auroral zone crossing and during the previous hour were |AL|<100nT, have been selected for the analysis. The IMF and solar wind plasma data from the NSSDC OMNIWeb database in the hours of the satellite pass were used for comparison with precipitation signatures. Data sets were examined separately for the IMF $B_z > 0$ and $B_z < 0$ intervals. More than 3700 passages were analyzed in all.

Figure 1 presents the number flux of precipitating ions in different regions versus solar wind density in the morning, pre-midnight and evening MLT sectors during periods of northward (a) and southward (b) IMF orientation. The vertical error bars representing standard deviation from the mean are also provided. In order not to overload the figure, these errors are shown, where it

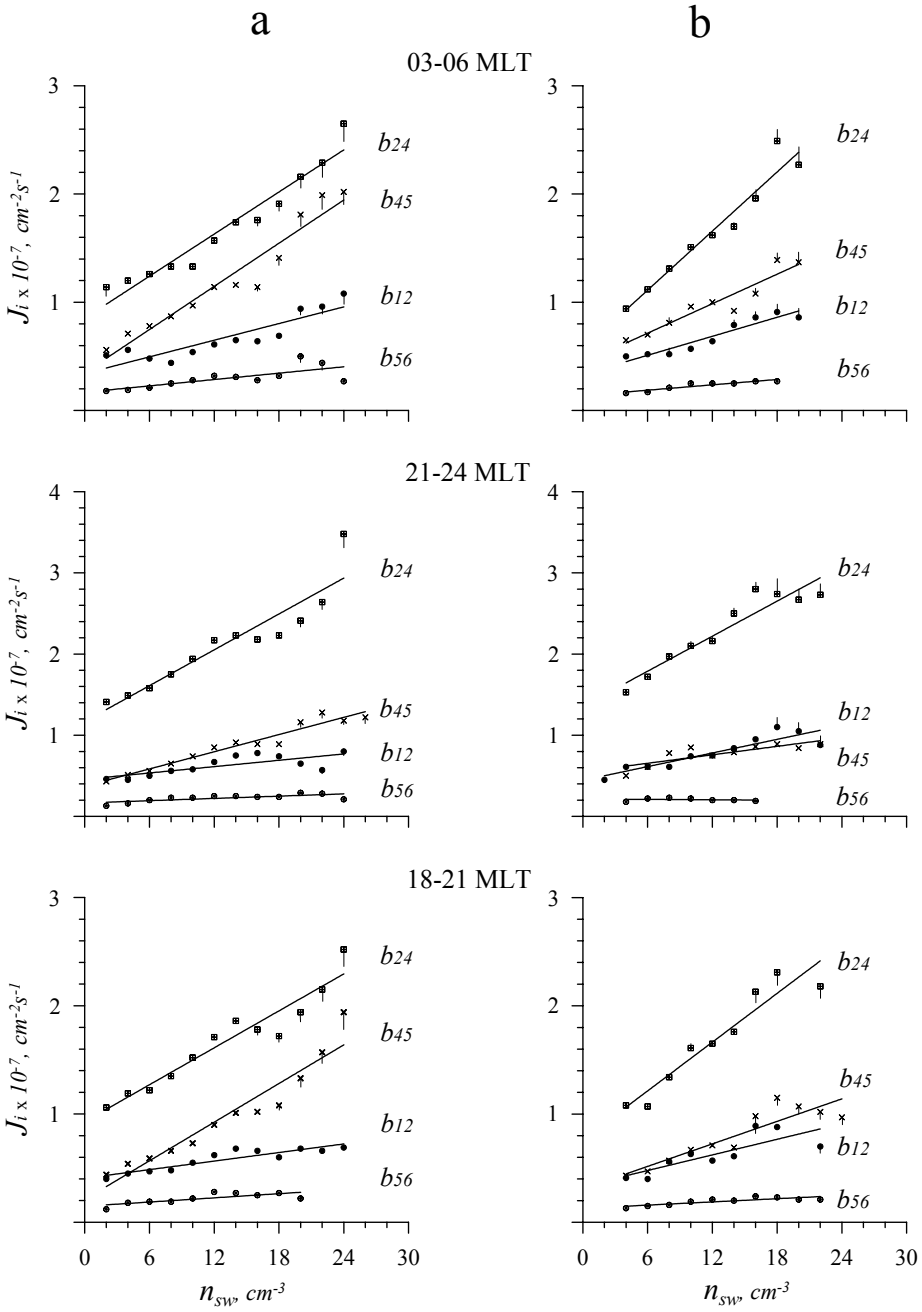


**Figure 1.** Ion number flux in four precipitation regions (*b1-b2i*, *b2i-b4s*, *b4s-b5* and *b5-b6*) versus solar wind plasma density in the morning, pre-midnight and evening MLT sectors during periods of northward (a) and southward (b) IMF orientation.

is possible, as half of deviation to either side. The average AL index value in all data sets was about 35 nT, and the average IMF $B_z$ component was equal to 2.3 nT and −1.2 nT for the northward and southward IMF orientation correspondingly. During IMF $B_z > 0$ Figure 1*a* clearly shows the enhancement of ion fluxes ($J_i$, $cm^{-2} \cdot s^{-1}$) in all night-time MLT sectors along with the increase in the solar wind plasma density ($n_{sw}$, $cm^{-3}$). Solid lines represent linear approximation of experimental points. Correlation coefficients, *r*, for all data sets are not less than 0.8. The most pronounced enhancements of the ion flux are observed in *b2i-b4s* and *b4s-b5* regions. In the *b2i-b4s* region the morning sector dependence is approximated by the formula:

$$J_{(2\text{-}4)} = (0.065\ n_{sw}+0.85)\ 10^7 \qquad r = 0.94$$

and in the *b4s-b5* region by expression:

$$J_{(4\text{-}5)} = (0.062\ n_{sw}+0.43)\ 10^7 \qquad r = 0.95.$$

In the pre-midnight and evening sectors respectively the similar expressions are as follows:

$$J_{(2\text{-}4)} = (0.074\ n_{sw}+1.17)\ 10^7 \qquad r = 0.86,$$

$$J_{(4\text{-}5)} = (0.038\ n_{sw}+0.38)\ 10^7 \qquad r = 0.97$$

and

$$J_{(2\text{-}4)} = (0.057\ n_{sw}+0.93)\ 10^7 \qquad r = 0.92,$$

$$J_{(4\text{-}5)} = (0.055\ n_{sw}+0.25)\ 10^7 \qquad r = 0.93.$$

The ion flux enhancement in the *b4s–b5* region looks more pronounced in the morning and in the evening in comparison with the pre-midnight sector. In *b1–b2i* and *b5–b6* regions dependence $J_i$ from $n_{sw}$ is expressed poorly enough in all considered MLT sectors. During the IMF $B_z<0$ (Figure 1*b*) the most essential enhancements of the ion flux are observed in the *b2i-b4s* region. The flux enhancement in the *b4s-b5* region during $B_z<0$ does not look as significant as during $B_z>0$.

Only a weak tendency of the electron flux to be increased is observed along with the increase of the solar wind plasma density.

Average ion energies in the *b2i-b4s* and *b4s-b5* regions during northward IMF periods versus solar wind density are shown in Figure 2*a*. As it is seen from Figures 1*a* and 2*a*, simultaneously with the number flux enhancement, the average precipitating ion energy in all MLT sectors decreases approximately by 2–4 keV when the solar wind plasma density increases from 2 $cm^{-3}$ to 24 $cm^{-3}$. The average energy of precipitating electrons in these regions (Figure 2*b*) undergoes the essential decrease as well.

## 3. Summary and discussion

The obtained results assume that the cold solar wind plasma effectively penetrates the plasma sheet region which maps along geomagnetic field lines in the *b2i-b4s* night-time precipitation region both during northward and southward IMF periods. In the distant plasma sheet, which maps in the *b4s-b5* region the solar wind plasma comes across the morning and evening flanks of the magnetosphere. We note that during IMF $B_z<0$, i.e. when the magnetic reconnection is in progress, the enhancement of precipitating ion fluxes are about the same as during the period of the IMF $B_z>0$.

The *b2i-b4s* region is placed between *b2i* and *b4s* boundaries, which in the notation of [*Newell et al*., 1996] are determined as follows: *b2i* is the point where the energy flux of ions has a maximum. The latitude of the *b2i* boundary coincides well with the position of isotropy boundary [*Newell et al*., 1998] and is a good proxy for the inner edge of the magnetospheric cross tail current sheet. The *b2i* and *b5* boundaries approximately coincide with the equatorward and poleward boundaries of the average auroral oval [*Vorobjev et al*., 2000]. In the new notation presented by *Starkov et al*. [2002] the *b2-b5* region was designated as the auroral oval precipitation, *AOP*. Spatially and spectrally structured electron spectra, which can be associated with discrete aurorae, are common for the *AOP* region in all MLT sectors. Thus the *b2i-b4s* region approximately corresponds to the equatorial part of the auroral oval and a *b4s-b5* region to its poleward part.

The *b1-b2* region named by *Starkov et al*., [2002] the diffuse auroral zone, *DAZ*, coincides well with the diffuse auroral luminosity equatorward of the auroral oval precipitation. To the pole of the *AOP*, between *b5* and *b6* boundaries, there is a soft diffuse precipitation region, *SDP*, which is associated with a weak diffuse luminosity (generally in the 630.0 nm emission) poleward of the auroral oval. The relative position of different precipitation boundaries during the magnetic periods and their dynamics during the substorm development are presented by *Vorobjev et al*., [2003]. The latitudinal width of the *AOP* region during the period of magnetic quietness is 3°–4°, and its equatorial part, *b2i-b4s*, is only about 1° of the latitude.

The pronounced decrease in the average electron energy observed with the increase of solar wind plasma density should lead to significant changes in the auroral luminosity inside the auroral oval. Figure 3*a* shows the behavior of electron energy fluxes (*JE,* $erg\ cm^{-2}\ s^{-1}$) in both *b2i-b4s* and *b4s-b5* pre-midnight regions during northward IMF periods versus solar wind plasma density. Since the electron number flux does not actually depend on the solar wind plasma density, the shape of curves in Figure 3*a* are defined mainly by changes in the electron

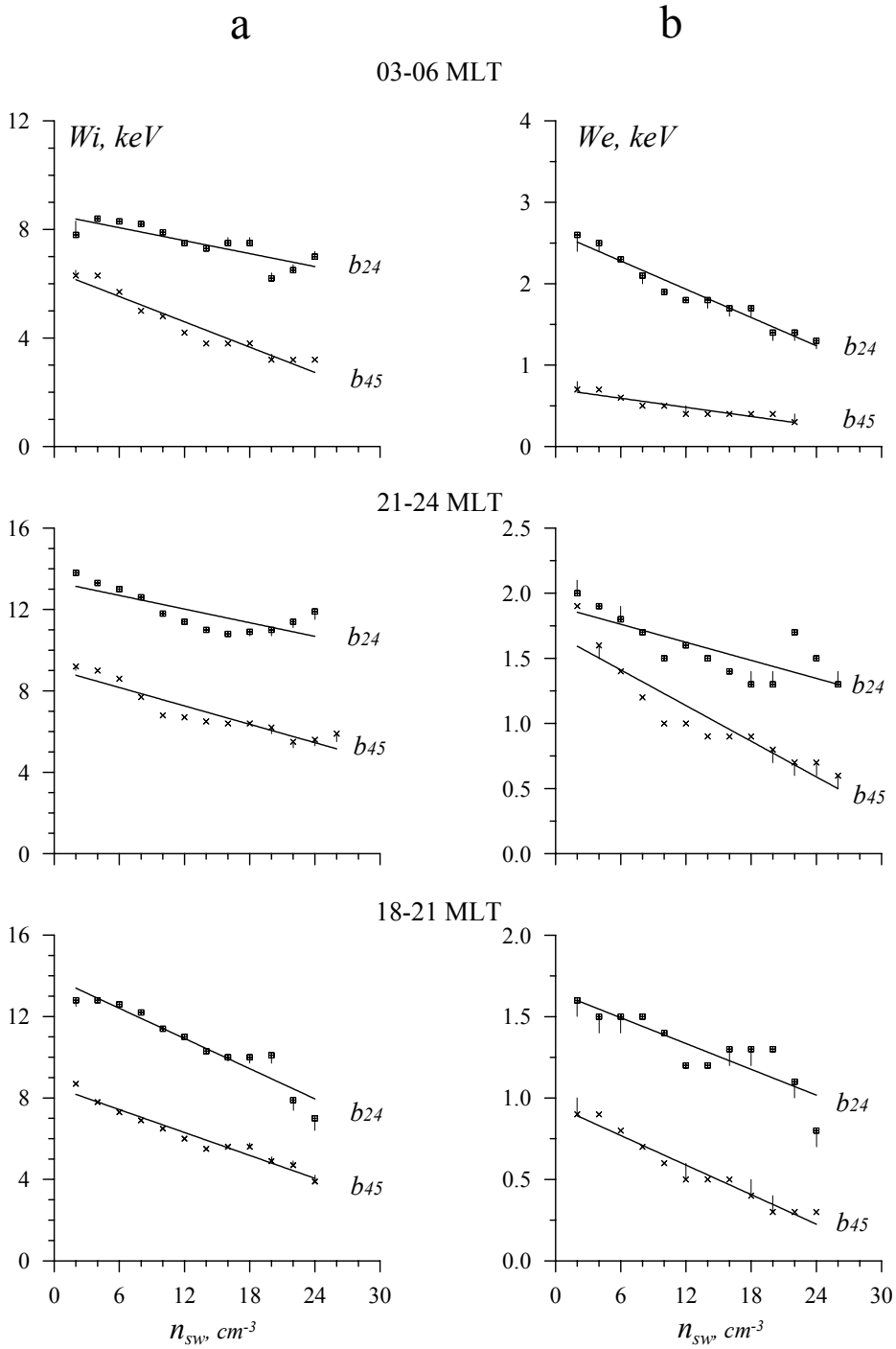


**Figure 2.** Average ion (a) and electron (b) energy in the *b2i-b4s* and *b4s-b5* regions during periods of the IMF $B_z>0$ versus solar wind plasma density.

average energy. As it can be seen from the figure, the most essential changes in the energy flux are observed in the *b4s-b5* region making the basic part of the average auroral oval.

Intensity of several auroral emissions is approximately proportional to the precipitating electron energy flux. Figure 3*b* illustrates the expected changes of the 391.4 nm 1NG $N_2^+$ band intensity in *b2i–b4s* and

*b4s–b5* zones during the solar wind density increase. For the conversion of precipitating electron energy flux in intensity of the 391.4 nm auroral emission it was accepted according to *Dalgarno et al*. [1965] that the flux of 1 *erg* $cm^{-2}$ $s^{-1}$ causes about 730 Rayleighs (R) of luminosity.

In Figure 3*c* the corresponding changes in the Lyman-Birge-Hopfield band intensity at about 170.0 nm (LBH-long) are shown, which could be registered by UVI Imager [*Torr et al*., 1995] onboard the Polar satellite.

The conversion of *ergs* $cm^{-2}$ $s^{-1}$ to Rayleighs for LBH-long band has been modeled by *Germany et al.* [1997] and is given as 1 *erg* $cm^{-2}$ $s^{-1}$ ≈ 110 *R*. Figures 3*b* and 3*c* show that the intensity of both auroral bands in the *b4s–b5* region, which make the basic part of the nightside auroral oval, decreased 3–4 times in the solar wind density increase from 2 to 26 $cm^{-3}$.

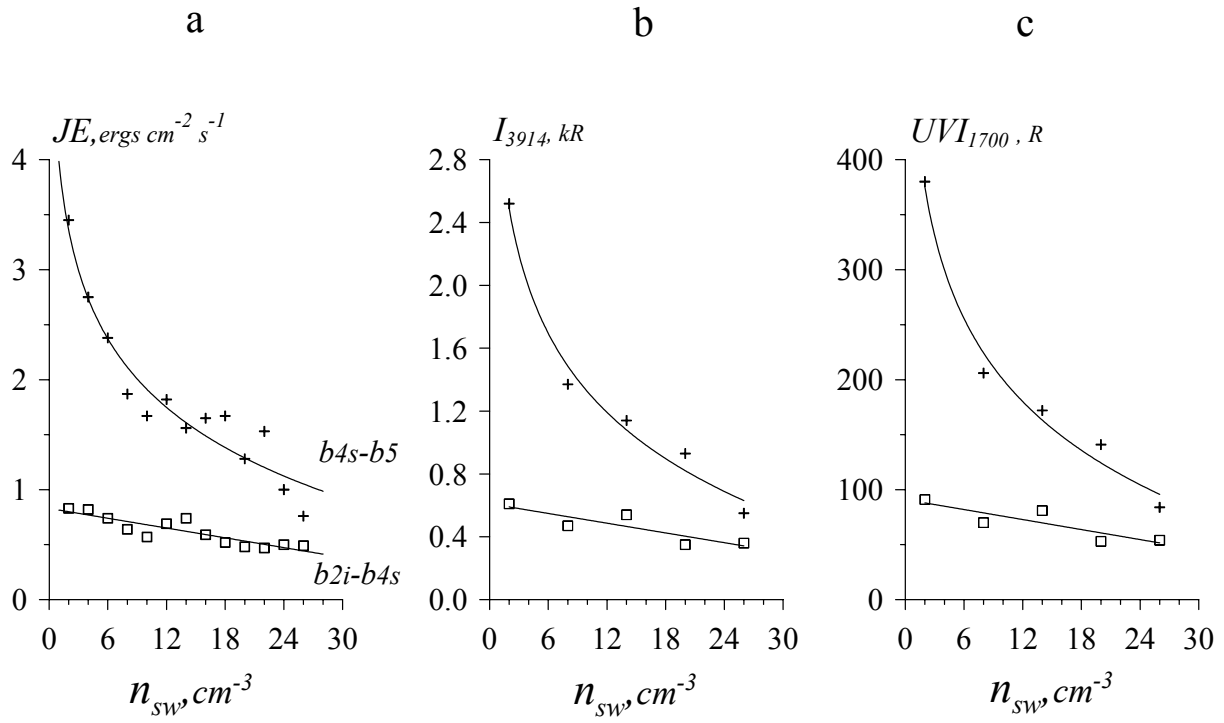


**Figure 3.** Changes of the electron energy flux (a), the intensity of 391.4 nm (b) and LBH-long (c) bands in *b2i–b4s* and *b4s–b5* regions in the pre midnight sector during periods of the IMF $B_z > 0$ depending on the solar wind plasma density.

The intensity of [OI] 557.7 nm and 630.0 nm auroral emissions is substantially determined by the chemical composition of the upper atmosphere which makes it extremely difficult to calculate their intensity. However, the average electron energy behavior allows one to roughly estimate the change of auroral intensity $I_{6300}/I_{5577}$ ratio. According to *Judge* [1972] model simultaneously with the solar wind plasma density increases it is possible to expect the enhancement of this ratio approximately from 0.5 up to 2, which corresponds to the occurrence of red aurorae of rather significant intensity.

These conclusions allow one to explain the results received earlier by *Liou et al*. [1998] and *Hviusova and Leontyev* [2002]. *Liou et al*. [1998] used the Polar UVI images at the LBH-long band for a correlative study of the energy deposition rate with the concurrent solar wind plasma and IMF observations. It was shown (their Figure 5*e*), that the midnight aurora had a trend of decreasing in power with the solar wind density increase.

*Hviuzova and Leontyev* [2002] have found out that during the magnetic quietness large (≥ 5 kR) intensities of the red oxygen emission (630.0 nm) were observed in the night-time aurorae generally during periods of the increased value ($n_{sw} > 10$ $cm^{-3}$) of solar wind plasma density. According to the results of our investigation the average electron energy in the auroral oval decreases essentially with the solar wind plasma density enhancement. It should lead to the decrease of the auroral luminosity in the UVI region as well as in the main 391.4 nm, 427.8 nm and 557.7 nm auroral emissions simultaneously with the enhancement of the

630.0 nm luminosity, which is caused by lower energy electron precipitation, i.e. the green aurorae are replaced with the red one.

**Acknowledgements.** The DMSP particle detectors were designed by Dave Hardy of AFRL, and data obtained from JHU/APL. We thank Dave Hardy, Fred Rich, and Patrick Newell for its use. We thank Drs J.H. King and N. Papitashvili for providing IMF and solar wind plasma observations in the NSSDC OMNIWeb database. The WDC for geomagnetism in Kioto provided magnetic activity indexes. The paper was supported by the RFBR grants 02-05-64807 and 99-05-65611, INTAS-2000-752. Authors acknowledge the support from the Division of Physical Sciences of the Russian Academy of Sciences (program DPS-16).

## References

Baumjohann, W., G. Paschmann and C. A. Cattell, Average plasma properties in the central plasma sheet, *J. Geophys. Res., 94*, 6597-6606, 1989.

Dalgarno, A., L. D. Latimer, J. W. McConkey, Corpuscular bombardment and $N_2^+$ radiation, *Planet. Space Sci., 13*, 1008, 1965.

Fairfield, D. H. *et al*., Simultaneous measurements of magnetotail dynamics by IMP spacecraft, *J. Geophys. Res., 86*, 1396-1414, 1981.

Hill, T. W., Origin of the plasma sheet, *Rev. Geophys. Space Sci., 12*, 379-388, 1974.

Judge, R. J. R., Electron excitation and auroral emission parameters, *Planet. Space Sci., 20*, 2081-2092, 1972.

Hviuzova, T.A. and S. V. Leontyev, Solar wind density influence on the auroral red line (630.0 nm) intensity, *Geomagnetism and Aeronony, 42*, 4, 519-521, 2002, (in Russian).

Lennartsson, W., and E. G. Shelley, Survey of 0.1–to 16–keV/e plasma sheet ion composition, *J. Geophys. Res., 91*, 3061-3076, 1986.

Lennartsson, W., A scenario for solar wind penetration of Earth's magnetotail based on ion composition data from the ISEE1 spacecraft, *J. Geophys. Res., 97*, 19921-19238, 1992.

Liou, K., P. T. Newell, C. –I. Meng, M. Brittnacher, G. Parks, Characteristics of the solar wind controlled auroral emissions, *J. Geophys. Res. 103*, 17543-17557, 1998.

Newell, P. T., Y. I. Feldstein, Yu. I. Galperin, C. –I. Meng, Morphology of nightside precipitation, *J. Geophys. Res. 101*, 10737-10778, 1996.

Newell, P. T., V. A. Sergeev, G. R. Bikkuzina, S. Wing, Characterizing the state of magnetosphere: testing the ion precipitation maximal latitude (b2i) and the ion isotropy boundary, *J. Geophys. Res. 103*, 4739-4745, 1998.

Starkov, G. V., B. V. Rezhenov, V. G. Vorobjev, Y. I. Feldstein, L. I. Gromova, Structure of dayside auroral precipitation, *Geomagnetism and Aeronony, 42*, 2, 186-194, 2002, (*in Russian*).

Terasawa, T., M. Fujimoto, T. Mukai et al., Solar wind control of density and temperature in the near – Earth plasma sheet WIND/GEOTAIL collaboration, *Geophys. Res. Let., 24*, 935-938, 1997.

Torr, M. R., D. G. Torr, M. Zukic et al., A far ultraviolet imager for the International Solar-Terrestrial physics mission, *Space Sci. Rev., 71*, 329, 1995.

Vorobjev, V. G., L. I. Gromova, B. V. Rezhenov, G. V. Starkov, Y. I. Feldstein, Variations of the boundaries of plasma precipitation and auroral luminosity in the night-time sector, *Geomagnetism and Aeronony, 40*, 3, 79-85, 2000, (in Russian).

Vorobjev, V. G., O. I. Yagodkina, Midnight electron precipitation pattern for substorm development, *this issue*, 2003.

# Plasma distribution in a dipole-like magnetosphere with azimuthal plasma flow around it

A. S. Leonovich[1,3], V. A. Mazur[1,3], and J. B. Cao[2,3]

[1] Institute of Solar-Terrestrial Physics (ISTP), Russian Academy of Science, Siberian Branch, Irkutsk 33, P.O.Box 4026, 664033, Russia
[2] Center for Space Science and Applied Research, Chinese Academy of Science, Chinese Academy of Science, Bejing, P.O. Box 8701, China
[3] Russian-Chinese Joint Research Center on Space Weather

**Abstract.** We have constructed an analytical model for an axisymmetric magnetosphere with azimuthal plasma flow. A dipole-like model of the geomagnetic field was used. It is shown that within the framework of this model of the magnetosphere, plasma at each magnetic shell moves with a constant angular velocity. The possibility of formation of a twin plasmapause is demonstrated. Abrupt changes in plasma density are directed across magnetic shells separating regions with strongly differing plasma velocities, as well as on the cylindrical surface whose radius coincides with the equatorial radius of the plasmapause.

## 1. Introduction

The main purpose of this work is construction of analytical magnetospheric model with dipole-like magnetic field lines and plasma flowing around it. This problem arises because of great disproportion between the development of field line resonance theory in the magnetosphere and theory of Kelvin-Helmholtz instability of magnetospheric magnetosonic oscillations, which are excited by solar wind stream flowing around the magnetosphere.

It is known, that these magnetosonic oscillations can be a source of resonant Alfven waves, excited in the magnetosphere [*Chen and Hasegawa*, 1974; *Southwood*, 1974; *Krylov and Lifhitz*, 1984]. Recently the theory of field line resonance has been constructed for models of a magnetosphere with a dipole or dipole-like magnetic field [*Krylov et al*., 1981; *Leonovich and Mazur*, 1989]. At the same time, the theory of Kelvin-Helmholtz instability exists currently only for models with a linear magnetic field [*McKenzie*, 1970; *Mann et al.*, 1999], which are rather far from reality. One of the main reasons for Kelvin-Helmholtz instability theory lagging behind, from our point of view, is the absence of a rather simple model of the magnetosphere with a dipole-like magnetic field and plasma on the move. The aim of our work is to construct a magnetospheric model, which will be suitable for theoretical investigations of Kelvin-Helmholtz instability of dipole-like magnetosphere, with plasma flowing around it. The basic requirement for such kind of model is self-consistency of its characteristics from the mathematical point of view. During the development of this model we have discovered some very interesting features, which are present in real magnetosphere. They can be registered by satellite observation.

## 2. Model of magnetosphere

The model of magnetosphere is presented in Figure 1. Curvilinear dashed lines correspond to the plasmapause ($x^1 = a_{\mathbf{p}}$) and magnetopause ($x^1 = a_{\mathbf{m}}$). The plasma moves only in the azimuthal direction $\vec{v} = (0, v_\varphi, 0)$. Solution of MHD equations

$$\rho_0 \frac{d\mathbf{v_0}}{dt} = -\nabla P_0 + \frac{1}{4\pi}[\mathrm{curl}\,\mathbf{B}_0 \times \mathbf{B}_0],$$

$$\frac{d\mathbf{B_0}}{dt} = \mathrm{curl}[\mathbf{v}_0 \times \mathbf{B}_0], \quad \frac{d\rho_0}{dt} + \mathrm{div}(\rho_0 \mathbf{v}_0) = 0,$$

$$\frac{d}{dt}\frac{P_0}{\rho_0^\gamma} = 0,$$

has led to the conclusion that the angular velocity of plasma in the model under consideration is constant on each magnetic shell and depends only on the coordinate $x^1$: $\Omega = v_\varphi / \rho \equiv \Omega(x^1)$. This means, that the arbitrary boundaries separating regions with sharply differing plasma velocities (plasmapause and magnetopause) must coincide with one of the magnetic shells.

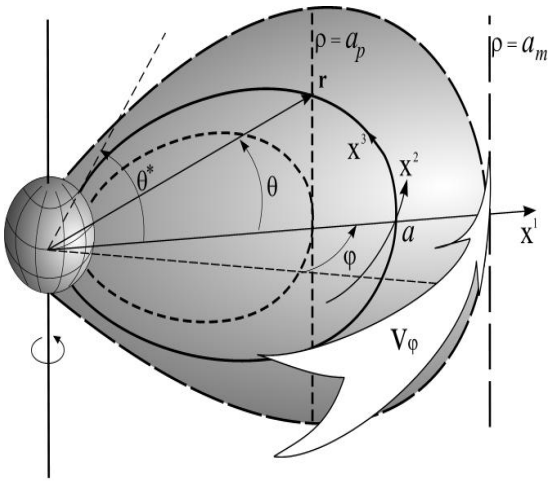


**Figure 1.** Model of the axisymmetric magnetosphere and coordinate systems: $(x^1, x^2, x^3)$ – curvilinear orthogonal coordinate system tied with magnetic field lines, $(a, \varphi, \theta)$ – coordinate system as used in calculations. Curvilinear dashed lines correspond to the plasmapause $\rho = a_p$ and magnetopause $\rho = a_m$.

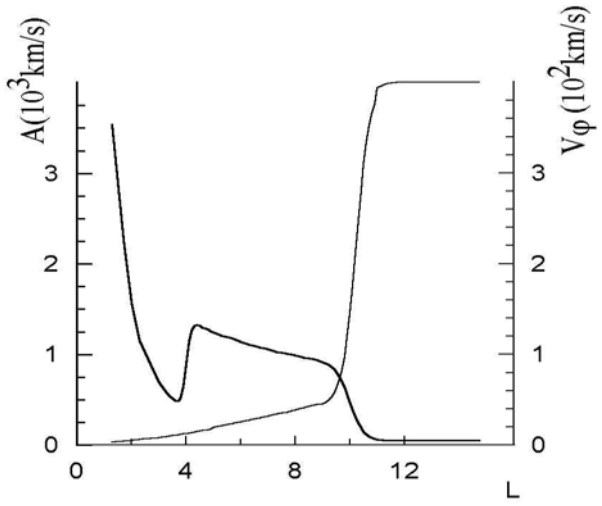


**Figure 2.** Distribution across magnetic shells: of the azimuthal plasma velocity $v_\varphi(a = L)$, and the Alfven velocity $A(a = L)$, where L – MacIlwain parameter.

The equilibrium of plasma rotating along the field line is sustained by the gas kinetic pressure gradient, and across magnetic shells by a total magnetic and gas kinetic pressure gradient. It is customary to use the surface where total kinetic and gas kinetic solar wind plasma pressure become equal to the geomagnetic field pressure $\beta = 8\pi p / B^2 = 1$ as the magnetospheric boundary.

It is evident that in the magnetospheric model under consideration this surface differs greatly from the magnetopause that was defined above as the boundary separating regions of rapidly moving solar wind plasma and slow convection of magnetospheric plasma. This surfaces match closely enough only in the near-equatorial region.

### 3. Boundary conditions

Figure 2 shows the equatorial distribution of the plasma velocity $v_\varphi(x^1 = L)$ and the Alfven velocity $A(x^1 = L)$, where $L$ is McIlwain parameter. These values are specific functions of the model. Such distribution of $A(x^1 = L)$ and $v_\varphi(L)$ leads to an abrupt jump of plasma density at the passage through the plasmapause ($L$=4).

The distribution of plasma concentration along magnetic field lines is determined by the solution of ideal MHD equations.

### 4. The results of numerical calculation

Figure 3 presents the distributions of plasma concentration *n* along the field line for different magnetic shells. The variation of *n* along field lines lying under the plasmapause in the plasmasphere (curve **1** – for L=2 and curve **2** – for L=4) proceeds monotonically, and along field lines outside the plasmasphere (curve **3** – for L = 6, curve **4** – for L=9, curve **5** – for L=12 and curve **6** – for L=15) it shows a sharp jump. The origin of this jump may be understood from the expression of concentration

$$n(a,\theta) = n(\rho,0)\frac{\Omega^2(a)}{\Omega^2(\rho)},$$

which follows from the theoretical investigation. The sharp change of $n(a,\theta)$ occurs on the magnetic shell where $\Omega(a)$ changes dramatically. This magnetic shell is defined as the plasmapause of the first type. It is mapped along field lines into the ionosphere to the main ionospheric trough. The jump is also caused by a sharp change of $n(\rho,0)$ in the place where the field line crosses the cylindrical surface $\rho = a_p$, where $a_p$ is an equatorial radius of the plasmapause. In accordance with the generally accepted criteria, such a surface should also be defined as the plasmapause of the second type.

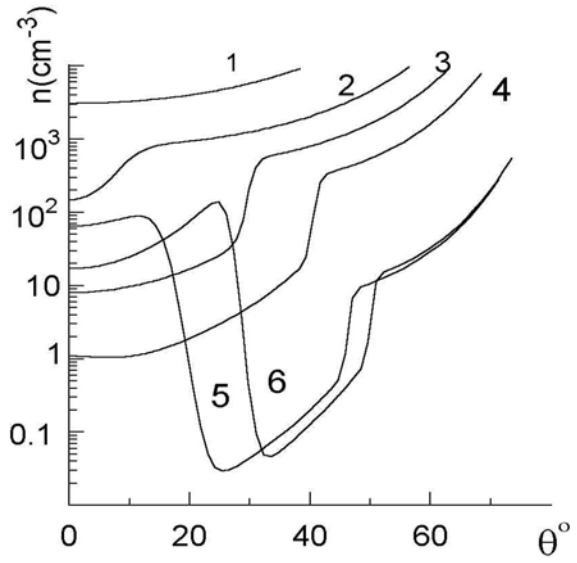


**Figure 3.** Distribution of the plasma density $n(a,\theta)$ along field lines at magnetic shells: 1) L=2; 2) L=4; 3) L=6; 4) L=9; 5) L=12; 6) L=15.

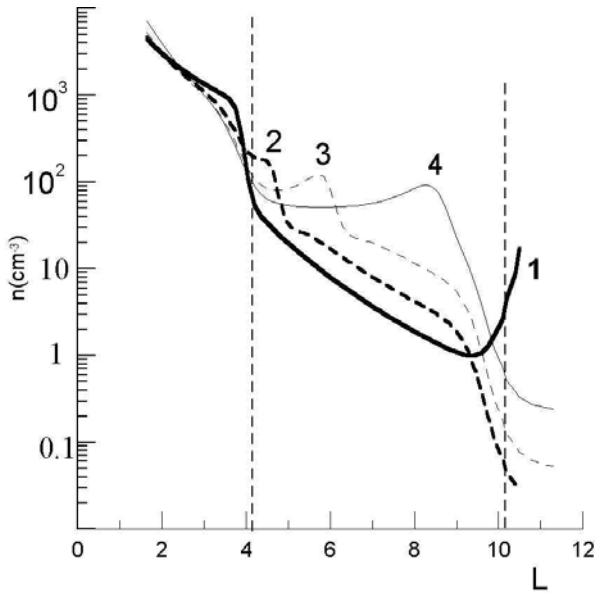


**Figure 4.** Distribution of plasma concentration along various trajectories of the satellite (at the projection to the meridional plane) calculated for model with "average" solar wind ($v_\varphi$ ~ 400 km/s).

1. Trajectory in the equatorial plane (inclination angle of the trajectory – $0^o$);
2. Trajectory under $20^o$ angle to the equatorial plane;
3. Trajectory under $30^o$ angle to the equatorial plane;
4. Trajectory under $40^o$ angle to the equatorial plane.

While the presence of the plasmapause of the first type associated with a sharp change of $\Omega(a)$ does not cause any special questions, the formation of the plasmapause of the second type is not quite an obvious phenomenon at present. Its unusual shape, cylindrical surface of radius $\rho = a_p$, is of course associated with quite the type of the plasma motion used in the model of the medium under consideration, the azimuthal rotation. Furthermore, plasma equilibrium is ensured by the equality of the centrifugal force and radial pressure gradient. In the real magnetosphere the plasma motion has much more complicated character. For that reason, the shape of the plasmapause of the second type can differ greatly from the one calculated in this paper. In any case, the presence of such a plasmapause and its possible shape needs further investigation using satellites.

If the satellite, moving in the magnetosphere under the definite angle to equator, crosses both of these surfaces, it must detect a double plasmapause (curves 2, 3, 4 in Figure 4), in contrast to satellite moving along equatorial plane (curve 1). It has been shown that in the magnetospheric model under consideration the existence of the plasmapause of two different types is possible. The plasmapause of the first type coincides with the magnetic shell, across which a sharp change of the plasma velocity occurs. In the magnetospheric model under consideration the plasmapause of the second type represents a cylindrical surface, the radius of the generatrix of which coincides with the equatorial radius of the plasmapause of the first type. When the satellite moves at a certain angle to the equatorial surface, a double (or of larger multiplicity) plasmapause must be observed.

**References**

Chen, L., and A. Hasegawa, A theory of long period magnetic pulsation–1, *J. Geophys. Res., 79*, 2054-5852, 1974.

Krylov, A. L., A. F. Lifshitz, and E. N. Fedorov, About resonance properties of the magnetosphere, (in russian) Izvestiya RAN SSSR, ser. *Fizika Zemli, 6*, 49-58, 1981.

Krylov, A. L., and A. F. Lofshitz, Quasy-Alfven oscillations of magnetic surfaces, *Planet. Space Sci., 32*, 481-489, 1984.

Leonovich, A. S., and V. A. Mazur, Resonance excitation of standing Alfven waves in an axisymmetric magnetosphere (monochromatic oscillations), *Planet. Space Sci., 37*, 1095-1108, 1989.

Mann, I. R., A. N. Wright, K. J. Mills, and V. N. Nakariakov, Excitation of magnetospheric waveguide modes by magnetosheath flows, *J. Geophys. Res., 104*, 333-353, 1999.

McKenzie, J. F., Hydromagnetic wave interaction with the magnetopause and the bow shock, *Planet. Space Sci.*, *18*, 1-23, 1970.

Southwood, D. J., Some features of field line resonances in the magnetosphere, *Planet. Space Sci.*, *22*, 423-492, 1974.

# Effect of solar wind parameters on velocity shear instability of magnetospheric boundary layers

V. V. Mishin

Institute of Solar-Terrestrial Physics (ISTP), Russian Academy of Science, Siberian Branch,
Irkutsk 33, P.O.Box 4026, 664033, Russia

**Abstract.** The effect of the interplanetary magnetic field (IMF) and the solar wind density on the regime of the magnetohydrodynamic (MHD) velocity shear instability of the magnetospheric boundary is considered. Its mode essentially differs at the dayside magnetosphere, where flow velocity in the magnetosheath is subsonic, and behind the meridian morning – evening, where the flow becomes supermagnetosonic. At the dayside boundary the instability can be a source of surface waves in the range of pulsations Pc2–4, their amplitude waning quickly deep in the magnetosphere, and the conditions of the instability development and dispersion properties of generated waves strongly depend on the IMF orientation. So, the dayside boundary is most unstable for the radial IMF and big values of plasma density when there is minimal value of the Alfven velocity in the magnetosheath. Solar wind negative pressure sharp changes cause impulsive development of the flute instability at the magnetopause during its short time (1–2 min) outward accelerated displacements. At the far magnetotail boundary in the region of hypersonic flow past the instability weakly depends on the IMF orientation and generates waves in the range of long-period geomagnetic pulsations with amplitude, weakly waning in space. The period of the most unstable perturbations (T~10 min) coincides with periods of: 1) the far tail boundary oscillations observed on ISEE– 3 and 2) high-latitude geomagnetic pulsations which are independent from orientation of IMF. Increase of magnetic pressure and density in the magnetosheath reduces stabilizing effect of compressibility. Here sluggish transonic oblique perturbations (concerning a direction of stream speed) predominate above usually taken into account fast longitudinal perturbations both on the value of growth rate, and on frequency bandwidth.

## 1. Introduction

At the magnetospheric boundary there is a sharp gradient of the flow velocity $\mathbf{v_0}$, the plasma density $\rho_0$, temperature $T$ and the magnetic field $\mathbf{B_0}$. In closed model used below we describe the magnetospheric boundary by a plane diffuse tangential discontinuity (TD) with the shear layer near the plane $z = 0$. The inhomogeneity of all quantities is specified only along the $z$ axis, and the vectors $\mathbf{v_0}$ and $\mathbf{B_0}$ are collinear to the plane $z = 0$. Here the velocity shear instability can develop. This instability is also named the Kelvin-Helmholtz instability. It is considered as the key excitation mechanism for magnetopause oscillations and associated geomagnetic pulsations [*Moskvin and Frank-Kamenetsky*, 1967; *Mishin*, 1981]. Besides, this instability can play an important role in the solar wind - magnetosphere interaction ensuring momentum transfer into the magnetosphere and forming diffuse boundary layers [*Boller and Stolov*, 1970; *Mishin and Morozov*, [*Boller and Stolov*, 1970; *Mishin and Morozov*, 1983; *Miura* 1982, 1992].

The nature of this instability is rather simple. The initial perturbation of a boundary causes concentration of streamlines and appearance of a wing lift owing to the theorem Bernoulli. At presence of the magnetic field its tensions counteract the generation of longitudinal perturbations (along the magnetic vector). For an adequate research of the influence of magnetic fields and plasma parameters on the development of the velocity shear instability with a finite transition layer it is necessary to carry out a numerical analysis. It is not a simple task. Therefore, for the analysis of the experimental data geophysicists often utilize the TD approximation, which gives the simple dispersion equation for slow subsonic flow past the magnetosphere.

The TD approximation considers instability of the plane boundary $z = 0$ of the zero width, where all parameters change their values. Vectors of the velocity $\mathbf{v_0}$ and the magnetic field $\mathbf{B_0}$ change their values and

directions, being in the plane parallel to the boundary ($\upsilon_z = B_z = 0$). For damping at $|z| \to \infty$ perturbations: $f_1(x,y,z,t) \propto \exp\{-\chi|z| + i(k_x x + k_y y - \omega \cdot t)\}$ linearization of the MHD equations gives for the vertical displacement $\zeta$ and the total pressure perturbation: $\Pi_1 = P_1 + \mathbf{B_1} \cdot \mathbf{B_0}/4\pi$:

$$\Pi_1 = \rho_0 (\Omega/\chi)^2 \frac{d\varsigma}{dz}, \qquad \frac{d\Pi_1}{dz} = \rho_0 \Omega^2 \varsigma. \tag{1}$$

Here:

$$\chi^2 = k^2 - \varpi^4 / [\varpi^2 (c_s^2 + a^2) - (\mathbf{k}\cdot\mathbf{a})^2 c_s^2] \tag{2}$$

$\Omega^2 = \varpi^2 - (\mathbf{k}\cdot\mathbf{a})^2$, $\varpi = \omega - \mathbf{k}\cdot\mathbf{v}_0(z)$; $\mathbf{k} = \{k_x, k_y, 0\}$ is a wave vector, $\omega = \mathrm{Re}(\omega) + i\gamma$.

For a positive growth rate (or increment) $\gamma > 0$ one has instability: $f_1(t) \propto \exp\{\gamma \cdot t\}$. Dispersion equation of the TD instability is derived analytically only for small values of magnetosonic Mach number $M_{ms} = \Delta\upsilon/(2c_m) << 1$, when the approximation of incompressible liquid is applicable (here $\Delta\upsilon = |\boldsymbol{\upsilon}_{\mathbf{II}} - \boldsymbol{\upsilon}_{\mathbf{I}}|$ is velocity difference, $c_s$ and $a$ are the sound and Alfven velocities); $c_m = \sqrt{(c_s^2 + a^2)}$ is the magneto-sound velocity. The equation looks like the following [*Mishin*, 1981]:

$$\omega = \{\mathbf{k}\cdot[(\rho\boldsymbol{\upsilon})_I + (\rho\boldsymbol{\upsilon})_{II}] \pm i\{\rho_I \rho_{II} (\mathbf{k}\cdot\Delta\boldsymbol{\upsilon})^2 - (\rho_I + \rho_{II})[(\mathbf{kB_I})^2 + (\mathbf{kB_{II}})^2]\}^{1/2}\}/(\rho_I + \rho_{II}) \tag{3}$$

In the homogeneous case $\rho = const$, $\mathbf{B} = const$ for parallel flow $\mathbf{k} \parallel \mathbf{v_0} \parallel \mathbf{B_0}$ there is instability $\gamma > 0$ for $\Delta\upsilon > 2a$.

The equation of motion describes an influence of the longitude magnetic field:

$$\rho[\partial\mathbf{v}/\partial t + (\boldsymbol{\upsilon}\cdot\nabla)\boldsymbol{\upsilon} - (\mathbf{B}\cdot\nabla)\mathbf{B}/(4\pi\rho)] = -\nabla(P + B^2/8\pi). \tag{4}$$

The Maxwell tensions $(\mathbf{B}\cdot\nabla)\mathbf{B}$ tend to stabilize longitude perturbations $(\mathbf{k}||\mathbf{B_0})$. For $M = \Delta\upsilon/2c_s \sim 1$ there is stabilizing influence of compressibility of the medium. *Landau* [1944] in the ordinary hydrodynamics ($\mathbf{B} = 0$) showed that longitudinal disturbances (with respect to the flow velocity vector $\mathbf{k} \parallel \mathbf{v}_0$) are stable ($\gamma = 0$) for $M \geq M_L = \Delta\upsilon/2c_s = \sqrt{2}$. But *Syrovatsky* [1954] found a presence of instability ($\gamma > 0$) for oblique perturbations $\cos\varphi = \mathbf{k}\cdot\mathbf{v_0}/k\upsilon_0 < M_L^{-1}$. However, his very important result was ignored for a long time.

Analysis of the influence of the IMF and plasma density on the instability of a sharp TD at the daytime magnetopause in detail was conducted by *Boller and Stolov* [1970] in the approximation of the incompressible liquid, which was proved by *Mishin* [1981]. The TD approximation is applicable only for wavelengths large in comparison with the transition layer's thickness, but this does not give a chance to estimate the increment of the most unstable short-wave perturbations. Besides it incorrectly features the compressibility effect and distortion effect of sharp gradients of plasma and field. From the other hand, in the papers dealing with the finite thickness of the boundary, its influence on all parameters is not usually considered (see references in [*Miura*, 1982-1999; *Mishin and Morozov*, 1983]). In the present paper we made an attempt to bridge this gap.

## 2. Instability at the dayside magnetospheric boundary

Here the plasma flow velocity in the magnetosheath is small: $M_{ms} = \Delta\upsilon/(2c_m) < 1$, and "incompressible" approximation is applicable. Perturbations here are the surface ones, fast damping from the boundary, because index (2) of exponential decrease of their amplitude is real and maximal: $\chi = \pm k$. Because the flow velocity difference is subalfvenic one, the instability can develop only for perpendicular flowing past geomagnetic field, at the low-latitude boundary layer (LLBL). But perturbations may be stabilized by the field $\mathbf{B_0}$ of the magnetosheath, which is dependent on the IMF direction. For average IMF orientation, the instability is more possible at the morning magnetopause than at the evening one. Non-radial IMF component causes an enhancement of the magnetic field in the magnetosheath and makes the whole dayside boundary more stable. Dayside geomagnetic pulsations Pc2-Pc4 are reduced by the increase of the IMF azimuth. Moreover, their frequency range corresponds to the instability range [*Mishin*, 1981].

Now for a more accurate analysis we have to take into account the presence of a finite tranzition layer. We describe the profiles of all the parameters by smooth functions following [*Mishin and Morozov*, 1983]:

$$\upsilon_0(z) = u(1+\tanh(z/d)),$$

$$\rho(z) = \rho_{00}\cdot[1+R\cdot(1+\tanh(z/d)]/(1+R),$$
$$B(z) = B_{00}\cdot[1-b\cdot(1+\tanh(z/d)]/(1-b).$$

For the homogeneous density and without parallel field ($\mathbf{B_0}\perp\mathbf{v_0}$) an analytical task solution exists [*Chandrasekhar*,1961; *Moskvin and Frank-Kamenetsky*, 1967; *Chandra*, 1973]. Dimensionless increment $\tilde{\gamma} = \gamma d/u$ has the maximum value (~0.2) and comes to zero at $\alpha_b = (kd)_b = 1$. At the LLBL there is a sharp density difference. For a static boundary it causes a displacement of the position of a maximum growth rate- $\gamma = \mathrm{Im}(\omega)$ and the short-wavelength boundary of the instability range $\alpha_b$ to the right (by as much as 40%) along the axis kd [*Morozov and Mishin*, 1981]: for $\rho = const$ there is $\alpha_b = 0.445$, for sharp density gradient $\Delta\rho/\rho \approx 1, \alpha_b = 0.7$ (middle curve on Figure 1). There is no reduction of maximum growth rate of instability, which gives the TD approximation.

The presence of the longitudinal magnetic field $\mathbf{B_0} \parallel \mathbf{v_0}$ causes weakening of the instability: the curve $\tilde{\gamma} = \tilde{\gamma}(kd)$ displaces downwards and to the left, i.e. there is a decrease of a maximal increment and contraction of the range of instability [*Chandra*, 1973; *Miura*, 1982, *Mishin and Morozov*, 1983]. The decrease of frequency

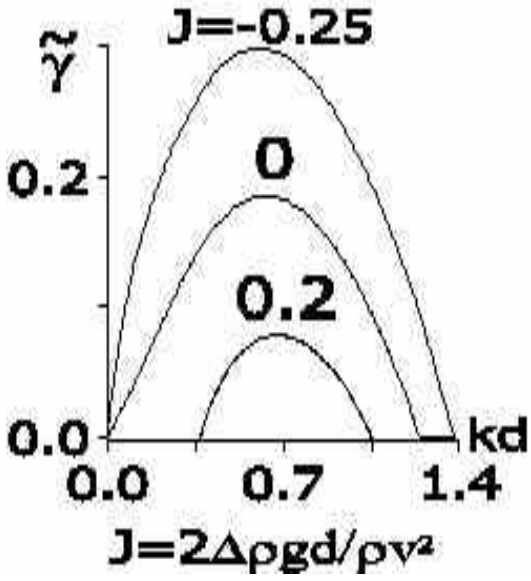


**Figure 1.** Normalized growth rate $\tilde{\gamma} = \gamma d/u$ as a function of *kd* for different values of Richardson number J, $M << 1$, $\rho_{II}/\rho_I = 10$.

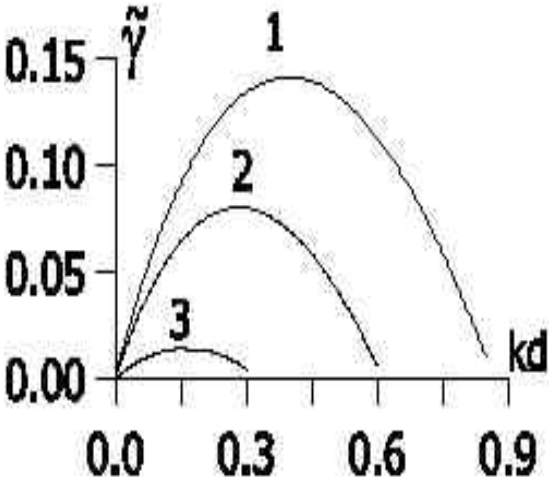


**Figure 2.** Normalized growth rate $\tilde{\gamma} = \tilde{\gamma}(kd)$ of longitude ($\mathbf{k} \parallel \mathbf{v_0}$) disturbances for different values the number M. Curves 1, 2, 3 correspond to following values: M = 0.5, 0.8, 1.2.

of generated oscillations by a magnetic field, is usually ignored.

It is necessary to note, that when both factors are present (the longitudinal magnetic field and density gradient), it is difficult to identify the effect from each of them.on the growth rate. In the TD approximation it is simply impossible. So, from the dispersion equation of TD it can be seen, that the value of an increment depends on the Alfven velocity, which is proportional to the field and inversely proportional to the radical from density. The numerical analysis, conducted by us, has proved, that the increase of plasma density in the magnetosheath reduces stabilizing effect of the longitude field also at presence of a finite transition layer. It is manifested not only by the increase of the growth rate, but also by the extension of the instability range.

Solar wind negative pressure sharp changes cause outward accelerated magnetopause motions and impulsive Raleigh-Taylor (R-T) instability [*Mishin*, 1993]. Its effect causes big values of the growth rate (see upper curve on Figure 1).

R-T (or flute) instability develops at the boundary between a heavy liquid and an underlying lightweight hot liquid: $\nabla\rho \uparrow\downarrow \mathbf{g}$. Its growth rate in the TD approximation is the following: $\gamma_{RT} \propto \sqrt{kg}$, where g- is resulting "gravitational" acceleration. In presence of both factors, Richardson number *J* characterizes their relative role in hydrodynamics (see Figure 1).

Experimental and model [*Mishin*, 1993] values of possible accelerations are 0.1-10 $km/s^2$, which is

enough for the instability development, even for strong IMF azimuth. An example of impulsive (1-2 min) generation of the flute instability was given by [*Parkhomov et al*., 2001] for two sudden impulses observed during propagation of the back front of the interplanetary magnetic cloud 11.01.1997. There were positive (01.20 UT) and negative (02.20 UT) pressure changes, caused accelerated inward and outward magnetopause motions. Pulsations were generated more intensively by the negative SW pressure change than by the positive one, which is in correspondence with the model by *Mishin* [1993].

In conclusion of this section we shall point out the following. The analysis of the instability of the daytime boundary by means of equation (3) can be done only qualitatively. The TD approximation can give incorrect results, as for the most unstable perturbations ($kd \sim 0.5$) the influence of inhomogeneities of all parameters does not appear too strong, as it is given in the equation (3). Therefore for adequate research it is necessary to carry out a numerical analysis in view of a smooth varying transition layer.

### 3. Velocity shear instability at the magnetotail boundary.

The flow velocity in the magnetosheath becomes supersonic after the morning – evening meridian.

In the ordinary hydrodynamics ($\mathbf{B_0}$=0) *Blumen* [1970]; *Blumen et al.* [1975] showed, that the shear layer instability develops for any Mach number, but the growth rate and range of supersonic perturbations are significantly smaller than those of subsonic disturbances. Thus, for M>1 the value of the growth rate reduces very quickly with increasing of M (Figure 2).

Supersonic velocity of shear layers generates perturbations with slow speed of amplitude damping ($\mathrm{Re}(\chi) \to 0$, $\mathrm{Im}(\chi) \approx k$) and weak growth in time ($\tilde{\gamma} < 10^{-3}$). From (2) it follows, that an influence of a compressibility of the medium is determined by the "wave" magnetosonic Mach number: $\tilde{M} = \varpi / kc_m$. As it follows from the equation (3), one has $\varpi \propto \mathbf{k} \cdot \mathbf{v_0} = k\upsilon\cos\varphi$ and $\tilde{M} \propto M\cos\varphi / \sqrt{1 + P_B / P}$. If the magnetic pressure $P_B$ is more than the thermal pressure $P$ ($P_B / P \geq 1$), the total pressure is essentially enlarged in comparison with the thermal pressure and the effective wave Mach number $\tilde{M}$ accordingly becomes essentially less (see Figure 3). Magnetic pressure increases full pressure and diminishes influence of the compressibility. So, the magnetic field may not only impact stabilizing effect by its longitude component, but can impact the opposite – destabilizing influence by its pressure. The latter effect is evident only for supersound velocity difference. In usually discussed subsound case its effect is not seen. So, we have the double effect of the magnetic field: stabilizing by the Maxwell tensions and destabilizing by its pressure (see equation (4)).

Second factor determining value of the Mach number is the angle $\varphi$ between the wave vector $\mathbf{k}$ and the velocity vector $\mathbf{v_0}$: $\tilde{M} \propto \cos\varphi$ [*Syrovatsky*, 1954].

At the near tail ($|x|<50R_E$) the speed of flow around passes the magnetosound "barrier" and the mode of transition takes place which is the least studied in the theory of turbulence. Besides in this region the stabilizing effect of the magnetic field still is essential, as the value of the flow velocity difference is comparable with the Alfven velocity. Here analysis is hampered also because of absence of the detailed satellite data of distribution of parameters near the boundary layers.

We shall consider the instability of the distant tail boundary, where the thorough observations on the ISEE-3 satellite were conducted [*Bame et al*., 1983]. In our papers [*Mishin and Morozov*, 1983, Matyukhin and *Mishin*, 1986] the possibility of the instability development there on oblique perturbations was shown. However in papers by *Miura* [1992, 1999] only the longitudinal perturbations $\mathbf{k} \parallel \mathbf{v_0}$ were considered, for which the increment was very small. On the basis of his research Miura made the conclusion that the instability in the region of hypersonic flow around the tail weakly influences the dynamics of the boundary layer. Let's prove the validity of outcome of our previous paper, using the improved algorithm [*Mishin*, 2002] for this purpose.

We consider the influence of the longitudinal magnetic field, the compressibility of the medium and the influence of the density inhomogeneity simultaneously. Nobody has done it before. But the necessity of simultaneous reviewing of effect of all three factors is stipulated by the fact that the longitudinal magnetic field and the compressibility of the medium shift a dispersion curve $\tilde{\gamma} = \tilde{\gamma}(kd)$ to the left on the axis $\alpha = kd$, and the density inhomogeneity on the contrary - to the right. Therefore, even if one of these factors is not taken into account an incorrect outcome will be received.

Now we examine the instability with respect to the density and magnetic field inhomogeneities, as well as the supersonic velocity difference on the geomagnetic tail boundary for a set of parameters obtained by the ISEE-3 satellite in the distant tail- region ($-220 < R_E < x < -50R_E$). Using ISEE-3 data [*Bame et al*., 1983] we calculated the dependence $\tilde{\gamma}(kd)$ in the most stable configuration: $\mathbf{B_0} \parallel \mathbf{v_0}$. Calculations were performed for three possible values of the velocity difference at the boundary: 1) $\Delta\upsilon$ = 250 km/s, 2) $\Delta\upsilon$ = 330 km/s, and 3) $\Delta\upsilon$ = 500 km/s. For all cases instability takes place, even in the case of small velocity jump (250 km/s). In the case

$\Delta\upsilon$ = 250 km/s instability arises with a sufficient growth rate, however, there is rather noticeable influence of the longitude magnetic field: for $\mathbf{k}\| \mathbf{B_0}$ the growth rate ($\tilde{\gamma} \le 0.02$) is 4 times less than for case $\mathbf{k}\perp\mathbf{B_0}$ ($\tilde{\gamma} \le 0.08$). Such instability enhancement can occur at the LLBL of the tail where the geomagnetic field can be perpendicular to the flow direction.

Note that *Sibeck et al*. [1987], based on analyzing the results obtained within the TD approximation, assumed that for existence of instability of longitude perturbations, it is necessary to have more drastic velocity difference $\Delta\upsilon \approx 400 km/s$. A strong magnetic field, in addition to having a stabilizing effect of the Maxwell tensions, significantly reduces the influence of the compressibility: when $\beta(z=0) = 0.65$, we have $M(z=0) = 2.24$, $M_a(z=0) = \Delta / (2a(z=0)) = 1.65$, $M_{ms}(z=0) = 1.33$. In fact, the effective wave number is less: $\tilde{M} \propto \tilde{\omega}/kc_m \le 1$, when $\cos\varphi \le 0.9$.

As the velocity difference on the boundary increases, the compressibility influence is enhanced, and the influence of Maxwell tensions decreases. Figure 3 illustrates the case: $M(0) = 3$, $M_a(z=0) = 2.2$,

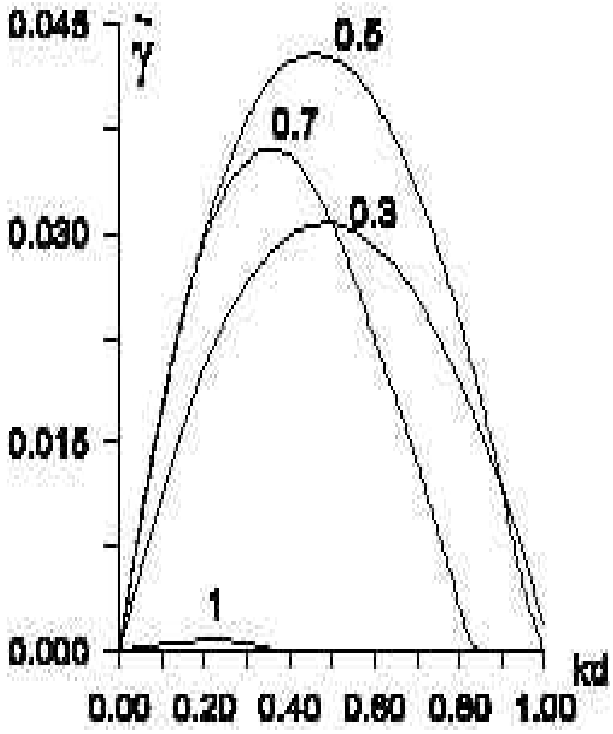


**Figure 3.** Instability of the distant tail boundary for velocity difference $\Delta\upsilon = 335\ km\ /\ s (M(0) = 3)$, $M_{ms}(0) = 1.33$ as a function of $\cos\varphi$. Case $\mathbf{v_0} \| \mathbf{B_0}$. $M_{ms}(0) = 1.77$ according to the value of the velocity difference $\Delta\mathbf{v} = 335 km/s$. With these parameters, the longitudinal field influence is rather weak, and the character of the influence of the angle $\varphi$ is the same as in the absence of Maxwell tensions. At the same time, an increase of the number $M(0) \to 3$ manifests itself in the decrease of the growth rate of longitudinal ($\cos\varphi \le 1$) disturbances and in the expansion of the opening of the angle $\varphi$ of generation of supersonic disturbances – the transition to surface disturbances is taking place when $\cos\varphi \le 0.7$.

In the case of a maximum possible velocity difference on the boundary $\Delta\upsilon = \upsilon_{II} = 500 km/s$, we have an enhancement of the compressibility influence: the generation of supersonic disturbances is over a wider range of values of the angle $\varphi$ ($\cos\varphi \le 0.5$), but with smaller growth rates as a consequence of an increase of Mach number: $M_{ms}(0) = 2.6$. In this case the role of the Maxwell tension becomes weak $M_a(z=0) = 3.3$. Maximum value of growth rate here is $\tilde{\gamma} = 0.035$ for $\cos\varphi = 0.4$, and longitude ($\cos\varphi = 1$) perturbations are really stabilized $\tilde{\gamma} < 0.001$.

Let us mark the destabilizing role of the density inhomogeneity. It is easy to see from the expansion of the instability range: the position of the short - wavelength boundary of subsonic oblique disturbances corresponds to the value of $\alpha_b \ge 1$ – i.e. it lies further from the boundary of subsonic disturbances in the case of an uniform density. In the latter case $\Delta\upsilon = 500 km/s$ for most unstable oblique disturbances we have the following values: $\alpha_{\max} = 0.4$, $\upsilon_{ph} = 0.28\upsilon_{II}$. The TD approximation gives much higher phase velocity of longitudinal disturbances: $\upsilon_{ph} = 0.9\upsilon_{II}$. So, the density inhomogeneity decreases the phase velocity of the generated disturbances and reduces the compressibility influence.

Thus we have demonstrated that the distant tail boundary for actually observed plasma parameters and the magnetic field are unstable at all latitudes; furthermore, the influence of the longitudinal magnetic field is almost indistinguishable when the velocity difference is $\Delta\upsilon \ge 335$ km/s.

The increase of the density in the solar wind after its intensification on the bow shock causes increase of the density in the magnetosheath and amplification of the density gradient at boundary layers. It renders a destabilizing effect on the boundary. At first, there is an extension of the instability range, as well as in conditions of subsonic flow past of the day time magnetosphere. Besides the increase of the density gradient reduces a convective phase velocity $\varpi/(kc_m)$, value of the effec-

tive wave number $\tilde{M}$ and accordingly the compressibility effect of the medium.

## 4. Conclusions

At the dayside magnetospheric boundary, where flow around the magnetosphere is submagnetosonic, the "incompressible" approximation is applicable. Here the MHD velocity shear instability generates surface oscillations in the range of geomagnetic pulsations Pc2-Pc4. The IMF azimuth reduces the instability and can stabilize it completely.

The increase of density, on the contrary, destabilizes the boundary, counteracting the stabilizing effect of a longitudinal magnetic field. The increase of the solar wind density after its additional amplification on the bow shock causes an increase of the density gradient at boundary layers. Thus there is a decrease of the Alfven velocity in the magnetosheath, increase of the growth rate and extension of the frequency range of the instability.

Besides the density gradient reduces a phase velocity, the value of the effective wave number $\tilde{M}$ and accordingly the compressibility effect of the medium. It is especially important at the boundary of the geomagnetic tail, where the instability is strongly attenuated by the compressibility of the medium. The effect of the magnetic field there has double character. On the one hand, at the near tail boundary there is the stabilizing effect of the longitudinal magnetic field, which is loosened at the far tail. On the other hand, here (especially in the region of the far tail) the not remarked earlier effect of weakening of the compressibility influence by the magnetic pressure appears [*Mishin*, 2002]. All this reduces the generation of transonic oblique perturbations in a broad band of angles $\varphi$, which are weakly attenuated by the magnetic field and are capable to explain generation of long-period oscillations of the far tail boundary and high-latitude geomagnetic pulsations, and also a formation of diffuse boundary layers.

In the non-stationary regime the sharp changes of the dynamic pressure of the solar wind cause accelerated displacements of the dayside magnetopause within 1–2 minutes, during which the flute instability "switches on", which excites short-lived oscillations in the range of periods 10-100 seconds observed on the Earth.

**Acknowledgements.** Work is supported by Russian Foundation for Basic Resarch, projects RFBR 01-05-64203 and RFBR/GFEN 02-05-39020.

## References

Bame, S. J., R. C. Anderson, J. R. Asbridge, D. N. Baker, W. C. Feldman, J. T. Gosling, E. W. Hones, D. J. McComas, R. D. Zwickl, Plasma regimes in deep geomagnetic tail: ISEE 3, *Geophys. Res. Let.*, *10*, 912-915, 1983.

Blumen, W., Shear layer instability of a inviscid compressible fluid, *J. Fluid Mech*., *46*, 763-775, 1970.

Blumen, W., P. G. Drazin, D. F. Billings, Shear layer instability of a inviscid compressible fluid, Part 2, *J. Fluid Mech*., *71*, 305-316, 1975.

Chandrasekhar, S., *Hydrodynamic and hydromagnetic stability*. Clarendon Press, Oxford, 1962.

Chandra, K., Hydromagnetic stability of plane heterogeneous shear flow. J. *Phys. Soc. Japan*, *34*, 539-546, 1973.

Landau, L. D., Stability of tangential discontinuities in compressible fluid, *Acad. Nauk U.S.S.R., Comps. Rendus (Doklady)*, *44*, 139-142, 1944.

Michalke, A., On the inviscid instability of the hyperbolic tangen profile, *J. Fluid. Mech*, *19*, 689-702, 1964.

Mishin, V. V., On the MHD instability of the Earth's magnetopause and it's geophysical effects, *Planet. Space Sci*., *29*, 359-363, 1981.

Mishin, V. V., A. G. Morozov, On the effect of oblique disturbances on Kelvin-Helmholtz instability at magnetospheric boundary layers and in solar wind, *Planet. Space Sci*., *31*, 821-828, 1983.

Mishin, V. V., and Yu. G. Matyukhin, A Kelvin-Helmholtz instability on the magnetopuse as a possible source of wave energy in the earth's magnetosphere, *Geomagn. Aeron., Engl. Transl., 26*, 806, 1986.

Mishin, V. V., On predominance of oblique disturbances in the supersonic shear layer instability of geomagnetic tail boundary, *Nonlinear problems in geophys., 10*, 2003 (to be published).

Miura, A., P. I. Pritchett, Nonlocal analysis of the Kelvin-Helmholtz instability in compressible plasma, *J. Geophys. R*es., *87*, 7431-7444, 1982.

Miura**,** A., Kelvin-Helmholtz instability at the magnetospheric boundary: dependence on the magnetosheath sonic Mach number, *J. Geophys. Res*., *97*, 10655-10675, 1992.

Miura, A., Self-organization in the two-dimensional magnetohydrodynamic transverse Kelvin-Helmholtz instability, *Geophys. Res., 104*, 395-411, 1999.

Morozov, A.G., V. V. Mishin, Influence of the magnetospheric boundary layer structure on Kelvin-Helmholtz instability, *Sov. Phys. Geomagnetizm i aeronomiya*, *21*, 1044-1049, 1981.

Moskvin, Yu. L., D. A. Frank-Kamenetsky, Geomagnetic micropulsations and the solar wind, *Sov. Phys.-Geomagnetizm i aeronomiya*, *7*, 144-149, 1964.

Sibeck, D. G., J. A. Slavin, E. J. Smith, ISEE-3 magnetopause crossings: evidence for the Kelvin-Helmholtz instability, *Magnetotail physics*, edited by T. Yz. Lui, 73-76, J. Hopkins Univ. Press, Baltimore, 1987.

Syrovatsky, S .I., Instability of tangential discontinuities in compressible medium, *Sov. Phys. -JETP*, *27*, 121-123, 1954.

# Magnetic cloud and magnetosphere-ionosphere response to the 6 November 1997 CME

A. Z. Bochev[1], and I. A. Dimitrova[2]

[1] Solar – Terrestrial Influences Laboratory -Bulgarian Academy of Sciences (BAS), 1113 Sofia, Bulgaria
[2] Space Research Institute – BAS, 1113 Sofia, Bulgaria

**Abstract.** In the present work we analyse the magnetic cloud (MC) at 1 AU on 9 November 1997. The appearance of a hotter and denser part (dense filament), with a radial extent of $10^6$ km, immediately behind the frontal part of the MC, is a distinctive feature of the event. The INTERBALL – Auroral Probe had a chance to observe field-aligned currents in mid – altitude magnetosphere during the substorm expansion phase intensification related to the dense filament. We emphasize the appearance of unusual "N"-shape magnetic structure, 3 min long, with an amplitude of 50 nT between field-aligned current region 1 and the magnetosphere lobe in late evening hours. To explain some of the MC features we refer to a model scenario of the 6 November coronal mass ejection.

## 1. Introduction

The coronal mass ejection (CME) appears to be the main real solar event responsible for geomagnetic storms [*Crooker*, 1994]. CME events were detected by space-born coronographs in the 70-s ([*Gosling et al*., 1976] for the SKYLAB mission). According to their visual features, the CME have an observable change in the coronal structure that (1) occurs within a time scale between a few minutes and several hours and (2) involves the appearance of a new, bright white-light feature in the coronograph field of view [*Hundhausen*, 1993]. In some works it is assumed that the CME propagates at 1 AU in the form of a magnetic cloud (MC), [*Burlaga et al*., 1988]. The 6 January 1997 CME, corresponding to a typical MC, appeared to be a remarkable event, which largely affected both the magnetosphere and ionosphere [*Fox et al*., 1998; *Nakamura et al*., 1998; *Thomsen et al*., 1998; *Yermolaev et al*., 1998; *Sanchez et al*., 1998]. Another unusual event was the 6 November 1997 CME, being related to the active region AR 8100 [*Maia et al*., 1999; *Dermendjiev et al*., 1999; *Pick et al*., 1999; *Mason et al*., 1999; *Mazur et al*., 1999; *Delann\'ee et al*., 2000; *Delann\'ee* and *Aulanier*, 2000]. It is remarkable for its very large-scale extent in latitude seen by both SOHO/LASCO/C2 coronograph and Nancy radioheliograph [*Maia et al*., 1999]. The present work is intended to investigate the 9 November MC and its magnetosphere -ionosphere response. For this purpose we analyze the magnetic field and plasma parameters in the interplanetary space at 1 AU (WIND data) during 9-10 November 1997.

In order to show field-aligned current (FAC) systems, we analyze data from the three-component flux-gate magnetometer [*Arshinkov et al*., 1995] aboard the INTERBALL-Auroral Probe satellite (or shortly INTERBALL-AU). The INTERBALL-AU spacecraft is spin stabilized along the X-axis directed to the Sun, its period being 120s. Orbital parameters: apogee $4R_E$ ($R_E$ is the Earth's radius), period 5.5hr, inclination $65^o$. The magnetometer X-axis is aligned with the spin axis, and the Y and the Z-axis are in the spin plane of the spacecraft.

## 2. Magnetic cloud at 1 AU

We analyse the magnetic field and plasma parameters in the interplanetary space at 1 AU on 09.11.1997 using the data from the WIND satellite (coordinates: X=144, Y=-44 and Z=20 computed in Earth's radius). The arrival of a shock is clearly seen at about 10:30 UT (Figure 1; Figure 2, panels 1-2). Note that the time in these plots has been shifted by 35 min to allow for MC propagation time from WIND. The frontal boundary of a large-scale magnetic structure corresponds to the Bz fast reversal from +4 nT to -5 nT at 18:00 UT (Figure 1 (2), panel 4 (1). Then a general positive trend of Bz dominates until 20:00 UT on 10 November (the rear boundary of this event, followed by irregular oscillations). Within these boundaries the radial extent of the event is about 0.3 AU. We identify this configuration as similar to a magnetic cloud (MC) [*Burlaga et al*., 1998; *Dermendjiev et al*., 1999; *Bochev*, 2000].

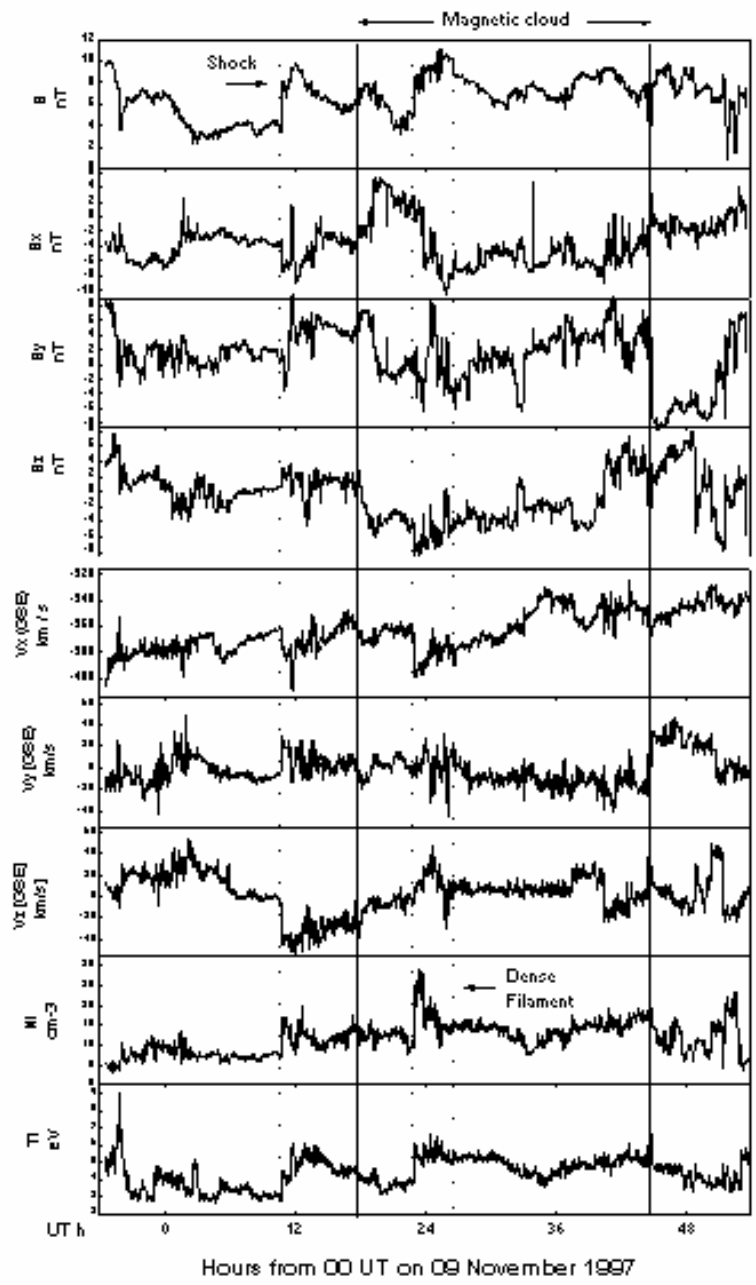


**Figure 1**. A plot of the magnetic field and solar wind parameters from November 8-11 (top to bottom): the magnetic field module $B$, the $B_x$, $B_y$ and $B_z$ components, the bulk velocity components ($V_x$, $V_y$ and $V_z$), the proton density ($N_i$), the ion temperature ($T_i$). Vertical lines indicate the shock (dot-dash line), the front boundary of the magnetic cloud and the stream interface (solid lines) and the dense and hotter part (dash lines).

Apart from this, we can identify some significant differences as compared with previous studies of MC:

(1) A pronounced step like change of $B$ from 5 to 9 nT (Figure 1, panel 1), in the interval 23:00 to 26:30 UT, delineates the region which is clearly indicated by the remaining plots: velocities, density and temperature (Figure 1). Note the appearance of a warmer and denser ($Ni$ = 25 cm$^{-3}$) region immediately after the frontal portion of the MC. Further in the text we denote this part of the MC, with the boundaries defined by $B$ and $Ni$, as dense filament;

(2) We observe relatively higher temperature $Ti$ = 6 eV (or 6.7 × $10^{4o}$K) in the dense filament as compared with the ambient solar wind ahead of the shock where $Ti$ = 3.5 eV (or 4.1 × $10^4$ $^o$K), (Figure 1, panel 9). The dense filament radial extent is large -more than $10^6$ km. More details about MC features are given elsewhere [*Dermendjiev et al*., 1999].

## 3. Magnetosphere - ionosphere response

We have calculated the energy coupling function ε (Appendix A) in order to make a quantitative estimation of the expected magnetosphere response (Figure 2, panel 3). The first separate enhancement ε = 5 × $10^{11}$ Watt, was on 09 November 1997 at 19 UT. Then we observed two larger enhancements: ε = 1.2x10 $^{12}$ (1.5 × $10^{12}$ ) Watt at about 23:00 (24:50) UT. The planetary Kp index increases from 1+ to 4. Ground based magnetograms from the Lovozero Magnetic Observatory, show a substorm onset at about 19:30 UT (Figure 2, panel 5). Then an enhancement begins at about 23:00 UT. After that, we examine the Hemisphere Power (briefly Power), issued by the Space Environment Centre, NOAA, Boulder, CO (available with time resolution of 30 or 60 min). This parameter is proportional to the auroral electrojet activity. As a whole we observe a dynamic picture in the form of three peaks of: 0.7 × $10^{11}$, 1 × $10^{11}$ and 1.2 × $10^{11}$ Watts at about 21:50, 23:30 and 26:30 UT respectively (Figure 2, panel 4). Three aspects stand out from these considerations:

(1) Before the arrival of the MC the magnetosphere was quiet. MC interaction with the magnetosphere provoked substorms and a magnetic storm;
(2) There is an indication of the substorm expansion phase intensification with the arrival of the MC dense filament at about 23 UT on 9 November 1997;

A large portion of the power transferred to the magnetosphere – ionosphere corresponds to the MC dense filament. Accordingly the hemisphere power reaches a maximum of 1.2 × $10^{11}$ Watt.

## 4. Field -aligned currents response (INTERBALL-AU data)

The INTERBALL -AU had a rare chance to monitor FACs exactly during the interaction of the MC dense filament with the magnetosphere. Here we are inclined to emphasize this period, taking into consideration a magnetogram recorded on 09 November 1997, from 22:48 UT to 24:00 UT. To characterize the magnetic field disturbances we have plotted for simplicity only the Bh component residuals (measured – IGRF model), $Bh = (B_y^2 + B_z^2)^{1/2}$, where $B_y$ and $B_z$ are spin plane components (Figure 3, panel 2). Corrected geomagnetic coordinates are shown at the bottom.

The orbit foot points cross the polar cap, and then the auroral oval at ≈22 MLT. Along this orbital interval the spacecraft altitude decreases from 3.87$R_E$ to 2.88$R_E$. In the magnetogram, a large-scale disturbance due to the FACs (Region 1 and Region 2) dominates. The disturbance amplitude is as large as 100 nT, which exceeds by a factor of three the normal quantities for these heights.

Next we try to show what is the portion of dissipated energy in the ionosphere. We assume that the FACs closure in the ionosphere appears to be the Pedersen currents under the condition of div **j** = 0. The general expression of Joule heating rate is Q = **j.** (**E** + **V** X **B**), where **j**, **E** and **V** are ionosphere current density, electric field and velocity respectively. Under **V** = 0, equipotentiality of magnetic field line (E = $\mathbf{E}_\perp$), and predomination of meridian orientation of the electric field $E_\perp$ = $\mathbf{E}_x$, Q will depend only on the transverse components of **j** and **E,** so that Q = $i_\perp$ $E_x$, where Pedersen current $i_\perp$ is expressed by FAC density $i_\perp = \int j_{//}\, dx$, where x is along the orbit. Assuming infinite current sheets for FAC density $j_{//} \cong \Delta B_h / (\mu\, \Delta l)$, where $\Delta B_h$ is $B_h$ amplitude, Δl is current sheet width, $\mu = 4\pi/10^7$. Then $i_\perp$ = 0.12 A/m and assuming E = 0.080 V/m in the ionosphere, for an unit area Q = 0.0096 Watt/m$^2$. Accepting for the half width of the auroral oval l = 500 km, in one hour MLT sector, we have the heating rate q = 0.26RQlsin θ [*Bochev*, 1999] or q = 1.3 × $10^{10}$ Watt for $R$ = 2.×.$10^4$ km and θ = 30$^o$. Then for a quarter of AO (half of the night sector) q = 0.8 × $10^{11}$ Watt. In this way we can assume that the dissipated energy of the FACs closure in the ionosphere was large; it corresponds to the Hemisphere Power, which indicates that the substorm overlaid not only on Kiruna-Lovozero sector but probably about 2 MLT hours to the west.

Apart from the enhanced large-scale currents, a zone of intense small-scale variations in the poleward edge of Region 1 could be revealed from 23:12 UT to 23:14 UT (Figure 3, panel 2). We denote this peculiar type of perturbation as "N"-shape structure. Originally this name was used in the TRIAD mission [*Iijima and Potemra*, 1978]. In this zone, peak to peak variations reach 50 nT (Figure 3, panel 2). Assuming a spatial interpretation, they could be related to a three-sheet current structure. Accordingly, high current densities $j_{//}$ = 2.$10^{-6}$ A/m$^2$ would be inherent to this zone. However, an interpretation in terms of time variations seems more probable: the dense filament as a pressure pulse, would

compress the magnetosphere and cause time variation in the magnetic field [*Cummings et al.*, 1969; *Cahill et al.*, 1986; *Potemra et al.*, 1989; 1990]. Recently an intriguing interpretation appeared [*Keiling et al.*, 2000).

## 4. Discussion and Conclusions

We have studied the magnetic fields and plasma parameters at heliocentric distance 1 AU. As one can trace in Figure 1, on 9 November the WIND registered a shock (10:30 UT) and sheath and then magnetic field and plasma configurations which we identify as similar to a magnetic cloud (MC); we point out well distinguished warm and dense filament in the MC frontal part. We shall dwell on the dense filament and its influence on the magnetosphere-ionosphere. The filament appears as a large pulse with a radial extent of more than 1 million km, characterized by southward magnetic field (Bz = –8 nT) and a high ion density (Ni = 25 $cm^{-3}$), (Figure 2, panel 1–2). It appears that the

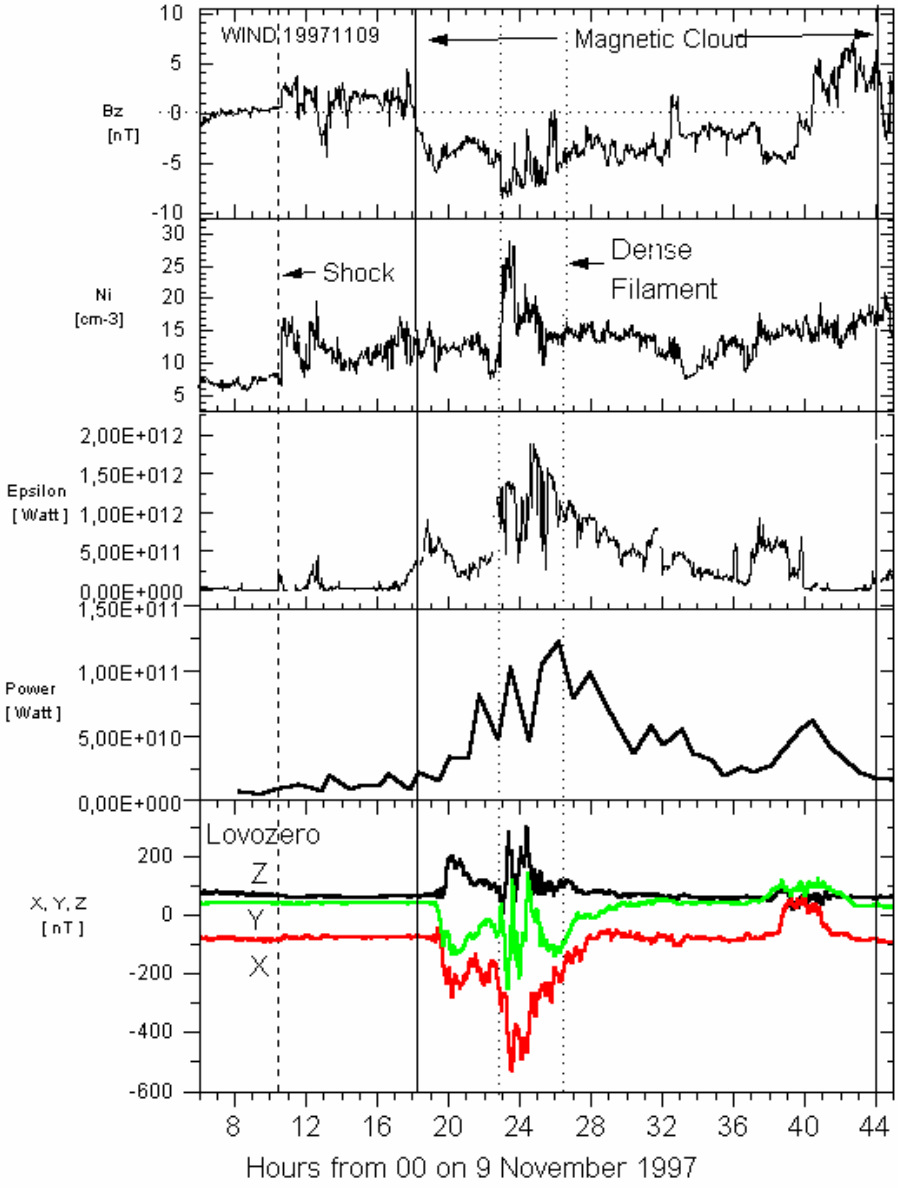


**Figure 2**. Panel 1 – magnetic cloud (MC) $B_z$ magnetic field component; panel 2 – ion density *Ni*; panel 3 – energy coupling function epsilon ($\varepsilon$); panel 4 – hemisphere power and Panel 5 magnetic field components at Lovozero Observatory. Vertical lines indicate: shock (dash), magnetic cloud (solid) and dense filament (fine dash).

strengthening of the reconnection at the nose of the magnetosphere due to these important parameters of the dense filament began a little before 22:56 UT. This moment could be identified by a sudden 20 nT increase of the GEOS-9/Bz component by the respective compressional wave in the dayside magnetosphere (data from GEOS are widely accessible). For the timing of the substorm development, apart from Lovozero (Figure 2, panel 5), we have examined other observatories too. For example Kiruna, which is closer to the INTERBALL footpoint, shows a similar record. In Figure 3, panel 1, a small portion of Kiruna magnetogram is presented. It is hard to obtain the exact timing of the substorm onset, however it is obvious that beginning from 23:08 UT there was a sharp and continuous decrease of the Bx component indicative for the expansion phase intensification. The substorm might have started even at earlier UT to the west of Kiruna, where was the INTERBALL conjunction. More important for us is that both observatories sensed almost simultaneously features characterising the expansion phase of a substorm during the INTERBALL transit.

We have emphasized the appearance of an unusual "N"-shape magnetic field structure between FAC Region 1 and the open field lines (magnetosphere lobe) registered by INTERBALL/magnetometer at 23:12 UT (Figure 3, panel 2). Note a sharper pulse in the middle of "N"-shape, time scale of 10 sec (30 km), dB/dt = 5 nT/s. This magnetic field disturbance would create a strong variation of electric field too. Sometimes the height integrated Pedersen conductivity is low at the poleward edge of the auroral oval, which gives some grounds to suppose a large electric field. Basically, if such an event occurs between the PSBL and the lobe simultaneously with the substorm expansion phase near to its conjunction, then we could suppose an association with a large Poynting fluxes transferred to the ionosphere via Alfven waves [*Keiling*., *Wygant et al*, 2000]. So the "N"-shape may be related to a transfer of significant amount of wave energy as large as the Joule heating ($10^{-3}$ Watt/m$^2$).

It was assumed that the MC (shock at 10:30 UT) on 9 November 1997 (at 1 AU) was directly related to the CME observed after 13:00 UT by the LASCO/SOHO on 6 November 1997 [*Dermendjiev et al*., 1999; *Mason et al*., 1999; *Mazur et al*., 1999]. We point out that the ejected plasma, in particular the dense filament, is distinguished for:

(1) comparatively higher temperature;
(2) increased plasma density and magnetic field;
(3) a large radial extent (about 1 million km.);

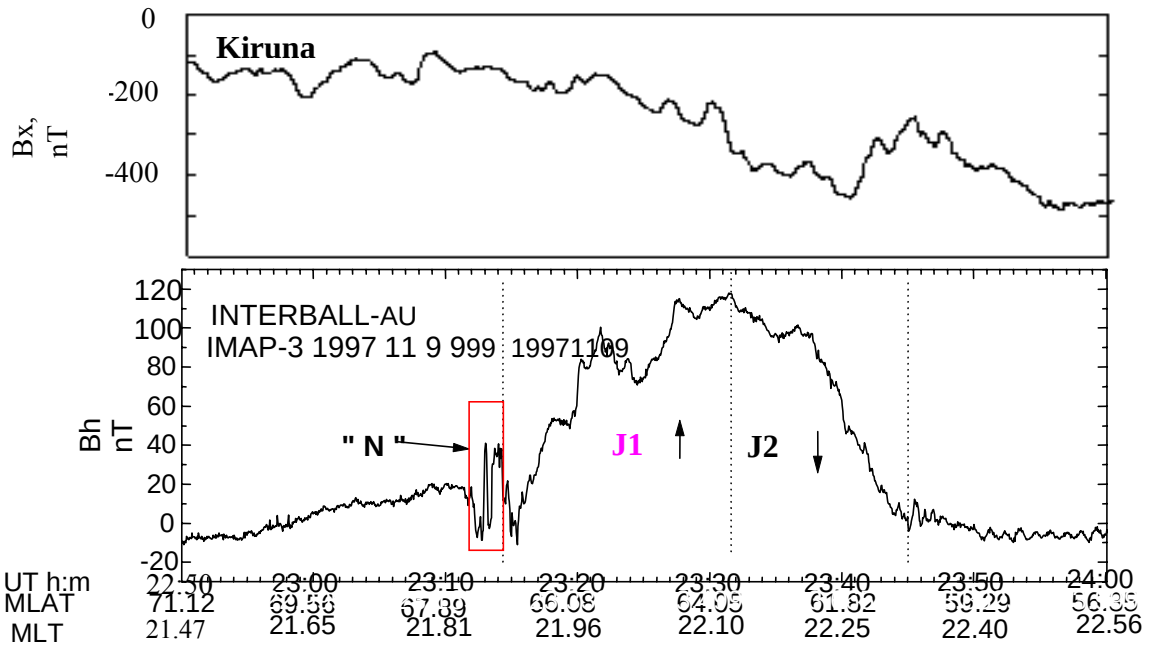


**Figure 3**. Panel 1 – The $B_x$ magnetic field component during expansion phase of a substorm. in Kiruna; panel 2 – INTERBALL-AU magnetogram suggestive for upward and downward large-scale field-aligned currents J1 and J2 (Region 1 and Region 2) and an "N"-shape structure at the poleward edge of Region 1.

(4) the location of hotter plasma in the frontal part of the ejection.

These features can be explained, e.g., by the hypothesis that this CME originated from "evaporation" from the chromospheric flaring area, due to the white light flare (WLF) [*Dermendjiev et al*., 1999]. A WLF was visually registered in the Haskovo Astronomical Observatory, Bulgaria, on 6 November 1997 between 11:45 UT and 11:50 UT very close to the W-S solar limb in the leading spot of a sunspot group in the active region 8100 [*Dermendjiev et al*., 1999]. Lord Carrington was the first to observe the appearance of WLF (on 01 September 1859) and severe magnetic storm two days later [*Carrington*, 1859]. The examined event contrasts the famous 6 January 1997 CME; its MC plasma at 1 AU was characterised as originating from erupting prominence [*Burlaga et al*., 1998]. One of their arguments was that the proton temperature of the maximum density region (dense filament) was exceptionally low ($Ti < 1.1 \times 10^4$ K). So the detected MC features in the Earth's environment could be attributed to the CME peculiar type. From these and other studies it appears that the MC at 1 AU can preserve basic structural peculiarities of its CME. Further studies will tell more about this large-scale magnetic field configuration, stable enough in the interplanetary space.

**Acknowledgement**. Dr. Ivan S. Arshinkov from the Scientific Industrial laboratory of Special Sensors and Systems ("SDS" Lab's) – Bulgarian Academy of Sciences (BAS), Sofia, Bulgaria, was the original principal investigator of the INTERBALL-Auroral Probe/magnetometer. Dr. Alexander Z. Bochev from the Solar-Terrestrial Influences laboratory (STIL) – BAS, Sofia, Bulgaria, has played that role since 1996. We acknowledge the WIND, GEOS-9, Lovozero and Kiruna data providers. We thank the referee for the helpful comments.

## Appendix A

The energy coupling function is $\varepsilon = V B^2 \sin^4(\theta/2) l_o^2$, [$10^{-7}$ Watt/s], where $V$ is the solar wind speed, $B$ is the IMF magnitude, $\theta = \tan^{-1}(|B_y/B_z|)$ for $B_z > 0$, $\theta = 180 - \tan^{-1}(|B_y/B_z|)$ for $B_z < 0$, $l_o = 7Re$ ($R_e$–Earth's radius). As originally defined, $\varepsilon$ is the energy flux integrated across an effective magnetopause cross sectional area. Ranges of ε given by Akasofu are: $\varepsilon \geq 10^{11}$ Watt for a substorm onset, $10^{11} < \varepsilon < 10^{12}$ Watt for a typical substorm and $\varepsilon > 10^{12}$ Watt for triggering of a magnetic storm [*Perrault and Akasofu*, 1978].

## References

Arshinkov, I. S., L. N. Zhuzgov, A. Z. Bochev, et al., Magnetic field experiment in the INTERBALL project (experiment IMAP). *Interball Mission and Payload. CNES*, 222-228, 1995.

Bochev, A. Z., Field-aligned currents during forcing of magnetosphere on 9-10 November 1997. *Compt. Rend. Acad. Bulg. Sci*., *53*, 12, 53-56, 2000.

Burlaga, R. F., Magnetic clouds and force-free fields with constant alpha. *Journ. Geoph.. Res*., *93*, 7217-7224, 1988.

Burlaga, L., et al. A magnetic cloud containing prominence material: January 1997. *J. Geoph. Res*., *103*, 277-295, 1998.

Cahill, L. J., et al., Electr. and magn. field observ. of standing waves in the magnetosph. *J. Geoph. Res*., *91*, 8895-8907, 1986.

Carrington, R. C., Description of a singular appearance seen in the Sun on September 1, 1859. *Mon. Not. Roy. Astr. Sos*., *20*, 13, 1859.

Gosling, G. T. et al., *Sol. Phys*., *386*, 1976.

Crooker, N., Replacing the solar myth. *Nature*, *367*, 595-596, 1994.

Cummings, et al., Standing Alfven waves in the magnetosphere. *Journ. Geophys. Res*., *74*, 778, 1969.

Delann\'ee, C., et al., Observation of the origin of CME in the low corona. *Astron. Astrophys*., *355*, 2000, 725-742.

Delann\'ee, C., G. Aulanier, CME associated with transequatorial loop and a bald patch flare. *Solar Phys*, 2001.

Dermendjiev, V. N., A. Z. Bochev, et al., The white light flare and CME on November 6, 1997 and the earth's magnetosphere response, *Magnetic fields and Solar Processes,* ESA, SP -448, *2*, 1999, 971–977.

Fox, N. J., et al., Cradle-to-grave tracking of the January 6-11, 1997, Sun-Earth connection event. G*eoph. Res. Lett*., *25*, 1998, 2461-2465.

Iiijima, T., T. A. Potemra, Large-scale chracteristics of field-aligned currents associated with substorms. *J. Geoph. Res*., *83*, 1978, No A2, 599-615.

Hundhausen, A. J. *J. Geoph. Res*., *98*, 1993, 13177.

Keiling, A., Wygant et al., Large Alfven wave power in the plasma sheet boundary layer during the expansion phase of substorms. Submitted to *Geoph. Res. Lett*., May 2000.

Maia, D., et al., Radio signatures of a fast coronal mass ejection development on November 6, 1997, preprint, to appear in *J. Geoph. Res*., 1999.

Mason, G. M., et al., Particle acceleration and sources in the November 1997 solar energetic particle events. *Geophys. Res. Lett*., *25*, 1999, 141-145.

Mazur, J. E. et al., Charge state of solar energetic particles using the geomagnetic cutoff technique:

SAMPEX measurements in the November 6, 1997 polar particle event. *Geoph. Res. Lett*., *25*, 1999, 173-177.

Nakamura, M. et al., Reconnection event at the dayside magnetopause on Jan.10, 1997. *Geoph. Res. Lett*., *25*, 1998, 2529-2533.

Perrault, P., S. -I. Akasofu . *J. R. Astr. Soc*., *54*, 1978, 547.

Pick, M., et al., Coronal mass ejections. *Proc. 9-th European Meeting on Solar Physics*, *Magnetic fields and Solar Processes,* ESA, SP-448, 2, 915-926, 1999.

Potemra, T. A. et al. Resonant geomagnetic field oscillations and Birkelands currents in the morning sector. *J. Geophys. Res*., *93*, 2661-2674, 1988.

Potemra, T. A. et al., Multisatellite and ground-based observ. of transient ULF waves. *J. Geoph. Res*., *94*, 2543-2554, 1989.

Sanchez, E. R. et al., Energy transfer between the ionosphere and magnetosphere during the January 1997 CME event. *Geoph. Res. Lett*., *25*, 1998, 2597-2601.

Thomsen, M. F. et al. The magnetospheric response to the CME passage of January 10-11, 1997 as seen at geosynchronous orbit. *Geoph. Res. Lett*., *25*, 1998, 2545-2549.

Yermolaev, Y. I. et al. Plasma populations in the magnetosphere during the passage of magnetic cloud on January 10-11, 1997: INTERBALL-TAIL observations. *Geoph. Res. Lett*., *25*, 2565-2569.

# Solar wind dynamic pressure fluctuations as the modulator of mid-latitude storm-time Pc1 geomagnetic pulsation activity

N. A. Zolotukhina and I. P. Kharchenko

Institute of Solar-Terrestrial Physics, Irkutsk, Russia

**Abstract.** We investigated the correlation between time variations of interplanetary space parameters and mid-latitude geomagnetic pulsations. Six magnetic storms were analyzed. Three magnetic storms revealed an obvious correlation between the intensity modulation of mid-latitude Pc1 and solar wind dynamic pressure ($P_{SW}$) variations. Pc1, modulated by solar wind dynamic pressure variations, were recorded in the maximum and in the early recovery phase of magnetic storms. The pulsations had amplitudes from a few nT to several hundred nT and lasted over 7 hours. Waves were observed as long as $P_{SW}$ increased or fluctuated. The modulation effect manifested itself as the start (or enhancement) of Pc1 after the increase in solar wind pressure and as the disappearance (attenuation) of the pulsations after the fall of $P_{SW}$. It is shown that series of Pc1 pulsations associated with $P_{SW}$–variations, were generated in mid-latitudes when regions of increasing solar wind dynamic pressure were recorded by spacecraft after intervals of a quasi-stationary negative $B_z$–component of the IMF of a duration of 4.5 hours or longer. This study is based on the data from the WIND and IMP8 spacecraft, as well as the data from Mondy (51.62° N, 100.75° E, L = 2.1) and Borok (58.03° N, 38.97° E, L = 2.9) magnetic observatories.

## 1. Introduction

The enhancement of the geomagnetic pulsation wave activity of different frequency ranges in the case where the magnetosphere is compressed by incoming solar wind inhomogeneities is one of the best known manifestations of solar-terrestrial connections. In the Pc1 range, this effect is the most conspicuous at high latitudes. It is related with two groups of events, namely:

- ion-cyclotron waves that were recorded in the outer magnetosphere simultaneously with isolated sudden impulses (SI). According to AMPTE/CCE data, the occurrence probability of ion-cyclotron waves in the Pc1 range during isolated sudden enhancements of the magnetic field, recorded by satellite, is 47% and it much exceeds the average probability of Pc1 registration in the outer magnetosphere, which is 10–20% [*Anderson and Hamilton*, 1993];
- pulsations in the Pc1 frequency range that were recorded at high-latitude magnetic observatories. According to *Kangas et al.* [1986], an enhancement of Pc1 wave activity on the ground after SI occurs in 2/3 of cases at least.

At this point we must also mention the increase in the probability of Pc1 occurrence before SI that was detected by *Gulielmi et al.* [2000], who suggested that it was associated with the compression of the magnetosphere by a specific structure of the interplanetary plasma ahead of the shock front.

## 2. Geomagnetic pulsations under study

In this paper we present a new group of wave phenomena, the generation and amplitude modulation of which are explicitly related to the increase of solar wind dynamic pressure ($P_{SW}$) and its fluctuations, respectively. They are geomagnetic pulsations in the Pc1 frequency range recorded in the maximum and in the early recovery phase of three magnetic storms in mid-latitudes.

Figure 1 shows the dynamic spectra of pulsations constructed using the data from induction magnetometers. For the October 19–20, 1995 storm, the figure shows the pulsation spectra constructed using the data from obs. Mondy (51.62° N, 100.75° E, L≈2.1, MLT ≈ UT+7); for the other two storms, the data were obtained from two observatories: Mondy and Borok (58.03° N, 38.97° E, L≈2.9, MLT ≈ UT+3). Local geomagnetic noon (▽) and local geomagnetic midnight (▼) of the observatories are indicated at the top of each panel. The spectral composition and the presence of "pearl"-like structures on dynamic spectra and analog

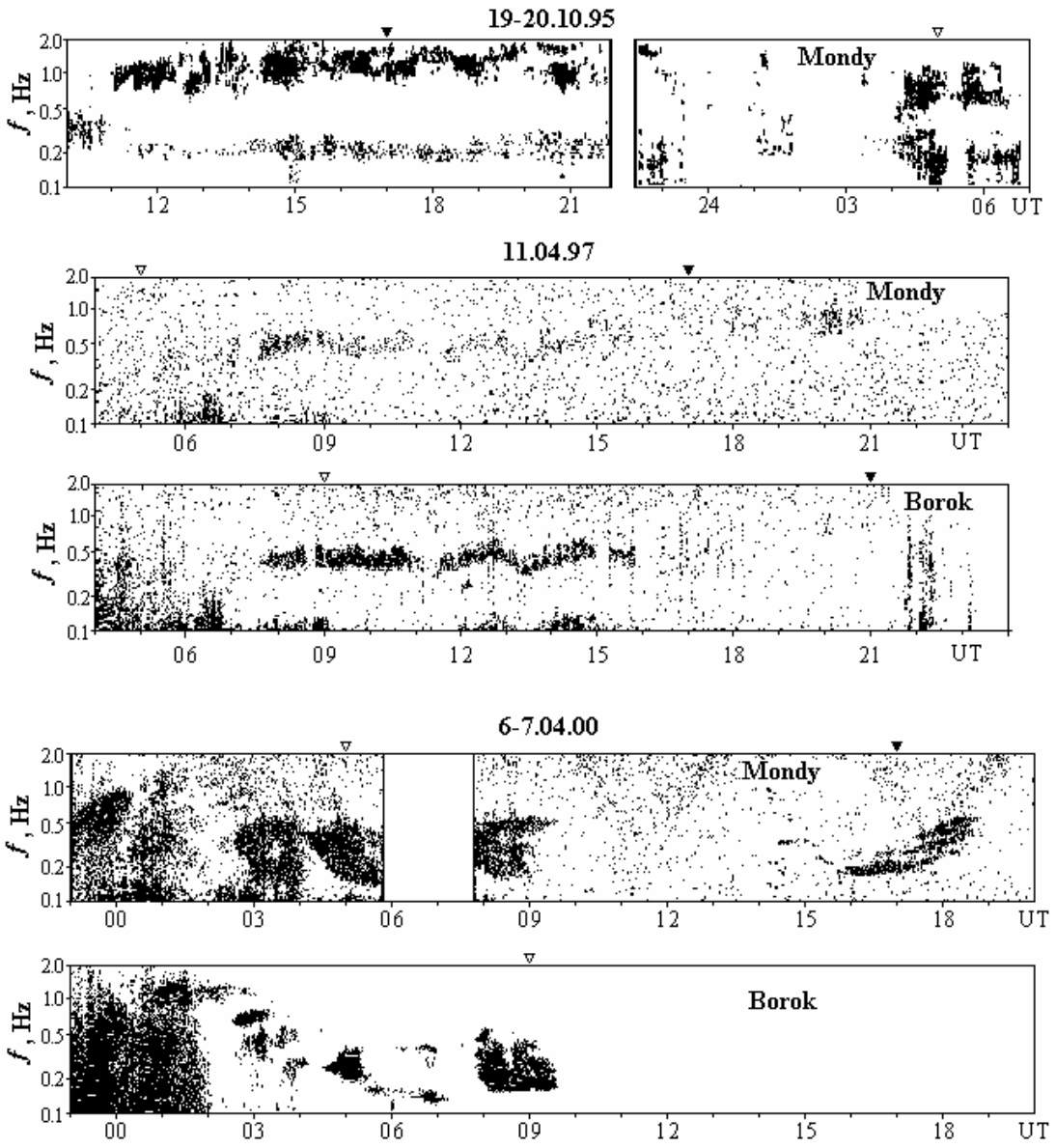


**Figure 1.** The dynamic spectra of geomagnetic pulsations. The time of the observatory's local noon and midnight is pointed by white and black triangular accordingly.

recordings permit us to attribute these pulsations to Pc1. The pulsations have amplitudes from a few nT to several hundred nT and are observed in all MLT sectors.

### 3. Geomagnetic activity temporal variations

Time variations of the $D_{st}$ and Kp–indices for the storms accompanied by long-lasting series of Pc1 are presented on three left-hand panels in Figure 2. For the sake of comparison, the $D_{st}$(UT) and Kp(UT) –dependencies are plotted at the right for the storms with no mid-latitude Pc1. The corresponding dates are indicated in the panels. Dark horizontal rectangles show the intervals of Pc1 recording. Open triangles designate local geomagnetic noon of obs. Mondy. The pulsations begin at the storm maximum (April 6-7, 2000) and at the first three hours (October 18–19, 1995 and April 10–12, 1997) of the storm recovery phase.

It is evident that the storms accompanied by series of mid-latitude Pc1 (Figure 2, left) have minimum values of $D_{st}$ ranging from ~ –80 to ~ –300 nT, and maximum

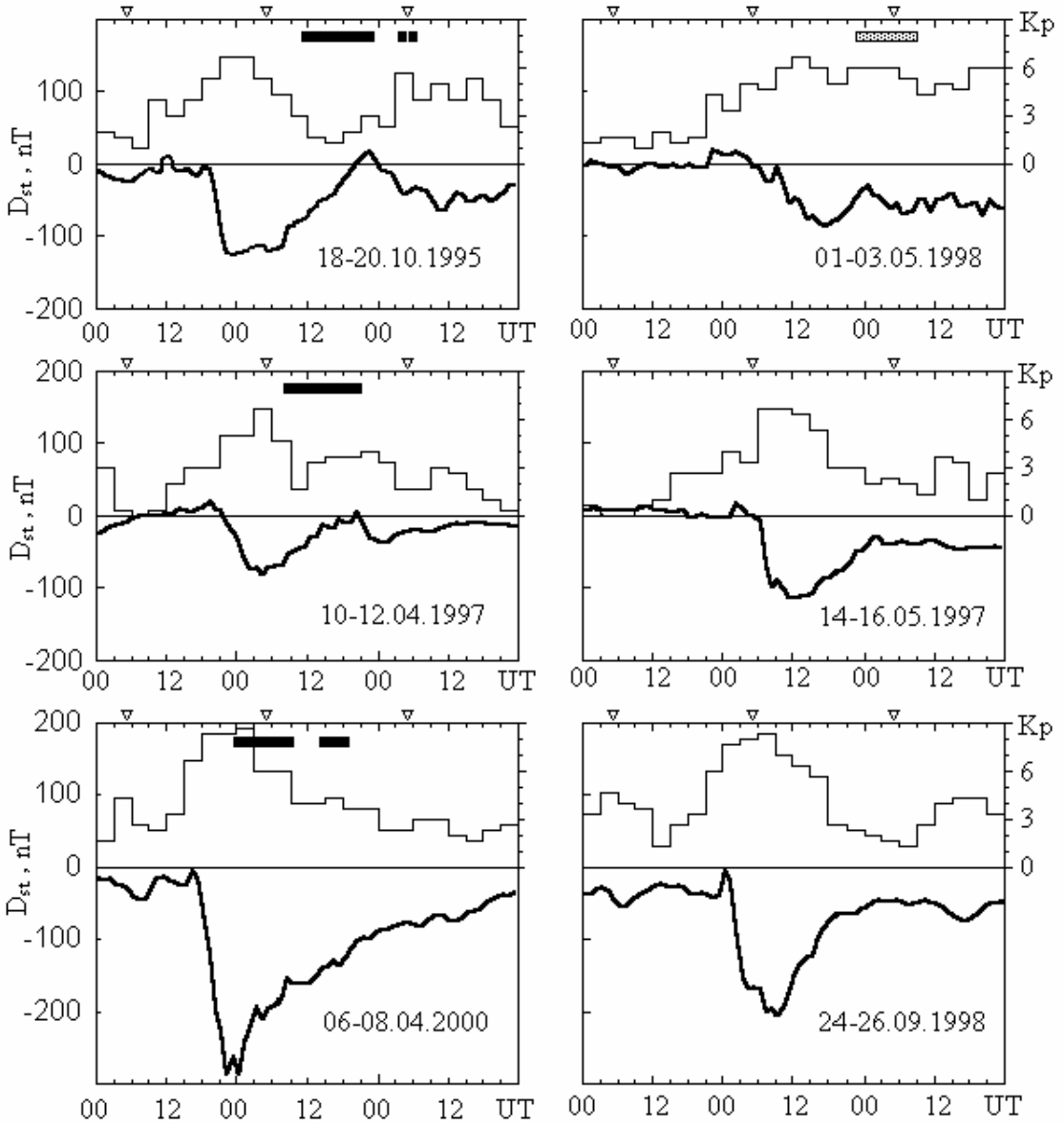


**Figure 2.** Temporal variations of Kp and $D_{st}$–indices during six geomagnetic storms.

values of Kp from ~7 to ~9. Note that identical characteristics correspond to the storms that are unaccompanied by series of Pc1 (Figure 2, right). Consequently, the storm intensity and the level of magnetic disturbance do not have a clear influence on the fact of presence or absence of series of Pc1 in the maximum and in the early stage of ring current decay.

## 4. Interplanetary conditions

We compare the characteristics of large-scale solar wind inhomogeneities that cause magnetic storms with the presence or absence of long-lasting Pc1 intervals in mid-latitudes. Three left-handed and three right-handed panels in Figure 3, respectively, present the corresponding (to these storms) variations of the two most geoeffective parameters of the interplanetary medium: solar wind dynamic pressure, and the $B_z$–component of the interplanetary magnetic field (IMF), constructed on the basis of the data from the WIND spacecraft. The values of $P_{SW}$ and $B_z$, obtained by IMP8, are shown by points instead of the missing WIND data, on the 14–16.05.97 panel of Figure 3 for the interval 14:21 – 16:14 UT of May 15. In the upper part of the panels, in accordance with the designations used in Figure 2, dark rectangles indicate series of Pc1.

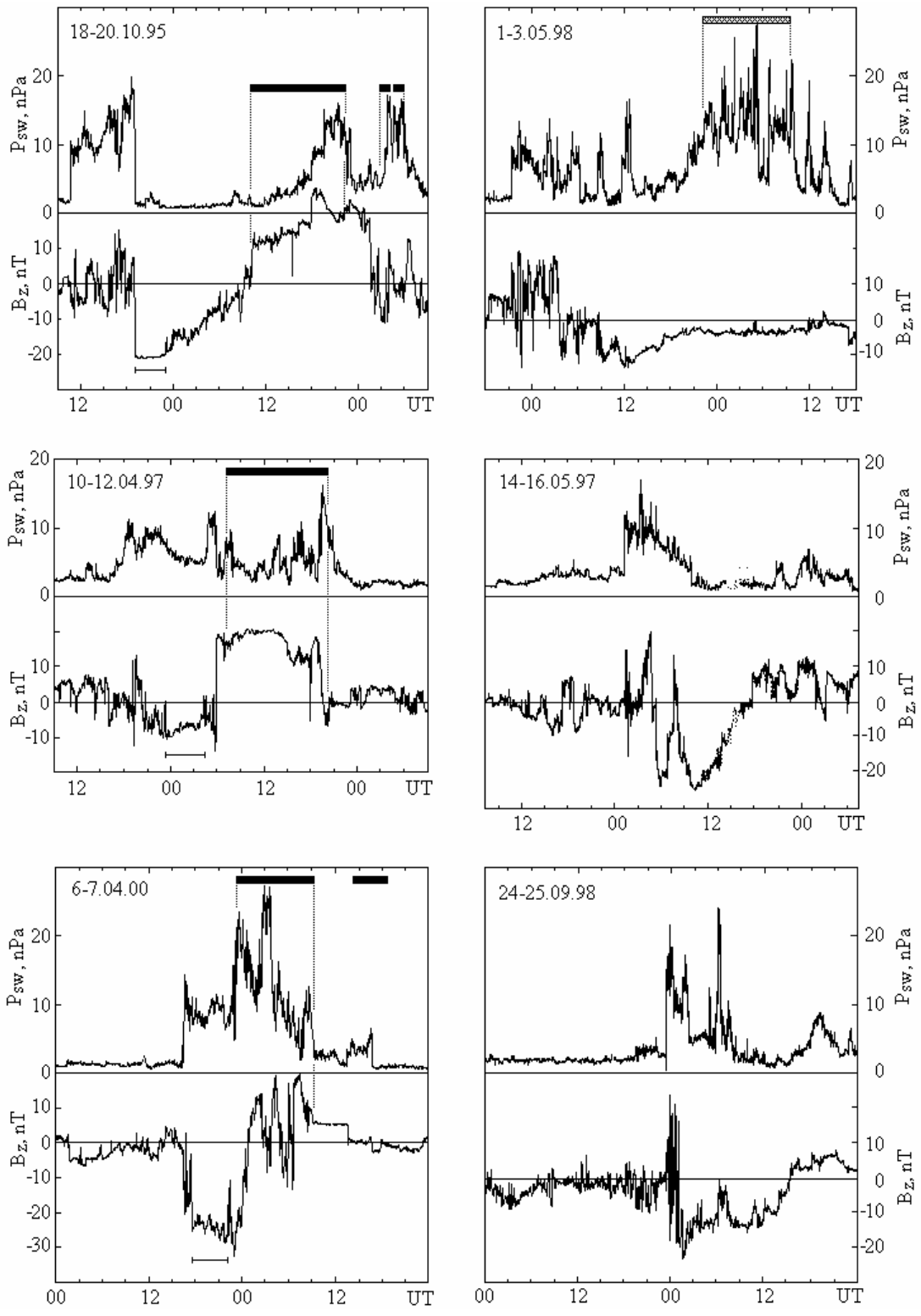


**Figure 3.** Temporal variations of the IMF $B_z$-component and solar wind dynamic pressure ($P_{SW}$).

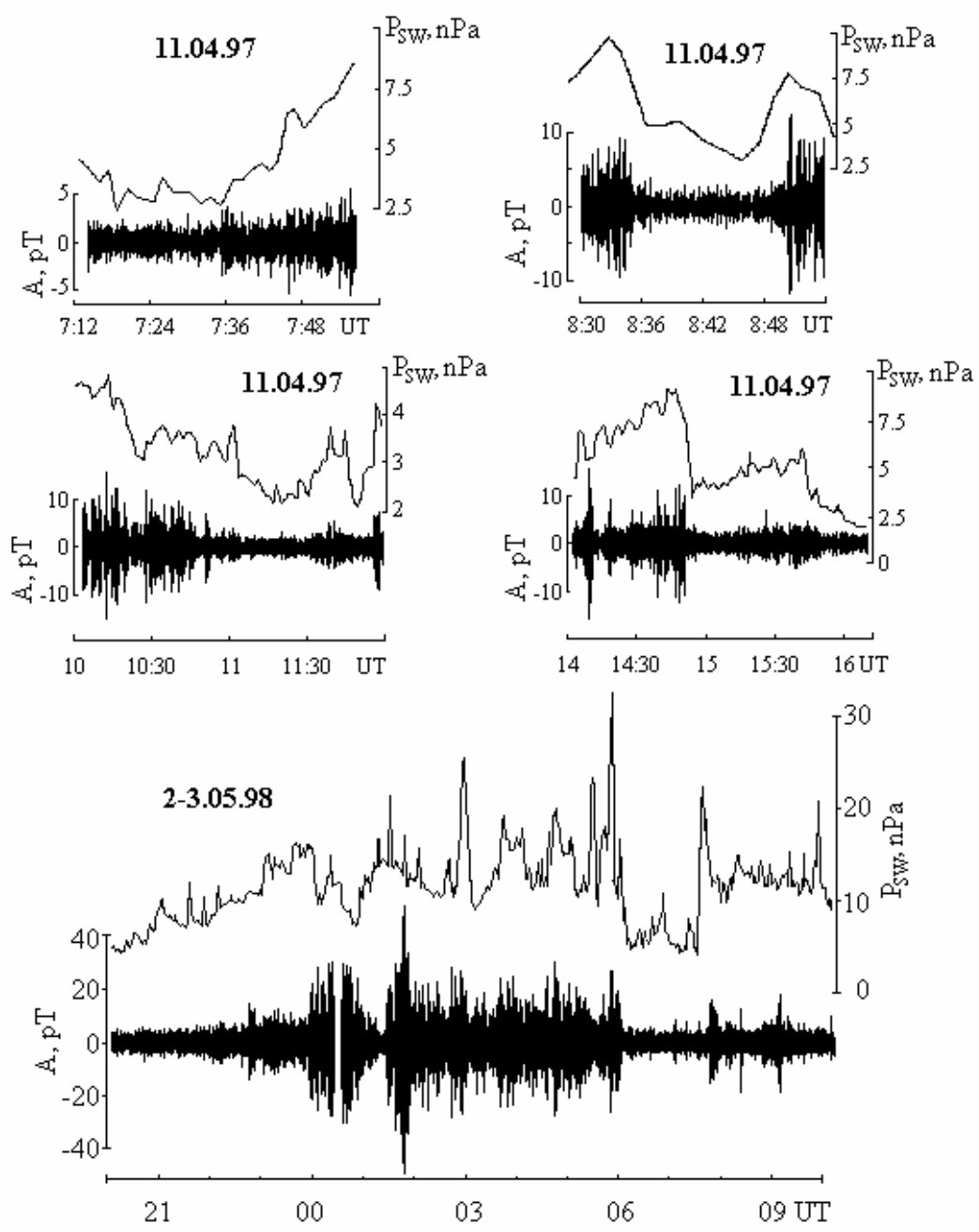


**Figure 4.** Examples of synchronous $P_{SW}$ and $A$ (Pc1 and Pc2 amplitude envelop) variations.

When constructing Figure 3, we took into account the propagation time of solar wind plasma from WIND to IMP8 and from WIND to the subsolar point of the magnetosphere.

Vertical dashed lines in Figure 3 show the boundaries of structures of interplanetary space that are responsible for the generation of mid-latitude Pc1. It is seen that the intervals of recording series of Pc1 in mid-latitudes correspond to regions of increasing or pulsating $P_{SW}$. The $P_{SW}$ structures follow the regions of the quasi-stationary southward $B_z$-component of the IMF, the standard deviations of $B_z$ in which do not exceed 15% of the mean values. The duration of recording the regions of the quasi-stationary $B_z < 0$ (it is shown as a horizontal line segment at the bottom of the $B_z$(UT) function) is 4.5 hours or longer in these cases. Note that interplanetary structures with increasing or non-monotonically varying dynamic pressure are also present on the

$P_{SW}$(UT)-dependencies plotted in the right-hand panels. In these cases, however, the areas of increasing $P_{SW}$ follow the regions of the strongly varying $B_z$-component of the IMF and are not accompanied by the occurrence of Pc1 in mid-latitudes. The exception is the May 1–3, 1998 storm that developed at the background of the smoothly increasing and weakly fluctuating $B_z$–component. According to the data from obs. Mondy, in this storm the increase of $P_{SW}$ corresponds to pulsations of the Pc2 frequency range, shown in Figure 3 by the shaded rectangle.

## 5. Amplitude modulation

In the events under consideration, the modulation effect of the mid-latitude Pc1 activity by solar wind dynamic pressure fluctuations shows up as a correlation between the occurrence or enhancement (disappearance or attenuation) of the pulsations and the increase (decrease) of $P_{SW}$. This correlation is most clearly pronounced around the noon meridian where there is a detailed correspondence between time variations of the pulsation amplitude envelope (A) and $P_{SW}$–variations. Examples illustrating the similarity of the $A$(UT) and $P_{SW}$(UT)-dependencies for the April 10-11, 1997 storm are presented in Figure 4. Note that a correlation between $A$(UT) and $P_{SW}$(UT) is observed not only for Pc1, shown in Figure 1, but also for Pc2 accompanying the May 1–3, 1998 storm.

## 6. Conclusion

It has been shown that the generation of long-lasting series of mid-latitude Pc1, observed in the maximum and in the early recovery phase of the magnetic storm, occurs during the interaction of the Earth's magnetosphere with regions of increased solar wind dynamic pressure. The intensity of mid-latitude pulsations within series is modulated by changes in solar wind dynamic pressure, which shows up most conspicuously in the dayside sector of the magnetosphere.

The origin of the pulsations under investigation is similar in these features to the nature of the wave phenomena described in the Introduction and presented in [*Anderson and Hamilton*, 1993; *Kangas et al*., 1986; *Guglielmi et al*., 2000]. However, unlike the cited references, long-lasting Pc1 may appear in mid-latitudes due to compression of the magnetosphere only under the condition that the increase of $P_{SW}$ is preceded by the region of the quasi-stationary negative $B_z$–component of the IMF that interacts with the Earth's magnetosphere for 4.5 hours or longer.

Our results show that the generation of long-lasting series of mid-latitude Pc1 in the maximum and in the early recovery phase of the magnetic storm requires an intense ring current penetrating inward the inner Earth's magnetosphere during enhanced magnetospheric convection.

The most probable source of pulsations under these conditions will be provided by the so-called "nose structures" produced in the inner ring current region adjacent to the plasmapause. "Nose structures" with a non-monotonic energy distribution of ring current ions were detected in [*Smith and Hoffman*, 1974] and calculated numerically in [*Zolotukhina and Bondarenko*, 1976]. Besides, for the waves to be recorded on the ground, it is necessary that the plasmapause (as the waveguide) lies over the observation point. Model calculations show that in the storm-time events considered in this study, which are accompanied by the generation of Pc1, the "nose structures" and the plasmapause could form at the Mondy and Borok observatories' latitudes.

## References

Anderson, B. J., D. C. Hamilton, Electromagnetic ion cyclotron waves stimulated by modest magnetospheric compressions, *J. Geophys. Res., 98*, 11369, 1993.

Guglielmi, A., J. Kangas, J. Kultima, A. Potapov, An increase in Pc1 wave activity prior to magnetic sudden impulses, *J. Geophys. Res., 105*, 25185, 2000.

Kangas, J., A. Aikio, J. V. Olson, Multistation correlation spectra associated with sudden impulses, *Planet. Space Sci., 34*, 543, 1986.

Smith, P. H., R. A. Hoffman, Direct observation in the dusk hours of the characteristics of the storm time ring current particles during the beginning of magnetic storms, *J. Geophys. Res., 79*, 966, 1974.

Zolotukhina, N. A., N. M. Bondarenko, Formation of the energy spectrum of particles in the drifting process from the tail deep into the magnetosphere, in *Issledovaniya po geomagnetizmu, aeronomii i fizike Solntsa, 39*, Moscow: *Nauka, 3*, 1975.

AURORAL PHENOMENA AND SOLAR-TERRESTRIAL RELATIONS
PROCEEDINGS OF THE CONFERENCE IN MEMORY OF YURI GALPERIN, 3-7 FEBRUARY 2003

# Solar wind – jovian magnetosphere coupling

E. S. Belenkaya

Institute of Nuclear Physics, Moscow State University, 119992, Moscow, Russia.

**Abstract.** A constructed model of the jovian magnetosphere is presented. The magnetospheric magnetic field consists of the planet dipole field, the field of the magnetotail current sheet, and the magnetodisc field. Magnetic fields of all magnetospheric sources are screened by the magnetopause currents. Interaction of the jovian magnetosphere with the solar wind magnetic field is considered. The purpose of this work is to study, using the magnetospheric magnetic field model, the electric fields, plasma motions, and auroral phenomena caused by the unipolar Jupiter's inductor and the solar wind MHD generator.

## 1. Introduction

The cool internal plasma in Jupiter's magnetosphere originates mainly from Io. This is one of the most important features of the jovian magnetosphere. Besides that, the plasma dynamics of the jovian inner and middle magnetosphere is driven by rotational forces. Pioneer 10, 11, Voyager 1, 2, Ulysses and Galileo reported corotational flow in the low-latitude regions of the Jupiter's magnetosphere, however, its rate was below that of rigid corotation for $r \geq 20R_J$ [*Hawkins et al.*, 1998].

The influence of the interplanetary magnetic field (IMF) on the jovian magnetosphere is revealed. Voyager 1 and 2 detected signatures of magnetic reconnection in the nightside of Jupiter's magnetosphere [*Nishida*, 1983]. *Goertz et al.* [1976], investigating the outbound Pioneer 10 pass, found the existence of field lines connected with IMF. The Ulysses observations also provide evidence for reconnection when the spacecraft reached open field lines most likely in the high-latitude cusp [*Smith and Wenzel*, 1993].

For this reason, a global model of the jovian magnetospheric field is needed, which is valid not only in the equatorial plane and near the planet, as most of the existing models are [*Hill et al.*, 1974; *Barish and Smith*, 1975; *Smith et al.*, 1975; *Beard and Jackson*, 1976; *Goertz*, 1976*a*, 1976*b*, 1979; *Engle and Beard*, 1980; *Acuna et al.*, 1983; *Connerney et al.,* 1981, 1998; *Khurana*, 1997], but also at high-latitudes, in the cusp, and in the outer regions of the magnetosphere, and which includes the IMF effects. This model should allow mapping of the electric potential along the high-conducting field lines to any point of the magnetosphere and ionosphere.

## 2. Short description of the model

The model presented here includes internal magnetospheric magnetic field sources screened by the magnetopause currents, and the IMF penetrated into the magnetosphere. Utilizing the approach used in the Earth's paraboloid model [*Alexeev*, 1986] we can construct a model of the jovian magnetosphere taking into account its individual characteristics. The magnetospheric magnetic field, $\mathbf{B}_m$, can be regarded as the sum of contributions from several sources: $\mathbf{B}_m = \mathbf{B}_d + \mathbf{B}_{sd} + \mathbf{B}_{TS} + \mathbf{b}k_J\mathbf{B}_{IMF} + \mathbf{B}_{MD} + \mathbf{B}_{sMD}$. Here $\mathbf{B}_d$ is Jupiter's dipole magnetic field; $\mathbf{B}_{sd}$ is the field of the currents on the magnetopause shielding the dipole field; $\mathbf{B}_{TS}$ is the field of the magnetospheric tail current system including the cross-tail currents and their closure currents on the magnetopause; $\mathbf{b}$ is a portion of the interplanetary magnetic field, $\mathbf{B}_{IMF}$, penetrating into the magnetosphere (the magnitude of $\mathbf{b}$ is about a factor of $k_J$ less than the $\mathbf{B}_{IMF}$); $\mathbf{B}_{MD}$ is the field of the magnetodisc currents; and $\mathbf{B}_{sMD}$ is the field of the currents on the magnetopause shielding the magnetodisc current field.

To calculate the magnetospheric magnetic field, the input parameters of the model should be defined: the distance from Jupiter's center to the subsolar point of the magnetopause, $R_{ss} = 100R_J$; the jovicentric distances to the inner, $R_{D2} = 18.4R_J$, and outer, $R_{D1} = 92.07R_J$, edges of the magnetodisc, respectively; the magnitude of the magnetic field created by the disc currents at the outer edge of the magnetodisc, $B_{DC} = 2.5$ nT; the distance from the planet's center to the inner edge of the magnetospheric tail current sheet, $R_2 = 65R_J$; the magnitude of the field of the tail currents at the inner edge of the tail current sheet, $B_t = -2.5$ nT.

The continuity equations for the magnetic field and electric current density: div$\mathbf{B} = 0$, div$\mathbf{j} = 0$ are valid for all model calculations. Here we will consider only the

dipole term in the representation of the internal jovian field. Moreover, we also neglect the 9.6° offset between Jupiter's magnetic dipole axis and the spin axis. As noted by *Hill*, [2001], the corrections due to dipole tilt and offset are not large, and the nondipole terms are ignorable relative to the dipole for $r >> R_J$. The jovian magnetic moment points northward, while the Earth's one – southward.

$\mathbf{B}_{sd}$ and $\mathbf{B}_{TS}$ out of the current regions (their thickness is assumed to be infinitesimal) are determined by the scalar potentials $V_{sd}$ and $V_{TS}$, respectively. $V_{sd}$ is an expansion in terms of Legendre polynomials for $r < R_{ss}$, and an expansion into a series of Bessel functions on the nightside for $r >> R_{ss}$. The scalar potential $V_{TS}$ is also an expansion into a series of Bessel functions.

In presented model, the axially symmetric current of the magnetodisc does not introduce an azimuthal magnetic field. Actually, a real current sheet structure is too complex and dynamic for modeling by any simple steady current. However, most of existing models do it. The characteristic features of the magnetodisc structure (the magnitude of the field decreases with the distance from Jupiter more slowly than for a dipole field and the direction of the field near the equatorial plane is radial) are reflected in our model. The radial magnetic field is associated with the azimuthal magnetodisc current, $\mathbf{j}_{MD\varphi}$, existing only inside the disc and directed to dusk in the dayside, and to dawn in the nightside (the azimuthal angle $\varphi$ is counted in the planet rotation direction). The radial dependence of this current is determined from the magnetic field observations. Following *Barish and Smith* [1975] and *Beard and Jackson* [1976], we assume the $r^{-2}$ current disc dependence.

The vector potential of the magnetodisc magnetic field is found in the form of an expansion in terms of associated Legendre polynomial functions. Model calculations show that the effective magnetic moment of the magnetodisc field, $M_{MD}$, exceeds Jupiter's dipole moment, $M_J$, by a factor ~ 2.6. The total model azimuthal current in the magnetodisc can be estimated as ~ $10^8$ A. The corresponding values in the *Connerney et al*. [1981] model is ~ $3 \cdot 10^8$ A.

The magnetopause is approximated by a paraboloid of revolution. The equation for the paraboloid in jovian solar–magnetospheric coordinates where the X–axis is directed to the Sun, $M_J$ is in the XZ plane, and Y points to dusk is of the form: $x/R_{ss} = 1 - (y^2 + z^2)/2\ R^2_{ss}$. Analysing the results of *Huddleston et al.* [1998] investigation of the average location and shape of the jovian magnetopause, we found that our approximation gives a rather rough but appropriate description of the magnetospheric boundary. *Joy et al*. [2002] derived a three-dimensional model of the jovian magnetopause by combining spacecraft observations with boundary characteristics inferred from a MHD simulation. Their magnetopause surface was approximated by a second order polynomial, and simulation results support our approach especially up to $200–250 R_J$ downstream.

## 3. Electric field caused by the planet's rotation

*Hill* [1979] wrote that the jovian atmosphere provides a viscous transfer of momentum from the rotating surface of the planet up into the ionosphere. The jovian magnetosphere tends to corotate with the planet because it is coupled electrodynamically to the ionosphere by highly conducting magnetic field lines. The region of rigid corotation is characterized by the dipole jovian magnetic field $\mathbf{B}_{d.}$ The corresponding electric potential of rigid corotation is $U_{rig} = B_{0J}\Omega_J (R^3_J/r) \sin^2 \theta$. In the equatorial plane $\theta = \pi/2$, $r = L$ and $U_{rig} = B_{0J}\Omega_J (R^3_J/L)$ for $L \le R_{D2}$. It is supposed that beyond $R_{D2}$ the partial corotation takes place. Due to the high field-aligned conductivity, the magnetic field lines are assumed to be equipotentials.

Summarizing observations by *Smith et al*. [1974], *Kane et al*. [1992; 1995; 1999], *Cheng and Decker* [1991], Cheng [1992], *Laxton et al*. [1997] we suggest that in the equatorial section of the jovian magnetosphere, the plasma corotates with an effective angular velocity $\Omega = \gamma\Omega_J$, where $\gamma = 1$ for $L \le R_{D2}$; $\gamma = 0.5$ for $R_{D2} < L \le R_{D1}$, $\gamma = 0.2$ for $R_{D1} < L \le R_c$, and $\gamma = 0$ for $L > R_c$, where $R_c$ is the equatorial boundary of the corotation region, beyond which the plasma does not even approximately corotate. At noon $R_c$ may coincide with the distance to the subsolar point $R_{ss}$ or with the equatorial distance to the last closed field line. At the other *LT*, $R_c$ is roughly approximated by the equatorial projection of the constant ionospheric latitude, which coincides with the footpoint of the noon field line with $L = R_c$.

Taking into account the differential rotation just described and the high conductivity of the magnetic field lines, we can correct the expression for the ionospheric rigid corotation electric potential including the feedback of the magnetosphere. So, the corotation electric potential at the ionospheric level can be written as

$$U_{cor} = \gamma\ B_{0J}\ \Omega_J R^2_J \sin^2 \theta + C = \gamma k_1 \sin^2 \theta + C,$$
$$k_1 = B_{0J}\ \Omega_J R^2_J = 377 \cdot\cdot 10^6\ V, \qquad (1)$$

where constants $\gamma$ and $C$ depend on the equatorial jovicentric distance L of the magnetic field line with the footpoint polar angle $\theta$. Constant $C$ provides potential continuity at the boundaries between the regions of different rotation regimes. We chose $C = 0$ for the region where corotation breaks down completely (for the region mapping in the equatorial plane to $L \ge R_c$).

## 4. Electric field caused by the solar wind MHD-generator

In spite of the large jovian dipole moment and strong magnetodisc field, a penetrating solar wind magnetic field of very small strength is significant for the global magnetospheric field line topology. We assume that $\mathbf{b} = k_J\mathbf{B}_{IMF}$, and $\mathbf{E} = k_J\mathbf{E}_{IMF}$ [*Alexeev*, 1986], where $\mathbf{B}_{IMF}$ and $\mathbf{E}_{IMF}$ are the undisturbed interplanetary magnetic and electric fields, respectively, upstream of the magnetopause, and **b** and **E** are their portions penetrating into the magnetosphere.

The electric potential generated in the jovian magnetosphere by the solar wind, $U_{sw}$, is

$$U_{sw} = k_2 y, \quad k_2 = k_J V_{SW} B_{IMFz} R_J, \qquad (2)$$

where y is measured in $R_J$. Most authors, following *Kennel and Coroniti* [1977], assume that the screening coefficient at the jovian magnetopause $k_J = 0.1$ as for the case of the Earth. The actual value of $k_J$ is not reliable known at present. In the next section we consider the magnetospheric field structure and electric field patterns generated by corotation and by the solar wind MHD–generator for different IMF.

## 5. The jovian magnetosphere for southward IMF

From Equation (1) it follows that lines of constant jovian latitude are equipotentials of the corotation elecrtic field. For southward IMF, these corotation equipotentials in the equatorial plane form a twin-vortical system with opposite senses of rotation (solid curves in Figure 1).

The electric potential distribution in Figure 1 is calculated for southward IMF with components: $B_{IMFx} = -0.26$ nT, $B_{IMFy} = 0$, $B_{IMFz} = -0.5$ nT and $k_J = 0.8$. The curve which marks the second distant vortex corresponds to the latitude −86° and to the electric corotation potential $U_{cor}$ =0; the ionospheric latitudes and electric corotation potentials for the curves of the first, nearest, vortex are shown in Figure 1.

Due to arising of the temporary field-aligned current along each equipotential magnetic field line, the equal potentials will be reached at the field line roots in a steady state. The same potential will be set up at the field line's equatorial crossing point.

For rigid corotation the field-aligned currents are equal to zero. When plasma moves at a different rate at some part of magnetic field line, the corresponding electric field there differs from that for rigid corotation, and arising field-aligned currents try to restore the equipotentiality of the magnetic field line. If the charge density cannot provide the necessary value of the current, the field-aligned voltages are required. At the field lines with maximum angular plasma velocity drop, the maximum field-aligned voltages occur. In our model, the maximum field-aligned potential drop arises at the ionospheric latitudes corresponding to the inner edge of the magnetodisc.

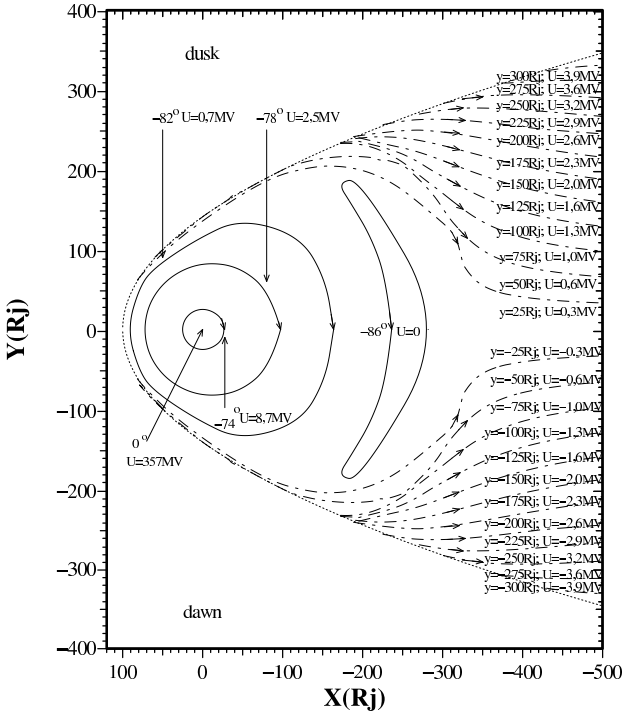


**Figure 1.** Equatorial projection of the corotation and solar wind electric field equipotentials.

The dashed-dotted curves in Figure 1 are the solar wind electric equipotentials: $y=const$ with the step $\delta y$ = 25 $R_J$ ($\delta U$ = 0.3 MV) mapped from the magnetopause to equatorial magnetosphere. The corresponding convection is directed tailward. The magnetopause is marked by the dotted curve.

For southward IMF, open field lines intersect the jovian equatorial magnetosphere. Our calculations show (see Figure 1) that a combination of corotation and tailward flows arises in the equatorial jovian magnetosphere for southward IMF. As a result, the anti-corotational and anti-sunward flows occur in the dawn sector, and anti-sunward flows in the same sense as corotation are formed in the dusk sector.

The influence of the southward IMF on the jovian magnetosphere significantly increases with the growth of $k_J$. However, the ionospheric projection of the magnetodisc (from ±74° to ±75° –76°) and of the final corotational boundary (±84°) is almost insensitive to the IMF penetration coefficient. For southward IMF at high jovian ionospheric latitudes (≥84° – 85°) the corotation is insignificant.

Twin–vortical high-latitude flow cells are formed on the open field lines in both polar caps due to reconnection with southward IMF. In Figure 2 the convection on the open field lines of the northern jovian polar cap is shown for the southward IMF: $B_{IMFx}$ = –0.26 nT, $B_{IMFy}$ = 0, $B_{IMFz}$ = –0.5 nT and $k_J$ = 0.8. For the Earth, at the low shear between the magnetosheath and magnetospheric fields, the convection on open field lines in both polar caps also has a twin-vortical structure with sunward flow near the cusp projection [*Belenkaya*, 1998]. Two vortices should also be excited near the cusp on high-latitude closed field lines (not shown in Figure 2).

The corotation braking in the equatorial magnetosphere leads to the partial stopping of a connected part of the ionosphere (this part rotates at the same rate, as implied by the mapped electric field). In particular, the region of the magnetospheric equatorial plane, where corotation is absent, maps to that zone of the ionosphere, which is prevented from rotating by the magnetosphere. For each constant latitude $\theta$, parameters $\gamma$ and $C$ (see Eq. (1)) are determined by the noon value of L – the equatorial point of the noon field line with the root co-latitude $\theta$. It follows from Figure 1 that the

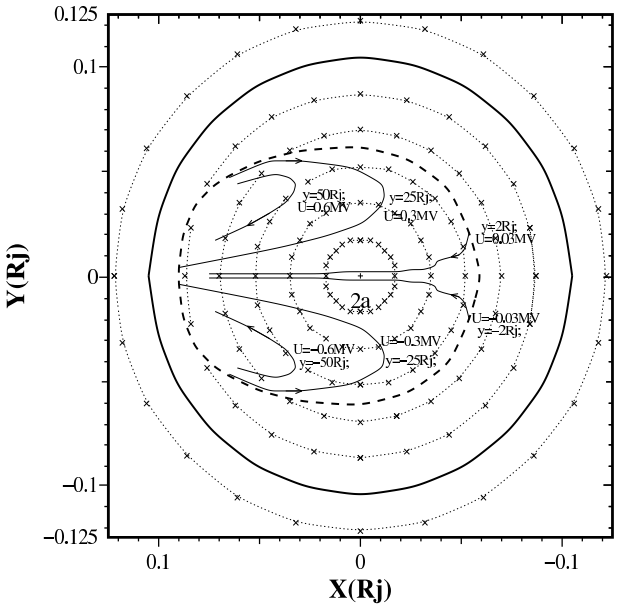


**Figure 2.** The northern jovian polar cap for southward IMF. Sun is at the left side. Circles dotted with crosses mark the lines of constant latitudes (from 83° to 90°). Dashed curve is the open field line boundary (possessing zero potential). Solid curves are the equipotentials of the solar wind electric field. The potential drop 1.2 MV across the open field line region is applied to the cusp projection (84.8°, 12:00 LT). The bold solid circle is the corotation boundary.

second vortex in the tail is located at $L > R_c$, where plasma does not rotate.

The electric corotation potential for chosen southward IMF with $k_J$ = 0.8 is determined by the constants $\gamma$ and $C$: $\gamma = 0$, $C = 0$ for $0° \le \theta < 6°$; $\gamma = 0.2$, $C = -0.8$ MV for $6° \le \theta < 8°$; $\gamma = 0.5$, $C = -3$ MV for $8° \le \theta < 16°$; $\gamma = 1$, $C = -17.3$ MV for $16° \le \theta \le 90°$.

Field-aligned currents which couple the magnetosphere and ionosphere are directed outwards from the ionosphere into the magnetospheric plasma sheet in the inner part of the region where the angular velocity of the plasma begins to depart from rigid corotation, while reversing at larger distances [*Hill*, 1979]. The main auroral oval is suggested to be connected with the regions of significant upward field-aligned currents [*Hill*, 2001; *Cowley and Bunce*, 2001]. *Cowley and Bunce* [2001] found that the field-aligned currents are directed out of the ionosphere into the current sheet throughout the whole of the middle magnetosphere region, from ~20$R_J$ out to ~100$R_J$ (see also [*Southwood and Kivelson,* 2001]). The angular radius of the auroral zone found by *Connerney et al.* [1981, 1998] and *Cowley and Bunce* [2001] is approximately 16° (see also [*Behannon et al.*, 1981]) with a latitudinal width of the main oval ~1°. In our model the magnetodisc corresponds to co-latitudes ~15–16°; the region in the equatorial magnetosphere where the main auroral processes might occur corresponds to the distances exceeding 18$R_J$ which is in good accordance with the results of *Clarke et al.* [1998] and *Hill* [2001].

For southward IMF, plasma does not corotate at $\theta$<6°, and we suggest that at the latitudes from ~ ±74° to ~ ±84° the auroral glows should partially follow the rotation of the magnetic field but for the higher latitudes their position should be determined by the reconnection effects.

The chosen southward direction of the IMF is close to those (of strength ~ 0.5 nT), which was measured by Ulysses upstream of Jupiter. In contrast with the Voyagers observations, in February 1992 Ulysses during the inbound passage found anti-corotation flow in the outermost low-latitude dawn-noon magnetosphere [*Phillips et al.*, 1993; *Staines et al.*, 1993; *Cowley et al.*, 1993, 1996].

*Phillips et al.* [1993] reported that the coexistence of magnetospheric and magnetosheath-like plasmas was observed by Ulysses in the jovian boundary layer. Encounters with open field lines occurred at the highest magnetic latitudes both inbound and outbound. The azimuthal flow velocity indicated a combination of corotation and tailward flow. As it follows from the analysis of the fluxes and anisotropies of energetic (MeV) ions and electrons measured during the first inbound traversal of the jovian dayside magnetosphere by the Ulysses in February 1992, the low-latitude

magnetopause was locally closed at the time of the spacecraft crossing. It was a tangential discontinuity, as expected for the small magnetic shear case (~20°) [*Edwards et al.*, 1996]. Despite the locally closed nature of the magnetopause, the existence of relativistic electron streaming in the boundary layer located just inside the magnetopause, suggests the intermittent presence of open flux tubes produced by reconnection [*Edwards et al*., 1996]. [*Cowley et al.,* 1993] suggested that the Ulysses data provide primary evidence for the occurrence of solar wind-magnetosphere coupling in the outermost regions of Jupiter's magnetosphere similar to those that occur at Earth. [*Cowley et al.,* 1993] concluded that the open flux tubes in the polar cap are being pulled anti-sunward by the flow of the solar wind and that the observations represent a part of a twin-vortical, high-latitude flow cell. These observations are in good accordance with results of our calculations (see Figures 1, 2).

For $B_{IMFz}$ = −0.5 nT, in the equatorial subsolar magnetosphere, open field lines occupy a region with the radial thickness ~1.2$R_J$ for $k_J$ = 0.1 and 5.3$R_J$ for $k_J$ = 0.8 (for comparison, *Tsyganenko* [2002] found the coefficient for the IMF penetration into the Earth's magnetosphere to be 0.15–0.8). The scale of the anti-corotational region in the noon outer low-latitude magnetosphere can be estimated as 8$R_J$ from the data published by *Desai and Simnett* [1996] and as 6$R_J$ from the data given by *Cowley et al*. [1996]. Both these estimations show that the value of $k_J$ = 0.8 is appropriate for $B_{IMFz}$ = −0.5 nT (the same result could be obtained, for example, for $B_{IMFz}$ ~ −1 nT and $k_J$ = 0.4).

For $k_J$ = 0.8 the large-scale reconnection with $B_{IMFz}$ = −0.5 nT causes the anti-sunward flows in the tail at $R_J$ >300$R_J$ (Figure 1). At the location of the second distant vortex in the equatorial magnetotail, the combination of the radial outflow and flow due to reconnection takes place (both of these flows are not shown in Figure 1). The latter flow consists of the tailward flow near flanks and sunward flow near the X−axis.

## 6. The jovian magnetosphere for northward IMF

Figure 3 presents the calculated magnetic field in the open jovian magnetosphere for the northward IMF. The reconnection occurs at the merging line located in the low latitude magnetopause and in the magnetotail. The IMF components are chosen to be $B_{IMFx}$ = −0.02 nT, $B_{IMFy}$ = 0, $B_{IMFz}$ = 0.5 nT, with $k_J$ close to 1. The neutral line intersects the midnight meridian at x = −130$R_J$. The ionospheric projections of this point have latitudes: 78.05° and −77.59° in the northern and southern midnight hemispheres, respectively. The ionospheric projections of the subsolar point are: 82.17°, 12:00, and −82.33°, 12:00. Our calculations show that for $B_{IMFz}$ > 0 beyond the neutral line the anti-sunward flow exists.

The angular radius of the ionospheric open field line region is of the order of 9° for northward IMF with $k_J$ ~1. The maximum potential drop across the open field line region in the northern polar cap (applied between its dawn and dusk edges) equals to 6 MV. Calculations for northward IMF with $k_J$ ~ 1 give the following values for the constants determining the corotation electric potential (Equation (1)) in the equatorial plane: $\gamma$ = 1, $C$ = –9.2 MV for 0° ≤ $\theta$ < 9°; $\gamma$ = 0.2, $C$ = −1.8 MV for 9° ≤ $\theta$ < 12°; $\gamma$ = 0.5, $C$ = −6,7 for 12° ≤ $\theta$ < 16°; $\gamma$ = 1, $C$ = −21 MV for 16° ≤ $\theta$ ≤ 90°.

For northward IMF, electric field generated by Jupiter's rotation is transmitted along open field lines outward to enforce the corotation of the magnetospheric plasma under assumption that magnetic field lines are perfect conductors. The rigid corotation can exist up to the distance at which the azimuthal speed equals the alfven speed (the so called, alfven distance). Beyond alfven distance the information about rigid corotation can not be transmitted along field lines with the alfven velocity. In the jovian tail lobe the alfven velocity is much higher (~$31\cdot10^3$ km·s$^{-1}$ [*Goldstein et al*., 1985, 1986]), than in the equatorial plane. So, the alfven distance in the Jupiter's tail lobe can be estimated as $2.5\cdot10^3$ $R_J$. As a result, for northward IMF, the corotation along open magnetic field lines can be transmitted up to magnetopause.

In Figure 3 the corotation electric field equipotentials (solid curves) form a vortex structure on the equatorial magnetospheric plane and on the magnetopause (we assume that corotation is stopped just outside the magnetopause [*Belenkaya*, 1996]). Contrary to the case of southward IMF, the corotation exists in the high-latitude ionosphere of both polar caps, because the open field lines connecting with the northward IMF do not intersect the equatorial magnetosphere where strong brake action of the corotation occurs due to the centrifugally driven radial outflow of the iogenic plasma concentrated near the equatorial plane. That is why corotation determines electric field distribution in most of the polar cap. Only in a small spot near the pole (from ~87° to 90°) the anti-sunward convection generated by the solar wind electric field prevails.

The ionospheric projection of the magnetodisc for the chosen northern IMF can be roughly approximated by a ring in the latitudinal range from ~74° to 76°. The corotation boundary in the equatorial plane can be set at ~81° (Figure 3). Thus, again we obtain the similar dimension of the suggested main auroral oval with the angular half width ~16°. *Behannon et al*. [1981] noted that if the polar cap size is estimated from the tail magnetic flux then it is of the order of ~10°; if magnetodisc currents are taken into account, then the

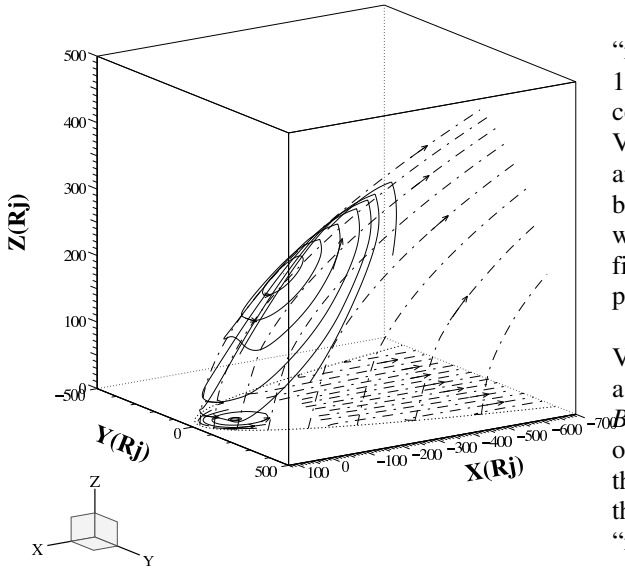


**Figure 3.** Three-dimensional jovian magnetosphere for northward IMF. Electric equipotentials of the corotation (solid curves) and solar wind (dashed-dotted curves) electric fields on the northern magnetopause and on the equatorial plane are shown. The distance between the dashed-dotted curves: $\delta y = 50R_J$ and corresponding $\delta U = 0.75$ MV. For the solid curves on the equatorial plane (from the outer to inner) the latitudes and electric corotation potentials are: 80°, 0.4 MV; 78°, 1.4 MV; 76°, 4.3 MV; 74°, 7.6 MV; 0°, 356 MV, respectively. For the solid curves on the magnetopause (from the outer to inner) the corresponding values are: 81°, 0 MV; 82°, −1.9 MV; 84°, −5.1 MV; 86°, −7.4 MV; 88°, −8.8 MV; 90°, −9.2 MV, respectively.

angular size of the auroral region is approximately ~16°.

A northward IMF was measured by Pioneer 10 inbound on 27 November 1973 [*Walker and Russell,* 1985; *Huddleston et al*., 1997]. *Huddleston et al.* [1997] emphasized that during the Voyager 1 inbound passage on 2 March 1979 the magnetic shear was large at the prenoon magnetopause and the IMF magnitude was reasonably stable. So, the low-latitude reconnection could occur.

Based on the Pioneer 10 and Voyagers measurements, *Cheng and Krimigis* [1989] stated that throughout most of the jovian magnetodisc plasma sheet, the corotation-dominated flow with roughly constant speed ~500 km/s is maintained (out to the dayside magnetopause and out to ~150$R_J$ on the nightside). *Kane et al*. [1992] also noted that during the Voyager inbound traversals the equatorial flow was in the corotation direction throughout much of the Jovian magnetosphere and anti-corotation flows were not observed.

Beyond ~150$R_J$ a nightside outflow termed the "magnetospheric wind" was discovered [*Krimigis et al.,* 1979; *Cheng and Krimigis,* 1989]. *Nishida* [1983] concluded that in the nightside jovian magnetosphere, Voyager 1 and 2 detected signatures of reconnection: the anti-sunward streaming events revealed by Voyagers beyond 150$R_J$ during the predawn outbound passages, were caused by a northward inclination of the magnetic field which suggests that the reconnection was in progress upstream of the observing site.

As it follows from Figure 3, the Pioneer and Voyagers observations can be roughly explained if we assume $B_{IMFz}$ ~0.5 nT and $k_J$ ~1 (or, for example, $B_{IMFz}$ ~1 nT and $k_J$ ~0.5). Our modeling results reproduce observations of the corotation-dominated flow throughout most of the jovian dawn magnetodisc from the dayside magnetopause up to the nightside "magnetospheric wind".

## 7. Conclusions

The global structure of the jovian magnetospheric magnetic field and the large-scale plasma flows is constructed for different IMF orientations and different values of its coefficient of penetration into the magnetosphere. The present model includes the ionosphere-magnetosphere coupling and the solar wind-magnetosphere interaction, which is most significant in the outer and high-latitude magnetosphere.

For southward IMF, from the model calculations it is found that the principal flows throughout the inner and middle magnetosphere are driven by the planetary rotation, and flows caused by the MHD solar wind generator prevail in the outer equatorial magnetosphere, on the polar caps, and in the magnetotail. In the dawn sector of the equatorial magnetosphere, the anti-corotational motion arises. In the ionospheric open field line region of each hemisphere two vortices exist for $B_{IMFx} \neq 0$, $B_{IMFz} < 0$ and one vortex for $B_{IMFx} = 0$, $B_{IMFy} \neq 0$, $B_{IMFz} < 0$.

The anti-corotational and anti-sunward flows in the morning sector of the equatorial magnetosphere and in the prenoon polar caps observed by Ulysses are explained in presented model by reconnection with southward IMF. The existence of such flows during the Ulysses flyby and their absence during the Voyagers and Pioneer 10 flybys may be due to the different orientations of IMF for these events.

For northward IMF, the corotation along open magnetic field lines is transmitted up to the northern and southern magnetopause (we assume that it is stopped just outside it). The corotation exists in the high-latitude ionosphere, on the most part of both polar caps. The corotation electric field equipotentials form a vortex structure in the equatorial magnetosphere. For $B_{IMFz} > 0$,

our model calculations show that contrary to the case of southward IMF, the corotation flow prevails throughout most of the jovian dawn magnetodisc from the dayside magnetopause up to the the nightside, where the tailward motion arises.

These results are in good accordance with the Pioneer 10 and Voyagers measurements of the corotation-dominated flow from the dayside magnetopause to ~150$R_J$ on the nightside, and a nightside outflow termed the "magnetospheric wind" beyond ~ −150$R_J$.

**Acknowledgments.** This work was supported partly by the RFBR Grant 01-05-65003. The author thanks I. I. Alexeev for valuable discussions.

## References

Acuna, M. H., K. W. Behannon, and J. E. P. Connerney, Jupiter's magnetic field and magnetosphere, in *Physics of the Jovian Magnetosphere, Cambridge, Plan. Sci. ser*, edited by A.J.Dessler, pp.1-50, Cambridge, Univ. Press, New York, 1983.

Alexeev, I. I., The penetration of interplanetary magnetic and electric fields into the magnetosphere, *J. Geomag. Geoelectr., 38*, 1199, 1986.

Barish, F. D., and R. A. Smith, An analytical model of the Jovian magnetosphere shape, *Geophys. Res. Lett., 2*, 269, 1975.

Beard, D. B., and D. J. Jackson, The Jovian magnetic field and magnetosphere, *J. Geophys. Res., 81*, 3399, 1976.

Behannon, K. W., L. F. Burlaga, and N. F. Ness, The Jovian magnetotail and its current sheet, *J. Geophys. Res., 86*, 8385, 1981.

Belenkaya, E., Generation of the magnetic field at the magnetopauses of the rapidly rotating planets, *J. Geophys. Res., 101*, 41, 1996.

Belenkaya, E., High-latitude ionospheric convection patterns dependent on the variable IMF orientation, J. *Atmosph. and Solar--Terrestrial Physics, 60/13*, 1343, 1998.

Cheng, A. F., A model of convection and corotation in Jupiter's magnetosphere: Ulysses predictions, *Geophys. Res. Lett., 19*, 221, 1992.

Cheng, A. F., and S. M. Krimigis, A model of global convection in Jupiter's magnetosphere, *J. Geophys. Res., 94*, 12003, 1989.

Cheng, A. F., and R. Decker, Nonadiabatic particle motion and corotation lag in the Jovian magnetodisk, *J. Geophys. Res., 96*, 12000, 1991.

Clarke, J. T., G. Ballester, J. Trauger, J. Ajello, W. Pryor, K. Tobiska, J. E. P. Connerney, G. R. Gladstone, J. H. Waite, Jr., L. B. Jaffel, and J. –C. Gerard, Hubble Space Telescope imaging of Jupiter's UV aurora during the Galileo orbiter mission, *J. Geophys. Res., 103*, 20217, 1998.

Connerney, J. E. P., M. H. Acuna, and N. F. Ness, Modeling the Joivian current sheet and inner magnetosphere, *J. Geophys. Res., 86*, 8370, 1981.

Connerney, J. E. P., M. H. Acuna, N. F. Ness, and T. Saton, New models of Jupiter's magnetic field constrained by the Io flux tube footprint, *J. Geophys. Res., 103,* 11929, 1998.

Cowley, S. W., and E. J. Bunch, Origin of the main auroral oval in Jupiter's coupled magnetosphere-ionosphere system, *Planet. Space Sci., 49*, 1067, 2001.

Cowley, S. W., M. K. Dougherty, T. M. Edwards, R. J. Forsyth, R. J. Hynds, and K. Staines, Ulysses observations of anti-sunward flow on Jovian polar cap field lines, *Planet. Space Sci., 41*, 987, 1993.

Cowley, S. W. H, A. Balogh, M. K. Dougherty, M. W. Dunlop, T. M. Edwards, R. J. Forsyth, R. J. Hynds, N. F. Laxton, and K. Staines, Plasma flow in the Jovian magnetosphere and related magnetic effects: Ulysses observations, *J. Geophys. Res., 101*, 15197, 1996.

Desai, M. I. and G. M. Simnett, Solar wind-driven flows in the Jovian magnetosphere, *J. Geophys. Res., 101*, 13115, 1996.

Edwards, T. M., A. Balogh, S. W. H. Cowley, G. Erdos, P. Ferrando, R. J. Forsyth, R. J. Hynds, C. Rastoin, A. Raviart, and K. Staines, Energetic ion and electron observations at Jupiter's dayside magnetopause: Implications for magnetopause location and boundary coupling processes, *Planet. Space. Sci., 44*, 371, 1996.

Engle, I. M., and D. B. Beard, Idealized Jovian magnetosphere shape and field, *J. Geophys. Res., 85*, 579, 1980.

Goertz, C. K., Jupiter's magnetosphere: Particles and fields, in Jupiter the Giant Planet, edited by T. Gehrels, pp. 23-58, University of Arizona Press, Tucson, Arizona, 1976*a*.

Goertz, C. K., The current sheet in Jupiter's magnetosphere, *J. Geophys. Res., 81*, 3368, 1976*b*.

Goertz, C. K., The Jovian magnetodisk, *Planet. Space Sci. Rev., 23*, 319, 1979.

Goertz, C. K., D. E. Jones, B. A. Randall, E. J. Smith, and M. F. Thomsen, Evidence for open field lines in Jupiter's magnetosphere, *J. Geophys. Res., 81,* 3393, 1976.

Goldstein, M. L., R. P. Lepping, and A. C. .Sittler, Jr., Magnetic field properties of Jupiter's tail at distances from 80 to 7500 Jovian radii, *J. Geophys. Res., 90*, 8223, 1985.

Goldstein, M. L., R. P. Lepping, and A. C. Sittler, Jr., Reply, *J. Geophys. Res., 91*, 7133, 1986.

Hawkins III, S. E., A. F. Cheng, and L. J. Lanzerotti, Bulk flows of hot plasma in the Jovian magnetosphere: A model of anisotropic fluxes of energetic ions, *J. Geophys. Res., 103*, E9, 20031, 1998.

Hill, T. W., Inertial limit of corotation, *J. Geophys. Res., 84*, 6554, 1979.

Hill, T. W., The Jovian auroral oval, *J. Geophys. Res., 106*, 8101, 2001.

Hill, T. W., A. J. Dessler, and F. C. Michel, Configuration of the Jovian magnetosphere, *Geophys. Res. Lett., 1*, 3, 1974.

Huddleston, D. E., C. T. Russell, G. Le, and A. Szabo, Magnetopause structure and the role of reconnection at the outer planets, *J. Geophys. Res., 102*, 24289, 1997.

Huddleston, D. E., C. T .Russell, M. G. Kivelson, K. K. Khurana, and L. Bennet, Location and shape of the Jovian magnetopause and bow shock, *J. Geophys. Res., 103*, 20075, 1998.

Joy, S. P., M. G. Kivelson, R. J. Walker, K. K. Khurana, C. T. Russell, T. Ogino, Probabilistic models of the Jovian magnetopause and bow shock locations, *J. Geophys. Res., 107*, N A10, 1309, doi:10.1029/2001JA009146, 2002.

Kane, M., B. H. Mauk, E. P. Keath, and S. M. Krimigis, A convected kappa distribution model for not ions in the Jovian magnetodisk, *Geophys. Res. Lett., 19*, 1435, 1992.

Kane, M., B. H. Mauk, E. P. Keath, and S. M. Krimigis, Hot ions in Jupiter's magnetodisk: A model for Voyager 2 low energy charged particle measurements, *J. Geophys. Res., 100*, 19473, 1995.

Kane, M., D. J. Williams, B. H. Mauk, R. W. McEntire, and E. C. Roelof, Galileo energetic particles detector measurements of hot ions in the neutral sheet region of Jupiter's magnetodisk, *Geophys. Res. Lett., 26*, 5, 1999.

Kennel, C. F., and F. V. Coroniti, Jupiter's magnetosphere, *Ann. Rev. Astron. Astrophys., 15*, 389, 1977.

Khurana, K. K., Euler potential models of Jupiter's magnetospheric field, *J. Geophys. Res., 102*, 11295, 1997.

Krimigis, S. M., T. P. Armstrong, M., W. I. Axford, C. O. Bostrom, C. Y. Fan, G. Gloeckler, L. J. Lanzerotti, E. P. Keath, R. D. Zwickl, J. F. Carbary, and D. C. Hamilton, Hot plasma environment at Jupiter: Voyager 2 results, *Science, 206*, 977, 1979.

Laxton, N. F., A. Balogh, S. W. H. Cowley, M. W. Dunlop, R. J. Forsyth, R. J. Hynds, and K. Staines, Origins of the first-order anisotropy of ~1 MeV protons in the Jovian magnetosphere during the Ulysses flyby: Flux gradients and plasma flows, *Planet. Space Sci., 45*, 1143, 1997.

Nishida, A., Reconnection in the Jovian magnetosphere, *Geophys. Res. Lett., 10,* 451–454, 1983.

Smith, E. J., and K. P. Wenzel, Introduction to the Ulysses encounter with Jupiter, *J. Geophys. Res., 98,* 21111, 1993.

Phillips, J. L., S. J. Bame, B. L. Barraclough, D. J. Mc-Comas, R. J. Forsyth, P. Canu, and P. J. Kellog, Ulysses plasma electron observations in the Jovian magnetosphere, *Planet. Space Sci., 41*, 877, 1993.

Smith, E. J., and K. P. Wenzel, Introduction to the Ulysses encounter with Jupiter, *J. Geophys. Res., 98*, 21111, 1993.

Smith, E. J., L. Davis, Jr., D. E. Jones, P. J. Coleman, Jr., D. S. Colburn, P. Dyal, C. P. Sonett, and A. M. A. Frandsen, The planetary magnetic field and magnetosphere of Jupiter: Pioneer 10, *J. Geophys. Res., 79*, 3501, 1974.

Smith, E. J., L. Davis, Jr., D. E. Jones, P. J. Coleman, Jr., D. S. Colburn, P. Dyal, C. P. Sonett, Jupiter's magnetic field, magnetosphere, and interaction with the solar wind: Pioneer 11, Science, 188, 451, 1975.

Southwood, D. J. and M. G. Kivelson, A new perspective concerning the influence of the solar wind on the Jovian magnetosphere, *J. Geophys. Res., 106*, 6123, 2001.

Staines, K., A. Balogh, S. W. H. Cowley, T. M. Edwards, R. J. Forsith, and R. J. Hynds, Ulysses observations of noncorotational flows in the outer dayside Jovian magnetosphere, *Planet. Space Sci., 41*, 931, 1993.

Tsyganenko, N. A., A model of the near magnetosphere with a dawn-dusk asymmetry. 1. Mathematical structure, *J. Geophys. Res., 107*, A8, 10.1029/2001JA000219, 2002.

Walker, R. J., and C. T. Russell, Flux transfer events at the Jovian magnetopause, *J. Geophys. Res., 90*, 7397, 1985.

---

Belenkaya, E. S., Institute of Nuclear Physics, Moscow State University, Moscow, 119899, Russia.

# Diffusive propagation of fast particles in the presence of moving shock

I. S. Petukhov, S. I. Petukhov, S. A. Starodubtsev, and V. E. Timofeev

Yu. G. Shafer Institute of Cosmophysical Research and Aeronomy SB RAS, 31 Lenin Ave., 677891 Yakutsk, Russia

**Abstract.** Temporal dynamics of spectrum shape and spatial distribution of particles, injected with the given spectrum impulsively in the vicinity of a moving plane shock front, has been determined in the framework of an analytic model. The condition to determine a degree of influence of the shock front on the particle propagation has been obtained, in which the magnitude of spatial diffusion coefficient of particles is of primary importance. It is shown that the regular (diffusive) acceleration mechanism affects strongly low-energy particles (an intensity maximum coincides with the shock front; intervals of hard and soft spectrum are formed) and weakly high-energy particles (the time of occurrence of a maximum in the intensity advances significantly an arrival moment of the shock front; a spectrum of particles is not changing). In the events, accompanying by the significant rise of a turbulence level, a degree of influence of the shock front on high-energy particles is subject to variation from weak to strong. It is manifested in the spatial distribution and spectrum form of particles. The dynamics of particle intensity calculated by using the diffusion coefficient and defined by the quasilinear theory for the measured turbulence level, qualitatively corresponds to the solar energetic particle intensity observed.

## 1. Introduction

Solar energetic particles (SEP) in gradually evolving events are generated by shock waves (see, for example, *Reames* [1999] and references therein). The SEP generation region is limited by the solar corona. Proton fluxes of 470 MeV to 21 GeV energies, a maximum of which occurs at the time when the shock in the atmosphere of the Sun reaches heights equal to 5–10 solar radii [*Kahler*, 1994] indicate it. It is also confirmed by the significant advancing of the occurrence time of maximum in the SEP intensity with kinetic energies more than 10 MeV, observed usually in interplanetary space relative to the shock front arrival moment. The change in the SEP acceleration efficiency reflects the spatial dependence of shock intensity on the background alfvenic turbulence levels, which are main factors in the regular acceleration mechanism. These factors are the strongest in the vicinity of the Sun and decrease with the distance from it [*Denskat and Neubaeur*, 1982]. Model calculations of the particles acceleration by the regular mechanism under the conditions, typical for the solar corona, show that the time needed for the shock to pass the solar atmosphere is quite sufficient to form the particle spectrum corresponding to the SEP characteristics observed [*Berezhko et al.,* 2001*a*,*b*].

The interaction of charged particles (it may be superthermal solar wind plasma ions; SEP remained in interplanetary space from preceding disturbances or SEP accelerated by the same shock in the solar corona) with the shock front in interplanetary space may lead to the formation of new particle populations. In the section of the shock front with the quasiperpendicular magnetic field there can appear particle beams with a soft spectrum due to the drift acceleration mechanism (see, for example, *Decker* [1981]). In the quasiparallel region of the shock front due to the regular (diffusion) mechanism the accelerated particle spectrum (ESP-events) can be formed (see, for example, *Lee* [1983]). The relative contribution from the each of the above-mentioned sources to the new particle populations in certain events is defined by amplitude of the injected particle flux, its dependence on the energy and time and also by the alfvenic turbulence level. For example, calculations based on self-consistent stationary [*Lee,* 1983] and nonstationary [*Berezhko et al.,* 1998] regular acceleration theory for solar wind protons and the generation of alfvenic turbulence corresponds sufficiently well to measurements [*Kennel et al.,* 1986; *Berezhko et al.,* 1998].

In recent years, to describe the SEP propagation in interplanetary space in the presence of a shock, a black box model is used, in which complex interaction processes of particles with a shock front and their injection

from the disturbed region are substituted by a fictitious source situated at the front and supplying particles to the region before the shock [*Kallenroude and Wibberenz,* 1997; *Lario et al.,* 1998; *Ng and Reames*, 1999]. The developed approach is useful in the statistical treatment of events and allows determining typical temporal profiles in the intensity and anisotropy of SEP in the period preceding the arrival of the disturbance. This knowledge is important for the forecast tasks, because it allows determining the SEP action limits under different conditions [*Lario et al.,* 1999]. The deficiency of this method, as in the case of all black box models, is the difficulty to study the contribution of different processes to the formation of registered SEP intensity and anisotropy.

*Lee and Ryan* [1986] realized another approach to the problem of SEP gradual event generation. The investigation of the analytical solution of the diffusion transport equation for the selected law of shock movement and diffusion coefficients shows:

1) at the time when the shock passes the solar corona (~100 min), the maximum energy in the accelerated particle spectrum reaches (0.1–1) GeV;
2) in the interplanetary space the value of maximum energy varies weakly;
3) temporal profiles of SEP intensity calculated for the Earth's orbit are similar to observed ones. Thus, the results obtained by *Lee and Ryan* [1986] confirm the close association between the regular acceleration mechanism and SEP events.

The analytical model describing the temporal dynamics of particle spectrum at their acceleration by the plane shock is also calculated by *Toptygin* [1983]. One can note the qualitative similarity of the solutions obtained. The quantitative difference of solution is due to the different geometry of space and also the accepted law of shock movement and diffusion coefficient of particles. The shortcoming of both models is the absence of relationship between the particle diffusion coefficients and the energy.

As an extension of preceding investigations, in this work the temporal dynamics of the particle spectrum in the presence of a plane shock for diffusion coefficients depending on the particle energy and also their change in time is studied.

The results are important to study the character of acting of the shock front in interplanetary space on features of SEP registered in the Earth's orbit.

## 2. The model

The SEP event from the moment of arising of the shock to the moment of it's arrival at the Earth's orbit can be divided in two stages: the first stage (duration is ~1 hour) is generation of SEP in the solar corona, the second stage (duration is ~1 day) is propagation in interplanetary space in the presence of a shock. Here we consider the second stage only which begins with the injection of the particle spectrum formed during the first stage.

Let's determine the distribution of fast charged particles in the phase space for the given particle flux being injected continuously to the plane shock front moving in unlimited space. To solve this task, we selected coordinate system with the beginning coinciding to the traveling shock front, and its X-axis directed contrarywise the shock speed. The solution of the transport equation in the diffusive approximation

$$\frac{\partial f_i}{\partial t} = k_i \frac{\partial^2 f_i}{\partial x^2} - u_i \frac{\partial f_i}{\partial x} \qquad (1)$$

with zero initial and boundary conditions at $x \to \pm\infty$ and sewing of solutions at the shock front defines the particle distribution in the presence of a shock ([*Berezhko et al.,* 1987], in detail). Here $f_i$ is the isotropic part of the distribution function of particles, $p$ is a momentum of particles; $u_1 = V_S - w$, $u_2 = u_1 / \sigma$ is a velocity of medium flow in the selected coordinate system; $k_i$ is a diffusion coefficient of particles; $V_S, w$ are velocities of a shock and medium flow, respectively, which is assumed to be constant; $\sigma$ is a degree of matter compression at the shock front. Thereby, the index 1 marks function and parameters of the region in front of the shock front (x<0), and the index 2 is the same but beyond the shock front (x>0).

The general solution in space with a plane geometry and diffusion coefficient of particles depending on the momentum only can be presented in the form of two analytic relations:

1) the distribution function of particles at the shock front depending on injected particle flux and
2) the distribution function of particles in space depending on the distribution function of particles at a front.

Based on the generation method [*Berezhko et al.,* 1987] the distribution function of particles at the front $f_0(p,t)$ can be written in the form

$$f_0(p,t)=\frac{3\sigma}{u_1(\sigma-1)}\int_{p_{\min}}^{p}\frac{1}{4\pi p'^3}\left(\frac{p}{p'}\right)^{-q}\frac{t_k^{3/2}}{\sqrt{2\pi d_k^2}}dp'\times$$

$$\times\int_{t_0}^{t}(t-t')^{-3/2}\exp\left[\frac{t_k^2}{d_k^2}-\frac{t_k(t-t')}{2d_k^2}-\frac{t_k^3}{2d_k^2(t-t')}\right] \quad (2)$$

$$J_{inj}(p',t')dt'$$

where $q=3\sigma/(\sigma-1)$; $J_{inj}$ is a density of charged injected particle flux, and following notations are introduced

$$t_k=\frac{3\sigma}{u_1^2(\sigma-1)}\int_{p'}^{p}(\kappa_1(p'')+\sigma k_2(p''))\frac{dp''}{p''}$$

is the average time and

$$d_k^2=\frac{6\sigma}{u_1^4(\sigma-1)}\int_{p'}^{p}(\kappa_1{}^2(p'')+\sigma^3k_2^2(p''))\frac{dp''}{p''}$$

is a dispersion.

In (2) it has been taken into account that the injected particle spectrum is limited on the side of small impulses, $p_{\min}$.

The distribution function of particles $f_i(x,p,t)$ in the region up and down the shock front is determined by the solution of (1) at the zero initial and boundary at $x\to\pm\infty$ conditions and at the boundary condition $f(x=0,p,t)=f_0(p,t)$. For the accepted model it can be found by using the Laplace integral transformation

$$f_i(x,p,t)=\frac{(-1)^i x}{\sqrt{4\pi\kappa_i}}\exp\left[\frac{u_i x}{2\kappa_i}\right]\int_{t_0}^{t}(t-t')^{-3/2} \quad (3)$$

$$\exp\left[-\frac{u_i^2(t-t')}{4\kappa_i}-\frac{x^2}{4\kappa_i(t-t')}\right]f_0(p,t')dt'$$

where $x$ is a distance from the front.

For the time-dependent injection of particles

$$J_{inj}(p',t')=N_{inj}(p')\delta(t'-t_0)$$

the equation (2) has a form

$$f_0(p,t)=\frac{3\sigma}{u_1(\sigma-1)}\int_{p_{\min}}^{p}\frac{N_{inj}(p')}{4\pi p'^3}\left(\frac{p}{p'}\right)^{-q} \quad (4)$$

$$\frac{t_k^{3/2}}{\sqrt{2\pi d_k^2 t^3}}\exp\left[\frac{t_k^2}{d_k^2}-\frac{t_k t}{2d_k^2}-\frac{t_k^3}{2d_k^2 t}\right]dp'$$

where $N_{inj}(p')$ is the differential spectrum of injected particles per an area unit of the front, $\delta(t'-t_0)$ is the delta-function.

In the case of injection of the monoenergetic particles beam and constant diffusion coefficients associated by a relationship $k_1/k_2=\sigma^2$ the solution of (4) coincides with the analogous expression obtained by *Toptygyn* [1983].

The relations (3) and (4) define the dynamics of the distribution function of particles in space and at the shock front, respectively, in the events with the diffusion coefficients independent of time.

It is known both from measurements in situ [*Winner, Wibberenz,* 1993; *Starodubtsev*, 2000] and from theoretical considerations [*Ng, Reames,* 1994] that the sufficiently strong SEP fluxes can change the turbulence level of MHD – waves during an event. The self–consistent dynamics of the SEP ion flux and turbulence based on the numerical models is studied by *Ng et al.* [1999].

In the framework of the simplified analytic model one can estimate the dynamics of particle flux. Let us assume that the particles propagate in two stages: the first stage is after the impulsive injection at the moment of time $t_0$ (the particle propagation in the time interval $(t_0,t_*)$ takes place with certain diffusion coefficients); the second stage is that at $t_*$ the diffusion coefficients vary by steps in the whole space and in the time interval $(t_*,t)$ the particle propagation is described by new diffusion coefficients. Analyzing the SEP events, we can use such a simplification because, as it is evident from measurements, at typical conditions in interplanetary space, $\Gamma\cdot t>>1$ is fulfilled, where $\Gamma$ is an increment of wave growth, $t$ is a duration of SEP event.

Under this approach, the first stage is described as before by the relation (3) and (4). In the case of the second stage, the particles are converting divided into two populations according to a criterion: whether they reach the shock front after $t_*$ or not. The spatial distribution of the first population of particles, i.e. when they do not reach the shock front, in each half-space is determined by a solution of (1) at zero boundary conditions and the given initial condition for the second stage of distribution $f_i(x,p,t_*)$ and is of a form:

$$f_i(x,p,t)=\frac{1}{\sqrt{4\pi k_i(t-t_*)}}\times$$

$$\times\exp\left[-\frac{u_i^2(t-t_*)}{4k_i}\right]\int_a^b f(x',p,t_*)\exp\left[\frac{u_i(x-x')}{2k_i}\right]\times \quad (5)$$

$$\times\left(\exp\left[-\frac{(x'-x)^2}{4k_i(t-t_*)}\right]-\exp\left[-\frac{(x'+x)^2}{4k_i(t-t_*)}\right]\right)dx'$$

where $f_i(x,p,t_*)$ is the spatial particle distribution in the corresponding half-space at the last moment of time of the first stage;

$$a=\begin{cases}-\infty, i=1\\ 0, i=2\end{cases},\quad b=\begin{cases}0, i=1\\ \infty, i=2\end{cases}.$$

The particle flux of the first population incident on the shock front is given by distribution (5) and it is

$$J_{inj,i}=4\pi p^2 k_i\left|\frac{\partial f_i}{\partial x}\right|_{x=0}=\frac{4\pi p^2}{\sqrt{4\pi k_i(t-t_*)^3}}\times$$

$$\times\exp\left[-\frac{u_i^2(t-t_*)}{4k_i}\right]\int_a^b(-1)^i x' f_i(x',p,t_*)\times \quad (6)$$

$$\times\exp\left[-\frac{u_i x'}{2k_i}\right]\exp\left[-\frac{x'^2}{4k_i(t-t_*)}\right]dx'$$

Thus, at the second stage, in each half-space there exist particles of the two populations, from which the spatial particle distribution of the first population particles is described by a relation (5), and the spatial distribution of the second population is described by (2) and (3). Thereby, in inner integrating of (2) the injected particle flux is equal to a sum of fluxes determined by (6) in the integration interval ($t_*, t$).

### 3. Results and discussion

In illustrated calculations presented in Figures 1, 2 the values $w=400$ km s$^{-1}$, $V_S=700$ km s$^{-1}$, $\sigma=3.5$ are used and it is assumed that at $t_0$ is taken as the beginning of the impulsive injection of protons took place whose differential power spectrum for a momentum is of a form $N_{inj}=N_0(p/mc)^{-5}H(p-p_{\min})$, where $N_0$ is a normalized constant, $H$ is the Heaviside function, $p_{\min}=0{,}014mc$ ($\varepsilon_{\min}=92$ keV). The diffusion coefficient in the region before the shock front is taken to be $k_1=k_{10}\varepsilon/1\text{MeV}$ (cm$^2$ s$^{-1}$). Figure 1 presents calculation results for three values of diffusion coefficient: the panels a, b for $k_{10}=4.2\cdot10^{19}$, the panels c, d for $k_{10}=2.1\cdot10^{20}$, the panels e, f for $k_{10}=1.1\cdot10^{21}$. The diffusion coefficient in the region 2 is taken to be $k_2=k_1/10$ for all variants of calculation.

The panels a, c, e show the proton intensity $J=p^2 f$ in the Earth's orbit depending on the time for 6 values of energy: 1 – 0.6 MeV; 2 – 1.6 MeV; 3 – 3.8 MeV; 4 – 9.3

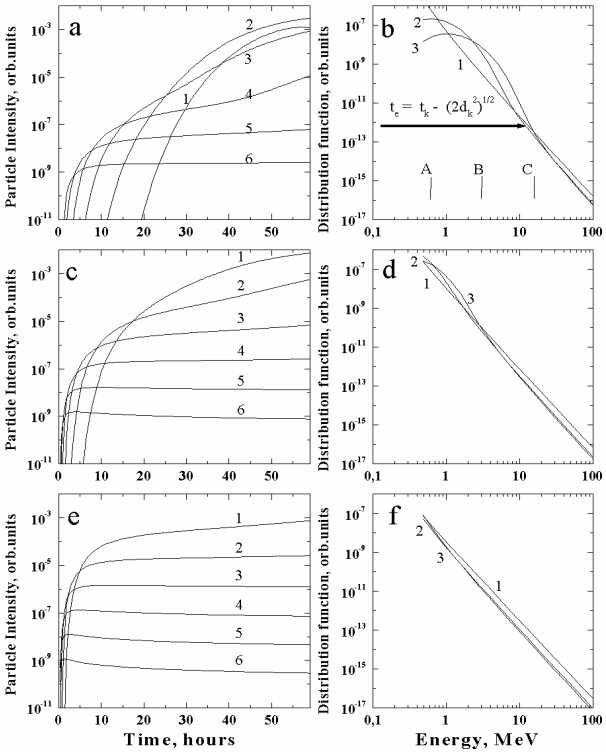


**Figure 1.** Intensity of particles for 6 values of energy (curves 1–6 in the panels a, c, e) at a fixed point of the region before the shock front depending on the time and the distribution function of particles at the shock front depending on the energy for 3 time moments (curves 1–3 in the panels b, d, f). Selected times are: 1 – a moment of the injection; 2– 30 hours after the injection; 3–60 hours after the injection, for used values of parameters it coincides with the moment of arrival of the shock front to a fixed point. The diffusion coefficient of particles is given in a form $k_1 = k_{10}\,(\varepsilon/1\text{ MeV})\cdot\text{cm}^2\cdot\text{s}^{-1}$, where: $k_{10}=4.2\cdot10^{19}$ in the panels a, b; $k_{10}=2.1\cdot10^{20}$ in the panels c, d and $k_{10}=1.1\cdot10^{21}$ in the panels e, f.

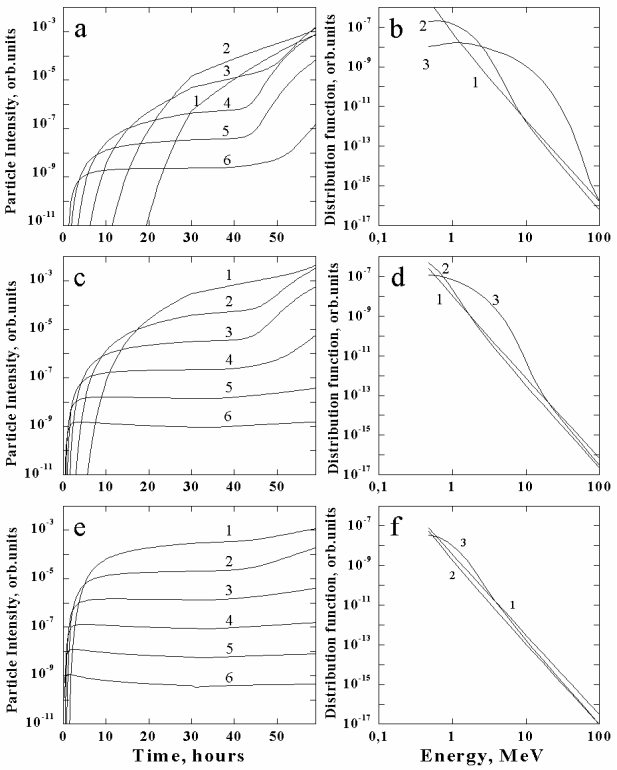


**Figure 2.** The same dependences as in Figure 1 with the difference that the diffusion coefficient in the upstream region of the shock front (30 hours after the injection) decreases by 10 times.

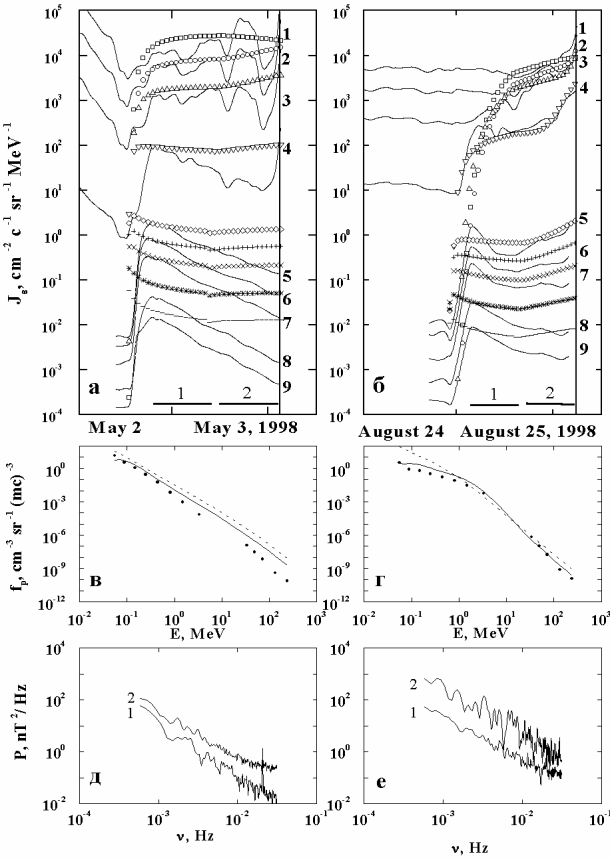


**Figure 3.** Intensity of SEP in the May 2, 1998 event registered in the orbit of the Earth's orbit in 9 energetic channels (solid curves 1–9 in the panel a) depending on the time. Curves of symbols are calculated intensities of particles with energies coinciding with a middle of corresponding energetic channel. The panel c presents the distribution function of particles at the shock front depending on the energy: the dashed and solid lines (calculation) correspond to the moment of injection and arrival of the shock front to the Earth's orbit; respectively; the points are measurements at the moment of arrival of the shock front to the Earth's orbit. The panel e gives the IMF power spectrum density measured in the Earth's orbit during 2 time intervals (curves 1, 2) marked by corresponding lines in the panel a. The panels b. d, f are the same for the August 24, 1998 SEP event.

MeV; 5 – 22.7 MeV; 6 – 55.2 MeV; the panels b, d, f present calculation results of the distribution function of protons at the shock front $f_0(p,t)$ according to (4) depending on the kinetic energy given in MeV. The distribution function of protons at the shock front in the panels b, d, f is indicated for three time moments: 1 – $t = 0.05t_e$; 2 – $t = 0.5t_e$; 3 – $t = t_e$, where $t_e = r_e / V_S$ is the arrival time of a shock to the Earth's orbit which for the above values is $t_e = 59.5$ h, $r_e = 1$ AU. As evident from Figure 1, two variants of intensity dynamics are possible for the particles of different energies: the first variant is that the intensity maximum occurs at the arrival moment of a shock front (curves 1–4 in the panel a; curves 1, 2 in the panel c); the second variant is that after the rapid rise the intensity either almost constant, or decreases up to the shock front arrival (rest curves in the panels a, c, e). The panels b, d, f show that as a result of interaction of particles with the shock front, a spectrum form varies only in the first variant of intensity dynamics. Note that the change in spectrum form is of different character: in the low-energy region (between A and B in the panel b) the spectrum becomes harder in comparison with the spectrum of injected particles, whereas in the high-energy region (between B and C) it becomes softer.

The boundary of an energy region in the injected particle spectrum, subjected to significant change due to the interaction with the shock front, is defined by relation

$$t = t_k - \sqrt{2d_k^2}\,, \qquad (7)$$

which is a consequence of the central limit theorem in probability theory for the given task ([*Berezhko et al,.* 1987], in detail). Here $t$ is duration of process; $t_k$ is the average time for the particle to perform $k$ cycles; $d_k^2$ is dispersion. Using the above expressions for the average time and dispersion (2) and also those taken in the calculation presented in the panel b and values from (7), we obtained for $t = t_e$

$$\varepsilon_* / 1MeV = \frac{r_e u_1^2 / V_S k_{10}}{\frac{3\sigma(1+0.1\sigma)}{2(\sigma-1)} - \sqrt{\frac{3\sigma(1+0.01\sigma^3)}{\sigma-1}}} \approx \approx 2.6 \frac{r_e u_1^2}{V_S k_{10}} \approx 12 \quad . (8)$$

The energy region marked by a solid line in the panel b corresponds well to the calculation. It is not difficult to verify that (7) and relations following from it, such as (8), correspond entirely to all calculations in the panels b, d, f.

It is known that the efficiency of particle interaction with the plane shock front (efficiency of regular acceleration mechanism) is defined by the acceleration time $t_{acc} \approx k_1 / u_1^2$ [*Berezhko et al.,* 1987]. As time $t$ passes the influence of a shock will be essential on such particles for which a condition $t_{acc} < t$ is fulfilled, or at $t = t_e$, $u_1^2 r_e / k_1 V_S \geq 1$ where the boundary value for the dimensionless combination of parameters is consistent with (8) within a numerical factor.

The calculation results presented in Figure 2 illustrate the influence of diffusion coefficients on the dynamics of the intensity and particle distribution functions at the shock front. The corresponding curves in Figures 1 and 2 are coincident with each other before the time moment $t_* = 0.5 t_e = 30$ h; the consequent difference in the dynamics is caused by the decrease of the diffusion coefficient by a factor of 10. From the comparison it will be obvious that the change of the diffusion coefficient is variously manifested in the intensity dynamics. This difference is related to a formation of the regions in hard and soft spectra (curve 2 in the panel b). The change of diffusion coefficients is weakly manifested in the dynamics of particles, the energy of which pertains to a region of hard spectrum (curves 1, 2 in the panel a) in comparison with analogous curves in Figure 1*a*. At the same time, the dynamics of intensity is changed for particles the energy of which pertains to the soft spectrum region (curves 3–6 in the panel a; curves 2–4 in the panel c and curves 2 in the panel e) in comparison with analogous curves in Figure 1. The change of diffusion coefficients slightly influences the behavior of curve 1 in the panels c, e, because an amplitude of injected particle spectrum in the energy region near $\varepsilon_{\min}$ can only decrease. Thus, in the events with varying diffusion coefficients the third variant of intensity dynamics is possible which is, in fact, a combination of two above variants: in the first part of the event the intensity rapidly reaches its maximum, and then weakly varies (the second variant of dynamics), in the second part of the event, after the decrease of diffusion coefficients there is an essential rise of intensity up to the shock front (the first variant of dynamics).

Figure 3 shows calculation results and variations of SEP events on May 2 and August 24, 1998. Curves 1–9 in the panels a, b are SEP intensity depending on the time registered in the Earth's orbit in 9 energetic channels: 1 – 0.047-0.065; 2 – 0.112-0.187; 3 – 0.31-0.58; 4 – 1.95-4.75; 5 – 27-41; 6 – 41-58; 7 – 58-88; 8 – 88-180; 9 – 180-300 MeV.

Curves from marks are the calculation for the energy corresponding to the center of energetic channel. Vertical solid line in the panels a, b is a moment of the shock arrival. Curves in the panels c, d are the distribution functions of SEP at the shock front: the dashed and solid curves are the calculation for the injection moment and shock front arrival moment to the Earth's orbit, respectively; points are measurements in the Earth's orbit. Curves marked by 1, 2 in the panels e, f are the power spectrum density of the interplanetary magnetic field (IMF) determined for two time intervals marked by horizontal lines in the panels a, b.

Results of measurements are obtained from two spacecraft − ACE: a) hourly data of SEP flux measurements (curves 1–4 in the panels a, b) are EPAM/LEMS30 experiment; b) hourly data of solar wind parameter measurements are SWEPAM experiment; c) hourly and 16-s data of IMF measurements are MAG experiment; and INTERBALL –2: hourly data of proton flux obtained with 10K-80 spectrometer (curves 5–9 in the panels a, b).

According to the measurements, the values of parameters used in calculations are following: for May 2 event $w = 500$ km s$^{-1}$ is the solar wind velocity in the region before the shock; $V_S = 1070$ km s$^{-1}$ is the shock speed according to the disturbance propagation time (note, that as a disturbance we take the shock registered at the beginning of May, 4 and not the weakly expressed disturbance arrived to the Earth's orbit at the end of May, 3); $\sigma = 4$ is a degree of compression matter in the shock front; $B = 6$ nT is IMF intensity before the shock; for the August 24 event: $w = 400$ km s$^{-1}$; $V_S = 1300$ km s$^{-1}$; $\sigma = 3$; $B = 6$ nT.

The diffusion coefficient used in these calculations is determined according to the quasilinear theory [*Lee,* 1983]. Taking into account numerical values the expres-

sion for it in the region before the shock front can be described in the form:

$$k_1 = \frac{3.6 \cdot 10^{11}}{P(\nu_0)} \left( \frac{B}{5nT} \right) \left( \frac{\varepsilon}{1MeV} \right)^{\frac{3-\alpha}{2}} \left( cm^2 / s \right),$$

where $P(\nu) = P(\nu_0)(\nu / \nu_0)^{-\alpha}$ is the IMF power spectrum density; $\nu_0 = 2.2 \cdot 10^{-3}$ $(B / 5nT)$ $(w / 400\ km/s)$ $(Hz)$ is the frequency of Alfven waves interacting resonance with protons whose energy equals 1 MeV. In the May 2 event, as it is followed from the panel e, $\nu_0 = 3.3 \cdot 10^{-3}$ $(Hz)$; $\alpha = 1.9$; $P(\nu_0) = 1(nT / Hz)$ that gives $k_1 = 4.3 \cdot 10^{21}$ $(\varepsilon/MeV)^{0.55}$ (cm$^2$ s$^{-1}$). According to measurements of the IMF power spectrum (curve 2 in the panel e), the diffusion coefficient in the second part of this event decreased by 3 times. In accordance with the data for the August 24 event (the panel f): $\nu_0 = 2.6 \cdot 10^{-3}$ (Hz); $\alpha = 1.5$; $P(\nu_0) = 6(nT / Hz)$ that gives $k_1 = 0.72 \cdot 10^{21}$ $(\varepsilon/MeV)^{0.75}$ (cm$^2$ s$^{-1}$), which decreases in the second part of event by 10 times. As concerns the diffusion coefficient of particles in the region beyond the shock front, it is taken in both events that $k_2 = k_1 / 10$ always.

As evident from results presented in the panels a, c, e the SEP event on May 2 took place on the background of the low level of turbulence, and it increased by the factor of 3 in the second part of the event. As a result, the manifestations of the regular acceleration mechanism in the temporal dynamics of SEP intensity are absent. Local variations in the low-energy SEP intensity (curves 1–3 in the panel a) are apparently caused by large-scale magnetic clouds from preceding disturbances, which at that time moment intersected the Earth's orbit. On the whole, the results of calculations for this event are qualitatively consistent with experiment.

The low-energy SEP dynamics in the August 24 event (curves 1–4 in the panel b) because of the higher turbulence level (curves 1, 2 in the panel f) is defined by the regular acceleration process. The results of calculations and measurements are consistent with each other. The reason of the significant increase of SEP intensity in the shock front in the channel of minimum registered energy (47–65 keV) remains unclear. The amplitude of spectrum for these energies it the regular acceleration is defined by the form of spectrum at lower energies unknown. By using an extrapolation in calculations for the spectrum of particles injected at the beginning of the event and given in the energy region of 30–47 keV, the intensity amplitude is essentially smaller than the registered one. Besides, an addition of a source of particles remained in interplanetary space from previous disturbances (curves 1–4 in the panel b for the August 24 event and their extrapolation up to 30 keV) increases insignificantly the intensity amplitude. It is possible that the considerable rise of the amplitude at the shock front is associated with the manifestation of drift acceleration mechanism (see, for example, *Decker*, [1981]).

The behavior of high-energy SEP intensity (curves 5–9 in the panel b) is of interest. According to (7) for parameter values taken in the August 24 event we obtain $\varepsilon_* \approx 3$ MeV. Nevertheless, in some energy interval (exceeding $\varepsilon_*$), the width of which depends on the diffusion coefficient value and the form of spectrum for particles in this energy region, weak manifestation of the regular acceleration mechanism can appear, namely, small intensity increase as particles approach the shock front and the spectrum softening. These manifestations exist in the dynamics of the SEP event intensity on August 24 up to the energy of 300 MeV. Probably, that is the reason of the increase of 500–700 MeV SEP intensity in the shock front in the November 6, 2001 event.

Thus, the significant decrease of the diffusion coefficient of particle motion in the region before the shock during the event intesifies the regular acceleration process. Results of IMF power spectrum measurements online can be used for a forecast of the high-energy SEP intensity increases up to the arrival moment of the shock front. It is important for Cosmic Weather problems.

## 4. Conclusion

The above investigation of the interaction process of fast particles with the moving shock front and the comparison of calculation results with measurements of the SEP intensity in interplanetary space allow to make the following conclusion.

The SEP generation region is limited by the solar corona. A character of the subsequence interaction of SEP with the shock front in interplanetary space is mainly defined by the diffusion coefficient value in the region before the front. As a result of the strong action of the regular acceleration mechanism, the energy spectrum form of the low-energy SEP varies, the regions of hard and soft spectrum are formed.

The intensity maximum of low-energy SEP coincides with the shock front. The high-energy SEP interact weakly with the shock front the form of their spectrum is not changed, and the intensity maximum moment in interplanetary space overtakes significantly the shock front arrival moment.

The energy boundary for the separation into low and high energy SEP according to the character of interaction with the shock front for typical conditions in interplanetary space is about 1 MeV.

In the events accompanied by the significant increase of the IMF power spectrum in the high-energy SEP intensity both variants can show up in the temporal dy-

namics, i.e.: the first intensity maximum is at the beginning of the event, the second maximum is the shock front arrival.

The dynamics of the particle intensity calculated in the framework of diffusion approximation with diffusion coefficients estimated according to the quasilinear theory for the measured IMF power spectrum qualitatively corresponds to the SEP intensity observed. On-line measurement data of the IMF power spectrum density during the event can be used for the forecast of high-energy SEP intensity increases up to the shock front arrival moment.

**Acknowledgments.** Authors thank the data preparation group on ACE EPAM, SWEPAM and MAG and ACE Science Center for spacecraft ACE data available by the address
http://www.srl.caltech.edu/ACE/ASC/level2/index.html.

The work has been carried out with partial financial support of the Russian Fund of fundamental investigations (grants 01-02-17278, 02-02-16096, 03-02-06897, 03-02-96026) and the grant of Leading Scientific School by G. F. Krymsky 422.2003.2.

## References

Berezhko, E. G., V. K. Yelshin, G. F Krymsky, and S. I. Petukhov, *The generation of cosmic rays by shock waves (In Russian),* 179 pp., Novosibirsk, Nauka., 1987.

Berezhko, E. G., S. I. Petukhov, and S. N. Taneev, Regular acceleration of particles at the fronts of interplanetary shock waves. *Astron. Lett., 24,* 122, 1998.

Berezhko, E. G., S. I. Petukhov, and S. N. Taneev, Acceleration of solar cosmic rays by shock in corona of Sun, *Izv. Akad. Nauk RAS, Fiz., (In Russian), 65,* 339, 2001*a*.

Berezhko, E. G., S. I. Petukhov, and S. N. Taneev, Shock acceleration of energetic particles in solar corona., *Proc. 27-th ICRC, Hamburg, Germany, 8,* 3215, 2001*b*.

Decker, R. B., The modulation of low-energy proton distribution by propagation interplanetary shock waves: A numerical simulation, *J. Geophys. Res., 86,* 4,537, 1981.

Denskat, K. U., and F. M. Neubaeuer, Statistical properties of low-frecuency magnetic field fluctuation in the solar wind from 0.29 to 1.0 AU during solar minimum conditions: Helios 1 and Helios 2., *J. Geophys. Res., 87,* 2,215, 1982.

Kallenroude, M. -B., and G. Wibberenz, Propagation of particles injected from interplanetary shocks: a black box model and its consequences for acceleration theory and data interpretation, *J. Geophys. Res., 102,* 22, 311, 1997.

Kahler, S. W., Injection profiles of solar energetic particles as functions of coronal mass ejection heights, *Astrophys. J., 428,* 837, 1994.

Kennel, C. F., F. V. Coroniti, F. L. Scarf, et al. A test of Lee's quasi-lear theory of ion acceleration by interplanetary traveling shocks, *J. Geophys. Res., 91,* 11,917, 1986.

Lario, D., B. Sanahuja, and A. M. Heras, Energetic particles events: efficiency of interplanetary shocks as 50 keV < E < 100 MeV proton accelerators, *Astrophys. J., 509,* 415, 1998.

Lario, D., B. Sanahuja, and A. M. Heras, A tool tomodel solar energetic particle events., *ESA. Workshop on Space Weather. (Ed. by N. Crosby, Noordwijk, WPP-115,* 343, 1999.

Lee, M. A., Coupled hydromagnetic wave excitation and ion acceleration at interplanetary traveling shocks, *J. Geophys. Res., 88,* 6109, 1983.

Lee, M. A., and J. M. Ryan, Time-dependent coronal shock acceleration of energetic solar flare particles, *Astrophys. J., 303,* 829, 1986.

Ng, C. K., and D. V. Reames, Focused interplanetary transport of ~ MeV solar energetic protons through self-generated waves, *Astrophys. J., 424,* 1032, 1994.

Ng, C. K., D. V. Reames, and A. J. Tylka, Effect of proton-amplified waves on the evolution of solar energetic particle composition in gradual events, *Geophys. Res. Lett., 26,* 2145, 1999.

Reames, D. V., Particle acceleration at the Sun and in the Heliosphere, *Space Sci. Rev., 90*, 413, 1999.

Starodubtsev, S. A., A study of the IMF fluctuation spectrum in the frequency range $10^{-4}$ – 1.67 $10^{-3}$ Hz during activity cycle development, *Phys. Chem. Earth (C), 25,* 133, 2000.

Toptygin, I. N. *Cosmic rays in the interplanetary magnetic fields (in russian),* 301 pp., Moscow, Nauka, 1983.

---

I. S. Petukhov, S. I. Petukhov, S. A. Starodubtsev and V. E. Timofeev, Yu. G. Shafer Institute of Cosmophysical Research and Aeronomy SB RAS, 31 Lenin Ave., Yakutsk 677891, Russia. (i_van@ikfia.ysn.ru)

AURORAL PHENOMENA AND SOLAR-TERRESTRIAL RELATIONS
PROCEEDINGS OF THE CONFERENCE IN MEMORY OF YURI GALPERIN, 3-7 FEBRUARY 2003

# Reconnection in the geomagnetic tail: a kinetic model of forced current sheet formation and evolution

V. I. Domrin and A. P. Kropotkin

Skobeltsyn Institute of Nuclear Physics, Moscow State University, 119992 Moscow, Russia

**Abstract.** A substorm activation in the geomagnetic tail is produced by a burst of magnetic reconnection in the tail current sheet (CS). A one-dimensional simulation model is constructed for analysis of the CS evolution. Magnetoplasma configuration slowly evolves forming eventually CS with the current carried by hot ions. Dynamics of the hot plasma structure formed this way and dynamics of the ambient cold plasma are examined on the kinetic equation basis; macroparticle code is used for ions while electrons are considered as a massless cold background. The plasma sheet evolution takes place under the influence of MHD disturbance, generated at the edge of the simulation box. This disturbance may be caused by e.g. fast tearing process occurring locally outside the simulation box. In the course of the simulated evolution, the electric field of the disturbance penetrates the central plane of the CS. This results in acceleration of ions in the CS; then accelerated ions escape CS along the field lines. Eventually the initial CS is replaced by specific steady-state nonlinear structure, Forced Kinetic Current Sheet. The current is carried by initially cold ions, which are brought into CS by convection from both sides. Magnetic field "annihilation" is a consequence: electromagnetic energy introduced into CS from both sides is transformed into energy of accelerated ions. MHD disturbance of rarefaction wave type appears spontaneously in the background plasma outside the CS.

## 1. Current sheets in space plasma and magnetic reconnection; relation to the problem of substorm dynamics

It is generally acknowledged (e.g. [*Syrovatskii*, 1971; *Parker*, 1979]) that slow, quasi-static evolution of magnetized space plasma objects often leads to formation of current sheets (CS) of relatively small thickness. Later development of the configuration is believed to involve transformation of stored magnetic energy into energy of plasma flows and dissipation. Actually this means formation of specific "dissipative structures" [*Nicolis and Prigogine*, 1977; *Haken*, 1983] and it is a manifestation of self-organization in open nonlinear systems. Relevant particular nonlinear dynamics is still an unresolved problem.

Small transverse scale of CS arising during quasi-static evolution may often mean that only its kinetic description is appropriate. On the other hand, we can treat CS locally as a one-dimensional structure.

In the case of the magnetosphere, its dynamics involves a phase of quasi-static evolution that is followed by a catastrophe of equilibrium [*Kropotkin and Sitnov*, 1997; *Kropotkin*, 2000; *Kropotkin et al.*, 2002*a*; *Kropotkin et al.*, 2002*b*]. In the global equilibrium state, i.e. on the quasi-static evolution stage, stability of the system is presumably dependent on the current density in the near-Earth portion of the magnetotail CS where transition takes place from the dipole-like to the tail-like field line structure (transition region, TR).

An intense CS thinning during substorm disturbances is a typical feature of TR [*Sergeev et al.*, 1993; *Baker et al.*, 1999]. Before the substorm activation (onset) the process may be treated as slow, quasi-static one [*Kropotkin and Lui*, 1995; *Schindler*, 1998] but during the activation it should become much faster. We suggest that it is induced by fast, explosion-like nonlinear process of current filamentation in the tearing mode that occurs in a somewhat more distant portion of the magnetotail [*Kropotkin*, 2000; *Kropotkin et al.*, 2002*a*,*b*]. In this paper we shall try to prove that outside the nonlinear tearing instability site the induced process of CS thinning eventually results in formation of a specific kinetic structure, namely an anisotropic forced kinetic CS (FKCS), whereas inside that structure, magnetic energy stored in the magnetotail transforms into the energy of ions accelerated inside such a CS. That structure provides merging of magnetic field lines,

and thus facilitates the global effect of magnetic reconnection.

In recent papers by these authors and their co-workers [*Kropotkin and Domrin*, 1995; *Kropotkin and Domrin*, 1996; *Kropotkin and Domrin*, 1997; *Kropotkin et al.*, 1997; *Sitnov et al*., 2000; *Sitnov and Sharma*, 2000] the theory of stationary FKCS was developed. A brief overview of this theory is presented in Section 2. In Sections 3 and 4 we analyze the process of FKCS formation. We have worked out special macroparticle code. Applying this code we obtained unique results, which allow (1) to observe and analyze the process of fast thinning of the initial CS under the influence of a pair of plasma flows transported to CS from both sides by initial MHD disturbances; (2) to demonstrate the process of FKCS generation, along with its accompanying structures. Section 5 contains arguments substantiating the adopted model of fast initial disturbance. This is done in particular for the sequence of events relevant to substorm activation. We also discuss the results from a more general viewpoint of a system nonlinear global restructuring involving fast magnetic reconnection arising in a burst-like manner.

## 2. "Forced" kinetic anisotropic current sheet

A theory of this regular nonlinear plasma structure is based on existence of a specific quasi-adiabatic invariant corresponding to ion oscillations about the central plane, during their motion on Speiser orbits, and also on connection of that invariant with the magnetic moment being the adiabatic invariant of the ion motion outside CS. The CS is presented as a self-consistent structure. By means of solution of a nonlinear integral equation, a profile of the equilibrium sheet was numerically determined, along with its dependence on features of the ion distribution function.

A solution exists if outside the CS the distribution function is highly anisotropic: there is a pair of counter-streaming ion flows along **B** with a relative velocity equal to $2V_A$, $V_A = B_0 / \sqrt{4\pi m n_c}$ is the Alfvén speed. The characteristic scale of the structure is determined by the Larmor radius $\rho_c = \sqrt{2T_c / m} / \Omega_0$ and the inertial length $\lambda_c$ of ions outside CS:

$$\delta = \sqrt{\pi\rho}\,\frac{c}{e}\,\frac{T_c^{3/2} n_c^{1/6}}{B_0^{4/3}} = \rho_c^{4/3} \lambda_c^{-1/3}$$

(ion flows outside the CS have shifted Maxwellian distributions with temperature $T_c$, $\Omega_0 = eB_0 / mc$).

In a real configuration, ions convecting in $z$ direction towards the CS in the crossed $E_y$ and $B_x$ fields, have near-zero $x$ component of the bulk velocity. At the same time, those ions that run away from the CS, having been accelerated by the electric field inside the CS, have the bulk velocity equal to $2V_A$ in that direction. The corresponding outward energy flux may be evaluated, and it coinsides with the inward Pointing flux value. That energy transformation is just a manifestation of magnetic merging in the CS.

## 3. Numerical simulation: the problem formulation and the solution method

We have worked out a one-dimensional model for numerical simulation of the CS evolution, in order to reveal the way in which a stationary FKCS type structure arises. Dynamics of the hot plasma ions belonging to the initial plasma sheet and of the surrounding cold plasma is described by kinetic equations. A solution for ions is found by means of a particle code; electrons form a massless background. Self-consistent electromagnetic fields are determined by solution of the Maxwell equations.

In the initial state the system consists of a hot plasma with the ion temperature $T$, forming a one-dimensional Harris-type CS, a uniform relatively cold plasma background (with parameters $n_c$, $T_C$ « $T$), and the magnetic field **B** ($B_t$ ($z$), 0, $B_n$). We set $B_n$ « $B_0$, $B_0$ being the tangential field $B_t$ at $z$ » $L_0$, $L_0$ is the characteristic scale of the Harris sheet. The plasma in CS is in equilibrium over the $z$ direction owing to the tangential field component $B_t$. Because of symmetry, simulation is carried out in the domain $0 < z < Z_0$; thickness of the simulation box (SB) $Z_0$ is much greater than $L_0$.

Evolution of the system is started by a MHD disturbance; it is a fast magnetosonic wave incident on the CS over the normal direction. Far from the CS the incident wave is set weak, and it propagates with the Alfvén velocity $V_A$. The wave magnetic field is directed along the $x$ axis while the electric field is in the $y$ direction.

At the SB outer boundary $Z_0$, the electric field of the incident wave, $E_i$ ($Z_0$, $t$) is set given: $E_i = 0$ at $t < 0$, $E_i = const \neq 0$ at $t > 0$. Resulting of the wave interaction with the CS, a reflected wave appears, propagating outwards. At the $Z_0$ boundary, the electromagnetic field is a sum of fields of the incident and the reflected waves. Setting the boundary condition we assume that the reflected wave is weak as well; this identifies its velocity outside the SB, namely the Alfven speed as well as the amplitude ratio of the wave electric and magnetic fields. The magnetic field $B_t$ at the second boundary of the SB, $z = 0$, is set equal to zero, due to symmetry.

For the particle motion, the boundary condition on the central plane, namely the mirror reflection, is determined by the problem symmetry. At the $Z_0$ boundary, particles can freely escape SB. Therefore the corresponding boundary condition involves both the inward convective ion flux and that outward freely escaping flux.

The translation symmetry over the *x*, *y* directions is effectively used. Then the field equations may be reduced to an ordinary differential equation for the *y* component of the vector potential. A full system of equations consists of equations of motion for separate particles, of a "material" equation coupling the current density and the electric field values, and of the Maxwell equations. Solutions of the equations are sought at particular instants (over a sequence of time steps with duration $\Delta t$). At every time step, $k\Delta t$, the number of particles is identified that are convected into the SB, and their distribution is generated. To calculate the smoothed current density $j_1$ at the spatial grid points, a linear weighting scheme is used. Then $j_1$ is inserted into a finite-difference equation for the vector potential. The equation is supplemented with conditions at both SB boundaries. Solution of the resulting set of algebraic equations is found by means of the Thomas algorithm. To solve the equations of motion of a particle, values of the magnetic and electric fields are recalculated at the particle position, by inverse interpolation from the grid points. Then solving the equations of motion, the particle position in the phase space is determined at the next time moment $(k + 1)\,\Delta t$.

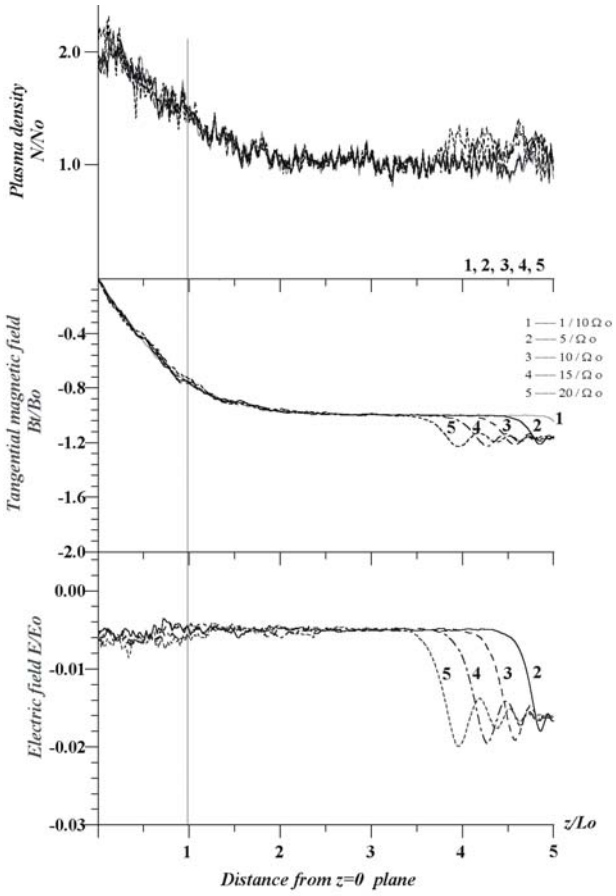


**Figure 1.** The initial phase of interaction of incident disturbance with the initial CS.

## 4. Numerical simulation: the results

The initial Harris sheet with the plasma (protons and electrons) density profile

$$n(z) / n(0) = cosh^{-2}\,(z/L_0)$$

is in equilibrium with the magnetic field $B_t(z)/B_0 = tanh\,(z/L_0)$, then $n(0) = B_0^2 / 8\pi T$ . The non-zero magnetic field component normal to the sheet is set $B_n = 0.2B_0$. The CS thickness is $L_0 = \rho / 0.0587$, $\rho = (2T / m)^{1/2} / \Omega_0$. The sheet is embedded in a uniform plasma with density which we have set equal to the maximum density of hot ions, $n_C = n(0) = N_0$. Results of two runs are presented in the paper. The time step is taken equal to $0.1\Omega^1{}_0$.

The Harris sheet was simulated with 10000 macroparticles in the first run, and with 15000 ones – in the second. Correspondingly was determined the number of macroparticles simulating the background plasma.

In Figure 1 the dependence on *z* is shown of the total (dimensionless) density $N(z) / N_0$, of the magnetic field intensity $B_t(z) / B_0$, and the electric field intensity $E(z) / E_0$ ($E_0 = V_A B_n / c$), for the time moments $t = 1/10\ \Omega_0$, $5/\ \Omega_0$, $10/\ \Omega_0$, $15/\ \Omega_0$, $20/\ \Omega_0$, correspondingly. (In this run the SB size was $5L_0$, and $T_c = 0.01T$). It is seen how in the uniform plasma a fast magnetosonic wave is propagating from the boundary, $z = Z_0$ in the form of a weak collisionless shock. Peak-to-peak distance equal to the wavelength of the shock oscillatory front, is $0.367L_0$, while according to theory it should be $2\pi / \lambda_C$ . The inertial length $\lambda_C$ is equal to $0.0578L_0$, and this yields a wavelength $0.363L_0$. In theory also, in the background plasma the wave propagates with the Alfvén velocity $V_A$. An estimate

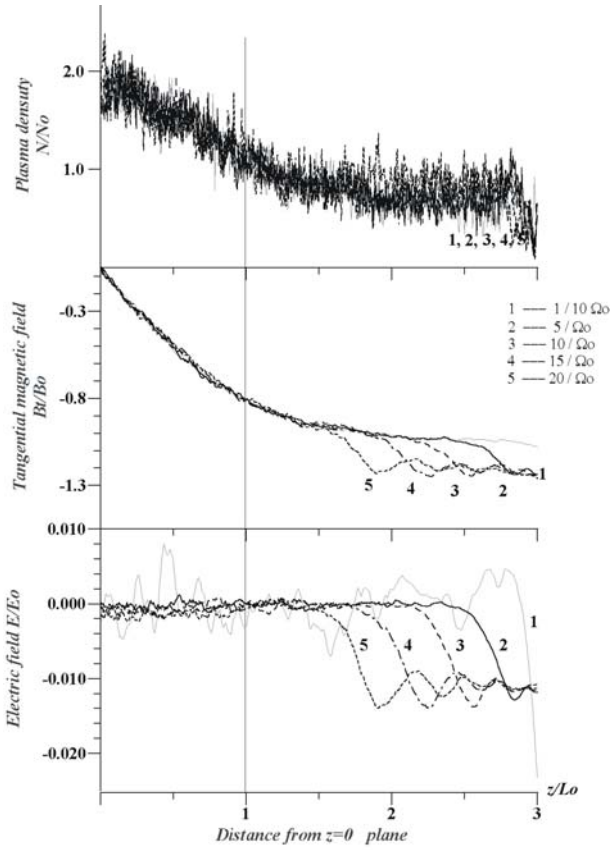


**Figure 2.** Profiles of plasma density, the magnetic field tangential component, and the electric field, for sequential moments of the CS evolution.

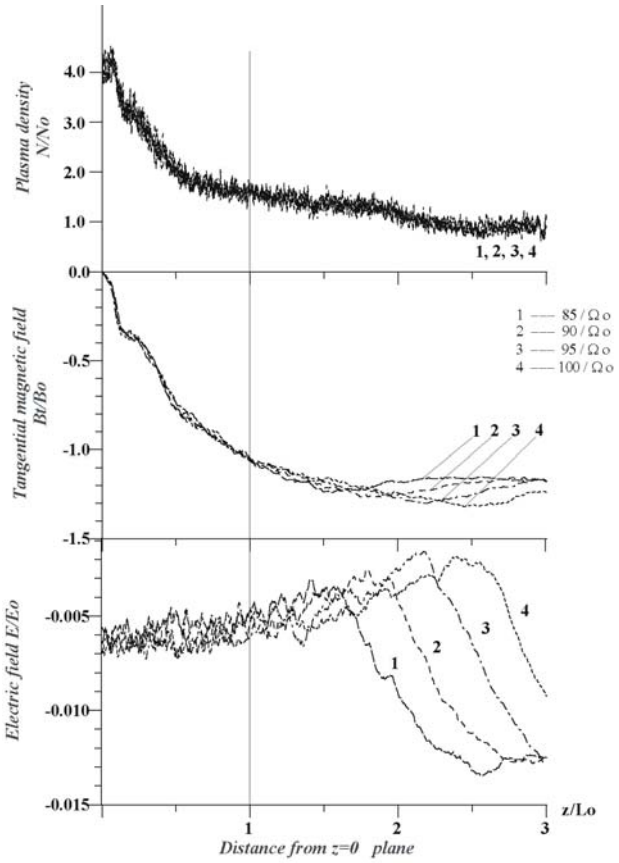


**Figure 3**. The same profiles for $85/\Omega_0 < t < 100/\Omega_0$.

based on simulation is 0.99 $V_A$. A very good consistency with theory is seen.

Figures 2-5 relate to a run with different initial parameters. For better spatial resolution, the SB size is reduced (down to $3L_0$) and at the same time, the number of grid points is doubled. The background plasma temperature is set equal to $T_c = 0.1T$. In Figure 2 corresponding to initial instants ($0.1/\Omega_0 < t < 20/\Omega_0$), a wave running to the central plane is seen again. The plasma density and magnetic field near another boundary, $z = Z_0$, stay undisturbed, and the electric field is nearly zero. During the time $30/\Omega_0 < t < 60/\Omega_0$ the wave propagates from the boundary of the Harris sheet to its central plane. In Figure 3 corresponding to $85/\Omega_0 < t < 100/\Omega_0$, a reflected wave is seen. In the $z = 0$ vicinity, the electric field is already nonzero. A sheet with enhanced plasma density and a sharp change of the magnetic field started to form at $t \sim 80/\Omega_0$.

In Figure 4, $305/\Omega_0 < t < 320/\Omega_0$, a structure is also seen which resembles the field profile in the initial Harris sheet. It stays there because of the hot plasma diamagnetism. In the vicinity of $z = 0$, over a time interval $\Delta t \sim 200/\Omega_0$, a thin embedded sheet has been formed.

At later time moments ($t>600/\Omega_0$, Figure 5) the central sheet gets even more pronounced. The wide $B_t$ minimum moves slowly towards the $z = Z_0$ boundary, and its profile now is fully different from the Harris one. The $E$ profile changes only slightly. While it is seen that there is still much hot plasma in the magnetic trap, it is now involved into the electric drift in the $x$ direction. At the same time, at $t \sim 650/\Omega_0$, a balance is established of the ion convective flux into the SB, and the flux of accelerated ions outgoing along the field lines.

The established thin central CS is that same FKCS, which is predicted by the theory, see Section 3. This is clear from comparison of the $B(z)$ profile with a theoretical profile calculated for the same value of the $v_{Tc}/V_{A0}$ parameter, taken from [*Sitnov et al.*, 2000], see Figure 6. The sheet thickness estimates taken at the $B_0/2$ level, differ for large $t \sim 1000/\Omega_0$ by several percent only.

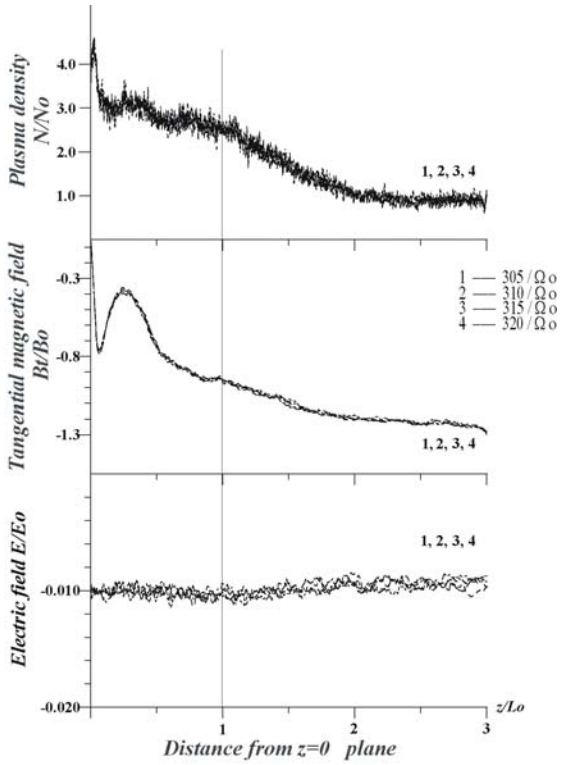


**Figure 4**. The same profiles for $305/\Omega_0 < t < 320/\Omega_0$.

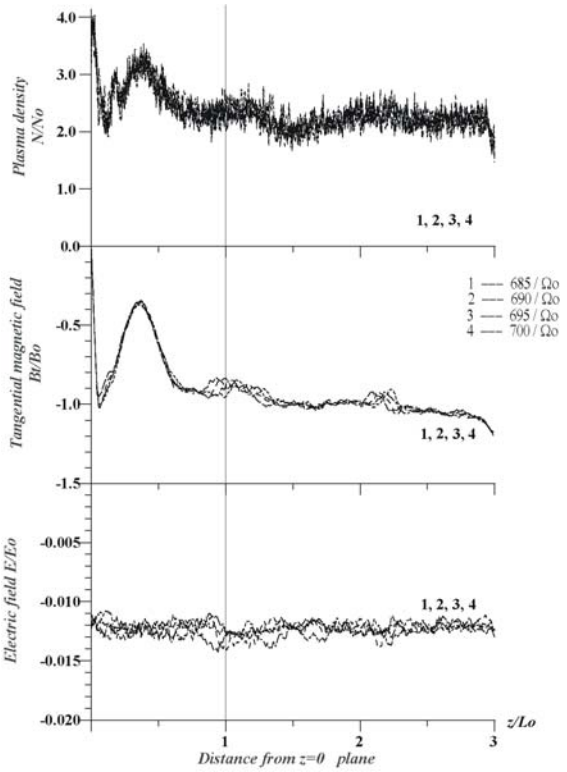


**Figure 5**. The same profiles for $t > 600/\Omega_0$.

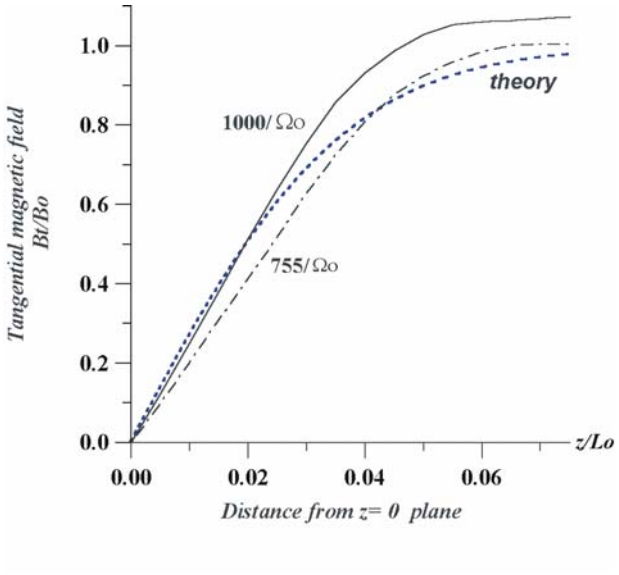


**Figure 6.** Comparison of the magnetic field profile with the theoretical profile of the FKCS.

Beginning with $t \sim 300/\Omega_0$, the electric field $E$ becomes quite uniform over the whole SB. According to the FKCS theory, we have $E/B_n = V_A/c$. In simulation, for $E$ we obtain $E/B_n = 0.97V_A/c$.

In Figure 7 energy spectra are presented, of all the ions existing in the outer portion of SB, $2.5L_0 < z < 3\,L_0$

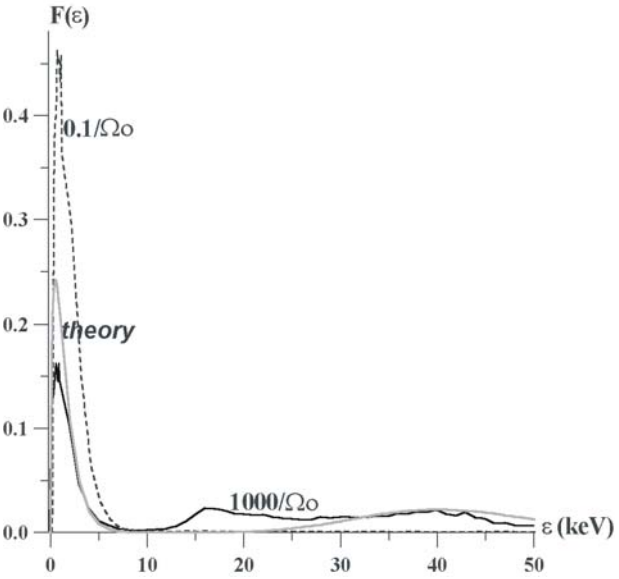


**Figure 7**. Energy spectra of ions at the edge of the simulation domain in a broad energy interval including practically all the particles.

(i.e. outside CS), at the initial moment and at the moment $t = 1000/\Omega_0$. At the initial moment, we can see a narrow peak of the background ions with energy 1 keV, and a wide low peak of particles with energy ~10 keV, belonging to the "wing" of the Harris sheet. The spectral density of particles with high energies (> 30 keV) is very low. At later times, the spectral density of low-energy particles diminishes by ~1.5 times but does not disappear, because ions convecting into SB are taken into account. At energies ~15 keV there appears a maximum that is presumably associated with magnetically trapped ions. Another wide maximum, at energies ~40 keV, is thought to correspond to particles escaping from SB with the doubled Alfvén velocity. The above conclusions are confirmed by comparison with the theoretical spectrum, which we have calculated for a stationary double-flow distribution function, namely a pair of mutually shifted Maxwellians, for FKCS with parameters adopted in simulation. That theoretical spectrum has the form

$$F(\varepsilon) = \frac{1}{\sqrt{\pi T_c}} \cdot$$

$$\cdot \left\{ \sqrt{\frac{\varepsilon}{T_c}} \exp\left( -\frac{\varepsilon}{T_c} \right) + \frac{1}{4V_0} \sqrt{\frac{2T_c}{m}} \cdot \right.$$

$$\cdot \left[ \exp\left( -\left( \sqrt{\frac{\varepsilon}{T_c}} - \sqrt{\frac{m}{2T_c}} V_0 \right)^2 \right) - \right.$$

$$\left. \left. - \exp\left( -\sqrt{\frac{\varepsilon}{T_c}} + \sqrt{\frac{m}{2T_c}} V_0 \right)^2 \right] \right\}$$

coupled with MHD modes. The disturbance propagates along the field lines towards the Earth. Propagating in a plasma with CS, such a disturbance gets deformed to a great extent; it is neither purely Alfvénic nor magnetosonic. However near the CS, at small distances as compared to its scale along the Sun-Earth line, $L_x$, the disturbance is reduced to a pair of fast magnetosonic waves incident from both sides on the initial CS, see Figure 8. Even if they are weak outside CS, as they interact with the CS, in the region with strongly depressed field $B$ inside the CS, the waves become nonlinear. Outside the CS reflected waves appear.

In the initial disturbance, behind the weak shock fronts, plasma moves only in the plane perpendicular to CS, as it is shown with the dashed line in Figure 7. Along with a good similarity in the profile for low energies (particles convecting slowly towards CS), and for high energies, $\varepsilon \sim 40$, there are considerable differences as well; they however, are quite expectable. Indeed, in simulation, a large portion of all the ions belongs to trapped hot ones originating from the initial Harris sheet. And they produce a wide middle maximum, at $\varepsilon > 10$ keV in simulation. Moreover, since both simulation spectra and the theoretical one, $F(\varepsilon)$, are normalized to unity in the same way: $\int F(\varepsilon) d\varepsilon = 1$, the presence of an additional population in the simulation results in diminishing of the area under the spectrum curve which corresponds to the FKCS particles alone, and therefore, to lowering of the curve itself, as compared to the theory. Note also that since the spectra are evaluated for particles from a wide region, which is a considerable part of the whole SB, they cannot present a detailed view of the particle energy distribution, being different at different distances from the central plane.

## 5. Discussion and conclusion

*MHD evolution of a disturbance induced in the near-Earth CS*

We briefly consider here how an MHD disturbance appears in the case of the geomagnetic tail, and what are the consequences.

At $B_n \neq 0$ and with non-zero background plasma density $n_c$ outside CS, in a system lacking full uniformity over $y$, the tearing mode occurs to be direction (convection). That is a cross-field, **E×B** drift of ions (and electrons). At the nonlinear stage, ions are accelerated in the **E** field inside the CS, rotated in the $B_n$ field, and ejected from the CS along the magnetic field lines. In such a manner, during the CS evolution, the plasma gets involved into motion along the $x$ axis; and this is just the way a well-known nightside particle injection may appear during a substorm.

*Comparison with MHD stationary solution*

The fast magnetosonic wave, with plasma moving towards the CS behind its front, propagates towards the CS with a certain large velocity, namely the Alfvén velocity $v_A$. I.e. this is a fast process, contrary to the earlier slow, quasi-static evolution. On the other hand, at the central plane the bulk velocity $v_z$ should be zero. In hydrodynamics, that is possible only if a reflected wave appears in such a way that $v_z = 0$ behind its front.

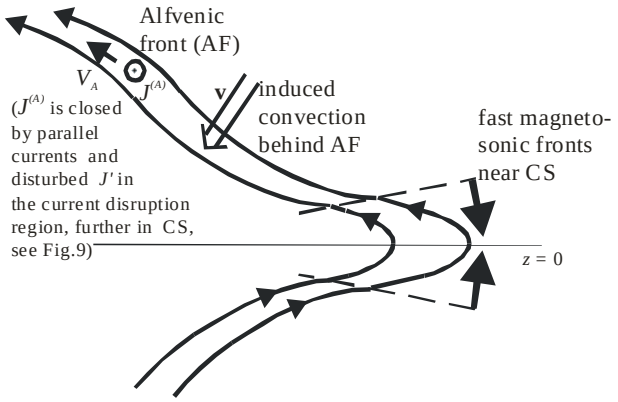


**Figure 8.** A pair of fast magnetosonic waves incident onto the initial CS.

Clearly, this is a situation which occurs in *Petschek's* [1964] solution; there a pair of slow MHD shocks forms a wedge just in such a way that $v_z = 0$ inside it while the normal to the shock front component $v_n$ is still nonzero.

Would the situation be the same in the collisionless plasma where the condition $v_z = 0$ may be fulfilled in quite another way, by means of severe anisotropy of the ion distribution function, namely by a pair of mutually penetrating flows?

Based on analysis of results of this numerical simulation, our answer is no. We have identified here a specific kinetic evolution pattern for the CS and the cold plasma flows being carried to its central plane by an initially given disturbance. A reflected wave is well seen in this case too. However, in a transient nonlinear regime, the field $E$ penetrates inside the CS and accelerates ions there. A transformation occurs of the electromagnetic energy into the energy of ion flows, i.e. magnetic merging takes place, in a way fully different from the MHD case presented by Petschek's solution.

*Relation to other one-dimensional current structures*

Actually the considered magnetic configuration is that of a rotational discontinuity. In MHD, for an ideally conductive fluid with density $n$, it should propagate with $v_Z = V_{AZ} B_Z / (4\pi n m_i)^{1/2}$ velocity. Note that no energy transformation occurs in that case.

On the other hand, we see that for collisionless plasma, ion anisotropy provides a possibility of a stationary structure with $v_z = 0$; that is FKCS. This structure provides an opportunity of magnetic field merging and energy transformation.

Presumably intermediate asymmetric situations are also possible. With thin current structure and small field normal component, ions on transient orbits coming to the CS, say, from $z = +\infty$, partly cross CS and go to $z = -\infty$, and partly are scattered back forming a counterstreaming field-aligned flow. So if there are less ions on transient orbits coming to the CS in opposite direction, from $z = -\infty$, we should get a net ion flow in the $-z$ direction. All such intermediate situations involve magnetic merging and energy transformation.

Another point is comparison with collisionless shocks. It is well known that a subcritical laminar shock also involves a kinetic small-scale nonlinear structure (a soliton), and regular ion flows are generated; so initially electromagnetic energy is transformed into energy of ion flows. Then interaction of those flows with the ambient plasma provides dissipation of electromagnetic energy, to ultimately form the shock. And this seems basically very similar to what occurs in the FKCS case.

*Spontaneous magnetic merging*

Note that while the nonlinear evolution with formation of FKCS can be initiated by a weak MHD disturbance (the particular threshold should be identified in further simulation runs), the amplitude of the electric field that establishes as a result of the nonlinear CS evolution, is finite and quite definite. Namely, it is determined by the background plasma density and by both tangential and normal magnetic field components: $E = B_t B_n / c \cdot (4\pi N_0 m)^{1/2}$. Thus the structure becomes a zone of a stationary spontaneous magnetic merging, or magnetic field "annihilation", with transformation of magnetic energy into the energy of accelerated ion flows. The effect of such a structure far from the CS still involves time dependence; it is a rarefaction wave propagating from CS, over the cold plasma. It is well known that transverse magnetosonic disturbances in a cold plasma are governed by the same equations as elastic disturbances in a gas with $\gamma = 2$. This allows to readily transfer results relating to one-dimensional motions in such a gas [*Landau and Lifshitz*, 1974] onto our case of the field $B_x$ disturbances propagating in the $z$ direction, with $B_z = const$, $B_z \ll B_x$.

The stationary FKCS may be viewed as a "sink" for hydromagnetic convective flows directed to the $z = 0$ plane on its both sides. Here escaping from FKCS flows of ions accelerated in the CS (and also flows of escaping electrons which are formed by a weak, with $T_e \ll T_i$, parallel electrostatic field) produce no influence on that flow pattern and the associated field $E_y$. This argument will be developed in more detail in our forthcoming paper.

*"Embedded" thin current sheet*

At those times when the central zone has almost stationary structure, over a much larger spatial scale and for a long time, remains though much deformed, the initial current structure. This is because of the hot plasma diamagnetism. Thus a structure known from

space observations, with a thin "embedded" CS, takes place in this simulation. A very thin structure stays very distinct in the central region of SD. Both in its shape, and quantitatively it corresponds to the forced kinetic current sheet (FKCS) predicted by the theory. It is seen that the initial nonlinear structure, the Harris type CS, is replaced by a fully different nonlinear structure, the FKCS with its accompanying hot plasma envelope; the transition is triggered with a weak "extraneous" MHD disturbance.

**Acknowledgments.** This paper is dedicated to the memory of Professor Yu. I. Galperin. He was interested in and appreciated the initial version of this study presented for the first time as a poster at a conference in Irkutsk, in autumn 2001.

The study was supported by grants of the Russian Foundation for Basic Research (N 99-05-65667), and of the Foundation "Universities of Russia" (N990600).

**References**

Baker, D. N., T. I. Pulkkinen, J. Buchner, and A. J. Klimas, Substorms: A global instability of the magnetosphere-ionosphere system, *J. Geophys. Res.*, *104*, 14601, 1999.

Haken, H., *Synergetics: An Introduction*, Springer-Verlag, New York, 1983.

Kropotkin, A. P., Explosion-type dynamics of the magnetotail current sheet: role of mode coupling in substorm onsets, in *Proc. 5-th Int. Conf. on Substorms*, St. Petersburg, Russia, 16-20 May 2000 (ESA SP-443, July 2000), p.127.

Kropotkin, A. P., and V. I. Domrin. Ion dynamics and induced reconnection in a thin plasma sheet, *Geomagn. and Aeronomy*, *35*, 1, 1995 (in Russian).

Kropotkin, A. P., and V. I. Domrin. Theory of a thin one-dimensional current sheet in collisionless space plasma, *J. Geophys. Res.*, *101*, 19893, 1996.

Kropotkin, A. P., and V. I. Domrin. Ion distribution function in a thin one-dimensional plasma sheet, *Geomagn. and Aeronomy*, *37*, 11, 1997 (in Russian).

Kropotkin, A. P., and M. I. Sitnov, Magnetospheric substorm dynamics from the viewpoint of open nonlinear systems theory, in *Problems of Geospace*, M. I. Pudovkin, B. P. Besser, W. Riedler, and A. M. Lyatskaya (eds.) Verlag Osterreich. Akad. Wiss., Wien, p.75, 1997.

Kropotkin, A. P., and A. T. Y. Lui, Quasi-static evolution of the magnetosphere: The substorm growth phase, *J. Geophys. Res.*, *100*, 17231, 1995.

Kropotkin, A. P., H. V. Malova, and M. I. Sitnov, The self-consistent structure of a thin anisotropic current sheet, *J. Geophys. Res.*, *102*, 22099, 1997.

Kropotkin, A. P., O. O. Trubachev, and K. Schindler, Nonlinear mechanisms of a substorm explosion in the magnetotail, *Geomag. and Aeronomy (English translation)*, *42*, 277, 2002a.

Kropotkin, A. P., O. O. Trubachev, and K. Schindler, Substorm onset: a fast restructuring of the magnetotail associated with explosion-like turbulence enhancement, *Geomag. and Aeronomy, (English translation)*, *42*, 286, 2002b.

Landau, L. D., and E. M. Lifshitz, *Course of Theoretical Physics*, vol.6, *Hydrodynamics*, Addison-Wesley-Longman-Reading, Mass., 1974.

Nicolis, G., and I. Prigogine, *Self-organization in nonequilibrium systems*, John Wiley and Sons, New York, 1977.

Parker, E. N., *Cosmical magnetic fields*, Oxford University Press, 1979.

Petschek, H. E., Magnetic field annihilation, *NASA Spec. Publ.*, *SP-50*, 425, 1964.

Schindler, K., Formation of thin current sheets and other recent developments in magnetospheric activity, *Astrophys. Space Sci.*, *264*, 289, 1998.

Sergeev, V. A., D. G. Mitchell, C. T. Russell, and D. J. Williams, Structure of the tail plasma/current sheet at ~11$R_E$ and its changes in the course of a substorm, *J. Geophys. Res*, *98*, 17345, 1993.

Sitnov, M. I., and A. S. Sharma, Magnetotail thin current sheet models and their role in substorm physics, in *Proc. 5-th Int. Conf. on Substorms*, St. Petersburg, Russia, 16-20 May 2000 (ESA SP-443, July 2000), p.113.

Sitnov, M. I., L. M. Zelenyi, Ch. V. Malova, and A. S. Sharma, Thin current sheet embedded within a thicker plasma sheet: self-consistent kinetic theory, *J. Geophys. Res*, *105*, 13029, 2000.

Syrovatskii, S. I., On generation of a current sheet in a plasma with frozen-in magnetic field, *Soviet JETP*, *60*, 1727, 1971 (in Russian).

# Storm-substorm coupling: Signatures of stormtime substorms

T. I. Pulkkinen[1], H. E. J. Koskinen[1,2], K. Kauristie[1], M. Palmroth[1],
G. D. Reeves[3], E. Donovan[4], H. J. Singer[5], J. A. Slavin[6],
C. T. Russell[7], and K. Yumoto[8]

[1]Finnish Meteorological Institute, Helsinki, Finland
[2]Department of Physical Sciences, University of Helsinki, Finland
[3]Los Alamos National Laboratory, Los Alamos, New Mexico, USA
[4]Department of Physics and Astronomy, University of Calgary, Calgary, Canada
[5]NOAA Space Environment Center, Boulder, Colorado, USA
[6]NASA Goddard Space Flight Center, Greenbelt, Maryland, USA
[7]Institute of Geophysics and Planetary Physics, University of California, Los Angeles, California, USA
[8]Department of Earth and Planetary Sciences, Kyushu University, Fukuoka, Japan

**Abstract.** It is shown that the evolution of magnetospheric and ionospheric activations during magnetic storms are different from isolated substorm activity. Even though these activations are often referred to as "stormtime substorms," it is shown that they are not all similar in characteristics, and that only a portion of the activations share properties usually associated with magnetospheric substorms. The activations are divided into distinct categories based on their ionospheric and magnetospheric signatures. It is concluded that the activations in different categories are caused by different physical processes. These results are discussed in the context of the importance of substorm activity to storm dynamics.

## 1. Introduction

The substorm injection hypothesis asserts that storms are composites of rapidly recurring substorms [e.g., *Chapman*, 1962]. In this case, the ring current is produced by ion injections following substorm onset. On the other hand, the convection hypothesis suggests that the stormtime ring current evolution is governed solely by the external driver, i.e., the solar wind and interplanetary magnetic field (IMF) conditions. The ring current would then be intensified as the strong convection electric field transports energetic ions into the inner magnetosphere [e.g., *Burton et al*., 1975].

The sizes of storms and substorms are classified using magnetic indices. The auroral electrojet (AE) indices are created from 12 northern hemisphere auroral region magnetometer recordings as upper (AU) and lower (AL) envelopes, and thus characterize the maximum intensity of the eastward and westward electrojet currents in the auroral region, respectively. The Dst-index and its high-resolution version, the SYM-H index, are weighted averages of several mid-latitude stations, and are generally interpreted to represent the intensity of the symmetric ring current encircling the Earth. In case of the substorm injection hypothesis, the AE index and its time history would predict the Dst index, while in case of the convection hypothesis the Dst index is determined from solar wind and IMF data alone. As both substorms and the ring current are driven by the southward IMF, there is a high degree of correlation between the indices, which has made it difficult to distinguish between the two views of storm evolution.

While there are two competing concepts for the storm evolution and its dependence on substorm activity, two points highlight the importance of substorm-like activations during storm evolution: Enhanced convection during strongly southward IMF can bring plasma to the ring current region [e.g., *Liemohn et al*., 2001], but convection alone cannot energize the particles to the observed several-hundred-keV [*Pulkkinen et al*., 2000]. Thus, substorms are dynamically important for the storm process. Furthermore, several studies have shown that the ionospheric dissipation in the form of Joule heating and particle precipitation accounts for a large part of the stormtime energy dissipation [*Lu et al*., 1998; *Turner et al.,* 2000]. As this dissipation occurs mainly as a consequence of substorm-like activity, substorms are also energetically important for the storm process.

Substorms are complex processes that involve a global reconfiguration of the magnetotail, intense field-aligned currents between the magnetosphere and the ionosphere, an intensification of the westward electrojet in the night sector, and expanding auroral activity. Substorms are characterized by three phases, the growth

phase during which the magnetotail current sheet is intensified and thinned, the expansion phase during which the substorm current wedge couples the magnetosphere and ionosphere via field-aligned currents, and the recovery phase when the activity subsides and the original configuration is slowly recovered [e.g., *Baker et al.*, 1996]. During magnetic storms, the inner magnetosphere is highly disturbed, and there is no a priori reason to assume that the substorm-like activations would have the characteristics of isolated substorms [*Pulkkinen et al*., 2002]. In this paper we examine the ionospheric and magnetospheric signatures of substorm-like activations during six storms. We conclude that there are several distinct types of these activations, which most probably result from different magnetospheric dynamic processes.

## 2. Data set

Six magnetic storms during 2000 and 2001 were selected for analysis. It was required that the selected storms had main phase maxima near 24 UT, which allows us to follow the main phase dynamics using the MIRACLE instrument network [*Syrjäsuo et al*., 1998], which is at local midnight at 2130 UT. Magnetic recordings from the IMAGE magnetometer network of MIRACLE, the SYM-H index, solar wind and IMF measurements from the Wind and ACE spacecraft, and ion and electron fluxes from the Los Alamos energetic particle detectors onboard geostationary satellites were all examined to characterize the activations. All data were available at 1-min temporal resolution or better. The storm dates and characteristics are given in Table 1.

| Date | $SYMH_{MIN}$ | <AL> | $<B_Z>$ | $<P_{SW}>$ |
|---|---|---|---|---|
| 06.04.00 | -320 | -580 | -23.1 | 21.9 |
| 15.07.00 | -347 | -845 | -15.2 | - |
| 17.09.00 | -203 | -440 | 1.7 | 13.5 |
| 06.11.00 | -176 | -370 | -7.0 | 5.5 |
| 11.04.01 | -280 | -519 | -4.0 | 22.2 |
| 22.10.01 | -219 | -496 | -5.0 | 8.4 |

**Table 1.** Storm events and characteristic activity parameters: Minimum of SYM-H, average of AL, average of IMF $B_Z$, and average of solar wind dynamic pressure $P_{SW}$ over the duration of the main phases of the storms.

For the first five storms, the analysis is performed for the storm main phase duration, when the substorm activity is most intense and the ring current is continuously intensifying. The last storm, on October 22, 2001, was characterized by an unusual development of the Dst index: Dst stayed at an almost stationary level for an extended period of about 24 hours. The substorm activity during that 24-hour period is examined separately from the five storm main phases.

## 3. Electrojet activations during storm main phase

The methodology used in the analysis is described in detail in *Pulkkinen et al.* [2002], and will only shortly be summarized here. The aim is to develop quantitative criteria that characterize the activations and hence allow for detailed examination of the causal relationships during the storm main phases. In order to avoid confusion, the events that are discussed are termed "activations" rather than "substorms", as it later becomes clear that all activations do not have all characteristics usually associated with substorms.

The IMAGE magnetometer recordings from the premidnight sector were examined in detail to identify the onset times and latitudes of the individual activations. For each event, the onset time, onset latitude, expansion propagation direction (poleward, equatorward, no expansion) were determined using data from the entire magnetometer chain. The level of electrojet activity at onset and level of electrojet activity at maximum were determined using the IL index [*Kallio et al.*, 2000] which is a proxy for the AL index in the Scandinavian local time sector (00 MLT at 2130 UT).

The geostationary orbit electron fluxes from the Los Alamos particle instruments averaged 10 min before and after the activation time were examined to determine whether the activations were associated with geosynchronous particle injections. The 10-min averaging ensures that some time is allowed for the particles to drift to the location of the spacecraft in cases where the observing spacecraft is not exactly at the injection location. Some of the activations were well-correlated with energetic particle flux enhancements at geosynchronous orbit, but at other times the flux changes were small or not coincident with the ground activations. Note that no difference was made between a true injection and a flux recovery to the previous level; only the absolute change around the onset time was considered.

The solar wind pressure and IMF $B_Y$ and $B_Z$ measurements from the ACE spacecraft were transitioned to the magnetopause using the solar wind velocity and $X$-distance of the spacecraft, assuming magnetopause location at $10R_e$ and 3 min for the transition through the magnetosheath. Pressure changes associated with the activations were evaluated from differences of 10-min averages before and after the activation. Similarly, IMF triggers were also defined as 10-min averages before and after the activations. The results discussed below were not sensitive to the actual

value of the integration time used; also longer periods (15 and 20 min) were used, and gave similar results. Thus, it is assumed that the 10-min averaging takes care of the possible timing errors due to solar wind transit time or due to spacecraft position relative to the injection front and substorm current wedge.

Such analysis for each of the five storm events give a set of activations characterized by the following properties: Onset time, onset latitude, expansion direction, IL at onset, IL minimum (largest negative deviation), IL intensification amplitude IL (minimum) – IL(onset), injection or no injection, solar wind pressure pulse and/or IMF $B_Y$ or $B_Z$ trigger. An injection was assumed when the flux more than doubled from before onset to after onset. A pressure pulse was more than 1-nPa change in the pressure from before onset to after onset. IMF triggers were considered to have more than 4-nT change in $B_Y$ or $B_Z$ from before onset to after onset. For all criteria, several values were used, but the results did not change very much. Thus, the general results are not sensitive to the details of how triggers were identified.

In total, 45 individual activations occurred during the five storm main phases. Detailed examination of the electrojet activations shows that they are not all similar: while some resemble isolated substorms, others show quite different behavior. The activation was defined to be a "substorm" if the electrojet (and auroral) expansion direction in the ionosphere was poleward and a geostationary orbit injection was observed. The "non-substorm" category included events where the expansion direction was equatorward and no injection was observed. Further, the data set was categorized to events that had an external trigger either in the form of a pressure pulse or IMF northward turning. Note that a single event can be a substorm or non-substorm simultaneously with being a triggered event. While "triggered" and "not triggered" events together include all events, there were events that did not fall into either "substorm" or "non-substorm" category.

Figure 1 shows the relationship between the IL value at substorm onset (IL(onset)) and the minimum value (maximum disturbance) reached during that activation (IL(min)). For higher activity before the onset (larger |IL(onset)|) the absolute value of the minimum is also larger. The mean of the intensification amplitude is –550 nT (solid line in figure), while the values range from a few hundred to over a thousand nT. As most of the events cluster along a straight line in the IL(onset) − IL(min) plane, it means that while the IL minimum (IL(min)) is dependent on the IL value at onset (IL(onset)), the intensification amplitude (IL(min) − IL(onset)) is independent of IL(onset). The different symbols highlight the events in the three categories discussed above: substorms, non-substorms, and triggered events. Substorms occur at all activity levels, and have all sizes, while the non-substorms are predominantly rather small activations.

The events in the "substorm" class are not well organized in any parameter: they have random intensification amplitudes, they occur at all latitudes, and during all electrojet and Dst activity levels (Figure 2). Substorms usually are not triggered by pressure pulses, but about 50% of the events occur in connection with an IMF northward turning. On the other hand, the events in the "non-substorm" class form a more coherent set of events: They have a intensification amplitude distribution roughly in the range of 300 – 600 nT, and they occur at typical auroral latitudes at 65 – 70° geographic latitude (Figure 2). Usually, events in this class are not triggered by either pressure pulses or IMF northward turnings. Furthermore, the speed of equatorward expansion is larger than what would be expected if it was caused by large-scale motion of the entire auroral oval during continuous driving.

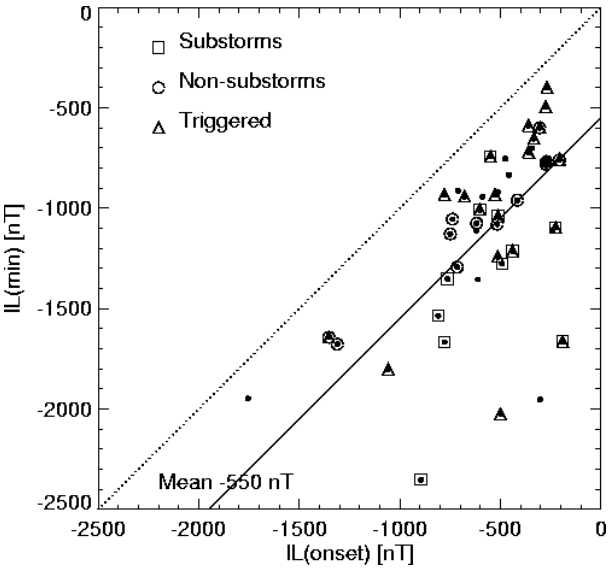


**Figure 1.** IL at onset vs. IL at maximum disturbance for all activations during the five storms (black dots). "Substorms" are indicated with squares, "non-substorms" with circles, and triggered events with triangles. The solid line shows the mean of all activations, –550 nT.

The events triggered by pressure pulses occur typically at low onset latitudes, expand poleward, but have no associated geostationary orbit injection, making them an independent category distinct from either substorms (poleward expansion + injection) or non-substorms (equatorward expansion + no injection) (Figure 3). The events triggered by northward turnings did not form a coherent set; events included in the "substorm" and "non-substorm" sets were part of this

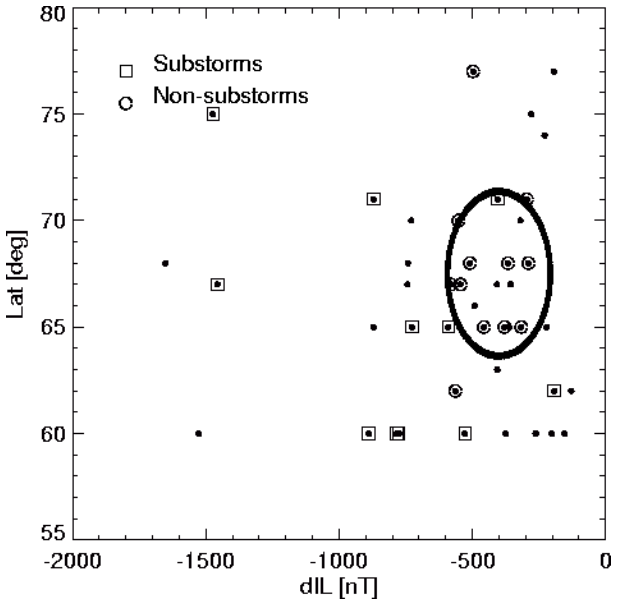


**Figure 2.** Intensification amplitude (dIL=IL(minimum) – IL (onset)) vs. onset latitude for all activations during the five storms (all points – black dots). "Substorms" are indicated with squares and "non-substorms" with circles.

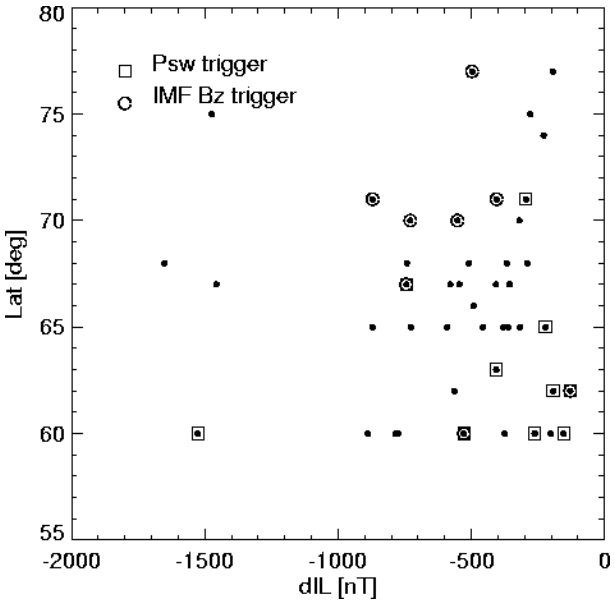


**Figure 3.** Intensification amplitude (dIL=IL(minimum) – IL(onset)) vs. onset latitude for all activations during the five storms (black dots). Pressure pulse triggered events are indicated with squares and IMF northward turning triggered events with circles.

category. Note also that the events that occur poleward of the typical auroral latitudes, near the poleward edge of the auroral oval, are not always associated with either IMF or solar wind pressure pulse triggers. Thus, solar wind pressure pulses during these storm periods do not cause activity near the high-latitude oval boundary, but are associated with dynamic events deep inside the magnetosphere. The wide spread in the onset latitudes is caused by the wide oval that has expanded equatorward both because of strong negative $B_Z$ producing open flux in the polar cap and because of the precipitation from the intensified ring current.

## 4. Electrojet activations during continuous Dst-activity

The storm on October 21–22, 2001, initiated when the sheath region of an interplanetary coronal mass ejection reached the Earth's magnetosphere. The interplanetary field was fluctuating, but $B_Z$ was mostly negative in the sheath region (Figure 4). The pressure was high, reaching above 40 nPa. The magnetic cloud (0140–1915 UT on Oct 22) followed with slowly rotating field. The leading edge of the cloud had positive or near-zero $B_Z$, negative $B_Z$ followed about 8 hours later. The solar wind velocity jumped at the shock arrival from below 400 km/s to almost 600 km/s, after which it gradually decreased to about 500 km/s.

The magnetospheric response to this driver was quite unusual. The SYM-H index showed a strong positive peak at 1645 UT on October 21, followed by a decrease to –130 nT by 1830 UT. Signs of slow recovery were visible during 0200-0800 UT, after that, SYM–H stayed at a level of about –150 nT for another 16 hours. In the ionosphere, substorm activity was quite strong outside a quieter period during 0200–0800 UT on Oct 22. The AL/AU indices were merged using data from three meridional magnetometer chains, the CANOPUS chain in Canada, the IMAGE magnetometer array in Scandinavia, and the 210 meridian chain in Eastern Asia.

The Los Alamos instruments onboard several geostationary satellites showed intense substorm activity (Figure 5). Particle injections were mostly clear and distinct from each other. As the GOES 8 and GOES 10 spacecraft moved to the nightside during early part of October 22, they recorded several clear substorm-associated magnetic field dipolarizations. During the substorm activity in the magnetotail the geosynchronous electron fluxes increased at all local times almost at the same time. The magnetotail magnetic field was highly taillike, with strong $B_X$ and small $B_Z$ that persisted also through the dipolarization events. This indicates that the cross-tail current was highly intensified and its inner edge reached geostationary orbit. The Polar spacecraft further out in the magnetotail at about $8R_E$ distance observed dipolarization events that occurred very close in time to the geostationary orbit dipolarizations and particle injections. Thus, it seems that the entire inner

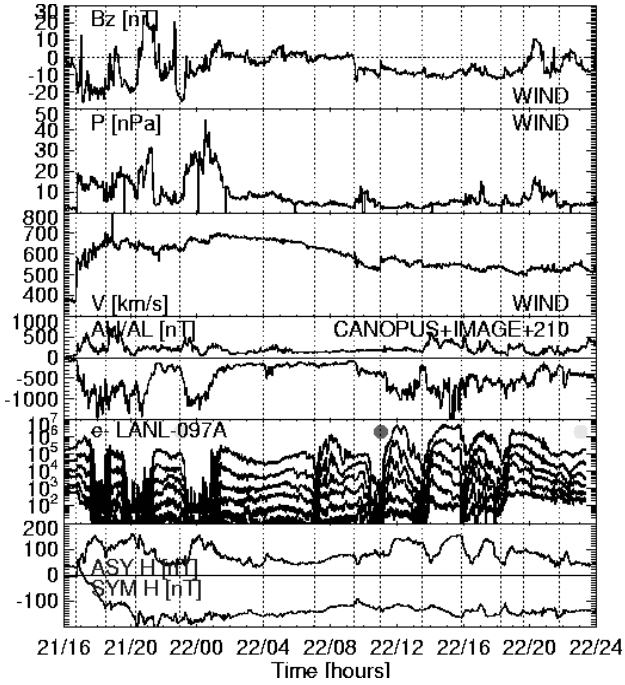


**Figure 4**. Storm on October 21-22, 2001. Panels from top to bottom: IMF $B_Z$, solar wind dynamic pressure, solar wind velocity, AU/AL indices, geostationary orbit electron fluxes (grey circle marks local midnight), and SYM-H and ASY-H indices.

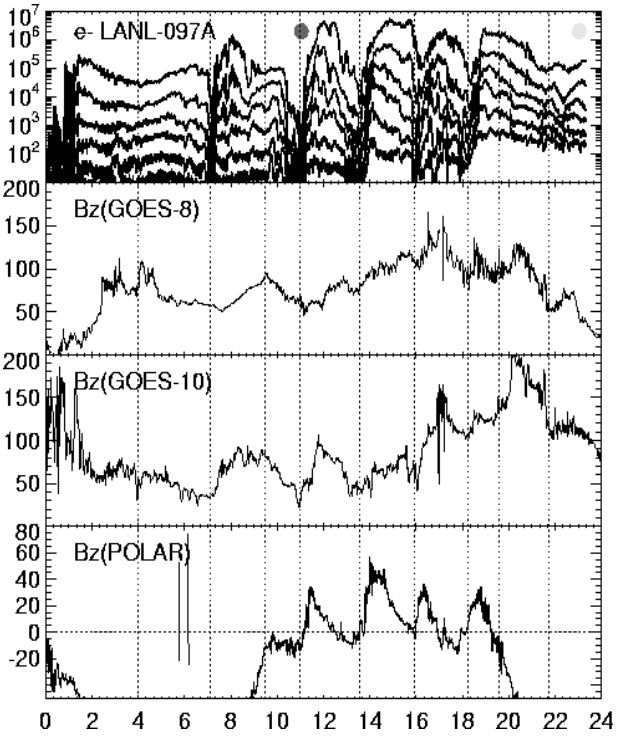


**Figure 5**. Storm on October 22, 2001 (0–24 UT). Panels from top to bottom: Geostationary orbit electron fluxes (grey circle indicates local midnight). $B_Z$ from GOES–8, $B_Z$ from GOES-10, and $B_Z$ from Polar all in units of nT.

magnetosphere responded in a coherent fashion.

The activations during the magnetic cloud passage thus form a distinct category characterized by global oscillatory motion of the entire inner magnetosphere. During that period, the magnetotail was in a relatively stretched configuration which persisted mostly even throughout the dipolarizations associated with the activation onsets.

## 5. Electrojet and Ring Current Relationship

Response of the ring current to electrojet enhancements has been a controversial issue in substorm dynamics: Event studies have asserted that a positive variation of the SYM-H index follows the substorm onset [e.g., *Ohtani et al.*, 2001], while other studies have concluded that storms evolve independent of substorm activity [*McPherron*, 1997]. A SYM-H decrease can be caused by enhanced ring current following the substorm energetic particle injection. On the other hand, an increase in the SYM–H index may follow the disruption of the cross-tail current near the inner edge of the plasma sheet. The total effect depends on the relative magnitudes of these and other contributing current systems.

In order to examine the response of the SYM–H index to the electrojet enhancements, Figure 6 shows a superposed epoch analysis of the SYM–H behavior before and after the electrojet activations. The top panels show all events, while the subsequent panels show results after the data have been categorized to “substorms”, “non-substorms”, pressure pulse triggered events, and the global oscillation events during the October 2001 storm. For substorms, the SYM–H increases, with positive gradient starting 5 min before the onset and lasting until 10 min after, indicative of storm-substorm coupling. For non-substorms, the profile is flat, indicating that there is no consistent change of SYM-H associated with these events. The pressure pulse triggered events also show a rapid increase of the SYM–H index promptly at onset, which probably comes from the magnetopause current systems rather than tail changes. Lastly, the global oscillation events produce a clear increase of the SYM–H index, beginning about 5 min before the onset and continuing about 15 min after the onset.

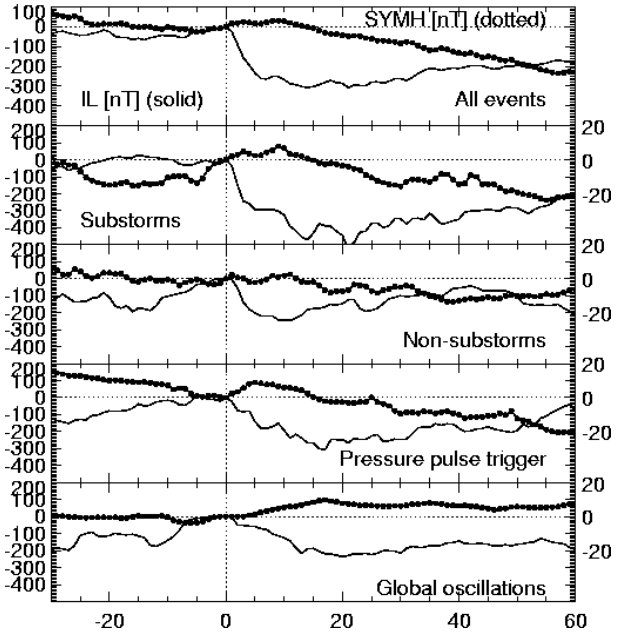


**Figure 6**. Superposed epoch analysis of the SYM–H behavior around substorm onsets (in minutes from onset). Panels from top to bottom: IL (solid thin line) SYM–H (dotted line) for all events, for substorm events, for non-substorm events, for pressure pulse triggered events, and for global oscillation events.

## 7. Summary and discussion

In this paper, we have categorized the stormtime electrojet activations into several distinct classes of events: The "substorms" had characteristics similar to those of isolated substorms: poleward electrojet and auroral expansion in the ionosphere, and an associated energetic particle injection at geostationary orbit. The "non-substorm" category was defined as a set of events during which the electrojet expanded equatorward, and during which no geostationary orbit injection was observed. Two classes of external triggers were also considered. While those that were triggered by IMF $B_Z$ northward turnings had no common characteristics, those triggered by pressure pulses were predominantly events that expanded poleward in the ionosphere, but were not associated with geostationary orbit injection. Finally, activations during a magnetic cloud passage on October 21, 2001 showed large-scale oscillations of the entire inner magnetosphere with nearly simultaneous particle flux enhancements and magnetic field dipolarizations at geostationary orbit and further tailward.

The activation occurrence frequency during the storm main phases was about one activation every 57 min [*Pulkkinen et al.*, 2002]. Furthermore, it was evident that there was a tendency that events in the "substorm" and "non-substorm" categories alternated such that a "substorm" was followed by a "non-substorm" and vice versa. On the other hand, during the magnetic cloud passage during the storm of October 2001, the global oscillations had a mean interval of about 140 min, and all activations had similar basic characteristics.

In the analysis, special emphasis was paid on finding parameters that control the size of the activations as measured by electrojet indices. However, the "substorm" class events had a random size distribution that is controlled by factors that are not easily parametrized either in terms of ionospheric state or the solar wind or IMF driver. On the other hand, the "non-substorm" events were consistently about 300–600 nT in magnitude. The global oscillation events caused activations in the ionosphere that had a variable size distribution with a mean of about 500 nT.

As storm-substorm coupling is closely related to the issue of coupling of the processes in the magnetotail and in the inner magnetosphere, it is useful to examine the correlation of the activations with changes in the SYM-H index. Also in this case, the different event categories showed distinct behavior: A superposed epoch analysis showed that "substorms" had the largest electrojet enhancement, and a clear positive change of SYM–H that started well before onset and maximized about 10 min after onset. The "non-substorms" showed no consistent signature in SYM-H. The pressure pulse triggered events showed a prompt increase of SYM-H at the onset time, maximizing rapidly about 5 min after onset. The global oscillations were associated with a slow increase of the SYM-H index beginning 5–10 min before onset and continuing about 15 min after onset.

Due to the complexity of the magnetotail activity during magnetic storms, it is not easy to analyze individual activations. *Reeves et al*. [2002] analyzed the activity during a storm in October 2000, and found similar oscillatory motion as reported in this paper; they termed the geosynchronous injections having "sawtooth" profile. Furthermore, they also report a similar repetition rate of about two hours of the sawtooth events.

The different characteristics of the classes of events discussed here imply that the events also have different generation mechanisms. "Substorms" are preceded by the formation of a thin current sheet in the inner magnetosphere, which is disrupted at substorm onset. This accounts for the increase of the SYM-H index, and would argue that the injection process is not very efficient in loading the ring current (see also *Reeves and Henderson* [2002], who reached similar conclusions using ENA images and geostationary particle observations). The "non-substorms" have no SYM-H signature, and propagate equatorward in the ionosphere. This would suggest that they are caused by flow channels (or large-scale BBFs) in the magnetotail, and that the activity does not reach the inner magnetosphere. Finally, the global oscillations during the magnetic cloud passage

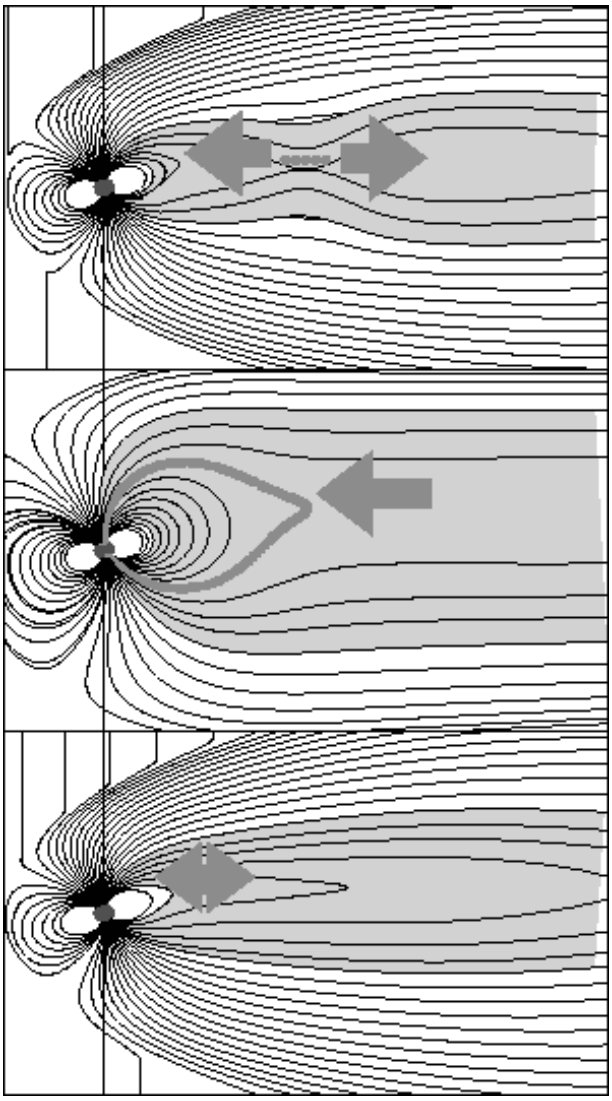

**Figure 7**. Schematic of the (top) "substorm" and (middle) "non-substorm" and (bottom) oscillating tail configurations.

occurred while the magnetotail was in quite stretched configuration; the intense currents in the inner magnetosphere were only partially disrupted at the activation onsets.

Figure 7 shows an illustration highlighting a possible scenario for the magnetotail dynamics during the different activation types. During substorm growth phase, the tail develops a thin current sheet, and the onset is associated with reconnection at the near-Earth neutral line [*Baker et al*., 1996]. The non-substorm activations are associated with fast flow channels intruding into the inner magnetosphere. During these activations, the tail current sheet is much thicker, and the flows do not necessarily reach the inner magnetosphere or geostationary orbit. While the flow burst onset is probably associated with reconnection, the ionospheric activations are associated with the field-aligned currents connecting the Earthward edge of the flow channel and the ionosphere [*Nakamura et al*., 2000, *Kauristie et al*., 2000, *Sergeev et al.,* 2000]. The global oscillations take place during a stretched magnetotail and relatively steady and strong driving [*Reeves et al.,* 2001].

A key question for the proposed scenarios is how the plasma sheet behaves during storm times. Isolated substorms are associated with reconnection first in a thinned plasma sheet and later in the lobes. This provides the characteristic signatures of injection of energetic particles to geosynchronous orbit and poleward expanding auroras. Here it is proposed (although not proven) that during storms the tail unloads energy also in different ways: Relatively strong flow bursts caused by closed-field-line reconnection within a thick plasma sheet couple to the ionosphere dissipating energy via Joule heating and particle precipitation. However, larger statistics and more detailed studies including observations in the magnetotail tailward of geostationary orbit are required before the final conclusions can be drawn.

The significance of substorms during storms is often reduced to the question of whether it is convection or substorms that produces the strong enhancement of the ring current [*McPherron,* 1997]. However, recent analyses have shown that the ring current is not necessarily the main sink of the solar wind energy during storms; the importance of the ionospheric precipitation and Joule heat have been emphasized in several studies [*Lu et al.*, 1998, *Tanskanen et al.*, 2002, *Turner et al*., 2001]. Thus, it is of importance to consider the entire system, including the ionosphere, the inner magnetosphere, and the energy leaving the tail in the form of plasmoids [*Ieda et al.*, 1998]. The results in this paper can be used to hypothesize that the tail response to the external driving depends on the tail configuration and its recent history: If the tail is near its nominal configuration, a normal substorm-like evolution of energy loading in the lobe and thin current sheet formation is a natural development. On the other hand, if the driving continues strong after the plasmoid release, the tail may not have time to recover from the previous activity, and the driving re-activates the post-plasmoid plasma sheet flows creating a strong flow channel in a dipolarized tail. In such a scenario, the driver properties and the magnetotail configuration strongly affect the type of activation that follows, which also controls the amount of energy dissipation either in the ring current or in the ionosphere. This would then imply that the substorms do not occur independent of storm activity, but that the storm phase, driver, and tail characteristics strongly affect the type of substorm-like activity that follows.

**Acknowledgments.** We thank the NSSDC for the CDAWeb facility. The ACE PI's of the MAG instrument (Dr. C. W. Smith) and SWEPAM instrument (Dr. D. McComas) are acknowledged for the use of their data. The WIND PI's of the MAG instrument (Dr. R. Lepping) and the SWE instrument (Dr. A. Lazarus) are acknowledged for the use of their data. The IMAGE magnetometer chain (PI Dr. A. Viljanen) is an international effort led by the Finnish Meteorological Institute. The 210MM database is being constructed by the Solar-Terrestrial Environment Laboratory, Nagoya University. The SYM-H data were obtained from World Data Center in Kyoto.

## References

Baker, D. N., T. I. Pulkkinen, V. Angelopoulos, W. Baumjohann, and R. L. McPherron, The neutral line model of substorms: Past results and present view, *J. Geophys. Res., 101*, 12,975, 1996.

Burton, R. K., R. L. McPherron, and C. T. Russell, An empirical relationship between interplanetary conditions and Dst, *J. Geophys. Res., 80*, 4204, 1975.

Chapman, S., Earth storms: retrospect and prospect, 17, J. Phys. Soc. Jpn., 6, 1962.

Ieda, A., S. Machida, T. Mukai, Y. Saito, T. Yamamoto, A. Nishida, T. Terasawa, and S. Kokubun, Statistical analysis of the plasmoid evolution with Geotail observations, *J. Geophys. Res., 103*, 4453, 1998.

Kallio, E. I. A., T. I. Pulkkinen, H. E. J. Koskinen, A. Viljanen, J. A. Slavin, and K. Ogilvie, Loading-unloading processes in the nightside ionosphere, *Geophys. Res. Lett., 27*, 1627, 2000.

Kauristie, K., V. A. Sergeev, M. Kubyshkina, T. I. Pulkkinen, V. Angelopoulos, T. Phan, R. P. Lin, and J. A. Slavin, Ionospheric signatures of transient plasma sheet flows, *J. Geophys. Res., 105*, 10677, 2000.

Liemohn, M. W., J. U. Kozyra, M. F. Thomsen, J. L. Roeder, G. Lu, J. E. Borovsky, and T. E. Cayton, Dominant role of the asymmetric ring current in producing the stormtime Dst*, *J. Geophys. Res*., 106, 10883, 2001.

Lu, G., et al., Global energy deposition during the January 1997 magnetic cloud event, *J. Geophys. Res., 103*, 11685, 1998.

McPherron, R. L., The role of substorms in generation of magnetic storms, in: *Magnetic Storms*, Geophysical Monograph 98, 131, 1997.

Nakamura, R., W. Baumjohann, V. A. Sergeev, M. Kubyshkina, M. Brittnacher, G. Parks, K. Liou, and T. Mukai, Fast flow bursts and auroral activations, Proceedings of the fifth International Conference on Substorms, ESA-SP 443, p. 319, ESA, The Netherlands, July 2000.

Pulkkinen, T. I., N. Yu. Ganushkina, V. F. Bashkirov, D. N. Baker, J. F. Fennell, J. Roeder, T. A. Fritz, M. Grande, B. Kellett, and G. Kettmann, Ring current enhancement due to substorm-associated inductive electric fields, in *Proceedings of the Fifth International Conference on Substorms*, edited by A. Wilson, ESA-SP 443, Estec, Noordwijk, the Netherlands, p. 451, 2000.

Pulkkinen, T. I., H. E. J. Koskinen, K. E. J. Huttunen, K. Kauristie, E. I. Tanskanen, M. Palmroth, G. D. Reeves, Effects of magnetic storms on substorm evolution, Sixth International Conference on Substorms, edited by R. M. Winglee, University of Washington, Seattle, 2002, pp. 464-471.

Reeves, G. D., and M. G. Henderson, The storm-substorm relationship: Ion injections in geosynchronous measurements and composite energetic neutral atom images, *J. Geophys. Res., 106*, 5833-5844, 2001.

Reeves, G. D., M. G. Henderson, R. M. Skoug, M. F. Thomsen, J. E. Borovsky, H. O. Funsten, P. C:son Brandt, D. J. Mitchell, J. -M. Jahn, C. J. Pollock, D. J. McComas, and S. B. Mende, IMAGE, POLAR, and geosynchronous observations of substorm and ring current ion injection, AGU Monograph on the Storm-Substorm Relationship, in press, 2002.

Sergeev, V. A., J. -A. Sauvaud, D. Popescu, R. A. Kovrazhkin, K. Liou, P. T. Newell, M. Brittnacher, G. Parks, R. Nakamura, T. Mukai, and G. D. Reeves, Multiple-spacecraft observation of a narrow transient plasma jet in the Earth's plasma sheet, *Geophys. Res. Lett., 27*, 851, 2000.

Syrjäsuo, M., et al., Observations of substorm electrodynamics using the MIRACLE network, in: *Substorms-4*, edited by S. Kokubun and Y. Kamide, Terra Scientific Publishing Company, Tokyo, p. 111, 1998.

Tanskanen, E. I., T. I. Pulkkinen, H. E. J. Koskinen, Substorm energy budget near solar minimum and maximum: 1997 and 1999 compared, *J. Geophys. Res., 107*, A6, 10.1029/2001JA900153, 2002.

Turner, N. E., D. N. Baker, T. I. Pulkkinen, J. L. Roeder, J. F. Fennell, and V. K. Jordanova, Energy content in the stormtime ring current, *J. Geophys. Res., 106*, 19149, 2001.

# Features of substorm onsets and expansions observed by CRRES

T. V. Kozelova[1], L. L. Lazutin[2], and B. V. Kozelov[1]

[1] Polar Geophysical Institute, Apatity, Murmansk region, Russia
[2] Scobeltsyn Institute of Nuclear Physics, Moscow State University, Russia

**Abstract.** Observations by the CRRES were used to study the characteristics of the dynamic behavior of the energetic particles and magnetic field in the near-Earth magnetosphere before and during the local dipolarization. Just before the local dipolarization onset the CRRES observed the oscillation of the *E* and *B* fields with quasi-period of ~ 50*s* that may be a coupled shear Alfven-slow magnetosonic mode. These data support drift-Alfven ballooning as possible mechanism for initiation of the substorm local onset in the near-geosynchronous plasma sheet.

## 1. Introduction

During substorm growth phase the magnetic field becomes more tail-like associated with the intensification of cross-tail current. The return of the B field to a more dipolar configuration, or 'dipolarization', is a well-known signature of the substorm expansion phase. The dipolarization is accompanied by the injections of the particles and high level of broadband magnetic fluctuations. *McPherron et al.* [1973] suggested the phenomenological model of the substorm current wedge (SCW) in which the pair of field-aligned currents (FACs) is associated with the region of the current disruption (CD). The investigation of the fine structure of the field and particle flux variations near substorm onset is very important for understanding of the mechanisms responsible for CD.

In the paper [*Lui et al*, 1988] it was shown that the CD region on r ~ 7–9$R_E$ consists of localized particle intensity enhancements (activations) with short duration (10–50*s*). The spatial scale of these activations can be of the order of the ion gyroradius $\rho_i$ [*Ohtani*, 1998]. *Roux et al.* [1991] detected large transient fluctuations in both the radial and azimuthal electric field components, associated with magnetic dipolarization. *Maynard et al.* [1996] using the observations from the CRRES satellite in the near-geosynchronous plasma sheet (PS) observed the brief cross-tail electric field reversals from dawn-dusk to the dusk-to-dawn, prior to the beginning of substorm. The substorm develops when significant Poynting flux flows in both field-aligned directions.

In this paper we used data from the CRRES satellite to examine the evolution of local conditions leading up to and during the substorm activation onsets. We investigated magnetic and electric field variations, the dispersionless injections of energetic electrons > 21.5 keV and protons > 37 keV, and the dynamics of the fine-scale structures of activation around the local dipolarization moments $T_{dip}$. We will also find a connection of large impulsive electric fields with the local magnetic field changes.

*Instrumentation.* The CRRES was launched in July 1990 into an 18.2° inclination orbit with apogee at a geocentric distance of 6.3$R_E$ and perigee at an altitude of 350 km. Here we are primarily interested in measurements taken by the electric field instrument [*Wygant et al*., 1992], the magnetometer [*Singer et al*., 1992] and the Electron and Proton Wide-Angle Spectrometer, also known as MEB [*Korth et al*., 1992]. The MEB instrument measures medium energy electrons (14 energy channels E1–E14: 21.5 – 31.5 – 40 – 49.5 – 59 – 69 – 81 – 94 – 112 – 129.5 – 151 – 177 – 208 – 242 – 285 keV) and protons (12 energy channels P1–P12: 37 – 54 – 69 – 85 – 113 – 147 – 193 – 254 – 335 – 447 – 602 – 805 – 3200 keV).

The time resolution of the **E** and **B** field data used in this study was 15 and 2 seconds respectively. The SM coordinate system was used here for **B** and **E** fields.

## 2. Substorm large impulsive electric fields

First we will consider certain features of E field variations associated with the local dipolarization.

*Substorm on March 6, 1991.* This substorm took

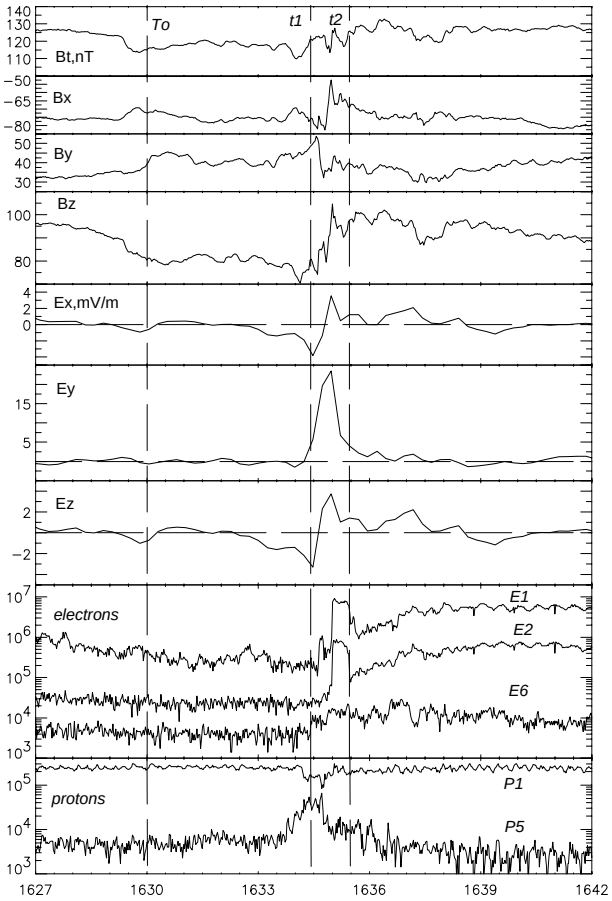


**Figure 1.** Substorm on March 6, 1991. Large impulse $E_y$ on the CRRES. From the top to the bottom: total $B$ field magnitude, **B** and **E** field components, electron and proton intensities in several channels.

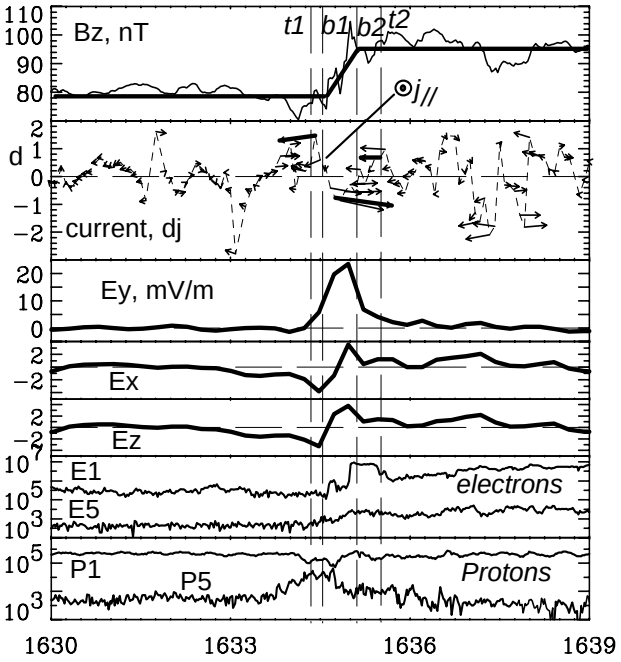


**Figure 2**. Substorm on March 6, 1991. **B** and **E** field components and current perturbation dj (in arbitrary units). Electron and proton intensities in two channels.

place near Dixon at about $T_o$ = 1630 UT. The CRRES (orbit 545) was located at $r$ ~5.56$R_E$, mlat = – 7.2°, ~21.5 MLT and magnetic longitude ~ 145°. Before $T_o$, the fluxes of the electrons in channel E1 and the protons P3–P5 were isotropic. The fluxes of protons in channels P1–P2 have maximum on PA = 90°. Thus the CRRES was located inside the PS near isotropic boundary of trapped energetic particles.

Figure 1 presents (from the top to the bottom): (1) – total magnetic field on the CRRES; (2–4) – magnetic field components and (5–7) – E field components; (8) – electron flux from the channels E1, E2 and E6, and (9) – proton flux from the channels P1 and P5.

In Figure 1 one can see a large (~ 24 mV/m peak) impulsive westward electric field $E_y$ in the interval 't1–t2'. This $E_y$ impulse has a short time duration of ~1 min and correlates with:

1) the magnetic field dipolarization;
2) the increases of B field variations on a finer time scale;
3) the onset of energetic electron injection.

*Perturbation currents*. Our interpretation of the magnetic field data are based on the following approach. We suppose that localized current perturbation in magnetosphere may be deduced from differential magnetic field perturbation d**B**(t) = **B**(t + dt) – **B**(t). The line current model was used to simulate equivalent current d**j**, associated with this perturbation d**B**. We assume that the current d**j** is restricted to the equatorial plane and have an arbitrary orientation. In the framework of this model, using the Biot-Savart law, we estimated the magnitude, orientation and location of the current d**j**. We will refer to this effective current as a "perturbation current" [*Kozelova et al*., 1996].

Figure 2 presents (from the top to the bottom): (1) – 2*s* values (thin solid line) and 30*s*-smoothed values (heavy solid line) of $B_z$ component measured by the CRRES; (2) – differential 30*s*-smoothed perturbation currents (in arbitrary units) for dt = 5*s* relative to the CRRES projection ($r_o$ = 5.5$R_E$) on XY plane. The positive distance 'd' is parallel to the **X** axis. Current flow to the right corresponds to eastward current $dj_E$.

One can see rapid dynamic changes in the magnitude, orientation, and location of the perturbation currents **dj**. In the interval 't1–t2', such kind of temporal sequence of currents **dj** is observed. At first, the westward current $dj_W$ appears Earthward the CRRES. Then the eastward current $dj_E$ appears (0.5–1)$R_E$ tailward the CRRES. Finally, the current $dj_W$ appears again Earthward the CRRES. The appearance of the current $dj_E$ may signify the occurrence of the CD. On Figure 2, the interval 'b1–b2', when current $dj_E$ exists, separates two states of magnetic field with different $B_z$ values. Thick lines denote the two states $B_z$=*const* and the transition between these states. This transition in the interval 'b1–b2' presents 'local dipolarization' on the CRRES location.

This interval 'b1–b2' has a short time duration ~ 40*s* and is observed near $E_y$ impulse peak. Since the $E_y$ field is westward, the eastward current $dj_E$ means that, locally, transiently, the PS region near the CRRES site is a generator, (**dj**·**E**) < 0. Before moment 'b1' and after moment 'b2', the westward current $dj_W$ means that this time the PS region near the CRRES is a load, since (**dj**·**E**) > 0.

*Injection of particles.* The $E_y$ impulse coincided with the onset of electron injection which has a fine structure and consists of, at least, two processes:

1) more smooth enhancements of electron fluxes and
2) bursts of particles.

The first electron burst and the reverse of the meridional component $E_x$ sign near the moment 'b1' coincide with the FAC from the ionosphere which is replaced Earthward. The proton injection occurred ~25*s* before $E_y$ impulse, when the $B_z$ component decreased and the meridional tailward component $E_x$ increased.

Thus, the impulse of the westward field $E_y$ coincides with the magnetic field dipolarization and has an inductive origin. The changes of **B** field configuration during this time may be described by the appearance of the differential eastward current $dj_E$ (or the decrease of the cross-tail current) on $r \sim 6.5R_E$. Since (**dj**·**E**) < 0, this current may be the driven current in the SCW model [*McPherron et al*., 1973].

The role of the PS region near the CRRES site changes during the $E_y$ impulse: firstly it is a load, then it becomes a generator and, finally, it is a load again. This may be interpreted as follows. The increase of the $E_y$ field and the injection of particles lead to the local enhancement in the current intensity. Then, the current sheet becomes unstable upto a cross-field current instability [*Lui et al*, 1991], which triggers the CD. During a short time, the local PS region near the CRRES becomes a generator.

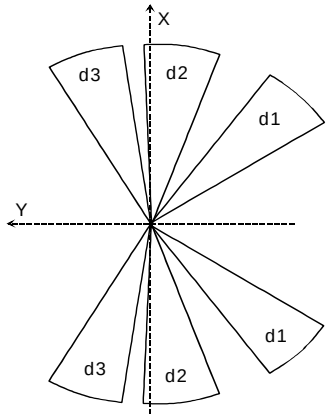


**Figure 3.** Scheme of the sectors on the XY−plane where the gyrocenters of the protons measured by different detectors d1−d3 are located.

## 3. Westward expansion of substorm activation in the magnetosphere

*Lui et al*. [1988] concluded that the CD region on $r \sim 7–9R_E$ consists of localized particle intensity enhancements (activation) with short duration (10–50*s*). The spatial scale of these active regions can be of the order of the ion gyroradius $\rho_i$ [*Ohtani*, 1998].

We used the particle data (with the best possible one second resolution) on the CRRES to study the dynamics of the fine-scale structures of activation near and during the local dipolarization on $r \sim 6R_E$. The proton flux anisotropy on three particle detectors was used to determine qualitatively the location of the acceleration region relative to the CRRES. A detector looking toward dawn (dusk) measured the $J_+$ (J_) intensity of the protons having the gyrocenters Earthward (tailward) of the CRRES. The gyrocenters of protons measured by different detectors d1–d3 located within the different sectors denoted by d1–d3, respectively. Figure 3 presents a sketch of these sectors. Here **X** is pointing toward the Sun (approximately Earthward in the midnight) and **Y** – westward. The $J_+$ (J_) intensity corresponds to the sectors on the plane with the X > 0 (X < 0).

*Substorm on February 27, 1991.* Starting at 1003 UT, a series of activations were observed at Barrow and Fort Simpson. More intensive activation lasted from 1021 to 1027 UT. This time the CRRES (orbit 527,

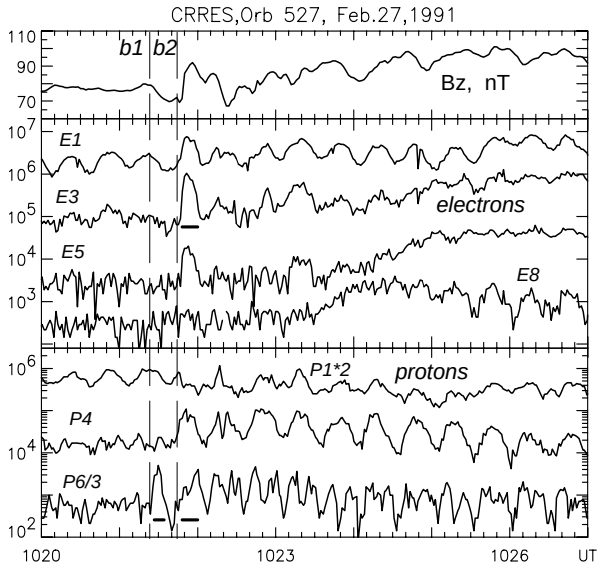


**Figure 4**. Substorm on February 27, 1991. Electron and proton flux changes in the several channels.

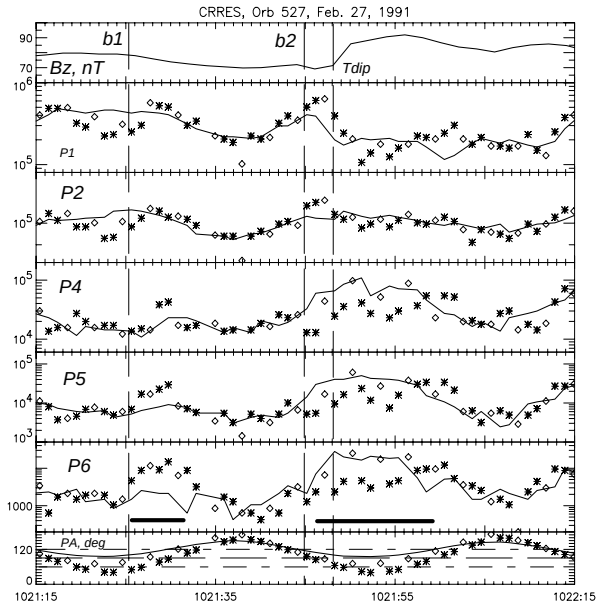


**Figure 5.** Substorm on February 27, 1991. Proton fluxes recorded by three detectors in the several energy channels. For different detectors (from East to West) the fluxes (and pitch angles) are shown with different symbol: solid line, rhombus and asterisk respectively.

23.57 MLT, mlat = –3.95°, and $r = 6.1R_E$ ) was located near the inner edge of the PS.

Figure 4 presents the $B_z$ component of the magnetic field and the electron and proton intensity in several channels. One can see that clear dispersionless burst of energetic electrons in the channels E1–E7 comes after the burst of energetic protons P6.

Figure 5 presentsprotons and their pitch angles (PA) obtained by three detectors d1–d3. It is necessary to remember that the phase when the PAs decrease (increase) corresponds to fluxes J+ (J_).

From Figures 4–5 one can see:

*Moment 'b' (22s before the Tdip).* First short (with the duration of 6s) burst of protons with the gyrocenters tailward of the CRRES was observed in the channels P4–P7 (85–250 keV) with very small dispersion. In the channel P4 ($\rho_i$ ~ 510 km), the intensity J_ increased with 3s delay from the burst in P6 ($\rho_i$ ~ 670 km), indicating the Earthward activity expansion velocity of 50 km/s. The proton burst was observed by the detectors d2–d3 only, indicating the westward gradient of proton population.

*Moment 'b2' (4 s before the Tdip).* Second burst of protons with gyrocenters Earthward of the CRRES was observed in the channels P1–P6 (37–193 keV) without dispersion. In the higher energy channels one can see the higher increases of proton flux $J_+$ on detector d1, what may indicate the source of the protons located eastward of the CRRES.

Dispersionless burst (with the duration of 15*s*) of energetic electrons in the channels E1–E7 (21.5–94.5 keV) occurs nearly simulteneously with the impulse of $B_z$ component. The lack of energy dispersion is an argument for local acceleration. The electron burst coincides with the decrease (drop) of the proton flux $J_+$ in the lowest energy channel P1 (37–54 keV). This proton drop begins eastward of the CRRES and expands westward with the velocity of 350 km/s.

*Substorm on Jan 24, 1991*. During this substorm the CRRES (orbit 445, 23.55 MLT, mlat = – 0.9°, and $r = 6R_E$) was located within PS [*Maynard et al*., 1996]. From the Figures 6–7 one can see:

1. Dispersionless injection of energetic electrons in the channels E1–E5 (21.5–69 keV) coincides with the drop of the proton flux $J_+$ in the lowest energy channel P1 (37–54 keV), which expands westward with the velocity of 130 km/s.
2. 20*s* before the electron injection, the precursor in the form of the proton increase with 2*s* dispersion is observed. This precursor propagates Earthward with the velocity of 150 km/s.

Thus, the analysis of several substorm events (see also [*Kozelova et al*., 2002]) shows that on $r \sim 6R_E$ the short interval of 30–40*s* consists of the temporal sequence of such phenomena: the proton injection with the dispersion in 2*s*, the proton injection without

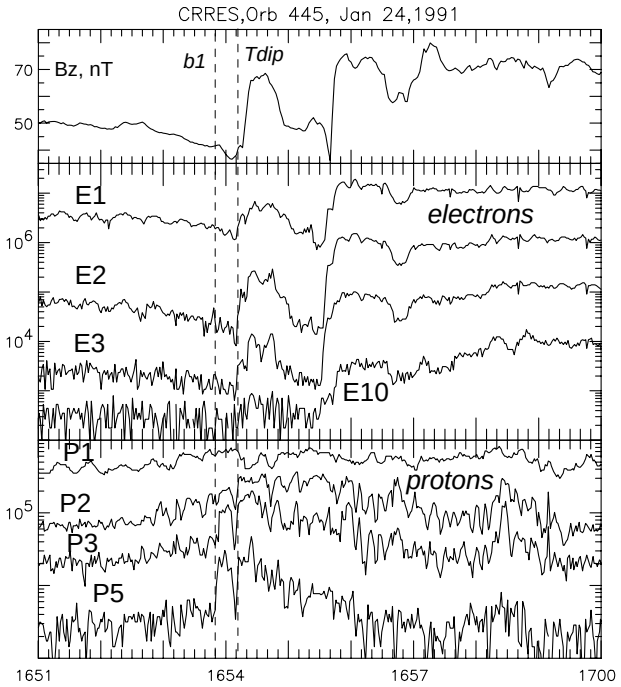


**Figure 6.** Substorm on January 24, 1991. Shown in the same format as Figure 4.

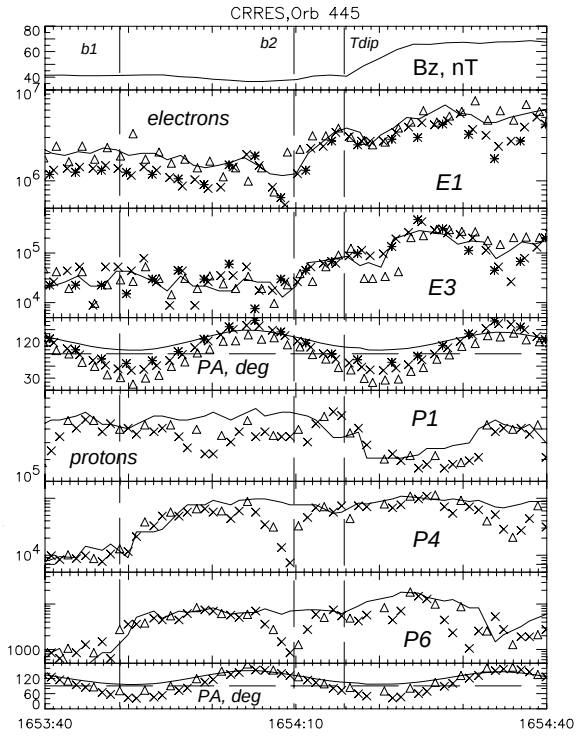


**Figure 7.** Substorm on January 24, 1991. Drop of the proton flux $J_+$ in channel P1 expands westward with the velocity of 130 km/s. Shown in the same format as Figure 5.

dispersion, the electron injection without dispersion (simultaneously with local dipolarization onset), and at last the electron injection with dispersion. This sequence may be a signature of westward and/or Earthward expansion of the substorm activation when new localized regions of impulsive particle accelerarion appear outside the initial position of the active region. The main results of the analysis of nearly dispersionless proton and electron injections are the following:

1. Sometimes the ion flux variations are noncoherent within a small spatial region comparable to the gyroradius (here $\rho_i \sim 350–1400$ km).
2. Dispersionless electron injection coincides with the local $T_{dip}$ and the drop of the 37–69 keV proton flux. This drop may expand westward with the velocity of 130–350 km/s.
3. Intensive higher energy proton burst develops just 20–30s prior to the $T_{dip}$. During this time the $B_z$ component decreases which is morphologically similar to the magnetic signature of the Explosive Growth Phase (EGP) [*Ohtani et al*., 1992].
4. Earthward expansion of the substorm activation occurred with the velocity of (50–150) km/s.

## 4. Oscillation of B and E fields before the local dipolarization

The magnetic fluctuations associated with the CD have been studied by several authors. *Holter et al*. [1995] obtained the oscillations at a low frequency with a period of 40–65*s* on $r = 6.6R_E$. *Roux et al.* [1991] observed similar oscillations in the electric field. They related these oscillations to the ballooning waves and the westward travelling surges. *Maynard et al*. [1996] presented the observations of brief electric field reversals from dawn-dusk to dusk-dawn before the substorm onset. *Erickson et al*. [2000] discovered that (1) quasi-electrostatic drift-wave oscillations with a period of 60–90*s* appear during the growth phase, (2) amplitude of *B* field oscillations with a period of 30*s* increases near local dipolarization onset.

Besides, higher frequency components of magnetic fluctuations during the CD are also observed. *Ohtani et al*. [1995] examined magnetic fluctuations that start almost simultaneously with ground substorm onsets. These fluctuations have typical time scales, which are several times larger than proton gyroperiod.

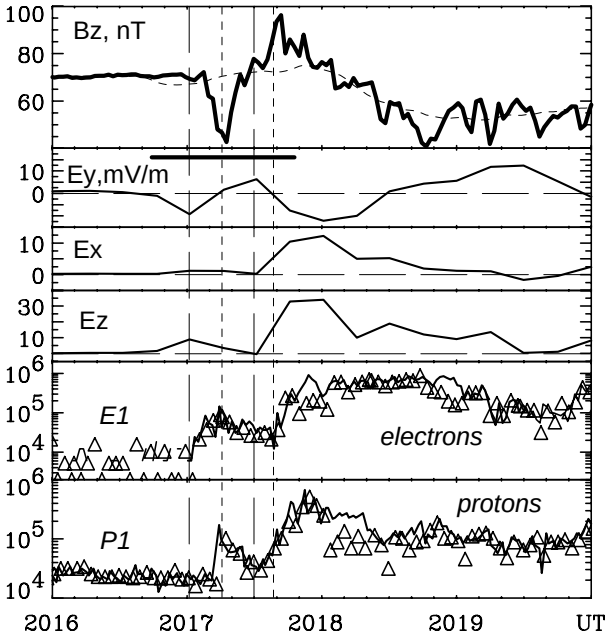


**Figure 8.** One oscillation of the $E_y$ and $B_z$ with quasi-period of 50*s* near the substorm onset on January 24, 1991. Substorm *B* onset on March 6, 1991.

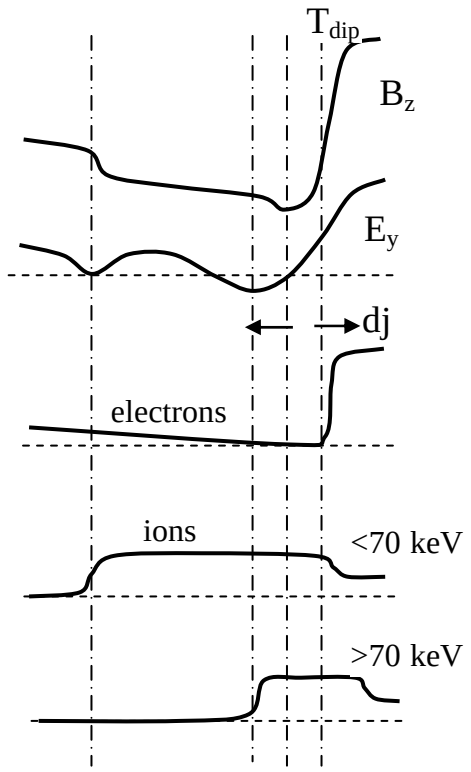


**Figure 9.** A scheme of changes in the fields, currents and particle fluxes near $T_{dip}$ from CRRES data.

These timescales are in good agreement with the predicted unstable wave frequencies from the cross-field current instability [*Lui et al*., 1991].

*Kozelova et al.* [2000] investigated the particle and field variations from the CRRES satellite near and prior to the beginning of dipolarization. The most significant result was an observation of one oscillation of the *E* and *B* fields with quasi-period of ~50 just before the $T_{dip}$ on March 6, 1991. This substorm occurred at $T_o$ = 2017 UT westward Dixon. The CRRES (orbit 545, $r \sim 5.59R_E$, mlat = $-14.8^o$, ~23.6 MLT) was located outside the current sheet plane. Large particle flux decreases and $\Delta B > 0$ during substorm growth phase, both these conditions are consistent with a thinning of the near-Earth plasma sheet.

Figure 8 presents: (1) $B_z$ component, (2–4) components of *E* field, (5–6) electron (proton) data in channel E1 (P1) from several detectors, respectively. One can see in Figure 8 that a large (~34 mV/m peak) impulsive component $E_z$ was observed simultaneously with particle injection and dipolarization. Just prior to the $T_{dip}$, one can see an oscillation of the $E_y$ with the quasi-period of ~50*s*. The CRRES observed also the similar variation in the magnetic field. The amplitude in the $B_z$ component is the largest.

One can suppose that the $B_z$ component in this interval is a sum $B_z = < B_z > + dB_z$, where $< B_z >$ is the 60*s*-smoothed value of $B_z$ (dashed line in Figure 8) and $dB_z$ is an oscillatory part of the $B_z$. The peak-to-peak amplitude of the *E* field is about 12 mV/m and of the *B* field is about 50 nT. One can reveal a phase shift ~ $90^o$ between $E_y$ and $B_z$ and $B_z$ lags $E_y$. This phase relationship between $E_y$ and $B_z$ field oscillations is an indication of the even (antisymmetric) mode of the standing wave.

Besides, in Figure 8, one can see the tendency to anticorrelation between particle fluxes and *B* field. This anticorrelation may be a signature of slow magnetosonic waves. Thus, the observed oscillation of the *E* and *B* fields may be interpreted as a coupled shear Alfven-slow magnetosonic mode. These oscillations may result from the ballooning instability.

## 5. Discussion

In this paper we review some features both of the structure of the *B* and *E* fields and of the plasma distribution occurring a few minutes before the onset of the substorm explosive phase. The most significant are the signatures of one oscillation with quasi-period of ~50*s* and with a phase shift ~$90^o$ between $E_y$ and $B_z$ observed just before the local dipolarization onset. These data support drift-Alfven ballooning as the possible mecha-

nism for initiation of the substorm local onset in the near-geosynchronous plasma sheet.

Examination of the local conditions leading up to CD is the main purpose of many scientific investigations. The known initial signatures of the field and particle flux changes in the near-geosynchronous plasma sheet detected just prior to CD are the following:

1. Appearance of intense beam of (10–70 keV) ions, the field becomes more tail-like, and non-adiabatic regime of ions in the thinning current sheet on r ~10$R_E$ [*Mitchell et al.*, 1990].
2. Sharp decrease of H component of magnetic field and the increase of energetic (68–385 keV) ion flux tailward of the spacecraft on $r < 9R_E$ [*Ohtani et al*., 1992]. Ohtani et al. explained it in terms of the explosive enhancement of the tail current intensity just to the CD. This is a signature of the EGP.
3. Large duskward shift of ion population close to the ion thermal speed on r ~ 8–9$R_E$ [*Lui*, 1995].
4. Brief cross-tail electric field reversals from dawn-dusk to the dusk-to-dawn, prior to the beginning of substorm on $r \sim 6.3–6.6R_E$ [*Roux et al*., 1991]. When the electric field turns eastward, ($\mathbf{j}\cdot\mathbf{E}$) < 0, the drift wave couples to the Alfven mode, and plasma kinetic energy is converted into electromagnetic energy, which flows mainly toward the ionosphere. These electric field reversals often correlate with changes in cross-tail currents and particle energies at the CRRES [*Maynard et al*., 1996] Quasi-electrostatic drift-wave oscillations with a period of 60-90*s* appear during the growth phase [*Erickson et al*., 2002].
5. Increase of magnetic field oscillations with 30-s period (after one or more such eastward reversals of the *E* field). Then the power flowing toward the ionospheree began an explosive increase (local explosive onset – LEXO) [*Erickson et al*., 2002].

*Erickson et al.* [2002] suppose that drift-Alfven ballooning in the near-geosynchronous PS is responsible for initiation of the SCW and substorm onset. They suppose also that the EGP is a signature of the ballooning phenomenon. *Cheng and Lui* [1998] consider the kinetic ballooning instability and suggest that the increase of energetic ion duskward flux observed during the EGP results from a resonance "the ballooning wave – magnetic drifting energetic ions". Then these ions may lead to the generation of higher-frequency cross-field current-driven instability.

Thus, in the recent studies *Maynard et al*. [1996] and *Erickson et al*. [2000] consider initial time variations in the field and particle fluxes before the dipolarization onset. But they do not notice the phase relationship between $E_y$ and $B_z$ field oscillation and standing wave structure that was obtained in our study. Figure 9 presents a scheme of the changes in the fields, currents and particle fluxes near $T_{dip}$ from CRRES observations.

## 6. Conclusion

Analysis of local conditions leading up to and during the substorm activation onsets in the near-Earth magnetosphere shows the following:

(1) Just before the local dipolarization onset, one oscillation (wavelet) with a quasi-period of ~50*s* and with a phase shift ~90° between $E_y$ and $B_z$ is observed. This oscillation has even (antisymmetric) mode standing wave structure with the tendency to anticorrelation between particle fluxes and *B* field. Thus, the observed oscillation of the *E* and *B* fields may be interpreted as a coupled shear Alfven-slow magnetosonic mode.

(2) 20–30*s* prior to the $T_{dip}$, an intensive higher energy proton burst is observed simulteneously with the $B_z$ component decrease that is morphologically similar to the magnetic signature of the Explosive Growth Phase [*Ohtani et al.*, 1992]. Earthward expansion of this burst occurred with the velocity of (50–150) km/s.

(3) Near the local dipolarization moment, the proton flux variations are noncoherent within a small spatial region comparable with the proton gyroradius (here $\rho_i$ ~ 350–1400 km).

(4) Simulteneously with the local dipolarization onset, dispersionless energetic electron injection and the drop of the lowest energy 37–69 keV proton flux are observed. This drop may expand westward with the velocity of 130–350 km/s.

(5) During the dipolarization, the impulse of induced westward electric field $E_y$ (1 min duration) is observed. The changes of **B** field in the time of $E_y$ maximum (duration ~ 40s) may be described by the differential eastward current $dj_E$ (or the decrease of the cross-tail current) on $r \sim 6.5R_E$. This current $dj_E$ is antiparallel to the observed westward Ey field, ($\mathbf{dj}\cdot\mathbf{E}$) < 0, and the plasma sheet region near the CRRES location becomes a generator for a short time.

These features support the drift-Alfven ballooning with a following generation of higher-frequency cross-field current-driven instability as a possible mechanism for initiation of the substorm local onset in the near-geosynchronous plasma sheet. The rapid development of some initial perturbation arising from any instability can lead to the nonlinear process of local *B* field reconfigu-

ration, which will in its turn induce a large *E* field and the particle acceleration.

**Acknowledgments.** Authors are thankful to Dr. N. Maynard for electric field data, Dr. A. Korth for energetic particle data, and H. Singer for magnetic field data from the CRRES spacecraft. Authors are grateful to Dr. Yuri Galperin for scientific interest to our papers during many years. The work is supported by grant RFBR-01-05-64827-a.

**References**

Cheng, C. Z., and A. T. Y. Lui, Kinetic ballooning instability for substorm onset and current disruption observed by AMPTE/CCE, *Geophys. Res. Lett., 25*, 4091, 1998.

Erickson, G. M., N. C. Maynard, G. R. Wilson, and W. J. Burke, Electromagnetics of substorm onset in the near-geosynchronous plasma sheet, *Proc. Fifth International Conference on Substorms, St. Petersburg. Russia.16-20 May 2000. ESA SP-443 (July, 2000)*, 385, 2000.

Holter, O., C. Altman, A. Roux, S Perraut, A. Pedersen, H. Pecseli, B. Lybekk, J. Trulsen, A. Korth, and G. Kremser, Characterization of low frequency oscillations at substorm breakup, *J. Geophys. Res., 100*, 1995.

Korth, A., G. Kremser, B. Wilken, W. Guttler, S. L. Ullaland and R. Koga, The electron and proton wide-angle spectrometer (EPAS) on the CCRES spacecraft, *J Spacecr. Rockets. 29*, 609, 1992.

Kozelova, T., L. Lazutin, B. Kozelov, and R. Rasinkangas, Dynamic injections, reconfiguration of magnetic field and equivalent magnetosperic cueernts asobserved by CRRES, *Proc. Third International Conference on Substorms (ICS-3). Versailles. France.12-17 May 1996. ESA SP-389 (October, 1996)*, 429, 1996.

Kozelova, T. V., B. V. Kozelov, and L. L. Lazutin, Substorm large impulsive electric fields observed by CRRES, *Proc. 5th International Conference on Substorms, St. Petersburg, Russia, 16-20 May, 2000, (ESA SP-443, July 2000)*, 393, 2000.

Kozelova, T. V., L. L. Lazutin, and B. V. Kozelov, Westward expansion of substorm activation in the magnetosphere, *Proc. XXV Annual Seminar "Physics of Auroral Phenomena", Apatity*, 25, 2002.

Lui, A. T. Y., R. E. Lopez, S. M. Krimigas, R. W. McEntire, L. J. Zanetti, and T. A. Potemra, A case study of magnetotail current sheet disruption and diversion, *Geophys. Res. Lett, 15*, 721, 1988.

Lui, A. T. Y., C. -L. Chang, A. Mankofsky, H. -K. Wong, and D. Winske, A cross-field current instability for substorm expansion, *J. Geophys. Res., 96.*, 11389, 1991.

Lui, A. T. Y., Observed features in current disruption and their implications to existing theories, *Space Plasmas: Coupling Between Small and Medium Scale Processes, Geophysical Monograph 86*, 149, 1995.

Maynard, N. C., W. J. Burke, E. M. Basinska, G. M. Erickson, W. J. Hughes, H. J. Singer, A. G. Yahnin, H. J. Hardy, and F. S. Mozer, Dynamics of the inner magnetosphere near times of substorm onsets *J. Geophys. Res., 101*, 7705, 1996.

McPherron, R. L., C. T. Russel, and M. P. Aubry, Satellite studies of magnetospheric substorms on August 15, 1968: Phenomenological models for substorms, *J. Geophys. Res., 78*, 3131, 1973.

Mitchell, D. C., D. J. Williams, C. Y. Huang, L. A. Frank, and C. T. Russell, Current carriers in the near-Earth cross-tail current sheet during substorm growth phase, *Geophys. Res. Lett., 17*, 583, 1990.

Ohtani, S., K. Takahashi, L. J. Zanetti, T. A. Potemra, R. W. McEntire, and T. Iijima, Initial signatures of magnetic field and energetic particle fluxes at tail reconfiguration: Explosive growth phase, *J. Geophys. Res., 97*, 19311, 1992.

Ohtani, S., T. Higuchi, A. T. Y. Lui, and K. Takahashi, Magnetic fluctuations associated with tail current disruption: ractal analysis, *J. Geophys. Res., 100*, 19135, 1995.

Ohtani, S., Earthward expansion of tail current disruption: dual-satellite study, *J. Geophys. Res., 103*, 6815, 1998.

Roux, A., S. Perraut, P. Robert, A. Morane, A. Pedersen, A. Korth, G. Kremser, B. Aparicio, D. Rodger, and R. Pellinen, Plasma sheet instability related to the westward traveling surge, *J. Geophys. Res., 96*, 17697, 1991.

Singer, H. J., W. P. Sullivan, P. Anderson, F. Mozer, P. Harvey, J. Wygant, and W. McNeil, Fluxgate magnetometer instrument on CRRES, *J. Spacecr. Rockets, 29*, 599, 1992.

Wygant, J. R., P. R. Harvey, F. S. Mozer, N. C. Maynard, H. Singer, M. Smiddy, W. Sullivan, and P. Anderson, The CRRES electric field/Langmuir probe instrument, *J. Spacecr. Rockets, 29*, 601, 1992.

# Statistic study of geomagnetic storm dependences on solar and interplanetary events during 1976-2000

Yu. I. Yermolaev[1], M. Yu. Yermolaev[1], A. A. Petrukovich[1],
G. N. Zastenker[1], L. M. Zelenyi[1], and J. -A. Sauvaud[2]

[1] Space Research Institute RAS, Moscow, Russia
[2] CESR, Toulouse, France

**Abstract.** We analyze 25-year sets of solar X-ray observations, measurements of plasma and magnetic field parameters in the solar wind and Dst index variations with the purpose of revealing the factors rendering the greatest influence on development of magnetospheric storms. Value of correlation between solar flares and magnetic storms (~30%) practically does not exceed a level of correlation of random processes. SOHO data on Earth-directed halo-CME for time interval 1996–2000 show that geoeffectiveness of CME is about 35%. The most geoeffective interplanetary phenomena are magnetic clouds (MC) which, as many believe, are interplanetary manifestations of CMEs and compressions in the region of interaction of slow and fast streams in the solar wind (Corotating Interaction Region, CIR): About 2/3 of all observed magnetic storms. For storms with $-100 < Dst < -60$ nT the numbers of storms from MC and CIR are approximately equal, and for strong storms with $Dst < -100$ nT the part of storms from MC is considerably higher. The analysis shows that our and another results are in good agreement if the direction of event tracing are taken into account: *Sun* $\rightarrow$ *Earth* or *Earth* $\rightarrow$ *Sun*. In summary the problems of reliability of a prediction of geomagnetic disturbances on the basis of observations of the Sun and conditions in the interplanetary space are discussed.

## 1. Introduction

Studying of processes providing transfer of disturbances from the Sun to the Earth by means of a solar wind (SW) was and remains the major element of solar-terrestrial physics and in particular to its practical part – "Space weather" program. Recently the quantity of publications on this topic steadily grows, but it is necessary to note, that at close general representations of authors about physical mechanisms of Sun's influence to the Earth there are appreciable divergences in quantitative estimations at the analysis of the same physical picture.

It has been historically developed in such a manner that originally from all active processes on the Sun the solar flares were discovered (see paper by *Gosling* [1993]), and during long time all disturbances in SW and the Earth's magnetosphere tried to connect extremely with solar flares (see, for example, the book by *Hargreaves* [1992]). After opening in the beginning of 70th years of other powerful solar process – coronal mass ejection (CME) long time CMEs were studied by only separate researchers and as a whole in consideration of a chain of solar-terrestrial connections were not used almost. However after known paper by *Gosling* [1993] the situation has sharply changed, and now CME is considered almost as the unique cause of all interplanetary and geomagnetic disturbances [*Webb*, 1995; *Crooker*, 2000; *Webb et al.*, 2000].

Nevertheless in the literature there are various estimations of CME geoeffectiveness from 35–45% [*Wang et al.*, 2002;*Yermolaev and Yermolaev*, 2003*a*] up to 83–100% [*Brueckner et al.*, 1998; *St.Cyr et al.*, 2000; *Zhang et al.*, 2003] (see also [*Webb et al.*, 1996; *Webb et al.*, 2000; *Crooker*, 2000; *Li et al.*, 2001; *Yermolaev and Yermolaev*, 2003*b*] ) and interplanetary CME (ICME), ejects and magnetic cloud (MC) geoeffectiveness from 25% [*Vennerstroem*, 2001] up to 82% [*Wu and Lepping*, 2002] (see also [*Gosling et al.*, 1991; *Gopalswamy et al.*, 2000, 2001; *Yermolaev et al.*, 2000; *Richardson et al.*, 2001; *Yermolaev and Yermolaev*, 2002; 2003*a*,*b*]) which do not agree with each other. Recently new papers with the statistical analysis of connection between geomagnetic storms and solar flares were published and they gave estimations 30-45% [*Park et al.*, 2002; *Yermolaev and Yermolaev*, 2002, 2003*a*], while in former works there are the data on geoeffectiveness of flares from 59% [*Krajcovic and Krivsky*, 1982] up to

88% [*Cliver and Crooker*, 1993]. We believe that both CMEs and flares are different (with different spatial and temporal scales) manifestations of one global process on the Sun (see for example discussions [*Harrison*, 1996; *Low*, 2001; *Forbes*, 2000; *Cliver and Hudson*, 2002] and references therein). A question, what from these processes is better to use as the indicator of the solar events resulting in interplanetary disturbances and then to the geomagnetic storms, remains open. Therefore in this paper we analysed data on connection between solar flares, CMEs, solar wind events and geomagnetic storms.

## 2. Data analysis

For the analysis we used the solar, interplanetary and magnetospheric data obtained via the Internet in the time interval of 1976–2000:

1. List of strong solar flares of importance $\geq M5$ (ftp://ftp.ngdc.noaa.gov/STP/SOLAR DATA/SOLAR FLARES/XRAY FLARES) and list of CME observations on SOHO spacecraft (1996-2000) (http://cdaw.gsfc.nasa.gov/CMElist/);
2. Parameters of plasma of the solar wind (velocity, temperature and density of ions) and the magnitude and three components of IMF (http://nssdc.gsfc.nasa.gov/);
3. Hourly average values of *Dst* index (http://nssdc.gsfc.nasa.gov/ and http://swdcdb.kugi.kyoto-u.ac.jp/dstdir/).

Before analysis we should compare more critically those data analysis methods used for study of between solar, interplanetaryand magnetospheric phenomena which were described in previous papers. Except for the ambiguity of comparison of the results connected with different approaches of event classification there is also an ambiguity connected with a technique of comparison of phenomena in two space areas. If for the analysis two phenomena with samples $X1$ and $X2$ were chosen and conformity was established for number of phenomena X12 then ”effectiveness” of process $X1 \rightarrow X2$ is usually defined as ratio of values $X12/X1$ which differs from ”effectiveness” of process $X2 \rightarrow X1$ equal $X21/X2 = X12/X2$, because samples $X1$ and $X2$ are selected by various criteria and can be different value. Thus the ”effectiveness” determined in different works depends on a direction of the process analysis. If to take into account that sometimes sample $X2$ is not fixed prior to the beginning of the analysis, i.e. the rule (or criteria) selection of events for sample $X2$ originally is not fixed the ambiguity of calculation of process ”effectiveness” can grow in addition.

As in solar-terrestrial physics we investigated 2-step process: the Sun – solar wind and the solar wind – magnetosphere, the presence of the data on an intermediate link can increase the reliability of estimations for all chain. Let us assume that there are data for sets on the Sun $X1$ and $Y1$, in interplanetary medium $Y2$ and $Z1$ and in magnetosphere $X2$ and $Z2$ for which estimations of ”effectiveness” of processes $X1 \rightarrow X2$ equal $X12/X1$, $Y1 \rightarrow Y2$ equal $Y12/Y1$ and $Z1 \rightarrow Z2$ equal $Z12/Z1$ were obtained. In this case it is natural to assume that ”effectiveness” of full process should be close to product of ”effectivenesses” of each parts, i.e. $X12/X1 = (Y12/Y1)(Z12/Z1)$. In particular it means the ”effectiveness” of full process cannot be higher ”effectiveness” of each of parts: $X12/X1 \leq Y12/Y1$ and $X12/X1 \leq Z12/Z1$. The published works contain the data sufficient for such analysis and we shall carry out it below.

It is important to note that authors frequently understand ”geoeffectiveness” of a phenomenon as completely different values obtained with the help of different procedures. In strict sense of this word, geoeffectiveness of the solar or interplanetary phenomenon is defined as percentage corresponding set of the solar or interplanetary phenomena resulted in occurrence of magnetic storms, and storms of the certain class. In other words, first of all it is necessary to select the solar or interplanetary phenomena by the certain rule, then to investigate each phenomenon from this list with occurrence of a storm using certain algorithm. The time of delay between the phenomena which should be stacked in some beforehand given ”window” is used as algorithm of comparison of the various phenomena: either characteristic times of phenomenon propagation between two points, or time delay determined on some initial data.

Very much frequently the authors act on the contrary and use the back tracing analysis: they take the list of storms as the initial list and extrapolate them back in the interplanetary space or on the Sun and search there for suitable phenomenon. This way defines not geoeffectiveness and allows to find candidates in the interplanetary space or on the Sun on the reason of the given magnetic storms. If to take into account that the phenomena of different classes are frequently used as such candidates if they only suited on time this is clear reason of divergence of results of many works.

We used the direct tracing of solar events: solar flares and Earth-directed halo-CME. In accordance with time delay between solar event and magnetic storm (see Figure 1) we classified solar events after which it is most probably (*a*, time delay of 2–4 days), probable (*b*, 1.5–2 and 4–5 days), less probable (*c*, 1–1.5 and 5–6 days) and impossible (*d*, <1 and >6 days) to observe the magnetic storms. Results of statistical analysis of solar flare and CME geoeffectiveness are presented in figures 2 and 3. It is necessary to note that time delay of 2–4 days

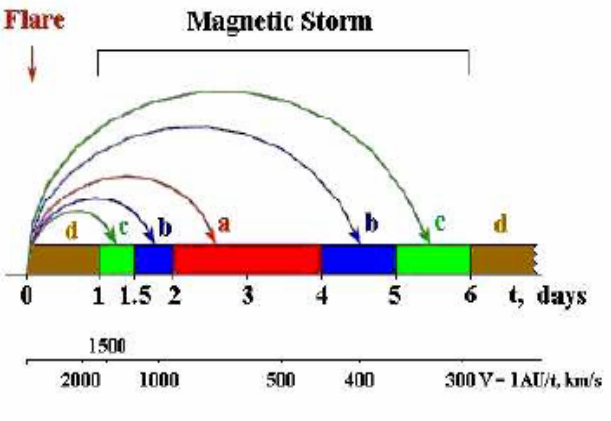


**Figure 1.** Schematic view of classification of solar sources of magnetic storms.

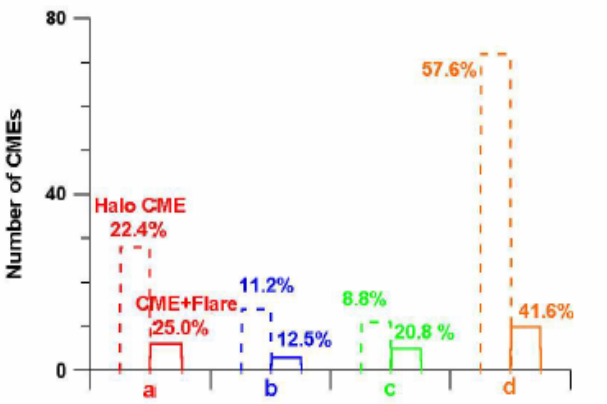


**Figure 3.** The number of CME accompanying and not by solar flares (continuous and shaped lines) after which it is most probably (a), probably (b), less probably (c) and impossibly (d) to observe the magnetic storms.

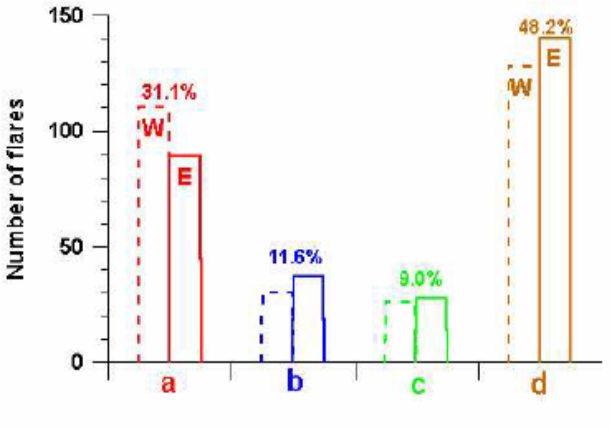


**Figure 2.** The number of west and east strong (importance ≥ *M*5) solar flares (shaped and continuous lines) after which it is most probably (a), probable (b), less probable (c) and impossible (d) to observe the magnetic storms.

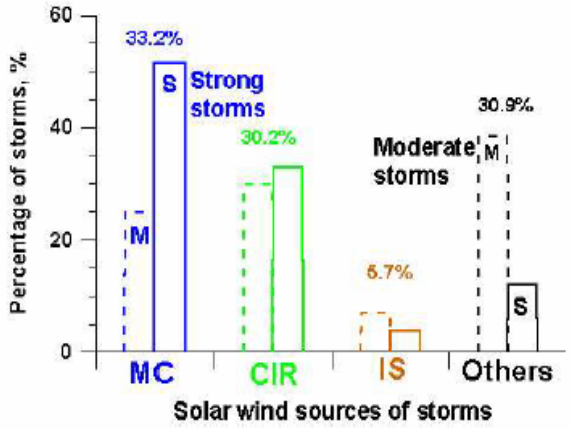


**Figure 4.** Solar wind types – sources for moderate (dashed line) and strong (solid line) magnetic storms.

corresponds to average velocity of disturbances 430–870 km/s on a line the Sun – Earth and it is usual velocity of SW in the orbit of the Earth.

Results of such analysis for 653 solar flares ≥ M5 are shown as histograms in the Figure 2 by shaped and continuous lines – for west and east flares respectively, and histograms ”a”, ”b”, ”c” and ”d” concern, respectively, to most probable sources (31.1 %) of storms, to probable (11.6 %) and less probable (9.0 %) sources and the flares which have not resulted in the storms (48.2 %). The total number of the west flares as a whole appeared more than east but after normalization on number of those and other types of flares the difference between distributions of west and east flares in all histograms practically disappears.

The set of CMEs registered on SOHO spacecraft during 1996–2000 contains 125 so-called Earth-directed halo-CMEs (i.e. CME occupying all space around the Sun on the corona images and as it is supposed moving in the direction of the observer, to the Earth), and 24 from them were accompanied by strong flares from already described set of strong flares. Applied to the CME the described above technique of definition of possible geoeffectiveness on the time delay between CME and magnetic storm gives low geoeffectiveness of CMEs (see. Figure 3): for type *a* 22.4 % and 25.0 %, for type *b* 11.2 % and 12.5 %, for type *c* 8.8 % and 20.8 %

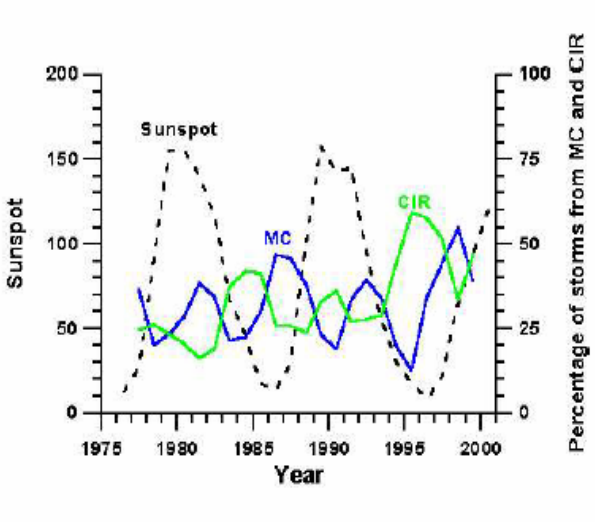


**Figure 5.** Time variation of part of the magnetic storms excited by MC (black line) and by CIR (grey line). Dashed line – the sunspot (scale on the left).

and for type *d* 57.6 % for all CMEs and 41.6 % for CMEs accompanied by solar flares. Thus, obtained geoeffectiveness of Earth-directed halo-CMEs appears below the geoeffectiveness of solar flares.

At the analysis of interplanetary sources we did not analyze all data file on SW and, using the time of observation of magnetic storms, we searched for interplanetary disturbances which could precede and result in moderate and strong magnetospheric disturbances. Therefore we used back tracing of events and geoeffectiveness of interplanetary disturbances discussed below has some other sense than mentioned above for solar flares and CMEs. Measurements of interplanetary parameters are available only for ~2/3 (404 events) of 618 moderate and strong magnetic storms and it allows us to estimate distribution between different geoeffective SW types with enough good statistics (see Figure 4): interplanetary sources of (in brackets for moderate and strong, respectively) magnetic storms in 33.2% (24.9% and 51.5%) cases are MCs, in 30.2% (29.9% and 32.8%) cases – CIRs, in 5.7% (6.9% and 3.7%) – ISs and in 30.9% (38.3% and 11.9%) – other SW types. Thus, in comparison with moderate storms the part of strong storms from MCs grows from ~1/4 up to ~1/2, from CIRs remains at a level ~1/3, and from ISs and other SW types appreciably falls.

The analysis of behavior of solar wind and IMF parameters (here they are not shown) for geoeffective events in the interplanetary space confirms the known fact that the sources of magnetospheric disturbances are events in which large negative (southward) IMF component is observed sufficiently long time. Just the similar situation is most frequently registered in MC, CIR and after IS passage. It is possible to explain this fact if the southward IMF component was in originally undisturbed solar wind as a result of dynamic processes during motion of MC, CIR and IS there is a compression and increase of all IMF components in the region of compression including IMF components parallel to the terrestrial magnetic dipole.

We investigated the change of a distribution of storms from MC and CIR in cycle during more than 2 solar cycles. For this purpose for each year we found the ratio of total number of moderate and strong storms respectively from MC and CIR to the number of storms for which it was possible to determine SW type. These results are presented in Figure 5. As the statistics of number of year average storms is not so large, especially in the minimum of cycle, to remove the high-frequency fluctuations connected with small statistics, we carried out smoothing these ratios by sliding average over three points. The Figure 5 confirms the conclusion made earlier [*Yermolaev and Yermolaev*, 2002]: curves for MC and CIR have 2 maxima for a solar cycle and change in antiphases.

## 3. Discussion

The results of comparison of CMEs, solar flares and the various interplanetary phenomena with magnetic storms for several last years are shown in table 1. First of all it is necessary to note, that we selected results on the comparing phenomena and the direction of tracing. For example, record "*CME → Storm*" means that for the initial data set the CME list was taken, the number of analyzed cases of CMEs is presented in a column "Number of events". The CMEs are compared with magnetic storms, the value of storm is defined by an index which is submitted in a column "Remarks". Thus, we summarized the published data by 6 types of phenomena comparison (3 space areas and 2 directions of tracing): *I: CME → Storm*, *II: CME → Magnetic clouds;Ejecta*, *III: Magnetic clouds; Ejecta → Storm*, *IV: Storm → CME*, *V: Storm → Magnetic clouds; Ejecta* and *VI: Magnetic clouds; Ejecta → CME*. In *II*, *III*, *V* and *VI* we included both magnetic clouds and ejecta (ICME) which are close under the physical characteristics, but in a column "Number of cases" we noted identification of authors by symbols MC (Magnetic clouds) and E (Ejecta). The table also presented data on *VII: Flare → SSC; Storm* and *VIII: Storm → Flare* correlations.

Geoeffectiveness of CME is shown as direct tracing *I: CME → Storm* which includes 5 data sets and changes from 35 up to 71% [*Webb et al.*, 1996; *Webb et al.*, 2000; *Plunkett et al.*, 2001; *Wang et al.*, 2002; *Yermolaev and Yermolaev*, 2003*a*,*b*]. Result 71% [*Webb et al.*, 2000] (later reproduced in papers by [*Crooker*,

2000; *Li et al.,* 2001] was obtained with rather small statistics of 7 cases. Other results obtained with statistics from 38 up to 132 CMEs are in a range of 35–50% and are in good agreement with each other. In our preliminary paper [*Yermolaev and Yermolaev,* 2003*a*] the result 35% was obtained for magnetic storms with *Dst* < –60 nT and if we include weaker storms with *Dst* < –50 nT in analysis (it corresponds to storms with *Kp*>5 like in work by *Wang et al.* [2002]) we obtain geoeffectiveness CME ~40% [*Yermolaev and Yermolaev,* 2003*b*]. Thus, it is possible to make a conclusion, that geoeffectiveness of halo-CME for magnetic storms with *Kp*>5 (*Dst* < –50nT) is 40–50% at suffciently high statistics from 38 up to 132 CMEs.

Results of back tracing analysis *IV: Storm → CME* contain 3 data sets with values from 83 up to 100% and at lower statistics from 8 up to 27 of strong magnetic storms with *Kp* > 6 and *Dst* < –100 nT [*Brueckner et al.,* 1998; *St. Cyr et al.,* 2000; *Li et al.,* 2001; *Zhang et al.,* 2003]. These results are in good agreement but they show not high geoeffectiveness of CME: they indicate that it is possible to find possible candidates on the Sun among CMEs for sources of strong magnetic storms with a high degree of probability. In Figure 6 it is evidently shown distinctions of results from types of comparisons *I: CME → Storm* (dark circles) and *IV: Storm → CME* (light triangles), and the statistics in initial data sets is shown on the bottom panel.

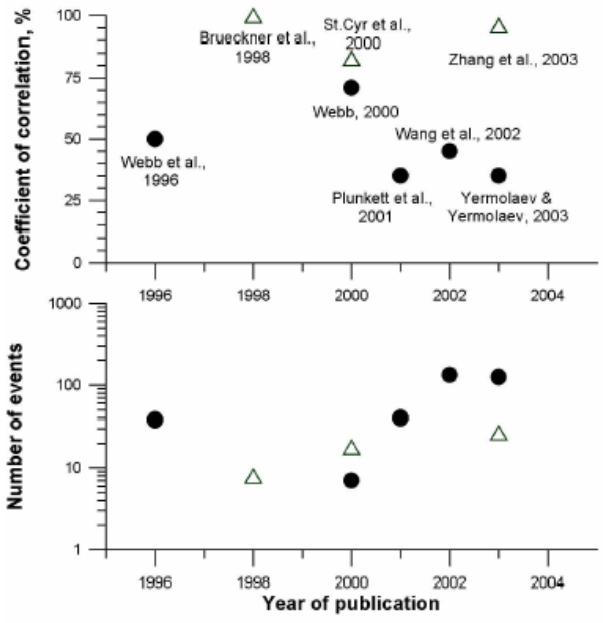


**Figure 6.** Effectiveness tracing *I: CME → Storm* (dark circles) and *IV: Storm → CME* (light triangles). Bottom panel – statistics of events.

**Table 1.** Correlation between solar, interplanetary and magnetospheric phenomena.

| N | % | Number of events | Remarks | Reference |
|---|---|---|---|---|
| | | | *I. CME → Storm* | |
| 1 | 50 | 38 | $Kp$ | *Webb et al.,* 1996 |
| 2 | 71 | 7 | $Dst < -50$ | *Webb et al.,* 2000; *Crooker,* 2000; *Li et al.,* 2001 |
| 3 | 35 | 40 | $Kp > 6$ | *Plunkett et al.,* 2001 |
| 4 | 45 | 132 | $Kp > 5$ | *Wang et al.,* 2002 |
| | 20 | 132 | $Kp > 7$ | |
| 5 | 35 | 125 | $Dst < -60$ | *Yermolaev and Yermolaev,* 2003a |
| | 40 | 125 | $Dst < -50$ | *Yermolaev and Yermolaev,* 2003b |
| | | | *II. CME → Magnetic cloud, Ejecta* | |
| 1 | 63 | 8 | Earth-directed halo-CME | *Cane et al.,* 1998 |
| | | | *III. Magnetic cloud, Ejecta → Storm* | |
| 1 | 44 | 327 E | $Kp > 5$ | *Gosling,* 1991 |
| 2 | | 28 MC | | *Gopalswamy et al.,* 2000 |
| | 67 | | $Dst < -60$ | *Yermolaev and Yermolaev,* 2002 |
| 3 | 63 | 30 MC | $Dst < -60$ | *Yermolaev et al.,* 2000 |
| 4 | | 48 MC | | *Gopalswamy et al., 2001* |
| | 57 | | $Dst < -60$ | *Yermolaev and Yermolaev,* 2003b |
| 5 | 19 | 1273 E | $Kp > 5\_$, Solar minimum | *Richardson et al.,* 2001 |
| | 63 | 1188 E | $Kp > 5\_$, Solar maximum | |
| 6 | 82 | 34 MC | $Dst < -50$ | *Wu and Lepping,* 2002 |
| | | | *IV. Storm → CME* | |
| 1 | 100 | 8 | $Kp > 6$ | *Brueckner et al.,* 1998 |
| 2 | 83 | 18 | $Kp > 6$ | *St.Cyr et al.,* 2000; *Li et al.,* 2001 |
| 3 | 96 | 27 | $Dst < -100$ | *Zhang et al.,* 2003 |
| | | | *V. Storm → Magnetic cloud, Ejecta* | |
| 1 | 73 | 37 | $Kp > 7\_$ | *Gosling,* 1991 |
| 2 | 25 | ? | $Dst(corr)$ | *Vennerstroem,* 2001 |
| 3 | 33 | 618 | $Dst < -60$ | *Yermolaev and Yermolaev,* 2003a |
| | 25 | 414 | $-100 < Dst < -60$ | |
| | 52 | 204 | $Dst < -100$ | |
| | | | *VI. Magnetic cloud, Ejecta → CME* | |
| 1 | 67 | 49 E | CME | *Lindsay et al.,* 1999 |
| 2 | 65 | 86 E | CME | *Cane et al.,* 2000 |
| | 42 | 86 E | Earth-directed halo-CME | |
| 3 | 82 | 28 MC | CME | *Gopalswamy et al.,* 2000 |
| | | | *VII. Flare → SSC, Storm* | |
| 1 | 35-45 | 4836 | $\geq M0$ | *Park et al.,* 2002 |
| 2 | 32 | 653 | $\geq M5$ | *Yermolaev and Yermolaev,* 2003a |
| | | | *VIII. Storm → Flare* | |
| 1 | 59 | 116 | $Kp > 7\_$ | *Krajcovic and Kriv-sky,* 1982 |
| 2 | 20 | 204 | $Dst < -100$ | *Yermolaev and Yermolaev,* 2003a |
| 3 | 88 | 25 | $Dst < -250$ | *Cliver and Crooker,* 1993 |

The comparison of direct and back tracings *II:* (*CME → Magnetic clouds*, *Ejecta*) and *V I:* (*Magnetic clouds*, *Ejec¡ta → CME*) for Earth-directed halo-CMEs shows that in the first case 63% is observed at small statistics of 8 events [*Cane et al.,* 1998], and in the second – 42% at statistics of 86 events [*Cane et al.,* 2000]. Other results are obtained for any CMEs [*Gopalswamy et al.,* 2000; *Lindsay et al.,* 1999] and are not so reliable as for first results. From comparison *III:* (*Magnetic clouds*, *Ejecta → Storm*) follows that correlation for magnetic clouds is a little bit higher 57–82% [*Gopalswamy et al.,* 2000; *Yermolaev et al.,* 2000; *Yermolaev and Yermolaev,* 2002; *Wu and Lepping,* 2002] than for ejecta – ~42 %(44% in paper by *Gosling et al.* [1991] and 41% – average of 19 and 63% [*Richardson et al.,* 2001]. Back tracimg *V:* (*Storm →! Magnetic clouds*, *Ejecta*) yields inconsistent results: 73% [*Gosling et al.,* 1991] and 25% [*Vennerstroem,* 2001] and it is necessary to emphasize that in both cases the definitions of storms and ejecta are different and in the first case the statistics is less (50 months and 32 years, i.e. more than in 7 times). For magnetic clouds in the period 1976–2000 our estimations 33% for moderate and strong storms (25% for moderate storms and 52% for strong storms) [*Yermolaev and Yermolaev,* 2002], are in good agreement with results of work by *Vennerstroem* [2001].

The analysis of a sequence of 2-step direct tracing *II:* (*CME → Magnetic clouds*, *Ejecta*) and *III:* (*Magnetic clouds*, *Ejecta → Storm*) allows us to estimate a probability of total process *CME → Storm* how product of probabilities and for magnetic clouds we obtain a value 0.63 * (0.57 – 0.82) = 0.36 – 0.52 which is close to above mentioned results 40-50% for the direct analysis of process *I:* (*CME → Storm*). For ejecta this approach resulted in less value. The analysis of a sequence of 2–step back tracing *V:* (*Storm → Magnetic clouds; Ejecta*) and *V I:* (*Magnetic clouds; Ejecta → CME*) does not allow us to obtain the high correlation *Storm → CME* in comparison with 83 – 100% in total process *IV* : (0.25 – 0.73) * 0.42 = 0.11 – 0.31. Thus, comparison of two-step and one-step processes for direct tracing *CME → Storm* are in good agreement while for two-step process for back tracing differs in several times from one-step process. It means that techniques of the analysis of processes (*Storm → Magnetic clouds; Ejecta*), (*Magnetic clouds; Ejecta → CME*) and (*Storm → CME*) require significant improvement.

As it has been shown above and in our previous study [*Yermolaev and Yermolaev,* 2003*a*] we carried out direct tracing events *Flare → Storm* and estimated geoeffectiveness of 653 solar flares of importance (on X-ray emission) ≥ *M*5 which in 32% cases resulted in magnetic storms with *Dst* < –60 nT. If we carry out back tracing *Storm → Flare* and take the list of strong magnetic storms with *Dst* < –100 nT, among the given set of flares only 20% can be sources of storm. In paper by *Krajcovic and Krivsky* [1982] in which back tracing *Storm → Flare* was analyzed on large set of solar flares (on optical emission), it was shown that for the period 1954–1976 for 116 storms with *Kp* > 7-, among flares were revealed 59% possible sources. In paper by *Cliver and Crooker* [1993] back tracing *Storm → Flare* also is analyzed and it was shown that for 25 strongest magnetic storms with *Dst* < –250 nT observed in 1957–1990, at least in 22 (88%) cases it is possible to offer solar flare as the candidate of source. High values of ”effectiveness” in papers by *Krajcovic and Krivsky* [1982] and *Cliver and Crooker,* [1993] besides the back direction of comparison of the phenomena, apparently, is connected with fact that even weak solar flares can be considered as possible sources of storms while in our work we analyzed only strong flares.

Comparison of events *Flare → SSC* (i.e. not with geomagnetic storms, and with the phenomena which frequently precede storms) was carried out in recent work [*Park et al.,* 2002] for 4836 flares of importance ≥*M*1 for the period September, 1, 1975 – December, 31, 1999. In result the estimation of geoeffectiveness for time of delay of 2–3 days for all flares was 35–45% and for long duration flares – a little bit more 50–55%.

The main interplanetary sources of moderate and strong magnetic storms are MC and CIR, each of which contains ~1/3 from all geoeffective SW types; and in comparison with moderate storms the part of strong storms from MC grows and reaches half of all geoeffective SW types, number of storms from CIR practically does not change, and from other SW types significantly falls. Our result on correlation of magnetic storms and MCs is in good agreement with the similar data of paper by *Gosling et al.* [1991] though in contrast with our paper there MCs were determined on the basis of counterstreaming electrons, and storms on *Kp* index. Our dependence of the part of the magnetic storms excited by MCs (as well as by CIRs) on the phase of solar cycle has two maxima for a cycle. Thus curves for storms from MCs and from CIRs change in an antiphase that was necessary to expect as the sum of parts of storms from MCs and from CIRs should be a constant close to 2/3, and 1/3 makes other SW types.

Observations of distribution of magnetic storms from SW streams such as MCs and CIRs carried out in period of 1979–1988 at distance 0.7 AU on *PVO* spacecraft [*Lindsay et al.,* 1995] showed that MC is more geoeffective in a maximum and CIR in a minimum of a solar cycle. Our results could be considered as totally coincided with observations on *PVO* spacecraft if our results would be ignored in the minimum of cycle in 1986–1988 (see Figure 5). As a whole the dependence obtained by us has more complicated character at the

extent longer period than in paper by *Lindsay et al.* [1995].

Irrespective of SW type which has resulted in magnetospheric storm, the southward IMF component (in GSM system of coordinates) with value from −5 up to −15 nT and duration from 1–3 h and more is always observed in the interplanetary space. Intervals of southward IMF components are observed more often (1) after shock wave, both isolated and connected with MC or CIR, (2) in the region of compression directly ahead of MC body and in CIR and (3) in MC body. Though models of a prediction of geomagnetic disturbances on the basis of SW and IMF measurements in real time in the libration L1 point (for example, on *WIND* (1994) and *ACE* (1997) spacecraft) have short-term character (about 0.5–1.0 hour), their reliability satisfies to practical criteria [*Petrukovich and Klimov* , 2000]. Reliable long-term (more than 1 day) techniques of prediction of magnetospheric disturbance for today do not exist. For such predictions it is required to begin the forecast with the analysis of the phenomena on the Sun and as we have already noted above, the reliability of available techniques for estimation of the geoeffective solar phenomena is insuffciently high.

## 4. Conclusions

The presented comparison of methods and results of the analysis of the phenomena on the Sun, in the interplanetary space and the Earth's magnetosphere shows on an example of our original data and the numerous published results that besides the methods used in each of areas the large importance for research of all chain of solar-terrestrial physics has also a way of comparison of the phenomena in various areas or direction of data tracing. For research of geoeffectiveness of the solar and interplanetary phenomena (i.e. their abilities to generate the magnetic storms on the Earth) originally it is necessary to select the phenomena, respectively, on the Sun or in the solar wind and then to compare the phenomenon with event at the following step of a chain. Thus the obtained estimations of CME influence on the storm both directly (by one step *CME* $\rightarrow$ *Storm*) and by multiplication of probabilities of two steps (*CME* $\rightarrow$ *Magnetic cloud;Ejecta* and *Magnetric cloud; Ejecta* $\rightarrow$ *Storm*) are close to each other and equal 40–50% [*Webb et al.*, 1996; *Cane et al.*, 1998; *Yermolaev et al.*, 2000; *Gopalswamy et al*., 2000; *Plunkett et al.*, 2001; *Wang et al.*, 2002; *Wu and Lepping*, 2002; *Yermolaev and Yermolaev*, 2002, 2003*a*,*b*]. This value strongly differs from results 83–100% obtained in papers by *Brueckner et al.* [1998]; *St.Cyr et al.* [2000] and *Zhang et al.* [2003] by search of back tracing correlation which characterizes not geoeffectiveness of CME and a probability to find the appropriate candidates among CME for magnetic storms. The obtained value 83–100% are not confirmed by the two-step analysis of sources of storms as at steps *Storm* $\rightarrow$ *Magnetic cloud; Ejecta* and *Magnetric cloud;Ejecta* $\rightarrow$ *CME* values are (25–73)% [*Gosling et al.*, 1991; *Vennerstroem*, 2001; *Yermolaev and Yermolaev*, 2002] and ~40% [*Cane et al.*, 2000], each of which is less than the factor obtained by the one-step analysis *Storm* $\rightarrow$ *CME*. Thus, to remove this contradiction the suggested in papers by *Brueckner et al.* [1998]; *St.Cyr et al.* [2000] and *Zhang et al.* [2003] techniques of the analysis of the data require the further development.

The obtained estimations of CME geoeffectiveness 40–50% are close to estimations of geoeffectiveness of solar flares 30–40% [*Park et al.*, 2002; *Yermolaev and Yermolaev*, 2003*a*] and exceed them only a little. As we have shown in paper by *Yermolaev and Yermolaev* [2002], for random distribution of solar processes and the magnetic storms the formally counted coeffcient of correlation can be 30–40%. It means that the obtained estimations of CME and solar flare geoeffectiveness can be result of random processes and therefore the forecast of geomagnetic conditions on basis of observations of the solar phenomena can contain high level of false alarm. Thus, there is a paradoxical situation at which the modern science in the retrospective approach successfully can explain an origin almost all strong geomagnetic disturbances, but can not predict their occurrence with a sufficient degree of reliability on the basis of observation of the Sun. To increase reliability of the forecast, the further analysis of the solar data and revealing of characteristics which would allow to select the phenomena among CMEs and/or flares with higher geoeffectiveness are required.

**Acknowledgments.** The authors gratitude the international scientific data centers SEC NOAA, NSSDC/GSFC NASA and WDC-C2 for the information, and also R. A. Kovrazhkin and J. L. Rauch for attention, the help and useful discussion of materials of the paper. The work was in part supported by grants INTAS 99-0078, RFBR 01-02-16182, 02-02-17160, Program N16 of Department of Physics Sciences RAS and by French – Russian scientific cooperation program (PICS grant APIC0090 and RFBR grant 00-02-22001).

## References

Brueckner, G. E., J. –P. Delaboudiniere, R. A. Howard, S. E. Paswaters, O. C. St. Cyr, R. Schwenn, P. Lamy, G. M. Simnett, B. Thompson, D. Wang, 1998. Geomagnetic storms caused by coronal mass

ejections (CMEs): March 1996 through June 1997. *Geophys. Res. Lett*., *25*, 15, 3019, 1998.

Cane, H. V., I. G. Richardson, O. C. St. Cyr, 1998. The interplanetary events of January-May, 1997, as inferred from energetic particle data, and their relationship with solar events. *Geophys. Res. Lett., 25*, 14, 2517, 1998.

Cane, H. V., I. G. Richardson, O. C. St. Cy,r 2000. Coronal mass ejections, interplanetary ejecta and geomagnetic storms. *Geophys. Res. Lett., 27*, 21, 359, 2000.

Cliver, E. W., N. U. Crooker, A seasonal dependence for the geoeffectiveness of eruptive solar events. *Solar Physics 145*, 2, 347, 1993.

Cliver, E. W., H. S. Hudson, CMEs: How do the puzzle pieces fit together? *J. Atmosp. and Solar-Terr. Phys., 64*, 2, 231-252, 2002.

Crooker, N. U., Solar and heliospheric geoeffective disturbances, *J. Atmos. and Solar-Terr. Phys., 62*, 1071, 2000.

Forbes, T. G., A review on the genesis of coronal mass ejections, *J. Geophys. Res., 105*, A10, 23153-23166, 2000.

Gopalswamy, N., A. Lara, R. P. Lepping et al., Interplanetary acceleration of coronall mass ejections, *Geophys. Res. Lett., 27*, 145, 2000.

Gopalswamy, N., A. Lara, S. Yashiro, M. L. Kaiser, R. A. Howard, 2001. Predicting the 1-AU arrival times of coronal mass ejections. *J. Geophys. Res., 106*, A12, 29207, 2001.

Gosling, J. T., The solar flare myth. *J. Geophys. Res., 98*, 18937, 1993.

Gosling, J. T., D. J. McComas, J. L. Phillips, and S. J. Bame, Geomagnetic activity associated with Earth passage of interplanetary shock disturbances and coronal mass ejections. *J. Geophys. Res., 96*, 7831, 1991.

Harrison, R. A., Coronal Magnetic Storms: a New Perspective on Flares and the 'Solar Flare Myth' Debate. *Solar Physics, 166*, 441-444, 1996.

Hargreaves, J. K., The Solar-Terrestrial Environment, Cambridge University Press, New York, 1992.

Krajcovic, S., L. Krivsky, Severe geomagnetic storms and their sources on the sun. Astronomical Institutes of Czechoslovakia, Bulletin, 33, N 1, 47, 1982.

Li Y., J. G. Luhmann T. Mulligan J. T. Hoeksema C. N. Arge, S. P. Plunkett, O. C. St. Cyr, Earthward directed CMEs seen in large-scale coronal magnetic field changes, SOHO LASCO coronagraph and solar wind. *J. Geophys. Res., 106*, A11, 25103, 2001.

Lindsay, G. M., C. T. Russell, J. G. Luhmann, Coronal mass ejection and stream interaction region characteristics and their potential geomagnetic effectiveness. *J. Geophys. Res., 100*, 16999, 1995.

Lindsay, G. M., J. G. Luhmann, C. T. Russell, J. T. Gosling, Relationship between coronal mass ejection speeds from coronagraph images and interplanetary characteristics of associated interplanetary coronal mass ejections. *J. Geophys. Res*., *104*, 12515, 1999.

Low, B. C., Coronal mass ejections, magnetic flux ropes, and solar magnetism. *J. Geophys. Res., 106*, A11, 25141-25164, 2001.

Park, Y. D., Y. –J. Moon, I. S. Kim, H. S. Yun, Delay times between geoeffective solar disturbances and geomagnetic indices, *Astrophys. and Space Science 279*, 4, 343-354, 2002.

Petrukovich, A. A., S. I. Klimov, The Use of Solar Wind Measurements for the Analysis and Prediction of Geomagnetic Activity. *Kosmicheskye Issledovaniva 38*, 5, 463, 2000. (In Russian, translated Cosmic Research 38, 5, 433.)

Plunkett, S. P., B. J. Thompson, O. C. St. Cyr, R. A. Howard, Solar source regions of coronal mass ejections and their geomagnetic effects. *J. Atmosp. and Solar-Terr. Phys., 63*, 389-402, 2001.

St. Cyr, O. C., R. A. Howard, N. R. Sheeley, S. P. Jr., Plunkett et al., Properties of coronal mass ejections: SOHO LASCO observations from January 1996 to June 1998. *J. Geophys. Res., 105*, A8, 18169, 2000.

Vennerstroem, S., Interplanetary sources of magnetic storms: Statistic study. *J. Geophys. Res., 106*, 29175-2914, 2001.

Wang, Y. M., P. Z. Ye, S. Wang, G. P. Zhou, J. X. Wang, A statistical study on the geoeffectiveness of Earth-directed coronal mass ejections from March 1997 to December 2000. *J. Geophys. Res., 107*, A11, 10.1029/2002JA009244, 2002.

Webb, D. F., Coronal mass ejections: The key to major interplanetary and geomagnetic disturbances. *Rev. Geophys., 33*, S1, 577-583, 1995.

Webb, D. F., B. V. Jackson, P. Hick, Geomagnetic Storms and Heliospheric CMEs as Viewed from HELIOS. In Solar Drivers of Interplanetary and Terrestrial Disturbances, ASP Conference Series 95, 167, 1996.

Webb, D. F., E. W. Cliver, N. U. Crooker et al., 2000. Relationship of halo coronal mass ejections, magnetic clouds, and magnetic storms. *J. Geophys. Res., 105*, 7491, 2000.

Wu, C. -C., R. P. Lepping, Effects of magnetic clouds on the occurrence of geomagnetic storms: The first 4 years of Wind. *J. Geophys. Res., 107*, A10, SMP 19-1 to SMP 19-8 10.1029/2001JA000161, 2002.

Yermolaev, Yu. I., G. N. Zastenker, N. S. Nikolaeva, The Earth's Magnetosphere Response to Solar Wind Events according to the INTERBALL Project Data. *Kosmicheskie Issledovaniia* 38, 6, 563, 2000. (in Russian, translated Cosmic Research, 38, 6, 527.)

Yermolaev, Yu. I., M. Yu. Yermolaev, Statistical relationships between solar, interplanetary, and geomagnetic disturbances, 1976–2000. *Kosmicheskie*

*Issledovaniia* 40, 1, 3, 2002. (in Russian, translated Cosmic Research 40, 1, 1.)

Yermolaev, Yu. I., M. Yu. Yermolaev, Statistical relationships between solar, interplanetary, and geomagnetic disturbances, 1976–2000, 2. *Kosmicheskie Issledovaniia* 41, 2, 115, 2003*a*. (in Russian, translated Cosmic Research 41, 2, 105).

Yermolaev, Yu. I., M. Yu. Yermolaev, Statistical relationships between solar, interplanetary, and geomagnetic disturbances, 1976–2000, 3. *Kosmicheskie Issledovaniia 41*, 2003*b* (in press).

Zhang, J., K. P. Dere, R. A. Howard, V. Bothmer, Identification of Solar Sources of Major Geomagnetic Storms between 1996 and 2000. *Astrophysical Journal 582*, 520, 2003.

---

Yuri I. Yermolaev, Michail Yu. Yermolaev, Anatoli A. Petrukovich, Georgy N. Zastenker, Lev M. Zelenyi, Space Research Institute RAS, Moscow, Russia.

Jean-Andre Sauvaud, CESR, Toulouse, France.

(Received 1 May, 2003; revised 1 May, 2003; accepted 1 May, 2003)

# Statistical relation of SAR arc dynamics to substorm and storm

I. B. Ievenko and V. N. Alexeyev

Institute of Cosmophysical Research and Aeronomy, Yakutsk, Russia

**Abstract.** The analysis results of statistical relation for 630,0 nm emission intensity in the mid-latitude red arc (SAR arc) and the velocity of its equatorward movement to geomagnetic activity indices *Dst*, *ASYM*, *AL* and *Kp* in the period of weak and moderate magnetic storms are presented. The work is based on 700 hours of spectrophotometric observations of SAR arcs at the Yakutsk meridian in 1987–2000. In particular, it has been found that the statistically significant positive relation of the arc intensity (log*I*) to the ring current appears at *Dst* ≤–50 nT. Dependences of log*(I)* on geomagnetic indices *ASYM*, *AL* and *Kp* are significant in two the samplings of data. This, most probably, points to the significant contribution of the asymmetric ring current originating during the substorm to the generation of a SAR arc. The observation results at the Yakutsk meridian, as a first approximation, are consistent with a conclusion by *Cole* [1965] about the relation of SAR arcs to the auroral activity at the beginning of magnetic storm main phase.

## 1. Introduction

It is well known that stable auroral red arcs (SAR arcs) are observed during the magnetic storms, determined by the geomagnetic *Dst* index variation. In the mechanism of SAR arc generation suggested by *Cole* [1965, 1970], their origin during the magnetic storm main phase has been considered. Subsequently, after the theoretical work [*Cornwell et al*., 1971] the idea about the formation of SAR arcs on the storm recovery phase has been established. According to this work during the recovery phase the extending plasmasphere overlaps near the Earth region of the ring current where as a result of the Landau damping of ion-cyclotron waves the cold electrons are heated. The superthermal electron flux along the magnetic field lines causes the intensification of atomic oxygen red line at the heights of ionosphere *F2* region in a form of midlatitudinal red arc which maps the newly formed boundary of the plasmasphere (plasmapause). At present, the conviction on the relationship of SAR arcs to the recovery phase of magnetic storm dominates [*Kozyra et al*., 1997]. At the same time, satellite investigations in 1980–1990 in specific cases point to the fact that the energetic particles of ring current penetrate into the outer plasmasphere in the period of the main phase of magnetic storm and/or during individual substorms [*Kozyra et al*., 1993, 1997]. Results of synchronous measurements at plasmaspheric and ionospheric heights on DE1 and DE2 satellites showed that the SAR arc can be observed at projection latitudes of the radial gradient in the cold plasma density inside the plasmasphere [*Horwitz et al*., 1986; *Brace et al*., 1988].

The authors [*Ievenko*, 1993, 1995a, 1999] have proved, that the occurrence and/or increase of brightness of SAR arc occurs during the substorm expansion phase. In the present work the statistical analysis of a relationship of the 630 nm emission intensity in the SAR arc *(I)* and the velocity of its equatorward movement *(V)* with magnetic *AL*, *Kp*, *Dst*, *ASYH* and *ASYD* indices has been carried out in order to determine the influence of substorm and storm activities on the arc dynamics. The statistical parameters of the analysed data are considered. The work has been carried out by the authors on the basis of original data of spectrophotometric observations at the Yakutsk meridian (st. Maimaga, CGMC: 57° N, 200° E) for the 1987 to 2000 period during 360 clear nights.

## 2. The observation methods and data analysis

To carry out the statistical analysis the observation data of mid-latitude red arcs obtained by the photometer scanning along the meridian have been used [*Ievenko*, 1993]. The registration of nightglow in the conditions of good atmosphere transparency has been carried out in the scanning regime in every 2 or 5 min at moonless nights during winter months. At the geographical latitude of Yakutsk 62° N from April to September the nights are white. The method of reference receiver has been used

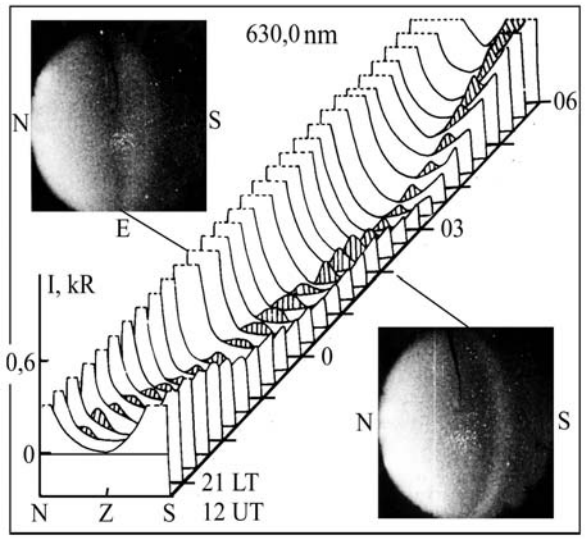


**Figure 1.** The example of registration of SAR arc and diffuse aurora by the scanning photometer and all-sky photocamera with the image amplifier on February 5, 1989 in the 630.0 nm emission.

for absolute energetic calibration of photometer [*Ievenko*, 1995*b*]. Examples of the observation of the diffuse aurora (DA) and SAR arc dynamics are presented in Figures 1 and 2.

In Figure 1 the arc-like band of luminosity equatorward of DA in the northern part of the sky is seen on images at 0020 and 0200 LT. On the three-dimensional diagram compiled from the individual scannograms the luminosity inhomogeneities with the pronounced intensity maximum in the meridional sections are hatched. The diagram well illustrates the red arc location along the meridian during the night. This example shows the possibility of unambiguous identification of SAR arcs by the scanning photometer data.

A wide red arc (Figure 2A) has been registered in the vicinity of the observation station zenith from 12.00 UT. In Figure 2B it is seen that after the sharp substorm onset (see the AL index graph in Figure 2) at 17.40 UT the arc intensity increases from 180 to 600 Rayleigh during an hour. At the same time the equatorward movement velocity of arc increases up to 25 m/s and it moves away from the boundary of DA. The detailed analysis of such a dynamics in subauroral luminosity is in [*Ievenko*, 1999]. The graphs in Figure 2C are the example of short data sampling from the whole data base which is used in this work for the statistical analysis. One can see that in this case there is the pronounced relationship between variations *I* and |*AL*|. The relationship of *I* to the |*Dst*| variation is less significant.

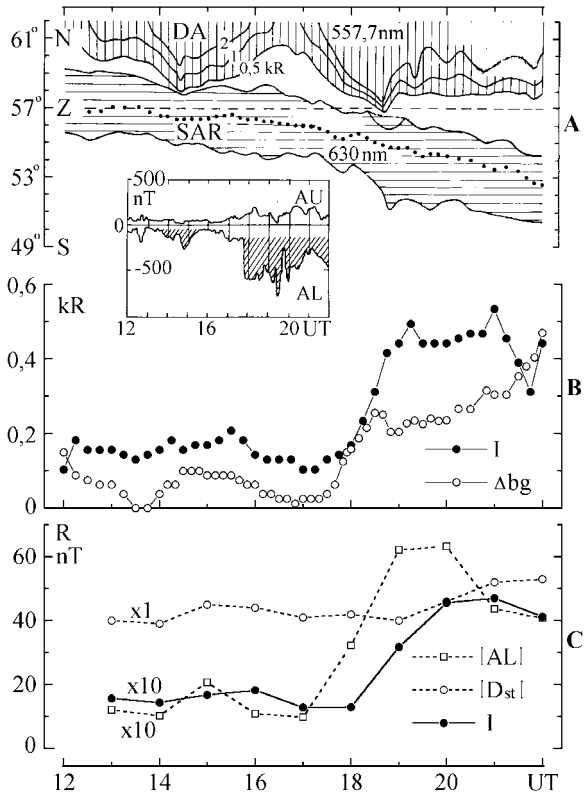


**Figure 2.** The example of data analysis during SAR arc observations at the Yakutsk meridian on December 4, 1989. From top to bottom: (A) projection of equatorial boundary of DA in 557,7 nm emission ($h$ = 110 km) and SAR arc ($h$ = 450 km) on the Earth's surface. The location of arc intensity maximum is marked by heavy dots; (B) intensity of SAR arc in the maximum and the background level of the 630,0 nm emission at the maximum latitude; (C) graphs of hourly average values of *I*, |*AL*| and |*Dst*| for the time interval of SAR arc observations.

### 3. Statistical characteristics for analyzed series of data

To carry out the statistical analysis the hourly averaged values of parameters *I* and *V* in Rayleigh and m/s respectively for ~700 hours of SAR arc observations for the 1989 to 2000 period have been calculated.

The averaging time of 1 hour has been taken according to the temporal scale of *Dst* index and the duration of the substorm active phase. The latitudinal location of SAR arc intensity maximum at the end of every hour has been also determined. Analyzing statistical dependences of arc dynamical parameters on the *Kp* index the corresponding operations have been carried for 3-hour time intervals. To determine the most probable values of studied parameters the analysis results of their distribution are presented in Figure 3.

Distribution for *AL* in Figure 3A noticeably differ from the normal ones. One should consider –230 nT as the most probable value for this parameter, which are mean value for fitted gaussoid. The mean values for *Dst* and *Kp* (1989-2000) in Figure 3B,C equal to –40 nT and 3,6 ($3_+$–$4_-$), respectively, are the most probable because their distributions are close to the normal. Both distributions of log*(I)* for 1989–1994 (D) and 1989–2000 (E) are close to the normal one with the most probable (mean) value *I* = 150–155 Rayleigh. Thus, the empirical rows of *I* have the logarithmically normal distributions. The histogram of *V* in Figure 3F for the observation period of SAR arc in 1989–1994 is close to the normal distribution with the mean *V* = 20 m/s.

## 4. Correlation relation of log*(I)* and *V* to geomagnetic activity indices

First the statistical data analysis of optical observations for 1989–1994 when the *AL* index is available, has been carried out. The calculation results of corresponding correlation coefficients are given in Table.

**Table**

| $r_{12}$ | $r_{12,3}$ | *N* (hours) | *P* |
|---|---|---|---|
| $r_{lg(I)\,AL}$ **-0,5±0,08** | **-0,44** | 360 | >0,999 |
| $r_{lg(I)\,Dst}$ **-0,3±0,09** | -0,12 | 360 | |
| $r_{lg(I)\,ASYM}$ **0,5±0,07** | **0,38** | 360 | >0,999 |
| $r_{V\,AL}$ **-0,4±0,09** | | 354 | >0,999 |

The coefficients, whose statistical significance is determined by the confidence level *P* >0,999, are stood out in heavy print. The correlation coefficient errors have been calculated for the confidence level *P* =0,95. The obtained coefficients show more significant relation of log*(I)* to *AL* and *ASYHD* (the vector sum of *ASYH* and

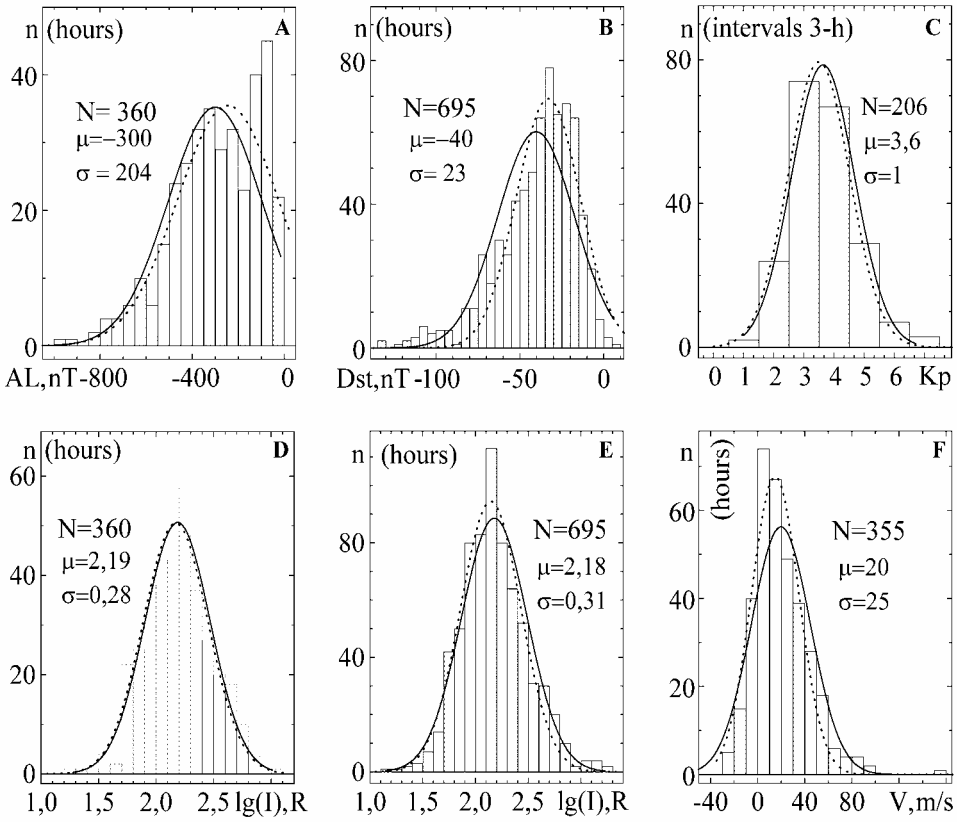


**Figure 3.** Distributions of geomagnetic indices *AL*, *Dst*, *Kp* and hourly averaged parameters log*(I)*, *V* of the SAR arc for the 1989–2000 period of observations. For each distribution the volume of sampling (*N*), the mean (μ) and standard deviation (σ) are indicated. On histograms the solid line is the normal distribution curves with the corresponding μ and σ and also the dotted line shows gaussoids fitted by the least-square method.

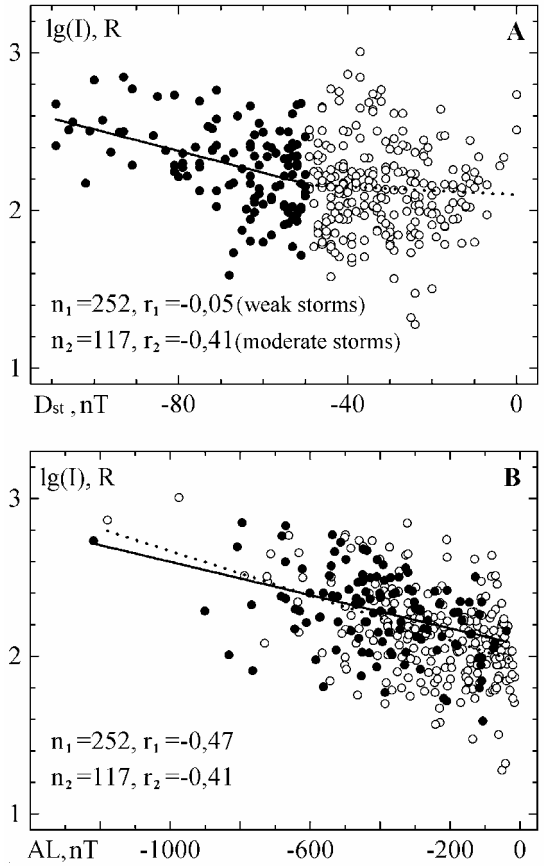


**Figure 4.** Correlation dependencies of log*(I)* on *Dst* and *AL* for the observation data samplings during weak and moderate magnetic storms for 1989-1994. In graphs the regression lines, correlation coefficients and sampling number for weak ($n_1$, $r_1$) and moderate ($n_2$, $r_2$) storms are presented. Distributions are marked by open and solid cycles for weak and moderate storms, respectively.

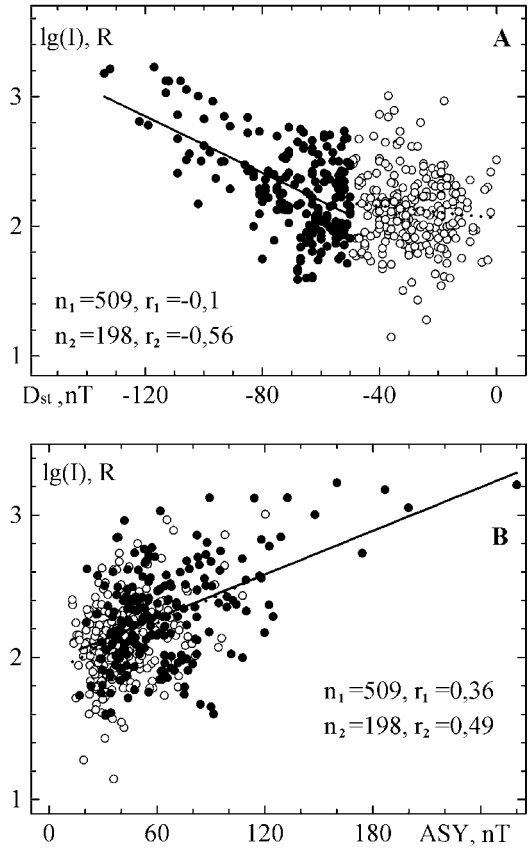


**Figure 5.** Correlation dependences of log*(I)* on *Dst* and *ASYHD* for the samplings during weak and moderate magnetic storms for 1989–2000. Designations are the same as in Figure 4.

*ASYD*) indices than to *Dst*. The partial correlation coefficients ($r_{12,3}$) of fixed values of *Dst* and *AL* in the table indicate that in the considered observation data base the values of log*(I)* are determined by *AL* and *ASYM* indices but not by *Dst*. The velocity of equatorward movement (*V*) of the SAR arc has the significant relation only to *AL* index of the auroral activity with $r_{V\,AL}$= –0,4.

To reveal the relation of SAR arc brightness to a ring current known from the literature [*Rees and Akasofu*, 1963; *Kozyra et al*., 1997] the sampling analysis of observation data during the weak and moderate storms with *Dst* ≥–50 and with –50≥ *Dst* ≥ –100 nT, respectively, according to a classification in [*Loewe and Prolss*, 1997] has been carried out. Figures 4 and 5 present the empirical distributions of log*(I)* depending on geomagnetic *AL*, *Dst* and *ASYHD* indices for the samplings in the indicated intervals of *Dst* values by observation data for 1989–2000. Statistical dependencies of log*(I)* and *V* on *Kp* are given in Figure 6.

From distributions in Figure 4 it is seen that the significant statistical relation of log*(I)* to *Dst* begins in the region of its values ≤–50 nT. Dependences of log*(I)* on *AL* are statistically significant (*P* >0,999) for the two samplings of data and have similar regression lines.

In Figure 5 the significant statistical dependence of log*(I)* on *Dst* appears in the region of *Dst*≤–50nT as well as in a number of data for 1989–1994 (Figure 4). In this case, this tendency is pronounced more statistically. The statistical dependence of log*(I)* on *ASYHD* is significant in both samplings but the correlation coefficient is greater at *Dst*≤–50nT.

The statistical relations of log*(I)* to *Kp* index in Figure 6 are significant (*P*>0,999) for both sampling as in the case of dependence on *AL*. Distributions have close regression lines. Correlation coefficient between *V* and *Kp* is of statistical significance with *P*>0,999 at *Dst* ≥–50nT.

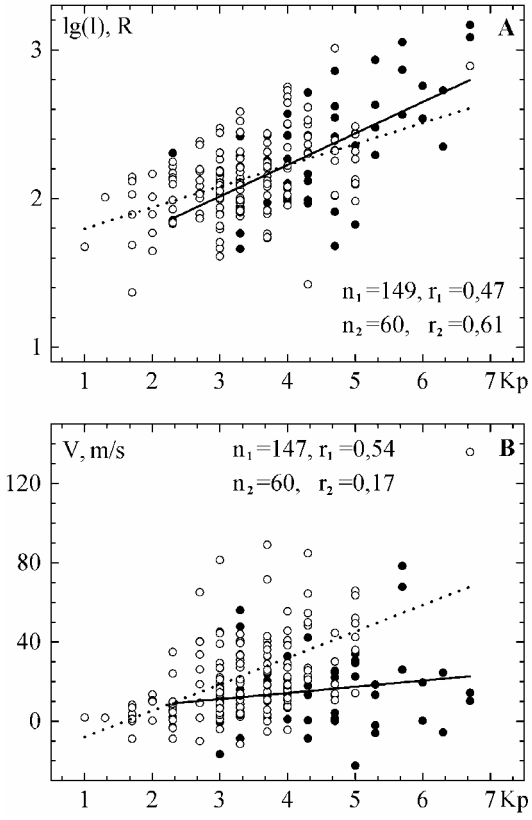


**Figure 6.** Correlation dependences of log*(I)* and *V* on *Kp* index during weak and moderate magnetic storms for 1989-2000. Designations are the same as in Figure 4.

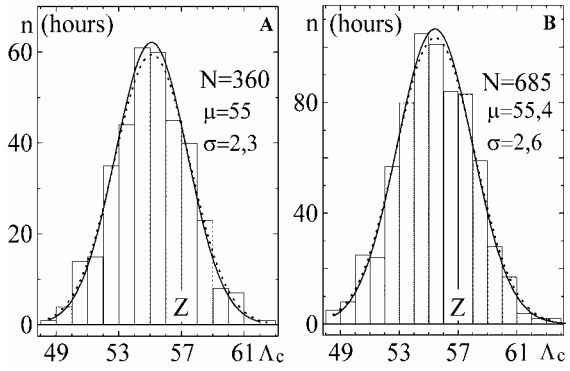


**Figure 7.** The latitudinal distribution of SAR arcs intensity maximum location by photometric observation data at the Yakutsk meridian for 1989–1994 (A) and 1989–2000 (B). *Z* is the observational station zenith; $\Lambda_c$ is the corrected geomagnetic latitude. Other symbols are as in Figure 3.

## 5. Latitudinal distribution of observation rate of SAR arc at the Yakutsk meridian

From the view-point of the understanding physical mechanisms of SAR arc formation, the latitudinal distribution of arcs observation rate is of interest. Histograms by observation data for 1989–2000 at the Yakutsk meridian are given in Figure 7.

It is seen that statistical distributions for two series of data are normal and have similar values of average μ and standard deviation σ. The most probable corrected geomagnetic latitude for the SAR arc observation (μ) is a median of these distributions and it is equal to 55–55,4° N (*L*=3). The half-width of both distributions is equal to ~6°. It is in agreement with earlier results in SAR arc investigations [*Hoch*, 1973].

## 6. Discussion and conclusion

A great body of the SAR arc spectrophotometric observation and DA data used in this work was obtained at *Dst* up to –130 nT. Correspondly revealed statistical regularities are applicable to the periods of weak and moderate magnetic storms. The appearance of the positive relation of the 630,0 nm emission intensity in an arc to the ring current at *Dst*<–50 nT is consistent with an early empirical result (*Rees and Akasofu*, 1963) concerning to the fact that this tendency is during major magnetic storms. At the same time, it should be pointed out that there are possible reasons of ambiguity in the dependence of the arc intensity on the *Dst* variation value.

In the first place, according to our results (*Ievenko*, 1994, 1995a, 1999) during substorms along with the SAR arc intensity increase there are also the 630,0 nm emission rise over the whole sky (background intensity) equatorward of DA. The example of such a dynamics in the arc and background intensity at the Yakutsk meridian is shown in Figure 2B. In turn, a SAR arc is conjugated along magnetic field lines with a radial gradient of cold plasma density inside of the plasmasphere on synchronous measurement data at plasmaspheric and ionospheric heights from DE1 and DE2 satellites (*Horwitz et al.*, 1986; *Brase et al.*, 1988). Most likely, a SAR arc maps in relief the cold plasma density gradient where the heat of plasmaspheric electrons by ring current energetic ions is enhanced. At the same time, this process takes place in the whole region of outer plasmasphere where the developing ring current penetrates. This causes the background increase in the 630,0 nm emission over the whole sky equatorward of DA. Thus, the 630,0 nm emission intensity in an arc reflects only partially the process of interaction of the ring current with the outer plasmasphere.

Secondly, observation data obtained by us in the periods of magnetospheric activity rise show that always there is an intensification in the 630,0 nm emission in the form of a band equatorward of DA in 557,7 or 427,8 nm

emission. The band intensity smoothly decreases to lower latitudes. During intense substorms in the meridional section of red luminosity the intensity maximum typical for a SAR arc is formed [*Ievenko*, 1993, 1995*a*]. This gives grounds to assume that a SAR arcs appears in the equatorial region of DA during the development of the partial ring current at the beginning of magnetic storm main phase. This SAR arc moves equatorward in the case when the activity will continue to rise [*Ievenko*, 1999]. The statistically significant correlation coefficients between lg*(I)* and *AL*, *ASYM* and *Kp* point to the regularity of this phenomenon. The latitudinal distribution of SAR arc observation rate obtained at the Yakutsk meridian with a median at corrected geomagnetic latitude ~55° does not contradict earlier results (for example, *Hoch*, 1973). We believe that observation results at the Yakutsk meridian are consistent with the conclusion by *Cole* [1965, 1970] on the relationship between SAR arcs and the auroral activity at the beginning of magnetic storm main phase, which he obtained on the base of generalization of early empirical data on mid-latitude red arcs.

In conclusion we summarize the statistical analysis main results of the influence of the substorm and storm on the SAR arc dynamics:

1. The SAR arc intensity during the weak magnetic storms of $Dst \geq -50$ nT is defined by the auroral *AL* and planetary *Kp* index with a correlation coefficient $r = -0.5 - 0.6$. The significant relation of arc intensity to *Dst* is absent, but it is essential with *ASYHD* index. It is assumed that the *AL* and *Kp*-dependence of log*(I)* is most likely caused by the considerable contribution of the asymmetric ring current arising during a substorm to the SAR arc generation.
2. In the samplings of data for the moderate storms of $-50 \geq Dst \geq -120$ nT the statistically significant dependence ($r = -0.5\ -0.6$) of arc intensity on the ring current intensity appears, that is in agreement with earlier results. In this case, the significant relation of log*(I)* to *AL* and *Kp* remains constant.
3. The velocity of SAR arc equatorward movement is of the significant dependence only on *AL* and *Kp* index with $r \approx -0.5$ and ~0,6 respectively, that can be indicative of a conditionallity of this phenomenon by penetration of the non-stationary convection electric field to plasmasphere latitudes during a substorm.
4. The latitudinal distribution of SAR arc observations rate at the Yakutsk meridian is close to the normal one with a median at $\Lambda c$=55° N ($L$=3) and it is of a half-width ~6°. It is supposed that this latitude interval of SAR arc observations is the statistical mapping of a more dynamic region of outer plasmasphere $L$-shells into which the ring current penetrates during substorms at $Kp$=3−5.
5. Most probable values of hourly averaged parameters of SAR arc and geomagnetic activity in used rows of data are: $I$ =150 Rayleigh, $V$ =20 m/s, $AL$ =−230 nT, $Ds\ t$=−40 nT and $Kp$ =3−4.

**Acknowledgments.** This work was partially supported by the Russian Foundation for Basic Research (project the Arctic 03-05-96081).

## References

Brace L. H., et al., F region electron temperature signatures of the plasmapause based on dynamics explorer 1 and 2 measurements, *J. Geophys. Res., 93,* 1896, 1988.

Cole K. D., Stable auroral red arcs, sinks for energy of Dst Main phase, *J. Geophys.Res., 70,* 1689, 1965.

Cole K. D., Magnetospheric processes leading to mid-latitude uroras, *Annales de Geophysique, 26,* 187, 1970.

Cornwell J.M., F.V. Coroniti and R.M. Thorne, Unified theory of SAR arc formation at the plasmapause, *J. Geophys. Res., 19,* 4428, 1971.

Hoch R. J., Stable Auroral Red Arcs, *Rev. Geophys. and Space Physics, 11,* 935, 1973.

Horwitz J.L., L.H. Brace, R.H. Comfort and C.R. Chappell, Dual-spacecraft measurements of plasma-ionosphere coupling , *J. Geophys. Res., 91,* 11203, 1986.

Ievenko I. B., Dynamics of diffuse aurora and SAR-arc during substorm, *Geomagn. Aeron. (English translation), 33,* 599, 1994.

Ievenko I. B., Substorm-induced pulsed particle precipitations in the SAR arc region, *Geomagn. Aeron. (English translation), 35,* 331, 1995*a*.

Ievenko I. B., Effects of magnetospheric activity on the plasmasphere as inferred from observations of diffuse aurora and SAR arc, *Geomagn. Aeron. (English translation), 39,* 697, 1999.

Ievenko I. B., *Absolute Energetic Graduation of Spectrophotometers by the Reference Receiver Method. Methodical Guidance (in Russian),* 24 pp., YaSC SD RAS, Yakutsk 1995b.

Kozyra J. U., A. F. Nagy and D. W. Slater, High-altitude energy source(s) for stable auroral red arcs, *Reviews of Geophysics, 35,* 155, 1997.

Kozyra J.U., et al., The role of ring current nose events in producing stable auroral red arc intensifications during the main phase: Observations during the september 19-24, 1984, equinox transition study, *J. Geophys. Res.*, *98*, 9267, 1993.

Kozyra J.U., et al., The role of ring current nose events in producing stable auroral red arc intensifications during the main phase: Observations during the september 19-24, 1984, equinox transition study, *J. Geophys. Res.*, *98*, 9267, 1993.

Loewe C. A. and G. W. Prolss, Classification and mean behavior of magnetic storms, *J. Geophys. Res.*, *102*, 14,209, 1997.

Rees M. H. and S. Akasofu, On the association between subvisual red arcs and Dst (H) decrease, *Planet. Space Sci.*, *11*, 105, 1963.

I. B. Ievenko, V. N. Alexeyev, Institute of Cosmophysical Research and Aeronomy, 31 Lenin Ave., Yakutsk 677891, Russia. (ievenko@ikfia.ysn.ru)

# Midnight electron precipitation pattern for substorm development

V. G. Vorobjev, and O. I. Yagodkina

Polar Geophysical Institute, Russian Academy of Sciences, Apatity, Murmansk region, Russia

**Abstract.** On the basis of DMSP F7 satellite observations for the whole of 1986 the empirical model of the midnight auroral precipitation during a substorm was constructed. The model includes the dynamics of different auroral precipitation boundaries during all substorm phases together with simultaneous changes in both an average electron precipitation energy and energy flow in different precipitation zones as well as the IMF and solar wind plasma behavior during the substorm. The analysis of the model shows two important features of precipitations. (1) During the magnetic quietness and just before the beginning of the substorm expansive phase the latitudinal width of the auroral precipitation in the nightside sector is about 5°−6° CGL. (2) Just before the substorm onset time a decrease of the precipitating electron energy in the equatorward part of auroral precipitations was observed simultaneously with an increase in the average precipitating electron energy and energy flows in the poleward part of auroral precipitations. The analysis of interplanetary medium parameters shows that on average during the progress of the substorm the solar wind dynamic pressure was about 1.5 times higher than during the period of magnetic quietness. Substorms occur, generally, during the southward IMF orientation and the substorm onset is not connected with the northern turn of the southward interplanetary $B_z$. In the winter season substorms were observed mainly during the positive interplanetary $B_y$ and in the summer season they were observed when the interplanetary $B_y$ was negative.

## 1. Introduction

DMSP satellites database for the whole of 1986 was created to investigate different types of auroral precipitation features. It contains more than 35000 satellite passes through the auroral zone almost around the magnetic local time. The description of the database will be presented below in more detail. Here we would only like to note that the level of geomagnetic activities and the phase of geomagnetic disturbances were determined for each of satellite passes. Such detailed information permits to examine the dynamics of different auroral precipitation boundaries and variations in the average energy and energy flux of precipitating particles in different parts of the auroral zone during a magnetospheric substorm. The model description of spatial distribution and basic characteristics of electrons precipitating into the polar ionosphere gives an idea of the behavior of various population sources in the distant magnetosphere during substorms and can be used to estimate the precipitation energy and its influence on ionospheric conductivity and the chemistry of the upper atmosphere.

*Sotirelis and Newell* [2000] published the boundary-oriented model of global configuration of electrons precipitating into the polar ionosphere based on DMSP spacecraft observations. An essential advantage of this model in comparison with the earlier published models [*Spiro et al.,* 1982; *Hardy et al.,* 1985] is not only large statistics (12 years of continuous observations) and rather high spatial resolution of global distributions, but also regulation of precipitating electron features for each satellite pass over the polar ionosphere relative to various auroral precipitation boundaries. Our database is based on more modest statistics (1 year of observations) but it has its own advantage: alongside with different auroral precipitation boundary co-ordinates, it contains additional information including interplanetary medium condition, magnetic activity indices and magnetospheric substorm phases. This information enables us to carry out finer investigations and to represent frequently the obtained dependencies in analytical form, which is handy for further applications. Thus *Vorobjev et al.* [2000] and *Starkov et al.* [2002] have published the quantitative correlations between the location of different auroral precipitation regions in the midnight and midday sectors and the magnetic activity level in the auroral zone, which was not possible in all previous models [*Spiro et al.*, 1982; *Hardy et al*., 1985]. *Sotirelis*

*and Newell* [2000] used the *b2i* boundary, the proxy for the ion isotropy boundary, to infer the magnetotail stretching. It is difficult to apply these models to a more detailed research particularly during the substorm development.

In the present paper the empirical model of a substorm in the midnight auroral precipitation is presented. The model contains the dynamics of different auroral precipitation boundaries during all substorm phases together with simultaneous changes in the average electron precipitation energy and energy flux in different precipitation regions as well as the IMF and solar wind plasma features during the substorm.

## 2. Data used and technique of processing

DMSP F7 spacecraft observations in the magnetic local time interval from 21 MLT to 24 MLT were used to study auroral precipitation features during substorms. The objects of investigation are *b1e, b2e, b2i, b4s, b5e* and *b6* boundaries according to notation suggested by *Newell et al.* [1996] and *Feldstein and Galperin* [1996] for nightside precipitations. In this notation the boundaries were numbered so that the number of the boundary grows with the increase of its latitudinal location. Indexes *e* and *i* refer to the electron and ion precipitation boundary, respectively.

*b1e* – the "zero-energy" electron boundary. According to results by *Vorobjev et al.* [2000] this boundary coincides well with the equatorward boundary of diffuse auroral luminosity.

*b2e* – the boundary where the electron average energy is neither increasing nor decreasing with latitude. It is supposed that this boundary is a proxy for the inner edge of the central plasma sheet. According to statistical study [*Vorobjev et al.*, 2000] *b2e* coincides with the equatorward boundary of the auroral oval.

*b2i* – the latitude where the energy flux of ions has the maximum. This boundary, a proxy for the ion isotropy boundary, corresponds to the earthward edge of magnetospheric cross tail current sheet [*Newell et al.,* 1996, 1998]).

*b4s* – the equatorward boundary of spatial structured electron precipitations (low correlation coefficient between the neighboring spectra).

*b5e* – the poleward boundary where an abrupt drop by the factor of at least 4 in the electron energy flux is observed. According to *Vorobjev et al.* [2000] this boundary coincides well with the poleward boundary of the statistical auroral oval.

*b6* – the poleward boundary of subvisual drizzle. It is supposed that *b6* often corresponds to the polar cap boundary.

Besides that standard information about different auroral precipitation boundaries co-ordinates and particles precipitation characteristics, interplanetary medium parameters and indexes of geomagnetic activity and substorm phases were determined for each satellite pass through the auroral zone. The substorm phase was determined from 1 minute averaged variations of AE and AL indexes at the time when the satellite encountered the *b2e* boundary. It only takes 2–3 min for the spacecraft to pass the precipitation zone from *b1* to *b5* boundaries. Magnetic activities were divided into four classes:

0 – the magnetic quiet period which consists of all quiet times, not only those preceding a substorm;
1 – the growth phase of substorm;
2 – the substorm expansive phase;
3 – the recovery phase of substorm;
4 – another type of magnetic activity.

Moreover, each of the 1, 2 and 3 classes was additionally divided into three time intervals corresponding to the initial, middle and final stage of each substorm phase (subphases). Such detailed separation allows one to obtain three experimental statistical points for each phase and to investigate the precipitation boundary dynamics and auroral electron characteristics during the magnetospheric substorm development in detail.

Observations obtained by DMSP F7 spacecraft with an orbiting period of approximately 100 minutes were used for the investigation. The duration of a typical isolated substorm from the beginning of the growth phase to the end of the recovery phase is about 2–3 hours. That is why in the course of any substorm there were only 2–3 DMSP passes occurring in different substorm phases. For this reason different points were related with different substorms. Our results describe an average or synthetic substorm consisting of three phases. Data belonging to the same stage of each substorm phase were summarized to determine the average level of auroral boundary locations, electron precipitations and interplanetary medium parameters. The average values of all quantities are shown in figures as points in the center of corresponding substorm subphase. The numbers of events per statistical cell are changed from 200–300 for different subphases to about 700 for the 0 and 4 classes.

Substorm phases were defined according to the classical reports by [*Akasofu et al*., 1966; *Kokubun*, 1970; *McPherron*, 1970; *Iijima and Nagata*, 1972], and others. The general feature of the growth phase was a slow growth of the magnetic activity prior to the rapid growth during substorm expansive phase. The beginning of a sharp magnetic activity level increase was determined as a substorm onset time. If the average duration of growth, expansive and recovery phases is about 45–60 min then the duration of each subphase is

about 15–20 min. To illustrate this point the variations of the average AL index value are shown as a histogram by a dashed line in Figure 1. In order to clarify the substorm phase and subphase selection, the model of corresponding magnetic disturbance shifted ahead in time by one half of substorm subphase is shown here by a solid line.

### 3. Observations and results

The histogram in the bottom part of Figure 1 displays the variations of the AL index during all magnetic activity intervals, which are marked along the horizontal axis. The histogram is constructed by 5 min averaged AL indexes as the average AL magnitude for satellite passes during the identical phase of magnetic disturbance.

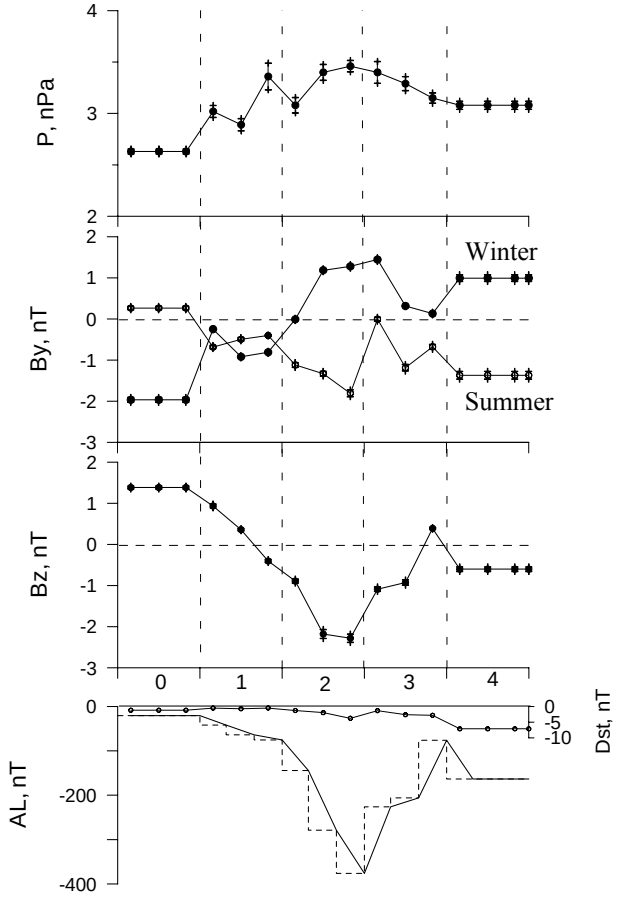


**Figure 1.** Variations of interplanetary medium parameters during the magnetospheric substorm. Solar wind dynamic pressure (P), variations of the IMF $B_y$ and $B_z$ components are shown from top to bottom. The bottom panel illustrates the AL and $D_{st}$ variations. The phases of magnetic disturbance are marked along the horizontal axis.

As it is seen from the figure the shape of the AL variation corresponds well to the typical magnetic substorm that testifies of rather a correct determination of magnetospheric substorm phases. The average level of magnetic activity during the period of the magnetic quietness was about −20 nT. The magnetic activity gradually increased during the substorm growth phase reaching about −85 nT just before the substorm onset. The average disturbance in the substorm maximum was −410 nT, and during the disturbance period (4) without the determined phase it was equal to about −125 nT. In Figure 1 the thin line with circles shows the changes of the $D_{st}$ index during the same periods. The average variation of this index is very insignificant and even during the substorm maximum it does not exceed −5 nT.

First, we examined the interplanetary medium parameters corresponding to each phase of magnetic disturbance. Crosses show the standard deviation of measured quantities. In three top panels of Figure 1 the average value of the solar wind dynamic pressure (P), and the IMF $B_y$ (separately for winter and summer seasons) and $B_z$ components are shown from top to bottom. The analysis of interplanetary condition demonstrates that on average the solar wind dynamic pressure was a little bit higher during the substorm than during the period of magnetic quietness.

Substorms occurred predominantly during periods of the southward IMF orientation and substorm onsets often were not associated with the northern turn of the interplanetary $B_z$.

Distributions of the IMF $B_y$ occurrence frequency of different sign and value during the summer and winter of 1986 are alike and approximately symmetrical to the nearly equal occurrence of positive (46% and 49%) and negative (54% and 56%, respectively) IMF $B_y$. However, in winter, substorms were generally observed during the positive interplanetary $B_y$ and in summer they occurred during the negative $B_y$.

In order to take into account the time history of the solar wind, another method was applied too. We took interplanetary parameters for the previous hour if the spacecraft pass occurred in the first half of any hour, and for the same hour if the pass took place during the second half of the hour. The results were qualitatively equal and only insignificant quantitative difference was observed.

The dynamics of different auroral precipitation boundaries during a substorm is illustrated in Figure 2. On the horizontal scale in this figure the active period with an unidentified substorm phase (4) is replaced by the period of magnetic quietness (0). So, the disturbance under investigation corresponds to the averaged isolated substorm. The variation of the average AL index value is shown in the bottom part of the figure. As the $D_{st}$ variations in the examined interval were insignificant, it is possible to consider that all changes in the latitudinal

location of the precipitation boundaries and auroral electron characteristics are caused generally by the substorm development.

Because of the relatively large statistical set, standard deviations are very small and actually slight for all quantities in our investigation. This is why in Figure 2 the root-mean-square errors were calculated for the boundary positions. In order not to overload the figure, these errors are shown as half of deviation to either side.

Figure 2 shows that the equatorward precipitation boundaries (*b1e, b2e, b2i, b4s*) move during both the growth and expansive substorm phases to lower latitudes and then return during the recovery phase to initial latitudes correlating well with changes in the AL index. The most equatorward boundary, *b1e,* shows the largest equatorward displacement of about 5° of corrected geomagnetic latitude (CGL), while the displacement of the *b4s* boundary was about 2.5°. Higher latitude precipitation boundaries (*b5e, b6*) only moved equatorward during the substorm growth phase. During the expansive phase the *b6* boundary returned to its undisturbed level, while the *b5e* boundary moved further

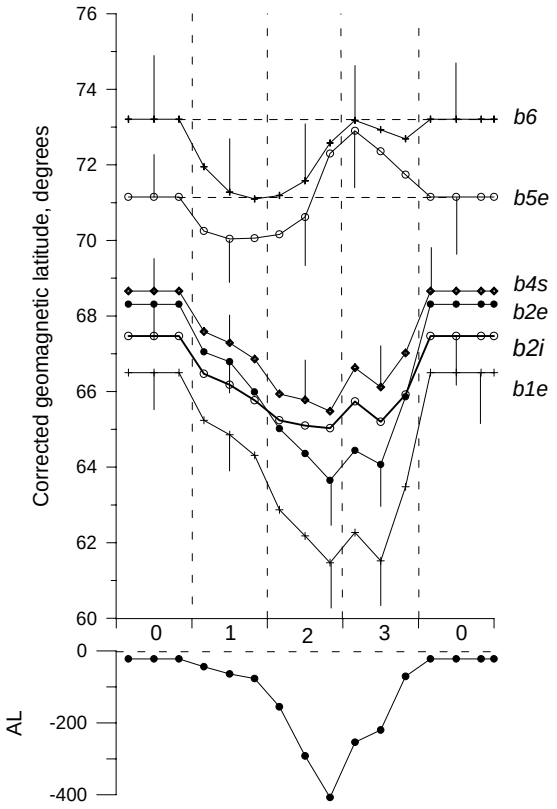


**Figure 2.** The auroral precipitation boundaries during the substorm. The label of a boundary is marked in the right part of figure. The bottom panel shows the AL index variations.

poleward at about 2° of latitude higher than its location during the quietness period.

Owing to such difference in the *b5e* and *b6e* boundaries dynamics, the region of soft precipitations between *b5e* and *b6* shrank sharply during the expansive phase. At the maximum of the substorm the polar cap boundary (*b6*) approximately coincided with the poleward boundary of the statistical auroral oval (*b5e*).

The *b2e* boundary is more dynamic than the *b2i*. During the average substorm of about 400 nT intensity, the equatorward displacement of *b2e* was about 5° of the latitude, while it was only ~2° CGL for the *b2i* boundary. During magnetic quietness *b2e* was placed poleward of the *b2i*, i.e. the inner edge of the magnetospheric cross tail current sheet was closer to the Earth than the central plasma sheet (CPS). By contrast, the isotropy boundary was observed inside the center plasma sheet during expansive and recovery phases of the substorm. The position of the *b2e* and *b2i* boundaries approximately coincided around the substorm onset time. Such interdependence in the auroral boundaries position occurred not only statistically but also for real individual disturbances. It is possible to suggest that the relative position of *b2e* and *b2i* boundaries can testify of the quiet or disturbed condition of the magnetosphere.

Besides the auroral precipitation boundary co-ordinates, the DMSP database contains the information about the average precipitating electron energy and energy flux in different precipitation regions. Taking into account that at midnight the position of the *b1e* and *b1i* boundaries and the *b5e* and *b5i* boundaries usually coincide well [*Newell et al.,* 1996; *Vorobjev et al.,* 2000] such kind of data are available for four precipitation regions: *b1e-b2i* – precipitations equatorward of the cross tail current sheet (diffuse auroral luminosity); *b2i-b4s* – precipitations from the earthward edge of the current sheet (the equatorial part of an auroral oval); *b4s-b5* – precipitations in the poleward part of the statistical auroral oval, and *b5-b6* – soft electron precipitation region poleward of the auroral oval. Precipitating electron characteristics in these regions are shown in Figure 3. To compute these characteristics we have selected one more temporal interval in the magnetospheric substorm development. In the 1–3 phase corresponding to the final stage of the substorm growth phase we have chosen the satellite passes closest to the substorm onset, the time of which we estimated as ($T_0$ – 5) ± 5 min. Only events with the sharply pronounced magnetic bay onset were selected for this investigation.

In Figure 3 the average electron precipitation energy and energy flux are standardized to those during magnetic quietness which levels in units (keV) for the average energy ($E_0$) and ($erg/cm^2\ s$) for the energy flux ($F_0$) are shown in the right part of Figures (a) and (b), respectively. Figure 3*a* illustrates changes of the average

electron precipitation energy in different regions during the substorm. As it is seen from the figure during the substorm expansive phase the average energy increase was as large as 2–3 times in all precipitation regions. The energy increase begins smoothly yet during the substorm growth phase. The most interesting is the decrease of the average auroral electron energy in the two low latitude regions (*b1-b2i* and *b2i-b4s*) and the simultaneous increase of energy in the two higher latitude regions *b4s-b5* and especially in *b5-b6* just before the substorm onset time. The energy decrease in the two low latitude auroral regions can correspond to the fading of both discrete and diffuse aurorae before the substorm onset found out by *Zaitseva et al*. [1976], *Pellinen and Heikkila* [1978] and *Kornilova et al.* [1989].

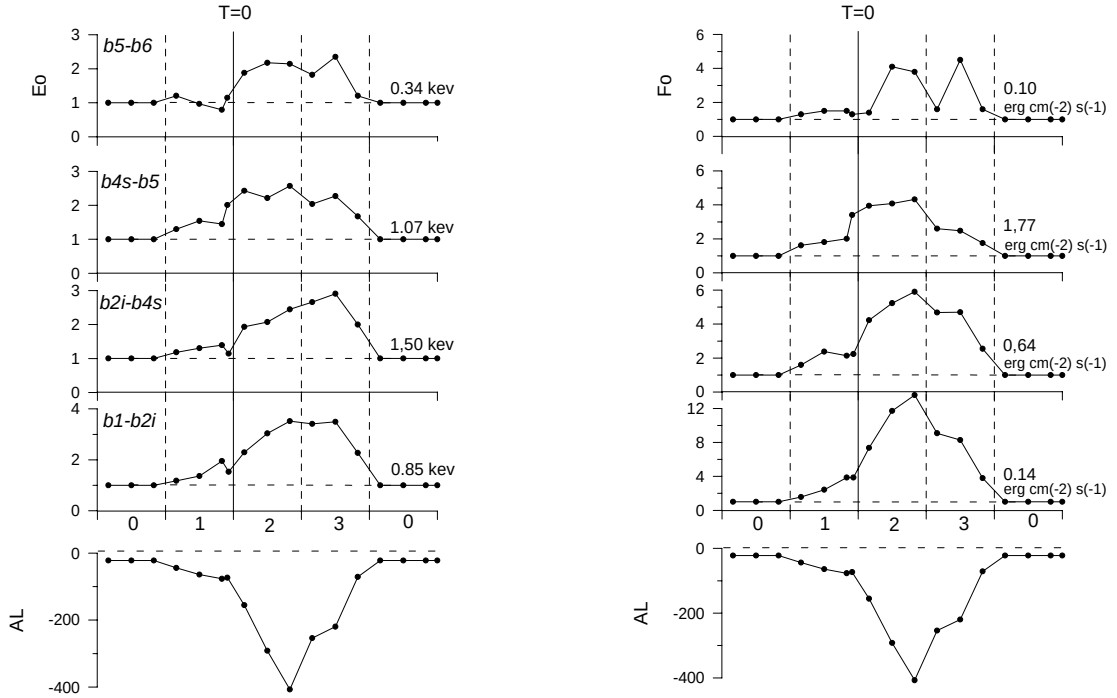


**Figure 3.** The average electron precipitation energy (a) and energy flux (b) in various precipitation regions during the substorm. They are standardized to those during magnetic quietness, which absolute levels are shown in the right part of Figures (a) and (b). The label of regions is marked in the left part of Figure (a). The bottom panel demonstrates the AL index.

Figure 3*b* shows the behavior of the average energy flux in the same precipitation zones as the average energy in Figure 3*a*. During the period of magnetic quietness the greatest power emitting occurred in the *b4s-b5* region corresponding to the poleward part of the statistical auroral oval. The precipitating electron energy flux in this region was about 3 times higher than in the equatorward part of the auroral oval (*b2i-b4s*) and more than ten times higher than in the *b1e-b2i* and *b5-b6* regions. As a whole, the energy fluxes, as well as the average electron energy, began to grow during the substorm growth phase and reached the maximum level at the end of the substorm expansive phase. The most essential increase of energy flux (more than ten times) this time was observed in the most equatorward precipitation region (*b1e-b2i*) corresponding to the region of diffuse auroral luminosity. Just before the beginning of substorm expansive phase, the energy flux in all regions remained about constant excepting the *b4s-b5* region where the flux increase of about 1.5 times was registered.

## 4. Discussion

The analysis of interplanetary medium conditions during substorms is extremely important for finding out whether the magnetospheric substorm is a consequence of internal magnetospheric instabilities or it is triggered by sharp changes in the interplanetary parameters ([*Lyons*, 1996] and references here). The general external sources of the substorm triggering can be a sharp decrease or a northern turn of the southward IMF $B_z$ component [*Caan et al.,* 1978; *Dmitrieva and*

*Sergeev*, 1983], impulsive changes of the solar wind dynamic pressure [*Kokubun et al.*, 1977; *Sauvaud*, 1998] and sharp variations in the IMF $B_y$ component [*Dmitrieva and Sergeev,* 1983; *Troshichev et al.,* 1986]. So*, Lyons* [1996] considered that the substorm expansive phase is caused generally by external sources. On the other hand, *Maltsev* [1998] showed from statistical data that the substorm onset was not associated with either sharp $|B_z|$ changes or solar wind dynamic pressure variations that in the author's opinion testifies of a spontaneous nature of substorms.

Our statistical results show that although on the average during the substorms the solar wind dynamic pressure was a little higher than during quietness periods, at the time of the substorm onset any essential or sharp changes in the dynamic pressure were not observed. The substorm expansive phase began generally during the southward IMF orientation and on the average the substorm onset was not associated with a decrease or a northern turn of the southward interplanetary $B_z$. In this point our conclusions coincide with the results obtained by *Maltsev* [1998]. The IMF $B_y$ component behavior is of interest. As one can see from Figure 1, in the winter season substorms were observed predominantly during the positive $B_y$ orientation and in summer when the $B_y$ was negative. A similar result has been earlier obtained by *Vorobjev and Zverev* [1982]. It is important to note here that according to our data the most essential changes in the interplanetary $B_y$ orientation were registered after the substorm onset. It is well known [*Sibeck et al.,* 1989; *Fairfield et al.,* 1990; *Vorobjev et al.,* 1999] that change of IMF $B_y$ orientation results in the change of a geometry foreshock upstream the Earth bow shock that in turn can be accompanied by sharp changes in the dynamic pressure put on the sunlit magnetopause. Moreover, *Vorobjev et al.* [2001, 2002] showed that the $B_y$ polarity essentially affects during a substorm development both the midnight latitudinal position of poleward electron precipitation boundaries (*b5* and *b6*) and the maximum latitude of auroral bulge. In this way, sharp changes of the $B_y$ orientation in an ecliptic plane can be one of important factors that influence the development of magnetospheric disturbances.

The width of the auroral precipitation in the midnight sector (Figure 2) during the period of magnetic quietness was about 6.5° of latitude and increased up to 11° to the maximum of the substorm expansive phase of about ~400 nT intensity. This expansion occurred generally due to the displacement of the equatorward precipitation boundary (*b1e*) to lower latitudes. In contrast with this, the width of the auroral oval during quiet periods is only ~ 2°-3° of the latitude [*Starkov and Feldstein,* 1967]. It is well known [*Akasofu*, 1964] that a substorm usually begins by a sudden growth of intensification of the auroral arc at the equatorward border of the auroral oval and is accompanied with the subsequent fast poleward displacement of bright auroral forms. *Samson et al.* [1992] showed that the auroral intensification at the substorm onset had occurred in the region of intensive proton penetration. Since the *b2i* boundary was determined as the latitude where the energy flux of ions had the maximum, the auroral break-up most likely occurs near the region of *b2i* and *b2e* boundaries crossing. The width of an auroral arc is a few km at most, while the width of the auroral precipitation region to the pole from the *b2i* and *b2e* crossing is about 5° of latitude. So, one can suggest that the auroral break-up occurs deeply in the magnetosphere in the transition region where the magnetic field lines change from dipole-like to extended ones in the tail. This result coincides with conclusions in the paper of *Samson et al*. [1992] where it is shown by scanning photometer data that the initial auroral intensification occurs at field lines which are about 5° of latitude equatorward of the polar cap boundary and cross the equatorial plane of the magnetosphere at $6–10R_e$.

It is interesting that the decrease of the average electron precipitation energy in the *DAZ* and in the equatorward part of the *AOP* region is about 5 min before $T$=0. This energy decrease can correspond to the fading in discrete aurorae and diffuse luminosity just before the beginning of the substorm [*Zaitseva and et al*., 1976; *Pellinen and Heikkila*, 1978; *Kornilova and et al.*, 1989]. Simultaneously with this energy decrease in the equatorial part of auroral zone, the enhancement in both the average electron precipitation energy and energy flux was observed in the poleward part of the *AOP* region. The energy flux increase was about 1.5 times compared to their average level at the final stage of the substorm growth phase. The increase in both the average auroral electron energy and energy flux in this region testifies of the fact that about 5 min before the substorm onset time an increase in auroral luminosity or occurrence of visual aurorae at CGLs of about 67°–71° can be expected, i.e. a few degrees poleward of the bright discrete aurorae of the auroral oval (substorm precursor).

This result can be an indirect evidence of the substorm mechanism suggested by *Shiokava et al.* [1997] and *Reeves* [1998]. In their "braking model" the formation of neutral line in the magnetospheric tail precedes the beginning of the substorm expansive phase determined by auroral break-ups, Pi2 bursts, the sharp beginning of magnetic bays, appearance of particle injections at geosynchronous distances etc. The beginning of the reconnection produces fast convective plasma flows that are directed earthward and tailward from the reconnection region. When the strong flows approach the dipole-like inner magnetosphere they are forced to slow down and divert around the Earth.

The braking process of the flow could cause an

azimuth pressure gradient, the strong inductive electric field, and vortical flows that in turn produce the field-aligned currents of the substorm current wedge. The compression pulses and fluctuations of the field-aligned currents generated in the braking point can be an initial cause of the Pi2 magnetic pulsations, the particle injections into the inner magnetosphere and appearance of other ground features of a substorm onset. Actually, *Nagai et al.* [1998] showed that magnetic reconnection most likely takes place in the limited area of the near-Earth plasma sheet at the distances of 20–30 $R_e$ downtail or nearer to the Earth [*Mukai et al.,* 1998; *Machida et al.,* 1998] a few minutes prior to the substorm onsets which were identified by Pi2 appearance. It suggests that at least in some particular cases the reconnection triggers the substorm. In the papers by *Fairfield et al.* [1998,1999] examples of high speed flows observed with the Geotail satellite were shown that were clearly associated with substorms and, in fact, preceded auroral break-ups and substorm injections. Thus, it cannot exclude the possibility that some substorms can be initiated by the magnetic reconnection in the tail and the occurrence of high-speed flows. However, we shall note that the analysis of optical data presented by *Yahnin et al.* [2000] did not discover any auroral precursor for several selected substorms.

## 5. Conclusions

DMSP F7 satellite observations for the whole of 1986 in the magnetic local time interval from 21 to 24 MLT were used to examine the different auroral precipitation boundary dynamics and precipitating electron features during all substorm phases. The general results can be summarized as follows:

1. The empirical model of the substorm in the midnight auroral precipitation is suggested. The model includes dynamics of different electron precipitation boundaries during all substorm phases together with simultaneous changes in average electron precipitation energy and energy flux in different precipitation zones as well as the IMF and solar wind plasma behavior during the substorm.
2. The analysis of observations shows that during magnetic quietness and just before the beginning of the substorm expansive phase the latitudinal width of the auroral precipitation in the nightside sector is about 6°-7°CGL.
3. For about 5 min prior to the substorm onset time a decrease in the average precipitating electron energy in the equatorward part of auroral zone was observed simultaneously with an increase in both the average precipitating electron energy and energy flux in the poleward part of the auroral precipitation zone.
4. The isotropy boundary position in the beginning of the substorm expansive phase ($T$=0) coincides with the inner edge of the central plasma sheet. During magnetic quietness and the substorm growth phase the isotropy boundary is placed closer to the Earth than the central plasma sheet, but in contrast, it is inside the main plasma sheet during the period of substorm expansive phase and magnetic disturbances.
5. On the average, during the substorm the solar wind dynamic pressure was about 1.5 that of the period of magnetic quietness. Substorms occurred predominantly during the southward IMF orientation and the substorm onset is not often associated with the northern turn or decrease of the southward interplanetary $B_z$. In winter substorms occurred generally during the positive interplanetary $B_y$ and in summer they were observed when the interplanetary $B_y$ was negative.

**Acknowledgements.** The DMSP particle detectors were designed by Dave Hardy of AFRL, and data obtained from JHU/APL. We thank Dave Hardy, Fred Rich, and Patrick Newell for its use. We think Drs J. H. King and N. Papitashvili for providing IMF and solar wind plasma observations in the NSSDC OMNIWeb database. The WDC for geomagnetism in Kioto provided magnetic activity indexes. The paper was supported by the RFBR grants 02-05-64807 and 99-05-65611, INTAS-2000-752 and ISSI, Bern.

## References

Akasofu, S. -I., The development of the auroral substorm, *Planet. Space Sci., 12*, 273, 1964.

Akasofu, S. -I., C. -I. Meng, D. S. Kimball, Dynamics of aurora. 4. Polar magnetic substorm and westward traveling surge. *J. Atmos. Terr. Phys*., *28*, 489, 1966.

Caan, M. N., R. L. McPherron, C. N. Russell, The statistical magnetic signature of magnetospheric substorm, *Planet. Space Sci., 26*, 269, 1978.

Dmitrieva, N. P., and V. A. Sergeev, Spontaneous and compelled beginning of a burst phase of the magnetospheric substorm and its preliminary phase duration, *Geomagn. Aeron*., *23*, 470, 1983. (in Russian).

Fairfield, D. H., W. Baumjohann, G. Paschmann, H. Luhr, D. G. Sibeck, Upstream pressure variations associated with the bow shock and their effects on the magnetosphere, *J. Geophys. Res., 92*, 4565, 1987.

Fairfield, D. H., T. Mukai, A. T. Y. Lui et al., Geotail observation of substorm onset in the inner magnetotail, *J. Geophys. Res., 103*, 103, 1998.

Fairfield, D. H., T. Mukai, T. Yamomoto et al., Earthward flow bursts in the inner magnetotail and their relation to auroral brightenings, AKR intensifications, geosynchronous particle injections and magnetic activity, *J. Geophys. Res., 104*, 355, 1999.

Feldstein, Ya. I., and Yu. I. Galperin, Structure of the auroral precipitations in the nightside sector of the magnetosphere, *Cosmic Research*, *34*, 227, 1996. (in Russian).

Hardy, D. M., M. S. Gussenhoven, E A. Holeman, Statistical model of auroral electron precipitation, *J. Geophys. Res., 90*, 4229, 1985.

Iijima, T., T, Nagata, Signatures for the substorm development of the growth phase and expansion phase, *Planet. Space Sci*., *20*, 1095, 1972

Kokubun, S., Polar substorm and interplanetary magnetic field, *Planet. Space Sci*., *18*, 697, 1970.

Kokubun, S., R. L. McPherron, C. T. Russell, Triggering of substorms by solar wind discontinuities, *J. Geophys. Res., 82*, 74, 1977.

Kornilova, T. A., M. I. Pudovkin, G. V. Starkov, Aurora damping before a breakup, *Geomagn. Aeron*., *29*, 503, 1989. (in Russian).

Lyons, L. R., Fundamental observational features, distinction from other disturbances, and external triggering, *J. Geophys. Res*., *101*, 13011, 1996.

McPerron, R. L., Growth phase of magnetospheric substorm, *J. Geophys. Res., 75*, 5592, 1970.

Machida, S., Y. Miyashita, A. Ieda et al., Time evolution of the Earth magnetotail associated with substorm onset: Geotil observations, Substorm-4. Edited by Kokubun S. and Kamide Y. Astrophysics and Space Science Library, Japan, 238, 149, 1998.

Maltsev, Yu. P., Search of relation between the substorm onset and the solar wind parameters, Substorm-4. Edited by Kokubun S. and Kamide Y. Astrophysics and Space Science Library, Japan, 238, 291, 1998.

Mukai, T., M. Hoshino, Y. Saito et al., Pre-onset and onset signatures for substorms in the near-tail plasma sheet: Geotail observations, Substorm-4. Edited by Kokubun S. and Kamide Y. Astrophysics and Space Science Library, Japan, 238, 131, 1998.

Nagai, T., M. Fujimoto, Y. Saito et al., Structure and dynamics of magnetic reconnection for substorm onset with Geotail observations, *J. Geophys. Res*., *103*, 4419, 1998.

Newell, P. T., Ya. I. Feldstein, Yu. I. Galperin., C. -I. Meng, Morphology of nightside precipitation, *J. Geophys. Res., 101*, 10737, 1996.

Newell, P. T., V. A. Sergeev, G. R. Bikkuzina, S. Wing, Characterizing the state of the magnetosphere: testing the ion precipitation maxima latitude (b2i) and the ion isotropy boundary, *J. Geophys. Res., 103*, 4739, 1998.

Pellinen, R. J., W. J. Heikkila, Observation of auroral fading before breakup, *J. Geophys. Res*., *83*, 4207, 1978.

Reeves, G. D., New perspectives on substorm injections, Substorm-4. Edited by Kokubun S. and Kamide Y. Astrophysics and Space Science Library, 238, Japan, 785, 1998.

Samson, J. C., L. R. Lyons, B. Xu, F. Creutzberg, P. Newell, Proton aurora and substorm intensifications, *Geophys. Res. Lett*., *19*, 2167, 1992.

Sauvaud, J. A., An attempt to characterize substorm drivers in the interplanetary medium, Substorm-4. Edited by Kokubun S. and Kamide Y. Astrophysics and Space Science Library, Japan, 238, 131, 1998.

Shiokava, K., W. Baumjohan, G. Haerendel, Braking of the high-speed flows in the near-Earth tail, *Geophys. Res. Lett., 24*, 1179, 1997.

Sibeck, D. G., W. Baumjohann, R. C. Elphic et al., The magnetospheric response to 8-minute period strong-amplitude upstream pressure variations, *J. Geophys. Res*., *94*, 2505, 1989.

Sotirelis, T., P. T. Newell, Boundary-oriented electron precipitation model, *J. Geophys. Res*., *105*, 18655, 2000.

Spiro, R. W., P. H. Reiff, Jr. L. J. Maher, Precipitating electron energy flux and auroral zone conductances – an empirical model, *J. Geophys. Res., 87*, 8215, 1982.

Starkov, G. V., and Ya. I. Feldstein, Variation of auroral oval zone boundaries, *Geomagn. Aeron*., *7*, 62, 1967. (in Russian).

Starkov, G. V., and Ya. I. Feldstein, Substorm in aurorae, *Geomagn. Aeron*., *11*, 560, 1971, (in Russian).

Starkov, G. V., B. V. Rezhenov, V. G. Vorobjev, Ya. I. Feldstein, L. I. Gromova, Structure of the auroral precipitations in the dayside sector, *Geomagn. Aeron*., *42*, 186, 2002, (in Russian).

Troshichev, O. A., A. L. Kotikov, B. D. Bolotinskaya, V. G. Andrezen, Influence of the IMF azimuthal component on the magnetospheric substorm dynamics, *J. Geomag. Geoelectr., 38*, 1075, 1986.

Vorobjev, V. G., and V. L. Zverev, Influence of solar wind parameters on geomagnetic activity, *Geomagn. Aeron*., *22*, 257, 1982, (in Russian).

Vorobjev, V. G., O. I. Yagodkina, V. L. Zverev, Morphological features of bipolar magnetic impulsive events and associated interplanetary medium signatures, *J. Geophys. Res., 104*, 4595, 1999.

Vorobjev, V. G., L. I. Gromova, B. V. Rezhenov, G. V. Starkov, Ya. I. Feldstein, Variations of the boundaries of plasma precipitation and auroral

luminosity in the night-time sector, *Geomagn. Aeron*., *40*, 79, 2000, (in Russian).

Vorobjev, V. G., O. I. Yagodkina, D. Sibeck, K. Liou, C. -I. Meng, Auroral conjugacy during substorm: Coordinated Antarctic ground and Polar Ultraviolet observations, *J. Geophys. Res., 106*, 24579, 2001.

Vorobjev, V. G., O. I. Yagodkina, G. V. Starkov, Ya. I. Feldstein, Influence of the IMF sector structure on the locations of auroral precipitation boundaries in the night-time sector, *Geomagn. Aeron*., 2002.

Yahnin, A. G., I. A. Kornilov, T. A. Kornilova et al., Do the observations confirm the high-speed flow breaking model for substorms? Fifth international conference on substorm. Edited by Wilson A. European Space Agency, SP-443, P.345, 2000

Zaitseva, S. A., B. M. Kuznetsov, M. I. Pudovkin, Auroral and current dynamics in the course of substorm progress, *Geomagn. Research*, *18*, 73, 1976, (in Russian).

# Filamentary structure of magnetospheric plasma

J. Błęcki[1], S. Savin[2], N. Cornilleau-Wehrlin[3], K. Kossacki[1]
M. Parrot[4], H. Rothkaehl[1], K. Stasiewicz, R.Wronowski[1],
O. Santolik[6], and J. -A. Sauvaud[7]

[1] Space Research Centre PAS, 00-716 Warsaw, Bartycka 18A, Poland
[2] Space Research Institute RAS, Moscow, Russia
[3] CETP/UVSQ, Velizy, France
[4] LPCE/CNRS, Orléans, France
[5] Space Physics Institute, Uppsala, Sweden
[6] Charles University, Prague, Czech Republic
[7] CESR/CNRS, Toulouse, France

**Abstract.** Plasma waves are one of the most significant features of plasma. They are a very sensitive indicator of the boundaries and inner structure of different regions in space plasmas. The data gathered onboard INTERBALL-1 and MAGION-4 in the polar cusp indicate that plasma wave intensity changes very rapidly with a characteristic period of the order of 1−50 seconds, which differs from the satellite rotation period. Comparison with plasma data suggests that it could be associated with real inner structure of the polar cusp. A similar effect has been seen in the data from PROGNOZ-8 and FREJA satellites. CLUSTER data also confirm these effects. The analysis of the wave and plasma data from these satellites associated with fine (filamentary) structures in the cusp is given in this paper. This kind of filamentary structure plasma is often associated with nonlinear stage of the current instabilities or nonlinear evolution of the Alfven waves. The polar cusp can be used as a laboratory for studies of the plasma non-linear processes. Discussion of possible source of this fine structure is presented at the end of this paper.

## 1. Introduction

Plasma turbulence is one of the most significant features of the polar cusp. Alfven, lower hybrid, electron and ion cyclotron waves are always observed there. Higher frequency waves at Langmuir and upper hybrid frequencies are also often seen in the cusps [*Potellette et al*., 1990; *Błęcki et al*., 1998; *Savin et al*., 1999].

Another general feature of magnetized plasma is a tendency to create filamentary structures in the field-aligned currents [*Perrat*, 1991]. This filamentation can be seen by optical and *X-ray* observations of the solar chromosphere and corona, in the cometary's tails and on the Earth in the aurora. Magnetospheric plasma indicates also a tendency to form subtle structures in the current flowing along magnetic field line. The polar cusp is a location where field-aligned currents are present [*Yamauchi et al*., 2000]. The information provided by the waves can be used for determination of the physical conditions in these plasma structures. Waves give information on the microphysics of the processes in plasmas. The temporal and spatial resolutions obtained from the wave spectra are the highest. This fact allows us to use the wave spectra as a main tool to study fine structure of the polar cusp.

PROGNOZ-8, MAGION-4, INTERBALL Tail Probe and CLUSTER with their orbits crossing the polar cusps – northern at high and southern at much lower altitudes, additionally FREJA at a lower orbit, give complementary information about the structure of polar cusps along their altitudes. Next section of this paper contains examples of observations of such structures in the polar cusp by the above-mentioned satellites. The last section dwells on the possible origin of the discussed structures.

## 2. Observations

*The outer cusp observations*

PROGNOZ-8 and INTERBALL satellites crossed the northern cusp at altitudes 8−10$R_E$ and the southern one at 3−4$R_E$. CLUSTER has a similar orbit, but FREJA was a low orbiting satellite with cusp crossings at the altitude of about 1700 km. Presented spectra are obtained either

by onboard processing of the signal or by wavelet analysis of the wave form in order to obtain highest spatial resolution.

Figure 1 presents an example of wavelet spectra obtained from wave form taken in the outer northern polar cusp at the distance to the Earth's $9R_E$ on 14.01.1981 by PROGNOZ-8. The interval of the measurements shown here has duration of 90 seconds. Rotation period of PROGNOZ-8 was 120*s*. At 10:02:02UT the satellite entered the structure with much higher wave activity. The time scale of this structure is 22s, but inner structures with time scales of 1–2*s* are clearly seen.

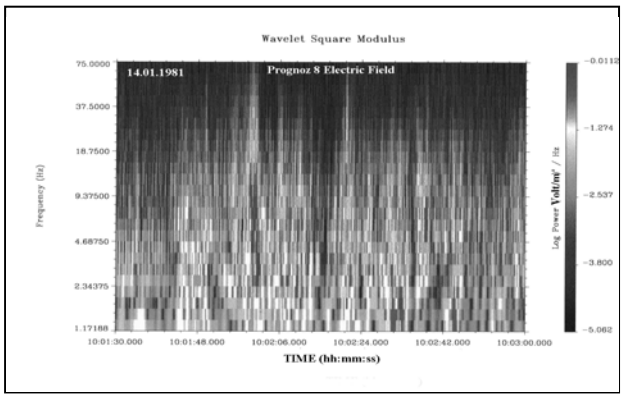


**Figure 1.** Example of wavelet spectra of electric field fluctuations registered in the outer polar cusp by PROGNOZ-8 satellite. At 10:02:02 the wave activity increases during 22*s*, but within this interval structures with duration of 1–2*s* can be clearly distinguished. (the wavelet analysis has been done with the SWAN software developed in LPCE – Orléans by Dominique Lagoutte and his colleagues).

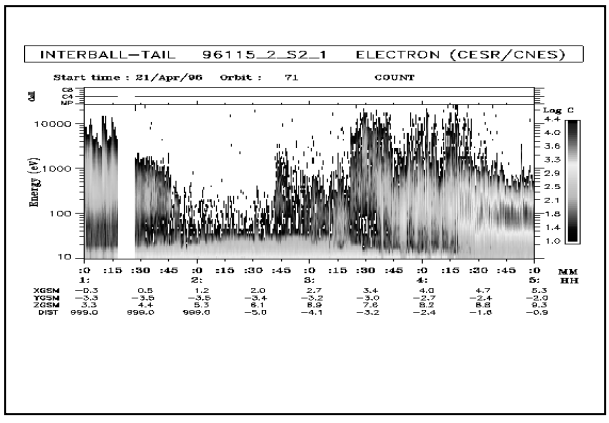


**Figure 2.** Dynamic spectra of the electron energy versus time, as obtained by the ELECTRON instrument on board INTERBALL-1 satellite. The cusp crossing is seen on 4:15–5:00UT.

The next example is taken from INTERBALL-1 and MAGION-4 measurements on 21 April 1996. Detailed descriptions of the wave experiments on board INTERBALL-1 and MAGION-4 are given in *Klimov et al.* [1997] and *Błęcki et al*. [1997]. Figure 2 contains the electron energetic spectra taken by the ELECTRON instrument on board INTERBALL-1. The outer cusp crossing is seen between 4:15 and 5:00 UT at a distance of about $9.5R_E$. Figure 3 presents the measurements of the electric currents within the cusp on board INTERBALL-1. The small-scale structure of the electric current has temporal scale of about 1*s*, which corresponds to the spatial scale of 3 km.

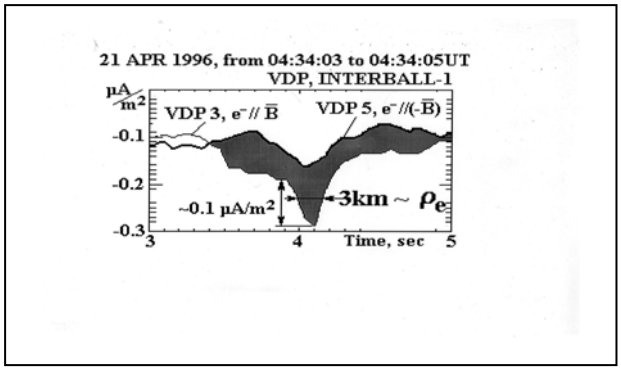


**Figure 3.** Registration of the electric current density by Faraday's cup on board INTERBALL-1 in the outer polar cusp. The maximum intensity of the current is concentrated within a small-scale structure with the size of 3 km.

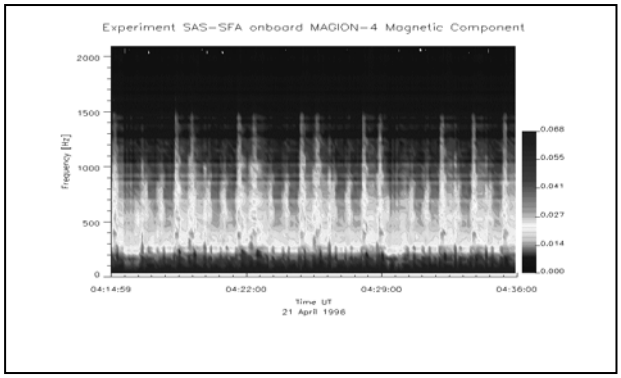


**Figure 4.** Spectrum of the magnetic field fluctuations obtained from the on board spectrum analyzer SAS – MAGION-4 in the outer polar cusp on 21 April 1996.

The wave spectra registered in the polar cusp and corresponding to the small scale structures are shown in Figure 4. The rotation of the satellite (period about 90*s*) is clearly seen in the periodic (42*s* equal to a half of rotation period) changes of the wave intensity, but

shorter variations with characteristic time of 2–4*s* can be also distinguished. The spectrum presented here occurred during INTERBALL-1 crossing of the structures shown in the previous figures. MAGION-4 was on the same orbit, but 10 min ahead of INTERBALL-1 on this day

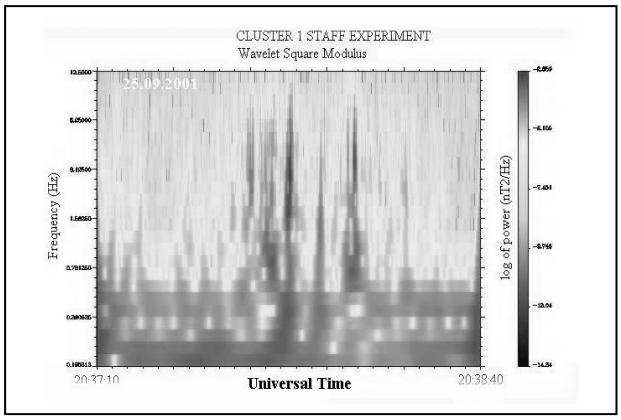


**Figure 5.** Wavelet spectra of the magnetic field variations from STAFF experiment on CLUSTER-1 spacecraft taken on 25.09.01 in the outer polar cusp. The time interval presented in this figure is 90s long.

The following examples are taken from CLUSTER satellites wave measurements. Figures 5 and 6 show 90*s* intervals of wavelet spectra of the magnetic field variations registered in the outer polar cusp by CLUSTER-3 and 1, respectively. The changes of the wave intensity are due to the satellites rotation (rotation period is 4 seconds), but inside these structures seen on 20:37:46 till 20:38:12 on CLUSTER-3 and 20:37:46 till 20:38:38 UT on CLUSTER-1 caused by rotation, shorter variations are distinguished with duration of 1*s*.

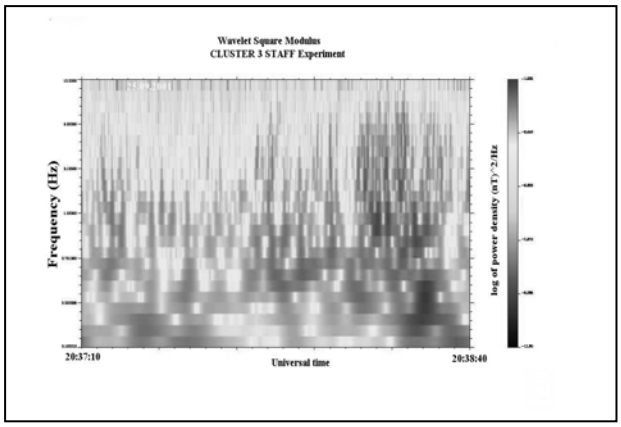


**Figure 6.** Same as Figure 5, but obtained by CLUSTER-3. The duration of the time interval is 90*s*.

The examples given above originated from the measurements made in the outer cusp at the distances of 8–10$R_E$. to the Earth center. All of them show the existence in this region of some structures with typical time scales. Two time scales can be distinguished – one of the order of 1–5*s* and a second one of the order of 20–30*s*. The two time scales correspond to the different spatial scales, 2–10 km and 40–60 km.

*The observations in the inner cusp*

FREJA has recorded the wave form of the magnetic and electric field variations in the polar cusp at the altitudes of about 1700 km. The wave form has been processed with FFT. Figure 7 contains the spectra of the electric component (upper panel) in the frequency range up to 1000 $H_z$ and magnetic component (lower panel) up to 2000 $H_z$. The duration of these measurements was 150*s*. A strong enhancement of the wave intensity can be seen in the interval 17:42:15–17:43:10. Within this interval, variations associated with the satellite rotation (6s) are seen but shorter changes with duration below 1s can be easily distinguished as well. The wave form (not shown in this paper) has even shorter variations of the intensity of the order of tenths of second. As in the outer polar cusp, two different time scales can be distinguished here – tenth of second and single seconds. It corresponds to two different spatial scales: hundreds meters and single kilometres.

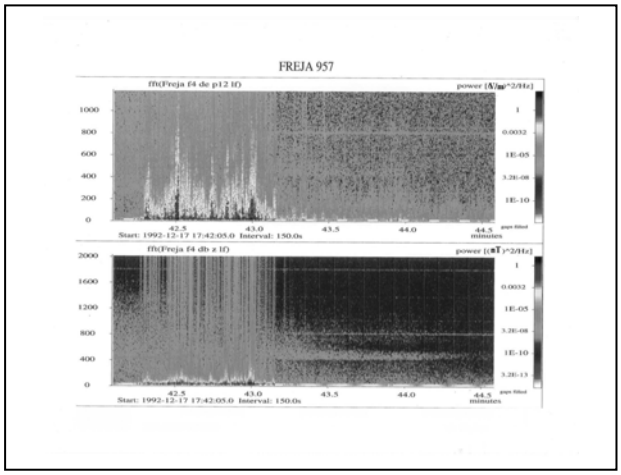


**Figure 7.** Spectra of the electric (upper panel) and magnetic field variations registered in the lower cusp by the FREJA satellite.

*Magnetospheric tail*

The plasma in the magnetospheric tail is rather thin both in the plasma sheet and in the plasma sheet boundary layer. But this region is the source of the field-

aligned currents which are closed in the aurora regions of the ionosphere.

The first registrations of the small-scale structures in the magnetospheric tail over the plasma sheet boundary were made by PROGNOZ-8 satellite [*Blecki et al* 1994]. Figure 8 shows the wave spectra of the electric field measured by PROGNOZ-8 in the vicinity of the plasma sheet boundary layer, but observed structures are clearly detached from it. The intensity of the waves indicates strong variability. This fact reflects the structure of the crossed formations. And again two different time (spatial) scales are clearly seen: about 2–5 minutes and about 30s respectively. This is a lower limit, as the time resolution of the spectra measurements on PROGNOZ-8 is equal to 30s.

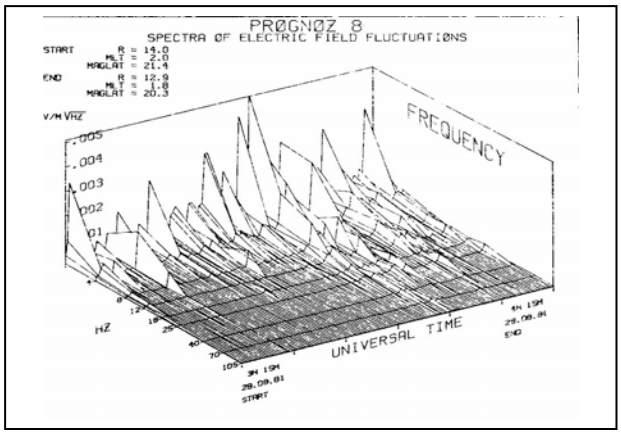


**Figure 8.** The spectra of the electric field obtained in the magnetospheric tail over the plasma sheet boundary layer. The structures are seen on 3:43–3:50 and 3:57–4:07UT, however internal substructure can be distinguished as well.

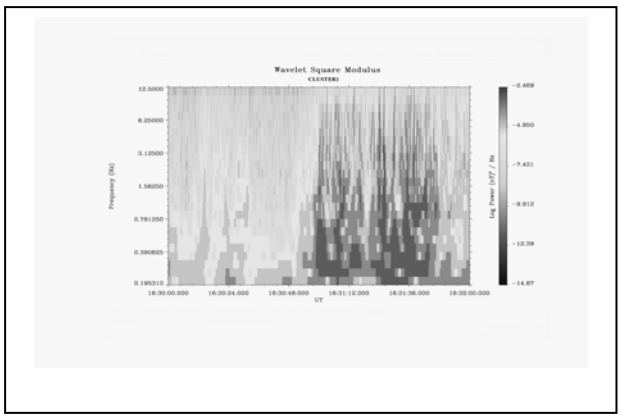


**Figure 9.** The wavelet spectrogram of the magnetic field variations in the magnetospheric tail registered by CLUSTER 1 satellite.

The wave magnetic component registered by CLUSTER satellites in the magnetospheric tail reveals the same feature.

This analysis provides much higher time resolution. One can see the 90*s* long structure with an internal substructure with typical time scales of 2–5*s*. This analysis gives much higher time resolution. One can see structure with duration of 90*s*, but with internal substructure with characteristic time scales of 2–5*s*.

Similar structures have been registered by INTERBALL-1 plasma instruments [*Grigorenko et al,* 2002].

## 3. Discussion

The wave spectra, which are the most sensitive indicator of the structure boundary within the cusp, reveal the existence of small-scale structures at all the altitudes visited by the above-mentioned satellites.

The typical time scales of these fine structures within wave spectra vary from single seconds up to tens of seconds in the outer cusp which corresponds to a spatial scale of 2–60 km. However two different scales can be distinguished here: first one in the outer cusp, large scales of the order of 20–60 km and thinner ones – 2–6 km, and second in the inner cusp, with large scales of the order of single kilometres and smaller ones of the order of hundreds meters.

Non-linear analysis of the kinetic Alfven waves shows the possibility of the filamentation of these waves with a minimum characteristic scale corresponding to those of Alfven soliton [*Bingham et al*., 2001]. The characteristic scale is of the order of the Alfven wavelength. Its minimum value can be expressed by the local electron density: $\lambda_a \geq 2.2 \times 10^8/n^{1/2}$ [m] if the plasma density $n$ is measured in $m^{-3}$.

Another non-linear mechanism that can lead to the filamentation is pinching of the field-aligned electric current [*Galperin et al*., 1986]. This mechanism can generate structures with a smallest size given by $L>c/\omega_p$ ($c$ is the light velocity and $\omega_p$ the plasma frequency). It can be also expressed by the electron local density as $10^7/n^{1/2}$ [m].

Both characteristic scales depend strongly on the altitude, and they are different in the outer and inner cusp. Assuming that proton density in the outer polar cusp is comparable to its value in the magnetosheath $10^7$–$10^8$ $m^{-3}$, the Alfven wavelengths can have values between 22 and 70 km, while the structures generated by the current pinching mechanism can be as small as 1–4 km. In the inner cusp at FREJA orbit altitudes the measured density is $10^9 - 10^{10}$ $m^{-3}$ which corresponds to Alfven wavelengths of 2.2–7 km and pinch generated structures of 100–300 m.

These structures observed in the magnetospheric tail have scales about 10 times bigger due to much smaller density in these regions of the magnetosphere.

Observations presented here are in good agreement with these hypotheses. To summarize one can say that structures often observed in the polar cusp and magnetospheric tail can be generated by a non-linear stage of Alfven waves evolution that produces large-scale structures and by non-linear pinching of the field-aligned current which generates small-scale structures.

**Acknowledgements**. This work has been supported by grant KBN 8T12E 047 21, RFFR 02-02-17160, 01-02-02009 and European Commission Research Training Network HPRN-CT-2001-00314.

## References

Bingham, R., R. A. Cairns, R. O. Dendy, et al., Auroral Particle Acceleration by Waves, *Phys. Chem. Earth*, *26*, 133-144, 2001.

Błęcki, J., S. Gadomski, J. Juchniewicz, et al., SAS Wave Experiment on Board Magion 4, *Annales Geophysicae*, *15*, 514-527, 1997.

Błęcki, J., H. Rothkaehl, K. Kossacki, et al., ULF-ELF-VLF-HF plasma wave observations in the polar cusp onboard high and low altitude satellites. *Physica Scripta, 75,* 259-263, 1998.

Galperin, Yu., L. Zelenyi, M. Kuznetsova, Pinching of the Field – Aligned Currents as a Possible Mechanism of the Aurora Ray Structures Formation, *Cosm. Res*., *XXIV*, 865-874, 1986.

Grigorenko, E. E., A. Fedorov, L. Zelenyi, Statistical Properties of Beamlets in the Earth's Magnetotail, *Adv. Space. Res., 30*, 1809-1816, 2002.

Klimov, S., S. Romanov, E. Amata, et al., ASPI Experiment: Measurements of Fields and waves onboard The INTERBALL-1 spacecraft, *Annales Geophysicae*, *15*, 514-527, 1997.

Perrat, A. L., Physics of the Plasma Universe, Springer Verlag, New York, Berlin, Heidelberg, London, Paris, Tokyo, Hong Kong, Barcelona, Budapest, 1991.

Pottelette, R., M. Malingre, N. Dubouloz, et al., High Frequency Waves in the Cusp /Cleft Regions, *J. Geophys. Res.*, *95*, 5957-5971, 1990.

Savin, S., E. Budnik, M. Nozdrachev., et al., On the Plasma Turbulence and Transport at the Polar Cusp Outer Border, *Czech. J. Phys.*, *49*, 679-693, 1999.

Yamauchi, M., R. Lundin, L. Eliasson, et al., Independency of the Dayside Field-Aligned Current: A Restriction to Cusp Models, in *Magnetospheric Current Systems*, Geophysical Monograph 118, pp.245-252, American Geophysical Union, Washington, 2000.

E-mail address of J.Błęcki:jblecki@cbk.waw.pl

# Dynamical behavior of the ring current ions in the dayside magnetosphere during strong geomagnetic storms

A. A. Gusev[1, 2], W. A. Gonzalez[1], U. B. Jayanthi[1], V. M. Pankov[2], G. Pugacheva[3], and N. J. Schuch[3]

[1] National Institute for Space Research, INPE, São José dos Campos, SP, Brazil
[2] Space Research Institute of RAN, Moscow, Russia
[3] Southern Regional Space Research Center/INPE, Santa Maria, Brazil

**Abstract.** Transport of ring current ions during the main phase of the geomagnetic storm is modeled. Particle trajectories are simulated by the Lorentz equation for dipole and Tsyganenko magnetic field models. The convection electric field is described by the $K_p$ dependent Volland-Stern model in the equatorial plane. Out of that plane the electric field is assumed to be the same as in the equatorial plane. This consideration implies the possibility of non-equipotentiality of geomagnetic field lines at least for $L \geq 6$ during strong magnetic storms. In our modeling energetic protons, typically of several tens of *keV*, start on the night side at $L=4$ or at $L=7$, and move initially under gradient magnetospheric drift largely confined to the equatorial plane. However, soon after crossing the noon-night meridian, the protons rather abruptly depart from the equatorial plane and deviate towards high latitude regions. This latter motion is essentially confined to a plane perpendicular to the equator, and it is characterized by finite periodic motion. The calculations indicate a small variation of the first adiabatic invariant along the ion orbit in the equatorial region with greater non-adiabatic variation at the point of ion departure from the equatorial region and later along the orbit. The greater the convection electric field, the higher is the energy of the protons participating in this off equatorial divergent flow. The more energetic ions, of hundreds *keV* and higher, however, continue their magnetic drift around the Earth uninterruptedly in equatorial plane and these ions form the symmetric ring current ion population. The numerical calculations described herein explicitly indicate that the perpendicular ion outflow can contribute to the morning-evening component of the magnetic field perturbation during geomagnetic storms, and can result in populating the high latitude and tail regions by the energetic protons.

## 1. Introduction

An appearance in the Earth's vicinity of a substantial negative IMF $B_Z$ component coupled to increased velocity of solar wind, leads to an increase in the magnitude of the large-scale magnetospheric convection electric field.

In the idealized case, the convection electric field vector located in the equatorial plane is directed along the morning to evening sectors. For quiet times, the geoelectric field strength is of the order of 0.1 *mV/m*, and is enhanced up to 10–20 *mV/m* during the main phase of great magnetic storms. Drift trajectories of the charged particles (energetic ions and electrons of about 3–300 *keV* energy) trapped in the magnetosphere can change dramatically due to these convection fields. Strong convection electric fields drive hot plasma particles from the tail region into the inner magnetosphere where their trajectories typically approach the Earth to distances of about 2–4 Earth radii, depending on the magnitude of the finite motion. In this case it is not necessary to check the solution by computing the reversed *E*-field (e.g., [*Roederer*, 1970]).

The flow of this hot plasma from the magnetotail is so strong that it creates a significant geoelectrical solenoid located at $L > 3$, which induces an almost-uniform perturbation magnetic field at $L < 3$ that is directed anti-parallel to the Earth's magnetic dipole axis. During strong magnetic storms this current-generated magnetic field sometimes reaches several hundreds of gamma as shown by measurements of the azimuthally symmetric component of the geomagnetic field variation, an effect which is associated with the $D_{st}$ index. Ring current ion transport, confined and divergent, in the disturbed magnetosphere is the subject of the present investigation.

## 2. Particle motion in geomagnetic and geoelectric fields

### 2.1. The two-dimensional case

Traditionally, the transport of ring current charged particles is simulated by the guiding center motion of equatorially mirroring particles (Nishida, 1971) with the second adiabatic invariant vanishing (i.e. $J = 0$). In this work the particle trajectories are simulated basing on the full Lorentz force equation for a particle motion in geomagnetic and geoelectric fields (i.e., Gusev and Pugacheva, 1982) instead of the guiding center approximation. The charged particle motion in magnetic field of strength $B$ and in an electric field of strength $E$ is described as

$$\frac{d(mV)}{dt} = q(E + \frac{1}{c}V \times B), \qquad (1)$$

where $q$, $m$, and $V$ are particle charge, relativistic mass, and velocity and $c$ is the light velocity. In a simple dipolar geomagnetic field, and in the absence of any electric fields, particles drift around the Earth due to the geomagnetic field gradient. Their leading center trajectories in a purely dipolar $B$-field are concentric circles around the dipole center. But in the presence of even small electric fields in the magnetospheric morning-evening direction, charged particles drift in $\boldsymbol{E}\times\boldsymbol{B}$ direction from the night side towards noon independent from the sign of their electric charge. Equation 1, is solved numerically applying the Runge-Kutta-Guills method. A corresponding Fortran code uses double and where necessary quadruple precision. The solution of the equation for the dipolar and for the IGRF model magnetic fields has a form of auto control whereby charged particles drift around the Earth with conservation of the $L$-shell parameter, and after one drift period approximately return to the initial starting point, i.e. performs a trajectory as is always made for infinite particle trajectories. For example, this is most often carried out for directional cosmic ray cutoff rigidities computed for neutron monitors.

Examples of trajectories of protons of 13.5–100 keV energy with $J = 0$ in a dipolar geomagnetic field with superposed dawn-dusk directed electric fields are shown in Figures 1a,b. These figures show particle orbits in the Earth's equatorial plane without any off-equator bounce oscillations (i.e., $V_Z = 0$). For modeling the proton orbits we used a combination of the corotation and convection electric fields. The former is defined by the potential $U_{COR} = -k(Re)^2/R$, and the latter is described in the equatorial plane by the model of Volland-Stern with dependence on geomagnetic activity in the interpretation of *Nishida* [1971]. Thus $U_{V\text{-}S} = AR^2 \sin a$, where $a$ is the angle between the direction of the field vector and the direction towards the sun (our $X$ axis), $R$ is the radial distance from magnetic dipole center, and with $A$ as the magnetic activity-dependent strength coefficient taken to be: $A = 0.0449/(1.-0.159K_P+0.009K_P^2)^3$, in units of $kV/R_e^2$ During a geomagnetic disturbance with $K_P$=8, the

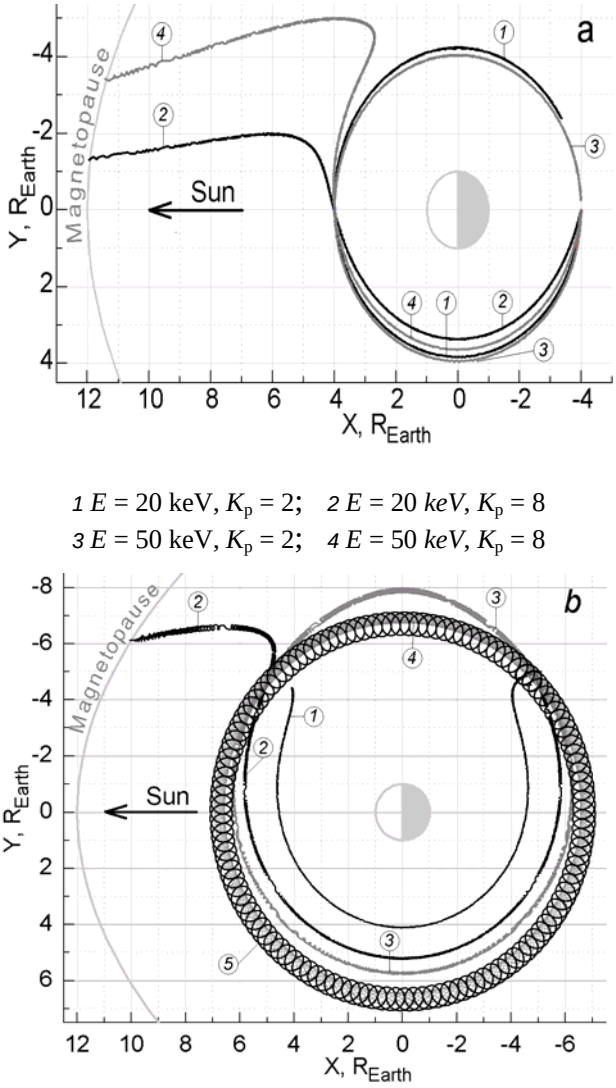


*1* $E$ = 20 keV, $K_p$ = 2; *2* $E$ = 20 *keV*, $K_p$ = 8
*3* $E$ = 50 keV, $K_p$ = 2; *4* $E$ = 50 *keV*, $K_p$ = 8

*1* $E$ = 13.5 *keV*; *2* $E$ = 50 *keV*,
*3* $E$ = 100 *keV*, *4* $E$ = 1 *MeV*,
*5* $E$ = 5 *MeV*,

**Figure 1.** Energetic proton 2-D trajectories in ortogonal dipolar geomagnetic and convection electric field of Volland-Stern model: ***a***) starting point at $L=4$ ($X = -4R_{Earth}$, $Y = 0$); ***b***) starting point at $L=7$ ($X = -7$ $R_{Earth}$, $Y = 0$). At higher energies, the Larmor rotation of the drifting ions is distinguishable because its gyration radius is comparable to the spatial scale sizes involved.

values of $E_{V\text{-}S}$ on the morning side at $L$=7 is 2.9 and at $L$=4 is 1.67 *mV/m*.In a quiet magnetosphere with $K_P$=1, the field values at these points are of 0.159 and 0.0917 *mV/m*. The same corrotation and convection electric field models were earlier used in the works of *Liemohn et al*. [2001]; *Delcourt et al*. [1998]; and *Ozturk et al*. [2001]. In this regard, we found comparable proton trajectories as shown herein as in *Liemohn et al*. [2001]. These are quite similar in purely two-dimensional approximations.

The magnetospheric convection electric field is defined as $\boldsymbol{E}_{conv} = -[\boldsymbol{V}_{SW} \times \boldsymbol{B}_{IMF}]$ where $\boldsymbol{V}_{SW}$ is the solar wind velocity and $\boldsymbol{B}_{IMF}$ is the near Earth interplanetary magnetic field (IMF). For idealized conditions when $\boldsymbol{V}_{SW} \equiv V_X$ and $\boldsymbol{B}_{IMF} \equiv B_Z$ one gets $E_Y = V_X B_Z$, i.e., the resulting magnetospheric electric field has only a dawn-dusk component. During an intense geomagnetic storm, such as the so-called "Bastilian Day" one of 14–15 July 2001, $B_Z$ is of ~ –50 *nT*, $\boldsymbol{V}_{SW}$ is of ~1000 *km/s*, and $E_Y$ = 50 *mV/m* (source: http://nssdc.gsfc.nasa.gov.omniweb), i.e. the electric field strength was substantially greater than that implied by the Volland-Stern model even for $K_P$ = 8.

The orbits of 20 *keV* to 50 *keV* protons starting on the night side at $L$ = 4 (Figure 1*a*) remain inside the inner magnetosphere during relatively low activity ($K_P$ = 2), it was expected. However, for disturbed times ($K_P$ = 8) they are forced out from inner zone towards the dayside magnetopause. Figure 1*b* shows the drift orbits of protons starting at $L$ = 7 (practically from the magnetotail). Protons with energies higher than ≈50 *keV* are well confined to the inner magnetosphere even during strong geomagnetic storms, and they form a roughly symmetric component of the magnetospheric ring current. However, protons below 50 *keV* move from the geomagnetic tail towards the magnetopause, and so leave the inner magnetosphere after residing and drifting there for about 3 hours, creating the partial asymmetric component of the magnetospheric ring current. This part of the ion flow is mainly responsible for the geomagnetic storm manifestation in the Earth's magnetic field, as $D_{st}$ index.

## 2.2. The three dimensional case

The electric field structure away from the Earth's equatorial plane is much less known. In 3-D modeling, we assume that the electric field would be the same as in the equatorial plane. It is clear that this implies non-equipotentiality of the geomagnetic field lines at magnetospheric off-equatorial locations, and we suppose that this is indeed possible for $L$ > 6 in a highly disturbed magnetosphere. Indeed, there is no compelling reason to suppose that field-aligned equipotentiality is fully maintained during geomagnetic storms at all times in the outer magnetosphere and the following computations of an electric field at $L$ > 6 during Bastilian Day geomagnetic storm of 15 July 2000 made for us by the Community Coordinated Modeling Center (CMCC, http://ccmc.gsfc.nasa.gov) showed that we were right in this assumption.

Adiabatic drift paths of equatorially mirroring low-energy protons in a dipolar magnetic field were described a long time ago, in 70's by Chen (1970). However, most of the ring current ions have a small nonzero second adiabatic invariant, i.e. they have a component of velocity perpendicular to equatorial plane different of zero, $V_Z \neq 0$, $J \neq 0$. To investigate the full 3-D proton trajectories in the storm time case, we use the same Equation 1 with the same initial conditions as in Figure 1, but with one crucial difference: the protons have a small initial $V_Z$ components of magnitude approximately $10^{-4} - 10^{-5} V$. This makes a dramatic difference in the drift-flow of these particles.

We traced various ion trajectories in the inner magnetosphere, utilizing both the purely dipolar and the Tsyganenko (1990) field models. The larger $E_{conv}$ values compared to those of the traditional Volland-Stern model (even with $K_P$ = 8) are necessary in order to obtain the appropriately larger $E$-fields corresponding to geomagnetic storm main phase conditions. We calculated the structure of the $E$-fields due to Volland-Stern model for $K_P$ = 8 to keep proper topology of the field, and multiplied those magnitudes by the factors of 2 to 5 to approximate the typically observed electric field magnitude values during intense geomagnetic storms.

In Figure 2, the 3-D view of a characteristic energetic proton orbit in the dipolar magnetic field is shown. Similar to the 2-D case, the ion travels westward from the night side of towards the dayside while remaining confined to the equatorial plane. The geoelectric field

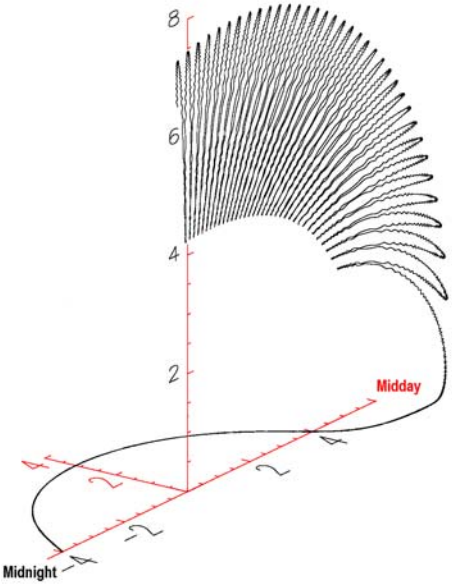


**Figure 2.** 3-D view of 50 keV proton orbit.

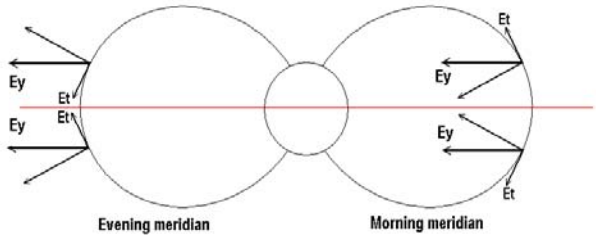


**Figure 3.** The perpendicular and tangential ($E_t$) components of morning-evening electric field ($E_Y$) projected on magnetic field lines in morning and evening meridians.

energizes the protons up in the motion in the electric field when approaching the local evening position, then ion decelerates and after the cross of the magnetic local noon, its velocity of magnetic drift around the Earth is decreased.

At the point where the magnetic drift velocity is approximately equal to zero, the particle abruptly leaves the equatorial plane, and it travels upwards towards middle and high geomagnetic latitudes. There is a reason, in our model, why a particle leaves the equatorial plane on the morning side of magnetosphere after crossing the noon-night line (see Figure 3): the dawn-dusk electric field $E_Y$ focuses particles onto the equatorial plane on the evening side due to the existence of a component $E_t$ tangential to magnetic field line. It is directed towards the equatorial plane on the evening side and away from it on the morning side. It presses the particles to the equatorial plane on the evening side decreasing their bounce oscillations and increases these bounce motions on the morning side. An ion leaving the equatorial plane essentially remains on a plane that is perpendicular to the Earth's equator plane, and its motion is effectively scattered by the defocusing action of this off-equatorial electric field. Drifting further in noon-midnight direction the proton crosses the midnight meridian and enters the area of the focusing electric field returning to the equatorial plane and thus closing its drift trajectory around the Earth.

The nature of the upper and the lower mirror points limiting bounce oscillations (Figure 2) in the morning hemisphere is different. The mechanism of reflection from the upper mirror point is the same as in the case of the absence of the electric field i.e. the increase of the geomagnetic field strength ("magnetic line density") along a geomagnetic field line. In spite of the acceleration of the proton by the tangential component of the electric field the increase of the magnetic field is enough to stop further proton motion towards the dipole center. Different from the case of the absence of the electric field the lower mirror point located in the same semi-sphere as the upper one. It is simply due to the fact that the parallel impulse of the proton is zeroed by the

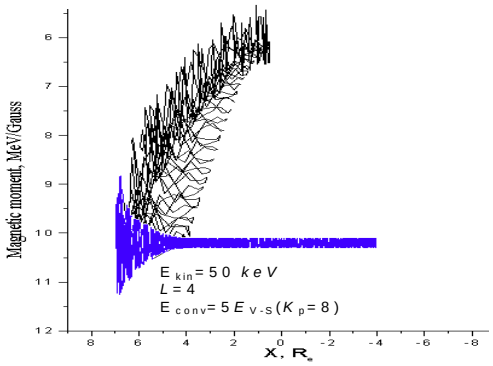


**Figure 4.** The variation of the proton magnetic moment ion along the trajectory when it moves in and out off equatorial plane.

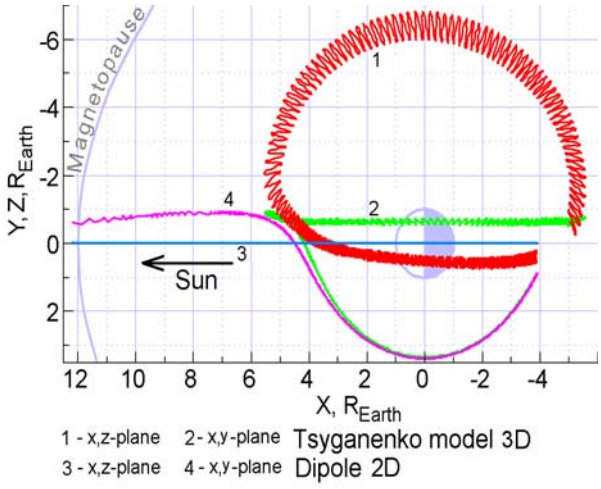


**Figure 5.** Projections of the simulated trajectories for proton of 135 keV energy moving in Tsyganenko and dipolar magnetic fields and convectional electric field equal to 5 fold of that for $K_P$ = 8 of Volland-Stern model.

tangential component of the electric field directed in this case opposite to the proton velocity. Thus the nature of the lower mirror point is essentially related to the presence of the electric field and has nothing to do with the dipole character of the geomagnetic field.

The particle motion in the geomagnetic field with the presence of electric field is not exactly adiabatic, and even the magnetic moment (the first adiabatic invariant) could well be slowly varied (if don't say, violated) by the processes herein described. Its instantaneous magnitude ($\mu = E_\perp/B$) for a 50 keV proton, which orbit is demonstrated in Figure 2, is shown in Figure 4. One can see that the magnetic moment is practically conserved along the path until it reaches $X \approx 4R_e$ (dark black lines).

The moment undergoes little variations around $\mu = 10.25$ MeV/Gauss, caused by ion gyration in the presence of electric fields. The strong variation of the invariant begins at $X > 4R_{Earth}$ and continues up to $X = 7\ R_{Earth}$, but the average value of the invariant still doesn't change much. In the crucial moment of the particle's departure from the equatorial plane, its first adiabatic invariant is slowly decreasing to $\mu \approx 6.0$ *MeV/Gauss.*

The numerical solution of Equation 1 is done with a double precision algorithm, and the solution was checked with 4-fold precision. A proton orbit was also traced back in time to the starting point shown in Figure 2, confirming the quality of the mathematical solution. The simulations were also made using the Tsyganenko (1990) magnetic field model. The results are illustrated in Figure 5 which shows the 3-D 135 keV proton orbit (lines with the numbers 1 and 2) with convection electric field 5 times larger than the Volland-Stern model at $K_P$=8. The orbit starting point is at $L = 4$ (longitude 166.67°). For comparison, the lines with the number 3 and 4 in this figure are the 2-D projections of a corresponding proton orbit for a purely dipolar magnetic field with the proton's second invariant $J$=0. All these particle trajectory examinations confirm the main result we have obtained: in the presence of an electric field, a significant part of the asymmetric ring current leaves the Earth's equatorial plane on the dayside magnetosphere.

Consequently, energetic ions flow into the middle and high latitudes, then populating the tail plasma. This motion remains finite and even periodic, as seen in Figures 2, 5. The modeling conducted here corresponds specifically to the $L = 4–7$ region. Recently, similar results were obtained for ions in the higher $L$-shell region at $L \geq 8$ (e.g., [*Delcourt et al*., 1998; *Obsturk et al*., 2001]). The reason of a sudden shift of ring current ions from the equatorial plane on the dayside in those cases is different from considered herein. Namely, there it is assumed that near the noon magnetopause near the equatorial plane the geomagnetic field has a small local maximum and two local minima in the adjacent regions both north and south of the equator on the same $L$-shell (e.g., [*Shabansky*, 1971[). Consequently, when a night-side particle which bounces symmetrically around the equator drifts toward noon and reach $L \approx 8$, it may shift out of the equatorial plane and so mirror about the northern and southern polar cusps with a violation of the second adiabatic invariant.

## 3. MHD equation numerical solution by CCMC for the Bastille day event

The NASA Community Coordinated Modeling Center (CCMC, 2002) has, on our request, run their 3-D numerical simulation software of the magnetospheric

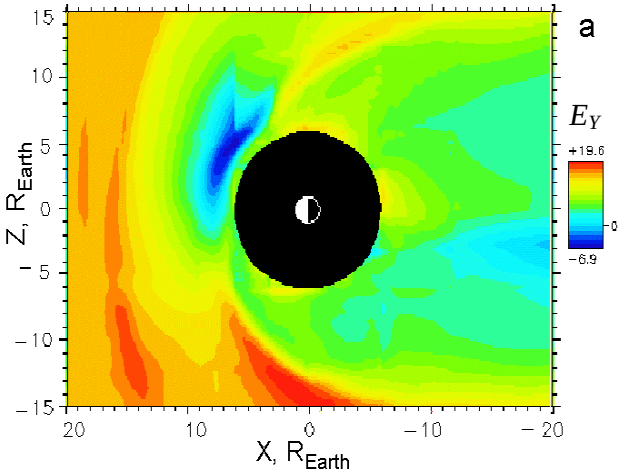


**Figure 6.** The $E_Y$ (a) electric field component (mV/m) in X, Z–plane simulated in NASA by CCMC for the 15.07.2000 event (UT22:36:00). X axis is directed towards the Sun, Y one is in dawn-dusk direction, Z one is toward the North. CCMC).

MHD equations for the "Bastille Day" (July 15 2000) magnetic storm. The physical models that are the basis for the CCMC software are described in the CCMC Web site (http://ccmc.gsfc.nasa.gov). Using the time-dependent solar wind input data one obtains magnetospheric time-dependent convection electric fields at $L > 6$ as an MHD equation solution. The computed MHD parameters also include the magnetic field and the plasma flow velocity components.

In Figure 6 we show the calculated $E_Y$ of the magnetospheric electric field strength in the (Z, X) noon-night meridianal plane (X is directed towards the Sun; Y is the dawn-dusk direction, and Z is towards the North) at the time of the approximate maximum of the $D_{st}$ development. We find that during several minutes near the geomagnetic storm maximum in the outer magnetosphere at $L$-shell between 6 and about 8 $R_{Eearth}$ there exists definite conditions in the (X, Z)–plane with a strong, of several *mV/m*, dawn-dusk electric field, $E_Y$, in the absence of a significant $E_Z$–component, and also a very small $E_X$ electric field component. As demonstrated above in this paper, these conditions could cause and sustain an effective energetic particle outflow from equatorial plane when they occur on the noon-side magnetosphere during such events. This could be another mechanism causing consequential energetic particle appearance in the middle and high latitudes of the magnetosphere and even in the magnetospheric tail. These aspects suggest that further analysis of the electric field structures on the front-side magnetosphere during event periods can shed light into energetic particle streaming and flows elsewhere in the Earth's magnetosphere.

## 4. Conclusion

The energetic particle orbital tracing conducted in this work was specially carried out for protons with energies as high as 50 to 135 keV, and with assumed geoelectric fields that for magnetic storm conditions are greater by factors of 2 to 5 compared to the Volland-Stern electric field model strength. As the CCMC modeling of 3-D numerical solution of MHD equations shows, these stronger electric fields are, however, quite natural during intense magnetic storms when the Earth's magnetosphere is severely perturbed. The results show that even the very energetic ring current ions participate in this charged particle outflow of the equatorial region during strong magnetic storms. In fact, the more negative the $B_Z$ component of the interplanetary magnetic field and the greater the solar wind velocity, the larger the magnitude of the dawn-dusk electric field. The natural consequence is that the more energetic ring current particles can leave the equatorial plane, thus contributing to the depletion of the ring current itself and its transformation into current of ions flowing out into the mid-latitude and cusp regions of the magnetosphere. This is in addition to the well-understood depletion mechanism by charge exchange losses of ring current ions.

The escaping energetic charged particle from the magnetospheric ring current could then populate the middle and high latitudes of the storm time magnetosphere, and possibly also some part of the geomagnetic tail region with tens keV protons and heavier ions.

Protons of the ring current that did not take part in this geoelectric field caused outflow continue to drift around the Earth forming the symmetric ring current component. The upward part of this ring current could conceivably create the morning-evening component of the magnetic field variation observed during geomagnetic storms, possibly with a significant *B*-field perturbation magnitude to that of the horizontal $D_{st}$ variation.

Our next step in this ongoing analysis will be to trace single particle orbit in the close-to-realistic magnetospheric electric and magnetic fields obtained by the CCMC MHD modeling to determine the spatial and energy distribution of the energetic particles outflow and its temporal evolution and duration during geomagnetic disturbed periods.

**Acknowledgements.** The authors devote the work to the memory of Dr. Yu. Galperin.

## References

Chen, A. J., Penetration of low energy protons deep into the magnetosphere, *J. Geophys. Res*, *75(A13)*, 2458-2467, 1970.

Chen, M. W., M. Schulz, L. R. Lyons, et al, Storm time transport of ring current and radiation belt ions, *J. Geophys. Res.*, *98*, 3835-3849, 1993**.**

Delcourt, D. C., and J. -A. Sauvaud, Recirculation of plasma sheet particles into high latitude boundary level, *J. Geophys. Res*, *103(A11)*, 26,521-26,532, 1998.

Gusev, A. A., and G. I. Pugacheva, About output of quasi-trapped electrons from the atmosphere, *Geomagn. Aeron.*, *22*, 487-489, 1982. (in Russian).

Liemohn, M. W., J. U. Kozira, M. F. Thomsen et al., Dominant role of the asymmetric ring current in producing the storm time $D_{st}$, *J. Geophys. Res*, *106(A6)*, 10,883-10,904, 2001.

Nishida, A. Geomagnetic diagnosis of the magnetosphere, Springer-Verlag, 180, pp.256, New York, 1971.

Öztürk, M. K., A. A. Chan, R. A. Wolf, Violation of the second invariant in a static magnetic field, (Abstract).International Workshop ISEC 2001: Radiation Belt Science and Technology, Queenstown, New Zealand, 2001.

Roederer, J., Dynamics of geomagnetically trapped radiation, Springer-Verlag, Heidelberg-New York, 1970.

Shabansky, V. P., Some processes in magnetosphere, *Space Sc. Rev*., *12(3)*, 299-418, 1971.

Tsyganenko, N. A., Quantitative models of the magnetospheric magnetic field: methods and results, *Space Sci. Rev*., *54*, 75-186, 1990.

---

CCMC group, http://ccmc.gsfc.nasa.gov, 2002.

# Electrostatic solitary structures associated with electron and ion beams in the auroral magnetosphere

A. V. Volosevich

State University, Mogilev, Belarus Republic

**Abstract.** Three-dimensional nonlinear theoretical model of the electrostatic solitary structures in the magnetospheric plasma with the electron and ion beams is constructed. Based on a series of works [*Volosevich and Galperin*, 2000; 2002*a*; 2002*b*] a modified Korteweg-de Vries-Zakharov-Kuznetzov (KdV-ZK) equation for plasma with electron and ion beams is derived. It is shown, that at presence of the ion and electron beams two types of structures are formed: the solitary structures moving with the velocity comparable to local ion-acoustic velocity, ion-acoustic structures (IAS) and the solitary structures moving with the velocity comparable to electron thermal velocity, electron acoustic structures (EAS). Characteristics of these solitary structures such as amplitude, phase speed and the oblateness ratio $R = l_\perp / l_\parallel$ ,(where $l_\parallel, l_\perp$ – field-aligned and perpendicular scale) are estimated.

## 1. Introduction

Small-scale solitary structures become one of the most interesting new features observable by modern high resolution rocket and satellite instruments in the auroral magnetosphere. The knowledge of these structures has progressed considerably, in particular, due to experiments on satellites S3-3, VIKING, FREJA, FAST, POLAR, INTERBALL-2 (see, for example, [*Mozer et al.*, 1980, 1997; *Ergun et al.*, 1997, 1998, 1999; *Bounds et al.,* 1999; *Franz*, 1998, 2000]). These structures have been observed in the plasma sheet boundary layer by the Geotail satellite [*Matsumoto, et al.,* 1994], by the Plasma Wave Instrument on the Polar satellite (2 to 8.5$R_e$ radial distance) [*Cattell et al.,* 1999]. Besides, there is a report on observation of solitary potential structures in the high-altitude cusp region (5 to 9$R_e$ *r*adial distance). Small-scale electrostatic structures are observed by Polar Electric Field Instrument (EFI) near 1*Re* altitude in the southern auroral zone. Solitary structures are identified in satellite electric field measurements (EFI) by their signature of bipolar electric field fluctuations of short duration oriented predominantly parallel to the magnetic field.

Many of these solitary structures were observed in association with the ion and electron beams within the auroral acceleration regions. These structures move mainly, or strictly, along the magnetic field. Some of them have field-aligned velocity comparable to the local ion-acoustic velocity with respect to the accompanying ion beam or speed of an ion beams (about several hundreds in km/s in the auroral zone), then they may be identified as ion acoustic structures (IAS). At the same time, both at these and at higher altitudes, solitary structures are moving with much faster velocities comparable to the accompanying electron beam drift speed or the speed of electron beams about 3000–4000 km/s. These are identified as electron acoustic solitary structures (EAS) [*Franz*, 1998, 2000*; Berthomier et al.*, 2000]. Such structures can exist inside the electric fields and are under certain conditions capable to support existence of these fields, representing moving carriers of a charge.

One-dimensional theoretical models of nonlinear structure formation in plasma were studied in numerous works. However, three-dimensional structures have been registered in experiments on FAST and POLAR satellites [*Franz*, 2000]. In these experiments the ratio of field-aligned components of an electric field to perpendicular component $E_\parallel / E_\perp$ or oblateness ratio $R = L_\perp / L_\parallel$ ( $L_\parallel, L_\perp$ – field-aligned scales and the scales perpendicular to the direction of the magnetic field which define its form) has been received on POLAR satellite. These experimental data have set the task of development of the three-dimensional theory of formation of electrostatic structures in magnetospheric plasma.

Despite the numerous observations of solitary structures, several questions concerning this phenomenon remain unanswered. For example, the physical mechanism of the solitary structures formation, their role in the auroral acceleration process have yet to be determined.

Such questions provided motivation for the theoretical study.

The purpose of the present work is the following:

- to develop the three-dimensional MHD theoretical models, describing formation of nonlinear electrostatic structures in magnetospheric plasma at presence of beams of charged particles.
- to research parametrical space, where solitary structures exist in various areas of the magnetosphere.
- to estimate the scales, amplitudes, velocity , spatial sizes of three-dimensional electrostatic structures and the factor $R = l_\perp / l_\parallel$ determining the form of structure.

## 2. MHD theory of formation of nonlinear electrostatic structures

Below we consider a fully ionized collisionless plasma in a uniform external magnetic field. The nonlinear evolution of the electrostatic waves in multicomponent plasma may be described by MHD set of equations:

Density $n_\alpha$, velocity $\vec{\upsilon}_\alpha$ and pressure $P_\alpha$ of the charged particles α -type are described by the of following fluid equations:

$$\frac{\partial \vec{\upsilon}_\alpha}{\partial t} + (\vec{\upsilon}_\alpha \nabla)\vec{\upsilon}_\alpha = -\nabla \frac{e_\alpha \varphi}{m_\alpha} - \frac{1}{n_\alpha m_\alpha}\nabla P_\alpha + \omega_{c\alpha}[\vec{\upsilon}_\alpha, \vec{e}_z] \quad (1)$$

$$\frac{\partial n_\alpha}{\partial t} + \nabla n_\alpha \vec{\upsilon}_\alpha = 0 \quad (2)$$

$$P_\alpha = C \cdot n_\alpha^\gamma \quad (3)$$

where: $\vec{\upsilon}_\alpha, n_\alpha, e_\alpha, m_\alpha, \omega_{c\alpha}, P_\alpha$ $-\alpha$, $\gamma$ – the velocity, density, charge, mass, cyclotron frequency, pressure of particles of the $\alpha$-type $\gamma$ – is the ratio of the specific heat at constant pressure to the specific heat at constant volume. For one-dimensional model $\gamma$ = 3 and for three-dimensional process $\gamma$ = 5/3. We shall assume, that the magnetic field is directed along Z axis. $\vec{B} = B_0 \vec{e}_z$, $\varphi$ – electrostatic potential.

For the normalized variables

$$\upsilon_\alpha \Rightarrow \frac{\upsilon_\alpha}{C_s},\ n_\alpha \Rightarrow \frac{n_\alpha}{n_{0\alpha}},\ \Phi = \frac{e\varphi}{kT_{ef}},\ C_s^2 = \frac{kT_{ef}}{m_i}, \quad (4)$$

where $m_i$ – ion mass, $T_{ef}$ – effective temperature of the electrons, $\Phi$-normalized potential, k – Boltzmann constant, we receive MHD system equations for the density and the velocity of the charged particles of the $\alpha$-type( $\alpha$ = e.i, electrons, ions):

$$\frac{\partial \vec{\upsilon}_\alpha}{\partial t} + (\vec{\upsilon}_\alpha \nabla)\vec{\upsilon}_\alpha = -K_\alpha \nabla \Phi + \omega_{c\alpha}[\vec{\upsilon}_\alpha, \vec{e}_z] - \sigma_\alpha \frac{\gamma}{\gamma - 1}\nabla n^{\gamma - 1} \quad (5)$$

$$\frac{\partial n_\alpha}{\partial t} + \nabla n_\alpha \vec{\upsilon}_\alpha = 0 \quad (6)$$

where:

$$\nabla \Rightarrow \frac{C_s}{\omega_{oi}}\nabla;\ K_\alpha = \frac{e_\alpha}{e}\frac{m_i}{m_\alpha};\ \sigma_\alpha = \frac{m_i}{m_\alpha}\frac{T_{0\alpha}}{T_{ef}};$$
$$\omega_{c\alpha} = \frac{\omega_{c\alpha}}{\omega_{0i}};\ t \Rightarrow \frac{1}{t \cdot \omega_{oi}};\ \omega_{oi}^2 = \frac{e^2 n_{0i}}{\varepsilon_0 m_i}; \quad (7)$$

To derive KdV-ZK three-dimensional equation describing the formation of electrostatic structures in the magnetospheric plasma with beams of charged particles, we make the following transformation of coordinates and time

$$x' = \varepsilon^{\frac{1}{2}} x;\ y' = \varepsilon^{\frac{1}{2}} y;\ z' = \varepsilon^{\frac{1}{2}}(z - Vt);\ \tau = \varepsilon^{\frac{3}{2}} t, \quad (8)$$

$V$ – the velocity of movement of structure and $\varepsilon$ – the small parameter measuring the weakness of the dispersion. We can take a reductive perturbation method to reach balance between the nonlinear and dispersive term, the same procedure as in [*Volosevich and Galperin*, 2000*a*, 2000*b*, 2002]. Then after simple transformations, defining first order component for velocities, density and potential, we determine: $\upsilon_{\alpha x}^{(1)}$, $\upsilon_{\alpha y}^{(1)}$, $\upsilon_{\alpha z}^{(1)}$. Then we receive the equation connecting value of the first and second order:

$$\frac{\partial \Phi_\alpha^{(1)}}{\partial \tau} + \frac{9V_\alpha^2 - \gamma\sigma_\alpha}{6a_\alpha V_\alpha}\,\Phi^{(1)}\frac{\partial \Phi^{(1)}}{\partial z} + \frac{V_\alpha^3}{2\omega_{c\alpha}^2}\frac{\partial}{\partial z}\Delta_\perp \Phi^{(1)} + L_\alpha = 0, \quad (9)$$

$$L_\alpha = \frac{a_\alpha K_\alpha}{2V_\alpha \tau}\left(\frac{\partial \Phi^{(2)}}{\partial z} - a_\alpha \frac{\partial n^{(2)}}{\partial z}\right), \quad (10)$$

For the definition $L_\alpha$ it is necessary to use Poisson equation for the chosen model of plasma. Defining $n^{(2)}$ from Poisson equation, after substituting Equation (10) in Equation (9) we receive three-dimensional equation KdV-ZK, describing formation of the solitary structures. We assume, that background plasma will consist of four populations of the charged particles.

1) Hot background electrons, which are in thermodynamic equilibrium with the effective temperature $T_{ef}$

$$n_e = n_{0e}\exp(\Phi) \quad (11)$$

2) Hot background positive ions with density $n_i$ and with equilibrium temperature $T_i$. The density of these ions submits to Boltzmann distribution

$$n_i = n_{0i}\exp\left(\frac{-e\varphi}{kT_i}\right) = n_{0i}\exp(-\Phi\beta), \quad \beta = \frac{T_{ef}}{T_i} \quad (12)$$

(3) The electron beam, moving along the direction of the magnetic field with the speed $V_{0e}$, which is described by the Equation (9) with parameters:

$$V_e = V - V_{0e},\ \sigma_e = \frac{m_i}{m_e}\frac{T_e^b}{T_{ef}},\quad a_e = \frac{V_e^2 - \gamma\sigma_e}{K_e},\ K_e = -\frac{m_i}{m_e} \quad (13)$$

4) The ion beam, moving along the direction of the magnetic field with the speed $V_{0i}$, with the parameters

$$V_i = V - V_{0i},\ \sigma_i = \frac{T_i^b}{T_{ef}},\quad K_i = 1,\ a_i = \frac{V_i^2 - \gamma\sigma_i}{K_i} \quad (14)$$

For the chosen four-component plasma Poisson equation is written as

$$\Delta\Phi = (1-\delta_e)e^{\Phi} + \delta_e n_e^b - (1-\delta_i)e^{-\beta\Phi} - \delta_i n_i^b \quad (15)$$

Here: $\delta_e = \frac{n_{eb}^0}{n_{0e}}$, $\delta_i = \frac{n_{ib}^0}{n_{0i}}$ – electron and ion density respectively, each normalized to the electron density equilibrium number.

Using equation of the first order, we receive the linear dispersion relation

$$\frac{\delta_e}{a_e} = \frac{\delta_i}{a_i} - (1-\delta_e) + \beta(1-\delta_i) \quad (16)$$

As it follows from Equation (16), linear phase speed of the structure's movement depends on relative density $\delta_e$, $\delta_i$, relative temperature $\sigma_i, \sigma_e$ of electron and ion beams, whereas $\beta$ is the relative temperatures of an electron and ion population of background plasma. We shall notice, that only at the certain values of these parameters the solitary structures are formed with certain speed of movement along the magnetic field's direction.

For the specific case when only an electron beam ($\delta_i = 0$) is present, the linear speed of the electron-acoustic structure is defined:

$$V_e = \left(\frac{m_i}{m_e}\left(\frac{5}{3}\sigma_i + \frac{\delta_e}{\lambda}\right)\right)^{\frac{1}{2}} + V_{0e} \quad (17)$$

and for the ion-acoustic structures with only ion beam if $\delta_e = 0$

$$V_i = \left(\frac{5}{3}\sigma_i + \frac{\delta_i}{\lambda}\right)^{\frac{1}{2}} + V_{0i}, \quad (18)$$

As follows from Equation (17) and Equation (18) for these special cases the velocity of ion – acoustic structures is close to the sound speed $C_s$, and for electron-acoustic structures it is close to thermal electron speed $V \sim \upsilon_{Te}$, however, when both ion and electron beams are present these speeds can considerably differ from $C_s$ or $\upsilon_{Te}$. We must notice that the linear velocity of structures depends on plasma parameters for the chosen models of plasma.

Further, from the Equation (15) for the second perturbations, we receive system of three equations for definition of $\frac{d\Phi^{(2)}}{dz}, \frac{dn_{eb}^{(2)}}{dz}, \frac{dn_{ib}^{(2)}}{dz}$. Defining $L_\alpha$ from Equation (10), then, substituting in the Equation (9) which have been written for the electrons and ions, finally we receive equation KdV-ZK for plasma with two beams of the charged particles

$$\frac{\partial \Phi^{(1)}}{\partial \tau} + a_1 \Phi^{(1)} \frac{\partial \Phi^{(1)}}{\partial z} + a_2 \frac{\partial^3 \Phi^{(1)}}{\partial z^3} + a_3 \frac{\partial}{\partial z} \Delta_\perp \Phi^{(1)} = 0 \qquad (19)$$

where coefficients $a_1, a_2, a_3$ are determined by the parameters of plasma.

$$a_1 = \frac{\alpha_2^i C_i - \alpha_2^e C_e - \lambda_1}{C_i - C_e}, \; a_2 = \frac{1}{C_i - C_e},$$

$$a_3 = \frac{\alpha_1^i C_i - \alpha_1^e C_e + 1}{C_i - C_e}, \; \lambda_1 = (1-\delta_e) - \beta^2 (1-\delta_i)$$

$$\alpha_1^i = \frac{V_i^3}{2\omega_{ci}^2}, \; \alpha_1^e = \frac{\hat{V}_e^3}{2\omega_{ce}^2}\sqrt{\frac{m_i}{me}},$$

$$\alpha_2^i = \frac{9V_i^2 - \gamma\sigma_i}{6a_i V_i}, \; \alpha_2^e = \frac{9\hat{V}_e^2 - \gamma\sigma_e}{6a_e \hat{V}_e}\sqrt{\frac{m_i}{m_e}}$$

$$C_i = \frac{2V_i\delta_i}{a_i^2}, \; C_e = -\frac{2\hat{V}_e\sqrt{\frac{m_e}{m_i}}\delta_e}{a_e^2}$$

$$a_e = -\left(\hat{V}_e^2 - \frac{5}{3}\sigma_e\right), \; \hat{V}_e = V_e\sqrt{\frac{m_e}{m_i}}, \; \omega_{ce} = \frac{\omega_{He}}{\omega_{oe}}$$

By investigating the dependences of the coefficients of the Equation (19) on the parameters of plasma, the electron and ions beams, we can define the characteristics of the structure: linear phase velocity of structure $V$, amplitude and the oblateness value ratio $R = L_\perp / L_\parallel$ ( $L_\parallel, L_\perp$ – field-aligned scales and the scales perpendicular to the direction of a magnetic field).

### 3. The basic numerical results

The Equation (19) can be analyzed by traditional methods, but some important conclusions for the diagnostic magnetospheric plasma can be received from the analysis of the coefficients of the Equation (19).

This equation was used for calculation of parametrical space (plasma parameters $\delta_i, \delta_e, \; \sigma_i, \sigma_e, \; \beta, V_{i0}$, $V_{0e}$) where electrostatic structures can form in four-component plasma.

As in the one-dimensional model the amplitude of structures is defined as $\Phi = 3M/a_1$ and the width $D = 2\sqrt{a_2/M}$, where $M$ is the structure velocity normalized to the ion acoustic speed (the Mach number). It is evident, that the amplitude of the soliton is positive for $a_1 > 0$ (compressive soliton) and negative for $a_1 < 0$ (rarefactive soliton) if we suppose that M>0 and $a_2 > 0$.

The oblateness ratio is defined as $R = L_\perp / L_\parallel = (a_3/a_2)^{1/2}$ and the structures' velocity along the magnetic field is determined from the dispersion equation, Equation (16).

Figure 1 shows the examples of amplitude variation of the potential and oblateness ratio of ion-acoustic electrostatic structures associated with ion beam ($\delta_e = 0$) as parameters $\delta_i, \beta, \sigma_i, M, \omega_{ci}$.

From these numerical results we can conclude that in plasma with ion beam the electrostatic potential is positive $\Phi > 0$, and in this plasma the compressive IAS are formed.

Amplitude of the IAS decreases as the parameter $\sigma_i$ (ion-to-electron relative temperature) increases for the fixed Mach number, which was chosen close to linear velocity, Figure 1(a). Also Figure 1(b) shows that as parameter $\beta$ (electron-to-ion relative temperature for the background plasma) increases, the amplitude de-

creases. Figures 2(a), 2(b) represent the similar dependences of amplitude on electrostatic potential and

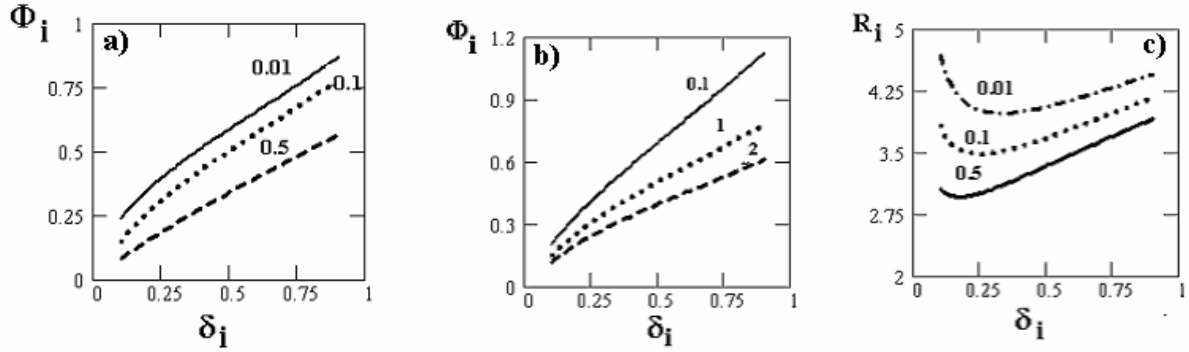


**Figure 1.** Dependence of the amplitude $\Phi_i$ (a), (b) and oblateness ratio $R_i$ (c), and $\delta_i$ for plasma with ion beam for the plasma parameters: $\delta_e = 0$, $\beta = 1$, , $V_d = 0$ M = 0.5, $\omega_{Hi} = 0.3$, (a) the parameter labeling the curve is $\sigma_i$ and $\beta = 1$, (b) the parameter labeling the curve is $\beta$, $\sigma_i = 0.1$.

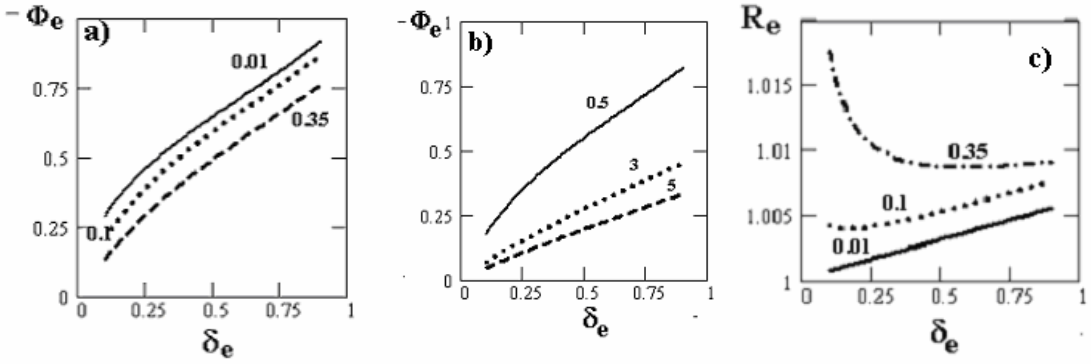


**Figure 2.** Dependence of the amplitude $\Phi_e$ (a), (b), and oblateness ratio $R_e$, (c), on $\delta_i$ for plasma with the electron beam and for plasma parameters: $\sigma_e$=0.1, $\delta_i = 0$ $V_d = 0$, $\omega_{ce} = 24$, (a) – the parameter labeling the curve is $\sigma_e$, and $\beta = 1$, (b) – the parameter labeling the curve is $\beta$ and $\sigma_e = 0.1$.

parameters $\delta_e, \beta, \sigma_e, M, \omega_{ce}$ for the plasma with the electron beam ($\delta_i = 0$). In this case rarefactive) solitary structure ($\Phi < 0$) is formed in plasma.

At presence of the ion and electron beams moving with the drift speed $V_d$ relative to each other, their formation as the slow structures with positive potential (Figure 3) and fast structures with negative potential (Figure 4) is possible.

The numerical calculations show that the parameter *R* determining the form of structure or the ratio of longitudinal scale to cross-section can change over a wide range depending on parameters of plasma. This parameter $R_e$ for electron-acoustic structures Figure 2 is less than for ion – acoustic structures $R_i$ (Figure 1) for the fixed plasma parameters.

Also we shall note that in narrow region of values of parameters $R_e$, $R_i$ slow structures with positive potential can be formed in plasma with ion and electron beams moving relative to each other (Figure 3*c*).

## 4. Conclusions and discussion of results

As it was pointed out above, in recent experiments onboard FAST, POLAR, GEOTAIL satellites with the use of high resolution technique three-dimensional small-scale moving density structures and electrostatic potential structures of soliton type have been registered

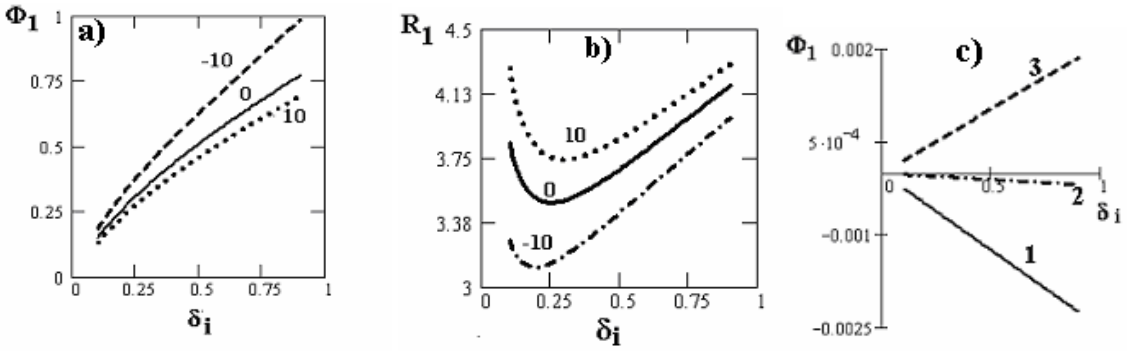


**Figure 3.** (a) – Dependence of the amplitude $\Phi_1$ for the slow structures on the parameter $\delta_i$; (b) – oblateness ratio $R_1$, for plasma with the ion and electron beams for the plasma parameters: $\delta_e = 0.1$, $\sigma_e = 0.1$, $\sigma_i = 0.1$ $\beta = 0.01$, $\omega_{ce} = 21.5$, $\omega_{ci} = 0.3$, M = 12.8, the parameter labeling the curve is $V_d$; (c) – is the amplitude $\Phi_1$, for plasma parameters: (1) – $\sigma_e = 5 \cdot 10^{-5}$; (2) – $\sigma_e = 10^{-5}$,(3) - $\sigma_e = 0$

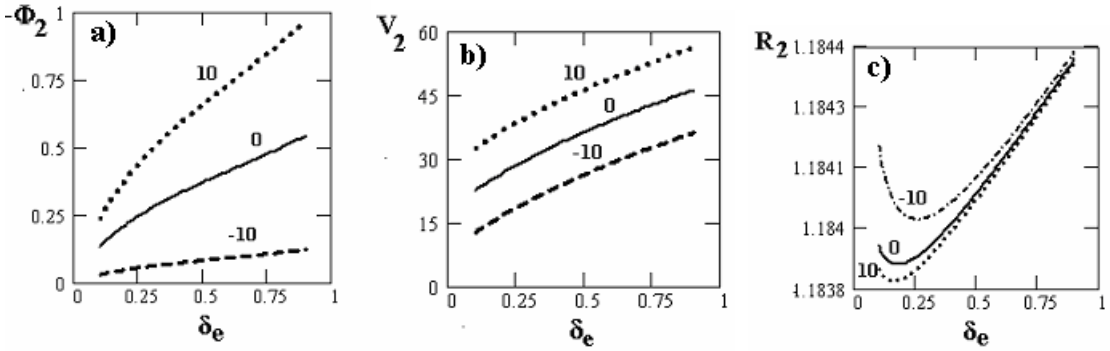


**Figure 4.** (a) Dependence of the amplitude $\Phi_1$ for the fast strucrures as the parameter $\delta_e$; (b) $V_2$ is the linear velocity and (c) oblateness ratio $R_1$ – for plasma with the ion and electron beams for the plasma parameters: $\delta_i = 0.1$, $\beta = 0.01$, $\omega_{ce} = 21.5$, $\omega_{ci} = 0.3$, $M = 12.8$, the parameter labeling the curve is $V_d$.

and estimated. By means of statistical analysis we estimated the scales (along) $l_{||}$ and the scales perpendicular to the direction of a magnetic field [*Franz et al*., 2000; *Ergun et al*., 1999]. In order to explain these experimental data we have to develop the theory of soliton structure formation and to estimate their parameters for real magnetospheric plasma conditions.

In the given work the conditions of formation of the three-dimensional localized moving structures in plasma with the ion and electron beams are investigated and the parameters of these structures are estimated. Three theoretical models, reflecting the formation of ion-acoustic and electron-acoustic soliton structures in plasma are considered. Three-dimensional fully nonlinear theory of ion acoustic and electron acoustic solitary structures is constructed in the four-component plasma which consists of hot background ions and electrons, and electron and ion beams. The theory is based on the derivation of the KdV-ZK equation and the MHD description of the ion and electron motions with self-consistent distribution and motion of all plasma components. Three theoretical models are calculated: plasma with ion, electron and both types of beams of the charged particles moving with respect to each other.

Reductive perturbation method was used to study the formation of three-dimensional structures in the selected models. This method proved to be efficient for small values of potential $\Phi = e\varphi / kT_e < 1$. Following this approach we receive the equation of KDV-ZK type (19) for perturbation of potential, which describes formation of quasi-stationary structures in the selected models of plasma. As the satellite-borne experiments have shown,

large amount of data has been obtained with values of potential $\Phi < 0.1$. POLAR experiments have registered soliton structures with relative values of potential $e\varphi / T_e < 0.1$, whereas S3-3 satellite registered $e\varphi / kT < 0.005$.

The data presented in [*Bound et al*., 1999] and other references support clearly the association of the electron soliton structures with electron beams, with considerably faster speeds and with amplitude potential polarity opposite to that of the ion- acoustic structures.

Our research has lead us to the following conclusions:

1. In the frame of this theory solutions for ion-acoustic and electron acoustic structures are obtained in a wide range of plasma parameters. Characteristics of ion-acoustic solitary structures and nonlinear waves include waveforms of density and electric field, field-aligned velocity, and the oblateness ratio $R = L_\perp / L_{||}$. The parameter space of such solutions is also determined.
2. From this numerical analysis we can conclude, that in plasma with an ion beams the electrostatic structures with positive potential moving with small speeds close to the sound speed are formed (compressive soliton). On the other hand, in plasma with an electron beams the structures with negative potential moving with much bigger speeds close to the electron thermal speed (rarefactive soliton), are formed.
3. At presence of the ion and electron beams moving with the drift speed $V_d$ with respect to each other, both structures can be formed as slow structures with the velocity close to the speed of a sound $V < C_S$ (Figure 3) and with positive and negative potential and fast structures with the velocity close to the thermal speed of electron and with negative potential (Figure 4).
4. The scale of structure of ion – acoustic type depends on the mass of ion, therefore it could be expected, that at presence of various sorts of ions, the scale of structure, speed of its movement and the maximal value of potential will depend on a sort of an ion beam. The value $\omega_{ci}$ is inversely proportional to $\sim\sqrt{m_i}$ ($m_i$ – mass of an ion) and the factor $R_i$ will grow for heavier ions. The speed of soliton structures which depends on ($He^+$, $O^+$, $H^+$) ion mass has been registered experimentally, and ion beams were correlated with these structures *Dombeck* [2001];
5. We can point out that an attempt to explain the experimental data [*Franz et al*., 2000] on a basis of the kinetic theory has led us only to the consideration of the factor $1 + \frac{\omega_{Oe}^2}{\omega_{ce}^2}$ without taking into account dependence on parameters of plasma. However, on the basis of the analysis, which has been led above, we can draw a conclusion that the form of soliton structures is defined not only by the relation, but by the plasma parameters as well, which results in occurrence of the structures of various forms.

Despite of many unresolved problems, studying of mechanisms of formation of three-dimensional electrostatic structures as an experimental method and by construction of various type of theoretical models is fruitful for research of mechanisms of generation of electromagnetic fields in magnetospheric plasma.

**Acknowledgments**. The work was supported in part by grant N-X01318 FBR of Belarus Republic.

## References

Berthomier, M., R. Pottelette, M. Malingre, Y. Khotyaintev, Electron-acoustic solitons in an electron-beam plasma system, *Physics of Plasmas*, *7*, 7, 2987-2994, 2000.

Bounds, S. R., R. F. Pfaff, S. F. Knowlton, F. S. Mozer, M. A. Temerin and C. A. Kletzing, Solitary potential structures associated with ion and electron beams near 1Re altitude, *J. Geophys. Res*., *104*, A12, 26709-28717, 1999.

Cattell, C., J. Dombeck, J. R. Wygant, M. K. Hudson, F. S. Mozer, Comparisons of Polar satellite observations of solitary wave velocity in the plasma sheet boundary and the high-altitude cusp to those in the auroral zone, *Geophys. Res. Lett*., *26*, 425-428, 1999.

Dombeck, J., C. Cattel, and J. Crumley, Observed trends in auroral wave structure characteristics using date from Polar, *J. Geophys. Res*. *106*, A5, 19013-19023, 2001.

Ergun, R. E., C. W. Carlson, J. P. McFadden, F. S. Mozer, G. T. Delory, W. Peria, C. Chaston, M. Temerin, R. C. Elphic, R. Strangeway, R. F. Pfaff, C. A. Cattell, D. M. Klumpar, E. G. Shelley, W. K. Peterson, E. Moebius, L. Kistler, FAST satellite observations of electric field structures in the auroral zone. *Geophys. Res. Lett*., *25*, 2025-2028, 1998.

Ergun, R. E., C. W. Carlson, J. P. McFadden, F. S. Mozer, G. T. Delory, W. Peria, C. Chaston, M. Temerin, I. Roth, L. Muschietti, R. C. Elphic, R. Strangeway, R. F. Pfaff, C. A. Cattell, D. M. Klum-

par, E. G. Shelley, W. K. Peterson, E. Moebius and L. Kistler, FAST satellite observations of large-amplitude solitary structures, *Geophys. Res. Lett., 25*, 2041-2044, 1998.

Ergun, R. E., C. W. Carlson, L. Muschietti, I. Roth and J. P. McFadden, Properties of fast solitary structures, *Nonlinear processes in Geophysics*, *6*, 187-194,1999.

Franz, J. R., P. M. Kintner, and J. S. Pickett, Polar observations of coherent electric field structures, *Geophys. Res. Lett., 25*, 1277-1280, 1998.

Franz, J. R., P. M. Kintner, C. E. Seyler, J. S. Pickett and J. D. Scudder, On the perpendicular scale of electron phase-space holes, *Geophys. Res. Lett., 27*, 169-172, 2000.

Galperin, Yu. I, A. V. Volosevich, The nonlinear localized electrostatic structures and their experimental diagnostics in magnetospheric plasma, *Cosmich Research*, *40*, 4, 1-10, 2002*a*.

Matsumoto, H., H. Kojima, T. Miyatake, Y. Omura, M. Okada, I. Nagano and M. Tsutsui, Electrostatic Solitary waves (ESW) in the magnetotail BEN wave forms observed by GEOTAIL, *Geophus. Res. Lett.*, *21*, 2915, 1994.

Mozer, F. S., C. A. Kletzing, Direct observation of large, quasistatic, parallel electric fields in the auroral acceleration region, *Geophys. Res. Lett., 25*, 10, 1629-1632, 1998.

Mozer, F.S., R. Ergun, M. Temerin, C. Cattel, J. Dombeck, J. Wygant, New features of time domain electric-field structures in the auroral acceleration region, *Phys. Rev. Lett., 79*, 1281, 1997.

Mozer, F. S., C. A. Cattell, M. K. Hudson, R. L. Lysak, M. A. Temerin and R. B. Torbert, Satellite measurements and theories of low altitude auroral perticle acceleration, *Space Sci. Rev., 27*, 155-213, 1980.

Volosevich, A. V., Yu. I. Galperin, F. M. Truhachev, Theoretical models of the spatially limited electrostatic structures and experiments in the auroral magnetosphere. Advances in *Space Research*, *30*, 7, 1677-1680, November 2002.

Volosevich, A. V. and Yu. I. Galperin, Nonlinear electrostatic waves and structures in collisionless magnetospheric plasmas, *Phys. Chem. Earth*., *1-2*, 85-91, 2000*a*.

Volosevich, A. V. and Yu. I. Galperin, Nonlinear electrostatic waves and moving localized structures in the outer plasmasphere and auroral magnetosphere, Cosmic Research (English version of *Kosmich. Issled*.), *38*, 514-525, 2000*b*.

# Numerical simulations of charged particle motion in the outer Earth's magnetosphere. 1. A study of Shabansky's effect

A. E. Antonova[1] and H. V. Malova[1,2]

[1] Skobeltsyn Institute of Nuclear Physics, Moscow State University, Moscow, Russia
[2] Space Research Institute, Russian Academy of Sciences, Moscow, Russia

**Abstract.** Particle behavior in Earth's outer magnetosphere is examined. Single particle trajectories in a vacuum 3D magnetospheric model field configuration are traced to study an effect predicted by V. P. Shabansky of particle drift shell branching, associated with two dayside off-equatorial field minima existing in the actual magnetosphere. “Full” motion equations are integrated for electrons, protons, and ions by the Runge-Kutta-Merson method. It is demonstrated that the branching studied on the modern theoretical basis [in *Antonova et al*., 2003] actually exists. Globally trapped particles that come sufficiently close to the interface between a region of trans-equatorial bounce oscillations and a region of oscillations about high-latitude field minima, are found to complete their azimuthal drift around the Earth via the cusp. Our computer code also can obtain the particles' injection time and site for energy dispersion events observed by *Lutsenko et al.* [2000] aboard INTERBALL 1 and 2.

## 1. Introduction

This work is primarily aimed to study in more detail a predicted by V.P. Shabansky effect of the particle drift shell branching, associated with two dayside off-equatorial magnetic field minima existing in the actual magnetosphere [*Shabansky*, 1968, 1971; *Shabansky and Antonova*, 1968]. Model concepts of energetic particle trapping in the dayside high-latitude outer magnetosphere (in the near-magnetopause cusp regions with highly depressed magnetic field) have long been put forward [*Shabansky*, 1968, 1971, 1972; *Shabansky and Antonova*, 1968].

In recent papers [*Antonova et al*., 2003a,b] violation of adiabaticity of the energetic particle bounce motion, which is caused by nonmonotonous change in magnetic field intensity along field lines near the dayside magnetopause, was theoretically examined, and a "jump" over second adiabatic invariant $I$ was evaluated. The violation happens at the separatrix, separating the regions of trans-equatorial bounce oscillations and oscillations about high-latitude field minima. A particle crosses the separatrix in the course of its longitudinal drift. It was demonstrated that the shell branching accompanied by this jump happens in a rather narrow zone on the equatorial plane adjacent to the dayside magnetopause.

The particles mirroring near the equator and traveling on the nightside through a region with a relatively weak field (about 40 nT), can, consequently, be globally trapped: instead of escaping through the magnetopause, they come into the dayside cusps regions.

An existence of enhanced fluxes of energetic particles in the zone of these high-latitude traps was revealed many years ago in experiments carried out aboard several, mainly Soviet, satellites and confirmed by recent measurements of energetic ions, protons, and electrons in the dayside cusps with POLAR and INTERBALL S/C (see, e.g., [*Antonova et al*., 2000, 2003] and references therein).

According to Shabansky' suggestion (see, e.g., [*Antonova and Shabansky*, 1975, 1976]) particles can be captured within autonomous traps near cusps and undergo cyclic drift only in this domain in either the northern or southern hemisphere, so that drift shell does not envelop the Earth. Some peculiarities of such a trapping have been studied in [*Antonova et al*., 2001]. *Sheldon et al.* [1998] demonstrated by numerical simulations a local trapping of energetic electrons in the outer cusp.

Numerical simulations of particle motion in model magnetic and electric fields performed by *Delcourt and Sauvaud* [1999] showed the possibility for particles starting in the magnetotail plasma sheet to arrive into the cusp and to remain in the cusp for some time before their escape.

The main objective of this paper is to examine the particle shell branching in a static magnetic field in order to separate an effect produced by that field.

## 2. Basic formulation

We calculate individual particle trajectories in a model 3D magnetospheric magnetic field configuration. The simulation region involves the entire magnetosphere.

The particle orbits were integrated numerically from the equations of motion by a Runge-Kutta-Merson scheme, without using any adiabatic or drift approximation. The time step was chosen to be small enough to ensure that the accumulated numerical errors were negligible. To estimate the accuracy achieved, different tolerance was used. The accuracy of our computer code was also tested by comparison with the orbits calculated for the dipole magnetic field.

By studying a large number of trajectories for various particle energies, it is possible to examine particle population patterns (and their evolution) in the outer Earth's magnetosphere.

Test particles move in combined magnetic field produced by the following sources: geomagnetic dipole, second (image) dipole, which imitates the effect of the solar wind, screening the geodipole field, i.e., the Chapman-Ferraro currents on the magnetopause, and dawn-dusk current across the magnetotail [*Antonova and Shabansky*, 1968]. This is a simple model which accounts for main features of the field in the outer magnetosphere and it was shown to agree well with observations [*Antonova et al.*, 1983].

Particle energy $E$, the magnetic moment $\mu$, and the second adiabatic invariant $I$ and their variations are evaluated numerically at each step. For instance, the change of energy $E$ over the entire run is found to be less than 0.04%, and this provides a check of the scheme accuracy.

## 3. Numerical simulations: the first results

Three images of a 30-keV proton trajectory are shown in Figure 1: (a) $X$ coordinate versus time, trajectory projections onto noon-midnight plane (b) and equatorial plane (c). Proton starts to travel in the magnetosphere near the equator, at a point that is close to but outside the branching region (GSM $X0$ = 5, $Y0$ = 10, $Z0$ = 0.001, $B_e$ = 33 nT, initial pitch angle $\alpha_0$ = 89.1°, tilt angle of geomagnetic dipole $\psi$ = 0; i.e., there is symmetry over the northern and the southern hemispheres). The proton moves azimuthally, initially near the equatorial plane. However, at a certain time, when it reaches the separatrix, the proton "escapes" from the equator. When the proton escapes, it continues to be trapped but it goes up into one of the dayside high-latitude cusps. Note that, in magnetic field without off- equatorial minima, this proton would exit the magnetosphere through the magnetopause.

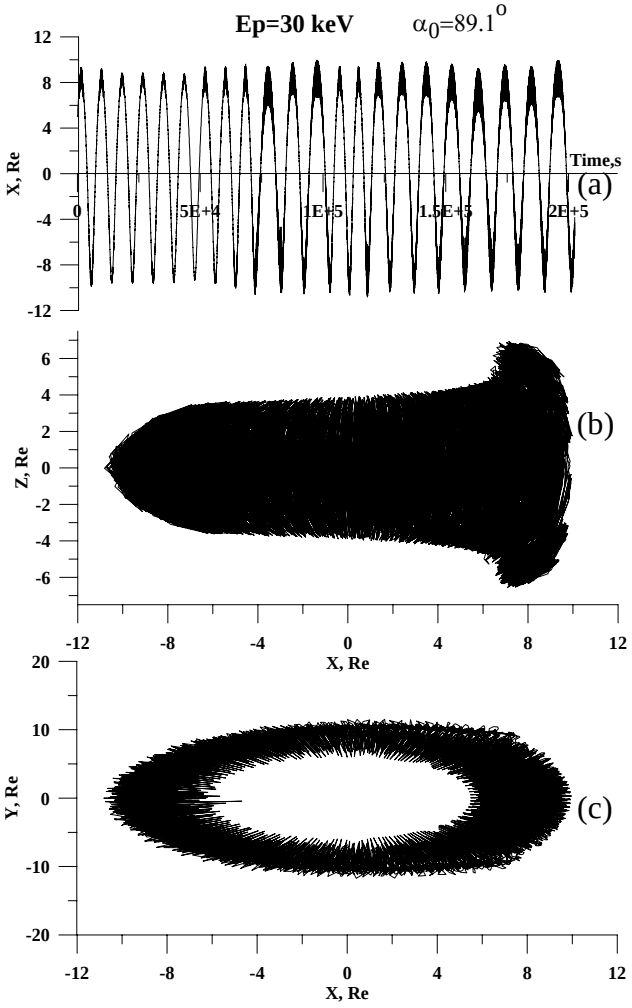


**Figure 1.** Three images of a 30-keV proton trajectory: (a) X coordinate versus time, trajectory projections onto noon-midnight plane (b) and equatorial plane (c). Proton starts to travel in the magnetosphere near the equator, at a point that is close to but outside the branching region (GSM $X0$=5, $Y0$=10, $Z0$=0.001, $Be$=33nT, pitch angle $\alpha_0$=89.1°).

It is seen that the proton is globally trapped in the magnetosphere, i.e., it executes many complete drift orbits round the Earth over a closed, 360° loop (without drastic change of the magnetic moment due to abrupt gradient of magnetic field near the inner edge of the magnetotail current sheet used in the model we applied).

For the run studied, after 6 complete drift orbits, its motion is markedly influenced near midnight when it approaches the current sheet, and it is subjected to pitch-angle scattering. But even so the proton continues to be globally trapped and to visit the dayside cusps.

Figure 2 presents three first excursions of a 10-keV

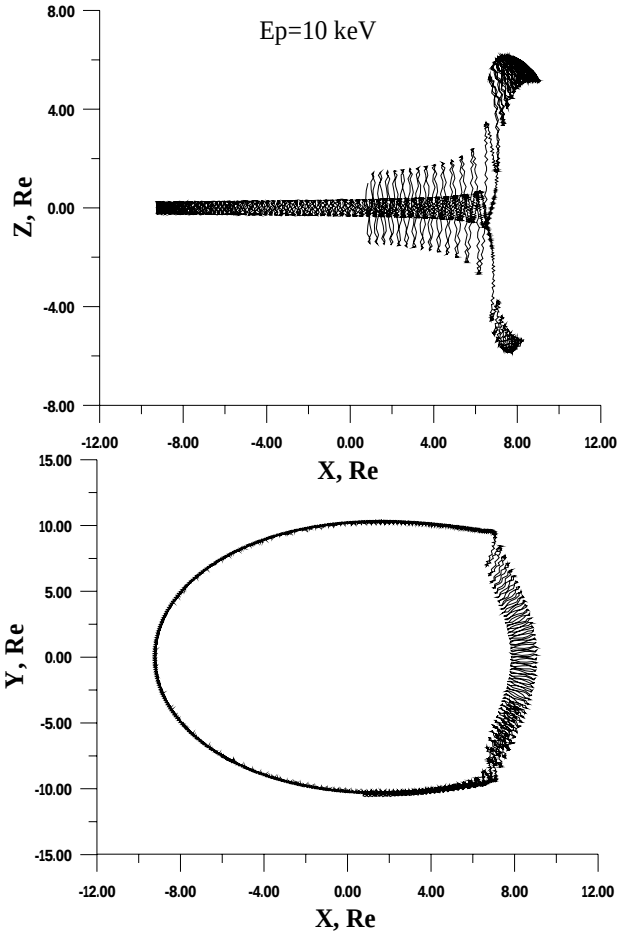


**Figure 2.** First excursions of a 10-keV proton into the southern and northern cusps projected onto noon-midnight plane *XZ* (top) and to equator *XY* (bottom); the proton with $\alpha_0$=89.1° starts at the same point as in Figure 1.

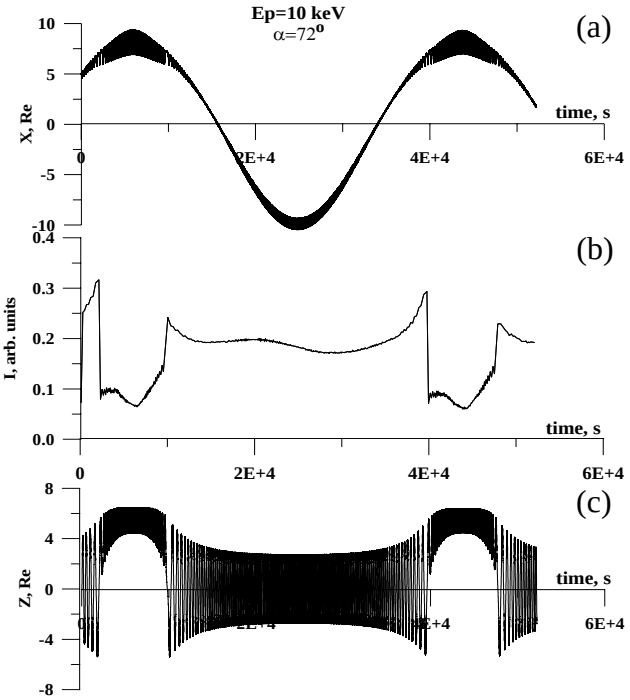


**Figure 3.** A fragment of time history of a 10-keV proton for the same initial parameters as in Figure 1 but for $\alpha_0$=72° and for the same image-dipole model but with the tail current excluded. (a) *X* and (c) *Z* coordinates and (b) second invariant *I* (arbitrary units).

proton into the southern (two times) and northern cusps, projected onto noon-midnight plane *XZ* (top) and to equator *XY* (bottom); the proton starts its drift outside the branching region but close to the separatrix with the same initial parameters as in Figure 1.

Figure 3 shows a fragment of time history (the first drift orbit out of more than 40 ones for that run) of a 10-keV proton for the same initial parameters as in Figure 2 but for $\alpha_0$ = 72° and for the same magnetic field model but with the tail current excluded. Beginning its motion, the particle drifts outside the branching region oscillating about equator and appears in the cusps.

When the particle crosses the separatrix, the second invariant *I* (panel b) is violated. According to Shabansky's hypothesis, for a symmetric case, the *I* value prior to this crossing is equal $2I_1$, where $I_1$ is the *I* magnitude inside the two-minima region. The simulation shows that accuracy of this relation corresponding to conservation of *I* is quite good; this is in accord with a relatively weak *I* violation [*Antonova et al*., 2003].

It is seen from Figure 3 that, despite a rather crude scheme used for the *I* test calculations (b), in the cusp region, the *I* magnitude is about a half of that seen outside the branching region. Nonmonotonic change of *I* inside the cusp is (possibly in part) due to the scheme we use.

Sudden increase in calculated *I* at the separatrix crossing is caused by a specific change of magnetic field intensity *B* profile along a field line: a transition from a dipole-like field profile ($B_{min}$ at the equator) to that with two off-equatorial minima and with a relative maximum at the equator. The transition occurs as follows: the *B* dependence on the field line arc length *s* becomes almost constant over a considerable (several $R_e$) distance *s* from the equator (on either side of it, for symmetric case). This *B* pattern provokes there a 'stagnation' so that the motion is no more quasi-periodical for some rather short time and the notion of bounce period then looses its sense. As the particle continues its drift round the Earth, it appears in a region where a *B* maximum exists on the equator, with two *B* minima of equal depth (for symmetric case) on both sides of the equator. At that

time, the particle is again in quasi-periodical motion while it becomes trapped in one of those $B_{min}$ pockets, depending on its bounce oscillation phase.

Every particle pass across the separatrix is accompanied by *I* violation. But despite this *I* behavior, the particle does not leave the magnetosphere and continues to be globally trapped during at least 20 days. It is also important to note that, in the run studied, magnetic moment remains practically unchanged.

An illustration of the transition from a dipole-like field profile ($B_{min}$ at the equator) to that with two off-equatorial minima and with a relative maximum at the equator is shown in Figure 4. A fragment of trajectory (*XZ* plane) of 100-keV positron that starts its motion prior to the separatrix - an interface separating the region of quasi-dipole magnetic field with a field minimum at the equator and the region with two off-equatorial minima which displace gradually from the equator along the field line. The initial parameters are the same as in Figure 1.

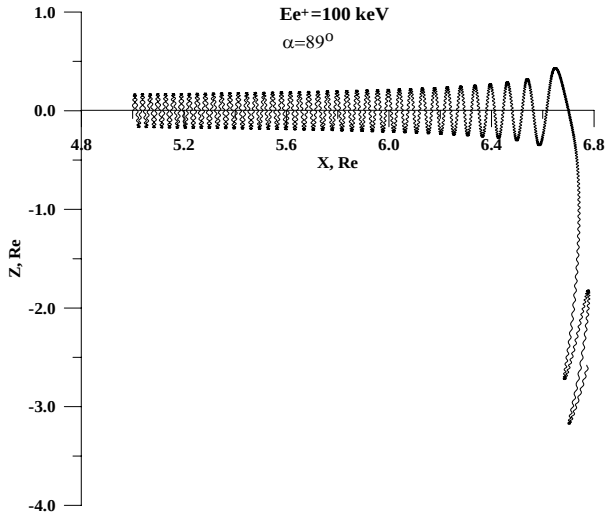


**Figure 4**. An illustration of the transition from a dipole-like field profile to that with two off-equatorial minima: a part of trajectory (*XZ* plane) of 100-keV positron that starts its motion prior to the separatrix and intersects it; the initial parameters are the same as in Figure 1.

It is clear from Figure 4 that when the particle approaches the separatrix, an amplitude *A* of its bounce oscillations (with respect to equator) progressively increases; i.e., particle mirror points move off the equator. This can be attributed to the field line straightening. In this region, magnetic field intensity along the field line becomes almost constant, it varies only slightly with the arc length *s* of the line. At the separatrix, a small field maximum appears at the equator, and the particle finds itself captured in the southern hemisphere (a choice of a hemisphere depends on the phase of its bounce oscillations).

Like in Figure 3, when the particle crosses the separatrix, its motion is not quasi-periodical for some short time. The particle entry into and exit from the region of off-equatorial minima is accompanied then by a sharp short-term rise in distance between mirror points. It is about 9 times as large as that seen at the particle start.

3D image of drift shells of a 10-keV proton, starting outside the branching region but close to the separatrix with $\alpha_0$=72° and the same input parameters as in Figure 3, and trapped in the magnetosphere for at least $1.7 \times 10^6$ s is presented in Figure 5. Now, the shells form a doubly-connected body due to V.P. Shabansky effect rather than a simply-connected one, typical of the inner magnetosphere [*McIlwain*, 1961].

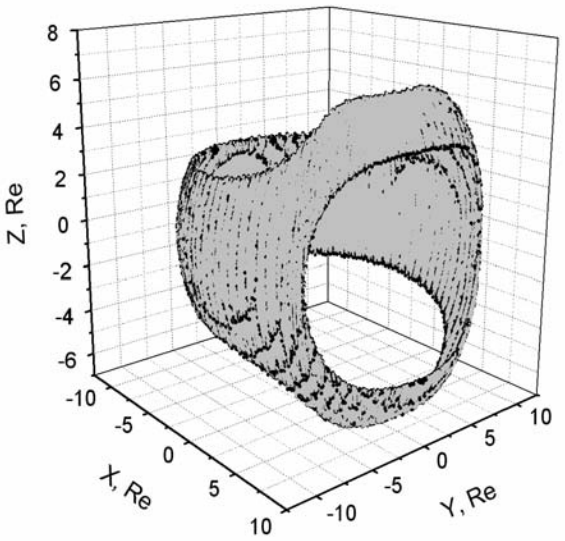


**Figure 5**. 3D image of drift shells of a 10-keV proton, starting outside the branching region but close to the separatrix with the same input parameters as in Figure 3 and trapped in the magnetosphere for at least $1.7 \times 10^6$ s.

We undertake also a backward tracing of particles in a model magnetospheric magnetic field to infer potential source regions for four energy dispersion events (structures in particle spectra) observed in auroral regions with INTERBALL 1 and 2 [*Lutsenko et al.*, 2000; *Lutsenko*, private communication, 2003]. We found that two events (June 28, 1997 and September 18, 1996) were consistent with sources located in the dusk-midnight sector. The third (March 10, 1998, 05:57-06:20 UT) and the fourth events were examined using the

dynamical paraboloid model [*Alexeev et al.,* 2001]. In the third event, there were two particle injection manifestations at the observation points. Our simulations show that the observed at ~9-10 MLT structures can originate from particle sources situated in the premidnight sector at ~21-23 MLT.

Figure 6 shows an example of test run series for backward orbit tracing of 318.7-keV proton drift (*XY* plane), for an energy dispersion event (the second injection) of March 10, 1998, observed at 06:11:28 UT, ~10 MLT aboard INTERBALL Auroral Probe. For the fourth event (February 13, 1997, 05:39-06:59 UT), particle pitch angle distribution was available and taken into consideration, and localized source sites, situated in dusk-premidnight sector, were found for 3 probable proton injections.

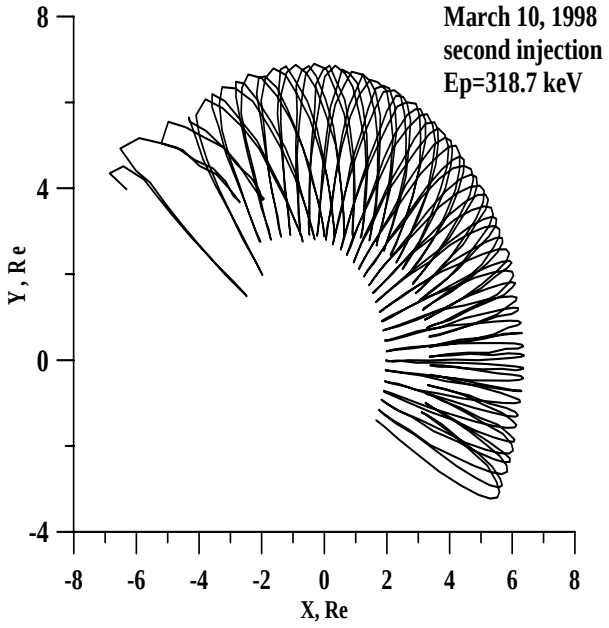


**Figure 6.** 318.7-keV proton drift orbit for the second injection of March 10, 1998, observed at 06:11:28 UT, ~10 MLT aboard INTERBALL; probable particle source is situated at ~22 MLT.

## 4. Discussion and conclusion

We considered here the particles, having a relatively small adiabatic invariant I and mirroring at a point with the magnetic field strength, that does not exceed local equatorial field maximum in the region of off-equatorial minima. These particles execute azimuthal drift all around the Earth, but in such a way that in the dayside sector their drift shell becomes "branched": particle bounce oscillations occur near either the northern or southern field minimum along the field line.

It has been demonstrated that the particle shell branching predicted by Shabansky actually exists.

An exchange between different particle populations is crucial for dynamics of radiation, trapped in the geomagnetosphere. Particle pitch-angle diffusion and diffusion across drift shells may take place and lead to that exchange.

Outer magnetosphere may be supplied with particles, arriving from dayside, via dayside cusps; or, on the contrary, particles injected during substorms from the magnetotail in quasi-dipole region of the night magnetosphere can leave magnetosphere owing to their arrival into a region of cusps along their branching trajectories.

Simulations undertaken show that particle population in the Earth's magnetosphere is significantly influenced by the presence of high-latitude field minima.

The key question in simulations of this sort is whether a field model chosen, which may contain sharp field gradients, would permit to avoid artifacts associated with these gradients.

**Acknowledgments.** This paper is dedicated to the memory of Professor Yu. I. Galperin. He was always interested in and appreciated the field and particle modeling, especially particle trapping in dayside cusps. We are grateful to Prof. A. P. Kropotkin for permanent interest to this work and valuable suggestions, to Dr. V. N. Lutsenko for useful discussions, and to Dr. V. V. Kalegaev for his assistance in adopting the paraboloid model subroutine into our computer codes.

## References

Alexeev I. I., V. V. Kalegaev, E. S. Belenkaya, S. Yu. Bobrovnikov, Ya. I. Feldstein, and L. I. Gromova, Dynamic model of the magnetosphere: Case study for January 9-12, 1997, *J. Geophys. Res*., *106*, 25,683, 2001.

Antonova, A. E., Yu. I. Gubar', and A. P. Kropotkin, Trapped energetic particles in a model magnetic field of the magnetospheric cusp, *Geomagn. Aeron. (in Russian), 41*, 8, 2001.

Antonova, A. E., Yu. I. Gubar', and A. P. Kropotkin, Effects in the radiation belts driven by the second adiabatic invariant violation in the presence of high-latitude field minima in the dayside cusps, *Geomagn. Aeron. (in Russian), 43*, 3, 2003a.

Antonova, A. E., Yu. I. Gubar', and A. P. Kropotkin, Effects in the radiation belts caused by the second adiabatic invariant violation in the presence of dayside off-equatorial magnetic field minima, *Adv. Space Res.*, 2003b, 31, 223, 2003b.

Antonova, A. E. and V. P. Shabansky, On the geomagnetic field structure at great distances from the Earth, *Geomagn. Aeron*., *8*, 801, 1968.

Antonova, A. E. and V. P. Shabansky, Particles and the magnetic field in the outer noon magnetosphere of the Earth, *Geomagn. Aeron*., *15*, 297, 1975. (p. 243, *English transl*.)

Antonova, A. E. and V. P. Shabansky, Energetic electron distribution in the Earth's outer magnetosphere, *Space Res.*, *16*, 539, 1976.

Antonova, A. E., V. P. Shabansky, and P. C. Hedgecock, Comparison of the magnetic field empirical model based on data from HEOS-1 and HEOS-2 satellites with analytical two-dipole model, *Geomagn. Aeron.*, *23*, 697, 1983. (p. 574, *English transl*.).

Delcourt, D. C. and J. -A. Sauvaud, Populating of the cusp and boundary layers by energetic (hundreds of keV) equatorial particles, *J. Geophys. Res.*, *104*, 22,635, 1999.

Lutsenko, V. N., private communication, 2003.

Lutsenko, V. N., T. V. Grechko, and K. Kudela, INTERBALL 2 and 1 observations of energy dispersion events in auroral zone for 30-500 keV ions and electrons. *Proc. 5th Int. Conf. on Substorms (ICS-5)*, St. Petersburg, 2000, ESA SP-443, p. 519, 2000.

McIlwain, C. E., Coordinates for mapping the distribution of magnetically trapped particles, *J. Geophys. Res.*, *66*, 3681, 1961.

Shabansky, V. P., Magnetospheric processes and related phenomena, *Space Sci. Rev.*, *8*, 366, 1968.

Shabansky, V. P., Some processes in the magnetosphere, *Space Sci. Rev.*, *12*, 299, 1971.

Shabansky, V. P., *Phenomena in the near-Earth space (in Russian)*, Moscow: Nauka, 1972, 272 p.

Shabansky, V. P. and A. E. Antonova, Topology of particle drift shells in the Earth's magnetosphere, *Geomagn. Aeron.*, *8*, 993, 1968.

Sheldon, R. B., H. E. Spence, J. D. Sullivan, T. A. Fritz, and J. Chen, The discovery of trapped energetic electrons in the outer cusp, *Geophys. Res. Lett.*, *25*, 1825, 1998.

---

A. E. Antonova, Skobeltsyn Institute of Nuclear Physics, Moscow State University, Vorob'evy Gory, Moscow, 119992 Russia.
(allaant@dec1.sinp.msu.ru).

H. V. Malova, Skobeltsyn Institute of Nuclear Physics, Moscow State University, Vorob'evy Gory, Moscow, 119992 Russia. Also at Space Research Institute, Russian Academy of Sciences, Moscow, Russia.
(mlv@dec1.sinp.msu.ru).

(Received 27 April 2003; accepted 00 June 2003).

# Partial ring current and polarization jet

V. Y. Trakhtengerts and A. G. Demekhov

Institute of Applied Physics, Nizhny Novgorod, Russia

**Abstract.** Intense precipitations of energetic charged particles into the ionosphere occur during magnetic storms. These precipitations are due to the cyclotron instability developing under the interaction of newly injected energetic particles with detached plasma regions. Such precipitation results in formation of a specific 3D current system, which ensures the quasineutrality and current continuity condition for the ionospheric and magnetospheric plasmas. The development of this current system is accompanied with generation of a northward electric field and formation of the polarization jet at the footpoints of the low-latitude edge of the partial ring current.

## 1. Introduction

Satellite data the clear evidence of the asymmetric ring current (ARC) formation during the main phase of a magnetic storm. Such a night-day asymmetry can influence the behavior of the *Dst* variation. Estimates by *Liemohn et al.* [2001] have illustrated the important contribution of the ARC to the *Dst* variation. In that paper, the RC asymmetry is related to the open trajectories of energetic ions which cross the magnetosheath and exit the magnetosphere. On the other hand, these ions can interact with electromagnetic ion-cyclotron (EMIC) waves as they meet the disturbed plasmapause and a tongue of the cold plasma density which appears at the main phase of a magnetic storm. This interaction leads to the precipitation of RC ions into the ionosphere [*Cornwall et al.*, 1970] and formation of an additional 3D current system inside the magnetosphere [*Trakhtengerts et al.,* 1996; *Grafe et al.,* 1996]. Formation of such a current system is accompanied by the generation of a strong northward electric field in the subauroral ionosphere, which can be associated with the polarization jet [*Filippov et al,* 1984; *Galperin*, 2002]. The polarization jet (PJ) was discovered by *Galperin et al.* [1973], *Galperin and Ponomarev* [1974] in the Kosmos-184 observations and revealed close relation to the ionospheric trough. [*Southwood and Wolf*, 1978] were the first who suggested a relation between these phenomena, known in the English literature as SAIDs (Subauroral Ion Drifts), to the ring-current penetration to the plasmasphere. Recent studies [*Khazanov et al.,* 2003] confirmed that the effects of energetic particle precipitation can diminish the screening effect of the RC, which prevents the electric field penetration to subauroral latitudes.

In this paper, we show that the precipitation of RC ions due to the cyclotron instability (CI) supplies an additional 3D current system at $L \leq 5$, comprising the currents of hot and cold plasma particles. A simple model of this current system is developed, which allows us to estimate the electric field structure and amplitude. These results are compared with the experimental PJ parameters, and a good agreement of the model and observations is shown.

## 2. Formation of the asymmetric RC

We start from the commonly accepted scheme, assuming that the RC is formed at the main phase of a magnetic storm due to the convection of hot ions ($W_i$ = 1–10 keV) in the enhanced electric field from the night-side plasma sheet to the evening and day side of the magnetosphere. The cold plasma density in the magnetosphere is redistributed simultaneously: a new plasmasphere of a smaller size is formed together with a plasmapause bulge of a cold plasma, which is stretched out in the evening sector towards the magnetosheath. Sophysticated simulations of this stage were performed by *Liemohn et al.* [2001]. Figure 1 shows two classes of trajectories, i.e., cold plasma particles and energetic ($W_p$ = 12 keV) protons, as calculated by *Liemohn et al.* [2001]. One can see that these trajectories cross each other in the plasmapause bulge region. We suggest that the entrance of energetic protons into the bulge with enhanced cold-plasma density is accompanied by the CI development and related precipitation of energetic protons. Schematic picture of this interaction is shown in Figure 2. The injected energetic protons and electrons drift to the evening and morning sides, respectively. Formation of the precipitation pattern under such conditions is supported by the analysis of NOAA satellite data, showing the precipitation of energetic protons and electrons [*Titova et al.*, 1998;

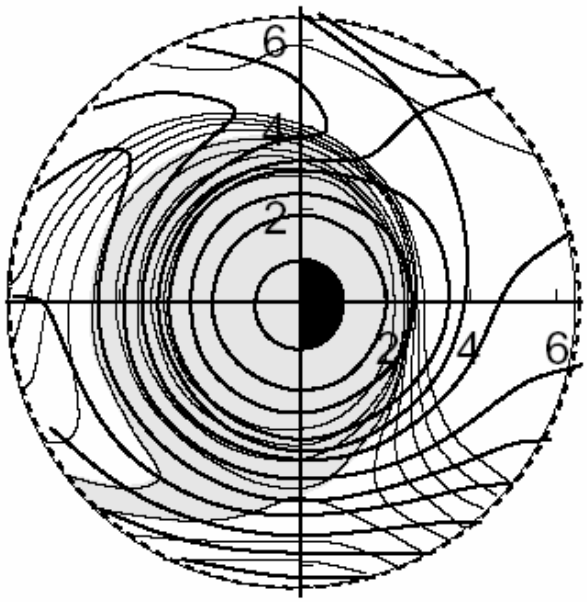


**Figure 1.** The crossing of convection trajectories of energetic and cold particles (results of *Liemohn et al.* [2001]). Thin and thick lines show tracjectories of cold plasma and protons with energy $W_p = 12$ keV at the boundary, respectively, and the gray area represents the plasmasphere.

*Yahnina et al.,* 2003]. The relaxation due to precipitation can change significantly the structure of the asymmetric ring current.

### 3. Field-aligned current of precipitating particles

We consider the interaction of the RC particles with the plasmapause bulge in the process of their intercourse due to the combined electric and magnetic drift. Here, we use the approximation of sharp gradient of the cold plasma density. In such a situation, energetic protons are involved into the cyclotron interaction starting from some boundary curve $L(\varphi)$, describing the form of a bulge in the equatorial cross-section (Figure 2). In the inner magnetosphere (the evening-day sector, $L \le 6$), the magnetic field is close to a dipole one. As for the effect of electric drift, it is important to supply the protons into this domain and to energize them, but it not significant within the cyclotron interaction region, so we neglect it here to avoid unnecessary lengthy calculations. In this case, we can write the bounce-averaged kinetic equation for the distribution function $F$ of energetic protons in the form

$$\frac{\partial F}{\partial t} + B\frac{\partial F v_{\|} B^{-1}}{\partial s} + \frac{v_{\mathrm{DM}}}{r\,\sin\theta}\frac{\partial F}{\partial \varphi} = \hat{D}^{\mu\mu} F\,, \qquad (1)$$

where the independent variables in the velocity space are the velocity modulus $\upsilon$ and the value $\mu = B_L/B \sin^2\alpha$ proportional to the magnetic moment, $B$ is the geomagnetic field, $\alpha$ is the pitch-angle, $(r, \theta, \varphi)$ are the geomagnetic polar coordinates ($\theta$ is the colatitude and $\varphi$ is the azimuthal angle), $\upsilon_{\|} = \pm\upsilon(1 - \mu B/B_L)^{1/2}$, $s$ is the path along the magnetic field line, $\hat{D}^{\mu\mu}$ is the operator of pitch-angle diffusion, and $\upsilon_{\mathrm{DM}}$ is the velocity of magnetic drift:

$$\vec{V}_{\mathrm{DM}} = \vec{\varphi}_0\, c\, \frac{W}{e}(1 + \cos^2\alpha)\,\frac{|\vec{B} \times \nabla B|}{B^3} \qquad (2)$$

(here, $W = m\upsilon^2/2$ and $e$ are the energy and charge of a particle, respectively, and $\vec{\varphi}_0$ is the unit vector in the azimuthal direction.

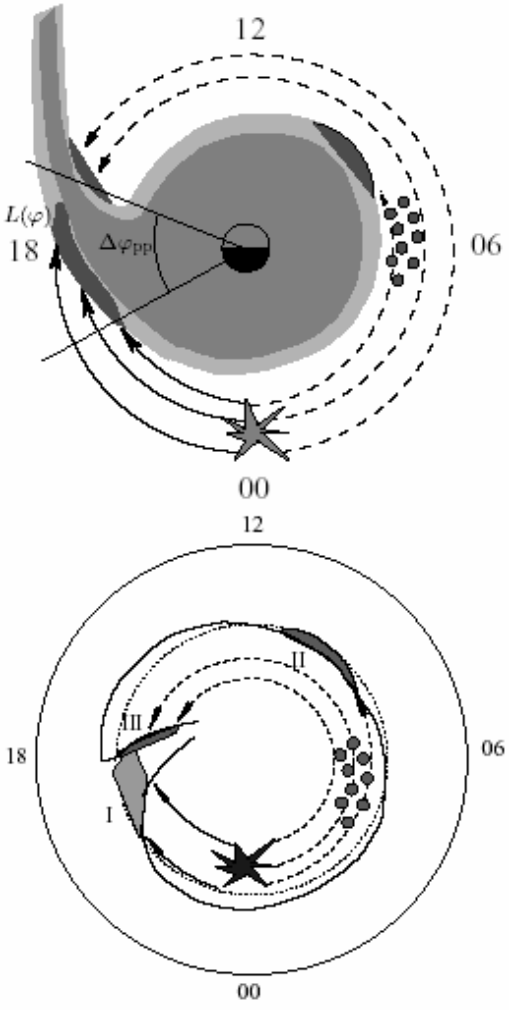


**Figure 2.** a) Schematic illustration of interaction of RC protons with the plasmapause bulge. b) The ionospheric projection of the plasmapause bulge.

Further, we consider the stationary case ($\partial F/\partial t = 0$) of the strong pitch-angle diffusion [*Kennel and Petschek*, 1966; *Bespalov and Trakhtengerts*, 1986], where the isotropization of the pitch-angle distribution takes place. In this case, the losses of RC protons are due to the precipitation through the loss cone with the flux density $S = F(s = \pm l/2)\ \upsilon_{\parallel c} \approx \frac{1}{2} F_L \upsilon$, where $F_L$ is the distribution function in the equatorial cross-section. Integrating (1) over the phase space and the volume of a magnetic flux tube with the unit cross-section at the ionospheric level, we obtain for the symmetric hemispheres:

$$\int_{-l/2}^{l/2} \frac{B_{\rm I}}{B}\, ds \int d^3\vec{v} \frac{V_{\rm DM}}{r\sin\theta}\frac{\partial F}{\partial \varphi} = 2S_{\rm A} \qquad (3)$$

where $S_{\rm A} = \frac{1}{2}\int (F\upsilon_{\parallel})_{s=l/2}\ \mathrm{d}^3\vec{\upsilon}$ is is the flux density of precipitating particles, and $B_{\rm I}$ is the magnetic field amplitude at the footpoint of the magnetic flux tube at the Earth's surface. Taking into account the definition of the kinetic pressure components

$$p_\perp = \int \frac{mv_\perp^2}{2} F\,\mathrm{d}^3\vec{v} \quad \text{and} \quad p_\parallel = \int m v_\parallel^2 F\,\mathrm{d}^3\vec{v} \qquad (4)$$

we can rewrite (3) in the form

$$j_{\parallel \rm I} \equiv eS_{\rm A} = \frac{c}{2}\int \frac{|\vec{B}\times\nabla B|}{B^3}\frac{\partial(p_\perp + p_\parallel)}{\partial\varphi}\frac{B_0}{B}\frac{\mathrm{d}s}{r\sin\theta} \qquad (5)$$

where $j_{\parallel \rm I}$ is the current density of hot particles at the ionospheric level. In the orthogonal dipole coordinate system $(\vec{s}_0, \vec{q}_0, \vec{\varphi}_0)$ ($\vec{s}_0 \parallel \vec{B}$, $\vec{q}_0 \perp \vec{B}$)

$$\frac{|\vec{B}\times\nabla B|}{B^3} = \frac{1}{B^2 h_q}\frac{\partial B}{\partial q} \qquad (6)$$

where

$$h_q = \frac{B_0 R_0^2}{Br\sin\theta} \quad \text{and} \quad h_\varphi = r\sin\theta \qquad (7)$$

are the Lamé coefficients, $R_0$ is the Earth radius, and $B_0 = B_{\rm I}(\theta = \pi/2)$.

Let us consider the case of the isotropic pressure $p_\parallel = p_\perp = p$. In this case,

$$j_{\parallel \rm I} = \frac{c}{2}\frac{B_{\rm I}}{B_0 R_0^2}\frac{\partial p}{\partial\varphi}\frac{\partial w}{\partial q}, \qquad (8)$$

where the magnetic flux tube volume $w$ is equal to

$$w = \int_{-l/2}^{l/2} \frac{\mathrm{d}s}{B} \simeq \frac{32}{35}\frac{R_0}{B_0 q^4}, \qquad (9)$$

and the value $q = (R_0/r)\sin^2\theta$ is constant along the dipole magnetic field line (actually, $q = L^{-1}$, and the latter equality in (9) is valid for $L >> 1$).

The current (8) can be presented as

$$j_{\parallel \rm I} = \frac{c}{2}\left(\frac{1}{h_\varphi}\frac{\partial p}{\partial\varphi}\cdot\frac{1}{h_q}\frac{\partial w}{\partial q}\right)_{\rm I} = \frac{c}{2}(\vec{s}_0[\nabla w\times\nabla p])_{\rm I} \qquad (10)$$

So, we obtained the well-known formula for the field-aligned current [*Vasyliunas*, 1970; *Tverskoi*, 1982] in the case where the current is determined by energetic precipitating particles.

## 4. RC relaxation and structure of the precipitation pattern

In the strong-diffusion limit, the precipitated flux density $S_A$ can be written as

$$S_{\rm A} = 2\pi\int_0^\infty\int_0^\infty F(s = l/2)v_\parallel\, v_\perp \mathrm{d}v_\perp\, \mathrm{d}v_\parallel . \qquad (11)$$

The integration limits over $\upsilon_\parallel$ in (11) are specified assuming that the distribution function $F(s = l/2)$ at the ionospheric level is isotropic for the downgoing protons and equal to zero for upgoing protons. On the other hand, the kinetic pressure near the equator is isotropic in this case and equal to if we take into account that, under the assumptions used here, $F_L \approx F(s = l/2)$ for $\upsilon_\parallel \geq 0$ and $F_L \approx F(s = -l/2)$ for $\upsilon_\parallel \leq 0$, then we can use Eqs. (11)-(12) to obtain the relation between $p$ and $j_\parallel$:

$$p = \frac{\overline{V}m}{e}j_\parallel, \quad \overline{V} = \frac{4\int_0^\infty v^4 F\,\mathrm{d}v}{3\int_0^\infty v^3 F\,\mathrm{d}v}. \qquad (13)$$

Note that it is valid only in the magnetic flux tube where the strong pitch-angle scattering takes place.

Now, taking into account Eqs. (9) and (13), we can rewrite Eq. (8) in the form

$$\frac{\partial p}{\partial\varphi} = -\delta p, \quad \delta = \frac{35R_0}{128 r_{B0}}\frac{L^{-5}}{(4 - 3/L)^{1/2}}, \qquad (14)$$

where $r_{B0} = \overline{V}/\Omega_{B0}$ is the effective gyroradius, and $\Omega_{B0}$ is the proton gyrofrequency at the equator for $r = R_0$.

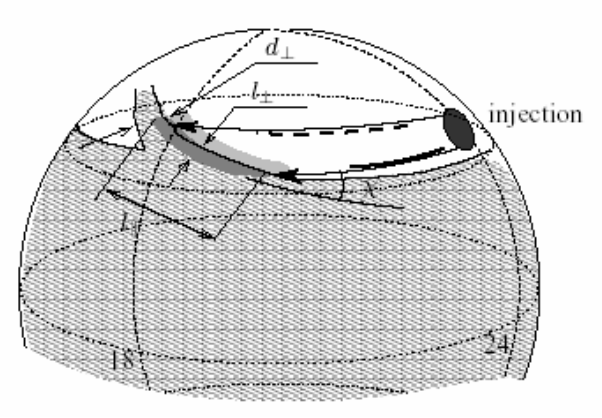


**Figure 3.** Schematic picture of the precipitation region at the ionospheric level.

The solution of (14) is written as

$$p(L,\varphi) = p_0(L)\exp[-\delta(\varphi-\varphi_0(L))]\,, \qquad (15)$$

where $\varphi_0(L)$ is the plasmapause bulge boundary and $p_0(L)$ is the RC pressure at this boundary in the equatorial plane. In the case of a sharp plasmapause, the current $j_\parallel$ is switched on at this boundary and decreases along φ similar to the pressure:

$$j_\parallel = \frac{ep_0(L)}{m_p\overline{V}}\,\exp[-\delta(\varphi-\varphi_0(L))]\,. \qquad (16)$$

The RC relaxation and the field-aligned current $j_\parallel$ of energetic protons are described by the formulas (15) and (16) in the interval

$$\varphi_0(L) \le \varphi \le \varphi_1(L)\,, \qquad (17)$$

where $\varphi_1$ is the boundary at which the CI is switched off due to a decrease in the RC ux density or a drop in the cold plasma density. It is clear that the pitch-angle diffusion can contribute to the formation of the partial RC if the precipitation leads to a significant variation in the pressure p at the interval $\Delta\varphi = \varphi-\varphi_0 = \delta^{-1} \le \pi$. This gives us an estimate for the maximum $L$ value, $L = L_{\max}$, at which the precipitation is important for the ARC formation:

$$L_{\max} \simeq \left(\frac{R_0}{2r_{B0}}\right)^{1/5} \qquad (18)$$

For energetic protons with $W_p$ ~20 keV, $L_{\max} \approx 5$. It follows from (18) that $L_{\max} \propto W_p^{0.1}$, i.e., depends very weakly on the energy of RC particles.

The geometrical shape and the scales of the precipitation region are determined by the position and the shape of the plasmapause in the region of its contact with drifting RC protons (Figures 2 and 3). In the simplest case, the ionospheric projection of this region can be approximated by a stripe forming an angle χ with the energetic ion drift velocity (Figure 3). The dimensions of this stripe are determined using Eqs. (16) and (17) and Figure 3. Taking into account the variation of the flux tube square along the field line, we obtain for the projections onto the Earth's surface:

$$\begin{aligned} l_\perp &= h_{\varphi \mathrm{I}}|\Delta\varphi|\,\sin\chi \\ l_\parallel &= R_0|\Delta\theta_\mathrm{I}|\,\sin^{-1}\chi\,, \end{aligned} \qquad (19)$$

where the subscript "I" determines the values at the Earth's surface, $h_{\varphi\mathrm{I}} = R_0 \sin\theta_\mathrm{I}$, and $\sin^2\theta_\mathrm{I}\, L^{-1}$. Finally, we have for $\Delta\varphi \sim \delta^{-1}$ and $\Delta L/L << 1$:

$$\begin{aligned} l_\perp &\simeq 3.4 r_{B0} L^{4.5}(4-3/L)^{1/2}\,\sin\chi \\ l_\parallel &\simeq \frac{R_0\Delta L}{2L(L-1)^{1/2}\sin\chi}\,, \end{aligned} \qquad (20)$$

Let us consider a quantitative example. Putting $W_p$ ~20 keV, $\Delta L \sim 1$, and $L \sim 4$, we obtain

$$\begin{aligned} \chi = \frac{\pi}{2}: &\quad l_\parallel = 460\ \mathrm{km} \quad l_\perp = 2000\ \mathrm{km} \\ \chi = 0.1: &\quad l_\parallel = 4600\ \mathrm{km} \quad l_\perp = 200\ \mathrm{km}\,. \end{aligned} \qquad (21)$$

Using (8), we can estimate the total field-aligned current of precipitated RC protons:

$$\begin{aligned} J_\parallel &= \left(\int j_\parallel\, h_q h_\varphi\, \mathrm{d}\varphi \mathrm{d}q\right)_\mathrm{I} \\ &\simeq \frac{c}{R_0^2}\int \frac{\partial w}{\partial q}\,[p_0(\varphi_0,q)-p(\varphi_1,q)]\,\mathrm{d}q \end{aligned} \qquad (22)$$

If the RC decay is signifcant ($L < 5$), i.e., $p << p_0$, and $p_0(\varphi_0, q)$ varies relatively slowly with $q$, then it is possible to present (22) in the form

$$J_\parallel = \frac{cR_0}{B_0}\,\frac{32p_0}{35}\,(L_2^4 - L_1^4) \simeq \frac{\Delta L}{L_{\mathrm{pp}}^3}\,\beta_{L\max}\, I_0 \qquad (23)$$

where $L_{\mathrm{pp}}$ is the plasmapause position, $I_0 = (16/35\pi)\, B_0 R_0\, c = 3\cdot 10^8$ A is a constant, $\beta_{L\,\max} = 8\pi p_{\max}/B_L^2$, and $\Delta L = L_2 - L_1 << L_{\mathrm{pp}}$. Taking, e.g., $\Delta L \sim 1$, $L_{\mathrm{pp}} = 4$, and $\beta_{L\,\max} = 0.05$, we obtain $J_\parallel \approx 230$ kA.

## 5. 3D current system related to precipitation

With injection of new energetic particles, formation of a new current system begins. The injection can be quasistationary, as in the case of enhanced magnetospheric convection, or nonstationary, as during substorm breakups. We consider the first case. Without precipitation, the convection current system includes the asymmetric ring current and its continuation into the magnetosheath and the plasma sheet. This current, generally speaking, can be closed in the magnetosphere without any ionospheric currents. Under real conditions, the field-aligned current (FAC) is generated, which is determined by distribution of the plasma pressure $p$ and by the structure of the magnetospheric magnetic field $B(r,\varphi)$. In the case of the isotropic pressure, this current is described by (10). The magnetospheric and field-aligned currents together with ionospheric currents form rather complicated 3D current system, which shields the convection electric field and prevents its penetration into the internal magnetosphere and ionosphere [*Volkov et al.*, 1985]. Precipitation directs the magnetospheric convection currents into the ionosphere and can remove this shielding. To estimate the electric fields and currents in this new 3D current circuit, we use a simple partial ring current model, shown in Figure 4. This model includes:

- the magnetospheric current $\vec{j}_M$ of energetic protons, which density can be written as a sum of the gyration current $j_c$ and the drift current $j_D$:

$$\vec{j}_{\rm M} = \vec{j}_c + \vec{j}_{\rm D} = -\frac{1}{c}\nabla \times \frac{p\vec{B}}{B^2} + en_p\langle\vec{V}_{\rm D}\rangle\,, \quad (24)$$

where

$$en_p\langle\vec{V}_{\rm D}\rangle = \frac{c}{2}\int (2W_{\parallel} + W_{\perp})\frac{\vec{B}\times\nabla B}{B^3}\,F\,{\rm d}^3\vec{v}\,;$$

- the field-aligned current $J_{\parallel}$ (22);
- and the ionospheric currents in the conjugate ionospheres with the current density

$$\vec{j}_{\rm I} = (\hat{\sigma}_{\rm N} + \hat{\sigma}_{\rm S})\vec{E}_{\rm I} \quad (25)$$

where $\vec{E}_I$ is the electric field at the ionospheric height.

In further calculations, we use the quasineutrality condition for the energetic-proton density $n_p$ and the cold-electron density $n_e$, the equipotentiality of the magnetic-field lines, and the current continuity equation

$$\mathrm{div}(\vec{j}_{\rm M} + \vec{j}_{\parallel}) \equiv \mathrm{div}(\vec{j}_{\rm D} + \vec{j}_{\parallel}) = \mathrm{div}(\vec{j}_{\parallel \rm I} + \vec{j}_{\rm I}) = 0\,. \quad (26)$$

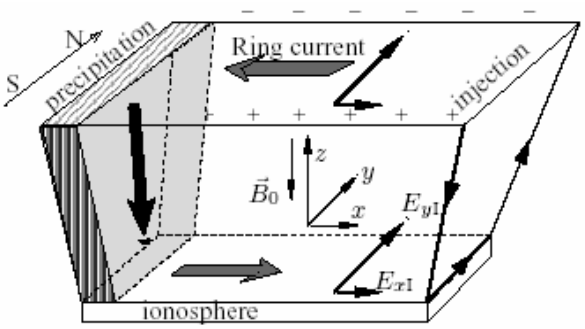


**Figure 4.** 3D current system with precipitation.

Here, the first identity represents the fact that $\mathrm{div}\,\vec{j}_{\rm c} = 0$, while the second and third equations describe current continuity at the magnetospheric and ionospheric heights. We employ the scheme in which field-aligned currents flow only in the injection and precipitation regions and along the northern and southern edges of the partial ring current (Figure 4). This scheme does not take into account details of the RC spatial structure but allows one to obtain useful integral relations. In our approximation, $\Delta L/L_{\rm pp} << 1$, the magnetospheric (and ionospheric) current stripe is thin and has the side boundaries directed along the total-velocity vector of energetic protons (Figure 5)

$$\vec{V}_\Sigma = \vec{V}_{\rm D} + \vec{V}_E = \langle\vec{V}_{\rm D}\rangle + c\frac{[\vec{E}\times\vec{B}]}{B^2} \quad (27)$$

In this geometry, shown in Figure 5, the $y$-component of the cold electron motion produces the polarization of the stripe and generates a Hall current loop (Figure 4). Integrating the first part of Eq. (26) over the coordinate $s$ along the magnetic field line and over $q$ across the magnetic field, we obtain the relation corresponding to the Hall current loop (the $y$-component of the current):

$$(\Sigma^e_{\rm HM} + \Sigma^{\rm S}_{\rm HI} + \Sigma^{\rm N}_{\rm HI})E_{x\rm I} = (\Sigma^{\rm N}_{\rm PI} + \Sigma^{\rm S}_{\rm PI})E_{y\rm I} \quad (28)$$

where

$$\Sigma^e_{\rm HM} = cenw \quad (29)$$

is the magnetospheric Hall conductivity, $w = \int_{-l/2}^{l/2} ds/B$, $\Sigma_{(H,P)I} = \Sigma^S_{(H,P)I} + \Sigma^N_{(H,P)I}$, $\Sigma^{S,N}_{(H,P)I} = \int \sigma^{S,N}_{(H,P)I}$ are the integral Pedersen (P) and Hall (H) conductivities of the Northern (N) and Southern (S) ionospheres. The integration of the second part of Equation (26) over the

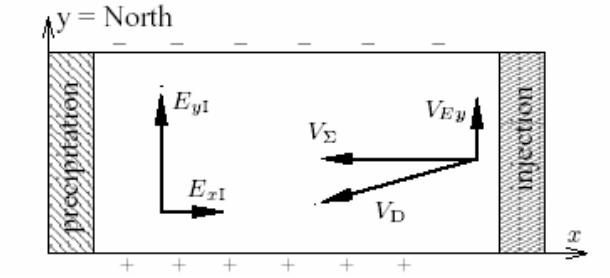


**Figure 5.** The ionospheric projection of the current stripe.

ionospheric height and the width of the stripe yields the relation

$$-\Sigma^e_{\mathrm{HM}} E_{y\mathrm{I}} l_\parallel + J_\parallel = [\Sigma_{\mathrm{PI}} E_{x\mathrm{I}} + \Sigma_{\mathrm{HI}} E_{y\mathrm{I}}]\, l_\parallel \qquad (30)$$

where the total field-aligned current $J_\parallel$ is determined by (22), $l_\parallel$ is the latitudinal stripe width at the ionospheric height, which is determined by (21). Using Eqs. (28) and (30), we obtain

$$E_{y\mathrm{I}} = \frac{(J_\parallel / l_\parallel)(\Sigma_{\mathrm{HM}} + \Sigma_{\mathrm{HI}})}{(\Sigma_{\mathrm{HM}} + \Sigma_{\mathrm{HI}})^2 + \Sigma^2_{\mathrm{PI}}} \qquad (31)$$

$$E_{x\mathrm{I}} = \frac{(J_\parallel / l_\parallel)\Sigma_{\mathrm{PI}}}{(\Sigma_{\mathrm{HM}} + \Sigma_{\mathrm{HI}})^2 + \Sigma^2_{\mathrm{PI}}} \qquad (32)$$

It follows from the quasineutrality condition that $J_\parallel \propto \Sigma_{\mathrm{HM}} \propto n_p$, so Eq. (31) shows that $E_{y\mathrm{I}}$ saturates with increase in $n_p$ and reaches the maximum value

$$E^{\max}_{y\mathrm{I}} \approx \frac{J_\parallel / l_\parallel}{c e n_p\, w} \approx \frac{\Delta w}{w} \frac{\overline{W}_p}{e l_\parallel} \approx \frac{8(L-1)^{1/2}}{eR_0} \overline{W}_p \qquad (33)$$

where we have used (3), (22), and (29), and $\overline{W}_p$ is the average kinetic energy of RC protons.

The dependence of $E_{x\mathrm{I}}$ and $E_{y\mathrm{I}}$ on $J_\parallel$ at constant $\overline{W}_p$ is shown in Figure 6. $E_{x\mathrm{I}}$ reaches its maximum value

$$E^{\max}_{x\mathrm{I}} = \frac{\Sigma_{\mathrm{PI}}\, E^{\max}_{y\mathrm{I}}}{2[\Sigma_{\mathrm{HI}} + \sqrt{\Sigma^2_{\mathrm{PI}} + \Sigma^2_{\mathrm{HI}}}]} \qquad (34)$$

for

$$\Sigma^2_{\mathrm{HM}} = \Sigma^2_{\mathrm{PI}} + \Sigma^2_{\mathrm{HI}}\,, \qquad (35)$$

where $E^{\max}_{yI}$ is determined by (33).

The above calculations of the 3D current system were performed actually for the particular case $\chi = \pi/2$. Under real conditions, $\chi$ can be rather small, and in this case some corrections are needed. On the other hand, the geometrical scales of the precipitation region do not enter the final results (31) and (32) for the electric field. This justifies the applicability of the results obtained in this Section for an arbitrary value of $\chi$.

## 6. Formation of the polarization jet

The structure and magnitude of the ionospheric electric field and the field-aligned cold-plasma current generated by the current of precipitated RC protons have good correspondence to the polarization jet. Indeed, according to the experimental data, PJ appears at the main phase of a magnetic storm in the night sector near the plasmapause position and correlates well with the ionospheric trough. The westward drift velocity in PJ reaches several km s$^{-1}$, the updraft velocity of cold electrons in the downward FAC region in the ionospheric F-layer, corresponding to PJ, can even exceed this value. According to the previous Section, the model gives the maximum westward velocity about 1 km s$^{-1}$ for the mean proton energy $\overline{W}_p$ = 24 keV and grows linearly with $\overline{W}_p$. This value is quite suitable for explaining PJ, but, according to (31), it is reached if $\Sigma_{\mathrm{HM}} >> \max(2\Sigma_{\mathrm{HI}}, 2\Sigma_{\mathrm{PI}})$. Under the conditions typical for the nighttime subauroral ionosphere, $\Sigma^S_{HI} + \Sigma^N_{HI} \sim \Sigma^S_{PI} + \Sigma^N_{PI} <\sim 10$ S. In accordance with (29) and (9), $\Sigma_{\mathrm{HM}}$ reaches this value at $L = 4$ for $n_p \sim 1$ cm$^{-3}$, which corresponds to the flux density $S_\mathrm{p} \sim 2{\cdot}10^8$ cm$^{-2}$ s$^{-1}$ ($\beta = 8\pi p / B^2_L \sim 0{,}1$), if $\overline{W}_p > 20$ keV.

The updraft velocity of cold electrons can be estimated from the equation ($E_{y\mathrm{I}} >> E_{x\mathrm{I}}$)

$$V_e \simeq \frac{2\Sigma_{\mathrm{PI}} E_{y\mathrm{I}}}{e n_{\mathrm{I}} l_\parallel} \qquad (36)$$

where $n_\mathrm{I}$ is the electron density in the ionospheric $F$-layer, and it is assumed that the latitudinal width of the field-aligned current region is equal to $l_\parallel/2$. Putting $\Sigma_{\mathrm{PI}}$ = 5 S, $E_{y\mathrm{I}}$ = 50 mV m$^{-1}$, $n_\mathrm{I} = 10^5$ cm$^{-3}$, and $l_\parallel$ = 460 km, we obtain from (36): $V_\mathrm{e} \sim 130$ m s$^{-1}$. Note that the electron density in the ionospheric trough can be much less than $10^5$ cm$^{-3}$. This is due to the nature of the ionospheric conductivity: the Pedersen conductivity $\Sigma_{\mathrm{PI}}$ is supplied by ions, and the field-aligned (Couling) conductivity $\sigma_\parallel$ is due to electrons, so the plasma density impoverishment takes place in a region of the inflowing field-aligned current.

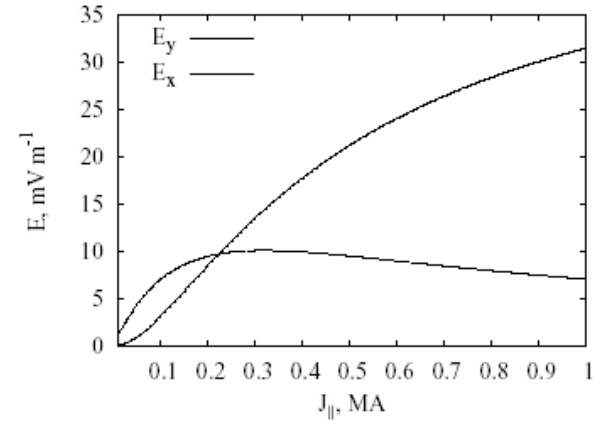


**Figure 6.** The dependence of the electric field $\vec{E}$ on the RC intensity $J_{\|}$ for $L = 4.4$, $\overline{W}_p = 24$ keV, $\Sigma_{HI} = \Sigma_{PI} = 5$ S, and $l_{\|} = 460$ km.

It is interesting that in the saturation regime, in which the electric field $E_{yI}$ is maximum and equal to (33), the velocity of electric drift $V_{EI} = cE_{yI}/B_I$ is close to the average magnetic drift velocity (2), which determines the magnitude of the magnetospheric RC. This fact has the clear physical sence (the magnetospheric Hall conductivity shunts the external (ionospheric) circuit in the case $\Sigma_{HM} >> (\Sigma_{HI}, \Sigma_{PI})$ and is supported by experimental data [*Khalipov et al.*, 2003].

The above calculations and quantitative estimates correspond to the strong pitch-angle diffusion regime, i.e., almost maximum values of precipitated energetic-proton fluxes observed experimentally [*Yahnina et al.*, 2003]. In more typical cases of moderate or weak pitch-angle diffusion, the developed scheme remains qualitatively valid, and only characteristic scales change. In particular, a decrease in the precipitated flux leads to the corresponding decrease in the RC decay rate $\delta$ as compared with Eq. (14) and increase in the azimuthal extent $\Delta\varphi \sim \delta^{-1}$ of the precipitation region. If $\Delta\varphi$ does not exceed the maximum value dictated by the azimuthal size $\Delta\varphi_{pp}$ of the cold-plasma bulge (see Figure 2), then the total field-aligned current $J_{\|}$ and the ionospheric electric field do not change as compared to our estimates (Eqs. (23) and (31) to (34)). In the opposite case ($\Delta\varphi > \Delta\varphi_{pp}$), both $J_{\|}$ and $E_I$ decrease by a factor $\Delta\varphi/\Delta\varphi_{pp}$.

## 7. Conclusions

The developed analytial approach to the problem of formation of the partial ring current with precipitation taken into account leads to important conclusions which are insensitive to the assumptions of the model. These conclusions are listed below.

1. Precipitation of RC protons due to the CI development at the plasmapause bulge plays the important role in the formation of partial ring current at $L \le 5$ (18).
2. The geometrical form and scales of the precipitation region are determined by the line of contact between the drifting energetic protons and the plasmapause, and are determined by Eq. (3).
3. The 3D current system includes the magnetospheric current generator (injection and precipitation of RC particles), the closing current chain of cold ionospheric particles and the Hall current loop, determined by the magnetospheric current of cold electrons (Figure 4).
4. The field-aligned current of cold electrons connected with the Hall current loop and the generated ionospheric northward electric field $E_{yI}$ are good candidates to explain the origin of the polarization jet.
5. The maximum value of the northward electric field (33) is close to the observed values of the electric field in the PJ; the corresponding electric drift velocity is close to the average magnetic drift velocity of RC particles.

**Acknowledgments.** This work was supported by the Russian Foundation for Basic Research (grant 02-02-17109), the General Physics Division of the Russian Academy of Sciences (Program No.16 for Basic Research), and INTAS (grant No. 99-0335).

## References

Bespalov, P. A., and V. Y. Trakhtengerts, The cyclotron instability in the Earth radiation belts, in *Reviews of Plasma Physics*, vol. 10, edited by M. A. Leontovich, pp. 155-192, Plenum, New York, 1986.

Cornwall, J. M., F. V. Coroniti, and R. M. Thorne, Turbulent loss of ring current protons, *J. Geophys. Res.*, *75*, 4699-4709, 1970.

Filippov, V. M., L. V. Shestakova, and Y. I. Galperin, A strip of fast ion drift in the subauroral F-region and its manifestation in the structure of subauroral ionosphere, *Cosmic Research*, *22*, 557-564, 1984.

Galperin, Y. I., Polarization Jet: characteristics and a model, *Ann. Geophys.*, *20*, 391-404, 2002.

Galperin, Y. I., and V. N. Ponomarev, Plasma convection in the polar ionosphere, during rapid subauroral ion drift events, *Ann. Geophys.*, *30*, 1-7, 1974.

Galperin, Y. I., V. N. Ponomarev, and A. G. Zosimova, Direct measurements of ion drift velocity in the upper ionosphere during a magnetic storm, 2. Results

of measurements during the November 3, 1967, magnetic storm, orbit, *Cosmic Research*, *11*, 283-292, 1973.

Grafe, A., V. Y. Trakhtengerts, P. A. Bespalov, and A. G. Demekhov, Evolution of the low latitude geomagnetic storm field and the importance of turbulent diffusion for ring current particle losses, *J. Geophys. Res.*, *101*), 24689-24706, 1996.

Kennel, C. F., and H. E. Petschek, Limit on stably trapped particle fluxes, *J. Geophys. Res.*, *71*, 1-28, 1966.

Khalipov, V. L., Y. I. Galperin, A. E. Stepanov, and E. D. Bondar, Formation of polarization jet during injection of ions into the inner magnetosphere, *Adv. Space Res.*, *31*, 1303-1308, 2003.

Khazanov, G. V., M. W. Liemohn, T. C. Newman, M. C. Fok, and R. W. Spiro, Self-consistent magnetosphere-ionosphere coupling: Theoretical studies, *J. Geophys. Res.*, *108*, 1122, doi:10.1029/2002JA009,624, 2003.

Liemohn, M. W., J. U. Kozyra, M. F. Thomsen, J. L. Roeder, G. Lu, J. E. Borovsky, and T. E. Cayton, Dominant role of the asymmetric ring current in producing the stormtime *Dst*, *J. Geophys. Res.*, *106*, 10,883-10,904, 2001.

Southwood, D. J., and R. A. Wolf, An assessment of the role of precipitation in magnetospheric convection, *J. Geophys. Res.*, *83*, 5227-5232, 1978.

Titova, E. E., et al., Strong localized variations of the low-altitude energetic electron fluxes in the evening sector near plasmapause, *Ann. Geophys.*, *16*, 25-33, 1998.

Trakhtengerts, V. Y., A. Grafe, P. A. Bespalov, and A. G. Demekhov, Modeling of asymmetric DR variation in presence of spatio-temporal variations of the plasmapause, *Adv. Space Res.*, *18*, 299-305, 1996.

Tverskoi, B. A., On field-aligned currents in the magnetosphere, *Geomagn. Aeron.*, *22*, 991-995, 1982.

Vasyliunas, V., Mathematical models of magnetospheric convection and its coupling to the ionosphere, in *Particles and Fields in the Magnetosphere*, edited by B. M. McComack, pp. 60-71, D. Reidel, Norwell, Mass., 1970.

Volkov, M. A., W. B. Lyatsky, and Y. P. Maltsev, On structure of electric field and currents in region of Harang discontinuity, *Geomagn. Aeron.*, *25*, 445-449, 1985.

Yahnina, T. A., A. G. Yahnin, J. Kangas, J. Manninen, D. S. Evans, A. G. Demekhov, V. Y. Trakhtengerts, M. F. Thomsen, R. G. D., and B. B. Gvosdevsky, Energetic particle counterparts for geomagnetic pulsations of Pc1 and IPDP types, *Ann. Geophys.*, *21*, 2281-2292, 2003.

---

A. G. Demekhov and V. Y. Trakhtengerts, Institute of Applied Physics of the Russian Academy of Sciences, 46 Ulyanov st., 603950 Nizhny Novgorod, Russia (andrei@appl.sci-nnov.ru, vyt@appl.sci-nnov.ru).

# Ground-based TV observations of auroral forms and results of comparison with particle data from the FAST satellite

V. R. Tagirov[1], V. A. Arinin[2], and M. Temerin[3]

[1] Polar Geophysical Institute, Russian Academy of Sciences, Apatity, Russia
[2] Institute of Explosion Physics, Russian Federal Nuclear Center, Sarov, Russia.
[3] Space Science Laboratory, University of California, Berkeley, USA

**Abstract.** We present the preliminary results of comparison of the energy and flux particle data obtained by FAST satellite and altitude measurements of corresponding auroral forms on February 9 1997. The satellite passed over the territory of Kola Peninsula in the interval from about 1923 to 1930 UT when two TV cameras operated in Loparskaya and Lovozero. The satellite data of electron energy flux (EEF) showed seven peaks during this period. In this paper we consider two of them in details when the satellite was at minimum distance from the zenith of both stations. According to the optical data the foot-point of the satellite crossed two different auroral bands whereas the satellite data showed that the bands differed noticeably by their characteristics. The first one was associated with the particle flux with wide energy spectrum from hundreds of eV to several KeV while the second one was formed mainly by hard particles with energies more than 10 KeV. For this case we used new triangulation technique, recently worked out for determination of altitudes of atmospheric luminous phenomena. The results showed good correspondence between measured altitudes of aurora and energy characteristics of particle flux registered onboard FAST satellite.

## 1. Introduction

The FAST satellite was built to obtain particle data with very high temporal resolution of about fractions of second. This gave an opportunity to observe spatial structures that map to a few tens of meters at the ionosphere with full energy and pitch angle resolution **[***Carlson et al.*, 1998]. We compared this data with high-resolution optical TV data from the Earth surface or aircraft [*Stenbaek-Nielsen et al.*, 1998]. Of course, the ground-based optical observations have some restrictions in comparison with aircraft observations, namely stationary position of the camera, dependence on auroral activity at the moment of satellite flight and weather conditions. On the other hand there are some advantages, for example, possibility of long-term observations, interaction with other programs and operation of more than one camera to cover large areas of sky.

Optical observations, performed simultaneously by two ground-based TV cameras, and FAST satellite particle measurements during very strong auroral activity are presented in this paper. Besides, we used new method of triangulation measurements of the altitude of auroral forms [*Arinin and Tagirov*, 2003] and compared them with energy characteristics of particle fluxes.

## 2. Results of observations

We present the preliminary results of the comparison of energy and flux particle data obtained by FAST satellite and altitude measurements of corresponding auroral forms on 9 February 1997. The satellite passed over the territory of Kola Peninsula from South to North within the interval from about 1923 UT to 1930 UT when two TV cameras operated in Loparskaya (latitude 68.62º, longitude 33.3º, geographic) and Lovozero (67.98º, 35.08º). The distance between them was about 71 km.

The auroral activity was very high and at least three substorms took place during that night. The satellite passed over Kola Peninsula during the very beginning of the second substorm when multiple auroral bands appeared in the sky, some of them being very active.

Electron flux characteristics are shown in Figure 1. The first panel from the top shows the energy spectra, pitch-angle distribution is presented in the second panel, the third panel presents energy flux, and particle flux is shown in the fourth panel. It is seen that there are seven peaks in EEF. TV image of the auroral display corresponding to the moment of the third peak of electron energy flux is shown in Figure 2. The solid line

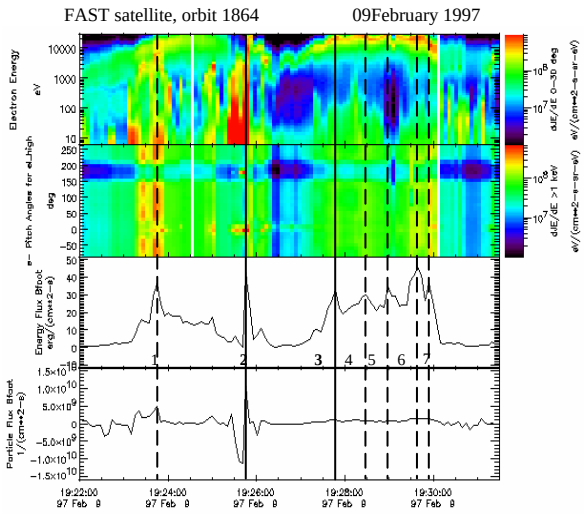


**Figure 1.** Electron flux data measured by FAST satellite during the pass over Kola Peninsula on February 09, 1997. The first panel from the top: energy spectra; the second panel: pitch-angle distribution; the third panel: energy flux; the forth panel: particle flux. Solid lines marked by bold numbers 2 and 3 show two instants, when the foot-point of FAST satellite was most closely located to the zenith of Loparskaya and Lovozero observatories.

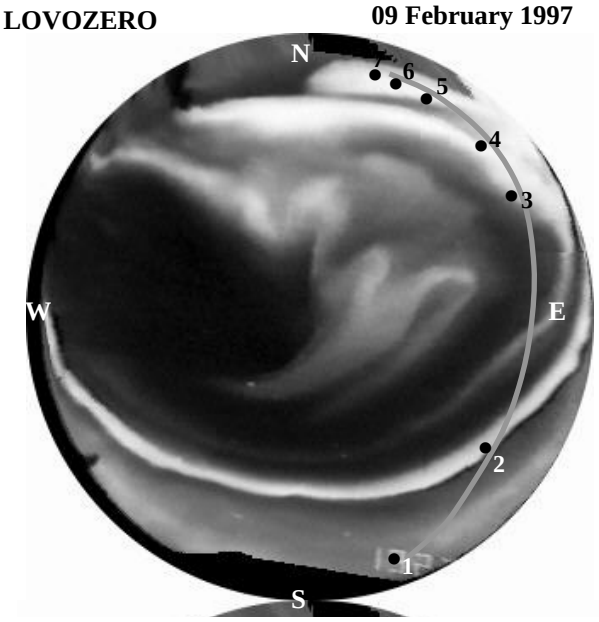


**19.27.47.05 UT**

**Figure 2.** TV image of auroral display in Lovozero corresponding to the 3rd peak of electron energy flux. Solid line shows a trace of the foot-point of the FAST satellite at 100 km altitude. Black dots indicate location of the foot-point corresponding to seven peaks of energy flux.

indicates the trace of the foot-point of FAST. Black dots show the location of the foot-point of the satellite at the instants of the EEF. It is evident from these data that the peaks of EEF are associated with auroral forms.

It is also seen from the satellite data that the peak values of energy flux varied: from 30 erg/cm$^2$s (the 4th peak) to 44 erg/cm$^2$s (the 6th peak). On the other hand, the energy of electrons and pitch-angle distribution varied considerably.

The instants 19:25:45:32 UT and 19:27:47:05 UT, which correspond to the second and the third peaks of energy flux intensity, are marked by solid lines and bold numbers 2 and 3 in Figure 1. At these moments the locations of FAST satellite foot-point was the closest to the zenith of Loparskaya and Lovozero observatories. All-sky TV images of auroral display from both observational sites and for both instants with the trace of the foot-point of the FAST satellite mapped to 100 km altitude and shown by the black curved lines at the right sides of the images are presented in Figure 3. The locations of the foot-point at the corresponding instants are indicated by black dots on the lines and shown by arrows.

At these moments the electron flux characteristics differed from each other considerably (see Figure 1). At the time of the 2nd peak the energy distribution became wider (from several eV to about 15 KeV). At this moment the flux of energetic electrons was sharply anisotropic and consisted of electrons having only 0 and 180° pitch-angles. Electron energy spectra show that the peak occurred at the very edge of the soft electron flux consisting of upward flowing particles, as seen from the particle flux data (lower panel in Figure 1). This corresponds to the downward field aligned currents. The particle flux data show that at the time of the peak itself the flow of electrons was mainly downward corresponding to upward FACs, although the pitch-angle data show some amount of upward flowing electrons.

At the moments of 3rd peak and the following peaks of energy flux the characteristics of particle flux changed considerably. It is seen from the energy spectra that there are four inverted V structures corresponding to peaks in EEF. The bulk of the electrons has energies in the range from 15 to about 22 KeV. Only at the moment corresponding to the last peak the energy decreased to the range between 7 and 15 KeV. Pitch-angle distribution has minimum around 180º for high-energetic fluxes, and it is approximately homogeneous at all other pitch-angles. So the characteristics of the particle flux were typical for those, that cause intense aurora.

For determination of the heights of auroral luminosity we applied new method proposed by *Arinin and Tagirov* [2003]. Briefly, it consists of several stages. At first using the positions of stars we remove all distortions, which could originate from optical and electronic channels of the equipment. The mathematical

method, which was used for improving the images, is called Gouraud network [*Gouraud*, 1971]. The network is constructed from triangles of minimal perimeter with stars as vertexes of triangles. By comparison of true positions of approximately 60-80 stars taken from the astronomical yearbook with measured ones the field of correction vectors can be constructed. Using this field the whole image can be improved. The images given in Figures 2 and 3 were obtained using this method. The second stage is the mapping of TV images to the geographical grid at a given altitude, each image being coloured in complimentary colours. At those places where auroras observed from each site coincide by altitude the sum of complimentary colours would give white colour. By varying the altitude one can determine the altitude of aurora in any place at that area where the projections of the images are superimposed on each other.

In this paper we determined the altitudes of aurora at the moments of the EEF peaks numbered as 2 and 3 (see Figure 1). Superimposed images of aurora from both stations are shown in Figure 4*a* for altitude equal to 90 km, the image from Loparskaya being coloured in red whereas Lovozero one being coloured in green. The arrow crossing the image shows the trace of footpoint of

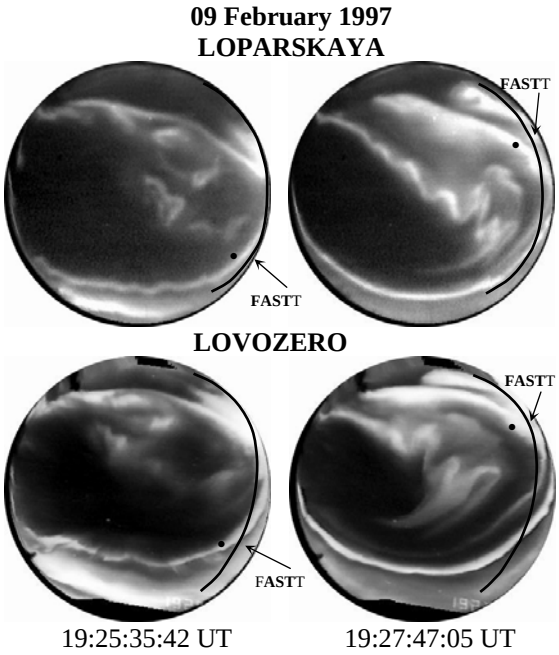


**Figure 3.** All-sky TV images from Loparskaya and Lovozero at the times of the 2nd and the 3rd peaks of electron energy flux (see Figure 1). The trajectory of the foot-point of the FAST satellite mapped to 100 km altitude is shown by the black curved lines at the right sides of the images. Location of the footpoint at the corresponding times are indicated by black dots on the lines and shown by the arrows.

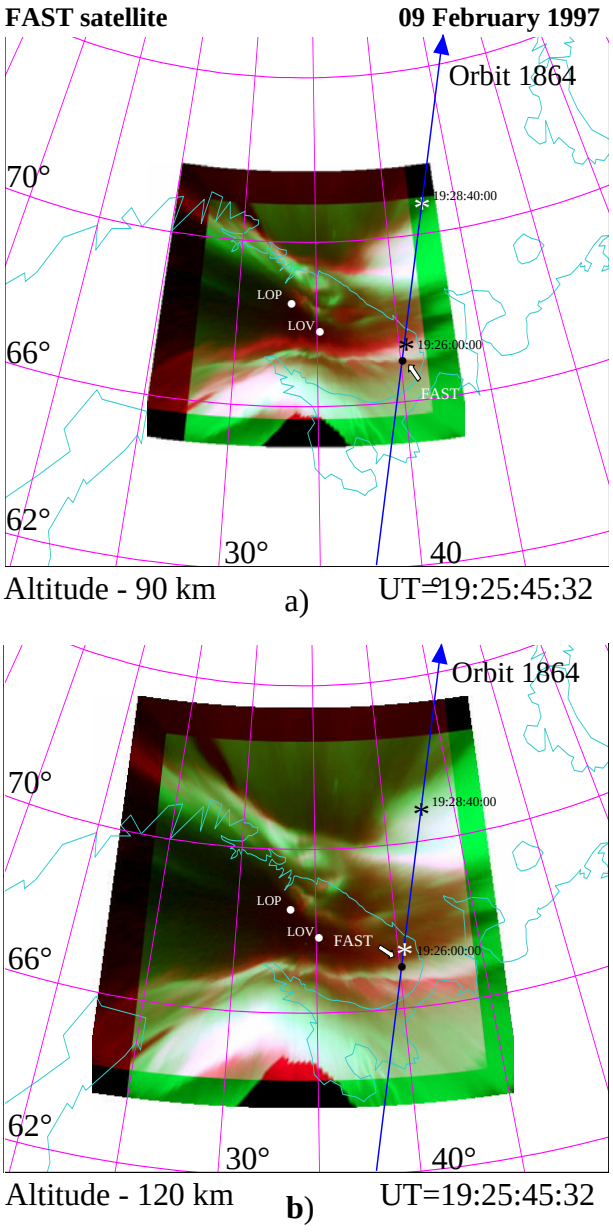


**Figure 4.** Images of aurora display at 19:25:45:32 UT on 09 February 1997 obtained by TV cameras at Loparskaya and Lovozero coloured by complimentary colours are superimposed on each other and mapped to the contour of the Kola Peninsula coastline. The Loparskaya image is coloured in red and Lovozero one in green. The assumed altitude of the display is 90km (a) and 120 km (b). The trace of footpoint of the FAST satellite over Kola Peninsula at altitude 100 km is shown by an arrow. The stars on this line show the positions of the satellite at two indicated moments. The Black dot shows the location of satellite foot point at the time when the second peak of the electron energy flux was registered on board of the satellite.

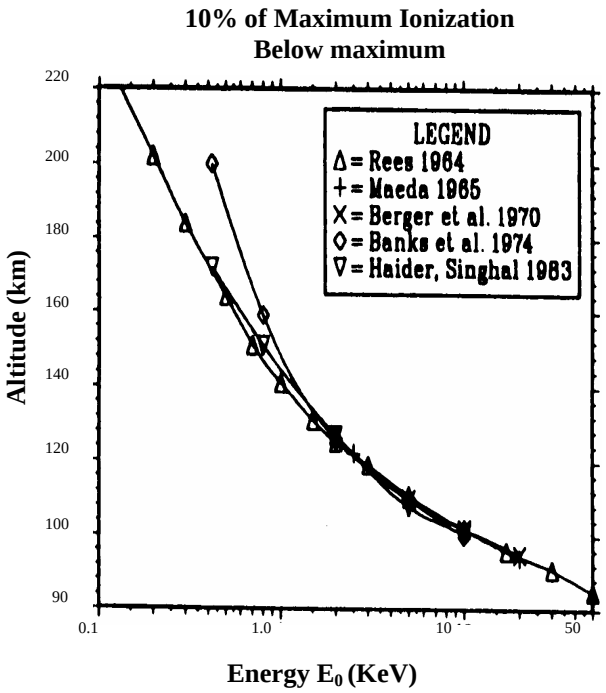


**Figure 5.** The altitudes of the ionization at 10% of maximum (below maximum) from five different authors in the energy range of 0.1-50 KeV [*Kaila*, 1988].

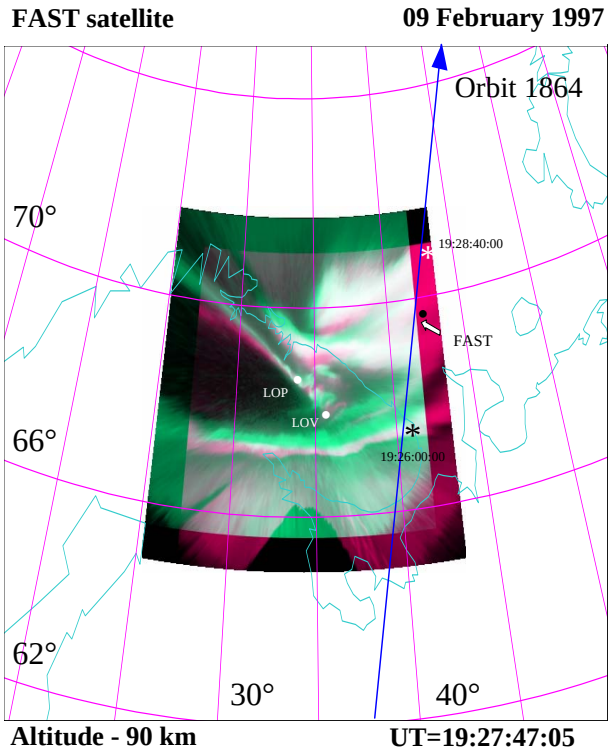


**Figure 6.** Images of auroral display constructed in the same way as in Figure 4 for the time 19:27:47:05 UT. The assumed altitude of the display is 90 km. The Black dot shows the location of satellite footpoint at the time when the third peak of the electron energy flux was registered on board of the satellite.

the satellite at 100 km altitude. Black spot on the arrow indicates the location of the foot point of the FAST satellite at 19:25:45:32 UT (2nd peak). It is located at the edge of the white band corresponding to the lower border of aurora. Figure 4*b* is constructed for the same moment, but for altitude equal to 120 km. In this case the location of FAST foot point takes place close to the opposite edge of the white area indicating the upper border of luminosity. So the bulk of luminosity fits the altitude range from ~90 to ~120 km, which corresponds to energies from about 15 KeV down to 2 KeV [*Kaila*, 1989]. It is in good agreement with those energies measured by FAST (see Figure.1).

Figure 6 is similar to the previous figure presenting auroral display at the moment of the 3rd peak in EEF (second solid vertical line in Figure 1). In this case the footpoint of the satellite was located further than in the previous one and we could not determine the lower border of aurora because the location of the footpoint of the satellite was out of field of view of Loparskaya TV camera. The field of view of the camera is the area, located above horizon higher than 12º elevation angle. Nevertheless the lower border of the auroral form is obviously located at the altitudes less than 90 km. We assume this because the footpoint of the satellite is just at the edge of Loparskaya camera field of view (FoV) while the white colored area is situated still further from the footpoint and from the edge. Setting of lower altitudes will get out the footpoint from the FoV of the Loparskaya camera. We were not able to determine the upper border of the auroral form due to the superposition of the auroral forms because of low elevation angle. So for the third peak of electron energy flux one can say that the luminosity of the auroral form was associated with particles with energies reaching 20–30 KeV. It is also, (as for the second peak), in agreement with the measurements onboard FAST satellite which show the same values of energy at the instants of the third and also successive peaks of electron energy flux.

### 3. Summary

We presented an example of simultaneous ground-based optical TV and satellite observations during strong auroral disturbance, which represented multiple auroral forms at break-up phase of substorm. The first results of altitude measurements of auroral forms by this new method and consequent determination of energy of

precipitating electron fluxes was in good agreement with the energetic characteristics measured on board of the FAST satellite.

**Acknowledgments.** We thank I. V. Okunev and A. V. Roldugin for carrying out TV observations in Loparskaya and Lovozero during winter season in 1996-1997.

**References**

Arinin, V. A. and V. R. Tagirov, Determination of volumetric brightness distribution of atmospheric luminous objects from all-sky TV images. Thes. Conf. p. 90.

Gouraud, H., Computer display of curved surfaces, Ph. Dr. Thesis, University of Utah, USA, 1971.

Carlson, C. W., R. F. Pfaff, and J. G. Watzin, The Fast Auroral SnapshoT (FAST) mission, *Geophys. Res. Lett., 25*, 12, 2013, 1998.

Kaila, K., Determination of the energy of electrons by the measurements of the emission ratio and altitude of aurorae. *Planet. Space Sci., 37*, 341,1989.

Stenbaek-Nielsen, H. C., T. J. Hallinan, D. L. Osborn, J. Kimball, C. Chaston, J. McFadden, G. Delory, M. Temerin, and C. W. Carlson, Aircraft observations conjugate to FAST: Auroral arc thickness. *Geophys. Res. Lett., 25*, 2073, 1998.

---

V. R. Tagirov, Polar Geophysical Institute, Kola Scientific Center, Russian Academy of Sciences, 184200, Apatity, Murmansk region, Russia.
E-mail: tagirov@pgi.kolasc.net.ru

V. A. Arinin, Institute of Explosion Physics, Russian Federal Nuclear Center, 607190, Sarov, Russia.

M. Temerin, Space Science Laboratory, University of California, Berkeley, CA 94709, USA.

# Dependence of the red auroral emission intensity on the parameters of the solar wind

T. A. Hviuzova, and S. V. Leontyev

Polar Geophysical Institut, Apatity, 184200, Russia

**Abstract.** This work deals with statistical research of the connection between the solar wind density and the intensity of red auroral emission (630.0 nm). It was found out that as a rule high (> 5 kR) intensities of red emission were observed when the solar wind density was more than 10 $cm^{-3}$. The distinct dependence of I630.0 on the solar wind density was observed, when the sign of IMF $B_z$ changed. Aurora was observed in the midnight sector of the auroral oval during 15 years.

## 1. Introduction

During the interaction of the Earth's magnetosphere with non-stationary flows of solar wind red auroras of type A are frequently observed, and it has been noticed, that the density of solar wind at that time was increasing [*Hviuzova and Leontyev*, 2001]. The recent research [*Terasawa et al.*, 1997] has shown, that there was a connection between the density of particles in the solar wind and that of particles in the plasma sheet. With the increase of the solar wind density, the density of the plasma sheet grows, especially at the positive $B_z$ component of IMF.

## 2. Observations and results

The data on aurora for 1970-1985 were obtained in Loparskaya by means of patrol spectrograph. The observations in zenith of station in the midnight sector of auroral oval were used, when the solar wind parameters were available [Interplanetary Medium Data Book, 1977; Interplanetary Medium Data Book-Supplement 3A, 1977-1985, 1986].

Among the selected events there were 187 cases when the intensity of red emission (630.0 nm) was more than 5 kR. The statistical processing has shown, that with probability of 0.87 they were observed when the density of the solar wind increased up to 10 $cm^{-3}$ and more. Unfortunately, these data were not enough to bring out the dependence of 630.0 nm emission intensity on the solar wind density because of the wide scattering of points, probably, due to the influence of other parameters.

According to results *Terasawa et al.* [1997] concerning the influence of the IMF $B_z$–component sign on solar wind − plasma sheet densities relationship, we have taken two samples of the data: the first corresponds to the $B_z$ transition from the positive value which lasted for a long period of time (several hours) to the negative one, the second, on the contrary, from the negative to the positive one. The moments of $B_z$ sign change were chosen from [Interplanetary Medium Data Book, 1977; Interplanetary Medium Data Book-Supplement 3A, 1977-1985, 1986]. There were detected 136 negative-to-positive changes and 97 positive-to-negative ones. The red line intensity and the solar wind density averaged for the period when $B_z$ sign remained unchanged before the change were chosen for each of these moments. Figure 1 shows the dependence of red line intensity on solar wind density.

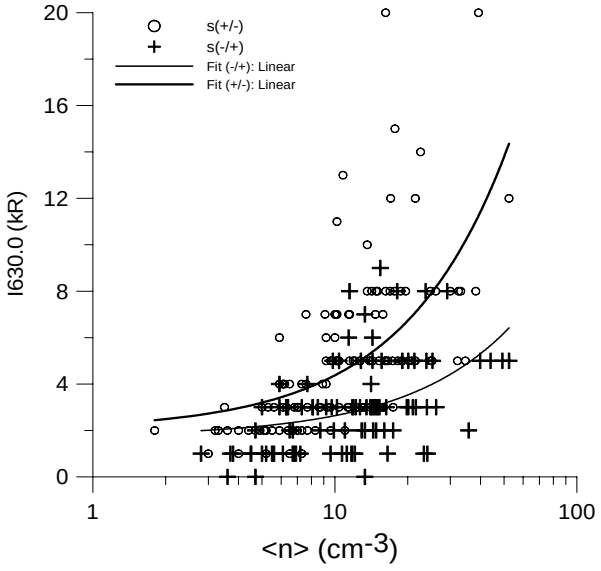


**Figure 1.** Dependence of the red auroral emission intensity upon the solar wind density.

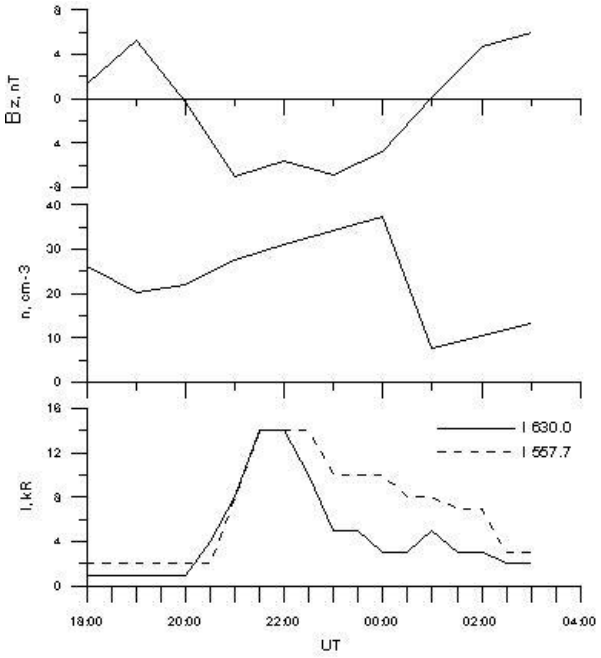


**Figure 2.** The solar wind parameters and the red and green emission intensities on 21-22 February, 1981 in Loparskaya.

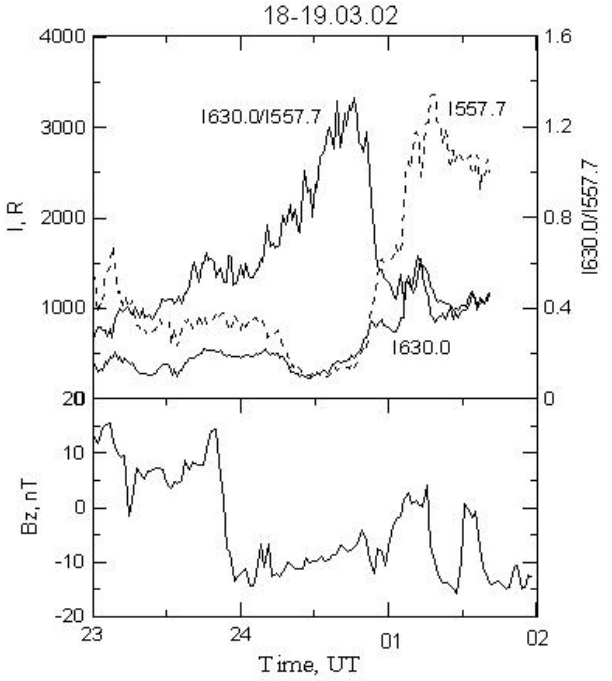


**Figure 3.** The behaviour IMF $B_z$ and auroral emissions for 18-19 March, 2002 in Tumanny. The field of view of photometer is 1.5º on a meridian and 8º on longitude, time resolution is 1 sampe / minute. As it is seen from Figure 3 there is a transition from $+B_z$ to $-B_z$ and transition from $-B_z$ to $+B_z$.

The lines give the approximation of these dependencies. The review of geomagnetic data at Loparskaya station has shown, that a positive step corresponds to the initial substorm phase, and the negative one corresponds to the recovery phase. The growth of red emission intensity with the increase of the solar wind density during the previous interval of time is clearly observed. The 630.0 nm intensity is approximately twice as large at the positive step, than at the negative one.

The example obtained on February 22-23, 1981 is shown in Figure 2. One can see that both steps are accompanied by an increase of red emission intensity. During the positive step this emission begins to grow earlier, than the intensity of green (557.7 nm) emission, and then they became equal. It is possible, that at this moment the power spectrum of precipitating particles has the broadband non-Maxwell form. The similar broadband spectra of precipitating particles were observed by *Shiokawa et al.* [1996].

These results are based on the hourly data therefore it would be useful to study the behaviour of auroral emissions with better time-resolution. On Figure 3 the behaviour of IMF and auroral emissions for 18-19.03.02 is shown. IMF was measured onboard the WIND satellite, and the intensity of emissions was measured by zenith photometer in Tumanny observatory (69.14 N, 35.82 E).

The first transition was accompanied by the increase of red emission without the change of green line intensity, which points to the broadening of the spectrum of precipitating particles. The second transition begins with increasing of red emission then the intensive green emission begins to increase, so that it equals the red emission and then exceeds it. Such behaviour of emissions points to the broadening of a spectrum of precipitating particles.

### 3. Discussion

The large intensities of red emission are observed, as a rule, at the increased (more than 10 $cm^{-3}$) density of the solar wind. In more simple situations one can observe the growth of intensity accompanied by the growth of the solar wind density. However, it is not the only factor determining the 630.0 nm intensity. IMF and its variability may affect it as well. We can suggest a qualitative explanation of such dependence. According to [*Terasawa et al.*, 1997], with the increased density of the solar wind the plasma sheet of the magnetosphere becomes dense and cold. The turn of $B_z$ IMF to the south

results in the growth of the electric field in the magnetosphere, and the occurrence of three-dimensional currents and field-aligned electric fields. The presence of dense cold plasma in the plasma sheet does not allow the field-aligned electric fields to be large, so the soft electrons which are responsible for excitation of red emission are precipitated. Under such conditions the plasma sheet becomes warmer, the field-aligned fields grow and, accordingly, the spectrum of precipitating particles becomes harder. At the negative step the situation is opposite: the turn of $B_z$ to north results in reduction of three-dimensional currents and field-aligned electrical fields and, accordingly, to the mitigation of a spectrum of precipitating particles.

Some other mechanisms of formation of broadband electrons are offered in [*Shiokawa et al.*, 1997]. However, as authors note, none of them are yet conclusive.

## 4. Conclusions

1. During the turns of IMF $B_z$ IMF component the growth of intensity of red (630.0 nm) emission with the growth of the solar wind density is observed. At the turn of $B_z$ to the south this intensity is approximately twice as large, as compared to the turn northward.
2. Large, more than 5 kR, intensities of red emission are observed, as a rule, with the increased values, more than 10 $cm^{-3}$, of the solar wind density.

## References

Hviuzova, T. A., S. V. Leontyev, The spectral characteristics of polar lights connected to non-stationary flows of the solar wind, *Geomagnetism and Aeronomie*, *41*, 337, 2001. (in Russian)

Shiokawa, K., K. Yumoto, C. -I. Meng, G. Reever, Broadband electrons observed by DMSP satellites during storm-time substorms, *Geophys. Res. Lett.*, *18*, 2529, 1996.

Shiokawa, K., C. -I. Meng, G. Reever, F. J. Rich, K. Yumoto, A multievent study of broadband electrons observed by the DMSP satellites and their relation to red aurora bserved at midlatitude stations, *J. Geophys. Res.*, *102*, 14237, 1997.

Terasawa, T., M. Fujimoto, T. Mukai, I. Shiinohara, Y. Saito, T. Yamamoto, S. Machida, S. Kokubun, A. J. Lazarus, J. T. Steinberg, and R. P. Lepping, Solar wind control of density and temperature in the near-Earth plasma sheet: WIND/GEOTAIL collaboration, *Geophys. Res. Lett.*, *24*, 935, 1997.

# Preliminary results of proton aurora observations acquired by CCD spectrograph

L. P. Borovkov, and B. V. Kozelov

Polar Geophysical Institute, Apatity, Murmansk region, Russia.

**Abstract**. Polar Geophysical Institute renews the spectral observations of aurora by a new CCD spectrograph. The spectrograph allows us to examine the red-green region of aurora spectrum with 1 A resolution in 15 seconds exposition. Preliminary results of observations of Balmer-alpha hydrogen emission profile are presented. Comparison with results of theoretical calculations is discussed. The observations are intended to study the substorm effects in proton precipitation.

## 1. Introduction

Proton precipitation in the upper high latitude atmosphere was discovered by optical spectroscopy method [*Vegard*, 1939]. Hydrogen emissions broadening and Doppler shift were used for energy spectra of the precipitating protons assessment [*Meinel*, 1951; *Galperin*, 1959; *Chamberlain*, 1961; *Eather*, 1967; *Omholt*, 1971; *Jones*, 1974].

Optical investigations of proton precipitation were being performed for many years in Polar Geophysical Institute [*Suhoivanenko*, 1961; *Evlashin et al*., 1972; *Totunova*, 1984; *Fedorova et al*., 1988]. Now we renew spectral optical measurements using up-to-date devices, e.g. computerized imaging spectrograph SpectraPro 306 of the Acton Research Corp. and CCD TV camera with microchannel image intensifier IPentaMax of the Princeton Instruments, inc.

We present experimental results of the hydrogen emission registration on December, 6-7, 2002 in Apatity. Magnetic disturbance amplitude did not exceed 400 nT, so auroral emissions were not too intensive. As a result, exposition time for spectra registration was set on 2 minutes. Total sensitivity of our apparatus decreases at the wavelength of less then 500 nm, for this reason we concentrate attention on Hα emission. The description of the device and the acquired spectra are given below.

## 2. Description of the device

The device consists of imaging spectrograph SpectraPro 306 of the Acton Research Corp. and intensified CCD camera IPentaMax of the Princeton Instruments.

Spectrograph SpectraPro 306

Focal length: 300 mm
Aperture Ratio: f/4
Optical design: Imaging Cherny-Turner with polished aspherical mirrors.
Grating with profiled grooves, 1200 gr/mm, 68×68 mm.
Resolution: 0.1 nm at 435.8 nm with 10 μm entrance slit.
Dispersion: 2.7 nm/mm.
Focal plane size: 27 mm wide x 14 mm high.
Free spectral interval ~25 nm with IPentamax camera.

CCD camera IPentaMax

CCD matrix 512×1024, 15×15 μm pixels with frame transfer.
Microchannel image intensifier fiber-optically coupled to CCD.
12 bits 5 MHz ADC converter.
Dark current ~20 electrons/pix at –20° C.
Up to 15 Images per second at full resolution.
Simultaneous digital and video signal.
Exposure range 50 μs to 23 hours.
Computer controls camera and acquires data via high speed serial connection.

The device is mounted to the ceiling on a gimbal and gets emissions through the plexiglass spherical window. The sketchy view of the device is presented in Figure 1. We can tilt the device's optical axis up to 45 degrees relative to the vertical direction in 2 orthogonal planes. Besides, we can turn the device (and the entrance slit) about the optical axis. The full aperture of the device with Nikkor fisheye lens is ~80 degrees.

The spectrograph and the camera are controlled by

their own original software, using low level program possibilities of the software, obtained with apparatus.

## 3. Experimental results

Presented data are results of the signal integration of the CCD strips from 100 to 199, which corresponds to the aperture angle range of 8–24 degrees to the north from zenith. Each figure contains 50 spectra, registered with the exposure of 120s.

In Figure 2 and Figure 3 first 100 spectra of 320 are shown, registered at night on December 6/7, 2002 in Apatity. Only OI 636.4 nm and $H_\alpha$ emissions are evident in Figure 2.

In Figure 3 one can see $1PGN_2$ bands (8,5) and (7,4) alongside with OI 636.4 nm and $H_\alpha$. $H_\alpha$ intensity variations are more pronounced comparing to those in Figure 2.

Each of the spectraum gives us $H_\alpha$ line profile and a possibility for comparing our experimental data and theoretical curve.

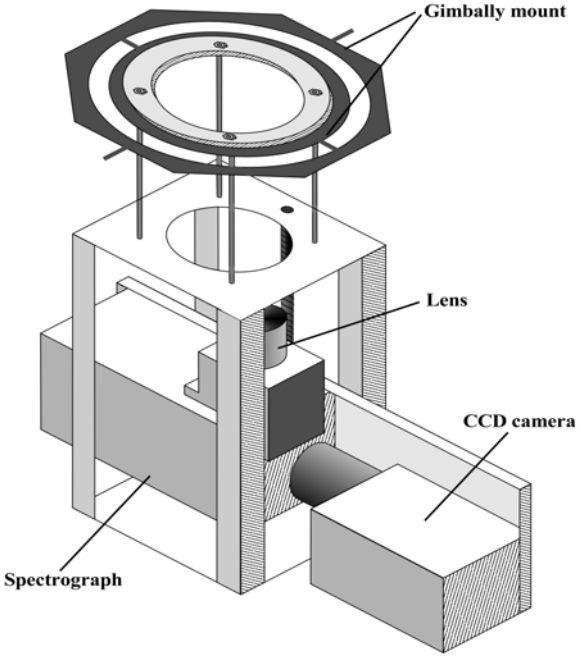


**Figure 1.** Diagram of the device.

## 4. Comparison with theoretical profiles and possible proton spectrum diagnostics

For this purpose we used the hydrogen profiles simulated by Monte-Carlo method. The basic numerical algorithm is the same as used in papers [*Kozelov*, 1993; *Kozelov and Ivanov*, 1994; *Kozelov et al*., 2002]. Several examples of simulated profiles are shown in Figure 4 for monoenergetic initial proton flux with pitch-angle distribution isotropic in downward hemisphere.

One can see that for view angles (angle between the magnetic field line and view line direction ) 10º – 30º the blue shoulder of the profiles has an identical shape. Therefore, we can estimate the characteristic energy of precipitated protons by position of the point of cross section of the approximation line with the background level, see Figure 5.

Experimental $H_\alpha$ profile from spectrum #48 in Figure 2 was used. If the wavelength corresponding to the point is L (in nm), then characteristic energy may be calculated as:

$$E\ (\text{keV}) \approx (L(\text{nm})/0.9575)^2,$$

where the coefficient (0.9575 nm) is equal to Doppler shift of Hα line for hydrogen atom with energy of 1 keV.

For presented observations the estimated characteristic energy was in the range of 15–26 keV. These values agreed well with the values expected from the statistical study [*Hardy et al*., 1989, 1991].

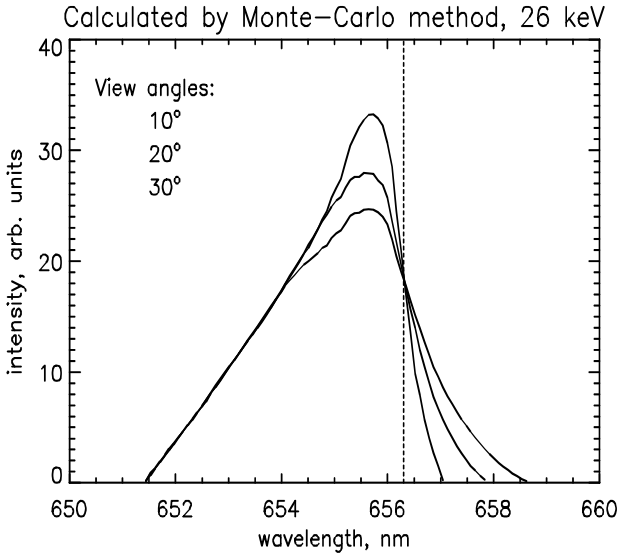


**Figure 4.** The Doppler profiles of $H_\alpha$ line simulated by Monte-Carlo method for monoenergetic initial proton flux with pitch-angle distribution isotropic in downward hemisphere.

## 5. Conclusion

Experimental device for optical spectra measurements has sensitivity and resolution, sufficient to register auroral $H_\alpha$ with the exposure of less then 1 min. Presented data are in good agreement with theoretical $H_\alpha$ profiles, obtained from Monte-Carlo simulation.

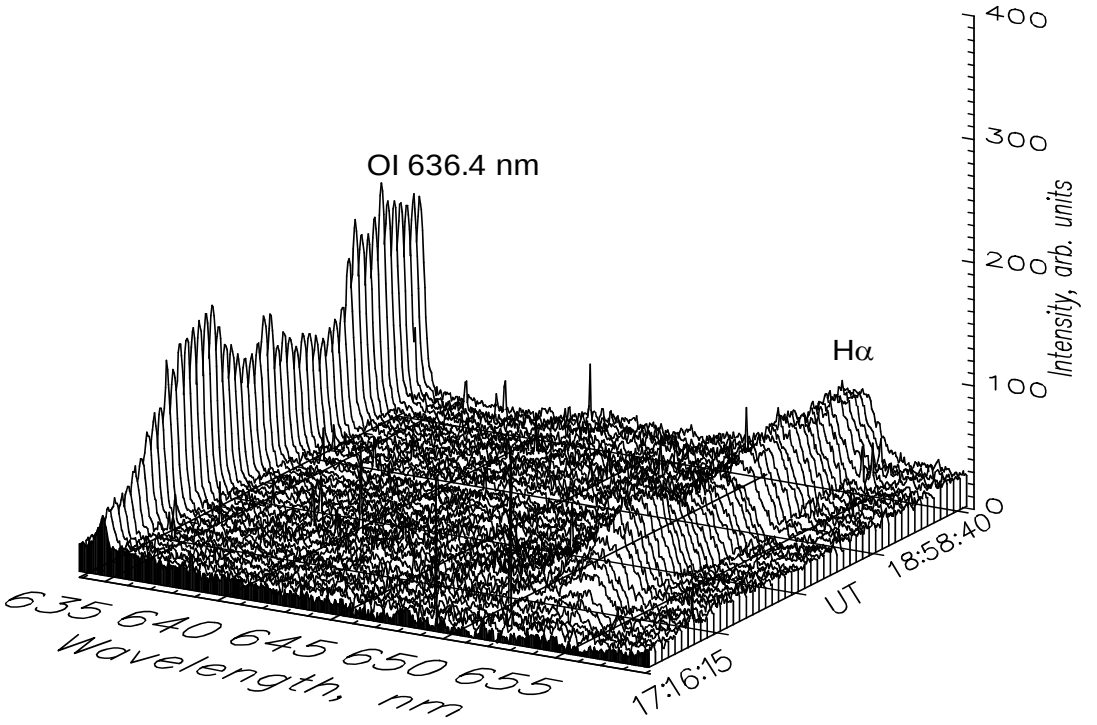


**Figure 2**. Auroral spectra of December 6, 2002, 17:16:15 – 18:56:40 UT. Exposure for each spectrum 2 min.

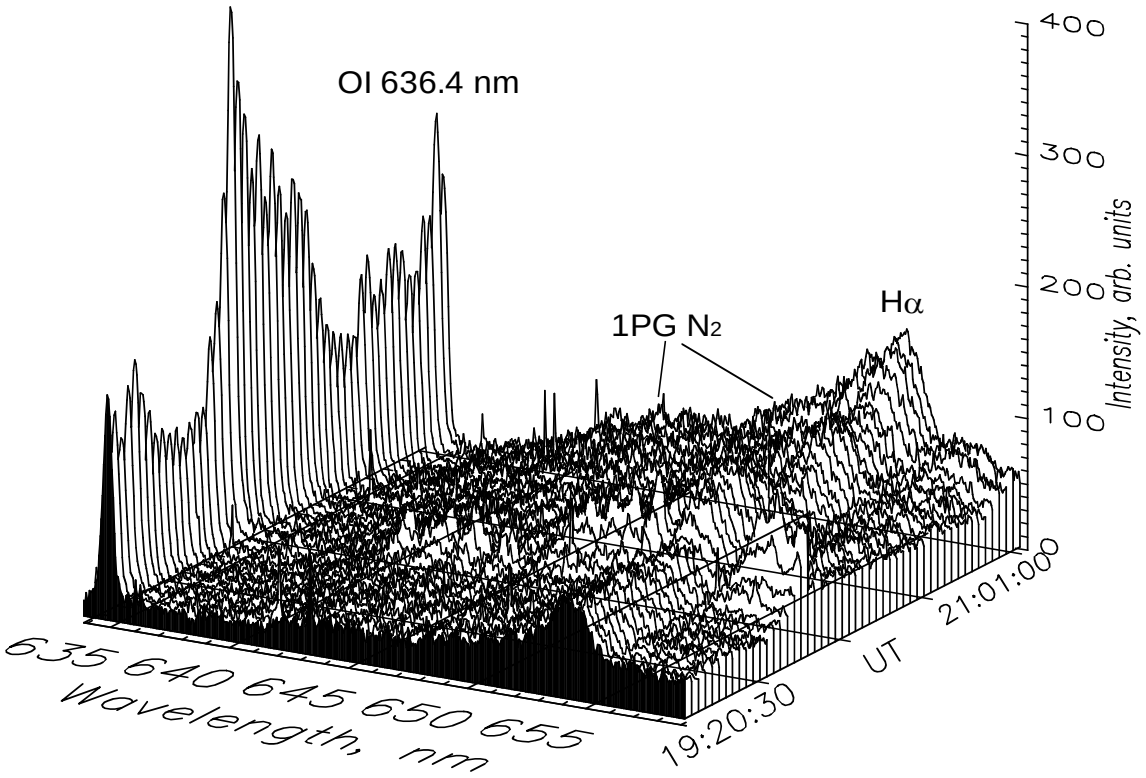


**Figure 3.** Auroral spectra of December 6, 2002, 19:20:30 – 21:01:00 UT. Exposure for each spectrum 2 min.

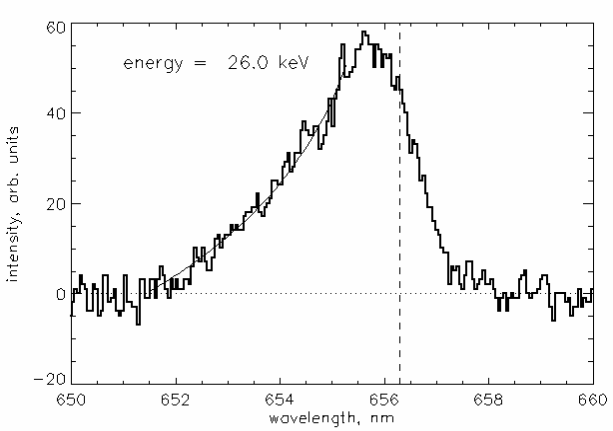


**Figure 5**. Estimation of characteristic particle energy: histogram – observed Doppler profiles of Hα line, solid line – the best fit theoretical approximation, dotted line – background level, dashed line – position of non-shifted Hα line. Experimental profile #48 from Figure 2 was used.

A simple method for precipitating protons energetic spectrum assessment in the case of the clear $H_\alpha$ was proposed.

## References


Chamberlain, J. W., Physics of the aurora and airglow, Academic Press, New York and London, 1961.

Eather, R. H., Auroral proton precipitation and hydrogen emissions, *Rev. Geophys*, *5*, 207-285, 1967.

Evlashin, L. S., Yu. L. Trutse, Ya. I. Feldstein, The effects of the ring current and polar electrojet on the oval of the proton aurora, *J. Atmos. Terrest. Phys, 34*, 859-866, 1972

Fedorova, N. I., L. L. Lazutin, V. E. Tsirs, Impulse increases of the proton aurora before substorm active phase, *Geomagnetism i Aeronomia*, *28*, 87-91, 1988.

Galperin, Yu. I., Hydrogen emission and two types of auroral spectra, *Planet. Space Sci, 1*, 57-62, 1959.

Jones, A. V., Aurora, Reidel Publ. Co, Dordrecht, p.301, 1974.

Hardy, D. A., M. S. Gussenhoven and D. Brautigam, A statistical model of auroral ion precipitation. *J. Geophys. Res*, *94*. 370-392, 1989.

Hardy, D. A., W. J. McNeil, M. S. Gussenhoven, D. H. Brautigam, A statistical model of auroral ion precipitation. 2. Functional representation of the auroral pattern. *J. Geophys. Res*, *96*. 5539-5547, 1991.

Kozelov, B. V. Influence of the dipolar magnetic field on transport of proton-H atom fluxes in the atmosphere, *Ann. Geophysicae*, *11*, 697-704, 1993.

Kozelov, B. V., and V. E. Ivanov. Effective energy loss per electron-ion pair in proton aurora, *Ann. Geophysicae*, *12*, 1071-1075, 1994.

Kozelov, B. V., V. E. Ivanov, and T. I. Sergienko, Variations in the intensity of auroral emissions in the region of combined electron and proton precipitation: Possibilities of diagnostics of plasma flux parameters, *Geomagnetizm i Aeronomiya*, English translation: *42*, 4, 486-490, 2002.

Omholt, A., The optical aurora, Springer-Verlag, 1971.

Suhoivanenko, P. Ya., Doppler speeds of protons in aurora from $H_\beta$ measurements, *Aurora and airglow*, *Results of the research on the International Geophys. Projects,* pub. House "Nauka", Moscow, *7*, 7-13, 1961.

Totunova, G. F., Investigation of auroral protons emission patterns and Doppler profile variations, *Aurora and airglow*, *Results of the research on the International Geophys. Projects,* VINITI, Moscow, *31*, 144-158, 1984.

Vaisberg, O. L., Pitch-angle and energy distribution of protons in aurora, Results of the research on the International Geophys. Projects, pub. House "Nauka", Moscow, *Aurora and airglow*, *8*, 36-42, 1967.

Vegard, L., Hydrogen showers in the auroral region, *Nature, 144***,** 1089-1090, 1939.


borovkov@pgi.kolasc.net.ru
kozelov@pgi.kolasc.net.ru

# Effect of the interplanetary magnetic field on the equatorial ionosphere dynamics on March 1998

L. Sizova[1], T. Maruyama [2], and K. Nozaki [3]

[1] IZMIRAN, Troitsk , Moscow region, 142190, Russia
[2] Hiraiso Solar Terrestrial Research Center, CRL, Ibaraki, Japan
[3] 4-2-1 Nukui-kitamachi, Koganey, CRL, Tokyo, Japan

**Abstract.** Variations of the virtual ionosphere height and critical frequency foF2 for Cebu Island are compared with the interplanetary magnetic field data. It is shown that these variations are defined to a significant degree by the direction of the $B_z$-component of the interplanetary magnetic field. The ionospheric heights and foF2 variations at Cebu during the northward IMF $B_z$ (the quiet period on 7 Mar 1998) and the southward IMF $B_z$ (the main phase on 10 Mar 1998 magnetic storm) are very large. Distinction in the heights between quiet and disturbed periods can reach up to100 km and more. The critical frequency foF2 is markedly lower during the southward IMF $B_z$. These phenomena can be explained mainly by the solar wind – magnetosphere – ionosphere coupling. We show that the field-aligned currents serve as a coupling agent between the auroral and the equatorial ionosphere.

## 1. Introduction

During geomagnetic storms intensive ionospheric currents change the quiet ionosphere, and short-term variations of the ionospheric characteristics are observed. Under these conditions the critical frequency foF2, virtual height h'F, drift velocities and other ionospheric characteristics are mainly defined by the state of the solar wind flowing around the Earth's magnetosphere. Numerous papers present the experimental and theoretical relations found by their authors between the solar wind and ionosphere parameters. The studies of *Zmuda and Armstrong* [1974], *Iigima and Potemra* [1978], *Foster et al.* [1989] and other authors led to the conclusion that the field-aligned currents constitute a major interconnection between the magnetosphere and auroral ionosphere. However, the equatorial ionosphere has been assumed to have a special advantage being free from the field-aligned currents. As it was shown by *Rastogi and Patel* [1978]; *Fejer et al.* [1979], the interplanetary magnetic field control on the ionosphere during geomagnetic disturbances is also pronounced at the equatorial ionosphere and they had explained the short-term equatorial ionospheric variations by the action of the auroral sources. From the up-to-date point of view the equatorial ionosphere characteristics depend on the action of the field-aligned currents too. *Zakharov* [1989]; *Denisenko and Zamai* [1992], *Kikuchi et al* [1996] using geomagnetic data, *Sizova and Pudovkin* [2000] using ionospheric data, had shown that the electric fields from the FAC can penetrate the equatorial ionosphere and cause the equatorial electric field variations.

The models of the relationship between the auroral and equatorial ionosphere cannot explain certain aspects of experimental data during magnetic disturbances. To clear up the nature of the short-term equatorial ionospheric variations additional investigations of ionospheric characteristics are required. The critical frequency foF2 and virtual heights h'F observed by an ionosonde become a good indicator of real layer heights and electron concentration and provide information about the equatorial ionosphere dynamics. From the practical point of view of Space Weather, the relationships between the solar wind and the ionosphere parameters can be used for its predicting. The change in the ionosphere height can be a good measure for predicting spread F or intense ionospheric scintillations. This paper continues the investigations mentioned above, and the critical frequency foF2 and virtual height changes at the equator are investigated and interpreted in terms of one of the possible sources of these changes.

## 2. Analysis of the experimental data

Variations of the critical frequency foF2 and virtual ionosphere height h'F for Cebu Island (124° E, 10.3° N;

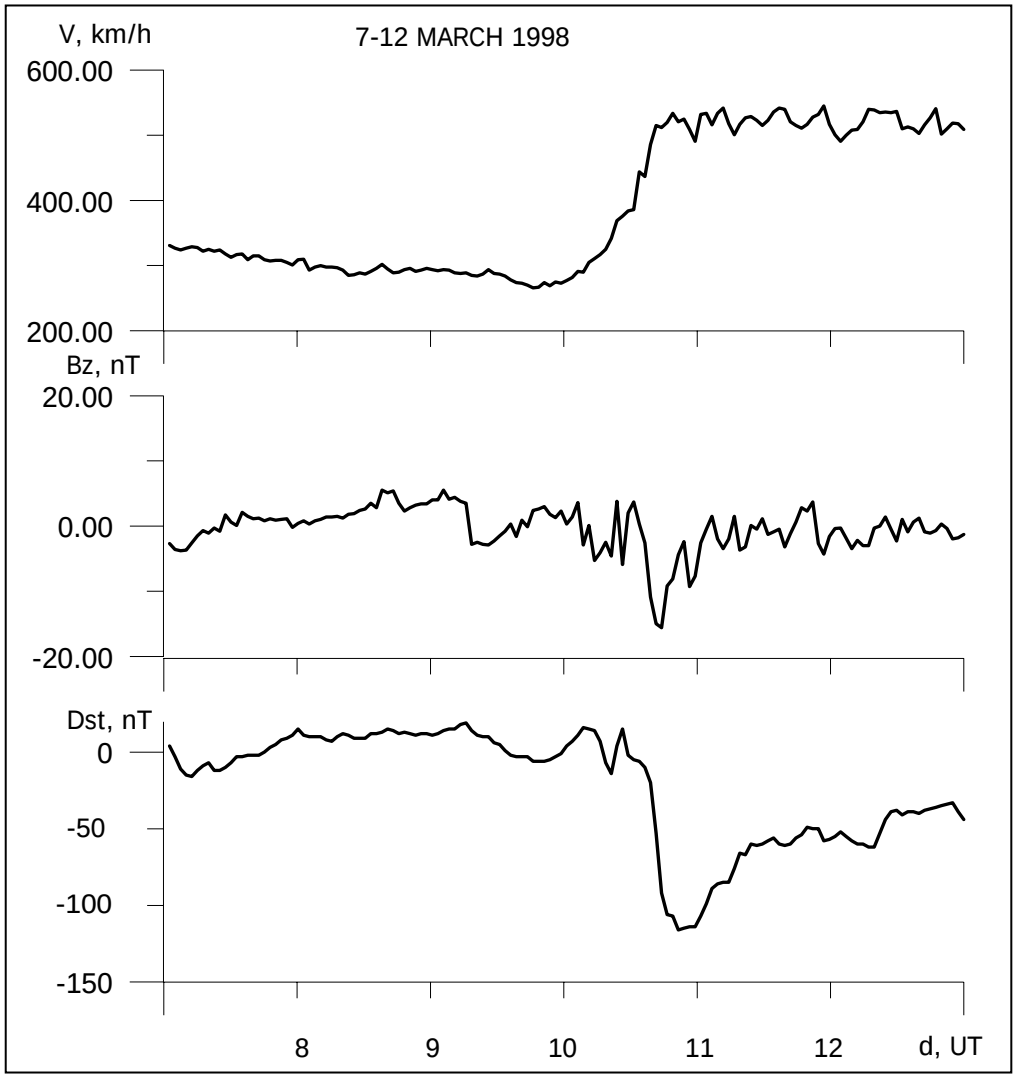


**Figure 1.** Hourly mean variations of the solar wind velocity – V km/s, the IMF $B_z$-component – $B_z$ nT, and Dst-field in nT for 7–13 March 1998.

2.4° N in diplatitude) are examined. Ionospheric observations at this station were conducted every 5 minutes from March, 2 to 12, 1998 during the first Western Pacific Ionosphere Campaign (West. Pac.). On 10 March the moderate geomagnetic storm with Dst = –120 nT occurred.

It was triggered by the negative $B_z$ component of the IMF of the solar wind from 1500 to 1930 UT. During this period the IMF $B_z$ reached –18 nT and the solar wind velocity was V = 550 km/s. In Figure 1 hourly mean variations of the solar wind velocity – V km/s, the IMF $B_z$–component – $B_z$ nT, and Dst-field for 7–13 March 1998 are presented.

Let us examine the foF2 and h'F data during the main phase of the geomagnetic storm on 10 Mar 1998 and the quiet day data on 7 March 1998. Figure 2 and 3 show these variations from 1200 to 2400 UT.

For convenience of comparison of the ionospheric data with the interplanetary and geomagnetic field data Universal Time is used in the figures. Local Time for Cebu is LT = UT + 8 h. The dashed lines of Figure 2 and Figure 3 show some typical examples of the quiet foF2 and h'F variations when $B_z$– component of the IMF is around zero (7 March 1998 data). It should be noted that the equatorial ionosphere varied in different ways during quiet and disturbed conditions at the equator. One can see sharp distinctions between the values of the ionospheric characteristics and the onsets of ionospheric disturbances on these days. Distinctions between quiet and disturbed periods in heights reach up to 100 km and more. For example, at 18 UT on 7 March and 10 March the heights were 200 km and 300 km, the foF2 were around 8 MHz and 2 MHz correspondingly. During the main phase of the geomagnetic storm the foF2 began to

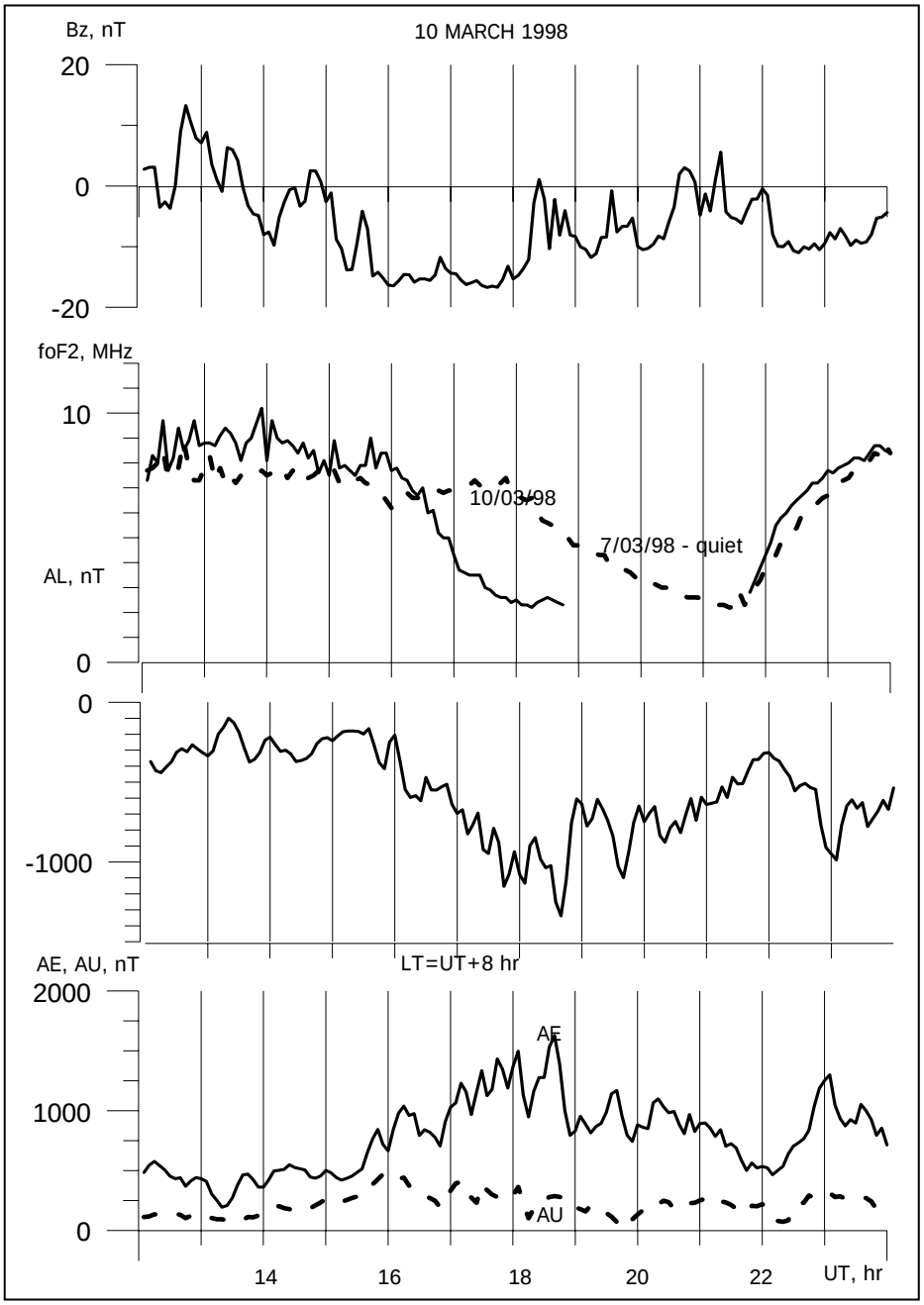


**Figure 2.** Variations of the $B_z$ IMF, critical frequency foF2 at Cebu, AL, AE, AU during the main phase of 10 March 1998 geomagnetic storm.

drop and h'F began to rise at two stations at 1630 UT, whereas for the quiet day it happened at 1800UT. Time delay between the IMF $B_z$ (5- min data of the IMP–8 are presented in Figure 2 and 3) and onset of the equatorial ionospheric disturbances was around 50 min.

Let us analyze 210 Magnetic Meridian data (STELAB, Nagoya University). Daily magnetograms from the high latitudes on 7 and 10 March 1998 are presented in Figure 4. During the quiet day when the IMF $B_z$ was around zero the westward polar electrojet was not observed in the auroral regions: at Kotelnyy (KTN), Tixie (TIK), Chokurdakh (CHD), Zyryanka (ZYK) and Magadan (MGD) stations. As it is seen from Figure 4 the strong westward electrojet was observed on 10 March 1998. It was associated with the IMF $B_z$ turning south. One can compare these magnetograms with AE, AL and AU indices. They show also strong westward auroral electrojet during the storm main phase.

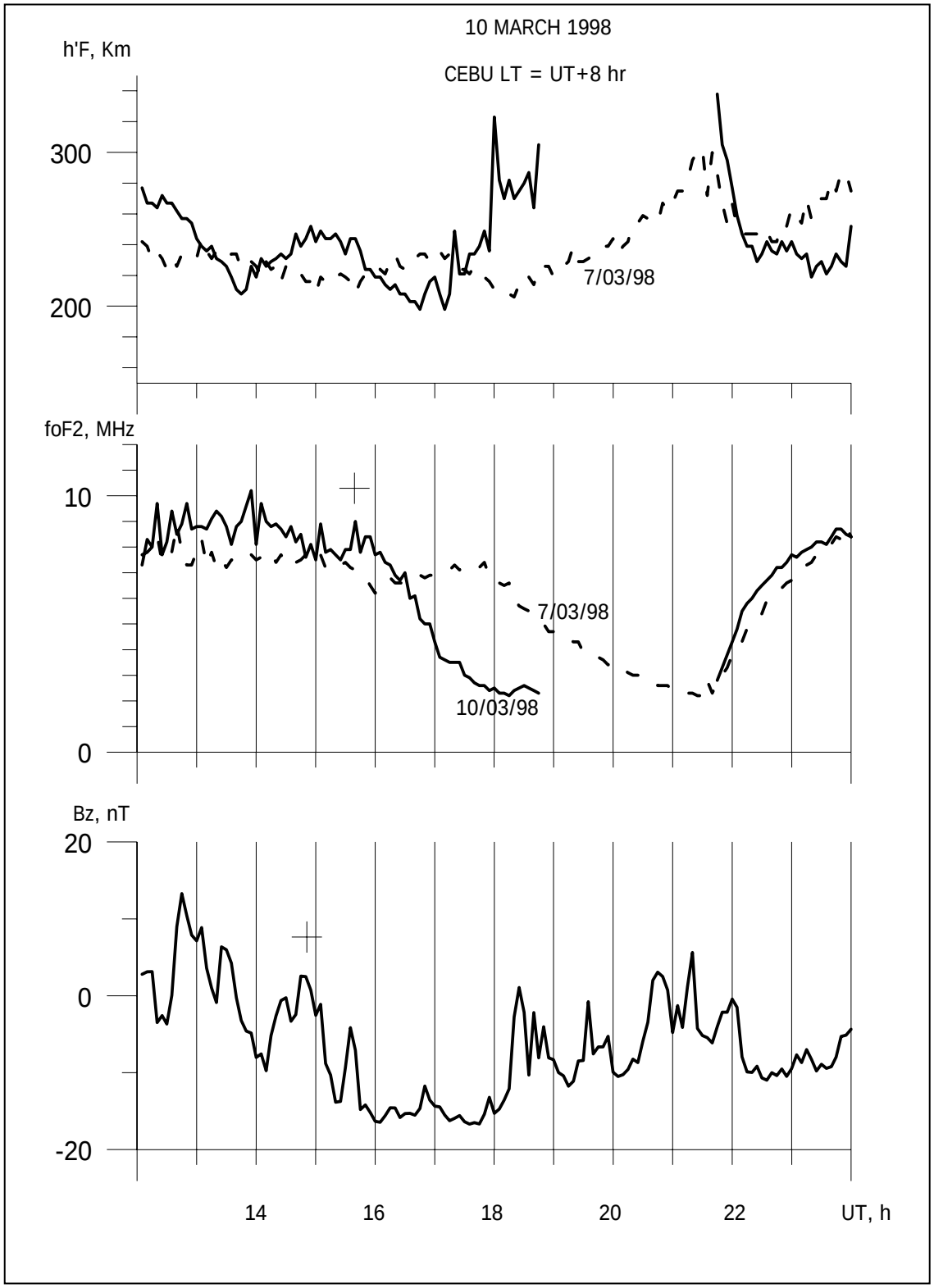


**Figure 3.** Variations of virtual height in km, critical frequency foF2 in MHz, and $B_z$ IMF in nT during the main phase of 10 March geomagnetic storm (solid lines), quiet day h'F and foF2 variations are presented by the dashed lines.

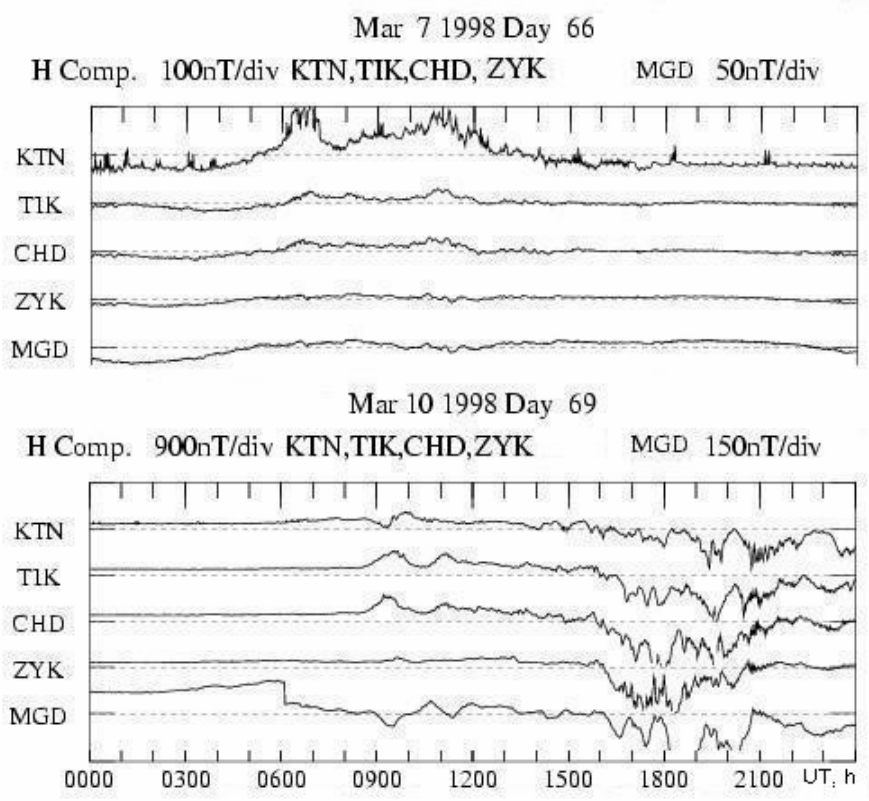


**Figure 4.** The high latitude magnetograms from the 210 Magnetic Meridian on 7 and 10 March 1998, one minute average data.

So, the clear-cut profile of the h'F rising and of the foF2 dropping at Cebu correlated with the disturbances of the $B_z$ IMF, observed at high latitudes.

### 3. Discussion

The examples considered in Figure 3 and 4 show that on 10 March 1998 during the southward IMF $B_z$ the strong westward auroral electrojet was observed. At the same time the equatorial ionosphere parameters at Cebu deviated greatly from the quiet day conditions. These examples allow us to assume that the southward IMF $B_z$ can form an additional eastward current system at the equatorial ionosphere. 50 min delay between the $B_z$ IMF and the equatorial ionospheric variations during the geomagnetic storm makes it possible to do this assumption. This current system can be connected with the Region II field-aligned currents (FAC) during the westward auroral electrojet formation at the night ionosphere. The mechanism of a similar current system formation at the equator by the field-aligned currents was proposed as far back as 1908 by Birkeland and has been further developed recently. According to the nowdays point of view, the electrodynamic relation between the solar wind and the geomagnetosphere and ionosphere is realized through the field–aligned currents. The field-aligned currents are closely connected with the auroral electrojets and the DP systems. The field-aligned current location and intensity are defined by the $B_z$ and $B_y$ components of the IMF. Taking into account these achievements, *Sizova and Pudovkin* [2000] explained the critical frequency foF2 and vertical drift variations during magnetic storms as the effect of the FAC. According to this model, the foF2 and h'F variations on 10 March 1998 at the nighttime equatorial ionosphere can be explained by the model presented in Figure 5. Electric fields from FAC of Region II can penetrate the low-latitude ionosphere through the midlatitudes and create the eastward equatorial electric field. This electric field decreases the nighttime equatorial electrojet, whereas the ionospheric plasma vertical drift velocity increases. In this case, the plasma moves upward away from the F layer, and F2 layer maximum is observed at

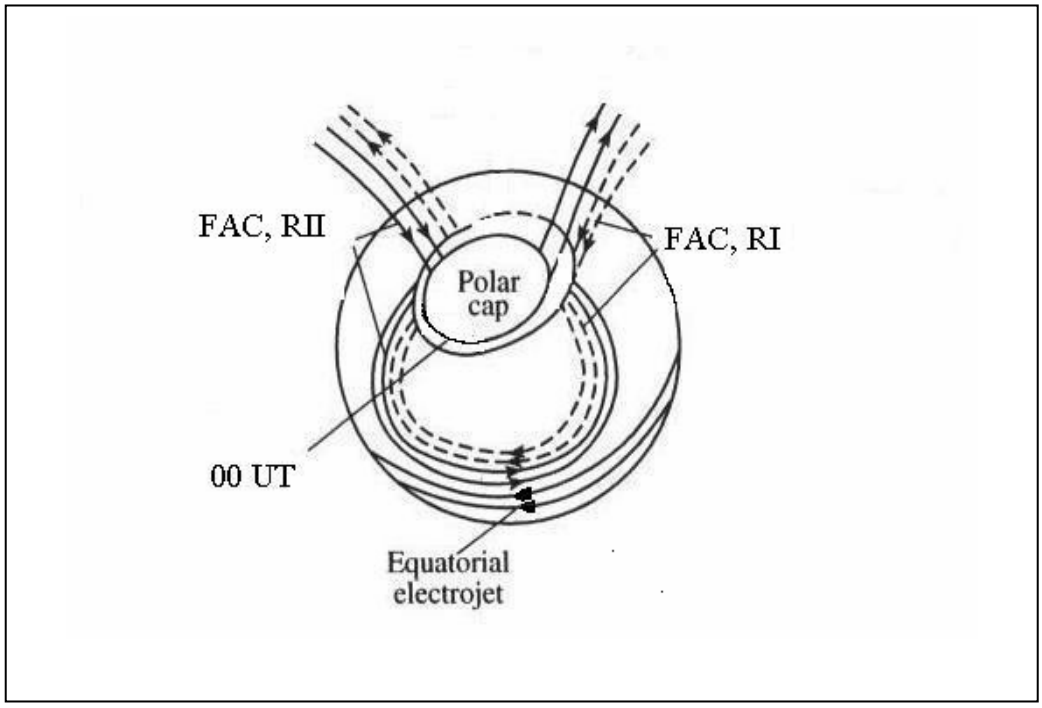


**Figure 5.** The model of the field-aligned currents of the Region I and Region II closing across the equatorial ionosphere.

great heights and one can see the foF2 depression connected with this movement of electrons. Therefore, the FAC are in continuous dynamics, becoming responsible for the complicated nature of height variations at the equator.

## 4. Conclusion

Effect of the IMF $B_z$ on the equatorial virtual heights h'F and critical frequency foF2 is shown. The FAC as one of the possible sources of these changes are discussed. The role of the IMF in the equatorial ionosphere dynamics can be estimated by examining the ionospheric characteristics during quiet and disturbed time. Taking into account time delay between the IMF and the ionospheric variations, this relationship can be used for the prediction of the equatorial ionosphere characteristics during magnetic storms.

**Acknowledgements.** This work was supported by Russian Basic Research Foundation, grant 01–05–64155. Our sincere thanks go to CDAWeb for IMP-8 data and to all the members of 210 MM magnetic Observation Group for their ceaseless support, and Shiokawa, STELAB, Nagoya University for data archives.

## References

Denisenko, V. V., and S. S. Zamay, Electric fields in the equatorial ionosphere, *Planet. Space Sci., 40***,** 941-952, 1992.

Fejer, B. G., C. A. Gonzales, D. T. Farley, M. C. Kelley, Equatorial electric field during magnetically disturbed conditions, *J. Geophys. Res., 84*, 5797, 1979.

Foster, J. C., T. Fuller-Rowell, and D. S. Evans, Quantitative pattens of large-scale field-aligned currents in the auroral ionosphere, *J. Geophys. Res., 94*, 2555-2564, 1989.

Iigima, T., and T. A. Potemra, Large-scale characteristics of the field-aligned currents associated with substorms, *J. Geophys. Res., 83*, 599-615, 1978.

Kikuchi, T., H. Luhr, T. Kitamura, O. Saka, and K. Schlegel, Direct penetration of the polar electric field to the equator during a DP event as detected by the auroral and equatorial magnetometer chains and the EISCAT radar, *J. Geophys. Res., 101*, 17161-17173, 1996.

Rastogi, G. and V. L. Patel, Effect of interplanetary magnetic field on the ionosphere over the magnetic equator. *Proc. Indian. Acad. Sci. Sect. A*, 82, 121-129, 1975.

Sizova, L. Z., M. I. Pudovkin, Disturbances of the daytime equatorial ionosphere associated with the Bz-component of interplanetary magnetic field, *Geomagn. Aeron.*, *40*, 246-249, 2000.

Zakharov, Y. Y., M. A. Nikitin , and O. A. Smirnov, The response of low-latitude fields to the action of magnetospheric source, *Geomagn. Aeron.*, *29*, 381-388, 1989.

Zmuda, A. J., and J. S. Armstrong, The diurnal variation of the region of vector magnetic field changes associated with field-aligned currents, *J. Geophys. Res.*, *79*, 2501-2502, 1974.

Yumoto, K., and the 210° MM Magnetic Observation Group, The STEP 210° magnetic meridian network project, *J. Geomag. Geoelectr.*, *48*, 1297, 1996.

lsizova@izmiran.rssi.ru
tmaru@crl.go.jp
nozaki@crl.go.jp

# Large-scale blobs of ionospheric plasma in the auroral region: Ground-based and satellite measurements

A. E. Stepanov[1] and V. L. Khalipov[2]

[1] Institute of Cosmophysical Research and Aeronomy, Yakutsk, Russia
[2] Space Research Institute, Moscow, Russia

**Abstract.** The data of high-latitude stations of Yakutian meridional chain (Tixie Bay, L=5.57 and Kotelny Island, L=8.2) and COSMOS–900 satellite recordings of polar ionospheric blobs are analyzed. Such blobs are characterized by the increased ionization (3–10 times higher than background ionization) and by the absence of the auroral particle precipitation. Ground-based ionospheric stations observe these blobs in the auroral oval and the polar cap region, basically, in the sector of 22.00–06.00 hours local time, and the satellite can cross them in the polar cap region. The criteria for blob identification in ground-based ionospheric data are determined. It is found that ground-based stations can register several blobs within one night. Their seasonal occurrence frequency with a maximum in winter months is given. Calculations of the blob drift trajectory were carried out with the use of stationary convection model IZMEM, with respect to interplanetary magnetic field. These calculations show that plasma blobs are formed in the dayside cusp region during sharp changes of interplanetary magnetic field parameters.

## 1. Introduction

The term blob or polar patch is used to describe a phenomenon in the system of dayside cusp/cleft region – polar cap – nightside auroral region, which is identified by optical, ionosonde and satellite measurements. The first description of ionospheric plasma blobs was based on measurements of Chatanika incoherent radar [*Banks et al.,* 1974]. Subsequent active studies of these formations in the polar ionosphere using satellite and ground-based data [*Buchau et al.,* 1983; *Weber et al.,* 1984, 1986; *Tsunoda,* 1988; *Baker et al.,* 1989; *Buchau and Reinisch* 1991; *Valladeres et al.,* 1994; *Sojka et al.,* 1994; *Coley and Heelis,* 1995; *Stepanov et al.,* 1999a, 1999*b*] revealed the following main parameters and features of a blob: blob is a region of nonlocaly increased electron density which is 3–10 times higher than the background level, with sizes of the order of 100–1000 km in the horizontal direction. A plasma blob drifts in anti-sunward direction across the polar cap with velocities of 250–1000 m/s. The electron temperature in blobs is low and unstructured, indicating that energetic particles do not precipitated into the blobs. In some cases blobs may also form simultaneously in geomagnetically conjugate regions.

The generation mechanism of large-scale blobs in the polar cap is still not clear. Some mechanisms of their formation were proposed in a number of experimental and model studies [*Stepanov et al.,* 1992; *Sojka et al.,* 1993; *Rodger et al.,* 1994; *Mingalev and Mingaleva,* 1995; *Anderson et al.,* 1996; *Walker et al.,* 1999], in which blobs are considered to originate in the dayside or cusp/cleft regions.

## 2. Experimental Results and Discussion

Ground-based measurements. The data of high-latitude ionospheric stations of vertical (VS) and oblique (OS) sounding of Yakutian meridional chain (Glong = 130$^o$) – Tixie Bay (L = 5.57) and Kotelny Isl. (L = 6.00) for 1981–1982, 1986 and 1990–1991 were analyzed. The analyzed period enveloped an interval approximately from 18.00 to 06.00 hours local time (09.00 UT – 20.00 UT; LT = UT + 9 hours). The stations operated in a standard mode in every 15 min.

Processing of the ground ionospheric data was precded by determination of the criterion or signature of plasma blobs, registered on VS and OS ionograms [*Mamrukov et al.,* 2000]. It is known that in blobs the electron density is increased and precipitating particles are not observed. Hence, in ionograms the tracks of reflections should be observed with the following basic criteria: the track of reflection from a plasma blob should have a critical frequency and it should be higher than the critical frequency of the regular F2-layer; these reflections should not be too diffuse; minimum frequency in the ionosphere ($f_{\min}$) should be about

1 – 1.5 MHz.

Figure 1 shows a sequence of ionograms from Tixie Bay station for December 8, 1981 when the reflections from plasma blobs were registered. It is seen that blob frequency is higher than the frequency of the regular layer (>10 MHz) and $f_{min}$ corresponds to the above criterion. For this event the velocity of plasma blob movement is about 400 m/s.

In Figure 2 variations of maximum frequencies of F2–layer over the Tixie Bay ionospheric station for several days are shown. An ordinate axis is frequency values in MHz, and an abscissa axis is Universal Time in hours (UT). Figure 2 shows that on November 10, 1981 the station recorded three intervals of successive frequency increases at 12.00 – 15.00 UT, close to 16.00 UT and at 17.00 – 20.00 UT, with maximum at ~8 MHz, ~9 and ~11 MHz,

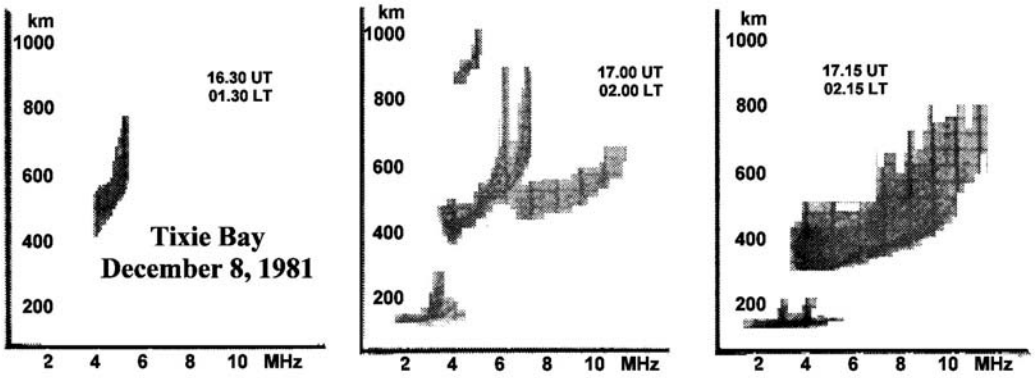


**Figure 1.** The series of ionograms obtained by Tixie Bay station on December 8, 1981 where the plasma blobs reflections were registered.

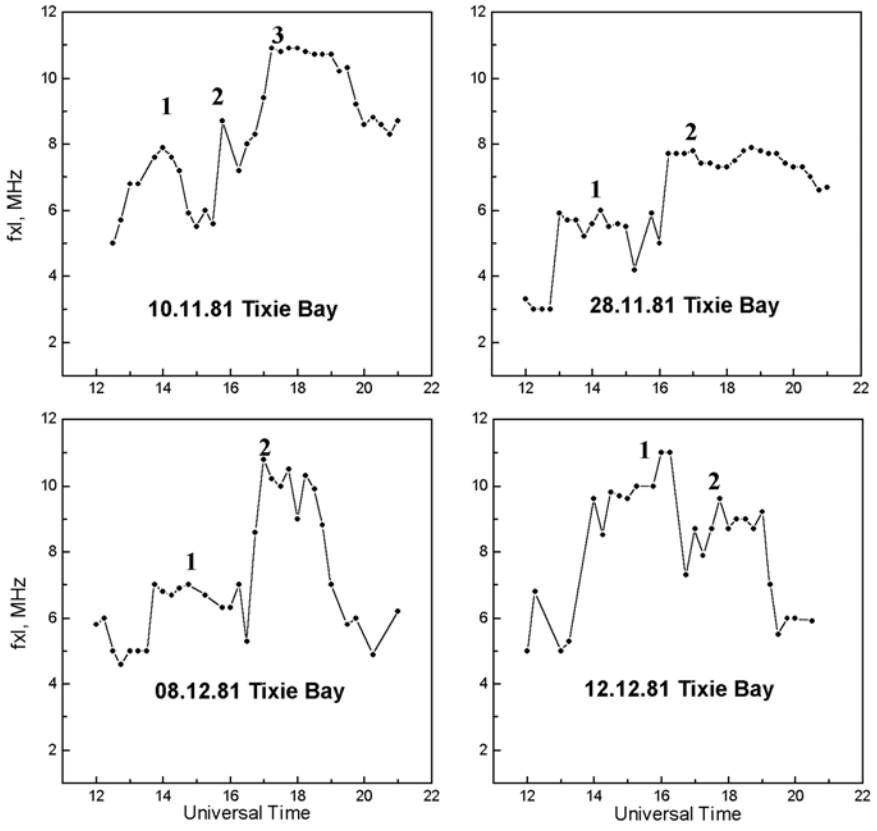


**Figure 2.** Variations of critical frequencies of F2 layer over Tixie Bay ionospheric station during 4 specific days-respectively.

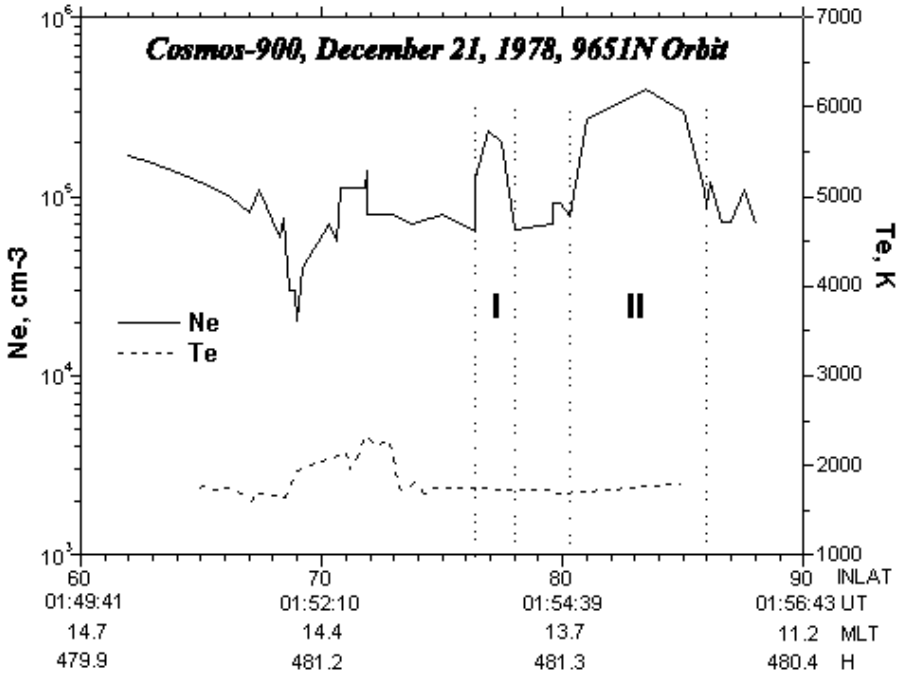


**Figure 3.** **I**onospheric plasma large-scale blobs recorded by the satellite in the polar cap (example).

Such abnormal raises of frequency (or density) in night hours, when there are no sources of plasma ionization at the F-layer heights, permit to assume that these regions of increased densities are generated not locally. A raise, and then decrease of frequency of radioreflections evidences that the blob at first enters "field of sight" of ionosonde and then goes out of it (multifrequency sounding was carried out along geomagnetic meridian toward North direction). The only possible reason for such behavior can be that the velocity of plasma drift is higher than corotation velocity at ionospheric heights. Later, the station can observe other blob hitting in "field of sight" of ionosonde.

Cosmos–900 satellite measurements. We also considered data of Cosmos-900 satellite for 1978–1979. Measurements of electron density and temperature at satellite altitude and invariant latitudes from 60 up to 90° were analyzed. Throughput November, 1978 – to August, 1979.

More than 700 passes in northern and southern hemispheres (407 passes in northern and 325 – in southern) were analysed. The plasma blobs in the satellite data were determined by the following signatures: 2 times or more increase of electron density above the background level; temperature of electrons is at the background level; the horizontal scale sizes should be more than 100 km.

In Figure 3 an example of satellite registration of large-scale blobs of ionospheric plasma in the polar cap on December 21, 1978 is shown. The satellite registered two plasma blobs (marked as I and II). Their horizontal scale sizes along the satellite trajectory are about 170 and 650 km, and electron density in the maximum of blobs is 4.3 and 5.7 times higher, than the density background level (about $10^5$ см$^{-3}$), respectively. Electron temperature during blob registration is as usual 1700-1800°K as usual.

Figure 4 illustrates the occurrence frequency of plasma blobs in ground-based and satellite data as a function of the month of the year. It is seen, that the blob occurrence frequency has maximum, both in ground-based and in satellite data, during winter months, whereas during summer months the blobs practically are not observed. This is possibly connected to the fact that in summer months it is difficult to identify blobs due to large background density of the ionosphere. The dashed line shows seasonal variations obtained in the southern hemisphere by COSMOS–900.

Model calculations. The model of stationary convection (IZMEM) was applied to calculations of drift trajectories of polar blobs [*Levitin et al.,* 1984]. This model is developed on the basis of high-latitude magnetic station data and it takes into account changes of $B_y$ and $B_z$ components of interplanetary magnetic field (IMF).

Figure 5*a* presents the general convection pattern for August 8, 1979 (23.43 UT) in polar coordinates of invariant colatitude and local magnetic time.

Here, positions of the polar cusp (two arcs marking an equatorial and polar boundaries of the cusp) and

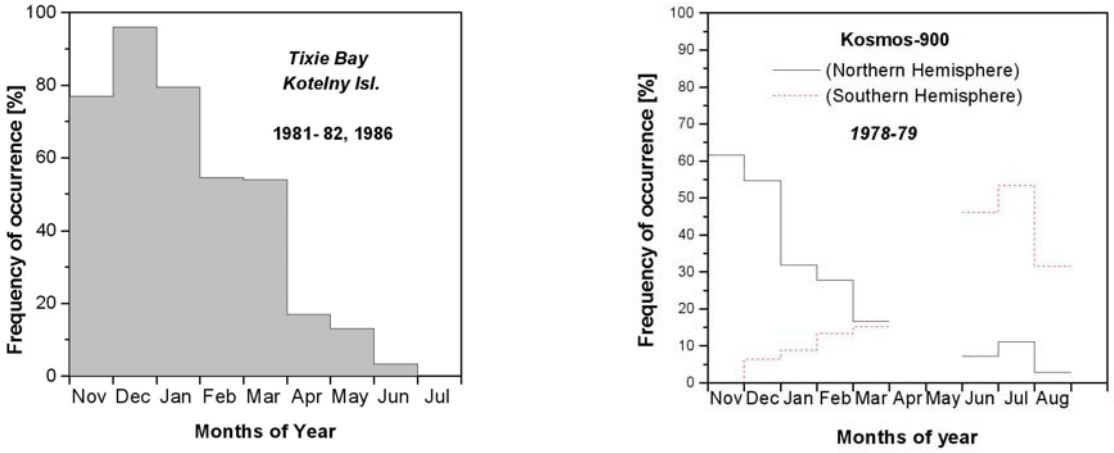


**Figure 4.** Plasma blob frequency recorded by the ground stations (left) and the satellite (right).

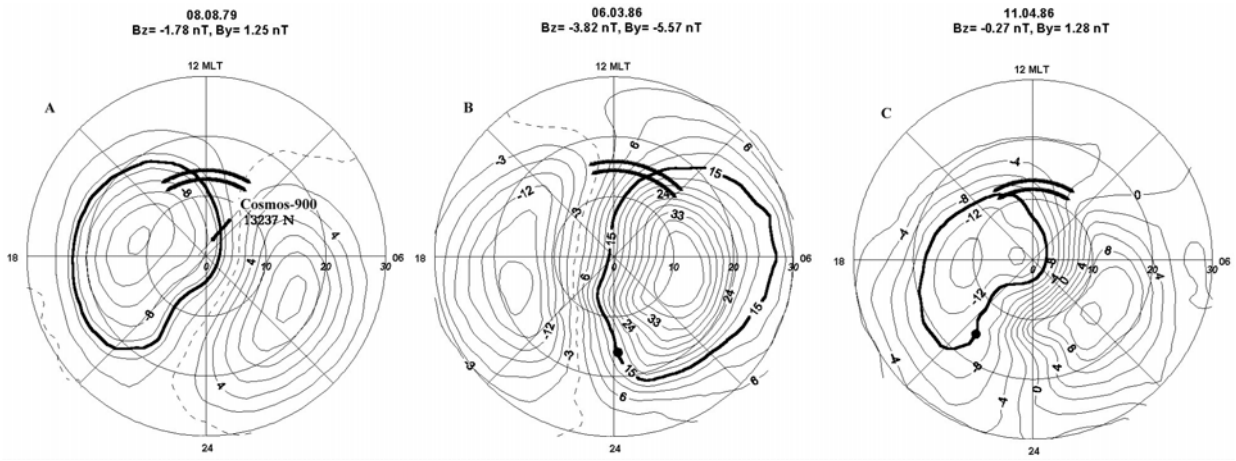


**Figure 5.** Blob drift trajectories for different IMF conditions.

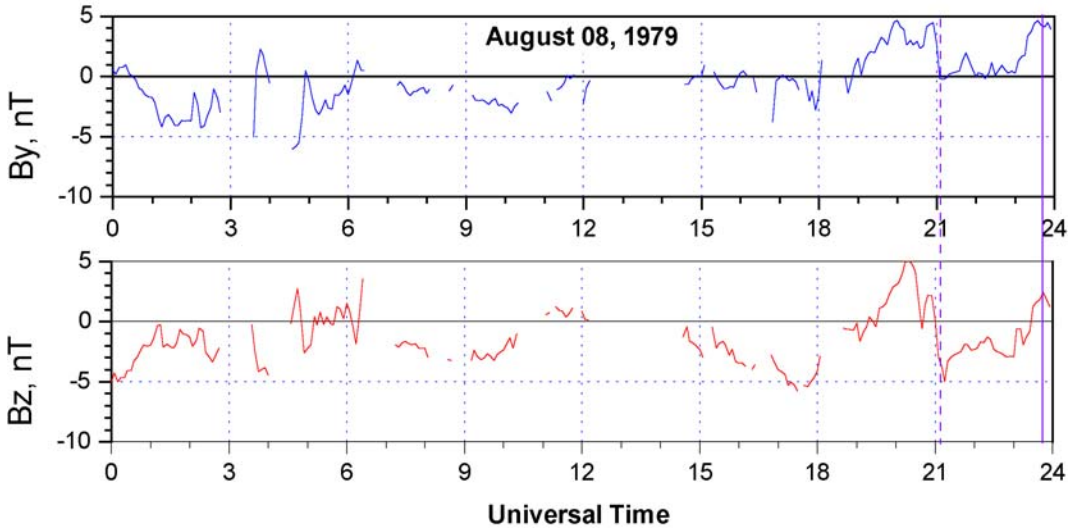


**Figure 6.** Variation of IMP parameters on August 8, 1979.

plasma blob measured by COSMOS-900 satellite, (bold segment on 13237N satellite orbit) are imposed on lines of large-scale convection calculated by IZMEM stationary model. The horizontal size of the blob is about 500 km. The latitude of the cusp equatorial boundary is calculated by the formula:

$$\Lambda_{\text{equat}} = 77.2 + 0.11\, B_z,$$

where the first term in the right part of a linear relation is invariant latitude in degrees, and $B_z$ value is in nT [*Newell et al.,* 1989]. Longitudinal extent of the cusp is about 1.5 hours on both sides from a midday meridian within $-3 < B_y < 3$ nT. The shift of the whole cusp region to the evening or morning side is observed during $B_y > 3$ and $B_y < -3$, correspondingly [*Maynard et al.*, 1997]. The IMP−8 satellite data shows the sharp changes of IMF parameters at 21.13 UT when $B_y$-component has varied from 4 down to 0 nT, and $B_z$–component – from 2 down to −4 nT within 15 minutes (Figure 6). After that moment and till the moment of satellite registration of plasma blob at 23.43 UT (about $\Delta t$ = 150 min), the values of IMF $B_y$ and $B_z$ remained on the same levels without sharp variations. Average values of IMF parameters which were used in model calculations for this time are the following: $B_z = -1.78$ nT and $B_y = 1.25$ nT. The planetary Kp index of geomagnetic activity was equal to 2. As it is seen from Figure 5*a*, the lines of convection corresponding to plasma blob position, originate in the cusp region. The distance between the cusp and blob's position is $S$ = 1228 km. Hence, the calculated velocity of plasma blob is $V_{cal}$ = 136 m/s, and model velocity is $V_{mod}$ = 176 m/s.

Figure 5*b* shows the case when the blob was observed by Kotelny Island station (ILat = 69.5°) on March 6, 1986 at 15.15 UT (00.15 LT). The position of the blob in invariant latitude is ILat = 74.1°. The values of IMF parameters are: for $B_z = -3.82$ nT and for $B_y = -5.57$ nT during the time interval of $\Delta t$ = 80 min. Planetary index of geomagnetic activity was Kp = 5–. As it can be seen, the lines of large-scale morning convection originate from cusp region again. The distance is $S$ = 3629 km, and the calculated and model velocities are, *Vcal* = 756 m/s, *Vmod* = 459 m/s, accordingly. Figure 5*c* presents the case from Tixie Bay station (ILat = 65.1°) on April 11, 1986 at 12.30 UT (21.30 LT). The values of IMF parameters are: $B_z = -0.27$ nT and $B_y = 1.28$ nT during time interval of $\Delta t$ = 375 min. A planetary index of geomagnetic activity was Kp = 1–. This time the lines of convection belong to the evening cell of large-scale convection and originate from cusp region also. The distance between the cusp and blob's position is $S$ = 3630 km. Calculated and model velocities are *Vcal* = 161 m/s, *Vmo*d = 224 m/s.

Thus, for the found cases of quasi-stationary convection after an impulse change of IMF parameters, the model calculations show that the formation of ionization blob happens in the dayside polar cusp/cleft region. It testifies the effectiveness of the generation mechanism of the blobs in the cusp region by non-adiabatic pressure of ionospheric plasma at the boundary of opposite plasma flows [*Stepanov et al*., 1992]. The discrepancies in calculated and model velocities of blobs (or transport time), in our opinion, are related to non-stationarity of large-scale convection, whereas in calculations on the basis of stationary model, the small-scale variations of IMF parameters are smoothed. Hence, more precise calculations with respect to non-stationary models of convection are necessary.

## 3. Conclusion

High-latitude ionospheric data from Yakutian meridional chain (Tixie Bay and Kotelny Island stations) and COSMOS-900 satellite for the winter, equinox and summer months were analyzed. The following results were obtained:

- Basing on the analysis of the large scope of ground-based and satellite data the criteria of plasma blobs at polar latitudes were defined;
- Winter is the time of utmost frequency of plasma blobs;
- The back-tracing modeling of trajectory of polar blobs, using stationary model of the electric field, shows that the blobs originate from dayside cusp/cleft region. Thus it is confirmed that blobs are formed in the dayside cusp during sharp changes of the interplanetary magnetic field.

**Acknowledgments**. This work was supported by grant No. 03–05–96081 of the Russian Foundation of Basic Research.

## References

Anderson, D. N., D. T. Decker, and C. E. Valladares, Modeling boundary blobs using time varying convection, *Geophys. Res. Lett., 23*, 579, 1996.

Baker, K. B., R. A. Greenwald, J. M. Ruohoniemi et al., PACE. Polar Anglo-American conjugate experiment, *EOS*, *70,* 785, 1989.

Banks, P. M., C. L. Rino, and V. B. Wickwar, Incoherent scatter radar observations of westward electric field and plasma densities in the auroral ionosphere, *J. Geophys. Res., 79,* 187, 1974.

Buchau, J., B. W. Reinisch, E. J. Weber, and J. G. Moore, Structure and dynamics of the winter polar cap F region, *Radio Sci., 18*, 995, 1983.

Buchau, J., and B. W. Reinisch, Electron density structures in the polar F-region, *Adv. Space Res*., *14,* N11(10), 29, 1991.

Coley, W. R., and R. A. Heelis, Adaptive identification and characterization of polar ionization patches, *J. Geophys. Res.*, *100,* 23819, 1995.

Levitin, A. E., Ya. I. Feldstein, R. G. Afonina et al., Model of large-scale electric field and currents in high-latitude ionosphere (I-VI), Moscow, Gidrometeoizdat, 1984.

Mamrukov, A. P., V. L. Khalipov, L. D. Filippov et al., Geophysical information on oblique echoes in high latitudes and their classification, *Irkutsk: Issled. Geomagn. Aeron. Fizike Solntsa (in Russian)*, *111*, 14, 2000.

Maynard, N. C., E. J.Weber, D. R.Weimer et al., How wide in magnetic local time is the cusp? An event study. *J. Geophys. Res., 102*, 4765, 1997.

Mingalev, V. S., and G. I. Mingaleva, Possible formation mechanism of "patches" and "blobs" ionization in ionosphere F-Layer, *Geomagn. and Aeron. (in Russian), 35*, N5, 136, 1995.

Newell, P. T., C. -I. Meng, D. G. Sibeck, and R. Lepping, Some low-altitude cusp dependencies on the interplanetary magnetic field, *J. Geophys. Res., 94*, 8921, 1989.

Rodger, A. S., M. Pinnock, J. R. Dudeney et al., A new mechanism for polar patch formation, *J. Geophys. Res*., *99*, 6425, 1994.

Sojka, J. J., M. D. Bowline, R. W. Schunk et al., Modeling polar cap F-region patches using time variyng convection, *Geophys.Res. Lett.*, *20*, 1783, 1993.

Sojka, J. J., M. D. Bowline, and R. W. Schunk, Patches in the polar ionosphere: UT and seasonal dependence, *J. Geophys. Res., 99,* 14959, 1994.

Stepanov, A. E., Yu. I. Galperin, C. Beghin, and A. A. Serov, Measurements of the large-scale ionospheric plasma blobs from Aureol-3 satellite at polar latitudes, *Cosmic Res.(in Russian), 30*, 534, 1992.

Stepanov, A. E., V. L. Khalipov, and E. K. Zikrach, Blob measurements in high-latitude ionosphere, *Irkutsk: Issled. Geomagn. Aeron. Fizike Solntsa, 109, part 2*, 168, 1999a.

Stepanov, A. E., V. L. Khalipov, E. K. Zikrach, and V. V. Afonin, Ionospheric plasma blob characteristics on ground-based and satellite measurements, in *Physics of Auroral Phenomena*, Proc.XXII Annual Seminar, Apatity, 97-100, 1999*b*.

Tsunoda, R. T., High latitude F-region irregularities: A review and synthesis, *Rev. Geophys., 26*, 719, 1988.

Valladeres, C. E., S. Basu, J. Buchau, and E. Friis-Christensen, Experimental evidence for the formation and entry of patches into the polar cap, *Radio Sci*., *29*, 167, 1994.

Walker, I. K., J. Moen, L. Kersley, and D. A. Lorentzen, On the possible role of cusp/cleft precipitation in the formation of polar-cap patches, *Ann. Geophys., 17*, 1298, 1999.

Weber, E. J., J. Buchau, J. G. Moore et al., F layer ionization patches in the polar cap, *J. Geophys. Res., 89*, 1683, 1984.

Weber, E. J., J. A. Klobuchar, J. Buchau et al., Polar cap F-layer patches: structure and dynamics, *J. Geophys. Res*., *91,* 12121, 1986.

---

A. E. Stepanov, Institute of Cosmophysical Research and Aeronomy, Siberian Branch of Russian Academy of Sciences, 677891, Yakutsk, 31 Lenin Ave., Russia.
a_l_stepanov@ikfia.ysn.ru

V. L. Khalipov, Space Research Institute, Russian Academy of Sciences, 117810, Moscow, 84/32 Pofsoyuznaya Str., Russia.
khalipov@iki.rssi.ru

# Influence of AGW of the lithospheric origin on the ionosphere before earthquakes

O. E. Gotynyan[1], V. M. Ivchenko[1], Yu. G. Rapoport[1], and M. Parrot[2]

[1] Kiev Taras Shevchenko National Univeristy, Kiev, Ukraine
[2] Centre National de la Recherche Scientifique, Orleans Cedex 2, France

**Abstract.** An accurate 2D numerical model for AGW excitation by lithospheric gas source taking into account reactive GW modes is proposed. Ionospheric F region response to excitation by AGW radiated from single lithospheric gas source into an ideal atmosphere is investigated. Considerable difference in the values of electron concentration relative change for AGW excited by lithospheric sources of different shapes is proven. AGW periods corresponding to maximal value of ionospheric response are found. Characteristic values and spatial and temporal scales of electron concentration disturbances in the F layer of ionosphere obtained in numerical simulation are close to those values of ionospheric disturbances observed before earthquakes and reported in literature.

## 1. Introduction

On the basis of observation data and theoretical results we can identify, roughly speaking, three channels of seismoionospheric coupling: electromagnetic channel [*Grimalsky et al*., 2002], electrostatic-photochemistry channel [*Grimalsky et al*., 2003] and acoustic-gravity wave [*Gohberg et al*., 1996; *Gohberg and Shalimov*, 1998; *Gotynyan et al*., 2001] channel. Combined effects such as electrostatic, AGW and electromagnetic effects [*Sorokin et al*., 2003] or AGW turbulent heating and photochemistry effects in the E-region of the ionosphere [*De Jager*, 1990] can also cause observable phenomena in the ionosphere before and during earthquakes. These effects are important for studying the processes of energy transmission from the lithosphere and troposphere to the ionosphere and for ionospheric monitoring using both ground-base technique and satellite observational systems.

The present work is dedicated to the AGW channel of seismoionospheric coupling. Physical basis of this channel is the phenomena observed in the lithosphere, mesosphere, lower thermosphere and ionosphere and also in the F-region of the ionosphere. There are such phenomena as green-house effect gas release from the lithosphere which is intensified before earthquakes [*Gohberg et al*., 1996; *Gotynyan et al*., 2001], sesmogravity oscillations with the periods of the order of 1 hour typical for AGW which can modulate gas release [*Gohberg et al*., 1996], wind generation and change diffusion coefficient due to AGW turbulence in the lower thermosphere which causes redistribution of atmosphere constituents by altitude before earthquakes [*Didebulidze et al.*, 1990], variations of intensity of ionospheric glows in E and F [*Gladyshev and Fishkova.*, 1994] regions of the ionosphere with periods typical for AGW (or gravity waves (GW), long-period branch of AGW), variations of plasma critical frequency [*Gohberg et al*., 1996; *Popov et al*., 1996]. Chain of processes: excitation of AGW as seeding factor of Rayleigh-Taylor instability [*Huang and Kelley*, 1996] – Rayleigh-Taylor instability development- growth of plasma bubbles in the F-region of the ionosphere accompanied by decrease of 630 nm line intensity before earthquakes [*Gladyshev and Fishkova.*, 1994] – development of plasma instabilities and turbulence on the edges of plasma bubbles with steep gradients of plasma density [*Ossakov*, 1981] can be caused also by AGW of the lithospheric origin. Recently evidences of an influence of AGW caused plasma turbulence on the equatorial anomaly were found in satellite data [*Molchanov et al*., 2002].

AGW channel of the coupling "lithosphere and lower atmosphere-ionosphere" is important not only for seismoionospheric monitoring. The same processes can be caused by AGW excited by cyclones, typhoons, hurricanes, volcano and other meteorological processes and natural hazards [*Gavrilov*, 1997]. Ionospheric effects caused by AGW propagating "from the below to the top" can be also used as very sensitive instrument in the "natural space plasma laboratory" for indication of plasma instabilities developing with AGW participation (such as Rayleigh-Taylor [*Huang and Kelley*, 1996], Perkins [*Huang et al.,* 1994], AGW-photochemistry [*De Jager*, 1990] and others types of instabilities).

In the papers [*Gohberg et al*., 1996; *Gohberg and Shalimov*, 1998] where the model of GW excitation by lithospheric green-effect gases was proposed, no real boundary conditions for lithospheric GW source have been used and reactive (non-propagating) modes of AGW have not been taken into account. Also, an influence of spatial (shape) and temporal (period) properties of AGW lithospheric source on the characteristics of ionospheric response (in particular, relative change of electron concentration in the F-region) have not been considered before. In the present paper an accurate numerical model of AGW excitation by of gases lithospheric origin is presented, see Section 2. Relations describing ionospheric response to excitation by AGW are presented in Section 3. The results of numerical calculations of AGW excited by 1D lithospheric gas source (using 2D numerical model for AGW and ionospheric response) are presented in Section 4. A role of reactive modes in the AGW excitation is considered. Ionospheric response to AGW in F region and influence of geomagnetic field obliqueness on a value of this response as well as temporal characteristic (period) of AGW lithospheric 1D source are investigated. To illustrate an influence on relative electron concentration change of the lithospheric AGW source spatial shape, 2D symmetrical lithospheric AGW source is considered and corresponding ionospheric response is investigated.

## 2. The model of the AGW generation and propagation

The set of hydrodynamics equations describing AGW with a heat source, source of mass and a force source is of the form [*Hines*, 1960]

$$\rho\frac{d\vec{\mathrm{v}}}{dt} = -\vec{\nabla}p + \rho\vec{g} + \rho\vec{F}\,,$$
$$\frac{d\rho}{dt} + \rho div\vec{\mathrm{v}} = Q\,, \qquad (1)$$
$$\frac{dp}{dt} + \vec{\mathrm{v}}\vec{\nabla}p = c^2(\frac{\partial\rho}{\partial t} + \vec{\mathrm{v}}\vec{\nabla}\rho) + A\rho\,,$$

where $\rho$, $\vec{\mathrm{v}}$, $p$, $\vec{g}$ and $c$ are density, velocity and pressure of neutral atmosphere and gravity acceleration, respectively, $d/dt \equiv \partial/\partial t + \vec{\mathrm{v}}\vec{\nabla}$, $\vec{e}_z$ and $\vec{F} = F_z\vec{e}_z$ are unit vertical vector (in $z$ direction) and the force function, respectively, $Q(\vec{r}, t)$ and $\mathrm{A}(\vec{r}, t)$ are densities of the mass and heat sources respectively which are determined by gases released from the lithosphere. In [*Gohberg et al*., 1996], the system (1) was solved for GW, long-period branch of AGW, without taking into account non-propagating (reactive) modes and with step-like source without specifying boundary conditions. An accurate model of AGW excitation with derivation of effective boundary conditions on the Earth surface was built first in [*Gotynyan et al*., 2001]. As the journal where the paper [*Gotynyan et al*., 2001] was published is hardly accessible for the western reader, we briefly review the "main points" of this model. Here we dwell on the influence on ionospheric response of spatial (shape) and temporal (period) characteristics of the lithospheric gas AGW source and consider an ideal and isothermal atmosphere. Periodical lateral (zero) boundary conditions are used for the AGW field at fictitious lateral walls (Figure 1) based far enough from the region where AGW field is calculated, to use discrete instead of continuous Fourier spectrum of AGW (Figure 1). The upper boundary condition is a condition of AGW radiation. The spatial distribution of 1D ground source vertical velocity is taken in the form [*Gohberg et al*., 1996; *Gotynyan et al*., 2001]

$$\mathrm{v}_z^{\mathrm{src}}(x) \approx \Delta z\, A \approx \frac{\Delta z}{gH}\frac{\omega k_b \Delta T}{m_n}\mathrm{ch}^{-2}\left(\frac{x}{l}\right), \qquad (2)$$

where $\Delta T$ (~3 K) is the amplitude of the temperature anomaly, caused by green-effect gases, $l$ (~100 km) is the lithospheric source width, $\Delta z$ (~3 m) is a thickness of near-ground gas layer, containing green-effect gases (such as $CO_2$), $\omega$ and $\tau = 2\pi/\omega$ are frequency and corresponding period of the lithospheric gas source (or equivalent frequency of lithospheric gas flow modulation), $k_B$, g and $H$ are Boltzmann constant, free-fall acceleration and atmosphere scale high, respectively, $m_n$ is an average mass of neutral atmosphere particles.

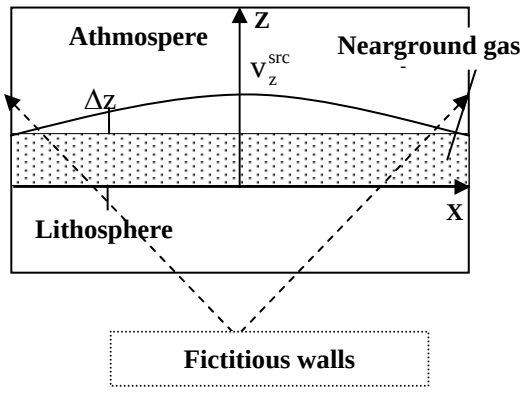


**Figure 1.** AGW source in near ground gas layer.

Reactive modes are taken into account in the present paper, in distinction to paper [*Gohberg et al*., 1996]. These modes do not propagate in the atmosphere. They are excited on medium inhomogeneities. In particular, lithospheric AGW source excites reactive AGW modes in the semi-infinite atmosphere. Although reactive modes cannot propagate themselves, they can change sufficiently amplitudes of propagating AGW modes dispersion law (in a case of 2D propagation of AGW excited by 1D lithospheric source, Figure 1) is [*Hines*, 1960]:

$$\omega^2 = \frac{c^2}{2}\left(k_{xm}^2 + k'^2_{zm} + \frac{1}{4H^2}\right) \pm \sqrt{\frac{c^4}{4}\left(k_{xm}^2 + k'^2_{zm} + \frac{1}{4H^2}\right)^2 - (\gamma-1)g^2 k_{xm}^2}, \quad (3a)$$

or

$$k_{zm}' = \pm\sqrt{k_{xm}^2\left(\frac{\omega_b^2}{\omega^2}-1\right) + \frac{\omega^2}{c^2} - \frac{1}{4H^2}}, \quad (3b)$$

where $m$ is number of the mode under consideration,

$$k_{zm} = \frac{i}{2H} + k'_{zm}, \quad (3c)$$

$k_{xm}$ and $k_{zm}$ are horizontal wave number and a real part of vertical wave number, respectively [*Hines*, 1960 ], time dependence for all variables is taken in the form $\sim e^{i\omega t}$, $c$ is the sound velocity, $\omega_b = \frac{g\sqrt{\gamma-1}}{c}$ is the Brunt-Vaisala frequency, the component $\frac{i}{2H}$ of a vertical wave number describes the effect of atmosphere stratification in the gravity field [*Hines*, 1960]. As follows from (3b), for modes with horizontal wave number satisfying the condition

$$k_{zm}'^2 = k_{xm}^2\left(\frac{\omega_b^2}{\omega^2}-1\right) + \frac{\omega^2}{c^2} - \frac{1}{4H^2} < 0, \quad (3d)$$

components $k'_{zm}$ of vertical wave numbers, $k_{zm}$ are purely imaginary and corresponding modes are

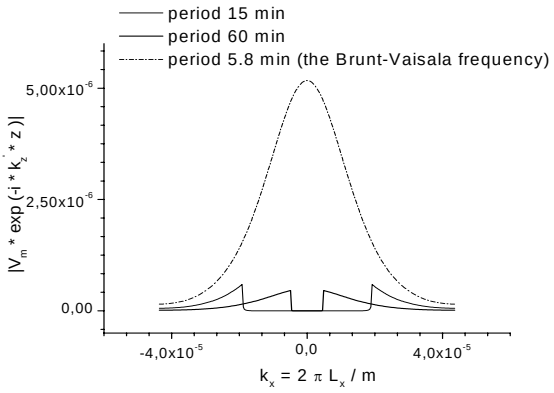


**Figure 2.** Dependence of amplitudes of harmonics on horizontal component of wave number for different periods of AGW at the altitude $Z$=250 km. $L_x$ is a distance between fictitious walls shown in the Figure1. The gap in the center corresponds to the reactive modes.

"reactive". Inscription "with reactive modes" in Figure 3 means that we do not neglect the term $\omega^2/c^2 - 1/4H^2$ in (*3b*) and therefore, in our model in distinction to [*Gohberg et al*., 1996], some of modes are reactive (solid curve in Figure 3). Amplitude of vertical velocity, $|\vec{v}_z|$, changes by more than one order of magnitude for AGW with the period of 15 min at altitude of 250 km if reactive modes are taken into account (Figure 3).

### 3. Influence of the AGW on the ionosphere

In accordance with drift approximation [*Kendall and Pickering*, 1967], inertialess ion (and electron) concentration, $N$, under conditions of neutrality and

$$\frac{m_e\nu_{en}}{eH_0} << \frac{m_i\nu_{in}}{eH_0} << 1,$$
$$|eN\vec{u}_i| << \frac{m_e\nu_{en}}{m_i\nu_{in}}|\vec{j}^{\parallel}|, \quad (4a)$$

is governed by the equation [*Kendall and Pickering*, 1967]:

$$\frac{\partial N}{\partial t} = -\nabla(N\vec{u}_i) + S - L. \quad (4b)$$

Here

$$\vec{u}_i \approx \vec{u}_i^{\parallel} = \vec{v}^{\parallel} - \frac{D_a}{2k_B T_i}[\vec{\nabla}^{\parallel}(p_e + p_i) - N m_i \vec{g}^{\parallel}], \quad (5)$$

$e$, $m_{e,i}$, $\nu_{en,in}$, are electron charge, electron and ion masses and electron-neutral and ion-neutral collision frequencies, respectively, $\vec{u}_i$ is ion drift velocity, index "$\parallel$" means projection of corresponding vector on the direction of geomagnetic field, $p_{e,i}$ are electron and ion pressure, respectively, $\vec{j}$ is plasma current, $D_a, T_i$ are ambipolar diffusion coefficient and ion temperature, respectively. $S$ and

$$L = \alpha N_N (N - N_{e0}) \quad (6)$$

are electron production and loss rates, respectively, $N_{e0}$ is steady-state concentration of charged particles in plasma. For the case of isothermal electrons and ions, $T_e = T_i$, ambipolar diffusion coefficient is

$$D_a = 2k_B T_i / (m_i \nu_{in} + m_e \nu_{en}) \approx 2k_B T_i / m_i \nu_{in}, \quad (7a)$$

$$\nu_{in,en} = q_{in,en} N_N, \quad (7b)$$

$$N_N = \rho / m_n$$

is a concentration of neutral particles, coefficients $\alpha$ and $q_{in,en}$ are described in [*Genkin et al.*, 1987] and [*Gershman*, 1974], respectively.

Linearization of equations (4*b*)–(7*a*) gives (for night conditions, when $S = 0$, or neglecting disturbances caused by the presence of $S$ in equation (4*b*))

$$\tilde{N}_{em} \equiv \tilde{N}_e(k_m) = \frac{G}{D},$$

$$G = -[D_B N_{e0} + \frac{\partial N_{e0}}{\partial z}\cos\theta]v_B + \hat{L}_1 \tilde{N}_N + \alpha N_{e0} \tilde{N}_N, \quad (8a)$$

$$D = D_t - \frac{D_a}{2} D_B^2 + \frac{1}{2H}(\frac{\partial D_a}{\partial z} + D_a D_z) + \alpha N_{N0}$$

Here $\tilde{N}_e = N - N_{e0}$, $\tilde{N}_N = N_N - N_{N0}$, $N_{N0}$ is steady-state concentration of neutral particles, $v_B$ is AGW velocity projection on the geomagnetic field direction, $D_t = i\omega, D_z = -ik_{zm}$, $D_B = \vec{e}_b \cdot \vec{\nabla} = -i(e_{bx}k_{xm} + e_{bz}k_{zm})$ $\vec{e}_b$ is a unit vector along geomagnetic field, $\theta$ is an angle between geomagnetic field and vertical direction, $\hat{L}_1 \tilde{N}_N$ describes an influence of AGW on the frequency of collisions between charged particles and neutrals and on the recombination intensity,

$$\hat{L}_1 \tilde{N}_N \equiv [\frac{D_a}{2}\frac{\partial N_{e0}}{\partial z}\frac{1}{N_{eo}} e_{zB} D_B + \frac{1}{2}\frac{\partial}{\partial z}(D_a \frac{1}{N_{N0}}\frac{\partial N_{e0}}{\partial z})]\tilde{N}_N + \frac{1}{2H}\frac{D_a}{N_{N0}}\frac{\partial}{\partial z}(N_{e0}\tilde{N}_N) \quad (8b)$$

Note that using linearized form of the system (1) and equation (7*b*), it is easy to express the value $\tilde{N}_N$ through the neutral particle's velocity projection, $v_B$. After collecting components of Fourier transform, one can get using (8):

$$\frac{N'_e}{N_{e0}}(x_n, z) = e^{z/(2H)} \sum_{m=-Nx/2}^{Nx/2} [\tilde{N}_{em} / N_{e0}] \cdot e^{-ik_{xm}x_n - ik_{zm}z}, \quad (9)$$

where $x_n = L_x \frac{n}{N_x}$, $L_x$ and $N_x$ are distance between fictitious lateral walls (shown in Figure 1) and number of Fourier harmonics taken into account, respectively, $n = \overline{1 - N_x/2, N_x/2}$ is integer number.

## 4. Results of numerical calculations

We would like to dwell on some features of AGW field with regard to the definite shape and spectrum characteristics of the lithospheric gas source. In the present paper we investigate one of the mechanisms of AGW influence on the ionospheric electron concentration, namely carrying out of charged particles

by neutral AGW "wind". We exclude the effects of AGW influence on recombination and collision frequency and put in the present calculations $\hat{L}_1 = 0, \alpha = 0$. Plasma parameters of the ionospheric F-region are taken from [*Kendall and Pickering*, 1967]. Figures 2, 3 illustrate the influence of the reactive modes on the excitation and penetration of the wave field through the atmosphere into ionospheric altitudes. Figure 2 shows, that in accordance with the condition (3*c*), a number of reactive modes increases with decreasing AGW frequency (below the Brunt-Vaisala frequency). For frequencies larger than Brunt-Vaisala frequency, there are no reactive modes. Figure 2 shows the result of multiplication of amplitudes, $V_m$ of the modes of lithospheric source with different horizontal wave numbers, $k_{xm}$, by exponential factor, $\exp(-ik_{zm}z)$, where $k_{xm}$ is determined by equations. (3*b*,*c*). For reactive modes (see equations. (3*b*-*d*)), $k_{xm}$ are imaginary, therefore reactive modes decay exponentially as altitude grows and turn into non-reactive modes (for which $k'_{zm}$ are purely real). At the same time, reactive modes correspond to the maximum of spectral distribution of the AGW source under consideration. By this reason reactive modes are of a great importance for the characterization of an influence of the lithospheric AGW source on the ionosphere. In calculations [*Gohberg et al*., 1996], the term $\frac{\omega^2}{c^2} - \frac{1}{4H^2}$ in expression (3*b*) was neglected, what is valid only for GW modes with very small frequencies, $\omega$ and large enough horizontal wave numbers, $k_{xm}$. As seen from equations. (3*b*, c), in this case reactive modes do not exist at all, in other words, values $k_{zm}'$ are real.

For comparison, we made calculations in the approximation [*Gohberg et al*., 1996], taking into account reactive modes (solid curve in Figure 3) and disregarding them (dashed curve in Figure 3). The amplitudes of vertical velocity, $|\tilde{v}_z|$, at the altitude of 250 km, determined using accurate dispersion low (3*a*,*b*) and in approximation [*Gohberg et al*., 1996] ("without taking reactive modes into account") differ for AGW with the period of 15 min more than by an order of magnitude. For AGW with the period of 60 min this difference is as big as about 4 times.

Figure 4 shows qualitative difference in spatial distribution of vertical velocity normalized to its maximum value for AGW with the frequencies equal to and lower than Brunt-Vaisala frequency (corresponding periods are 5.8 min and 15 and 60 min, respectively). These distributions have one and two spatial peaks in the first and second cases respectively.

Figure 5 illustrates spatial distributions of the vertical and horizontal velocity amplitudes for AGW with the period of 60 min. As seen from Figure 5, for AGW with the period of 60 min, maximum value of horizontal velocity exceeds sufficiently (in few times) maximum value of vertical velocity at the altitude of 250 km. Numerical calculations (not presented here) show that for AGW with the period of 15 min maximum values of amplitudes of horizontal and vertical velocities are comparable. We would like to point out, that all numerical calculations for 1D lithospheric source of AGW with different frequencies are done using equation (1) where all others parameters, except frequencies, are the same. Spatial distributions of electron concentration relative changes for 15 and 60 mins periods are presented in Figures 6*a* and *b*., respectively. Maximum value of electron concentration relative change caused by AGW with the period of 60 min exceeds sufficiently the corresponding value for AGW with the period of 15 min (Figures. 6*a* and 6*b*, respectively).

As seen from Figure 6, for AGW with smaller period, 15 min., the distribution of electron concentration relative change, $N_e'/N_{e0}$, has larger spatial asymmetry than for AGW with larger period, 60 min. This is caused by the following reason.

In accordance with equation (8a), $|N_e'/N_{e0}| \sim |v_B|$ (in the considered case $\hat{L}_1 = 0$, $\alpha$=0).

In oblique geomagnetic field and in the absence of vertical AGW velocity component, $v_z$, the absolute

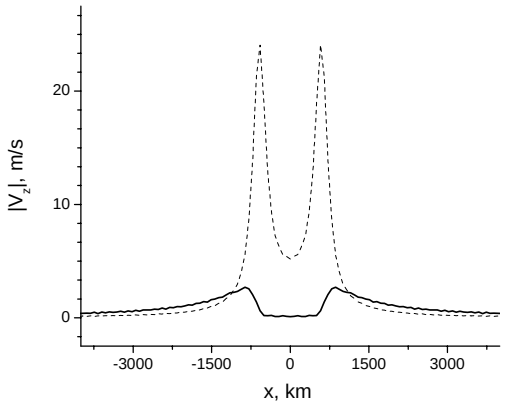


**Figure 3.** Spatial distribution of the AGW vertical velocity taking into account reactive modes (solid curve) and disregarding them (dotted line). AGW period is 15 min, altitude is 250 km; AGW are excited by 1D lithospheric source described by equation (1).

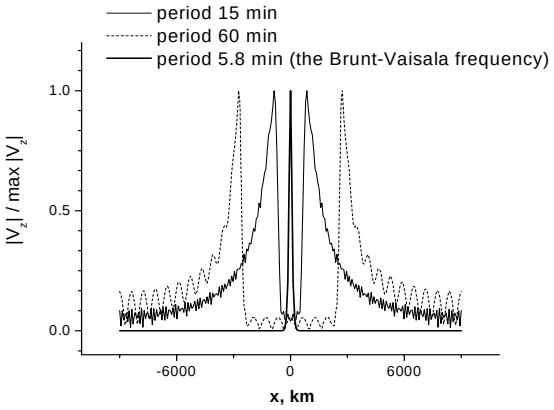


**Figure 4.** Spatial distribution of AGW vertical velocity, normalized on the maximum value, for different periods at the altitude of 250 km (for 1D lithospheric source).

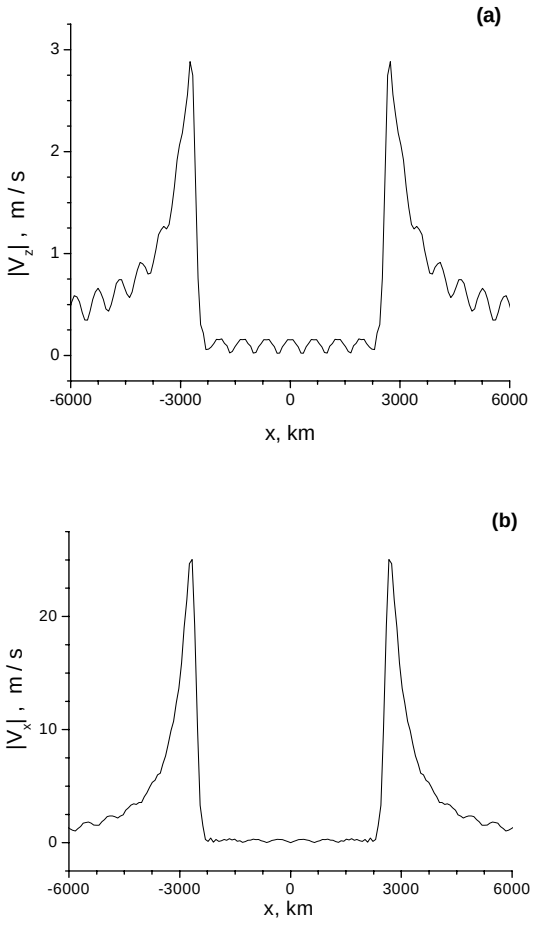


**Figure 5.** Spatial distribution of the velocity of AGW excited by 1D lithospheric source with period 60 min.: (a) – vertical velocity; (b) – horizontal velocity.

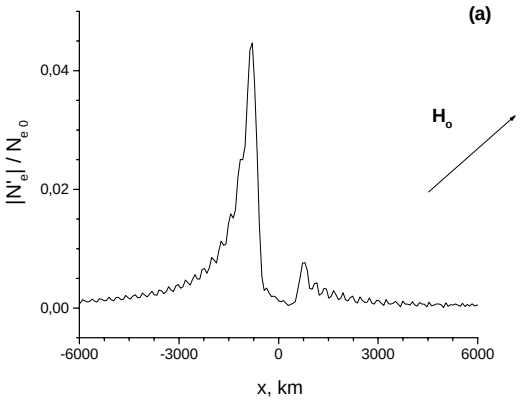


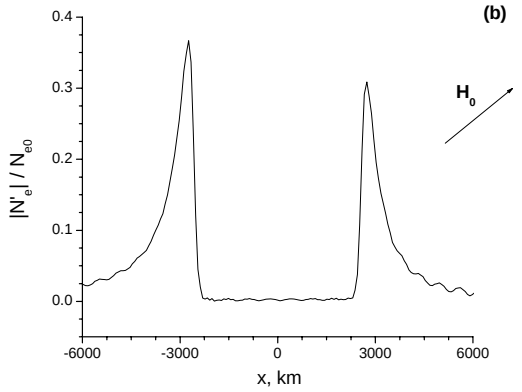


**Figure 6.** Spatial distribution of the electron concentration relative change at the altitude of 250 km (AGW are excited by 1D lithospheric source): (a) – period of AGW is 15 min; (b) – period of AGW is 60 min. Angle between magnetic field and vertical direction, $\theta$, is equal to 45°.

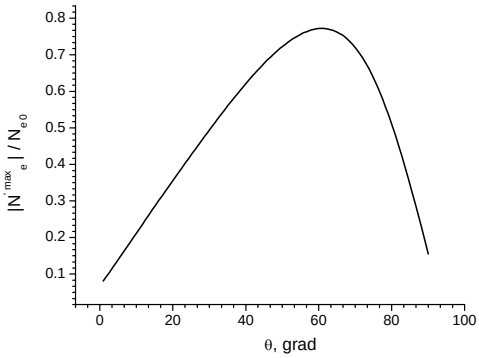


**Figure 7.** Dependence of the value of maximum in electron concentration spatial distribution on the angle between magnetic field and vertical direction, $\theta$ (for 1D lithospheric gas source). Width of source, AGW period and altitude are equal to 100 km, 73 min. and 250 km, respectively.

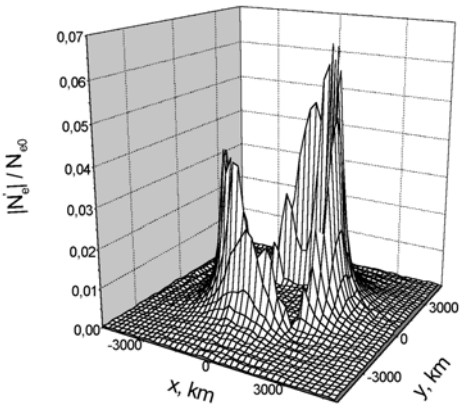


**Figure 8.** The spatial distribution of the electron concentration relative change caused by AGW radiated by 2D lithospheric symmetrical source with the period of 50 min and characteristic dimension 100 km. Altitude is 250 km, angle between geomagnetic field and vertical direction is 60°, angle between directions of the geomagnetic field horizontal projection and X axis is 45°.

value of AGW velocity projection on geomagnetic field direction, $|v_B|$ would be the same for AGW propagating to both sides X > 0 and X < 0 (Figure 5) from the lithospheric source. Therefore, spatial asymmetry in the $N_e'/N_{e0}$ distribution is caused by the presence of both vertical and horizontal components of AGW velocity (Figure 5). Horizontal AGW velocity exceeds vertical velocity for AGW with the periods of both 60 min. (Figure 5) and 15 min. (not shown here). But for AGW source with the period of 60 min. relative difference between horizontal and vertical AGW velocity at 250 km (Figure 5) is larger than for AGW with the period of 15 min. Therefore contribution of vertical AGW velocity component into the value $|v_B|$ is relatively smaller and spatial asymmetry of the $N_e'/N_{e0}$ distribution is also smaller for the AGW with the period of 60 min., than for AGW with the period of 15 min. (Figure 6). Figure 7 shows that for given parameters of 1D lithosperic gas source and the altitude of 250 km, maximum value of ionospheric response, $N_e'/N_{e0}$ is reached when the angle between magnetic field and vertical direction, $\theta$, is equal to 60°.

Spatial distribution of the electron concentration relative change is presented in Figure 8 for symmetrical 2D source. It illustrates the effect of the lithospheric AGW source spatial shape. As seen from Figure 8, spatial asymmetry of $N_e'/N_{e0}$ distribution in 3D case for symmetrical AGW source is determined by angles of geomagnetic field inclination relative to both horizontal and vertical axes. The value of ionospheric response to AGW radiated by 1D lithospheric source (which can be also considered as "very elongated" 2D source and can correspond to elongated fracture in the Earth crust) (Figures 6*b*, 7) is almost one order of magnitude larger than the corresponding value for 2D symmetrical lithospheric source (Figure 8). Dependence of maximum in the spatial distribution of the electron concentration relative change at the altitude of 250 km on AGW period is investigated (figures are not presented here). It is shown that maximal possible ionospheric responses at 250 km correspond to AGW periods, $\tau$ equal to 73 min and ~40 min for 1D and symmetrical 2D lithospheric AGW sources, respectively. By their order of magnitude these periods are close to the ones of typical plasma frequency variations observed prior to earthquakes [*Gohberg et al.*, 1996; *Popov et al.*, 1996]. These calculations as well as calculations presented in Figures 6 and 8 show rather strong dependence of ionospheric response on spatial (shape) and temporal (period) characteristics of the lithospheric AGW source.

The following conclusions can be made on the basis of presented modelling.

## 5. Conclusions

1. Numerical 2D model of AGW excitation by lithospheric gas source in the ideal atmosphere is developed. Different types of the "excitation forces" of AGW are compared and numerical convergence (of an order of 1.5% for 500 spatial modes) is proven. Reactive modes are taken into account. Their presence leads to the change of velocity amplitude at the altitude of 250 km by an order of magnitude and several times change for AGW with the periods of 15 min and 1 hour respectively .

3. Values of AGW velocity amplitudes are of the order of few dozens of km/s, and relative change of electron concentration reaches few dozens of percents at the altitudes of 250 km for AGW with the periods of the order of 1 hour and spatial scales of the order of thousand kilometers. Absolute values as well as spatial and temporal characteristics of ionospheric response to AGW excitation coincide by an order of magnitude with the results of observations [*Gohberg et al.*, 1996; *Popov et al.*, 1996; *Meister et al.*, 2002; *Liperovsky et al.*, 2002] of ionospheric F-layer

response to the processes of strong earthquake's (M > 4.5–5) preparation.

4. In the inclined geomagnetic field spatial distribution of electron concentration relative change in the ionospheric F-layer has considerable asymmetry. Maximum value of ionospheric response is achieved when the angle between magnetic field and vertical directions reaches 60°.
5. Spatial (shape) and temporal (frequency) characteristics of lithospheric gas source affect substantially the value of ionospheric response to AGW excitation. Amplitudes of ionospheric response to AGW excited by 2D symmetrical source are almost by an order of magnitude less than for 1D lithospheric source. Dependence of maximum in relative electron concentration distribution, $N'^{\max}_e / N_{e0}$, on AGW period has maximum. The periods of 1D lithospheric source and symmetrical 2D lithospheric source are as long as 73 min. and ~40 min, respectively.

More detailed study of the influence of lithospheric source's spatial and temporal characteristics on the ionospheric response taking into account realistic atmosphere model including wind, non-isothermity, losses and AGW and plasma instabilities will be a subject of the further works.

**References**


De Jager, P. C., An instability of acoustic waves caused by radiation and the influence of chemical reactions on it. *J. Geophys. Res*., *95,* 10,017, 1990.

Didebulidze, G. G., L. M. Fishkova, A. D. Pataraya and T. I. Toroshelidze, Investigation of the night sky airglow near the epicenter of the earthquake Proceed. Of the JointVarenna-Abastumani-ESA-Nagoya-Potsdam workshop on "Plasma Astrophysics", Telavi, Georgia, USSR, 4-12 June 1990 (ESA SP-311, Aug. 1990), pp. 321-327.

Gavrilov, N. M., Parametrization of momentum and energy deposition from gravity waves generated by tropospheric hydrodynamic sources. *Ann. Geophysicae*, *15*, 1570, 1997.

Genkin, L. G., L. M. Eruhimov, E. N. Myasnikov, M. M. Shvarts, To the question of generation and buoyancy of isothermal ionospheric and chromospheric "bubbles". *Izvestiya Vuzov Radiofizika* (in Russian), *30*, 567, 1987.

Gershman, B. N., Dynamics of ionospheric plasma, Moskow, *Nauka*, 1974.

Gladishev, V. A., L. M. Fishkova, Optical research of seismoactivity effects of the ionosphere. In: Electromagnetic phenomena related to earthquake prediction. Ed. M. Hayakawa, Y. Fujinawa. TERRAPUB Tokyo, pp. 375-380, 1994.

Gohberg, M. B., A. K. Nekrasov, S. L. Shalimov, To the influence of nonstable release of green-effect gases in seismically active regions on the ionosphere, *Physics of the Earth* ("*Fizika Zemli*", in Russian), *8*, 52, 1996.

Gohberg, M., S. Shalimov, Lithosphere-ionosphere coupling mechanism and its application to the earthquake in Iran on June 20, 1990. A review of ionospheric measurements and basic assumptions, *Physics of the Earth and Planetary Interiors*, *105*, 211, 1998.

Gotynyan, O. E., V. M. Ivchenko, Yu. G. Rapoport, Model of the internal gravity waves excited by lithospheric greenhouse effect gases, *Space Science and Technology* ("Kosmichna nauka i tehnologiya"). *7*, 26, 2001.

Grimalsky, V. V., I. Kremenetsky, O. K. Cheremnykh, and Yu. G. Rapoport, Spatial and frequency filtration properties of ULF EM radiation of lithospheric origin in the lithosphere-ionosphere-magnetosphere system, in: Seismo Electromagnetics: Lithosphere-Atmosphere-Ionosphere Coupling. Eds. M. Hayakawa and O. A. Molchanov, pp. 363-370, TERRUPUB, Tokyo, 2002.

Grimalskiy, V. V., M. Hayakawa, V. N. Ivchenko, Yu. G. Rapoport, and V. I. Zadoroznii, Penetration of electrostatic field from the lithosphere into the ionosphere and its effect on the D-region before earthquake *Journl. of Atmos. Solar-Terrestr. Phys*., *65*, 391, 2003.

Huang, C. -S., C. A Miller, and M. C. Kelley, Basic properties and gravity wave initiation of the midlatitude F region instability. *Radio Sci*., *29*, 395, 1994.

Huang, C. S., C. Kelley, Nonlinear evolution of equatorial spread of F2. Gravity wave seeding of Rayleigh-Taylor instability, *J. Geophys. Res*., *A101*, 293, 1996.

Hines, C. O., Internal atmospheric gravity waves at ionospheric heights. *Can. J. Phys., 38*, 1441, 1960.

Kendall, P. C., and W. M. Pickering, Magnetoplazma diffusion at F2-region altitudes, *Planet Space Sci*, *15*, 825, 1967.

Liperovsky, V. A., C. V. Meister, K. V. Popov, E. V. Liperovskaya, O. A. Molchanov, A. S. Silina, On the time scales of some seismo-ionospheric effects. In: Seismo Electromagnetics: Lithosphere-Atmosphere-Ionosphere Coupling. Eds. M. Hayakawa and O. A. Molchanov, pp. 325-327, TERRUPUB, Tokyo, 2002.

Meister, C. V., E. V. Liperovskaya, O. A. Molchanov, O. A. Pokhotelov, O. A. Alimov, To the question of spatial scales of seismo-ionospheric effects. In: Seismo Electromagnetics: Lithosphere-Atmosphere-

Ionosphere Coupling. Eds. M. Hayakawa and O. A. Molchanov, pp. 329-3331, TERRUPUB, Tokyo, 2002.

Molchanov, O. A., M. Hayakawa, V. V. Afonin, O. A. Akentieva, E. A. Mareev, V. Yu. Trakhtengerts, Possible influence of siesmicity by gravity waves on the ionospherivc equatorial anomaly from data of IK-24 satellite. 2. Equatorial anomaly and small-scale ionospheric turbulence. In: Seismo Electromagnetics: Lithosphere-Atmosphere-Ionosphere Coupling. Eds. M. Hayakawa and O. A. Molchanov, pp. 287-296, TERRUPUB, Tokyo, 2002.

Ossakov, S., Spread-F theories- a review *J. Atmos Terrestr. Phys*., *43*, 437, 1981.

Popov, K. V., V. A. Liperovskiy, and O. A. Alimov Modification of spectra of night ionospheric F2 layer density variations during the periods of earthquake preparation *Physics of the Earth*, *1*, 93-96, 1996 (in Russian).

Sorokin, V. M., V. M. Chmirev, and A. K. Yashenko, Ionospheric generaion mevchanism of geomagnetic pulsations observed on the Earth's surface before earthquakes. *J. Amos. Solar-Terrestr. Phys*., *64*, 21, 2003.

# Computer simulation of acoustic gravity waves transport from a ground-based source up to ionospheric altitudes

V. O. Rapoport[1], P. A. Bespalov[2], N. A. Mityakov[1],
M. Parrot[3], and N. A. Ryzhov[1]

[1] NIRFI, Nizhny Novgorod, Russia
[2] Institute of Applied Physics, Russian Academy of Science, Nizhny Novgorod, Russia
[3] LPCE/CNRS, Orlean, France

**Abstract.** During the earthquakes infrasonic and acoustic gravity waves may be generated. This phenomenon may be caused by the earth surface motion or by large release of gas prior to the earthquakes. Such waves can propagate up to ionospheric altitudes. The ionospheric disturbances could be detected by satellite or ground-based systems, and this information is useful for the earthquakes activity monitoring. To study this opportunity more in detail we designed an experiment with an artificial ground-based source of monochromatic low frequency acoustic waves. In this report the problem of computer simulation of low frequency acoustic-gravity waves propagation in non-isothermal atmosphere is described. Numerical simulations for wave intensity at ionospheric altitudes (E-layer) were performed for several types of ground-based acoustic sources. The simulations were carried out for waves in the windless stratified media. The temperature profile typical of the standard atmosphere was taken.

## 1. Basic assumptions and equations

Let consider the model problem of acoustic gravity waves in a plane layers of the non-isothermal atmosphere with the temperature profile typical for standard atmosphere [*Brasseur and Solomon*, 1986]. We shall ignore viscosity of the atmosphere assuming that wave frequency is low enough. We shall ignore the influence of winds, though it can significantly affect the results of the actual experiment.

For the basis of calculations we shall take the regular two dimensional linearized set of atmospheric gas dynamics

$$\frac{\partial u}{\partial t}+\frac{1}{\rho_0}\frac{\partial p}{\partial x}=0, \qquad (1a)$$

$$\frac{\partial w}{\partial t}+\frac{1}{\rho_0}\frac{\partial p}{\partial z}-g\frac{\rho}{\rho_0}=0, \qquad (1b)$$

$$\frac{\partial \rho}{\partial t}+\rho_0\frac{\partial u}{\partial x}+w\frac{d\rho_0}{dz}+\rho_0\frac{\partial w}{\partial x}=0, \qquad (1c)$$

$$\frac{\partial p}{\partial t}+w\frac{dp_0}{dz}=c_s^2\left(\frac{\partial \rho}{\partial t}+w\frac{d\rho_0}{dz}\right). \qquad (1d)$$

Here $g$ is an acceleration of gravity, $x$ is the horizontal coordinate, $z$ is the vertical coordinate, $\rho_0(z)$ is the density of the atmosphere, $\rho$ and $p$ are small

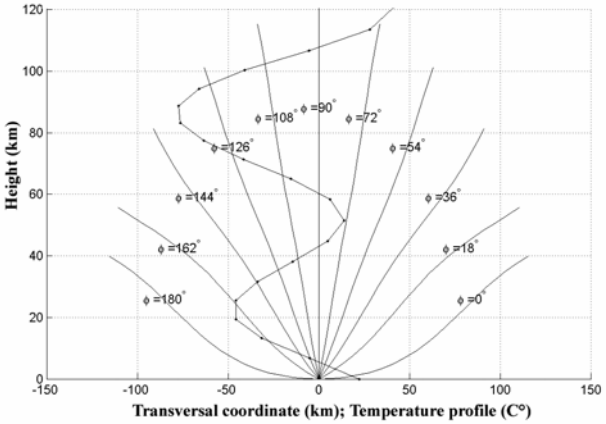


**Figure 1.** The picture shows the ray traces of infrasonic wave in ray approximation. Numbers on picture are zenith angles. The typical temperature profile is shown as well.

perturbations of density and pressure, $w$ and $u$ are vertical and horizontal components of the gas velocity. To simplify the evolution of the equations it is convenient to introduce new field variables

$$W = (\rho_0/\rho_Z)^{1/2}\, w, \quad P = (\rho_0/\rho_Z)^{-1/2}\, p,$$

where $\rho_E$ is the density at the ground level. We have in adiabatic approximation that, $c_S^2 = \frac{\partial p}{\partial \rho}$,

where $C_S$ is the sound velocity. For the monochromatic signal in plane atmosphere layers the solution of the system (1) for field variables can be presented as expansion on transversal wave numbers $k_\perp$. Then for the processes **exp**$(-i\omega t + ik_\perp x)$, we can reduce the system (1) to the following form [*Gossard and Hooke*, 1975]:

$$\frac{\partial P(\omega, k_\perp, z)}{\partial z} = -\Gamma P(\omega, k_\perp, z) + i\frac{P_z}{\omega}\left(\omega^2 - N^2\right) W(\omega, k_\perp, z), \tag{2a}$$

$$\frac{\partial W(\omega, k_\perp, z)}{\partial z} = \Gamma W(\omega, k_\perp, z) + i\frac{1}{\omega\rho_E c_S^2}\left(\omega^2 - k_\perp c_S^2\right) P(\omega, k_\perp, z). \tag{2b}$$

Here $N$ is the Brunt-Vaisala frequency, and $\Gamma$ is the Eckart parameter. For a non-isothermal atmosphere

$$N^2 = \frac{(\gamma-1)g^2}{c_S^2} + \frac{g}{T}\frac{\partial T}{\partial z},$$

$$\Gamma = \frac{(2-\gamma)g}{2c_S^2} - \frac{1}{2T}\frac{\partial T}{\partial z}.$$

where $\gamma$ is the adiabatic exponent.

The equations (2) can be written in more convenient form

$$\frac{\partial P(\omega, k_\perp, z)}{\partial z} = -\Gamma P(\omega, k_\perp, z) + ikZ_0 W(\omega, k_\perp, z), \tag{3a}$$

$$\frac{\partial W(\omega, k_\perp, z)}{\partial z} = i\frac{k}{Z_0} P(\omega, k_\perp, z) + \Gamma W(\omega, k_\perp, z). \tag{3b}$$

Here

$$k^2 = \frac{\left(\omega^2 - N^2\right)\left(\omega^2 - c_S^2 k_\perp^2\right)}{\omega^2 c_S^2},$$

$$Z_0 = \rho_E c_S \left(\frac{\omega^2 - N^2}{\omega^2 - c_S^2 k_\perp^2}\right)^{1/2}.$$

To prepare the equations (3) for numerical calculations it is convenient to introduce dimensionless impedance

$$Z = \frac{P}{WZ_0}.$$

After such substitution we find, that dimensionless impedance satisfies the nonlinear first order Rikkaty equation. This equation can be written in the following form

$$\frac{\partial Z}{\partial z} = i\kappa(1 - Z^2) - 2\chi Z, \tag{4}$$

where $$\chi = \Gamma + \frac{\partial \log Z_0}{2\partial z}$$

Then we shall introduce a boundary condition for ($z\to\infty$) for the equation (4). We consider infrasonic and gravity waves separately bearing in mind that for selected frequencies $k^2 \neq 0$. First of all we shall search for an escaping wave, and for the infrasonic mode it is necessary to substitute $P$ and $W$ proportional to **exp**$(ikz)$. After such substitution we obtain $k^2\,(z\to\infty) = k^2 - \Gamma^2$ and hence

$$Z(z\to\infty) = \left(1 - \frac{\chi^2}{\kappa^2}\right)^{1/2} + i\frac{\chi}{\kappa}. \tag{5}$$

The numerical solutions of the equation (4) with boundary condition (5) are easily found. So we can determine the dependence of the dimensionless impedance on the heights.

Vertical component of the gas velocity in acoustic gravity wave is defined by another linear equation of the first order

$$\frac{\partial W}{\partial z} = (ikZ + \Gamma) W. \tag{6}$$

Let us discuss boundary conditions for this equation. In our case we must assign disturbances the vertical component of the gas velocity in infrasonic wave at the ground level

$$W(\omega, k_\perp, 0) = W_{source}(k_\perp). \qquad (7)$$

(Here we suppose that $k_Z > 0$ everywhere). The numerical solution of the system (4) and (6) with boundary conditions (5) and (7) is carried out as follows. For each transversal wave number $k_\perp$ we solve boundary problems and then it is easy to find the general solution of the task with a model emitter. Then the general solution for vertical velocity is equal to

$$w = \left(\frac{\rho_E}{\rho_0}\right)^{1/2} \cdot \int W \exp(-i\omega t + ik_\perp x) dk_\perp . \qquad (8)$$

## 2. Results of calculation

The results of calculations for ground-based infrasonic wave emitter. It has the power of 1000 W and size of ~1 km. Frequency is assumed to be 0.1 Hz.

The results of calculations for internal gravity wave source on the surface. Frequency is assumed to be 0.001 Hz.

## 3. Conclusion

In this work the calculations for transport of different frequency acoustic gravity waves were performed.

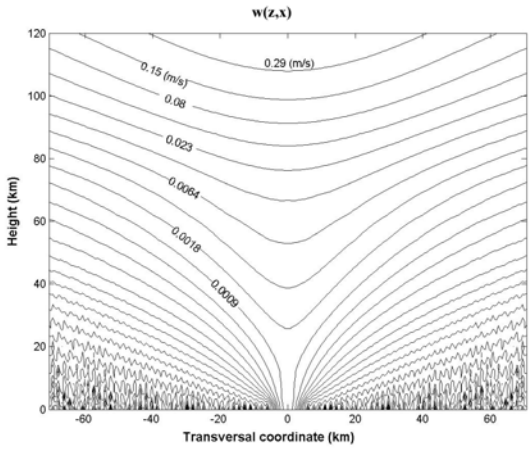


**Figure 2.** Two-dimensional distribution of the infrasonic wave field for rather high altitudes (specifically for the velocity amplitude in m/s).

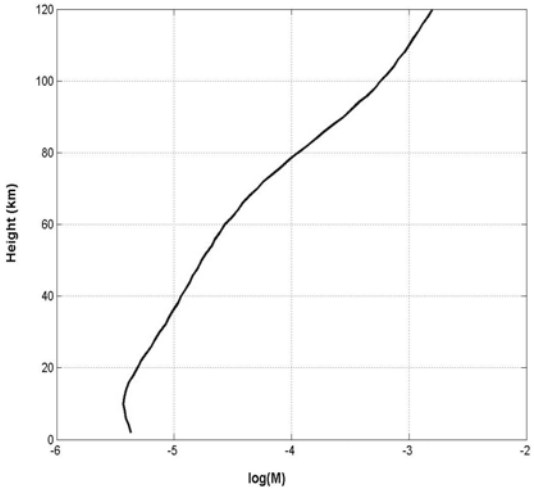


**Figure 3.** The Mach number in the infrasonic wave field over the emitter location.

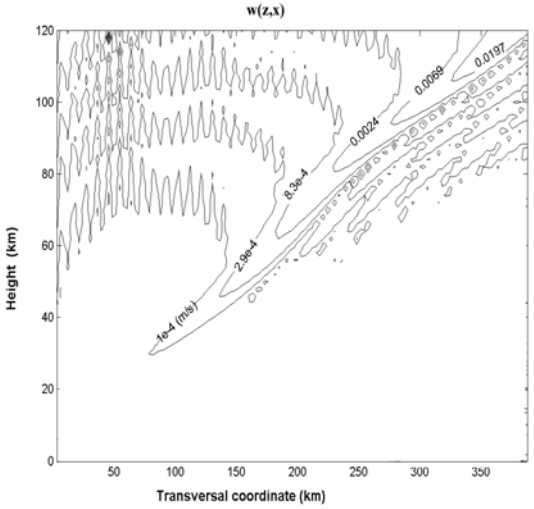


**Figure 4.** Two-dimensional distribution of the internal gravity wave field (specifically for velocity amplitude).

We examine the cases of monochromatic infrasonic and internal gravity waves produced by ground-based source.

For infrasonic exciter next parameters were assumed: frequency – 0.1 Hz; power – 1000 W; horizontal size approximately 1 km. The main results are as follows:

- The region with rather high disturbance has a spot-like form.
- The "spot" is located above the emitter and it's size is about 50 km at the height of 120 km.
- The amplitude of velocity field in this "spot" reaches the value of 0.55 m/s. The Mach number

at the height of 120 km was more than 0.001 due to reduction of density, which promises appreciable probability of detection.

For the internal gravity wave case we assumed that the frequency was 0.001 Hz, power – 1 kW, horizontal size 1 km. The main results are:

- The "spot", it's size being about 50 km, is located 370 km away from the exciter at the height of 120 km.
- The Mach number at the height of 120 km was ≈ 0.05 m/s which 10 km less compared to the case of infrasonic source.

Thus, the calculation shows the possibility of successful ionospheric experiment based on propagation of quasi-monochromatic infrasonic waves from the ground-based emitter.

**Acknowledgements.** The work was partly funded by INTAS grant No. 01–0456, and Russian Foundation for Basic Research grants No. 01–02–17796 and No. 01–02–16680.

## References

Brasseur, G., S. Solomon, Aeronomy of the middle atmosphere. D. Reidel Publishing Company, Dordrecht, 1986.

Gossard, E., W. Hooke, Waves in the atmosphere. Elsevier Scientific Pubblishing Company, Amsterdam – New York, 1975.

# Helioactivity and properties of global tropical cyclogenesis

V. V. Afonin and E. A. Sharkov

Space Research Institute. Profsouznaya str., 84/32. Moscow, 117997. Russia.

**Abstract.** Properties of global cyclogenesis and its relation to the solar activity are studied by analyzing time series of daily numbers of cyclones and the solar activity index F10.7. The study is based on available in SRI time series of number of cyclones (with the account for their lifetime) over 19 years from 1983 to 2001. The first exploratory analysis of relationship between the TC genesis and solar activity index F10.7 has shown that although any given cyclone may be considered as an chaotic event, they arise and evolve under the action of strong control of the Sun. Properties of tropical cyclogenesis and the Earth atmosphere as a unique system in its interaction with the solar emission are presented. It was concluded that the process of TC formation is actually controlled by that part of solar energy which is absorbed by the atmosphere, rather than by the Earth's surface and the TC-effective heating of atmosphere is caused by UV and IR regions of the solar irradiance spectrum.

## 1. Introduction

The study on solving the fundamental problem of atmosphere and ionosphere physics – revealing possible relationship between ionospheric disturbances and heliogeophysical factors with processes of formation and evolution of tropical cyclones (cyclogenesis) and energy balance of cyclonic formations was initiated in Space Research Institute of Russian Academy of Sciences. This study is aimed at solving one of the most unclear problem: revealing the physical mechanisms of intensification and evolution of cyclonic formations.

The solar energy inflows into the atmosphere-Earth's surface system both directly in the form of electromagnetic emissions and through the sun energetic particles via numerous Sun-Magnetosphere-Ionosphere-Troposphere interactions. As the Earth's atmosphere constitutes complicated thermo-aerodynamic structure with complicated kinetic characteristics, the TC genesis may display relations with both direct solar activity indicators and geomagnetic activity processes.

The study is based on available in SRI time series of number of cyclones (with the account for their lifetime) over 19 years from 1983 to 2001 and large database of ionospheric data from three satellites. The study provides for extending the available data bases to create the complex database to be used for search for relationship between different parameters including spatio-temporal relations in the atmosphere and ionosphere dynamics in altitude range 0–3000 km, for revealing the role of heliogeophysical factors in processes of formation and evolution of cyclones and in energy balance of cyclonic formations in terrestrial atmosphere, and for revealing the degree of mutual influence of cyclonic formations and atmosphere-ionosphere system.

The complex computerized database will include the data on tropical cyclones, lower and middle atmosphere,

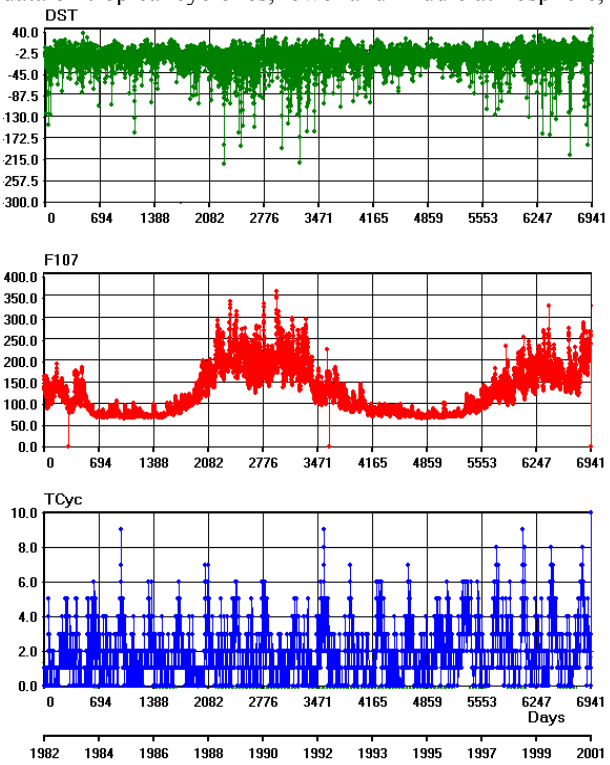


**Figure 1.** Time variations of global number of TC (nTC), F10.7, and $D_{ST}$ over 19 years.

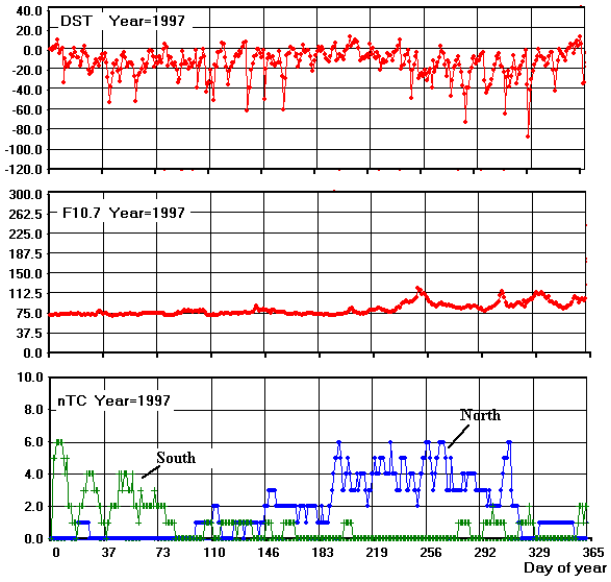


**Figure 2.** Annual variations of nTC, F10.7 и $D_{ST}$.

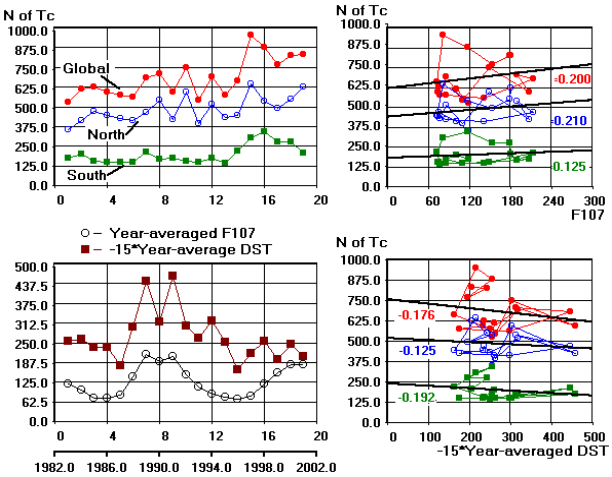


**Figure 3.** (Left) Long scale time variations of year-averaged values for global nTC and separately for Northern and Southern hemispheres with similarly computed values for F107 and $D_{ST}$. (Right) Scatter plots of nTC (global, southern, and northern) against (upper) F10.7 and (lower) DST and corresponding linear regressions (black lines). Correlation factors are indicated by numbers under regression lines.

ionosphere, solar and geophysical indexes, energetic particles in near Earth space, solar wind and emissions in view of investigation of relationship between the tropical cyclogenesis and heliogeophysical factors.

As the first step, we present results of the first exploratory analysis of relationship between the TC genesis time series and solar activity index F10.7.

## 2. Data bases and general analysis

The TC data base, available in SRI, exists in electronic form [*Sharkov*, 2000; *Pokrovskaya and Sharko*, 2001].

The TC database includes detailed set of parameters for each cyclon and allow sorting by any of these parameters. Time variations of global number of TC (nTC), F10.7, and $D_{ST}$ over 19 years are shown in Figure 1. Solar-geophysical parameters ($K_p$, sunspot number Z, $D_{ST}$, and F10.7 were taken from Internet.

The ionospheric data base includes the electron density Ne and electron temperature Te from a number of satellites, including Cosmos-900, Intercosmos-24 (Activnyi), and Intercosmos-25 (APEX). Each of these satellites was operating 2–3 years and had long-time (~1 day) onboard memory. For this first-step study we used only the global number of cyclones, separated in some cases by hemispheres, and the solar activity index F10.7.

**Annual variations** of $D_{ST}$, F10.7 and nTC (tropical cyclogenesis) for minimal solar activity are shown in Figure 2. The quantity nTc is the number of TC at a given day of a year with the account of their lifetime (the global snapshot for a day). The nTc values are separated by hemispheres (green crosses for Southern and blue dots for Northern hemisphere). The scatterplots of global nTc against F10.7 (not shown) clearly show the absence of any correlation. From this figure (and many other similar plots) we may conclude:

- The time series of daily values of nTC, F10.7, and DST show no significant correlation.
- The time series of daily values of nTC, show clear season variation. Year nTC maximums at the North and the South are distinctly spaced in time. In both hemispheres the nTC maximum is observed only during the local summer. Practically no TC are observed during local winter. The intensity of TC in the south is slightly less than in the north.
- Difference in nTC for minimum and maximum SA (represented by F10.7) is mush less that the ratio of corresponding values of F10.7.

To check if TC and F107 are correlated in large time scales (more than 1 year) we compared year-averaged values for nTC, global and separately for Northern and Southern hemispheres, with similarly computed values for F107 and $D_{ST}$ (Figure 3). To present data in the same plot the DST values were scaled by a factor –15. Right panels show scatterplots of each of 3 TC parameters against F10.7 (upper) and $D_{ST}$ (lower). Black lines are corresponding linear regressions. Numbers below these

lines are correlation factors, all of them do not exceed 0.210. It is evident that in large time scales of years no correlation between nTC and the solar and geomagneric activity represented by F10.7 and $D_{ST}$ parameters is observed [*Afonin and Sharkor*, 2003].

Do the TC have "history"? Is it stochastic or somehow "organized" events? To answer these questions we have computed autocorrelation functions nTC and F10.7 time series for maximal and minimal SA, Figure 4. In computing we used circular shift of initial series. More correctly would be to extend initial year time series at both sides by time series for preceding and subsequent years, but this would not change significantly the results.

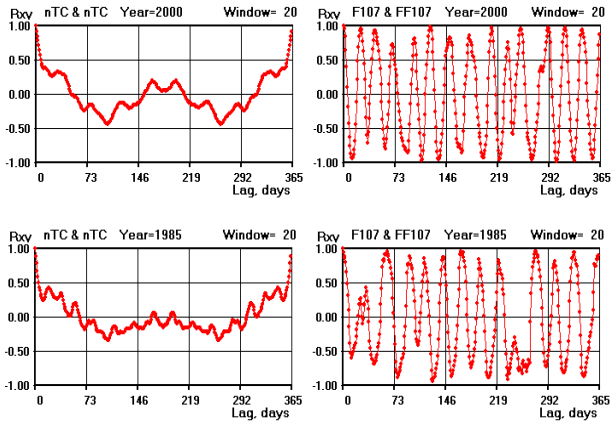


**Figure 4.** Autocorrelation functions for nTC (left) and F10.7 (right) year time series for maximal (2000) and minimal (1985) solar activity.

It is seen that nTC values are autocorrelated during times less than ≤ 4 days, i.e., it is short-living phenomena without long "history" (note that we use time series nTC with account for their lifetime). At larger time lags there is no mutual dependence, each TC may be considered as an stochastic event. On the contrary, the F10.7 time series are well autocorrelated with period close to 27 days and significant 27-day autocorrelation preserves even during solar minimum.

In subsequent analysis we shall use the wavelet transform (WT). As in many cases the WT is considered as nice qualitative pictures, and in most papers, including this, authors use their own program codes, it is reasonable to "calibrate" the WT method, or, in other words, to answer the question: if the WT method can be used for quantitative in addition to qualitative estimates? This has been done and described in details in [*Afonin and Sharkov*, 2003*a*], confirming that our code (using Morlet wavelet) produce correct quantitative estimates.

We have analyzed the "model cyclone" year time series with parameters close to that of real. The model time series consists of two sine half-waves overlayed by noise with the same amplitude. Figure 5 shows the model year time series (upper panel) and its WT-spectrum. The WT-spectrum shows frequency-temporal variations of the signal components. The amplitude (in this case the component power) is color coded (right scale). The time scale (abscissa) show days of year. The frequency axis, LgF, is logariphmic, the minimal [lgF = 0,0] is below, and the maximal frequency lgF = 2,26 is at the top. For convenience, two other scales at the left show corresponding frequencies between $F_{min}$ = 1 (period T = 1 year) and $F_{max}$ = 182,5 (period T = 2 days, the Nyquist frequency of given time series) and corresponding time scales in days.

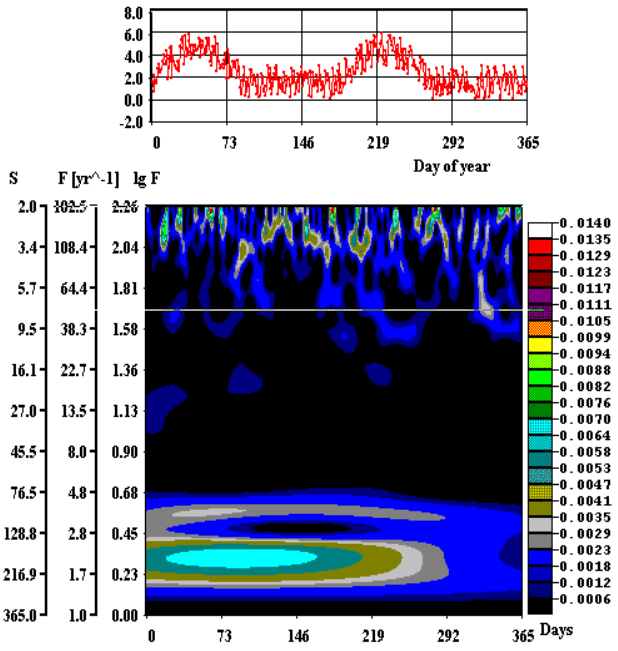


**Figure 5.** WT spectra of model quasi-random TC time series.

As is seen from Figure 5, this quasi-random time series contain mainly time structures with time scales $S \sim 1–3$ days and practically no structures with $S > 10$ days. Therefore WT-spectra of real TC time series the structures with $S \le 10$ days should be neglected; in all real spectra they have much less amplitudes and reflect the randomness of the TC formation process. Large scale structures, corresponding to annual and semi-annual variations are seen in lower part of the spectrum. As the time resolution in this part of the spectrum is small, such large-scale structures should be analyzed using larger time series. In this case of year time series these spectral structures should be considered as qualitative.

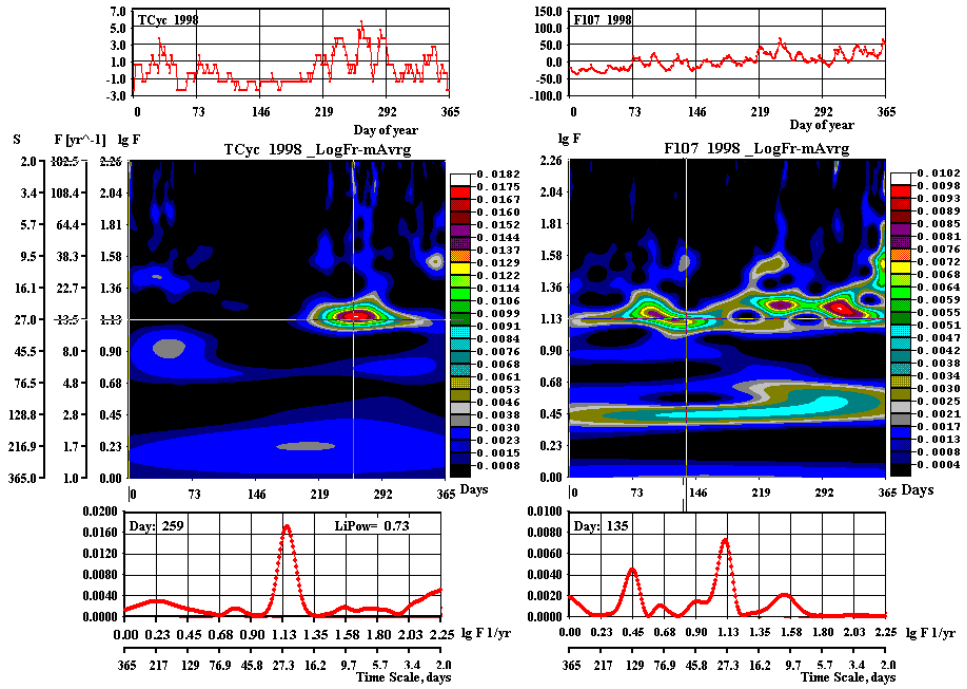


**Figure 6.** WT spectra of global TC time series (left) and F10.7 in solar maximum (1998 ).

### 3. Search for 27-day periodicity (S27)

It is known that the TC formation probability is maximal in locations with highest surface temperature [*Sharkov,* 2000]. As the main initial energy for TC–genesis comes from the Sun, it is reasonable to look for 27-day (S27) variability in TC time series, in spite that the cyclone formation mechanism is not well understood.

**Search for S27 in year time series.** WT spectra of TC and F10.7 year time series for maximal SA are shown in Figure 6. In all spectra the vertical cursors (horizontal lines) are set at the frequency f27, corresponding to 27-day component. The section of WT spectrum along the frequency axis for indicated day of year is shown at the lower panels. This format will be used for all subsequent figures.

Variations of F10.7. In Figure 6 (and in all other similar plots) the presence of f27 component is evident. During SA maximum it displays most clearly. The spectral maximums not always fall on the f27 line, but they are rather close to it. The amplitude variations of this component are rather large. However, it is unlikely to expect the continuity of this spectral line (constancy of amplitude) due to finite length of the sample, evident long term variations in F10.7, as well as due to the fact that 27-day variation in the solar activity is not a single factor of F10.7 variations. These additional factors may "shift" the f27 frequency visible in WT spectra. In this case we can only say that the f27 component is present in WT spectra of F10.7 practically at all times and presents the most pronounced feature.

In TC variations three main features are visible. The first is that the most intensive components fall into mentioned range of time scales $S$ = 10–80 days, quite different to the model WT spectrum (Figure 5). The second is that the most intensive response is in f27 component. During the SA minimum f27 is largest component at the North, while in the South the f27 is absent, and two maximums approximately at the first subharmonic (~54 days) and the second harmonic (~15 days) are observed. It should be noted that in this case the WT-spectra are normalized to the unit value for the whole spectrum power, thus each point presents the instant power of corresponding components. As was shown in Figure 2 the TC displays clear season effect, therefore left part of each TC WT-spectrum results from southern nTC, and the right part from northern nTC. At the minimum of SA we see about the same pattern.

The ratio of characteristic peak amplitudes at the left side to those in the right side is, according to the color scales, about 50%; as the total intensity of TC at the south is less than in the north, the real ratio, if to make WT separately for the northern TC and the southern TC, should be higher.

**Search for S27 in 4- and 5-year time series.** To check the above results we have performed the same procedure for longer time series. WT spectra of global

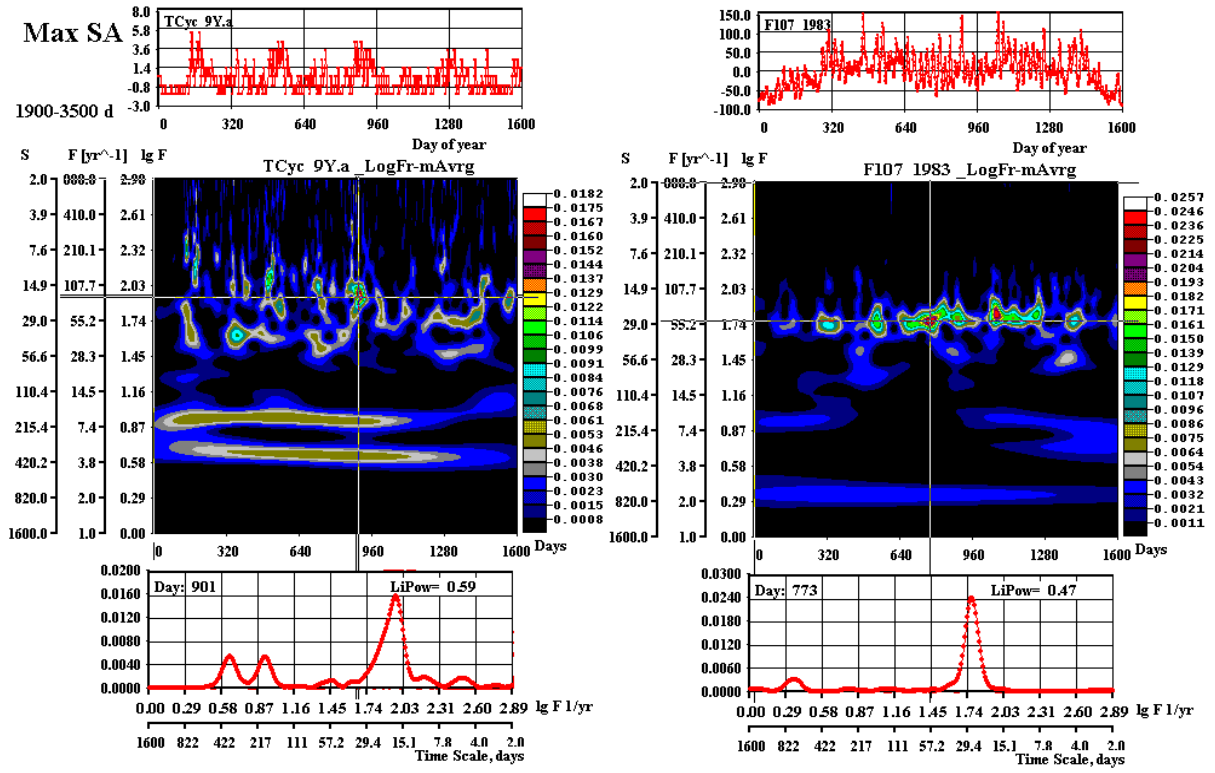


**Figure 7.** WT spectra of global TC (left) and F10.7 (right) for time series 1600 days around the maximum of solar activity.

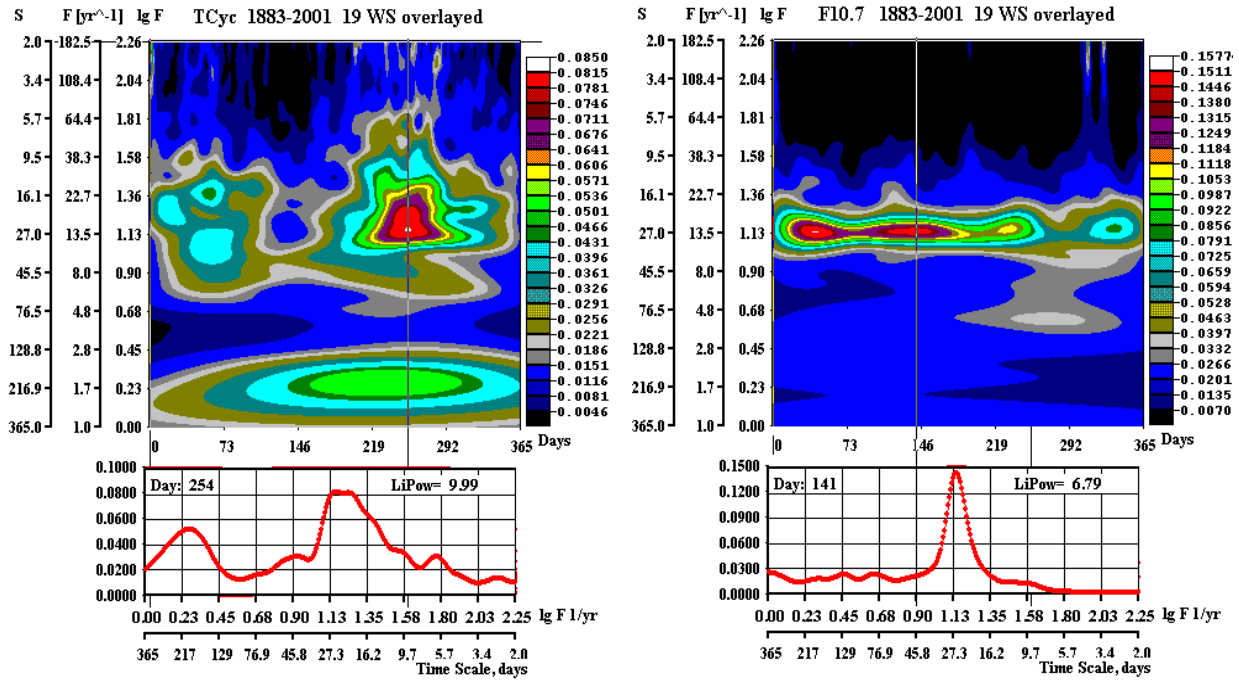


**Figure 8.** WT spectra of global TC (left) and F10.7 averaged over 19 years.

TC 1600 day time series (left) and F10.7 (right) during maximal SA are shown in Figure 7. In this case the $F_{min}$ corresponds to time scale S = 1600 days. The annual and semi-annual structures, reflecting seasonal effect, are clearly seen. What about the TC-genesis as a system, in this case we also can see that the characteristic time scales of nTC form an isolated region in the frequency space, as they are separated in the frequency space both from the "noise" region ($S$ < 10 days) and year and half-year variations and fall into 10–80 days range. The maximal response in this range corresponds to f27 or it is close to f27. In addition, some spectral maxima are observed at frequencies close to harmonics and subharmonics of f27. These frequencies may represent own (possibly resonance) frequencies, and/or they may reflect the external action on the whole global system.

**Average WTS over 19 years.** WT spectra, computed for each of 19 years, were averaged, and the result is shown in Figure 8. This figure confirm the above conclusions. In F10.7 WT spectrum the most pronounced component is 27-day (S27), there are practically no other marked components. In nTC spectrum two distinct regions are evident – the $S$ = 10–80 days region and semi-annual structure reflecting well defined seasonal effect in the process of TC genesis. In this $S$ = 10–80 day region the most pronounced is $S$ = 27 day component, observable in Northern hemisphere practically at all times. In southern hemisphere the maximal response is observed most often at frequencies close to harmonics and subharmonics of main frequency f27. The f27 maximum appears to be the forced response at the frequency of external solar action.

Responces at harmonics and subharmonics of f27 indicate to nonlinearity of the tropical cyclogenesis system. The fact that in most cases responces do not coincide with f27 and its harmonics and subharmonics allow to assume that the tropical cyclogenesis reflects complicated behavior of aero-thermo-hydrodynamical system the Earth's surface-atmosphere having its own, possibly resonant, frequencies.

## 4. Effect of solar heat input to the Earth's atmosphere

Clear season variation in nTC assumes that direct heat inflow from the Sun constitutes the main controlling agent for formation and evolution of tropical cyclogenesis in the Earth's atmosphere. In this paper we shall search for possible correlation between nTC time series with direct heat inflow into the Earth's atmosphere, rather than to the atmosphere-surface system. We consider two characteristic latitudes, the tropic of Cancer and tropic of Capricorn, between which the sun moves during a year. For both locations the Table lists zenith angles $\alpha$ for two times during the year, summer and winter solstices. Between these dates the $\alpha$ angle varies linearly. According to cosine law the heat energy from the sun, reaching the top of the earth atmosphere and further absorbed by the atmosphere and by the earth's surface, is $S = S_0 \cos(\alpha)$, where $S_0$ is the heat absorbed at $\alpha = 0$, i.e. when the sun is in zenith of the point considered. Here we neglect the reflected part of the solar emission and consider only the relative to the year maximum solar heat input $Sp = S(\alpha) / S_0$ (in %). Variations of zenith angles $\alpha$ and heat input Sp during a year are shown in Figure 9 for Northern (left) and Southern (right) hemispheres on upper panels. Here black line is the angle $\alpha$ between the local vertical and the highest Sun elevation at the noon, and the red line is relative heat inflow Sp (in %).

| Latitude | $\alpha$/Date of $S_{max}$. | $\alpha$/Date of $S_{min}$. |
|---|---|---|
| 22.5° Cancer | 0° / June 22 | 45° / Dec. 22 |
| -22.5° Capricorn | 0° / Dec. 22 | 45° / June 22 |

Blue line, labeled as nTc shows the observed number of TC for each day of the year summed up over 19 years. We see that both curves, Sp and nTc are symmetric, and while the Sp curve is centered relative the summer solstice day ($N$ = 173), the nTc curve has significant, more than two month, delay. That is why no correlation between nTc and F10.7 time series was found in previous analysis [*Afonin and Sharkov*, 2003*a*].

The green line (snTc) is the same nTc curve, but shifted to the coincidence with the maximum of heat input Sp curve. Now we see that both Sp and shifted snTc curves are symmetric relative to the summer solstice day, and both have maximum at this day. We see that while the heat input fall off as $\cos(\alpha)$, the number of cyclones do the same much faster. It means that some agent exists that decreases the TC formation probability.

To see how well both curve are correlated the shifted TC time series, snTc, was plotted against the heat input curve Sp (midlle panels). Both wings of snTc curve practically coincide with each other, confirming thereby that the rate of TC formation depend on the heat input. The dependence nTc(Sp) is strongly nonlinear. The important feature is existence of some critical value of heat input Spc, below which the number of cyclones vanishes. This value is, as is seen from Figure 9, about 70% of the year maximum. This dependence was approximated by exponential function $Y=exp((Sp–Spc)/C)$, where $Spc$ is critical value of Sp, and $C$ is a constant. This function approximates the observed shifted curve snTc rather well. Lower panels show maps of mean square error for fitting the $Y=exp((Sp–Spc)/C)$ function to the year variation of snTC, shifted by $Lag$ days. The minimums are very narrow; note that limits of ordinate in these maps are 74 and 78 units of 100, and 7.5 and 8.5 for abscissa. From these maps one can see that the TC-genesis responds to the

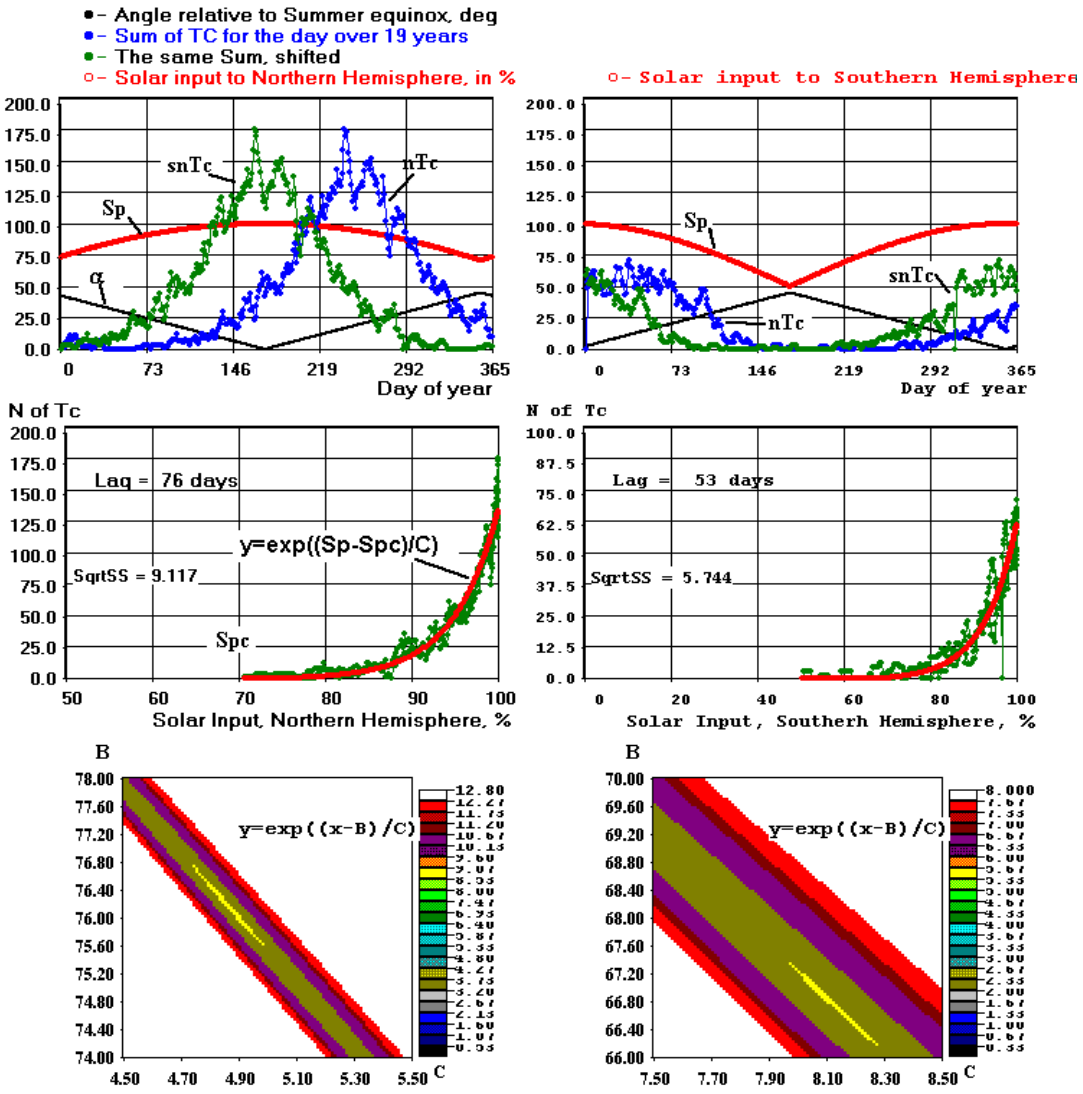


**Figure 9.** Role of solar heat input, see text.

external action with *lag* equal 76 and 66 days in Northern and Southern hemispheres, respectively.

Rather well correlation between the solar heat input and TC-genesis imply that it constitutes the direct agent controlling the main harmonic component TC genesis time series.

Exponential dependence of approximating function on Sp may give some clue on the nature of the agent, which actually controls the process of TC formation. It is well known that any radiation, propagating in a media, decays according to an exponential law. Thus, we may conclude that the process of TC formation is actually controlled by that part of solar energy which is absorbed by atmosphere, rather than by the Earth's surface.

It is known that ozone is completely effective in removing all radiation short of 300 nm, and longward of about 1μm large segments of the spectrum are removed by atmospheric water vapor [*Rottman,* 1997]. It is clearly seen in Figure 4 of *Harvey* [1997]. Thus, the TC-effective heating of atmosphere may be caused by UV and IR regions of the solar irradiance spectrum.

The question arises, why direct comparison between the year time series of TC and F10.7 show no linear correlation. From above it is clear that the reason is the existence of rather large response time, 76 or 66 days in different hemispheres. On the other side, the absence of linear correlation in time scales of years can not be explained by this delay and needs explanation.

We can assume that the reason is in the magnitude of critical level of heat input to the whole system Earth's surface-atmosphere. The 70% of the total solar irradiance, *Qsunt*, incident on the top of the atmosphere, are absorbed by the atmosphere (19%) and by the Earth's surface (51%) [*Smithson et al.*, 2002]. About 99% of the heat, absorbed by the Earth's surface, *Qsurf=0.51Qsunt*, comes from visible and infrared wavelengths [*Fligge et*

*al.,* 2001]. As is well known, the amplitude of the solar total irradiance variation is slightly less than 0.1% [*Harvey,* 1997]. Thus, Qsurf is practically constant and it is very "inertial", as the whole system the surface-atmosphere has very large response times, at least, more than 66 days according this paper. On the other side, the heat, absorbed by the Earth's atmosphere, *Qatm=0.19Qsunt*, is very variable, as variability of UV-part solar spectrum is tens-hundreds times larger than at $\lambda$>300 nm (in visible and IR regions) [*Harvey*, 1997], and it depends on the atmosphere properties (density, temperature, chemical composition etc.). That is why we do not see the large-scale (years) correlation between nTc and the solar activity.

The exponential dependence of nTc on the solar heat input in this case may be understood if the critical level of energy deposited into the whole system is close to the ratio *Qsurf/(Qsurf+Qatm),* i.e, to 0.51/(0.51 + 0.19) = 0.73. In another words, the heat *Q = 0.51Qsunt* is close but not enough to form a cyclone, and even small enhancement due to *Qatm* starts "to work". The critical level of the solar heat input into the atmosphere (~70% of year maximum), obtained in this paper, is in excellent agreement with above value 0.73.

This explains also result obtained in the above spectral analysis and in [*Afonin and Sharkov,* 2003*a*] of existence 27-day component in time-frequency spectra of nTc time series, as practically all atmosphere characteristics display 27-day variation.

These results are also confirmed by the known fact that most of cyclones are formed in two near-equatorial bands at ~15°–20° latitude.

## 6. Conclusions

The first exploratory analysis of relationship between the TC-genesis and solar activity index F10.7 time series have shown that

(1) The year time series of daily values of nTc, F10.7, and DST show no significant correlation.

(2) The time series of daily values of nTc, show clear season variation. Year nTc maximums at the North and the South are distinctly spaced in time. In both hemispheres the nTC maximum is observed only during the local summer. Practically no TC are observed during local winter. The intensity of TC in the south is slightly less than in the north.

(3) Difference in nTC for minimum and maximum SA (represented by F10.7) is mush less that the ratio of corresponding values of F10.7.

(4) The nTc values are autocorrelated during times less than ≤ 4 days, i.e., it is short-living phenomena without long "history". At larger time lags there is no mutual dependence, each TC may be considered as an stochastic event. On the contrary, the F10.7 time series are well autocorrelated with period close to 27 days and significant 27-day autocorrelation preserves even during solar minimum.

(5) In large time scales (years) no correlation between nTc and the solar and geomagneric activity represented by F10.7 and $D_{ST}$ parameters is observed.

(6) The 27-day component (S27) is the most pronounced component in WT spectra of F10.7 obtained from year time series; there are practically no other marked components.

(7) The global TC-genesis has its own characteristic time scales. These scales form an isolated region in the frequency space with time scales $S$ = 10–80 days, as they are separated in the frequency space both from "noise" region (time scales $S$ < 10 days) and year and half-year variations. The half-year structure reflects the presence of well defined seasonal effect in tropical cyclogenesis.

(8) In one-year time spectra the response of global TC-genesis on external action with 27day period is observed at frequencies which are close to this forcing frequency, subharmonics, and at second harmonics. In 19–year averaged spectrum the most pronounced in the region $S$ = 10–80 days is $S$ = 27 day component, observed in Northern hemisphere practically at all times. In Southern hemisphere the maximal response is observed most frequently at frequencies close to harmonics and subharmoncs of main frequency f27 ($S$ = 27 days).

(9) The heat input of the Sun into terrestrial atmosphere constitutes the direct agent controlling the main harmonic component of TC-genesis.

(10) The TC-genesis responds to the heat inflow from the sun with significant delay. The response time (phase delay) of TC-genesis to the solar heat input constitutes about 76 days in Northern and 66 days in Southern Hemisphere.

(11) A critical level of solar heat input exists, below which no TC are generated.

(12) The magnitude of critical solar heat input is about 70% of the year maximum.

(13) Exponential dependence of function approximating observed number of cyclones against relative solar heating evidences that the solar heat, causing maximal action on the global TC-genesis, is released in the atmosphere, rather than at the Earth's surface, i.e. it comes from EUV and IR ranges of the solar emission spectrum.

(14) The tropical cyclogenesis reflects complicated non-linear behavior of the whole thermo-aero-

hydrodynamical system The Earth's surface – atmosphere, displaying its own dynamical properties and characteristic time scales and (possibly resonant) frequencies.

**Acknowledgments.** The authors are grateful to L. M. Zelenyi for useful discussions. This work was supported by the Russian Foundation for Basic Research, project N$^{o}$ 03-05-64143.

**References**

Afonin, V. and E. A. Sharkov, Global Tropical Cyclogenesis And Solar Activity, *Geomagn. Aeron*., (in press), 2003*a*.

Afonin, V. and E. A. Sharkov, On impact of the solar UV-emission absirption in the Earth's atmosphere on tropical cyclogenesis, *Geomagn. Aeron*., (in press), 2003*b*.

Fligge, M., S. K. Solanki, J. M. Pap, C. Fröhlich, and Ch. Wehrli, Variations of solar spectral irradiance from near UV to the infrared-measurements and results, *J. Atm. and Solar-Terr. Phys., 63,* 1479–1487, 2001.

Harvey, K. L., The solar activity cycle and sun-as-a-star variability in the visible and infrared, Proceedings of The Second Annual Lowell Observatory Fall Workshop, October 5-7, 1997.

Pokrovskaya, I. V. and E. A. Sharkov, Tropical cyclones and tropical disturbances of the World Ocean: chronology and evolution. Version 2.1 (1983-2000), Poligraph-Service, Moscow, 2001.

Rottman, G., Observations of the Sun at ultraviolet wavelengths: 1 to 400 nm, Proceedings of The Second Annual Lowell Observatory Fall Workshop, October 5-7, 1997.

Sharkov, A. Eugene, Global tropical cyclogenesis, Springer-Praxis, Chichester, UK, 2000.

Smithson, P., K. Addison, and K. Atkinson, Fundamentals of the physical environment, Routledge, 3rd edition, 2002.

# Ballistic lifetime aspects in the problem of the AES orbit selection for the space physics experiments

V. I. Prokhorenko

Space Research Institute, Russian Academy of Sciences, Moscow, Russia

**Abstract.** This article examines methodological principles involved in AES orbit selection for Solar-Terrestrial physics experiments. The main criteria for orbit selection are the scientific goals and the topological structure of the regions being explored. Based on them, the family of possible orbits is characterized by certain free parameters. To select among the free parameters the domain of those which give long-lived AES orbits, a qualitative analysis of the long-term evolution of such orbits under lunisolar gravitational perturbations is conducted. It should be noted that orbit selection involves more than formal mathematics: as a rule, there exist many more requirements and constrains than the number of available free parameters. This makes the art of orbit selection a matter of compromises, requiring intelligent communication between all those planning the mission. This article is intended to explain various aspects of the long-term AES orbits evolution under the influence of lunisolar gravity perturbations and is addressed to readers other than specialists in celestial mechanics.

## 1. Introduction

This paper describes a geometrical method for the analysis of the long-term evolution of the Artificial Earth's Satellites (AES) orbits, under the influence of lunisolar gravitational perturbations.

The orbits being considered have high apogee and high inclinations, and as an example we use the high-apogee orbits of the PROGNOZ AES series, launched between 1972 and 1995, with a typical semi-major axis of about 16.7 $R_E$.

The evolution of the elliptical orbit of a satellite of negligible mass, located at the point *P*, is considered in the framework of the restricted three-body problem. The satellite moves in the attractive field of a mass *M* at a central point *S*, subject to gravitational perturbations of a mass $M_1$ at point *J*, moving around *S* along a circular orbit with radius $a_1$.

Initially we assume that the Moon's orbital plane is co-planar with the ecliptic plane. That allows us conducting qualitative analysis of the four-body problem, using the satellite version of the analytical solution (AS) of the doubly averaged restricted circular three-body problem, obtained by *Lidov* [1961].

In the first part of the article we characterize orbits by two parameters, the constants ($c_1$ and $c_2$) of the first integrals of the AS. Using these, we develop a geometrical method to select long-lived orbits and to analyze their long-term evolution. The constants $c_1$ and $c_2$depend of the initial values of three AES orbital elements, $e_0$ (eccentricity), $i_0$ (inclination), $\omega_0$ (pericenter argument), where the angular elements are measured relative to the orbital plane of the disturbing body.

In the second part we take into account the fact that the Moon's orbit and the ecliptic plane make a 5.15° angle, as well as the Moon's orbital precession with an 18.6-year period. This forces us to deal with time-dependent perturbations. In studying this effect we numerically solve the complete system of differential equations (ESDE), taking into account the perturbations of the bodies at their actual locations.

The numerical experiments show a significant effect of the launch date on the ballistic lifetime of orbits whose initial orbital elements are otherwise the same.

The first example is the investigation of the ballistic lifetime of the PROGNOZ-6 AES (launched 22.IX.1977). The analytical solution suggests the periodical evolution of the orbital elements ($e$, $i$, $\omega$) with the period of 9.9 years. According to the ESDE numerical calculations, the real launch date (1977) results in the quasi-periodic orbital elements ($e$, $i$, $\omega$) varying with a period of 8 years, and a ballistic lifetime of about 40 years. A hypothetical "bad" launch date (1988) would lead to the satellite's collision with the Earth 7 years later.

We also consider two launch dates of the PROGNOZ-2 AES, one actual (29.VI.1972) and the other hypothetical (29.VI.1981). The analytical estimation gives the ballistic lifetime of about 16 years. Numerical ESDE calculation predicts in the first case a satellite collision

with the Earth within 8 years, as confirmed by observations. Had the spacecraft been launched at the hypothetical launch date, the quasi-periodic evolution of its orbital elements ($e$, $i$, $\omega$) would have had a period of 12 years, and the ballistic lifetime would have been about 60 years.

These examples indicate the presence of some effect going beyond the scope of the analytical solutions used earlier. What parameters are responsible for this effect? We found that one of these parameters was the angular distance, $\varphi$ (0°, 360°), between the ascending nodes of the orbits of the AES and the Moon in the ecliptic plane. The initial value of $\varphi_0$ depends on $\Omega_0$, the initial value of the right ascension of the ascending node of the AES orbit, and on the date of the launch, which in turn determines the ascending node position of the Moon's orbit.

Assuming that the Moon's orbit precesses at a nearly constant rate, one can predict the evolution of the parameter j from that of $\Omega$. The semi-major axis a of the satellite's orbit plays key role in the evolution of the $\Omega$, beside parameters $c_1$ and $c_2$. It thus appears that we can use ($\varphi_0$, $a$) as the additional parameters for the investigation of the orbital elements evolution, taking into account the precession of the orbit of disturbing body.

## 2. Analytical solutions of the satellite version of the double-averaged restricted circular three-body problem

The double averaged system of the differential equations [*Lidov*, 1961] is obtained by independent averaging of the perturbing function relative to the mean motions of a satellite and the perturbing body, in the Hill's approach: $\alpha = a/a_1 << 1$, where $a$ is the semi major-axis of the Point P (satellite) orbit. The first term of the expansion of the perturbation function on $\alpha$ was used.

The general solution of the double averaged equations includes three first integrals (1–3) and two independent quadratures (4), (5).

$$c_0 = a; \qquad (1)$$

$$c_1 = \varepsilon \cos^2 i; \qquad (2)$$

$$c_2 = (1-\varepsilon)(2/5 - \sin^2\omega \sin^2 i); \qquad (3)$$

$$N - N_0 = -\frac{1}{A}\int_{\varepsilon_0}^{\varepsilon} \frac{d\varepsilon}{(1-\varepsilon)\,\varepsilon^{1/2}\sin^2 i \sin 2\omega}; \qquad (4)$$

$$\Omega - \Omega_0 = -A\int_{N_o}^{N} \frac{\cos i\,((1-\varepsilon)\sin^2\omega + \varepsilon/5)dN}{\varepsilon^{1/2}}, \qquad (5)$$

where

$$A = \frac{15}{2}\pi\frac{M_1}{M}\left(\frac{a}{a_1}\right)^3 \varepsilon_1^{-3/2},$$

$a$ is the semi-major axis, $\varepsilon = 1 - e^2$, $e$ is the eccentricity; $i$, $\omega$, and $\Omega$ are the inclination, the argument of the pericenter, and the right ascension of the ascending node (RAAN) of the satellite's orbit, $N$ is the orbit number, the angular elements are measured in relation to the orbit plane of the perturbing body (Point J); $\varepsilon_1$ is a parameter $\varepsilon$ of the Point $J$ orbit. The constants $c_0$, $c_1$, $c_2$ are determined by the initial values of the orbital elements:

$$c_0 = a_0, \quad c_1 = \varepsilon_0 \cos^2 i_0,$$

$$c_2 = (1 - \varepsilon_0)(2/5 - \sin^2 i_0 \sin^2\omega_0). \qquad (6)$$

As it follows from expressions (2), (3) the domain of the possible value of $c_1$ is the segment (0,1). The maximum value corresponds to $\varepsilon = 1$ and $i = 0$. The domain of the possible value of $c_2$ consists of the segments ($c_{2\min}$ ($c_1$), $c_{2\max}$ ($c_1$)) determined for each value of $c_1$ by the following expressions:

$$c_{2\min} = \begin{cases} -3/5(1-\sqrt{5/3c_1}) & \text{by} \quad c_1 \le 3/5 \\ 0 & \text{by} \quad c_1 > 3/5 \end{cases}$$

$$c_{2\max} = 2/5(1-c_1).$$

For $c_1 = 0$ the segment of the possible $c_2$ values is (–0.6; 0.4).

It should be mentioned that Moiseev [*Moiseev*, 1945] was the first to obtain the integral (2). Kozai obtained the similar solution in a more extent statement in 1962 [*Kozai*, 1962]. Gordeeva [*Gordeeva*, 1968] expressed quadrature (4) via elliptical integral of the first kind. Vashkov'yak [*Vashkov'yak*, 1999] expressed the quadrature (5) via elliptical integrals of the first and third kinds.

## 3. Geometrical analysis of the orbital elements' long-term evolution

Following [*Prokhorenko*, 2001] for the geometrical analysis of the orbital elements long-term evolution we use the spherical coordinate system Or$\theta\lambda$, where $r = \varepsilon$ (0, 1), $\theta = i$ (0°, 180°) is co-latitude, $\lambda = \omega$ (0°, 360°) is longitude, and the corresponding Cartesian coordinate system OXYZ.

The sphere of the unit radius is completely filled by all possible values of the orbital elements $\varepsilon$, $i$, and $\omega$. The expressions (2) and (3) describe two families of the rotation surfaces in this coordinate system. The first fam-

ily corresponds to $c_1$=*const* ($0 \le c_1 \le 1$). The rotation axis coincides in this case with the OZ axis. The second family of the rotation surfaces is formed by $c_2$=*const* ($-0.4 \le c_2 \le 0.6$). In this case the rotating axis coincides with the OY axis. Each couple of the parameters $c_1$ and $c_2$ values determines the closed line representing the cross-section of two surfaces $c_1$=*const* and $c_2$=*const*.

Figure 1 shows the cross-sections of family of surfaces $c_1$=*const* by the pair of meridian planes: $\omega$ = 90° and 270°.

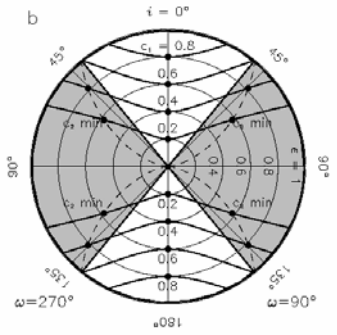


**Figure 1.**

Figure 2 shows the family of the closed lines $c_2$=*const* on the surface $c_1$ = 0.2 projected to the OXY plane. Here and in the following figures the shaded area shows the domains corresponding to the negative value of $c_2$. The arrows indicate the directions of motion along the integral curves during the evolution of the orbital elements. The isolated singular points in the regions of negative (positive) $c_2$ values correspond to the local minimum (maximum) of this parameter. For $c_1$ = *0* all integral curves converge into the singular saddle point $\varepsilon$ = 0.

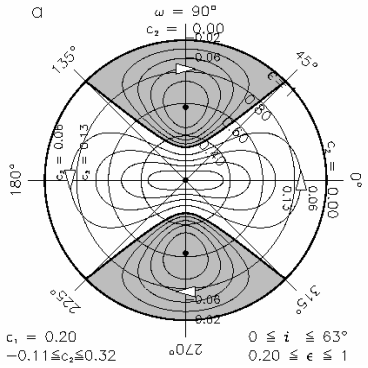


**Figure 2.**

The main properties of DAS solutions became quite visible for two type of the pericenter's argument ω evolution: the rotation type in the domain of the positive $c_2$ values, and libration type in the domains of the negative values of $c_2$.

In the first case $\omega$ changes in the counterclockwise direction with the period of $2\pi$, and $\varepsilon$ reaches its maximum (minimum) values at the points $\omega$ = 0° and 180° ($\omega$ = 90° and 270°), in the second case ω changes in the clockwise direction in bounded regions near $\omega$ = 90° or 270°, the minimum and maximum values of $\varepsilon$ are reached at the same point $\omega$ = 90° (or 270°). Variations of the parameters $\varepsilon$, $i$ in both cases have a libration character; the period of these parameters evolution in case of rotation (libration) types of ω evolution is equal to half (entire) period of ω evolution.

## 4. Geometrical interpretation of a satellite collision with the central body

To formalize the collision of a satellite with the central body Lidov [*Lidov*, 1961] introduced the finite radius, $R$, of a central body. The critical value $\varepsilon$*, corresponding to the collision of a satellite with a central body, is estimated as

$$\varepsilon^* = (2a_* - 1)/a_*^2, \qquad (7)$$

where $a_* = a/R$.

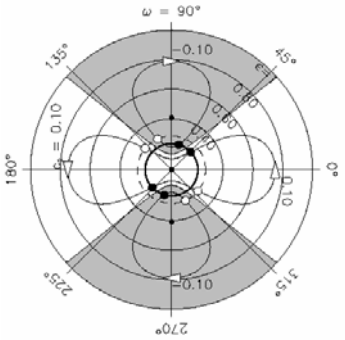


**Figure 3.**

Figure 3 shows the geometrical interpretation of the collision. Examples of the integral curves for $c_2$ = 0.1, and $c_2$ = −0.1 are shown (both for $c_1$ = 0.1). The solid line represents the trace of the spherical surface of the collision for the case of $\varepsilon$* = 0.234 ($a_*$ = 8.0).

The solid symbols mark the "collision points" of the integral curves considered. Empty symbols mark the "starting points" belonging to the spherical surface of radius $\varepsilon_0$ ($\varepsilon_0 > \varepsilon$*). The trace of the spherical surface of radius $\varepsilon_0$ on surface $c_1$ = 0.1 is shown by a dashed line.

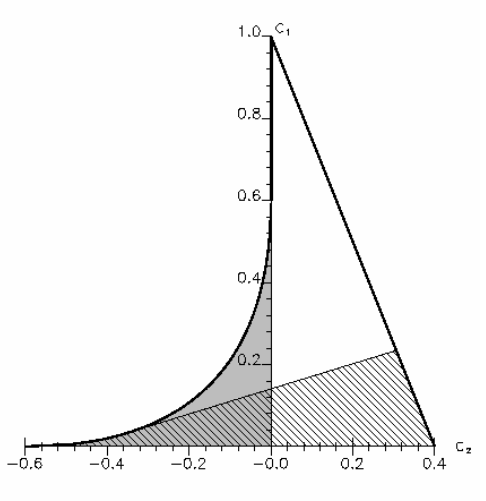


**Figure 4.**

In the space of the parameters $c_1$, $c_2$, the area associated with the orbits of finite ballistic lifetime is shown in Figure 4 as a hatched region at $a_* = 8.0$, $\varepsilon^* = 0.234$. This area is estimated by conditions obtained by Gordeeva [*Gordeeva*, 1968]: $c_1 < 0.6\,\varepsilon^{*2}$ or $c_2 > (1-\varepsilon^*)(c_1/\varepsilon^* - 0.6)$.

## 5. Parametrical analysis of the period of the orbital elements' long-term evolution and ballistic lifetime

The parametric analysis of the mentioned solutions in the domain of possible values of $c_1$, $c_2$ reveals certain latent regularities of the evolution [*Prokhorenko*, 2002*a*; 2002*b*] and helps to develop the graphical method for the selection of long-live AES orbits.

One may present the time-dependence of the orbital elements' long-term evolution as a product of the independent factors, using quadrature (4) and applying the theory of similarity and dimensionality

$$t_* - t_{*0} = \frac{4}{15} a_*^{-3/2} \frac{\mathrm{L}(c_1, c_2, \varepsilon_0, \varepsilon, \omega_0)}{L_D}, \quad (8)$$

$$\mathrm{L}(c_1, c_2, \varepsilon_0, \varepsilon, \omega_0) = -\int_{\varepsilon_0}^{\varepsilon} \frac{d\varepsilon}{(1-\varepsilon)\varepsilon^{1/2} \sin^2 i \sin 2\omega}. \quad (9)$$

The non-dimensional parameter of the perturbation similarity, $L_D$:

$$\mathrm{L_D} = \mu_{*1} a_{*1}^{-3} \varepsilon_1^{-3/2} \mu_*^{-1/2}, \quad (10)$$

depends only on the dynamic characteristics of the central and disturbing bodies. The asterisk (*) marks the non-dimensional parameters:

$$a_* = a/l,\ t_* = t/\tau,\ M_* = M/m,\ \mu_* = \mu\ \tau^2/l^3,$$

related to the characteristic size, $l=R$ (radius of the central body), time, $\tau$, and mass, $m = l^3/f\ \tau^2$, where $f$ *is* the gravity constant, $\mu$ is the product of the mass to the gravity constant.Following [*Gordeeva*, 1968], we express the period, $T_*$, of the long-term evolution of the parameters $\varepsilon$ and $i$ via doubled quadrature $L$ calculated in the limits $\varepsilon_{min}$, $\varepsilon_{max}$.

$$\mathrm{T}_* = \frac{4}{15} a_*^{-3/2} \frac{|\mathrm{L_C}(c_1, c_2)|}{\mathrm{L_D}}, \quad (11)$$

$$|L_C(c_1, c_2)| = 2\,L\,(c_1, c_2, \varepsilon_{min}, \varepsilon_{max}, \pi/2).$$

One can estimate the majorante of the ballistic lifetime, $\mathrm{T_{B*}}$, via doubled quadrature L calculated in the limits $\varepsilon^*$, $\varepsilon_{max}$, using $\omega_0(\varepsilon^*)$ belonging to the II or IV quarters.

$$\mathrm{T_{B*}} = \frac{4}{15} a_*^{-3/2} \frac{|\mathrm{L_B}(c_1, c_2, a_*)|}{\mathrm{L_D}}, \quad (12)$$

$$|L_B(c_1, c_2, a_*)| = 2\,L\,(c_1, c_2, \varepsilon^*, \varepsilon_{max}, \omega_0(\varepsilon^*)).$$

The function $\mathrm{T_{B*}}$ is determined only in the region of the finite ballistic lifetime, where inequality: $\varepsilon_{max} > \varepsilon^* > \varepsilon_{min}$ is fulfilled.

For any fixed values $a_*$, and $c_1$, $c_2$ belonging to the domain of the finite ballistic lifetime, the following inequality is fulfilled: $\mathrm{T}_* > \mathrm{T_{B*}} > \mathrm{T_{BR*}}$. Here $\mathrm{T_{BR*}}$ is the ballistic lifetime estimated for arbitrary $\varepsilon_0$ belonging to the segment: $\varepsilon_{max} \geq \varepsilon_0 > \varepsilon^*$.

Considering a period of the orbital elements' long-term evolution (11) and a majorante of the ballistic lifetime (12) as the product of independent factors we find some latent regularities.

**The dynamical parameter of the perturbation similarity, $L_D$,** plays a role of the scaling factor. Using this parameter we can reduce the problem of $n$+2 bodies to the problem of three bodies (in the case of the coplanar orbits of $n$ ($n > 1$) perturbing bodies). The coefficient $L_{Dn}$ for reduced three-body system can be expressed as a sum of $n$ perturbation similarity parameters, $L_D(j)$, calculated for $j = 1, \ldots, n$ independent three body systems. This transformation is based on the principle of additivity of the small perturbations.

**The factor $a_*^{-3/2}$** means that it is possible to decrease the periods of the orbital elements long-term evolution and ballistic lifetime by increasing the semi-major axis.

We call **the functions $L_C$ ($c_1$, $c_2$) and $L_B$ ($c_1$, $c_2$, $a_*$)** orbital configuration parameters. The signs of $L_C$ and $L_B$ are the same as the sign of $c_2$. The values of $|L_C(c_1, c_2)|$ in the $c_1$ and $c_2$ domain are shown in Figure 5*a* by izolines of the corresponding surface. The magnitude varies from 6 to 13 with unit step. The sections of the surface $|L_C(c_1, c_2)|$ by the planes $c_1$=*const* (for $0 < c_1 < 0.6$) are shown in Figure 5*b*.

The values of $|L_B(c_1, c_2, a_*)|$ as a function of $c_1$ and $c_2$ in the region of the finite ballistic lifetime are shown in Figure 5*c* for $a_* = 16$, $\varepsilon^* = 0.12$. The remaining part of the $c_1$, $c_2$ domain show the izolines of the function $|L_C(c_1, c_2)|$.

The function $|L_C(c_1, c_2)|$ sharply increases while $c_2$ moves closer to zero (see Figure 5*b*).

The behavior of the functions $|L_C(c_1, c_2)|$ and $|L_B(c_1, c_2, a_*)|$ demonstrates the existence of a symmetric solutions in the regions of different types of the perigee argument evolution.

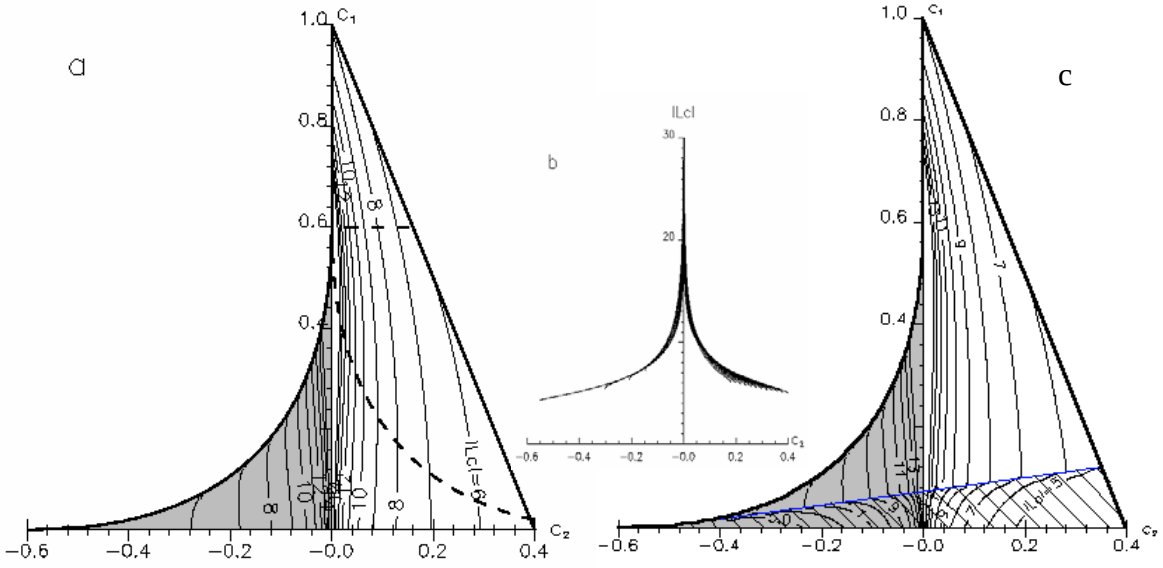


**Figure 5.**

This suggests that both the period and the ballistic lifetime of the corresponding orbits sharply increase near the plane $c_2 = 0$.

## 6. Geometrical tool for the long live orbit selection

Now we can formulate several recommendations that may be valuable in practical terms in the orbit design taking into account optimizing the ballistic lifetime of a satellite.

One should use the parameters $c_1$ and $c_2$ for a qualitative parametric analysis. The accessible domain for these parameters depends on the range of the possible initial orbital elements.

**The role of the satellite's semi-major axis value as a parameter:** Parameter $a_* = a/R_E > 1$ determines the critical value ε* (7) of the parameter ε and the region of domain $c_1$, $c_2$ associated with the orbits of the finite ballistic lifetime. In the mentioned region parameter $a_*$ determines the function $|L_B(c_1, c_2, a_*)|$, proportional to the majorante of the ballistic lifetime, for each point of this region.

The decrease in the parameter *a* leads to the increase in the part of the domain $c_1$, $c_2$ associated with the orbits of finite ballistic lifetime. When *a*-value is close to $R_E$, $a_* = 1$, the mentioned domain replaces the entire domain of $c_1$, $c_2$.

In Figure 6*b*, the hatched region is associated with the orbits of the finite ballistic lifetime corresponding to $a_* = 8$ ($\varepsilon^* = 0.234$). The level lines of the function $|L_B(c_1, c_2, 8)|$ and $|L_C(c_1, c_2)|$ are shown the same way as they were in Figure 5.

**The role of the initial value of the pericenter's radius, $r_{p0}$, parameter $\varepsilon_0$:** The values of the parameters *a*, and $r_{p0}$ determine the initial value of the parameter $\varepsilon_0$. The borders of the segment ($\varepsilon^* < \varepsilon_0 \le \varepsilon_{max}(c_1, c_2)$) of $\varepsilon_0$ possible values correspond to $r_{p0} = R_E$ and $r_{p0} = a$.

In Figure 6, the fixed initial values of the pericenter altitude, $h_{p0} = 5000$ km; $r_{p0} = 1.78\ R_E$; $e_0 = 0.777$, and $\varepsilon_0 = 0.4$ are used, as an example. The spherical surface of radius $\varepsilon_0 = 0.4$ is shown in Figure 6*a* as a projection to the equatorial plane.

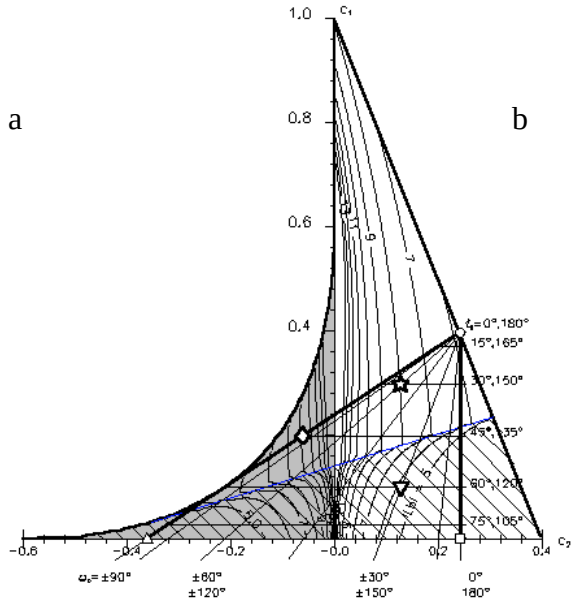


**Figurte 6.**

The parallels, corresponding to the constant values of the inclination $i_0$, are shown as circles, while the meridians, corresponding to the constant values of $\omega_0$, are shown as beams.

The transformation (6) maps the spherical surface to the tree-angled domain of $c_1$, $c_2$ space. This domain is bounded by the right-angled triangle with the sum of two cathetus length equal to unity. One of the triangle cathetus with the length $\varepsilon_0$ is parallel to the $c_1$ axis and corresponds to the fixed value of $c_2 = 0.4\ (1-\varepsilon_0)$. The other cathetus lies on $c_2$ axis from $-0.6\ (1-\varepsilon_0)$ to $0.4(1-\varepsilon_0)$.

The empty symbols show the characteristic points of the sphere and its images. The apex of the triangle is the image of the pole of the spherical surface. The parallels corresponding to the $i_0$ = const are mapped onto the lines $c_1$=const, the meridians are mapped into the beams, focused in the apex of the triangle. The orthogonal grid is mapped onto the oblique grid. The image of the circle $i_0 = 90°$ is one of the cathetus of the triangle. The other cathetus is the image of the meridians $\omega = 0$ and $\omega = 180°$. The meridians $\omega_0 = 90°$ and $\omega_0 = 270°$ are preimages of the hypotenuse.

In the case of $\varepsilon_0 = 0$, the triangle degenerates into a segment of the $c_2$ axis, while in the case of $\varepsilon_0 = 1$ it becomes the segment of the $c_1$ axis.

While $\varepsilon_0$ approaches $\varepsilon^*$, the greatest part of the accessible region of $c_1$, $c_2$ fades into the region of the finite ballistic lifetime. The increase of $\varepsilon_0$ (by increasing of $r_{p0}$) changes the balance to the benefit of the orbits with the periodic character of the orbital elements evolution.

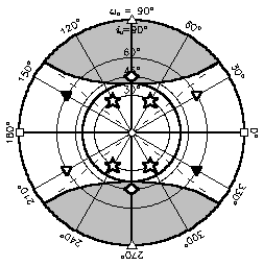

In this context we should mention the following non-trivial circumstance. For the orbits with finite ballistic lifetime, fixed value of the semi-major axis, and other initial data being equal an increase in $r_{p0}$ does not lead to an increase in ballistic lifetime of the orbits, but the opposite is true (see Figure 3).

**The role of free parameters $i_0$, $\omega_0$:** Using the oblique grid in Figure 6*b* one can find the images of the initial values of $i_0$, $\omega_0$ (associated with the selected fixed value of $\varepsilon_0$) in the space $c_1$, $c_2$. The additional information regarding the magnitudes of the functions $L_C(c_1, c_2)$ and $L_B(c_1, c_2, a_*)$ shown in Figure 6*b* suggests the way of selecting the initial values of the $i_0$, $\omega_0$, which provides an increase in the ballistic lifetime or helps to reach the region of the periodical evolution of the orbital elements.

Three versions of the $c_1$, $c_2$ samples are shown in Figure 6*b* by different symbols. In Figure 6*a* the same symbols mark the corresponding initial values of $i_0$, $\omega_0$. The version labelled by the symbol $\nabla$ corresponds to the region of the finite ballistic lifetime. In this case, the initial value of $\omega_0$ should be taken from quarters II or IV to provide the increase of $\varepsilon$ and the pericenter's radius (see Figure 3). The corresponding points in Figure 6*a* are labelled by the empty symbols, whereas the alternative points are labelled by the solid symbols.

**The region of the possible values of the free parameters $i_0$, $\omega_0$, the role of the RAAN $\Omega_{e0}$:** Let us consider a special important case, namely, the orbit family with the fixed initial value of the inclination to the Earth's equatorial plane, $i_{e0}$. The initial value of the inclination to the ecliptic plane, $i_0$, depends on the initial value of the RAAN, $\Omega_{e0}$. The possible values of $i_0$ belong to the segment $(i_{e0} - \delta, i_{e0} - \delta)$, where $\delta$ is the inclination of the ecliptic plane to the Earth's equatorial plane.

The relation between the angular elements measured in relation to the Earth's equatorial plane ($i_e$, $\omega_e$, $\Omega_e$) and the ones measured in relation to the ecliptic plane ($i$, $\omega$, $\Omega$) is expressed by the following formulae:

$$\begin{gathered}\cos i = \cos\Omega_e \sin i_e \sin\delta + \cos i_e \cos\delta;\\ \cos\Delta\omega = (\sin i_e \cos\delta - \cos\Omega_e \cos i_e \sin\delta)/\sin i;\\ \sin\Delta\omega = -\sin\delta \sin\Omega_e / \sin i;\ \omega = \omega_e + \Delta\omega; \qquad (13)\\ \cos\Omega = (\cos\Omega_e \cos\delta \sin i_e - \sin\delta \cos i_e)/\sin i;\\ \sin\Omega = \sin\Omega_e \sin i_e / \sin I\end{gathered}$$

## 7. Application to the AES orbits subjected by lunisolar gravitational perturbations. Influence of the Moon's orbit precession

We have applied the described above geometrical method to the retrospective analysis [*Nazirov et al.*, 2002] of the AES orbit PROGNOZ series long-term evolution.

The assumption of the co-planarity of the Moon's orbit and ecliptic planes allows applying the analytical solution of the three-body problem to the problem of four bodies.

The non-dimensional parameter of the perturbation similarity, $L_D$, for three body systems (see Table) was calculated with the help of the characteristic size, $l$, time, $\tau$, and the dynamic parameters of the central and perturbing body as follows:

$$l = R_E = 6371200 \text{ m}, \quad \tau = 365 \text{ days};$$
$$\mu = 0.39860044\ 10^{15}\ \text{m}^3/\text{s}^2 \text{ (Earth)};$$
$$\mu_1 = 0.4902799\ 10^{13}\ \text{m}^3/\text{s}^2, \quad a_1 = 0.3844109 \text{ m},$$
$$\varepsilon_1 = 1 \text{ (Moon)}; \quad \mu_2 = 0.13271244\ 10^{21}\ \text{m}^3/\text{s}^2,$$
$$a_2 = 0.1495979\ 10^{12} \text{ m}, \quad \varepsilon_2 = 1 \text{ (Sun)}.$$

**Table**

| Body system | Earth – AES – Moon | Earth – AES – Sun | Earth – AES – Moon + Sun |
|---|---|---|---|
| | 1 | 2 | 3 |
| **$L_D$** | 0.00219 | 0.00101 | 0.00320 |

The values of $L_D$ in columns 1 and 2 were calculated using the formula (10); the corresponding value in column 3 is just a sum of the columns 1 and 2 values.

To verify the validity of the mentioned assumption, we have performed a numerical experiment in order to compare the estimations with and without taking into account the Moon's orbit precession.

For the numerical experiments, the exact system of the differential equations (ESDE) was used (the lunisolar gravitation perturbations were taken into account).

The values of the periods $T_*$ of the long-term evolution and majorante of the ballistic lifetime $T_{B*}$ as a function of $c_2$ are shown in Figure 7*a* by solid and dashed lines. These values are estimated as functions of $c_2$ by formulas (10), (11), using $c_1$= 0.0179, $a_*$ = 16.12, and $L_D$ from the third column of the Table. The time is measured in years.

For two selected versions of the orbit, we have applied a series of hypothetical launch dates, belonging to the common period of the Moon's orbit precession.

Diamonds show the value of ballistic lifetime, $T_{BR}$, calculated numerically for the INTERBALL-1 type orbits associated with various hypothetic dates of launch. Another version, shown by the circle, corresponds to the hypothetical orbit V4, whose initial data differ from the INTERBALL-1 orbit data only in the value of the perigee argument ($\omega_0$ = 322.6°).

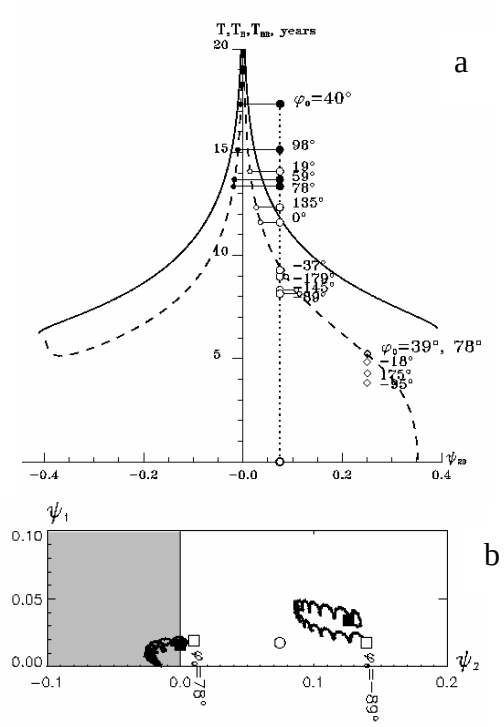


**Figure 7.**

The values of $T_{BR}$ ($c_1$, $c_2$, $\varphi_0$) (in years) are shown as a function of $c_2$ for various launch dates, and are labelled by a corresponding value of the parameter $\varphi_0$. Parameter $\varphi_0$ ($0° \le \varphi_0 \le 360°$) is determined as the initial value of the angular distance between the ascending nodes of the satellite's and Moon's orbits in ecliptic plane.

The solid (empty) circles mark the versions of the orbits with a perigee argument evolution of a libration (rotation) type detected during the exact calculation. The versions of discrepancy between $T_{BR}$ ($c_1$, $c_2$, $\varphi_0$) and $T_{B*}(c_1, c_2)$ vary within the range from –1.5 to 8.5 years.

We accept the discrepancy as the result of the shift of the arguments of the function $T_{BR}$ from its initial point ($c_1$, $c_2$) to the point ($c_1+\Delta c_1$, $c_2+\Delta c_2$). The arguments' shifts: $\Delta c_1 = c_{1s} - c_1$, $\Delta c_2 = c_{2s} - c_2$ are determined from the equality

$$T_{BR}(c_1, c_2, a_*, \varphi_0) = T_{B*}(c_{1s}, c_{2s}, a_*).$$

To study this shift effect let us consider the functions of the orbital elements $\psi_1$ (t) = $\varepsilon \cos^2 i$, and $\psi_2$(t) = $(1 - \varepsilon)(2/5 - \sin^2\omega \sin^2 i)$ with the initial values equal to $c_1$ and $c_2$ (see (2), (3), (6)). In Lidov's AS, these functions being constant are the first integrals.

It is noteworthy that the domain of possible values of both pairs: functions $\psi_1$(t), $\psi_2$(t) and parameters $c_1$, $c_2$ are just the same.

To understand the nature of the shift effect, we examine the functions $\psi_{1m}(t) = \varepsilon_m \cos^2 i_m$, and $\psi_{2m}(t) = (1 -$

$\varepsilon_m)(2/5 - \sin^2\omega_m \sin^2 i_m)$, where index m marks the orbital elements measured relative to the plane of the Moon's orbit.

One can use the relations (13) for the estimation of the orbital elements measured in relation to the Moon's orbit ($i_m$, $\omega_m$) on the basis of the orbital elements ($i$, $\omega$) measured in relation to the ecliptic plane. For this, in (13) the parameters: $i_e$, $\omega_e$, $\Omega_e$, $i$, $\omega$, $\delta$ have to be replaced correspondingly by $i$, $\omega$, $\varphi$, $i_m$, $\omega_m$, $\delta_m$, where $\delta_m$ is inclination of the Moon's orbit to the ecliptic plane (5.15°).

The domain of the values of the functions $\psi_{1m}(t)$ and $\psi_{2m}(t)$ is the same as that of $c_1$ and $c_2$, but the initial values of $\psi_{1m}(t)$ and $\psi_{2m}(t)$ do not equal to $c_1$ and $c_2$ and depend on $\varphi_0$.

The behavior of functions $\psi_{1m}(t)$ and $\psi_{2m}(t)$ for the hypothetical orbit V4 is shown in Figure 7b. Two versions of a launch date are used ones that result in the greatest shifts (on different sides). The empty (solid) square shows the initial (final) position of $\psi_{1m}(t)$, $\psi_{2m}(t)$. The initial value of $\varphi_0$ is shown near the empty square. The empty circle shows the position of the point $\psi_1(t_0) = c_1$, $\psi_2(t_0) = c_2$.

A more detailed study of the $\varphi$-factor will be addressed elsewhere. To constrain the discussion it must be mentioned that the role of the $\varphi$-factor is more prominent for $c_1$, $c_2$ in the vicinity of $c_2 = 0$ and near the borders of the region of the finite ballistic lifetime.

One of the cases mentioned in the Introduction (the orbits of the PROGNOZ-6) is used for the illustration of this thesis. We introduce the cylindrical coordinate

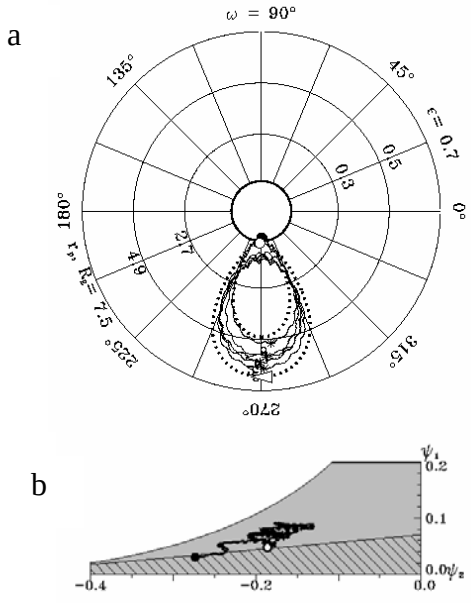


**Figure 8.**

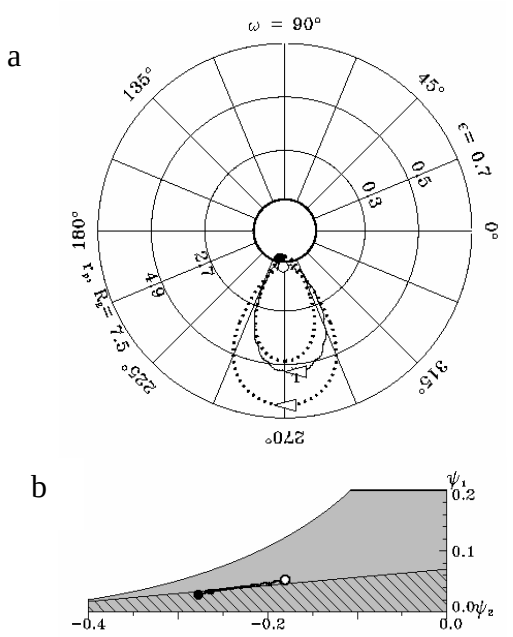


**Figure 9.**

system $O\varepsilon\omega\psi_1$, more convenient for the case when $\psi_1$, $\psi_2$ are the functions of time.

Figure 8 (9) shows the AES orbit PROGNOZ-6 orbital elements $\varepsilon(t)$, $\omega(t)$ evolution (a) and the behavior of the functions $\psi_1(t)$, $\psi_2(t)$ (b) for the actual (hypothetical) launch dates with $\varphi_0 = 225°$ ($\varphi_0 = 80°$).

These figures demonstrate the importance of the shift of $\psi_1(t)$. This shift accounts for the displacement of the orbit into (or out of) the region of the finite ballistic lifetime.

**Acknowledgements.** This paper is a tribute of the memory of Yuri I. Galperin. The research presented here started when Yuri was alive and he displayed a keen interest in it. Unfortunately, he passed away before the main results were obtained.

**References**

Gordeeva, Yu. F., Time dependence of the elements long-period oscillations in the restricted three-body problem, *Kosm. Issled.* (*In Russian*), *6* (4), 536, 1968.

Nazirov, R. R, V. I. Prokhorenko, A. I. Sheikhet, A retrospective geometric analysis of the long-term evolution of orbit and the ballistic lifetime for satellites of the Prognoz series. *Kosm. Issled. 40* (5), 501, 2002.

Lidov, M. L., Evolution of the orbits of the artificial planetary satellites under action of the gravitation

perturbations of the external bodies, *Isskusstv. Sputniki Zemli* (*in Russian*), *8*, 5, 1961.

Prokhorenko, V. I., Study of satellite situation mission, *Acta Astronautica*, *10*, 499, 1983.

Prokhorenko, V. I., A geometric study of solution to restricted circular double-averaged three-body problem, *Kosm. Issled.*, *39* (6), 583, 2001.

Prokhorenko, V. I., Investigations of the period of evolution of elliptical orbits in the double-averaged three-body problem, *Kosm. Issled*., *40* (1), 48, 2002*a*.

Prokhorenko, V. I., Investigations of the ballistic lifetime for elliptical orbits under action of gravitation perturbation of the external bodies, *Kosm. Issled*., *40* (3), 264, 2002*b*.

Vashkov'yak, M. A., Evolution of the orbits of distant Uranus' satellites, *Letters in A. J.*, *25* (7), 554, 1999.

# Space distribution of the dust continuum around Halley comet nucleus obtained by the three-channel spectrometer onboard VEGA 2

P. V. Stoeva, V. C. Guineva, and R. Werner

Central Solar-Terrestrial Influences Laboratory, Bulgarian Academy of Sciences,
Stara Zagora Department, Bulgaria

**Abstract.** Space distribution of the solar light scattered by dust particles in Halley comet coma towards the Sun and in the near tail is investigated using spectra measured by the three-channel spectrometer (TKS), onboard VEGA 2 interplanetary station. Monochromatic composed images in 5260Å are constructed from consequently registered two-dimensional images. The composed image for 9 March1986 includes 7 pictures, and for 10 March 1986 – 5 pictures. Radial profiles – proxy for intensity as a function of the projected distance to the nucleus $p$ are also used in the research. Two strong jets are observed. One of them is in the direction towards the Sun and expands up to $p$ = 19500 km from the nucleus, and the other one is perpendicular to it and reaches $p$ = 19000 km. The inner coma dust continuum tomographic reconstruction shows that a model of isotropic and anisotropic dust ejection can approximately describe the region near the nucleus. Investigation of the dust angular distribution reveals the existence of inhomogeneities in the form of rings or shell structures. The radial profile of the intensity in solar direction is divided into 2 parts. For $p$ < 1000 км the slope is approximately –0.7, and for $p$ > 1000 km it is about –1.1. The weaker slope near the nucleus is explained by the greater optical depth of the inner coma or by the quick change of the scattering angle. In antisolar direction, in the near tail, a weaker intensity of the dust continuum is observed, which decreases with the increasing of the distance between VEGA 2 and comet nucleus. The intensity increasing, obtained far from the nucleus, and the radial profile maxima are probably connected with a dust shells formation due to jet activity and nucleus rotation.

## 1. Introduction

Among the small bodies of the Solar system comets are among the most beautiful objects, keeping information about its origin. Comets are a conglomerate of water ice, complicated molecules based on hydrogen, carbon, nitrogen and oxygen, and dust.

Spectral studies give a lot of information about the nucleus, the coma and the tail of the comets. Most of them have an asymmetric dust coma. Space experiments have already completely proved that the solid material – dust and gas – was released from active regions on the solar side of the nucleus. The outgassing from the night side of the comet presents a small part of the total activity. Depending on the outgassing rate and direction of ejection from the nucleus, under the action of the solar radiation pressure, gravitational force, fragmentation and drag forces, dust particles form the dust tail in antisolar direction.

The comet spectrum consists of emissions of the neutral and ionized constituents of the gas coma complimented with the solar continuum emission, reflected by the central nucleus and dust coma particles. In order to investigate the comet's glow itself, it is necessary to separate glow of the continuum and molecular bands. The continuum is basically in the visible part of the spectrum. Its intensity changes with the heliocentric distance.

Space distribution of the Halley comet continuum glow has a sharply expressed jet structure in Sun direction [*Werner et al.,* 1993]. Towards the tail, the dust continuum intensity decreases as a whole, but repeated increase of the glow (dust shell structures) far from the nucleus is observed [*Trotignon et al.,* 1987, *Larson et al.,* 1987, *Stoeva et al.,* 1999*b*].

## 2. Experiment and measurements

Two-dimensional images giving the space distribution of Halley comet dust and gas constituents are obtained using the data measured on 9 and 10 March

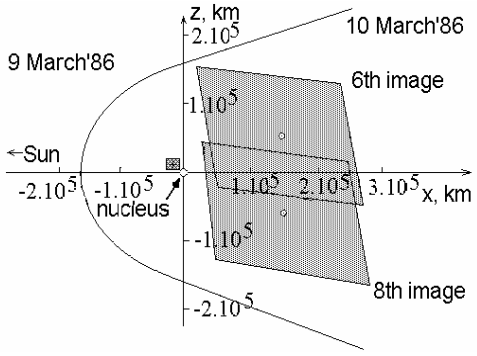


**Figure 1**. Displacement of the scanned by the three–channel spectrometer (TKS) on board VEGA 2 areas in relation to the Halley comet nucleus, on 9 and 10 March 1986.

1986 (in the coma towards the Sun and in the near tail accordingly) by the visible channel of the three-channel spectrometer (TKS), onboard VEGA 2 interplanetary station. The three-channel spectrometer (TKS) onboard VEGA is a joint work of specialists from Bulgaria, France and the former Soviet Union [*Gogoshev et al.,* 1985]. It consists of a Cassegrain telescope with a scanning device and a spectrometer with holographic gratings. The optical beam is separated in three spectral channels – UV – 120÷290 nm, visible – 275÷715 nm, and IR – 950÷1900 nm. The detector is linear, Reticon type and consists of 1024 elements (pixels). Every element covers 6 Å from the registered spectrum.

It is mounted on an automatic stabilized platform with a TV camera. The main goals of the project are: investigation of the gas and dust coma composition, determination of the gas production rate and the lifetime of the cometary constituents (lifetime of the parent and daughter molecules).

TKS scanned in 2.5° x 1.5° rectangular area in 7 consecutive rows, each with 15 points (105 scanner positions). The slit is 26′55″ × 29″ in size. Scientific data was being received for about 2 hours. Far from the comet TKS registered 1 spectrum in each of these 105 spatial regions and they all form a single picture of the cometary glow. This way of scanning is named mode A. In the period of closest approach, during the last 33 minutes, when the distance between the VEGA 2 and the Halley comet was less than 150000 km, TKS scanned only in the central line and this is mode B. VEGA – comet distance decreased from 516000 km to 8030 km and the projected distance to the nucleus decreased from 20000 km to 250 km during the 9 March 1986 encounter. The initial time of measuring on 9 March is UT 04:12:38. Spectra measured from 4524s to 9009s board time, read from the initial time, are used. The area of the observed region is 22000 km × 17000 km. At the beginning of measurements, nucleus position is obtained by TKS and TV camera images comparison. At the end of measurements, nucleus position is calculated using measured intensities and the Hazer model [*Stoeva*, 1999]. Co-ordinates of the nucleus are (1.1°, –1.3°) from the image centre. On 10 March the initial time of measuring is UT 04:56:35. Spectra measured from 3600s to 6980s board time are used. The VEGA – comet distance reaches 6 million km and the projected distance to the nucleus increases from 20000km to 300000 km. Scanned area is 210000 km × 180000 km and the nucleus' co-ordinates are (1.1°, –0.3°) except for the 8$^{th}$ picture when the nucleus is outside the TV camera field of view. For the 8$^{th}$ picture we determine (1.05°, –0.3°) as co-ordinates of the nucleus. Supposing that for 20 minutes space distribution is not substantially changed we combine 8$^{th}$ and 6$^{th}$ picture. As a result we obtain space distribution of the dust and different cometary gases in a larger area – 210000 km × 330000 km. The TKS scanning areas and their position towards the nucleus are schematically shown in Figure 1. Because of the VEGA – comet short distance, on 9 March scanned areas are much smaller than those scanned on 10 March 1986. On 9 March TKS line of sight is directed from us to the graph and on 10 March – vice versa.

### 3. Monochromatic composed images

Dust continuum intensity or the intensity of solar light scattered by the dust particles near the nucleus is investigated and defined for every spectrum [*Werner et al.,* 1989]. This is the integral intensity or monochromatic surface brightness in the column along the line of sight measured in Rayleight.

The image of each picture is reconstructed from data measured in the TKS 105 scanner positions. They are obtained by adapted regularizing algorithm of Tichonov using interpolating generalizing spline. [*Nikolov et al.*, 1989]. Dust continuum intensity is obtained by averaging the values of 5 consecutive pixels, centered on the corresponding dust line in the spectrum measured in a specific scanner position. Each line is characterized by different distance between the VEGA station and the comet, $r$ and the distance between the nucleus and the line of sight, $p$. The image plane is perpendicular to the averaged position of the line of sight. Spectra registered for about 10 min are used to obtain the monochromatic image.

Monochromatic composed images of the dust continuum are constructed in Sun direction using all the 7 pictures registered in mode A, 9 March 1986. Dimensions of the 1$^{st}$ picture are around 15000 km × 14000 km and of the last when the image is the smallest – about 7000 km × 3600 km. Five pictures on 10 March 1986 are used for obtaining such images in antisolar

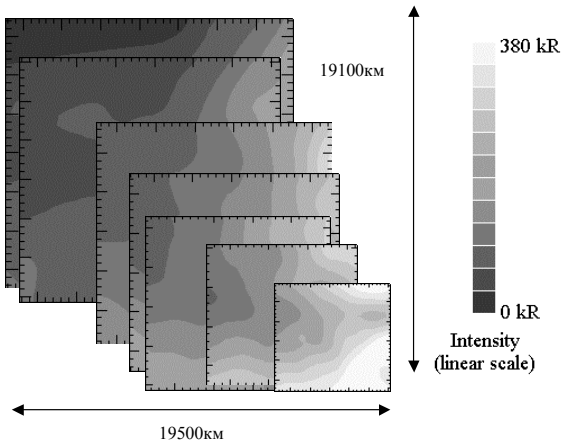


**Figure 2.** Monochromatic composed image of the dust continuum at 5260 Å in the Halley comet coma towards the Sun, 9 March 1986. Two strong jets are clearly distinguished - one of them is directed to the Sun (to the left, 2° under the X-axis) and the other jet is turned upwards.

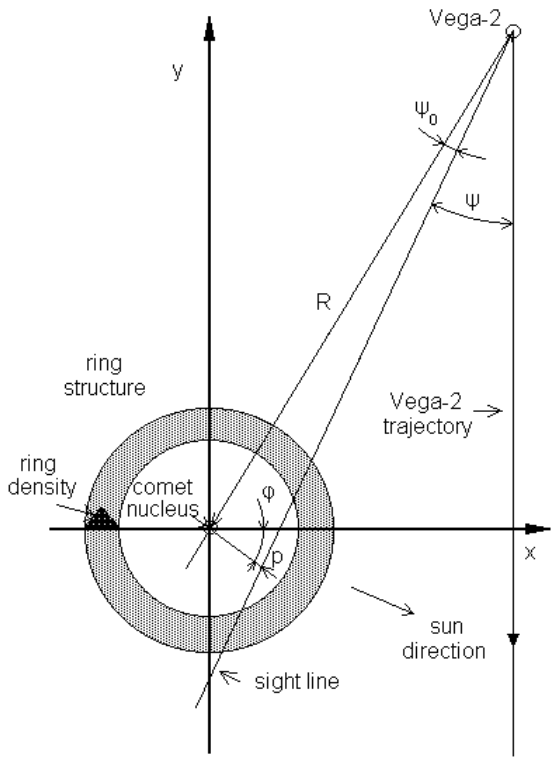


**Figure 3.** Geometry of the VEGA 2 observations for TKS scanning of the Halley comet in mode B (only in the central line).

direction. They are put one on another according to the image structure and nucleus position.

The composed images of the dust continuum glow space distribution are made in 5260Å. This is a representative spectral line as the distribution in all the 11 dust lines in the region 4100Å – 6840Å, free of other gas emissions, almost coincides with that of 5260Å line [*Stoeva et al.,* 1999*a*].

## 4. Dust continuum in solar direction

Two strong jets are clearly distinguished on each of the images obtained on 9 March. Sun is to the left, –5° in the image plane and –35° in the plane perpendicular to it. One of them is directed to the Sun (–2°, which is under the x-axis) and the second jet is ejected approximately upwards. How they are placed in all the coma space in Sun direction could be seen from the composed image (Figure 2). The Sun jet stretches up to $p$=19 500km and the other – up to $p$=19 100km. Dust space distribution is investigated in jet and free of jet zones.

In the quiet zones – without jets, when the comet outgassing is homogeneous – dust concentration decreases with $r^2$ and consequently intensity of the scattered light is proportional to $1/p$. Dust continuum intensity in jet zones decreases more slowly in comparison with the jet-free zone intensity. Similar to these, jets in space distribution of OH, CN, $C_2$ and $C_3$ are also observed. The gas to dust ratio in jet and free of jet

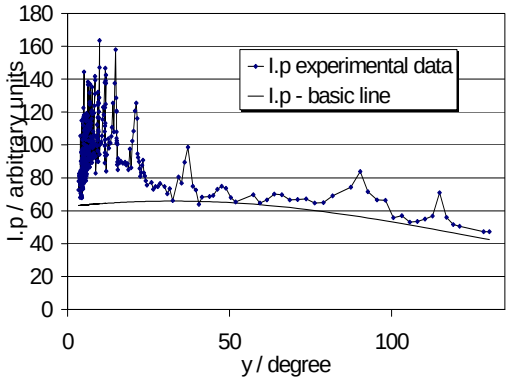


**Figure 4.** Investigation of the dust scattering near the nucleus by the analysis of the variation of the product $I.p$ as a function of angle $\psi$. The basic line of the $I.p$ series can be approximately described as a combination of isotropic and anisotropic dust ejection.

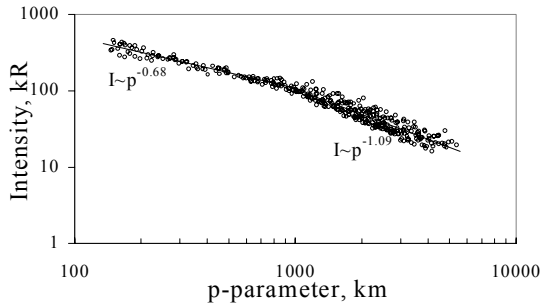


**Figure 5.** Dust distribution around the Halley comet nucleus. It is stronger in the hemisphere towards the Sun and shows a distinct jet structure.

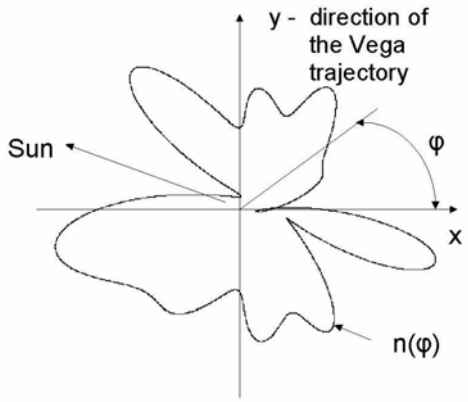


**Figure 6.** The intensity of the solar light scattered by the dust particles, integrated along the line of sight, for the 5260 Å wavelength, for all scanner positions in mode B versus *p*-parameter, compared to model calculations (the solid line).

zones remains approximately one and the same which means that a strong correlation exists between gas emission and dust continuum intensities. It can be supposed that the observed jet consists of a gas and dust mixture.

Jets in Halley comet coma are directly connected with the nucleus and that is the reason to be considered as one of the most remarkable phenomena registered by the VEGA 2 and Giotto stations. If we want to reconstruct the dust distribution in a plane formed by the VEGA 2 trajectory and the comet the tomographic problem (determining the dust concentration in given projections) should be resolved. The inner coma dust scattering was investigated in mode B. Figure 3 shows the geometry of observations and TKS scanning in this mode. The dust scattering near the nucleus can be studied by the analysis of the variation of the *I.p* product as a function of angle $\psi$ (the angle between the line of sight and the VEGA trajectory) (Figure 4). *I* represent the measured values of the dust continuum around 5260 Å. At the beginning of the measurements in the range up to $\psi$=30° a large number of peaks is registered with almost chaotic distribution. With the approach of the VEGA 2 station to the comet, the presence of peaks strongly decreases. The basic line of the *I.p* series is not a constant and can be approximately described as a combination of isotropic and anisotropic ($\sim cos\varphi$) dust ejection. The difference between function $I.p(\psi)$ and the basic line describes the deviation of the real distribution from the combined model. Figure 5 shows the angular dust distribution obtained by reconstruction of the dust number density $n(\varphi) = n(r, \varphi).r^2$, neglecting the scattering indicatrice. TKS experimental date, in the range of 150 km < $p$ < 500 km, for the intensity in the region of 30°< $\psi$ <130° (see Figure 4) are used. The reconstructed n(φ) distribution can be qualitatively compared with the data measured by dust detectors SP1 [*Vaisberg et al.,* 1986] and SP2 [*Mazets et al*., 1987] onboard VEGA 2,. As most important we can point out that the obtained two strong jets in sun direction correspond to dust peaks obtained about 10–20s before and 30–110s after the VEGA 2 closest approach. The obtained jets' distribution in the data field is also in good agreement with the results of *Celnik et al.* [1987]. In the $\psi$ < 30° the remaining structures can be explained by the inhomogeneities in the form of rings or shell structures with a center in the nucleus [*Werner,* 2000]. The dust distribution in the ring structure is assumed as a triangle with a maximum in the middle of the ring (Figure 3). The sightline crosses quaziperiodically the narrow rings and the obtained intensities rapidly change (peaks on Figure 4).

Radial profiles of the intensity *I* of the scattered light can compliment the space distribution investigation. That is why the nucleus position should be precisely determined [*Stoeva,* 1999]. Radial profile of the intensity in 5260Å wavelength, for all scanner positions in mode B is presented in Figure 6. The VEGA – comet distance is in the region of 9334 km ÷ 152853 km and $p$ accordingly is 136÷5936 km. One can distinguish two parts of the graph – one from the beginning to $p$ = 1000 km, and the other from $p$ = 1000 km to the end. The intensity can be described by a power law $I \sim p^s$ where s determines the slope at logarithmic presentation of the *I(p)* dependence. The slope is determined by linear regression using least squares method. A 95% confidence interval for *(n-2)* degrees of freedom for the Student distribution (*t*-criterion) is used. For $p$ = 0÷1000 km 116 spectra are included and the slope is $s_1$=–0.68±0.02. For $p$ > 1000 km the slope is

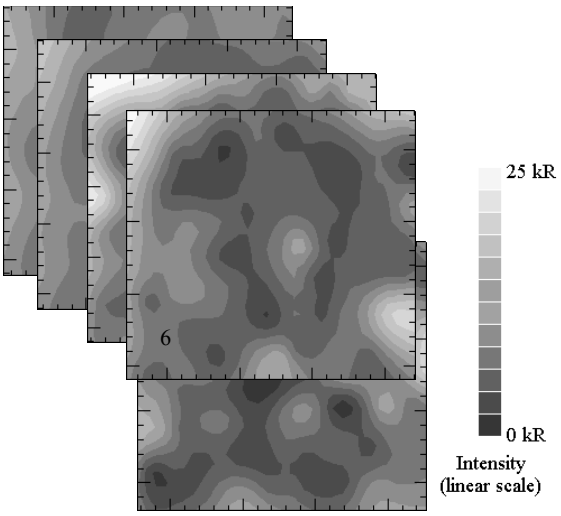


**Figure 7.** Monochromatic composed image of the dust continuum at 5260 Å in the Halley comet coma, in antisolar direction, 10 March 1986. Here a weaker intensity is observed, which gradually decreases. An increasing is evident in the left part of the image, at about 200000 km from the nucleus.

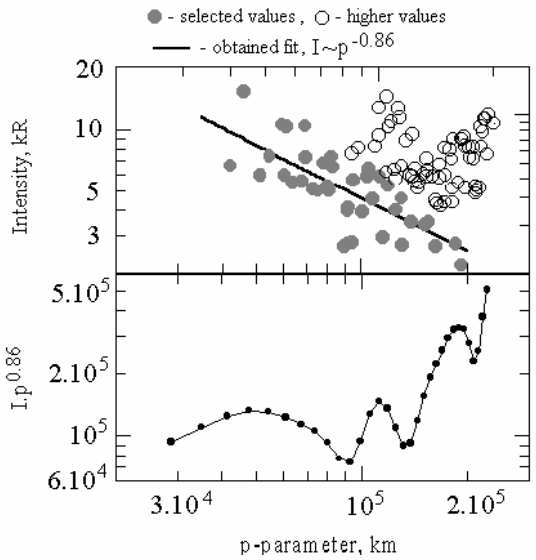


**Figure 8**. Dependencies of the 5260 Å continuum intensity (up), and of the product of the intensity and the obtained fit (down) on the perpendicular distance. Grey dots represent the selected values used for determining the overall decrease. White dots show the higher values forming maxima.

$s_2$=–1.09±0.05 and 245 spectra are included. It means that near the nucleus a flattening of the spatial brightness profile or decreasing of the continuum glow intensity is observed. The reason is the greater optical thickness of the inner coma near the nucleus or the fast change of the scattering angle, which leads to scattering indicatrice change. The flattening maybe also due to the fact that the measured spectra near the nucleus are from the two jets which cannot be clearly distinguished. This is in good agreement with the ground-based observations of *Umbach et al.* [1998] who also obtained –1.1 gradient of the overall coma. Comparing our results with that of *Goidet-Devel et al.* [1997] we have found that they use different values for the *p*-parameter, which depends on the TKS optical axis angular displacement $\psi_0$ towards the VEGA – Halley comet straight line. We use 1.7° but they use 3°. That is why their $p_{Fr}$ =3000 km corresponds to our $p_{Bul}$ = 1000 km. For $p_{Bul}$ > 1000 km ($p_{Fr}$ > 3000 km) the slope obtained by *Goidet-Devel et al.* [1997] is steeper and may be due to the lesser number of spectra taken from the free of jet zone.

## 5. Dust continuum in antisolar direction

In the near tail region dust continuum brightness is lower than in the coma in sunward direction. As a whole, the intensity decreases with increase of the distance to the nucleus but intensity increasing obtained at a distance of about 200000 km from the nucleus can be seen on all the images. On the composed image on 10 March (Figure 7) the increasing is evident on the left part of all the pictures for which the Sun is to the right (–4° in the image plane and 22.5° in the plane perpendicular to it, see Figure 1). Radial profile of the dust continuum for 6$^{th}$ picture is shown in Figure 8. Grey dots represent the selected values used for determining the overall decrease, and the white dots are the higher values forming maxima. A linear regression is calculated and it is shown with a straight line. T–criterion for 95% confidence interval is applied. The obtained gradient is $s$= –0.862±0.21, which is in good agreement with the result of *Umbach et al.* [1998] for the 3650Å dust continuum in the near tail region of the Halley comet.

In order to stress on the deviations from the obtained dependence, intensities are multiplied by $p^{0.862}$. Thus, they emerge as peaks above a horizontal line – at the bottom of Figure 5. Three maxima are outlined – around 50000 km, 115000 km and 190000 km. Such maxima are observed in the local brightness profiles and dust flux profiles beyond 35000 km by Giotto data [*Levasseur Regourd et al.,* 1990]. Maybe these are the dust shells observed in the dust space distribution on 10 March 1986.

Modeling by *Trotignon et al.* [1987], using one dust source, 54±5h rotation period and 300m/s dust particles

radial velocity shows an additional increasing in the middle of the space distribution [*Stoeva*, 1999] which is evident in the radial profile at the bottom of Figure 6.

## 6. Conclusions

- Space distribution of the dust continuum brightness is investigated in the Halley comet coma towards the Sun and in the near tail region.
- Two strong jets are observed in solar direction. One of them is in Sun direction and stretches up to about $p$ = 19500 km to the nucleus. The other is perpendicular to it and reaches $p$ = 19100 km.
- A tomographic reconstruction of the dust continuum distribution near the nucleus has been made. Shell structures with a center in the nucleus can be also observed.
- Radial profile of the intensity towards the Sun is divided into two. For $p$ < 1000 km the slope is approximately –0.7, and for $p$ > 1000 km – about –1.1. The weaker slope near the nucleus can be explained with the greater optical thickness of the inner coma or the fast scattering angle change. The same effect would be reached if the data used were from jet zones where the intensity slowly decreases.
- In antisolar direction the dust continuum brightness is weaker. It decreases with the distance to the nucleus. Registered increasing in the whole region of observation, at about 200000km from the nucleus and maxima in the radial profile are probably connected with dust shells formation, caused by the jet activity and rotation of the nucleus.

## References


Celnik, W. E. and Th. Schmidt-Kaler, Structure and dynamics of plasma-tail condensations of P/Halley comet 1986 and inferences on the structure and activity of the cometary nucleus, *Astron. Astrophys*. *187*, 233-248, 1987.

Gogoshev, M., Ts. Gogosheva, S. Sargoitchev et al., Three channel spectrometer for the Halley's comet Investigation, *Adv. Sp. Res*., *5*, 12, 133–136, 1985.

Giodet-Devel, B. and J. Clairemidi, P. Rousselot et al., Dust spatial distribution and redial profile in Halley's inner coma, *Icarus*, *126*, 78-100, 1997.

Larson, S., Z. Sekanina, D. Levy, S. Tapia, and M. Senay, Comet P/Halley near-nucleus phenomena in 1986, *Astron. Astrophys*. *187*, 639-644, 1987.

Levasseur-Regourd, A. C., N. McBride, E. Hadamcik et al., Similarities between in situ measurements of local dust light scattering and dust flux impact data within the coma of 1P-Halley, *Astron. Astrophys.*, *348*, 636-641, 1999.

Mazets, E. P., R. Z. Sagdeev, R. L. Aptecar, Dust in comet P/Halley from Vega observations, *Astron. Astrophys*. *187*, 699-706, 1987.

Nikolov, B. A., R. Werner, S. Spasov, Image Formation by Generalized Spline Functions, *Comptes rendus de l'Academie Bulgare des Sciences,* Tome *42*, 8, 1989.

Stoeva, P. Vl., Spectrometry of the Dust Continuum and Ultraviolet OH Emission of the Halley Comet, Stara Zagora, *PhD Thesis* (In Bulgarian), 86-90, 1999.

Stoeva, P., R. Werner, V. Guineva, St. Staykova, Investigation of the Halley comet dust size distribution by the Vega-2 interplanetary station visual spectra, *in Tenth International School on Quantum Electronics: Laser physics and Applications,* Peter A. Atanasov, Dimitar V. Stoyanov, Editors, Proceedings of SPIE, 3571, 307-311, 1999*a*.

Stoeva P., R. Werner, V. Guineva, Halley Comet dust images obtained on 10 March 1986, by TKS onboard VEGA 2, *in Proceedings of the Sixth national conference with an international participation, on contemporary problems of the solar-terrestrial influences, 18-19 November 1999, Sofia* (in Bulgarian), 173, 1999*b*.

Trotignon, J. G., C. Beghim, R. Grard et al., Dust observations of comet P/Halley by the plasma-wave analyser, *Astron. Astrophys., 187*, 83-88, 1987.

Umbach, R., K. Jockers, and E. H Geyer et al., Spatial distribution of neutral and ionic constituents in comet P/Halley, *Astron. and Astrophys. Suppl. 127*, 479-495, 1998.

Vaisberg, O. L., V. N. Smirnov, L. S. Gorn, Dust coma structure of comet Halley from SP-1 detector measurements, *Nature*, *321*, 274-276, 1986.

Werner, R., V. Guineva, P. Stoeva et al., Investigation of Halley comet's jets using data from the three-channel spectrometer aboard VEGA-2 interplanetary station, *COSPAR Colloquia*, *4*, 135-138, 1993.

Werner, R., P. Stoeva, V. Guineva et al., An investigation of the reflected by comet Halley solar light and the gas emissions' distribution using data from board VEGA-2, *Adv. in Space Res., 3*, 9, (3)225–(3)228, 1989.

Werner, R., Dust shells in the Halley comet coma, *Fourth General Conference of the Balkan Physical Union*, Veliko Turnovo, 22–27 August, 2000, poster 2P–027, 2000.

# Mathematical modeling of $H_2O$ molecules injection into the F2-region of the Earth's ionosphere

V. V. Medvedev[1], S. A. Ishanov[1], and L. V. Zinin[1,2]

[1]Kaliningrad State University, Kaliningrad, Russia
[2]Space Researah Institute, Moscow, Russia

**Abstract.** The numerical model of ionosphere-plasmasphere coupling which was designed for the analysis of F2-layer depletions produced by water vapours injection is described. In the case of water vapours injection atomic oxygen ions reacts with water molecules. Due to water molecules photodissociation additional H atoms react with oxygen ions. So, such injection leads to the formation of a region with low plasma density, so-called ionospheric "holes". The numerical model of ionosphere-plasmasphere coupling was used for simulation of these processes. The model includes a set of magneto hydrodynamic equations (continuity, momentum and energy) for electrons and ions, and neutral atmosphere with winds calculations. The equations were integrated along magnetic field lines. The mechanisms forming and filling "hole" is discussed.

## 1. Introduction

In the case of an injection of water vapours, atomic oxygen ions undergo charge transfer reactions:

$$O^+ + H_2O \rightarrow H_2O^+ + O\,. \qquad (1)$$

Such injection leads to the formation of region with decreased plasma density, ionospheric "holes". The investigation of this processes is carried out using a numerical model of ionosphere – plasmasphere coupling, in which the transfer equations for charged components are integrated along geomagnetic field lines.

The aim of this paper is to describe the mathematical model, which can simulate the formation and filling process of ionospheric "holes" produced by molecules $H_2O$ in the F region.

## 2. Modelling equations for background plasma

The model of the ionosphere-plasmasphere system reported here relies on numerical solutions for partially ionized plasma for the $H^+$, $O^+$, $N_2^+$, $NO^+$, $O_2^+$, $H_2O^+$, $H_3O^+$, $OH^+$, ions and electrons. Continuity equation writing along the field lines is:

$$\frac{\partial n_i}{\partial t} + B\frac{\partial (n_i V_i)}{\partial s} = P_i - \alpha_i \cdot n_i\,. \qquad (2)$$

Ions transport equation (inertial terms $\frac{dV_e}{dt}$ and $\frac{dV_i}{dt}$ were ignored) is:

$$n_i V_i = \frac{n_i}{R_i + S_{ij}}[m_i g \sin I + S_{ij}V_j + R_i V_{nx}\cos I - \frac{k}{n_e}\frac{\partial (n_e T_e)}{\partial s} - \frac{k}{n_i}\frac{\partial (n_i T_i)}{\partial s}]\,. \qquad (3)$$

Electron and ions temperature equations are:

$$\frac{3}{2}kN_e\frac{\partial T_e}{\partial t} = B\frac{\partial}{\partial s}\left(\frac{\lambda_e}{B}\frac{\partial T_e}{\partial s}\right) + \sum_i \frac{3m_e N_e}{m_i}\nu_{ei}k(T_i - T_e) + Q_e - L_{en}\,, \qquad (4)$$

$$\frac{3}{2}kn_i\frac{\partial T_i}{\partial T} = B\frac{\partial}{\partial s}\left(\frac{\lambda_i}{B}\frac{\partial T_i}{\partial s}\right) + 3n_i\nu_{ie}k(T_e - T_i) + \sum_n \frac{3m_i n_i}{m_i + m_n}\nu_{in}k(T_n - T_i) + Q_i - L_i\,, \qquad (5)$$

where $T_e$, $T_i$ are temperatures of electrons and ions, I – magnetic dipole angle, $\lambda_{i,e}$ – heat conductivity coefficients for the ion (i) and electron (e) gas, $Q_{i,e}$, $L_{i,e}$ –

are the heating and cooling rates of a respective component.

The heating rate of thermal electrons by photoelectrons is calculated:

$$Q_e^{eT} = \int_o^{E_m} E \cdot Q(E) dE + 4\pi\chi N_e \left[ \Phi_0(E_m) + \int_{Em}^{\infty} \Phi_0(E) \frac{dE}{E} \right]. \quad (6)$$

where $E$ is electron energy, $E_m$ is the energy limit for the not Maxwellian function, $Q(E)$ is photo ionization rate, $\chi$ = 2.6 10–12 eV cm$^{-2}$, $\Phi_0(E)$ – part from the heat flux determined from a self-consistent solution of the kinetic equation for the electrons heated above.

Macroscopic average wind velocities $V_{nx}$, $V_{ny}$ are given by the differential equations

$$\frac{\partial V_{ny}}{\partial t} = \frac{\xi}{\sin^2 I} \frac{\partial^2 V_{ny}}{\partial s^2} - \frac{1}{\rho} \sum_{j=1}^{5} n_j R_j V_{ny} - 2\Omega \sin\varphi V_{ny} - \frac{1}{\rho} \frac{\partial P}{\partial y}, \quad (7)$$

$$\frac{\partial V_{nx}}{\partial t} = \frac{\xi}{\sin^2 I} \frac{\partial^2 V_{nx}}{\partial s^2} - \frac{1}{\rho} \sum_{j=1}^{5} n_j R_j (V_{nx} - V_j \cos I) + 2\Omega \sin\varphi V_{ny} - \frac{1}{\rho} \frac{\partial P_n}{\partial x}. \quad (8)$$

Main neutral components H, O, $O_2$, $N_2$ and neutral temperature $T_n$, are calculated by the MSIS model [Hedin et. al., 1977].

For the components O($^1$D), N($^2$D), N($^4$S), NO, $N_2^{(v)}$, $H_2O$, OH, H, continuity and momentum equations are:

$$\frac{\partial n_i}{\partial t} = \frac{\partial (n_i \cdot V_i)}{\partial z} - \alpha_i n_i + P_i, \quad (9)$$

$$V_i = \frac{\sum_{j \neq i} S_{ji} n_j V_j}{\sum_{j \neq i} S_{ji} n_j} - D_i \left[ \frac{\partial \ln n_i}{\partial z} + \frac{\partial \ln T}{\partial z} + \frac{1}{H_i} \right], \quad (10)$$

$D_i = \dfrac{kT}{m_i \sum_{j \neq i} S_{ji} n_j}$ – molecular diffusion coefficient for different species,

$H_i = \dfrac{kT_n}{m_i g}$ – scale height, g – gravitational constant, $P_i$ and $\alpha_i$ are the chemical production and loss terms.

The distribution of initial density of the exhaust molecules [$H_2O$] water vapour is described by a hydrodynamics equation

$$n(z) = n(z_0) \cdot \frac{T(z_0)}{T(z)} e^{-\int_{z_0}^{z} \frac{dz}{H}}, \quad H = \frac{kT}{mg}, \quad (11)$$

where $n(z_0)$, $T(z_0)$ are density and temperature on the $h_m$F2 altitude F2, $n(z_0)$=[$H_2O$]=1.0 10$^7$ cm$^{-3}$, $h_mF2$=250 km in our case.

At the upper and bottom boundary (400 km and 120 km) it was assumed that the flux equals zero for all the neutral species except H. For H the flux is thermal flux.

### 3. The results of a numerical calculation

In case of the undisturbed F2-layer the dominant [$O^+$] is lost in the reactions (12)=(14)

$$O^+ + N_2 \rightarrow NO^+ + N \quad (12)$$

$$O^+ + H \rightarrow H^+ + O \quad (13)$$

$$O^+ + O_2 \rightarrow O_2^+ + O \quad (14)$$

$$H_2O + h\nu \rightarrow OH + H \quad (15)$$

$$H_2O^+ + e \rightarrow \begin{cases} O + H_2 \\ H_2 + O(^1D) \\ OH + H \end{cases} \quad (16)$$

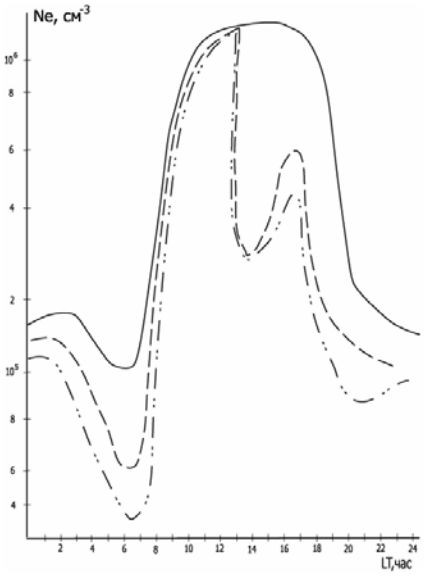


**Figure 1**. The time variations of electron density ($N_{e\,max}$ F2) in the F2 region. Solid curve is undisturbed density, dashed and dashed – dotted curves are $N_{e\,max}$ F2 variations after ejection of $[H_2O]_{maxF2}$ = 10$^7$ cm$^{-3}$ without and with reaction (15) – (16).

In the case of the injection of water vapors the dominant reactions are (15), (16). For the [H] (15), (16) is an addition reaction in the backgrounds reaction and it decreases electron density (Figure 1). Calculations were made for L=3.

It is known that the reaction (1) proceeds approximately $10^3$ times more rapidly, compared with $N_2$ and $O_2$ (12), (14).

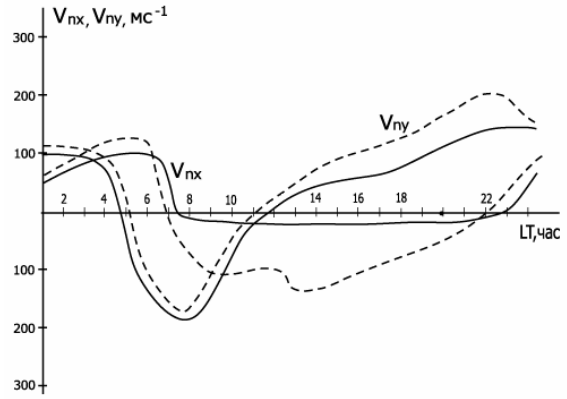


**Figure 2.** Time variations $V_{nx}$, $V_{ny}$ for the $h_mF2$ layer without $H_2O$ (solid line) and with $H_2O$ (dashed line).

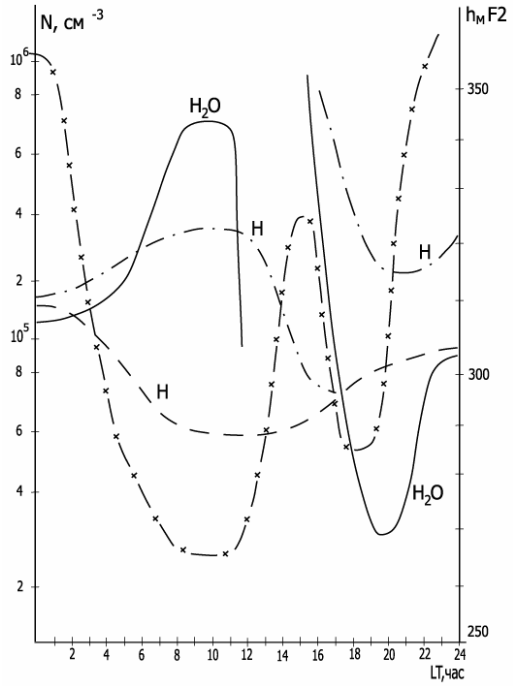


**Figure 3.** Time variations of the $h_mF2$ (dashed and "star" curve), $H_2O$ density (solid curve) and H density (dashed curve – without reaction (15), (16) and dashed – dotted curve – with (15), (16) reactions).

Those reactions lead to the formation (in F2-region) of regions with decreased plasma density (Figure 1). Similar results were obtained by *Mendillo et al*. [1975], *Brushkin et al*. [1988], *Ishanov et al.* [1989].

In this time the $V_{nx}$ velocity increases by absolute value (Figure 2).

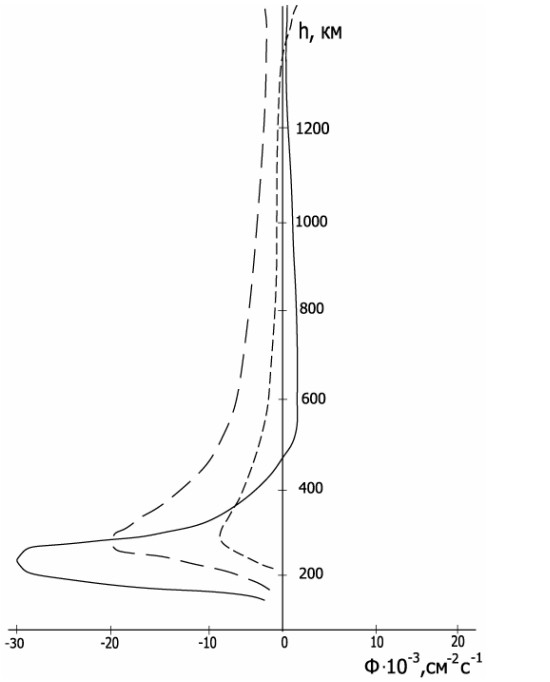


**Figure 4.** The height distribution of the charged particle flux (solid curve – undisturbed, small dashed is after ejection without reaction (15), (16), long dashed is with reaction (15), (16).

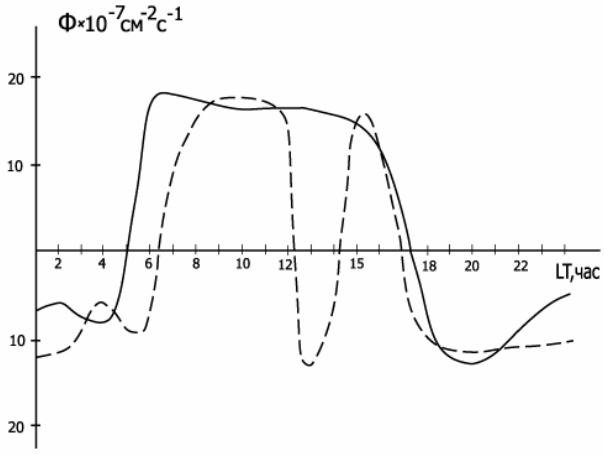


**Figure 5.** The time variation of the charged particle flux (solid curve is undisturbed, dashed curve is after ejection for the h = 600 km).

It can be explained as a result of the decreasing plasma density (decreasing ions braking). During the next 3–4 hours the electron density increases and maximum of the F2 layer moves upward (Figure 3) due to the process photoionization.

The decreased $[N_e]$, increased $V_{nx}$ Figure 2 (decrease ions braking) and lowered $h_mF2$ is a result of formation of the flow from plasmasphere in to the ionosphere.

The particle flux is directed from the plasmasphere in to the ionosphere during day-time making "block" at the height ≈ 400 km (Figure 4 – Figure 5).

**Acknowledgments.** This paper is dedicated to the memory of Professor Yu. I. Galperin. The work is supported by Russian Foundation for Basic Research, projects RFBR 01-01-00718 and RFBR 03-02-16749.

**References**

Bruskin, L. G., M. A. Koen and I. M. Sidorov, Modelling of Neutral-Gas releases into the Earth's Ionosphere, *Pageop.*,. *127*, 2/3, 415-446, 1988.

Ishanov, S. A., V. K. Latishev, V. V. Medvedev, Modeling of the disturbances in the ionosphere F2-layer during anthropogenic influences, in "Models in the nature utilization". Kaliningrad. KSU, 1989, p. 136 (in Russian).

Mendillo, M. and J. M. Forbes Artificially created Holes in the Ionosphere, *J. Geophys. Res., 83*, A1, 151-162, 1978.

Zinn, J., C. D. Sutherland, S. N. Stone and L. M. Duncan, Ionospheric effects of rocet exhaust products HEAO-C Skylab, *Atmos Terr. Phys., 44*, 12, 1143–1171, 1982.

# The electric potential of a spacecraft injecting an electron beam into the Earth's ionosphere

V. A. Fedorov

Mintz Radio Engineering Institute, ul. 8 Marta 10/1, Moscow, Russia

**Abstrac**t. The problem of the electric potential value for the spacecraft injecting an electron beam into the Earth's ionosphere is considered. The formulas defining the spacecraft's electric potential in the equilibrium state as a function of experimental parameters are derived. It is shown that the presented theoretical results are in a good agreement with both the results of numerical modeling and experimental data. A comparison of different models of spacecraft charge neutralization is performed. An explanation is given for the facts related to the difficulties of interpretation of the mechanisms of spacecraft charge neutralization within a period less than the time of ionization of neutral particles and plasma heating by the injected beam.

## 1. Introduction

When carrying out active space experiments using the electron spacecraft-injected beam as a tool for geophysical investigations in the Earth's ionosphere *Grannal*' [1985], usually the condition

$$I_b/I_{0H}\,| >> 1 \qquad (1)$$

is met, where $I_b \approx -(10^{-3} \div 1)$ A is the beam current, $I_{0H}$ is the thermal current of ionospheric plasma electrons collected by the spacecraft surface at $I_b = 0$. For instance, if a spacecraft has a spherical shape, then with allowance made for the Earth's magnetic field ($\overline{H}_0$), we have $I_{0H} = I_0 (1+r_{eT}/R_0)^2$, where $I_0 = 2\pi R_0^2 e n^0_e v_{eT}$; $R_0$ is the spacecraft radius; $e$ is the electron charge; $n^0_e v_{eT}$, and $r_{eT} = |v_{eT}|/\omega_{eH}$ are the density, velocity, and cyclotron radius of thermal plasma electrons, respectively; and $\omega_{eH}$ is the electron cyclotron frequency. On the basis of typical dimensions of spacecraft or their modules carrying electron accelerators and the specific features of the ionospheric plasma at different altitudes of electron beam injection, $h_I \approx 150 - 30000$ km, it can be shown that $I_{0H} \approx 10^{-2} \div 10^{-6}$ A.

However, the spacecraft $\varphi_0$ values measured in ionospheric experiments carried out at $|I_b / I_{0H}| >> 1$ and without special systems of neutralization of spacecraft charge were found to be much less than theoretical estimations, *Beard and Johnson* [1961] and *Parker and Murphy* [1967] and *Linson* [1969]. To resolve this contradiction, the hypotheses on new mechanisms of spacecraft charge neutralization $Q$ in addition to the collection of thermal ionospheric plasma electrons by the spacecraft surface were suggested *Cambou et al*. [1975] and *Galeev et al*. [1976] and *Lyakhov and Managadze* [1977] and *Volokitin and Mishin* [1978] and *Zhulin et al*. [1979] and *Managadze* [1979]. These mechanisms result in the increase of electron density due to ionization of neutral particles of plasma and spacecraft emanated gases by plasma electrons flowing to the spacecraft surface, or they result in the heating of plasma electrons by the injected beam, which enlarges their average thermal velocity. However, the mechanisms of spacecraft charge neutralization $Q$ suggested cannot take place within the period $0 \le t < t_{ion}$, $t_H$, where $t_{ion}$ is the time of ionization of neutral particles, and $t_H$ is the time of plasma heating by the electron beam *Fedorov* [1983]. Thus, the positive charge will be accumulated on the spacecraft surface during this period after the beginning of electron beam injection, because condition (1) is fulfilled, which leads to the partial loss of electron beam energy or, if the charge is large enough, to the cut-off of beam electrons.

The cut-off of beam electrons occurs, if the time of ionization of neutral particles, $t_{ion}$, exceeds the time of the cut-off of beam electrons, $t_b$. If so, the mechanisms of spacecraft charge neutralization based on the ionization of neutral particles begin to work only after the time $t > t_{ion} \approx [n_0 \sigma(w_*)_{N_2} v_*]^{-1}$, where $n_0$ is the density of neutral particles near the spacecraft, $\sigma(w_*)_{N_2}$ is the cross section of ionization by an electron with energy $w_* \sim m_e v_*^2/3$, $v_*$ is the effective velocity of plasma electrons, and $m_e$ is the electron mass. In this case, ionization in the field of plasma discharges of various kinds appears if the density of neutral particles is

higher than the critical value, $n_0 > n_\kappa = 3\cdot10^{11} \div 10^{12}$ cm$^{-3}$ *Galeev et al*. [1976], i.e., it is possible at altitudes $h_I \lesssim 130$ km *Fedorov* [1983]. For instance, if the injection altitude is $h_I = 200$ km ($n_0 = 5.5\cdot10^9$ cm$^{-3}$ $<n_\kappa$, $\sigma(w_*)_{N_2} = 3\cdot10^{16}$ cm$^2$, $V_* = 4\cdot10^8$cm/s *Gurevich and Shvartsburg* [1973]) at $R_0 = 50$ cm, $I_b = -0.1$ A, and $W_b = 10$ keV, we have $t_{ion} = 1.5$ ms. This value is much larger than $t_b$ in the field of the charging spacecraft at typical parameters of these experiments, i.e., $t_{ion} >> t_b = W_b R_0/eI_b) \approx 5$ μs, where $R_0 = 50$ cm, $I_b = -0.1$ A, $W_b = 10$ keV. Eventually, the heating of plasma electrons by the injected beam requires the time $t_H = 10^2/\omega_0$ *Volokitin and Mishin* [1978], where $\omega_0$ is the plasma frequency. In the case of daytime experiments, we have $t_b \geq 2.5\ \mu s \approx t_b$ at $h_I = 200$ km and $\omega_0 \leq 4\cdot10^7$ s$^{-1}$. In the case of nighttime experiments, when the electron density is much lower as compared to the day time, $t_H >> t_b$ *Fedorov* [1983].

Thus, taking into account theoretical results *Beard and Johnson* [1961] and *Parker and Murphy* [1967] and *Linson* [1969], as well as the mechanisms of spacecraft charge neutralization suggested in *Cambou et al*. [1975] and *Galeev et al*. [1976] and *Lyakhov and Managadze* [1977] and *Volokitin and Mishin* [1978] and *Zhulin et al*. [1979] and Managadze [1979], one cannot explain the experimental data concerning the spacecraft $\varphi_0$ value at altitudes $h_I > 130$ km and the absence of the electron beam cut-off within the time interval $0 \leq t < t_{ion}, t_H$. Later, theoretical works investigated the process of satellite charge variation and plasma dynamics within this time interval for isotropic injection of electrons at $\overline{H}_0 = 0$ *Fedorov* [1983], as well as for injection of an electron beam along $\overline{H}_0$ *Fedorov* [2000]. On the basis of the results of *Fedorov* [1983], a theory of spacecraft charge neutralization was constructed *Fedorov* [1983[1]], [1984] [1984[1]] for the case of $\overline{H}_0 = 0$, and a formula was derived (see (13) in *Fedorov* [1984[1]]) determining the spacecraft $\varphi_0$ values. They were found to be lower than the values following from formulas found in *Beard and Johnson* [1961] and *Parker and Murphy* [1967] and *Linson* [1969] and were comparable with measurements made in the course of the Zarnitsa-2 and ARAKS experiments, whose initial conditions (or close to them) were applied in *Fedorov* [1983]. The results of *Fedorov* [2000] obtained at $\overline{H}_0 \neq 0$ were not used to determine spacecraft $\varphi_0$ and to suggest new mechanisms of spacecraft charge neutralization. Hence, the problem of spacecraft $\varphi_0$ value and of mechanisms of spacecraft charge neutralization in active space experiments with injection of electron beams in the magnetically active plasma within the time interval $0 \leq t < t_{ion}, t_H$ remains open.

## 2. Association of spacecraft potential with parameters of experiment and ionospheric plasma

From the aforesaid it follows that the spacecraft charge will increase after the electron injection have started. If the current $I_b$ is compensated by the current $I_c$ at $\varphi_0 < W_b/|e|$, then later on, the spacecraft charge should not be higher than the maximum value achieved. In the opposite case, $\varphi_0$ will exceed the value $\varphi_0 = W_b/|e|$, and the electron beam cut-off will take place. Let us refer to the state of a system composed of the plasma and the spacecraft injecting the electron beam, which appears as a result of equality of the currents $I_b$ and $I_c$, as the equilibrium state. The equilibrium state in this system was observed in numerical experiments *Fedorov* [1983, 2000] in two forms

$$|I_b| = I_c, \qquad \partial/\partial t = 0, \qquad (2)$$

$$|I_b| = < I_c >, \qquad \partial/\partial t \neq 0 \qquad (3)$$

where <f> is the mean value of functions characterizing the processes in plasma ($Q$, $\varphi_0$, $I_c$, and so on), for which the expression $|(f - <f>)/<f>| << 1$ was true. The system state determined by Eqs. (2) was realized in the case of isotropic electron injection at $\overline{H}_0 = 0$ *Fedorov* [1983]. The state determined by (3) was realized in the case of electron beam injection along $\overline{H}_0$, and it represented a beat-like oscillating regime with the fundamental frequency $\omega_0$ being modulated by the frequencies $\omega_{eH}$ and $2\omega_{eH}$ *Fedorov* [2000].

The results of *Fedorov* [1983, 2000] led us to conclusion that (1) damped plasma harmonic oscillations are generated after the beginning of the electron injection; (2) equilibrium states (2) and (3) become established within the time $t_p \approx 5\mu s \ll t_{ion}$ at $|e|\varphi_0 \ll W_b$; and (3) ionospheric plasma ions have no time to escape from the disturbed plasma region within the time $t \approx t_p$. It should be emphasized that variations of $\varphi_0$ and plasma parameters within the time interval $0 < t < t_p$ were not investigated in the majority of experiments, because the time resolution of devices used for measuring $\varphi_0$ was $t \approx 1 \div 10$ ms *Grannal'* [1985], which far exceeds $t_{p,b}$. The sole exception is the CHARGE-2 experiment ($h_I \approx 160 \div 260$ km, $I_b = -(6 \div 48)\ 10^{-3}$ A, $W_b = 1$ keV *Myers et al*. [1990] and *Banks et al*. [1990]), one of its goals being to investigate the transition regimes of $\varphi_0$ establishment with a time resolution of $0.1\mu s$. The measurements of $\varphi_0$ have shown (see Figure 4 in *Myers et al*. [1990]) that (1) the equilibrium state of Eq. (3) type for plasma processes occurring in the spacecraft neighborhood is established in a time less than $5\mu s$; (2)

for time periods $0 < t < 50\ \mu s$ and $50 < t < 100$ μs, $\langle\varphi_0\rangle \cong 40$ and 50 V, respectively; (3) the deviation of $\varphi_0$ from $\langle\varphi_0\rangle$ within the interval $5 < t < 50\mu s$ is 4–10 V; (4) one can assume that all the functions characterizing the processes in plasma ($Q$, $\varphi_0$, $I_c$, and so on) oscillate with the frequency $\omega \approx \omega_0$. Thus, the basic features of plasma dynamics are close in both numerical and *in situ* experiments.

In order to find the functional connection between the satellite's $\langle\varphi_0\rangle$ value and experimental parameters and characteristics of the ionospheric plasma, let us consider the following scheme of the experiment, using a spherical coordinate system with the origin at the satellite center (the $Z$ axis and $\overline{H}_0$ are parallel and like directed). Let the electron beam be injected into the ionosphere at altitudes $h_I > 130$ km along $\overline{H}_0$ from a satellite of radius $R_0$ under conditions of the established equilibrium state of Eq. (3) type. If so, it follows from the results of *Fedorov* [2000] that there is a charge of a large value on the satellite's surface, while the electric field $\overline{E}$ with components $\overline{E}_R$, $\overline{E}_\theta$, and $\overline{E}_\varphi$, oscillating with frequencies $\omega_0$ and $\omega_{eH}$, exists in the satellite's neighborhood. The joint action of the fields $\overline{E}$ and $\overline{H}_0$ on the plasma results in different kinds of drifts of plasma electrons across $\overline{H}_0$. They lead to additional (apart from $I_{0H}$) currents onto the satellite's surface, which enlarges the current $\langle I_c\rangle$.

Under conditions of these space experiments, $\langle I_c\rangle$ consists of three components *Frank-Kamenetskii* [1964] that make the main contribution to its value, i.e.,

$$\langle I_c\rangle \approx \langle I_E\rangle + \langle I_P\rangle + \langle I_T\rangle. \qquad (4)$$

Here, $\langle I_E\rangle$ is the electric current of the drift of plasma electrons due to the action of $\langle\overline{E}_\varphi\rangle$ and $\overline{H}_0$, $\langle I_p\rangle$ is the current of polarization drift of plasma electrons appearing due to the varying component of $\overline{E}$; and

$$\langle I_T\rangle \approx I_0\left(1 + \frac{r_{eT} + r_{eH}}{R_0}\right)^2 \qquad (5)$$

is the thermal current of plasma electrons that flows along the *magnetic tube* onto the satellite surface at the electron beam injection and is collected from the efficient plane of radius $(R_0+r_{eT}+r_{eH})$, perpendicular to $\overline{H}_0$ ($r_{eH}$ is the cyclotron radius of an electron rotating in $\langle\overline{E}_R\rangle$, $\langle\overline{E}_\theta\rangle$ and $\overline{H}_0$). Accounting for (4) and (5), the equality in (3) can be written as

$$\frac{|I_b| - \langle I_p\rangle - \langle I_E\rangle}{I_0} = \left(1 + \frac{r_{eT} + r_{eH}}{R_0}\right)^2. \qquad (6)$$

The functions $\langle I_E\rangle$, $\langle I_P\rangle$, and $r_{eH}$ appearing in (6) are represented as functions of $\varphi_0$ and experimental parameters as follows.

$$\begin{aligned}\langle I_E\rangle &\sim en_e^0 \int_{S(R=R_0)} \langle v_E\rangle dS \\ &\sim \frac{\pi}{2|v_{eT}|}\sqrt{\frac{2|e|}{m_e}}\langle\varphi_0\rangle I_0\end{aligned} \qquad (7)$$

where

$$\langle v_E\rangle \sim c\frac{\langle E_\varphi\rangle}{H_0} \sim -\langle v_{eR}\rangle \sin\theta + \langle v_{e\theta}\rangle \cos$$

is the velocity of electric drift of plasma electrons, $c$ is the velocity of light, $\langle v_{eR}\rangle$ and $\langle v_{e\theta}\rangle$ are the components of a slowly varying component of the velocity vector of plasma electrons ($|\langle v_{e\theta}\rangle/\langle v_{eR}\rangle| \ll 1$ *Fedorov* [2000]), $\langle E_\varphi\rangle$ is the azimuth component of the slowly varying component of $\overline{E}$. Formula (7) is valid if $|\langle E_\varphi\rangle/H_0| \ll 1$ and $(d|\overline{E}|/dR) \ll 1$ on the interval $R_0 < R < R_0 + r_{eH}$, and $\omega_{eH} \gg \nu$, where $\nu$ is the frequency of collisions of plasma electrons with other particles. These conditions mean that the plasma electrons must be non-relativistic, adiabatic, and magnetized.

$$\begin{aligned}\langle I_P\rangle &\sim en_e^0 \times \\ &\int_{S(R=R_0)} \langle v_P\rangle dS \sim \frac{\pi}{2}\frac{\omega}{\omega_{eH}}\frac{c\left|\langle\tilde{E}_0(R_0)\rangle\right|}{|v_{eT}|H_0} I_0\end{aligned} \qquad (8)$$

where

$$\begin{aligned}\langle v_P\rangle &\approx \left(m_e c^2/|e|H_0^2\right)(d\langle\tilde{E}\rangle/dt)\sin\theta \\ &\sim (\omega/\omega_{eH})(c/H_0)\langle\tilde{E}_0\rangle \sin\theta\end{aligned}$$

is the velocity of polarization drift of plasma electrons, $\langle\tilde{E}_0\rangle$ and $\omega$ are the amplitude and frequency of the slowly varying component of $\overline{E}$. The use of (8) requires the fulfillment of the condition $\omega \ll \omega_{eH}$, under which the motion of plasma electrons is adiabatic.

$$r_{eH}\left(< R >, \theta = \pi/2\right) \sim \frac{1}{\omega_{eH}} \sqrt{\frac{2|e|}{m_e} < \varphi_0 > \left(\frac{R_0}{< R >}\right)^{\kappa}} \qquad (9)$$

where $<\varphi>=<\varphi_0>(R_0/<R>)^{\kappa}$ is the law of $<\varphi>$ distribution in the satellite's neighborhood presented by a power law function, and $0 \le k \le 2$ *Al'pert et al*. [1964]. Under conditions of the equilibrium state, the mean of the coordinate $R$ in (9) must be constant, since $|I_b| = <I_c>$, and determined by the maximum distance from where an electron can arrive onto the satellite's surface; so, it must be taken as $<R>=R_0+r_{eH}$. If so, (9) can be written as

$$r_{eH}\left(< R >, \theta = \pi/2\right) \sim \frac{1}{\omega_{eH}} \sqrt{\frac{2|e|}{m_e} < \varphi_0 > \left(\frac{R_0}{R_0 + r_{eH}}\right)^{\kappa}} \qquad (10)$$

### 3. Spacecraft electric potential at electron beam injection into the earth's ionosphere

Before expressing the satellite's $<\varphi_0>$ as a function of parameters of the ionospheric plasma and experiment, let us evaluate the ratio $(|I_b| - <I_p>)/I_0$ appearing in (6), at which $r_{eH} = 0$, $R_0$. These $r_{eH}$ values correspond to certain values of $<\varphi_0>$, namely, $<\varphi_0> \approx 0$, $\Phi_0$, where $\Phi_0 = (\omega_{eH}R_0)^2/(2|e|/m_e)$ is the characteristic $<\varphi_0>$ of a satellite, when $r_{eH} = R_0$ and the kinetic energy of plasma electrons is $W_e = |e\ \Phi_0|$ *Grannal'* [1985]. The achievement of the above $r_{eH}$ values is possible at $(|I_b| - <I_p>)/I_0 \ge 1$, because in the case of $I_b = 0$ we have $<\varphi_0> = \varphi_{eT} < 0$, where $\varphi_{eT}$ is the thermal potential of the ionospheric plasma. The value of the ratio $(|I_b| - <I_p>)/I_0$ found at $r_{eH} = 0$, $R_0$ as a function of $r_{eT}/R_0$ at various $h_I$ presents an estimate, which will be necessary to choose the signs, corresponding to real satellite $<\varphi_0>$ values, in formulas deter-mining $<\varphi_0>$. The comparison of the values of this ratio, calculated at particular values of $r_{eT}$ and $R_0$, with $|I_b|$, $<I_p>$, and $I_0$ values will permit conclude that either $r_{eH}/R_0 < 1$ or $r_{eH}/R_0 \ge 1$. And if the value of the ratio $r_{eH}/R_0$, is specified, it is possible to get the value of $(|I_b| - <I_p>)/I_0$. In this case, the found values of the above ratios will serve as a criterion to choose the formula determining the satellite's $<\varphi_0>$.

Let $r_{eH} = 0$. Then we get from (6)

$$< \varphi_0 > \sim \frac{\Phi_0}{4}\left(\frac{4r_{eT}}{\pi R_0}\right)^2 \times \left[\frac{|I_b| - < I_p >}{I_0} - \left(1 + \frac{r_{eT}}{R_0}\right)^2\right]^2 \qquad (11)$$

Since $r_{eH} = 0$, upon assuming $<\varphi_0> = 0$, in (11), we find

$$\frac{|I_b| - < I_p >}{I_0} = \left(1 + \frac{r_{eT}}{R_0}\right)^2 \qquad (12)$$

Hence, $|I_b| - <I_p> = I_0(1+r_{eT}/R_0)^2 = I_{0H}$. If $<I_p> = 0$, the injection current is equal to the thermal current of the ionospheric plasma flowing onto the satellite's surface at $<\varphi_0> = 0$. Substituting particular values of the ratio $r_{eT}/R_0$, into (12), we have

$$\frac{|I_b| - < I_p >}{I_0} \cong \begin{cases} 1, \text{ if } r_{eT}/R_0 << 1 \\ 4, \text{ if } r_{eT}/R_0 = 1 \\ (r_{eT}/R_0)^2, \text{ if } r_{eT}/R_0 >> 1 \end{cases} \qquad (13a,13b,13c)$$

The relations between $r_{eT}$ and $R_0$, appearing in (13a)–(13c) correspond to the altitudes $h_I \approx 150 \div 1000$ km (the $F$ layer of the Earth's ionosphere), $h_I \approx R_E \div 2R_E$, and $h_I \ge 3R_E$ (the lower boundary of the Earth's plasma-pause), respec-tively, where $R_E$ is the Earth's radius *Al'pert et al*. [1964].

Let $r_{eH} = R_0$. Then, we get from (6)

$$< \varphi_0 > \sim \frac{\Phi_0}{4}\left(\frac{4r_{eT}}{\pi R_0}\right)^2 \times \left[\frac{|I_b| - < I_p >}{I_0} - \left(2 + \frac{r_{eT}}{R_0}\right)^2\right]^2 \qquad (14)$$

The equality $r_{eH} = R_0$ implies $<\varphi_0> \sim \Phi_0$. Substituting this relation into (14), we find that

$$\frac{|I_b| - < I_p >}{I_0} \sim \frac{\pi R_0}{2r_{eT}} + \left(2 + \frac{r_{eT}}{R_0}\right)^2 \qquad (15)$$

Hence, we have for certain values of the ratio $r_{eT}/R_0$

$$\frac{|I_b| - < I_p >}{I_0} \sim \begin{cases} \pi R_0/2r_{eT} + 4, \text{ if } r_{eT}/R_0 << 1 \\ \pi/2 + 9, \text{ if } r_{eT}/R_0 = 1 \\ (r_{eT}/R_0)^2, \text{ if } r_{eT}/R_0 >> 1. \end{cases} \qquad (16a,16b,16c)$$

Notice that setting $r_{eH} = R_0$ in (10), we find that $<\varphi_0> \sim 2^{\kappa} \cdot \Phi_0$, where it must be $\kappa = 0$, since this requirement results in $<\varphi_0> \sim \Phi_0$, when $W_e = |e\ \Phi_0|$.

When determining the value of the satellite's $<\varphi_0>$, let us first consider the case of $\kappa = 0$ in (10), which excludes the dependence of $<\varphi>$ and $r_{eH}$ on $R$, i.e., $<\varphi>$ and $r_{eH}$ are constant. Then, substituting (7) into (6), we get

$$x^2 + 2\left(1 + \frac{r_{eT}}{R_0} + \frac{\pi R_0}{4r_{eT}}\right)x + \left(1 + \frac{r_{eT}}{R_0}\right)^2 - \frac{|I_b| - < I_p >}{I_0} = 0 \quad (17)$$

where $x = r_{eH}/R_0$. Solving (17) and replacing $r_{eH}$ in the solution by (10), where $\kappa = 0$, we find

$$< \varphi_0 > \sim \Phi_0 \times \left[ -\left(1 + \frac{r_{eT}}{R_0} + \frac{\pi R_0}{4r_{eT}}\right) \pm \sqrt{\left(1 + \frac{r_{eT}}{R_0} + \frac{\pi R_0}{4r_{eT}}\right)^2 - \left(1 + \frac{r_{eT}}{R_0}\right)^2 + \frac{|I_b| - < I_p >}{I_0}} \right]^2 \quad (18)$$

Notice that it is possible to derive Eqs. (12) and (15) from (18) by setting $<\varphi_0> = 0$, and $\Phi_0$, respectively. In doing so, (12) is derived independent of sign in front of the radical, while only positive sign provides (15).

If one sets $(4r_{eT}/\pi R_0)(|I_b| - <I_p>)/I_0 << 1$ in (18), whence it follows $r_{eT}/R_0 << 1$ as well as $r_{eH}/R_0 << 1$ (see (16*a*)), and chooses the positive sign in front of the radical, then

$$< \varphi_0 > \sim \frac{\Phi_0}{4}\left(\frac{4r_{eT}}{\pi R_0}\right)^2 \left(\frac{|I_b| - < I_p >}{I_0}\right)^2 \quad (19)$$

and, upon setting $r_{eT}/R_0 >> 1$, we arrive at

$$< \varphi_0 > \sim \Phi_0 \left(\sqrt{\frac{\pi}{2} + \frac{|I_b| - < I_p >}{I_0}} - \frac{r_{eT}}{R_0}\right)^2 \quad (20)$$

In (20), the relation $\pi/2 + (|I_b| - <I_p>)/I_0 \geq (r_{eT}/R_0)^2$ (see (13*c*) and (16*c*)) must be satisfied by virtue of the fact that $<\varphi_0> \geq 0$. Hence it follows that the term "$\pi/2$" in (20) can be neglected as $(|I_b| - <I_p>)/I_0 >> 1$. Notice that determination of the satellite's $<\varphi_0>$ value by (19) and (20) leads to underestimated results as compared with real values, because the requirement $\kappa = 0$ makes it impossible to take into account the $\varphi$ decrease with increasing distance. When (20) is used, this circumstance makes the strongest effect, because $r_{eT}/R_0 >> 1$.

Let us now consider the case of setting $0 \leq \kappa \leq 2$ in (10), i.e., $r_{eH} = f(R)$.

(a) We assume $r_{eH}/R_0 < 1$ and $r_{eT}/R_0 \ll 1$. By determining $r_{eH}$ from (6) in a linear approximation and substituting it together with (7) into (10), taking the accepted inequalities into account, we find

$$\frac{\kappa}{8}(z-1)^2 + \frac{1}{2}(z-1) - \frac{2r_{eT}}{\pi R_0}\frac{|I_b| - < I_p >}{I_0} = 0 \quad (21)$$

where $z = (|I_b| - <I_E> - <I_p>)/I_0$. If $\kappa = 0$, the solution to Eq. (21) for $<\varphi_0>$ is expressed by the formula

$$< \varphi_0 > \sim \frac{\Phi_0}{4}\left(\frac{4r_{eT}}{\pi R_0}\right)^2 \left(\frac{|I_b| - < I_p >}{I_0} - 1\right)^2 \quad (22)$$

This formula differs from (19) by the term "1," which is related to the use of the linear approximation to derive (21), while (17) was found without this approximation.

If $\kappa \neq 0$, then the solution to Eq. (21) has the form

$$< \varphi_0 > \sim \frac{\Phi_0}{4}\left(\frac{4r_{eT}}{\pi R_0}\right)^2 \times \left[\frac{|I_b| - < I_p >}{I_0} - 1 + \frac{2}{\kappa}\left(1 \pm \sqrt{1 + \kappa\frac{4r_{eT}}{\pi R_0}\frac{|I_b| - < I_p >}{I_0}}\right)^2\right]^2 \quad (23)$$

At $(|I_b| - <I_p>)/I_0 \approx 1$ and without reference to the sign in front of the radical in (23), we obtain $<\varphi_0> \approx 0$. If one assumes the sign in front of the radical be negative and $\kappa(4r_{eT}/\pi R_0)(|I_b| - <I_p>)/I_0 << 1$, formula (23) transforms to (22) or (11) (where $r_{eT}/R_0 << 1$). If we assume additionally that $(|I_b| - <I_p>)/I_0 >> 1$, we get (19) from (22) and (23). However, together with this requirement, the fulfillment of the condition $(|I_b| - <I_p>)/I_0 << \pi R_0/\kappa 4r_{eT}$ (see (16*a*)) is required, which presents an upper limitation on the ratio of currents, as the condition $r_{eH}/R_0 < 1$ is taken. Notice that after the transformation of (23) into (11), (12), and (22), the dependence of $<\varphi_0>$ on "$\kappa$", disappears; in this case, the transformation to (11) is possible because the inequality $r_{eH}/R_0 < 1$ also valid in the case of $r_{eH} = 0$, which takes place at $(|I_b| - <I_p>)/I_0 = 1$.

(b) Let $r_{eH}/R_0 \geq 0$ and $r_{eT}/R_0 << 1$. Substituting $r_{eH}$ from (6) into (10), we arrive at the equation

$$z^{1/2+\kappa/4} - z^{\kappa/4} + \frac{2r_{eT}}{\pi R_0}z - \frac{2r_{eT}}{\pi R_0}\frac{|I_b| - < I_p >}{I_0} = 0 \quad (24)$$

If $\kappa = 0$, the solution to (24) has the form

$$< \varphi_0 > \sim \frac{\Phi_0}{4}\left(\frac{4r_{eT}}{\pi R_0}\right)^2 \times \left\{\frac{|I_b| - < I_p >}{I_0} - \left(\frac{\pi R_0}{4r_{eT}}\right)^2 \left[1 \pm \sqrt{1 + \left(\frac{4r_{eT}}{\pi R_0}\right)^2 \frac{|I_b| - < I_p >}{I_0}}\right]^2\right\}^2 \quad (25)$$

which differs from (18), because it was derived with the use of the condition $r_{eT}/R_0 \ll 1$.

Let $\kappa = 1$. If $r_{eH}/R_0 > 1$ and a $z \gg 1$ (see (6)), the term $(2r_{eT}/\pi R_0)z \ll z^{3/4}$, $z^{1/4}$ in Eq. (24) can be neglected. Taking into account that from (16a) we have $(|I_b| - \langle I_p \rangle)/I_0 > \pi R_0/4r_{eT}+4$ (at $r_{eH}/R_0 > 1$), the solution to (24) is written as

$$\langle \varphi_0 \rangle \sim \frac{\Phi_0}{4}\left(\frac{4r_{eT}}{\pi R_0}\frac{|I_b| - \langle I_p \rangle}{I_0}\right)^2 \times \left[1 - \left(\frac{2r_{eT}}{\pi R_0}\right)^{4/3}\left(\frac{|I_b| - \langle I_p \rangle}{I_0}\right)^{1/3}\right]^2 \quad (26)$$

Setting $\kappa = 2$ in (24), we have

$$\langle \varphi_0 \rangle \sim \frac{\Phi_0}{4}\left(\frac{4r_{eT}}{\pi R_0}\right)^2 \left[\frac{|I_b| - \langle I_p \rangle}{I_0} - \frac{1}{4}\left(1 \pm \sqrt{1 + 2\frac{4r_{eT}}{\pi R_0}\frac{|I_b| - \langle I_p \rangle}{I_0}}\right)^2\right]^2 \quad (27)$$

If one sets $(4r_{eT}/\pi R_0)(|I_b| - \langle I_p \rangle)/I_0 \ll 1$ in (25) and (27) and chooses the negative sign in front of the radical, then formula (19) is obtained, where $\langle \varphi_0 \rangle$ does not depend on "κ". This occurs due to the fact that the taken inequality results in $(|I_b| - \langle I_p \rangle)/I_0 \ll \pi R_0/4r_{eT}$, i.e., $r_{eH}/R_0 \ll 1$, (see (16a)), so the value of $r_{eH}$ rather weakly influences the $\langle I_T \rangle$ value.

Taking into account all said above at deriving the formulas related to the satellite's $\langle \varphi_0 \rangle$, we give below without derivation the formulas for $\langle \varphi_0 \rangle$ of a rocket (the case of cylindrical symmetry). If the rocket axis makes an angle $\alpha < \pi/2$ with $\overline{H}_0$, then at $r_{eH}/r_p > 1$, $r_{eT}/r_{eH} \ll 1$, and $(|I_b| - \langle I_p \rangle - \mu)/I_0 \cos\alpha \gg 1$ we have

$$\langle \varphi_0 \rangle \sim \frac{\Phi_0}{4}\left[\frac{2r_{eT}}{l_p \cos\alpha}\left(\frac{|I_b| - \langle I_p \rangle - \mu}{I_0 \cos\alpha}\right)\right]^2 \quad (28)$$

while at $r_{eH}/r_p < 1$ and $r_{eT}/r_{eH} \ll 1$

$$\langle \varphi_0 \rangle \sim \frac{\Phi_0}{4}\left(\frac{2r_{eT}}{l_p \cos\alpha}\right)^2 \times \left\{\frac{|I_b| - \langle I_p \rangle - \mu}{I_0 \cos\alpha} - 1 + \frac{2}{\kappa}\left[1 \pm \sqrt{\kappa \cos\alpha \frac{2r_{eT}}{l_p}\left(\frac{|I_b| - \langle I_p \rangle - \mu}{I_0 \cos\alpha} - 1\right)}\right]\right\}^2 \quad (29)$$

where $r_p$ and $l_p$ are the radius and length of the rocket, respectively, and $\mu = (2l_p/\pi r_p)I_0 \sin\alpha$.

## 4. Comparison with experimental results

Let us find the satellite's $\langle \varphi_0 \rangle$ in the numerical experiment of *Fedorov* [2000], modeling the behavior of plasma dynamics during the electron beam injection into the Earth's ionosphere with an equilibrium state of type (3), i.e., in the oscillating regime, with the following initial conditions: $R_0 = 50$ cm, $I_b = -0.5$ A, $W_b \approx 10$ keV, $n_e^0 \approx 5 \cdot 10^5$ cm$^{-3}$, $|v_{eT}| = 2 \cdot 10^7$ cm/s, $H_0 = 0.45$ Oe, $\omega_{eH} = 8 \cdot 10^6$ s$^{-1}$, and $r_{eT} = 2.5$ cm. From the initial conditions we have $I_0 = 2.5 \cdot 10^{-2}$ A, $\Phi_0 \approx 44.5$ V. Assuming $\langle \tilde{E}(R_0) \rangle \approx 0.1 \cdot |\tilde{E}\omega_{eH}(R_0)| \approx 5 \cdot 10^{-5}$ CGSE units (see the $E_R$ plot in Figure 2 of *Fedorov* [2000]) and $\omega/\omega_{eH} \approx 0.1$ in (8), we obtain $\langle I_p \rangle \approx 6 \cdot 10^{-4}$ A $\ll |I_b|$. In this case, $r_{eH} = \langle v_{eR} \rangle/\omega_{eH} \approx 16$ cm $< R_0$ (see the $\langle v_{eR} \rangle$ plot in Figure 5 of *Fedorov* [2000]) and $r_{eT}/R_0 \ll 1$; therefore, we take advantage of formulas (23) and (27), for which applicability conditions are met, with $\kappa = 2$ (because $\kappa = 1$ corresponds to very high values of the satellite's $\langle \varphi_0 \rangle$. *Fedorov* [1983[1]] and *Al'pert et al.* [1964]) and the positive sign in front of the radical. By this way, we find that $\langle \varphi_0 \rangle \approx 22$ and 21 V respectively, while it follows from *Fedorov* [2000] that in the equilibrium state at $R \approx R_0$ and $t = 4\mu s$ we have $m_e \langle v_{eR} \rangle^2 / 2 \approx 19$ eV, i.e., these values are in a good agreement. Notice that if the value of $r_{eH}$ is unknown, then from (16a) we have $(\pi R_0/2r_{eT}) + 4 \approx 34$, while $(|I_b| - \langle I_p \rangle)/I_0 \approx 20$; whence it follows that $r_{eH}/R_0 < 1$.

Let us interpret the results of the JIKIKEN experiment *Grannal'* [1985] related to the determination of the satellite's $\langle \varphi_0 \rangle$ at the electron beam injection at the altitudes close to the plasmapause altitude. Taking the following initial conditions of the experiment: $|I_b| = 0.25 \div 1.0$ mA, $W_b \approx 0.1 \div 0.2$ keV, $R_0 = 40$ cm, and plasma parameters at altitudes $R_E$ and $3.5R_E$, respectively, as follows: $n_e^0 = 5 \cdot 10^3$ and 5 cm$^{-3}$, $|v_{eT}| = 6 \cdot 10^7$ and $1.3 \cdot 10^8$ cm/s, $H_0 = 10^{-1}$ and $10^{-2}$ Oe, $\omega_{eH} = 1.8 \cdot 10^6$ and $1.8 \cdot 10^5$ s$^{-1}$, $r_{eT} = 32$ and 640 cm *Al'pert et al.* [1964], we find that $I_0 \approx 0.5$, and $10^{-3}$ mA, and $\langle I_p \rangle \ll |I_b|$. If the beam injection occurs at altitudes lower than the plasmapause, for instance, at $h_I \approx R_E$, then $|I_b|/I_{0H} = |I_b|/I_0(1 + r_{eT}/R_0)^2 < 1$. Hence, $\langle \varphi_0 \rangle \sim \varphi_{eT}$. If the beam injection occurs after crossing the plasmapause, for instance, at $h_I \approx 3.5R_E$, then $|I_b|/I_{0H} = |I_b|/I_0(1 + r_{eT}/R_0)^2 \geq 1$. In order to determine the satellite's $\langle \varphi_0 \rangle$ under this condition, it is necessary to refer to formula (20). However, this formula cannot be

employed, because one of the criteria of applicability of expression (7), with taking initial conditions of the JIKIKEN experiment at $h_I \approx 3.5R_E$, into account, is not met, namely, $|<E_\varphi>/H_0| \sim 1$. Therefore, in order to find the value of the satellite's $<\varphi_0>$ in this case, system of Eqs. (11)–(17) from *Fedorov* [2000] was numerically solved. As a result, it was found that $|e|<\varphi_0>W_b$ at the electron beam injection after crossing the plasmapause, i.e., the beam cutoff occurs, which was actually observed in the JIKIKEN experiment.

Let us determine $<\varphi_0>$ for the *Eridan* rocket in the ARAKS project (the rocket launch to the "North") *Gringauz* [1976] and *Managadze* [1979] and *Grannal*' [1985]. As initial conditions, we take $h_I \approx 160$ km, $r_p = 28$ cm, $l_p = 140$ cm, $I_b = -0.5$ A, $W_b \approx 10$ keV, $n_e^0 \approx 1.8\cdot10^5$ cm$^{-3}$, $|v_{eT}| = 1.6\cdot10^7$ cm/s, $r_{eT} \approx 2$ cm, $H_0 \approx 0.45$ Oe. Taking into account that the rocket axis was directed under the angle $\alpha=6°$ with respect to $\overline{H}_0$, we get: $I_0 \approx 2.2\ 10^{-3}$ A, $\Phi_0 \approx 14$ V, $I_p \approx 1.4\cdot10^{-3}$ A at $\left|<\tilde{E}(R_0)>\right| \approx 3\cdot10^{-4}$ CGSE units [10]. From (16a) we have $\pi R_0/2r_{eT} + 4 \approx 34$ and $(|I_b| - <I_p>)/I_0 \approx 20$, i.e., $r_{eH}/r_p > 1$. Applying formula (28), we have $<\varphi_0> \approx 150$ V, which is in a good agreement with the experimental data given in *Fedorov* [1983[1]], [1984]. It should be noted that in spite of the functioning plasma generator and the possibility of plasma–beam discharge at $h_I \approx 150$ km, the background plasma density is taken as $n_e$. This is made due to the virtual stability of $<\varphi_0>$ at altitudes $130 \le h_I \le 200$ km ($150 \le <\varphi_0> \le 130$ V). This circumstance indicates that electrons produced by the plasma generator did not arrive at the rocket, and they are to be considered as the conducting medium [*Managadze,* 1979], while the plasma–beam discharge occurs up to altitudes $h_I < 130$ km *Galeev et al*. [1976].

## References


Al'pert, Ya. L., et al., *Iskusstvennye sputniki v razrezhennoi plazme* (Artificial satellites in a rarefied plasma), Moscow: Nauka, 1964.

Banks, P. M., et al., CHARGE-2 rocket observations of vehicle charging and charge neutralization, *Adv. Space Res*., *10*, 133, 1990.

Beard, D. B. and F. S. Johnson, Ionospheric limitation on attainable satellite potential, *J. Geophys. Res*., *66*, 4113, 1961.

Cambou, F., et al., The zarnitza rocket experiment on electron injection, *Space Res*., vol. XV, Berlin: Akademic, 491, 1975.

Fedorov, V. A., Measurement of potential of an Earth's satellite at the initial stage of carrying out Active experiments in the ionosphere, *Fizika Plazm*y, *9*, 874, 1983.

Fedorov, V. A., Distribution of electric field potential in the vicinity of a satellite injecting electrons in a steady-state regime at the initial stage of Active experiments in the ionosphere, *Geomagn. Aeron*., *23*, 427, 1983[1].

Fedorov, V. A., Mechanism of damping of plasma oscillations at the initial stage of injection of electron beams from a spacecraft in the ionosphere in Active experiments, *Geomagn. Aeron*., *24*, 205, 1984.

Fedorov, V. A., Electric potential of satellites in Active experiments at the initial stage of injection of electron beams in a steady-state regime, *Kosm. Issled*., *22*, 588, 1984[1].

Fedorov, V. A., Plasma dynamics in the vicinity of an Earth's satellite and neutralization of its electric charge at injection of electron beam in the ionosphere, *Fizika Plazm*y, *26*, 287, 2000.

Frank-Kamenetskii, D. A., *Lektsii po fizike plazmy* (Lectures in Plasma Physics), Moscow: Atomizdat, 1964.

Galeev, A. A., et al., The discharge in the near-rocket region at injection of electron beams into the ionosphere, *Dokl. Akad. Nauk SSS*R, *231*, 71, 1976.

Grannal', B., Ed. *Iskusstvennye puchki chastits v kosmicheskoi plazme* (Man-made beams of particles in space plasma), Moscow: Mir, 1985.

Gringauz, K. I. and N. M. Shutte, Altitude changes of the electrical potential of the eridan rocket during ARAKS experiment, *Preprint of Space Res. Inst., Acad. Sci. USS*R, Moscow, no. D-223, 1976.

Gurevich, A. V. and A. B. Shvartsburg, *Nelineinaya teoriya rasprostraneniya radiovoln v ionosfere* (Nonlinear theory of propagation of radio waves in the ionosphere), Moscow: Nauka, 1973.

Linson, L. M., Current-voltage characteristics of an electron-emitting satellite in the ionosphere, *J. Geophys. Res*., *74*, 2367, 1969.

Lyakhov, S. B. and G. G. Managadze, Beam-plasma discharge near the rocket in the Zarnitsa-2 experiment, *Fizika Plazm*y, *3*, 1370, 1977.

Managadze, G. G., The processes of charge neutralization and determination of rocket potential under injection of powerful electron beam in the Araks experiment, *Fizika Plazm*y, *5*, 1100, 1979.

Myers, N. B., et al. Vehicle charging effects during electron beam emission from the CHARGE-2 experiment. *J. Spacecr. Rockets, 27*, 25, 1990.

Parker, L. W. and B. L. Murphy, Potential buildup on an electron-emitting ionospheric satellite, *J. Geophys. Res*., *72*, 1631, 1967.

Volokitin, A. S. and E. V. Mishin, Initial stage of rocket neutralization at injection of electron beam in the ionosphere, *Fizika Plazm*y, *4*, 947, 1978.

Zhulin, I. A., et al., Investigation of electric fields in near-rocket region at injection of electron beam from the rocket, *Geomagn. Aeron*., *19*, 812, 1979.

## ALPHABETICAL LIST OF AUTHORS

AFONIN V. V.
*Space Research Institute, Russian Academy of Sciences Moscow, Russia*
vafonin@iki.rssi.ru

ALEXEEV I. I.
*Institute of Nuclear Physics, Moscow State University, Moscow, Russia*
alexeev@dec1.sinp.msu.ru

ALEXEYEV V. N.
*Institute of Cosmophysical Research and Aeronomy, Russian Academy of Sciences, Yakutsk, Russia*

ANTONOVA E. E.
*Institute of Nuclear physics, Moscow State University, Moscow, Russia*
allaant@dec1.npi.msu.su

ANTONOVA A. E.
*Skobeltsyn Institute of Nuclear Physics, Moscow State University, Moscow, Russia*
allaant@dec1.sinp.msu.ru

ARININ V. A.
*Institute of Explosion Physics, Russian Federal Nuclear Center, Sarov, Russia*
arinin@gdd.vniief.ru

BAISHEV D. G.
*Istitute of Cosmophysical Research and Aeronomy, Russian Academy of Sciences, Yakutsk, Russia*

BELENKAYA E. S.
*Institute of Nuclear Physics, Moscow State University, Moscow, Russia*
elena@dec1.sinp.msu.ru

BERTHELIER J. -J.
*Centre d'étude des Environnements Terrestre et Planetaries, Saint-Maur, France*
jean-jacques.berthelier@cetp.ipsl.fr

BESPALOV P. A.
*Institute of Applied Physics, Russian Academy of Sciences, Nizhny Novgorod, Russia*
peter@appl.sci-nnov.ru

BLAGOVESHCHENSKY D. V.
*St.-Petersburg University of aerospace instrumentation, St.-Petersburg, Russia*
dvb@aanet.ru

BLECKI J.
*Space Research Centre, Polish Academy of Sciences, Warsaw, Poland*
jblecki@cbk.waw.pl

BOBROVNIKOV S. Y.
*Institute of Nuclear Physics, Moscow State University, Moscow, Russia*

BOCHEV A. Z.
*Central Solar-Terrestrial Influences Laboratory, Bulgarian Academy of Sciences (BAS), Sofia, Bulgaria*
stil@bas.bg

BOROVKOV L. P.
*Polar Geophysical Institute, Russian Academy of Sciences Apatity, Russia*
borovkov@pgi.kolasc.net.ru

BOROYEV R. N.
*Institute of Cosmophysical Research and Aeronoy, Russian Academy of Sciences, Yakutsk, Russia*

BOUHRAM M.
*Centre d'étude des Environnements Terrestre et Planetaries, Saint-Maur, France*

CAO J. B.
*Center for Space Science and Applied Research, Chinese Academy of Science, Bejing, China*

CHUGUNIN D.
*Space Research Institute, Russian Academy of Sciences, Moscow, Russia*
dimokch@iki.rssi.ru

CHUGUNOVA O. M.
*Institute of the Physics of the Earth, Russian Academy of Sciences, Moscow, Russia*

CORNILLEAU-WEHRLIN N.
*Centre d'étude des Environnements Terrestre et Planetaries/CNRS, Velizy, France*

DEMEKHOV A. G.
*Institute of Applied Physics, Russian Academy of Sciences, Nizhny Novgorod, Russia*
andrei@appl.sci-nnov.ru

DIMITROVA I. I.
*Space Research Institute – BAS, Sofia, Bulgaria*

DONOVAN E.
*Department of Physics and Astronomy, University of Calgary, Calgary, Canada*

DOMRACHEV V. V.
*Space Research Institute, Russian Academy of Sciences, Moscow, Russia*
vdomrachev@pisem.net

DOMRIN V. I.
*Institute of Nuclear Physics, Moscow State University, Moscow, Russia*
dmr@dec1.sinp.msu.ru

DUBOULOZ N.
*Laboratoire de Physique et Chemic de l'Environnement/Observatoire de Nancay, Orleans, France*

EIGES P. E.
*Space Research Institute, Russian Academy of Sciences Moscow, Russia*

ENGEBRETSON M. J.
*Augsburg College, Minneapolis, USA*

FEDOROV V. A.
*Mintz Radio Engineering Institute, Moscow, Russia*
f_v99@mail.ru

FEJER B. G.
*Center for Atmospheric and Space Science Utah State University, USA*
bfejer@cc.usu.edu

FŐRSTER M.
*Max Planck Institute of Extraterrestrial Physics, Garching, Germany*

GELLER M. A.
*Stony Brook University*
mgeller@notes.cc.sunysb.edu

GLADYSHEV V.
*Institute of the Physics of the Earth, Russian Academy of Sciences, Moscow, Russia*

GOLOVKOV V. P.
*IZMIRAN, Moscow, Russia*

GONCHAROVA M. YU.
*Polar Geophysical Institute, Russian Academy of Sciences, Apatity, Russia*
marina@pgi.kolasc.net.ru

GONZALEZ W. A.
*National Institute for Space Research, INPE, São José dos Campos, SP, Brazil*

GOTYNYAN O. E.
*Taras Shevchenko Kyiv National University, Kyiv, Ukraine*

GRIGORIEV S.
*Kaliningrad State University, Kaliningrad, Russia*
grigoriev@mathc.albertina.ru

GUSEV A. A.
*Space Research Institute, Russian Academy of Sciences Moscow, Russia*

GUINEVA V. C.
*Solar-Terrestrial Influences Laboratory, Stara Zagora Department, Bulgarian Academy of Sciences, Stara Zagora, Bulgary*

HAMELIN M.
*Centre d'étude des Environnements Terrestre et Planetaries, Saint-Maur, France*

HAYOSH M.
*Charles University, Faculty of Mathematics and Physics, Prague, Czech Republic*

HVIUZOVA T. A.
*Polar Geophysical Institute, Russian Academy of Sciences, Apatity, Russia*

IEVENKO I. B.
*Institute of Cosmophysical Research and Aeronomy, Russian Academy of Sciences, Yakutsk, Russia*

ISAEV S. V.
*Radiophysical Research Institute, Nizhny Novgorod, Russia*

ISHANOV S. A.
*Kaliningrad State University, Kaliningrad, Russia*
math@dekan.albertina.ru

IVCHENKO V. M.
*Taras Shevchenko Kyiv National University, Kyiv, Ukraine*

JAYANTHI U. B.
*National Institute for Space Research, INPE, São José dos Campos, SP, Brazil*

KALEGAEV V. V.
*Institute of Nuclear Physics, Moscow State University, Moscow, Russia*
klg@dec1.sinp.msu.ru

KAURISTIE K.
*Finnish Meteorological Institute, Geophysical Research, Helsinki*

KHALIPOV V. L.
*Space Research Institute, Russian Academy of Sciences Moscow, Russia*
khalipov@iki.rssi.ru

KHARCHENKO I. P.
*Institute of Solar-Terrestrial Physics, Irkutsk, Russia*

KLEIMENOVA N. G.
*Institute of Physics of the Earth, Moscow, Russia*
kleimen@uipe-ras.scgis.ru

KORNILOV I. A.
*Polar Geophysical Institute, Russian Academy of Sciences, Apatity, Russia*
kornilov@pgi.kolasc.net.ru

KORNILOV O. I.
*Institute of Physics, St.-Petersburg State University, St.-Petersburg, Russia*

KORNILOVA T. A.
*Polar Geophysical Institute, Russian Academy of Sciences, Apatity, Russia*
kornilova@pgi.kolasc.net.ru

KOSKINEN E. J.
*Finnish Meteorological Institute, Helsinki, Finland*
*Department of Physical Sciences, University of Helsinki, Finland*

KOSSACKI K.
*Space Research Centre PAS, Warsaw, Poland*

KOVRAZHKIN R. A.
*Space Research Institute, Russian Academy of Sciences, Moscow, Russia*
kovrazhkin@romance.iki.rssi.ru

KOZELOV B.V.
*Polar Geophysical Institute, Russian Academy of Sciences, Apatity, Russia*
kozelov@scientist.com

KOZELOVA T.V.
*Polar Geophysical Institute, Russian Academy of Sciences, Apatity, Russia*
kozelov@scientist.com

KOZYREVA O. V.
*Institute of Physics of the Earth, Moscow, Russia*

KROPOTKIN A. P.
*Institute of Nuclear Physics, Moscow State University, Moscow, Russia*
apkrop@dec1.sinp.msu.ru

LANZEROTTI L.
*AT&T Bell Laboratories, NJ*

LAZUTIN L. L.
*Institute of Nuclear Physics, Moscow State University, Moscow, Russia*
lazutin@dec1.npi.msu.su

LEONOVICH A. S.
*Irkutsk 33, P.O.Box 4026, 664033, Russia*
leon@iszf.irk.ru

LEONTYEV S. V.
*Polar Geophysical Institute, Russian Academy of Sciences, Apatity, Russia*

MALINGRE M.
*Centre d'étude des Environnements Terrestre et Planetaries, Saint-Maur, France*

MALOVA H. V.
*Institute of Nuclear Physics, Moscow State University, Moscow, Russia*
*Space Research Institute, Russian Academy of Sciences, Moscow, Russia*
mlv@dec1.npi.msu.ru

MALTSEV YU. P.
*Polar Geophysical Institute, Russian Academy of Sciences, Apatity, Russia*
maltsev@pgi.kolasc.net.ru

MANNINEN J.
*Sodankylä Geophysical Observatory, Finland*

MARUYAMA T.
*CRL, Koganey, Tokyo, Japan*

MAZUR V. A.
*Irkutsk 33, P.O.Box 4026, 664033, Russia*

MEDVEDEV V. V.
*Kaliningrad State University, Kaliningrad, Russia*
math@dekan.albertina.ru

MISHIN V. M.
*Institute of Solar-Terrestrial Physics Russian Academy of Science, Irkutsk, Russia*

MISHIN V. V.
*Institute of Solar-Terrestrial Physics Russian Academy of Science, Irkutsk, Russia*
vladm@iszf.irk.ru

MITYAKOV N. A.
*NIRFI, Nizhny Novgorod, Russia*

MULARCHIK T. M.
*Space Research Institute, Russian Academy of Sciences, Moscow, Russia*
tmularchik@romance.iki.rssi.ru

NEMECEK Z.
*Charles University, Faculty of Mathematics and Physics, Prague, Czech Republic*
zdenek.nemecek@mff.cuni.cz

NOZAKI K.
*CRL, Koganey, Tokyo, Japan*

OSTAPENKO A. A.
*Polar Geophysical Institute, Russian Academy of Sciences, Apatity, Russia*

OVCHINNIKOV I. L.
*Skobeltsyn Institute of Nuclear Physics Moscow State University, Russia*

PALMROTH M.
*Finnish Meteorological Institute, Helsinki, Finland*

PANCHENKO M.
*Space Research Centre, Polish Academy of Sciences, Torun, Poland*
panch@ncac.torun.pl

PANKOV V. M.
*Space Research Institute, Russian Academy of Sciences, Moscow, Russia*

PARROT M.
*Laboratoire de Physique et Chemic de l'Environnement/CNRS, Orleans, France*
mparrot@cnrs-orleans.fr

PETRUKOVICH A. A.
*Space Research Institute, Russian Academy of Sciences, Moscow, Russia*
apetruko@iki.rssi.ru

PETUKHOV I. S.
*Yu. G. Shafer Institute of Cosmophysical Research and Aeronomy SB Russian Academy of Sciences, Yakutsk, Russia*

PETUKHOV S. I.
*Yu. G. Shafer Institute of Cosmophysical Research and Aeronomy SB Russian Academy of Sciences, Yakutsk, Russia*

PILIPENKO V. A.
*Institute of the Physics of the Earth, Russian Academy of Sciences, Moscow, Russia*
pilipenko@augsburg.edu

PLOTNIKOV I. YA.
*Institute of Cosmophysical Research and Aeronomy, Russian Academy of Sciences, Yakutsk, Russia*

PROKHORENKO V. I.
*Space Research Institute, Russian Academy of Sciences, Moscow, Russia*
vprokhor@iki.rssi.ru

PUDOVKIN M. I.
*Institute of Physics, St.-Petersburg State University, St.-Peterburg, Russia*

PUGACHEVA G.
*Southern Regional Space Research Center/INPE, Santa Maria, Brazil*

PULKKINEN T. I.
*Finnish Meteorological Institute, Helsinki, Finland*
tuija.pulkkinen@fmi.fi

RAPOPORT V. O.
*NIRFI, Nizhny Novgorod, Russia*
wr@nirfi.sci-nnov.ru

RAPOPORT YU. G.
*Kiev Taras Shevchenko National Univeristy, Kiev, Ukraine*

REEVES G. D.
*Los Alamos National Laboratory, Los Alamos, New Mexico, USA*

REZHENOV B. V.
*Polar Geophysical Institute, Russian Academy of Science, Apatity, Murmansk region, Russia*

RICHARDSON J. D.
*Center for Space Research, MIT, Cambridge MA, USA*

RODGER A.
*British Antarctic Survey, Cambridge, UK*

ROTHKAEHL H.
*Space Research Centre, Polish Academy of Sciences, Warsaw, Poland*

RUSSELL C. T.
*Institute of Geophysics and Planetary Physics, University of California, Los Angeles, California, USA*

RYLINA I.
*Kaliningrad State University, Kaliningrad, Russia*

RYZHOV N. A.
*NIRFI, Nizhny Novgorod, Russia*
ryna@nirfi.sci-nnov.ru

SAFRANKOVA J.
*Charles University, Faculty of Mathematics and Physics, Prague, Czech Republic*
jana.safrankova@mff.cuni.cz

SAMSONOV A. A.
*Institute of Physics, St.-Petersburg State University, St.-Petersburg, Russia*
samsonov@geo.phys.spbu.ru

SANTOLIK O.
*Charles University, Prague, Czech Republic*
ondrej.santolik@mff.cuni/cz

SAUVAUD J. -A.
*Centre d'Etude Spatiales des Rayonnements – CNRS, Toulouse, France*

SAVIN S.
*Space Research Institute, Russian Academy of Sciences, Moscow, Russia*

SCHOTT J. -J.
*Ecole et Observatoire des Sciences de la Terre, Strasbourg, France*

SHARKOV E. A.
*Space Research Institute, Russian Academy of Sciences, Moscow, Russia*

SHEVYREV N. N.
*Space Research Institute, Russian Academy of Sciences, Moscow, Russia*
shevyrev@iki.rssi.ru

SHIRAPOV D. SH.
*ESSTU, Ulan-Ude*
shir@esstu.ru

SCHUCH N. J.
*Southern Regional Space Research Center/INPE, Santa Maria, Brazil*

SINGER H. J.
*NOOAA, Space Environment Center, USA*

SIZOVA L.
*Institute of Terrestrial Magnetism, Ionosphere and Radiowave Propagation, Russian Academy of Sciences (IZMIRAN), Troitsk, Moscow region, Russia*
isizova@izmiran.rssi.ru

SLAVIN J. A.
*NASA Goddard Space Flight Center, Greenbelt, Maryland, USA*

STARODUBTSEV S. A.
*Institute of Cosmophysical Research and Aeronomy, Russian Academy of Sciences, Yakutsk, Russia*

STASIEWICZ K.
*Space Physics Institute, Uppsala, Sweden*

STEPANOV A. E.
*Institute of Cosmophysical Research and Aeronomy, Russian Academy of Sciences, Yakutsk, Russia*
a_e_stepanov@ikfia.ysn.ru

STERN D.
*Greenbelt, Maryland*

STOEVA P. V.
*Central Solar-Terrestrial Influences Laboratory, Bulgarian Academy of Sciences, Stara Zagora Department, Bulgaria*

TAGIROV V. R.
*Polar Geophysical Institute, Russian Academy of Sciences, Apatity, Russia*
tagirov@pgi.kolasc.net.ru

TEMERIN M.
*Space Science Laboratory, University of California, Berkeley, USA*

TIMOFEEV V. E.
*Institute of Cosmophysical Research and Aeronomy, Russian Academy of Sciences, Yakutsk, Russia*
vetimofeev@ikfia.ysn.ru

TRAKHTENGERTS V. Y.
*Institute of Applied Physics, Russian Academy of Science, Nizhny Novgorod, Russia*
vyt@appl.sci-nnov.ru

VELICHKO V. A.
*Institute of Cosmophysical Research and Aeronomy, Russian Academy of Sciences, Yakutsk, Russia*
vitvel@ikfia.ysn.ru

VESELOVSKY I. S.
*Institute of Nuclear Physics, Moscow State University, Moscow, Russia*
veselov@dec1.sinp.msu.ru

VOLOSEVICH A. V.
*Mogilev State University, Mogilev, Belarus*
avolos@rambler.ru

VOROBJEV V. G.
*Polar Geophysical Institute, Russian Academy of Sciences, Apatity, Russia*
vorobjev@pgi.kolasc.net.ru

WERNER R.
*Solar-Terrestrial Influences Laboratory, Stara Zagora Department, Bulgarian Academy of Sciences, Stara Zagora, Bulgary*

WRONOWSKI R.
*Space Research Centre, Polish Academy of Sciences, Warsaw, Poland*

YAGODKINA O. I.
*Polar Geophysical Institute, Russian Academy of Sciences, Apatity, Russia*
oksana@pgi.kolasc.net.ru

YAGOVA N. V.
*Institute of the Physics of the Earth, Russian Academy of Sciences, Moscow, Russia*

YERMOLAEV M. YU.
*Space Research Institute, Russian Academy of Sciences, Moscow, Russia*

YERMOLAEV YU. I.
*Space Research Institute, Russian Academy of Sciences, Moscow, Russia*
yermol@hotbox.ru

YUMOTO K.
*Department of Earth and Planetary Sciences, Kyushu University, Fukuoka, Japan*

ZASTENKER G. N.
*Space Research Institute, Russian Academy of Sciences, Moscow, Russia*
gzastenk@iki.rssi.ru

ZELENYI L. M.
*Space Research Institute, Russian Academy of Sciences, Moscow, Russia*
lzelenyi@plasma.rssi.ru

ZININ L. V.
*Kaliningrad State University, Kaliningrad, Russia*
lzinin@econom.albertina.ru

ZOLOTUKHINA N. A.
*Institute of Solar-Terrestrial Physics, Irkutsk, Russia*
zolot@iszf.irk.ru

## AUTHOR INDEX